CRC Handbook of THERMOELECTRICS

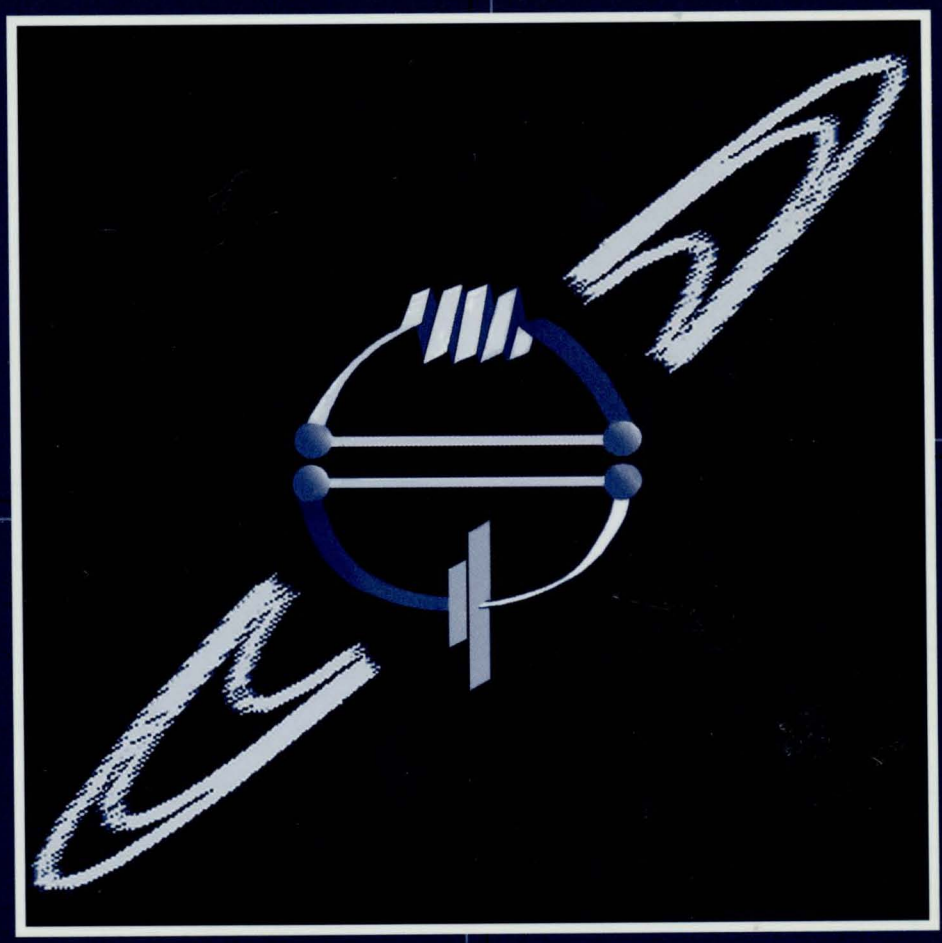

Edited by D.M. Rowe

CRC Handbook of
THERMOELECTRICS

Edited by D.M. Rowe, Ph.D., D.Sc.

CRC Press
Boca Raton London New York Washington, D.C.

Library of Congress Cataloging-in-Publication Data

CRC handbook of thermoelectrics / edited by D. M. Rowe.
p. cm.
Includes bibliographical references and index.
ISBN 0-8493-0146-7
1. Thermoelectric materials. I. Rowe, D.M.
TK2950.C73 1994
620.1'1297—dc20 94-11425
CIP

Visit the CRC Press Web site at www.crcpress.com

International Standard Book Number 0-8493-0146-7
Library of Congress Card Number 94-11425
Printed in the United States of America 4 5 6 7 8 9 0
Printed on acid-free paper

Preface

The truly remarkable T.V. pictures of the rings of Saturn transmitted to Earth from the Voyagers 1 and 2 spacecraft captured the imaginations of people throughout the world. No less remarkable is the source of electrical power which enabled the information to be transmitted from the spacecraft after more than a decade into its mission and from over 1.5 billion miles in space.

The power source is not a solar cell as one may at first think. The craft is too far from the sun to receive sufficient light energy to power the transmitters. On-board power is provided by an RTG (radioisotope thermoelectric generator) which utilizes the Seebeck effect in converting the heat from a radioactive heat source directly into electrical energy. The Seebeck effect and the reverse phenomenon, the Peltier effect, are the principal elements of thermoelectrics—the science and technology associated with thermoelectric generation and refrigeration.

There is no journal exclusive to thermoelectrics. Information on this activity is scattered throughout the scientific literature with articles regularly appearing in learned society journals and more recently in the popular press. For the past twenty or so years, the proceedings of The Intersociety Energy Conversion Engineering Conference (IECEC) have served as a source of information on thermoelectric research, albeit primarily on space activities. Since 1974 the proceedings of the International Conference on Thermoelectrics (ICT) have been a source of information on thermoelectrics in general. Scientific articles on thermoelectrics have also appeared periodically in journals such as Space Nuclear Power Systems, Applied Energy, Journal of Power Sources, and a number of non-English publications.

It is intended that this handbook should serve both as the authoritative reference text on thermoelectrics for the professional scientist and engineer and as a source of general information on thermoelectrics for the well-informed layman. This handbook is comprised of fifty-five chapters written by sixty-one of the leading authorities in their field. The chapters are review-type contributions which cover current activities in thermoelectrics.

I have viewed my role as an acquisition rather than a copy editor and, although I have taken the liberty of rephrasing on occasion in order to clarify the meaning, every attempt has been made to preserve the international flavor of the handbook.

I am indebted to my colleagues in the thermoelectric community who unselfishly spent their most precious commodity, time, in writing contributions for the handbook and meeting deadlines. I am also indebted to my publishing editor Navin Sullivan for his encouragement at all stages in preparing the manuscripts and to Sara White for re-typing the majority of the chapters. Finally special thanks to my father, the late A. J. Rowe, B.Sc., some of whose interest in science I like to think has rubbed off on me.

David M. Rowe
Cardiff, Wales

Contributors

L. I. Anatychuk
Institute of Thermoelectricity
Chernovtsy, Ukraine

Terry Aselage
Sandia National Laboratories
Albuquerque, New Mexico, U.S.A.

B. J. Beaudry
Iowa State University
Ames, Iowa, U.S.A.

Gary L. Bennett
National Aeronautics and Space Administration (retired)
Washington, DC, U.S.A.

C. M. Bhandari
University of Allahabad
India

Ulrich Birkholtz
Universität Karlsruhe
Karlsruhe, Germany

Alexander Borshchevsky
Jet Propulsion Laboratory
Pasadena, California, U.S.A.

Richard J. Buist
TE Technology
Traverse City, Michigan, U.S.A.

Edward J. Burke
Marlow Industries Inc.
Dallas, Texas, U.S.A.

Alexander T. Burkov
A. F. Ioffe Physico-Technical Institute of RAS
St. Petersburg, Russia

M. Cassart
Université Catholique de Louvain
Louvain-La-Neuve, Belgium

M. H. Cobble
New Mexico State University
Las Cruces, New Mexico, U.S.A.

Bruce A. Cook
Ames Laboratory
Iowa State University
Ames, Iowa, U.S.A.

David Emin
Sandia National Laboratories
Albuquerque, New Mexico, U.S.A.

V. Fano
University of Parma
Parma, Italy

Mikhail I. Fedorov
A. F. Ioffe Physico-Technical Institute of RAS
St. Petersburg, Russia

Gao Min
Kunming Institute of Physics
Kunming, China

H. J. Goldsmid
University of New South Wales
Australia

Erwin Groβ
Universität Karlsruhe
Karlsruhe, Germany

K. A. Gschneidner, Jr.
Iowa State University
Ames, Iowa, U.S.A.

William C. Hall
Teledyne Brown Engineering
Hunt Valley, Maryland, U.S.A.

S. H. Han
Ames Laboratory
Iowa State University
Ames, Iowa, U.S.A.

J. Harringa
Ames Laboratory
Iowa State University
Ames, Iowa, U.S.A.

Robert F. Hartman
Martin Marietta Corporation
Valley Forge, Pennsylvania, U.S.A.

Jean Paul Issi
Université Catholique de Louvain
Louvain-La-Neuve, Belgium

Takenobu Kajikawa
Shonan Institute of Technology
Fujisawa, Japan

K. Kishimoto
Shonan Institute of Technology
Kanagawa, Japan

T. Koyanagi
Yamaguchi University
Ube, Japan

S. A. Ktitorov
A. F. Ioffe Physico-Technical Institute of RAS
St. Petersburg, Russia

V. L. Kuznetsov
A. F. Ioffe Physico-Technical Institute of RAS
St. Petersburg, Russia

Lionel M. Levinson
General Electric Company
Schenectady, New York, U.S.A.

Robert S. Lewandowski
General Electric Company
Schenectady, New York, U.S.A.

Raymond Marlow
Marlow Industries Inc.
Dallas, Texas, U.S.A.

Kakuei Matsubara
Yamaguchi University
Ube, Japan

Kenji Matsuura
Osaka University
Osaka, Japan

Alan G. McNaughton
Global Thermoelectrics Inc.
Calgary, Canada

J. Mondt
Jet Propulsion Laboratory
Pasadena, California, U.S.A.

K. Nagao
Yamaguchi University
Ube, Japan

I. A. Nishida
National Research Institute for Metals
Ibaraki, Japan

Toshitaka Ohta
Electrotechnical Laboratory
Tsubuka, Japan

Daniel D. Pollock
State University of New York
Buffalo, New York, U.S.A.

Yu I. Ravich
A. F. Ioffe Physico-Technical Institute of RAS
St. Petersburg, Russia

R. M. Redstall
British Telecom Research Laboratories
Ipswich, UK

David Michael Rowe
University of Wales
Cardiff, UK

Stanislas Scherrer
Ecole des Mines
Nancy, France

Hubert Scherrer
Ecole des Mines
Nancy, France

A. Nancy Scoville
ThermoTrex Corporation
Waltham, Maryland, U.S.A.

E. A. Skrabek
Orbital Sciences Corporation
Germantown, Maryland, U.S.A.

Glen A. Slack
Rensselaer Polytechnic Institute
Troy, New York, U.S.A.

John G. Stockholm
Marvel Thermoelectric
Vernouillet, France

Ulrich Stöhrer
Universität Karlsruhe
Karlsruhe, Germany

M. Stordeur
Martin Luther University, Halle-Wittenberg
Halle, Germany

R. Studd
British Telecom Research Laboratories
Ipswich, UK

R. Taylor
University of Manchester Institute of Science and Technology
Manchester, UK

D. S. Trimmer
Teledyne Brown Engineering
Hunt Valley, Maryland, U.S.A.

Kin-ichi Uemura
Institute for Thermoelectric Technologies Japan
Yokohama, Japan

Jan W. Vandersande
Jet Propulsion Laboratory
Pasadena, California, U.S.A.

M. V. Vedernikov
A. F. Ioffe Physico-Technical Institute
St. Petersburg, Russia

Cronin B. Vining
Consultant
Webster Groves, Missouri, U.S.A.

H. Hugh Woodbury
General Electric Company
Schenectady, New York, U.S.A.

V. K. Zaitsev
A. F. Ioffe Physico-Technical Institute of RAS
St. Petersburg, Russia

Table of Contents

SECTION C Measurement of Thermoelectric Properties

SECTION D Thermoelectric Materials

SECTION E Thermoelectric Generation

SECTION F Generator Applications

SECTION G Thermoelectric Refrigeration

SECTION H Applications of Thermoelectric Cooling

List of Symbols

A	cross-sectional area; total area; resonant scattering intensity
A_n, A_p	cross sectional area of the n and p legs, respectively
Å	Angstrom unit
A'	material parameter
B	magnetic field; elastic constant for hard sublattice; magnetic field strength
B'	strength of phonon-electron scattering
C	specific heat/unit mass; thermal conductance of thermoelectric material
C_{11}	longitudinal elastic constant
C_V	specific heat at constant volume
E_A	activation energy
E	energy of charge carriers
E_F	Fermi energy
E_g	energy band gap
E_b	potential barrier height
$\boldsymbol{F}$	force; pulverizing force
$F(\eta)$	Fermi-Dirac integral
G	reciprocal lattice vector
G_i	average stiffness constant
$H(t)$	Heavidide unit step function
I	electrical current
I	current in multistage generator
I_r	current ratio
I_b	phonon mean-free-path
K	thermal conductance; heat transfer conductance through a thermocouple
K_n	kinetic coefficient
L	length; length of thermoelements
L	Lorenz number
L_{ij}	Onsager coefficient
L_e	generalized Fermi integral
L, $\mathcal{L}$	Lorenz factor
M	atomic mass; separation of the chemical potential from the resonant band center
N	number of thermoelements in the module
N^0	thermal conductance
N_a	number of atoms per unit volume
N_I	impurity density
N_e, N_h	equivalent extrema (or valleys) in conduction or valence bands, respectively
N_v	number of valleys in conduction or valence band; vacancy concentration
P	electrical power, pressure; Peltier coefficient
P_c	"realistic" power output
P_0	electrical power output
$\boldsymbol{P_0}$	electrical power output of MTEG
P_r	power ratio
P_{max}	maximum power output
Q	heat flow; thermal input
Q_c	heat pump capacity at cold junction
Q_h	thermal input
$\boldsymbol{Q_h}$	thermal input to MTEG
Q_0	heat rejected
R	electrical resistance; device resistance; electrical resistance of a single thermocouple; reflectivity
$\boldsymbol{R}$	MTEG resistance
R^*	effective internal resistance for a single thermocouple
R_H	Hall coefficient
R_c	electrical contact resistance
$\boldsymbol{R_c}$	MTEG contact resistance
R_{cc}	cold temperature contact resistance
$\boldsymbol{R_{cc}}$	cold temperature MTEG contact resistance
R_{ch}	hot temperature contact resistance
R_{ch}	hot temperature MTEG contact resistance

R_l	external load resistance
R_t	total resistance
$\boldsymbol{R_t}$	MTEG total resistance
S	entropy
S_c	heat exchanging surface area corresponding to a single thermocouple (cold flow side)
S_w	heat exchanging surface area corresponding to a single thermocouple (warm flow side)
S_{Te}	thermoelectric Seebeck coefficient = $NB_{Te}{}^{*}\ S_{Te}$
T	absolute temperature
T_{av}	average temperature
T_c	cold junction temperature; cold fluid temperature
T_{cj}	cold junction temperature
T_h	hot junction temperature
T_w	warm fluid temperature
T_{wj}	warm junction temperature
T^e	eutectic temperature
T^{liq}	liquidus temperature
ΔT	temperature difference
ΔT_c	temperature difference between the electrode at the cold junction and the cold flow
ΔT_{teg}	temperature difference across a block of thermoelectric semiconductor
ΔT_w	temperature difference between the electrode at the warm junction and the warm flow
U	weighted mobility
U_n, U_p	weighted carrier mobility for electrons and holes, respectively
$U(T)$	phonon energy density
V	voltage; terminal voltage; load voltage; volume
$\boldsymbol{V}$	MTEG load voltage
V_H	Hall voltage
V_N	Nernst voltage
V_{RL}	Reghi-Leduc voltage
V_S	Seebeck voltage
V_{oc}	open circuit voltage
$\boldsymbol{V_{oc}}$	open circuit voltage
V_r	voltage ratio
V_E	Ettinghausen voltage
V_a^c	critical potential
V_{open}	open terminal voltage
ΔV	potential difference along a sample
W	ratio of flow of electrical energy, strength of carrier-phonon coupling
x	concentration (number of atoms in a formula unit)
$X(a)$	electronegativity of element a
ΔX	electronegativity of compounds
Z	thermoelectric figure-of-merit of material
Z^*	optimal Ioffe figure-of-merit
Z_{opt}	optimal figure-of-merit
Z_c, Z_{np}	thermoelectric figure-of-merit of thermocouple
Z	reduced phonon frequency
ZT	dimensionless figure-of-merit
a	inter-atomic spacing; mean hopping distance
a_0	Bohr constant
c	atomic concentration of an alloy component
d	density; diameter; potential barrier separation
dS	area element of a constant energy surface in the wave vector space
e	electronic charge
f	Fermi-Dirac distribution function
h	Planck constant; heat transfer coefficient
h_{ec}	heat transfer conductance between the cold flow and the cold electrode per unit area
h_{ew}	heat transfer conductance between the warm flow and the warm electrode per unit area
h_{lec}	heat transfer coefficient between the cold flow and the inner surface of the heat transfer tube
h_{lew}	heat transfer coefficient between the warm flow and the inner surface of the heat transfer tube

h_{2ec}	heat transfer conductance through the insulator and the heat transfer tube faced to the cold flow per unit area
h_{2ew}	heat transfer conductance through the insulator and the heat transfer tube faced to the warm flow per unity area
$\boldsymbol{i}$	electric current density
$\boldsymbol{j}$	electron flow
$j(k)$	Heisenberg current operator
k	Boltzmann constant; absorption coefficient
k_0, k_B	Boltzmann constant
$\boldsymbol{k}$	wave vector; conduction electron wave vector
$\boldsymbol{k}_T$, $\boldsymbol{k}_L$	transverse and longitudinal components of the electron (or hole) wave vector
l	length; length of thermoelements; width of soliton wall; phonon mean-free-path
l_e, l_p	mean-free-path of electron or hole, respectively
l_s	barrier width
m_0	free electron mass
m_c	conductivity (initial) effective mass
m_d	density-of-states effective mass
m^*	density-of-states effective mass
m_d	density-of-states effective mass; density-of-states effective mass in a single valley
m_1, m_2, m_3	effective mass components along principal axes
m^*_{L0}	longitudinal component of effective mass
m^*_{T0}	transverse component of effective mass
n	carrier concentration; reflectivity coefficient; number of stages in multistage generator
n_{opt}	optimum carrier concentration
q	electronic charge; thermal flow; elastic constants for the soft sublattice
q_c	heat flux at the cold junction
q_w	heat flux at the warm junction
$\boldsymbol{q}$	wave vector; quantity of heat
q^{-1}	reciprocal of penetration depth
r	scattering parameter; thermal resistivity
r_H	Hall factor
s	scattering parameter
s_{ph}	acoustic phonon-drag effect
t	time
t_{av}	average temperature of thermoelectric material
$t_{1/2}$	half-rise time
u	mobility
u_0	barrier amplitude
$\boldsymbol{u}_i$	displacement vector
$\boldsymbol{u}_{ij}$	deformation tensor
v	velocity; velocity of sound; conduction electron velocity; heat pulse dissipation function
v	elastic constants for the soft sublattice
v_L	average sound (phonon) velocity
v_s	sound (phonon) velocity
v_q	constant phonon velocity
w	weight; thermal current density
x	fractional content; reduced energy of charge carriers
z	figure-of-merit of single material
Γ	resonant band width
Γ_{ijk}	inter-sublattice interaction constant
Θ_D	Debye temperature
Ω	angular frequency
Ω_0	average atomic volume
Ψ	$=\gamma_n/\gamma_p$
α	Seebeck coefficient; thermoelectric power, thermopower, thermal expansion coefficient
α_i	impurity thermoelectric power
α_n, α_p	Seebeck coefficient of n and p legs
α_{ph}	phonon thermoelectric power
α_r	thermoelectric power reference electrode
α_s	thermoelectric power of the sample under investigation
α_{Te}	thermoelectric material Seebeck coefficient

β	Thomson coefficient; non-parabolicity parameter
χ	reduced phonon frequency; thermal conductivity
χ_L	lattice thermal conductivity
χ_e	electronic thermal conductivity
χ_b	un-enhanced thermoelectric power
ε	charge carrier energy
ε_b	potential barrier height
ε_l	deformation potential
γ	Carnot efficiency; Thomson coefficient; average anhamonicity of bonds
γ_i	$=A_i/l_i$ i=n,p
η	reduced energy of charge carrier; generation efficiency; reduced Fermi energy, reduced barrier height
η_c	Carnot efficiency
η_t	thermodynamic efficiency
η_t	MTEG thermodynamic efficiency
δ	$=\delta_c=R_c/R$
δ_{ch}	$=R_{ch}/R$
δ_i	cubic root of atomic volume
λ	thermal conductivity; wavelength
λ_L	lattice thermal conductivity
λ_e	electronic thermal conductivity
λ_{Te}	thermoelectric material thermal conductivity
λ_c	thermal contact conductivity
λ_{min}	minimum lattice thermal conductivity of crystals
λ_n, λ_p	thermal conductivity of the n and p legs
λ_0	virtual crystal thermal conductivity
λ_{st}	known (standard) thermal conductivity
λ_s	enhanced thermoelectric power
λ_{total}	total thermal conductivity
λ'	thermal diffusivity
μ	carrier mobility; chemical potential; $=R_0/R$
μ_{cl}	classical Hall mobility
μ^*	reduced Fermi energy
μ_a	carrier mobility due to alloy scattering only
μ_c	carrier mobility in low carrier concentration limit
μ_n, μ_p	electron and hole mobility, respectively
μ_H	Hall mobility
π	Peltier coefficient
ρ	electrical resistivity; porosity
ρ_c	electrical contact resistivity
ρ_i	"ideal" power output; impurity contribution to the resistivity
ρ_n, ρ_p	electrical resistivity of n and p legs
ρ_{ph}	phonon contribution to resistivity
ρ_{Te}	thermoelectric material electrical resistivity
σ	electrical conductivity
σ_0	electrical conductivity in absence of resonant scattering
τ	relaxation time; conduction electron relaxation time
τ_0	energy independent factor of relaxation time
τ_{ac}	carrier relaxation time due to acoustic phonon scattering
τ_{imp}	carrier relaxation time due to ionized impurity scattering
τ_{res}	carrier relaxation time due to resonance scattering
τ_{pd}	phonon relaxation time due to point defect scattering
τ_{pe}	phonon relaxation time due to charge carrier scattering
ω	angular frequency; phonon frequency
ω_0	characteristic frequency of resonance mode
ω_D	Debye frequency
$\omega(\varepsilon, T)$	conductivity of electrons on a constant energy surface e(k)=const
ζ	Fermi energy
ξ	reduced Fermi energy
ξ_{opt}	optimum reduced Fermi energy
ξ_g	reduced band-gap
ψ	eigenfunction

ϕ	generator conversion efficiency; coefficient of performance
ϕ_c	$=1+2\ \delta_{ch}$
Φ	$=P_0/A_t$
$\Phi_{(x)}$	displacement of the soft sublattice atoms

ABa_{C0}	area of cooled base
ABa_{He}	area of heated base
AFin	area of fin
ATe	area of one thermoelectric element
Cxt	thermal conductance of seal
$cp_{\cdot Co.in}$	heat capacity of cooled fluid
effFin	Fin efficiency = average t of fin/t at base of fin
GF	geometric factor of thermoelectric element
hFin	convection coefficient of fin
Lte	length of thermoelectric element
Nb_{te}	number of thermoelectric elements in the module
P_{C0}	cooling power
P_{he}	heating power
Qco	mass flow rate of cooled fluid
Rco	electrical resistance of cold side heat exchanger if in circuit
RHe	electrical resistance of cold side heat exchanger if in electrical circuit
ReCo	electrical resistance $Re_{TE}/2+R_{Co}$
ReHe	electrical resistance $Re_{TE}/2+R_{He}$
$RtBa_{Co}$	thermal resistance of cooled base
$RtBa_{He}$	thermal resistance of heated base
$RtHy_{Co}$	thermal hydraulic resistance of cooled base
$RtHy_{He}$	thermal hydraulic resistance of heated base
tFL_{Co}	temperature of cooled fluid
$tFL_{Co.ex}$	temperature of cooled fluid at exit of building block
$tFL_{Co.in}$	temperature of cooled fluid at inlet of building block
tFL_{He}	temperature of heated fluid
tTe_{Co}	temperature of thermoelectric material at the cooled end
tTe_{He}	temperature of thermoelectric material at the heated end
Ct_{Te}	thermoelectric thermal conductance = Nb_{Te}* GF* k_{Te}
Re_{Te}	thermoelectric electrical resistance = Nb_{Te}* r_{Te}/GF

AMD	Accident Model Document
ASC	absolute Seebeck coefficient
ASE	absolute Seebeck effect
BOL	beginning of life
CBCF	carbon bonded carbon fiber
CVD	chemical vapor deposition
DOE	Department of Energy
DOD	Department of Defense
EIS	environmental impact statement
EPA	Environmental Protection Agency
FEPF	fine weave pressed fabric
GIS	graphic impact shell
GDS	ground demonstration system
GPHS	general purpose heat source
HMS	higher manganese silicides
HSR	heat sink resistance
HTSC	high temperature superconductor
ICB	ion cluster beam
INSRP	Interagency Nuclear Safety Review Panel
LEC	lower expansion coefficient
LPE	liquid phase epitaxy
LTT	low temperature tetragonal phase
MA	mechanical alloying
MBE	molecular beam epitaxy

MTEG	multicouple (multi-stage) thermoelectric generator
NOAA	National Oceanic and Atmosphere Administration
NPS	nuclear powered source
NRAD	Nuclear Risk Analysis Document
NRC	Nuclear Regulatory Committee
NSC	National Security Council
OSTD	Office of Science and Technology Police
PGEC	phonon glass and an electron single crystal
QID	quasi one-dimensional
RDD	Reference Design Document
RSC	relative Seebeck coefficient
RSE	relative Seebeck emf.
SAR	safety analysis report
SER	safety evaluation report
SP	space power
SNAP	systems for nuclear auxiliary power
SQL	size quantum limit
TAGS	tellurium-antimony-germanium-silver
TED	thermoelectric device
THM	traveling heater method
TZM	traveling zone melted
XRD	X-ray diffraction
ZM	zone-melting

1
Introduction

David M. Rowe
University of Wales, Cardiff
U.K.

In 1823 Seebeck reported the results of experiments in which a compass needle was deflected if placed in the vicinity of a closed loop, formed from two dissimilar conductors, when one of the junctions was heated.[1] Seebeck erroneously concluded that the interaction was a magnetic phenomenon and, in pursuing this line of thought, attempted to relate the Earth's magnetism to the temperature difference between the equator and the Poles. Nevertheless, he did investigate the phenomenon in a large number of materials, including some we now call semiconductors, and arranged them in order of the product $\alpha\sigma$, where α is the Seebeck coefficient and σ the electrical conductivity. The Seebeck coefficient is expressed in volts per degree, or more often in microvolts per degree μVK^{-1}. The Seebeck series formed in this way is very similar to the present-day thermoelectric series and, had Seebeck employed the first and last members of his series in a thermocouple, he could have converted thermal energy into electricity in 1821 with an efficiency of about 3%, which compares very favorably with the most efficient steam engine of the day. With the benefit of hindsight it is apparent from Seebeck's account that the phenomenon observed was caused by an electric current flowing in the circuit and that he had discovered the so-called thermoelectric effects.

Some 12 years later, a complementary effect was discovered by Peltier,[2] who observed temperature changes in the vicinity of the junction between dissimilar conductors when a current passed. Although Peltier used the Seebeck effect in his experiments as a source of weak currents, he failed to appreciate the fundamental nature of his observations, or to relate the effect to the findings of Seebeck. The true nature of the Peltier effect was explained by Lenz[3] in 1838. He concluded that, depending upon the direction of the current flow, heat is absorbed or generated at a junction between two conductors and demonstrated this by freezing water at a bismuth-junction and melting the ice by reversing the direction of current flow.

The lack of interest and slow progress in thermoelectric application which followed the discovery of thermoelectric phenomena are understandable when one recalls that much more exciting discoveries were made during this period. This was the era of electromagnetism, with the initial discoveries of Oersted being followed by investigations of researchers such as Ampere and Laplace and culminating in the formulation of the laws of electromagnetic induction by Faraday.

Thermoelectricity enjoyed a temporary revival from 1850 with the development of thermodynamics when interest focused on all forms of energy conversion. In 1851[4] W. Thomson (Lord Kelvin) established a relationship between the Seebeck and Peltier coefficients and predicted the existence of a third thermoelectric effect, the Thomson effect, which he subsequently observed experimentally. This effect relates to the heating or cooling in a single homogeneous conductor when a current passes along it in the presence of a temperature gradient.

The possibility of using thermoelectric phenomena in the generation of electricity was considered in 1885 by Rayleigh who first calculated, although incorrectly, the efficiency of a thermoelectric generator. In 1909[5] and 1911[6] Altenkirch gave a satisfactory theory of thermoelectric generation and refrigeration and showed that good thermoelectric materials should possess large

0-8493-0146-7/95/$0.00+$.50

Seebeck coefficients with low thermal conductivity (λ) to retain the heat at the junction and low electrical resistance to minimize Joule heating. These desirable properties were embodied in a so-called figure-of-merit Z, where $Z = \alpha^2\sigma/\lambda$ and the unit of Z is 1/K. At a given absolute temperature T, since Z may vary with T, a useful nondimensional figure-of-merit is ZT.

Although the properties favorable for thermoelectric applications were well known, the important advantages offered by Seebeck's mineral semiconductors were overlooked with the attention of researchers focused on metal and metal alloys. In these materials the ratio of the thermal conductivity to electrical conductivity is a constant (Wiedemann-Franz-Lorenz law) and it is not possible to reduce one while increasing the other. Consequently, the metals best suited are those with the highest Seebeck coefficients. Most metals possess Seebeck coefficients of 10 μVK^{-1} or less, giving associated generating efficiencies of a fraction of 1%, which are uneconomical as a source of electrical power. Similar considerations also led to the conclusion that thermoelectric refrigeration was an uneconomic proposition.

Renewed interest in thermoelectricity accompanied the development in the late 1930s of synthetic semiconductors that possessed Seebeck coefficients in excess of 100 $\mu V/K$ and in 1947 Telkes[7] constructed a generator that operated with an efficiency of about 5%. In 1949 Ioffe[8] developed a theory of semiconductor thermoelements and in 1954 Goldsmid and Douglas demonstrated that cooling from ordinary ambient temperatures down to below 0°C was possible.[9] Unfortunately, in semiconductors the ratio of the thermal to electrical conductivity is greater than in metals owing to their poorer electrical conductivity. It was not obvious that semiconductors were superior thermoelectric materials and, apart from the Soviet activities, interest again waned. Research into compound semiconductors for possible transistor application in the 1950s resulted in new materials with substantially improved thermoelectric properties and in 1956 Ioffe and his co-workers[10] demonstrated that the ratio could be decreased if the thermoelectric material is alloyed with an isomorphous element or compound. Spurred on by possible military applications a tremendous survey of materials was undertaken, particularly at the RCA Laboratories in the U.S., which resulted in the discovery of a few semiconductors with ZT approaching 1.5.

A "modern" thermoelectric convertor consists, in essence, of a number of alternate ingot-shaped n- and p-type semiconductor thermoelements, which are connected electrically in series with metal connecting strips, sandwiched between two electrically insulating but thermally conducting ceramic plates to form a module. Provided a temperature difference is maintained across the module, electrical power will be delivered to an external load and the device operates as a generator. Conversely, when an electric current is passed through the module, heat is absorbed at one face of the module, rejected at the other face, and the device operates as a refrigerator.

In a thermoelectric generator the efficiency of conversion of heat into electricity depends upon the temperature difference ΔT over which the device operates, on its average temperature of operation, T, and on the performance of the thermoelectric material through its figure-of-merit. The figure-of-merit also determines both the maximum temperature depression and the maximum coefficient of performance of a thermoelectric refrigerator. Consequently, materials that possess large Z values over the intended temperature range of operation are desirable in both generation and refrigeration.

Established thermoelectric materials conveniently fall into three categories depending upon their temperature range of operation. Bismuth telluride and its alloys have the highest figures-of-merit, are extensively employed in refrigeration, and have a maximum operating temperature of around 450 K. Alloys based on lead telluride have the next highest figures-of-merit with silicon germanium alloys having the lowest. Lead telluride and silicon germanium are used in generator applications with upper operating temperatures of around 1000 and 1300 K, respectively.

In the early 1960s a requirement for autonomous sources of electrical power arose from the exploration of space, advances in medical physics, and the exploitation of the Earth's resources in increasingly hostile and inaccessible locations.[11] Thermoelectric generators are ideally suited to such applications, where their reliability, absence of moving parts, and silent operation outweigh their relatively high cost and low efficiency (typically less than 5%). Advantage can be taken of the simplicity and ruggedness of thermoelectric generators compared with thermomechanical conversion devices.[12]

In situations where periodic refueling is possible and oxygen available, fossil fuel is employed as a heat source. Hydrocarbon fuel has an energy density some 50 times that of a chemical battery and so, provided that the conversion efficiency is better than 2%, a hydrocarbon-fueled system can provide a much lighter and less bulky source of long-term electrical energy than batteries. When annual refueling is not possible, or oxygen is not available, radioactive isotopes serve as heat sources, enabling the generators, which are referred to as radioisotope thermoelectric generators or RTGs, to operate unattended for extended periods, in some instances, such as the Voyager spacecrafts launched in 1977, for longer than 17 years.[13]

Following the fivefold increase in the price of crude oil in 1974, a closer look was taken at the possibility of large-scale production of electricity by the thermoelectric effect. Apart from an abundant supply of easily utilized heat, it was concluded that the economic large-scale thermoelectric generation of electricity would require the cheap production of substantial amounts of semiconductor material, accompanied by a significant improvement in the material figure-of-merit. However, concern over the depletion of the ozone layer in the late 1980s and a general public interest in environmentally friendly energy sources have been accompanied by a renewed interest in thermoelectric generation as a potential source of large-scale electrical power using waste heat.[14,15]

Thermoelectric cooling has also enjoyed success in domestic food refrigerators, air conditioning, and numerous novel applications where the facility to vary the cooling capacity of the device to match the particular application has proved an important factor.[16] Although large-scale thermoelectric cooling is unlikely ever to match the performance of freon systems, in some applications its modularity and reliability does offer certain advantages.[17] Significant advances have also been made in the miniaturization of thermoelectric devices, particularly in the development of miniature detectors and sensors[18,19] and power sources.[20]

In recent years multistage thermoelectric cooling modules have been developed with as many as six stages enabling temperatures of below 170 K to be achieved with commercial devices.[21] However, the figure-of-merit of bismuth telluride-based alloys decreases with a reduction in temperature and renewed interest has been shown in materials such as the bismuth-antimony alloys whose thermoelectric performance can be improved by the application of a magnetic field.[22] Another magnetic phenomenon, "the Ettingshausan effect", has also proved to be an efficient refrigeration process at low temperatures.[23]

Thermoelectric cooling below 150 K has been constrained by the nonavailability of material with a reasonable figure-of-merit at these temperatures apart from n-type bismuth antimonide. The possibility of using a high T_c superconductor (HTSC) as a passive thermoelement was first explored by Goldsmid et al.[24] and successfully demonstrated a couple of years later.[25,26]

Successful commercial exploitation of thermoelectric devices depends to a large degree in increasing the material's figure-of-merit. This in turn is closely dependent upon the formulation of an adequate theoretical model. Solid-state theory has greatly assisted in this direction. Although the models available are, at best, rough approximations of the actual materials, they do provide a useful insight into the desirable basic properties of materials for refrigeration and generation. Models have been developed for all three of the established families of thermoelectric materials.[26–29] In recent years the upper limit to figure-of-merit has been reinvestigated,[30] but realization of the same in practice depends upon many factors, not the least of which is whether or not the material can be prepared.

It is in high-temperature thermoelectric generation that the vast majority of basic research effort is being concentrated with a view to increasing the material figure-of-merit and the device's upper operating temperature. Materials under development are based on the lanthanum chalcogenides and boron-carbon compounds.[31] Attempts to improve the performance of materials based upon silicon germanium alloys continues. The major effort, which was initially directed at reducing the lattice thermal conductivity by introducing additional disorder into the alloy structure,[32–36] is being shifted to improving the electrical power factor.[37]

Further research into, and development of, thermoelectrics is assured with the continuation of a number of U.S. space projects. In addition, the increased Japanese interest and involvement across the whole spectrum of thermoelectric activities is a pointer to a future increase in the commercial exploitation of this unique energy conversion phenomenon.

References

1. Seebeck, T. J., Magnetic polarization of metals and minerals, *Abhandlungen der Deutschen Akademie der Wissenschaften zu Berlin*, 265, 1822–1823.
2. Peltier, J. C., Nouvelles experiences sur la caloricite des courans electrique, *Ann. Chim.*, LV1 371, 1834.
3. Ioffe, A. F., *Semiconductor Thermoelements and Thermoelectric Cooling*, Infosearch, London, 1957.
4. Thomson, W., On a mechanical theory of thermoelectric currents, *Proceedings of the Royal Society of Edinburgh*, 91, 1851.
5. Altenkirch, E., Uber den Nutzeffeckt der Thermosaule, *Physikalische Zeitschrift*, 10, 560, 1909.
6. Altenkirch, E., Electrothermische Kalteerzeugung und Reversible Electrische Heizung, *Physikalische Zeitschrift*, 12, 920, 1911.
7. Telks, M., The efficiency of thermoelectric generators, *Int. J. Appl. Phys.*, 18, 1116, 1947.
8. Ioffe, A. F., *Energeticheskic osnovy termoelektricheskikh baterei iz poluprovoduikov*, Academy of Sciences of the USSR, Moscow, 1949.
9. Goldsmid, H. J. and Douglas, R. W., The use of semiconductors in thermoelectric refrigeration, *Br. J. Appl. Phys.*, 5 (11), 386, 1954.
10. Ioffe, A. F., Airapetyants, S. V., Ioffe, A. V., Kolomoets, N. V., and Stilbans, L. S., On increasing the efficiency of semiconducting thermocouples, *Dokl. Akad. Nauk SSSR*, 106, 931, 1956.
11. Rowe, D. M. and Bhandari, C. M., *Modern Thermoelectrics*, Holt Technology, 1983.
12. Cooke-Yarborough, E. H. and Yeats, F. W., Efficient thermo-mechanical generation of electricity from the heat of radioisotopes, *Proc. Xth IECEC*, August 1975, 1033.
13. Rowe, D. M., United States thermoelectric activities in space, *Proc. VIIIth Int. Conf. Thermoelectric Energy Conversion*, Scherrer, S. and Scherrer, H., Eds., July 10–13, 1989, Nancy, France, 133.
14. Rowe, D. M., Thermoelectric generation, *Watt Report, 1992*, Cook, A. W., Ed., 28th Consultative Conference, to be published on behalf of the U.K. Watt Committee on Energy by IEE, 1993.
15. Matsuura, K., Rowe, D. M., Koumoto, K., Min, G., and Tsuyoshi, A., Design Optimisation for a Large Scale Low Temperature Thermoelectric Generator, *Proc. XIth International Conference on Thermoelectrics*, University of Texas at Arlington, October 7–9, 1992, 10.
16. Goldsmid, H. J., *Applications of Thermoelectricity*, Methuen Monograph, Worsnop, B. L., Ed., 1960.
17. Blankenship, W. P., Rose, C. M., and Zemanick, P. P., Applications of Thermoelectric Technology to Naval Submarine Cooling, *Proc. VIIIth Int. Conf. Thermoelectric Energy Conversion*, Scherrer, S. and Scherrer, H., Eds., July 10–13, 1989, Nancy, France, 224.
18. Anatychuk, L. I., Moldavasky, M. S., Rasinkov, V. V., and Tsipko, N. K., Thermoelectric batteries for pyrometers, *Proc. Xth Int. Conf. Thermoelectrics*, Rowe, D. M., Ed., Cardiff, Wales, September 10–12, 1991, 108.
19. Van Herwaarden, A. W., Van Duyn, D. C., Van Oudheusden, B. W., and Sarro, P. M., Integrated Thermopile Sensors, *Sensors and Actuators*, A21–A23, 621, 1989.
20. Rowe, D. M., Miniature Thermoelectric Convertors, U.K. Patent No. 87 14698, 1988.
21. Goldsmid, H. J., *Electronic Refrigeration*, Pion Limited, London, 1986.
22. Smith, G. E. and Wolfe, R., Thermoelectric properties of bismuth antimony alloys, *J. Appl. Phys. (USA)*, 33 (3), 841, 1962.
23. Delves, R. T., The prospect of Ettinghausen and Peltier cooling at low temperatures, *Br. J. Appl. Phys.*, 13 (9), 440, 1962.
24. Goldsmid, H. J., Gopinathan, K., Matthews, D. N., Taylor, K. N. R., and Baird, C. A., High T_c superconductors as passive thermoelements, *J. Phys. D, Appl. Phys.*, 21 (2), 344, 1988.
25. Vedernikov, M. V., Kuznetsov, V. L., Ditman, A. V., Melekh, B. T., and Burkov, A. T., Efficient thermoelectric cooler with a thermoelectrically passive high T_c superconducting leg, *Proc. Xth Int. Conf. Thermoelectrics*, Cardiff, Wales, September 10–12, 1991, 96.
26. Sidorenko, N. A. and Mosolov, A. B., Cryogenic thermoelectric coolers with passive high T_c superconducting legs, *Proc. XIth Int. Conf. Thermoelectrics*, University of Texas at Arlington, October 7–9, 1992, 289.
27. Stordeur, M. and Sobotta, H., Valence band structure and thermoelectric figure-of-merit of $(Bi_{1-x}Sb_x)_2Te_3$ single crystals, *Proc. 1st European Conf. Thermoelectrics*, Rowe, D. M., Ed., Cardiff, Wales, 1988, 209.

28. Bhandari, C. M. and Rowe, D. M., Theoretical analysis of the thermoelectric figure-of-merit, *Energy Conversion and Management,* 20, 113, 1980.
29. Bhandari, C. M. and Rowe, D. M., *Thermal Conduction in Semiconductors,* Wiley Eastern Ltd., 1988.
30. Vining, C. B., The thermoelectric figure-of-merit ZT=1; fact or artifact, *Proc. XIth Int. Conf. Thermoelectrics,* University of Texas at Arlington, October 7–9, 1992, 223.
31. Wood, C., Materials for high temperature thermoelectric energy conversion, *Proc. Ist European Conf. Thermoelectrics,* Rowe, D. M., Ed., Cardiff, Wales, 1988, 1.
32. Rowe, D. M. and Shukla, V., The effect of phonon-grain boundary scattering on the thermoelectric conversion efficiency of heavily doped fine grained hot pressed silicon germanium alloys, *J. Appl. Phys.*, 52, 7421, 1981.
33. Pisharody, R. K. and Garvey, L. P., Modified silicon germanium alloys with improved performance, *Proc XIIIth Intersociety Energy Conversion Engineering Conference,* San Diego, CA, August, 20–25, 1963, 1978.
34. Vining, C. B., Laskow, W., Hanson, J. O., Van der Beck, R. R., and Gorsuch, P. D., Thermoelectric properties of pressure sintered $Si_{0.8}Ge_{0.2}$ thermoelectric alloys, *J. Appl. Phys.*, 69, 4333, 1991.
35. Slack, G. A. and Hussain, M. A., The maximum possible conversion efficiency of silicon germanium generators, *J. Appl. Phys.*, 70 (5), 2694, 1991.
36. Rowe, D. M., Fu, L. W., and Williams, S. G. K., Comments on the thermoelectric properties of pressure sintered $Si_{0.8}Ge_{0.2}$ thermoelectric alloys, *J. Appl. Phys.*, 73, 4683.
37. Flurial, J. P., Borshchevsky, A., and Vandersande, J., Optimisation of the thermoelectric properties of hot pressed n-type SiGe materials by multiple doping and microstructure control, *Proc. Xth Int. Conf. Thermoelectrics,* Cardiff, Wales, September 10–12, 1991, 156.

Section A
General Principles and Theoretical Considerations

2
Thermoelectric Phenomena

Daniel D. Pollock
State University of New York
Buffalo, New York, U.S.A.

2.1 Introduction

An electrical potential (voltage) is generated within any isolated conducting material that is subjected to a temperature gradient; this is the *absolute Seebeck effect, ASE. The absolute Seebeck coefficient, ASC,* is defined as the instantaneous rate of change of the ASE with respect to temperature at a given temperature: ASC = $[d(ASE)/dT]_T$. The least complicated example of the way in which this phenomenon is used is to form a thermocouple composed of two dissimilar conductors, or thermoelements, by electrically joining one set of their ends. The application of a temperature difference, or gradient, between the ends of this device will produce a voltage across its unpaired terminals that is a function of the temperature distribution.[1-4]

The resulting voltage is the *relative Seebeck emf, RSE,* Figure 1. It results only from the difference between the internal potentials, or ASEs, within the individual conductors of which it is composed. The *relative Seebeck coefficient, RSC,* is the instantaneous rate of change of the RSE with temperature at a given temperature: RSC = $[d(RSE)/dT]_T$. The Seebeck effect does not arise as a result of the junction of the dissimilar materials, nor is it directly affected by the Thomson or the Peltier effects; the latter two thermal effects are present only when current flows in a thermoelectric circuit and are not voltages. These responses are in contrast to that of the relative Seebeck effect, which exists as long as the temperature gradient is maintained, regardless of whether current flows or not. It turns out that the relative Seebeck potential is the driving force for the current flow that is

0-8493-0146-7/95/$0.00+$.50

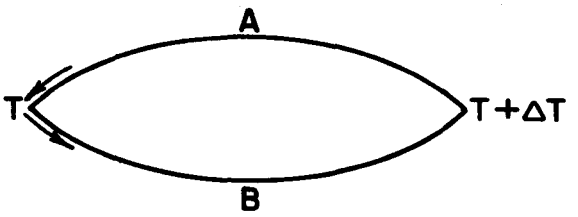

FIGURE 1 Thermodynamic circuit for the relative Seebeck coefficient. (From Pollock, D.D., *Thermoelectricity: Theory, Thermometry, Tool,* ASTM Special Technical Publication 852, American Society for Testing and Materials, Philadelphia, PA, 1985. With permission.)

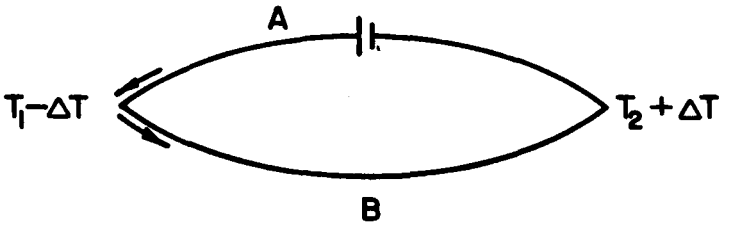

FIGURE 2 Thermodynamic circuit for the Peltier effect. (From Pollock, D.D., *Thermoelectricity: Theory, Thermometry, Tool,* ASTM Special Technical Publication 852, American Society for Testing and Materials, Philadelphia, PA, 1985. With permission.)

responsible for the Peltier and Thomson effects in thermoelectric circuits in the absence of other applied voltages.

Too frequently the RSE has been *incorrectly* described in the literature as being a consequence of the external contact potential, or Volta effect, between dissimilar materials. *The external contact potential is not a thermoelectric effect.* An external contact potential is induced when two different materials are brought sufficiently close to each other, but are not in physical contact, so that electron transfer between them results in a common Fermi energy level in each. This mechanism is independent of temperature and vanishes virtually instantaneously ($\sim 10^{-15}$ s) when the materials make physical contact. *The external contact potential has no relationship whatsoever to any thermoelectric phenomenon.*[5]

The greatest application of the Seebeck effect is in thermoelectric thermometry. This results from the fact that thermoelectric circuits convert thermal energy into electrical energy. The open-circuit (null-balance) emf obtained by this means is the RSE, which can be used to measure temperature. Thermocouples composed of standardized metallic conductors are very widely used for the accurate, sensitive, and reliable measurement and/or control of temperature.

Peltier showed that heat is absorbed or liberated when a current crosses an interface between two different conductors; see Figure 2.[6] This also occurs within nonhomogeneous conductors at concentration gradients or at phase interfaces within multiphase materials. The *Peltier effect* is the reversible change in the heat content at an interface between dissimilar conductors that results from the flow of current across it.

The *Peltier coefficient,* π_{AB}, is the change in the reversible heat content at the junction of conductors A and B when unit current flows across it in unit time, where $\pi_{AB} = \pi_A + \pi_B$ and π_A and π_B are the respective *absolute Peltier coefficients* of the conductors. The direction in which current flows across a junction and the values of π_A and π_B determine whether heat is liberated or absorbed. The Peltier effect is a result of the change in the entropy of the electrical charge carriers as they cross a junction. It is not an emf despite the fact that π_{AB} can be expressed in energy units involving volts. The Peltier effect, like the Seebeck effect, is unrelated to the contact potential.

For a constant current, the Peltier effect is proportional to the RSC, and at any fixed junction temperature, it is proportional to the current. These reversible effects are independent of the shape or dimensions of the junction. This is in contrast to *Joule heating* which is a function of dimensions,

does not require a junction, or change its sign, and is irreversible. Applications of the Peltier effect include thermoelectric devices for refrigeration and for power generation.

The *Thomson effect* is the reversible change of heat content within any single homogeneous conductor in a temperature gradient when an electric current passes through it, Figure 3.[7–10] This may occur in any nonisothermal segment of a conductor. The *Thomson coefficient* is the reversible change of the heat content within a single conductor per unit temperature gradient per unit current flow. Thomson termed it the "specific heat of electricity". The Thomson effect is *not* a voltage, although, like the Peltier effect, it can be expressed in energy units involving volts.

The Thomson effect is a manifestation of the direction of flow of electrical carriers with respect to a temperature gradient within a conductor. These absorb energy (heat) flowing in a direction opposite to a thermal gradient, increasing their potential energy; and, when flowing in the same direction as a thermal gradient, they liberate heat, decreasing their potential energy.

2.2 Thermodynamics

The thermodynamic relationships between thermoelectric effects are important in order to understand the basic phenomena, and because the quantum mechanic treatments are based on them. The thermodynamics relates the thermoelectric effects and the quantum mechanics explains their mechanisms.[11]

The thermodynamic analysis given here is essentially that of Thomson.[12,13] More rigorous treatments are given by Benedict[14] and Callen.[15,16]

A thermoelectric circuit can be treated as very closely approximating a "reversible heat engine". The very small irreversible thermal (Joule) losses can be neglected as shown in the following approximation. The current in a closed thermometric thermoelectric circuit is about 10^{-3} A. The electrical resistance of the thermoelements is small (usually minimized in order to achieve maximum sensitivity), being usually much less than 10 Ω. This gives a negligible irreversible heat loss (I^2R) of considerably less than 10^{-5} W.

Let two dissimilar conductors, A and B constitute a closed circuit, see Figure 1, in which the colder junction is at temperature T and the hotter junction is at T + ΔT and both are maintained by heat reservoirs. The RSE generated by the temperature difference is E_{AB}. The RSC (the change in emf per Kelvin) is dE_{AB}/dT so the electrical energy is expressed as

$$I\,E_{AB} = I\frac{dE_{AB}}{dT}\Delta T \tag{1}$$

and, for unit current flowing in the thermoelectric circuit,

$$E_{AB} = \frac{dE_{AB}}{dT}\Delta T \tag{2}$$

The other energy factors in a closed thermoelectric circuit are the Peltier effects (changes in the heat contents at the junctions) and the Thomson effects (changes in the heat contents in the individual conductors). These thermal energies are expressed as:

Peltier effects (at the junctions) (3a)

Heat absorbed at the hotter junction = $\pi_{AB}(T + \Delta T)$

Heat liberated at the colder junction = $-\pi_{AB}(T)$

Thomson effects (within the conductors) (3b)

Heat absorbed in conductor B = $\beta_B(\Delta T)$

Heat liberated in conductor A = $-\beta_A(\Delta T)$

where π and β are the Peltier and Thomson coefficients, respectively.

A thermoelectric circuit approximates a reversible heat engine so the thermal and electrical energies can be equated. For unit current flow in the circuit,

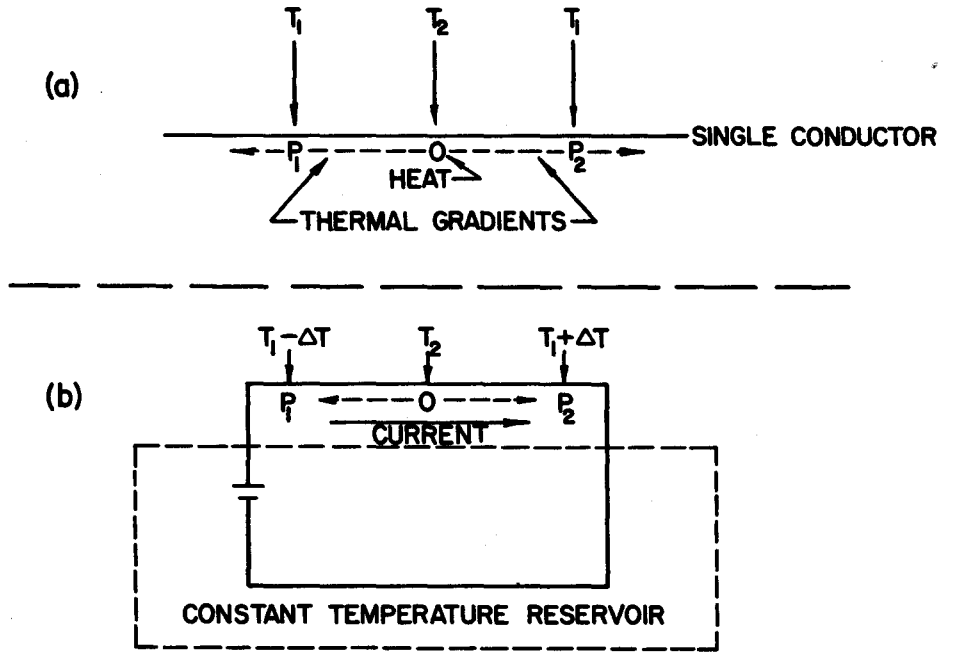

FIGURE 3 (a) Opposing thermal gradients in a single conductor in an open circuit. (b) Asymmetrical thermal gradients caused by the Thomson effect in a single conductor in a closed circuit. (From Pollock, D.D., *Thermoelectricity: Theory, Thermometry, Tool,* ASTM Special Technical Publication 852, American Society for Testing and Materials, Philadelphia, PA, 1985. With permission.)

$$\frac{dE_{AB}}{dT}\Delta T = \pi_{AB}(T + \Delta T) - \pi_{AB}(T) + (\beta_B - \beta_A)\Delta T \tag{4}$$

Equation 4 is divided through by ΔT to obtain

$$\frac{dE_{AB}}{dT} = \frac{\pi_{AB}(T + \Delta T) - \pi_{AB}(T)}{\Delta T} + (\beta_B - \beta_A) \tag{5}$$

The fraction on the right is a difference quotient. This gives, for the condition in which ΔT approaches zero, the instantaneous rate of change of the Peltier effect with respect to temperature. Thus, Equation 5 is expressed as

$$\frac{dE_{AB}}{dT} = \frac{d\pi_{AB}}{dT} + (\beta_B - \beta_A) \tag{6}$$

This is the fundamental thermodynamic theorem for closed thermoelectric circuits; it shows the *energy* relationship between the *electrical* Seebeck effect and the *thermal* Peltier and Thomson effects. These components of Equation 6 represent distinct thermal phenomena that are induced by the RSE that arises solely from the temperature (energy) gradient in conductors A and B. While the Peltier and Thomson effects may be expressed in energy units involving voltage, they are purely thermal in character.

It must be emphasized that Equation 6 is derived for closed circuits with no external electrical sources. The RSC, as represented by dE_{AB}/dT, is nonzero in open thermoelectric circuits, while the Peltier and Thomson heat changes are zero for this case. This arises because the current is zero, while their coefficients remain unchanged. Thus, Equation 6 does not hold for the case in which no current flows. This clearly demonstrates that *the RSE should not be considered to be the physical consequence of the Peltier and Thomson effects.* This may be restated as: the thermal terms in Equation 6 may *not* be converted to their electrical equivalents to "explain" the Seebeck effect.

The electrical Seebeck effect is the driving force for the currents that give rise to the thermal Peltier and Thomson effects in closed circuits. These thermal effects can introduce small temperature errors in thermoelectric thermometry, but the IR voltage losses can cause much larger decreases in the accuracy of such emf readings. It is for these reasons that the most accurate thermoelectric thermometry employs null-balance (open-circuit or zero-current) measurements.

The approximation that thermoelectric circuits may be treated as being thermodynamically reversible simplifies the analyses of their relationships. Thus, the net change in the entropy of the surroundings of a closed thermoelectric circuit may be approximated as being equal to zero. While this is not rigorous, it simplifies the problem and gives results that are in excellent agreement with experimental findings.[14] This simplifies the analyses of the thermodynamic properties of thermoelectric circuits based on the net entropy changes of their surroundings as represented by the thermal reservoirs in the following analysis.

Two additional reservoirs are positioned at the midpoints of conductors A and B. Each of these central reservoirs is maintained at a temperature that is the average of those at the hotter and colder junctions, Figure 4. These provide a means to evaluate the average change in the entropy of the surroundings of each of the thermoelements in the circuit.

A unit quantity of electricity is made to flow through the circuit. The approximation of reversibility permits the assumption that the net change in the entropy, $\Delta\mathcal{S}$, of all of the reservoirs (at the junctions and along the conductors) is zero. This enables the net entropy change of the surroundings of a thermoelectric circuit to be given as

$$\Delta\mathcal{S} \cong \frac{-\pi_{AB}(T+\Delta T)}{T+\Delta T} + \frac{\pi_{AB}(T)}{T} - \frac{\beta_B(\Delta T)}{T+\frac{\Delta T}{2}} + \frac{\beta_A(\Delta T)}{T+\frac{\Delta T}{2}} = 0 \tag{7}$$

The first two terms of Equation 7 are multiplied by $\Delta T/\Delta T$ to obtain

$$\Delta\mathcal{S} \cong \left[\frac{-\frac{\pi_{AB}(T+\Delta T)}{T+\Delta T} + \frac{\pi_{AB}(T)}{T}}{\Delta T}\right]\Delta T - \frac{\beta_B(\Delta T)}{T+\frac{\Delta T}{2}} + \frac{\beta_A(\Delta T)}{T+\frac{\Delta T}{2}} = 0 \tag{8}$$

In the limit, as ΔT approaches zero, the difference quotient within the brackets is $-\frac{d}{dT}\left(\frac{\pi_{AB}}{T}\right)$. Its substitution into Equation 8 yields

$$\Delta\mathcal{S} \cong -\frac{d}{dT}\left(\frac{\pi_{AB}}{T}\right)\Delta T - \frac{\beta_B(\Delta T)}{T+\frac{\Delta T}{2}} + \frac{\beta_A(\Delta T)}{T+\frac{\Delta T}{2}} = 0 \tag{9}$$

Using the definition of the Thomson coefficient, $\Delta T = 1K$, and since T is much greater than 1K, $T + \Delta T/2 = T + 1/2 \cong T$. This approximation permits Equation 9 to be written more simply as

$$\frac{d}{dT}\left(\frac{\pi_{AB}}{T}\right) \cong \frac{\beta_A}{T} - \frac{\beta_B}{T} \tag{10}$$

The indicated derivative reduces Equation 10 to

$$\frac{T\frac{d\pi_{AB}}{dT} - \pi_{AB}}{T^2} \cong \frac{\beta_A}{T} - \frac{\beta_B}{T} \tag{11}$$

Equation 11 is simplified and rearranged as

$$\frac{\pi_{AB}}{T} \cong \frac{d\pi_{AB}}{dT} + \beta_B - \beta_A \tag{12}$$

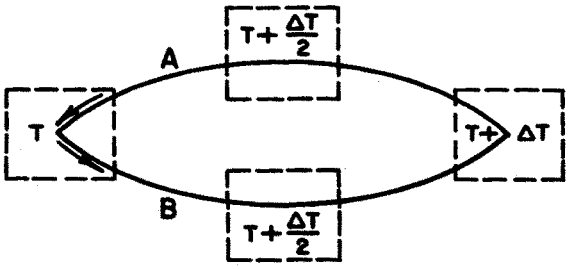

FIGURE 4 Closed thermoelectric circuit for the analysis of thermal phenomena. (From Pollock, D.D., *Thermoelectricity: Theory, Thermometry, Tool*, ASTM Special Technical Publication 852, American Society for Testing and Materials, Philadelphia, PA, 1985. With permission.)

Equation 12 represents the entropy change at a thermoelectric junction in a closed circuit because π_{AB} is the change in the heat content of the junction, and, divided by the absolute temperature, is (by the Nernst definition) the change in entropy of the junction for the given temperature.[17]

Equation 12, relating the Peltier and Thomson coefficients, is helpful as a means for the selection of materials for use in Peltier devices. Equation 12 is reexpressed for clarity as

$$-\frac{d\pi_{AB}}{dT} \cong -\frac{\pi_{AB}}{T} + (\beta_B - \beta_A) \tag{13}$$

If a maximum Peltier effect exists, $d\pi_{AB}/dT = 0$. This is used to obtain the optimum relationship between the two thermal effects as

$$\pi_{AB} \cong (\beta_B - \beta_A)T \tag{14}$$

Where data are available for the Thomson coefficients, the best combinations of thermoelements may be selected by means of simple calculations.

The fundamental thermodynamic theorem (Equation 6) is used in Equation 12 to obtain

$$\frac{\pi_{AB}}{T} \cong \frac{dE_{AB}}{dT} \tag{15}$$

Equation 15 gives the RSC of a thermocouple as a direct measure of the change in the entropy at a thermoelectric junction in closed circuits and may be rewritten as

$$\pi_{AB} \cong \frac{dE_{AB}}{dT} T \tag{16}$$

Equation 16 is helpful in understanding the operation of Peltier devices. It shows why combinations of thermoelements with large Peltier effects must be used for power generation or for refrigeration. The thermal efficiency is low in either case.

Another important relationship between the Seebeck and Thomson effects is obtained by starting with the derivative of Equation 16:

$$\frac{d\pi_{AB}}{dT} \cong \frac{dE_{AB}}{dT} + T\frac{d^2E_{AB}}{dT^2} \tag{17}$$

Equation 17 is reexpressed for clarity as

$$\frac{d\pi_{AB}}{dT} - \frac{dE_{AB}}{dT} \cong T\frac{d^2E_{AB}}{dT^2} \tag{18}$$

A similar expression is obtained from Equation 6:

$$\frac{d\pi_{AB}}{dT} - \frac{dE_{AB}}{dT} \cong -(\beta_B - \beta_A) \tag{19}$$

Equations 18 and 19 are equated to obtain

$$T\frac{d^2E_{AB}}{dT^2} \cong -(\beta_B - \beta_A) \tag{20}$$

which can be rewritten as

$$\frac{d^2E_{AB}}{dT^2} \cong \frac{\beta_A - \beta_B}{T} \tag{21}$$

The integration of Equation 21 provides the relationship being sought in the form of

$$\frac{dE_{AB}}{dT} \cong \oint_0^T \frac{\beta_A - \beta_B}{T}\,dT \cong \oint_0^T \frac{\beta_A}{T}\,dT - \oint_0^T \frac{\beta_B}{T}\,dT \tag{22}$$

Equation 22 is integrable because the quantities β/T are entropies, and based on the third law of thermodynamics, they approach zero as the temperature approaches zero.[17] On this basis, the thermoelectric energy of a thermocouple in a simple closed circuit is responsible for the difference between the entropies of the components of which it is composed. The restrictions noted for Equation 6 also hold for Equation 22. The Seebeck effect may not be ascribed to the algebraic difference of Thomson effects.

The use of Equation 22 in Equation 16 leads to another important relationship between the Thomson and Peltier coefficients. For closed thermoelectric circuits,

$$\pi_{AB} \cong \frac{dE_{AB}}{dT}\,T \cong \left(\oint_0^T \frac{\beta_A}{T}\,dT - \oint_0^T \frac{\beta_B}{T}\,dT\right)\mathrm{T} \tag{23}$$

Equation 23 may be simplified as

$$\pi_{AB} \cong \pi_A - \pi_B \tag{24}$$

In other words, since the integrals in Equation 22 are entropies, π_A and π_B are the entropies of the individual components forming a thermoelectric junction. Thus, the Peltier effect arises as a result of the entropy difference between the components of a junction. Heat (energy) is evolved when the carriers flow from a component with higher entropy to one with lower entropy. Heat is absorbed in the opposite case.

Equation 24 is one of the bases for the statements made earlier that the Peltier effect has no relation to contact potential.

Equation 22 permits the RSC of a thermocouple in a closed circuit to be given in terms of the entropy difference between its components. It is the thermodynamic basis for the concept that in terms of the energies involved, the RSC of a thermocouple is the algebraic sum of the ASCs of its component thermoelements. However, despite its common misinterpretation, Equation 22 does not hold for open-circuit emf measurements because, as noted in reference to Equation 6, the Thomson heat changes are zero, and the RSC is nonzero for this case.

The independence of the RSC of the Thomson effects arises solely from the fact that the potential difference (ASE) that exists in each of the thermoelements composing a thermocouple in a temperature gradient is present in open circuits. And, in a way analogous to Equation 22, the open-circuit RSC of a thermocouple is give by

$$\frac{dE_{AB}}{dT} = \alpha_A - \alpha_B \tag{25}$$

in which α_A and α_B are the ASCs of its components. Equation 25 is of fundamental importance because it permits the study and evaluation of the properties of individual thermoelements without

the need for recourse to any other thermoelements. The natures of α_A and α_B are best described by quantum mechanics, rather than thermodynamics, because of the special properties of the electrical carriers involved.[11]

One of the least complicated ways to visualize the concept of absolute Seebeck properties is to consider a thermocouple made of a normal conductor and a superconductor. The ASCs of superconductors are zero at temperatures lower than that at which they undergo the transition to superconduction.[18] A temperature gradient induces no potential difference (emf) within the superconductor (its ASE equals zero), but does produce one in the normal conductor. The emf generated by this thermocouple is just that originating in the normal thermoelement. At present, this technique is applicable to temperatures below about 120 K.

Elemental lead (Pb) is sometimes used for thermoelectric reference purposes. This means that it is used as a reference thermoelement (with established thermoelectric properties) as one leg of a thermocouple. The ASCs of other thermoelectric materials then are calculated using Equation 25. One reason lead is used is that its ASC is comparatively small with respect to most other thermoelectric materials. So, when lead is used as a reference thermoelement, the RSC of the thermocouple largely arises as a result of the ASC of the other thermoelement. This technique is limited by the relatively low melting point of Pb, and it now is used for reference purposes at temperatures below room temperature.

Very pure platinum now is generally used as a reference thermoelement. Its high melting point, established thermoelectric properties, and stability in oxidizing atmospheres make it more useful over a broader range than lead.

Reference materials with formally standardized ASCs are yet to be established.

The thermodynamic reference temperature and that of absolute thermoelectric properties is 0 K, Equation 22. Any convenient, readily reproducible temperature can be used for practical reference purposes. The melting point of ice at one atmosphere pressure, 0°C, is most generally used in thermometry as the practical reference temperature because of its ready availability and ease of practical reproducibility.[19]

2.3 Thermoelectric Laws

The relationships discussed here were developed primarily for thermoelectric thermometry. When two thermoelements of the same homogeneous material form a thermocouple, no emf will be produced because α_A and α_B in Equation 25 are identical.

It also follows from Equation 25 that if no temperature difference exists between the ends of a *homogeneous* conductor, the net emf along the conductor will be zero even though temperature gradients exist between its ends. In this case any number of conductors can be connected in series and their net emf will be zero. Series of conductors can be made to form the measuring junction of a thermocouple with no effect on its calibration. This effect is included in the *Law of Intermediate Conductors* that states that the ASCs of any *homogeneous* conductors are zero when their ends are at the *same* temperature.

Another law of the same name states that the RSCs of two thermocouples composed of thermoelements A-C and C-B, each of whose junctions are at the same temperatures, may be expressed as $dE_{AB}/dT = \alpha_A - \alpha_C + \alpha_C - \alpha_B = \alpha_A - \alpha_B$. Thermoelements, such as Pt, that are common to both thermocouples are used in this way to pair thermoelements. In this case the contribution of the common thermoelement is denoted above by α_C.

A fourth law is the *Law of Successive Temperatures.* This law is a consequence of integrating Equation 25 over successive temperature ranges, where T_o is a reference temperature and $T_o < T_1 < T_2 < T_3$,

$$E_{AB} = \int_{T_o}^{T_1} (\alpha_A - \alpha_B)dT + \int_{T_1}^{T_2} (\alpha_A - \alpha_B)dT + \int_{T_2}^{T_3} (\alpha_A - \alpha_B)dT \qquad (26)$$

which is the same as

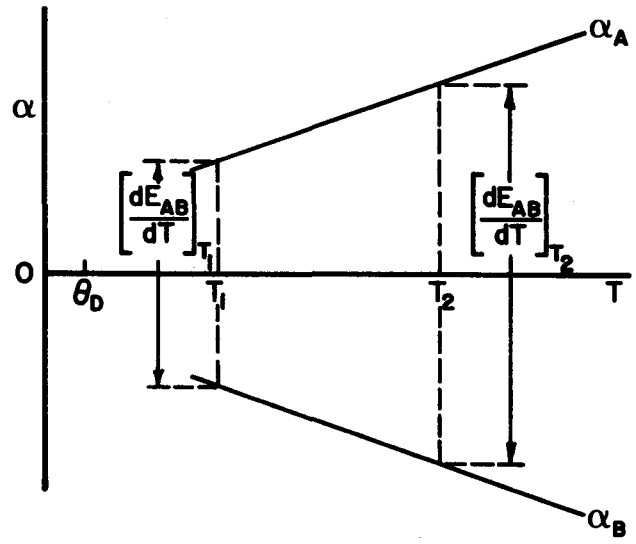

FIGURE 5 Schematic diagram of the thermoelectric properties of a thermocouple in terms of its component thermoelements. (From Pollock, D.D., *Thermoelectricity: Theory, Thermometry, Tool*, ASTM Special Technical Publication 852, American Society for Testing and Materials, Philadelphia, PA, 1985. With permission.)

$$E_{AB} = \int_{T_o}^{T_3} (\alpha_A - \alpha_B) dT \tag{26a}$$

In effect, the emf of a given thermocouple composed of homogeneous thermoelements can be measured or represented by the sum of its emfs over successive temperature ranges. This is very useful in the calibration of thermocouples and in the establishment of emf-temperature characteristics over wide temperature ranges. Equation 26 is also of help in understanding the influence of circuitry, including extension wires, in thermoelectric thermometry.[20]

2.4 Absolute Thermoelectric Properties

Thermocouple properties can only be explained by the concept of absolute thermoelectric properties because, as was shown previously,

$$\frac{dE_{AB}}{dT} = \alpha_A - \alpha_B \tag{25}$$

In other words, the ASC of each component of a thermocouple must be understood in order to understand the thermoelectric properties of a thermocouple.[21] Two widely differing pairs of thermoelements are discussed here as a means of understanding the thermoelectric characteristics of most thermocouples.

The first case is that of two thermoelements whose ASCs have both different signs and slopes; Figure 5. The RSC of thermocouple A-B is obtained graphically from Figure 5 for any temperature by means of the algebraic sum indicated by Equation 25.

The individual ASCs of the thermoelements A and B are given for $T > \theta_D$, where θ_D is the Debye temperature, as

$$\alpha_A = C_1 + m_A T \tag{27a}$$

and

$$\alpha_B = C_2 + m_B T \tag{27b}$$

Here C_1 and C_2 are empirical constants and the respective slopes are m_A and m_B. The RSC of thermocouple A-B, Equation 25, is obtained as

$$\frac{dE_{AB}}{dT} = C_3 + (m_B - m_A)T \quad \text{or} \quad dE_{AB} = [C_3 + (m_B - m_A)T]dT \tag{28}$$

where another empirical constant $C_3 = C_2 - C_1$. Equation 28 represents an element of area between the curves so that the RSE generated by thermocouple A-B is the area between the curves obtained by integration over the temperature range between the reference and measuring junctions. It will be noted that the lower temperature (reference temperature) may be selected as that being most convenient. If the reference junction is selected and maintained at a given temperature, T_o, the emf of thermocouple A-B is expressed using Equation 28 as

$$E_{AB} = \int_{T_o}^{T} [C_3 + (m_B - m_A)T]dT \tag{29}$$

The integration of Equation 29 over the temperature range of interest gives the emf of thermocouple A-B as

$$E_{AB} = C_3(T - T_o) + 1/2 \,.\, (m_B - m_A)(T^2 - T_o^2) \tag{30a}$$

or as

$$E_{AB} = E_o + C_3(T - T_o) + 1/2 \,.\, (m_B - m_A)(T^2 - T_o^2) \tag{30b}$$

where E_o is a constant of integration, when Equation 26 is used, to account for the emf between 0K and T_o. Equation 30b includes a term that contains the difference of squares of the temperatures. It is a nonlinear function of temperature. High degrees of thermoelectric nonlinearity were originally considered to be undesirable for use in thermometry because they required both more complex expressions than those given by Equations 30a and 30b and correspondingly more expensive measuring/controlling instrumentation. This problem is no longer of concern with contemporary equipment.

The most desirable situation is one in which the ASCs of two thermoelements A and D are parallel functions of temperature. In this ideal case, the slopes will be equal ($m_A = m_D = m$) and the ASCs are given by

$$\alpha_A = C_1 + mT \tag{27a}$$

and

$$\alpha_D = C_4 + mT \tag{31}$$

Then, $\alpha_D - \alpha_A = C_4 - C_1 = C_5$, another constant, because the temperature-dependent terms vanish, and the RSC of couple A-D is

$$\frac{dE_{AD}}{dT} = C_4 - C_1 = C_5 \tag{32}$$

Thus, the RSE of this thermocouple is

$$E_{AD} = \int_{T_o}^{T} C_5 dT = C_5(T - T_o) \tag{33}$$

where T_o again is a reference temperature.

The emf of couple A-D is a linear function of the temperature difference. A relationship of this kind was considered by manufacturers of thermometric devices to be ideal when contrasted to that shown by couple A-B, Equation 30a. Components associated with thermoelectric thermometry and electrical circuits based on linear behavior are more readily made and calibrated than those based on nonlinear responses of sensing devices. This would simplify the production of more accurate and more economical temperature measuring and control devices.

This practical consideration is one of the reasons for the relatively few combinations of metals and alloys in common use as components of standard thermocouples. While no two thermocouple alloys have exactly the same slopes, pairs of thermoelements are available with relatively small differences between their slopes, Equation 27. This causes the quadratic term of Equation 30a to be relatively small compared to the linear term. None of these thermocouples have ideally linear thermoelectric characteristics. To a good first approximation such thermocouples are considered to approach a linear emf-temperature characteristic.

On the basis of the foregoing, it is seen that the temperature-dependent terms of Equations 27a and 27b are of fundamental importance in the understanding of the absolute thermoelectric properties of thermocouple elements. As noted previously, these are best described by quantum mechanics because of the nature of the electrical carriers.[11]

Acknowledgment

I am deeply indebted to Dr. R.P. Reed, of the Sandia National Laboratories, for his helpful comments and for the terminology used in this chapter.

References

1. Seebeck, T. J., Ueber den magnetismus der galvenische kette, *Abh. K. Akad. Wiss. Berlin*, 289, 1821.
2. Seebeck, T. J., Magnetische polarisation der metalle und erze durck temperatur-differenz, *Abh. K. Akad. Wiss. Berlin*, 265, 1823.
3. Seebeck, T. J., *Ann. Phys. (Leipzig)[2]*, 6, 1, 1826.
4. Seebeck, T. J., Methode, Platinatiegel auf ihr chemische reinheit durck thermomagnetismus zu prufen, *Schweigger's J. Phys.*, 46, 101, 1826.
5. Pollock, D. D., *Physics of Engineering Materials*, Prentice Hall, Englewood Cliffs, NJ, 1990, 330.
6. Peltier, J. C. A., Nouvelles expériences sur la caloricité des courants electrique, *Ann. Chem. Phys.*, 56, 371, 1834.
7. Thomson, W., An account of Carnot's theory of the motive power of heat, *Proc. R. Soc. Edinburgh*, 16, 541, 1849.
8. Thomson, W., On a mechanical theory of thermo-electric currents, *Philos. Mag. [5]*, 3, 529, 1852.
9. Thomson, W., Account of researches in thermo-electricity, *Philos. Mag. [5]*, 8, 62, 1854.
10. Thomson, W., On the electrodynamic qualities of metals, *Philos. Trans. R. Soc. London*, 146, 649, 1856.
11. Pollock, D. D., *Thermocouples, Theory and Properties*, CRC Press, Boca Raton, FL, 1991, chap. 5.
12. Bridgeman, P. W., *The Thermodynamics of Electrical Phenomena in Metals*, Dover, New York, 1961, chap. 2.
13. Roesser, F., Thermoelectric Thermometry, *J. Appl. Phys.*, 11, 388, 1940.
14. Benedict, R. P., *Fundamentals of Temperature, Pressure and Flow Measurements*, 3rd ed., Wiley-Interscience, New York, 1984, chap. 7.
15. Callen, H. B., Application of Onsager's reciprocal relations to thermoelectric, thermomagnetic and galvanomagnetic effects, *Phys. Rev.*, 78, 1349, 1948.
16. Callen, H. B., Irreversible thermodynamics of thermoelectricity, *Rev. Mod. Phys.*, 26, 237, 1954.
17. Darken, L. S. and Gurry, R. W., *Physical Chemistry of Metals*, McGraw-Hill, New York, 1953, 191.
18. Pollock, D. D., *Physical Properties of Materials for Engineers*, CRC Press, Boca Raton, FL, 1993, sect. 6.8.3.
19. Roeser, W. F. and Lonberger, S. T., *Methods of Testing Thermocouples and Thermocouple Materials*, NBS Circular 590, National Bureau of Standards, U.S. Government Printing Office, Washington, D.C., 1958.
20. Reed, R. P., Thermoelectric thermometry: a functional model, in *Temperature, Its Measurement and Control in Science and Industry, 5*, American Institute of Physics, New York, 1982, 915.
21. Thomson, W., On an absolute thermometric scale, *Philos. Mag. [4]*, 33, 313, 1848.

3

Conversion Efficiency and Figure-of-Merit

H. J. Goldsmid
University of New South Wales, Australia

3.1 Ideal Model

In order to obtain an expression for the conversion efficiency of a thermoelectric device, the rather idealized thermocouple shown in Figure 1 is considered. The thermocouple consists of a positive (p) and negative (n) branch (thermoelement) to which are attached metallic conductors A, B, and C of supposedly zero electrical resistance. The branches are of length L_p and L_n and of cross section area A_p and A_n where, in general, the ratios L_p/A_p and L_n/A_n are different from one another. In spite of suggestions to the contrary,[1] the steady-state condition is unaffected by the shape of the branches; they are shown of constant cross section area merely for convenience. An important assumption is that heat is transferred from the heat source at B to the heat sink at AC solely by conduction along the branches of the thermocouple. It should be clear that the connection of any number of such couples, electrically in series and thermally in parallel, affects the power handling capacity of the convertor but not its efficiency.

The thermocouple can be used in two ways. If a voltage source is connected across A and C so that an electric current is driven through the couple, it acts as a heat pump (or, more specifically, if A is negative and C is positive, as a refrigerator). Heat is pumped from the source at an absolute temperature T_1 to the heat sink at temperature T_2 by means of the Peltier effect. Alternatively, if a resistive load is placed across A and C, the supply of heat at B and its removal at AC causes an electric current to flow around the circuit due to the Seebeck effect; in other words, the thermocouple acts as a generator. It can be shown that the coefficient of performance of the couple when used as a refrigerator and its efficiency when used as a generator can both be related to a parameter, known as the figure-of-merit, that incorporates certain of the material properties of the two arms.

3.2 Thermoelectric Refrigeration

Cooling Power

The theory of the thermoelectric refrigerator will be discussed first. It is important to realize that, although the Peltier and Seebeck effects require junctions between thermoelements for their manifestation, they are essentially bulk phenomena, i.e., they depend on bulk rather than surface properties of the materials. Thus, when an electric current flows through a conductor it transports heat, which reveals itself in the Peltier effect when it has to be liberated or absorbed as the current passes

0-8493-0146-7/95/$0.00+$.50

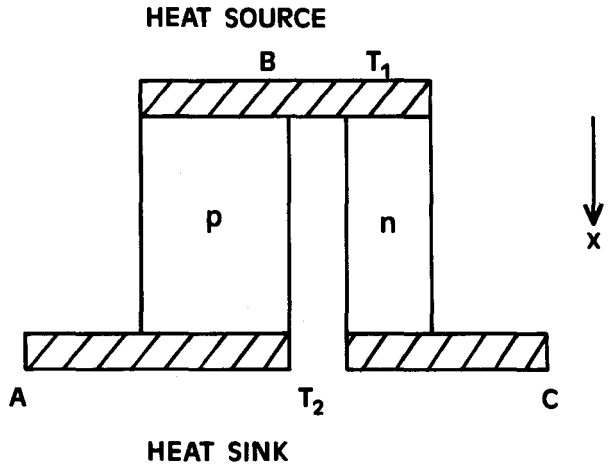

FIGURE 1. Thermocouple for heat pumping or generation.

into another conductor in which the heat transported is different. Thus, in the two branches, the heat transported from the source to the sink is

$$\left.\begin{aligned} q_p &= \alpha_p IT - \lambda_p A_p \, dT/dx \\ q_n &= -\alpha_n IT - \lambda_n A_n \, dT/dx \end{aligned}\right\} \tag{1}$$

in the two branches respectively, where α is the absolute Seebeck coefficient, I is the current, λ is the thermal conductivity, and dT/dx is the temperature gradient. From Kelvin's second law, the Peltier coefficient is given by αT, where T is the absolute temperature. It should be noted that α_p is positive and α_n is negative so that, in both cases, the Peltier heat flow αIT is opposed by the heat conduction $\lambda A dT/dx$.

The rate of heat generation per unit length within each branch, due to the Joule effect, is $I^2\rho/A$, where ρ is the electrical resistivity, which is the reciprocal of the electrical conductivity σ. This heat generation implies that the temperature gradient is nonuniform, where

$$\left.\begin{aligned} -\lambda_p A_p \frac{d^2T}{dx^2} &= \frac{I^2\rho_p}{A_p} \\ -\lambda_n A_n \frac{d^2T}{dx^2} &= \frac{I^2\rho_n}{A_n} \end{aligned}\right\} \tag{2}$$

For the present purposes it is assumed that the Seebeck coefficient is independent of temperature, which means that the Thomson effect is absent. This assumption can be reconsidered later.

Setting the boundary condition that $T = T_1$ at $x = 0$ (i.e., at the heat source) and also setting $T = T_2$ at $x = L_p$ or L_n (i.e., at the heat sink), Equation 2 can be solved to find

$$\left.\begin{aligned} \lambda_p A_p \frac{dT}{dx} &= -\frac{I^2\rho_p (x - L_p/2)}{A_p} + \frac{\lambda_p A_p (T_2 - T_1)}{L_p} \\ \lambda_n A_n \frac{dT}{dx} &= -\frac{I^2\rho_n (x - L_n/2)}{A_n} + \frac{\lambda_n A_n (T_2 - T_1)}{L_n} \end{aligned}\right\} \tag{3}$$

Equations 1 and 3 can be combined to obtain the rate of heat flow at $x = 0$,

$$\left.\begin{aligned} q_p (x = 0) &= \alpha_p IT_1 - \frac{\lambda_p A_p (T_2 - T_1)}{L_p} - \frac{I^2\rho_p L_p}{2 A_p} \\ q_n (x = 0) &= -\alpha_n IT_1 - \frac{\lambda_n A_n (T_2 - T_1)}{L_n} - \frac{I^2\rho_n L_n}{2 A_n} \end{aligned}\right\} \tag{4}$$

If, then, q_p and q_n are added at x = 0, the cooling power q_C at the heat source is obtained.

$$q_C = (\alpha_p - \alpha_n)IT_1 - K(T_2 - T_1) - I^2R/2 \tag{5}$$

where the thermal conductance of the two branches in parallel is

$$K = \frac{\lambda_p A_p}{L_p} + \frac{\lambda_n A_n}{L_n} \tag{6}$$

and the electrical resistance of the two branches in series is

$$R = \frac{L_p \rho_p}{A_p} + \frac{L_n \rho_n}{A_n} \tag{7}$$

Equation 5 reveals the interesting result (often assumed without proof) that half the Joule heating ($I^2R/2$) arrives at the heat source while, presumably, the other half turns up at the heat sink.

Figure-of-Merit

When Equation 5 is inspected, it is seen that the Peltier cooling term $(\alpha_p - \alpha_n)IT_1$ varies linearly with the electric current I, whereas, of course, the Joule heating term $I^2R/2$ varies as the square of the current. This means that there must be a particular current I_q at which the cooling power reaches its maximum value. This current is easily found by setting $dq_C/dI = 0$ which occurs when

$$I_q = \frac{(\alpha_p - \alpha_n)T_1}{R} \tag{8}$$

and the maximum cooling power is then

$$(q_C)_{max} = \frac{(\alpha_p - \alpha_n)^2 T_1^2}{2R} - K(T_2 - T_1) \tag{9}$$

This equation reveals that a positive cooling effect cannot be achieved if the temperature difference between the junctions is too great. In fact, there is a maximum temperature difference $(T_2 - T_1)_{max}$ which is found by setting $(q_C)_{max} = 0$. Clearly,

$$(T_2 - T_1)_{max} = \frac{(\alpha_p - \alpha_n)^2 T_1^2}{2KR} \tag{10}$$

The figure-of-merit of the thermocouple is defined as

$$Z = \frac{(\alpha_p - \alpha_n)^2}{KR} \tag{11}$$

so Equation 10 can be rewritten as

$$(T_2 - T_1)_{max} = \frac{1}{2} Z T_1^2 \tag{12}$$

It will be shown later that the same figure-of-merit applies for thermoelectric generation. However, at this point, some of the implications of Equation 12 should be considered. Also, the usual situation should be discussed where the required temperature difference $(T_1 - T_2)$ is less than the maximum that can be achieved.

Thermoelectric refrigeration is unlikely to be practical unless the maximum temperature difference is a significant fraction of the absolute temperature. For example, this method of cooling would be dismissed out of hand if it were not able to yield a source temperature $T_1 = 273$ K (i.e., 0°C) with a sink temperature of, say, $T_2 = 303$ K (i.e., 30°C). If these values are substituted into Equation 12 it is found that they correspond to a value of Z equal to 0.8×10^{-3} K^{-1}. This was,

in fact, the order of magnitude of the figure-of-merit for the thermocouples available in the early 1950s when development work started on new thermoelectric materials based on semiconductors.[2,3] This work eventually led to thermocouples having a figure-of-merit of the order of 3×10^{-3} K^{-1} with a corresponding maximum temperature depression of some 80 K.[4] Sometimes use can be made of the dimensionless figure-of-merit ZT instead of Z and it becomes clear that, in seeking new thermoelectric materials, one should be looking for values of ZT of the order of unity or greater.

It will be apparent that the figure-of-merit Z, as defined by Equation 12, is a characteristic not of a pair of materials but, rather, of a particular couple, since it includes terms that involve the relative dimensions of the thermoelements. For a given pair of materials, the highest value of Z is reached when the product RK is minimized. Of course, R rises and K falls as the ratio of length to cross section area increases and, indeed, a thermocouple can be designed for a given cooling power and electric current by altering the ratio in both arms. What is important, however, is to maintain a preferred relationship between L/A in one arm and the other. It is, in fact, a trivial exercise to show that RK is minimized when

$$\frac{L_n A_p}{L_p A_n} = \left(\frac{\rho_p \lambda_n}{\rho_n \lambda_p}\right)^{1/2} \tag{13}$$

When this equation is satisfied it is indeed possible to talk about the figure-of-merit of a pair of materials, giving it the value

$$Z = \frac{(\alpha_p - \alpha_n)^2}{[(\lambda_p \rho_p)^{1/2} + (\lambda_n \rho_n)^{1/2}]^2} \tag{14}$$

This figure-of-merit embodies the properties that common sense leads us to expect to be relevant. The Seebeck (and Peltier) coefficients are required to be large and of opposite signs in the two materials. In addition the thermal conductivity and the electrical resistivity should be low. In other words, the reversible thermoelectric effects should dominate over the irreversible effects of heat conduction and Joule heating.

Actually, Equation 14 is rather cumbersome when attempting to find a good thermoelectric material, be it p-type or n-type, since it involves the properties of both thermoelements. It is for this reason that the figure-of-merit of a single material is encountered, defined as

$$z_{p,n} = \frac{\alpha_{p,n}^2}{\rho_{p,n} \lambda_{p,n}} \tag{15}$$

Only in special cases can this figure-of-merit z be accurately related to the true figure-of-merit Z. One such case is when the p-type and n-type materials are exactly equivalent to one another apart from the sign of the Seebeck coefficient. In other words $\alpha_p = -\alpha_n$ and $\lambda_p \rho_p = \lambda_n \rho_n$. Then $Z = z_p = z_n$. It is fortunate that this situation holds, at least approximately, for the materials that are used in thermoelectric refrigeration at ordinary temperatures.

Another case of some practical importance occurs when $\lambda\rho$ for one branch is negligibly small compared with that for the other branch. This is true, for example, if one of the branches is a superconductor.[5] If an n-type thermoelement, say, is combined with a superconductor to form a couple, the denominator on the right-hand side of Equation 14 becomes equal to $\lambda_n \rho_n$. Furthermore, the absolute Seebeck coefficient of any superconductor is effectively zero so the numerator becomes α_n^2 and then $Z = z_n$.

It will be realized that the common practice of equating the figure-of-merit of a couple with the average of the values of z for the two branches can lead to substantial errors but the single-material figure-of-merit is widely used in the literature and there is no doubt that it is of conceptual value. There does not seem to be any better quantity to employ when dealing with just one material.

Coefficient-of-Performance

Turning now to the optimization of the current through a refrigerating couple when $(T_2 - T_1)$ is less than its maximum value, the performance of any refrigerator is usually assessed in terms of a quantity known as the coefficient of performance ϕ, defined as the ratio q_C/W, where W is the rate at which electrical energy is supplied. Looking at the branches separately,

$$\left.\begin{aligned} W_p &= \alpha_p I (T_2 - T_1) + \frac{I^2 \rho_p L_p}{A_p} \\ W_n &= -\alpha_n I (T_2 - T_1) + \frac{I^2 \rho_n L_n}{A_n} \end{aligned}\right\} \tag{16}$$

It will be seen that electrical power is used to overcome the Seebeck effect as well as the Joule effect. The total power is

$$W = (\alpha_p - \alpha_n) I (T_2 - T_1) + I^2 R \tag{17}$$

The coefficient-of-performance is

$$\phi = \frac{q_C}{W} = \frac{(\alpha_p - \alpha_n) I T_1 - \frac{1}{2} I^2 R - K (T_2 - T_1)}{(\alpha_p - \alpha_n) I (T_2 - T_1) + I^2 R} \tag{18}$$

It is found that the optimum current, i.e., the one that yields the maximum coefficient-of-performance, by setting $d\phi/dI$ equal to zero. This gives a current

$$I_\phi = \frac{(\alpha_p - \alpha_n)(T_2 - T_1)}{R[(1 + Z T_M)^{1/2} - 1]} \tag{19}$$

where T_M, equal to $(T_1 + T_2)/2$, is the mean temperature. The corresponding coefficient-of-performance is

$$\phi_{max} = \frac{T_1[(1 + Z T_M)^{1/2} - T_2/T_1]}{(T_2 - T_1)[(1 + Z T_M)^{1/2} + 1]} \tag{20}$$

Multistage Refrigerators

It has been seen that there is a limit to the temperature depression that can be achieved using a single-stage refrigerator. However, in principle (but not in practice) any required temperature depression can be achieved (provided that T_1 is above the absolute zero) by using thermoelectric refrigerators in cascade. Multistage units are also of some use in improving the coefficient-of-performance when the temperature depression is close to the limit for a single stage.

The optimum design of a multistage thermoelectric refrigerator is no simple matter since the effective figure-of-merit for one stage is bound to be different from that for some other stage at a different mean temperature. However, something of the problem can be appreciated by discussing the general case.

Suppose that there are N stages, the Nth stage being that which operates at the lowest temperature. Then the nth stage ($n < N$) must have a cooling power that is the sum of that at the source and the electrical power used at N, $(N - 1)$, . . . and $(n + 1)$ stages. The coefficient-of-performance (COP) of the nth stage is designated ϕ_n and the cooling power at the Nth stage as q_N. The rate of working for the nth stage is $q_N(1 + 1/\phi_N)(1 + 1/\phi_{N-1}) \ldots (1 + 1/\phi_{n+1})$ and heat is delivered to the sink at the rate $q_N(1 + 1/\phi_N)(1 + 1/\phi_{N-1}) \ldots (1 + 1/\phi_1)$. The overall COP is $\phi = [(1 + 1/\phi_N)(1 + 1/\phi_{N-1}) \ldots (1 + 1/\phi_1) - 1]^{-1}$.

In order to get some idea of the likely value of the overall COP it can be assumed that each of the stages operates at some COP ϕ'. Then $\phi = [(1 + 1/\phi')^N - 1]^{-1}$. By using this relation it can easily be shown that the overall COP is going to be very low whenever the required temperature

difference is significantly greater than the maximum for a single stage. Nevertheless, multistage refrigerators using as many as six or more stages have been produced for special applications.

A common feature of all multistage refrigerators is their pyramidal shape. The Nth stage consists of no more than one or two thermocouples. Then, if the same current is used throughout, subsequent stages use rapidly increasing numbers of couples so as to pump the ever-increasing amount of heat that has to be passed on.

3.3 Thermoelectric Generation

Suppose that a load of resistance R_L is connected across the thermocouple in Figure 1 at A and C. It will also be supposed that the source supplies heat at the rate q so as to maintain a temperature difference $(T_1 - T_2)$ between the junctions. The emf produced by the generator is $(\alpha_p - \alpha_n)(T_1 - T_2)$ and this yields useful power across the load given by

$$W = \left[\frac{(\alpha_p - \alpha_n)(T_1 - T_2)}{(R_L + R)}\right]^2 R_L \tag{21}$$

Next, consider the rate at which heat is supplied by the source. Most of this heat is conducted to the sink through the thermocouple branches but it should not be forgotten that some is used to balance the Peltier effect associated with the flow of current. Also, just as for the case of thermoelectric refrigeration, half of the Joule heating in the arms finds its way to the source. If all these terms are included

$$q = K(T_1 - T_2) + (\alpha_p - \alpha_n) IT_1 - I^2R/2 \tag{22}$$

where the current I is equal to $(\alpha_p - \alpha_n)(T_1 - T_2)/(R_L + R)$.

The efficiency η is equal to W/q and its value depends to some extent on the way that the load is matched to the resistance of the generator. The condition for maximum power transfer is obtained if R_L and R are made equal to one another. However, if this condition is satisfied, the efficiency can never exceed 50% of the ideal thermodynamic value $(T_1 - T_2)/T_1$. Therefore, it is assumed that the load resistance is chosen so as to yield maximum efficiency. If the ratio R_L/R is denoted by m, it is required that $d\eta/dm = 0$. As shown by Ioffe,[2] the optimum value of m, identified as M, is given by

$$M = (1 + ZT_M)^{1/2} \tag{23}$$

Substituting this value into Equation 22, the efficiency is given by

$$\eta = \frac{(T_1 - T_2)}{T_1} \cdot \frac{(M - 1)}{(M + T_2/T_1)} \tag{24}$$

It will be seen that the ideal thermodynamic efficiency is degraded by the factor $(M - 1)/(M + T_2/T_1)$. The efficiency rises as M becomes greater. Since M depends only on the source and sink temperatures and on Z, it can be concluded that the same figure-of-merit holds for generation and refrigeration.

Consider the limiting cases of $ZT_M \ll 1$ and $ZT_M \gg 1$. When $ZT_M \ll 1$, $\eta \rightarrow [(T_1 - T_2)/T_1][ZT_M/2(1 + T_2/T_1)]$ so that the ideal efficiency is multiplied by a factor that is very much less than unity. On the other hand, when $ZT_M \gg 1$, $\eta \rightarrow (T_1 - T_2)/T_1$ which is the ideal thermodynamic efficiency. It so happens that currently available materials yield ZT_M of the order of unity at most temperatures of interest. If $ZT_M = 1$, $M = 1.4142$. $(M - 1)/(M + T_2/T_1)$, of course, depends on T_2/T_1 as well as on M. Typically, for a generator using a small temperature difference (i.e., one that works off low-grade heat) T_2/T_1 is close to unity and $(M - 1)/(M + T_2/T_1)$ would be about 0.17. As T_1/T_2 rises, this factor increases somewhat, reaching 0.21 when $T_1 = 2T_2$ and about 0.29 when $T_1 \gg T_2$. It is seen, then, that it is at present possible to obtain something like one quarter of the ideal thermodynamic efficiency using thermoelectric generation.

3.4 Temperature-Dependent Parameters

It has been assumed that α, ρ, and λ are all temperature independent. In practice, of course, this is never the case and a numerical computation must normally be made to find ϕ or η using parameters measured over the temperature range in question. Nevertheless, a reasonable estimation of the performance may be made using averaged parameters. The use of averages for ρ and λ seems to present little difficulty, since the irreversible effects that they characterize are taking place throughout the elements. Ioffe,[2] in fact, has proposed the averaging of the product $\rho\lambda$ rather than the separate parameters over the range of temperature that is applicable.

The Seebeck coefficient presents a little more difficulty. Consider the case of the thermoelectric refrigerator. Then there will be additional heating or cooling depending on the sign of the Thomson coefficient $\gamma = Td\ \alpha/dT$. It has been shown[6] that if the average value of α over the required temperature range is used, rather than the value at the cold junction, this takes care of the Thomson effect for most practical purposes. Thus, it is reasonable to use a figure-of-merit given by

$$Z = \frac{<\alpha_p - \alpha_n>^2}{(<\rho_p\ \lambda_p>^{1/2} + <\rho_n\ \lambda_n>^{1/2})^2} \tag{25}$$

where the angular brackets indicate temperature-averaged quantities. This approach is more likely to give a better approximation for thermoelectric refrigeration, where the temperature differences are generally a small fraction of the absolute temperature, than for thermoelectric generation, where the temperature differences can be much larger.

References

1. Landecker, K., *Proceedings, First International Conference on Thermoelectric Energy Conversion*, Arlington, Texas, IEEE, New York, 1976, 150.
2. Ioffe, A. F., *Semiconductor Thermoelements and Thermoelectric Cooling*, Infosearch, London, 1957.
3. Goldsmid, H. J. and Douglas, R. W., *Br. J. Appl. Phys.*, 5, 1954, 386.
4. Rosi, F. D., Abeles, B., and Jensen, R. V., *J. Phys. Chem. Solids*, 10, 1959, 191.
5. Goldsmid, H. J., Gopinathan, K. K., Matthews, D. N., Taylor, K. N. R., and Baird, C. A., *J. Phys. D: Appl. Phys.*, 21, 1988, 344.
6. Goldsmid, H. J., *Electronic Refrigeration*, Pion, London, 1986.

4

Thermoelectric Transport Theory

C. M. Bhandari
University of Allahabad
India

4.1 Introduction

To understand the behavior of a thermoelectric semiconductor[1-12] in all its details it is desirable to have a clear understanding of the kinds of problems one may encounter. It is not possible to give a comprehensive account of the vast spectrum of semiconductor transport phenomena in the span of one chapter. Understandably, the emphasis will be on those aspects that have a relevance in thermoelectric applications. A cursory glance at the best known thermoelectric materials in various temperature ranges of operation indicates that one often has to deal with a multivalley semiconductor with or without intervalley scattering of carriers.[13-18] The carriers may be scattered primarily by acoustic and optic phonons, neutral and ionized impurities, and to a lesser extent by grain boundaries.

Thermoelectric materials are usually heavily doped, and quite often narrow-band-gap materials. Both these situations make it imperative that, in a rigorous theoretical analysis, the effects of non-parabolicity of the energy bands are taken into consideration. At the upper end of the temperature range of operation of a thermoelectric device, minority-carrier effects make their presence felt, and their influence on various transport coefficients should not be overlooked. A number of material properties influence its thermoelectric behavior; on the other hand thermoelectric investigations yield valuable information about the same. In several situations even simple considerations may lead to meaningful results. Consequently, it is desirable to start with a sample representation of these and then gradually progress to more sophisticated and realistic models.

0-8493-0146-7/95/$0.00+$.50

4.2 Transport Processes in Semiconductors

Transport Coefficients

The theory of thermoelectric transport is essentially the domain of transport in semiconductors with the behavior of metals of minor interest. Semiconductors display almost all the essential features and complications of transport phenomena in solids. The relevant transport processes involve a flow of charge or energy or both. These "flows" arise due to external causes such as an electric field and temperature gradient which are referred to as "forces". In general, any force may give rise to any flow and the relationships between various "forces" and "flows" define the various transport coefficients that are characteristic of electrons (and holes) and phonons in the material.[13,19,20] Assuming that the electron and phonon systems depart only slightly from their equilibrium distributions a linear relationship can be obtained between "forces" and "flows". The choice of the "forces" depends upon certain considerations regarding the flow of electron and energy.

Consider a solid in contact with two reservoirs, one of energy, and the other of electrons. In the steady state a steady flow is maintained through the solid as are the differences in electrochemical potential (μ) and temperature (T) between the two points.

A good choice of the forces are grad(μ/T) and grad(1/T). The components of the flows of electrons ($\vec{j}$) and of energy ($\vec{w}$) are given by

$$\begin{aligned} -j_i &= \sum_{k=1}^{3} L_{ik}^{(1)} \frac{\delta}{\delta x_k}\left(\frac{\mu}{T}\right) + \sum_{k=1}^{3} L_{ik}^{(2)} \frac{\delta}{\delta x_k}\left(\frac{1}{T}\right) \\ w_i &= \sum_{k=1}^{3} L_{ik}^{(3)} \frac{\delta}{\delta x_k}\left(\frac{\mu}{T}\right) + \sum_{k=1}^{3} L_{ik}^{(4)} \frac{\delta}{\delta x_k}\left(\frac{1}{T}\right) \end{aligned} \tag{1}$$

The total energy flow can be written as a sum of W_e and W_p where e and p refer to the electron and phonon systems, respectively. In that case $L^{(3)} = L_e^{(3)} + L_p^{(3)}$ and the set of coefficients L_{ik} provide a complete description of the transport properties of the solid. The number of independent coefficients is reduced by taking the crystal symmetry into account.

The electric current density ($\vec{i} = -e\vec{j}$) and thermal current density ($\vec{w}$) can be expressed[19] in terms of grad(μ) and grad(T)

$$\begin{aligned} \vec{i} &= \frac{1}{e}\,\sigma \cdot grad\mu - \sigma \cdot \alpha \cdot gradT \\ \vec{w} &= \left(\pi - \frac{\mu}{e}\right)\vec{i} - \lambda \cdot gradT \end{aligned} \tag{2}$$

σ, α, π, and λ are, in general, second-order tensors which are related to the coefficient $L^{(n)}$ defined earlier. The advantage of writing the electric and thermal current densities as in Equation 2 is obvious: these parameters are easily obtainable in practice.

Electron Distribution and Boltzmann Equation

Statistical methods are employed when dealing with equations involving a large number of particles. A probability distribution function of $f(\vec{k},\vec{r},t)$ is introduced which describes the occupancy of allowed energy states. The most probable number of electrons in a volume element $d\vec{k}$ of the $\vec{k}$-*space* at time t is given by $(2/8\pi^{-3})\, f(\vec{k},\vec{r},t)d\vec{k}$. The function f around a point may change due to a number of mechanisms: external fields, diffusion, and collision processes. The total rate of change of f is given by

$$\frac{df}{dt} = \left(\frac{\delta f}{\delta t}\right)_{field} + \left(\frac{\delta f}{\delta t}\right)_{diff} + \left(\frac{\delta f}{\delta t}\right)_{coll} \tag{3}$$

In the steady state (df/dt) = 0. Substituting for the field and diffusion terms

$$-\left(\frac{\delta f}{\delta t}\right)_{coll} = +\vec{v}_k \cdot \vec{\nabla}_r f + \frac{1}{\hbar}\vec{F} \cdot \nabla_k f \tag{4}$$

Here $\vec{F}$ refers to an external force.

The basic problem is to solve this equation for $f(k)$. There are, in general, two methods to solve the Boltzmann equation. The variational method,[13] although more rigorous, is unsuitable for routine use due to its complicated procedure. On the other hand the relaxation time approach is widely used and is particularly useful in data analysis. It is possible to obtain a solution of the Boltzmann equation if one assumes the existence of a relaxation time $\tau(\vec{k})$ defined by

$$\left(\frac{\delta f}{\delta t}\right)_{coll} = -(f(\vec{k},\vec{r}) - f_o)/\tau(\vec{k}) \tag{5}$$

Electron Scattering Mechanisms

The next step is to obtain suitable expressions for the relaxation time for various electron (or hole) scattering processes. Among the important mechanisms that scatter electrons are phonons. In general, acoustic phonon scattering is invariably present, whereas in materials with two or more atoms per unit cell optical phonons also take part in the scattering. An electron in the state described by the electron wavevector $\vec{k}$ is scattered to a state described by $\vec{k}'$ as a result of an interaction with a phonon of wavevector $\vec{q}$. The problem is reduced to obtaining the matrix element of the interaction energy between initial and final states and then to calculate the transition probability. To simplify matters one usually considers the "adiabatic approximation", in which electron wavefunctions are assumed to keep pace with the ionic motion. The energy conservation condition has to be satisfied. The momentum of the electron-phonon system may be conserved (Normal or N-process) or it may change by a reciprocal lattice vector (Umklapp or U-process). The scattering terms require a knowledge of the phonon distribution which, in turn, requires knowledge of the electron distribution. The problem is simplified if the phonon distribution is replaced by its equilibrium value. The assumption implies that the electron and the phonon systems produce entropy independently of each other. This amounts to neglecting the phonon-drag effects which are a direct consequence of the coupling of the entropy production in the two systems via the electron-phonon interaction.[13,14,19] The scattering by vibrational modes is contributed to both by acoustic and optical phonons, although the latter are significant at higher temperatures and in polar semiconductors.

4.3 The Electronic Transport

Single Spherical Band Model

In several cases it is possible to express the carrier relaxation time in terms of carrier energy E

$$\tau(E) = aE^s \tag{6}$$

s is referred to as the scattering parameter and takes different values for various scattering mechanisms. The proportionality constant "a" may, among other things, be a function of temperature.

The carrier mobility can be written as

$$\mu = (e/m_c^*)\langle\tau\rangle \tag{7}$$

where m_c^* is the conductivity (inertial) effective mass, and $\langle\tau\rangle$ is the average of τ(E) over all energies.

$$\langle\tau\rangle = \frac{\int_o^\infty \tau(E)E^{3/2}\left(\frac{\delta f_o}{\delta E}\right)dE}{\int_o^\infty E^{3/2}\left(\frac{\delta f_o}{\delta E}\right)dE} \tag{8}$$

where $f_o = [1 + \exp(\eta - \xi)]^{-1}$.

η and ξ are the reduced carrier energy (E/kT) and reduced Fermi energy (E_F/kT), respectively. With the help of these equations the carrier mobility is obtained as[18]

$$\mu = \frac{2}{3} a(kT)^s (e/m_c^*)\, F_{s+1/2}(\xi)/F_{1/2}(\xi) \tag{9}$$

$F_l(\xi)$ are Fermi integrals defined by

$$F_l(\xi) = \int_o^\infty \frac{x^l dx}{[1 + \exp(x - \xi)]} \tag{10}$$

The Fermi energy depends upon carrier concentration and effective mass through the relation

$$n = \frac{4}{\sqrt{\pi}} (2\pi m^* kT/h^2)^{3/2} F_{1/2}(\xi) \tag{11}$$

With mobility and carrier concentrations known in terms of the Fermi energy, one can obtain the electrical conductivity. The dimensionless electrical conductivity is given by[21]

$$\sigma' = \left(\frac{k}{e}\right)^2 \frac{T}{\lambda_L} \sigma = \beta F_{s+1/2}(\xi)/(s + 1/2)! \tag{12}$$

where

$$\beta = 2(2\pi k)^{3/2} k^2 A'/eh^3 \tag{13}$$

and

$$A' = T^{5/2} m^{*3/2} \mu/\lambda_L \tag{14}$$

Here λ_L refers to the lattice thermal conductivity.

β and A′ are usually referred to as material parameters. Increased performance requires a large mobility to lattice thermal conductivity ratio and a higher value for the effective mass. The thermoelectric figure-of-merit is usually defined by $z = \alpha^2\sigma/\lambda$ where α, σ, and λ refer to the Seebeck coefficient and electrical and thermal conductivity of the thermoelement material. A high value of the material parameter A′ would indicate a high figure-of-merit.

Two-Band Conduction

A serious shortcoming of the single band conduction model is that the Seebeck coefficient tends to become very large as the Fermi level diverges from the band edge. This difficulty can be avoided by considering a second band or by making the assumption that, instead of diverging indefinitely from the band edge with a decrease in carrier concentration, the Fermi level approaches its intrinsic value.[6,23] In the non-degenerate limit the inclusion of the second band is essential. A simple two-band model[22,23] can be considered with both the bands having parabolic energy-wavevector relationships. There will be a contribution to the electric current density from both the bands. If the electrical conductivity contributions from the two bands are represented by σ_e and σ_h then the total electrical conductivity is given by $\sigma = \sigma_e\, \sigma_h$. However, the total Seebeck coefficient is not a simple sum of the individual contributions from the two bands; rather, it is given by

$$\alpha = (\alpha_e\sigma_e + \alpha_h\sigma_h)/(\sigma_e + \sigma_h) \tag{15}$$

The electronic thermal transport can also be considered with the heat flux densities from the two bands given by[7]

$$\vec{w}_e = \alpha_e T \vec{i}_e - \lambda_e \frac{\delta T}{\delta x} \tag{16}$$

$$\vec{w}_h = \alpha_h T \vec{i}_h - \lambda_h \frac{\delta T}{\delta x} \tag{17}$$

The contributions from the Peltier effect have been expressed in terms of partial Seebeck coefficients. To satisfy the condition of zero current (for defining thermal conductivity) i_e and i_h must be equal and opposite. This gives

$$i_e = -i_h = \frac{\sigma_e \sigma_h}{\sigma_e + \sigma_h}(\alpha_h - \alpha_e)\frac{\delta T}{\delta x} \tag{18}$$

With the help of Equations 16 and 17 one obtains

$$\lambda = \lambda_e + \lambda_h + \frac{\sigma_e \sigma_h}{\sigma_e + \sigma_h}(\alpha_h - \alpha_e)^2 T \tag{19}$$

Here λ is the electronic contribution to the thermal conductivity (usually referred to as λ_e). The total electronic contribution is not simply the sum of the conductivities of the two bands. The third term arises from the fact that a heat flow can take place without a charge flow. Electron-hole pairs are created at the hot end by the absorption of energy from the source. These pairs move down the temperature gradient and recombine at the cold end, releasing the energy of recombination. This process is sometimes referred to as bipolar thermodiffusion.[25] In narrow band gap semiconductors the inclusion of the other band in theoretical formulations significantly affects the various transport properties.

Multivalley Effects

In several semiconductors the transport properties cannot be adequately described in terms of a single spherical band model. The conduction and valence band structures possess several equivalent extrema. In silicon the conduction band has six minima along the [100] direction at points close to the zone boundary. The equal energy surfaces near the minima are ellipsoids of revolution with energy near the band edges given by[15,20]

$$E(\vec{k}) = \frac{\hbar^2}{2}\left[\frac{k_1^2}{m_1} + \frac{k_2^2}{m_2} + \frac{k_3^2}{m_3}\right] \tag{20}$$

suffixes 1, 2, and 3 refer to the components along the principal directions of the equal energy ellipsoids. For an electron in the conduction band a density-of-states effective mass is defined (for a single valley) as

$$m_d^* = (m_1 m_2 m_3)^{1/3} \tag{21}$$

The conductivity (or inertial) effective mass is given by

$$m_c^{*-1} = \frac{1}{3}(m_1^{-1} + m_2^{-1} + m_3^{-1}) \tag{22}$$

The total density-of-states effective mass is given by

$$m_{d,t}^* = N_v^{2/3}(m_1 m_2 m_3)^{1/3} \tag{23}$$

N_V being the number of equivalent valleys in the band under consideration.

Material Parameter

The material parameter (Equation 14) determines the thermoelectric "worth" of a material. A large value for A′ corresponds to a good thermoelectric performance. Let A_s' and A_e' represent the material parameter[5] corresponding to a single spherical valley and that corresponding to an ellipsoidal energy surface. One can then write[5]

$$A_e'/A_s' = (m_2 m_3/m_1 m^*)^{1/2}\frac{\langle \tau_e \rangle \lambda_s}{\langle \tau_s \rangle \lambda_1} \tag{24}$$

Here λ_i and m_i are the components of the thermal conductivity and effective mass tensors along the principal axis. If it is assumed that the same type of scattering is predominant in both the cases then the energy terms in the relaxation time averages cancel out. The constants appearing in the two relaxation rates can also be assumed to be the same. Further assuming that the density-of-states effective masses are the same in the two cases, one gets[5]

$$A'_e/A'_s = (m_2m_3/m_1^2)^{1/3}(\lambda_s/\lambda_1) \tag{25}$$

Next consider N_V equivalent ellipsoidal energy surfaces of the type described. Defining the corresponding material parameter as A'_m one can write

$$A'_m/A'_s = \frac{\lambda_s}{\lambda_m}\frac{N_v}{3}(m_1m_2m_3)^{1/3}[m_1^{-1} + m_2^{-1} + m_3^{-1}] \tag{26}$$

If it is assumed that the density-of-states effective mass corresponding to a single valley is the same as that for the single ellipsoidal valley and is given by Equation 21, the two transverse components can be taken to be equal, i.e., $m_2 = m_3$ and $m_1 = \gamma m_2$ and Equation 26 can be expressed as

$$A'_m/A'_s = \frac{\lambda_s}{\lambda_m}N_v(1 + 2\gamma)/3\gamma^{2/3} \tag{27}$$

Implicit in this derivation is the assumption that the scattering of the charge carriers between different valleys can be ignored. It is concluded from these arguments that a large number of equivalent valleys tend to increase the material parameter and hence improve the thermoelectric performance. One may look at it from a different angle. The parameter A′ is proportional to $\mu m^{*3/2}$, and for N_V valleys $m_d^* = N_v^{2/3}\ (m_1m_2m_3)^{1/3}$. For the case of acoustic phonon scattering of the carriers one obtains

$$\mu^{-1}\alpha\ m_c^*(m_1m_2m_3)^{1/2} \tag{28}$$

This gives

$$A_{ac}\ \alpha\ N_v/m_c^* \tag{29}$$

A number of equivalent extrema along with a small conductivity effective mass appears to favor the thermoelectric performance. For polar optical mode scattering similar conclusions are obtained.

Intervalley Scattering

The apparent favorable effect on the thermoelectric performance of a number of valleys in the conduction or valence bands may be offset by the presence of additional scattering of carriers between these valleys.[15,17,18] Both high-energy acoustic and optical phonons take part in the intervalley scattering. The conservation of momentum requires that only short-wavelength phonons near the band-edge participate in the scattering. These phonons have frequencies which are almost independent of the wavevector. Which of the modes interact with the carriers depends upon the symmetries of the initial and final states. For example, in silicon there are two kinds of situations for intervalley scattering: those between opposite valleys (such as <100> to <$\bar{1}$00>), denoted as a g-process, or those between non-opposite valleys (such as <100> to <010>), referred to as an f-process. The former requires longitudinal optical phonons, whereas the latter requires a combination of longitudinal acoustic and transverse optical phonons.[14]

The effect of this additional scattering[17] can be taken into consideration in a relatively simple manner as outlined by Herring. As described previously the phonons participating in this process lie near the zone boundary where the acoustic and the optical branches are either degenerate or close to each other. The average phonon energy taking part in the usual intravalley scattering (either emission or absorption) is considerably lower than that of the carriers, whereas this is not the case for phonons taking part in the intervalley scattering. In a simple model the frequency of

the phonon participating in the intervalley scattering can be approximated by an average of the transverse and acoustic mode frequencies at the zone boundary. The total relaxation time of carriers can be obtained by the addition of the inverse relaxation rates usually followed in all relaxation time approaches. Following Herring's method W_1 and W_2 are defined by the strengths of the coupling of carriers to intra- and intervalley phonons. The intervalley scattering relaxation time is then given by[15,17,26]

$$\tau_{iv}^{1} = \frac{W_2\{[(E/k\theta_i) + 1]^{1/2} + \exp(\theta_i/T)Re[(E/k\theta_i) - 1]^{1/2}\}}{[exp(\theta_i/T) - 1]} \tag{30}$$

Here $\theta_i = \hbar w_i/k$.

Herring calculated the temperature dependence of the mobility (μ/μ_o) vs. (T/θ_i) where $\mu_o = \mu_{ac}\,(T/\theta_i)^{3/2}$. Using this framework and taking W_2/W_1 as an adjustable parameter the effect of the intervalley scattering can be obtained and compared with the observed values of the electronic thermal conductivity and the electrical conductivity. However, an independent determination of W_2/W_1 would be desirable.

4.4 Non-Parabolicity of the Energy Bands

Energy Dependence of the Effective Mass

In a large number of situations the energy of the carriers can be satisfactorily expressed assuming a quadratic variation with the wavevector. The simplification arises from the utilization of the first term of a more general expansion of $E(\vec{k})$. A more rigorous theoretical formulation requires the inclusion of the next higher order term in the expansion and results in a deviation from the usual parabolic relationship. The effect of this deviation becomes pronounced at high carrier densities. Moreover, narrow-band-gap semiconductors are likely to show a significant degree of non-parabolicity even at low carrier densities. Heavy doping of thermoelements makes it imperative that the effects of band non-parabolicity are taken into consideration.[27–33]

In obtaining expressions for various transport coefficients an approach similar to the one adopted by Kane[28] can be considered. Defining the longitudinal and transverse components of the carrier wavevectors by k_L and k_T, it follows that:

$$\frac{\hbar^2}{2}\frac{2k_T^2}{m_{TO}^*} + \frac{\hbar^2}{2}\frac{k_L^2}{m_{LO}^*} = E\left(1 + \frac{E}{E_g}\right) \tag{31}$$

m_{LO}^* and m_{TO}^* refer to the longitudinal and transverse components of the effective mass tensor near the band extrema. The effective mass becomes energy dependent and is given by

$$m_j^* = m_{jO}^*(1 + 2E/E_g) \tag{32}$$

Effect on the Transport Coefficients

The effect of the energy dependence of the effective mass is likely to be significant in narrow-band-gap semiconductors. Expressions can be obtained for the relevant transport coefficients for a particular type of carrier scattering. Scattering by acoustic phonons is invariably present and the corresponding relaxation time which takes account of the non-parabolicity is given by[31–33]

$$\tau_{ac}^{-1}\ \alpha\ [\eta(1 + \beta_g^{\eta})]^{1/2}(1 + 2\beta_g\eta) \tag{33}$$

Here $\eta = E/kT$ is the reduced carrier energy, and $\beta_g = kT/E_g$ is the inverse of the reduced band gap. The transport coefficients can be expressed in terms of the generalized Fermi integrals defined by

$${}^{n}_{L}I^{m}_{l}(\xi,\beta_g) = \int_0^{\infty}\left(-\frac{\delta f}{\delta\eta}\right)\eta^n[\eta(1 + \beta\eta)]^m(1 + 2\beta_g\eta)^l d\eta \tag{34}$$

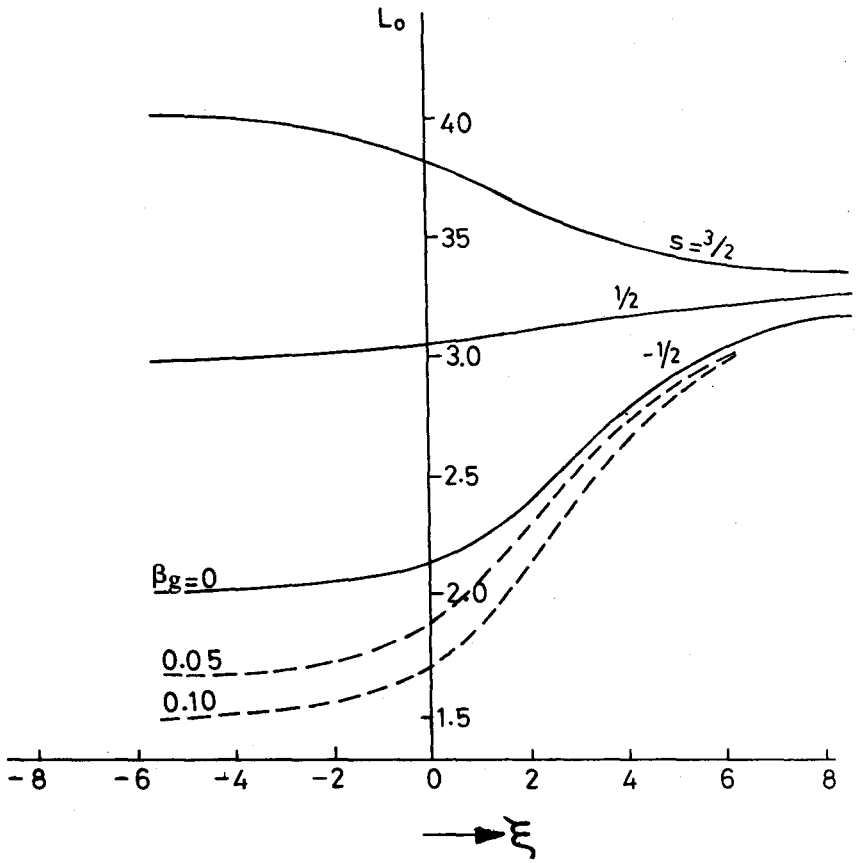

FIGURE 1 Lorenz factor L_o plotted against reduced Fermi energy ξ for different values of the scattering parameter s. The effect of band non-parabolicity is incorporated into the calculations through the parameter β_g.

The indices *n, m, l* take different values for various scattering processes. The carrier concentration is given in terms of Fermi level by

$$n = \frac{(2m^*_{do}kT)^{3/2}}{3\pi^2\hbar^3} {}^0L_0^{3/2} \tag{35}$$

The reduced electrical conductivity is given by

$$\sigma' = \frac{N\gamma T}{m^*_c\lambda_L} {}^0L^1_{-2} \tag{36}$$

where $\gamma = k^2hC_{11}/3\pi^2\varepsilon_1^2$. C_{11} and ε_1 refer to the longitudinal elastic constant and the deformation potential, respectively.

If one defines ${}^1L^1_{-2}/{}^0L^1_{-2} = \delta$, the reduced Seebeck coefficient and the Lorenz factor are given by the following equations:

$$\alpha' = [\delta(\xi) - \xi] \tag{37}$$
$$L_0 = {}^2L^1_{-2}/{}^0L^1_{-2} - \delta^2$$

In Figure 1 the variation of the Lorenz factor is displayed with the reduced Fermi energy for several values of the scattering parameter s corresponding to a parabolic band. The parameter β_g takes into account the effect of band non-parabolicity. Figure 2 shows the calculated variation of λ_c/λ_L for bismuth telluride at 300 K. The calculations include the effect of non-parabolicity of the conduction band along with the intervalley scattering. The figure also displays the estimated effect

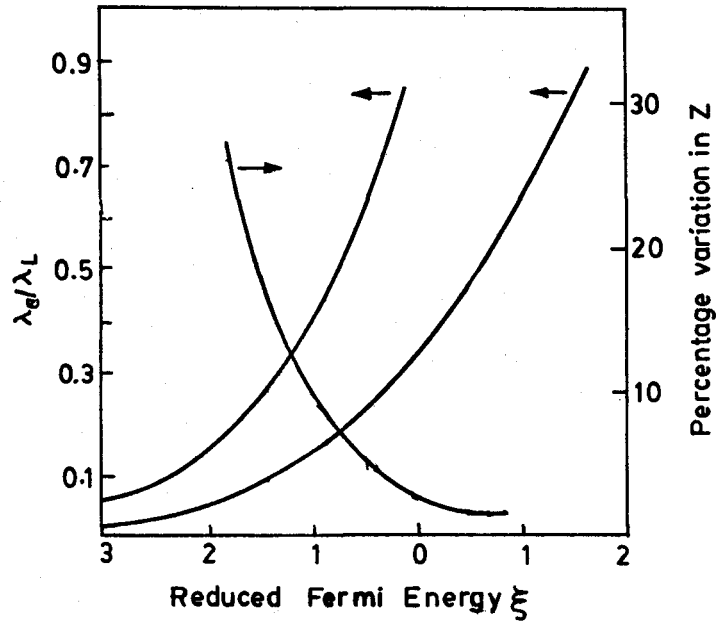

FIGURE 2 Calculated variations of λ_e/λ_L plotted against ξ in bismuth telluride at 300 K. The parameters pertain to a polycrystalline material. The effect of intervalley scattering is included ($W_2/W_1 = 0.5$). Also displayed is the effect of minority carriers. The percentage change corresponds to the estimated change corresponding to single band conduction.

of the minority carriers on the thermoelectric figure-of-merit Z. The quantity plotted is the estimated percentage change in Z if only single band conduction is taken into consideration.

4.5 Thermal Transport

A low thermal conductivity material is obviously a good choice for a thermoelement provided the power factor $\alpha^2\sigma$ is not affected adversely. The means to achieving this have formed the central theme of most of the thermal conductivity studies in the context of thermoelectric applications.[1–12] The requirement of heavy doping to enhance the electrical conductivity, on the other hand, gives rise to a significant electronic contribution to the thermal conductivity. Theoretical considerations[6,7,34,35] lead to the conclusion that higher values of Z can be obtained when $\lambda_e \sim \lambda_L$. This can be realized when the dependence of Z on the following two factors is considered: the electrical properties of the material and a degradation in performance due to parasitic heat loss.[35] The requirement for the electronic thermal conductivity to be comparable to the lattice contribution is due to a balance in the interplay of the effectiveness of the two factors.

Several methods of obtaining a minimum in λ_L have been outlined:[6,7,36] in solid solutions, this is achieved by a selective scattering of phonons by lattice disorder, and in fine-grained materials use is made of the selective scattering of phonons by the grain-boundaries. Although there has been substantial progress in this area a significant breakthrough is unlikely, since (1) the mechanism employed to scatter phonons is likely to scatter the charge carriers, and (2) a large electronic thermal conductivity accompanies a high electrical conductivity, large λ_e, which is a necessary price to be paid. Details of the minimization of thermal conductivity is described elsewhere in the handbook.

4.6 Phonon Drag

In the theory of phonon heat transport electrons play the role of scattering centers whereas they themselves are assumed to be in equilibrium. In the same manner the phonon system is assumed

to be in equilibrium while describing electronic transport even though they act as scattering agents. These assumptions are not always valid and a proper account has to be taken of the resulting "phonon drag" on electrons and "electron drag" on phonons. First proposed by Gurevich,[37] a number of authors have described the drag effects in metals[38–42] and later in semiconductors.[25,43–45] A simple treatment due to Bailyn[41] is given here to illustrate the basic mechanism.

Consider phonons moving along a bar of length δx. The phonon spectrum is assumed to consist of one average acoustic branch. Let $\delta N(\vec{q})$ be the number of phonons of wavevector $\vec{q}$ that will be annihilated before reaching the cold end in order to satisfy the boundary conditions. The annihilation occurs due to the interaction with electrons by momentum-conserving or momentum-destroying processes, or by processes which do not involve electrons, such as the impurity scattering. If $\alpha'(\vec{q};\vec{q} + \vec{G})$ is the relative probability that any one of the excess phonons will be destroyed by an Umklapp (momentum-destroying) process then

$$\alpha'(\vec{q};\vec{q} + \vec{G}) = \frac{B(\vec{q};\vec{q} + \vec{G})}{B_0 + \sum_{G'} B(\vec{q};\vec{q} + \vec{G}')} \tag{38}$$

B values represent absolute probabilities and B_0 refers to the sum of probabilities for all processes other than electron-phonon scattering. The sum in the denominator includes all Umklapp processes in which a given phonon may participate. During each Umklapp process the phonons transfer a momentum $\hbar(\vec{q} + \vec{G})$ to the electron system. Thus, the probable x-component of the momentum transferred to the electronic system is

$$P_x = \delta N(\vec{q})\alpha'(\vec{q};\vec{q} + \vec{G}_n)[\hbar(\vec{q} + \vec{G})]_x \tag{39}$$

The force on the electron from phonons of wavevector $\vec{q}$ is given by

$$F_x(\vec{q}) = \Sigma \frac{\delta N}{\delta x}\frac{\delta x}{\delta t}[\hbar(q + G]_x\alpha'(\vec{q};\vec{q} + \vec{G}) \tag{40}$$

δt is the time taken by the phonon of wavevector $\vec{q}$ before being annihilated. Further,

$$\delta x/\delta t(\vec{q}) = [\vec{\nabla}\omega(\vec{q})]_x \tag{41}$$

With the substitution $F_x = -|e|\ \varepsilon_x N$, one obtains

$$\alpha_g = \varepsilon_x/\left(\frac{\delta T}{\delta x}\right) = (3Ne)^{-1}\Sigma\Sigma\alpha'(\vec{q};\vec{q} + \vec{G})\hbar(\vec{q} + \vec{G})\nabla_q\omega\frac{\delta N}{\delta T} \tag{42}$$

A relatively simple calculation[46,47] of α_g can be made at low temperatures when phonon-phonon collisions are few. The phonon-electron collisions are assumed to be relatively abundant. A metallic conductor is considered with a temperature gradient dT/dx. It is further assumed that the phonon system behaves as a perfect gas which exerts a pressure $P = U(T)/3$ on the electron system, where $U(T)$ refers to the phonon energy density. The temperature gradient gives rise to a pressure gradient, or a net directed force per unit volume, F_x, on the electrons.

$$F_x = -\frac{dP}{dx} = -\frac{1}{3}\frac{dU}{dT}\frac{dT}{dx} \tag{43}$$

The force gives rise to a current which is proportional to the temperature gradient. This is the so-called phonon drag thermoelectric current. In an open circuit an electric field ε_x will be set up to balance F_x. One can write $Ne\varepsilon_x = F_x = 0$, N being the concentration of the conduction electrons. Further,

$$Ne\varepsilon_x = \frac{1}{3}\frac{dU}{dT}\frac{dT}{dx} \tag{44}$$

Defining $C_l = dU/dT$ (the lattice specific heat per unit volume)

$$\alpha_g = \frac{\varepsilon_x}{dT/dx} = C_l/3Ne \tag{45}$$

The phonon drag affects both α and σ. However, the effect on σ is not as pronounced as that on α. The difference is due to the fact that the latter is a first-order effect, whereas the former is of the second order.[48]

4.7 In a Magnetic Field

Application of a magnetic field has a profound effect on the transport coefficients in addition to a whole range of galvanomagnetic and thermomagnetic phenomena.[13] These diverse phenomena are very useful in the understanding of the electronic structure of solids. The Lorenz force acting on an electron in a magnetic field of a few kilogauss is usually greater than the force exerted by usually attainable electric fields within the solid, and is therefore a powerful tool to probe into an electronic structure.[13,49] The Boltzmann equation in the presence of a magnetic field now includes an extra term

$$(\dot{f}_k)_{mag} = -\frac{e}{\hbar}(\vec{v} \times \vec{B})(\delta f_k/\delta \vec{k}) \tag{46}$$

The effect of a magnetic field is quite unlike that of an electric field. While considering the latter f_k^o is substituted for f_k, giving rise to a drift which is balanced by the scattering processes. It follows that

$$e(\vec{v} \times \vec{B})\frac{\delta f_k^0}{\delta k} = e(\vec{v} \times \vec{B})\frac{\delta f_k^0}{\delta E_k}\frac{\delta E_k}{\delta k} = e(\vec{v} \times \vec{B}) \cdot \vec{v}\hbar\frac{\delta f_k^0}{\delta E_k} \tag{47}$$

This obviously equals zero. The velocity vectors rotate about the field without a change in energy. The effect of the magnetic field has to be considered by considering the next term in the expansion of f_k. The magnetic field has the effect of changing the direction of motion of the electrons; it thereby acts as a sort of scattering agent. This scattering is asymmetric, being always to one side for a given field and type of carrier. In general, the effect of a magnetic field is to increase the electrical resistance. In the case of magnetoresistance the general rule is expressed as

$$\frac{\Delta\rho}{\rho_0} = F\left(\frac{B}{\rho_0}\right) \tag{48}$$

ρ_o is the resistivity in zero field and F is a function which depends upon the material and the geometrical configuration. Obviously the magnetoresistance depends upon the relative orientation of the field and the current. Usually two configurations are considered, the transverse, when $\vec{B}$ and $\vec{i}$ are perpendicular, and the longitudinal, when they are parallel.

Bipolar effects are of importance in the context of thermomagnetic effects. In thermoelectric applications the presence of both types of carriers has to be avoided to obtain a high value for the figure-of-merit. However, the bipolar effects are not always undesirable.[7]

A detailed discussion of various thermo-galvanomagnetic phenomena is available in the literature.[50,51]

4.8 Low-Dimensional Systems

Quantum Size Effects in Two-Dimensional Systems

The study of systems that are spatially restricted in one or two dimensions has drawn a good deal of attention during recent years.[52] When the de Broglie wavelength λ_D of an electron is comparable

to the size of the sample, quantum size effects become important and significantly influence the transport properties. Fabrication of thin films and quantum-well-wires using advanced techniques such as MBE have made it possible to conceive devices based upon these effects. The study of electronic transport in these systems requires a knowledge of electron-scattering mechanisms. The important scattering mechanisms remain the same (acoustic and optic phonons, ionized and neutral impurities) with different energy dependences.[53–56] Once the relaxation time is known the usual Boltzmann equation approach can be followed to obtain the transport coefficients.[57,58] The variation of the Fermi energy with carrier concentration may also be quite different and characteristic of the system considered. Model calculations based on these ideas indicate future possibilities in the context of thermoelectric applications.

A simple two-dimensional system can be considered in which electrons are confined to move in a plane. The behavior of the quasi-two-dimensional (Q2D) gas is characterized by eigenfunctions Ψ_k and energy ε_k, given by

$$\Psi_k = A^{-1/2}\exp(ik_x x + ik_y y) \tag{49}$$

$$\varepsilon_k = \hbar^2(k_x^2 + k_y^2)/2m^* \tag{50}$$

Here $\vec{k} = (k_x, k_y)$ is a two-D vector, and A = ab is the area of the rectangular plane of length a and breadth b. The density-of-states function $Z(\varepsilon)$ is independent of the carrier energy

$$Z(\varepsilon) = 2\sum_k \delta(\varepsilon - \varepsilon_k) = Am^*/\pi\hbar^2 \tag{51}$$

This can be compared with the parabolic variation of the density-of-states for the bulk material. The Fermi level for the Q2D-gas is also characteristic of the system. This can be obtained from the usual normalization condition

$$\sum_k f_0(\varepsilon_k) = N$$

N being the total number of electrons. The Fermi energy is given by[53]

$$E_F = kT \ln[\exp(\pi\hbar^2 n_s / m^* kT) - 1] \tag{52}$$

where $n_s = N/a$ is the surface density of carriers.

As the density-of-states and Fermi levels are different from that of the bulk material, the transport coefficients are expected to differ. The energy dependences for the various relaxation rates are also different and thus influence the transport properties. The relaxation times for scattering by acoustic phonons and by impurities are found to be energy independent in the Q2D model considered.[53,59]

A more realistic situation arises when the motion along the third dimension is also included, the motion being quantized in accordance with the requirements of a one-dimensional box of thickness d (between z = 0 and z = d). The eigenfunctions and eigenvalues are given by

$$\Psi = (2/\Omega)^{1/2}\exp[ik_x x + ik_y y]\sin(l\pi z/d) \tag{53}$$

$$\varepsilon = \hbar^2(k_x^2 + k_y^2)/2m^* + l^2\varepsilon_o;\ l = 1,2,3,\ldots. \tag{54}$$

where $\varepsilon_o = \pi^2\hbar^2/2m^*d^2$.

This model gives results pertaining to a bulk gas if $d \gg D$, and the earlier simple Q2D model if $d \ll D$.

Quasi-One Dimensional Systems

Consider a gas of carriers confined to move in a long thin wire embedded in an insulating cladding. The wire may be taken to be of square cross section (sides *a*) and length L along the Z-direction. The eigenfunctions and eigenvalues are given by

$$\Psi_{n,l,k}(x,y,z) = \frac{2}{\sqrt{abL}} \sin(n\pi x/a) \sin(l\pi y/a) \exp(ikz) \tag{55}$$

$$\varepsilon_{n,l,k} = \frac{\pi^2\hbar^2}{2m^*}\left(\frac{n^2 + l^2}{a^2}\right) + \hbar^2k^2/2m^* \tag{56}$$

where k is the electron wavevector along the z-direction.

It is of interest to consider the size-quantum limit (SQL) which assumes that all electrons are populated in the ground state ($n = n' = l = l' = 1$). This situation may arise if the wire is thin and the energy differences between sub-bands become large and the inter-sub-band transitions are not allowed in a certain temperature range. As regards the scattering one may take acoustic phonon scattering to be the dominant scattering. The energy dependence of the relaxation time is $E^{+1/2}$ instead of the usual $E^{-1/2}$ for the bulk material, and is given by[56]

$$\tau_{ac}^{-1}(SQL) = D\,E_k^{-1/2} \tag{57}$$

where D is a constant independent of carrier energy.

In the nondegenerate limit the Fermi energy is given by[57]

$$E_F = k\,T\,ln\left(\frac{\sqrt{2\pi}\hbar n_e a^2}{\gamma\delta\sqrt{mkT}}\right) \tag{58}$$

where $\gamma = \sum_n \exp(-n^2E_n^o/kT)$.

$$\delta = \sum_l \exp(-l^2E_l^o/kT)$$

The Seebeck coefficient for the Q1D system in the SQL and nondegenerate limit is given by[57]

$$\alpha^{Q1D} = \frac{k}{e}\left\{2 - ln\left[\left(\frac{2\pi}{m^*kT}\right)^{1/2}\hbar n_e a^2\right]\right\} \tag{59}$$

This can be compared with the Seebeck coefficient for the bulk material. α^{Q1D} increases with a decrease in a. For parameters pertaining to the GaAs system the results obtained by Kubakaddi and Mulimani[57] show that for a <110 A at 300 K, α^{Q1D} may be greater than the corresponding bulk value.

The low-field mobility for a nondegenerate Q1D gas as obtained by Lee and Vassell[56] is given by

$$\mu = \frac{2e}{m^*kT}\sum_{n,l}\int_0^\infty dE_{nlk}E_{nlk}^{1/2}\tau(E_{nlk})\exp(-E_{nlk}/kT)x \left[\sum_{n,l}\int dE_{nlk}E_{nlk}^{-1/2}\exp(-E_{nlk}/kT)\right]^{-1} \tag{60}$$

The mobility can be calculated as a function of temperature for various values of the dimension parameter a assuming the size-quantum limit. Calculations have also been presented for various scattering mechanisms and, over a certain range of temperature and the parameter a, the mobility is found to be greater than that for the corresponding bulk material. Figure 3 gives the variation of the mobility of a Q1D gas with temperature and the dimension parameter.

Phonon drag effects have also been discussed in low-dimensional systems by a number of workers.[60–62] The phonon drag thermopower is found to peak at a certain temperature; for AlGaAs the temperature is around 13 K.

Among the future thermoelectric materials multilayered systems utilizing the quantum-size effect are under active consideration. With advanced techniques such as molecular-beam epitaxy new exotic material systems are close to being realized in practice.

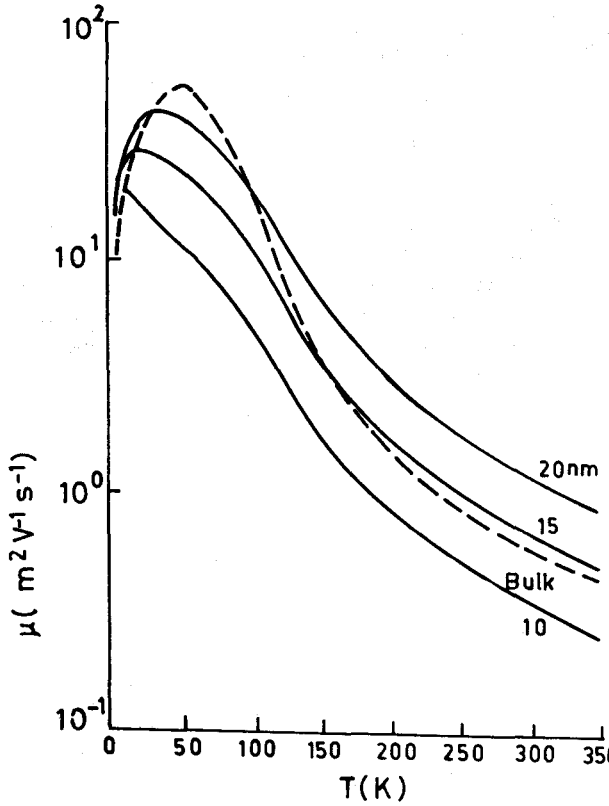

FIGURE 3 Electron mobility plotted against temperature for different values of the dimension parameter a in quasi-one-dimensional structures. The broken curve shows the three-dimensional case. (From Lee, J. and Vassell, M. O., *J. Phys. C: Solid State Phys.*, 17, 2525, 1984. With permission.)

References

1. Ioffe, A. F., *Semiconductor Thermoelements and Thermoelectric Cooling*, Infosearch, London, 1957.
2. Cadoff, I. B. and Miller, E., *Thermoelectric Materials and Devices*, Reinhold, New York, 1959.
3. Goldsmid, H. J., *Applications of Thermoelectricity*, Methuen Monograph, London, 1960.
4. Egli, P. H., Ed., *Thermoelectricity*, John Wiley & Sons, New York, 1960.
5. Ure, R. W. and Heikes, R. R., Eds., *Thermoelectricity: Science and Engineering*, Interscience, London, 1961.
6. Rowe, D. M. and Bhandari, C. M., *Modern Thermoelectrics*, Holt Saunders, London, 1983.
7. Goldsmid, H. J., *Electronic Refrigeration*, Pion Ltd., London, 1988.
8. Rosi, F. D., Hockings, E. F., and Lindenblad, N. E., Semiconducting materials for thermoelectric power generation, *RCA Rev.*, 22, 82, 1961.
9. Burshteyn, A. I., *Semiconductor Thermoelectric Devices*, Temple Press, London, 1964.
10. Rosi, F. D., Thermoelectricity and thermoelectric power generation, *Solid State Electron.*, 11, 833, 1968.
11. Wright, D. A., Materials for direct conversion thermoelectric generators, *Metall. Rev.*, 15, 147, 1970.
12. Rowe, D. M., Thermoelectric power generation, *Proc. Inst. Electr. Eng.*, 125 (11R), 1113, 1978.
13. Ziman, J. M., *Electrons and Phonons*, Cambridge University Press, London.
14. Ridley, B. K., *Quantum Processes in Semiconductors*, Oxford University Press, New York, 1981.
15. Seeger, K., *Semiconductor Physics*, Springer-Verlag, Berlin, 1973.
16. Bhandari, C. M. and Rowe, D. M., *Thermal Conduction in Semiconductors*, Wiley Eastern Ltd., New Delhi, 1988.
17. Herring, C., Transport properties of a many valley semiconductor, *Bell Systems Tech. J.*, 34, 237, 1955.

18. Long, D., Scattering of conduction electrons by lattice vibrations in silicon, *Phys. Rev.*, 120, 2024, 1960.
19. Callen, H. B., *Phys. Rev.*, 73, 1349, 1948.
20. Drabble, J. R. and Goldsmid, H. J., *Thermal Conduction in Semiconductors*, Pergamon Press, Oxford, 1961.
21. Ure, R. W., Jr., Practical limits to thermoelectric figure-of-merit II, *Energy Convers.*, 12, 45, 1972.
22. Simon, R., Thermoelectric figure-of-merit of two-band semiconductors, *J. Appl. Phys.*, 33, 1830, 1962.
23. Rittner, E. S. and Neumark, G. F., Theoretical bound on the thermoelectric figure-of-merit of two-band semiconductors, *J. Appl. Phys.*, 34, 2071, 1963.
24. Parrott, J. E., *Rev. Int. Hautes Temper. Refract. Fr.*, 16, 393, 1979.
25. Price, P. J., Ambipolar thermodiffusion of electrons and holes in semiconductors, *Philos. Mag.*, 46, 1252, 1955.
26. Bhandari, C. M. and Rowe, D. M. Electronic contribution to the thermal conductivity of narrow band gap semiconductors—effect of nonparabolicity of bands, *J. Phys. D: Appl. Phys.*, 18, 873, 1985.
27. Zawadzki, W., *Adv. Phys.*, 23, 437, 1974.
28. Kane, E. O., Band structure of indium antimonide, *J. Phys. Chem. Solids*, 1, 249, 1957.
29. Ravich, Y. I., Efimova, B. A., and Tamarchenko, V. I., Scattering of current carriers and transport phenomena in lead chalcogenides, *Phys. Status Solidi (b)*, 43, 11, 1971.
30. Kolodziejczak, J. and Zhukotynski, S., *Phys. Status Solidi*, 5, 145, 1964.
31. Ravich, Y. I., Efimova, B. A., and Smirnov, I. A., in *Semiconducting Lead Chalcogenides*, Stil'bans, T. S., Ed., Plenum, New York, 1970.
32. Smirnov, I. A. and Ravich, Y. I., *Sov. Phys. — Semiconductors*, 1, 739, 1967.
33. Rowe, D. M. and Bhandari, C. M., Electronic thermal transport in thermoelectric materials — effect of band nonparabolicity, *Fifth International Conference on Thermoelectric Energy Conversion*, Arlington, 1986, p. 62.
34. Chasmar, R. P. and Stratton, R. J., The thermoelectric figure-of-merit and its relation to thermoelectric generators, *J. Electron. Control*, 7, 52, 1959.
35. Goff, J. F. and Lowney, J. R., The integral formulation of the thermoelectric figure-of-merit: effect of lattice thermal conduction, *11th IECEC*, p. 1561.
36. Parrott, J. E., Thermal conductivity: a guide to improved thermoelectric materials, *Proceedings of the 1st International Conference on Thermoelectrics*, 1987, p. 186.
37. Gurevich, J., *Phys. USSR*, 9, 447, 1945.
38. Klemens, P. G., *Austr. J. Phys.*, 7, 520, 1954.
39. Hanna, I. I. and Sondheimer, E. H., *Proc. R. Soc. A*, 239, 247, 1957.
40. Bailyn, M., Transport in metals: effect of nonequilibrium phonons, *Phys. Rev.*, 112, 1587, 1958.
41. Bailyn, M., The phonon drag component of the thermoelectric power of the alkali metals at low temperatures, *Philos. Mag.*, 5, 1059, 1960.
42. Collins, J. G. and Ziman, J. J., *Proc. R. Soc. A*, 264, 60, 1961.
43. Frederikse, H. P. R., Thermoelectric power of Ge below room temperature, *Phys. Rev.*, 92, 248, 1953.
44. Herring, C., Theory of thermoelectric power of semiconductors, *Phys. Rev.*, 96, 1163, 1954.
45. Price, P. J., Theory of transport effects in semiconductors: thermoelectricity, *Phys. Rev.*, 104, 1223, 1956.
46. MacDonald, D. K. C., *Thermoelectricity — An Introduction to the Principles*, John Wiley & Sons, 1962.
47. Herring, C., *Proc. Int. Coll. Garmisch-Partenkirchen*, Vieweg, Braunschweig, 1958.
48. Huebener, R. P., Thermoelectric power of lattice vacancies in gold, *Phys. Rev.*, 146, 502, 1966.
49. Jan, J. P., Galvanomagnetic and thermomagnetic effects in metals, *Solid State Phys.*, 5, 1, 1957.
50. Tsidilowski, I. M., *Thermomagnetic Effects in Semiconductors*, Infosearch, London, 1962.
51. Putley, E. H., *The Hall Effect and Related Phenomena*, Butterworths, Sevenoaks, Kent, 1960.
52. Ando, T. and Mori, S., Electronic properties of a semiconductor superlattice, *J. Phys. Soc. Jpn.*, 47, 1518, 1979.
53. Arora, V. K. and Awad, F. G., Quantum size effects in semiconductor transport, *Phys. Rev. B*, 23, 5570, 1981.
54. Ridley, B. K., *J. Phys. C: Solid State Phys.*, 15, 5899, 1982.
55. Lee, J. and Spector, H. N., *J. Appl. Phys.*, 54, 3291, 1983.

56. Lee, J. and Vassel, M. O., Low-field electron transport in quasi-one-dimensional semiconducting structure, *J. Phys. C: Solid State Phys.*, 17, 2525, 1984.
57. Kubakaddi, S. S. and Mulimani, B. G., Thermopower enhancement in semiconducting quantum-well wires for acoustic phonon scattering, *J. Appl. Phys.*, 58(9), 3643, 1985.
58. Kearney, M. J. and Butcher, P. N., A calculation of the effect of sub-band structure of the thermopower of a quasi-one-dimensional wire, *J. Phys. C: Solid State Phys.*, 19, 5429, 1986.
59. Kawaji, S., *J. Phys. Soc. Jpn.*, 27, 906, 1969.
60. Nicholas, R. J., *J. Phys. C: Solid State Phys.*, 18, L695, 1985.
61. Fletcher, R., Maan, J. C., and Weimann, G., Experimental results on the high field thermopower of a two-dimensional electron gas in a GaAs-$Ga_{1-x}Al_xAs$ heterojunction, *Phys. Rev. B*, 32, 8477.
62. Cantrell, D. G. and Butcher, P. N., A calculation of the phonon-drag contribution to thermoelectric power in two-dimensional systems, *J. Phys. C: Solid State Phys.*, 19, L429, 1986.

5

Optimization of Carrier Concentration

C. M. Bhandari
University of Allahabad
India

David M. Rowe
University of Wales,
Cardiff, U.K.

5.1 Introduction

The thermoelectric figure-of-merit is defined by $Z = \alpha^2\sigma/\lambda$ where α, σ, and λ refer to the Seebeck coefficient, electrical conductivity, and the thermal conductivity of the thermoelectric material. This parameter is of central importance in any program to optimize the thermoelectric properties.[1–13] The Seebeck coefficient and electrical conductivity depend strongly on the Fermi level,[6,14,15] which in turn depends upon the carrier concentration, the carrier effective mass, and the temperature. In theoretical formulations it is convenient to express the thermoelectric transport coefficients in terms of the Fermi energy E_F (conventionally measured from the band edges). Since the thermal conductivity depends only weakly on the carrier concentration (n) the general effect of an increase in carrier concentration would manifest itself in the figure-of-merit, through the power factor $\alpha^2\sigma$ (Figure 1).

5.2 Single Band Conduction

Classical Statistics

It is convenient to start from simple theoretical considerations and then gradually develop more refined models. Consider a single band (either an electron or hole band) with the usual parabolic density-of-states distribution and assume that the carriers obey classical statistics. The Seebeck coefficient[3] can be expressed as

$$\alpha = \mp\frac{k}{e}(5/2 + s - \xi) \qquad (1)$$

The signs $\mp$ refer to the contributions from electrons and holes, respectively. $\xi = (E_F/kT)$ is the reduced Fermi energy, k is the Boltzmann's constant, T the absolute temperature, s refers to the

0-8493-0146-7/95/$0.00+$.50

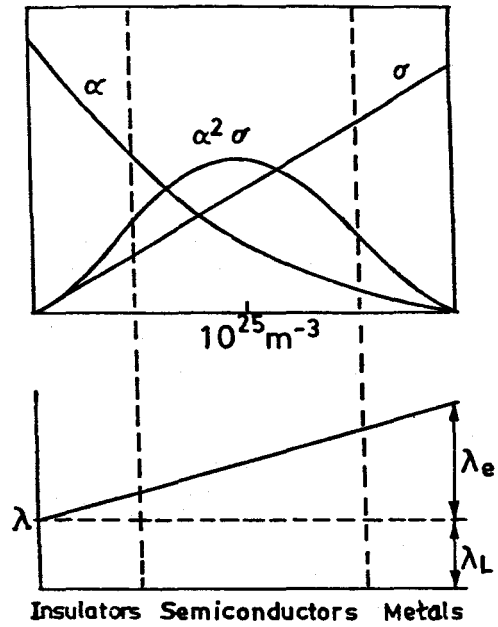

FIGURE 1 Dependence of α, σ, λ, and $\alpha^2\sigma$ on the concentration of free carriers (schematic).

scattering parameter, and it is assumed that the carrier relaxation time can be expressed in terms of the carrier energy in a simple way, i.e., τ is proportional to E^s.

The electrical conductivity is given by

$$\sigma = ne\mu_c \tag{2}$$

where μ_c is the carrier mobility in the low carrier concentration limit. The carrier concentration is related to the reduced Fermi energy by the equation

$$n = 2(2\pi m^* kT/h^2)^{3/2}\exp \xi \tag{3}$$

The thermal conductivity is written as a sum of the lattice and the electronic components, i.e., $\lambda = \lambda_L + \lambda_e$. Evidently ξ affects the thermal conductivity only through the electronic contribution λ_e.

In addition $\lambda_e = L_o\,(k/e)^2\sigma T$, where the dimensionless quality L_o is referred to as the Lorenz factor. In the limit of low carrier concentration it can be shown[3,6] that $L_o = (5/2 + s)$. When the following parameters are introduced:

$$\begin{aligned} F &= \frac{\mu_c}{\lambda_L}\left(\frac{m^*}{m}\right)^{3/2} \\ G &= (2\pi mkT/h^2)^{3/2} \end{aligned} \tag{4}$$

the thermoelectric figure-of-merit can, after some rearrangement, be expressed as

$$Z = (5/2 + s - \xi)^2/\left[\left\{2\frac{k^2}{e}FG\exp\xi\right\}^{-1} + (5/2 + s)T\right] \tag{5}$$

Optimum Fermi Level

The figure-of-merit varies with the Fermi level and the optimum value of ξ which maximizes Z is obtained by setting $dZ/d\xi = 0$. This gives[3]

$$\xi_{opt} + 4(5/2 + s)\frac{k^2}{e}FGT\exp\xi_{opt} = \frac{1}{2} + s \tag{6}$$

In general, the lattice contribution to the thermal conductivity is large. Neglecting the second term in Equation 6, which amounts to neglecting λ_e, gives:

$$\xi_{opt} = s + \frac{1}{2} \tag{7}$$

When the electron scattering is by acoustic phonons and ionized impurities the scattering parameter s takes values of $-1/2$ and $+3/2$, respectively, with corresponding ξ_{opt} values of 0 and 2. Including the electronic thermal conductivity will amount to a reduction in ξ_{opt}. Obviously, the thermoelectric material has to be doped heavily to obtain Fermi levels well within the bands. Corresponding values of the optimum carrier concentrations can be estimated from Equation 3.

Optimum Seebeck Coefficient

An estimate[16] for the optimum Seebeck coefficient that maximizes Z can be obtained by differentiating Z with respect to α at constant temperature and equating $dZ/d\alpha$ to zero. Classical statistics gives $d(\log \sigma)/d\alpha = e/k$, for all scattering mechanisms. Consequently,

$$\alpha_{opt} = -2\frac{k}{e}[1 + (\lambda_e/\lambda_L)] = -172[1 + (\lambda_e/\lambda_L)]\ \mu\ V/K \tag{8}$$

In this model higher values for Z_{max} are obtained[6,16] when $\lambda_e/\lambda_L \sim 0.5$, $\alpha_{opt} \sim 250\ \mu V/K$, $Z_{max}T \sim 4/L_o$. In the case of acoustic phonon scattering $Z_{max}T \approx 2$.

The results predicted by this simple model are not unrealistic. A more rigorous theoretical model can be formulated which takes into account several important features that characterize a thermoelectric semiconductor,[6,7,17,18] viz., the presence of several equivalent valleys in the conducting band, with or without intervalley electron scattering, minority carrier effects, and possible deviations from the parabolic E-$\vec{k}$ relationship.

Fermi-Dirac Statistics

The use of classical statistics in describing the behavior of the carriers is justified only in the limit of low carrier concentration. As the thermoelectric material is heavily doped, Fermi-Dirac statistics must be employed. The expressions for the Seebeck coefficient and the Lorenz factor then take the form[3,6]

$$\alpha = \mp\frac{k}{e}(\delta - \xi) \tag{9}$$

where

$$\delta = \frac{(s + 5/2)F_{s+3/2}(\xi)}{(s + 3/2)F_{S+1/2}(\xi)} \tag{10}$$

and

$$L_o = \frac{(s + 7/2)F_{s+5/2}(\xi)}{(s + 3/2)F_{s+1/2}(\xi)} - \delta^2 \tag{11}$$

$F_\ell(\xi)$ are the Fermi integrals.

The electrical conductivity is given by $\sigma = \sigma_0\varepsilon$, where

$$\sigma_o = 2(2\pi m^* kT/h^2)^{3/2}\, e\mu_c \tag{12}$$

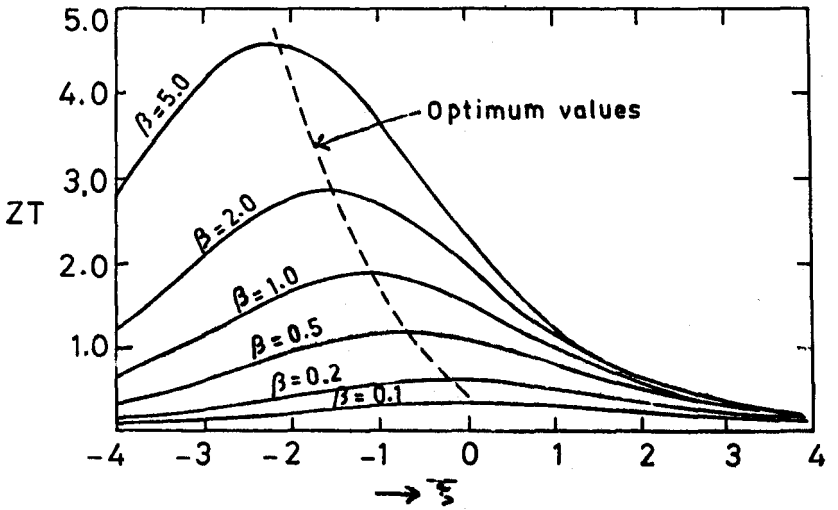

FIGURE 2 Dimensionless figure-of-merit (ZT) plotted against reduced Fermi energy (ξ) for s = −1/2. (From Chasmar, R. P. and Stratton, R. J., *J. Electron. Control*, 7, 52, 1959. With permission.)

and

$$\varepsilon = F_{s+1/2}(\xi)/(s + 1/2)! \tag{13}$$

These equations enable the dimensionless thermoelectric figure-of-merit to be expressed as

$$ZT = (\delta - \xi)^2 / \left[L_o + \left\{ \frac{\sigma}{\lambda_L} T(k/e)^2 \right\}^{-1} \right] \tag{14}$$

It is convenient to work with the dimensionless quantity, σ′, referred to as the reduced electrical conductivity, where

$$\sigma' = (\sigma/\lambda_L) T(k/e)^2 \tag{15}$$

The dimensionless figure-of-merit is then given by[6]

$$ZT = \frac{(\delta - \xi)^2}{L_o + 1/\sigma'} \tag{16}$$

In addition

$$\sigma' = \beta F_{s+1/2}(\xi)/(s + 1/2)! \tag{17}$$

with

$$\beta = \frac{2(2\pi k)^{3/2} k^2}{eh^3} A' \tag{18}$$

$$A' = T^{5/2} m^{*3/2} \mu / \lambda_L \tag{19}$$

The dependence of the Fermi level on carrier concentration is now given by

$$n = \frac{4}{\sqrt{\pi}} (2\pi m^* kT/h^2)^{3/2} F_{1/2}(\xi) \tag{20}$$

The parameters A′ and β, which make their appearance in the expression for the figure-of-merit, are referred to as the material parameters, since for a given scattering mechanism and Fermi level, the figure-of-merit depends on the physical properties of the material only through these parameters. A plot of ZT vs. ξ for scattering by acoustic phonons is displayed in Figure 2.

5.3 Two-Band Conduction

Idealized Models

Although the materials are heavily doped by the addition of n- or p-type impurities, the presence of the second band and the invariable presence of minority carriers have a significant effect on the thermoelectric properties. Narrow-band-gap semiconductors are usually good thermoelectric materials and are quite likely to exhibit the minority carrier effects at the upper end of their temperature ranges of operation. Following Rittner and Neumark[20] an insight into the conditions that favor a high figure-of-merit can be obtained for a simple two-band model[19–22] of a semiconductor with several equivalent extrema in its conduction or valence bands.[17,18,21] The lattice contribution to the thermal conductivity is neglected in these considerations.

The conduction and valence bands are considered as having N_e and N_h equivalent extrema (or valleys), respectively. If σ_1 represents the contribution of a single valley to the electrical conductivity, then:

$$\sigma_{e,h} = N_{e,h}\,\sigma_{1e,h} \tag{21}$$

where the suffices e and h refer to the electron and hole contributions from the two bands. The total electrical conductivity is a sum of the contributions from the two bands, i.e., $\sigma = \sigma_e + \sigma_h$. Also, the Seebeck coefficient appropriate to a two-band conduction model is written as

$$\alpha = (\alpha_e\,\sigma_e + \alpha_h\,\sigma_h)/(\sigma_e + \sigma_h) \tag{22}$$

The total Seebeck coefficient is then given by[20]

$$\alpha = \frac{k}{e}\left[-\frac{(\delta_e - \xi_e)}{1 + \sigma_h/\sigma_e} + \frac{(\delta_h - \xi_h)}{1 + \sigma_e/\sigma_h}\right] \tag{23}$$

and the ratio σ_e/σ_h by

$$\sigma_e/\sigma_h = \gamma^2\{F_{s_e+1/2}(\xi_{s_e})/(s_e + 1/2)!\}/\{F_{s_h+1/2}(\xi_{s_h})/(s_h + 1/2)!\} \tag{24}$$

where suffices s_e and s_h refer to the scattering parameters for the electron and hole systems, respectively. The density-of-states effective masses for electrons and holes are given as

$$m^* = N^{2/3}(m_1 m_2 m_3)^{1/3} \tag{25}$$

where m_1, m_2, and m_3 are mass components along principal axes. N refers to the number of equivalent valleys in the band (N_e or N_h). If the parameter s is taken to be the same for the two bands, and classical statistics is used, then

$$A = [s + 5/2 - \xi] \tag{26}$$

$$L_o = s + 5/2 \tag{27}$$

and

$$\sigma_e/\sigma_h = \gamma^2\exp(\xi_g + 2\xi) \tag{28}$$

Here $\xi_g = E_g/kT$ is the dimensionless energy band gap. In the present model $\lambda_e/\sigma T$ is independent of ξ, (ξ_g) and γ and a variation in these parameters will affect Z only through α. It is therefore sufficient to consider the dependence of α on these parameters, which yields the following:

$$\alpha = \frac{k}{e}\,[-M \tanh \xi' + \xi' - 1n\gamma] \tag{29}$$

where $\xi' = \xi + \xi_g/2 + 1n\gamma$ and $M = s + 5/2 + \xi_g/2$.

For a given γ, the optimum Fermi level corresponding to a maximum Z is given by

$$\begin{aligned}\xi_{opt} &= -\xi_g/2 + 1n[\sqrt{M} + \sqrt{M-1}] - 1n\gamma, \text{ for } \xi' > 0 \\ &= -\xi_g/2 - 1n[\sqrt{M} + \sqrt{M-1}] - 1n\gamma, \xi' < 0\end{aligned} \tag{30}$$

A detailed study of the conditions under which the upper bound on Z can be raised reveals that the parameter γ is of central importance.[20] The model predicts a large value of Z for high values of m_h^*/m_e^* and m_e^*/m. These results pertain to a highly simplified model and cannot be applied, as such, to realistic situations. However, they do point towards possible directions in which to look for future developments.

Realistic Situations

Simon[19] has outlined a procedure which provides a reasonable estimate of Z_{max} (i.e., Z at the optimum carrier concentration) from the measured values of α, σ, and λ on a sample which is not too heavily doped. Implicit in the procedure is the assumption that the scattering parameter s is independent of ξ, an assumption invariably present in most calculations. When more than one scattering mechanisms operate simultaneously a mixed scattering model has to be adopted.[6,15]

In practical situations a two-band conduction model can be considered and appropriate parameters selected from among the known thermoelectric materials. The maximization of Z can then be considered with respect to variations in ξ. The bipolar contribution to the thermal conductivity is included and is given by

$$\lambda_b = T\left(\frac{k}{e}\right)^2 \frac{\sigma_e \sigma_h}{\sigma_e + \sigma_h} [\delta_e + \delta_h + \xi_g]^2 \tag{31}$$

Using this model the dimensionless figure-of-merit is written as[22]

$$ZT = \frac{(\alpha_e' \sigma_e' - \alpha_h' \sigma_h')^2}{(\sigma_e' + \sigma_h')(1 + \sigma_e' L_{oe} + \sigma_h' L_{oh}) + \sigma_e' \sigma_h' (\delta_e + \delta_h + \xi_g)^2} \tag{32}$$

Ure[22] used these equations and optimized Z with respect to variations in ξ. He selected various parameters, such as the effective mass and the elastic constant, from among the best-known thermoelectric materials. Ure's result slightly overestimates Z but the calculation can be made more rigorous by choosing all the relevant parameters from a particular material.

This formulation can yield valuable information about the effect of minority carriers on various transport coefficients. Z may change considerably due to the effect of the second band as a result of the contributions to α and σ, and also through the thermal conductivity which now includes a contribution due to electron-hole pairs. These aspects have been discussed in detail for bismuth telluride.[23]

Goff and Lowney[24] reformulated ZT in integral form and used it to analyze the thermoelectric behavior of lead telluride. The analysis emphasizes the effect of changing the values of internal parameters arbitrarily. As expected, setting $\lambda_L = 0$, for example, increases ZT. In this case the lower carrier concentrations yield larger Z, unlike the normal situation (i.e., with normal values of λ_L), where larger carrier concentrations correspond to larger ZT. Nevertheless such considerations can be helpful in material development programs.

5.4 Further Considerations

Multivalley Structure with Intervalley Scattering

It has often been emphasized that the presence of a number of equivalent valleys in the bands has the effect of increasing the figure-of-merit, provided, of course, that the scattering of carriers between different valleys can be avoided.[18,25–27] For such scattering to take place high-energy phonons are required and these may not be available in sufficient numbers at low temperatures. At elevated temperatures the intervalley scattering of carriers may partly offset[27] the gain in the figure-of-merit.

Non-Parabolic Energy Bands

Another unavoidable complication arises due to the deviation from the parabolic energy-wavevector relationship.[28–32] In obtaining the transport coefficients for non-parabolic bands an approach is usually employed which takes account of the electron energy dispersion: [21,28,31]

$$\frac{\hbar^2}{2}\frac{2k_T^2}{m_{To}^*} + \frac{\hbar^2}{2}\frac{k_L^2}{m_{Lo}^*} = E\left(1 + \frac{E}{E_g}\right) \tag{33}$$

where k_L and k_T are the longitudinal and transverse components of the electron (or hole) wavevector and m_{Lo}^* and m_{To}^* are the components of the effective mass tensor near the band extremum. The effective mass now becomes energy dependent, with

$$m_j^* = m_{jo}^*(1 + 2\eta\beta_g) \tag{34}$$

where $\beta_g = \xi_g^{-1}$ is the inverse of the energy band gap, and $\eta = E/kT$ is the reduced carrier energy. For large band gaps $\beta_g \ll 1$ and the effective mass take a constant value as in parabolic bands. The calculated transport coefficients based on these considerations are significantly different in narrow-band-gap semiconductors; the Lorenz factor and electrical conductivity are reduced compared to values obtained using the parabolic model.

Bhandari and Rowe have taken these aspects into consideration and obtained estimates for the possible effects of valleys with and without additional scattering, and deviations from band parabolicity.[29,30] This model can be used in analyzing known data as well as in investigating the role of various parameters in enhancing the figure-of-merit. The power factor $\alpha^2\sigma$ is of prime importance when optimizing with respect to ξ. Situations can also be considered in which the number of valleys is increased while the other parameters are fixed. Studies of the silicon-germanium system indicate that $\alpha^2\sigma$ (max) increases by a factor slightly less than N_v in the absence of intervalley scattering. This sets an upper limit on the increase in Z due to the number of valleys. Interestingly n_{opt} also exhibits a corresponding increase. In a "model calculation" based on the $Si_{70}Ge_{30}$ system at room temperature a sixfold increase in N_v has the effect of multiplying $\alpha^2\sigma$ by a factor of 5.0, whereas n_{opt} is multiplied by a factor of 6.2. For $N_v = 6$, pertaining to the situation in silicon, $n_{opt} \sim 2.5 \times 10^{25}$ m^{-3}. It is important, of course, to note that to take maximum advantage of these considerations n_{opt} should stay well below the solubility limit.

5.5 Improved Materials

Optimum Carrier Concentration

The introduction of "additives" may enhance the thermoelectric performance of a material, as has been reported for silicon-germanium. Significant improvements in the figure-of-merit accompany the addition of gallium phosphide to the silicon-germanium system.[35–38] This increase appears primarily due to an increase of $\alpha^2\sigma$; and in particular due to an increase in σ. The mechanism for the phenomenon is not well understood and there have been various investigations to identify it.[38,39] High-temperature annealing is found to have a profound effect on the reported increase in performance. Normally the maximum figure-of-merit occurs at concentrations that are not normally attainable in practice, as is the case with silicon-germanium. The introduction of gallium phosphide followed by annealing appears to raise the dopant solubility limit and is accompanied by an increase in $\alpha^2\sigma$. For standard $Si_{0.80}Ge_{0.20}$ samples the optimum carrier concentration is around $(1.4 - 1.8) \times 10^{26}$ m^{-3}, whereas for silicon-germanium alloys to which gallium phosphide has been added it is found to be around 2.2×10^{26} m^{-3}. It should be pointed out that the Seebeck coefficient is not expected to change significantly as it depends on log n. Hall effect measurements appear to confirm this.

The above explanation appears reasonable but it cannot possibly account for the reported magnitude of increase in the figure-of-merit. Theoretical estimates based on fairly rigorous calculations[30,39] can be employed in assessing the possible increase in the figure-of-merit which

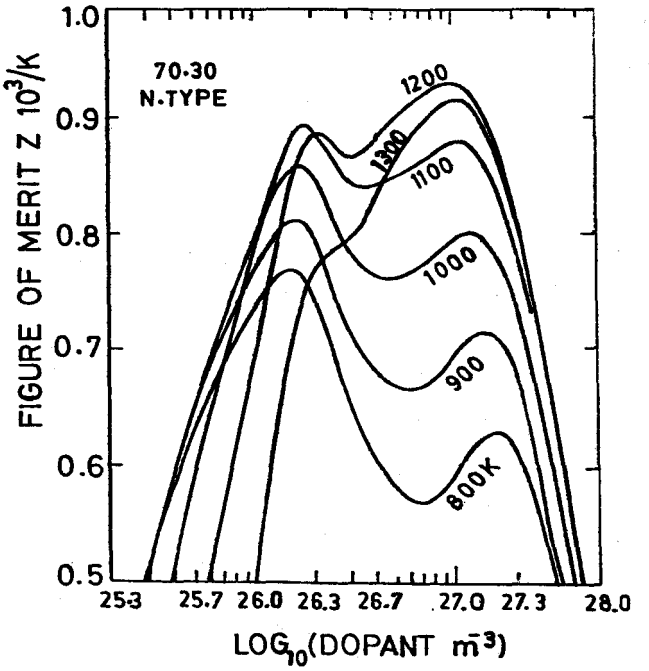

FIGURE 3 Z vs. dopant concentration for n-type samples of $Si_{.70}Ge_{.30}$; $m^*(L)/m_o = 2$, where L refers to the L-band; λ_L obtained from the measured λ. (From Slack, G. A. and Hussain, M. A., *J. Appl. Phys.*, 70(5), 2694, 1991. With permission.)

accompanies an increase in carrier concentration. In the case of $Si_{0.70}Ge_{0.30}$ alloy a plot of $\alpha^2\sigma$ vs. n at 300 K shows a 12.5% rise in the power factor when n increases by a factor of 1.6 just before the maximum. This is about half the reported increase in the figure-of-merit in silicon-germanium-gallium phosphide annealed samples. The effect of heat treatment on the electrical power factor is not yet fully understood, neither is the reported (almost unchanged) thermal conductivity. At these high doping levels the electronic contribution is not negligible and changes in the electrical conductivity should be reflected in a change in the electronic thermal conductivity. Microstructure studies by scanning electron microscopy have revealed the presence of new phases. This has been particularly important in other high-temperature materials, such as the lanthanum chalcogenides $La_{3-x}Te_4$, with $0 < x < 1/3$; these are among the best-known high-temperature thermoelectric materials with the figure-of-merit showing a maximum around a temperature of 1273 K. However, even similar samples appear to behave differently. Microscopic examination of the material reveals[38] new phases and structures which are dependent on the methods and processes used in chemically synthesizing the compound and subsequent hot-pressing. The presence of oxy-telluride phases have been reported indicating the possibility of varying degrees of oxygen contamination. It is relevant to any clear understanding of the sample behavior that the sample history is known, including any previous thermal annealing. Slack and Hussain's[40] analysis of the thermoelectric behavior of the silicon-germanium system does not support the reported effectiveness of GaP doping and grain-boundary scattering in enhancing the figure-of-merit. Using a model with one valence and two conduction bands they obtained the dependence of the figure-of-merit on carrier concentration at several temperatures (300 to 1300 K), as shown in Figure 3. The curves show two distinct maxima, the left one (at lower n) being usually higher than the other. However, above 1130 K the maximum figure-of-merit shifts to the right side, and n_{opt} is around 10^{27} m^{-3}. This is somewhat higher than other reported values of n_{opt}.[38] These calculations, however, neglect the non-parabolic nature of the energy bands and intervalley scattering, both of which may be significant at the doping levels and temperatures considered.

Dopant Precipitation and Solubility

Often in thermoelectric semiconductors, the dopants possess retrograde characteristics which are strongly temperature dependent[41] and the dopant concentration may well exceed the solubility limit.[42] This can considerably influence the material's properties when operated over a period of time. For example, the effect of phosphorus precipitation on the room temperature Seebeck coefficient of $Si_{63.5}Ge_{36.5}$ alloy[43] shows that the precipitation is very fast over the temperature range 700 to 800 K, with the carrier concentration decreasing by around 50% after only 1 h. However, the process is reversible and suitable annealing procedures may redissolve the dopant. The precipitation of boron is slower than that of phosphorus and is fastest in the range 1000 to 1200 K. A theoretical analysis of the dopant precipitation has been provided by the Lifshitz-Slyozov model,[44] and the long-term behavior of the material can be predicted from the results of relatively short-term heat treatment.[45]

As regards the dopant solubility the mechanism is not difficult to understand when both n- and p-type impurities are present. Considering the reaction

$$e^+ + e^- = (e^+e^-) \tag{35}$$

it can be seen that the formation of electron-hole pairs (e^+ e^-) depletes the solution of electrons, and consequently more donors are ionized leading to a greater solubility. The effectiveness of the process depends upon the degree of dissociation of electron-hole pairs. Studies on the solubility of lithium in germanium show that the presence of gallium considerably increases the lithium solubility.[46] For example, the concentration of lithium in pure germanium at room temperature goes up from its normal value of 10^{20} m^{-3} to about 10^{24} m^{-3} when doped with gallium. However, these considerations must be investigated much more comprehensively before a quantitative understanding can be achieved of the reported increase in the figure-of-merit.

New Materials

Recent advances in new materials must include a mention of the low dimensional systems[47–53] — thin films and micro-thin wires operating in the size-quantum limit. The mobility and the Seebeck coefficient in these systems may be favorably influenced in a particular temperature range and for a certain range of film thicknesses. Advanced preparation techniques like molecular beam epitaxy can be used to prepare exotic new material structures, such as synthetic superlattices and the strained-layer heterostructures. The figure-of-merit may be increased by these and other factors, such as the effect of strain on the phonon properties, electrical conductivity enhancement by modulation doping, and carrier confinement in quantum wells. The carrier densities pertaining to the onset of degeneracy in these systems may be lower than that in the bulk and this may have some relevance in achieving optimization of the carrier concentration.

References

1. Ioffe, A. F., *Semiconductor Thermoelements and Thermoelectric Cooling*, Infosearch, London, 1957.
2. Cadoff, I. B. and Miller, E., *Thermoelectric Materials and Devices*, Reinhold, New York, 1959.
3. Goldsmid, H. J., *Applications of Thermoelectricity*, Methuen Monograph, London, 1960.
4. Egli, P. H., Ed., *Thermoelectricity*, John Wiley & Sons, New York, 1960.
5. Ure, R. W. and Heikes, R. R., Ed., *Thermoelectricity: Science and Engineering*, Interscience, London, 1961.
6. Rowe, D. M. and Bhandari, C. M., *Modern Thermoelectrics*, Holt Saunders, London, 1983.
7. Goldsmid, H. J., *Electronic Refrigeration*, Pion Ltd., London, 1988.
8. Rosi, F. D., Hockings, E. F., and Lindenblad, N. E., Semiconducting materials for thermoelectric power generation, *RCA Rev.*, 22, 82, 1961.
9. Burshteyn, A. I., *Semiconductor Thermoelectric Devices*, Temple Press, London, 1964.
10. Rosi, F. D., Thermoelectricity and thermoelectric power generation, *Solid State Electron.*, 11, 833, 1968.

11. Wright, D. A., Materials for direct conversion of thermoelectric generators, *Metall. Rev.*, 15, 147, 1970.
12. Rowe, D. M., Thermoelectric power generation, *Proc. Inst. Electr. Eng.*, 125(11R), 1113, 1978.
13. Bhandari, C. M. and Rowe, D. M., Silicon-germanium alloys as high temperature thermoelectric materials, *Contemp. Phys.*, 21(3), 219, 1980.
14. Hutner, R. A., Rittner, E. S., and DuPre, F. K., Fermi levels in semiconductors, *Philips Res. Rep.*, 5, 188, 1950.
15. Fistul, V. I., *Heavily Doped Semiconductors*, Plenum, New York, 1969.
16. Chasmar, R. P. and Stratton, R. J., The thermoelectric figure of merit and its relation to thermoelectric generators, *J. Electron. Control*, 7, 52, 1959.
17. Ziman, J. M., *Electrons and Phonons*, Cambridge University Press, London, 1960.
18. Ridley, B. K., *Quantum Processes in Semiconductors*, Oxford University Press, New York, 1981.
19. Simon, R., Thermoelectric figure-of-merit of two-band semiconductors, *J. Appl. Phys.*, 33, 1830, 1962.
20. Rittner, E. S. and Neumark, G. F., Theoretical bound on the thermoelectric figure-of-merit of two-band semiconductors, *J. Appl. Phys.*, 34, 2071, 1963.
21. Bhandari, C. M. and Rowe, D. M., *Thermal Conduction in Semiconductors*, Wiley Eastern Ltd., New Delhi, 1988.
22. Ure, R. W., Jr., Practical limits to the thermoelectric figure-of-merit. II, *Energy Convers.*, 12, 45, 1972.
23. Bhandari, C. M. and Rowe, D. M., Minority carrier effects on thermoelectric figure-of-merit, *Proceedings of the 1st European Conference on Thermoelectrics*, Cardiff, 1987, p. 178.
24. Goff, J. F. and Lowney, J. R., The integral formulation of the thermoelectric figure of merit: effects of lattice thermal conduction, *Proceedings of the 11th IECEC*, 1976, p. 1561.
25. Herring, C., Transport properties of a many valley semiconductor, *Bell System Tech. J.*, 34, 237, 1955.
26. Seeger, K., *Semiconductor Physics*, Springer-Verlag, Berlin, 1973.
27. Bhandari, C. M. and Rowe, D. M., The behaviour of a multivallied semiconductor, *Proceedings of the Vth International Conference on Thermoelectric Energy Conversion*, Arlington, 1984, p. 38.
28. Kane, E. O., Band structure of InSb, *J. Phys. Chem. Solids*, 1, 249, 1957.
29. Rowe, D. M. and Bhandari, C. M., Electronic thermal transport in thermoelectric materials — effect of band non-parabolicity, *Proceedings of the Vth International Conference on Thermoelectric Energy Conversion*, Arlington, 1984, p. 62.
30. Bhandari, C. M. and Rowe, D. M., Electronic contribution to the thermal conductivity of narrow band gap semiconductors — effect of non-parabolicity of bands, *J. Phys. D: Appl. Phys.*, 18, 873, 1985.
31. Ravich, Y. I., Efimova, B. A., and Smirnov, I. A., *Semiconducting Lead Chalcogenides*, Stil'bans, T. S., Ed., Plenum, New York, 1970.
32. Ravich, Y. I., Efimova, B. A., and Tamarchenko, V. I., *Phys. Status Solidi (b)*, 43, 11, 1971.
33. Rowe, D. M. and Bhandari, C. M., A review of lead telluride technology at UWIST, *Sixth International Conference on Thermoelectric Energy Conversion*, Arlington, 1986, p. 43.
34. Bhandari, C. M. and Rowe, D. M., unpublished.
35. Pisharody, R. K. and Garvey, L. P., Modified Si-Ge alloys with improved performance, *Proc. 13th IECEC*, 3, 1963, 1978.
36. Vining, C., personal communication.
37. Vandersande, J. W., Wood, C., and Draper, S., *Proc. Spring Meet. Mater. Res. Soc.*, Anaheim, CA, 1987, p. 21.
38. Wood, C., Materials problems in high temperature thermoelectric energy conversion, *1st European Conference on Thermoelectrics*, Cardiff, 1987, p. 1.
39. Rowe, D. M., Min, G., and Bhandari, C. M., The effect of high temperature heat treatment on the electrical power factor of Si-Ge/GaP alloys, *Proc. 2nd Asian Thermophys. Prop. Conf.*, 1989, p. 145.
40. Slack, G. A. and Hussain, M. A., The maximum possible conversion efficiency of Si-Ge thermoelectric generators, *J. Appl. Phys.*, 70(5), 2694, 1991.
41. Trumbore, F. A., Solid solubilities of impurity elements in Ge and Si, *Bell Systems Tech. J.*, 39, 205, 1960.

42. Ekstrom, L. and Dismukes, J. P., Precipitation of phosphorus from solid solution in Ge-Si alloys, *J. Phys. Chem. Solids*, 857, 1966.
43. Savvides, N. and Rowe, D. M., Precipitation of phosphorus from solid solution of Si-Ge alloys and its effect on thermoelectric transport properties, *J. Phys. D: Appl. Phys.*, 14, 723, 1981.
44. Lifshitz, I. M. and Sloyozov, V. V., *J. Phys. Chem. Solids*, 19, 35, 1961.
45. Raag, V., Comprehensive thermoelectric properties of n and p-type $Si_{78}Ge_{22}$, *Proc. 2nd Int. Conf. Thermoelectric Energy Conversion*, Arlington, 1978, p. 5.
46. Glazov, V. M. and Zemskov, V. S., *Physiochemical Foundation of Semiconductor Doping*, Nauwa, Moscow, 1967.
47. Ando, T. and Mori, S., Electronic properties of a semiconductor superlattice. I. Self consistent calculation of subband structure, *J. Phys. Soc. Jpn.*, 47, 1518, 1979.
48. Arora, V. K. and Awad, F. G., Quantum size effects in semiconductor transport, *Phys. Rev. B*, 23, 5570, 1981.
49. Ridley, B. K., *J. Phys. C: Solid State Phys.*, 15, 5899, 1982.
50. Lee, J. and Spector, H. N., *J. Appl. Phys.*, 54, 3291, 1983.
51. Lee, J., and Vassel, M. O., Low-field electron transport in quasi-one-dimensional semiconducting structures, *J. Phys. C: Solid State Phys.*, 17, 2525, 1984.
52. Kubakaddi, S. S. and Mulimani, B. G., Thermopower enhancement in semiconducting quantum-well wires for acoustic phonon scattering, *J. Appl. Phys.*, 58(9), 3643, 1985.
53. Whall, T. E. and Parker, E. H. C., Preparation of advanced materials by MBE, *1st European Conf. on Thermoelectrics*, Cardiff, 1987, p. 51.

6

Minimizing the Thermal Conductivity

C. M. Bhandari
University of Allahabad
India

6.1 Introduction

The study of heat transport[1–5] in semiconductors requires a knowledge of a number of material properties. On the other hand, heat transport studies can yield useful information on several of these properties. In addition to this, a knowledge of the thermal conductivity and the means by which it can be increased or decreased in a selective manner is of considerable practical importance.[5]

The thermoelectric performance[6–10] of a material is characterized by the so-called figure-of-merit $\alpha^2\sigma/\lambda$, where α, σ, and λ refer to the Seebeck coefficient and the electrical and thermal conductivity of the material, respectively. The thermal conductivity of a semiconductor has two main components: the lattice (phonon) component (λ_L), and the electronic (or hole) component (λ_e). The electronic thermal conductivity is written as

$$\lambda_e = \left(\frac{k}{e}\right)^2 L_0\, \sigma T \tag{1}$$

In semiconductors the Lorenz factor L_0 varies with the level of doping. This is discussed in terms of the Fermi level, which relates to the energy E_F measured from the band edge. It is convenient to introduce a reduced Fermi energy $\xi = E_F/kT$, and reduced energy band gap $E_g/kT = 1/\beta_g$; the Lorenz factor in a semiconductor depends upon ξ, β_g, and the particular carrier scattering mechanism. The variation of L_0 with β_g incorporates into the calculation the influence of the second band, which manifests itself in deviations from the parabolic energy-wavevector relationships.[5,11,12] The Lorenz factor can be calculated as a function of ξ and β_g, with the latter taking account of the non-parabolicity of the energy bands. For the usual parabolic band model a relaxation time τ can be defined for the carriers which varies as E^s, where E refers to the carrier energy. The scattering parameter s takes on different values for different scattering mechanisms. The figure-of-merit can be optimized with respect to the variation of ξ, and its optimum value is given by $\xi_{opt} = 1/2 + s$. In a simple theoretical framework the figure-of-merit is expressed in terms of various parameters and maximizes with respect to variations in α, yielding[13]

$$\alpha_{opt} = -2\frac{k}{e}[1 + (\lambda_e/\lambda_L)] \tag{2}$$

0-8493-0146-7/95/$0.00+$.50

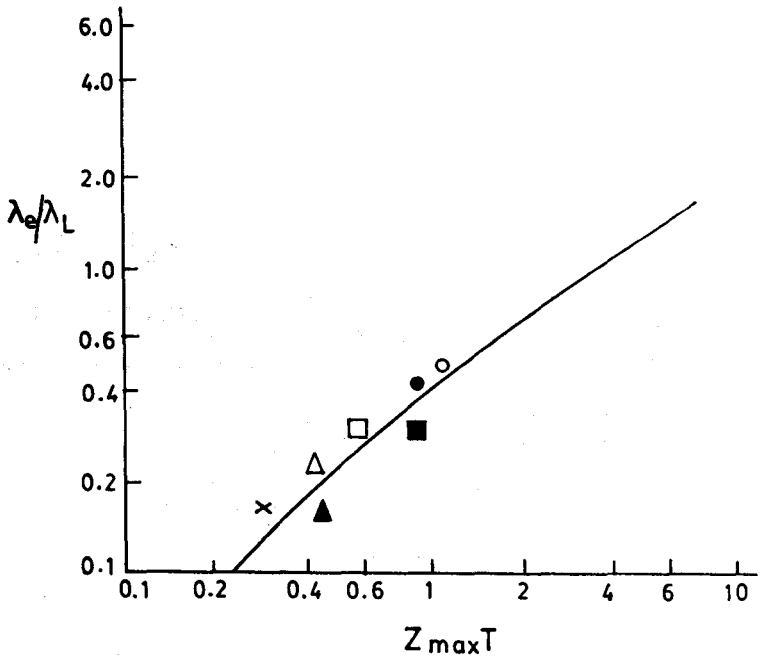

FIGURE 1 Maximum dimensionless figure-of-merit for several thermoelectric materials plotted against the ratio $\lambda_e\lambda_L$ at 300 K. (○) p-type Sb_2Te_3–25% Bi_2Te_3–3% Sb_2Se_3; (●) n-type Bi_2Te_3–5% Sb_2Te_3–5% Sb_2Se_3; (□) p-type Bi_2Te_3; (■) n-type Bi_2Te_3; (△) p-type PbTe; (▲) n-type PbTe; (x) p-type $AgSbTe_2$. (From Rosi, F. D., *Solid State Electron.*, 11, 833, 1968. With permission.)

The maximum figure-of-merit in its dimensionless form (Z_mT) is then given by

$$Z_mT = \frac{4}{L_0}(\lambda_e/\lambda_L)[1 + (\lambda_e/\lambda_L)] \tag{3}$$

Higher values of Z_mT are obtained when $(\lambda_e/\lambda_L) \sim 0.5$. The variation of Z_mT against (λ_e/λ_L) for several thermoelectric semiconductors is displayed in Figure 1; the good agreement with the highly idealized theoretical formulation should be noted.

6.2 Requirement of Low Thermal Conductivity

"Good thermoelectric materials" obviously require a low thermal conductivity to prevent a significant portion of the heat from flowing down the temperature gradient. Most of the thermal conductivity studies that relate to thermoelectric materials have dealt primarily with the question of reducing the thermal conductivity without resulting in an adverse effect of the electrical power factor $\alpha^2\sigma$. However, there are considerable problems in achieving this objective. As the thermoelectric semiconductors are heavily doped, a significant contribution to thermal conductivity arises from the electrons (or holes). The nature of the problem is better realized when one considers the dependence of the figure-of-merit on two factors: the electrical properties of the material as incorporated in the power factor $\alpha^2\sigma$ and a degradation due to heat loss.[14] The fact that a significant λ_e is invariably present needs to be taken into account in any thermal conductivity minimization program.

Thermoelectric materials should possess a low value of thermal conductivity to reduce the loss of heat by conduction, and a reasonably large energy band gap to minimize the effect of the minority carriers.[15] Usually the materials with large band gaps possess large lattice thermal conductivity. A plot of E_g vs. λ_L for a number of commonly used semiconductors is displayed[16]

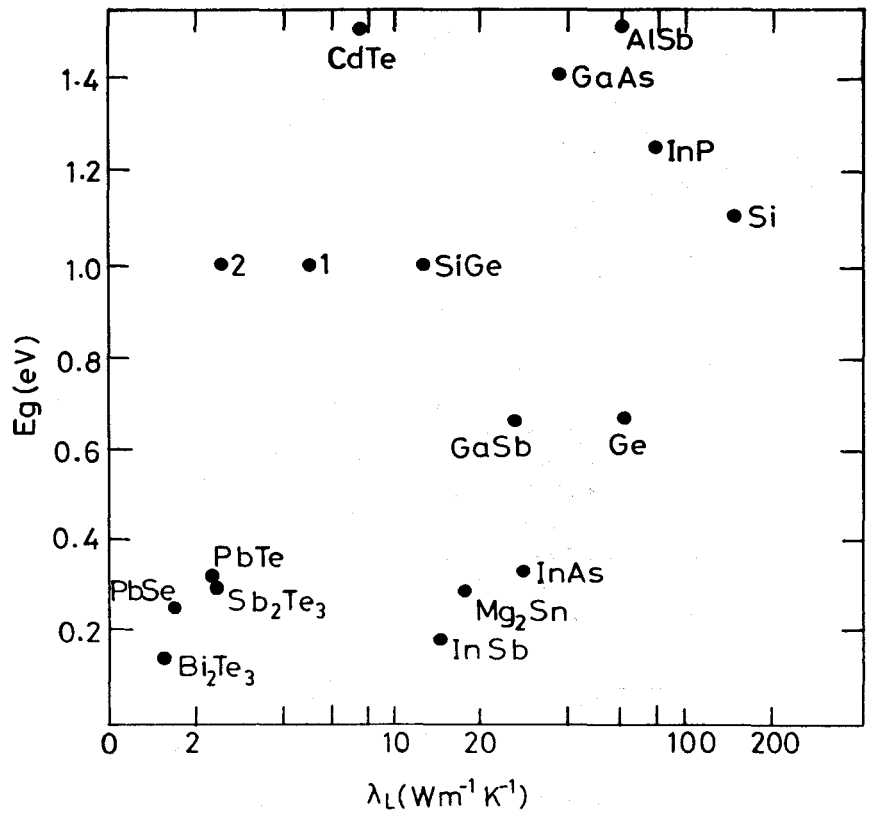

FIGURE 2 Lattice thermal conductivity and energy gap for various semiconductors. Si-Ge refers to 80–20 composition. (1) SiGe doped, 10^{26} m^{-3}; (2) doped fine-grained. (From Bhandari, C. M. and Rowe, D. M., *Proc. Second Int. Conference Thermoelectric Energy Conversion*, Arlington, 1978. With permission.)

in Figure 2. Any attempt to reduce λ_L without significantly affecting the band gap and the power factor $\alpha^2\sigma$ could lead to a better choice of thermoelectric material. For example, the effect of alloy disorder on λ_L in materials like Si-Ge alloys is significant (over a wide range of composition), whereas the band gap varies almost linearly when silicon is added to germanium.

6.3 Reducing the Lattice Thermal Conductivity

Alloy Disorder

A reduction in the lattice thermal conductivity can be achieved in several ways. The effect of introducing point-defects as in an alloy has been described in the context of Si-Ge alloys. The aim has primarily been to seek a selective scattering of phonons. Any mechanism that scatters phonons more effectively than the electrons (or holes) is likely to enhance the electrical to thermal conductivity ratio. Among the important scattering mechanisms that tend to reduce the phonon mean free path are scattering by other phonons, lattice defects, electrons and holes, and grain boundaries. One of the most thoroughly understood mechanisms related to defect scattering is based upon mass-difference scattering.[2–5,17] The usefulness of solid solutions in thermoelectric applications was realized at an early stage and various recipes were put forward to improve the figure-of-merit by decreasing the thermal conductivity. The thermal conductivity of bismuth telluride-based solid solutions is displayed in Figure 3. Reductions of the phonon mean free path in solid solutions is analyzed in terms of mass-difference scattering with an associated phonon relaxation time.[17]

$$\tau_{pd}^{-1} = \Gamma\omega^2 g(\omega)/6N \tag{4}$$

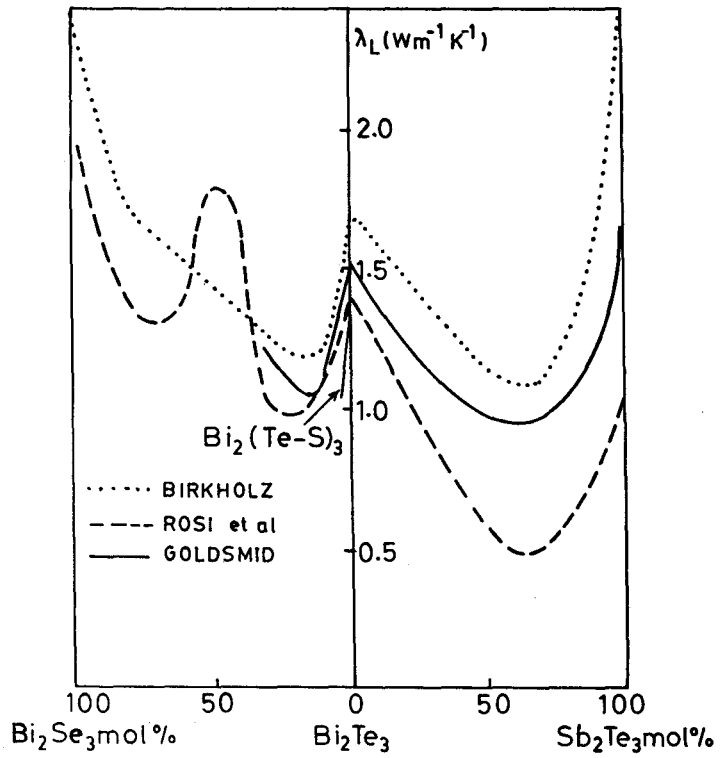

FIGURE 3 Lattice thermal conductivity of n-type Bi_2Te_3 alloys at 300 K. (From Goldsmid, H. J., in *Materials Used in Semiconductor Devices*, Hogarth, C. A., Ed., Interscience, 1965. With permission.)

Γ, which is a measure of the strength of the scattering, is given by

$$\Gamma = \Sigma f_i \left(1 - \frac{M_i}{\overline{M}}\right)^2 \tag{5}$$

f_i is the fractional concentration of the impurity of mass M_i, and $\overline{M} = \Sigma f_i M_i$ is the mean atomic mass. For the Debye model $g(\omega) \alpha \omega^2$ and the familiar Rayleigh expression is obtained

$$\tau_{pd}^{-1} = \Omega_o \Gamma \omega^4 / 4\pi v_s^3 \tag{6}$$

$\Omega_0 = V/N$ is the average atomic volume, v_s is the average sound (phonon) velocity, and ω refers to the phonon frequency. Obviously this method of reducing λ_L is useful in alloys such as silicon-germanium where the atomic masses of the components differ considerably. In general an impurity atom differs from the host atoms in its mass, size, and the force constants. A generalized expression which takes these various factors into account can be written as[21,22]

$$\Gamma_i = f_i \left[(\Delta M_i/M)^2 + 2\{(\Delta G_i/G) - 6.4\,\gamma(\Delta\delta_i/\delta)\}^2\right] \tag{7}$$

G_i is the average stiffness constant of the nearest-neighbor bonds from the impurity to the host atom and G the corresponding quantity for the host. δ_i is the cube root of the atomic volume for the *i*th impurity in its own lattice and $\delta = \Sigma f_i \delta_i'$; γ represents the average anharmonicity of the bonds.

Resonance Scattering

Resonance scattering corresponds to a process in which phonons combine to excite a localized mode. Certain impurities in particular host lattices give rise to a scattering which results in small

dips or undulations in the thermal conductivity curves. The process may be understood in terms of inelastic scattering of phonons at the impurity modes.[23–25] A resonance scattering relaxation time together with the usual scattering mechanisms is required to explain the results. The dip in the λ-T curve can be reproduced[26] by using an additional relaxation time given by[25]

$$\tau_R^{-1}(\omega) = R\omega^2 T^n/[(\omega_0^2 - \omega^2)^2 + D\,\omega_o^2\omega^2] \tag{8}$$

R depends upon the concentration of the impurities and D refers to damping; ω_0 is the frequency characteristic of the resonance mode. For monatomic disturbances (such as KCl:NaCl) n = 2 gives a good agreement, whereas in systems like KCl:KNO_2, n = 0 is found to be more appropriate.

Scattering by Charge Carriers

Heavy doping of the thermoelectric material necessitates a detailed investigation of the role of carriers as (1) agents aiding the flow of heat down the temperature gradient, and (2) scattering centers for the phonons, thereby opposing the flow of heat. For some doping levels the two contributions may be comparable. The thermal conductivity of a particular sample of n-InSb is reported[27] to be higher than that of the corresponding undoped material; on the other hand a p-type sample of InSb shows a lower λ. Qualitatively this could be explained on the basis of a larger mobility of electrons than that of the holes. A large mobility may lead to a large electrical conductivity and hence an enhanced λ_e. The effect of additional phonon scattering on λ_L is obviously less significant than the additional electronic contribution to the flow of heat. The same could not be said for the p-type sample for obvious reasons. Ziman[28,29] investigated the scattering of phonons by carriers and obtained the relaxation time

$$\tau_{pe}^{-1} = \frac{\varepsilon^2 m^{*2} kT}{2\pi\hbar^4 \rho v_L}\left\{z - \ln\left[\frac{1 + \exp(\psi + z/2)}{1 + \exp(\psi - z/2)}\right]\right\} \tag{9}$$

where $z = \hbar\omega/kT$ and

$$\psi = \hbar^2\omega^2/8m^* v_L^2 kT + m^* v_L^2/2kT - E_F/kT \tag{10}$$

Here ε is the strength of the electron-phonon interaction and E_F is the Fermi energy. v_L refers to the average phonon velocity and the various other parameters have their usual meanings. This expression has been derived for the longitudinal phonons. The expression can be simplified with the inverse relaxation rate expressed[3,5] in terms of z, i.e., $\tau_{pe}^{-1} = B'z$, where the proportionality constant B′ represents the strength of phonon electron scattering.

The role of the carriers as scattering centers along with that as heat carriers is displayed[30] in Figure 4 in which the thermal conductivity of n-Bi_2Te_3 is plotted against electrical conductivity. The region of the minimum is of obvious interest in thermoelectric applications. A theoretical analysis[31] of the results must take into account the effects of the multivalley band structure, nonparabolicity of bands and that of the minority carriers. The bipolar contribution to thermal conductivity is significant in the region beyond the minimum.

Scattering by Grain Boundaries

The phonon mean free path may be limited by crystal dimensions. A mean free path ($\bar{l}_b$) can be defined which is related to the crystal size; $\bar{l}_b = 1.12$ D, for a specimen with square cross section of side D. Berman and coworkers[32] have presented a detailed theory of boundary scattering which takes into account different surface conditions.

Earlier accounts of boundary scattering portrayed it as a low-temperature phenomenon. However, in highly disordered materials, boundary scattering may become significant at high temperatures.[33] A high degree of disorder effectively scatters short-wavelength phonons with the net heat conduction being primarily due to long-wavelength phonons. These may then be scattered effectively by the grain boundaries and result in significant reduction in thermal conductivity. Experiments on thin specimens of silicon showed a pronounced decrease in the thermal conductively due to boundary scattering which was enhanced in samples irradiated with neutrons.[34,35]

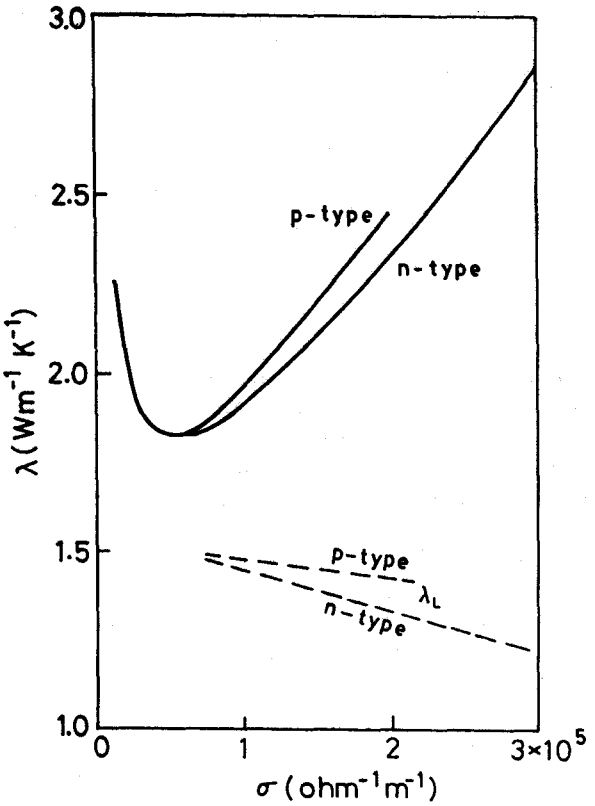

FIGURE 4 Thermal and electrical conductivities of n-type Bi_2Te_3 at 300 K. (Goldsmid, H. J., *Proc. Phys. Soc.*, 72, 17, 1958. With permission.)

Parrott[36] further explored the consequences of grain boundary scattering in fine-grained materials. Considering the high temperature limit ($\hbar\omega/kT \ll 1$, ω referring to average phonon frequency), it is possible to obtain compact simplified formulae for the thermal conductivity which take into account phonon scattering by phonons, grain boundaries, disorder, and electrons. The phonon relaxation times for the Umklapp process is given by

$$\tau_U^{-1} = A_U z^2 \quad (z = \hbar\omega/kT) \tag{11}$$

The Normal process relaxation time is assumed to have the same frequency dependence with $\tau_U = k_0\tau_N$, where k_0 is an adjustable parameter. The thermal conductivity can be conveniently expressed[36–38] in terms of the conductivity of the virtual perfect crystal (λ_0), in which phonon-phonon scattering is the only mechanism which limits the phonon mean free path. The remainder of the expression accounts for all other phonon scattering processes. The thermal conductivity is given by

$$\lambda/\lambda_0 = (1 + 5k_0/9)^{-1}\left\{L_2 + \frac{k_o(1 + k_0)^{-1}L_4^2}{0.2 - k_0(1 + k_0)^{-1}L_6}\right\} \tag{12}$$

where

$$L_n = \int_0^1 \frac{x^n dx}{Ax^4 + x^2 + Bx + C} \tag{13}$$

The parameters representing the strengths of the scattering by alloy disorder, free carriers, and grain boundaries are given by

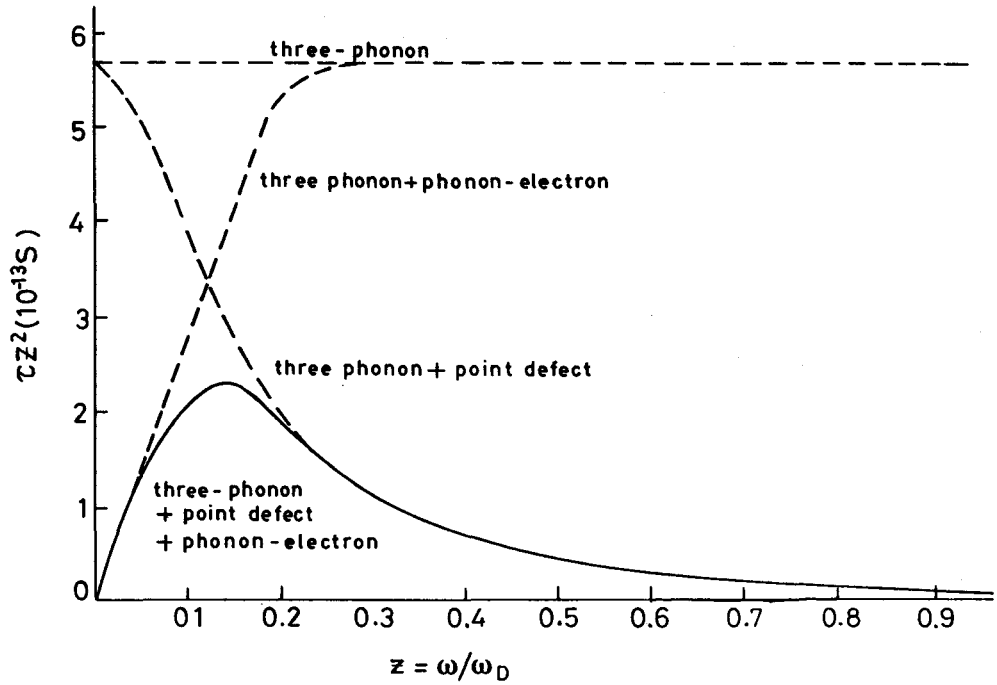

FIGURE 5 Integrand in the thermal conductivity expression plotted against reduced phonon frequency ω/ω_D for various phonon scattering processes. (From Steigmeier, E. F. and Abeles, B., *Phys. Rev. A*, 136, 1149, 1964. With permission.)

$$A = \frac{\pi\lambda_0\Gamma\Omega_0\omega_D}{2v_s^2k(1 + 5k_0/9)} \tag{14}$$

$$B = \frac{2\pi^2\lambda_0 v_s\hbar B'}{\omega_D^2k^2T(1 + 5k_0/9)} \tag{15}$$

$$C = 2\pi^2\lambda_0V_s^2/Lk\omega_D^3(1 + 5k_0/9) \tag{16}$$

With the help of these equations it is possible to explore the effects of the different scattering processes which operate in relevant thermoelectric materials. The factor $(1 + 5k_0/9)$ takes into account (in an approximate way) the special role of the N-processes. The parameters A, B, C represent the strength of scattering by alloy disorder, electron-phonon, and grain boundaries. To appreciate the relative roles and strengths of these phonon scattering mechanisms it is instructive to plot[39] the integrand of the thermal conductivity integral against the reduced phonon frequency x (Figure 5). In a pure (unalloyed) undoped, single crystal ($A = B = C = 0$) the integrand is almost independent of x. The effect of alloying ($A > 0$) is to reduce the integrand considerably in the high-frequency region. The high-frequency phonons having been effectively scattered, most of the heat is carried by low-frequency phonons. The boundary scattering can then effectively scatter low-frequency phonons. It is easy to appreciate the increased effectiveness of boundary scattering in the presence of alloy disorder. Bhandari and Rowe[38] have also discussed the effect of dispersive phonon branches on the lattice thermal conductivity.

6.4 Fine-Grained Materials

Improving the Ratio of Electrical to Thermal Conductivity

An understanding of the relative roles of the various mechanisms in limiting the phonon mean free path may find application in thermoelectric material development. The preparation of fine-grained materials of the required grain size and with the required degree of disorder can effectively

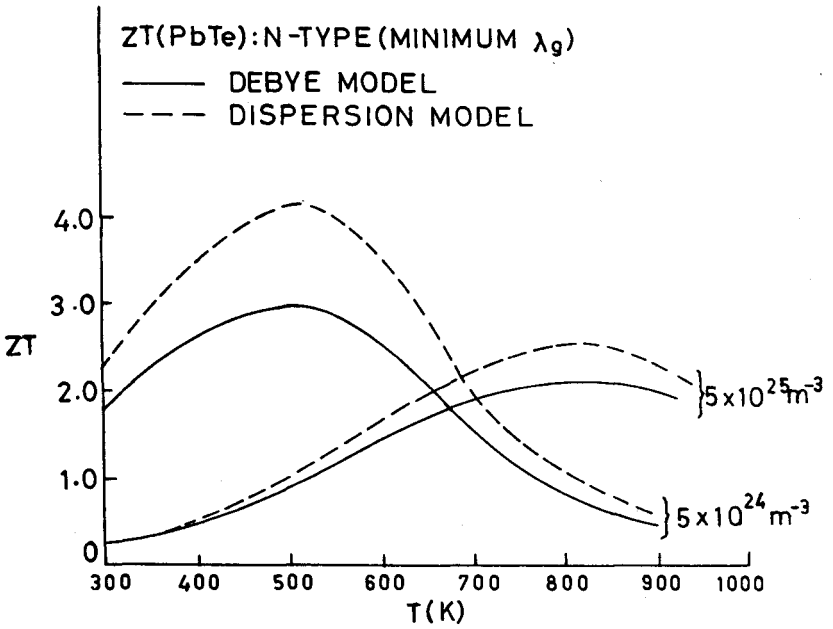

FIGURE 6 ZT plotted against temperature for the Debye and dispersive models. (From Goff, G. F. and Lowney, J. R., *Proc. 11th IECEC*, 1976, p. 1561. With permission.)

reduce the thermal conductivity. Implicit in these considerations is the realization that the electrical conductivity is not significantly influenced by the grain boundaries. Various studies have suggested appreciable improvement in the figure-of-merit of fine-grained silicon-germanium alloys.[40,41] The study was extended[42,43] to lead telluride-based alloys; a grain size of 1 μm could reduce the lattice thermal conductivity of these alloys by around 11 to 13%. Several review papers[41,44–46] present details of the state of the art.

Slack and Hussain[47] have discussed the changes in the electrical and thermal conductivities of Si-Ge alloys that accompany boundary scattering and their results are not in agreement with the earlier reported improvements in the electrical to thermal conductivity ratio. Sample preparation and history are important and need to be taken into consideration before conclusions can be drawn about the degree of effectiveness of grain boundary scattering in improving thermoelectric materials.

Other Considerations

Most of the efforts towards reducing the thermal conductivity described so far have been related to limiting the phonon mean free path l. The simple equation for the thermal conductivity expresses it in terms of the lattice specific heat, sound (phonon) velocity, and l. The simple Debye model is usually used for describing phonon modes, and does not distinguish between various polarizations, and assumes a constant phonon velocity v_q = v. However, this is not always justifiable and the phonon branches may exhibit strong dispersion which has a profound effect on phonon transport. Among the better-known thermoelectric semiconductors, silicon-germanium and lead telluride have strongly dispersed phonon branches. At high frequencies the group velocity becomes very small and in some cases even negative. This may have two consequences: λ_L may be lower than that obtained on the basis of the Debye model, and the alloy disorder may become less effective as the high-frequency phonon contribution has been reduced due to the dispersive effects.

Goff and Lowney[14] obtained the lower bound of λ_L in PbTe by assuming $(l_q)_{min}$ = lattice spacing. This gives the high-temperature values of λ_{min} as 0.126 W/mK and 0.06 W/mK for the Debye and dispersive models, respectively. A plot[14] of ZT vs. T obtained with these λ_L values is shown in Figure 6. It is interesting to note that ZT now has a higher value for lower carrier concentrations,

Table 1. Calculated Values of Various Thermoelectric Parameters for n-Type $Si_{0.70}Ge_{0.30}$ Alloy at 300 K

f	n (10^{26} m^{-3})	$-\alpha$ ($\mu V/K$)	σ (10^2 Ω^{-1} m^{-1})	λ_e (10^{-1}	λ_L W/mK)	Z (10^{-3} K^{-1})
0.0	1.25	136.5	1191.6	8.73	42.73	0.432
0.3	0.65	184.2	662.3	4.85	21.51	0.852
0.6	0.45	213.1	471.5	3.46	13.59	1.256
1.0	0.35	233.5	374.6	2.74	9.00	1.740

(From Slack, G.A. and Hussain, M., *J. Appl. Phys.* 70 (5), 2694, 1991. With permission.)

whereas for normal λ_L values the situation was the reverse. These considerations might have implications in future material research programs.

6.5 Towards a Minimum Thermal Conductivity

The efforts to reduce λ_L are likely to continue in spite of a significant λ_e, which seems to be ignored in theoretical formulations. The concept of a minimum of thermal conductivity was first discussed by Roufosse and Klemens.[48] Slack[49] elaborated the theoretical framework and calculated λ_{min} for a number of crystals. In general both acoustic and optical phonons contribute and their contributions to λ_{min} have been obtained by Slack. The theoretically obtained values of λ_{min} are then compared with the observed values which refer to the high-temperature values obtained by extrapolating the observed thermal conductivity to the melting point. The results for a number of crystals with two atoms per unit cell have been reported.[49] It is to be noted that the observed thermal conductivity at the melting point for some rocksalt structure materials is higher than the calculated minimum by a factor of 2. For adamantine crystals this may increase to 7. This serves to indicate that even at the melting point the lowest thermal conductivity has not been reached and that there is scope for further reduction.

Understandably the minimum refers to a value of thermal conductivity when the phonon mean free path is close to the phonon wavelength. This is essentially similar to the amorphous case and therefore data on amorphous samples can provide an estimate of λ_{min}. For $Si_{70}Ge_{30}$ Slack and Hussain used $\lambda_{min} = 0.9$ W/mK in their calculations. In general any sample may have its λ_L between two limits:

$$\lambda_G \geq \lambda_L \geq \lambda_{min} \tag{17}$$

where λ_G is the thermal conductivity value in pure samples determined from the observed values. It could be obtained as a $T^{-1/2}$ variation[20,50] for temperatures above room temperature. Slack and Hussain express thermal conductivity in resistivity terms and define a parameter f where

$$1/\lambda_L = (1 - f)/\lambda_G + f/\lambda_{min} \tag{18}$$

The parameter f represents the fraction of the progress made towards achieving λ_{min}. Table 1 presents the results of their calculations for silicon germanium at 300 K. A calculation like this is useful in the context of thermoelectric material research. However, for a quantitative estimate of the electronic transport coefficients the effect of band non-parabolicity[10–12] must be taken into consideration, particularly at the high doping levels required for thermoelectric applications.

References

1. Ziman, J. M., *Electrons and Phonons*, Cambridge University Press, London, 1960.
2. Drabble, J. R. and Goldsmid, H. J., *Thermal Conduction in Semiconductors*, Pergamon Press, London, 1961.
3. Parrott, J. E. and Stuckes, A. D., *Thermal Conductivity of Solids*, Pion Limited, London, 1975.
4. Berman, R., *Thermal Conduction in Solids*, Clarendon Press, Oxford, 1976.
5. Bhandari, C. M. and Rowe, D. M., *Thermal Conduction in Semiconductors*, Wiley Eastern Limited, New Delhi, 1988.

6. Ioffe, A. F., *Semiconductor Thermoelements and Thermoelectric Cooling*, Infosearch, London, 1957.
7. Cadoff, I. B. and Miller, E., Eds., *Thermoelectric Materials and Devices*, Reinhold, New York, 1959.
8. Goldsmid, H. J., *Applications in Thermoelectricity*, Methuen Monograph, London, 1960.
9. Ure, R. W. and Heikes, R. R., Eds., *Thermoelectricity: Science and Engineering*, Interscience, London, 1961.
10. Rowe, D. M. and Bhandari, C. M., *Modern Thermoelectrics*, Holt Saunders, London, 1983.
11. Ravich, Y. I., Efimova, B. A., and Smirnov, I. A., in *Semiconducting Lead Chalcogenides*, Stil'bans, T. S., Ed., Plenum, New York, 1970.
12. Ravich, Y. I., Efimova, B. A., and Tamarchenko, Scattering of current carriers and transport phenomena in lead chalcogenides (I), *Phys. Status Solidi(b)*, 43, 11, 1971.
13. Chasmar, R. P. and Stratton, R. J., The thermoelectric figure of merit and its relation to thermoelectric generation, *J. Electron. Control*, 7, 52, 1959.
14. Goff, G. F. and Lowney, J. R., The integral formulation for the thermoelectric figure-of-merit: effects of a lattice thermal conductivity, *Proceedings of 11th IECEC*, 1976, p. 1561.
15. Bhandari, C. M. and Rowe, D. M., Minority carrier effects of the thermoelectric figure-of-merit, *Proceedings of 1st European Conference on Thermoelectrics*, 1988, p. 178.
16. Rowe, D. M. and Bhandari, C. M., Fine-grained Si-Ge alloys as superior thermoelectric materials, *Proceedings of 2nd International Conference on Thermoelectric Energy Conversion*, University of Texas at Arlington, 1978, p. 32.
17. Klemens, P. G., The scattering of low frequency lattice waves by lattice imperfections, *Proc. Phys. Soc. (London) A*, 68, 1113, 1955.
18. Goldsmid, H. J., in *Materials Used in Semiconductor Devices*, Hogarth, C. A., Ed., John Wiley, Interscience, London, 1965, 165.
19. Birkholz, U., *Z. Naturforsch.*, 13a, 780, 1958.
20. Rosi, F. D., Abeles, B., and Jensen, R. V., *J. Phys. Chem. Solids*, 10, 191, 1959.
21. Carruthers, P., *Rev. Mod. Phys.*, 33, 92, 1961.
22. Abeles, B., Lattice thermal conductivity of disordered semiconductor alloys at high temperatures, *Phys. Rev.*, 131, 1906, 1963.
23. Holland, M. G. and Neuringer, L. J., *Proceedings of the International Conference on Physics of Semiconductors*, Exeter, The Institute of Physics and Physical Society, London, 1962, p. 35.
24. Vook, F. L., Thermal conduction of electron-irradiated silicon, *Phys. Rev. A*, 140, 2013, 1965.
25. Wagner, M., Influence of localized modes on thermal conductivity, *Phys. Rev.*, 131, 1443, 1963.
26. Walker, C. T. and Pohl, R. O., Phonon scattering by point defects, *Phys. Rev.*, 131, 1433, 1963.
27. Stuckes, A. D., Thermal conductivity of indium antimonide, *Phys. Rev.*, 107, 427, 1957.
28. Ziman, J. M., The effect of free carriers on lattice conduction, *Philos. Mag.*, 1, 191, 1956.
29. Ziman, J. M., The effect of free carriers on lattice conduction, *Philos. Mag.*, 2, 292, 1957.
30. Goldsmid, H. J., *Proc. Phys. Soc.*, 72, 17, 1958.
31. Bhandari, C. M. and Agrawal, V. K., Thermal and electrical transport in bismuth telluride, *Indian J. Pure Appl. Phys.*, 28, 448, 1990.
32. Berman, R., Foster, E. L., and Ziman, J. M., Thermal conduction in artificial sapphire crystals at low temperatures, *Proc. R. Soc. A*, 231, 130, 1955.
33. Goldsmid, H. J. and Penn, A. W., Boundary scattering of phonons in solid solutions, *Phys. Lett. A*, 27, 523, 1968.
34. Savvides, N. and Goldsmid, H. J., The effect of boundary on the high temperature thermal conductivity of silicon, *J. Phys. C: Solid State Phys.*, 6, 1701, 1973.
35. Savvides, N. and Goldsmid, H. J., *Phys. Status Solidi (b)*, 63, K89, 1974.
36. Parrott, J. E., The thermal conductivity of sintered semiconductor alloys, *J. Phys. Chem.*, 2, 147, 1969.
37. Meddins, H. R. and Parrott, J. E., The thermal and thermoelectric properties of sintered Ge-Si alloys, *J. Phys. C: Solid State Phys.*, 9, 1263, 1976.
38. Bhandari, C. M. and Rowe, D. M., Boundary scattering of phonons, *J. Phys. C: Solid State Phys.*, 11, 1787, 1978.
39. Steigmeier, E. F. and Abeles, B., *Phys. Rev.*, 136, 1149, 1964.
40. Rowe, D. M and Bhandari, C. M., Effect of grain size on the conversion efficiency of semiconductor alloys at high temperatures, *Appl. Energy*, 6, 347, 1980.

41. Bhandari, C. M. and Rowe, D. M., Silicon-germanium alloys as high temperature thermoelectric materials, *Contemp. Phys.*, 21, 219, 1980.
42. Bhandari, C. M. and Rowe, D. M., The effect of phonon grain boundary scattering, doping and alloying on the lattice thermal conductivity of lead telluride. *J. Phys. D: Appl. Phys.*, 16, L75, 1983.
43. Rowe, D. M. and Bhandari, C. M., Lattice thermal conductivity of small grain size PbSnTe and PbGeTe thermoelectric materials, *Appl. Phys. Lett.*, 47, 256, 1985.
44. Rowe, D. M. and Bhandari, C. M., Preparation and thermal conductivity of doped semiconductors, *Prog. Cryst. Growth Charact.*, 13, 233, 1986.
45. Rowe, D. M. and Bhandari, C. M., A review of lead telluride technology at UWIST, *Sixth Int. Conf. on Thermoelectric Energy Conversion*, Arlington, 1986, p. 43.
46. Parrott, J. E., Thermal conductivity: a guide to improved thermoelectric materials, *Proceedings of the 1st European Conference on Thermoelectrics*, Cardiff, 1988, p. 187.
47. Slack, G. A. and Hussain, M., The maximum possible conversion efficiency of Si-Ge thermoelectric generators, *J. Appl. Phys.*, 70(5), 2694, 1991.
48. Roufosse, M. and Klemens, P. G., *J. Geophys. Res.*, 79, 703, 1974.
49. Slack, G. A., The thermal conductivity of nonmetallic crystals, in *Solid State Physics*, Turnbull, D. and Ehrenreich, H., Eds., Academic Press, New York, 1979, 34.
50. Abeles, B., Beers, D. S., Cody, G. D., and Dismukes, J. P., Thermal conductivity of Ge-Si alloys at high temperature, *Phys. Rev.*, 125, 44, 1962.

7

Selective Carrier Scattering in Thermoelectric Materials

Y. I. Ravich
Ioffe Technical Physical Institute
St. Petersburg, Russia

7.1 Introduction

Carrier scattering may be called selective when carriers of one energy are scattered considerably more strongly than those of a different energy, i.e., when the relaxation time and the mean free path are strongly energy dependent. If the relaxation time of comparatively energetic ("hot") carriers is substantially higher than that of low-energy ("cold") ones, such selective scattering increases the mean carrier energy in the flow, hence, the Seebeck (α) and Peltier (P) coefficients. The presence of selective scattering, besides the conventional phonon scattering, may increase the $\alpha^2\sigma$ product (power factor) and the figure-of-merit Z, despite a decrease of the electric conductivity σ.

The relative increase of the thermoelectric parameters can be particularly large when the carriers are degenerate, i.e., when the chemical potential $\mu > 0$. In this case, the contributions to the Seebeck coefficient of the hot electrons with $\varepsilon > \mu$, and of the cold ones with $\varepsilon < \mu$, are of opposite signs. If the relaxation time depends smoothly on energy, then these contributions will largely cancel out. In the presence of selective scattering, if it is strong enough, they do not cancel one another.

Coulomb scattering by charged impurity centers is selective to some degree. However, two other mechanisms, namely, resonant scattering by impurity and defect centers and scattering by potential barriers at grain and crystallite boundaries, exhibit a considerably higher selectivity.

7.2 Resonant Scattering

Resonant scattering in thermoelectrics and its effect on the thermoelectric parameters have been studied both experimentally and theoretically.[1-7] Resonant scattering by impurity atoms and defects occurs when there are quasi-local states in an allowed energy band. On jumping from the band into an impurity state, carriers reside in it for a certain time and are ejected back into the band with a different momentum. The finite lifetime of the carrier in the impurity state, i.e., the nonstationary nature of the impurity state, results in a broadening of the level. Other mechanisms can also produce broadening, such as carrier exchange between the level in question and other bands, impurity wave function overlap, a spread in the impurity level positions because of sample inhomogeneities, and interactions between disordered impurity atoms and defects.

0-8493-0146-7/95/$0.00+$.50

If the level broadening is not too large, the carriers with energies close to the level will be predominantly scattered, so that the resonant scattering relaxation time should be strongly energy dependent. If the resonance level lies below the chemical potential in a degenerate sample, carriers with negative values of ε-μ are primarily involved in scattering and their contribution to the mean flow energy decreases and results in an increased Seebeck coefficient.

The energy dependence of the density-of-states in a resonant band can be approximated by a bell-shaped Lorenz function, the reciprocal relaxation time of the resonant scattering being described by the same function. The resonant relaxation time as a function of energy can be represented in the form

$$\tau_{res} = \tau_{res}^{(0)}\left[1 + \left(\frac{\varepsilon - \varepsilon_i}{\Gamma/2}\right)^2\right] \tag{1}$$

where Γ is the resonant band width including all relevant broadening processes, $\tau_{res}^{(0)}$ is the minimum value of τ_{res} reached at the impurity band center, $\varepsilon = \varepsilon_i$. The parameter $\tau_{res}^{(0)}$ is inversely proportional to the concentration of the impurities or defects responsible for the resonant states. While in the simplest cases it lends itself to a straightforward calculation, it is usually fitted using experimental data.

The transport coefficients that determine the thermoelectric figure-of-merit (α, σ, and electronic thermal conductivity λ_e) are calculated for the case where both the resonant impurity scattering and the conventional acoustic phonon scattering described by the relaxation time $\tau_{ac}(\varepsilon)$ are present. The total relaxation time τ is presented in terms of the following dimensionless functions and parameters:

$$\psi(x) = \frac{\tau}{\tau_{ac}} = \left(1 + \frac{\tau_{ac}}{\tau_{res}}\right)^{-1} = \left[1 + \frac{A}{1 + \left(\dfrac{x}{\Gamma^*/2} + M\right)^2}\right]^{-1} \tag{2}$$

$$A = \frac{\tau_{ac}(\mu)}{\tau_{res}^{(0)}},\ M = \frac{\mu - \varepsilon_i}{\Gamma/2},\ x = \frac{\varepsilon - \mu}{kT},\ \Gamma^* = \frac{\Gamma}{kT} \tag{3}$$

The parameter A is proportional to the resonant scattering intensity and describes the partial contribution of the resonant scattering at an energy $\varepsilon = \varepsilon_1$ corresponding to the center of the impurity band. The quantity M relates to the separation of the chemical potential from the band center and is directly connected with the impurity band filling, K ($K \geq 0.5$ for $M \geq 0$). The transport integrals should be calculated bearing in mind that $\Psi(x)$ is a fast varying function, just as an energy derivative of the Fermi-Dirac function. An approximation based on these properties yields the following expressions:

$$\sigma/\sigma_0 = I_0, \tag{4}$$

$$\alpha = \frac{k}{e}\frac{I_1 + I_2/\mu^*}{I_0}, \tag{5}$$

$$L = \frac{\lambda_e}{\sigma T} = \left(\frac{k}{e}\right)^2 \frac{I_2}{I_0} - \alpha^2, \tag{6}$$

where σ_0 is the electric conductivity in the absence of the resonant scattering ($A = 0$, $\psi = 1$), L is the Lorenz number. The integrals

$$I_n = \int_{-\mu^*}^{\infty} \left(-\frac{df}{dx}\right) \psi(x) \cdot x^n dx \ (n = 0,1,2) \tag{7}$$

were calculated numerically for various values of the parameters A, M, $\Gamma^*/2$ and μ^*.

Presented here are the numerical results obtained for the case of moderately strong degeneracy, $\mu^* = 6$, and the impurity band halfwidth of k_0T ($\Gamma^*/2 = 1$). Figure 1 displays the dependence of $\alpha^2\sigma$ on A for different values of M. The highest value of $\alpha^2\sigma$, which is three times the corresponding value in the absence of the resonant scattering, is reached at $A = 10$, $M = 2$. The smooth

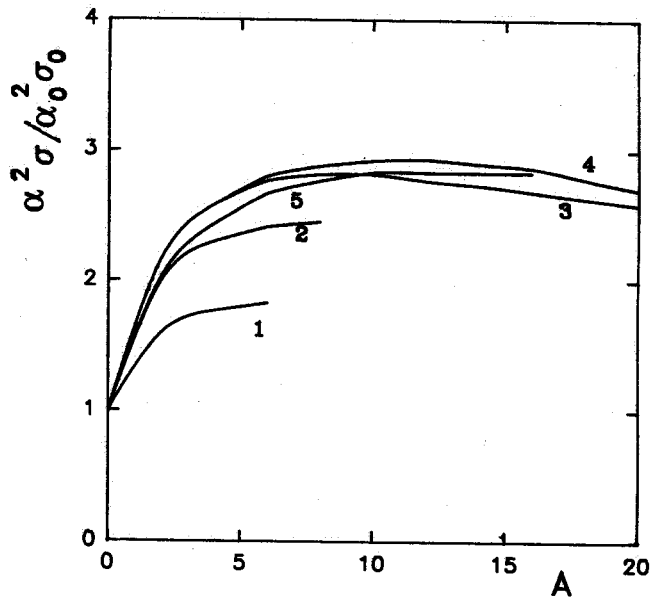

FIGURE 1 Calculated $\alpha^2\sigma$ product reduced to its value in the absence of resonant scattering vs. parameter A characterizing the scattering intensity, for $\mu^* = 6$, $\Gamma^*/2 = 1$. Parameter M specifying the position of the resonant band center relative to chemical potential is 0.5 (curve 1), 1.0 (2), 1.5 (3), 2.0 (4), 2.5 (5).

behavior of the curves implies that the pronounced gain in $\alpha^2\sigma$ is obtained over a broad range of A (from 1 to a few tens) and M (from 0.5 to a few times one). The optimum value, $A = 10$, usually corresponds to a fairly high impurity concentration ($\approx 10^{20}$ cm^{-3}), and the optimum $M = 2$ to a high band filling ($K \approx 0.85$). A separate analysis of the electric conductivity and of the Seebeck coefficient has revealed that the former decreases with increasing A by the same factor by which the thermopower increases, resulting in an increase in $\alpha^2\sigma$.

The selective resonant scattering markedly affects the dependence of α and $\alpha^2\sigma$ on the degeneracy μ^*. While in conventional acoustic phonon scattering $\alpha^2\sigma$ decreases with increasing chemical potential for $\mu^* > 1$, in the case of selective scattering the thermopower remains constant, about 100 μV/K with increasing chemical potential and carrier concentration, for the fixed optimum values of A and M, so that $\alpha^2\sigma$ increases with carrier concentration. Thus, resonant scattering substantially increases the optimum carrier concentration which now becomes dominated by such factors as the impurity solubility, mechanical strength at high impurity concentrations, etc.

According to the Wiedemann-Franz relation, the threefold drop of σ at the optimum values of A and M brings about a corresponding decrease of the thermal conductivity. The calculations also show that resonant scattering reduces the Lorenz number L, primarily due to the increase of α^2 in Equation 6. For instance, for $\Gamma^*/2 = 1$ and $\mu^* = 6$ the value of L decreases by a factor 1.65 as A increases from 0 to 10. Thus, resonant scattering reduces the electronic thermal conductivity as a result of the decrease in both σ and L. This leads to an increase of the figure-of-merit Z in samples where the electronic conductivity is not small compared with the lattice contribution.

It thus follows that resonant scattering can be used to increase substantially the figure-of-merit by doping a thermoelectric material with an impurity which creates resonant levels close to the allowed band edge. Optimum band filling can be achieved by additional doping with an electrically active impurity which does not itself produce levels near the band edge. Positive effects from resonant scattering can be achieved only with double doping, which not only creates a large number of resonant states, but provides conditions favorable for a high degree of their filling by carriers.

Lead telluride was doubly doped with thallium which produced a resonant level in the valence band near the edge of the second extremum, and with sodium used as the additional impurity.[2,5] Lead telluride samples containing 1 at.% thallium and 1 at.% sodium possessed a hole concentration of about 10^{20} cm^{-3} and a hole reduced chemical potential, $\mu^* \approx 6$ at room temperature.

In singly doped samples with the same concentration, the maximum of Z is observed to occur at about 750 K and Z drops dramatically with decreasing temperature down to room temperature. This results in a decrease of the mean value of Z and of the thermoelectric generator efficiency over the temperature range ≈300 to 900 K. The drop becomes much smaller in doubly doped samples due to the resonant scattering by thallium atoms. An evaluation of the resonant scattering parameters for this sample corresponding to a temperature of 300 K yields for A and M values of the order 1. While they are less than the optimum values, the resonant scattering offers a possibility of increasing the Seebeck coefficient from 56 μV/K in sodium-doped samples up to 140 μV/K for double doping, with the conductivity dropping by two to three times. The values of $\alpha^2\sigma$, and Z at 300 K turn out to be two to three times larger than those in samples with the same hole concentration obtained by single doping.

Resonant scattering is observed to occur also in In-doped n-type lead telluride (PbTe) and lead selenide (PbSe),[8–10] and in In-doped p-type tin telluride (SnTe).[11]

Low temperatures are favorable for making resonant scattering comparable with the phonon contribution. This is why the use of resonant scattering is promising for use in thermoelectric cooling materials. However, the existence and properties of resonant states in low-temperature thermoelectrics have been studied less thoroughly than those for the IV–VI semiconductors. Nevertheless, there is convincing experimental and theoretical evidence for the existence of resonant states in bismuth telluride[12,13] and in bismuth.[14]

7.3 Scattering by Potential Barriers

The presence of potential barriers can result in a strong dependence of the mean free path on energy near the chemical potential, if their height is close to the Fermi level.[15–17] Carriers of energy lower than the barrier height, $\varepsilon < \varepsilon_b$ ("cold"), are stopped, while most of those with energy above the barrier height, $\varepsilon > \varepsilon_b$ ("hot"), pass through it. The selective effect of a barrier becomes most pronounced when the energy mean free path, l_e, is much greater than that in momentum, l_p.[18]

The case particularly favorable for thermoelectric applications is when the mean barrier separation d is much greater than the momentum mean free path and substantially smaller than that in energy,

$$l_p \ll d \ll l_e \tag{8}$$

Under these conditions, the "cold" carriers will be practically excluded from the flow directed perpendicular to the barriers, the "hot" ones being only weakly affected by the presence of the latter. Their effect in the limiting case (Equation 8) can be evaluated using a simple model for the relaxation time τ, in which $\tau = 0$ for $\varepsilon < \varepsilon_b$, and depends relatively weakly, e.g., by a power law, on energy for $\varepsilon > \varepsilon_b$ similar to the relaxation time in samples without potential barriers. Thus, this model predicts a jump in the relaxation time at $\varepsilon = \varepsilon_b$. In the case of strong degeneracy ($\mu^* \gg 1$), this model yields the following expressions for the electrical conductivity σ, Seebeck coefficient α, and Lorenz number L:

$$\sigma/\sigma_0 = (1 + e^{\eta})^{-1} \tag{9}$$

$$\alpha = \frac{k}{e} \cdot [\eta + (1 + e^{\eta}) \cdot \ln(1 + e^{-\eta})] \tag{10}$$

$$L = \left(\frac{k}{e}\right)^2 \cdot \{2(1 + e^{\eta}) \cdot F_1(-\eta) - (1 + e^{\eta})^2 \cdot [\ln(1 + e^{-\eta})]^2\} \tag{11}$$

where σ_0 is the conductivity in the absence of barriers, $F_1(\eta)$ is the Fermi integral, and

$$\eta = (\varepsilon_b - \mu)/kT \tag{12}$$

Figure 2 presents the dependencies of the Seebeck coefficient, conductivity, and $\alpha^2\sigma$ product, reduced to the corresponding values for barrier-free samples, on the quantity η in the region where

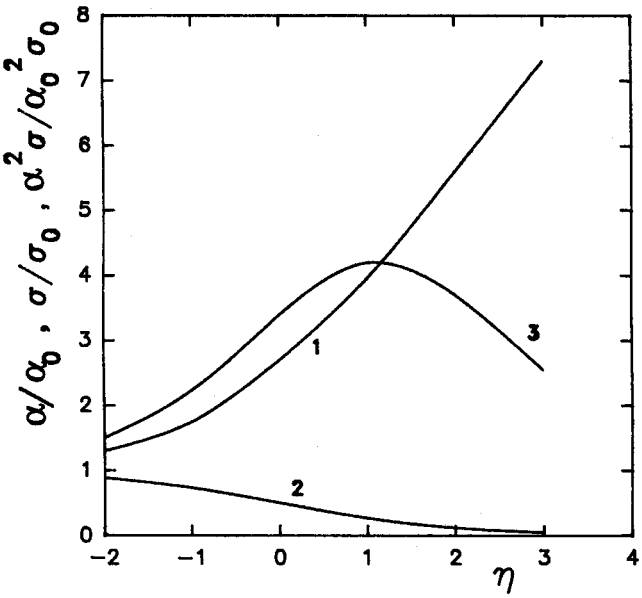

FIGURE 2 Calculated Seebeck coefficient (curve 1), electric conductivity (2), and $\alpha^2\sigma$ product (3), reduced to the corresponding values in the absence of barriers for $\mu^* = 6$, vs. reduced barrier height η.

$|\eta|$ is not much greater than one calculated using Equations 9 and 10. The value of α_0 was taken for the particular case of moderately strong degeneracy, $\mu^* = 6$, a standard carrier dispersion law, and acoustical phonon scattering. It follows from the calculations that the Seebeck coefficient increases and the conductivity decreases in the presence of barriers, while the $\alpha^2\sigma$ product increases by about a factor 4 if the barrier height is close to the Fermi level ($\eta = 0$ to 2).

This increases with the degree of degeneracy μ^*. As in the case of the resonant scattering (see Section 7.1), the presence of barriers significantly increases the optimum degree of degeneracy.

At the same time, in the more realistic case where the inequality (Equation 8) does not hold, the increase in the $\alpha^2\sigma$ product is somewhat less than that obtained in the idealized model. However, it is still substantial over a broad range of variation of l_p/l_e and d/l_p.[18]

In the presence of barriers, the figure-of-merit Z can also increase due both to the increase of $\alpha^2\sigma$, and a decrease of the electronic thermal conductivity $\lambda_e = L\sigma T$; this falls because of the reduction in the electric conductivity and the Lorenz number. In particular, Equation 11 shows that for $\eta = 0$ the effect of the barriers decreases the Lorenz number by 2.5 times.

The above mechanism of enhancing the thermoelectric parameters has been experimentally verified in epitaxial films of *n*- and *p*-type lead chalcogenides.[15–17] The films about 1 μm thick were grown on different substrates, and had small crystallites with their boundaries perpendicular to the film surface. Thus, the carrier and heat flows propagating along a film crossed the potential barriers at the crystallite boundaries. The experimental data suggest that the barrier height was about equal to the Fermi level. The authors[15,16] believed that this barrier height is established automatically under the influence of shallow levels at the crystallite boundaries representing dislocation walls, irrespective of the carrier concentration. The levels originated possibly from the elastic deformation of the crystal near dislocations.

Besides the changes in the electric conductivity and the Seebeck coefficient in films compared with bulk samples, the existence of barriers is experimentally supported by a clearly pronounced anisotropy of the magnetoresistance measured at two magnetic field orientations, namely, perpendicular to the film surface (i.e., along the barriers) and in the film plane.[19] The observed magnetoresistance anisotropy differed qualitatively from that typical of single crystals. Further experimental evidence for the existence of barriers is the extremely slow relaxation of the photoconductivity of films.[20]

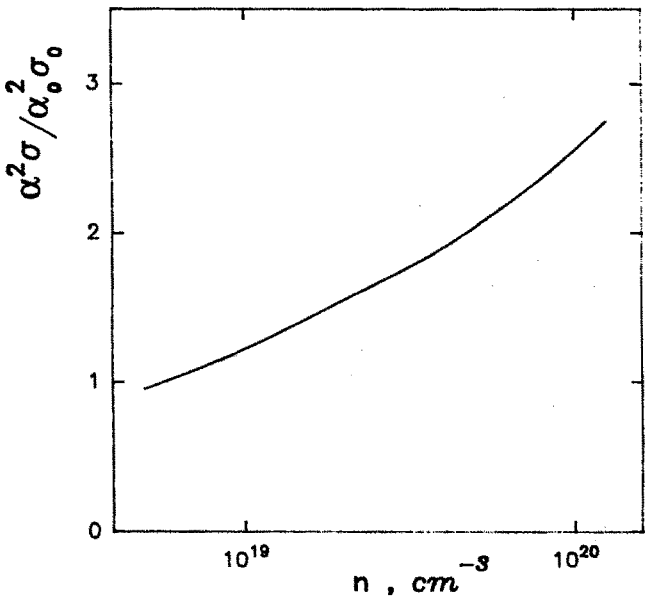

FIGURE 3 The $\alpha^2\sigma$ product obtained[15] on *n*-lead telluride films at 300 K and reduced to the corresponding values for bulk samples, vs. electron concentration.

Figure 3 displays the experimental dependence of the $\alpha^2\sigma$ product, at room temperature, on electron concentration in *n*-type lead telluride films grown on mica substrates.[15] In the concentration range of around 10^{19} to 10^{20} cm^{-3}, the $\alpha^2\sigma$ product is seen to be about twice the corresponding value for bulk samples with the same electron concentration. Such a behavior is observed to prevail throughout the temperature range 100 to 300 K, as well as for films on polyamide substrates,[17] and in *n*- and *p*-type lead selenide.[16]

The values of the thermoelectric parameters obtained for films are not an upper limit. The positive effect of potential barriers on the thermoelectric properties can be enhanced by properly choosing the dopant[21] and the degree of deviation from stoichiometry,[17] as well as by optimization of the crystallite size relative to the mean free path length.

The creation of barriers capable of charge-selective scattering appears promising. If a barrier scatters the minority carriers more strongly than the majority ones, the suppression of the minority carrier mobility may shift the onset of mixed conduction and ambipolar diffusion to higher temperatures and, hence, increase the figure-of-merit averaged over the working temperature interval.

References

1. Kaidanov, V. I. and Nemov, S. A., Effect of thallium impurity on hole scattering in lead telluride, *Fiz. Tekh. Poluprovodn.*, 15, 542, 1981 (in Russian).
2. Kaidanov, V. I., Nemov, S. A., Ravich, Y. I., and Zaitsev, A. M., Influence of resonance states on Hall effect and electric conductivity in PbTe under simultaneous doping by thallium and sodium, *Fiz. Tekh. Poluprovodn.*, 17, 1613, 1983 (in Russian).
3. Nemov, S. A., Ravich, Y. I., and Zaitsev, A. M., Peculiarities of the transverse Nernst-Ettingshausen effect in conditions of high resonance scattering in PbTe < Tl >, *Fiz. Tekh. Poluprovodn.*, 19, 636, 1985 (in Russian).
4. Kaidanov, V. I. and Ravich, Y. I., Deep and resonance states in IV–VI type semiconductors, *Sov. Phys. Usp.*, 145, 51, 1985 (in Russian).
5. Kaidanov, V. I., Iordanishvili, E. K., Naumov, V. N., Nemov, S. A., and Ravich, Y. I., Effect of charge carrier resonance scattering on the kinetic coefficients in the absence of a magnetic field, *Fiz. Tekh. Poluprovodn.*, 20, 1102, 1986 (in Russian).

6. Ravich, Y. I. and Vedernikov, M. V., On a possibility of increasing the thermoelectric figure-of-merit through resonance charge carrier scattering, in *Proc. IX Int. Conf. on Thermoelectrics (USA)*, Vining, C. B., Ed., JPL, Pasadena, 1990, 278.
7. Nemov, S. A. and Ravich, Y. I., Resonance-state density from data of thermopower in PbTe < Tl >, *Fiz. Tekh. Poluprovodn.*, 22, 1370, 1988 (in Russian).
8. Kaidanov, V. I., Melnik, R. B., and Chernik, I. A., Study on indium-doped lead telluride, *Fiz. Tekh. Poluprovodn.*, 7, 759, 1973 (in Russian).
9. Chernik, I. A., On temperature-dependent part of electron mobility in indium-doped lead telluride, *Fiz. Tekh. Poluprovodn.*, 14, 80, 1980 (in Russian).
10. Prokofieva, L. V., Gurieva, E. A., Zhumaksanov, S. M., Konstantinov, P. P., Mailina, K. R., Ravich, Y. I., and Stilbans, L. S., Peculiarities of In donor action in PbSe, *Fiz. Tekh. Poluprovodn.*, 21, 1778, 1987 (in Russian).
11. Bushmarina, G. S., Grusinov, B. F., Drabkin, I. A., Lev, E. Y., and Yuneev, B. M., Some peculiarities of In doping action in SnTe, *Fiz. Tekh. Poluprovodn.*, 18, 2203, 1984 (in Russian).
12. Pecheur, P. and Toussaint, G., Tight binding studies of crystal stability and defects in Bi_2Te_3, in *Proc. 8th Int. Conf. on Thermoelectric Energy Conversion*, Scherrer, H. and Scherrer, S., Eds., INPL, Nancy (France), 1989, 176.
13. Kulbachinskii, V. A., Brandt, N. B., Cheremnykii, P. A., Azou, S. A., Horak, J., and Lostak, P., Magnetoresistance and Hall effect in Bi_2Te_3 < Sn > in ultrahigh magnetic fields and under pressure, *Phys. Status Solidi (b)*, 150, 237, 1988.
14. Falkovsky, L. A., On impurity states in substances with narrow gaps, *Zh. Eksp. Teor. Fiz.*, 68, 1529, 1975 (in Russian).
15. Gudkin, T. S., Drabkin, I. A., Kaidanov, V. I., and Sterlyadkina, Special features of electron scattering in PbTe thin films, *Fiz. Tekh. Poluprovodn.*, 8, 2233, 1974 (in Russian).
16. Bytensky, L. I., Gudkin, T. S., Iordanishvili, E. K., Kazmin, S. A., Kaidanov, V. I., Nemov, S. A., and Ravich, Y. I., *Fiz. Tekh. Poluprovodn.*, 11, 1522, 1977 (in Russian).
17. Boikov, Y. A., Goltsman, B. M., Gudkin, T. S., Dedegkaev, T. T., Zhukova, T. B., Iordanishvili, E. K., and Shmuratov, E. A., On anomalous growth of thermopower coefficient in *n*-PbTe films, *Fiz. Tverd. Tela*, 22, 1226, 1980 (in Russian).
18. Moizhes, B. Y., Naumov, V. N., and Nemchinsky, V. A., personal communication, 1977.
19. Bytensky, L. I., Gudkin, T. S., Kazmin, S. A., Kaidanov, V. I., Ozerova, L. A., and Ravich, Y. I., Anisotropy in magnetoresistance of PbSe films with potential barriers, *Fiz. Tekh. Poluprovodn.*, 13, 300, 1979 (in Russian).
20. Grigoriev, A. V., Kazmin, S. A., and Kaidanov, V. I., Effect of IR lighting on kinetic coefficients in PbTe films with potential barriers, *Fiz. Tekh. Poluprovodn.*, 17, 934, 1983 (in Russian).
21. Bytensky, L. I., Kazmin, S. A., Kaidanov, V. I., Ravich, Y. I., and Saveliev, A. V., Effect of doping impurity sort on electrophysical properties of lead selenide films, *Fiz. Tekh. Poluprovodn.*, 16, 113, 1982 (in Russian).

8

Thermomagnetic Phenomena

H. J. Goldsmid
University of New South Wales
Australia

8.1 Thermogalvanomagnetic Effects

The application of a magnetic field to an electrical conductor both modifies those properties that are involved in thermoelectric energy conversion, i.e., the thermoelectric coefficients, the electrical resistivity, and the thermal conductivity, and introduces a number of new phenomena, some of which can be utilized in their own right for refrigeration or generation. The complete range of phenomena are often referred to as the thermogalvanomagnetic effects.

The most familiar of these magnetic effects are the Hall effect and the magnetoresistance, two phenomena that do not require the application of a temperature gradient. The Hall effect is commonly used in the study of all types of semiconductors since it reveals, at least approximately, the concentration of charge carriers (when they are of only one type) and, together with the electrical conductivity, it enables the mobility of the charge carriers to be estimated. The magnetoresistance is, perhaps, of more concern, since it directly affects one of the parameters involved in the thermoelectric figure-of-merit. A phenomenon that is closely related to the magnetoresistance is the magnetothermal resistance, that is, the change in thermal resistivity due to a magnetic field. The magnetoresistance tends to be larger than the magnetothermal resistance, since the latter is associated with only the electronic part of the thermal conductivity and not the lattice component. Thus, the effect of a magnetic field is to increase the product $\rho\lambda$ and the figure-of-merit can only benefit if the increase in α^2 is still greater. Sometimes, indeed, the Seebeck coefficient may fall as a magnetic field is applied, but there is at least one known case where the use of a magnetic field is beneficial.

8.2 Bismuth-Antimony as a Thermoelectric Material

It has been realized for many years that certain of the bismuth-antimony alloys become superior, as negative thermoelectric materials, to the Bi_2Te_3-Bi_2Se_3-Sb_2Te_3 alloys when the temperature falls well below the ordinary ambient value. It has been found that the superiority of the bismuth-antimony alloys becomes even greater, particularly in the region of liquid nitrogen temperature, when a transverse magnetic field is applied.[1] The effect is strongest when the electric current passes in the trigonal direction of a single crystal and when the magnetic field is applied in the bisectrix direction.

It should be noted that pure bismuth has long been used as a negative thermocouple material, for example, in thermal detectors, and, indeed, in single crystal form it has the relatively high

0-8493-0146-7/95/$0.00+$.50

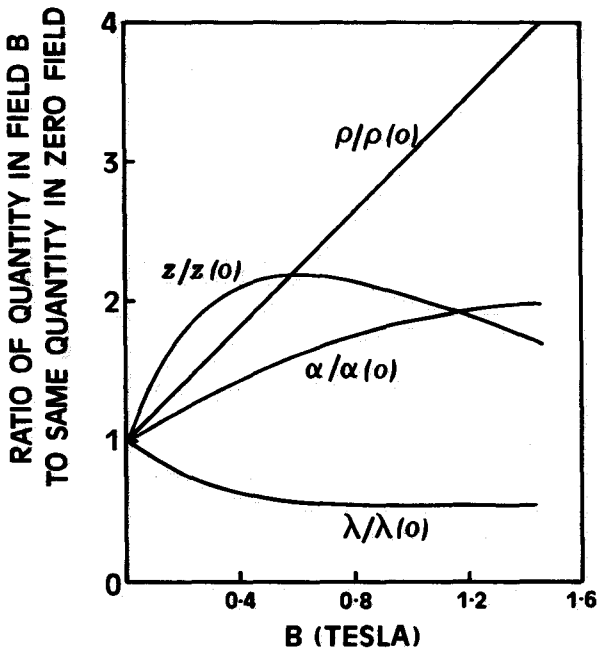

FIGURE 1 Relative change of thermoelectric properties of $Bi_{0.88}Sb_{0.12}$ at 160 K in a magnetic field. The electrical and thermal flows are in the trigonal direction and the magnetic field is along the bisectrix direction.[1]

figure-of-merit of 1.7×10^{-3} K^{-1} at 100 K.[2] Whereas bismuth is a semimetal, some of the bismuth-antimony alloys display semiconducting behavior and this enables larger Seebeck coefficients to be obtained, but a more significant factor, perhaps, is the reduction in the lattice thermal conductivity on the formation of a solid solution.[3] Thus, at about 100 K, the figure-of-merit has a value of more than 4×10^{-3} K^{-1} for a single crystal of the alloy $Bi_{0.88}Sb_{0.12}$ in the absence of a magnetic field.[4] The application of a transverse magnetic field causes the figure-of-merit to rise substantially. For example,[1] at 160 K the figure-of-merit rises from 3.4×10^{-3} K^{-1} to 7.6×10^{-3} K^{-1} as the field rises from zero to 0.6 T.

The behavior of the individual properties is shown in Figure 1. Although the electrical resistivity rises by a factor of more than 2, this is partly offset by the fall in thermal conductivity, but the most striking effect (as compared with observations on other materials) is the considerable increase in the Seebeck coefficient. The value of the latter in zero field is -130 μV K^{-1}, with a value of -260 μV K^{-1} being reached in a field of about 1.5. T. Smith and Wolfe[4] were unable to explain such a large increase in terms of normal extrinsic semiconductor behavior and suggested that it was due to the influence of the transverse thermomagnetic effects. However, before discussing this point any further, it might be mentioned that, to date, no positive branch material that is at all comparable with the negative bismuth-antimony alloys has been found. This may not matter if, in due course, superconductors that can carry sufficiently high currents at the required temperatures are developed. Such materials could then be used as "passive" branches in conjunction with the "active" bismuth-antimony alloys.[5]

Perhaps the most direct evidence that the transverse effects are responsible for the large increase in the Seebeck coefficient in a magnetic field is provided by the experiments of Ertl et al.[6] These authors measured the magneto-Seebeck coefficient for samples of different length-to-width ratio cut from the same crystal of $Bi_{0.93}Sb_{0.07}$. They found that, whereas in zero field all the samples had the same Seebeck coefficient (-90 μV K^{-1} at 80 K), they had very different values in a field of 0.5 T. For example, the sample with a length-to-width ratio of 0.71 had a Seebeck coefficient of -100 μV K^{-1} while that with a length-to-width ratio of 2.55 had a Seebeck coefficient of about -145 μV K^{-1}. One would indeed expect such a shape dependence if any of the transverse thermogalvanomagnetic phenomena were involved. Other evidence is provided by the work of Thomas

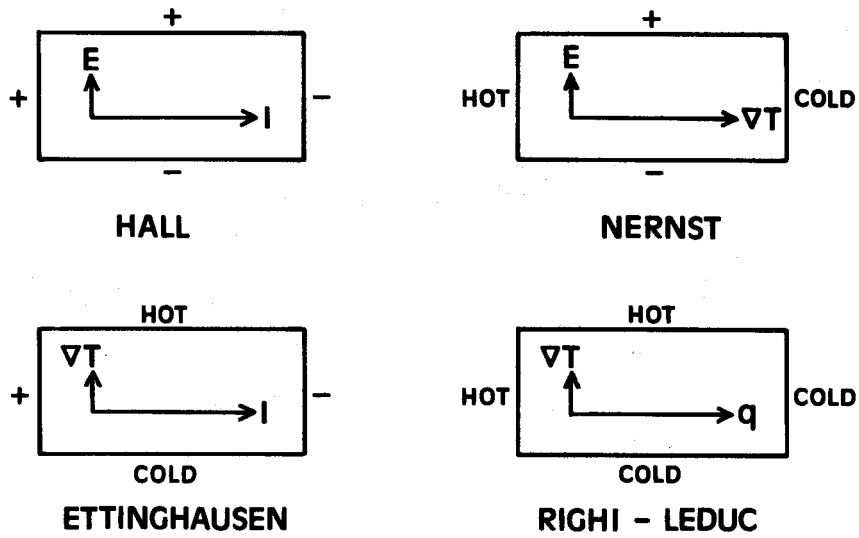

FIGURE 2 Transverse thermogalvanomagnetic effects. The coefficients are positive if the directions are as shown in the diagram. E represents electric field, I represents electric current, ∇T represents temperature gradient, and q represents heat flow.

and Goldsmid,[7] who showed that when there is only one type of carrier, in this case $Bi_{0.95}Sb_{0.05}$ doped with tellurium, the rise in Seebeck coefficient in a magnetic field is much smaller than when there are both electrons and holes present. As shall be seen, it is the simultaneous presence of electrons and holes that makes the transverse thermomagnetic effects large.

If, then, it is the transverse effects that are responsible for the large thermoelectric figure-of-merit of bismuth-antimony in a magnetic field, one might expect to be able to use these effects directly. Thus, for the remainder of this chapter, attention will be concentrated on the transverse phenomena.

8.3 Transverse Thermomagnetic Effects

The four transverse thermogalvanomagnetic effects are shown in Figure 2. Of minor importance in this context are the Hall effect (a transverse electric field produced by a longitudinal electric current) and the Righi-Leduc effect (a transverse temperature gradient produced by a longitudinal heat flow). Of more interest are the Nernst effect (a transverse electric field produced by a longitudinal heat flow) and the Ettingshausen effect (a transverse temperature gradient produced by a longitudinal electric current), since these are the transverse analogues of the Seebeck and Peltier effects, respectively. In principle, the Nernst effect could be used in the generation of electricity from heat. It has, in fact, been suggested that a thermal radiation detector based on the Nernst effect would be much faster than the more familiar radiation thermopile.[8] However, it is difficult to conceive of a situation in which a transverse thermomagnetic generator would be of practical value. On the other hand, a transverse thermomagnetic refrigerator, based on the Ettingshausen effect, could well be useful at low temperatures. Figure 3 shows a schematic diagram of such a device.

In practice a transverse thermomagnetic device is complicated by the distortion of the electrical and thermal flow patterns by the presence of the end and side contacts, but, in principle, these effects can be minimized and they shall be ignored here. An expression can be found for the rate q_y of transverse heat flow that results from the longitudinal current I_x. This expression can contain the Ettingshausen coefficient or, more conveniently, the Nernst coefficient N, defined as the transverse electric field produced by unit longitudinal temperature gradient, there being a unit magnetic field in the mutually perpendicular direction. The two coefficients are related to one another by thermodynamics, just as the Peltier and Seebeck coefficients are inter-related. Using analogous

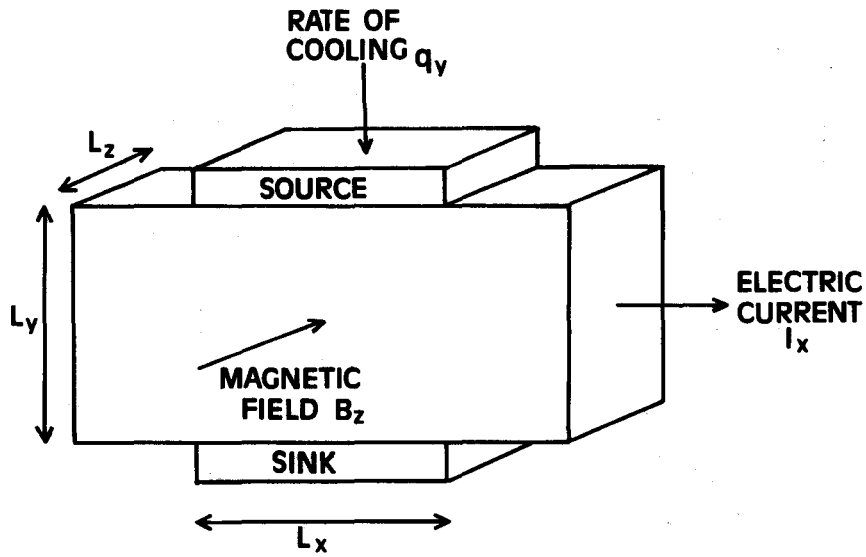

FIGURE 3 Schematic thermomagnetic refrigerator.

processes to those used in calculating the cooling power of a thermoelectric refrigerator,[9] one finds that

$$q_y = \frac{N B_z I_x T_1 L_x}{L_y} - \frac{\lambda L_x L_z (T_2 - T_1)}{L_y} - \frac{I_x^2 \rho L_x}{2 L_z L_y} \tag{1}$$

where L_x, L_y, and L_z are the dimensions of the sample in the three directions, T_1 and T_2 are the source and sink temperatures, respectively, ρ is the electrical resistivity, λ is the thermal conductivity, and B_z is the magnetic field strength. The expression for the cooling power of a Peltier device becomes identical with Equation 1 if the differential Seebeck coefficient $(\alpha_p - \alpha_n)$ is replaced by NB_zL_x/L_y, the thermal conductance is replaced by $\lambda L_xL_z/L_y$ and the electrical resistance is replaced by $\rho L_x/L_zL_y$. This means that a thermomagnetic figure-of-merit can be defined as

$$Z_E = \frac{(N B_z)^2}{\rho \lambda} \tag{2}$$

which has the same significance for Ettingshausen cooling as the thermoelectric figure-of-merit Z has for Peltier cooling.* In particular, the maximum temperature depression is given by

$$(T_2 - T_1)_{max} = Z_E T_1^2/2 \tag{3}$$

In spite of the similarity between Ettingshausen and Peltier cooling, there are some important differences. The first difference, of course, is that only one material is involved. Then, the expression that replaces the Seebeck coefficient involves not only the Nernst coefficient and the magnetic field but also the ratio L_x/L_y, that is, the relative dimensions in the directions of electrical and thermal flow. This means that, in principle, one can change the cooling power (but not the coefficient of performance) for a given electric current just by altering the relative dimensions of the sample. This advantage stems from the separation of the directions of heat flow and electrical flow.

*A word of caution must be added here. All the thermogalvanomagnetic effects depend strongly on the set boundary conditions. For example, the Hall effect is much larger for a long sample than for a short one. The essential question is whether or not transverse flows exist. Suffice it to say that it is the so-called adiabatic figure-of-merit that is used here. The Nernst coefficient and the thermal conductivity are defined for zero transverse temperature gradient while the electrical resistivity is defined for zero transverse electric current and temperature gradient and zero longitudinal heat flow.

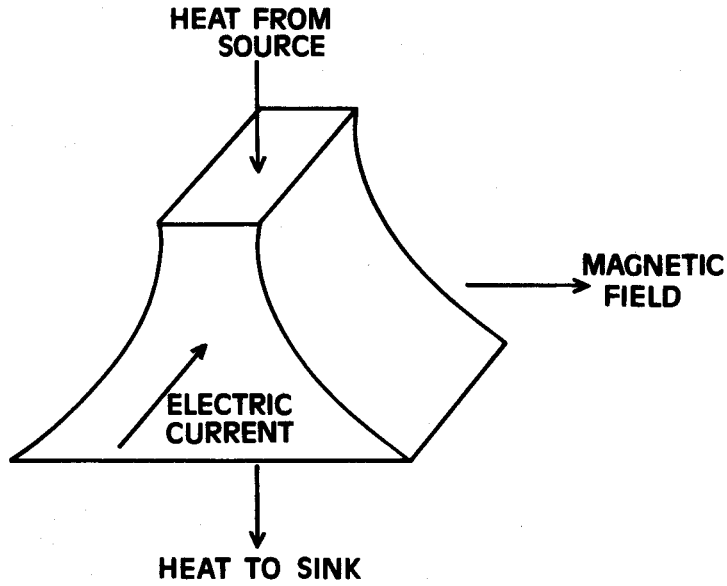

FIGURE 4 Principle of the thermomagnetic cascade.

Another advantage that has the same origin is apparent when one wishes to improve either the maximum temperature depression or the coefficient of performance by using a multistage device or cascade. A thermoelectric cascade is complicated to construct, involving, as it does, large numbers of thermocouples in the higher temperature stages. A thermomagnetic cascade with the ideal infinite number of stages is obtained by shaping a single sample of material into the exponential form shown in Figure 4.

8.4 Bipolar Flow

It is apparent that thermomagnetic refrigerators have certain practical advantages over ordinary Peltier coolers which offset the disadvantage of having to apply a magnetic field. However, these advantages are of little consequence if the coefficient of performance for a given temperature depression is much poorer. In other words, the Ettingshausen figure-of-merit Z_E must become at least comparable with the thermoelectric figure-of-merit Z in the temperature range of operation.

It can be shown quite easily that the transverse thermomagnetic phenomena are going to be small and ineffective for energy conversion purposes when there is only one type of carrier. In fact, the only reason that the thermomagnetic effects exist at all in this case is that some of the charge carriers are more strongly scattered than others. The Ettingshausen effect then depends on the more energetic carriers being deflected preferentially to one side of the sample while the less energetic carriers move to the other side so as to maintain electrical neutrality, as shown in Figure 5(a). However, when electrons and holes are present, as in Figure 5(b), the action of the magnetic field is to drive both types of carrier to the same side of the sample and, since they carry charges of opposite sign, electrical neutrality is not destroyed. Evidently, an essential feature of a good thermomagnetic material is that both electrons and holes should be present. Also, both carriers should have a high mobility, since the thermomagnetic effects all depend on the product of this quantity with the magnetic field. In fact, one usually requires the product of the mobility μ and the magnetic field B to be at least of the order of unity or, preferably, $(\mu B)^2 \gg 1$. Since it is desirable that the magnetic field be provided by a permanent magnet, we are normally restricted to values of B that are somewhat less that 1 T. Consequently we require electron and hole mobilities of the order of several $m^2\ V^{-1}\ s^{-1}$. Generally speaking, such mobilities are only found, even for favorable materials, at rather low temperatures, so we must regard Ettingshausen cooling essentially as a

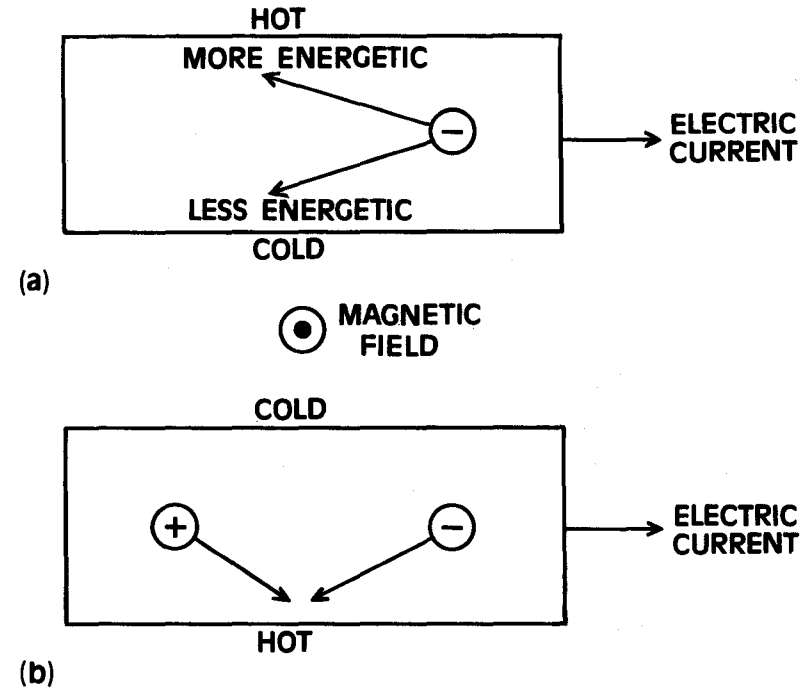

FIGURE 5 Ettingshausen effect in (a) extrinsic semiconductor and (b) intrinsic semiconductor or semimetal.

technique for well below room temperature and, probably, for the region of liquid nitrogen temperature or less.

In a thermoelectric refrigerator made from extrinsic materials, the electrons travel in one branch whereas the positive holes travel in the other branch. On the other hand, in a thermomagnetic refrigerator, the electrons and holes share a common lattice. This means that the effect of the lattice heat conductivity on the figure-of-merit is halved. Furthermore, it may be shown that, as $(\mu B_z)^2$ becomes much greater than unity, the ratio $(NB_z)^2/\rho$ rises to some limiting value while λ falls to λ_L, the lattice conductivity. In effect, the harmful influence of the electronic thermal conductivity has been removed. If one makes a comparison[10] between a thermomagnetic refrigerator having equal numbers of electrons and holes of equal mobility and a thermoelectric refrigerator made from the same material but with one branch containing only electrons and the other branch only holes, we find, as $(\mu B_Z)^2 \gg 1$:

1. A factor of 2 is gained for the thermomagnetic device because both carriers share the same lattice.
2. The thermal conductivity of the thermomagnetic cooler contains only the lattice contribution.
3. The term $(NB_z)^2/\rho$ in the thermomagnetic figure-of-merit may be somewhat greater than $(\alpha_p - \alpha_n)^2/\rho$ for the thermoelectric figure-of-merit if the usually assumed carrier scattering mechanism (acoustic mode lattice scattering) applies.

Overall, then, one might hope to improve the performance of electronic refrigerators by using the Ettingshausen rather than the Peltier effect. However, one must set against this the fact that one has to find a single material in which both the electron and hole properties are favorable whereas, of course, in a thermoelectric device one can combine the best n-type conductor with the best p-type conductor. Furthermore, in order that both electrons and holes be present in the requisite numbers, it is necessary that the energy gap should be close to zero; doping to achieve the preferred carrier concentration is no longer possible. Although the ideal material has yet to be found, some of the bismuth-antimony alloys come close enough to yielding reasonably attractive values for the thermomagnetic figure-of-merit.

8.5 Thermomagnetic Materials

It has already been shown that the reason for the improvement in a magnetic field of the bismuth-antimony alloys as thermoelectric materials is the presence of the transverse thermomagnetic effects. It is, therefore, sensible that one should look at these materials first as possible candidates for Ettingshausen cooling devices. It turns out that they are the only materials that one need consider at the present time.

It is not immediately obvious that the thermomagnetic figure-of-merit will be superior to the thermoelectric figure-of-merit, since the hole mobility is substantially less than the electron mobility. It is likely that the best alloy for Ettingshausen cooling will have a lower concentration of antimony than the best thermoelectric alloy. This is because the mobility generally falls as the antimony concentration increases and mobility is rather more important for Ettingshausen cooling than for Peltier cooling. Thus, in their work on thermomagnetic materials, Yim and Amith[11] employed the alloy $Bi_{0.99}Sb_{0.01}$. In the preferred orientation, with the heat flow in the binary direction and the electric current in the trigonal direction and in a magnetic field of up to 0.8 T, the highest thermomagnetic figure-of-merit observed was about 2.9×10^{-3} K^{-1} at 115 K, which is somewhat lower than the best thermoelectric figure-of-merit in a magnetic field at this temperature. However, more recently, Horst and Williams[12] have improved the purity of their single crystals and have thereby achieved lower carrier densities. As a result, using the alloy $Bi_{0.97}Sb_{0.3}$, a value of Z_ET equal to 1.0 has been reached at 150 K in a magnetic field of 1.0 T. This corresponds to Z_E of about 6.67×10^{-3} K^{-1} and a value of this order was observed down to about 80 K. At this temperature the required magnetic field was only about 0.5 T. It is apparent that the thermomagnetic figure-of-merit can be comparable with the best thermoelectric figure-of-merit and, considering the other advantages of using the transverse mode, there seems little doubt that Ettingshausen cooling is preferable at around liquid nitrogen temperature.

Although Horst and Williams[12] found it impractical to make an exponentially shaped sample, they did produce an element of trapezoidal shape having a ratio of width at the sink to width at the source of 12:1. They reported a temperature depression of about 50 K at a temperature of 156 K in a field of 1.6 T and a temperature depression of about 10 K at a temperature of 77 K in a magnetic field of about 0.6 T. The thermal load was 75 mW at 158 K and 20 mW at 77 K. It appears, then, that thermomagnetic refrigeration at low temperatures is close to being practical, if it is not already so. In this connection, it may be worth noting that Horst and Williams have projected a rise of Z_E by a factor of more than 2 at liquid nitrogen temperature, which they claim would result from further purification of their crystals.

References

1. Wolfe, R. and Smith, G. E., *Appl. Phys. Lett.*, 1, 5, 1962.
2. Gallo, C. F., Chandrasekhar, B. S., and Sutter, P. H., *J. Appl. Phys.*, 34, 144, 1963.
3. Cuff, K. F., Horst, R. B., Weaver, J. L., Hawkins, S. R., Kooi, C. F., and Enslow, G. W., *Appl. Phys. Lett.*, 2, 145, 1963.
4. Smith, G. E. and Wolfe, R., *J. Appl. Phys.*, 33, 841, 1962.
5. Gopinathan, K. K., Goldsmid, H. J., Matthews, D. N., and Taylor, K. N. R., *Proceedings, Seventh International Conference on Thermoelectric Energy Conversion*, Arlington, Texas, IEEE, New York, 1988, 58.
6. Ertl, M. E., Pfister, G. R., and Goldsmid, H. J., *Br. J. Appl. Phys.*, 14, 161, 1963.
7. Thomas, C. B. and Goldsmid, H. J., *Phys. Lett.*, 27, 369, 1968.
8. Paul, B. and Weiss, H., *Solid State Electron.*, 11, 979, 1968.
9. O'Brien, B. J. and Wallace, C. S., *J. Appl. Phys.*, 29, 1010, 1958.
10. Goldsmid, H. J., *Electronic Refrigeration*, Pion, London, 1986.
11. Yim, W. M. and Amith, A., *Solid State Electron.*, 15, 1121, 1972.
12. Horst, R. B. and Williams, L. R., *Proceedings, Third International Conference on Thermoelectric Energy Conversion*, Arlington, Texas, IEEE, New York, 1980, 183.

Section B
Material Preparation

9
Preparation of Thermoelectric Materials from Melts

Alexander Borshchevsky
Jet Propulsion Laboratory/California Institute of Technology
Pasadena, California, U.S.A.

9.1 Introduction

After the important discovery of the Seebeck and Peltier effects in 1821[1] and 1834,[2] various materials were identified as being thermoelectric. Even some minerals tested by Seebeck, which are considered semiconductors today, displayed thermoelectric properties. It was not until the late 1940s, however, that Ioffe theoretically showed[3] that semiconductors could be used as thermoelectric materials with reasonably high efficiencies. Before that, the Seebeck effect was used almost exclusively for temperature measurements by thermocouples made of metals and metal alloys. Metal wires for thermocouples have been manufactured in large quantities for many years, and the technology of metals thermometry is well known and widely reported.

The discovery of compound semiconductors in the 1950s gave rise to the development of modern thermoelectric materials, the best and most promising of which are chemical compounds and solid solutions. They differ basically from electronic and optoelectronic materials such as silicon (Si), gallium arsenide (GaAs), and related compounds because of different requirements. To obtain high thermoelectric efficiencies, one of the requirements is that the materials should possess carrier concentrations of up to 10^{20} cm^{-3}, whereas electronic materials should have much lower concentrations. At such high carrier concentrations, thermoelectric semiconductors tend to exhibit low carrier mobility, which in turn lowers the thermoelectric efficiency, unless perfect specimens

0-8493-0146-7/95/$0.00+$.50

are prepared. In most cases achieving the combination of high carrier concentration and perfect crystalline structure in a semiconductor presents a very difficult challenge for technologists. For this reason the preparation of "modern" thermoelectric material depends strongly upon the successful development of crystal technology.

To facilitate characterization of the material, the specimens need to be as free of defects as possible. One of the major obstacles to achieving that goal is grain boundaries. The only way to eliminate these defects is to grow single crystals. The alternative is to minimize them by growing polycrystalline ingots with very large grains.

It is well known that silicon (Si) and germanium (Ge) were classified as metals before the early 1940s, when pure single crystals of these elements were grown and were found to be semiconductors. This discovery laid the foundation for the work of Shockley, Bardeen, and Brattain and resulted in the invention of the transistor in 1948, which started the "semiconductor revolution".

The synthesis, alloying, and crystal growth of semiconducting materials have progressed tremendously in recent years and have been adequately described in the literature. For this reason only a short discussion of some basic aspects and a brief description of techniques are given in this chapter. At the same time, the specifics of the most important established methods of thermoelectrics preparation are emphasized.

The objective in this chapter is to familiarize the reader with the preparation of thermoelectric materials from a melt. The examples of preparation methods presented should indicate the direction of current research.

9.2 Phase Relationships

The vast majority of modern thermoelectric semiconductors are solid solutions or chemical compounds. In order to understand the process of preparing these materials from a melt and to be able to obtain reproducible results, a good knowledge of solid-liquid equilibrium phase diagrams is required. Even in the simplest case of congruently melting/crystallizing chemical compounds, at least the accurately measured melting point is needed, which is a part of the phase diagram. Most thermoelectric semiconductors contain elements from groups V and VI of the periodic table, so that at the elevated processing temperatures their partial pressures over a solid or liquid become appreciable. Thus, not only solid-liquid equilibrium conditions but also the more complicated solid-liquid-vapor relationship become important. In other words, it is almost impossible to manufacture material in a controllable fashion without knowledge of the related phase diagram or at least part of it.

Very good reviews of phase diagrams are available[4,5] and here only those that are necessary for the preparation of thermoelectric materials from a melt are discussed. Three binary phase diagrams in generalized form are considered. They represent three major types of element interaction: eutectic, solid solutions, and peritectic. Figure 1 is a synthetic phase diagram that demonstrates the formation of the chemical compound AB from elements A and B. If the vapor pressure of A and/or B can be neglected, the AB crystal is prepared from the stoichiometric melt *a* by lowering the temperature so that only the phase transformation $AB_{liq} \leftrightarrows AB_{sol}$ takes place, resulting in AB crystallization. This process is called *congruent* crystallization of a stoichiometric melt. It is congruent because liquid AB transforms into solid AB without any compositional changes. It should also be noted that this process occurs at a constant temperature, T^{M}_{AB}.

The left-hand part of the diagram can be considered as a separate binary system, A-AB, the simplest eutectic interaction between the components during solidification of the melt. As can be seen, the crystals of AB and A precipitate from nonstoichiometric melts *b* and *c*, respectively, representing an *incongruent* phase transformation in which the original liquid compositions do not correspond to the solidified materials. Moreover, the original melts change their compositions during crystallization along the corresponding liquidus lines. It should also be noted that here the crystallization takes place not at a constant temperature but within a temperature range between the liquidus points of the original melts and the solidus point, which in this case is a eutectic temperature, T^{e}_{A-AB}.

In a more realistic situation, represented by the AB-B system shown on the right-hand side of Figure 1, the crystallization of melts *d* and *f* causes the crystals of solid solutions of B in AB and

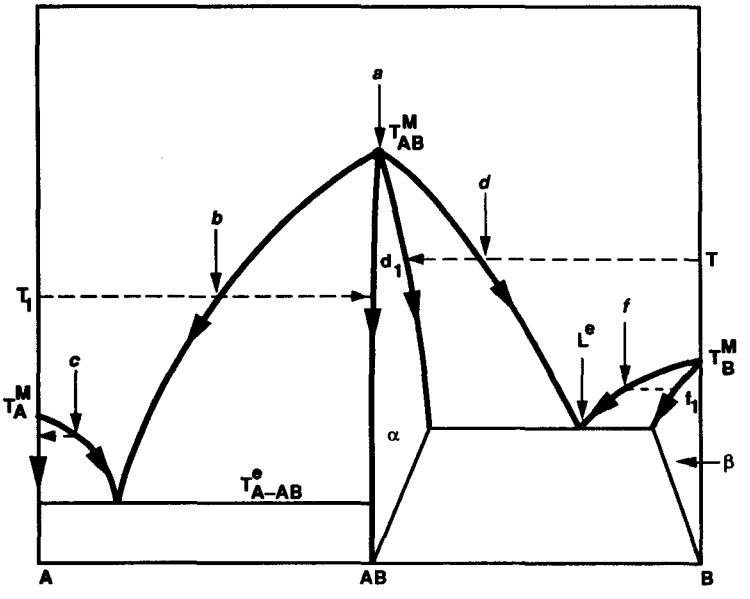

FIGURE 1 Eutectic phase diagram.

AB in B to solidify between corresponding solidus points (d_1 and f_1), along the solidus lines, and an eutectic temperature, T^e_{AB-B}. If the diffusion rates in the solid are low, which is usually the case, the crystallized solid solutions will have variable compositions and will require homogenization.

If a complete series of solid solutions is formed between elements A and B, the phase diagram looks like the one shown in Figure 2. Melt *a* starts to crystallize at liquidus point T^{liq}_a, producing the first crystal of *x* composition. Further lowering the temperature changes the liquid composition along the liquidus line and changes the composition of the precipitating crystals along the solidus line. Without fast diffusion in the solid, a very substantial separation occurs so that B-rich parts of the solidified material might neighbor A-rich grains or even almost pure component A. This usually happens during actual semiconducting material processing due to very low diffusion rates in the solid.

The most important high-temperature thermoelectric material, Si-Ge solid solution, is a typical example (see Section 9.3). Again, as in systems A-AB and AB-B (Figure 1), the process described here is crystallization of a nonstoichiometric melt during incongruent phase transformation. It should also be mentioned that this case relates to molten metal solution crystal growth (Section 9.3) because a "concentrated" solid solution of composition *x* is produced by crystallization of a "diluted" liquid solution *a*.

The third type of binary phase diagram, which is particularly important in the broad search for modern thermoelectric semiconductors, is shown in Figure 3. Many new phases that might turn out to be promising thermoelectric semiconductors are formed by the so-called peritectic reaction at a constant temperature, T^{per}. This is a solid + liquid $\leftrightarrows$ solid ($\alpha + L^P \leftrightarrows \beta$) reaction, unlike the eutectic reaction, which is liquid $\leftrightarrows$ solid + solid ($L^e \leftrightarrows \alpha + \beta$, Figure 1, AB-B system), also at a constant temperature, T^e_{AB-B}. Ideally, the stoichiometric melt *a* starts crystallization at the liquidus point when the solid solution α precipitates and changes its composition, then the temperature drops until it reaches T^{per} at c. Meanwhile, the original liquid *a* changes its composition to L^P. At this constant temperature, T^{per}, the peritectic reaction should occur if equilibrium is maintained. The result is a peritectic phase which might be a homogeneous composition, AB (chemical compound), or a solid solution, β.

In fact, peritectic reactions almost never reach completion because of very slow kinetics, and the solidification process in this case will result in a multiphase ingot that will have the desired phase, AB or β, as inclusions. However, the shape of the phase diagram in Figure 3 suggests another way to prepare a peritectic phase from the melt. The crystallization of melts with concentrations

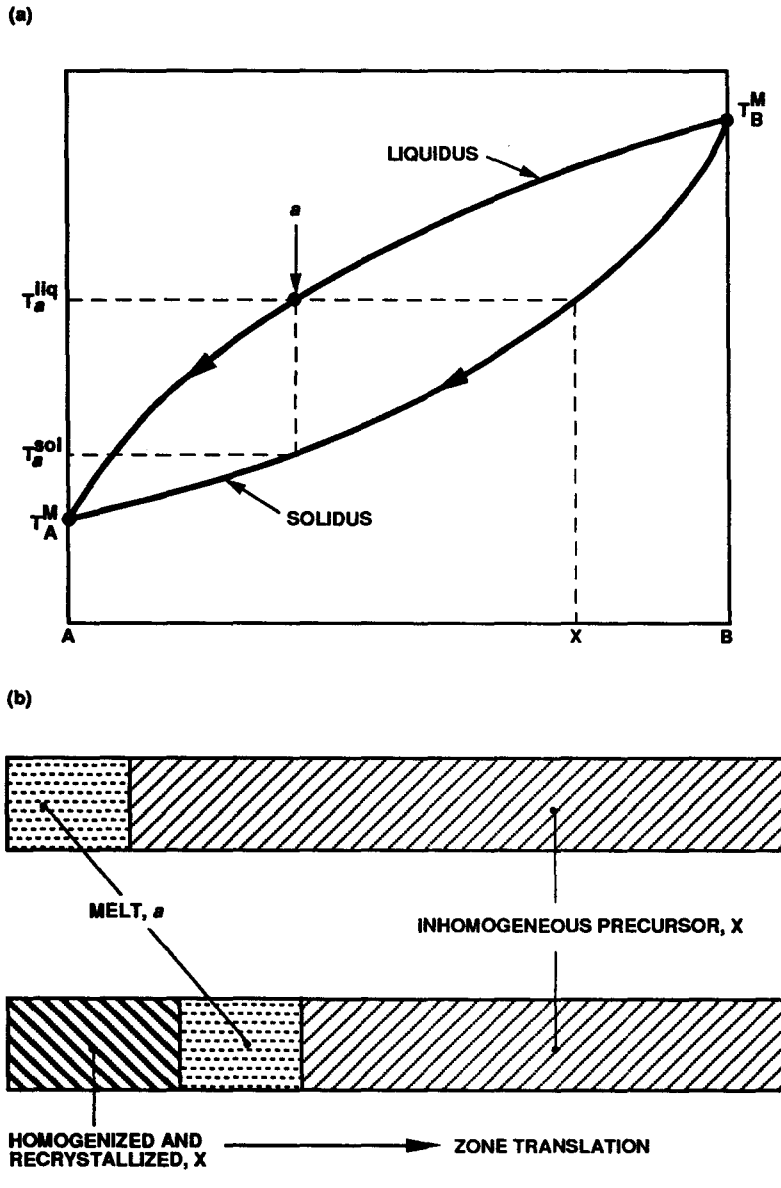

FIGURE 2 Solid solution phase diagram.

between points p and e, e.g., melt *b*, can be conducted similarly to the processing of melt *d* in Figure 1, system AB-B.

As discussed below, some of the established thermoelectric semiconductors contain three or even four elements. Ternary and quaternary phase diagrams are not always available, and when they are, it is very difficult to work with them in practice. The best way to use them is to divide them into simpler *pseudo-* (or *quasi-*) diagrams. Figure 4 shows a generalized compositional ternary phase diagram. If congruent compounds are formed between the participating elements, lines can be drawn between them and the elements, and there is a very high probability that those lines constitute *pseudo*-binary systems within the ternary. In this event, section A-BC might be treated as AB-B in Figure 1 or A-B in Figure 2; or section A-BC_2 might look like A-B in Figure 1, etc. Then those pseudo-binaries in practice can be used in the same way as simple binaries. This process of ternary diagram sectioning is called *triangulation* and is a common way for metallurgists to work with complicated systems.

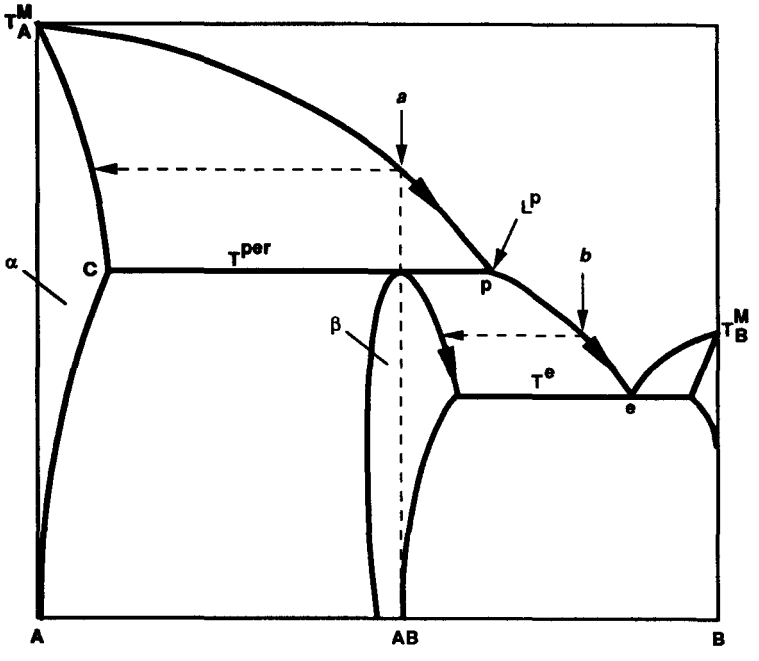

FIGURE 3 Peritectic phase diagram.

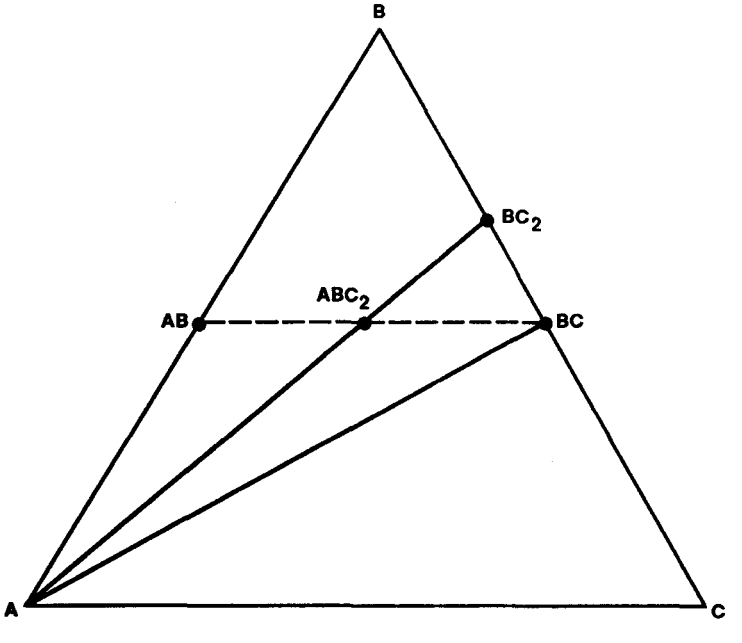

FIGURE 4 Compositional ternary phase diagram.

The diagram in Figure 4 is compositional only, and it is obvious that the full ternary system requires three-dimensional space to be fully described. The fourth possible variable, pressure, must again be constant as in binaries; otherwise, the full ternary diagram will require four-dimensional space. The temperature axis is not shown here. It would be the third dimension, perpendicular to the page. As for the quaternary diagrams, they are even more complex, are almost never fully available, and cannot be considered practical. Only parts of them, reduced to ternaries or binaries,

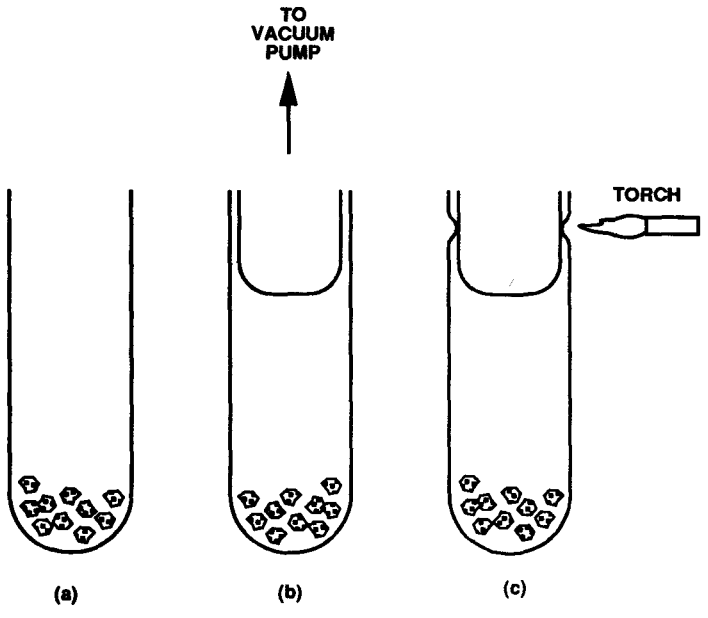

FIGURE 5 Synthesis/alloying ampoule preparation.

can be used. For example, the important thermoelectric material based on the quaternary bismuth-tellurium-selenium-antimony "Bi-Te-Se-Sb" can be described by the pseudo-ternary system Bi_2Te_3-Sb_2Te_3-Sb_2Se_3.

9.3 Synthesis/Alloying

Modern thermoelectric materials, from a technological point of view, can be roughly divided into three categories: low-temperature materials (group V chalcogenides based on bismuth telluride), middle-temperature materials (group IV chalcogenides based on lead telluride), and high-temperature materials (silicon-germanium solid solutions). The melting points and approximate total pressures of volatile elements over the melts of the major phases are shown in Table 1.

The preparation of chemical compounds and solid solutions from a melt begins with melting the elemental constituents together, a process referred to as *synthesis* or *alloying*. It is essential to use high-grade elements of guaranteed purity and to take all necessary precautions to prevent contamination during handling, synthesis, and crystal growth. A common way to synthesize the chalcogenides is to use sealed, clear quartz ampoules of up to 25-mm bore. The preweighed materials are placed into the tube (Figure 5a), followed by a quartz plug (Figure 5b). The tube is then evacuated to between 10^{-5} and 10^{-6} torr and sealed circumferentially with a hydrogen torch (Figure 5c).

Before use, the quartz is usually washed in soapy water, cleaned with solvents (e.g., acetone, methanol), aqua regia (HNO_3 + 3HCl), and hydrofluoric acid (HF) diluted with high-purity water, rinsed in pure water, and dried. Most of the high-purity commercially available elements are oxidized on the surface, and it is essential to remove the oxides from the ingredients before synthesis. This can be done by etching or by reduction of the element. For example, lead placed in an alumina or graphite boat can be reduced at 700°C in a stream of pure hydrogen. The presence of oxygen causes the solidifying ingot to stick to the quartz walls due to a chemical reaction between lead oxide and silica. This introduces stresses into the material and can even break the ampoule and expose the hot ingot to the air. In addition, any oxygen in the chalcogenides changes the electrical properties of the final product. To prevent sticking alone, quartz containers can be coated with carbon by pyrolitically cracking toluene in a nitrogen stream at 1050°C.[7] The vibrational stirring can be used during synthesis to homogenize the melt.[8]

Table 1. Melting Temperatures and Total Vapor Pressures of Major Thermoelectric Materials

Temp. Range	Low-Temperature Materials			Middle-Temperature Materials				High-Temperature Materials
Material	Bi_2Te_3	Sb_2Te_3	Sb_2Se_3	PbTe	PbSe	GeTe	SnTe	Si_{80} Ge_{20}
T^M, °C	585	621	612	917	1076	725	806	1350
P^{tot}, torr at T^M	4	1	2	10	100	40	1	$\ll 1$

Table 2. Comparison of Nominal and Actual SiGe Bulk Precursor Composition

Composition/Element	Si	Ge	Ga	P
Nominal, at.%	77.5	18.5	2.00	2.00
Actual, at.%	77.5	19.0	1.75	1.75

The synthesis (alloying) of silicon germanium is a more complicated procedure. The most "efficient" thermoelectric material in this system, both n- and p-types, contains about 80 at.% of silicon and 20 at.% of germanium ($Si_{80}Ge_{20}$). The high liquidus point of this composition, 1350°C, does not allow the use of vacuum-sealed silica tubes for processing. The quartz glass softens at 1250 to 1300°C, resulting in collapse of the ampoule. Also, due to the very large gap between the liquidus and solidus points of this composition (1350 − 1280 = 70°C) and very low diffusion rates in the solid alloys, a heavy segregation occurs during crystallization, resulting in separation of the solid silicon-rich and germanium-rich grains. The usual metallurgical homogenization by annealing cannot be performed in a reasonable period of time.[9]

Additionally, the extremely high affinity of silicon for oxygen makes preliminary etching of the silicon unreasonable. As soon as silicon is exposed to air or water after etching, a thin film of oxide forms on the surface immediately. Therefore, the use of large pieces of silicon (and germanium) to minimize the surface area is recommended.

Alloying of $Si_{80}Ge_{20}$ is done in a radio frequency furnace.[10] The large pieces (10 to 20 mm) of silicon and germanium, together with dopant, boron for p-type and phosphorus for n-type materials, are placed into an open quartz crucible. Improved n-type alloy can also be doped with gallium phosphide. The crucible is inserted into a graphite susceptor in the furnace chamber, and the chamber is vacuum pumped. After purging of the chamber by argon, a slight overpressure of argon is established (1.1 atm), and the temperature is raised to between 1370 and 1400°C within 2 to 3 h. Eddy currents develop an intensive stirring motion so that the homogenization of the melt can be achieved in 40 to 50 min at maximum temperature. After this, the melt is cast inside the chamber into the water-cooled copper mold, resulting in 12.5-mm diameter by 100-mm high fine-grained ingots. The bulk wet chemical analysis of the ingots shows reasonable agreement with nominal composition; an example is shown in Table 2. This material, with segregated microstructure but fine grains, serves as a precursor for the homogeneous ingot preparation (see Section 9.4).

9.4 Crystal Growth

Crystal growth, which is the next step in material preparation from the melt, can be carried out in many different ways. The same material can be grown by different methods with different levels of success. Bearing in mind preparation is from *melts*, we divide all possible processes into two major categories for convenience, while acknowledging that this categorization is not absolute.

Category 1: Growth from stoichiometric melts, i.e., from melts with the composition of certain stoichiometric compounds, resulting in a crystal of the same (or nearly the same) composition.

Category 2: Growth from nonstoichiometric melts, i.e., from melts with composition that does not correspond to the grown material. This process may equally result in either stoichiometric (e.g., chemical compound) or nonstoichiometric (e.g., solid solution) crystal growth.

Each method is briefly described below and illustrated by its application in the crystal growth of thermoelectric materials.

Stoichiometric Melts

Bridgman Method (Br)—The classical Bridgman method consists of a slow lowering of a crucible containing the melt from the higher temperature zone, through the temperature gradient, into the lower temperature zone (Figure 6a). As the crucible crosses the melting point between the zones, the melt directionally crystallizes and, under certain conditions, may result in a single crystal.

Using this simple arrangement, single crystals of lead telluride and lead selenide measuring 1.25 cm in diameter and 6 cm long were grown.[11] The upper and lower temperatures in the zones were 950 and 850°C for lead telluride and 1110 and 1010°C for lead selenide. Sealed quartz ampoules with pointed bottoms were lowered at a rate of less than 1 cm/h.

More recently, the Bridgman method has been successfully employed for bismuth telluride, antimony telluride, and some solid solutions based on these binaries, e.g., Bi-Te-Sb.[12,13] The high-purity elements were melted in hydrogen and kept under this reducing atmosphere for 2 d. Then the elements were placed into a precleaned quartz tube, sealed, synthesized, and the melts crystallized by the Bridgman method technique. The resulting ingots, 14 mm in diameter, were completely or partially single crystalline with the cleavage planes parallel to the growth axis.

The as-grown crystals were characterized and it was concluded that a certain deviation of the composition from that desired had taken place. The knowledge of the related phase diagrams was used for the following corrective isothermal annealing process. The single crystalline specimens were sealed into quartz tubes under a vacuum of 10^{-7} torr, together with a binary or ternary alloy (source) specially synthesized. The source composition was thermodynamically tied, at a certain temperature to specimen composition. At this temperature, the annealing process was carried out for about 7 to 10 d, allowing the specimen and the powdered source to reach equilibrium between solid, liquid, and vapor phases by means of diffusion, and to anneal the defects. This corrective isothermal annealing allowed record high thermoelectric efficiencies of over 3×10^{-3} K^{-1} to be obtained for both n- and p-type group V chalcogenides.[14,15]

The Bridgman method has also been used in a horizontal configuration. The horizontal boat, in this case, provides a free top surface of the growing material, minimizing mechanical stresses characteristic of vertically grown ingots when the solidifying melt is completely surrounded by the crucible. In the horizontal arrangement, only about 3/5 of the circumference of the melt and crystal are in contact with the surrounding surface of the vessel. Although the horizontal arrangement with the large free melt surface increases the dissociation and evaporation of compounds, good materials can be obtained. P-type $(Bi_2Te_3)_{25}(Sb_2Te_3)_{72}(Sb_2Se_3)_3$ + excess Te ingots with diameters of 25 mm were successfully grown in a horizontal Bridgman furnace.[16] As a countermeasure to the evaporation of volatile components of the melt (Te, Se, Sb), the ampoules were backfilled with argon to a pressure of 600 torr. Very high figures-of-merit were measured on parts of these ingots.

Gradient Freeze (GF)—The gradient freeze process eliminates any moving parts in the apparatus, ampoule, or furnace. Instead of lowering the crucible through the temperature gradient (Figure 6a), the *frozen* temperature gradient extended over the whole ampoule length (Figure 6b), is moved electronically, rather than physically, in contrast to the typical Bridgman apparatus. Correspondingly, the liquid-solid interface is translated up and crystal growth occurs. Such a system can be used not only vertically, but horizontally as well, and is sometimes called the *horizontal Bridgman* (HB) method.

The gradient freeze vertical arrangement has been used recently for the growth of promising new high-temperature materials.[17,18] A refractory compound, "ruthenium silicide" (Ru_2Si_3), congruently melting at 1700°C, has been grown (Figure 1, system A-AB, melt *b;* or system AB-B, melt *d*). High-purity ruthenium and silicon, in stoichiometric ratio, were placed in a pyrolytic boron nitride pointed-bottom crucible. Boron nitride was found to be the most appropriate

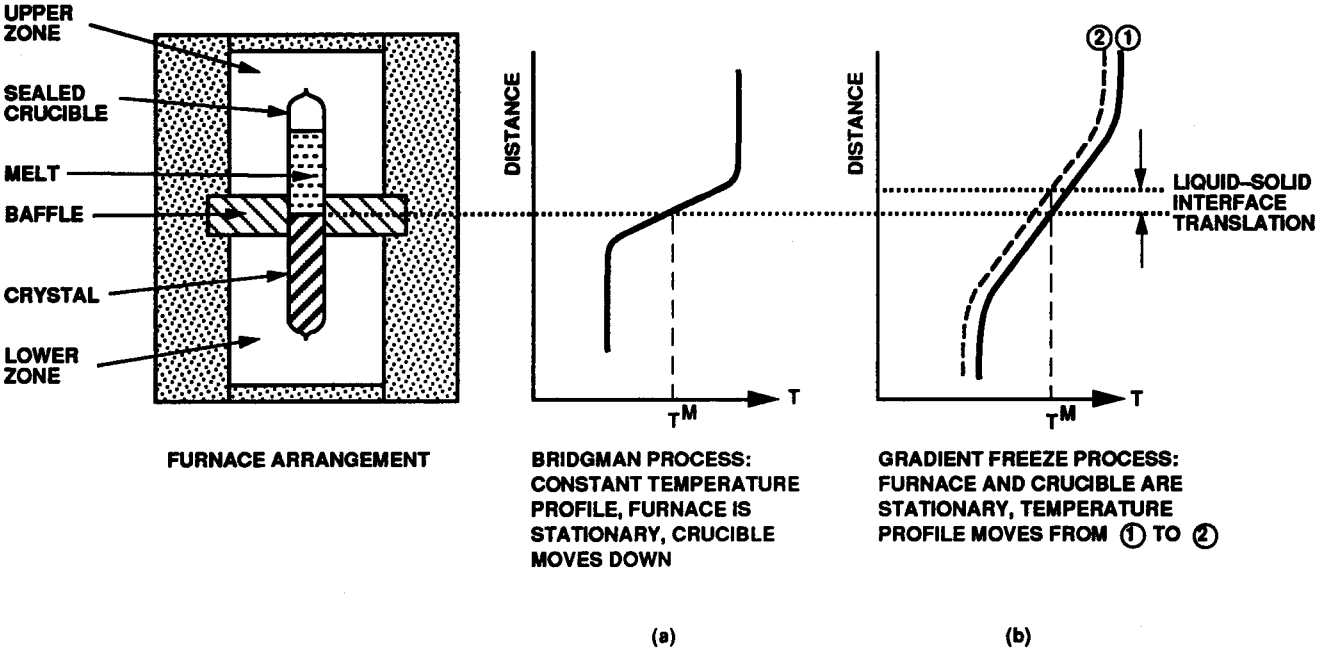

FIGURE 6 Bridgman/gradient freeze apparatus and process schematic.

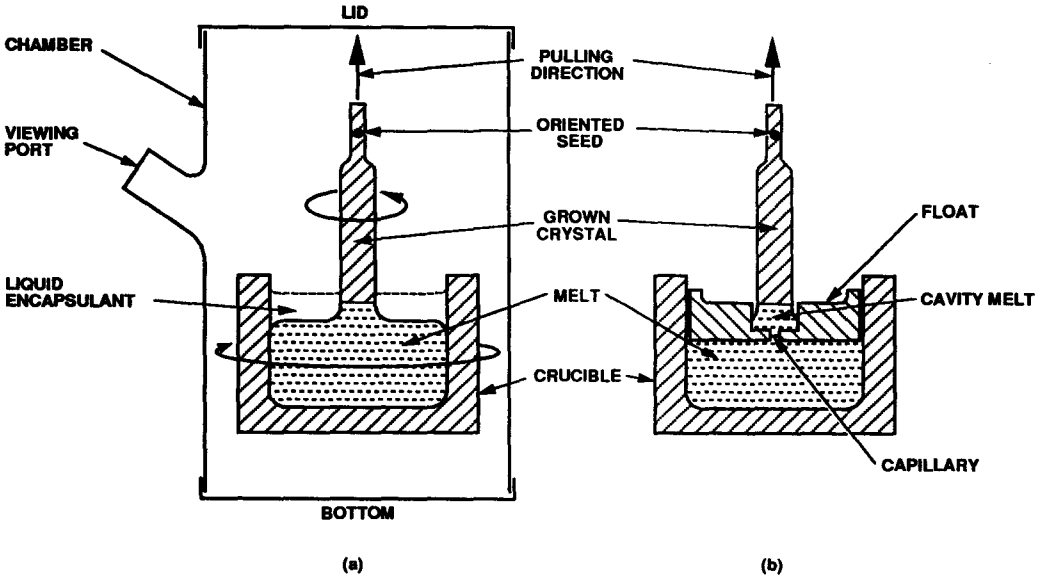

FIGURE 7 Czochralski method.

container material for ruthenium silicide, in spite of some dissociation and consequent contamination of the melt and crystal by boron. After synthesis of the compound at a minimum of 1765°C, the temperature gradient of 30 to 32°/cm was stabilized and growth occurred at rates of 0.8 to 3 cm/d. Single crystalline ingots of the compound with typical dimensions of 12 mm in diameter by 20 mm high were obtained and their thermoelectric properties measured.

Czochralski Method (Cz)—One of the most thoroughly investigated and widely used methods is Czochralski (Cz), also known as *crystal pulling*. The principle of the method is shown in Figure 7a. The material to be grown is melted in a crucible. A crystallographically oriented seed is then dipped into the melt and slowly pulled up. Rotations of the seed or the crucible with the melt (or both at the same time in counterdirections) can be applied during the pulling. The rotation attains thermal symmetry and stirs the melt. The Czochralski process is a "real-time" technique whereby the seeding, size, and diameter of the crystal can be monitored visually through the viewing port of the chamber while the crystal is growing. This is a great advantage because the operator can remelt the crystal or part of it if it grows polycrystalline and can start the process again. The crystal grows without contact with the crucible, which eliminates the sticking problem and decreases the dislocation density. Ideally, the material is suitable for Czochralski if it is congruently melting (Figure 1, compound AB) and has a low vapor pressure and a low viscosity.

Some of the thermoelectric materials, despite deviations from the ideal, were successfully grown using this technique. Reasonably large single crystals of lead telluride (2 cm in diameter, 75 g in weight) were grown from stoichiometric melts or melts slightly shifted from stoichiometry.[19] The chamber was fabricated from clear quartz, with the lid and bottom machined from boron nitride. The lid and bottom accommodated resistance heaters so that their temperatures as well as the chamber temperature were maintained above the condensation point of the volatile component (tellurium). A slight positive pressure of argon was maintained in the chamber during the synthesis, growth, and cooling. Dislocation densities of crystals obtained ranged from 6×10^4 to $2 \times 10^6/cm^2$.

A better way to prevent the loss of volatile components during the process is achieved by *liquid encapsulation* (LE). The same apparatus can be used as in Figure 7a. A liquid blanket of molten boric oxide (B_2O_3) is placed on the surface of the semiconductor melt, and inert gas pressure which exceeds the decomposition pressure is applied. Boric oxide is a glass with a softening point of about 450°C, and in the 900 to 1450°C range it is a liquid with low viscosity, colorless and transparent,

and having a very low vapor pressure. Because of the transparency of this liquid blanket, the seeding is usually easily seen. It also does not react chemically with many important semiconducting melts and has been successfully used for gallium arsenide and gallium phosphide crystal pulling. It was also used for crystal growth of lead telluride and lead selenide.[20] The compounds were presynthesized in separate furnaces in graphite crucibles under B_2O_3, cooled, and transferred in the crucibles to a Czochralski apparatus. Nitrogen pressure was established (1 atm for PbTe) and the pulling performed. High-quality crystals of lead telluride about 25 mm in diameter and 75 mm long were grown.

The double-crucible technique is a further development of Czochralski, which was intensively used for growing bismuth telluride-based thermoelectric materials.[21,22] This technique is illustrated schematically in Figure 7b. The pulling is realized not from the crucible but from the cavity in the float. During growth, a constant flow of the melt from the crucible, through the capillary, replenishes the melt in the cavity. The main features of the process are (1) a negligible diffusion of dopant from the cavity back to the melt in the crucible and (2) a much larger proportion of the melt in the crucible than in the cavity.

Obviously, the composition of the melt in the cavity can differ considerably from the composition of the melt in the crucible. But, after a relatively short period of time from the beginning of pulling, the cavity melt remains unchanged, resulting in uniform crystal composition. Single crystals of bismuth telluride about 130 mm long can be grown by this method. The first 10 to 20 mm of the crystals were compositionally nonuniform, but the remainder was very uniform. The Seebeck coefficient measured along the crystal was 150 ± 3 μV/°C.[22] In addition, the float protects the surface of the melt from evaporation of volatile ingredients, and the capillary "filters" the oxides. The shapes of the cavity and capillary can be made rectangular so that rectangular crystals can be readily grown. The shaping of the pulled crystal during the processing is based on a principle formulated in the 1950s.[23] Crystals of bismuth telluride and antimony telluride of rectangular cross section, 1 to 3 mm thick, 8 to 12 mm wide, and 100 mm long,[22,24] were grown perpendicularly to the c axis of the hexagonal lattice under pressure of pure helium 1.4 to 1.7 atm.

This technique, due to the principle of quasi-dynamic equilibrium established during processing, has been employed successfully for the growth of many different bismuth telluride-based solid solution compositions,[25,26] including quasi-ternary Bi_2Te_3-Bi_2Se_3-Sb_2Te_3.[27] It has been used even in a manufacturing environment to grow crystals of Bi-Te-Sb solid solutions with diameters of 35 mm and lengths of 150 mm.[28] Formally, according to our classification, the growth of solid solutions belongs to category II processes, from nonstoichiometric melts. It is mentioned here only because of its very close similarity to the processes used in group V chalcogenides.

Zone Melting (ZM)—Zone melting is a term given to a large number of techniques having in common the partial melting of a long ingot and then traversing the molten zone along the ingot. Thus, the main function performed by zone melting is redistribution of the impurities or phases present in a charge. A factor that plays a major role in zone melting is called the *distribution,* or *segregation, coefficient.* This coefficient has to be taken into consideration in any process involving melting-crystallization. For example, if this coefficient k = (solubility of B in solid AB)/(solubility of B in liquid AB) = $d_1/d \ll 1$, at processing temperature T (Figure 1), the concentration of "impurity" B in the melt zone will be higher than in the solid. After several passes of the zone through the ingot in one direction, the impurity concentrates at the end of the ingot, thus resulting in zone refining of AB. A detailed description of zone melting can be found in Reference 29.

The concept of zone melting is easily understood from the schematic in Figure 8. Zone melting can be used for (1) impurity removal (not characteristic for thermoelectric material where dopant concentration is expected to be relatively high) and (2) uniform doping. The latter use of zone melting can be applied when a small amount of dopant is present or when the average composition of the charge corresponds to the middle part of the solid solution diagram (Figure 2). Then the zone repeatedly passes through the ingot in both forward and reverse directions until the middle part of the ingot becomes uniform. This zone melting technique is well known to metallurgists as *zone leveling* and apparently requires many reciprocating passes through the charge. A better leveling technique for concentrated solid solutions is described later in Section 9.4.

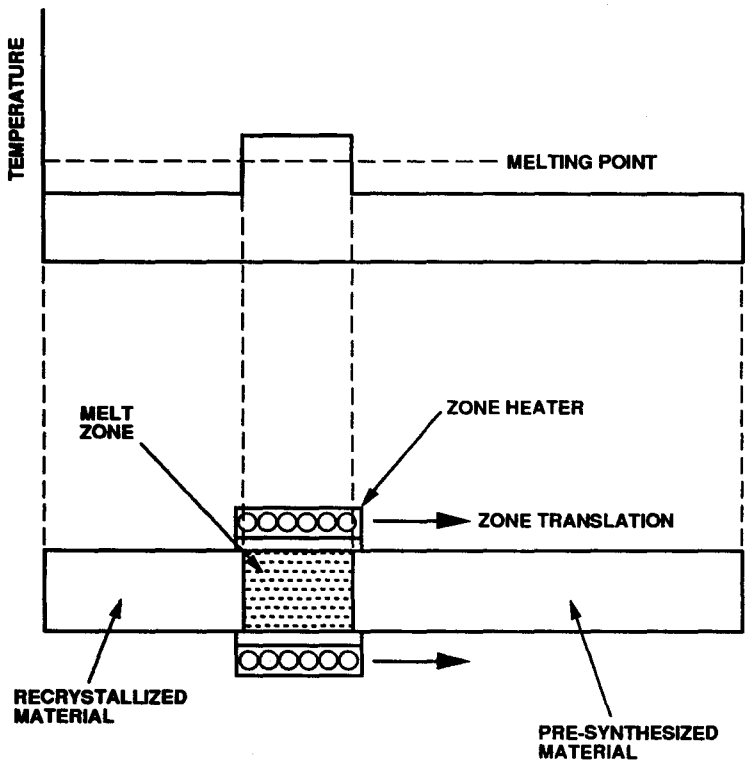

FIGURE 8 Zone melting schematic.

One recent publication[30] deals with zone melting of a Bi_2Te_3-Sb_2Te_3 quasi-binary system (Figure 2 type). One of the compositions processed, $Bi_{1.6}Sb_{0.4}Te_3$ with 2 at.% extra tellurium, was synthesized in an evacuated and sealed quartz tube coated with carbon. After zone melting, mostly single-phase material was found along the ingot except for about a 1-cm long two-phase part at the end. The electrical and thermal properties along the single-phase part of the ingot (8 cm) were measured, and their strong dependence upon the position in the ingot was attributed to the extra tellurium introduced. Due to the very narrow gap between T^{liq} and T^{sol} of this composition (according to Reference 31, it is only 5°C) and relatively fast diffusion in the solid, the strong major phase segregation was not observed. It was also due to precise knowledge of the solidus curve on the corresponding phase diagram.[32]

Nonstoichiometric Melts or Molten Metal Solutions

Gradient Freeze (GF)—A broad search for new thermoelectric materials brings to the attention of researchers a number of chemical compounds and solid solutions that have not been previously considered. Some of these materials are difficult to synthesize and grow because of their nature and unknown phase diagrams. The GF technique can be used successfully to grow peritectic compounds of interest from metal solutions. A schematic of the GF apparatus is shown in Figure 6b, and its principle of operation is described below. Some more details can also be found in Reference 33.

GF was employed for growth of one of the potential thermoelectric materials, iridium triantimonide.[34] $IrSb_3$ is a peritectically formed compound and can be grown from solution in Sb. The antimony side of the Ir-Sb binary system corresponds to the AB-B part of the diagram shown in Figure 3, where AB can be considered as $IrSb_3$ and B as antimony. Ir and Sb, in a ratio similar to

melt *b*, were sealed in a pointed-bottom quartz ampoule and processed with a growth rate of 0.3°/h at a temperature gradient of 45°/cm in an apparatus similar to the one shown in Figure 6b. The crystallization of melt *b* (Sb) (Figure 3) started at the bottom of the ampoule, resulting in precipitation of compound AB ($IrSb_3$) until the melt reached composition *e*, after which the remainder of the melt solidified as eutectic. The final ingot consisted of two parts. The lower part was the compound, and the upper part was a eutectic mixture between the compound and antimony. Iridium triantimonide has been cut, measured, and found to be an attractive p-type semiconductor with high mobility (1200 $cm^2/V \cdot s$ for a carrier concentration of 10^{19} cm^{-3} at room temperature). At 600°C the mobility value is still high (650 $cm^2/V \cdot s$), and the resistivity is 1 $m\Omega \cdot cm$. The Seebeck coefficient was measured as 150 $\mu V/K$.

Zone Leveling (ZL)—Zone leveling is one of the versions of zone melting described below in the discussion of the traveling solution method. As opposed to several reciprocating zone passes, this version is performed using only one zone pass and is based on the phase relationship shown in Figure 2. Again, we consider this process as a crystallization of metal solution because "dilute" liquid solution *a* crystallizes, resulting in "concentrated" solid solution *x*. It is obvious that if the liquid *a* composition, which loses component B during crystallization, is constantly replenished by B, the crystallizing composition *x* is the only product of the process.

Zone leveling of a very difficult and the most important high-temperature thermoelectric material, $Si_{80}Ge_{20}$ solid solution, is a perfect example of the use of this technique. It was described in 1957,[35] investigated in more detail and applied later,[36] and more recently applied again with some changes.[37] Figure 2b and the phase diagram above (2a) fully represent the principle of the process. Two precursors of silicon germanium are alloyed: $a(Si_{52.5}Ge_{47.5})$ for zone melt, and $x(Si_{80}Ge_{20})$ for homogenization, e.g., composition leveling. They are loaded into the processing boat (graphite, glassy carbon, carbon-coated quartz), sealed under vacuum in a quartz tube, and zone melted (Figure 8) at a constant temperature T_a^{liq} (Figure 2a). One pass of the zone is usually employed. Two processes take place simultaneously during the zone passing on both liquid-solid interfaces: melting of inhomogeneous precursor *x*, on the right interface, and crystallization of homogeneous composition *x*, on the left interface. At each given time the quantity of crystallized material is equal to the quantity of melted precursor. Therefore, a constant composition of the melt is maintained, and a perfectly homogeneous $Si_{80}Ge_{20}$ solid-solution ingot is obtained. It was found[10] that a radio frequency (RF) coil used as a zone heater, instead of the conventional resistance furnace, helps to avoid deterioration of the quartz ampoule. In this case the graphite boat (crucible) also played the role of an RF susceptor. Two resistance furnaces mounted on both sides of the RF coil maintained sufficiently high pressure in the ampoule, when phosphorus (or gallium phosphide) was a dopant, and prevented phosphorus sublimation during the process. In this case the whole heating assembly was stationary and the ampoule was translated. The travel rate was about 2 mm/h, which was slow enough to provide homogeneous recrystallization of the charge. Thus, intercrystalline liquation was avoided.

One more advantage of this version of zone leveling should be noted: the process is performed at a much lower temperature than T^{liq} of $Si_{80}Ge_{20}$. The processing temperature corresponds to T^{sol} of the alloy (1280°C) vs. T^{liq} = 1350°C, and the sealed quartz container can easily survive even when a conventional heater is used.

Liquid Phase Epitaxy (LPE)—Liquid phase epitaxy is the growth of a material epitaxially on an oriented, single-crystalline substrate seed from the solution of the material in an appropriate solvent. Usually the material is grown in the form of a thin (10 nm to 100 μm) layer over the polished and etched wafer. The layers reproduce the structure of the substrate (*epitaxy*) as in any other seeded crystal growth. The basics of the process are illustrated by Figure 1 for AB epitaxial growth from solution *b* over substrate AB. A diluted solution of AB in solvent A is heated to T_1. At this temperature, melt *b* is brought into contact with substrate AB. According to the phase diagram, melt *b* and substrate AB are in thermodynamic equilibrium, and no changes are expected at T_1. By lowering the temperature, AB precipitates from the melt and grows epitaxially on the substrate of the same composition until the substrate is withdrawn from the melt. By introducing

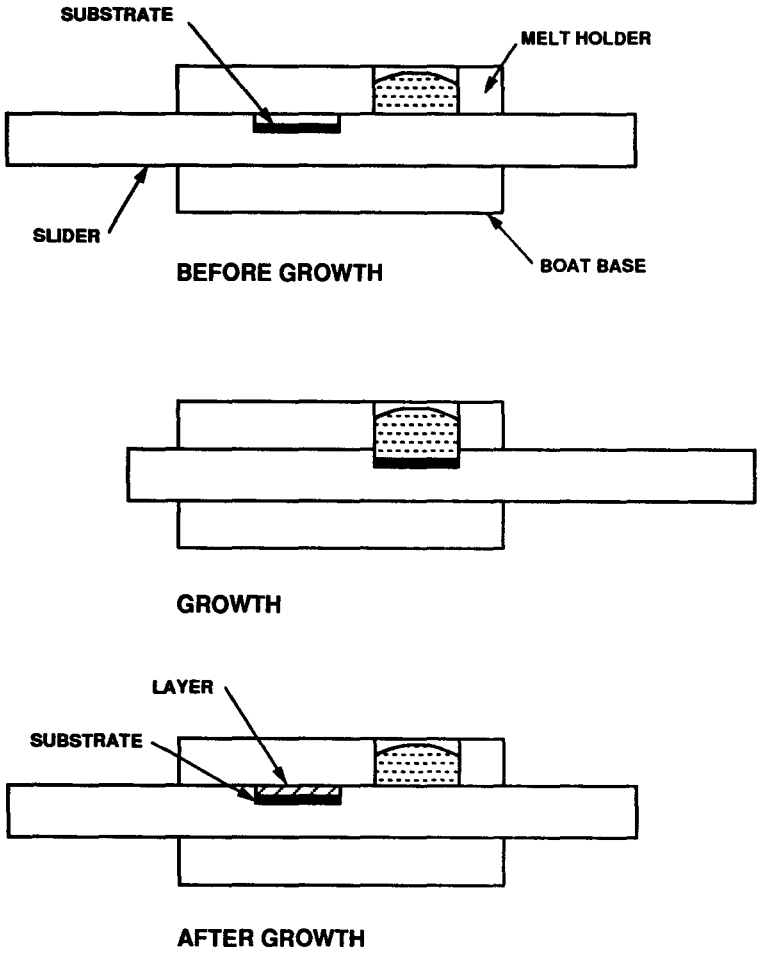

FIGURE 9 The LPE slider boat system.

a dopant into the melt, the doped layer can be grown on an undoped substrate. A solid solution α of d_1 concentration can also be grown on substrate AB at temperature T from melt *d*.

The major obvious advantages of liquid phase epitaxy are: (1) it can be performed at substantially lower temperatures than bulk growth of the same material from a stoichiometric composition; (2) consequently, the vapor pressures over the melts can be much lower during liquid phase epitaxy, thus eliminating a big loss of volatile elements and simplifying the process; (3) solid solutions of certain composition can be grown. Liquid phase epitaxy has been so widely used in research and manufacturing of semiconductors that a large number of apparatus designs have been developed. A simplistic horizontal configuration of liquid phase epitaxy apparatus is shown in Figure 9. This is the graphite slider boat system, usually operated in a purified hydrogen atmosphere. The slider, with the substrate and solution located separately, are heated to a certain temperature. The slider is then moved to the right so that the substrate is in contact with the melt. The temperature is lowered and the growth occurs, after which the slider with substrate and grown layer is moved to the left, terminating the growth. A more detailed description of liquid phase epitaxy is given in Reference 38.

The use of liquid phase epitaxy in thermoelectric research can be illustrated by the development of improved silicon-germanium material. The difficulties of this high-temperature solid solution have been noted in Section 9.3. It has been found[39] that silicon-germanium solid solutions can be more heavily doped when crystallized from metallic liquid solutions, at lower temperatures than T^{liq}. In this case the use of a solvent, which is also a dopant, is beneficial because the solvent-dopant atoms are incorporated in the silicon-germanium alloy, according to their solid solubility

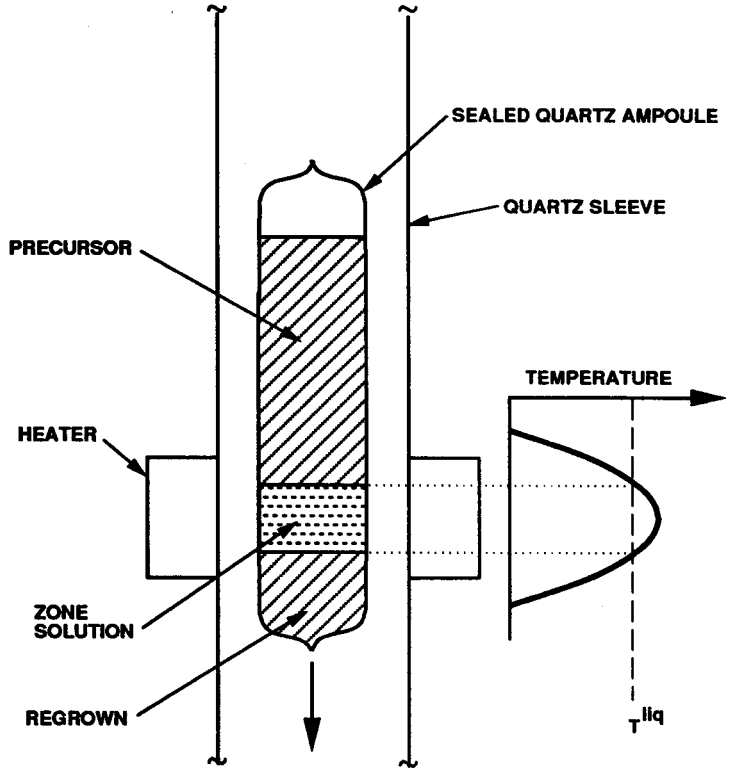

FIGURE 10 Traveling solvent method schematic.

at the temperatures of growth. $Si_{80}Ge_{20}$ layers 10 to 100 μm thick were grown from solution in gallium with gallium phosphide addition on (111) oriented substrates.[39] Temperatures of growth ranged from 750 to 900° C with cooling rates of 30 to 40°C/h (compared to $Si_{80}Ge_{20}$ T^{liq} = 1350°C). These low growth temperatures were used because of the selected melt composition of $Si_{7.7}Ge_{24.8}Ga_{67.5}$, which produced a $Si_{79.9}Ge_{19.9}Ga_{0.2}$ crystalline layer at 900°C. Liquid phase epitaxy experiments proved the feasibility of enhancing the phosphorus-dopant solid solubility in silicon-germanium material in the presence of gallium. This multiple doping had more recently improved the thermoelectric energy conversion efficiency of $Si_{80}Ge_{20}$,[40] which is widely employed in radio-isotope thermoelectric generators (RTGs).[6]

Traveling Solution Method (TSM)—The traveling solution method (sometimes called traveling solvent method or traveling heater method, THM) is one of the zone melting techniques, and the process is almost the same as zone leveling. It is the recrystallization of a concentrated solution through a dilute solution and is usually carried out vertically with one pass of the molten solution zone. The vertical configuration of the apparatus (Figure 10) provides a more symmetrical thermal field applied to the charge and improved uniformity of composition and properties in grown ingot cross sections. The traveling solution method has been successfully employed for crystal growth of several well-established thermoelectric materials, and has resulted in high-quality samples.

The binaries bismuth telluride and antimony telluride have been grown in the form of single crystals,[14] but the most exciting results were achieved on several ternary compositions of ternary Bi-Sb-Te solid solutions.[15] The success was based on the precise knowledge of the ternary phase diagram, in particular its Te-corner, quasi-ternary Te-Bi_2Te_3-Sb_2Te_3.[31] With this knowledge, the precise initial compositions of the material for zone solution and precursor corresponding to the processing temperature were chosen, separately synthesized, and placed into the quartz growth chamber, with the zone solution ingot on the pointed bottom and the precursor ingot on the top (see Figure 10). When the processing temperature, T^{liq}, is established, part of the precursor dissolves in the zone solution, thermodynamic equilibrium on the solid-liquid interface at T^{liq} is

achieved, and lowering of the ampoule begins. Homogeneous single crystals of several ternary solid solutions with exactly the desired composition were obtained and, after corrective saturation annealing (see above), characterized. The best value of thermoelectric efficiency calculated for $Bi_9Sb_{31}Te_{60}$ alloy is 3.2×10^{-3} K^{-1}. A very important feature of this approach, based on appropriate phase diagram knowledge, is reproducibility of growth conditions and, consequently, the properties of the grown material. Also, the growth is possible at temperatures lower than the melting point of the alloy.

Another example of the traveling solution method applied to thermoelectric material preparation is silicon-germanium solid solution growth.[39] In this case, solvents such as gallium and tin were used with growth temperatures between 800 and 900°C (compared to $T^{liq} = 1350$°C for $Si_{80}Ge_{20}$).

9.5 Concluding Remarks

A brief review has been given of the preparation of thermoelectric materials from melts. Melt preparation techniques usually involve vacuum or protective atmospheric environments, which are ideally suited to research into further understanding of the synthesis of initial precursors and crystal growth mechanisms, but which are less suitable for manufacturing due to factors such as long turn-around times. Nevertheless, the manufacturing of the "best performance materials" relies upon careful choice of these environments. One of the melt preparation stages, synthesis/alloying, is almost always inevitable during material processing.

It is strongly emphasized that the processes described require knowledge of composition-temperature or even composition-temperature-pressure phase diagrams. This knowledge helps to select the appropriate method of preparation, apparatus design, and processing.

Not all methods of thermoelectric material preparation from melt were included in this chapter. Some of them were only briefly discussed in recent publications (e.g., Bi-Te-Sb melt quenching followed by hot pressing[41]) and could prove to be beneficial for manufacturing in the future. Such methods as liquid phase epitaxy have not so far found wide application in the preparation of thermoelectric materials. However, the miniaturization of electronics might lead to development and manufacturing of thermoelectric generators and cooling devices based on thin layers produced by liquid phase epitaxy (as well as by other techniques).

References

1. Seebeck, T. J., Magnetische polarisazion der metalle und erze durch temperatur-differenz, *Abhandlungen der Deutschen Akademie der Wissenschaften zu Berlin,* 1822, p. 265.
2. Peltier, J. C., Nouvelles experiences sur la caloricité des courants electriques, *Annales de Chimie,* LVÉ, 371, 1834.
3. Ioffe, A. F., *Energeticheskie Osnovy Termoelektricheskikh Batarei iz Poluprovodnikov,* Akademia Nauk SSSR, Moscow, 1949.
4. Rhines, F.N., *Phase Diagrams in Metallurgy,* McGraw-Hill, New York, 1956.
5. Alper, A. M., *Phase Diagrams: Materials Science and Technology,* Academic Press, New York, 1970.
6. Wood. C., Materials for thermoelectric energy conversion, *Rep. Prog. Phys.,* 51, 459, 1988.
7. Beels, R. and De Sutter, W., Pyrolytic coating of quartz and ceramic vessels used for zone melting, *J. Sci. Instrum.,* 37, 397, 1960.
8. Borshchevsky, A. and Tretiakov, D.N., On the influence of vibrations on the crystallization of some semiconductors, *Krist. Tech.,* 3, K69, 1968.
9. Stöhr, H. and Klemm, W., Über zweistoffsysteme mit germanium. I, *Z. Anorg. Chem.,* 241, 305, 1939.
10. Borshchevsky, A., Fleurial, J.-P., Vandersande, J. W., and Wood, C., Preliminary results on zone-leveling of multidoped SiGe thermoelectric alloys, in *Proc. 7th Symp. Space Power Syst.,* p.I, Inst. for Space Nuclear Power Studies, Albuquerque, 1990, 229.
11. Lawson, W. D., A method of growing single crystals of lead telluride and lead selenide, *J. Appl. Phys.,* 22, 1444, 1951.

12. Scherrer, S., Scherrer, H., Chitroub, M., and Fleurial, J. P., Thermoelectric optimization of bismuth telluride and alloys by stoichiometric deviation, in *Proc. 6th Int. Conf. Thermoelectric Energy Conversion*, The University of Texas, Arlington, 1986, 25.
13. Gailliard, L., Caillat, T., Scherrer, H., and Scherrer, S., Influence of elaboration technique on the electrical properties of Sb_2Te_3, in *Proc. VIII Int. Conf. on Thermoelectric Energy Conversion*, Scherrer, S. and Scherrer, H., Eds., Nancy, France, 1989, 12.
14. Scherrer, S., Scherrer, H., and Caillat, T., Recent development in compound tellurides and their alloys for Peltier cooling, in *Proc. IX Int. Conf. on Thermoelectrics (USA)*, Vining, C. B., Ed., JPL, Pasadena, 1990, 1.
15. Caillat, T., Carle, M., Fleurial, J.-P., Scherrer, S., and Scherrer, H., Thermoelectric properties of single crystal alloys $Bi_8Sb_{32}Te_{60}$, $Bi_9Sb_{31}Te_{60}$ and $Bi_{10}Sb_{30}Te_{60}$ grown by the T.H.M. method, in *Mat. Res. Soc. Symp. Proc.*, Allred, D. D., Vining, C. B., and Slack, G. A., Eds., 234, 189, 1991.
16. Day, G. G., Stoner, B. R., Jesser, W. A., and Rosi, F. D., Processing effects on figure of merit for Bi_2Te_3-Sb_2Te_3-Sb_2Se_3 alloys, in *Proc. VIII Int. Conf. on Thermoelectric Energy Conversion*, Scherrer, S. and Scherrer, H., Eds., Nancy, France, 1989, 35.
17. Ohta, T., Vining, C. B., and Allevato, C. E., Characteristics of a promising new thermoelectric material: ruthenium silicide, in *Proc. 26 Intersoc. Energy Conv. Eng. Conf.*, vol. 3, American Nuclear Society, 1991, 196.
18. Vining, C. B. and Allevato, C. E., Intrinsic thermoelectric properties of single crystal Ru_2Si_3, in *Proc. X Int. Conf. Thermoelectrics*, Rowe, D. M., Ed., Babrow Press, Cardiff, U.K., 1991, 167.
19. Cronin, G. R., Jones, M. E., and Wilson, O., The growth of crystals from compounds with volatile components, *J. Electrochem. Soc.*, 110, 582, 1963.
20. Metz, E. P. A., Miller, R. C., and Mazelsky, R., A technique for pulling single crystals of volatile materials, *J. Appl. Phys.*, 33, 2016, 1962.
21. Leverton, W. F., Floating crucible technique for growing uniformly doped crystals, *J. Appl. Phys.*, 29, 1241, 1958.
22. Airapetyants, S. V. and Shmelev, G. I., Method for growing uniform monocrystals of alloyed semiconductor materials, solid solutions, and intermetallic compounds of a given composition determined by the composition of the melt, *Sov. Phys. Solid State*, 2, 689, 1960.
23. Stepanov, A. V., New method of producing articles (sheets, tubes, rods, various sections, etc.) directly from the liquid metal, *Sov. Phys. Techn. Phys.*, 4, 339, 1959.
24. Abrikosov, N. Kh., Ivanova, L. D., and Fetisova, T. I., Preparation and investigation of Te- and Se-doped single crystals of Sb_2Te_3 and $(Bi_{0.5}Sb_{1.5})Te_3$, *Inorg. Mater.*, 12, 689, 1976.
25. Abrikosov, N. Kh., Ivanova, L. D., Karpinskii, O. G., Svechnikova, T. E., and Chizhevskaya, S. N., Preparation and properties of bladed single crystals of solid solutions based on Sb_2Te_3 and Bi_2Te_3, *Inorg. Mater.*, 13, 525, 1977.
26. Abrikosov, N. Kh., Ageev, Y. I., Ivanova, L. D., Kutasov, V. A., Petrov, A. V., Sagaidachnyi, I. A., Svechnikova, T. E., and Chizhevskaya, S. N., Single crystals of thermoelectric materials based on solid solutions of Bi and Sb chalcogenides, *Inorg. Mater.*, 15, 1083, 1979.
27. Abrikosov, N. Kh. and Ivanova, L. D., Single crystals of solid solutions of the system Bi_2Te_3-Bi_2Se_3-Sb_2Te_3, *Inorg. Mater.*, 15, 926, 1979.
28. Anatychuk, L. I., Klim, V. A., and Kshevetsky, A. A., Properties of Bi-Te-Sb single crystals grown by the Czochralski method for thermoelectric cooling, in *Mat. Res. Soc. Symp. Proc.*, Alfred, D. D., Vining, C. B., and Slack, G. A., Eds., 234, 197, 1991.
29. Pfann, W. G., *Zone Melting*, 2nd ed., John Wiley & Sons, New York, 1966.
30. Aivazov, A. A., Thermoelectric properties of $(Bi_{0.8}Sb_{0.2})_2Te_3$ solid solutions grown by zone melting technique, *Proc. IX Int. Conf. on Thermoelectrics (USA)*, Pasadena, 1990, 36.
31. Caillat, T., Carle, M., Perrin, D., Scherrer, H., and Scherrer, S., Study of Bi-Sb-Te ternary phase diagram, *J. Phys. Chem. Solids*, 53, 227, 1992.
32. Aivazov, A. A., Anukhin, A. I., and Gavrilenko, I. S., Zone melting characteristics of complex semiconductors, *Inorg. Mater.*, 27, 780, 1991.
33. Borshchevsky, A., Caillat, T., and Fleurial, J.-P., Two-zone Bridgman furnace with sharp thermal gradient, *NASA Tech Briefs*, 18, 68, 1994.
34. Caillat, T., Borshchevsky, A., and Fleurial, J.-P., Search for new high temperature thermoelectric materials, in *Proc. 27th Intersoc. Energy Conv. Eng. Conf.*, Vol. 3, American Nuclear Society 1992, p. 499.

35. Mitrenin, B. P., Troshin, N. E., Tsomaya, K. P., Vlasenko, V. A., and Gubanov, Yu. D., Possibility of homogeneous Si-Ge alloys preparation by zone melting, *Voprosy Metallurgii i Fiziki Poluprovodnikov* (in Russian), Petrov, D. A., Ed., AN SSSR, Moscow, 1957, 59.
36. Dismukes, J. P. and Ekstrom, L., Homogeneous solidification of Ge-Si alloys, *Trans. Met. Soc. AIME*, 233, 672, 1965.
37. Deitch, R. H., Molten metal solution growth, in *Crystal Growth*, 2nd ed., Pamplin, B. R., Ed., Pergamon Press, Oxford, 1980, chap. 11.
38. Fleurial, J.-P. and Borshchevsky, A., Si-Ge-Metal ternary phase diagram calculations, *J. Electrochem. Soc.*, 137, 2928, 1990.
39. Borshchevsky, A. and Fleurial, J.-P., Growth of heavily doped Si-Ge from metallic solutions, *J. Cryst. Growth*, 128, 331, 1993.
40. Fleurial, J.-P., Borshchevsky, A., and Vandersande, J., Optimization of the thermoelectric properties of hot-pressed n-type SiGe materials by multiple doping and microstructure control, *Proc. X Int. Conf. Thermoelectrics*, Babrow Press, Cardiff, U.K., 1991, 156.
41. Gogishvili, O. Sh., Zaldastanishvili, M. I., Krivoruchko, S. P., Lalykin, S. P., and Ovsyanko, I. I., Thermogenerator and thermoelectric cooler materials produced by melt jet impinging, *Proc. IX Int. Conf. on Thermoelectrics* (USA), Pasadena, 1990, 36.

Literature

1. Ioffe, A. F., *Thermoelements and Thermoelectric Cooling*, Infosearch, London, 1957.
2. Goldsmid, H. J., *Thermoelectric Refrigeration*, Plenum, New York, 1964.
3. Abrikosov, N. Kh., Bankina, V. F., Poretskaya, L. V., Skudnova, E. V., and Shelimova, L. E., *Poluprovodnikovye Soedinenia, ikh Poluchenie i Svoistva*, (in Russian, Semiconducting Compounds, Preparation and Properties) Nauka, Moscow, 1967.
4. Goltsman, B. M., Kudinov, B. A., and Smirnov, I. A., *Thermoelectric Semiconductor Materials Based on Bi_2Te_3*, Nat. Techn. Info. Center, U.S. Department of Commerce, Washington, D.C., 1973.
5. Pamplin, B. R., Ed., *Crystal Growth*, 2nd ed., Pergamon Press, Oxford, 1980.
6. Rowe, D. M. and Bhandari, C. M., *Modern Thermoelectrics*, Holt, Rinehart and Winston, London, 1983.
7. Goltsman, B. M., Dashevsky, Z. M., Kaidanov, V. I., and Kolomoets, N. V., *Plenochnye Termoelementy, Fizika i Primenenie* (in Russian, Film Thermoelements, Physics and Application), Nauka, Moscow, 1985.

10

Powder Metallurgy Techniques

A. Nancy Scoville
ThermoTrex Corporation
Waltham, Massachusetts, U.S.A.

10.1 Introduction

Powder metallurgy is broadly defined as the process whereby powders are compacted and then sintered at elevated temperatures to form a dense body with a well-defined, coherent grain structure. The compaction can occur at either room temperature or at elevated temperatures, which is commonly known as hot-pressing. Powder metallurgy techniques are used to fabricate a variety of common thermoelectric materials, including silicon-germanium (SiGe) and lead telluride (PbTe). It has also been investigated for bismuth telluride (Bi_2Te_3)-based systems. After a brief summary of powder metallurgical processes, the application of powder processing to SiGe and Bi_2Te_3 will be discussed.

For a more complete analysis of the sintering process, excellent texts are available.[1–3] The discussion presented here is largely based on Kingery, Bowen, and Uhlmann.[1]

10.2 Powder Metallurgy Processes

Pressureless Sintering

In this process, the thermoelectric powder is compacted at room temperature and then sintered at elevated temperature at ambient pressure. This process is particularly attractive from a manufacturing perspective. Simple tool steel dies are used to compact the powder. The material can be pressed to the device element size, eliminating the need for wafering and dicing steps. The powder is compacted in a short time so that the material can be processed quickly and high-speed dies are available that can press many hundreds of elements per hour.

During sintering two processes occur simultaneously; the grain size increases while the pore size and volume decrease. As the average grain size increases, smaller grains are consumed and the total number of grains decreases. The rate at which grain growth occurs is governed by the rate at which individual atoms can move across the grain boundary. This has been shown[1] to increase exponentially with temperature.

As the grains are growing, the number and size of the pores are also decreasing. The controlling variables for densification are particle size and the mechanism by which material is transported

0-8493-0146-7/95/$0.00+$.50

across the grain boundary. The densification rate decreases with increasing particle size. The transport mechanism will vary based on system parameters, but two mechanisms are especially important, diffusion from the grain boundary to the adjacent particles and diffusion from one grain to another. The diffusion coefficients will vary depending on the controlling diffusion mechanism and are affected by the composition and temperature as well as the cleanliness and shape of the grain boundaries.

In systems where no chemical processes are occurring, the sintering rate has been shown to decrease with time, thus long sintering times do not significantly improve the properties. Of course in systems where sintering is used as the synthesis technique and the reaction mechanism is solid state diffusion, a longer time may be required to allow complete reaction of material.

Hot Pressing

Hot-pressing is often used in systems where pressureless sintering is not practical. In pressureless sintering, capillary pressures provide the driving force for densification. If this pressure is not sufficient for rapid densification, external application of pressure at high temperatures is required. Densification occurs in precisely the same way whether or not external pressure is applied. The application of external pressure simply increases the rate at which these processes occur. In addition, plastic deformation can be important, especially in the early stages when contact stresses are significant.

Liquid-phase sintering can also be important in hot-pressing. Densification will occur at lower temperatures in the presence of a small amount of liquid phase. If the solid is soluble in, and is wet by the liquid, an extra capillary pressure develops from the filling of the interparticle space by the liquid. This allows the particles to rearrange to give a more efficient packing. Material transport is also increased as the solid dissolves in the liquid phase. This process is especially important in the SiGe system, especially in the early stages, due to the presence of molten elemental germanium.

In general, hot pressing is not as economically desirable as pressureless sintering, since it is not practical to fabricate individual elements. Instead, large compacts are pressed which must then be wafered and diced. Therefore, whenever possible pressureless sintering is preferred over hot pressing.

10.3 Silicon-Germanium

The powder metallurgical processing of SiGe has been extensively investigated since the late 1960s.[4] Powder processing, in the form of hot pressing, was initially investigated as a mechanism for increasing the carrier concentration since the dopant solubility decreases near the liquidus of the alloy.[3] Since that time, considerable improvements in the figure-of-merit of SiGe have been accomplished through manipulation and control of the powder processing techniques.

Two areas of improvement have been especially dependent on control of powder processing. The first is the improvement in electrical performance with heavily doped silicon germanium/gallium phosphide (SiGe/GaP) and the second is the reduction in thermal conductivity from increased phonon scattering.

Power Factor Improvements

In recent years. the most significant improvement has been the ability to increase the solubility of phosphorus by the addition of GaP.[6] In order to achieve a high power factor, a multiphase microstructure must be attained. Key to this microstructure are minor variations in the alloy composition throughout the material.[7] A typical[8] microstructure is shown in Figure 1. While the majority of the grains are fully alloyed, there are areas slightly enriched in Si and other areas slightly enriched in Ge. The Ge-rich regions are also enriched in dopant and these areas act as reservoirs for dopant during thermal cycling.

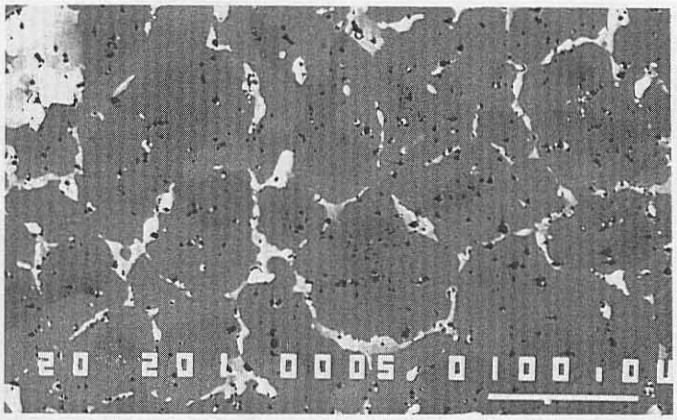

FIGURE 1 Micrograph of hot-pressed SiGe/GaP. The light areas are richer in Ge and have a higher dopant concentration than the Si-rich SiGe (dark areas).

While this structure could be obtained in zone-leveled material,[9] the grain sizes were considerably larger than for hot-pressed material. The smaller grain size of hot-pressed material resulted in formation of more dopant-rich phases and a higher carrier concentration. When elemental silicon and germanium are hot pressed, the resulting compact is composed of a distribution of alloy compositions. Thus, only a short anneal is required to distribute the dopant and form a coherent grain structure.[10]

Thermal Conductivity Improvements

The second area of performance improvements involves lowering the thermal conductivity without adversely impacting the electrical properties. Merely reducing the grain size will reduce the thermal conductivity, but the electrical conductivity will be similarly affected, resulting in no net improvement. A new approach has been investigated based on introducing a small amount of very fine (50 Å) particles into the SiGe grains.[11] These particles should scatter the phonons but not impact the electrical properties.

To effectively scatter the phonons the inert particle must be inside the grain, not at the grain boundary. As the powder is sintered, the thermoelectric grains will grow and incorporate the inert particle. Particles this small present several problems in pressing and sintering. These particles are very reactive because over 50% of the atoms are on the surface. The oxidation rate is sufficiently rapid that air exposure, even at room temperature, will result in pyrolysis. Therefore the powder must be fabricated and stored in an inert atmosphere. Once pressed, the grain size has increased sufficiently so that handling in air is not a problem.

Attempts to press these materials using the parameters developed for more conventional sized powders were unsuccessful. During the temperature ramp significant melting of the germanium occurred, most likely exacerbated by latent heats of mixing at essentially the molecular level. Thus, the ramp cycle had to be slowed and extended. Additionally even though densification occurred the degree of grain growth was insignificant at the pressing temperatures normally used. Grain growth was only observed after pressing at temperatures just below the liquidus followed by an extensive heat treatment. The difficulty in achieving grain growth may be related to grain pinning.[1] Since the primary energy for grain growth is temperature, higher temperatures are required.

Fine-particle p-type SiGe to which no inclusions were added has been fabricated with Zs equivalent to conventionally prepared SiGe.[12] The ability of this process to incorporate 40- to 100-Å particles inside the grain has been demonstrated. A 2-μm SiGe grain is shown in Figure 2; several small inclusions are clearly visible. To date, the concentration of particles has not been sufficiently high to dramatically reduce the thermal conductivity. However, moderate reductions have been achieved.[13]

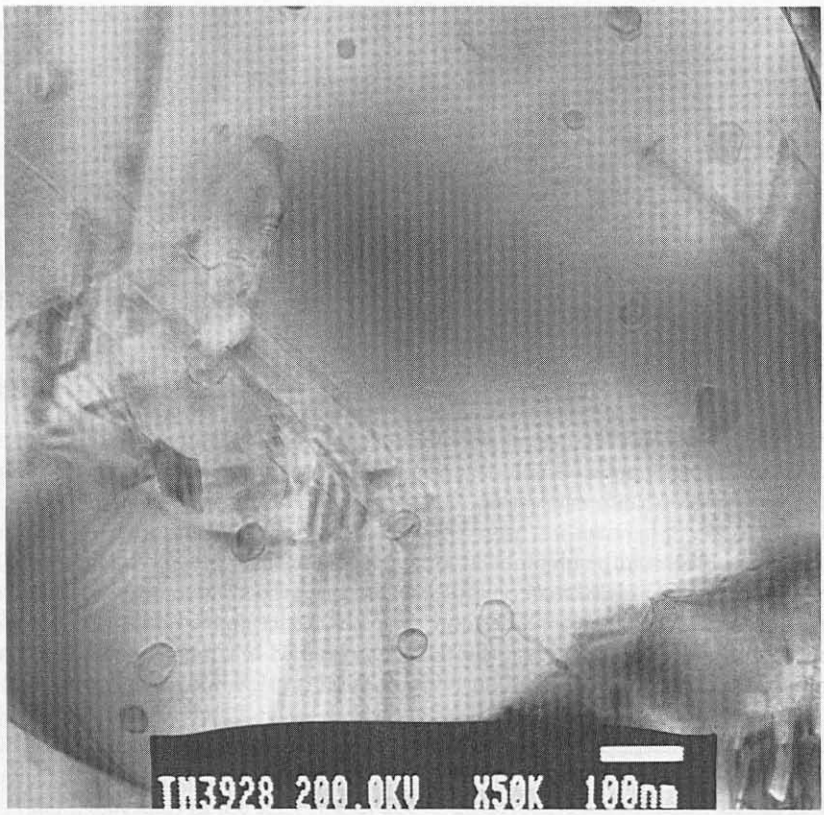

FIGURE 2 Transmission electron micrograph of hot-pressed spark-eroded SiGe. Note dark inclusions inside grain.

10.4 Bismuth Telluride Alloys

Bismuth telluride and its alloys with antimony telluride (Sb_2Te_3) and bismuth selenide (Bi_2Se_3), hereafter collectively referred to as Bi_2Te_3, crystallize in a highly anisotropic hexagonal crystal structure with the c-axis almost seven times longer than the a-axis.[14] As expected this results in anisotropic behavior in the thermoelectric properties, particularly the electrical and thermal conductivities. For this reason, most work done on Bi_2Te_3 systems has focused on highly oriented crystalline material.

The key issue to address in sintered Bi_2Te_3, then, is the potential degradation in performance as a result of random orientation. In fact, although the available data are quite limited it is not clear that any significant degradation would occur. In order to understand this one must look closely at the trade-off in anisotropy in the thermal conductivity and electrical resistivity. The Seebeck coefficient is not affected by the orientation. In Bi_2Te_3, the electrical conductivity is high along the a-axis, while the thermal conductivity is highest along the c-axis.[15] Thus, the degree to which these properties cancel controls the degradation in Z. A simple weighted average analysis showed that the Z in randomly oriented p-type material may be only 6% less than highly oriented materials. In n-type material the electrical anisotropy is greater and a 20% reduction would result.[15] In a randomly oriented material prepared by powder processing, the thermal conductivity may be reduced over the crystalline value as a result of grain boundary scattering so that these estimates may be pessimistic.

The change in lattice thermal conductivity as a function of grain size has been evaluated, and as expected significant reductions are observed. The lattice conductivity plotted vs. grain size is

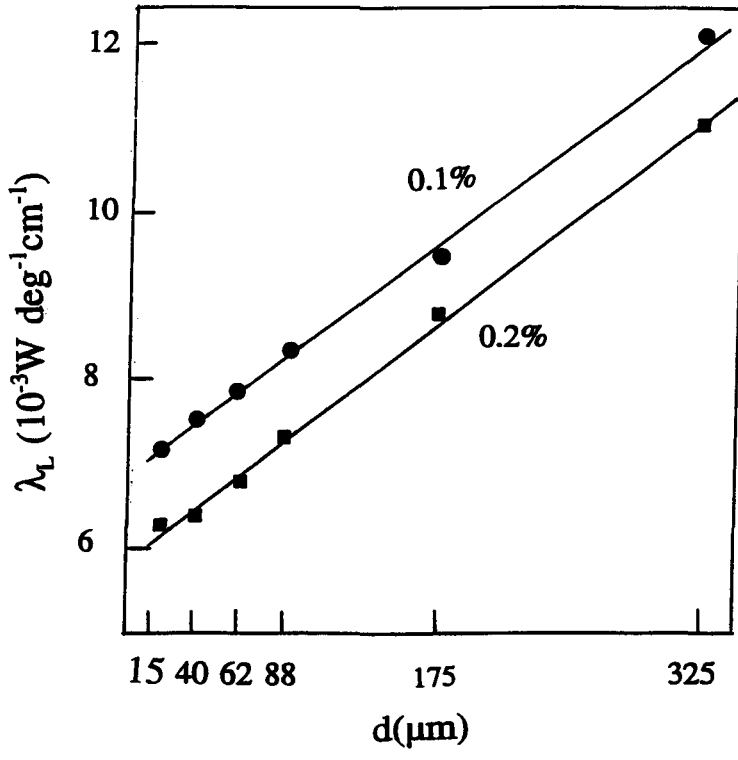

FIGURE 3 Lattice thermal conductivity vs. grain size, d, for p-type Bi_2Te_3 alloy. (From Jaklovszky, J. et. al., *Phys. Status Solidi (A)*, 27, 329, 1975. With permission of VCH Publishers. Copyright 1975.)

shown in Figure 3. For 15-μm grain size, the lattice conductivity is reduced by 40% over crystalline Bi_2Te_3.[16] The conductivity increases with increasing grain size and at 325 μm is the same as crystalline material.[17] In order to realize an improvement in Z from this lattice reduction, the electrical resistivity must not be similarly affected. In this study, as expected, the electrical resistivity was found to decrease with increasing grain size such that the figure-of-merit reached a maximum for 80-μm grain size, as shown in Figure 4. This result indicates that there is potential for sintered material; however, in this system the observed Z in the p-type system was 14% less than comparable materials and a 30% reduction was observed for n-type. Given the simple analysis discussed above, such a significant reduction in the thermal conductivity should have resulted in comparable if not improved Zs. Further analysis of this system reveals that the electrical resistivity is higher than expected based on random orientation.

The degradation in electrical behavior is most likely the result of oxidation of the powdered alloy. All the Bi_2Te_3-based materials are susceptible to oxidation and the amount of oxide increases as the particle size is decreased. Oxide layers can passivate the surface and prevent electrical transport through the material. A recent study[18] on hot-pressed Bi_2Te_3 provides further evidence that oxide formation most likely resulted in degradation of performance in the above-mentioned work. In this study similar-sized material, 37 to 74 μm, was used. Prior to pressing the powder was annealed in a hydrogen atmosphere for 24 h at 400°C. The powder was then hot pressed at 500°C. In this system the electrical properties were not appreciably degraded over crystalline material, while the thermal conductivity was reduced. The maximum figure-of-merit was 2.74×10^{-3} K^{-1} in good agreement with the crystalline material of the same composition.

Thus, it appears from these results that powder processing is a viable synthesis route for Bi_2Te_3-based systems. Control of the grain size and the processing ambient is required to achieve high figure-of-merit.

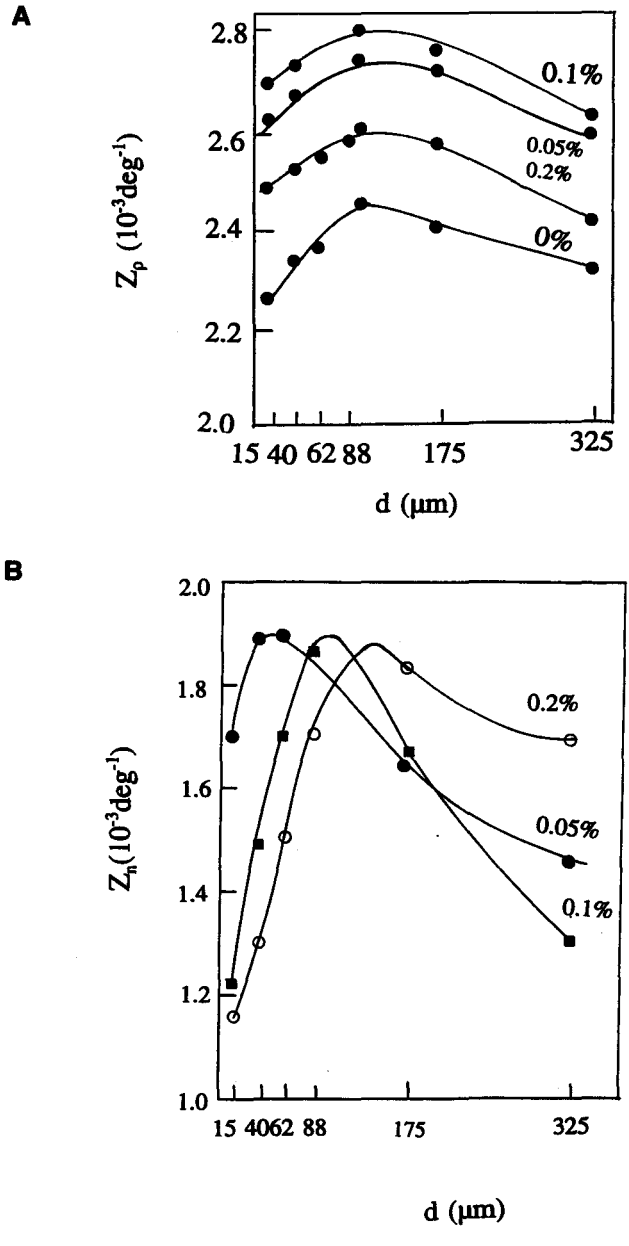

FIGURE 4 Figure-of-merit as a function of grain size for n-type (a) and p-type (b) Bi_2Te_3 alloy. (From Jaklovszky, J. et al., *Phys. Status Solidi (A)*, 27, 329, 1975. With permission of VCH Publishers. Copyright 1975.)

10.5 Conclusion

Powder metallurgy is a powerful tool for fabrication of thermoelectric materials. As with any process, identification and control of key process parameters are required to reproducibly achieve high-quality materials. While it is relatively straightforward to achieve high density and compositional control, the microstructure must also be controlled. This requires development of a detailed understanding of the relationship between processing parameters, microstructure, and thermoelectric performance.

References

1. Kingery, W. D., Bowen, H. K., and Uhlmann, D. R., *Introduction to Ceramics,* 2nd ed., John Wiley & Sons, New York, 1976, chap. 10.
2. Kuczyuski, G. C., Hooten, N. A., and Gibson, C. F., Eds., *Sintering and Related Phenomena,* Gordan and Breach, New York, 1986.
3. Coble, R. L. and Burke, J. E., in *Progress in Ceramic Science,* Vol. 3, Burke, J. E., Ed., Pergamon Press, New York, 1963.
4. Rosi, F. D., *Solid State Electron.,* 11, 833, 1968.
5. Wolf, H. F., *Silicon Semicondutor Data,* Pergamon Press, Oxford, 1969.
6. Vandersande, J. W., Wood, C., Draper, S. L., Raag, V., Alexander, M., and Masters, R., *Proc. 5th Symp. Space Nuclear Power,* Albuquerque, NM, 1988, 629.
7. Fleurial, J. P., Borshchevsky, A., and Vandersande, J. W., *Proc. 8th Symp. Space Nuclear Power,* Albuquerque, NM, 1988, 451.
8. Fleurial, J.P., private communication.
9. Borshchevsky, A., Fleurial, J. P., and Vandersande, J. W., *Proc. 25th Intersoc. Energy Conv. Eng. Conf.,* Reno, NV, 1990, 397.
10. Scoville, A. N., Bajgar, C., Vandersande, J. W., and Fleurial, J. P., *Proc. 26th Intersoc. Energy Conv. Eng. Conf.,* Boston, MA, 1991, 224.
11. Beaty, J. S., Rolfe, J. L., and Vandersande, J. W., *Proc. 25th Intersoc. Energy Conv. Eng. Conf.,* Boston, MA, 1990, 379.
12. Beaty, J. S., Rolfe, J. L., and Vandersande, J. W., *Proc. 8th Symp. Space Nuclear Power Systems,* Albuquerque, NM, 1991, 446.
13. Beaty, J. S., Rolfe, J. L., and Vandersande, J. W., *Proc. 9th Symp. Space Nuclear Power Systems,* Albuquerque, NM, 1992, 332.
14. Nakajima, S., *J. Phys. Chem. Solids,* 24, 479, 1963.
15. Goldsmid, H. J., *Electronic Refrigeration,* Pion Ltd., London, 1986.
16. Jaklovszky, J., Ionescu, R., Nistor, N., and Chiculita, A., *Phys. Status Solidi (A),* 27, 329, 1975.
17. Rosi, F. D., Abeles, B., and Jensen, R. V., *J. Phys. Chem. Solids,* 10, 191 1959.
18. Imaizumi, H., Yamaquchi, H., Haibe, H., and Nishida, I., *Proc. 6th Int. Conf. in Thermoelectrics,* Arlington, TX, 1986.

11

PIES Method of Preparing Bismuth Alloys

Toshitaka Ohta
Electrotechnical Laboratory
Ibaraki, Japan

Takenobu Kajikawa
Shonan Institute of Technology
Japan

11.1 Introduction

The PIES method (pulverized and intermixed elements sintering method[1,2]) is becoming recognized as a front-runner material preparation technique for use in the next generation of thermoelectric material. It has been reported that the thermoelectric figure-of-merit of PIES material is comparable to that of material prepared from the melt.[3,4] In addition it has a number of advantages over the melt technique: first, low-energy inventory for preparation, low cost, and a short processing period; second, increased homogeneity; third, a potential for reducing grain size, which favors a reduction in the material's thermal conductivity.[5] Fourth, it requires less specialized equipment and skills. This improvement in material preparation is significant, especially in the preparation of widely used thermoelectric materials, such as bismuth alloys, silicon germanium,[4,6] and new potential thermoelectric materials.[7,8]

It has been generally believed for 30 years that "the sintering of a pressed mixture of powdered elements is not totally satisfactory" because of the accompanying low thermoelectric figures-of-merit.[9] Evidently the PIES method can overturn this commonly held view because the figures-of-merit of PIES materials are much better than those of pseudo-PIES materials made by using conventional ball milling at the pulverizing and intermixing stage. Consequently, understanding the mechanisms responsible for the observed increase in the figure-of-merit is a main consideration as it may prove possible to use the PIES method to achieve similar improvements in other thermoelectric materials.

Bismuth alloys are the most widely used thermoelectric materials, especially in commercial thermoelectric refrigeration.[9] Consequently, bismuth alloys have always been of interest as thermoelectric materials. However, in previous studies bismuth alloys have been almost exclusively prepared by the conventional melt technique followed occasionally by conventional sintering.[10–13] The properties of bismuth alloys prepared by the PIES method are quite different from the conventional bismuth alloys.

0-8493-0146-7/95/$0.00+$.50

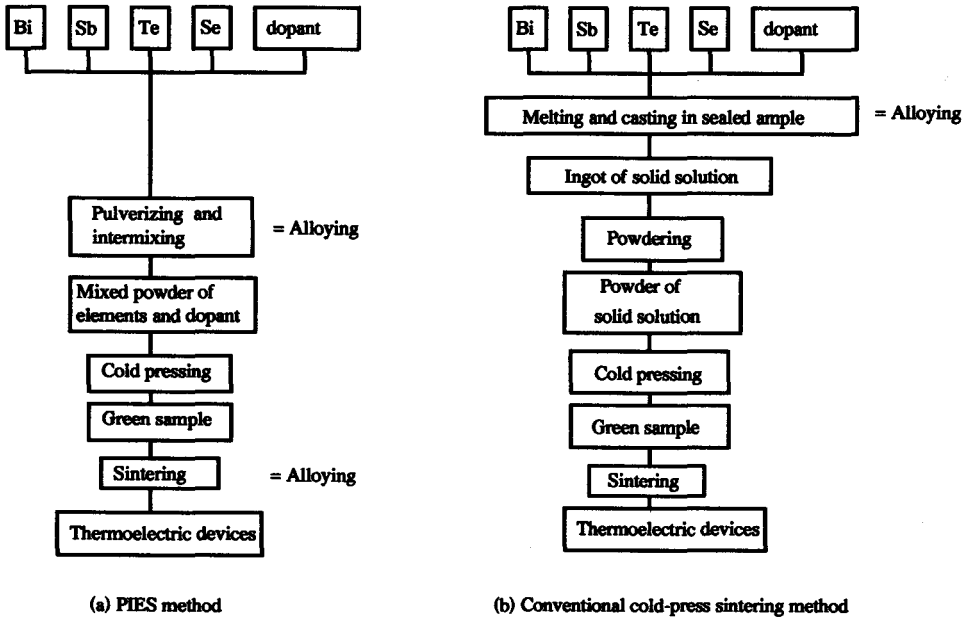

FIGURE 1 Pulverized and intermixed elements sintering (PIES) method.

11.2 PIES Method

PIES is a technique in which crystalline intermetallic or element powders are co-pulverized through a sequence of collision events inside a high-energy ball mill and yield alloys without using a melting process. PIES includes mechanical alloying (MA) in which the co-pulverization itself yields alloy. Although MA has been used widely over the past 10 years, neither PIES nor MA had been applied to thermoelectric semiconductors until it was first successfully used on bismuth telluride-type materials.[1]

Today PIES is successfully applied not only to bismuth alloys,[2,3,14,15] but also to a number of thermoelectric materials, for example, silicon germanium alloys,[6,16] rare earth sulfides,[17,18] and transition metal semiconductors such as Re_3Ge_7, chromium disilicide, and $Mo_{13}Ge_{23}$.[7,19]

The PIES method consists of several stages as shown in Figure 1, in which the conventional cold-press-sintering method is also presented as a comparison.[1,4,7,8] There are two important aspects of the stages in the PIES method. One is that the melting and casting process, which is indispensable in the conventional method and requires a long time, high temperature, and a sealed tube, is not required. It can be replaced by "pulverizing and intermixing" in the atmosphere, which correspond to the "powdering" process in the conventional method. The second is that the powdered mixture of several elements is alloyed at the "pulverizing and intermixing" stage and/or the "sintering" stage, of considerable significance for industrial application.

The PIES method with MA is discussed in Chapter 12; therefore, the PIES method without MA is described in this chapter. The manufacturing sequence is as follows.

Stage 1: Raw material elements are weighed in the ratio of the intended thermoelectric alloy and the appropriate amount of dopant added.

Stage 2: Pulverizing and intermixing can be dry or wet and is performed in atmosphere using a high-energy ball mill. An optimum intermixing time is selected in order to obtain a mixture with a particle size of a few microns or less.

Stage 3: Ethanol is added to the powdered mixture of elements. It is sieved into 50- to 150-mesh grain size and then cold pressed.

Stage 4: The green sample is finally sintered, then hot pressed or hot isostatic pressed (HIP).

The details of each process are as follows.

Raw material, which consists of the component elements in a ratio equal to that of the intended thermoelectric alloy, is pulverized and intermixed thoroughly. This is the most important process in the PIES method. In order to obtain a fine intermixture a planetary-type ball mill, impulsion-type pulverizer, jet-type pulverizer, or a tower-type grinder should be used.

In the case of a planetary ball mill, the pulverizing force F is given by

$$F = n(m/d)v^2\ t/W \tag{1}$$

where W is the loaded mass; n is the number of balls; m the mass of a ball; d the pot diameter; v the ball speed; and t the mixing time.

The ball milling speed can be expressed as

$$v = (d\ \pi\ n')/60 \tag{2}$$

where d is the mill diameter and n′ the rotation speed of the mill.

A large pulverizing force F is required to apply the PIES method successfully. The mean particle-diameter of the resulting raw material mixture ranges from submicron to a few microns.

The mixture is sieved with polyvinyl alcohol and cold-pressed at 0.5 to 1.5 × 10^8 Pa using single spindle press equipment to form the green. Initially the green was sintered at atmospheric pressure in an inert gas. However, the thermoelectric performance of the compact was not good enough for commercial use. The composition of the alloy differed a little from that expected because of the sublimation of certain components. In addition, the composition at the surface and interior of the compact differed and resulted in inhomogeneous properties. Therefore, in order to improve the material performance and reproducibility, preheating and hot isostatic pressing procedures were employed.

11.3 Preparation of Bismuth Alloys

The typical conditions for preparing bismuth alloys are as follows:

1. The constituent elements are weighed according to the required composition ratio. For n-type bismuth alloy the ratio of Bi:Sb:Te:Se is 1.8:0.2:2.85:0.5 and 0.2 to 0.375 mol% of SbI[3] is added as dopant. In the case of p-type alloy the ratio of Bi:Te:Sb is 0.5:3.0:1.5 and 2.5 wt% of Se is added as dopant. The purity of the materials is 5 nines.
2. Pulverizing and intermixing is wet, using ethanol as the solvent, and is carried out in a planetary-type ball mill. Intermixing time is more than 10 h and results in a typical average particle size of 3.3 μm.
3. The powder mixture is sieved into 50 to 150 μm using 1.0 cc of ethanol per grain of powder and then pressed at a pressure of 2.7 × 10^8 Pa in a single spindle press.
4. The green sample is preheated in argon gas under atmospheric pressure.
5. The green is hot isostatic pressed at 2 × 10^8 Pa and at a temperature of 730 K.

11.4 Solid Solution Formation Process and Morphology

The solid solution formation of n-type $(Bi,Sb)_2(Te,Se)_3$[14] is monitored at each stage of the sintering process by X-ray diffraction and microprobe analysis.

X-Ray Diffraction

In Figure 2 the X-ray diffraction (XRD) spectra of the samples 0 to 5 listed in Table 1 are shown. Figure 2(a) shows the spectra of the pulverized powder and samples 0 to 2, whereas Figure 2(b) shows the spectra of samples 3 to 5.

The pulverized powder and green sample (sample 0) have some peaks corresponding to elements such as Bi, Te, and Sb. On the other hand, in the preheated sample (sample 1), which is

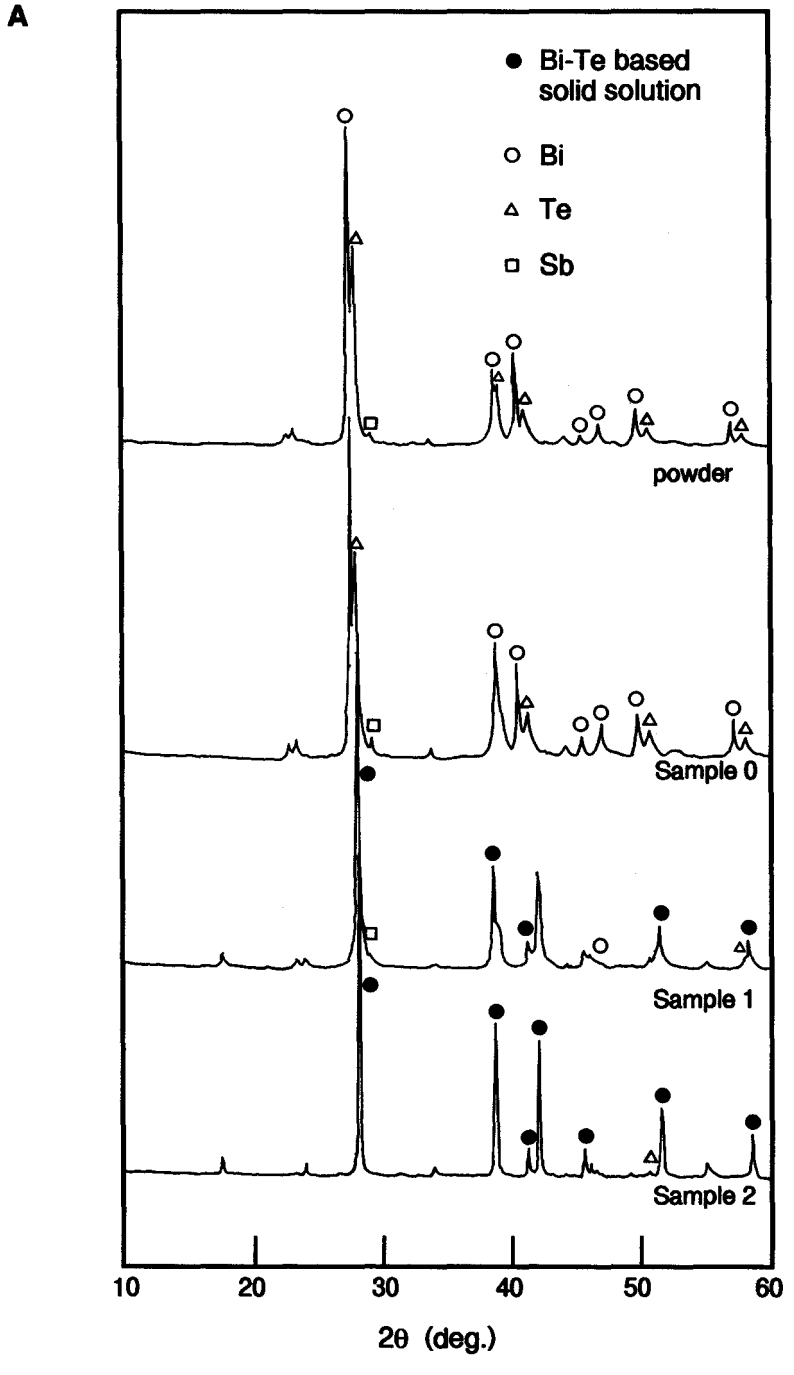

FIGURE 2a XRD spectra of powder and samples 0 to 2.

subjected to a 10-h preheating at 473 K, the peaks correspond to those of the solid solution Bi-Te alloy. However, the solid solution formation is insufficient as is confirmed by the presence of peaks corresponding to the elements and by the large width of the solid solution peak.

Sample 2 is preheated for 10 h at 473 K and then its temperature increased up to 678 K. Small element peaks and a solid solution peak with a relatively small half-width are observed.

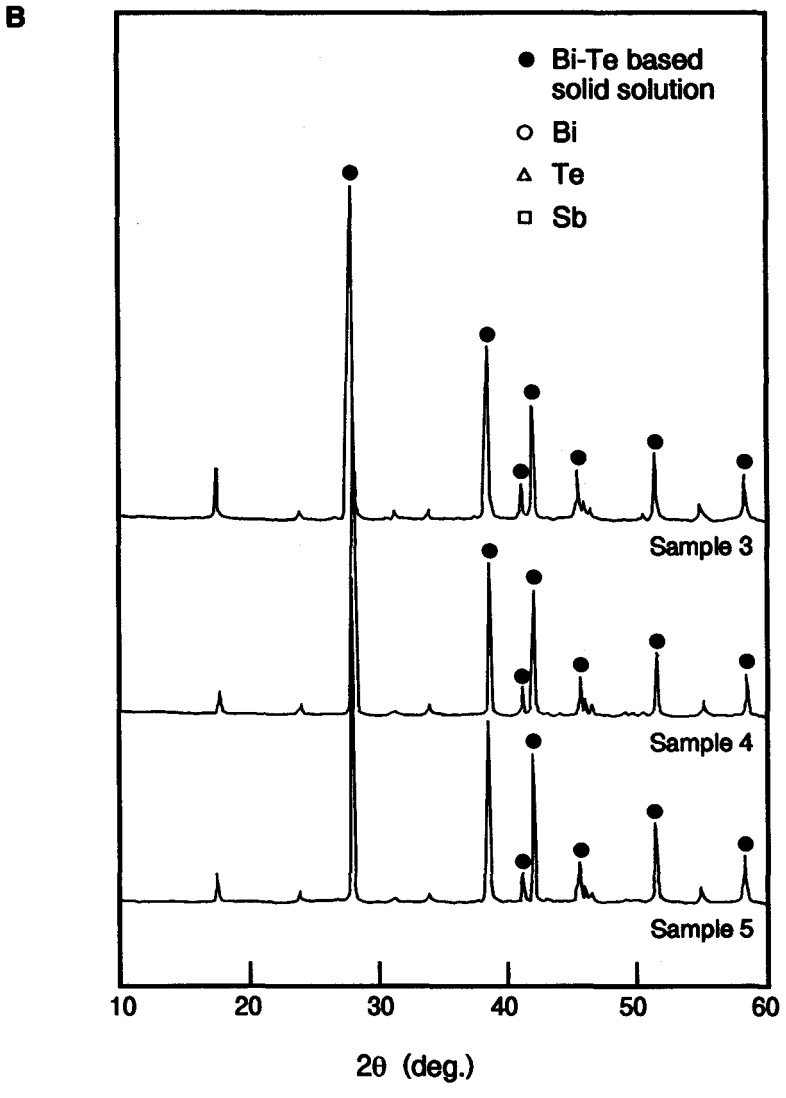

FIGURE 2b XRD spectra of samples 3 to 5.

Table 1. Table of Sample Numbers and Sampling Conditions

Sample No.	Sampling Conditions
0	Green
1	After 10 h preheating (473 K)
2	At 678 K
3	Just after the sintering temperature (733 K)
4	After 1 h sintering
5	After 10 h sintering

From Ohta, T. et al., in *Proc. IX Int. Conference on Thermoelectrics*, Vining, C.B., Ed., Jet Propulsion Lab., California Institute of Technology, Pasadena, 1990, 16. With permission.

Sample 3 is quenched just after reaching the sintering temperature (733 K). Element peaks are not observed and the main "solid solution peak" has become sharper.

Samples 4 and 5 are sintered for 1 h and 10 h, respectively. The half-width of sample 4's "solid solution peak" is smaller than that of sample 3, while there is almost no difference between samples 4 and 5.

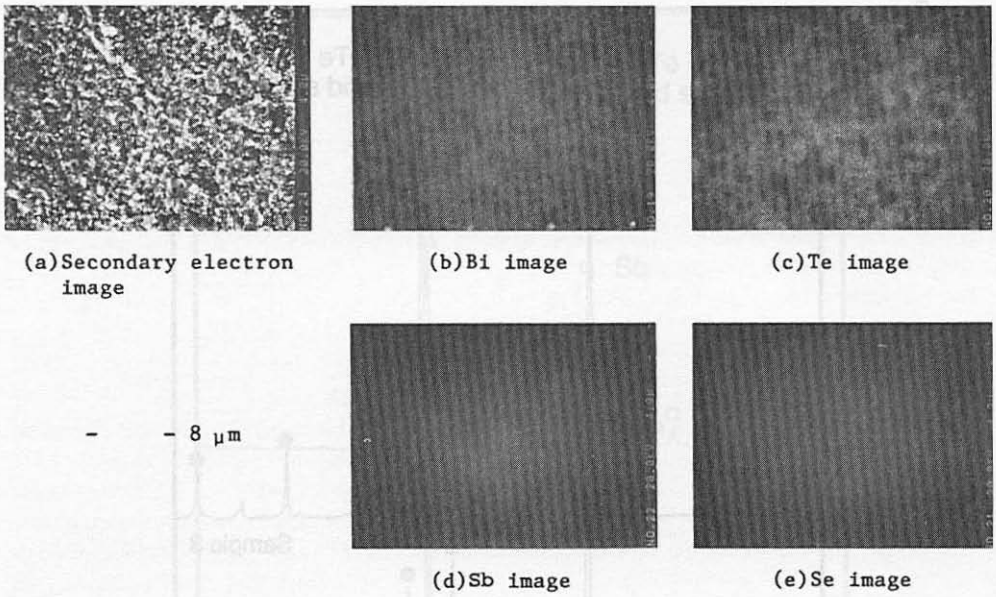

FIGURE 3 SEM-EPMA image of sample 0. (From Ohta, T. et al., in *Proc. IX Int. Conference on Thermoelectrics*, Vining, C.B., Ed., Jet Propulsion Lab., California Institute of Technology, Pasadena, 1990, 16. With permission.)

The XRD charts show that the solid solution formation has already begun at the preheating process. Evidently, diffusion and reaction processes have occurred even at 473 K because of the existence of low-melting-point materials such as Bi (M.P.: 544 K) and Te (M.P.: 623 K).

Microprobe Analysis

Figures 3 to 8 show the SEM images and the distribution of elements. The majority of the particles are submicron, while the mean particle size measured using a particle size meter is 3.3 μm, which is the result of cohesion.

According to the SEM images obtained after the preheating process, Figure 4(a), solid-phase diffusion has resulted in some links between particles, although isolated particles are still dominant. A SEM image obtained at 678 K as shown in Figure 5(a) indicates clearly the presence of crystal growth of 2 μm. Figure 6(a) shows that crystal growth is continuing, with crystals up to about 10 μm in diameter present immediately after the sintering temperature at 733 K, which is the intended value for the PIES method. Figure 6(a) also shows the existence of non-reacted and isolated particles. Figure 7(a) and Figure 8(a) are similar to Figure 6(a), but the isolated particles are reduced and accompanied by a decrease in porosity.

The X-ray images of individual elements are shown in Figure 3(b) to (e). The figures show that the distributions of Bi and Te are uniform at the green sample stage except for the region where other elements exist on the surface. However, the distributions of Sb and Se are localized as islands, since the content of these elements is too low to obtain a uniform distribution in spite of high-energy ball milling for a long time. In Figure 4, (b) to (e), the island-like distributions of Sb and Se disappear after preheating at 473 K. These X-ray images confirm that all elements in the intermixture are able to diffuse in the solid phase at 473 K. Figure 5, (b) to (e), shows that the distributions of Bi and Te, the major constituents, are uniform at 678 K. The actual distribution of Sb, however, is rather more localized than indicated by the signal intensity. Figure 6, (b) to (e), shows the additional improvement in the distributions of Bi and Te just after the sintering temperature. On the other hand, Sb continues to be localized. The crystals in Figure 6(a) are observed not as the shadow in the X-ray images of Bi, Te, and Se, but as the shadow in the X-ray image of Sb.

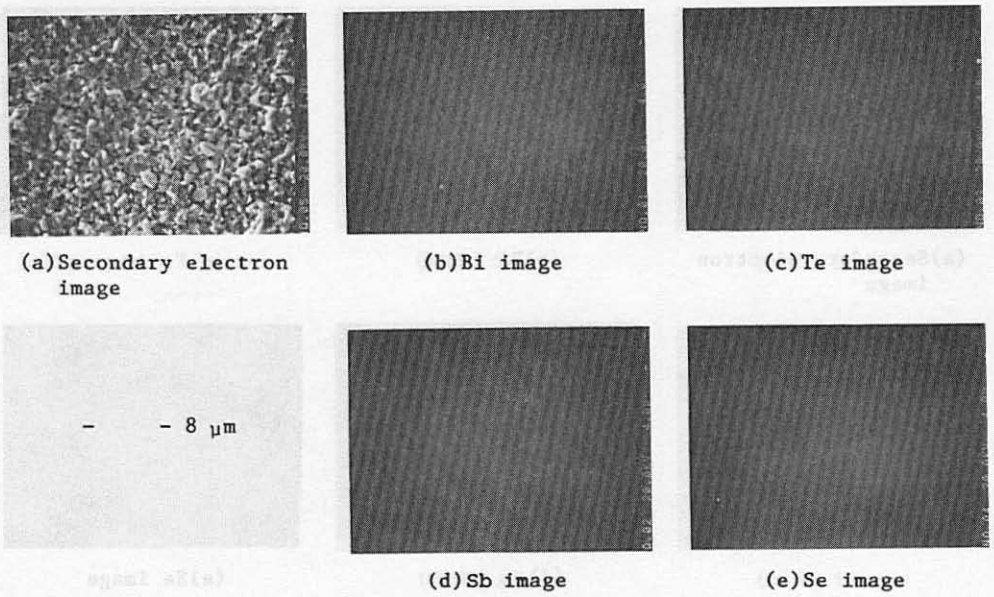

FIGURE 4 SEM-EPMA image of sample 1. (From Ohta, T. et al., in *Proc. IX Int. Conference on Thermoelectrics,* Vining, C.B., Ed., Jet Propulsion Lab., California Institute of Technology, Pasadena, 1990, 16. With permission.)

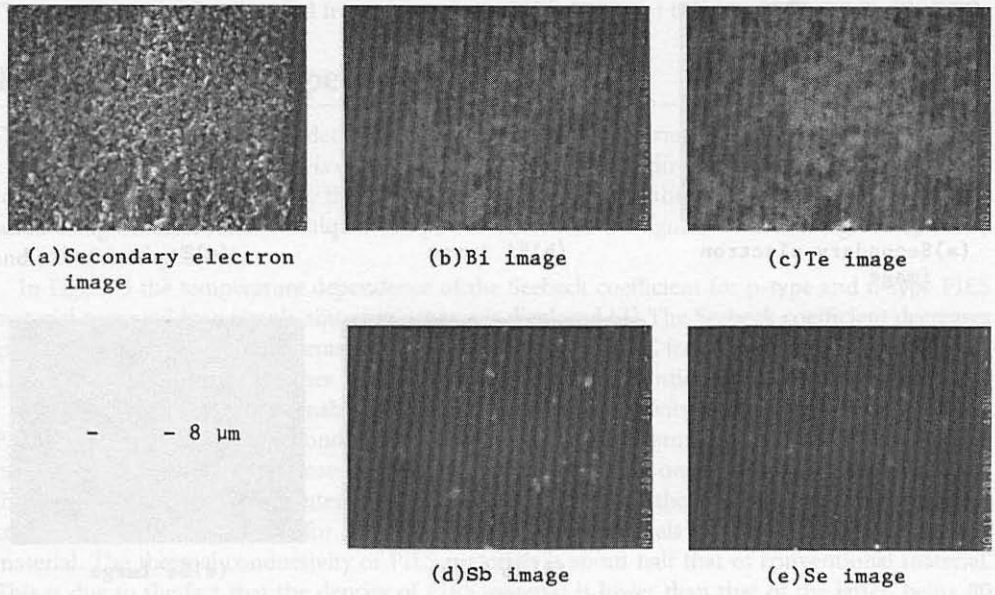

FIGURE 5 SEM-EPMA image of sample 2. (From Ohta, T. et al., in *Proc. IX Int. Conference on Thermoelectrics,* Vining, C.B., Ed., Jet Propulsion Lab., California Institute of Technology, Pasadena, 1990, 16. With permission.)

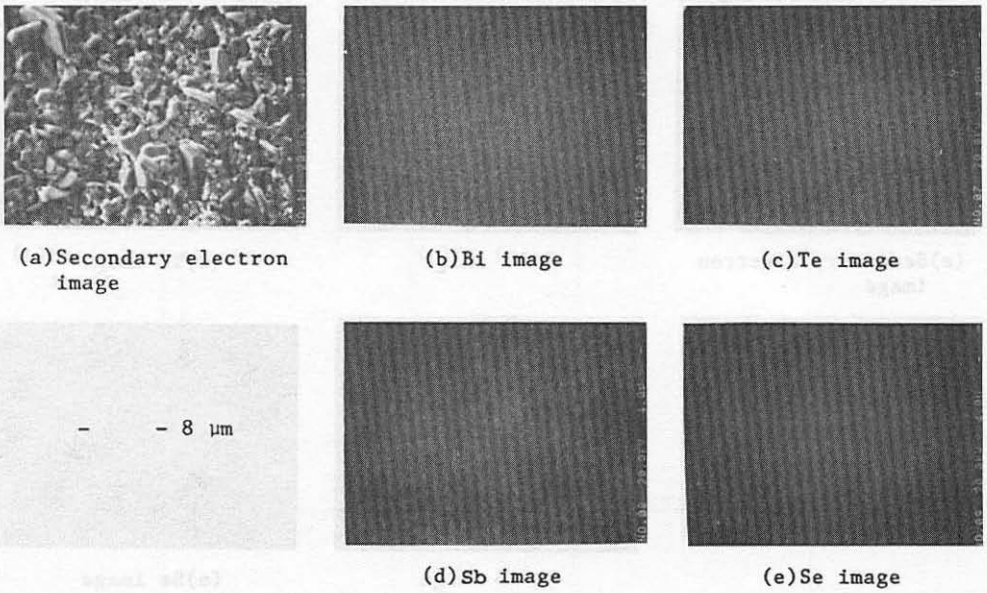

FIGURE 6 SEM-EPMA image of sample 3. (From Ohta, T. et al., in *Proc. IX Int. Conference on Thermoelectrics*, Vining, C.B., Ed., Jet Propulsion Lab., California Institute of Technology, Pasadena, 1990, 16. With permission.)

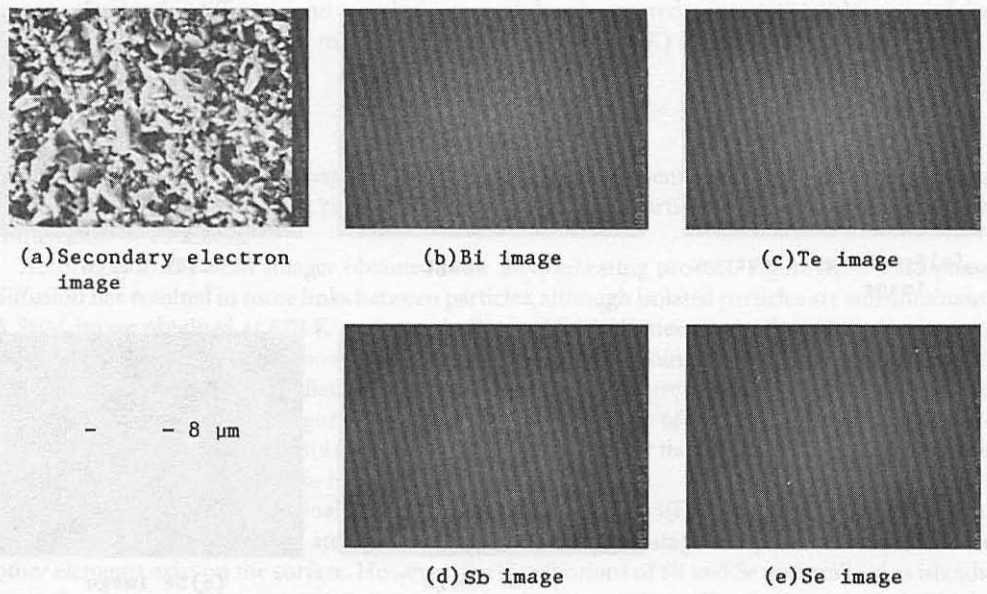

FIGURE 7 SEM-EPMA image of sample 4. (From Ohta, T. et al., in *Proc. IX Int. Conference on Thermoelectrics*, Vining, C.B., Ed., Jet Propulsion Lab., California Institute of Technology, Pasadena, 1990, 16. With permission.)

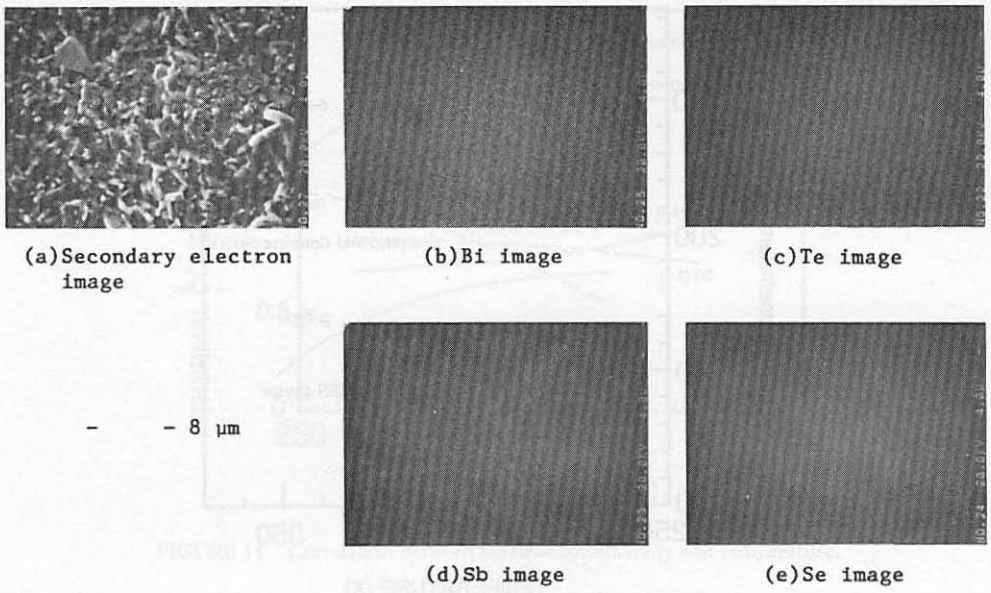

FIGURE 8 SEM-EPMA image of sample 5. (From Ohta, T. et al., in *Proc. IX Int. Conference on Thermoelectrics*, Vining, C.B., Ed., Jet Propulsion Lab., California Institute of Technology, Pasadena, 1990, 16. With permission.)

Therefore, it is suggested that this crystal is the solid solution of Bi, Te, and Se but excludes Sb. This result can also be obtained from the analysis of Figure 7, (b) to (e), and Figure 8, (b) to (e).

11.5 Thermoelectric Properties

The Seebeck coefficient (α) is determined from the thermoelectric motive force generated when a temperature difference of 5 K is established in the longitudinal direction of the sample. Electrical conductivity (σ) is measured by the four-probe method and the thermal conductivity (λ) is measured using the laser-flash technique. The power factor and the figure-of-merit are given by ($\alpha^2\sigma$) and ($\alpha^2\sigma/\lambda$), respectively.

In Figure 9 the temperature dependence of the Seebeck coefficient for p-type and n-type PIES material prepared by a simple sintering process is displayed.[1,15] The Seebeck coefficient decreases gradually with increasing temperature over the range 270 to 350 K for both p- and n-type material. The PIES materials have a higher Seebeck coefficient than conventionally sintered ones.

Figure 10 shows the relationship between electrical conductivity and temperature for p-type PIES materials. The electrical conductivity decreases with temperature. In addition, PIES materials made by a simple sintering process have an electrical conductivity one third to one half times lower than that of conventionally sintered material. Figure 11 shows the correlation between thermal conductivity and temperature for p-type and n-type PIES materials and a conventionally sintered material. The thermal conductivity of PIES materials is about half that of conventional material. This is due to the fact that the density of PIES material is lower than that of the latter, being 80 and 95% that of the theoretical density, respectively. The density of PIES material is lower because a small part of the component elements evaporates during the sintering process. Table 2 shows a comparison of the composition before and after the sintering processes. The ratio of tellurium decreases due to the sintering process.

There are a number of reasons why the thermoelectric performance of PIES material is worse than that of a conventionally sintered material.

1. The latter is sintered in a sealed tube while PIES material is sintered in a flow of argon gas. Consequently, its composition changes and its density decreases.

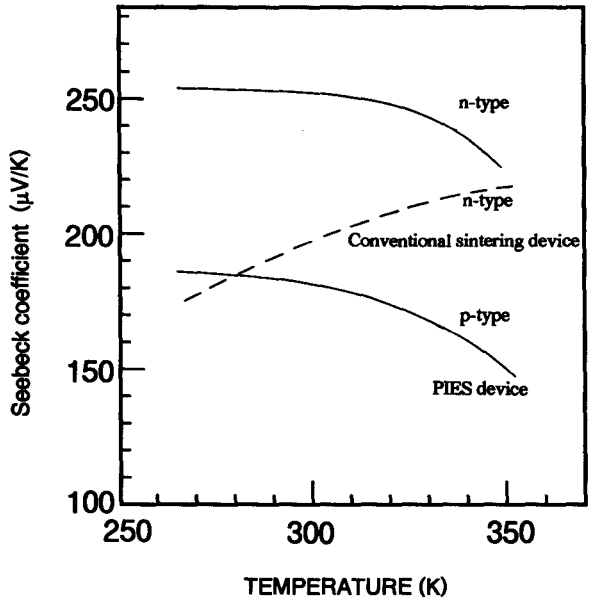

FIGURE 9 Correlation between Seebeck coefficient and temperature.

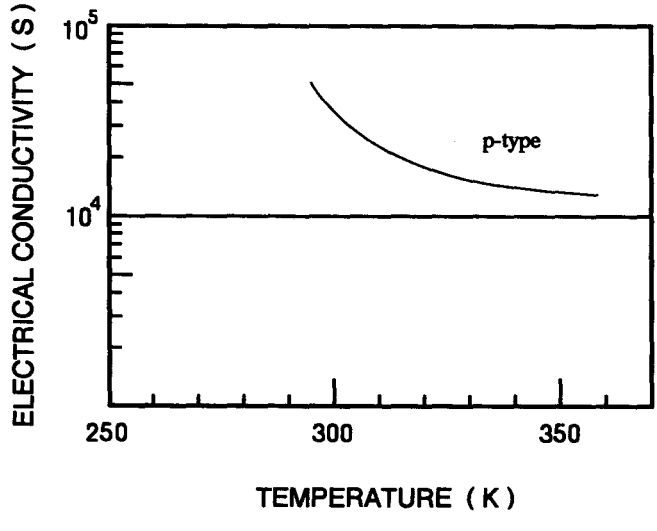

FIGURE 10 Correlation between electrical conductivity and temperature for p-type PIES material.

Table 2. Composition Before and After Sintering

	Bi	Te	Sb	Se
Initial composition (wt%)	15.13	54.43	26.44	2.49
Composition of sintered body (wt%)	18.27	48.79	29.80	2.94

From Tokiai, T. et al., in *Proc. IX Int. Conference on Thermoelectrics*, Vining, C.B., Ed., Jet Propulsion Lab., California Institute of Technology, Pasadena, 1990, 48. With permission.

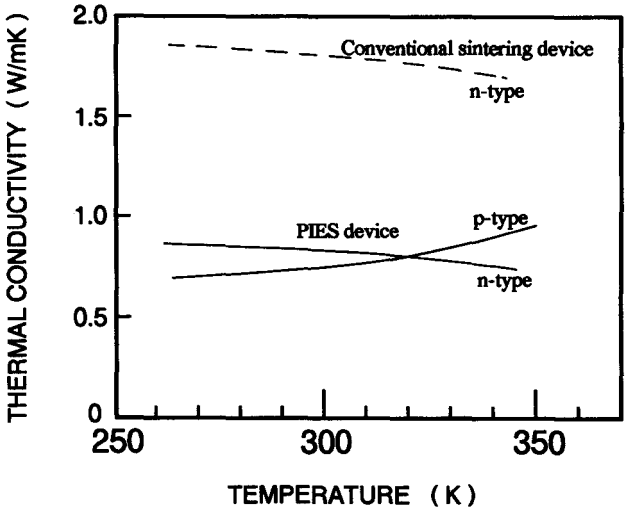

FIGURE 11 Correlation between thermal conductivity and temperature.

Table 3. Thermoelectric Properties of Various PIES Methods

	HIP-PIES	Preheated PIES	Simply Sintered PIES	Conventional Sintering
Seebeck coef. (μV/K)	200	185	183	160
Electrical conductivity × 10^5 (S/m)	0.95	0.45	0.31	1.45
Thermal conductivity (W/mK)	1.3	0.9	0.71	1.4
Figure-of-merit × 10^{-1} (K^{-1})	2.83	1.71	1.46	2.8

2. A large particle size of raw material (100 to 200 μm) is used on conventional sinterary, while PIES material has a small particle size of around 2.5 μm. Hence, the PIES raw material powder is more *oxidized* and accompanied by an increase in electrical resistivity.

It is possible to minimize the electrical resistivity and improve the figure-of-merit by adjusting the initial composition ratio so as to obtain the final optimum composition which has a Seebeck coefficient of about 200 μV/K. The reduction in density increases the electrical resistivity on one hand, and decreases the thermal conductivity on the other hand. From the macroscopic point of view the presence of pores in the material is neutral with respect to the figure-of-merit.

In the case of PIES materials, since pulverizing and uniform intermixing are essential, oxidation is inevitable. Therefore, oxidized compact should be reduced by some means such as annealing them in hydrogen. In the case of a conventionally hot-pressed compact, this has resulted in a large improvement in the figure-of-merit.[20] Consequently, since the PIES material should be much more oxidized than conventionally hot-pressed material, an improvement in performance can be expected.

In order to sufficiently improve the thermoelectric performance and the reproducibility of the PIES material, the preheating and HIP processes replaced the sintering process. The density of preheated PIES material is 91% of the theoretical value, while the density of HIP-PIES material is 99%. The electrical conductivity can be doubled while maintaining a small change in the Seebeck coefficient. The thermal conductivity is 1.4 times higher than that of a simple sintered PIES material (increases from 0.9 W/mK to 1.3 W/mK). Table 3 shows the room temperature thermoelectric properties for each processed PIES material. The dependence of the figure-of-merit on temperature is shown in Figure 12. The performance of HIP-PIES material is comparable to that of the commercial melt grown and hot-pressed material.

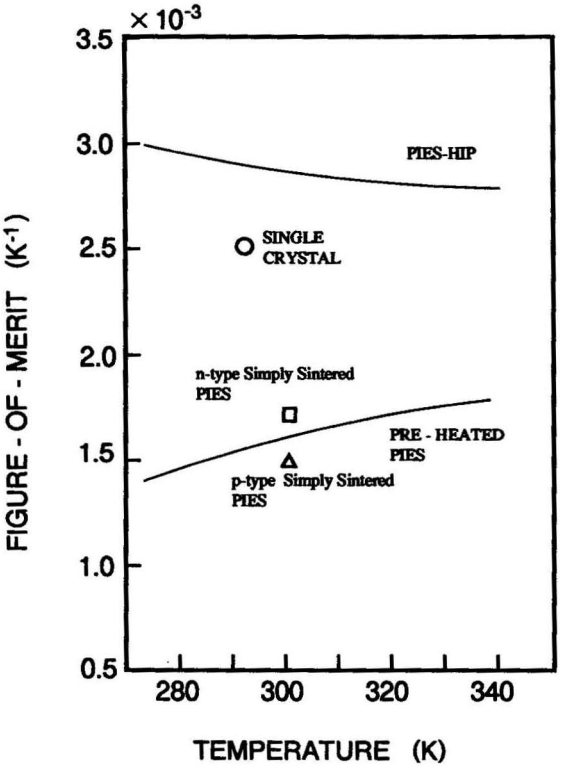

FIGURE 12 Dependency of figure-of-merit on temperature.

11.6 Effect of Pulverizing and Intermixing

The key to successful PIES method is high-energy ball milling in a pulverized and intermixed process. The effect of high-energy ball milling is demonstrated by comparing high-energy ball milling and the conventional method. Then, the thermoelectric properties and X-ray diffraction chart of a PIES material and a conventional ball-milling material are investigated.

Table 3 gives thermoelectric properties, at 300 K, for both PIES and conventional ball-milled material. The Seebeck coefficient (α) of the PIES material is 40 to 60 μV/K higher than that of the conventional material. The electrical conductivity of the former is 5.5 times higher than the latter, while the thermal conductivity is the same. Consequently, the figure-of-merit of the PIES material is about one order higher than material prepared by conventional ball-milling.

Figure 13 is an X-ray diffraction chart of both materials. The chart of the PIES material is considerably different from that of the conventional ball-milling material. The main peak of the solid solution of Bi-Sb-Te is symmetrical, while that of the conventional one is asymmetrical. This is caused by the overlap of the Bi, Te, and Sb peaks and the peaks of oxides of Sb which indicate that considerable amounts of Bi, Te, and Sb remain in solid solution. X-ray diffraction analysis reconfirmed that the simple sintering process after conventional ball-milling results in incomplete alloying, which has been expected by the common view for the last 30 years.

Thus, the high-energy ball milling facilitates the total transformation to solid solution by a single sintering process.

11.7 Future Prospects

The PIES method that includes mechanical alloying (MA) is a low energy-cost process for preparing thermoelectric materials because of the elimination of the melting and casting processes which require a long time, a high-temperature environment, and sealing.

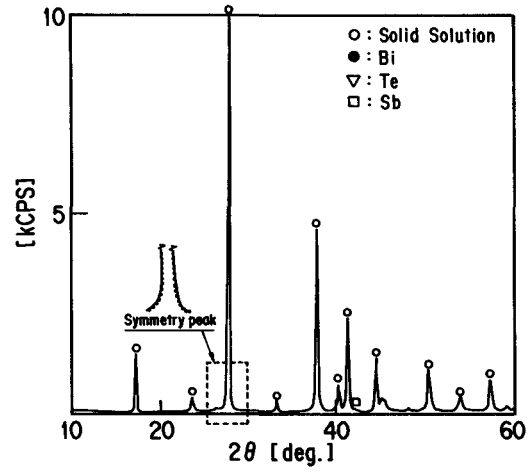

(a) PIES device (After sintering)

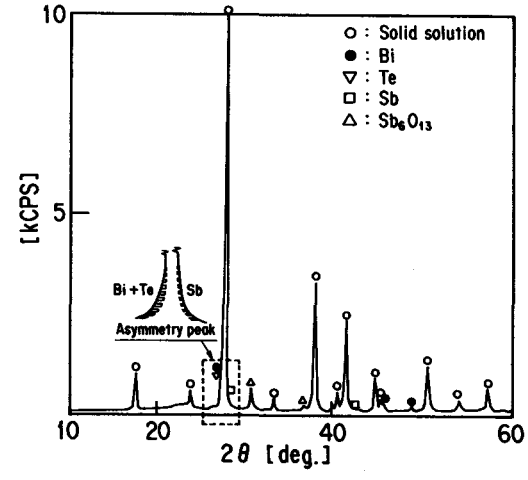

(b) Conventional ball milling device (after sintering)

FIGURE 13 XRD spectra of PIES material and conventional ball-milling material. (From Ohta, T. et al., in *Proc. Eighth Int. Conference on Thermoelectric Energy Conversion*, Scherrer, H. and Scherrer, S., Eds., Institut National Polytechnique de Lorrane, Nancy, 1989, 7. With permission.)

Simple sintering, sintering after preheating, and hot isostatic pressing (HIP) after preheating are optional as the final stage of the PIES method to improve thermoelectric performance, reproducibility, and mechanical properties. The room temperature figure-of-merit of PIES material is 2.8×10^{-3} K^{-1} and is competitive with commercial hot-pressed materials.

X-ray diffraction analysis makes it clear that the solid solution formation in the PIES method occurs at the preheating stage. Furthermore, in MA the solid solution is formed at the pulverizing and intermixing stage, which leads to another feature, that is, producing fine-grain sized material.

Traditionally, a PIES-like method has been used in the production of oxide dispersed-strengthened alloys and the production of alloys from components that have widely differing melting temperatures.[21] The alloying process occurs through solid-state diffusion rather than through the formation of local melts.[22] This suggests that the PIES method could be an alternative to the conventional melt-technique method of preparing thermoelectric materials, which involves melting-casting-grinding-hot pressing.

References

1. Ohta, T., Uesugi, T., Tokiai, T., Nosaka, M., and Kajikawa, T., Pulverized and intermixed elements sintering method on $(Bi,Sb)_2(Te,Se)_3$ based n-type thermoelectric materials, in *Proc. Eighth Int. Conference on Thermoelectric Energy Conversion*, Scherrer, H. and Scherrer, S., Eds., Institut National Polytechnique de Lorrane, Nancy, 1989, 7.
2. Ohta, T., Uesugi, T., Tokiai, T., Nosaka, M., and Kajikawa, T., Pulverized and intermixed elements sintering method for $(Bi,Sb)_2(Te,Se)_3$ based n-type thermoelectric materials, *Trans. IEE of Japan*, Vol. 111-B, 670, 1991 (in Japanese).
3. Tokiai, T., Uesugi, T., Fukumoto, K., Hirayama, A., Ito, K., Ohta, T., and Kajikawa, T., Thermoelectric characteristics of Bi-Te based PIES materials after-sintering (II), in *Proc. 1992 Spring Meeting of the Japan Institute of Metals*, Japan Institute of Metals, Tokyo, 1992 (in Japanese).
4. Cook, B.A., Beaudry, B.J., Harring, J.L., and Barnett, W.J., Mechanical alloying as an alternative method of producing n-type $Si_{80}Ge_{20}$ thermoelectric materials, in *Proc. IX Int. Conference on Thermoelectrics*, Vining, C.B., Ed., Jet Propulsion Lab., California Institute of Technology, Pasadena, 1990, 234.
5. Rowe, D.M. and Shukla, V.S., The effect of phonon-grain boundary scattering on the lattice thermal conductivity and thermoelectric conversion efficiency of heavy doped fine-grained, hot-pressed silicon germanium alloy, *J. Appl. Phys.*, 52, 7421, 1981.
6. Han, S.H., Cook, B.A., and Gschneidner, K.A., Jr., Effect of the doping process on the electrical activity of phosphorous in $Si_{80}Ge_{20}$, in *Proc. Eleventh Int. Conference on Thermoelectrics*, Rao, K.R., Ed., The University of Texas at Arlington, Arlington, 1992, 57.
7. Caillat, T., Fleurial, J.P., and Borshchevsky, A., Use of mechanical alloying to prepare and investigate new potential thermoelectric materials, in *Proc. Eleventh Int. Conf. on Thermoelectrics*, Rao, K.R., Ed., The University of Texas at Arlington, Arlington, 1992, 240.
8. Ohta, T., P-type thermoelectric characteristics of polycrystal ruthenium sesquisilicide, in *Proc. Eleventh Int. Conf. on Thermoelectrics*, Rao, K.R., Ed., The University of Texas at Arlington, Arlington, 1992, 74.
9. Goldsmid, H.J., *Thermoelectric Refrigeration*, Plenum Press, New York, 1964, 199.
10. Yim, W.M. and Rosi, F.D., Compound tellurides and their alloys for Peltier cooling — a review, *Solid-State Electron.*, 15, 1121, 1972.
11. Durst, T., Goldsmid, H.J., and Harris, L.B., Production of alloys of bismuth telluride for solar thermoelectric generators, *Sol. Energy Mater.*, 5, 181, 1981.
12. Kaibe, H., Tanaka, Y., Sakata, M., and Nishida, I., Anisotropic galvanomagnetic and thermoelectric properties of n-type Bi_2Te_3 single crystal with the composition of a useful thermoelectric cooling material, *J. Phys. Chem. Solids*, 50, 945, 1989.
13. Caillat, T., Carle, M., Fleurial, J.P., Scherrer, H., and Scherrer, S., Thermoelectric properties of single crystal alloys $Bi_8Sb_{32}Te_{60}$, $Bi_9Sb_{31}Te_{60}$, and $Bi_{10}Sb_{30}Te_{60}$ grown by the T.H.M. method, in *Modern Perspectives on Thermoelectrics and Related Materials*, MRS Symp. Proc. 234, Allred, D.D., Vining, C.B., and Slack, G.A., Eds., Material Research Society, Pittsburgh, 1991, 189.
14. Ohta, T., Sugimoto, K., Tokiai, T., Nosaka, M., and Kajikawa, T., Solid solution formation process on $(Bi,Sb)_2(Te,Se)_3$ based n-type thermoelectric materials by PIES method, in *Proc. IX Int. Conference on Thermoelectrics*, Vining, C.B., Ed., Jet Propulsion Lab., California Institute of Technology, Pasadena, 1990, 16.
15. Tokiai, T., Ohta, T., Nosaka, M., Sugimoto, K., and Kajikawa, T., Characteristics of $(Bi,Sb)_2(Te,Se)_3$ based p-type thermoelectric materials by PIES method, in *Proc. IX Int. Conference on Thermoelectrics*, Vining, C.B., Ed., Jet Propulsion Lab., California Institute of Technology, Pasadena, 1990, 48.
16. Cook, B.A., Beaudry, B.J., Harringa, J.L., and Barnette, W.J., Oxygen effects in mechanical alloyed $Si_{80}Ge_{20}$ doped with GaP and P, in *Modern Perspectives on Thermoelectrics and Related Materials*, MRS Symp. Proc. 234, Allred, D.D., Vining, C.B., and Slack, G.A., Eds., Material Research Society, Pittsburgh, 1991, 111.
17. Han, S.H., Gschneidner, K.A., Jr., and Beaudry, B.J., Preparation of a metastable high temperature phase (γ-Dy_2S_3) and a metastable high pressure phase (γ-Y_2S_3) by mechanical alloying and mechanical milling, *Scr. Metall. Mater.*, 25, 295, 1991.
18. Han, S.H., Gschneidner, K.A., Jr., and Beaudry, B.J., Preparation of the metastable high pressure γ-R_2S_3 phase (R = Er, Tm, Yb and Lu) by mechanical milling, *J. Alloys Compounds*, 181, 463, 1992.

19. Caillat, T., Borshchevsky, A., and Fleurial, J.P., Search for new high temperature thermoelectric materials, in *Proc. 27th Intersociety Energy Conversion Engineering Conference*, Vol. 3, McFadden, B. and Bland, T.J., Eds., Society of Automotive Engineers, Warrendale, 1992, 3.499.
20. Kaibe, H., Sakata, M., Isoda, Y., and Nishida, I., Thermoelectric properties of n-type sintered $Bi_2Te_{2.85}Se_{0.15}$, *J. Jpn. Inst. Metals*, 53, 958, 1989 (in Japanese).
21. Sundaresan, R. and Froes, F.H., Mechanical alloying, *J. Metals*, 39(8), 22, 1987.
22. Schwarz, R.B. and Koch, C.C., Formation of amorphous alloys by the mechanical alloying of crystalline powders of pure metals and powders of intermetallics, *Appl. Phys. Lett.*, 49, 146, 1986.

12

Preparation of Thermoelectric Materials by Mechanical Alloying

B. A. Cook, J. L. Harringa, and S. H. Han
*Ames Laboratory, Iowa State University**
Ames, Iowa, U.S.A.

12.1 Introduction

Mechanical alloying (MA) was first developed to produce oxide dispersion-strengthened (ODS) alloys.[1] The numerous commercial applications of MA for producing high-strength (Ni, Fe, and Al) alloys by ODS have been reviewed by Sundaresan and Froes.[2] Synthesis of amorphous alloys is an area that has received considerable attention in recent years. Weeber and Bakker[3] and Koch[4] have reviewed amorphization by MA. These publications show the impact of this technique on materials synthesis, a subject which was also reviewed earlier by Koch.[5] Mechanical alloying (MA) is a high-energy ball mill technique used to produce alloyed powder through solid-state reactions. MA occurs basically through a repeated process of fracture and cold welding of powder particles trapped between grinding balls. Although the processing is done at ambient temperature, the localized heat generated by collisions of the balls with the materials being alloyed can raise the temperature of the alloy 100 to 350 K depending on the thermal properties of the materials. This temperature increase is not sufficiently large to cause melting or recrystallization in most cases, but does provide a driving force for the interdiffusion of the components along atomically clean fracture surfaces.[5]

Davis and Koch[6] demonstrated the application of MA to the brittle system of silicon-germanium. Preparation of n-type Si-Ge alloys doped with phosphorus and gallium phosphide, and of p-type alloys doped with B (SiB_4) was accomplished by Cook et al.[7] The advantages of MA over conventional melting/grinding hot-pressing techniques were demonstrated in this study. One is that it is a room temperature process which removes the problem of volatilization of dopants such as phosphorus. Also, the process reduces the problem of inhomogeneous Si-Ge alloys that arises from dendritic segregation caused by the wide separation of the solidus and liquidus in the Si-Ge phase diagram. In addition, the MA process may allow for the incorporation of nanometer-sized inclusions to act as phonon scatterers, as suggested by White and Klemens.[8]

*The Ames Laboratory is operated for the U.S. Department of Energy by Iowa State University under contract no. W-7405-ENG-82. This project was supported by the Office of Special Applications.

12.2 Experimental Devices

Among the many ball mill variations, three basic types encompass the bulk of mechanical alloying applications: the attritor, the planetary, and the vibratory. In an attritor mill, an impeller is rotated inside a tank filled with grinding balls and the materials to be processed. Microscopic fracture and cold welding occur in the powder particles trapped between the rapidly agitated balls. This type of mill has been used extensively in the production of high strength, oxide dispersion-strengthened (ODS) superalloys and MA of ductile metal powders.

The second common type of ball mill is the planetary type, which consists of a rotating vessel of radius r and angular frequency ω mounted on a platform of radius R (>r) which rotates in the opposite direction with angular frequency Ω, ideally such that $\omega/\Omega \approx 2$. The centrifugal force caused by the rotation of the vessel and platform continuously moves the powder and balls to the tangential edge of the vessel. Depending on the value of ω/Ω, the grinding medium is either pinned to the inner wall of the vessel or the combined motion of the platform and vessel causes an apparent curved trajectory such that the balls impact the vessel wall, trapping powder between them. A characteristic of both the attritor and planetary mills is that the processing time required for alloy formation can be rather lengthy.

The third type of mill is a vibratory mill in which a sealed vial is shaken in a complex three-dimensional motion at high frequency, typically on the order of 15 to 20 Hz. Powder particles trapped between the milling balls and the vial walls undergo high-energy compressive impact forces which generate fracture, cold welding, and some heat. The most popular vibratory mill of this type used for mechanical alloying is the Spex 8000 mixer/mill (Spex Industries, Edison, NJ). This device can prepare a small quantity of homogeneous $Si_{80}Ge_{20}$ thermoelectric powder from elemental precursor materials in 4 to 6 h. This type of mill more thoroughly mixes the powders and breaks down larger chunks of precursor material than the attritor or planetary mills. Chunk material can thus be used as a starting material rather than powders which are usually used to prepare ODS superalloys by MA. This is advantageous in that reduced oxygen levels in the final consolidated alloys can be obtained compared to the use of fine powders.

Various milling configurations have been examined using the Spex 8000 design. Milling has been carried out in a flat-ended WC vial with WC grinding balls,[10] a flat-ended hardened steel vial with steel balls,[11–14] and a round-ended hardened steel vial with steel balls.[14] Use of a WC vial causes alloy formation at a more rapid rate than in the steel vial (4 h vs. 6 h), but excessive WC contamination and formation of WSi_2 in the case of silicon-based alloys can have deleterious effects on the thermoelectric properties of the materials. The round-ended steel vial can require nearly twice as much time to form an alloy compared to the flat-ended counterpart.[14] Iron contamination from the flat-bottomed vial in Si-Ge alloys has been measured at 1000 to 5000 ppm as determined by scanning laser mass spectrometry. A Fritsch P5/4 (Fritsch Industries, Idar Oberstein, Germany) planetary mill has been evaluated in the production of 50-g quantities of doped $Si_{80}Ge_{20}$ powder, with typical milling times on the order of 100 h at intermediate rotational frequencies.[9] The powder tends to agglomerate into a hard compact on the bottom of the tank, which necessitates periodically stopping the device and breaking up the milled material from the tank bottom.

12.3 Materials Preparation

Si-Ge-Based Alloys

A Spex 8000 mill was used to prepare n-type Si-Ge alloys using elemental phosphorus as the dopant and the additive gallium phosphide, which has been reported to increase the solid solubility of phosphorus in the Si-Ge matrix.[15] P-type alloys were also prepared doped with boron (SiB_4) powder. For both the n- and p-type alloys weighed portions of the constituents in the form of +20 mesh chunks were sealed in a flat-end hardened steel vial with hardened steel balls. After the charge was milled continuously for 6 h, X-ray diffraction patterns showed a heavily cold-worked, single-phase alloyed powder with a diamond cubic structure. The (111) line of the X-ray pattern of these powders showed a slight asymmetry, which was attributed to incomplete alloying. The alloy powder was consolidated into a dense compact by vacuum hot pressing, which is the common

Table 1. Oxygen Content of Silicon Powder, Chunk Silicon, and Single-Crystal Silicon Determined by Neutron Activation Analysis (Values Are in Parts per Million Atomic)

Type of Silicon	Oxygen Content
Powdered	13,340
Chunk	1,600
Single crystal	900

Table 2. Oxygen Content of Alloys Prepared from the Various Grades of Si and Powdered and Chunk Ge[a]

	Oxygen Content		
Materials	Powdered Si and Ge	Chunk Si and Ge	Single-Crystal Si and Chunk Ge
Si, Ge, GaP, and P mixture	16,000	800	[b]
MA (6 h)	22,100	4,600	[b]
As-hot-pressed	22,200	5,700	2,500
Heat treated	23,000	6,000	[b]

[a]The oxygen content of the unalloyed Ge was not determined.
[b]Not determined.

method used in the preparation of Si-Ge thermoelectrics.[16] The density of the hot-pressed $Si_{80}Ge_{20}$ compacts was greater than 99% of theoretical density. X-ray diffraction analysis of the as-pressed compacts indicated the formation of a homogeneous, crystalline, single-phase alloy.

The amount of second-phase oxygen contained in the $Si_{80}Ge_{20}$ alloys can have a pronounced effect on the thermoelectric properties. Cook et al.[11] determined the oxygen content of silicon purchased as −325 mesh powder, +20 mesh 99.9999% pure chunks, and a float-zone single crystal by neutron activation as shown in Table 1. Alloys with the nominal composition of $Si_{0.747}Ge_{0.187}(GaP)_{0.016}P_{0.034}$ were mechanically alloyed and hot pressed. In that study, three alloys, each using a different grade of Si and Ge, were prepared, all using the same source of GaP and P. Alloys prepared from fine powders (−325 mesh Si and −100 mesh Ge) were found to contain high oxygen contents, in the 20,000 parts per million atomic (ppma) range, as determined by neutron activation. Alloys prepared from +20 mesh chunk Si and +20 mesh Ge chunks were found to have lower oxygen contents, in the 5000 to 6000 ppma range. A third set, prepared from +20 mesh Ge and float-zone Si, was found to have the lowest oxygen content of the three, in the 2000 to 3000 ppma range. Table 2 summarizes the oxygen levels observed in the materials at various steps during the MA process. As can be seen, the samples prepared from Si and Ge powders contained considerably higher levels of oxygen than those using Si and Ge in chunk form. Additional oxygen pickup during processing probably results from the handling of the submicron powders, even though this was performed under a purified inert atmosphere. Using TEM, Cook et al.[11] observed second-phase particles within the grains of the alloy containing 0.57 at.% oxygen and clean grain boundaries. In the same study the alloy containing 2.2 at.% oxygen showed a large number of second-phase inclusions at the grain boundaries as well as within the grains. The second-phase particles exert a pinning force on the grain boundaries and inhibit grain growth during hot pressing. Cook et al.[11] found that the grain size of the alloys was strongly dependent on the purity of the Si used. The alloys prepared from the purchased Si powder, which had the highest oxygen content, had submicron grains, whereas the alloys with the lower oxygen, chunk Si, had grains in the 3.5- to 18-μm size range. The low oxygen alloys had superior electrical properties compared to the high oxygen alloys. The high oxygen alloys did have lower thermal conductivity values than their low oxygen counterparts, but the effect on electrical properties, particularly electron mobility for n-type alloys, dominated. As a result, low oxygen alloys consistently had higher figures-of-merit.

Cook et al.[12] examined the effects of varying the P/Ga ratio in mechanically alloyed $Si_{80}Ge_{20}$ alloys. Alloys with nominal P/Ga ratios ranging from 1.0 to 4.0 were prepared and the final P and Ga contents of some of the alloys were determined. The results showed a difference of, at most,

30% between the actual and nominal P/Ga ratios. Phosphorus losses consistently exceeded that of Ga. It was also observed that grain size depended on the amount of P present in the alloys. Average electrical power factors (S^2/ρ) between 300 and 1000°C ranged from 30.4 to 34.6 for the compositions examined. An integrated average figure-of-merit between 300 and 1000°C of 0.93×10^{-3} °C^{-1} was measured in alloys prepared with 0.63 at.% GaP and a P/Ga ratio of 3.0:1.

The solubility of P alone in $Si_{80}Ge_{20}$ alloys prepared by mechanical alloying was examined by Han et al.[17] Hall effect measurements indicated enhanced solubility of P over previously known solubility levels of conventionally prepared materials reported by Vandersande et al.[15]

P-type materials doped with SiB_4 have been prepared by MA in both a Spex 8000 vibratory mill and a Fritsch P5/4 planetary mill. Low hot-pressing temperatures as reported by Cook et al.[10] resulted in poor electrical properties. Subsequent hot pressings at 1200°C produced alloys comparable to state-of-the-art p-type alloys. The use of a Fritsch mill was explored in order to scale up the production of MA powders to 50+ g quantities.[9] Electrical properties were slightly inferior to the alloys produced via Spex milling. Experiments to determine optimum alloying configurations for the Fritsch mill have not been performed.

New Alloys

MA has also been applied to systems other than Si-Ge. Caillat et al.[18] have examined a number of alloys for possible use as thermoelectrics. These include $CrSi_2$, Re_3Ge_7, $Mo_{13}Ge_{23}$, and $(CrSi_2)_x(Cr_{11}Ge_{19})_{1-x}$ with $x > 0.8$. Preliminary results on these new materials were presented in their paper.[18]

Rare Earth Sulfides

Cu-Dy_2S_3 compounds have been examined as thermoelectric materials because of their high melting points (~1500°C) and low thermal conductivities (~20 mW/cm-°C). In these systems, copper is a dopant and dysprosium sesquisulfide is the host material. Therefore, the carrier concentration varies with the amount of Cu. Mechanical alloying is a reliable process to prepare alloys in which the two components have widely different melting points. This is especially true of the Cu-Dy_2S_3 system. When copper is added to Dy_2S_3 as a dopant by the melting technique, it is very difficult to maintain the nominal composition because at the melting point of Dy_2S_3 (1775°C) the vapor pressure of copper exceeds 5 mm. However, since MA is a solid-state diffusion process, material loss by vaporization is negligible. In addition, MA can also produce the metastable high temperature or the metastable high pressure γ-rare earth sesquisulfide compounds.[19,20]

The experimental procedure followed by Han et al.[19] was to seal Cu and η-Dy_2S_3 in a tungsten carbide vial in a helium-filled glove box and MA for 6 h in a Spex 8000 mixer/mill using three 10-mm diameter tungsten carbide balls. The weight ratio of balls to powders was 4.7:1. During MA, $Cu_x(\eta\text{-}Dy_2S_3)_{1-x}$ was transformed into $Cu_x(\gamma\text{-}Dy_2S_3)_{1-x}$ at room temperature. γ-Dy_2S_2 is a high-temperature phase which exists above 1190°C. It is believed that the preparation of the metastable high-temperature or high-pressure γ-rare earth sesquisulfide by MA (or mechanical milling) is associated with the destabilization of the equilibrium structure due to the free energy increase induced by the defect accumulation during MA or MM. At this point, it was noted that Cu did not affect the phase transition of Dy_2S_3.[19] The metastable high-temperature $Cu_x(\gamma\text{-}Dy_2S_3)_{1-x}$ was converted into the equilibrium $Cu_x(\eta\text{-}Dy_2S_3)_{1-x}$ after hot pressing at 1100°C with a pressure of 138 MPa (20 ksi) for 1 h. Usually, 6 h of MA introduced about 0.05 at.% tungsten into the $Cu_x(Dy_2S_3)_{1-x}$ powders as an impurity.

12.4 Summary

Mechanical alloying is a relatively new technique that can be used to prepare a large variety of thermoelectric materials. Alloying near ambient temperature permits introduction of volatile dopants without loss. Increased solubilities of dopants and homogeneous alloys have been prepared.

Metastable high-pressure and high-temperature structures have been prepared by this technique at room temperature. Applications of MA are growing rapidly.

References

1. Benjamin, J. S., Mechanical alloying, *Sci. Am.*, 234, 40, 1976.
2. Sundaresan, R. and Froes, F. H., Mechanical alloying, *J. Metals*, 39, 22, 1987.
3. Weeber, A. W. and Bakker, H., Amorphization by ball milling. A review, *Physica B*, 153, 93, 1988.
4. Koch, C. C., Amorphization by mechanical alloying, *J. Non-Crystalline Solids*, 117/118, 670, 1990.
5. Koch, C. C., Materials synthesis by mechanical alloying, *Annu. Rev. Mater. Sci.*, 19, 121, 1989.
6. Davis, R. M. and Koch, C. C., Mechanical alloying of brittle components: silicon and germanium, *Scr. Metall.*, 21, 305, 1987.
7. Cook, B. A., Beaudry, B. J., Harringa, J. L., and Barnett, W. J., The preparation of Si-Ge thermoelectric materials by mechanical alloying, *Proc. Intersociety Energy Conversion Engineering Conference*, Vol. 2, Jackson, W. D. and Hull, D. A., Eds., Institute of Electrical and Electronics Engineers, New York, 1989, 693.
8. White, D. P. and Klemens, P. G., Thermal conductivity of thermoelectric $Si_{0.8}Ge_{0.2}$ alloys, *J. Appl. Phys. A*, 4258, 1992.
9. Cook, B. A., Harringa, J. L., and Beaudry, B. J., A solid state approach to the production of kilogram quantities of $Si_{80}Ge_{20}$ thermoelectric alloys, *Proc. Tenth Symposium Space Nuclear Power and Propulsion*, El-Genk, M. S. and Hoover, M. D., Eds., American Institute of Physics Conf. Proc. 271, Part 2, New York, 1993, 777.
10. Cook, B. A., Beaudry, B. J., Harringa, J. L., and Barnett, W. J., Thermoelectric properties of mechanically alloyed p-type $Si_{80}Ge_{20}$ alloys, *Proc. Eighth Symposium on Space Nuclear Power Systems*, El-Genk, M. S. and Hoover, M. D., Eds., American Institute of Physics Conf. Proc., Part 1, New York, 1991, 431.
11. Cook, B. A., Harringa, J. L., Han, S. H., and Beaudry, B. J., Parasitic effects of oxygen on the thermoelectric properties of $Si_{80}Ge_{20}$ doped with GaP and P, *J. Appl. Phys.*, 72, 1423, 1992.
12. Cook, B. A., Harringa, J. L., Beaudry, B. J., and Han, S. H., Optimization of the P/Ga ratio in n-type $Si_{80}Ge_{20}$ thermoelectric alloys prepared by mechanical alloying, *Proc. of the Eleventh International Conference on Thermoelectric Energy Conversion*, Rao, K. R., Ed., The University of Texas at Arlington, TX, 1992, 28.
13. Cook, B. A., Harringa, J. L., and Beaudry, B. J., Oxygen effects in mechanically alloyed $Si_{80}Ge_{20}$ doped with GaP and P, *Mater. Res. Soc. Proc.*, 234, 111, 1991.
14. Harringa, J. L., Cook, B. A., and Beaudry, B. J., Effects of vial shape on the rate of mechanical alloying in $Si_{80}Ge_{20}$, *J. Mater. Sci.*, 27, 801, 1992.
15. Vandersande, J. W., Borshchevsky, A., Parker, J., and Wood, C., Dopant solubility studies in n-type GaP doped Si-Ge alloys, *Proc. of the Seventh International Conference on Thermoelectric Energy Conversion*, Rao, K. R., Ed., The University of Texas at Arlington, TX, 1988, 76.
16. Lefever, R. A., McVay, G. L., and Baughman, R. J., Preparation of hot-pressed silicon-germanium ingots. III. Vacuum hot pressing, *Mater. Res. Bull.*, 9, 863, 1974.
17. Han, S. B., Cook, B. A., and Gschneidner, K. A., Jr., Effect of the doping process on the electrical activity of phosphorus in $Si_{80}Ge_{20}$, *Proc. of the Eleventh International Conference on Thermoelectric Energy Conversion*, Rao, K. R., Ed., The University of Texas at Arlington, TX, 1992, 57.
18. Caillat, T., Fleurial, J.-P., and Borshchevsky, A., Use of mechanical alloying to prepare and investigate new potential thermoelectric materials, *Proc. of the Eleventh International Conference of Thermoelectric Energy Conversion*, Rao, K. R., Ed., The University of Texas at Arlington, TX, 1992, 240.
19. Han, S. H., Gschneidner, K. A., Jr., and Beaudry, B. J., Preparation of a metastable high temperature phase (γ-Dy_2S_3) and a metastable high pressure phase (γ-Y_2S_3) by mechanical alloying and mechanical milling, *Scr. Metall. Mater.*, 25, 295, 1991.
20. Han, S. H., Gschneidner, K. A., Jr., and Beaudry, B. J., Preparation of a metastable high pressure γ-R_2S_3 phase (R = Er, Tm, Yb and Lu) by mechanical milling, *J. Alloys Compounds*, 181, 463, 1992.

13

Preparation of Thermoelectric Films

K. Matsubara,
T. Koyanagi, K. Nagao,
and K. Kishimoto
Yamaguchi University
Japan

13.1 Basic Concepts of Preparing Thermoelectric Thin Films

A number of ways of fabricating thin films which have been widely adopted as a key technology in the semiconductor industries involve sputtering, ion beam deposition, molecular beam epitaxy (MBE), and activated evaporation. Recently, the technique of preparing semiconductor films from aqueous solutions has attracted considerable interest and has been adopted as an alternative way of producing films of semiconductors and a number of other materials.[1,2]

The investigation of films is of great interest both for the understanding of the transport mechanism of carriers and for technical applications of the films, e.g., in thermoelectric thin film devices such as sensors or coolers in microelectronics. A number of papers on the preparation of thermoelectric films have been published in the literature.

In this chapter the current studies on thermoelectric films are reviewed and attention focused on the possibility of improving the thermoelectric figure-of-merit value using techniques based on the use of charged particles such as high-energy (2 to 16 eV) electrons, ions, and radicals. The fundamental effects of charged particles with different kinetic energies can be observed in the early stage of the film growth. A correct amount of ionized particles activates the nucleation process and greatly influences the critical parameters of the film, such as its nucleation density, crystalline structure, adhesion strength, and surface morphology. The density of nucleation can be controlled by varying the kinetic energies of the ionizing vaporized particles.

13.2 Preparation of Films and their Properties

Silicon, Germanium, and Related Alloy Films

The thermoelectric properties of amorphous films of Si and Ge have been studied by several authors. Amorphous silicon (*a*-Si) films have been prepared by the decomposition of silane (SiH_4) gas in a radio frequency glow discharge plasma.[3] The experiments were carried out on a series of amorphous films containing small amounts of phosphine. The thermoelectric power α in *a*-Si films (*n*-type) are as high as 3 mV/K at room temperature. This anomalous thermoelectric power is explained in terms of a phonon drag model, and electron transport takes place predominantly in the extended states just above the mobility edge, where the electron mean free path is very short. A pronounced effect on the thermoelectric power can be observed in *a*-Si(Al) films prepared by co-sputtering Si and Al in a glow discharge plasma in the presence of H_2 gas.[4]

0-8493-0146-7/95/$0.00+$.50

Studies have also been done on amorphous germanium (*a*-Ge) films prepared by the decomposition of germane (GeH_4) gas in a radio frequency glow discharge.[5] The thermoelectric power is negative, and it was concluded that the electron transport of the *a*-Ge films takes place predominantly by phonon-assisted hopping. In addition, the electrical and thermoelectric properties of amorphous films of SiGe alloys have been studied by Nasredinov and coworkers.[6] They also carried out a study of the Mössbauer effect attributed to ^{119}Sn impurity atoms and discussed the transport mechanism of the films.

Heavily doped SiGe alloy films prepared by glow discharge decomposition have been studied by measuring both the electrical conductivity and the thermoelectric power.[7] The electrical conductivity increases up to 250 S/cm at the transition temperature from the amorphous state to the microcrystalline state. The films have a large Seebeck coefficient of 160 μV/K. An examination of both X-ray diffraction and Raman scattering revealed that the films are composed of a random mixing of Si-Si, Si-Ge, and Ge-Ge bonds.

Nagels and Rotti[8] employed a model for a highly disordered semiconductor having a band of localized energy levels, particularly filled, near the middle of the mobility gap. Using an expression of the electrical conductivity based on variable-range hopping, it was shown that the thermoelectric power exhibits a simple temperature dependence of a form $\alpha/T \propto T^{-1/n+1}$, where n is an integer. The theory is applied to some results obtained on amorphous silicon carbide.

Borides and Carbides: BC, BP Films

Dense polycrystals of boron carbide with various compositions were synthesized by a thermal chemical vapor deposition (CVD) method using a reaction involving BCl_3, CH_4, and H_2.[9] The results of electrical conductivity and thermoelectric power measurements indicated that the thermoelectric power increased with increasing boron content from B_4C to $B_{13}C_{12}$. Thermally activated hopping due to small polarons was observed to be a dominant conduction mechanism at high temperatures. A marked effect of the microstructure on the thermoelectric properties of B_4C films was observed.

A detailed study of the thermoelectric properties of boron phosphide (BP) thin films has been carried out at high temperatures ranging from 300 to 1200 K.[10] The structure and electrical properties have also been investigated for films grown at various temperatures. The thermoelectric power of the films (*n*-type) is of the order of 300 to 500 μV/K.

3d-Transition Metal Silicides: $FeSi_2$, CoSi Films

Among the 3d-transition metal silicides, the preparation of films of iron disilicide ($FeSi_2$) and their properties have been extensively studied. According to Birkholz et al.,[11] β-$FeSi_2$ has semiconducting transport properties, while α-$FeSi_2$ exhibits metallic behavior. Preliminary work on films of $FeSi_2$ alloys was undertaken by Geserich and coworkers.[12]

Stoichiometric $FeSi_2$ films can be deposited in an ultra-high vacuum system by an electron beam gun onto a fused silica substrate maintained at room temperature. Thin layers of $FeSi_2$ deposited at room temperature have an amorphous structure. The layers undergo a phase transformation into crystalline β-$FeSi_2$ on heating at high temperatures.

The conduction mechanism of $FeSi_2$ films prepared by electron beam evaporation has been studied in detail by Theiner and Geserich.[13] The temperature dependence of the *dc*-conductivity and *IR*-reflectance measurements reveals that the structural transition is accompanied by a metal-insulator transition of the Anderson type with a minimum metallic conductivity of about 400 S/cm.

$FeSi_2$ thin films have also been prepared by the furnace reaction of ion beam sputtered iron layers with single crystal silicon wafers.[14] X-ray diffraction indicates that the films are orthorhombic β-$FeSi_2$ with a single-phase structure, and a direct energy gap of 0.87 eV is obtained for the optical measurements of the films.

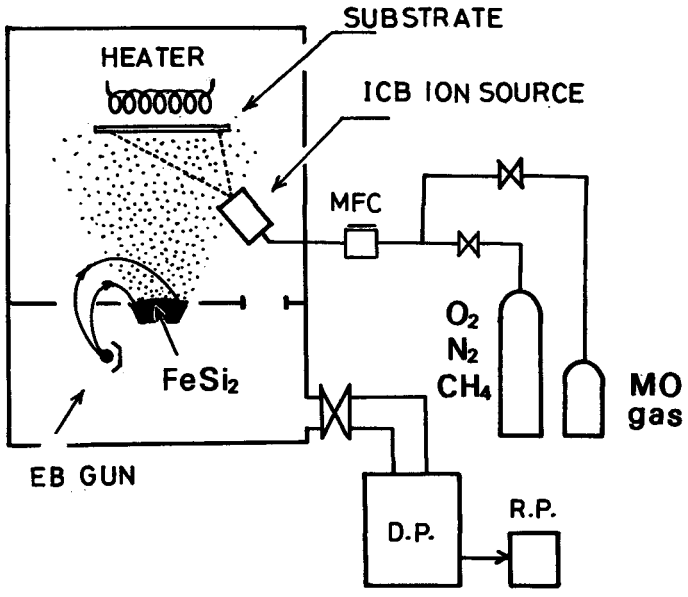

FIGURE 1 Schematic diagram of ion-assisted deposition system which is equipped with an electron beam gun and a cluster ion source.

The preparation of $FeSi_2$ films by ion cluster beam (ICB) deposition and ion-assisted deposition has been studied.[15,16] Figure 1 shows the schematic diagram of an ion-assisted evaporation system. This is composed of a 5-kW electron beam gun and an ICB-type sub-ion source, which is equipped to facilitate the flow of ions of a reactive gas (e.g., oxygen O_2, methane CH_4) or semiconducting gas (SiH_4) into the vacuum chamber where these ions react with metal vapor evaporated from the *EB*-gun. Figure 2 shows a TEM image and HEED pattern of the $FeSi_2$ film, which reveals a granular structure. In the TEM image, the dark area consists of β-$FeSi_2$ grains (100 to 200 Å in diameter) dispersed in amorphous SiO_2.

The thermoelectric power α for the films is compared with that for a film prepared by ICB deposition in Figure 3. All films exhibit a *p*-type thermoelectric power, which is due to the Si-O bonds in the films. For films with a granular structure, the thermoelectric power increases and its peak shifts toward higher temperatures with an increase in the atomic ratio of Si/Fe. The peak value of α for the film with Si/Fe = 3.8 is about +4.0 mV/K at 900 K. Figure 4 shows the electrical conductivity σ as a function of temperature, from which the conduction mechanism can be explained in terms of a tunnel model.

The thermoelectric power and electrical conductivity of $Cr_{0.28}Si_{0.72}(O,N)$ and $Fe_{0.2}Si_{0.8}(O,N)$ thin films have been investigated by Gladun and coworkers.[17] The films were prepared by reactive sputtering in Ar/O_2 and Ar/N_2. The microstructure of the films is changed by annealing from an amorphous to a partially crystallized structure. Above a critical concentration of the reactive gas, the crystalline structures of $CrSi_2$ and $FeSi_2$ change to a granular structure. The thermoelectric power of the films obeys percolation theory and reaches the values of bulk materials. Based on these results a thermocouple of Cr-Si-N films has been developed which is of use as a very sensitive sensor.

Chemical vapor deposition (CVD) processes have been utilized for most of the silicides, with the notable exception of cobalt silicide (CoSi). Polycrystalline cobalt silicide films have been prepared by West and Beeson[18] using CVD of $Co_2(CO)_8$ or $HCo(CO)_4$ as a Co source and SiH_4 or Si_2F_6 as a Si source. CoSi stoichiometry is obtained at 300°C using SiH_4 and at 225°C when Si_2H_6 is the Si precursor. The electrical resistivities of the films deposited near CoSi stoichiometry are typically 200 μΩcm following annealing at 900°C.

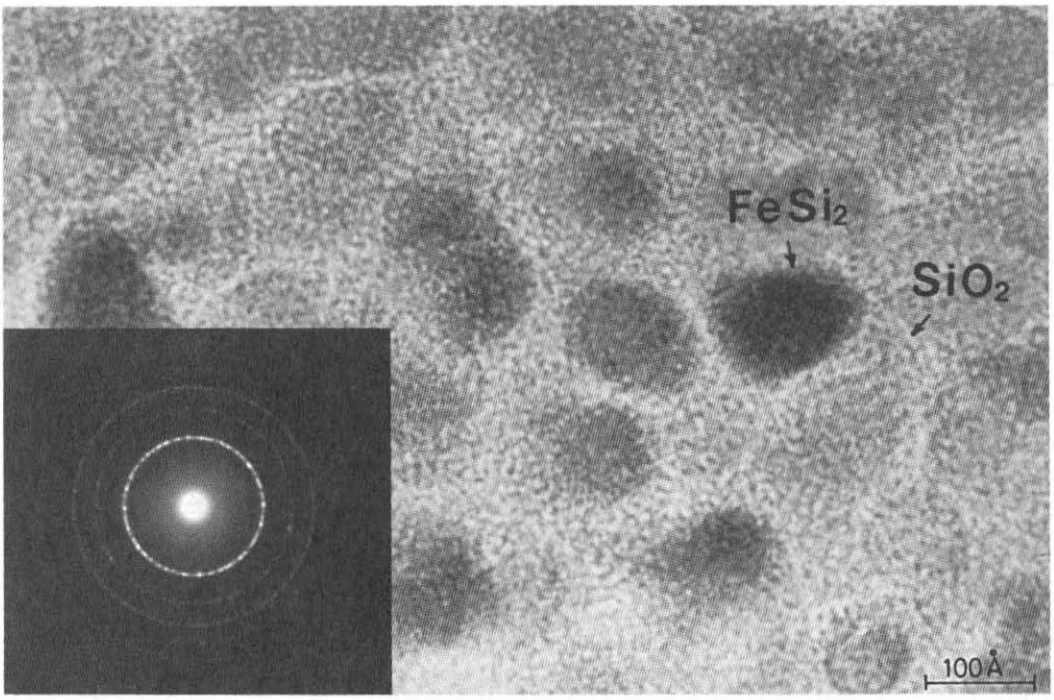

FIGURE 2 Transmission electron microscope (TEM) structure and HEED pattern of a granular film containing $FeSi_2$ microcrystals (100 Å in size) and SiO_2, deposited on a glass substrate by ion-assisted deposition.

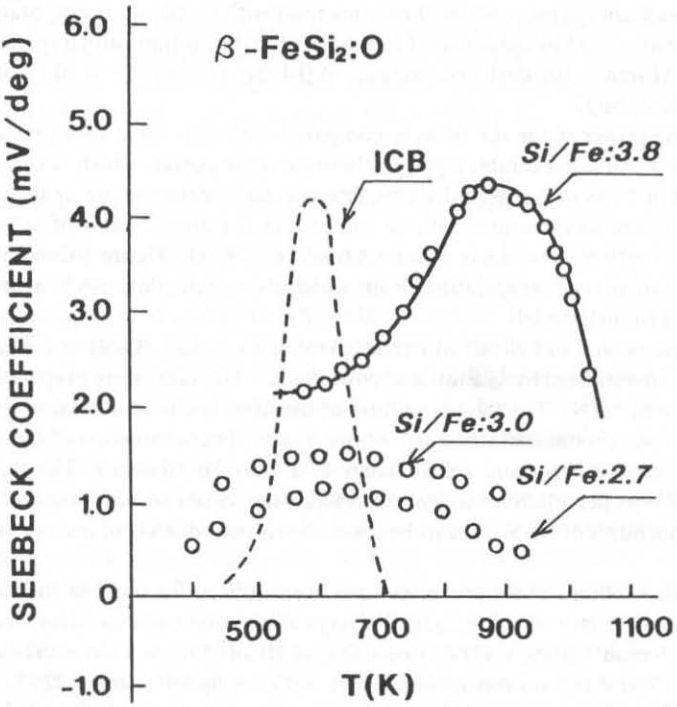

FIGURE 3 Thermoelectric power α as a function of temperature for granular films with different Si/Fe ratios, which are compared with a result for an amorphous film deposited by ionized cluster beam (ICB).

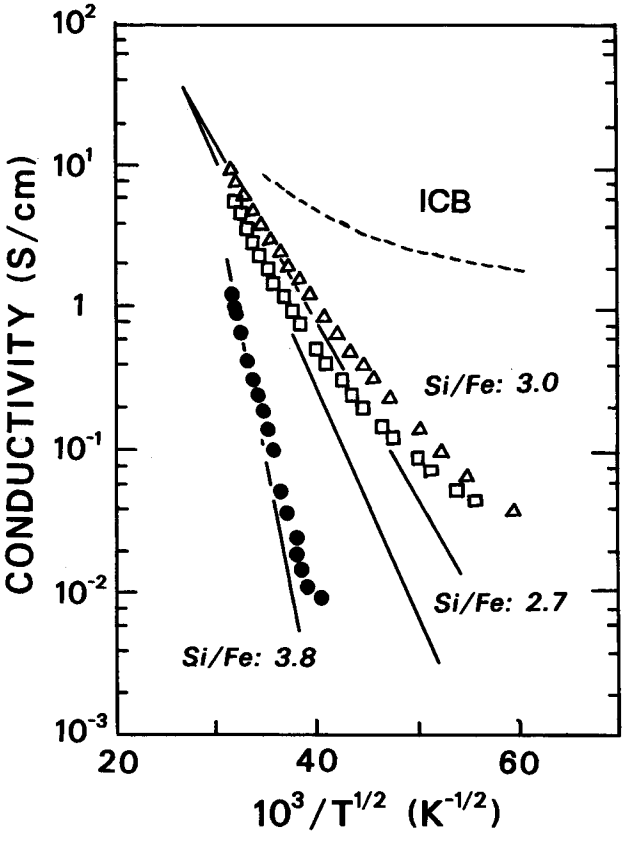

FIGURE 4 Electrical conductivity σ vs. $1/T^{1/2}$ for the granular films with different values of a Si/Fe ratio, indicating that the film for Si/Fe = 3.8 obeys a tunnelling conduction.

Chalcogenides: Bi, Sb, Te, and Related Materials

Thin bismuth films with thicknesses ranging from 20 to 400 nm have been prepared by evaporating bismuth (99.999%) from a boat-shaped tantalum heater at a pressure of 4×10^{-4} Pa with a deposition rate of 10 Å s^{-1} on to an organic substrate foil at 300 K.[19] The lattice thermal conductivity λ_{ph} of the films is about 0.01 W/Kcm, and the result is in good agreement with a modified Mayadas-Shatzkes model of phonon scattering in polycrystalline films.

Studies of the electrical conductivity and the thermoelectric power of vacuum-deposited bismuth and antimony films have been undertaken by Akhtar and Khawaja.[20] In bismuth films having a thickness of 20 to 70 nm, an oscillational resistivity is observed, which may be related to a quantum size effect. The thin films have been evaluated as a detector of Q-switched Nd-glass laser. The electrical and galvanomagnetic properties of vacuum-evaporated polycrystalline Bi films have been studied by Schnelle and Dillner.[21] Application of the films is directed at the development of highly sensitive bolometers, and this is achieved by appropriate acceptor doping.

Using the ICB deposition technique, a fundamental study to clarify the effects of ions in the film growth process was made on bismuth films deposited simultaneously on a glass and on an aluminum-coated glass substrate. Figures 5a and 5b show the experimental results. The thickness of the aluminum thin film was ~300 Å, the surface of which was earthed to remove the electrostatic charge. On a glass substrate, the film grew along the <003> and <006> axes, that is, the *c*-axis which is perpendicular to the substrate surface. However, when the aluminum-coated glass was not earthed, a strong peak corresponding to a (102) plane was observed. These results suggest that the presence of ions on the substrate surface has a large influence on the *c*-axis orientation during the film growth.

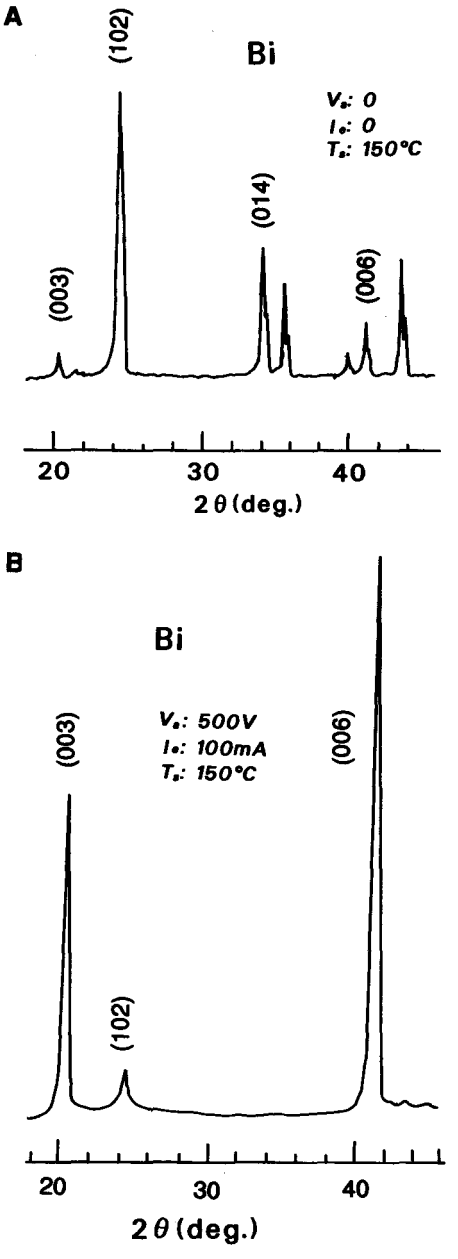

FIGURE 5 *X*-ray diffraction patterns of bismuth films deposited by ionized cluster beams at $T_s \sim 70°C$ onto a glass (a) and a thin *Al*-coated glass substrate, which is grounded (b).

The transport properties of flash-evaporated Bi_xSb_{1-x} films have been studied by Volkein and coworkers.[22] The films were prepared on a silicon wafer with native oxide SiO_2 on the surface. The electrical conductivity, Hall coefficient, magnetoresistivity, thermoelectric power, and thermal conductivity of the films were measured. The figure-of-merit was estimated to be 2.9×10^{-3} K^{-1}.

Thin films of Bi_xSb_{1-x} have been prepared by ion-beam mixing.[23] Ion-beam mixing in the Bi/Sb system using Ne^+, Ar^+, and Kr^+ ions in the energy range 40 to 110 keV has been studied by Rutherford backscattering analysis. The mixing is found to increase linearly with the energy converted into atomic displacement at the Bi/Sb interface. Alloys of Bi_xSb_{1-x} ($0 < x < 0.5$) have been produced. The thermoelectric power of fully mixed alloys reaches a maximum value at an alloy composition of $Bi_{0.87}Sb_{0.13}$. The thermoelectric power for partially mixed alloys exhibits almost the same dependence on the Ar^+ dose as on the amount of mixing.

Studies on Bi_2Te_3 thin films have been prepared by George and Pradeep,[24] using reactive evaporation. The electrical conductivity, Hall coefficient, and thermoelectric power were measured in the temperature range from liquid nitrogen to 350 K. The films prepared were *n*-type with a carrier concentration of 1.25×10^{20} cm^{-3} at room temperature. The temperature dependence of the Hall mobility varied as $T^{-1.8}$, indicating lattice scattering.

Sputtered thin films of Bi_2Te_3 and PbTe using a target of the stoichiometric compounds have been studied by Shing et al.[25] The morphology of these sputtered films was established to be polycrystalline by X-ray diffraction (XRD) and revealed the existence of nonstoichiometric crystalline phases. The carrier concentration and Hall mobility of Bi_2Te_3 film were 7.2×10^{20} cm^{-3} and 15 cm^2/Vs at room temperature, respectively. The corresponding values of PbTe films are 5.6×10^{19} cm^{-3} and 38 cm^2/Vs.

The preparation of Bi_2Te_3 films has been carried out using ionized cluster beam (ICB).[26] Figure 6 shows XRD patterns of Bi_2Te_3 thin films, which were prepared under the following conditions: $V_a \sim 1$ kV, $I_e \sim 200$ mA, and substrate temperatures up to 300°C. The diffraction peaks which correspond to the (003), (006), (0,0,15), (0,0,18), and (0,0,21) planes of Bi_2Te_3 indicate that a *c*-axis orientation of the Bi_2Te_3 films can be observed above $T_s \sim 200°C$. The thermoelectric power α of the Bi_2Te_3 films was ~ 200 $\mu V/K$ (*n*-type) at 450 K, and the conductivity $\sigma \sim 700$ S/cm. The conductivity was reduced by half in comparison with the value for thermally grown Bi_2Te_3 crystal. This is probably due to the anisotropic structure of the film. That is, the *c*-axis of the film orients perpendicular to the substrate surface, and the temperature difference was at a right

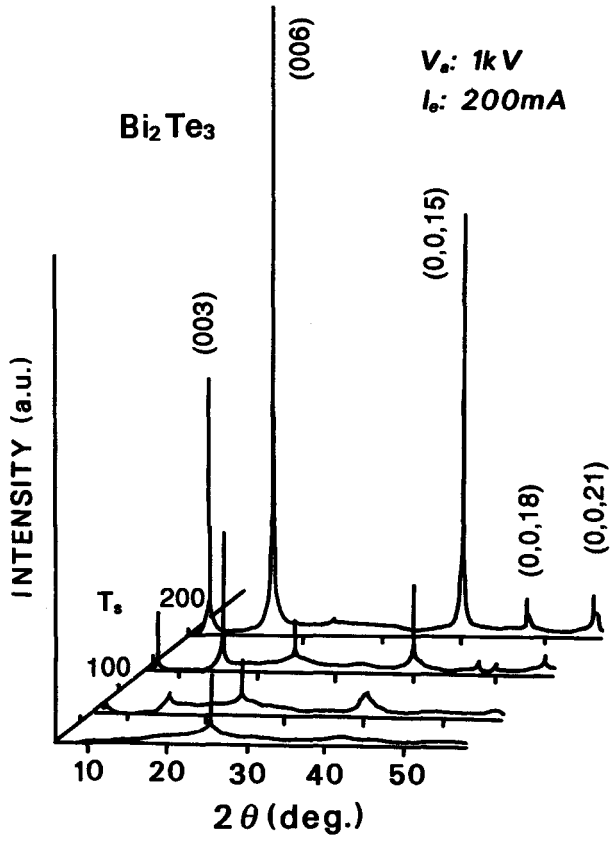

FIGURE 6 X-ray diffraction peaks of Bi_2Te_3 films, deposited on a glass substrate with varying substrate temperatures T_s, when I_e = 200 mA, $V_a \sim 3$ kV, and $P = 10^{-3}$ Pa.

angle to the axis. In general, it is not possible to measure the electrical conductivity along the film thickness; and the authors have assumed that the result for the *c*-axis oriented film is reasonable from the results for a single crystal grown by the Bridgman method, $\sigma_\perp \sim 5 \times 10^2$ S/cm and $\sigma_{\cdot\cdot} \sim 10^2$ S/cm.[27]

The thermoelectric properties of Sb_2Te_3 (*p*-type) films deposited on a glass substrate by vacuum evaporation have been studied by Krishna Moorthy and Shivakumar.[28] It has been shown that the temperature dependence of the thermoelectric power is related to the thickness of the films. Studies on the electrical conductivity and thermoelectric power of amorphous Sb_2Te_3 thin films and the amorphous-crystalline transition are reported by Das et al.[29] The films were vacuum-deposited on a glass substrate. The transition temperature is estimated to be about 340 to 370 K from the measurement of electrical resistivity, X-ray, and electron diffraction patterns.

The crystal growth of PbTe thin films on a glass substrate has been studied using ICB deposition.[30] The results are shown in Figure 7, indicating that the deposition at high value of V_a was effective in enhancing the crystal growth along the <200> axis, because PbTe has an NaCl-type crystal structure. Epitaxial film growth at a low substrate temperature is of great importance in the realization of hybridized semiconductor devices, consequently epitaxial growth of PbTe on a Si(111) substrate has also been examined. The lattice misfit between the two is less than 1.5%. The thermoelectric power α and electrical conductivity σ for a *p*-type film were ~500 μV/K and 20 S/cm at 350 K, respectively, and the Hall mobility was $\mu_e \sim 400$ cm²/Vs.

Lead telluride (PbTe) films have been prepared by depositing thin alternate layers of Pb and Te, and alloying by solid-state interdiffusion.[1,2] This technique (electrodeposition method) may provide a cheaper alternative method of preparing thermoelectric materials.

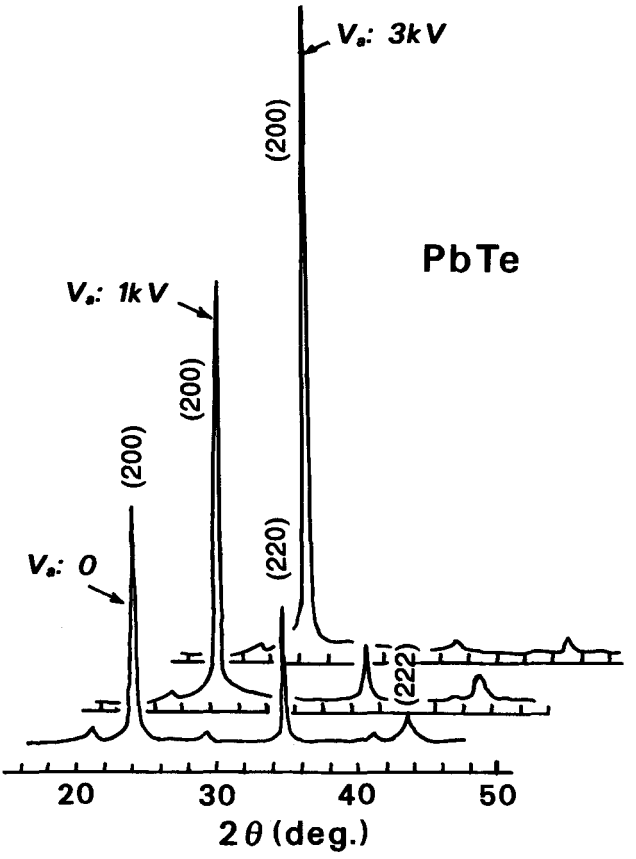

FIGURE 7 X-ray diffraction peaks of PbTe films, deposited on glass substrates with varying acceleration voltage V_a when $I_e \sim 100$ mA, $T_s = 150°C$, indicating that a preferential orientation arises along the *c*-axis of the films.

The transport mechanisms in amorphous films, e.g., *a*-Ge_xTe_{1-x}, have been studied extensively by Vanderplas and Bube.[31] The carrier transport in these chalcogenides exhibit characteristics of conduction both in extended states and in localized states at the Fermi level. This is explained in terms of a small poloron conduction model.

The thermoelectric properties of magnetron sputtered $Bi_{0.5}Sb_{1.5}Te_3$ films have been investigated by Stolzer and Stordeur.[32] Analytical studies indicate that the films have polycrystalline structures. Measurements of the electrical conductivity, thermoelectric power, and Hall coefficient of the films were undertaken, and the conduction mechanism was explained in terms of an anisotropic parabolic one-valence band model.

Other Materials: ZnSb, ZrO_2, RuO_2 Films

Zinc antimonide films were prepared by the simultaneous deposition of Zn and Sb clusters onto a glass substrate using ICB deposition.[33] Stoichiometric ZnSb films with a single phase could be successfully prepared. In general, polycrystals of ZnSb were grown from a zinc-antimony melt by a peritectic reaction. This material normally involves the eutectic compositions of ZnSb, Zn_4Sb_3, and Zn_3Sb_2; consequently, it is very difficult to grow a homogeneous polycrystal or a single crystal of ZnSb.

The ZnSb films prepared by ICB have a preferred orientation along a <102> axis perpendicular to the substrate surface, which is peculiar to an orthorhombic structure. From the result of RDF (X-ray distribution function) of the amorphous ZnSb films, it was found that the preferential

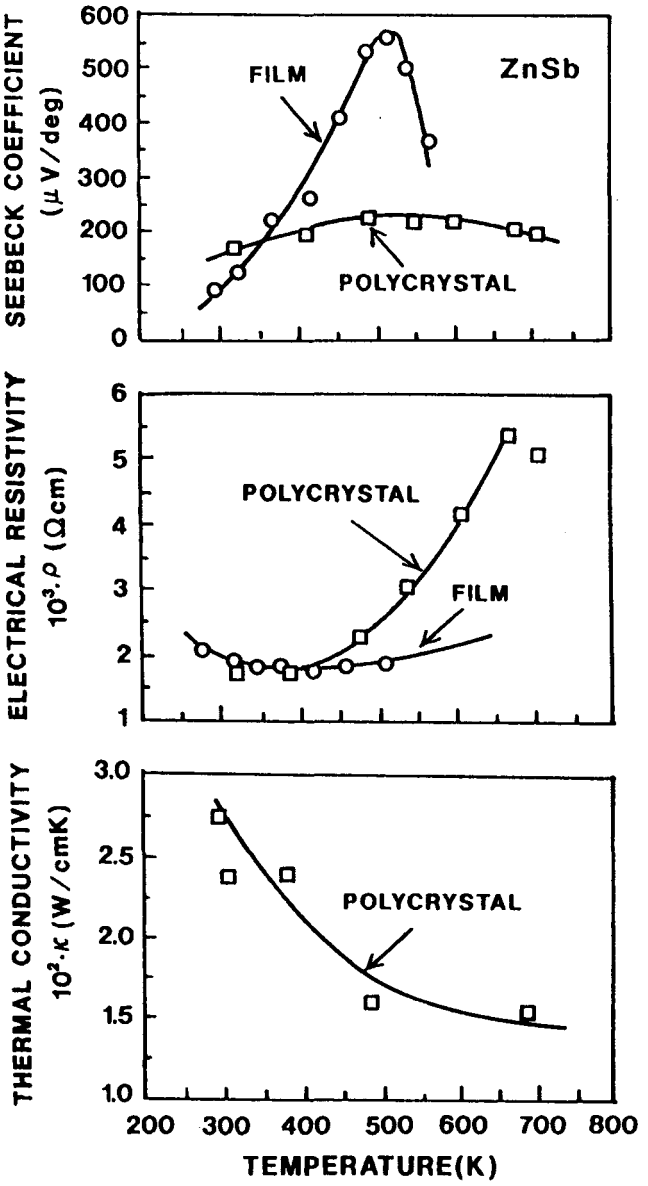

FIGURE 8 Temperature dependence of thermoelectric power α, electrical resistivity ρ, and thermal conductivity λ of stoichiometric ZnSb film prepared by ICB, compared with those of a ZnSb polycrystal.

(X-ray distribution function) of the amorphous ZnSb films, it was found that the preferential orientation along the <102> axis was ascribed to the tetrahedral bonding between pairs of Zn and Sb atoms, which was pronounced when only Zn clusters were ionized.

The thermoelectric properties of stoichiometric ZnSb films have been evaluated. Generally polycrystal ZnSb has a thermoelectric power $\alpha \sim 220$ μV/K, electrical resistivity $\rho \sim 2.5 \times 10^{-3}$ Ωcm, and a thermal conductivity $\lambda \sim 0.016$ W/cmK at 520 K.[34] In Figure 8, the thermoelectric properties of a ZnSb film are compared with reported data on polycrystal ZnSb. The figure-of-merit of a typical ZnSb film deposited by the ICB technique is compared with polycrystal ZnSb in Figure 9. The Seebeck coefficient of stoichiometric ZnSb films is about 580 μV/K, which is about three times that of polycrystal ZnSb. The corresponding Z value is estimated to be about 1×10^{-2} K^{-1} at 520 K.

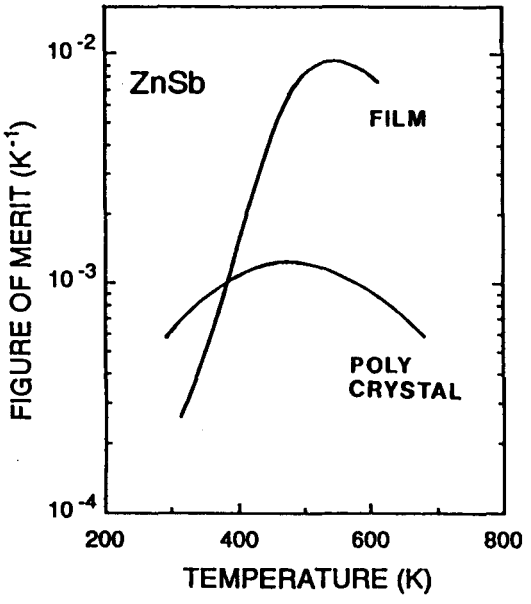

FIGURE 9 The figure-of-merit values of a typical ZnSb film deposited by the ICB technique, compared with that of a ZnSb polycrystal.

Sputtered thin films of ruthenium oxide (RuO_2) and iridium oxide (IrO_2) have potential application in very fast sensors[35] and have been studied to characterize their thermoelectric and electrical conductance parameters.

References

1. Muraki, M. and Rowe, D. M., Structure and thermoelectric properties of thin film lead telluride prepared by electrolytic deposition, in *Proc. 10th Int. Conf. on Thermoelectrics*, Rowe, D. M., Ed., Babrow Press, Cardiff, 1991, 174.
2. Muraki, M. and Rowe, D. M., On the possibility of preparing thermoelectric semiconductor films from aqueous solutions, in *Proc. 9th Int. Conf on Thermoelectrics*, Vining, C. B., Ed., Jet Propulsion Lab., Pasadena, 1990, 62.
3. Jones, D. I., Spear, W. E., and LeComber, P. G., Phonon drag in amorphous silicon, *Commun. Phys.*, 1, 39, 1976.
4. Le, Xu, Foiles, C. L., and Reinhard, D. K., Thermopower of amorphous Si(Al), *J. Non-Cryst. Solids*, 47, 355, 1982.
5. Jones, D. I., Spear, W. E., and LeComber, P. G., Transport properties of amorphous germanium prepared by the glow discharge technique, *J. Non-Cryst. Solids*, 20, 259, 1976.
6. Nasredinov, F. S., Andreev, A. A., Golikova, O. A., Kurmantaev, A. N., and Seregin, P. P., Electrical properties of amorphous films of silicon-germanium alloys, *Fiz. Tekh. Poluprovodn.*, 17, 1871, 1983.
7. Kodato, S., Si-Ge alloy films with very high electrical conductivity and thermoelectric power, *J. Non-Cryst. Solids*, 77–78, 893, 1985.
8. Nagels, P., Rotti, M., and Govers, R., Thermoelectric power due to variable-range hopping, *J. Non-Cryst. Solids*, 59–60, 65, 1983.
9. Koumoto, K., Seki, T., Pai, C. H., and Yanagida, H., CVD synthesis and thermoelectric properties of boron carbide, *J. Ceram. Soc. Jpn.*, 100, 853, 1992.
10. Yugo, S. and Kimura, T., Thermoelectric power of boron phosphide at high temperatures, *Phys. Status Solidi (a)*, 59, 363, 1980.
11. Birkholz, U., Fruehauf, A., and Schelm, J., Insulator-metal transition in $FeSi_2$, in *Proc. 10th Int. Conf. Phys. Semicond.*, Cambridge, USA, 1970, 311.
12. Geserich, H. P., Sharma, S. K., and Theiner, W. A., Some structure, electrical and optical investigations on a new amorphous material: $FeSi_2$, *Philos. Mag.*, 27, 1001, 1973.

13. Theiner, W. A. and Geserich, H. P., Anderson transition in $FeSi_2$ films, *Phys. Status Solidi (b)*, 89, 441, 1978.
14. Bost, M. C. and Mahan, J. E., Optical properties of semiconducting iron disilicide thin films, *J. Appl. Phys.*, 58, 2696, 1985.
15. Matsubara, K., Koyanagi, T., and Takagi, T., in *The 1st European Conf. on Thermoelectrics*, Peter Peregerinus Ltd., London, 1988, chap. 18.
16. Matsubara, K., Koyanagi, T., and Takagi, T., Amorphous $FeSi_2$ films as a new thermoelectric material prepared by ionized-cluster beam (ICB) technique, in *Proc. 6th Int. Conf. on Thermoelectric Energy Conversion*, Rao, K. R., Ed., University of Texas, Arlington, 1986, 1.
17. Gladun, C., Heinrich, A., Monch, I., Schumann, J., and Thomas, J., Thermoelectric power and sensor application of semiconducting CrSi and FeSi thin films, Rao, K. R., Ed., University of Texas, Arlington, 1992, 92.
18. West, G. A. and Beeson, K. W., Chemical vapour deposition of cobalt silicide, *Appl. Phys. Lett.*, 53, 740, 1988.
19. Volklein, F. and Kessler, E., Analysis of the lattice thermal conductivity of thin films by means of a modified Mayadas-Shatzkes model: the case of bismuth films, *Thin Solid Films*, 169, 1986.
20. Akhtar, S. M. J. and Khawaja, E. E., A study of the resistivity and thermoelectric power of thin films of Sb and Bi, *Phys. Status Solidi (a)*, 87, 335, 1985.
21. Schnelle, W. and Dillner, U., Electrical and galvanomagnetic properties of undoped and doped polycrystalline bismuth films. I. Preparation and experimental characterization, *Phys. Status Solidi (a)*, 115, 505, 1989.
22. Volkein, F., Baier, V., Dillner, U., and Kessler, E., Transport properties of flash-evaporated $(Bi_{1-x}Sb_x)_2Te_3$ films. I. Optimisation of film properties, *Thin Solid Films*, 187, 253, 1990.
23. Ibrahim, A. M., Thompson, D. A., and Davies, J. A., Thin film alloys of $Bi_{1-x}Sb_x$ produced by ion-beam mixing and their thermoelectric properties, *J. Mater. Res.*, 2, 313, 1987.
24. George, J. and Pradeep, B., Preparation and properties of co-evaporated bismuth telluride (Bi_2Te_3) thin films, *Solid State Commun.*, 56, 117, 1985.
25. Shing, Y. H., Chang, Y., Mirshafii, A., Hayashi, L., Roberts, S. S., Josefowicz, J. Y., and Tran, N., Sputtered Bi_2Te_3 and PbTe thin films, *J. Vac. Sci. Technol. A.*, 1, 503, 1983.
26. Kyosaka, M., Saito, T., Matsubara, K., and Takagi, T., Preparation of Bi-Sb-Te films by ICB technique, in *Proc. 6th Symp. on Ion Sources and Ion-Assisted Technol.*, Takagi, T., Ed., Tokyo, 1982, 415.
27. Imaizumi, H., Yamaguchi, H., Kaibe, H., and Nishida, I., Thermoelectric properties of *n*-type $Bi_2(Te,Se)_3$ by hot pressing, in *Proc. 7th Int. Conf. on Thermoelectric Energy Conversion*, Rao, K. R., Ed., University of Texas, Arlington, 1988, 141.
28. Krishna Moorthy, P. A. and Shivakumar, G. K., Thermoelectric power of Sb_2Te_3 films, *Cryst. Res. Technol.*, 21, 783, 1986.
29. Das, V. D., Soundarajan, N., and Pattabi, M., Electrical conductivity and thermoelectric power of amorphous Sb_2Te_3 thin films and amorphous-crystalline transition, *J. Mater. Sci.*, 22, 3522, 1987.
30. Matsubara, K., Takaoka, H., Shigeno, K., Kuriyama, Y., and Takagi, T., Preparation of PbTe films by ICB technique, in *Proc. 6th Symp. on Ion Sources and Ion-Assisted Technol.*, Takagi, T., Ed., Tokyo, 1982, 399.
31. Vanderplas, H. A. and Bube, R. H., Thermoelectric power of amorphous compound semiconductors, *J. Non-Cryst. Solids*, 24, 377, 1977.
32. Stolzer, M. and Stordeur, M., Properties of magnetron sputtered thermoelectric $Bi_{0.5}Sb_{1.5}Te_3$ films, Rao, K. R., Ed., University of Texas, Arlington, 1992, 260.
33. Koyanagi, T., Matsubara, K., Takaoka, H., and Takagi, T., Crystallographic and thermoelectric properties of ZnSb films prepared by ICB technique, in *Proc. 6th Symp. on Ion Sources and Ion-Assisted Technol.*, Takagi, T., Ed., Tokyo 1982, 409.
34. Telkes, M., Solar thermoelectric generators, *J. Appl. Phys.*, 25, 765, 1954.
35. Kreider, K. G., Thin film ruthenium oxide-iridium oxide thermocouples, *Mater. Res. Soc. Symp. Proc.*, 234, 205, 1991.

Section C
Measurement of Thermoelectric Properties

14
Calculation of Peltier Device Performance

Richard J. Buist
TE Technology, Inc.
Traverse City, Michigan, U.S.A.

14.1 Introduction

The proliferation of high-speed personal computers has provided the means for more sophisticated approaches to design and engineering. The current technology for most scientists and engineers in the thermoelectric (TE) industry is to rely on the analytical formulas for thermoelectric design that were derived from temperature-independent assumptions. Others have derived a "temperature-averaging" methodology for the thermoelectric material parameters in an attempt to partially account for the effects ignored by the temperature-independent method. However, even this technique is inaccurate.

As a consequence, computers have been used to merely facilitate the output while the level of sophistication in thermoelectric design theory has still suffered. Computers have not been fully exploited and current design theory is mostly based on unnecessary simplifications yielding imprecise results.

0-8493-0146-7/95/$0.00+$.50

The numerical method presented in this chapter overcomes these inadequacies but is still simple to use and easy to understand. It is based on the well-understood analytical formulas but is applied in such a way as to overcome the inadequacies of a purely analytical approach. It requires a computer, but applies the power of the computer to obtain a higher level of precision.

Calculations via the numerical method are presented in this chapter and comparisons are made with the most common short-cut methods for modeling, designing, and optimizing thermoelectric devices. Conclusions derived emphasize the need for applying the power and speed of computers to close the gap between theory and experiment.

14.2 Constant Parameter Theory

In order to set the framework for the numerical method some of the basic thermoelectric equations derived from the simplifying assumptions made over 30 years ago are reviewed. The heat balance at the cold junction of a thermoelectric pellet (hereafter referred to as a pellet) is given by:

$$Q_c = \alpha I T_c - I^2R/2 - K(T_h - T_c) \tag{1}$$

where Q_c is the heat pumped at the cold junction, α is the Seebeck coefficient, I the electrical current, T_c the cold junction temperature, R the electrical resistance, K the thermal conductance, and T_h the hot junction temperature. The voltage across this pellet is given by:

$$V = \alpha(T_h - T_c) + IR \tag{2}$$

The heat rejected by the hot side of the pellet, Q_h, is equal to the sum of Q_c plus the power consumed, IV. This yields the following expression for T_c:

$$T_c = T_h - (\alpha I T_h + I^2R/2 - Q_h)/K \tag{3}$$

These "closed-form" or "analytical" equations were derived by applying the simplifying assumption that the thermoelectric parameters α, R, and K were invariant with temperature. This assumption only holds for very small $(T_h - T_c)$ differentials.

Nevertheless, these formulas, plus various optimization formulas derived therefrom, have been very useful to scope and define thermoelectric phenomena and provide insight into the "zero-order" thermoelectric cooling effects (useful, yes; accurate, no). However, properly applied, they provide the basis for precision as well as usefulness.

14.3 Thermoelectric Material Parameters

The most essential input to an accurate thermal model for a pellet is the temperature-dependent thermoelectric material parameters: Seebeck coefficient, electrical resistivity, thermal conductivity, and figure-of-merit. For purposes of illustrating the numerical design model, data were collected on an n-type sample of "bismuth-telluride" using the thermoelectric technology computer automated test system, Model TF-101. This is a bipolar system which takes advantage of computerized high speed, high resolution, voltage, and temperature measurements.

Simultaneous, direct measurements of Seebeck coefficient, electrical resistivity, and figure-of-merit were made on the pellet. Thermal conductivity was determined from these three parameters. Tests were made at temperatures from −50 to 60°C at very low level applied currents producing low (approximately 4°C) temperature differentials and avoiding errors potentially brought on by secondary effects.

Results are presented in Figures 1 to 4. Five tests of each parameter were performed at each temperature point. The observed close-packed data clusters illustrate the degree of repeatability of the tests. The smooth curve through the Seebeck, resistivity, and thermal conductivity data are graphic representations of second-order polynomial equations derived via a least-squares curve-fitting process. Again, the deviation from each data cluster from these curves serves to further validate the repeatability and stability of the tests.

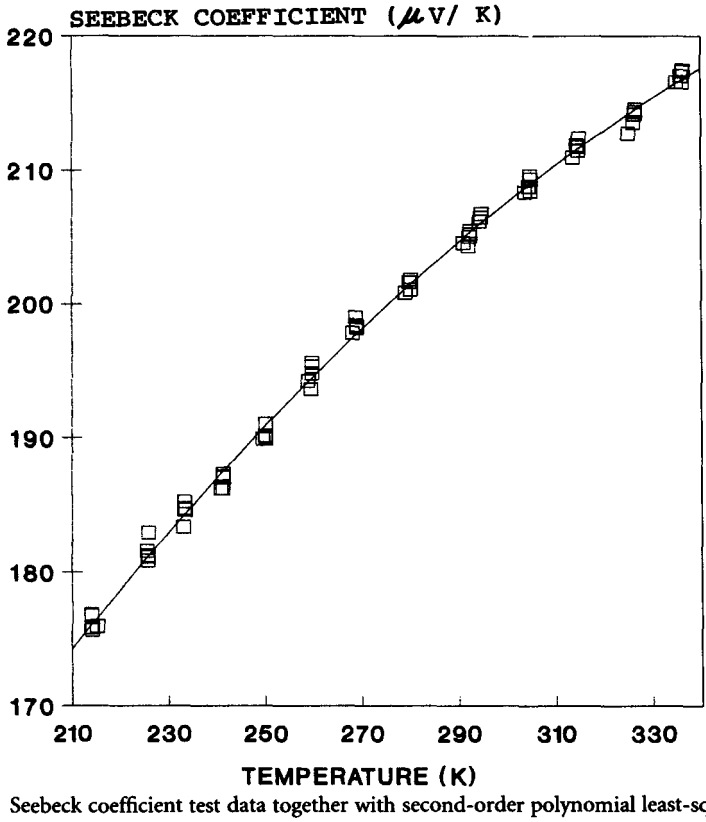

FIGURE 1 Seebeck coefficient test data together with second-order polynomial least-squares curve.

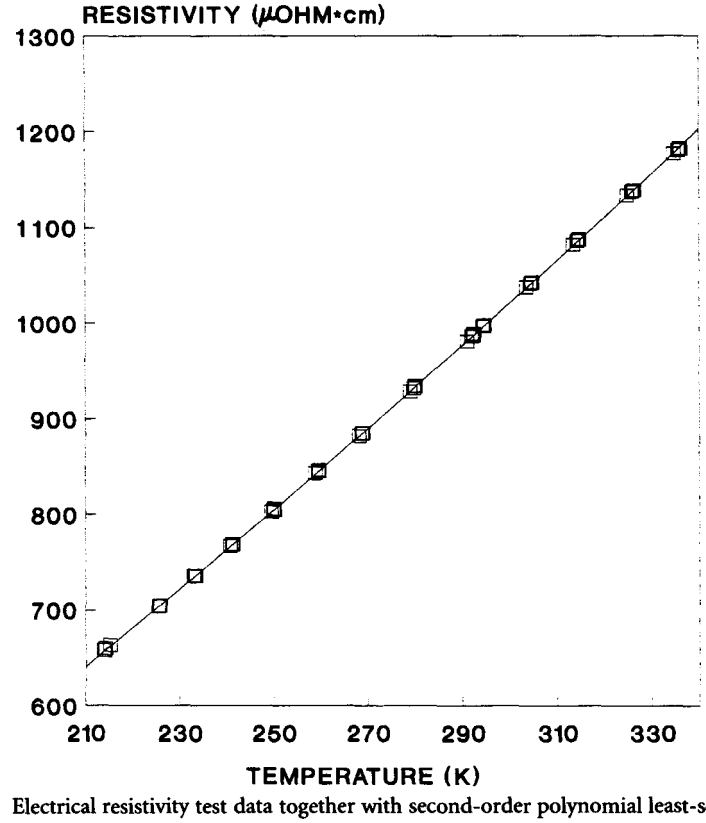

FIGURE 2 Electrical resistivity test data together with second-order polynomial least-squares curve.

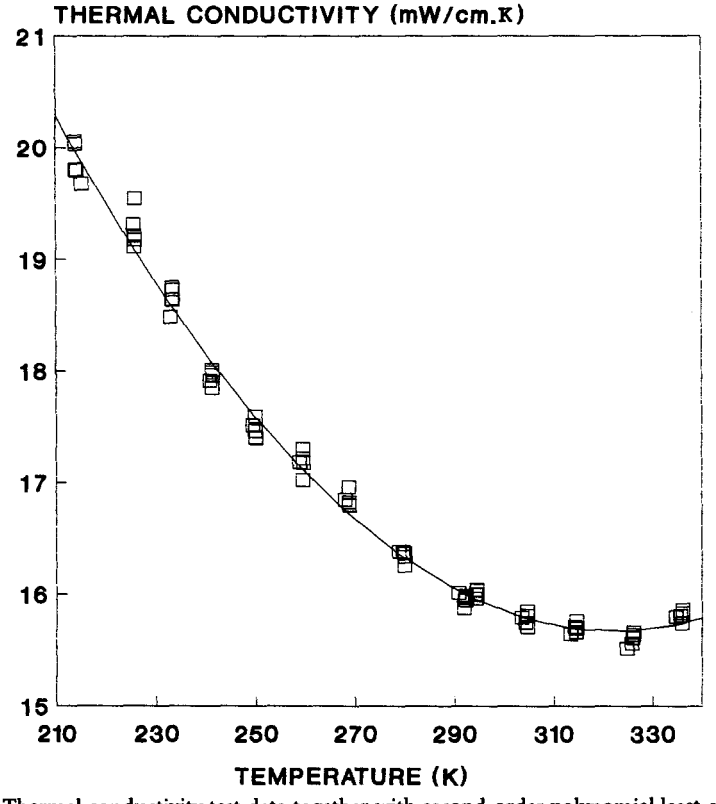

FIGURE 3 Thermal conductivity test data together with second-order polynomial least-squares curve.

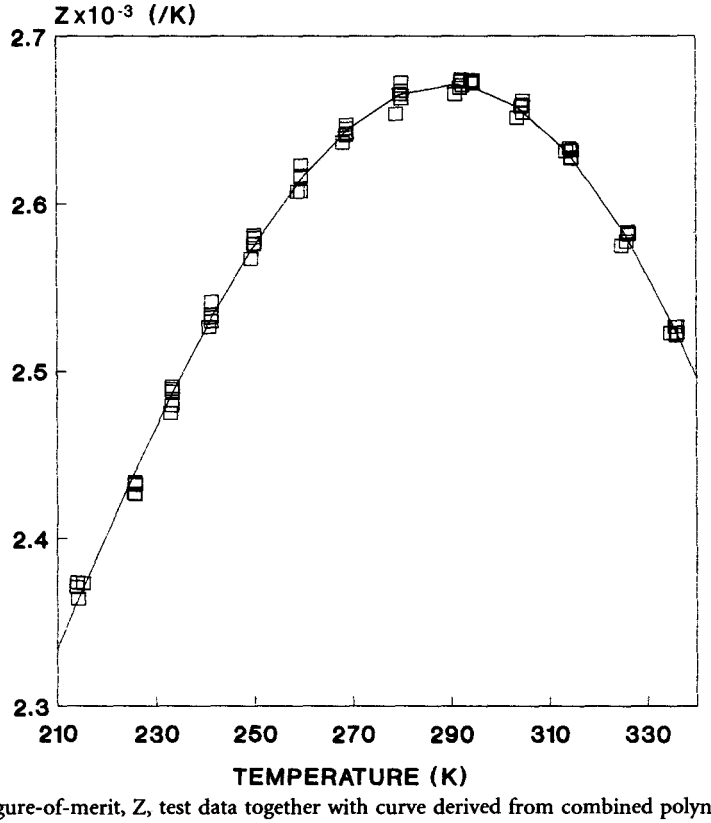

FIGURE 4 Figure-of-merit, Z, test data together with curve derived from combined polynomials graphed in Figures 1 to 3.

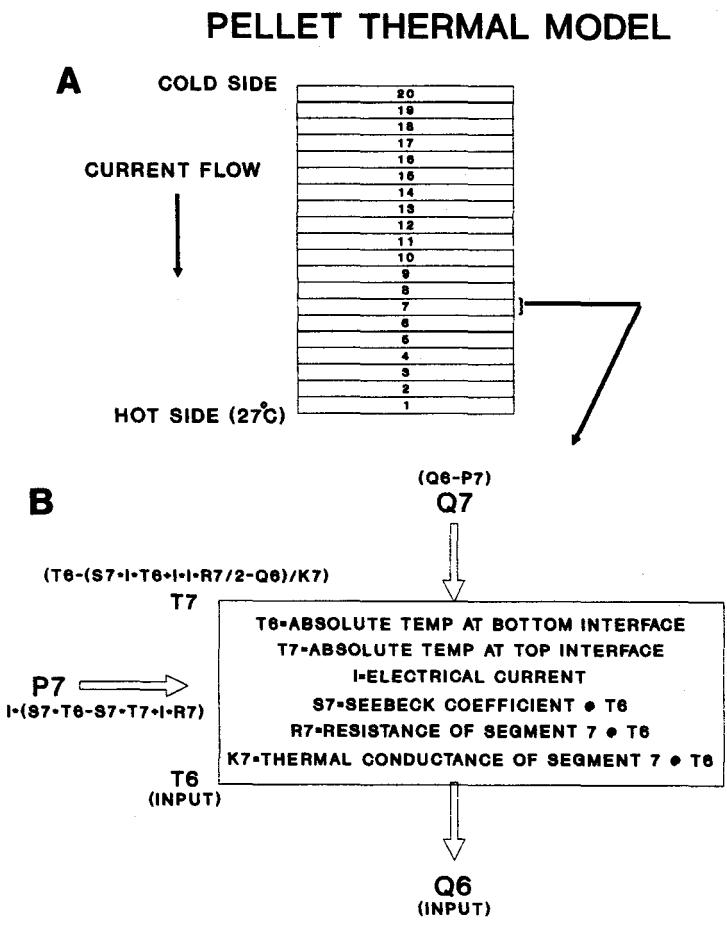

FIGURE 5 (a) Twenty-segment thermal model for a thermoelectric pellet; (b) detailed parameter description for segment #7.

The curve through the figure-of-merit vs. temperature data is *not* a curve-fit of that data, at least directly. Each point on this curve was calculated from the formulas derived from the other three data sets. As such, this complex curve and its close matching with the figure-of-merit data represent the quality of curve-fitting process for the other three parameters. Only the curve-fit formulas of these three parameters were used in constructing the model.

14.4 Thermoelectric Pellet Numerical Model

The simple, analytical Equations 1, 2, and 3 are accurate as long as the thermoelectric properties do not vary over the region where these formulas are applied. Therefore, if we break a pellet into many, infinitesimal segments, each segment will meet the stated criteria, at least in the limiting case of many, many segments.

Figure 5a is an illustration of a 20-segment model of a pellet. Each segment is an equal-sized "slice", but has its own, individual set of thermoelectric material parameters defined by its temperature and the formulas applied from Figures 1 to 3. The detailed applications of Equations 2 and 3 are illustrated in the expanded segment #7, given in Figure 5b. Calculations were also performed using an 8-segment model and it was discovered that the difference was less than 1%. Nevertheless, the 20-segment case was used for the calculations presented in this chapter, and this was essentially equivalent to the limiting case.

Note that the base temperature of the segment was used to determine the material properties. Actually, either could be used since the boundary temperatures converge in the limiting case. Use of the base temperature eliminates the need for unnecessary iterations.

The calculation sequence starts from the base of the pellet. Two "free" variables are arbitrarily chosen: (1) Q_o = heat rejected by the pellet and (2) T_o = base temperature. The calculation sequence could commence at the top of the pellet, but it is not nearly as effective since only the final iteration would be significant for this option. In contrast, two iterations will usually suffice and the results from both are used to define the heat pumping slope and intercept plus all of the device parameters needed to define the pellet performance.

Furthermore, by starting from the base, even the performance of a pellet on a "soft" heat sink can be quickly determined with no more iterations than for a constant hot side temperature. That is, T_o is calculated from the following equation from the "free" iteration variable, Q_o:

$$T_o = T_a + Q_o * HSR \tag{4}$$

where T_o is the thermoelectric pellet base temperature, T_a the ambient temperature, Q_o the heat rejected by the thermoelectric pellet, and HSR is the heat sink resistance.

14.5 Performance Calculations

To illustrate the operation and results of the model, T_h (T_o) was set equal to 27°C and calculations were performed from the bottom of the pellet to the top yielding a "net" cooling value, Q_c (Q_{20}), at the temperature T_c (T_{20}) for a given current, I. A new value for Q_o was then selected by simply subtracting Q_{20} for the original Q_o value and repeating the process. This process was repeated once or twice until Q_c was sufficiently close to zero and the value of T_c was recorded together with the current and the calculated voltage.

The current, I, was parametrically varied and the corresponding values of T_c and voltage recorded for each value of I until the value of I for the coldest T_c value was determined. Profiles of the key parameters under this condition (maximum current) are given in Figures 6 to 10. Figure 6 is the temperature profile in the pellet and Figures 7 to 10 illustrate the variance of each thermoelectric material parameter across the pellet. These data clearly illustrate how inappropriate it is to assume constant parameters for an entire pellet.

It is interesting to note that, although the Seebeck coefficient and resistivity monotonically increased from the cold to hot end of the pellet, the power consumption distribution is relatively uniform, as observed from Figure 11. This graph has a very expanded Y-axis to illustrate the slight curvature evident. It maximizes in the middle of the pellet rather than being maximum at the hot side as one might expect from the parameter profiles (especially resistivity). This curve clearly illustrates the importance and impact of the Seebeck voltage which, of course, is driven by the steeper temperature gradient at the cold end.

The overall cooling performance and voltage for each value of current from zero to the maximum current is given in Figures 12 and 13 (numerical method). Note that for all of these calculations the pellet is operating in a zero heat load condition. This is true for all calculations presented in this chapter. The addition of heat load is relatively simple to accommodate by calculating the heat absorbed by convection and radiation at the periphery of each segment (Q_p) and inserting the quantity, $-Q_p$, right after Q_h in Equation 3.

14.6 Comparison with Other Methodologies

To illustrate the significance of the results, a comparison of these "numerical" calculations was made with results obtained from three typical "short-cut" methodologies.

Method 1: $P(T_{hot})$

This is the simplest of all methods and the most widely used, especially in the early days of thermoelectric design and analysis when computers were not so prolific. It consisted of assuming the

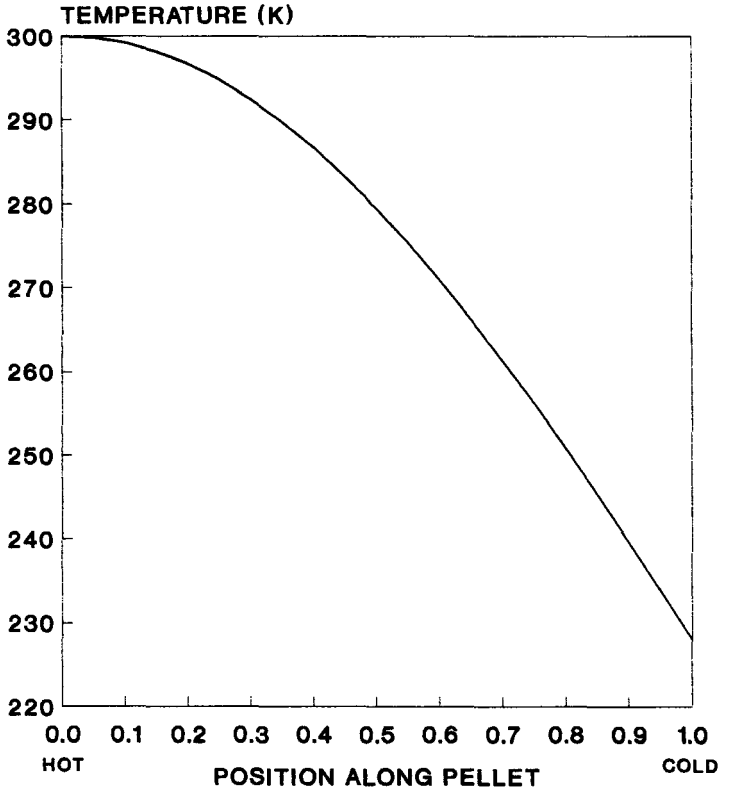

FIGURE 6 Calculated temperature profile within n-type pellet #N1 operated at maximum current and T_h = 27°C.

thermoelectric material properties were constant and equal to the values at T_h (in this case, 27°C). This yielded instant results, requiring no iterations whatsoever. Essentially, the entire pellet was treated exactly as one segment of the numerical method. Since the figure-of-merit is typically maximum at T_h, it was expected that this method would overestimate the ΔT producible by a pellet.

Method 2: $P(T_{avg})$

This method is very similar to method 1, except that the constant thermoelectric material properties used were determined from the *average* temperature (T_{avg}) of the operating pellet. As such, this method is necessarily iterative in order to determine T_{avg}. However, only three or four iterations were needed to establish adequate closure. This method is usually expected to give more accurate results than method 1, because the material parameters used in the equations take temperature dependence into account.

Method 3: P_{avg}

This method is also similar to method 1, but uses more scientifically averaged thermoelectric material parameters. That is, since Seebeck voltage is a temperature gradient-produced quantity, the average Seebeck coefficient was determined by integrating the Seebeck coefficient with respect to temperature from T_h to T_c. The average thermal conductivity and electrical resistivity are spatially dependent and thus were determined by an integral average with respect to position along the

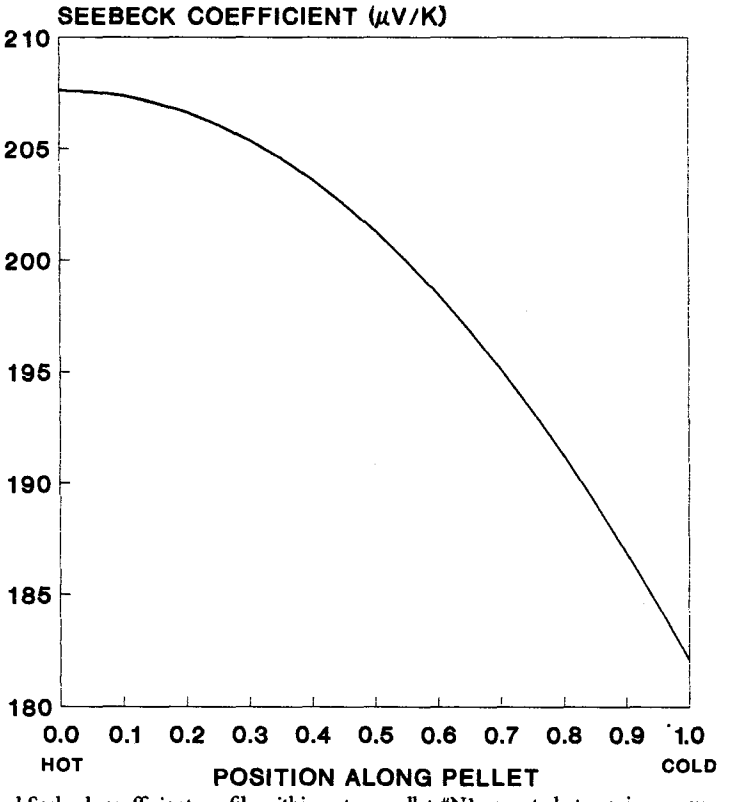

FIGURE 7 Calculated Seebeck coefficient profile within n-type pellet #N1 operated at maximum current and T_h = 27°C.

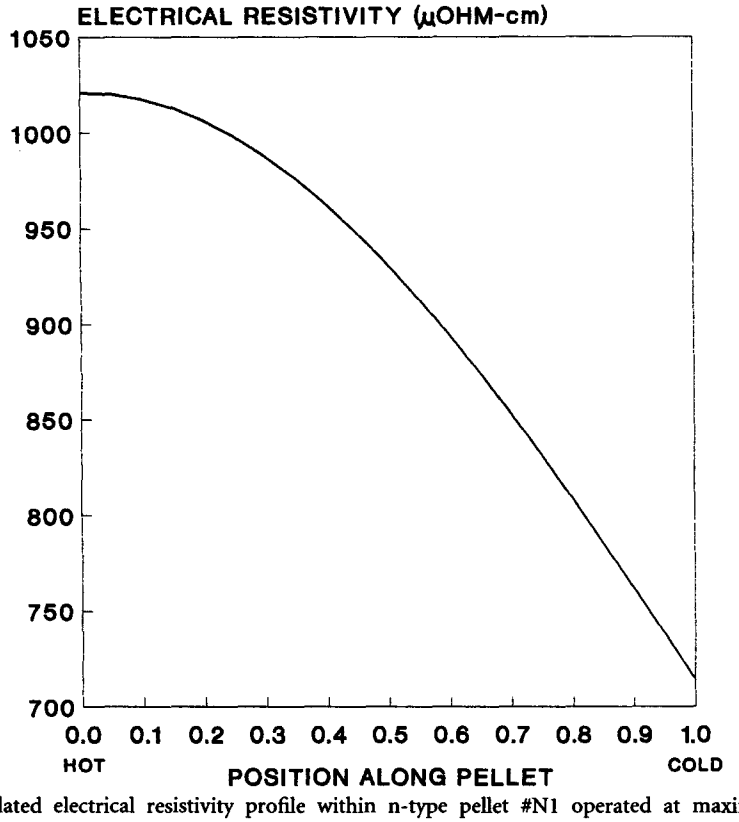

FIGURE 8 Calculated electrical resistivity profile within n-type pellet #N1 operated at maximum current and T_h = 27°C.

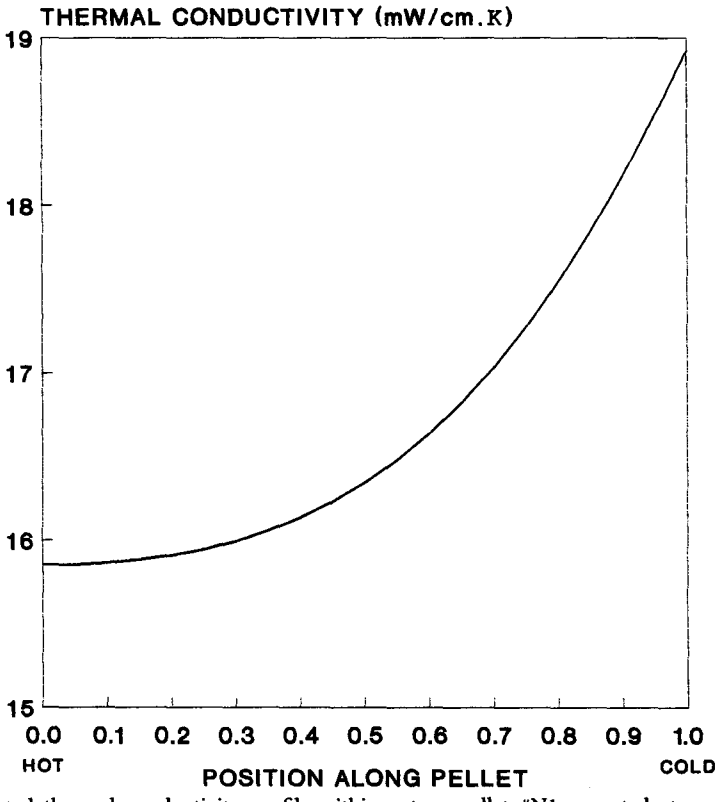

FIGURE 9 Calculated thermal conductivity profile within n-type pellet #N1 operated at maximum current and T_h = 27°C.

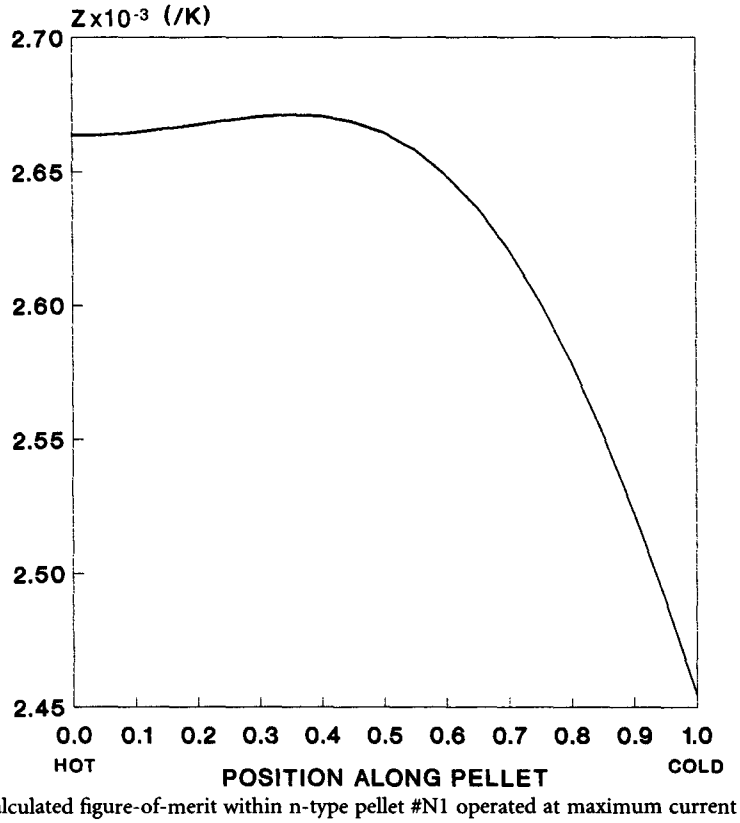

FIGURE 10 Calculated figure-of-merit within n-type pellet #N1 operated at maximum current and T_h = 27°C.

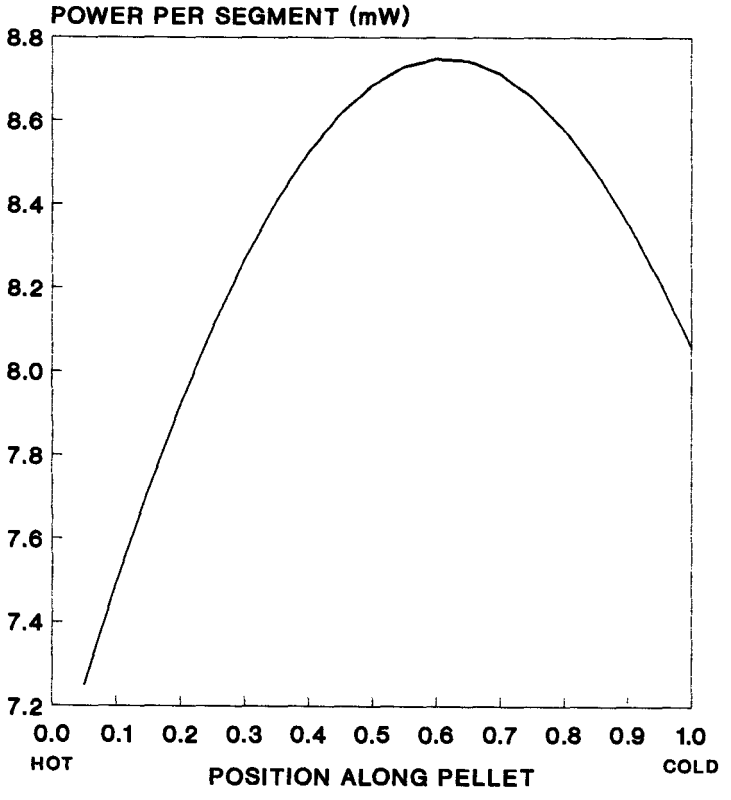

FIGURE 11 Calculated power consumption distribution within n-type pellet #N1 operated at maximum current and T_h = 27°C.

pellet. This is a much more complicated way of defining the "effective" average parameters which were expected to be the most accurate of all the "short-cut" methods.

These three methods were derived so that the analytical Equations 1, 2, and 3, plus the various optimized formulas derived therefrom, could be used. This provided means to model, optimize, and analyze thermoelectric designs.

Calculations were made in accordance with each of these three methods and comparisons were made with the 20-segment numerical method presented in this chapter. The results are shown in Figures 12 and 13. The calculated cooling performance (at zero heat load) for the entire operating electrical current range is given in Figure 12a. As expected, at fairly low currents, there is not much difference between any of the methods. However, the $P(T_{hot})$ method clearly overestimates ΔT as discussed earlier, but only for the low level values of current. The surprise is that even this method still *underestimates* the maximum ΔT. In fact, none of the methods seems to fit very well at high current, especially the expected, more accurate P_{avg} method! (See Figure 12b.) This is a surprising result. The true (numerical) maximum ΔT is actually higher than one would project from even the highest figure-of-merit point within the thermoelectric pellet. This is unexpected since the figure-of-merit does, indeed, drop well below this maximum point under operation (see Figure 10). The answer to this apparent anomaly is that the numerical method includes the effect of Thomson cooling, and compared to the P_{avg}, method 3, it can account for as much as four extra degrees centigrade of cooling and extends the maximum current.

The calculated voltage of the operating thermoelectric pellet is shown in Figures 13a and 13b. Note that the P_{avg}, method 3, voltage vs. current calculations agree extremely well with the numerical method. This lends credence to the integral averaging philosophy adopted, at least for modeling the true "dynamic impedance" of the pellet. Nevertheless, the fact remains that maximum ΔT is underestimated by every one of the short-cut methods to varying degrees.

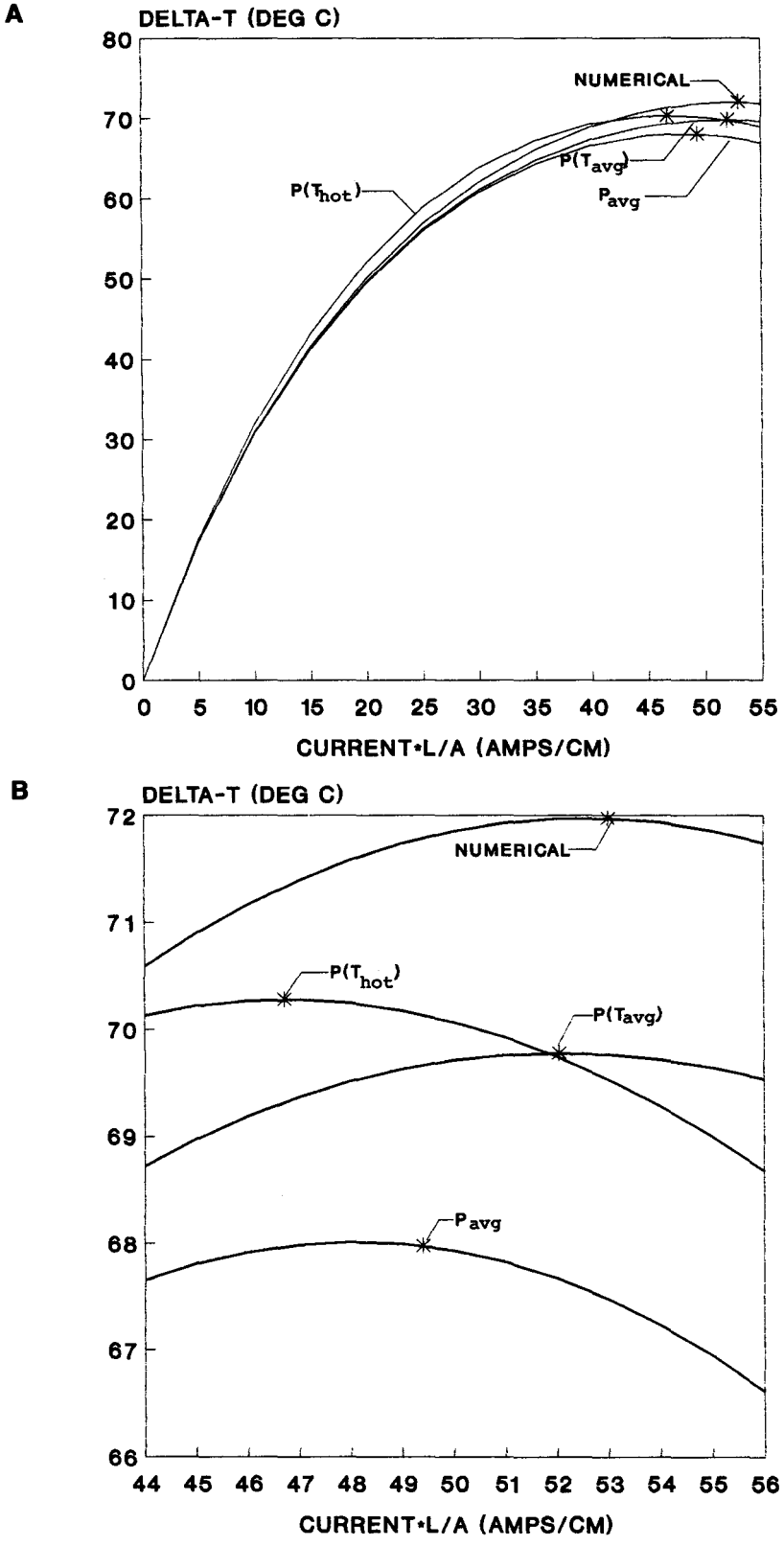

FIGURE 12 (a) Cooling performance calculation comparison between the numerical method and three different constant parameter methods (T_h = 27°C). (b) Expanded data from (a) to illustrate region around maximum current.

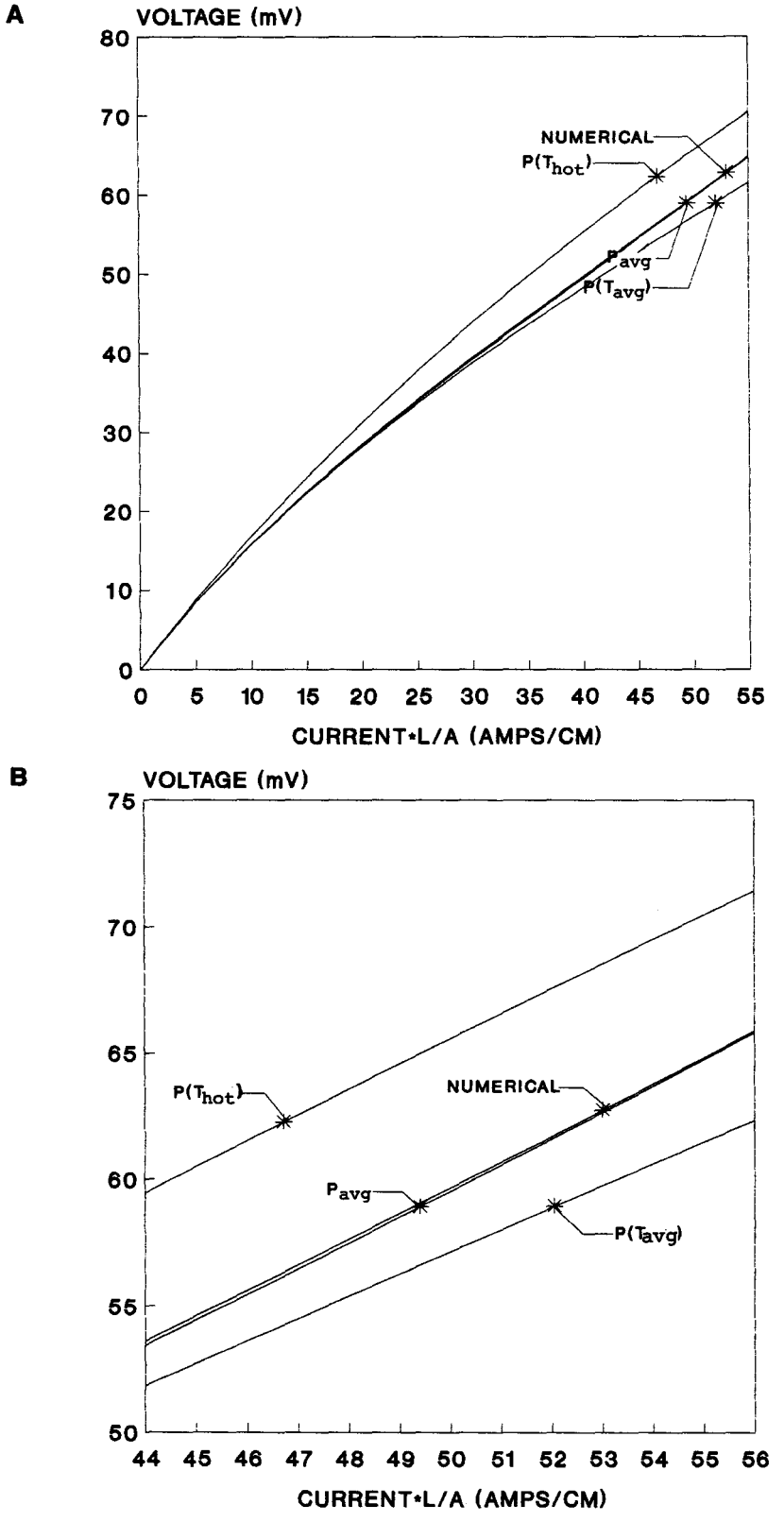

FIGURE 13 (a) Voltage calculations for cases given in Figure 12a. (b) Voltage calculations for cases given in Figure 12b.

It is clear that, given the figure-of-merit profile in Figure 10, there will be no average figure-of-merit determinable from this graph that will explain the numerically derived maximum ΔT. Any averaging technique will bring the figure-of-merit down from its maximum value, which is already too low to explain the numerically calculated, maximum ΔT.

14.7 Conclusions

A numerical method has been described which is both simple and rigorous. It is based on the simplified equations with which all thermoelectric designers are familiar but applied in a way that meets the criteria for mathematical accuracy. The results clearly indicate that the "usual" thermoelectric material property averaging techniques do not produce accurate results, especially at currents near the maximum cooling. They also do not predict accurate optimization values for maximum current and maximum ΔT. The optimization values for maximum coefficient of performance are expected to also be in error.

Essentially, it has been concluded that a material property averaging technique is not adequate for the precision level demands placed on thermoelectric design engineers. The numerical technique presented herein offers a solution which is easy to use, easy to install, and, with the help of a computer, is sufficiently fast.

15

Measurements of Electrical Properties

I. A. Nishida
National Research Institute for Metals
Tokyo, Japan

15.1 Introduction

The thermoelectric properties of materials are evaluated by measurements of the quantities which occur in the figure-of-merit, i.e., the electric resistivity ρ, thermoelectric power α, and thermal conductivity λ as a function of temperature. These quantities are closely related to more fundamental parameters, such as carrier mobility μ, effective mass m^*, and carrier concentration n.

These fundamental parameters can be evaluated by the additional measurement of the Hall coefficient R_H. Measurements of electrical conductivity, thermoelectric power, and Hall coefficient are carried out by detecting the corresponding voltage drop V_r, the thermoelectromotive force V_o, and Hall voltage V_H, irrespective of the measuring methods (AC or DC) or the apparatus employed. Therefore, precise voltage detection is an important aspect of the measurements of thermoelectric parameters.

Numerous techniques have been employed in the measurements of ρ and R_H,[1-6] and many of them have been especially modified to satisfy the conditions dictated by the thermoelectric (TE) materials being investigated. However, if an electrical current is passed through a "good" TE material, the Peltier effect produces a temperature difference between the two current probes. The voltage V_o is then added to V_r in the measurement of ρ and the thermomagnetic voltage V_{TM} added to V_H when measuring Hall voltage. In the nonadiabatic condition V_{TM} is relatively small and, if the distance between the Hall voltage probes is small (b in Figure 1), then V_{TM} is reduced to less than 2% of V_H. However, occasionally V_o can increase to more than 20% of V_r even in the nonadiabatic condition.

The most common method of nullifying V_o is to use an alternating current (AC) which instantaneously reverses V_r. However, since Peltier heat pumping is produced by the applied current, an alternating V_o is added to V_r.[4,5] Chopped direct current[7] and magnetic field[8] techniques do not nullify V_o and V_{TM} completely.[4,5] The most dependable method to separate V_r from V_o is the currently available high-speed and high-resolutional DC measurement technique.[9]

As mentioned above, the detected voltage is sensitive to a number of factors, such as the positions of the voltage probes and thermocouples, method of contacting or joining to a specimen, and whether they are located in the correct positions. This is particularly true for the measurement

0-8493-0146-7/95/$0.00+$.50

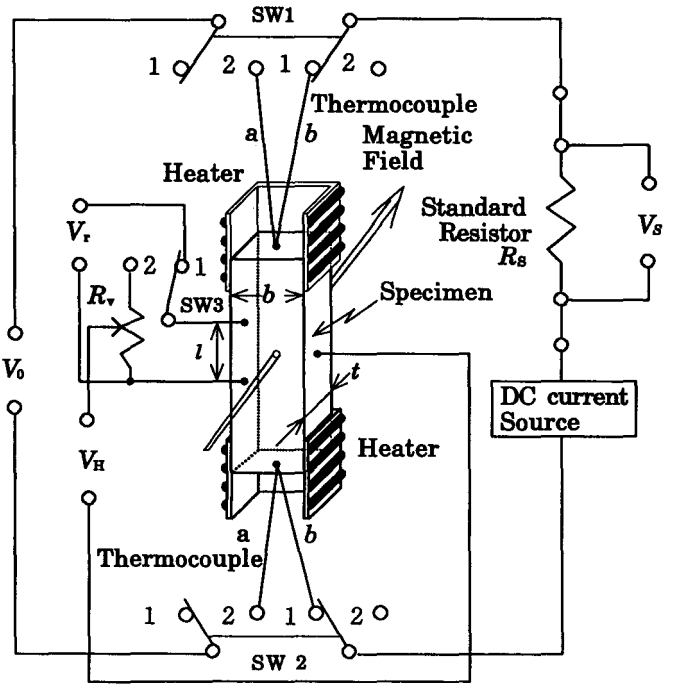

FIGURE 1 Schematic circuit for measuring the resistivity, Hall coefficient, and thermoelectric power.

of α, when the junctions of the two pairs of thermocouples must be located so that the measurement of the temperature and the thermoelectromotive force are made at the same points.[10] Since the measurement error in α is double when estimating the figure-of-merit Z, the thermoelectric power must be measured very accurately.

15.2 Measurement of Resistivity

Basic Measurement

The basic equation for the experimental determination of resistivity is

$$\rho = \frac{A\Delta V}{I\Delta x} \tag{1}$$

where $\Delta V/\Delta x$ is the potential gradient along the specimen, A is the cross-sectional area, and I is the specimen current. As shown in Figure 1, the potential drop V_r between the two probes is compared with the potential drop V_s across a standard resistor R_s. Equation 1 for a parallelepiped specimen becomes

$$\rho = R_s \frac{V_r\, bt}{V_s\, l} = \frac{V_r A}{I l} \tag{2}$$

where b is the width of a specimen, t is its thickness, and l is the distance between the resistivity probes (voltage probes).

The voltage can be measured using a modified ADVANTEST TR-68701 high-speed, high-resolution digital voltage meter in conjunction with a low thermoelectric voltage scanner.[11] The DC current through the specimen is provided by an ADVANTEST TR-6143 constant current source. For typical semiconductors and metals, the effect of contact resistance and inherent thermoelectric voltage can be nullified by changing the current direction and/or varying the current

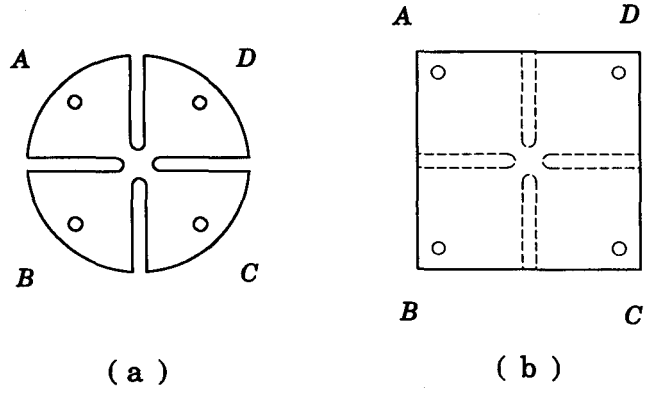

FIGURE 2 Specimen shapes for the van der Pauw's method: (a) ideal shape, (b) practical one.

values. The accuracy of measurement is then determined by the precision with which the specimen's dimensions are known, i.e., *b*, *t*, and *l*, and by the degree of homogeneity in the specimen. For "good" thermoelectric materials, the measurement error in V_0 due to Peltier pumping is minimized using the measuring technique described in Section 15.4.

Van der Pauw's Method

For basic measurements, a long parallelepiped specimen is required in order to homogenize the current density between the voltage probes. Without such a restriction, the van der Pauw method[12,13] is commonly used for the electrical characterization of small-size wafers and thin film. An ideal specimen shape for this method is shown in Figure 2a. In practice it is very difficult to fabricate, and a square shape as shown in Figure 2b is usually employed. Then error in measurement can be decreased by cutting deep into the specimen along the broken lines, as indicated in Figure 2b.

The resistivity is given by

$$\rho = \frac{\pi t(R_{AB,CD} + R_{BC,DA})}{2\ ln2} f \tag{3}$$

where t is the thickness of a specimen. $R_{AB,\,CD}$ is defined by V_{CD}/I_{AB}, where V_{CD} is the voltage drop between probes C and D when the electrical current is passed between a probe A and B. Analogously, $R_{BC,\,DA}$ is defined as V_{DA}/I_{BC}. f is a coefficient which is a function of the ratio R, defined as $R_{AB,\,CD}/R_{BC,\,DA}$. When $R > 1$, then

$$\frac{R-1}{R+1} = \frac{f}{ln2} \cosh^{-1}\left\{\frac{\exp(ln2/f)}{2}\right\}. \tag{4}$$

When the four probes are arranged with a mirror symmetry, $R_{AB,\,CD} = R_{BC,\,DA}$ and $f = 1$, Equation 3 is then given as

$$\rho = \frac{\pi t}{ln2} R_{AB,\,CD}. \tag{5}$$

f-values are presented as a function of R in the original literature.[12] For $R = 2$, f can be regarded as unity within a 5% error. However, R can become larger than 100 depending on the various shapes of the specimens under investigation. In this case numerical analysis is required to calculate the f-values to more than three figures of accuracy and depends on the accuracy in measuring the specimen thickness.

Montgomery[14] developed a novel method to calculate the resistivity tensors from the voltage-current ratio using only a single specimen.[14,15] This method, referred to as the Montgomery

method, is suitable for the anisotropic resistivity measurement on layered structure materials such as oxide superconductors and Bi_2Te_3-type compounds. The two components of the resistivity tensor can be obtained using a rectangular parallelepiped specimen in the shape of a very thin plate along the c-axis.

15.3 Measurement of the Hall Coefficient

The basic equation for the experimental determination of the Hall coefficient is

$$R_H = \frac{V_H\, t}{I\, B} \tag{6}$$

where V_H is the potential difference between the Hall probes and B is the applied magnetic field. The Hall coefficient determination is carried out employing the circuit shown in Figure 1 (SW1 and -2 are in No. 1 position; SW3 is in No. 2 position). The variable resistor R_r is used to nullify the voltage between the Hall probes before applying the magnetic field.[4,16] A magnetic field perpendicular to the direction of the electric current flow in the specimen produces a potential V_H across the specimen, which is mutually perpendicular to the direction of the magnetic field and to the direction of the current. The Hall coefficient is given by

$$R_H = R_s \frac{V_H\, t}{V_s\, B} \tag{7}$$

The carrier concentration n and mobility μ are related by the following relations:

$$n = \frac{\lambda_H}{eR_H} \tag{8}$$

$$\rho = \frac{1}{ne\mu} \tag{9}$$

where λ_H is the Hall factor which depends on the carrier scattering parameter r and the degree of degeneracy, viz., $\lambda_H = 1$ for degenerate acoustic phonon scattering and $\lambda_H = 3\pi/8$ for nondegenerate acoustic phonon scattering.

The Hall coefficient R_H using van der Pauw's method is given by

$$R_H = \frac{t}{B}\Delta R_{BD,\,AC} \tag{10}$$

where $\Delta R_{BD,\,AC}$ is the change in the potential when a magnetic field B is applied.

15.4 Peltier Effect on the Resistivity Measurement

Consider a parallelepiped specimen of n-type unidirectionally solidified $Bi_2Te_{2.85}Se_{0.15}$ with $\rho = 1.019 \times 10^{-5}\ \Omega m$, $\alpha = -200\ \mu V/K$, and $Z = 2.6 \times 10^{-3}/K$ in the a-axis direction. It is 15 mm long with $l = 1.5$ mm, $b = 3.0$ mm, and $t = 0.5$ mm (Figure 1). If a current of 10 mA is passed through the specimen, a temperature difference of 3.9 K between the ends of the specimen produced by Peltier pumping would result in a thermoelectric voltage V_o of 78 μV between the voltage probes under adiabatic condition.[4] In addition a V_r of 101.9 μV is generated by the specimen resistance. Then, the detected voltage V_l between the voltage probes has a 78% greater value than that of V_r, because the sign of V_o coincides with that of V_r. Since, in practice it is not possible to make measurements under perfect adiabatic conditions, V_o obtained is considerably smaller than 78 μV. Table 1 shows the measurement results of V_l in the steady state for the specimen described above when adhered to a high thermal conductivity Al_2O_3 plate. Measurements were made in air and in vacuum. The time dependence of V_l when measured under vacuum conditions

Table 1. Effects of the Peltier Heat Pumping on Measured Resistivities for n-Type Unidirectionally Solidified $Bi_2Te_{2.85}Se_{0.15}$ in the a-Axis Direction

Current Density	Adiabatic Condition		Calculated	In Vacuum		In Air	
(mA/mm²)	ΔT (K)[a]	V_0 (μV)	V_r (μV)	V_0 (μV)	V_r (μV)	V_0 (μV)	V_r (μV)
6.667	0.39	78	101.9	18.18	101.89	13.63	101.92
33.333	1.80	360	509.5	111.92	509.55	65.12	509.70
66.667	3.24	680	1019	224.95	1019.2	125.0	1019.5

[a]ΔT is the temperature difference between voltage probes.

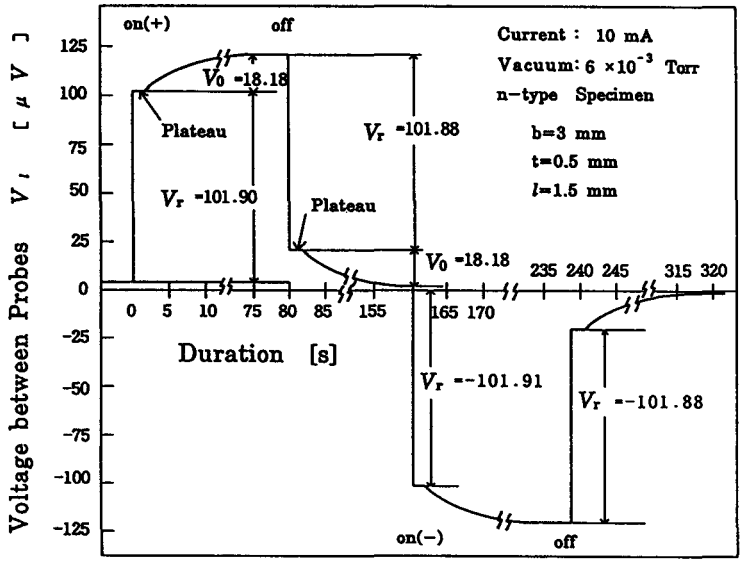

FIGURE 3 Effects of the Peltier heat pumping on the voltage between the probes V_l as a function of current duration.

is displayed in Figure 3. The plateau regions just after turning the current on and off have a duration of 1.1 ~ 1.3 s. During this time the effect of the temperature difference derived from Peltier pumping is negligibly small. However, after 1.3 s Peltier heat flows into the region between the voltage probes, with the result that V_l increases with increasing V_0. The dependence of V_0 on the current duration and measurement conditions has an effect on the measurement error. The error increases to more than 12.3% of V_r in an air atmosphere and increases with a decrease in current. Peltier heat has a similar influence when measuring the Hall effect, as discussed in the next section. Therefore, for high-precision resistivity measurements V_l must be detected within the duration of the plateau in Figure 3. The results suggest that it is important to maintain a sufficient distance between the current and voltage probes regardless of the measurement techniques, viz., DC, AC, and chopping methods.

15.5 Peltier Effect on the Hall Coefficient Measurement

When the current is passed through the specimen shown in Figure 1, the Peltier heat produces a temperature difference which results in thermal flow. The direction of the thermal flow depends on the sign of the mobile charge carrier in the thermoelectric material. The signs of the voltage V_E, V_N, and V_{RL} which are derived from the Ettinghausen, Nernst, and Righi-Leduc effects, respectively, are reversed by reversing the directions of the current and/or the magnetic field. These voltages coincide with that of the Hall voltage and are added to it.

Assuming that an electrical current of 10 mA is passed through a specimen similar to that employed for the resistivity measurement, the measurements being made at 300 K under adiabatic conditions, the voltages V_H, V_E, V_N, and V_{RL} will be

$$V_H = 2.50\ \mu V$$
$$V_E = 0.0065\ \mu V$$
$$V_N = 0.42\ \mu V$$
$$V_{RL} = 0.051\ \mu V$$

and the voltage detected is $V_{total} = 2.9975\ \mu V$.

The increment ratio of V_H is 19%, but it is considerably smaller than that of V_o. The voltage derived from the Nernst effect is the main additional contribution to the Hall voltage with only 2.3% due to the remaining contributions. The voltage due to the thermomagnetic effects is proportional to the specimen width.[4] Consequently when the specimen width is decreased to 1.5 mm, V_{total} is equal to 2.7385 μV and the measuring error is reduced to 9.5%. As indicated in Table 1 the influence of the Peltier effect on the resistivity ρ is around 20% in a vacuum condition (6.3×10^{-3} torr), V_H can be measured within an error of 2.2% for $b = 1.5$ mm. Also, under an air atmosphere the 17% contribution due to the Peltier heat will be comparable with that under an adiabatic condition; the error in V_H can be reduced to 1.5%. Therefore, as in the case of resistivity measurement, it is important to measure the Hall voltage within such a short duration that the Peltier heat has had insufficient time to flow into the region between the Hall voltage probes.

15.6 Measurement of Thermoelectric Power

The voltage V_o produced between two junctions of two dissimilar materials per unit temperature difference between the thermocouples is defined as the thermoelectric power of the one material relative to the other. This voltage can be measured by setting SW1 and SW2 to No. 2 positions in Figure 1. The temperature difference ΔT can be measured by means of two thermocouples. The average thermoelectric power of the sample α_{sa} as a function of the average temperature of the two thermocouples is given by

$$\alpha_{sa} = \frac{V_o}{\Delta T} \tag{11}$$

If the thermocouples spot-welded to the specimen are composed of chromel *a* and constantan *b*, the thermoelectric power of the specimen α_s is given by

$$\alpha_s = \alpha_{sa} + \alpha_a \tag{12}$$

where α_{sa} is the thermoelectric power of chromel. α_{sa} can be obtained from the slope of the thermoelectric voltage V_o as a function of the temperature difference ΔT. This temperature difference is maintained within ±2 K along the length of the specimen by the stabilized DC powered small subheaters. It is necessary to measure V_o under steady-state condition. If α_{sa} varies considerably with temperature, then the linear relationship cannot be obtained between V_o and ΔT. The relative thermoelectric power of the chromel-constantan thermocouple at 300 K is 40.55 μV; consequently, a voltage less than 150 nV must be detected precisely in order to measure ΔT within ±2 K at several points with an accuracy of more than 1%.

The thermoelectric power in the extrinsic conduction region based on a single band model is given by

$$\alpha = \pm \frac{k}{e} \left\{ \frac{(2 + r)F_{r+1}(\eta^*)}{(1 + r)F_r(\eta^*)} - \eta^* \right\} \tag{13}$$

where k is the Boltzmann's constant, e the electric charge, and η^* the reduced Fermi energy.[4,10]

The positive and negative signs refer to holes and electrons, respectively. $F_r(\eta^*)$ is the well-known Fermi-Dirac integral:

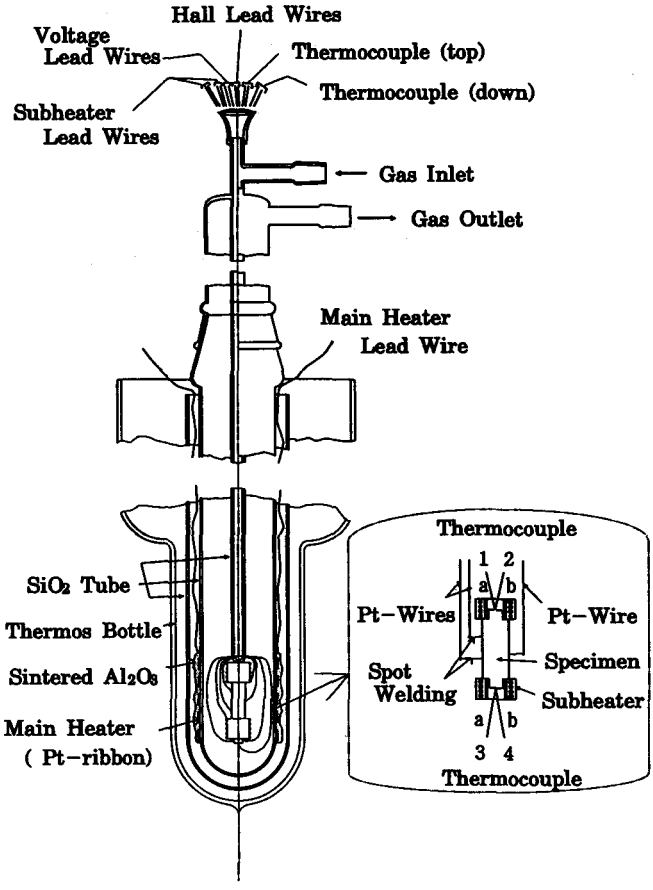

FIGURE 4 Apparatus for measuring the temperature dependence of the thermoelectric properties.

$$F_r(\eta^*) = \int \frac{\varepsilon^{*r}}{\exp(\varepsilon^* - \eta^*) + 1} d\varepsilon^* \tag{14}$$

Ohsugi et al.[17] have proposed a novel calculating procedure for $F_r(\eta^*)$ with an arbitrary real index r. Their method reduces the total error in calculation to 10^{-7} at any η^* through the use of a personal computer.

The carrier concentration is related to η^* and the effective mass m^* by the following relation:

$$n = \frac{4\pi}{h^3}(2m^*kT)^{3/2}F_{1/2}(\eta^*) = \frac{\lambda_H}{eR_H} \tag{15}$$

where h is Planck's constant.[4,10] Thus, m^* can be calculated by determining η^* from Equation 14 and substituting the values into Equation 15.

15.7 Measurement of the Temperature Dependence of Electrical Properties

An apparatus used to measure the temperature dependence of the thermoelectric parameters is shown in Figure 4. The apparatus is constructed of transparent quartz and pyrex glass, is lightweight, and easy to handle. The subheaters which maintain a temperature difference along the specimen are made of a resintered Al_2O_3 tube around which 50-μm diameter platinum wire is wound. Al_2O_3 cement is used to coat the surface of the heaters and to locate and hold the platinum

wires. Platinum wires 0.3 mm and 75 μm in diameter are used as the heater and voltage detection leads, respectively, because of their associated low thermal noise. The specimen-holder part of the apparatus is inserted into a thermos bottle filled with liquid nitrogen.

The main heater used to provide elevated temperatures consists of a ribbon of 20 wt% Pd-Pt alloy noninductively wound around a transparent quartz tube and fixed with Al_2O_3 cement. It is possible to set the apparatus at any required temperature in a range between 77.4 and 1200 K by adjusting the heater current. This method is suitable for Hall effect measurement, since a stable temperature can be obtained even in the presence of a magnetic field. A thermocouple of alumel-constantan, chromel-alumel, or platinum-platinum containing 13 wt% rhodium, is used to measure the temperature. Two pairs of thermocouples are attached to the top and bottom of the specimen, as shown in Figure 4, by soldering or percussion welding. These thermocouples are calibrated below room temperature using suitable refrigerants such as liquid nitrogen and dry ice in acetone and above room temperature by comparing against a standardized thermocouple of Pt-Pt/13% Rh.

References

1. Peason, G. L. and Bardeen, J., Electrical properties of pure silicon and silicon alloys containing boron and phosphorus, *Phys. Rev.*, 75, 865, 1949.
2. Dauphinee, T. M. and Mooser, E., Apparatus for measuring resistivity and Hall coefficient of semiconductors, *Rev. Sci. Instrum.*, 26, 660, 1955.
3. Lavine, J. M., Alternate current apparatus for measuring the ordinary Hall coefficient of ferromagnetic metals and semiconductors, *Rev. Sci. Instrum.*, 29, 970, 1958.
4. Putley, E. H., *The Hall Effect and Related Phenomena*, Butterworth, London, 1960, chaps. 2–3.
5. Harman, T. C., Measurement of pertinent thermoelectric properties, in *Thermoelectric Materials and Devices*, Cadoff, I. B. and Miller, E., Eds., Reinhold, 1967, chap. 6.
6. Lupu, N. Z., Tallan, N. M., and Tannhauser, D. S., Apparatus for measuring the Hall effect of low-mobility samples at high temperature, *Rev. Sci. Instrum.*, 38, 1658, 1967.
7. Rowe, D. M. and Bunce, R. W., Apparatus for measuring resistivity and Hall coefficient of heavily doped semiconductors at high temperature, *J. Phys. E*, 4, 902, 1971.
8. Lomas, R. A., Hampshire, M. J., and Tomlinson, R. D., A sensitive method of Hall measurement, *J. Phys. E*, 5, 819, 1972.
9. Buist, R. J., Thermoelectric material property, *Thermoelectric News*, Thermoelectric Technology, Inc., June 1991, 6.
10. Ioffe, A. F., *Semiconductor Thermoelements and Thermoelectric Cooling*, Infosearch, London, 1957, chaps. 2–3.
11. Nishida, I. A., Okamoto, M. A., Isoda, Y., and Masumoto, K., On the study of utilization for $FeSi_2$ thermoelectric elements, *Natl. Res. Inst. Metals*, 6, 149, 1985 (in Japanese).
12. Van der Pauw, L. J., A method of measuring specific resistivity and Hall effects of discs of arbitrary shape, *Philips Res. Rep.*, 13, 1, 1958.
13. Van der Pauw, L. J., A method of measuring the resistivity and Hall coefficient on lamellae of arbitrary shape, *Philips Techn. Rev.*, 20, 220, 1958/1959.
14. Montgomery, H. C., Method for measuring electrical resistivity of anisotropic materials, *J. Appl. Phys.*, 42, 2971, 1971.
15. Logan, B. F., Rice, S. O., and Wick, R. F., Series for computing current flow in a rectangular block, *J. Appl. Phys.*, 42, 2975, 1971.
16. Heikes, R. R. and Ure, R. W., *Thermoelectricity; Science and Engineering*, Interscience, London, 1961, chaps. 11–12.
17. Ohsugi, I. T., Kojima, T., and Nishida, I. A., A calculation procedure of the Fermi-Dirac integral with an arbitrary real index by means of a numerical integration technique, *J. Appl. Phys.*, 63, 5179, 1988.

16

Measurement of Thermal Properties

Roy Taylor
University of Manchester and UMIST
U.K.

16.1 Introduction

The term thermal properties is usually assumed to cover those material properties which change with the application of heat. Hence the term includes properties such as thermal expansion, specific heat, thermal diffusivity, and thermal conductivity. However, since the intrinsic worth of a thermoelectric material is defined by its figure-of-merit $Z = \alpha^2\sigma/\lambda$ where α is the Seebeck coefficient, σ is the electrical conductivity, and λ is the thermal conductivity, only the thermal conductivity of the parameters listed above is of special interest.

However, thermal conductivity measurements are not only difficult but, equally important, time consuming, since steady-state conditions are invariably required. Hence, during the past three decades there has been an inexorable shift towards the determination of basic thermal transport data using thermal diffusivity (a) techniques. This may be readily converted to thermal conductivity ($\lambda = a\rho c$ where ρ is density and C is specific heat). However, it must be emphasized that accurate specific heat data are needed to generate reliable thermal conductivity data. The overriding advantages of diffusivity measurement techniques are their extreme rapidity and the ability to generate large volumes of data very quickly. Diffusivity techniques are now used almost exclusively for measurements above room temperature on bulk materials.

Thermoelectric materials are being actively researched for the direct conversion of thermal energy to electric energy and for electronic refrigeration. Hence, the thermal transport properties of the various classes of material being studied are of interest over the temperature range up to 2000 K[1] or in the latter case at temperatures as low as 100 K.[2] Measurements are needed for bulk material and for material available as thin film. Various techniques are or have been used, depending on the temperature range to be covered and material availability. The techniques in common use are discussed in this chapter.

0-8493-0146-7/95/$0.00+$.50

16.2 Thermal Conductivity Measurements of Bulk Material

Below room temperature, thermal conductivity is the parameter almost invariably measured either by absolute or comparative methods. Radiation transfer is conveniently small and the measurements are less susceptible to extraneous heat losses. Above room temperature heat losses become more significant and more difficult to quantify as the temperature increases. However, below room temperature, basic thermal conductivity methods are still widely used and the principal methods are described below.

Absolute Axial Heat Flow or Thermal Potentiometer

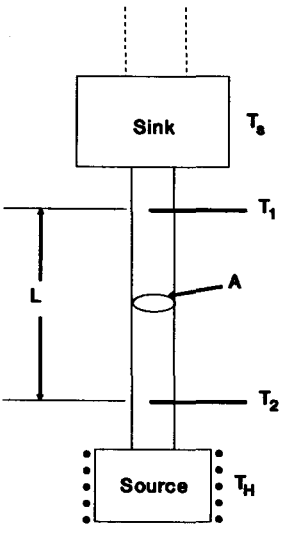

FIGURE 1 Schematic of axial heat flow apparatus.

This method is most widely used for measurements at low temperatures and modern equipment differs little in principle from that used by Lees more than 80 years ago.[3] An excellent review of the experimental requirements is given by White.[4] If all the heat supplied to the source $\dot{Q}$ ($= \partial q/\partial T$) is conducted along the rod of uniform cross section A and distance L between thermometers (Figure 1), then at any point

$$\lambda(T) = \frac{\dot{Q}}{A}\frac{\partial L}{\partial T} \tag{1}$$

and the mean conductivity between points 1 and 2 separated by a distance L is given by

$$\lambda(T) = \frac{\dot{Q}}{A}\frac{L}{\Delta T} \tag{2}$$

where $\Delta T = T_2 - T_1$. This assumes that the temperature is uniform across any element of the cross section, and that heat losses by conduction through any residual gas, by electrical leads from T_1 and T_2, and by radiation are negligible.

The choice of specimen geometry is dictated by the conductivity to be measured, by thermometer sensitivity, and by the maximum and minimum values of $\dot{Q}$ that can be tolerated. In practice, the length should be sufficiently great that the distance between source end 2 and sink end 1 is greater than the diameter. For low conductivity materials equilibrium times become very long unless L/A is made small. Typically for thermoelectric material, diameters of 3 to 4 mm are preferred and $L/A \leq 10$.

To allow as wide a temperature range as possible, the heat sink, which is loosely coupled to a refrigerator block, is coupled to an electric heater. Temperatures may be measured using either resistance thermometers[5–8] or thermocouples. Typical thermocouples for low-temperature use[9,10] are Au + 0.03% Fe/Chromel and Au + 2.1% Co vs. magnesium or copper. Various versions of this apparatus have been constructed for use on semiconductors and thermoelectric material at 300 K.[9,11] As a typical example, the apparatus of Slack[9] is shown in Figure 2. The temperatures are determined with respect to the heat sink, the absolute temperature of which is measured by means of a helium gas thermometer bulb. The outer can is inserted into different cryogenic liquids. The post heaters serve to bring the heat sink to any temperature in the range 3 to 300 K. A vacuum of $\sim 10^{-6}$ torr is maintained and a radiation shield minimizes radiation losses above 200 K. It is perhaps worth mentioning that a number of papers reporting low-temperature data on thermoelectric material refer to measurements made using "standard techniques" without giving more details. These are almost certainly the axial heat flow method. This technique has also been used for thermal conductivity measurements of high Tc superconductors.

Apparatus has been constructed to measure thermal conductivity above room temperature and various excellent systems have been devised.[12–14] The important fact here is to avoid spurious heat loss from the heaters, but more especially from the sample. The essential experimental requirement is the elimination, as far as possible, of radiation losses and this is achieved by a series of guard

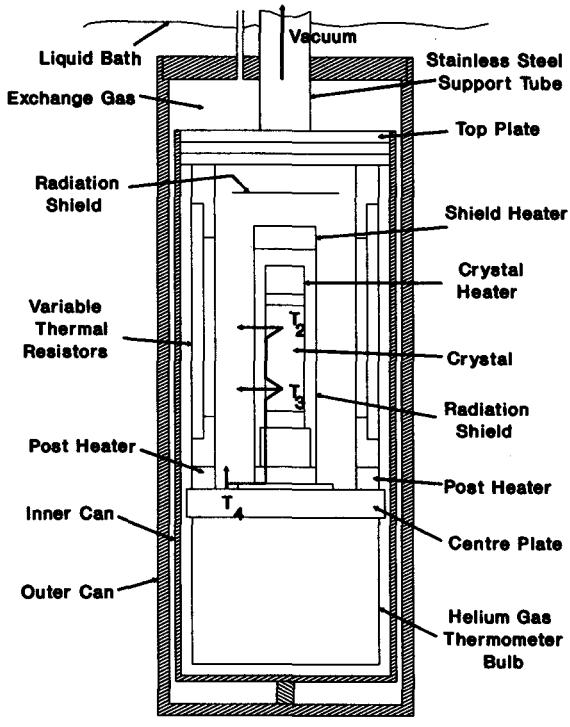

FIGURE 2 Schematic of experimental assembly for low-temperature thermal conductivity measurements (after Slack[9]).

heaters whose temperature is matched to that of the sample. Such equipment has, however, been used to measure the thermal conductivity of semiconductors and thermoelectrics.[15] Because it has been superceded in recent years by other techniques it will not be reviewed further. However, a useful critique of measurement of thermal conductivity at high temperatures by this technique is given by Laubitz.[16]

Comparative Methods

The comparative method determines the thermal conductivity λ of a material with respect to that of a suitable reference material. The unknown, whose thermal conductivity is to be measured, is sandwiched between two cylinders of a reference material of known thermal conductivity. The temperature gradients in the unknown and the standards are measured. If the cross sections are equal then

$$\lambda = \frac{\lambda_{ST}(\Delta T/\Delta x)_{ST}}{(\Delta T/\Delta x)} \tag{3}$$

where λ_{ST} is the known thermal conductivity of the standard and $(\Delta T/\Delta_x)_{ST}$ and $(\Delta T/\Delta x)$ are the temperature gradients of standard and test sample, respectively.

The thermocouples are usually located near the interfaces between the specimen and standards. The whole specimen-standard assembly is shielded by a matched guard heater. A typical short specimen assembly is based on the design of Francl and Kingery,[17] who used chromel/alumel thermocouples placed on silver plates separating the sample and standards. Thin layers of indium amalgam were used to overcome the problem of contact resistance. In an improved version Morris and Hust[18] placed the thermocouples in the sample and standards and used a heated ceramic radiation shield in three segments around sample and standards. This enabled the method to be

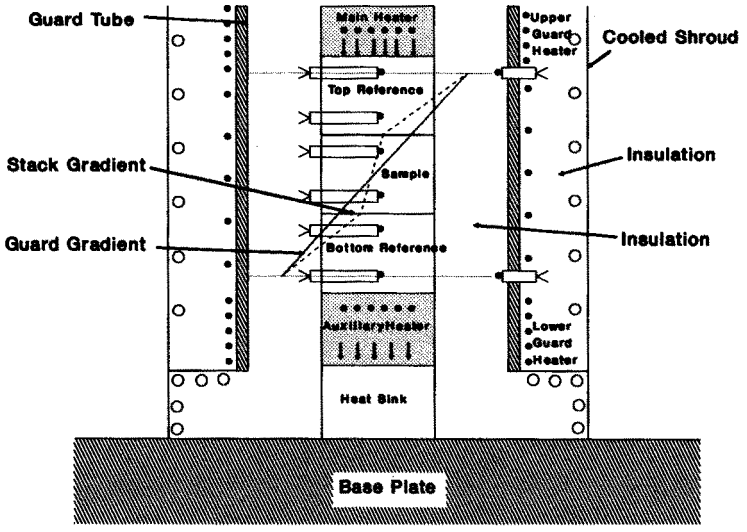

FIGURE 3 Comparative method schematic assembly.

used at temperatures up to 1000 K.[19] A typical assembly is shown in Figure 3. Important design features are

1. Accurate control of heaters on the outer cylindrical guard tube to minimize radial heat losses
2. Elimination of contact resistances at interfaces by the application of pressure or heat transfer media
3. Selecting a suitable thickness of sample relative to the reference material chosen

This method does not possess the high accuracy of absolute methods and has a reported precision of ~3% and an absolute accuracy of 5%.[20]

Other Thermal Conductivity Methods

Two absolute methods that could be used for thermoelectric material are the Kohlrausch method[21] and the radial heat flow method. The former is applicable to electrical conductors and the source of heat is a current passing through the sample. The thermal conductivity is calculated from the temperature distribution established. In principle the method may be used for thermoelectric material, but it has proven to have limited applicability. In radial heat flow apparatus there are various configurations which employ a central source of power and monitor the radial flow of heat outwards. A variety of configurations have been used and this method has been used for thermoelectric material.[22] Of all the thermal conductivity measurement techniques the radial heat flow method has the widest operating temperature range, and versions have been reported for operation at temperatures up to ≥2000 K. The major difficulties for application to thermoelectric material are the difficulties of fabricating homogeneous samples of the relatively large sizes needed.

16.3 Thermal Diffusivity Methods

Numerous outstanding scientists of the 19th and early 20th centuries appreciated the application of non-steady-state methods to measure thermal transport and an impressive mathematical bibliography has been built up.[23,24] They usually measure diffusivity, λ', and involve a solution to the complete differential equation for heat flow

$$\lambda' \left(\frac{\partial^2 T}{\partial x^2} \right) = \frac{\partial T}{\partial t} + \mu T \tag{4}$$

where μ is the coefficient of surface heat loss which takes into account heat loss by radiation conduction and convection. Depending on the boundary conditions chosen, a wide range of solutions to Fourier's equation are possible and a variety of ingenious techniques have been developed. Most non-steady-state methods are of recent origin and two factors are responsible for their development. First, time is the parameter usually measured and advances in the field of instrumentation, such as oscilloscopes and, later, digital data acquisition systems and microcomputers, have meant that time can be measured very accurately. Second, heat losses have a smaller influence when measurement times are short and are generally amenable to manipulation either by inclusion in the differential equation or by measurement and calibration. This approach is strikingly different from steady-state methods where heat losses must be accurately quantified or eliminated entirely if large errors are to be avoided. Non-steady-state methods may be divided into two general categories, periodic and transitory temperature methods. Within each category one technique which has been employed in measurements on thermoelectric materials will be reviewed. For a more critical review the reader is referred to Danielson and Sidles.[25]

Angstrom's Method

Originally developed in 1861,[26] this was the first periodic method to gain widespread acceptance. In its original version a long (semi-infinite) rod was used. However, this has been modified and improved by numerous investigators and has become a useful method for measuring thermal diffusivity at temperatures up to 1800 K. The theory is based on the fact that if a heat source, whose temperature varies sinusoidally with time, is located at one end ($x = 0$) of a semi-infinite radiating rod these temperature oscillations will propagate long the rod with a velocity V

$$V = \omega/\beta \tag{5}$$

where ω is the angular frequency and β the phase shift per unit length.

If the temperature is measured at two points $x = x_1$ and $x = x_2$ the thermal wave will have an amplitude decrement given by

$$q = \frac{\exp(-bx_1)}{\exp(-bx_2)} = \exp b \tag{6}$$

where $l = x_2 - x_1$.

The general solution to the differential equation (Equation 4) is given by

$$T(x,t) = A_o\exp^{-b_o x} + A_1\exp^{-bx}\cos(\omega t - \beta x + \varepsilon) \tag{7}$$

A_o, A_1, and ε are arbitrary constants

$$b_o = \sqrt{\mu\lambda'} \tag{8}$$

$$b = \left\{\frac{1}{2\lambda'}\left[\sqrt{\mu^2 + \omega^2} + \mu\right]\right\}^{\frac{1}{2}} \tag{9}$$

and

$$\beta = \left\{\frac{1}{2\lambda'}\left[\sqrt{\mu^2 + \omega^2} - \mu\right]\right\}^{\frac{1}{2}} \tag{10}$$

From Equations 5 and 6

$$b_1\beta = \frac{\omega ln q}{lV} \tag{11}$$

and from Equations 9 and 10

$$b_1\beta = \frac{\omega}{2\lambda'} \tag{12}$$

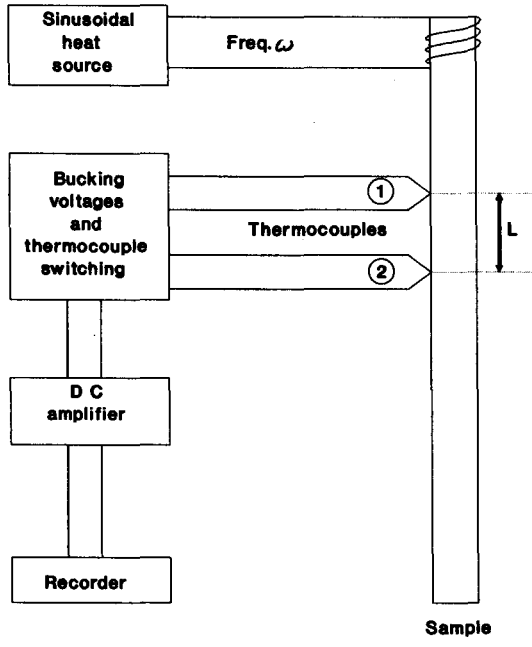

FIGURE 4 Schematic diagram of Angstrom's method for measuring thermal diffusivity (after Sidles and Danielson[27]). (With permission of John Wiley & Sons, Inc., New York, NY, and the estate of Paul H. Egli, Mt. Rainier, MD.)

Eliminating $\alpha_1\beta$ a simple expression for the experimental determination of thermal diffusivity (λ') is obtained:

$$\lambda' = \frac{lV}{2lnq} \tag{13}$$

For accurate measurement the period would be typically 120 s, sample diameters 3 to 9 mm, and lengths 500 to 300 mm. In later versions higher frequencies and shorter samples were used. The thermal diffusivity may be determined from measurements of the velocity and amplitude decrement using a single recorder/amplifier system (Figure 4) or by using two DC amplifiers and an X-Y plotter to generate an ellipse whose parameters define the thermal diffusivity.[27]

In the late 1950s and early 1960s this appeared a promising technique for the measurement of thermal diffusivity of thermoelectric material and has been used for a variety of different materials.[28–32] Unfortunately, after such early promise the Angstrom method is now little used to measure the thermal properties of these materials. One reason is the difficulty of obtaining suitably long specimens using the normal fabrication techniques of pressing and sintering. The second, and more important reason, was the advent of the flash technique which requires a specimen geometry that is readily available during the production of bulk thermoelectric materials.

Pulse or Laser Flash Method

This technique was first described by Parker et al.[33] in 1961 and since its inception it has been estimated[34] that >75% of all diffusivity results published in the primary scientific literature, and by implication derived thermal conductivity data, since the 1970s have been obtained using this single technique. The method has been widely used for the measurement of thermal diffusivity of thermoelectric materials since the late 1960s.[35–37] Since the technique is perceived to be such an important one it has been reviewed on a number of occasions.[38–40]

The application of the flash method in its original and most widely used form is limited to materials that can be rendered thin enough to be representative of bulk material and still satisfy

the requirement that the half rise time be within the limits 0.040 to 0.500 s. Specimens are usually in the form of a small disc 5 to 15 mm in diameter and thickness from 0.5 to 5 mm. Thermal diffusivity values from 1×10^{-3} to 1×10^{-7} m s^{-1} are readily measurable by this method and measurements have been made over the temperature range 100 to 3000 K. Two extensions to the technique have been developed: the radial flash method (which will not be reviewed) and multi-layer techniques (see Section 16.4).

One face of a disc sample is irradiated by a short pulse of heat from a laser, electron beam, or flash lamp, irradiation times being ≤1 msec. The resultant temperature rise of the opposite surface is recorded, from which the thermal diffusivity is computed from temperature rise vs. time data. According to Carslaw and Jaeger,[23] if the sample has an initial steady temperature distribution T(x,o) the temperature T(x,t) at anytime (t) and location (x) after the flash is incident at t = 0 on the face $x = 0$ is given by

$$T(x,t) = \frac{1}{L}\int_o^L T(x,O) + \frac{2}{L}\sum_{n=1}^{\infty} \exp\left(\frac{-n^2\pi^2\lambda' t}{L^2}\right) \tag{14}$$
$$x \cos\frac{n\pi x}{L}\, T(x,O) \cos\left(\frac{n\pi x}{L}\right)$$

If the pulse of energy (Q) is uniformly and instantaneously absorbed in a small depth g at the surface x = O then at the instant the temperature distribution is

$$T(x,O) = Q/DCg \qquad O < x < g$$
$$T(x,O) = O \qquad g < x < L$$

With these initial conditions Equation 14 becomes

$$T(x,t) = \frac{Q}{DCL}\left[1 + 2\sum_{n=1}^{\infty} \cos\frac{n\pi x}{L}\,\frac{\sin(n\pi g/L)}{n\pi g/L}\exp\frac{-n^2\pi^2\lambda' t}{L2}\right] \tag{15}$$

for opaque materials g is sufficiently small so sin(nπg/L) = nπg/L. With this approximation the rear face temperature at $x = L$ is given by

$$T(x,t) = \frac{Q}{DCL}\left[1 + 2\sum_{n=1}^{\infty} (-1)^n \exp\frac{-n^2\pi^2\lambda' t}{L^2}\right] \tag{16}$$

Two dimensionless parameters V and ω may be defined:

$$V(L,t) = T(L,t)/T_m$$
$$\omega = \frac{\pi^2\lambda' t}{L^2}$$

where T_m is the maximum temperature of the rear face. Hence (Figure 5):

$$V(L,t) = 1 + 2\sum_{n=1}^{\infty} (-1)^n \exp(-n^2\omega) \tag{17}$$

Since V varies from 0 to 1, in principle any fractional temperature rise can be used to calculate α. In practice most researchers use the half rise time (V = 0.5). When V = 0.5, ω = 1.37, and

$$\lambda' = \frac{1.37L^2}{\pi^2 t_{1/2}} \tag{18}$$

where $t_{1/2}$ is the time taken for the rear face to attain half its maximum temperature rise.

It is important to appreciate that an energetic pulse is concentrated in a very thin surface layer causing an appreciable temperature increase in this region. The technique relies on the fulfillment of relatively stringent boundary conditions, namely

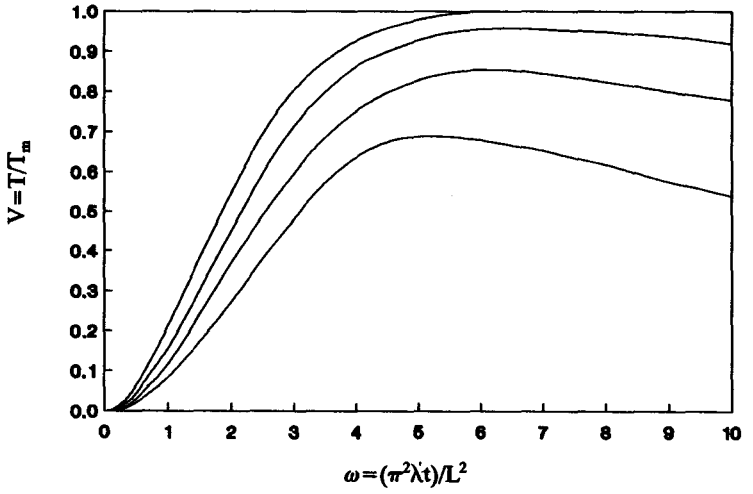

FIGURE 5 Thermogram flash technique, including the effect of heat losses.

1. The pulse of energy is uniformly absorbed in a small depth at the surface x = 0
2. The heat pulse dissipation time is of negligible duration
3. The measurement time is sufficiently short so that no heat losses occur from the sample

In addition, there are four basic experimental requirements:

1. A uniform, short-duration pulse source
2. A means of heating (or cooling) to adjust the measurement temperature
3. Sensors to detect the temperature transient
4. Recording and analysis facilities

Lasers are almost exclusively used to generate the heat pulses, usually Nd glass lasers at an operating wavelength of 1.06 μm, although historically flash tubes[33] and electron beams have also been used.[41] Laser dissipation times are typically 0.5 to 1.5 msec and variable laser powers in the range 20 to 100 J are used. The apparatus usually consists of a vacuum/unit atmosphere system with a specimen holder and either a furnace (or chiller) to obtain the desired measurement temperature. Furnace requirements are a matter of personal choice or are dictated by the temperature range to be covered. Because of the small size of the sample, the furnace can be small and of low thermal inertia, enabling rapid change of specimen temperature. For modest temperatures up to 1200°C (1473 K) an ordinary AC wound furnace is adequate.[35] At higher temperatures (up to 2000 K) refractory metal furnaces are widely used.[34] For measurements up to 3000 K induction heated or graphite susceptors have been used.[42,43] A schematic experimental configuration is shown in Figure 6.

Measurement of the transient temperature change forms the most crucial part of any heat pulse measurement system. The selection of a sensor depends on the temperature range to be covered and detectors that have been used include thermocouples, infrared (IR) detectors, or automatic optical pyrometers. The time response of the detector is crucial. Below the threshold of optical IR detectors thermocouples are necessary and it is important that an intrinsic thermocouple must be used (i.e., the specimen itself completes the electrical circuit). However, even for an intrinsic thermocouple there is a time delay. Henning and Parker[44] showed that the time to attain 95% of steady temperature $t_{0.95}$ is

$$t_{0.95} = \frac{25}{\pi} \frac{D^2}{\lambda_s'} \frac{\lambda_T}{\lambda_s} \tag{19}$$

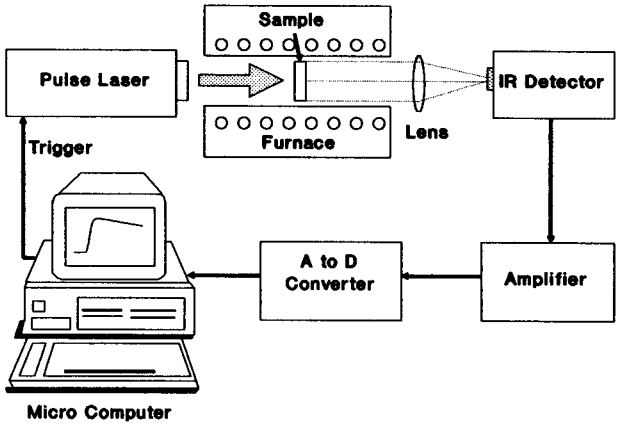

FIGURE 6 Schematic diagram of laser flash experimental requirements.

D is the wire diameter, λ_s' and λ_s are the diffusivity and conductivity of the substrate, and λ_T is the thermal conductivity of the wire. In reality[45] the actual behavior is a step change followed by an exponential rise to a final value

$$\frac{T_T - T_o}{T_\infty - T_o} = 1 - (1 - \lambda_s')e^{b^2 t^*} \, erfc(b\sqrt{t^*}) \tag{20}$$

T_o and T_∞ are initial and final temperatures, t^* is a dimensionless time ($= 4\alpha_s t/D_t^2$), and $b = (1 + 0.667\ \lambda_T/\lambda_s)^{-1}$.

Walter et al.[46] have shown the limitations of thermocouples in a series of experiments on low diffusivity materials. This is particularly relevant to thermoelectric materials so, if thermocouples must be used, these should be made from low thermal conductivity materials. These inherent problems can be avoided by the use of non-contact sensors with response times in the microsecond range, of which the following are representative:

1. In Sb, sensitive to 5 μm, cooled at 77 K
2. $Hg_xCd_{1-x}Te$, sensitivity 5 to 14 μm, cooled to 230 K
3. PbS, sensitive to 3.2 μm, used at room temperature
4. Photomultipliers and silicon photodiodes for use at temperatures >1000°C

All detectors require suitable amplification of the signal, together with a data collection analysis system. While the response of a non-contact sensor may be one to two orders of magnitude faster than required for the flash method, the detector signal is fed to amplifiers and filters whose response can affect the transient reading. Although traditionally this has been done with oscilloscopes, photographing the traces, or even by high-speed chart recorders, in recent years the advent of digital data acquisition systems and more recently microcomputers has meant that such systems are an integral part of modern measurement systems. These form the basis for fast, simple, and accurate data acquisition and analysis.

Boundary conditions for the flash technique require that the heat pulse be uniform, of short duration compared to the transient time through the sample, which itself should be sufficiently short so that no heat losses occur. Deviation from the ideal boundary conditions influences the result and gives rise to error. The non-measurement errors are primarily

1. Finite pulse time effects
2. Heat losses
3. Non-uniform heating

The first two are readily amenable to mathematical analysis. Analyses have been derived by various authors for finite pulse time effects.[47–50] The most detailed analysis is given by Taylor and Clark,[49]

who developed closed solutions for experimental cases and demonstrated results experimentally. They also showed how diffusivities may be corrected at percentage rise times other than $t_{1/2}$. Diffusivity is calculated from

$$\lambda' = \frac{C_1 L^2}{C_2 t_x - \tau} \tag{21}$$

where C_1 and C_2 are constants whose values depend on the shape of the heat pulse, which has a dissipation time τ. Taylor and Clark assume a triangular pulse approximated by a Kronecker-delta function of intensity $2/\tau$ with a maximum occurring at $\beta\tau$ ($o < \beta < 1$). Diffusivity calculated using Equation 12 increases as $t_{1/2}$ approaches τ so to avoid finite pulse time effects $t_{1/2} \gg \tau$. The correction to a finite pulse time effects is <0.2% when $t_{1/2} \geq 75\tau$.

The problem of heat losses is less clear-cut because the effect of heat losses occurring from different parts of the sample can vary depending on the geometrical configuration. A number of authors have analyzed the effect of heat losses.[47,50–53] Experimentally, the problem of heat losses is shown by a relatively short maximum temperature followed by a small decline. The calculated value of α decreases and a family of curves may be generated corresponding to different degrees of heat loss (Figure 5). Effectively, as heat losses increase, the constant in Equation 6 (= 1.37 in the adiabatic case) decreases in nonlinear fashion.

Some of the models are difficult to apply to an experimental situation, require fairly accurate estimations of the heat loss parameter, and rely on iteration methods. From a pragmatic point of view, radiation losses may be corrected for using the methods of Cowan[52] or Clark and Taylor.[53] Cowan's method consists of determining the value of V_x where V_x is the value of V, at either $5t_{1/2}$ or $10t_{1/2}$, and finding the ratio of this to $V(t_{1/2})$. Predicted curves showing the variation of ω/π^2 ($= \lambda' t_{1/2}/L^2$) with these ratios have been generated. Clark and Taylor[53] present an analysis based entirely on the rising portion of the heating curve. They show that the ratio of time at a higher percentage rise to time at a lower percentage rise decreases with increasing heat loss. The experimental times are ratioed at various fractional rises $t_{0.8}/t_{0.4}$, $t_{0.8}/t_{0.2}$, $t_{0.7}/t_{0.3}$, and the correct value of ω/π^2 may be selected from pregenerated curves.

While the problems of finite pulse time effects and heat losses are amenable to mathematical analysis and hence correction, non-uniform heating can occur in all flash diffusivity experiments for a variety of reasons. Very little research has been done, but some results of the effects of non-uniform beams have been published.[55–57] However, it must be said that a comprehensive study of the effect of non-uniform heating is a formidable task. To ameliorate this effect requires experimental care. Three facts in particular need to be regularly checked.

1. Regular checks of laser beam uniformity using photographic or laser footprint paper
2. A check of the system optics every time a specimen is inserted into the system
3. Ensure that the specimen front surface is of uniform emissivity

16.4 Films and Coatings

The technology to deposit thin films or coatings has made tremendous advances in the last 15 years. Thermoelectric semiconductors are one of several classes of material of current technological interest. However, it would be dangerous to assume that films have the same properties as bulk material. To measure the thermal transport properties of such coatings, a number of promising transient methods have been developed over the past 20 years. Brief surveys covering some of these have already been conducted.[54,55] Before briefly reviewing these methods it is necessary to point out that for a coating two thermal conductivities may be defined and measured: (1) through thickness normal to the surface and (2) a radial conductivity parallel to the surface.

Techniques will measure one or the other and there is no reason to suppose the two values to be identical for any given coating, since preferred orientations are likely to exist in any layer. The methods described in the previous section are not, in general, applicable or capable of adaptation to measure the thermal properties of films and coatings. The single exception is the flash diffusivity technique, described below.

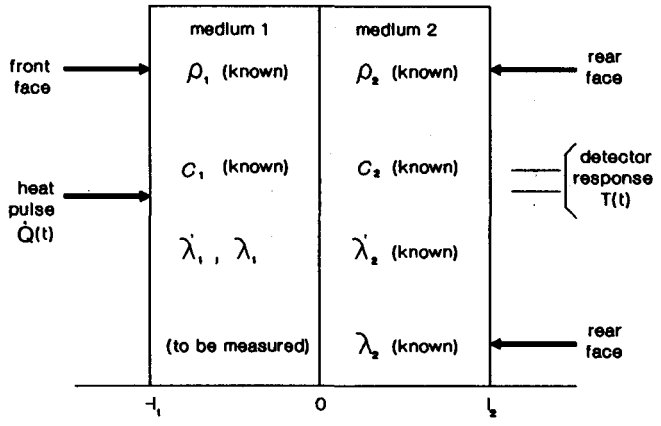

FIGURE 7 Schematic two-layer sample for flash technique.

Flash Diffusivity Technique

This technique measures the through thickness diffusivity of a coating. In the early 1970s a number of papers were published with analyses whereby the thermal diffusivity of one layer of a two-layer sample may be determined,[56–58] or even of one layer of a three-layer sample or the contact resistance between two layers of known diffusivity.[58] The experimental requirements are identical to those for the normal flash technique. Various computer programs exist to calculate the thermal diffusivity of an unknown layer from a half rise time measured in the conventional manner. A typical analysis is given by Bulmer and Taylor.[57]

$$V(t) = 1 - 2\gamma_2 \sum_{k=1}^{\infty} x \frac{(1 - \exp \beta_k^2/\gamma_2) \exp(-\beta_k^2 t/U_2)}{\beta_k^2 \cos(\beta_k X) \cos(\beta_k) - \Omega(X) \sin(\beta_k X) \sin(\beta_k)} \tag{22}$$

where β_k is the positive root of

$$H \sin(\beta X) \cos(\beta) + X \cos(\beta X) \sin(\beta) = 0 \tag{23}$$

and

$$X = (L_1/L_2)\left(\frac{\lambda_2'}{\lambda_1'}\right)^{\frac{1}{2}} \tag{24}$$

$$\lambda_2 = \frac{L_2^2}{\lambda_2' \tau} \tag{25}$$

$$U_2 = \lambda_2 \tau \tag{26}$$

$$H = (\rho_1 C_1 L_1)(\rho_2 C_2 L_2)^{-1} \tag{27}$$

$$\Omega(X) = (X + H/X)(H - 1)^{-1} \tag{28}$$

The subscripts 1 and 2 refer to front and rear layers, respectively. The heat pulse τ is approximated for a laser pulse by

$$F(t) = 1 - H(t - \tau) \tag{29}$$

where H(t) is the Heaviside unit step function defined as $H(t - \tau) = 0 (0 < t < \tau)$.

For layer 1, the "known" layer, knowledge of thickness, specific heat, density, and thermal diffusivity is required, whereas for the unknown layer it is still necessary to know length, density, and specific heat in order that the film or coating diffusivity be calculated (Figure 7). To ensure optimal accuracy it is desirable that the unknown layer constitutes as large a fraction of the total thermal

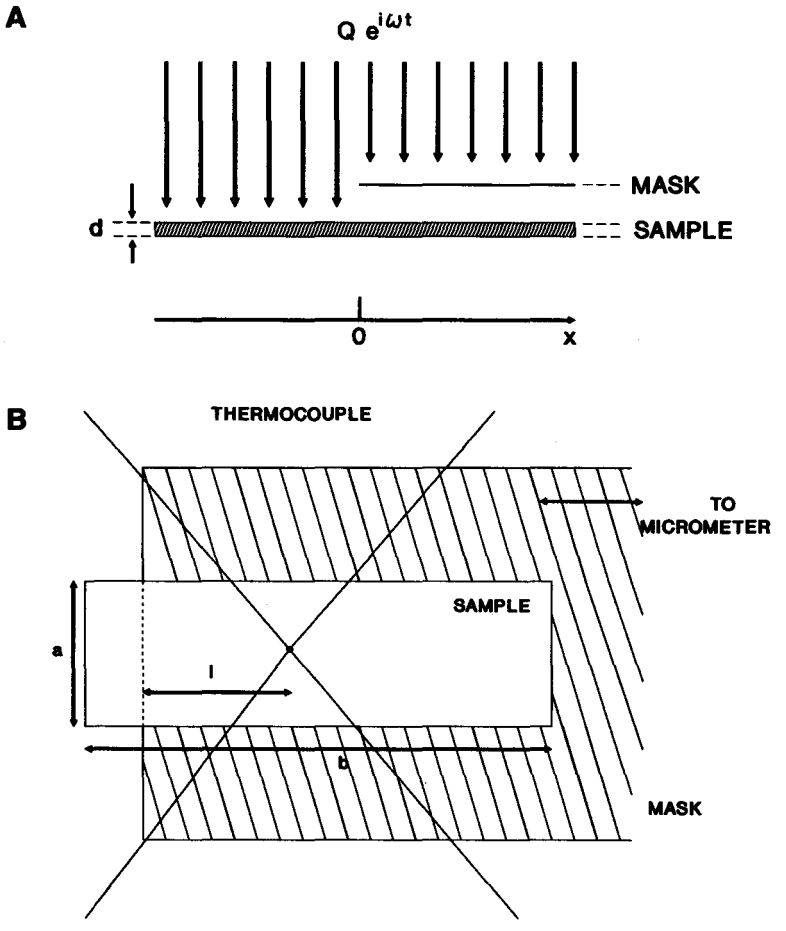

FIGURE 8 (a) Cross-sectional view of AC thermal diffusivity measuring system; (b) schematic view of rear face of AC thermal diffusivity sample (after Hatta et al.[60]).

barrier as possible, and certainly not less than 20%. This raises the question of desirable film/substrate combinations and this question has never been adequately addressed in the scientific literature. Ideally, the flash diffusivity technique is best suited to thick (>100 μm) films of relatively low thermal diffusivity. A "back of the envelope" calculation suggests that, for the thermoelectric materials currently being investigated, the two-layer flash method would be suitable for films >~100 μm.

AC Calorimetry

This method measures the thermal diffusivity parallel to the plane of the surface and is an adaptation of AC calorimetry[59] to measure thermal diffusivity.[60,61] While the method was developed originally for polymer films its use has been extended to self-supporting films (<0.01 mm) of all types of materials and to films on substrates, provided that the substrate thermal conductivity is ≤10 W m^{-1} K^{-1}. In this system (Figure 8) a part of a thin sample is shadowed by a mask from chopped light and a periodic energy wave is imparted to the remaining part of the sample. The AC temperature at a position of the sample lying under the mask at a distance x from the edge is detected using a fine thermocouple wire, attached to the sample by silver paste. Heat propagates into the shadowed region and decays with increase in x. The relation between T and n is given by

$$T = Q/2\omega\rho d \exp(-kx) \tag{30}$$

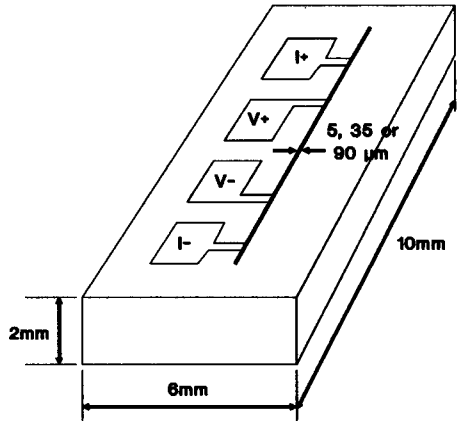

FIGURE 9 Evaporated metal pattern produced by photolithography for the 3ω technique (after Cahill and Pohl[62]).

where Q is the amplitude of the thermal flux/unit area, ω is the angular frequency, d the sample thickness, ρ the density, and C the specific heat/unit mass. k is the thermal decay constant, $(\omega/2\lambda')^{1/2}$, and from this the thermal diffusivity may be estimated. In order to treat the sample as a one-dimensional system (i.e., no conduction component perpendicular to the plate), the sample thickness should satisfy the condition $kd \leq 0.1$ or $\omega(d^2/2\lambda') \leq 0.1$.

Hence the thinner the sample the better; so for frequencies in the range 1 to 25 Hz, the maximum film thickness depends on its anticipated diffusivity. So for a thermoelectric material with $\lambda' \sim 2 \times 10^{-2}$ cm^2 s^{-1}, a *maximum* thickness would be <250 μm. In principle, it is possible to extend the method to measure through thickness thermal diffusivity, though at a decrease in accuracy.[62]

3ω Technique

A novel and interesting technique developed originally for glasses and other amorphous solids[62] has been extended to the measurement of thermal properties of thin films.[63] This is similar to the hot wire or hot strip techniques[64,65] in that a single element is used both as a heater and for temperature measurement. The difference is that measurements are made in the frequency rather than the time domain.

A thin metal strip is evaporated on to the specimen in such a way as to form a heater line (Figure 9). The application of an AC current of frequency ω will generate a temperature wave of frequency 2ω to diffuse into the substrate. The wavelength or reciprocal of penetration depth (q^{-1}) is given by

$$(q^{-1}) = (\lambda'/2\omega)^{1/2} \tag{31}$$

This technique probes the sample to a depth (q^{-1}) which, depending on λ and ω, is $\sim 10^{-3}$ to 10^{-5} m. By increasing frequency the technique is readily adapted to measure the thermal conductivity of thin films. Basically, the temperature wave is confined to the film if the thickness $d \geq /|q^{-1}|$. The technique has been used to measure the thermal conductivity of 50-μm films of α-Ge and α-Si.

Other Techniques for Film Measurement

Thermal transport properties of coatings are of interest for a number of materials, not merely thermoelectrics. At one extreme we have thermal barrier coatings ≥150 μm thick of conductivity ≤1 W m^{-1} K^{-1}, whereas at the other there are thin diamond films <5 μm thick with a thermal

conductivity of ≥ 1000 W m^{-1} K^{-1}. Measurement of the latter presents the more severe challenge and a number of techniques are being researched that may ultimately prove to be applicable to thin film thermoelectrics. Two of these are pulsed photothermal radiometry[66] and the photoacoustic technique.[67,68] In the former, a specimen is heated with a CO_2-TEA laser to produce 60-mJ, 50-μm pulses and the resultant thermal history is monitored by an IR detector. From the slope of the cooling curve the diffusivity of the coating may be obtained. The technique is primarily being researched as a nondestructive testing technique but has the capability to be adapted as a thermal diffusivity measurement method. In the photoacoustic method the sample is enclosed in a cylindrical shell filled with gas, the sample excited by a modulated radiative beam, and a microphone used to detect pressure versions corresponding to a temperature modulation.

16.5 Conclusion

Methods for the measurements of the thermal conductivity of thermoelectric materials have been reviewed. The techniques covered are steady state, methods for low-temperature measurements, diffusivity techniques for high-temperature measurements, and methods for measuring the thermal conductivity or diffusivity of thin films. The flash technique has received the most comprehensive coverage since it is the most widely used, and hence important, technique for measuring thermal transport properties of thermoelectric materials. However, a number of interesting variants and techniques of potential applicability have also been covered.

References

1. Wood, C., Materials problems in high temperature thermoelectric conversion, in *The First European Conference on Thermoelectrics*, Rowe, D.M., Ed., Peter Peregrinus, London, 1988, 1.
2. Goldsmid, H.J., Electronic refrigeration, in *The First European Conference on Thermoelectrics*, Rowe, D.M., Ed., Peter Peregrinus, London, 1988, 342.
3. Lees, C.H., Conductivities of methods and alloys at low temperatures, *Philos. Trans. R. Soc. A*, 208, 301, 1908.
4. White, G.K., Measurement of solid conduction at low temperature, in *Thermal Conductivity*, Vol. 1, Tye, R.P., Ed., Academic Press, London, 1969, 69.
5. Black, W.C., Rosch, W.R., and Wheatley, J.C., Speer carbon resistors as thermometers for use below 1°K, *Rev. Sci. Instrum.*, 35, 587, 1964.
6. Kunzler, J.E., Gabelle, T.H., and Hull, G.W., Germanium resistance thermometers suitable for low temperature calorimetry, *Rev. Sci. Instrum.*, 28, 96, 1957.
7. Lindenfield, P., Carbon and semiconductor thermometers for low temperatures, in *Temperature. Its Measurement and Control in Science and Industry*, Vol. 3, Part 1, Herzfeld, C.M., Ed., Reinhold, New York, 399, 1962.
8. Klein, M.V., Phonon scattering in sodium chloride containing oxygen, *Phys. Rev.*, 122, 1393, 1961.
9. Slack, G.A., Thermal conductivity of CaF_2, MnF_2, CoF_2 and ZnF_2 crystals, *Phys. Rev.*, 122, 1451, 1961.
10. Berman, R., Brock, J.C.F., and Huntley, D.J., Properties of gold + 0.03 at% iron thermoelements between 1 and 300°K and behaviour in a magnetic field, *Cryogenics*, 4, 233, 1964.
11. Brinson, M.E. and Dunstan, W., Thermal conductivity and thermoelectric power of heavily doped n-type silicon, *J. Phys. C Solid State Phys.*, 3, 483, 1970.
12. Ditmars, D.A. and Ginnings, D.C., Thermal conductivity of beryllium oxide from 40° to 750°C, *J. Res. Natl. Bur. Stand.*, 59, 93, 1957.
13. Armstrong, L.D. and Dauphine, T.M., Thermal conductivity of metals at high temperatures. I. Description of the apparatus and measurements on iron, *Can. J. Res. A*, 25, 357, 1947.
14. Powell, R.W. and Tye, R.P., Thermal and electrical conductivities of nickel-chromium (Nimonic) alloys, *Engineer*, 209, 729, 1960.
15. Busch, G. and Steigmeier, E.F., Thermal and electrical conductivities, Hall effect and thermoelectric power of InSb, *Helv. Phys. Acta*, 34, 1, 1961.

16. Laubitz, M.J., Measurement of thermal conductivity of solids at high temperature by using steady state linear and quasi-linear heat flow, in *Thermal Conductivity*, Vol. 1, Tye, R.P., Ed., Academic Press, London, 1969, 111.
17. Francl, J. and Kingery, W.D., Thermal conductivity. IV. Apparatus for determining thermal conductivity by a comparative method, *J. Am. Ceram. Soc.*, 37, 80, 1954.
18. Morris, R.G. and Hust, J.G., Thermal conductivity measurements of silicon from 30° to 425°C, *Phys. Rev.*, 124, 1426, 1961.
19. Morris, R.G. and Martin, J.C., Thermal conductivity measurements of silicon from 680 to 1000°K, *J. Appl. Phys.*, 34, 2388, 1963.
20. Mirkovich, V.V., Comparative method and choice of standards for thermal conductivity determination, *J. Am. Ceram. Soc.*, 48, 387, 1965.
21. Kohlrausch, F., Electrochemical relations, *Preuss. Akad. Wiss. Berlin, S. Ber.*, 38, 711, 1899; *Ann. Phys.*, 1, 132, 1900.
22. Birkholz, U., Untersuchung der intermetallischen Verbindung Bi_2Te_3 Sourie der festen Lösungen $Bi_{2-x}Sb_xTe_3$ und $Bi_2Te_{3-x}Se_x$ hindsichtlich ihner Eignung ab Material fur Halbleiter — Thermoelemente, *Z. Naturforsch.*, 13a, 780, 1958.
23. Carslaw, H.S. and Jaeger, J.C., *Conduction of Heat in Solids*, 2nd ed., Oxford University Press, New York, 1959.
24. Jakob, M., *Heat Transfer*, John Wiley & Sons, New York, 1949.
25. Danielson, G.C. and Sidles, P.H., Thermal diffusivity and other non-steady state methods, in *Thermal Conductivity*, Vol. 2, Tye, R.P., Ed., Academic Press, London, 1989.
26. Angstrom, A.J., Neue Methode des Warmeleitungsvermogen der Korper zu bestimmen, *Ann. Phys. Chem.*, 114, 513, 1861.
27. Sidles, P.H. and Danielson, G.C., Thermal diffusivity measurements at high temperature, in *Thermoelectricity*, Egli, P.H., Ed., John Wiley & Sons, New York, 1960, 270.
28. Abeles, B., Beers, D.S., Cody, G.D., and Dismukes, J.P., Thermal conductivity of Ge-Si alloys at high temperatures, *Phys. Rev.*, 125, 44, 1962.
29. Steigmeier, E.F. and Kudman, I., Acoustical-optical phonon-scattering in Ge Si and III-V compounds, *Phys. Rev.*, 141, 767, 1966.
30. Shanks, H.R., Maycock, P.D., Sidles, P.H., and Danielson, G.C., Thermal conductivity of silicon from 300–1400°K, *Phys. Rev.*, 130, 1743, 1963.
31. Kudman, I. and Steigmeier, E.F., Thermal conductivity and Seebeck coefficient of InP, *Phys. Rev.*, 133, A166J, 1964.
32. Dismukes, J.P., Ekstrom, L., Steigmeier, E.F., Kudman, I., and Beers, D.S., Thermal and electrical properties of heavily doped Ge-Si alloys up to 300°K, *J. Appl. Phys.*, 35, 2899, 1964.
33. Parker, W.J., Jenkins, R.J., Butler, C.P., and Abbott, G.L., Flash method for determining thermal diffusivity, heat capacity and thermal conductivity, *J. Appl. Phys.*, 32, 1679, 1966.
34. Taylor, R.E., Critical Evaluation of Flash Method for Measuring Thermal Diffusivity, Report PRF-6764, National Science Technical Information Service, Springfield, Virginia, 1973.
35. Rowe, D.M. and Shukla, V.S., The effect of thermal conductivity and thermoelectric conversion efficiency of heavily doped fine grained hot pressed silicon germanium alloy, *J. Appl. Phys.*, 52, 7421, 1981.
36. Vining, C.B., Zoltan, A., and Vandersande, J.W., Determination of the thermal diffusivity and specific heat using an exponential heat pulse, including heat loss effects, *Int. J. Thermophys.*, 10, 259, 1989.
37. Wood, C. and Zoltan, A., Simple high temperature thermal diffusivity apparatus, *Rev. Sci. Instrum.*, 55, 235, 1984.
38. Righini, F. and Cezairliyan, A., Pulse method of thermal diffusivity measurements (a review), *High Temp.-High Press.*, 5, 481, 1973.
39. Taylor, R.E. and Maglic, K.D., Pulse method for thermal diffusivity measurement, in *Compendium of Thermophysical Property Measurement Methods*, Vol. 1, Maglic, K.D., Cezairliyan, A., and Peletskii, V.V., Eds., Plenum Press, New York, 1984, 305.
40. Taylor, R., Measurement of thermal diffusivity by the laser flash method, in *First European Conference on Thermoelectrics*, Rowe, D.M., Ed., Peter Peregrinus, London, 1987, 107.
41. Walter, A.J., Dell, R.M., and Burgess, P.C., Measurement of thermal diffusivities using a pulsed electron beam, *Rev. Int. Mtes. Temp. at Refract.*, 7, 271, 1970.

42. Weilbacher, J.C. and Van Craeynest, J.C., Appareil de mésure de la diffusivité thermique a trés haute temperature, *Rev. Int. Mtes. Temp. at Refract.*, 7, 268, 1970.
43. Taylor, R., Construction of apparatus for heat pulse thermal diffusivity measurements, *J. Phys. E. Sci. Instrum.*, 13, 1197, 1980.
44. Henning, C.D. and Parker, R., Transient response of an intrinsic thermocouple, *J. Heat Transfer ASME*, 39, 146, 1967.
45. Taylor, R.E., Critical evaluation of flash method for measuring thermal diffusivity, *Rev. Int. Htes. Temp. at Refract.*, 12, 141, 1975.
46. Walter, A.J., Dell, R.M., Gilchrist, K.E., and Taylor, R., A comparative study of the thermal diffusivities of stainless steel, hafnium and zircaloy, *High Temp.-High Press.*, 4, 439, 1972.
47. Cape, J.A. and Lehman, G.W., Temperature and finite pulse-time effects in the flash method for measuring thermal diffusivity, *J. Appl. Phys.*, 34, 1909, 1963.
48. Larson, K.B. and Koyama, K., Correction for finite pulse-time effects in very thin samples using the flash method of measuring thermal diffusivity, *J. Appl. Phys.*, 38, 465, 1977.
49. Taylor, R.E. and Clark, L.M., III, Finite pulse time effects in flash diffusivity method, *High Temp.-High Press.*, 6, 65, 1974.
50. Heckman, R.C., Error analysis in flash diffusivity technique, in *Proc. 14th Int. Thermal Conductivity Conf.*, Klemens, P.G. and Chu, T.K., Eds., Plenum Press, New York, 1976.
51. Watt, D.A., Theory of thermal diffusivity by pulse technique, *Br. J. Appl. Phys.*, 17, 231, 1960.
52. Cowan, R.D., Pulse method of measuring thermal diffusivity, *J. Appl. Phys.*, 34, 926, 1963.
53. Clark, L.M., III and Taylor, R.C., Radiation loss in the flash method for thermal diffusivity, *J. Appl. Phys.*, 46, 714, 1975.
54. Tye, R.P., Measurement of thermal conductivity and related properties, a half century of radical change, *High Temp.-High Press.*, 23, 1, 1991.
55. Kobayasi, K., Recent developments in measurement techniques for thermal conductivity and thermal diffusivity, *J.S.M.E. II*, 31, 1, 1988.
56. Larson, K.B. and Koyama, K., Measurement by the flash method of thermal diffusivity, heat capacity and thermal conductivity in two layer composite samples, *J. Appl. Phys.*, 39, 4408, 1968.
57. Bulmer, R.F. and Taylor, R., Measurement by the flash method of thermal diffusivity of two layer composite samples, *High Temp.-High Press.*, 6, 491, 1974.
58. Lee, H.J. and Taylor, R.E., Determination of thermophysical properties of layered composites by the flash method, in *Thermal Conductivity*, Vol. 14, Klemens, P.G. and Chu, T.K., Eds., Plenum Press, New York, 1976, 423.
59. Salamon, M.B., Garnier, P.R., Golding, B., and Buehler, E., Simultaneous measurement of thermal diffusivity and specific heat near phase transitions, *J. Phys. Chem. Solids*, 35, 851, 1974.
60. Hatta, I., Sasuga, Y., Kato, R., and Measan, A., Thermal diffusivity measurement of thin films by means of an A.C. calorimetric method, *Rev. Sci. Instrum.*, 56, 1643, 1985.
61. Hatta, I., Thermal diffusivity measurements of thin film and multilayered composites, *Int. J. Thermophys.*, 11, 293, 1990.
62. Cahill, D.G. and Pohl, R.O., Thermal conductivity of amorphous solids above the plateau, *Phys. Rev.*, 835, 4067, 1987.
63. Cahill, D.G., Fischer, H.E., Klitsner, T., Swartz, E.T., and Pohl, R.O., Thermal conductivity of thin films; measurement and understanding, *J. Vac. Sci. Tech.*, A7, 1259, 1989.
64. Gustaffson, J.E., Chohan, M.A., and Khan, M.A., Thermal transport studies using pulse transient hot strip measurements of vitreous silica produced by vacuum deposition, *High Temp.-High Press.*, 17, 35, 1985.
65. Gustaffson, J.E. and Karawicki, E., Transient hot-strip probe for measuring thermal properties of insulating solid and liquids, *Rev. Sci. Instrum.*, 54, 744, 1983.
66. Cielo, P., Pulsed photo thermal evaluation of layered materials, *J. Appl. Phys.*, 56, 230, 1984.
67. Rejab, A.B., Britton, B., and Stephens, R., Thermal diffusivity of powders and porous media, *High Temp.-High Press.*, 17, 695, 1985.
68. Hsiao, W., Qinrui, Y., Minghua, L., and Tonggen, X., Measurement of thermal conductivity of sheet materials using a photoacoustic technique, *Proc. 1st Asian Thermophysics*, Props Conf. (1986), 253.

17
Z-Meters

Hugh H. Woodbury,
Lionel M. Levinson, and
Robert S. Lewandowski
General Electric Company
Schnectady, New York, U.S.A.

17.1 Introduction

The thermoelectric figure-of-merit, Z, is defined as:

$$Z = \alpha^2/(\lambda\rho)$$

where α is the Seebeck coefficient, λ the thermal conductivity, and ρ the electrical resistivity.[1] Z is a common measure of the effectiveness of a material to function in a thermoelectric couple for heating or cooling applications. A knowledge of the temperature dependence of Z is important in optimizing couples for specific applications.

A Z-meter is an instrument that simultaneously measures, on one sample, the three thermoelectric parameters of interest as a function of temperature from which Z can be calculated. Putley[2] describes an apparatus which he used to measure the Peltier heating and cooling when a small current was passed through a sample. The resulting small temperature difference gives rise to a Seebeck voltage, and the thermal conductivity can be calculated from the steady-state conditions. Independently, Harman et al. used the same idea in a Z-meter.[3] An interesting feature of this approach is that ZT, where T is the absolute temperature, can be directly determined from the experimental data as a ratio of the various measured voltages. Lisker briefly outlines a general analysis of this approach, pointing out that a variety of different but related measurements which lead to Z or ZT can be carried out.[4] A number of experimental variations of these ideas have been proposed, including the study of films. Accurate measurement of α, λ, and ρ requires care. In particular, measurement of the thermal conductivity is difficult and needs a steady-state condition and adiabatic thermal insulation of the sample or appropriate corrections for the lack thereof.[5]

The primary interest of the above cited authors was the study of materials for thermoelectric cooling, i.e., making measurements near or below room temperature, although Putley's apparatus employed a sample holder that could be heated to 700°C,[8] while Phillips[6] and Kaplan[7] have described Z-meters that operate in the range 100 to 600°C. They essentially involve a classical arrangement for directly measuring α, λ, and ρ on rod-shaped samples. The need for establishing different thermal conditions for each measurement, i.e., a moderate temperature gradient for α, a low gradient for λ, and a zero gradient for ρ, illustrates a major difficulty in these approaches. Automated versions of this classical stationary approach have been described by Wartanowicz and Goschorski[8] and by Vedernikov et al.[9]

An alternative approach to Z-meters employs a large temperature difference across the sample.[10–12] The total Seebeck voltage, thermal conductance, and electrical resistance are essentially simultaneously measured as a function of the temperatures of the ends of the sample. The data are then deconvoluted to obtain the temperature dependence of α, λ, and ρ, from which the temperature dependence of Z is determined. A computer is used to record the data, and the method

0-8493-0146-7/95/$0.00+$.50

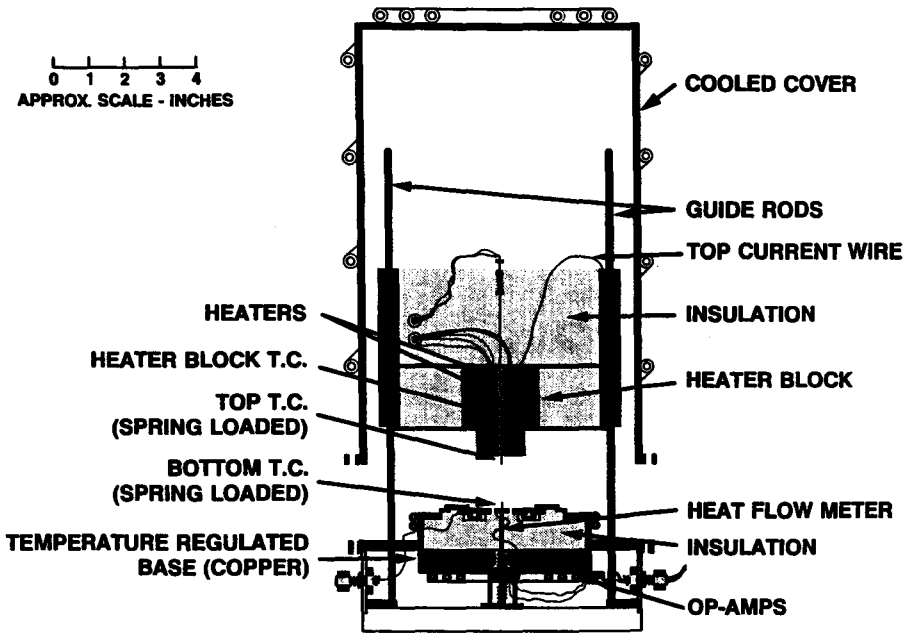

Figure 1 Overall schematic of the large temperature difference apparatus, which is shown here without a sample and with the cover slightly lifted. Not shown are the supports for the top thermocouple and the top bracing to carry the added weights to increase the contact pressure on the ends of the sample.

results in a fully automated system for a complete temperature run. This is one of its principal advantages. A description of such a meter is given in Section 17.2. This description provides a context for discussion of more general Z-meter problems, which are considered in Section 17.3.

Section 17.4 gives a summary and recommendations for the use of Z-meters. The promises of Z-meters are many, including the automated, reproducible measurement of the basic thermoelectric parameters and not relying on data taken on different samples or in sequence on the same sample. For example, the trade-off between the Seebeck coefficient and electrical resistivity for semiconductors is well known, and typical sample-to-sample variations or variations following thermal cycling in which the active dopant concentrations change can give misleading results if measurements are carried out in sequence or on different samples.

17.2 A Large Temperature Difference Z-Meter

Design Features

In this section we give the detailed design specifications, operation and calibration features, and data analysis for a particular large temperature difference Z-meter. This meter has been used successfully by the authors to up to 700°C for samples 6.3 mm square by 1 to 1.5 cm long. While this meter was constructed to measure specific thermoelectric materials having properties similar to those of PbTe alloys, the authors believe this type of meter has a broader usefulness and the details given here relate to general Z-meter design considerations.

The features of the Z-meter are shown in Figures 1 and 2. Construction details are as follows: the top and bottom supports for the heater block are quartz disks secured to the stainless steel cylinder with screws "padded" with high-temperature silicone rubber. This upper assembly is guided with Teflon* bearings on stainless steel rods. The insulation is quartz wool throughout. An

*Teflon is a registered trademark of E I du Pont de Nemours and Company Inc., Wilmington, DE.

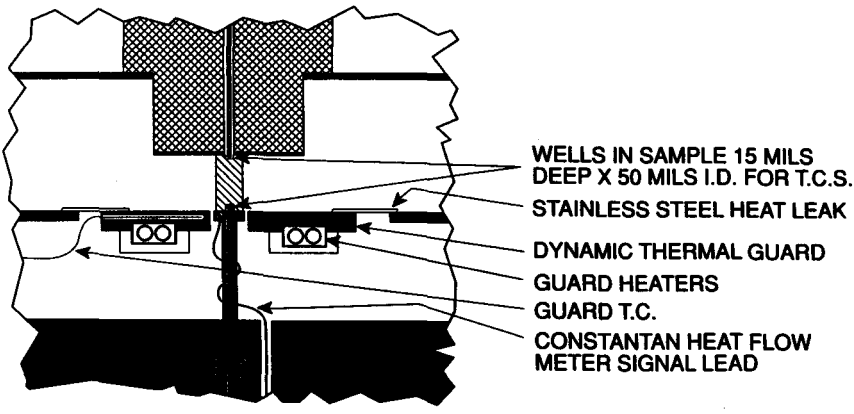

FIGURE 2 Details of the sample area and heat flow meter of the large temperature difference apparatus. Not shown are the sample end gaskets and the insulation (quartz wool) which surrounds the sample.

additional 1-kg weight is placed on top of the stainless steel cylinder to counter the force of the spring-loaded upper and lower thermocouples and to increase the contact pressure on the sample ends.

In order to preserve the face of the bottom of the heater block, a thin sheet of Pt is brazed onto it and is then machined and polished. A 5-ml Grafoil* gasket is used at the top while two 2-ml indium gaskets are used at the bottom to provide uniform electrical and thermal contacting. The bottom of the sample never gets above 120°C. The apparatus is evacuated and back-filled with argon before a measurement run.

One objective of the design is to create a vertical heat flow pattern adjacent to the sample by creating uniform temperature planes at the top and bottom of the sample. The bottom of the heater block forms the top plane while a dynamic thermal guard ring around the top of the heat flow meter forms the bottom plane. This guard ring is maintained close to the temperature of the bottom of the sample by comparing the reading of the guard thermocouple with the heat flow meter output signal. The difference signal is used to control the guard heaters in a standard analog control loop.

The dynamic thermal guarding of the heat flow meter and the use of cooling coils around the outside shield improve the reproducibility from run to run and significantly decrease the time required to bring the system into thermal equilibrium before a run begins.

Molybdenum was the choice for the heater block because of its higher thermal conductivity over high-temperature alloys such as Inconel. This provides a higher maximum temperature at the top of the sample for a given (maximum) temperature rating of the heaters as well as maintaining a more uniform temperature plane.

Some electrical considerations are as follows: the heat flow meter is made of copper to give rapid thermal response. A 5-ml constantan wire is secured to the top of the square copper pedestal comprising the meter. This wire and the copper meter and base become a thermocouple pair which generates the meter output signal. The upper thermocouple is a 5-ml platinum-platinum/10% rhodium pair in a 47-ml O.D. zirconia tubing. The lower thermocouple is a copper-constantan pair in similar zirconia tubing. Both of these thermocouples are referenced to the base, which is maintained at 25°C with a VWR Model 1145 Constant Temperature Circulator (VWR Scientific Inc., San Francisco, CA).

The leg-pairs of the thermocouples are each brought to the inputs of AD708 operational amplifiers (Analog Devices, Inc., Norwood, MA) connected in an instrumentation mode. The time constant is designed to be 100 msec and the measured input noise is $<0.5\ \mu V$. In order to measure the Seebeck voltage, the Pt and Cu legs of the upper and lower thermocouples are carried to a fourth AD708, also with a time constant of 100 msec. All of the op-amps are mounted such that

*Grafoil is a registered trademark of Union Carbide Corp., New York, NY.

they are in thermal contact with the base, which provides excellent stability. Occasionally the system is permitted to equilibrate for 24 to 48 h, at which time the zero offset readings are read and stored by the computer.

To measure the resistivity, a square wave current pulse is passed through the sample. This pulse is computer-controlled in timing and duration as well as magnitude. Typically it is 60 msec positive and 60 msec negative and ±1 A and 0.1 A in magnitude. The ohmic voltage drop across the sample is measured through the same thermocouple legs used for measuring the Seebeck voltage. However, they feed a parallel AD708 with a time constant of 4.7 msec. The faster response time of this circuit minimizes distortion of this pulse.

The outputs from the five op-amps plus a current signal derived from the voltage drop across a 1-Ω standard resistor are fed into a DT2801/5716A 16-bit A/D board (Data Translation, Inc., Marlboro, MA) plugged into a PC. Care is taken to balance the impedances of all lines to maintain a high CMRR.

Operation and Calibration

The end faces of the samples are ground using simple jigs to ensure that they are planar and parallel. Accurately centered and defined thermocouple wells (see Figure 2) are made using a clockmaker's precision drill press with 50-ml diamond drills (Diamond Microdrill #S50, Amplex Corp., Bloomfield, CT).

To begin a measurement run, data near room temperature, typically from 25 to 50°C, are first obtained by applying low power to the heater block. Also, the voltage waveform at the output of the current square wave generator is monitored with a digital scope. This initial testing provides (1) a check on the sample integrity, (2) a check on the electrical and thermal contacting, (3) a check to optimize the software-controlled A/D channel gains and the magnitude of the current pulse (for new samples with unknown characteristics), and (4) approximate, near room temperature values for the thermoelectric parameters before the sample is thermally cycled. The initial near room temperature measurements check for any sample hysteresis.

Following the initial checks, full power of 200 W is applied to the heater block, which brings it to 500–600°C in about 30 min. After a holding period of 30 min, the heater block power is turned off and the whole assembly is allowed to cool. The upper thermocouple is continuously monitored by the computer, and at preset intervals (typically 10°C), data collection is initiated. Each data collection cycle consists of reading the upper and lower thermocouples, the heat flow meter, and the Seebeck voltage. The current pulse is then generated, and the current and sample ohmic voltages are measured. A complete set of data is taken in 150 msec. The last data point is usually taken at 30°C, 5°C above the base. The entire temperature range is covered in 6 to 12 h. Since the data collection is under computer control, run-to-run reproducibility is very good.

The temperature measurements are better than 0.1°C on a relative basis. The absolute temperature values are no better than typical thermometry accuracy but are not critical in the analysis.

Analysis of Data

To convert the Seebeck voltages, electrical resistances, and the sample thermal conductances to the Seebeck coefficient, resistivity, and thermal conductivity as a function of temperature, it is necessary to deconvolute the experimental data. This is done using the following relationships:

$$\text{Measured Seebeck voltage} = V_s = \int_{T_c}^{T_h} \alpha \cdot dT \tag{1}$$

$$\frac{\partial V_s}{\partial T_h} = \alpha(T_h) - \alpha(T_c)\frac{\partial T_c}{\partial T_h} \tag{2}$$

$$\text{Measured heat flow} = Q = (A/L)\int_{T_c}^{T_h} \lambda \cdot dT \tag{3}$$

$$(L/A) \cdot \frac{\partial Q}{\partial T_h} = \lambda(T_h) - \lambda(T_c) \frac{\partial T_c}{\partial T_h} \tag{4}$$

$$\text{Measured resistance} = R = (1/Q)\int_{T_c}^{T_h} \rho \cdot \lambda \cdot dT \tag{5}$$

$$\frac{\partial(R \cdot Q)}{\partial T_h} = \rho(T_h) \cdot \lambda(T_h) - \rho(T_c) \cdot \lambda(T_c) \cdot \frac{\partial T_c}{\partial T_h} \tag{6}$$

where A is the cross-sectional area and L the length of the sample minus the depths of the thermocouple wells. The essence of the formulations of Equations 1, 3, and 5 is that the integrals are independent of the actual temperature gradient in the sample and hence are functions only of T_h and T_c.

$\alpha(T_h)$, $\lambda(T_h)$, and $\rho(T_h) \cdot \lambda(T_h)$ are solved iteratively using equations 2, 4, and 6. Note that when most of the temperature drop is across the sample $(\delta T_c/\delta T_h) \ll 1$. Also, $\alpha(T_c)$, $\lambda(T_c)$, and $\rho(T_c)$ do not change rapidly with (T_h). Thus, $\alpha(T_h)$, $\lambda(T_h)$, and $\rho(T_h)$ can be determined quickly and accurately in a simple iterative computer program. The partial derivatives are calculated using a finite difference method to determine the slopes of the desired quantities as a function of T_h. Three- and five-point slope calculations have been used.

17.3 Design Considerations: Problems, Promises, and Solutions

A *Z*-meter is inherently an instrument whose design requires compromises. As one example, proper electrical resistivity measurements require a uniform sample temperature while thermal conductivity and Seebeck coefficient measurements require a (small) temperature gradient. Furthermore, a four-point probing technique is required for λ and ρ measurements to minimize end contact effects, but standard-type side probes will disturb the axial heat flow. The arrangement shown in Figures 1 and 2 appears to be a suitable compromise.

While the Seebeck coefficient measurement is the simplest because it is independent of sample geometry, it does require corrections because of the thermoelectric power of the probe leads[13] and also accurate temperature measurements. An attractive feature of the design is that both the top and bottom thermocouples are thermally guarded, the top by the essentially uniform temperature of the heater block and the bottom by the low temperature gradient in the heat flow meter. The use of zirconia sleeving instead of silica reduces the heat transport by the sleeving.

Although the total resistance of the sample is little changed by the wells, the distortion of the equipotential lines under the wells, which is basically a function of the radius of the wells, is significant. Computer modeling for 50-ml diameter wells in a 6.3-mm square cross section sample indicates that an effective length can be used to correct for the wells when calculating the resistivity. Specifically, $L(\text{eff}) = (L - 0.095)$ cm where L is the length between well bottoms. For 1- to 1.5-cm long samples, this correction is essentially independent of well depths up to the 35 ml which were modeled. The potential along the bottom of the wells varies little near the center, which means that the size of the thermocouple bead and its location in the well are not critical.

The effect of the wells on the thermal conductivity are not important because (1) the wells are not a thermal void because of the presence of the thermocouple wires/sleeving and argon and (2) the heat flow meter is usually calibrated with a reference sample having an identical geometry to the test samples. However, an absolute calibration of the heat flow meter was made using the known properties of copper. Up to 300°C, the results agree within 2% with a Pyroceram 9606 reference sample.[14] This degree of agreement is fortuitous (although the temperature dependence is not) because the accuracy of the calculation is limited by the ability to model the foot and shoulder of the heat flow meter.

Typically 80% of the temperature drop is across the sample and 20% across the heat flow meter. The large temperature drop in the sample means that the final values obtained for any one parameter at a given temperature are not spatially averaged over the sample. Specifically, since the

temperature of the hot end is changing most rapidly, it contributes the bulk of the signal during a run. Also, because of the temperature dependence of the various parameters, the weighted contribution of each part of the sample changes with temperature. To check the assumption of sample uniformity, runs can be repeated with the sample turned over.

A final anomalous situation is that a thermal steady-state condition never exists in this instrument. Usually, under such conditions, corrections for the heat capacity of the sample have to be made. However, as long as the thermal mass of the heater block is much larger (>100:1) than the thermal mass of the sample, this correction can be neglected. Under such conditions, taking data as the instrument naturally cools, the heat flowing through the sample from the heater block is always large compared to the internal heat of the sample. The cooling rates at 600°C, for example, are of the order of 10°C/min while it may take 1 or 2 h to cool from 40 to 30°C. These are the proper rates and cannot be speeded up without making heat capacity corrections. It is important in the deconvolution to obtain data near the base temperature, although this takes the bulk of the time. In practice, one simply lets the meter collect data overnight.

The above assumes that the major heat loss of the heater block is entirely through the sample. Good insulation around the heater block is thus important in order to minimize the size of the heater block, i.e., its total thermal mass.

Insulation around the sample is also critical. The assumption of only axial heat flow, i.e., no radial flow into or out of the sample, is only approximated because, for most materials, the thermal conductivity changes significantly with temperature. This results in a nonuniform temperature gradient in the sample; however, the apparatus was designed to create a uniform gradient outside the sample. The mismatch between these gradients will produce a radial heat flow, which is believed to be the largest source of error for the heat conductivity and electrical resistivity values above 300°C.

Close-fitting, ideal thermal insulation around the sample would resolve this problem (as it would resolve many problems in thermal measurements). Looking to the future, high-temperature aerogels might approximate such a material.

At present, several approaches to the radial heat flow/insulation problem can be considered. One is to design for samples with large cross-sectional areas. Also, calibration should be done with reference samples which have a similar temperature dependence of the thermal conductivity. This is just as important as choosing a reference sample with similar average values. In any case, the relative comparison of samples of the same material is still valid even if the absolute values are in error.

The use of vacuum would greatly improve the thermal insulation. However, the thermal contacting to the ends of the sample and of the thermocouples with the sample would be severely degraded.

A final solution to the nonuniform temperature gradient across the sample is to design a "low temperature gradient" meter, i.e., one in which the temperature drop across the sample is 20% or less of the total. The general principles and analysis involved are the same as described above. The design problems, however, shift to the heat flow meter where the response time of the heat flow meter and thermal guarding of the lower thermocouple would be two of many considerations.[15]

A high signal-to-noise ratio is important because changes in the slopes of the measured data as a function of temperature, i.e., point-by-point differences, determine the final temperature dependence of the desired parameters. An alternative procedure is to fit the raw data to analytical functions, thereby smoothing the data, and then taking the derivatives of the functions. The functions cannot be too complicated or they will reflect the noise rather than average the data. However, our experience is that simple functions cannot fit the data over the full temperature range. Fitting fourth-degree polynomials over 100 to 200°C intervals and matching the parameters at the interval edges have proven successful.

By thermally isolating the base and using a refrigerant in the base cooling coils, the meter could be used to study materials for cooling applications down to −40°C. Since a much more limited temperature range is usually of concern for such materials, many of the problems mentioned above are reduced. Also, with the preamps thermally tied to the lower temperature, a reduction in amplifier noise would be realized.

Anisotropic materials, e.g., bismuth telluride,[16] with grain sizes a significant fraction or larger than the size of the wells present formidable problems. The only satisfactory procedure we have found using our meter is to first measure the resistivity at room temperature on a large area sample or test puck using soldered contacts. This test puck is then cut into several smaller samples to fit the *Z*-meter where standard runs are carried out. The temperature-dependent resistivity values obtained are then normalized to the original room temperature values obtained on the original piece. Since spatial nonuniformities are often found in large test pucks, e.g., from the center to the edges, more than one sample measurement in the *Z*-meter is often required per test puck.

Alternatively, samples could be prepared for the *Z*-meter without wells but with soldered metal end pieces. An emphasis in our design is to make sample preparation as simple as possible. Wells are included to get "four point probe" contacting to eliminate contact impedance when using pressure contacts and gasketing material. For high-temperature studies, this appears to be the simplest procedure because high-temperature brazing would otherwise be required, and there could be problems of chemical reactions or welding to the bottom of the heater block. However, for low-temperature anisotropic materials, metal end contacts appear to offer significant advantages.

17.4 Summary and Recommendations

The inherent advantages of an automated *Z*-meter are such that the inability to create a universal meter for any type of sample over extreme temperature ranges should not preclude its use. *Z*-meters do have a place in a serious thermoelectrics laboratory and as an instrument for quality control. This is especially true for research and development directed towards the improvement of a particular material where timely, relative measurements are important. Such measurements would be useful for many common thermoelectric materials for cooling and low temperature (<700°C) generator applications.

A meter has been described which functions well on an absolute scale up to 300°C and on a relative scale up to 700°C. It employs a large temperature difference across the sample, which means that the results and the temperature stress on the sample reflect real-life situations. Data are not taken under thermal equilibrium conditions and the experimental design takes this into consideration. Key requirements for this type of meter are (1) the use of a computer to control the sequence of data collection, (2) a well-defined thermal geometry, and (3) a high signal-to-noise ratio in the thermometry and voltage probes. Many of the problems and solutions described will be common to any such meter.

References

1. Ioffe, A. F., *Semiconductor Thermoelements and Thermoelectric Cooling,* Infosearch Ltd., London, 1957, 38.
2. Putley, E. H., Thermoelectric and galvanomagnetic effects in lead selenide and telluride, *Proc. Phys. Soc. B (London),* 68, 35, 1955.
3. Harman, T. C., Special techniques for measurement of thermoelectric properties, *J. Appl. Phys.,* 29, 1373, 1958; Harman, T. C., Cahn, J. H., and Logan, M. J., Measurement of thermal conductivity by utilization of the Peltier effect, *J. Appl. Phys.,* 30, 1351, 1959. (See also Kaganov, M. A., Lisker, I. S., and Mushkin, I. G., On the problems of measuring thermoelectric properties of semiconductors, *Soviet Phys. Solid State,* 1, 905, 1959.
4. Lisker, I. S., Determining an efficiency criterion for semiconductor materials, *Soviet Phys. Solid State,* 8, 1042, 1966.
5. See, e.g., Herincky, C. and Monfils, A., Electrical determination of the thermal parameters of semiconducting thermoelements, *Br. J. of Appl. Phys.,* 10, 235, 1959; Airapetyants, S. V., Measurement of the thermoelectric properties of semiconductors at high temperatures by the Harman method, in *Thermoelectric Properties of Semiconductors,* Kutasor, V. A., Ed., Consultants Bureau, New York, 1964; Campbell, M. R. and Hogarth, C. A., A correction to the theory of Harman's method of determining the thermoelectric figure-of-merit, *International Journal of Electronics,* XIX, First Series,

571, 1965; Al-Obaidi, T. A. A. and Goldsmid, H. J., Determination of the thermoelectric figure-of-merit from thermal conductivity measurements, *Energy Conversion*, 9, 131, 1969; Efremov, A. A. and Pushkarskii, A. S., The measurement of the thermoelectric figure-of-merit of semiconductors in the presence of heat transfer at the junctions, *High Temp.-High Press.*, 2, 171, 1970; Trefroy, J. U., Thin film characterizations using the Harman technique, *Proc. Fourth International Conference on Thermoelectric Energy Conversion*, University of Texas, Arlington, 1982, 79.

6. Phillips, L. S., The measurement of thermoelectric properties at high temperatures, *J. Sci. Instrum.*, 42, 209, 1965.
7. Kaplan, M., Thermoelectric properties of rare earth chalcochromites, *Proc. Fourth International Conference on Thermoelectric Energy Conversion*, University of Texas, Arlington, 1982, 37.
8. Wartanowicz, T. and Goschorski, M., Automatic measurement of thermoelectric material properties, *Proc. Seventh International Conference on Thermoelectric Energy Conversion*, University of Texas, Arlington, 1988, 156.
9. Vedernikov, M. V., Konstantinov, P. P., and Burkov, A. T., Development of automated techniques of measuring the temperature dependences of the transport properties of thermoelectric materials, *Eighth International Conference on Thermoelectric Energy Conversion*, Nancy, 1989, 45.
10. Van Wynsberghe, R., Rapid simultaneous measurement of thermoelectric material properties, *Proc. Sixth International Conference on Thermoelectric Energy Conversion*, University of Texas, Arlington, 1986, 28. This paper provided the motivation for our own work but it is noted that it has serious methodological flaws.
11. Yoshida, I. and Yunoki, I., Automatic measuring system of thermoelectric properties with a desk-top computer, *Proc. Sixth International Conference on Thermoelectric Energy Conversion*, University of Texas, Arlington, 1986, 39.
12. Woodbury, H. H., Lewandowski, R. S., Levinson, L. M., and Loughin, S., A *Z*-Meter measurement on SiGe using a large-temperature-difference apparatus, *Proc. IXth International Conference on Thermoelectrics*, Pasadena, 1990, 303.
13. Cusack, N. and Kendall, P., The absolute scale of thermoelectric power at high temperature, *Proc. Phys. Soc. (London)*, 72, 898, 1958.
14. Powell, R. W. et al., Thermal Conductivity of Selected Materials, National Standard Reference Data Systems, U.S. Department of Commerce, Washington, D.C., 25 November 1966. A least squares fit to the curves from 0°C to 700°C gives $k = 24.7 + 5456/(T + 334)$mW/cm-sec where T is in C.
15. Wu et al. have approached the problem of radial heat flow by measuring the temperature profile along hot and cold probes to a sample, and from this determining and correcting for heat loss in the sample. Wu, C. T., Lu, C. W., and Chou, D. J., The computer aided TE properties measurement system, *Proc. IXth International Conference on Thermoelectrics*, Pasadena, 1990, 312.
16. Goldsmid, H. J. and Situmorang, M., Sintered bismuth telluride alloys — problems of orientation, *Eighth International Conference on Thermoelectric Energy Conversion*, Nancy, 1989, 1.

18

Methodology for Testing Thermoelectric Materials and Devices

Richard J. Buist
TE Technology, Inc.
Traverse City, Michigan, U.S.A.

18.1 Introduction

A method was developed in the early 1960s by Harman and Honig[1] for testing the AC resistance and figure-of-merit, Z, of a thermoelectric material sample. This method provided a direct measurement of Z, but lacked precision and reproductibility, primarily due to the mechanical and electronic limitations of the instrumentation.

A new method has been developed which is based on a similar concept but has some fundamental differences which give rise to improvements in accuracy and reproducibility. The fundamental similarity is that both techniques are designed to resolve the voltage components of a thermoelectric device. The fundamental difference is that the Harman[1] method does this by measuring the *resistive* component, whereas the new method measures the *Seebeck* component.

This new test method presented in this chapter is referred to as the "TRANSIENT" test method. The TRANSIENT method applies to completed, modular devices as well as individual thermoelectric material samples. It provides for the direct measurement of all the parameters needed to characterize the thermoelectric properties of materials or devices under test.

The key to the TRANSIENT method is a computer-driven, high-speed, high-resolution, integrating voltage measurement system which is capable of accurately resolving the voltage components in an active thermoelectric device or sample. The subsequent computer analysis yields values for the Seebeck coefficient, α, electrical resistivity, ρ, thermal conductivity, λ, and figure-of-merit, Z. These parameters are measured simultaneously on the same sample via an absolute method which requires no reference or standard material for comparison.

Data are presented illustrating the application of this method over a wide temperature range with an extremely high level of reproducibility.

0-8493-0146-7/95/$0.00+$.50

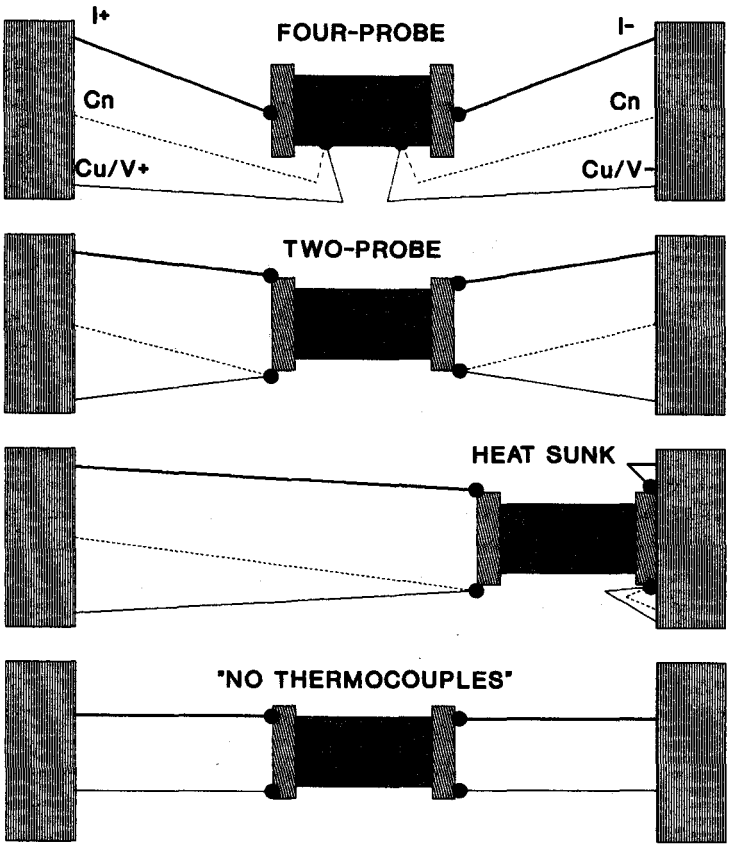

Figure 1 Optional test configurations for a TE pellet sample.

18.2 Optional Test Configurations

The term, "thermoelectric device" (TED), referred to in this chapter consists of either a thermoelectric sample pellet or a module composed of one or more pairs of n- and p-type thermoelectric pellets. The versatility of the TRANSIENT test method allows for many different test configurations for both types of TEDs.

Figure 1 illustrates four different test configurations for a thermoelectric pellet sample. The first of these is a suspended sample employing a four-probe technique. This test method is necessary whenever the contact resistance is unknown or significant compared to the resistance of the thermoelectric pellet. Copper/constantan (Cu/Cn) thermocouples are attached directly to the thermoelectric pellet by resistance welding or some other suitable process. The copper halves of these thermocouples also serve as voltage probes. Difficulties with this configuration are that: (1) current flow through the TE pellet can be disturbed by the presence of the thermocouples; (2) voltage pick-up in the probes can result in significant errors in the thermocouple readings; (3) precise measurements of the probe separation are usually very difficult to obtain; and (4) the voltage and temperature "planes" are affected by the probes and, therefore, are not nearly as well defined at the probes as they are at the opposite ends where high-conductivity end caps are applied.

The indicated two-probe configuration is recommended for most thermoelectric materials where good contacts are relatively easy to obtain. However, care should be taken to place the current and thermocouples at opposite edges of the end caps in order to avoid voltage pick-up in the thermocouples. Essentially, the thermocouple should not be placed in a position on the end cap where current "lines" will intersect it. Tests were performed on a TE pellet sample to monitor the

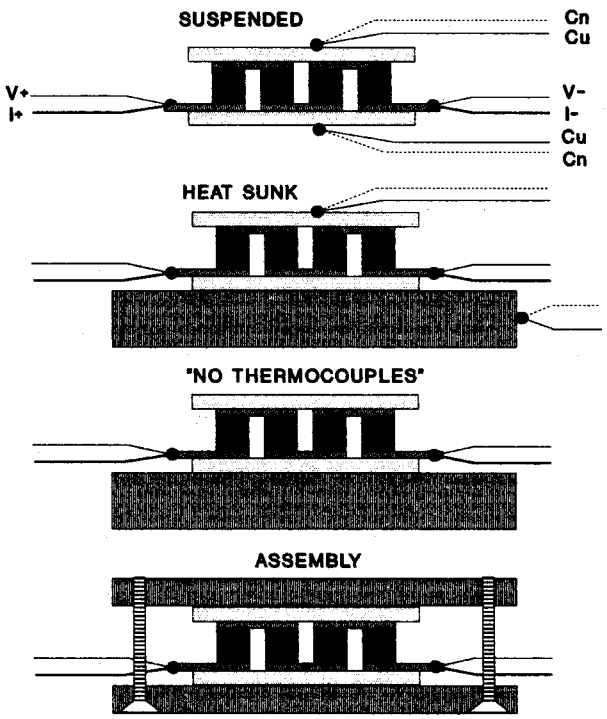

FIGURE 2 Optional test configurations for a TE module.

thermocouple reading with and without applied current and zero voltage pick-up was confirmed. The configuration referred to in Figure 1, HEAT SUNK, is also applicable and, in fact, was used to obtain the temperature-dependent data presented in this chapter. There were some slight differences in the correction factors and in the TED time constant, but, due to the bipolar test sequence employed, there was essentially no *significant* error difference between the SUSPENDED and HEAT SUNK configurations. The primary advantageous feature of the HEAT SUNK configuration is that the TED can be thermally attached to the top of a multistage thermoelectric cooler to control its temperature yet maintain a high degree of TED temperature stability.

The NO THERMOCOUPLES configuration is used to obtain ρ and ZT measurements. Very simple connections can be used to obtain "quick" data on these two key material parameters. These tests are very effective for screening samples prior to more rigorous testing. This mode is especially effective for rapid testing of TE modules and will be discussed in more detail below.

Examples of some test configurations for a thermoelectric module are given in Figure 2. The SUSPENDED and HEAT SUNK configurations are essentially the same. The difference in the correction factors between these two configurations is even less than for the thermoelectric pellet samples. The method used to attach the thermocouples was simply to apply a tiny "dab" of thermal compound into which the thermocouple junction was imbedded. It was held in place under compression with Scotch Tape. This has proven to be a very effective technique when properly applied.

Unlike the thermoelectric pellet samples, the thermocouples will not be in contact with the active circuit and voltage pick-up will not be a factor. However, care must be taken to attach voltage probes directly onto the input tabs but not under the same junction as the current probes. This must be done in order to avoid the voltage created by contact resistance, especially if "alligator" clips are used. Dual contact "Kelvin clips" are excellent for this purpose and were used in the measurement of the module test data presented herein.

As mentioned above, the NO THERMOCOUPLES configuration provides the ultimate in simplicity, in "hook-up" and test speed. As will be discussed below, the parameters *measured* using

this configuration are ρ and ZT. This is sufficient to assure the quality of production of the thermoelectric modules. Furthermore, since a ±3°C of the error in absolute temperature, T, produces only 1% error, the figure-of-merit, Z, is extractable even if the temperature of the thermoelectric module is only approximately known, such as in the ambient test of thermoelectric modules.

8.3 Device Performance Forecasts

In order to translate the measured parameters into meaningful thermoelectric module parameters, algorithms have been developed which provide a dependable projection of the Seebeck coefficient using ρ, Z, and certain thermoelectric material factors which can be derived from prior tests using thermocouples applied on previous modules or TE materials. This algorithm process involves the determination of the parameter Q_s which is related to the effective mass times mobility product. The shape of the Q_s "response surface" as a function of the measured ρ and ZT yields a means to calculate the Seebeck coefficient with quite dependable results, as shown below. Thermal conductivity can be determined from the other three parameters and enables full characterization of the TE module to be undertaken at ambient temperature.

The Q_s parameter, plus another calculated parameter related to lattice thermal conductivity, Q_λ, provide the keys to a dependable method of forecasting the temperature dependence of each of the thermoelectric material parameters. These data are used in combination with a temperature-dependent thermal model to forecast the performance of the tested TE module over the entire continuum of thermal and electrical parameters with remarkable accuracy. The key device performance characteristics of the TED are calculated, such as ΔT_{max}, I_{max}, V_{max}, and Q_{max}. This information is projected for any selected hot side temperature enabling pass/fail forecasting under any conceivable final use of the TED. Thus, this test, taking only about 1 min to carry out, can be used to determine whether or not the TED under test will perform properly in the final product.

The TRANSIENT test can be made on a completed assembly as long as the TE power leads can be accessed. Of course, the test time will be increased due to increased thermal masses in contact with the TE module, but this test will still take less time than a full performance test. Furthermore, the TRANSIENT test provides other key system information in addition to a full set of projected system performance curves. That is, comparison with prior TE module test data will yield the overall loss conductance of the system. This will provide a simple, fast, and accurate means of evaluating the quality or effectiveness of a given thermoelectric assembly with no extra test time. Another important output from the TRANSIENT test is the overall time constant of the system. This information is very useful where system cool-down time is of interest.

These tests can also be used to define potential failure modes. If tests are made before and after an observed degradation or on a returned thermoelectric module or assembly, the material parameter data extracted via the TRANSIENT test can provide insight as to what caused the failure. For example, if the electrical resistivity increased without a corresponding increase in Seebeck coefficient, the failure would most likely be due to failed contacts or mechanical fracture in the thermoelectric material. If it did vary with α (yielding not much change in Q_s), it would imply a change in the material properties, probably resulting from contaminant diffusion, perhaps due to overheating.

8.4 Thermoelectric Device Voltage

In order to understand the nature and detail of the TRANSIENT test method, a review of some of the basic effects of a TED is appropriate. As an electrical current, I, is applied to a TED, it will develop a voltage, V. If Ohm's law were the only relationship to apply, the resulting voltage would be in direct proportion to the applied current. The constant of proportionality would be the electrical resistance, R. However a TED does not follow Ohm's law. This is because a "good" TED will have a significant *device* Seebeck coefficient, α, and low enough thermal conductance, K, to support a temperature differential, ΔT. This will result in the creation of a significant additive

Seebeck voltage, V_o. The resulting expression for the voltage across a TED is, therefore, given by the following equation:

$$V_i = V_o + V_r \quad (1)$$

where $V_o = \alpha^*\Delta T$ and $V_r = I^*R$.

At first glance, it might also be surmised that if the current is kept very low, perhaps a ΔT will not be generated and the first term can be ignored. This is *definitely not the case!* In fact, the V_o term can be proportionally larger for small currents. After all, it can easily be non-zero even when the current, and therefore V_r, is zero.

The quantities V_i, I, and ΔT can be measured, but it is not easy to separate the two components of voltage, V_o and V_r. The Harman[1] method resolves these two voltage components by creating a bipolar square-wave AC current using a mechanical chopper. Thus, V_r reverses polarity but V_o does not. The resulting voltage signal is passed again through the same chopper used to generate the AC current in order to convert the AC voltage to DC for measuring purposes. There are several problems with this experimental set-up, including noise generated by the opening and closing of electrical contacts and a momentary "dead-band" during each half-cycle. Some improvements have been made over the years using more sophisticated electronic switching, but fundamental problems still exist in obtaining precise measurements.

One of these fundamental problems is that the Peltier effect is still in operation during the half-cycle of applied current and this voltage does rise during each on-cycle. A typical TE pellet 1.14 mm long has a time constant of less than 1 s. Consequently, at the typical applied current frequency of 40 Hz, the voltage will rise as much as 5% during each half-cycle. This introduces corresponding errors in the measurement of V_r. Higher frequencies will lower this error but will create other errors in the voltage measurement due to inductance in the circuit.

The use of commercial AC resistance meters does not solve the problem. They typically employ sinusoidal applied currents and measure the RMS AC voltage. They are not sufficiently accurate for thermoelectrics because the resulting instantaneous sinusoidal Peltier effect will not be in phase with the "slower" Joule and thermal conduction effects. This very complicated thermal situation can seriously affect the accuracy of the readings. This can be demonstrated by simply monitoring the "AC-resistance" of a TED using a commercial AC resistance or voltage meter and quickly heating one surface with a lighted match. An anomalous transient AC resistance reading will be clearly evident, which cannot be explained by the temperature dependence of the TED resistance. This simple test confirms the inability of AC meters to resolve accurately the Seebeck and resistive voltage components to the precision levels needed to characterize thermoelectric materials or devices.

The solution to this problem is not to measure V_r, but measure V_o. If the current is removed and the "residual" voltage is *instantaneously* measured, that measured voltage will essentially be V_o. The problem is that the time constant for the initial decay of V_o, immediately after the current is removed, is extremely short. This will be the case even if large thermal masses are attached to the ends of the TED to slow it down. There will be a significant initial decay as a consequence of the time constant of the TE pellet which is usually very small in size and even a few milliseconds will result in significant voltage decay and uncertainty of the true V_o. Nevertheless, the TRANSIENT test and analysis technique described herein is capable of precisely determining V_o.

The situation is shown graphically in Figures 3 and 4. As current is applied in accordance with Figure 3, the voltage across the TED will be that shown in Figure 4. The voltage rises instantaneously to the value V_r, and then asymptotically to a value of $V_i = V_r + V_o$ at steady state. As the current is shut off, the voltage drops instantaneously to V_o and decays exponentially to zero. An important aspect of the hardware is to ensure that the current waveform is extremely "clean", i.e., does not contain any "spikes" or anomalies. The method is checked with a high-speed, high-resolution oscilloscope to assure that this condition is met.

The key to the TRANSIENT method is to reconstruct accurately the detail for the waveform of the actual voltage at the precise instant of switching. The key to this reconstruction is the utilization of a high-speed, high-resolution, programmable, integrating, analogue-to-digital (A/D) computer board.

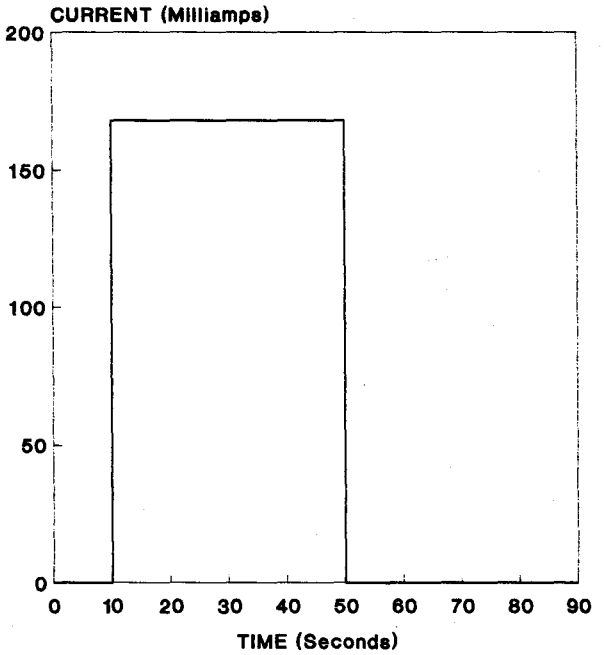

FIGURE 3 Current pulse applied to a TED.

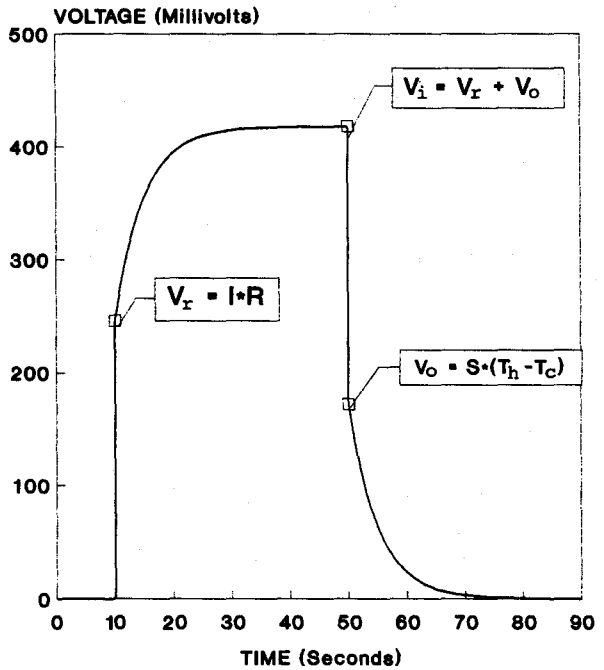

FIGURE 4 TED transient voltage due to the current pulse shown in Figure 3.

The A/D board also includes a remote terminal board which contains specially designed isothermal terminals for thermocouples together with self-contained reference junction compensation. It has 16-bit resolution which produces sub-microvolt resolution of the millivolt voltage signals obtained from single TE pellet samples. By way of software selection, a "filter mode" facilitates integration of the instantaneous voltage over a specified period of time (approximately

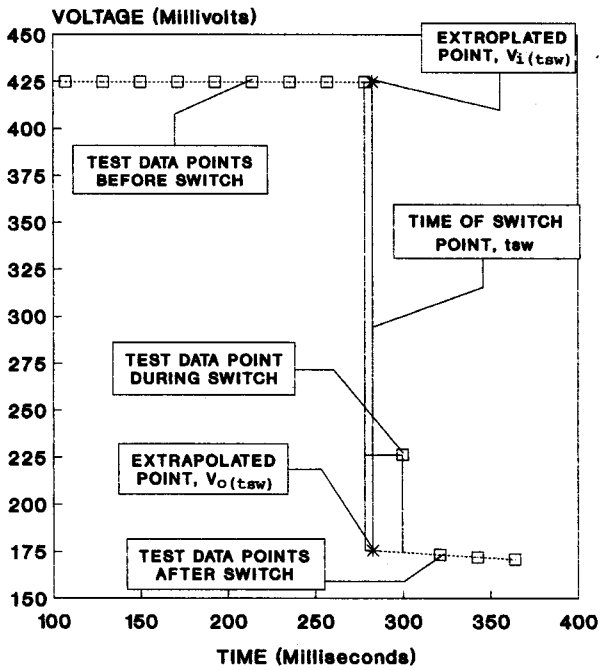

FIGURE 5 Determination of switch time, t_{sw}, and corresponding voltages $V_{i(tsw)}$ and $V_{o(tsw)}$.

20 msec). This filter mode is one of the keys to this method since it yields the time-averaged voltage over this period even for the unusual waveform produced during the switching.

The waveform analysis process is illustrated in Figures 5 and 6. Each square represents an actual measured voltage data point of a thermoelectric module. These data are obtained via repetitiously measuring the thermoelectric module voltage at a known frequency, referred to herein as the "burst" measurement. Approximately 275 msec from the start of the burst measurement, the applied current to the thermoelectric module is abruptly shut off. When this happens, an "intermediate voltage" reading is evident and is followed by the decaying "residual" voltage. The intermediate voltage reading represents the average voltage made up of the $V_i(t)$ voltage *prior* to switching plus the rapidly decaying $V_o(t)$ voltage *after* switching. This data point is used to determine the exact instant of switching, t_{sw}. That is, several test points are curve-fitted with a linear regression process to define the equation of the $V_i(t)$ curve. Actually, a simple averaging process would probably suffice, but the slope from this regression serves the dual purpose of double-checking temperature stability. That is, whenever the slope is not very nearly equal to zero, the test is automatically recycled. This check is applied as an additional constraint to the stability check discussed below.

A similar process is applied to the first few initial points following the intermediate data point in order to define the equation of the $V_o(t)$ curve. It is plotted against some of the initial test data points after switching, as shown in Figure 6. Although the nature of the voltage decay is exponential, it is not a *simple* exponential since it is made up of several discrete masses connected together. In fact, a simple exponential does not fit very well for the initial set of data points. Further discussion on this subject is given below. In the final analysis the linear regression of the first three points yields the most dependable extrapolation of the time-dependent $V_o(t)$ voltage nearby the true switching time, t_{sw}. Incidentally, a 1.26% error would have resulted from simply accepting the first measured voltage for the value of V_o. This error could be as much as 6% for small suspended TE pellet samples.

The time, t_{sw}, is calculated by constructing the original waveform using the two curve-fit equations described above and the switching time, t_{sw}, as a variable. An expression for the area under this zig-zagged broken line can be obtained from the time interval of the last test point before t_{sw}

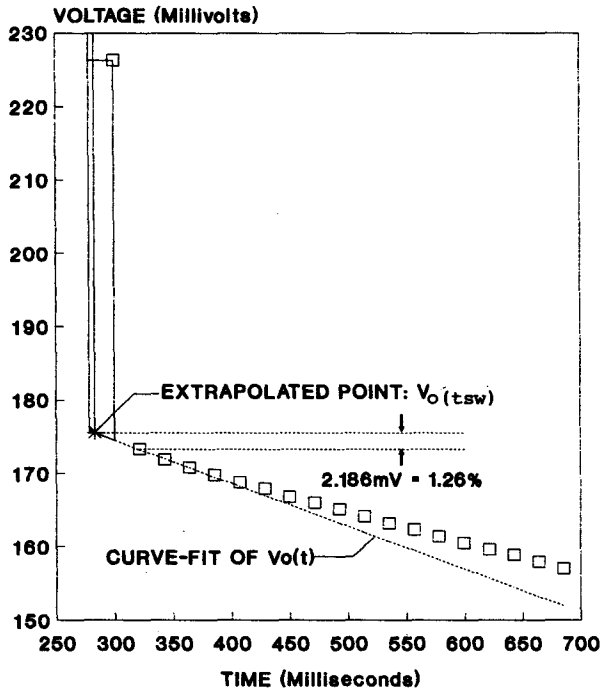

FIGURE 6 Analysis of data immediately following the switch point.

and the "test data point during switch", shown in Figure 5. This expression is set equal to the area over that same time interval using the constant voltage defined by the measured "test data point during switch". With t_{sw} determined therefrom, the true values of $V_i = V_i(t_{sw})$ and $V_o = V_o(t_{sw})$ are defined using the respective extrapolation formulas for $V_i(t)$ and $V_o(t)$. Note that these values are for the same instant in time, t_{sw}. The current I and temperatures T_h and T_c are measured prior to initiating the burst measurement, but many checks and double-checks should be made to make sure the TED under test is extremely stable prior to initiating the burst test, as discussed in more detail below.

18.5 Temperature Stability

Actual test data of an "extended burst" test on the TE module example presented above are given in Figure 7. This graph is a line graph of over 2500 test points and illustrates, among other things, the excellent, low-scatter characteristics of the test system. However, the main point of these data and the similar TE pellet test given in Figure 8, is to serve as the basis for determining the time constant of the TED under test. This parameter for each case is shown in Figures 9 and 10, respectively. The time constant can be calculated from the slope change between data points over the 2-s burst test. The relatively large amount of scatter is due to the fact that there is not much time between points (yielding a small denominator) and not much difference in measured voltage between points (yielding low resolution for the numerator). Nevertheless, the average calculated time constant is quite well defined and highly reproducible. This is essentially "free" data since it is a basic necessity of the TRANSIENT test technology. The resulting time constant can be used to characterize system cool-down and to determine the time needed for TED temperature stabilization. That is, using five to six times the time constant for stabilization time, yields approximately 24 and 60 s for the TE module and TE pellet stabilization times, respectively. This agrees quite well with the corresponding test data given in Figures 7 and 8.

The significance of this result is that this *tested* stabilization time is compared with the actual "wait time" prior to initiating the burst sequence. If the wait time had been less, the test was

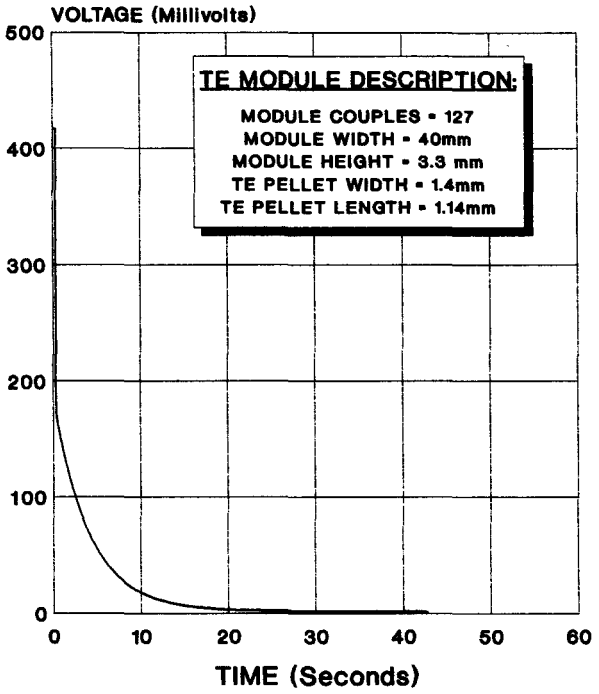

FIGURE 7 Transient test data from a TE module.

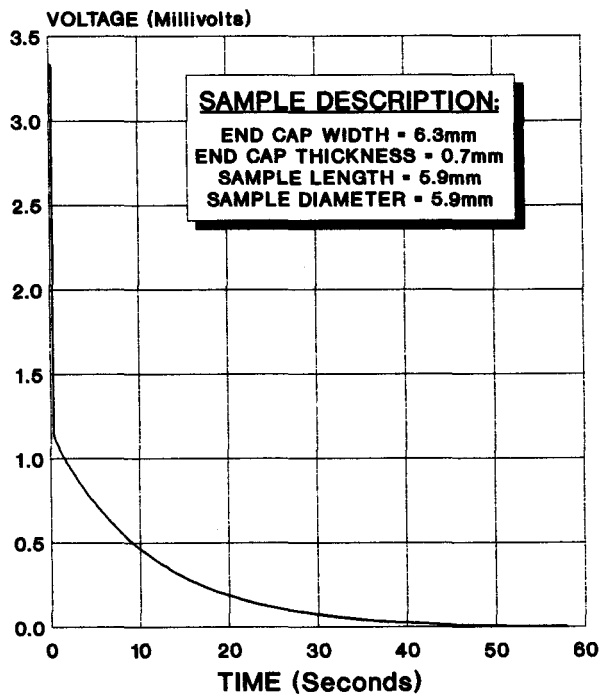

FIGURE 8 Transient test data from a TE pellet sample.

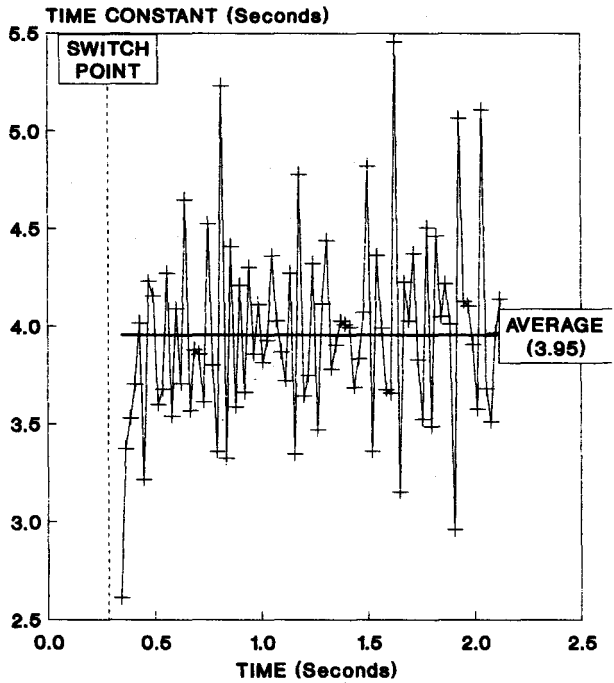

FIGURE 9 Time constant calculations from a point-to-point analysis of data taken from Figure 7.

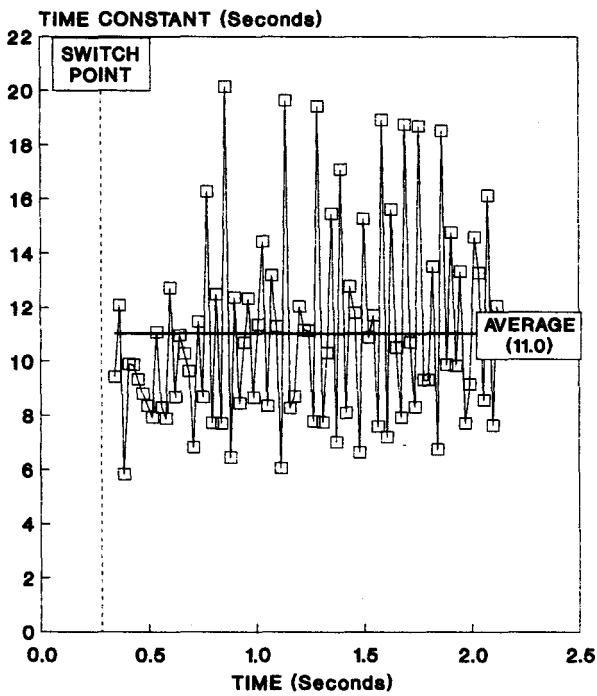

FIGURE 10 Time constant calculations from a point-to-point analysis of data taken from Figure 8.

automatically recycled, forcing the tested stabilization time on this and all subsequent tests, at a minimum. This process is repeated for each test and the stabilization time is automatically updated as required. The effectiveness of this feature is that it not only allows complete and dependable automation while maintaining test precision but minimizes the wait time and, thus, maximizes overall test speed.

The increase in the calculated time constant for the TE module in Figure 9 immediately after the switch point should be noted. This is a result of the composite thermal structure of the thermoelectric module as discussed above. This effect is indicative of the impact of the lower time constant of the basic TE pellet(s) composing the TE module and the imperfect diffusivity of the composite structure of conducting tabs and ceramic plates. Within a few hundred milliseconds, the data more exactly correspond to a simple exponential decay with a time constant consistent with the overall thermal mass of the system. Thus, the average time constant as calculated is appropriate to determine the minimum test stabilization time. In Figure 10 the initial rise is not evident for a relatively large TE pellet; this is because the composite thermal structure is much less complicated and consists of a relatively small copper end cap.

18.6 Bipolar Testing

All TRANSIENT tests are made via a two-step, bipolar process. The test being performed using one polarity of applied current, the current is reversed, and the test repeated. The primary purpose of this bipolar process is that it reduces the magnitude of the correction factors and maximizes the overall accuracy of the results.

This reversal process corrects for any thermal emfs in the test circuit and for any imperfections in the thermocouples which might cause them not to be totally identical. Since the accuracy of the test results is mostly affected by temperature *differences*, this reversal process totally cancels any unbalance or zero off-sets.

Bipolar testing is actually the key to precision testing of all the parameters of the TED, each parameter being calculated from voltage and/or temperature *differences*. The equations for each parameter derived below reveal this fact. For example, the Seebeck coefficient is calculated from two basic quantities: V_o and ΔT. V_o, in turn, is actually the *difference* between two voltage measurements and ΔT is the *difference* between two temperature measurements. Application of the bipolar method further corrects for any zero offset in voltage and any unbalance of thermocouples. Essentially, the accuracy of the results is mostly dependent on the *linearity* of the measurement system, which is an inherently excellent feature of the A/D board used in the TRANSIENT test system.

18.7 Thermal Modeling and Equation Derivations

One of the key features of the TRANSIENT test method is the utilization of a very low test current. It is calculated from the input geometry of the TED under test to yield approximately 4°C across the TED. This corresponds to approximately 1/50th of the current that would normally produce maximum ΔT. This magnitude of ΔT provides adequate signal for accuracy but not so much that it will take the TED below dew point and introduce large condensation heat loads which are difficult to accurately quantify. Also, since the ΔT is so small, the assumption of constant parameters assists making the closed form, simplified heat source equations quite rigorous. These low currents also facilitate testing of extremely high current TE material wafers.

The first step in formulating the equations for determining the TE material parameters is to set up expressions for each component of heat flow for the chosen test configuration. These expressions are summarized in Table 1. They include all active and parasitic heat sources applied to a SUSPENDED or HEAT SUNK TE module. Very similar expressions can be obtained for TE pellet samples and each of the configurations described above.

Table 2 is a set of equations formed from the sum of each corresponding expression taken from Table 1. It should be noted that the wire conduction losses and Joule heat terms are zero as a result

Table 1. Junction Heat Load Calculations for a TE Module

Heat Load Description	Heat Entering Cold Junction	Heat Exiting Hot Junction
	Positive Test Mode	
1. Module Peltier	$-N^*\alpha^*I^*T_c$	$-N^*\alpha^*I^*T_h$
2. Module conduction	$N^*\lambda^*(T_h - T_c)/L$	$N^*\lambda^*(T_h - T_c)/L$
3. Internal radiation	$R_i(T_h^4 - T_c^4)$	$R_i(T_h^4 - T_c^4)$
4. External radiation	$R_e(T_a^4 - T_c^4)$	$R_e(T_h^4 - T_a^4)$
5. Convection	$H^*(T_a - T_c)$	$H^*(T_h - T_a)$
6. Air conduction	$K_a^*(T_h - T_c)$	$K_a^*(T_h - T_c)$
7. Wire conduction	0	$W^*(T_h - T_w)$
8. Module Joule	$I^{2*}R/2$	$-I^{2*}R/2$
9. Wire Joule	0	$-I^{2*}R_w$
	Negative Test Mode	
1. Module Peltier	$-N^*\alpha^*I'^*T_{c'}$	$-N^*\alpha^*I'^*T_{h'}$
2. Module conduction	$N^*\lambda^*(T_{h'} - T_{c'})/L$	$N^*\lambda^*(T_{h'} - T_{c'})/L$
3. Internal radiation	$R_i(T_{h'}4 - T_{c'}4)$	$R_i(T_{h'}^4 - T_{c'}^4)$
4. External radiation	$R_e(T_{a'}^4 - T_{c'}^4)$	$R_e(T_{h'}^4 - T_{a'}^4)$
5. Convection	$H^*(T_{a'} - T_{c'})$	$H^*(T_{h'} - T_{a'})$
6. Air conduction	$K_a^*(T_{h'} - T_{c'})$	$K_a^*(T_{h'} - T_{c'})$
7. Wire conduction	$W^*(T_w - T_{c'})$	0
8. Module Joule	$I'^{2*}R/2$	$-I'^{2*}R/2$
9. Wire Joule	$I'^{2*}R_w$	0

Table 2. Sum of Junction Heat Load Calculations for a TE Module

1. Module Peltier	$Q_p = -N^*\alpha^*(I^*(T_h + T_c) + I'^*(T_{h'} + T_{c'})$
2. Module conduction	$Q_\lambda = 2^*N^*\lambda(T_h - T_c + T_{h'} - T_{c'})/L$
3. Internal radiation	$Q_{ri} = 2^*K_{ri}^*(T_h - T_c + T_{h'} - T_{c'})$
4. External radiation	$Q_{re} = K_{re}^*(T_h - T_c + T_{h'} - T_{c'})$
5. Convection	$Q_c = H^*(T_h - T_c + T_{h'} - T_{c'})$
6. Air conduction	$Q_a = 2^*K_a^*(T_h - T_c + T_{h'} - T_{c'})$
7. Wire conduction	$Q_w = 0$; since $T_w = T_h = T_{c'}$
8. Module Joule	$Q_{mj} = 0$; since $I \approx I'$
9. Wire Joule	$Q_{wj} = 0$; since $I \approx I'$

Where	N	= total number of thermoelectric pellets
	α	= thermoelectric material Seebeck coefficient
	I, I′	= Electrical current in POS & NEG modes
	T_h, $T_{h'}$	= Hot junction temperatures in POS & NEG modes
	T_c, $T_{c'}$	= Cold junction temperatures in POS & NEG modes
	λ	= thermoelectric material thermal conductivity
	L	= Length/area of thermoelectric pellet
	R_i	= $\sigma^*\varepsilon^*$internal surface area
	R_e	= $\sigma^*\varepsilon^*$external surface area
	σ	= Boltzman constant
	ε	= Effective emissivity (including shape factor)
	H	= Convection coefficient * external surface area
	K_a	= Air conductivity * internal space area
	W	= Sum of wire thermal conductances
	R	= Thermoelectric module electrical resistance
	R_w	= Electrical current wire electrical resistance
	T	= $(T_h + T_c)/2$
	$T_h^4 - T_c^4$	= $4^*T^{3*}(T_h - T_c)$
	K_{ri}	= $4^*T^{3*}R_i$
	K_{re}	= $4^*T^{3*}R_e$

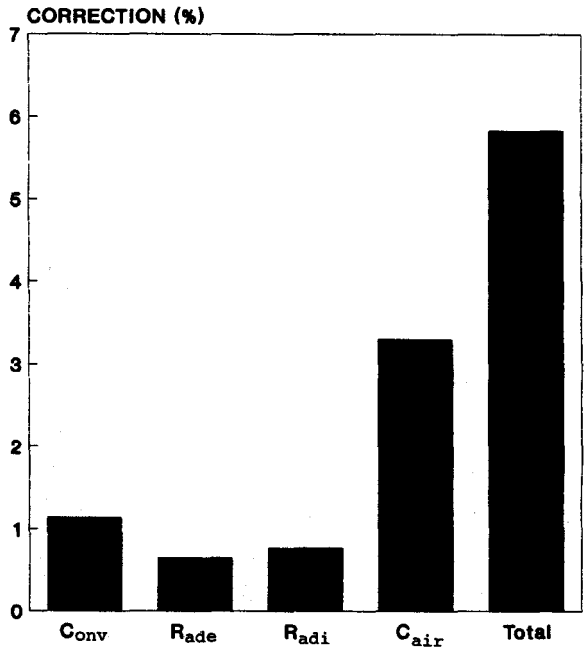

FIGURE 11 Correction factors for the TE module identified in Figure 7 tested in ambient air.

of using the same absolute value of applied current in each mode of the bipolar process; the radiation terms reduce to $T_h^4 - T_c^4$. Since T_h and T_c are set by the experiment to be a small ΔT, the first term in the Taylor expansion is an excellent approximation, as indicated in Table 2. The result is that each term below the Peltier term contains the same temperature expression.

The heat balance equation is given by

$$-Q_p = Q_k + Q_{ri} + Q_{re} + Q_c + Q_a \tag{2}$$

Substitution of the expressions from Table 2 yields an equation for α/λ (Seebeck coefficient/thermal conductivity) as a function measured parameters multiplied by an overall correction factor, C:

where
$$C = 1 + R_{adi} + R_{ade} + C_{onv} + C_{air}$$
$$R_{adi} = K_{ri}{}^*L/N/\lambda$$

$$\alpha/\lambda = \frac{C^*Da}{L^*IT_a} \tag{3}$$

$$R_{ade} = K_{re}{}^*L/N/\lambda/_2$$
$$C_{onv} = H^*L/N/\lambda/_2$$
$$C_{air} = K_a{}^*L/N/\lambda$$
$$IT_a = I^*(T_h + T_c)/2 + I'^*(T_{h'} + T_{c'})/2$$
$$D_a = (T_h - T_c + T_{h'} - T_{c'})$$

The overall correction factor, C, is equal to 1 plus a series of dimensionless correction factors derived from each remaining source of parasitic heat load. Each correction factor is a function of λ itself, requiring an iterative calculation process. However, since these factors are typically quite small, convergence is usually achieved in just a few iterations.

Figures 11 and 12 are the calculated correction factors obtained from actual tests made on the TE module and sample described above. It is observed that the total correction factor is only 6%.

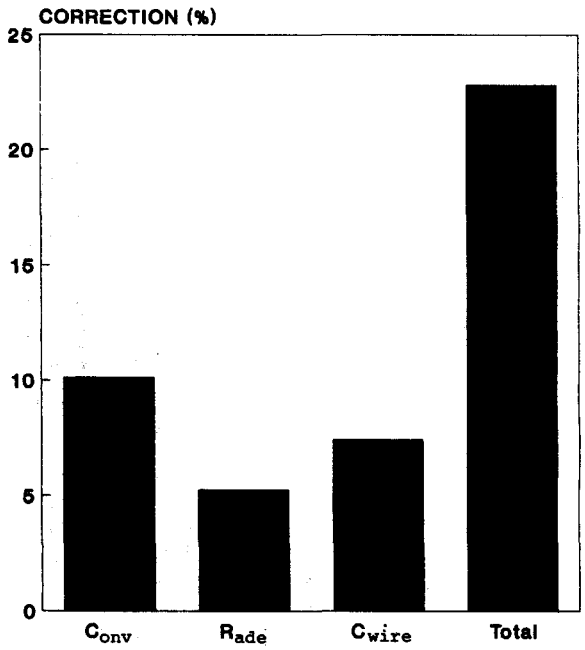

FIGURE 12 Correction factors for the TE pellet identified in Figure 8 tested in ambient air.

Thus, if the total uncertainty in the model for the correction factors were as high as 20%, the overall uncertainty of the final calculation of λ or Z would only be 1.2%.

The correction factors for the TE pellet sample are much larger, as illustrated in Figure 12, yielding a potential uncertainly of 6%. Half of that is due to convection heat loading which will disappear in a vacuum. Also, reducing the TE sample and end cap sizes dramatically lowered these factors, as illustrated in Figure 13. These data are determined from actual tests on a smaller, 2 mm square × 1.65 mm long thermoelectric pellet sample mounted on top of a multistage thermoelectric cooler in a vacuum. As observed, the total correction factor varies between 2 and 4% over the indicated temperature range yielding an overall uncertainty of less than ½%.

Comparison testing in a vacuum vs. air has provided a very accurate means of empirically establishing the overall convection and air conduction coefficients used in the corresponding correction terms. This further improves the accuracy of the correction coefficients and of the final test data.

The voltage equations for the TED under test are given by

$$V_o = N^*\alpha^*(T_h - T_c) + \alpha_w{}^*(T_h - T_c) \tag{4}$$

$$V_o' = N^*\alpha^*(T_h' - T_c') + \alpha_w{}^*(T_h' - T_c') \tag{5}$$

$$V_i = N^*\rho^*L^*I + V_0 \tag{6}$$

$$V_i' = N^*\rho^*L^*I' + V_o' \tag{7}$$

Note that the α_w is the thermopower of the voltage wires and must be included for all TE pellet calculations. It is included throughout all formulas but simply set to zero for TE modules since both voltage probes will be at the same temperature.

The calculation of α and ρ are obtained from the set of voltage equations:

$$\alpha = \frac{V_{oa}}{N^*D_a} - \alpha_w \tag{8}$$

$$\rho = \frac{V_{ia} - V_{oa}}{N^*L^*I_a} \tag{9}$$

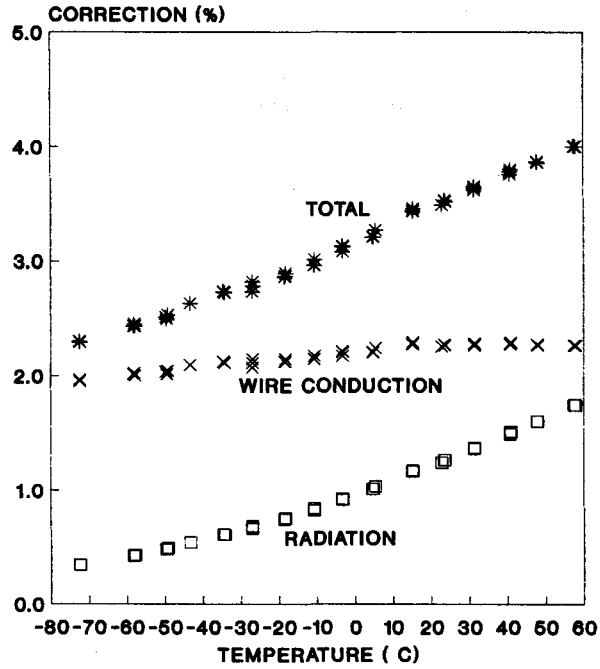

FIGURE 13 Correction factors for a 2 mm square × 1.6 mm long TE pellet sample mounted onto the top stage of a multistage thermoelectric cooler in a vacuum of 10 mtorr.

where

$$V_{oa} = (V_o + V_{o'})/2$$
$$V_{ia} = (V_i + V_{i'})/2$$
$$I_a = (I + I')/2$$

The equation for λ is formed by dividing Equation 8 by Equation 3 to yield the following equation:

$$\lambda = \frac{L^*IT_a^*V_{oa}}{C^*N^*D_a^*D_a} + \frac{L^*IT_a^*\alpha_w}{C^*D_a} \tag{10}$$

The equation for Z is formed by multiplying Equation 8 by Equation 3 and dividing by Equation 9 to yield the following equation:

$$Z = \frac{C^*I_a^*V_{oa}}{IT_a^*(V_{ia} - V_{oa})} - \frac{C^*I_a^*\alpha_w/N/D_a}{IT_a^*(V_{ia} - V_{oa})} \tag{11}$$

Note that each term on the right side of Equations 8 to 10 is *measurable* yielding a truly *absolute* test methodology for each thermoelectric material parameter. Also, the second terms of Equations 10 and 11 go to zero for a TE module or when α_w can be ignored compared to α. If this is applied together with the realization that I_a/IT_a is nearly equal to 1/T, Equation 11 reduces to the well-known Harman[1] formula:

$$ZT = \frac{V_{oa}}{(V_{ia} - V_{oa})} \tag{12}$$

This simplified formula accounts for the fact that the resultant Z test data (presented below) exhibits very low scatter, since it is primarily dependent on V_o and V_i which can be accurately measured using the TRANSIENT test method.

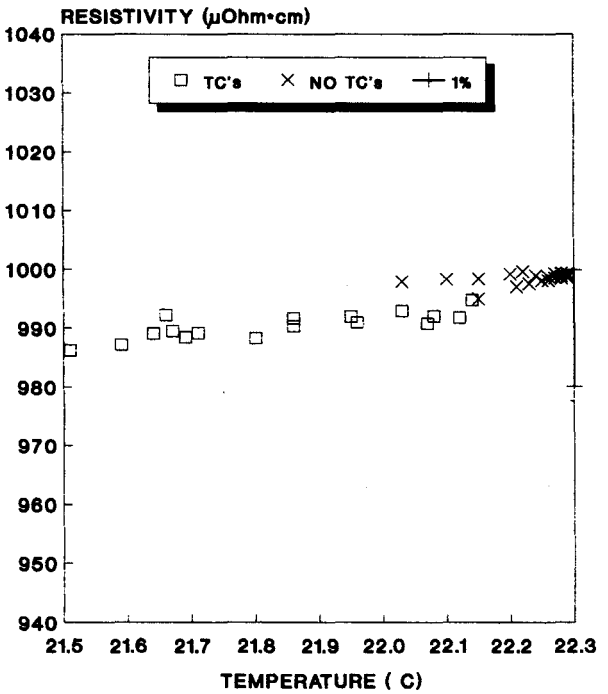

FIGURE 14 Electrical resistivity test data taken on the TE module tested via the SUSPENDED and NO THERMOCOUPLES configurations.

18.8 TE Module Test Results

To illustrate the output obtainable from the TRANSIENT test system, the TE module described in Figure 7 is tested via the SUSPENDED and NO THERMOCOUPLES configurations in ambient air. The results are plotted as a function of temperature in order to separate temperature-dependent effects from data scatter.

Electrical resistivity and Z data are given in Figures 14 and 15. As expected, the scatter is less than 1% for both parameters (1% reference bar at the far left border of the graph). Furthermore, there is no significant difference between the test results with and without thermocouples.

Seebeck coefficient data are given in Figure 16. The following observations were made: (1) the scatter in the data taken using thermocouples is significantly higher than that with no thermocouples. This is due to the resolution limitation of the measured small ΔT of the TED and the imperfect thermocouple attachment of a thermal grease dab and Scotch Tape. With this taken into consideration, the observed maximum deviation of less than 1% is very good. The Seebeck scatter of TE pellet tests is typically better because of the better thermal contact of the thermocouples. This is validated in the temperature-dependent data presented below. (2) There is approximately 1% separation between the algorithm-derived Seebeck coefficient and the measured Seebeck. This level of agreement validates the dependability and effectiveness of the algorithm. (3) The scatter in the NO THERMOCOUPLES data is very low as might be expected since it was calculated from the low scatter ρ and Z data.

Thermal conductivity data are given in Figure 17. Basically, the same observations made for the Seebeck data also applied to these data. However, the scatter is a little larger for the THERMOCOUPLE case and the separation between test configurations is approximately 2%. This is still considered very good considering the complexity of the thermal algorithm used to forecast this parameter.

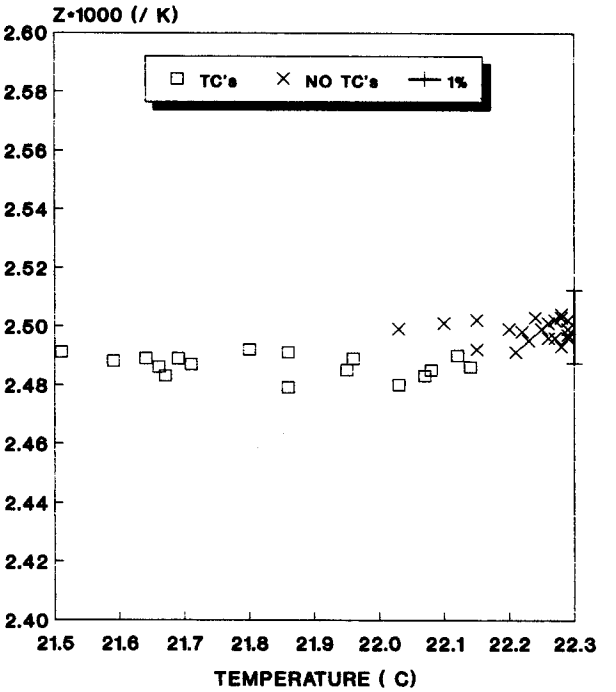

FIGURE 15 Figure-of-merit test data taken on the TE module tested via the SUSPENDED and NO THERMOCOUPLES configurations.

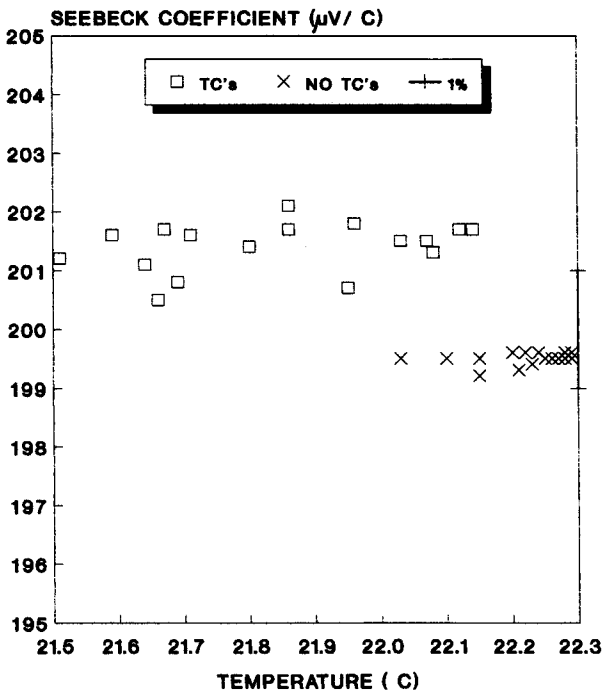

FIGURE 16 Seebeck coefficient test data taken on the TE module tested via the SUSPENDED and NO THERMOCOUPLES configurations.

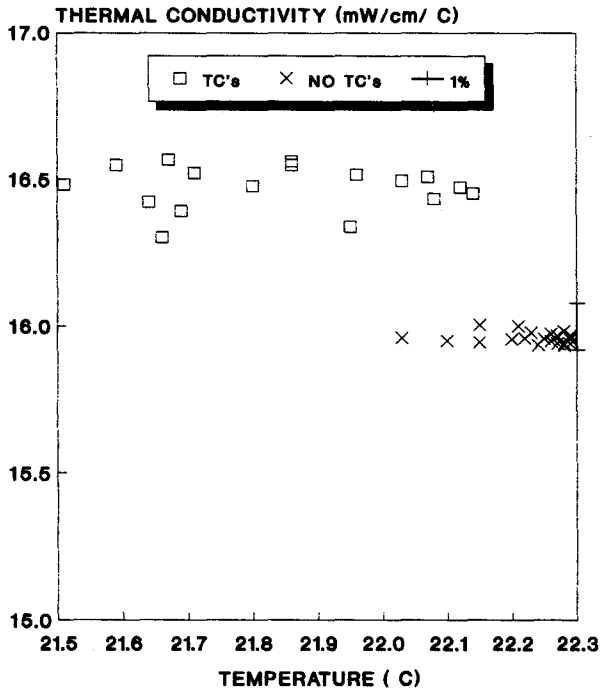

FIGURE 17 Thermal conductivity test data taken on the TE module tested via the SUSPENDED and NO THERMOCOUPLES configurations.

18.9 Temperature-Dependent Test Data

Temperature-dependent TRANSIENT testing is performed on one "standard" and one "special" TE pellet sample. Both samples are 2 mm square × 1.65 mm long TE pellets mounted on top of a multistage TE cooler in a vacuum. The correction factors calculated from the "standard" test data are presented in Figure 13.

This configuration is particularly effective whenever extreme precision of all results is required. For "unusual" thermoelectric materials, it is also useful to test at least one TED from these materials to "calibrate" the algorithms used in the NO THERMOCOUPLES test mode and to project temperature dependence for thermal modeling thermoelectric module performance parameters.

The test data collected on both samples (tested three times each) are given in Figures 18 to 21. The following observations are made: (1) the resistivity scatter is *very* low since the data were not dependent on thermocouples, correction factors, or vacuum level. (2) The Seebeck scatter is not quite as good because of the dependence on ΔT measurements. Nevertheless, the scatter is still quite low because of the care given to precision thermometry. (3) The thermal conductivity scatter is largest, as expected, since these measurements are affected by correction factors, thermocouples, and vacuum level. (4) The Z scatter is better than the thermal conductivity scatter because it is not affected by thermocouples, as explained above. (5) Overall, the reproducibility is excellent to the point that it is difficult to identify the three separate measurements made for each parameter at each temperature point.

Finally, the importance of the precision and flexibility of the TRANSIENT test methodology presented herein is exemplified in Figure 21. The Z vs. temperature for the standard sample is typical for "normal bismuth-telluride" TE materials. If only tested at room temperature, the "special" TE material produced at TE Technology, Inc. would not have identified any significant Z enhancement. However, its low-temperature Z data represent unusually high performance. It would greatly improve the cooling performance of a low-temperature multistage cascade.

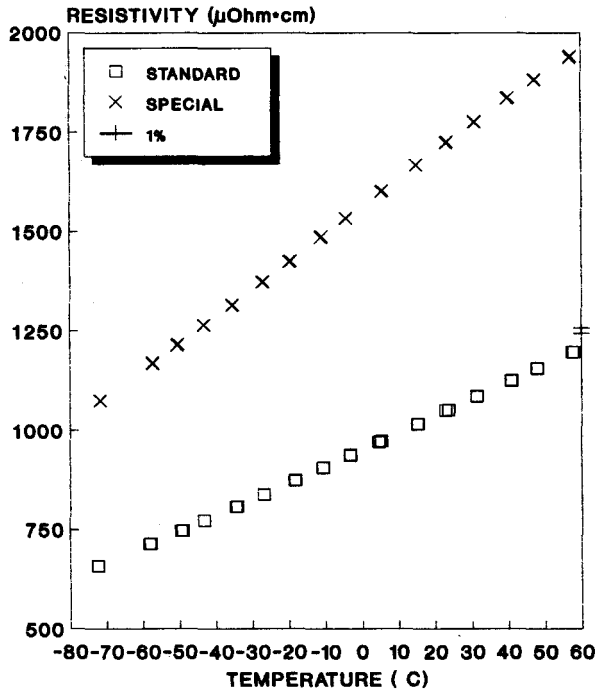

FIGURE 18 Electrical resistivity test data taken on standard and special n-type TE pellets as identified in Figure 13.

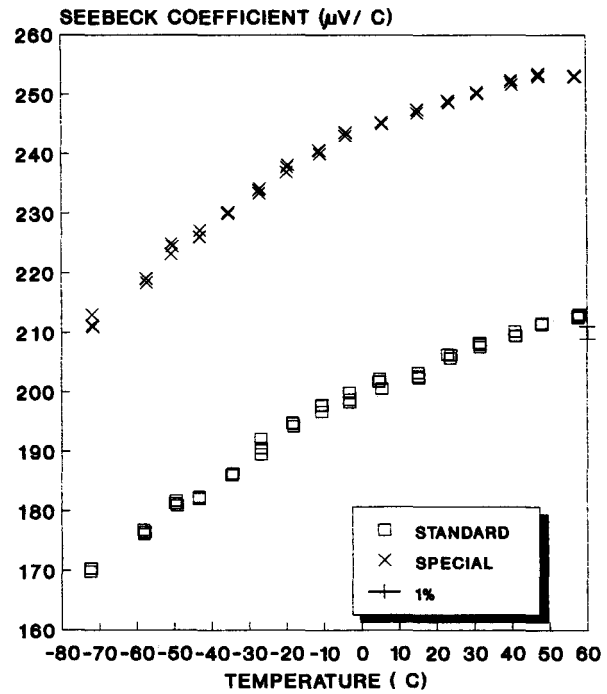

FIGURE 19 Seebeck coefficient test data taken on standard and special n-type TE pellets as identified in Figure 13.

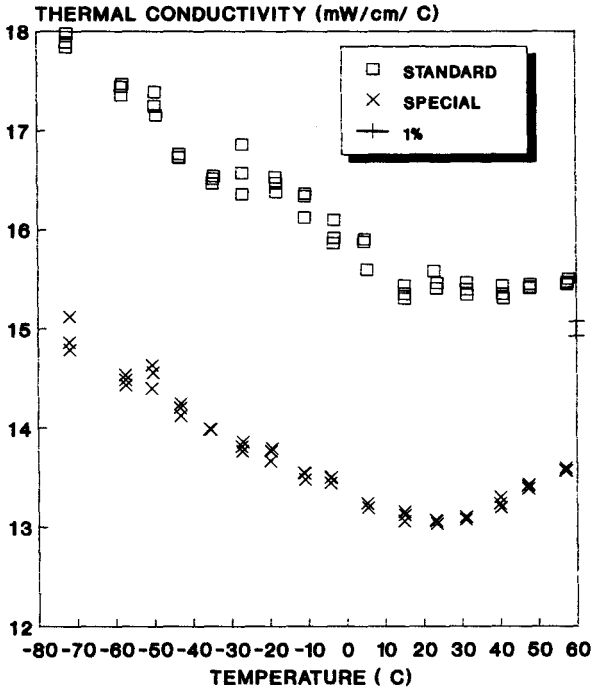

FIGURE 20 Thermal conductivity test data taken on standard and special n-type TE pellets as identified in Figure 13.

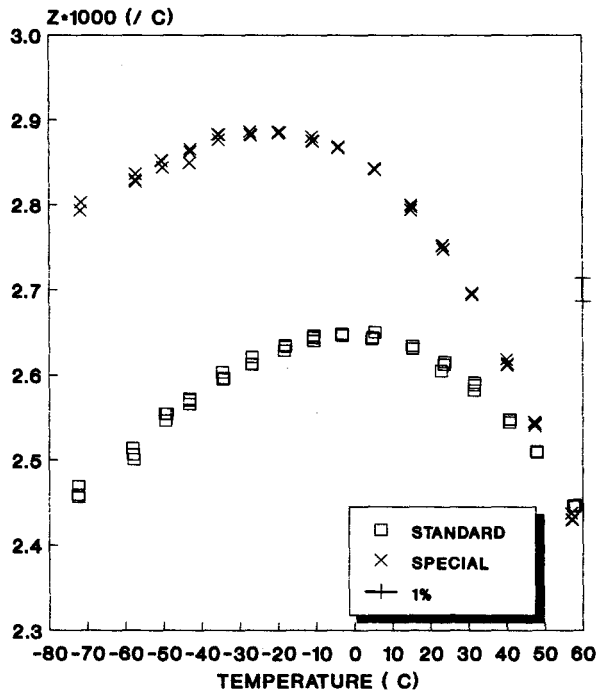

FIGURE 21 Figure-of-merit test data taken on standard and special n-type TE pellets as identified in Figure 13.

18.10 Discussion and Summary

A new TRANSIENT test methodology has been developed and described in detail. It provides the basis for a high-speed, high-precision measurement system for thermoelectric ingots, wafers, pellets, modules, and systems. It offers significant improvements on, but maintains all advantageous features of, the Harman[1] test method.

The TRANSIENT technique employs a detailed thermal model automatically created for the TED under test by the computer software. The software drives a PC computer with a special A/D board plugged into an expansion slot of the computer. The test sequence employs a transient technique and extracts the key TE material parameters by analysis of the digital waveform data. Rigorous formulas are used which separate the "zero-order" TE material, Z, and thermal conductivity terms from several correction terms involving internal radiation, external radiation, air conduction, external convection, and, in the case of single TE pellets, conduction through the test wires and thermocouples.

Data have been presented on TE modules and samples which validate the performance claims for this test method. It is simple, fast, accurate, and very easy and affordable to use. Since it is particularly accurate in its measurement of ZT, this test technology is presented with the expectation that it will virtually eliminate conflicts in thermoelectric quality claims that might otherwise arise between the various thermoelectric organizations of the world.

Reference

1. Harman, T. C. and Honig, J. M., *J. Appl. Phys.*, 13, 440, 1962.

Section D
Thermoelectric Materials

19
Bismuth Telluride, Antimony Telluride, and Their Solid Solutions

H. Scherrer and
S. Scherrer
Ecole des Mines, Parc de Saurupt
Nancy, France

19.1 Introduction

In this chapter the author's recent results on the thermoelectric properties of bismuth telluride and its solid solutions are presented. Many authors[1-7] have previously studied these materials and presented the results of room temperature measurements made on "good" thermoelectric materials. However, these studies are relatively old and the data dispersed throughout the literature. In most of the samples previously studied, it is difficult to relate the thermoelectric properties to the physical state of the material. The intrinsic properties are hidden by doping effects or an excess of one of the components; the starting materials usually being thermodynamically badly defined.

0-8493-0146-7/95/$0.00+$.50

The studies of bismuth telluride by Satterthwaite and Ure[7] and Brebrick[8] revealed a region of existence bounded by a solidus line at high temperatures. The resulting deviation from stoichiometry can be expressed in terms of inherent defects which are electrically active and related to the thermoelectric properties.

Following a brief introduction to the general properties of Bi_2Te_3 and its solid solutions the results of a characterization of high-quality, single crystals, grown using the traveling heater method (THM) are presented. This preparation method requires knowledge of the thermodynamic solid-liquid equilibrium of the materials. Binary and tertiary phase diagrams of (Bi-Te), (Bi-Se), (Bi-Sb-Te), and (Bi-Te-Se) systems are presented.

The characterization of the samples, saturated by the annealing technique under specified thermodynamic conditions, is carried out along the solidus line (corresponding to the maximum stoichiometric deviations). These characterizations have been done through electrical, thermal, and Seebeck coefficient measurements. The results are discussed in terms of the optimum figure-of-merit of the material.

19.2 General Properties of Bi_2Te_3, Sb_2Te_3, and Their Solid Solutions

Although many authors[9–11] have described the compound bismuth telluride (Bi_2Te_3) as a rhombohedric structure of the space group (R3m), it is easier to represent this structure by an hexagonal cell. The hexagonal cell is formed by the stacking of layers, perpendicularly to the c-axis, of like atoms following the sequence:

$$-Te^{(1)}\text{-}Bi\text{-}Te^{(2)}\text{-}Bi\text{-}Te^{(1)}\text{-}$$

(The superscripts refer to the two types of bonding.)

This sequence is called a quintet and the hexagonal cell is formed by three quintets. The lamellar structure of Bi_2Te_3 and the weakness of $Te^{(1)}$-$Te^{(1)}$ bonds between two quintets are responsible for the easy cleavage along the planes perpendicular to the c-axis (i.e., along the basal planes). Besides this striking mechanical anisotropy, most of the semiconductor parameters also possess a strong anisotropy. The $Te^{(1)}$-$Te^{(1)}$ bonds are considered to be of Van der Waals type,[12,13] whereas the $Te^{(1)}$-Bi and Bi-$Te^{(2)}$ bonds are of ionic-covalent type.[14,15] The parameters of the hexagonal cell are

$$a = 4.3835 \text{ Å}, c = 30.360 \text{ Å (at 77 K)}[16]$$

A table of the general properties of the materials can be found in *Thermoelectric Refrigeration* by Goldsmid.[3]

The details of the multivalley type of band structure (multiple ellipsoidal energy surfaces) have been obtained by extrapolating optic and galvanomagnetic measurements.[17] The forbidden energy gap of Bi_2Te_3 was found to be 0.16 eV at 300 K and 0.18 eV at 0 K.[18–22]

The rhombohedric structure of antimony telluride belongs to the same space group (R3m) as bismuth telluride. In the hexagonal cell the sequence of stacked layers is

$$-Te^{(1)}\text{-}Sb\text{-}Te^{(2)}\text{-}Sb\text{-}Te^{(1)}$$

The parameters of the hexagonal cell have been determined experimentally by many authors:[23,24]

$$a = 4.25 \text{ Å} \qquad c = 29.96 \text{ Å}$$
$$a = 4.264 \text{ Å} \qquad c = 30.428 \text{ Å}$$

The lamellar structure leads to a strong anisotropy of the semiconductor parameters. Infrared transmission investigations[25,26] have provided an estimate for the forbidden energy gap of between 0.25 and 0.30 eV. The multivalley type of band structure has been studied by Von Middendorf et al.[27]

The $(Bi_{1-x}Sb_x)_2Te_3$ solid solutions constituted from the isomorphous compounds, Sb_2Te_3 and Bi_2Te_3, crystallize in the same rhombohedric structure (R3m). The bismuth atoms are substituted

for the antimony atoms. The parameters of the hexagonal cell have been obtained by different authors:[28,29] for example, if x = 0.75,

$$a = 4.295 \text{ Å} \qquad c = 30.35 \text{ Å}$$
$$a = 4.275 \text{ Å} \qquad c = 30.45 \text{ Å}$$

The density varies linearly as a function of the mole percent Sb_2Te_3 in Bi_2Te_3 (x = 0.75, d = 6.892 g cm^{-3}). The solid solutions prepared with $x \geq 0.5$ present a p-type conductivity. Volotskii et al.[30] have described a band structure with two conduction bands and two valence bands. Optical studies[31] give an estimated energy gap, at room temperature, equal to 0.166 eV and 0.155 eV for x = 0.9 and 0.7, respectively. Based on a six-valley model with and without one parabolic valence band,[32,33] the energy gap is estimated at 0.190 and 0.180 eV for x = 0.75 and 0.7, respectively. A second valence band has been identified by measurements of the Shubnikov-De Haas effect.[34,35]

In the same way, the solid solutions $Bi_2(Te_{1-x}Se_x)_3$ are formed by the substitution of Te atoms with selenium (Se). Initially the Se atoms, being more electronegative, take the place of the $Te^{(2)}$ atoms, and increase the ionic bonds.[36] Some interesting optical-transmission studies[37,38] show that the energy gap increases on adding Bi_2Se_3 to Bi_2Te_3, reaching a value of 0.31 eV for x = 0.3.[39,40] If more Te atoms are replaced, the Se atoms occupy the $Te^{(1)}$ sites. The presence of Bi-$Se^{(1)}$ bonds would decrease the ionicity of the Bi-$Se^{(2)}$ bonds, and lead to a decrease in the energy gap. The sharp discontinuity, at x = 0.3, probably indicates a change in the band structure. Likewise, the parameter *a* of the hexagonal cell decreases linearly with the content of selenium atoms (4.38 to 4.15 Å).[39–41] However, the parameter *c* decreases linearly to 30 mol% Bi_2Se_3 in Bi_2Te_3 (x = 0.3), then deviations from Vegard's law are observed corresponding to the substitution of $Te^{(1)}$ atoms by Se atoms.

19.3 Binary Compounds Bi_2Te_3 and Sb_2Te_3

Preparation by THM (Traveling Heater Method) and Saturation Annealing Technique

A simplified schematic description of the traveling heater method[42] is shown in Figure 1. In this method a molten zone passes through a polycrystalline ingot (source ingot), in a quartz ampoule sealed under high vacuum. The source ingot is prepared by the synthesis of high-purity components with the stoichiometric composition of the compound to be prepared (Bi_2Te_3, Sb_2Te_3 or a ternary solid solution). A dissolution interface is observed in the upper part of the furnace and a crystallization interface at the lower part.

Binary or ternary phase diagrams (Bi-Te, Sb-Te, Bi-Sb-Te, and Bi-Te-Se) are necessary in order to employ the THM process because, at a given temperature, solid and liquid must be in equilibrium at each interface. This method allows single crystals to be prepared at a temperature lower than the melting temperature and consequently of high quality. The transfer of the zone through the source ingot improves the purity of the material by a zone melting process. In general the ingots have an orientation such that the cleavage planes are parallel to the growth axis (i.e., perpendicular to the c-axis).

The solidus line can be explored using a saturation annealing technique,[43] as described below. The technique involves the equilibration under isothermal conditions of any alloy powder of known composition outside the solidus line with a crystal of arbitrary initial defect concentration. Samples cut from the monocrystalline ingot are saturated in a sealed quartz ampoule (10^{-7} torr) in the presence of the powdered ingot in an isothermal furnace at the desired temperature. The composition of the saturating source depends both on the sample composition and the temperature. In the case of bismuth telluride, using the diagram[44] partially shown in Figure 2, the atomic source composition is chosen such that the three phases, solid, liquid, and gas, are present in equilibrium. The sample then acquires the solidus composition by means of atomic exchange with the gas phase at the desired temperature. To obtain good homogeneous samples, the saturation process is carried out for at least 7 d.

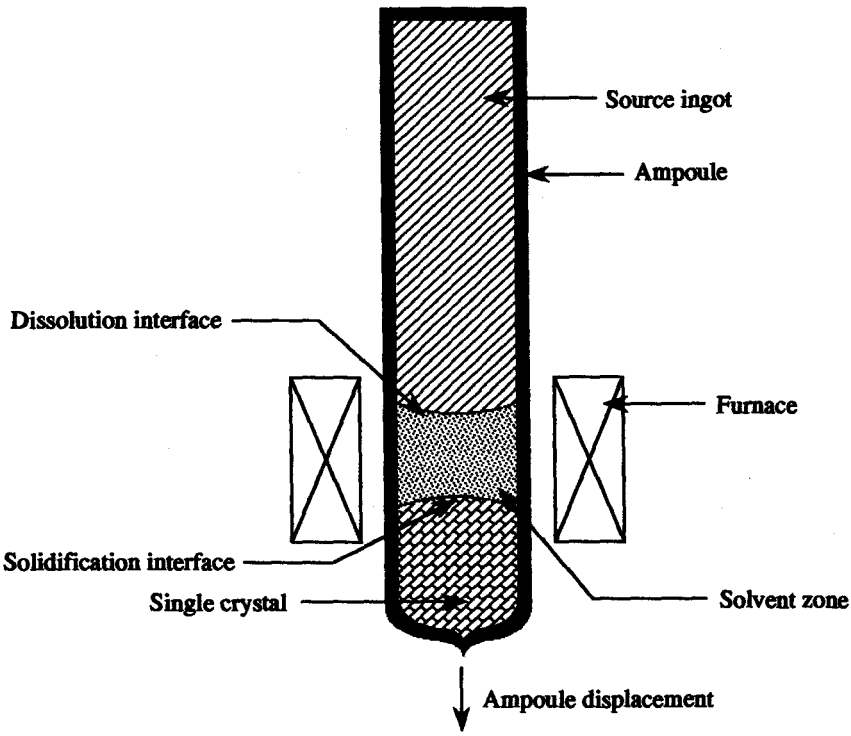

FIGURE 1 Schematic of the traveling heater method.

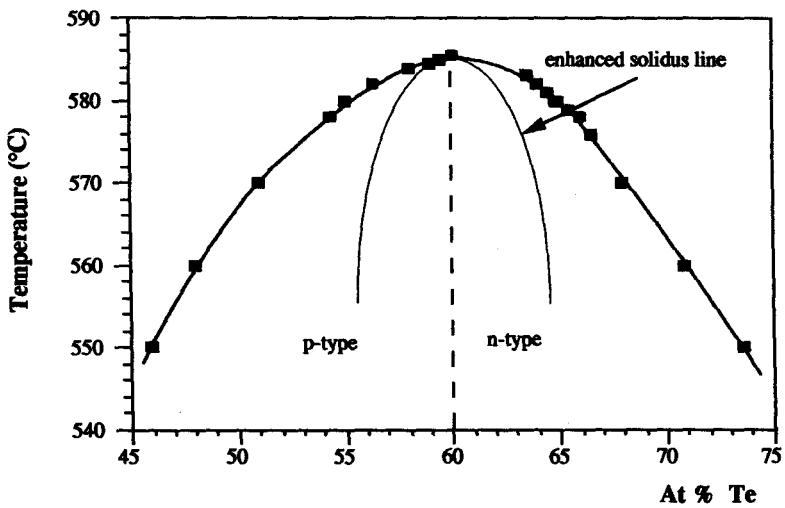

FIGURE 2 Phase diagram of Bi-Te in the region around Bi_2Te_3.

Experimental Results for the Bi_2Te_3 Compound

Single crystals of n- and p-type were grown by THM at different temperatures. Saturated samples of known composition which correspond to annealing temperatures from 570°C to the melting point, 585.5°C, for the bismuth-rich side, and from the melting point to 560°C for the chalcogenide-rich side, were characterized. These results[45] are reported in Tables 1 and 2. The measurements are performed in a direction parallel to the cleavage planes.

In Figure 3 the number of excess carriers is displayed as a function of annealing temperatures. It may be noted that the carrier concentrations on the p-type side are greater than on the n-type

Table 1. Experimental Results for p-Type Bi_2Te_3

Saturation temperature °C	570	578	582	584	584.5	585	585.5
At.% Te	51.5	54.3	56.3	58	59	59.5	60
α $\mu V K^{-1}$	141	162	156	116	145	174	227
ρ μ Ω.m	13.3	5.5	4.8	5.9	7.6	17.8	19.5
λ $W m^{-1} K^{-1}$	1.83	2.06	2.22	2.88	2.41	1.84	1.73
R_H 300 K $cm^3 c^{-1}$	0.0302	0.0296	0.0299	0.118	0.147	0.294	0.310
R_H 100 K $cm^3 c^{-1}$	0.0340	0.0246	0.0283	—	0.196	0.244	—
μ_H 300 K $cm^2 V^{-1} s^{-1}$	23	54	66	200	194	180	—
μ_H 100 K $cm^2 V^{-1} s^{-1}$	78	181	214	—	1330	943	—
$p.10^{19}$ cm^{-3}	18	25.5	22	4.2	3.3	2.5	2.0
$Z.10^{-3}$ K^{-1}	0.82	2.32	2.28	0.79	1.15	0.924	1.53

Table 2. Experimental Results for n-Type Bi_2Te_3

Saturation temperature °C	560	576	578	579	580	581	582	583
At.% Te	70.5	66.5	66	65.5	65	64.5	64	63.5
α $\mu V K^{-1}$	−115	−127	−174	−189	−198	−240	−247	−224
ρ μ Ω.m	2.6	4.5	6.9	8.0	8.1	10.0	14.3	17.9
λ $W m^{-1} K^{-1}$	3.24	2.8	2.53	2.37	2.27	2.02	1.92	2.05
R_H 300 K $cm^3 c^{-1}$	−0.038	−0.098	−0.117	−0.135	−0.152	−0.214	−0.246	−0.520
R_H 100 K $cm^3 c^{-1}$	−0.0428	−0.120	−0.117	−0.184	−0.183	−0.272	−0.320	−0.179
μ_H 300 K cm^2 $V^{-1} s^{-1}$	152	171	178	168	189	212	173	227
μ_H 100 K cm^2 $V^{-1} s^{-1}$	652	1284	1417	1371	1523	1893	1546	2504
$n.10^{19}$ cm^{-3}	14.6	5.2	3.5	3.4	3.4	2.3	1.9	0.7
$Z.10^{-3}$ K^{-1}	1.37	1.16	1.74	1.89	2.15	2.89	2.23	1.36

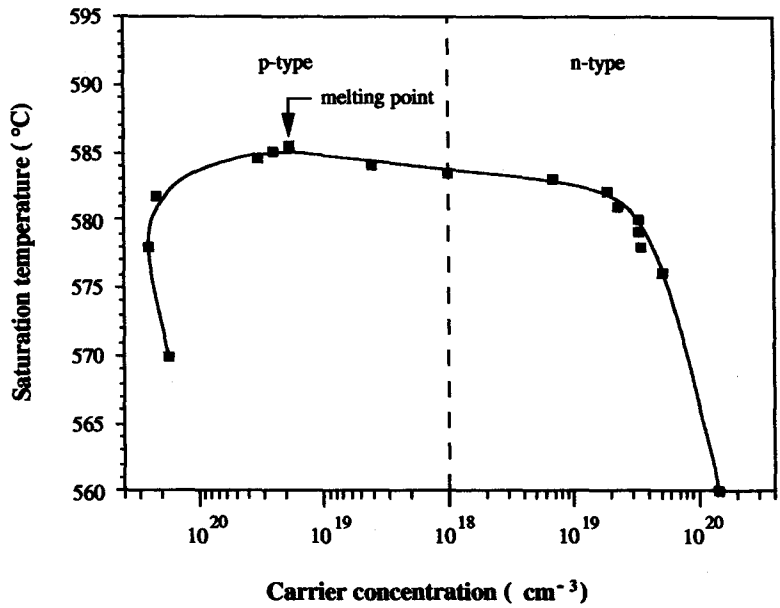

FIGURE 3 Solidus of Bi_2Te_3 for different saturation temperatures plotted as a function of carrier concentration. (From Reference 45 with permission.)

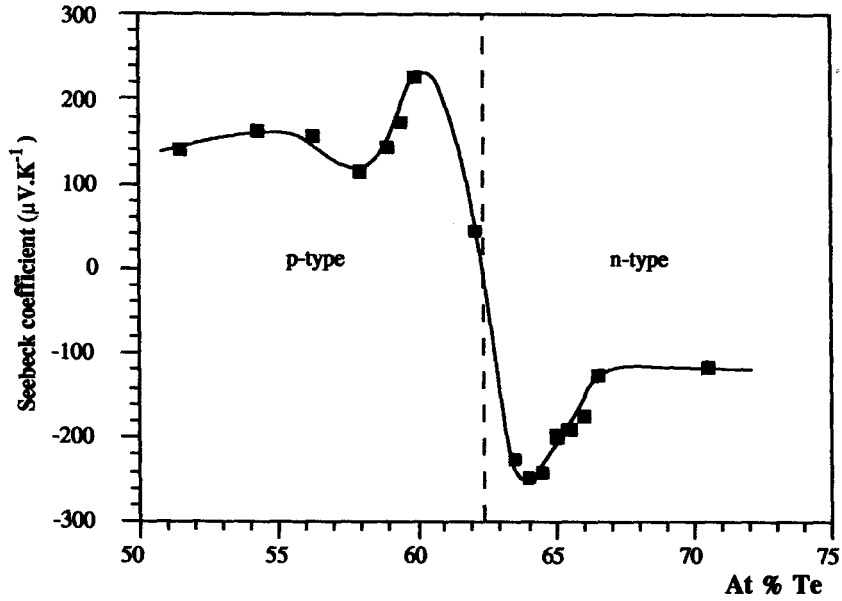

FIGURE 4 Seebeck coefficient as saturation temperature for both n- and p-type Bi_2Te_3. (From Reference 45 with permission.)

side. It is found that the change in type occurs at 583.5°C, a value in good agreement with the results of Satterthwaite and Ure.[7] Moreover, samples were made as near as possible to the melting point of 585.5°C, in keeping with the result of Zhukov et al.[46]

The concentration of charge carriers is directly related to the concentration of inherent defects. The major defects are of an antistructure type[47,48] and are responsible for deviations from stoichiometry. Therefore, it can be concluded that the solubility of tellurium, on the Te-rich side, is always found to increase with carrier concentration as the annealing temperature decreases. However, for the Bi-rich side, below the annealing temperature of 582°C, a retrograde solubility of bismuth is observed with decreasing annealing temperature. It should be noted that measured values of Hall coefficient R_H at 100 K must be used to determine the solidus line.[49] At this temperature, all the defects are ionized and the carrier concentrations calculated from Hall effect data are "apparent" concentrations.

The Hall mobilities are derived from the Hall coefficient R_H and the electrical conductivity σ. Between 100 and 200 K the product $R_H\sigma$ also gives the conduction mobility because R_H is constant. As expected for n-type samples, the carrier mobility decreases when the carrier concentration increases. For the p-type samples, this behavior is modified by the retrograde solubility. The measured values for all the samples remain far greater than in the case of samples grown[50] by the Bridgman method because of better crystal quality.

The Seebeck coefficient α at room temperature as a function of the liquidus composition for various samples is shown in Figure 4. The results confirm the change in type at 583.5°C when $\alpha = 0$. For the p-type material the behavior of the Seebeck coefficient is related to the carrier concentrations and shows the effects of retrograde solubility. For n-type a maximum value of 250 $\mu V\ K^{-1}$ was found.

The plot of the electrical resistivity ρ vs. the liquidus composition is shown at room temperature in Figure 5. As can be seen, for the p-type material ρ has a minimum value of $\rho_m = 4{,}75\ \mu\Omega m$ at about 56 at.% Te, and then increases in samples richer in bismuth, because of the retrograde solubility on the Bi-rich side. In addition, the electrical resistivity of n-type samples is always found to decrease towards a low value of $\rho = 2\ \mu\Omega m$ for samples richer in tellurium. The dotted lines show the Bridgman-grown material:[50] it can be seen that for high excess concentration, the electrical resistivity is far greater using the simple Bridgman technique, due to the difference between the Hall mobilities.

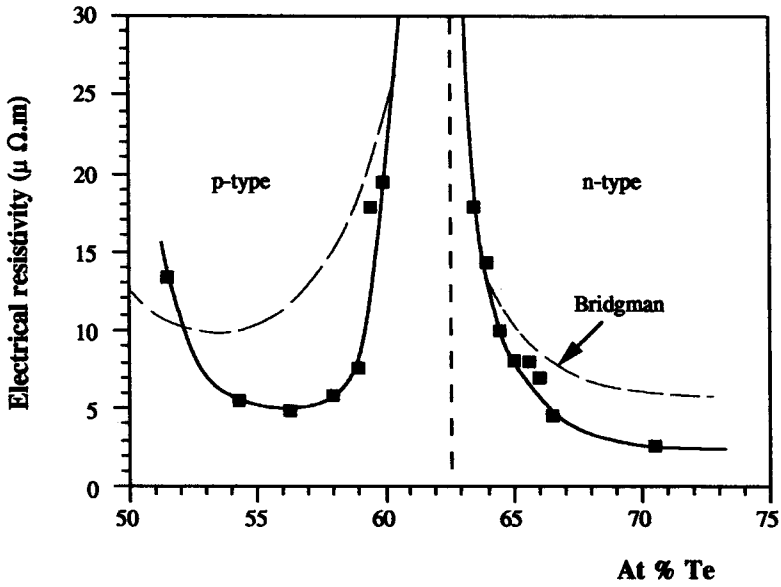

FIGURE 5 Electrical resistivity as the liquidus composition for both n- and p-type Bi_2Te_3. The dotted lines are for Bridgman-type single crystals. (From Reference 45 with permission.)

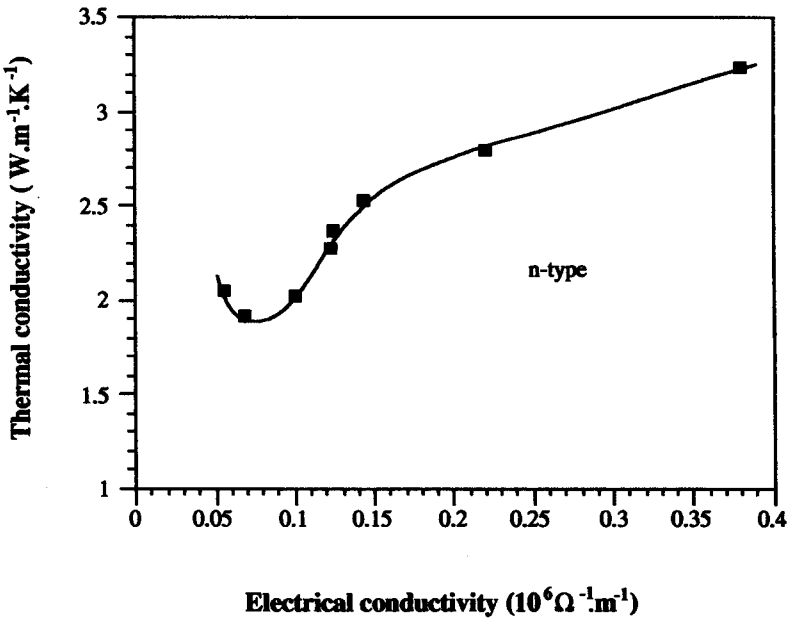

FIGURE 6 Thermal conductivity as a function of the electrical conductivity for n-type Bi_2Te_3.

Figure 6 displays the thermal conductivity λ for n-type material as a function of electrical conductivity σ. At room temperature, the values of λ vary between 1.9 and 3.3 W m^{-1} K^{-1} and the lattice thermal conductivity is estimated at λ_L = 1.7 W m^{-1} K^{-1} (for σ = 0).

In Figure 7 the behavior of the thermal conductivity as a function of the liquidus composition is displayed. On the bismuth-rich side the thermal conductivity exhibits a maximum value (λ = 2.88 W m^{-1} K^{-1}) due to a retrograde solubility. Measurements in a direction perpendicular to the cleavage planes were carried out[33] and the results reported in Table 3. As the electrical

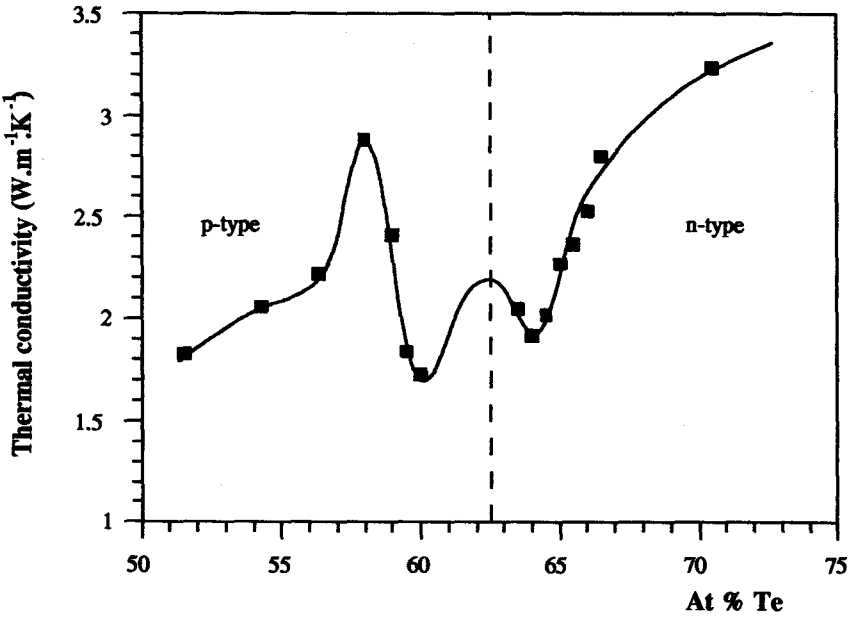

FIGURE 7 Thermal conductivity as the liquidus composition for both n- and p-type Bi_2Te_3. (From Reference 45 with permission.)

Table 3. Experimental Results of Anisotropy

Saturation temperature °C	560	576	578	579	581	583
ρ_{33}/ρ_{11}	6.67	5.30	5.30	5.40	5.11	4.2
ρ_{11} μ Ω.m	2.6	4.5	6.9	8.0	10.0	17.9
$\lambda_{11}/\lambda_{33}$	2.51	2.13	2.12	2.05	2.02	2.0
λ_{11} W m^{-1} K^{-1}	3.24	2.80	2.53	2.27	2.02	2.05
n.10^{19} cm^{-3}	14.6	5.2	3.5	3.4	2.3	0.7

resistivity ρ_{11} increases the experimentally determined anisotropy ratio ρ_{33}/ρ_{11} leads to the theoretically predicted ratio[51] of 4. Likewise, the anisotropy ratio $\lambda_{11}/\lambda_{33}$ decreases from 2.5 to 2 with decreasing stoichiometric deviations.

Finally, the Seebeck coefficient is reasonably isotropic, with only a slight change of about 10% between α_{33} and α_{11} with:

$$(\alpha_{11} - \alpha_{33})/\alpha_{11} \leq 0.10$$

This agrees with the experimental values of Goldsmid,[52] who found a variation of 25 μV °C^{-1} for a value of 200 μV K^{-1} °C^{-1} for the α_{11} Seebeck coefficient.

From the measurements, it can be deduced that the anisotropic figure-of-merit is maximum in a direction parallel to the cleavage planes and

$$Z_{11} \approx 2 \times Z_{33}$$

The figure-of-merit $Z_{11} = \alpha^2\sigma/\lambda$ is plotted against the liquidus composition in Figure 8. The best values are obtained for n-type material. It can be seen that in n-type material, Z_{11} has a maximum value of 2.9×10^{-3} K^{-1} at about 64% Te.

From this figure it is clear that very close control of the stoichiometric deviation is necessary to obtain an optimum value of Z_{11}. In the case of the (Bi-Se-Te) solid solutions, as discussed later, this maximum in the figure-of-merit is less critical. The optimum value of Z_{11} for n-type samples corresponds to a charge carrier concentration of 2.10^{19} cm^{-3}.

Because of the low value of the energy gap (0.16 eV) the material is partially degenerate, and the corresponding Fermi level should not be far from the bottom of the conduction band at room

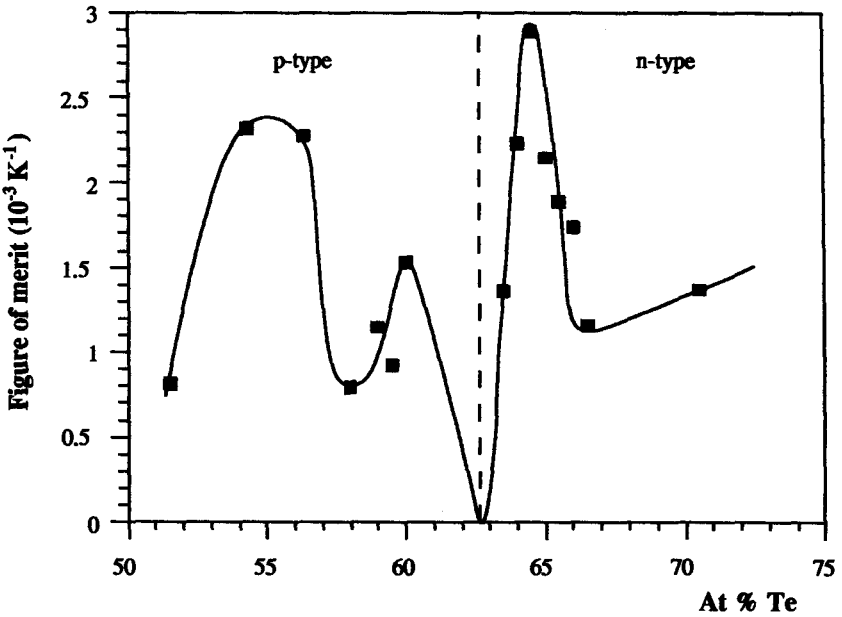

FIGURE 8 Figure-of-merit as the liquidus composition for both n- and p-type Bi_2Te_3. (From Reference 45 with permission.)

temperature. For small stoichiometric deviations, electrical conduction by minority carriers cannot be neglected. The experimental results of Bi_2Te_3 at 300 K indicate the significant effect of two-band conduction upon all the thermoelectric parameters.[53]

Experimental Results for the Sb_2Te_3 Compound

Preparation and annealing techniques are the same as described in the previous section and enable measurements to be carried out (at 300 K) on samples with well-defined stoichiometry.[42] Figure 9 shows the apparent carrier concentrations against the solidus temperatures between 558°C and the melting point of the compound on the Sb side and between the melting point and 500°C on the Te side.

The behavior of Sb_2Te_3 is strongly p-type in spite of the deviations from the stoichiometric composition with carrier concentration between 10^{20} and 10^{21} cm^{-3}. The melting point of the compound is not congruent, a retrograde solubility being observed on the lower concentration side.

Some authors (Eichler and Kurg,[54] Gaidukova et al.,[55] Langhammer et al.,[56] Simon and Eichler,[57] Stölzer et al.,[31] Stordeur and Simon[58]) have studied the thermoelectric properties of the compound Sb_2Te_3 as a function of carrier concentration and their anisotropy. Yet, the published results refer to a few samples only and are usually doped.

The present authors have used controlled samples to investigate the effect of stoichiometric deviation on the thermoelectric properties. Figures 10, 11, 12, and 13 show the mobility, resistivity, Seebeck coefficient, and the thermal conductivity dependence on the carrier concentration. These parameters are measured along the cleavage planes (ρ_{11}, α_{11}, λ_{11}) and in the perpendicular direction (ρ_{33}, α_{33}, λ_{33}). All these results are collected in Tables 4 and 5. The different behavior of these parameters should be noted when the hole carrier concentration (ρ) is below or above 3.10^{20} cm^{-3} and also the anisotropic variation of the thermoelectric power.

The results are related to a complex valence band structure. When the carrier concentration increases, two sub-bands which correspond to different effective mass values are progressively occupied by the holes. Below $\rho = 3.10^{20}$ cm^{-3}, a mixed-scattering model[59] that takes into account the ellipsoidal surfaces of constant energy explains the behavior of the thermoelectric parameters.

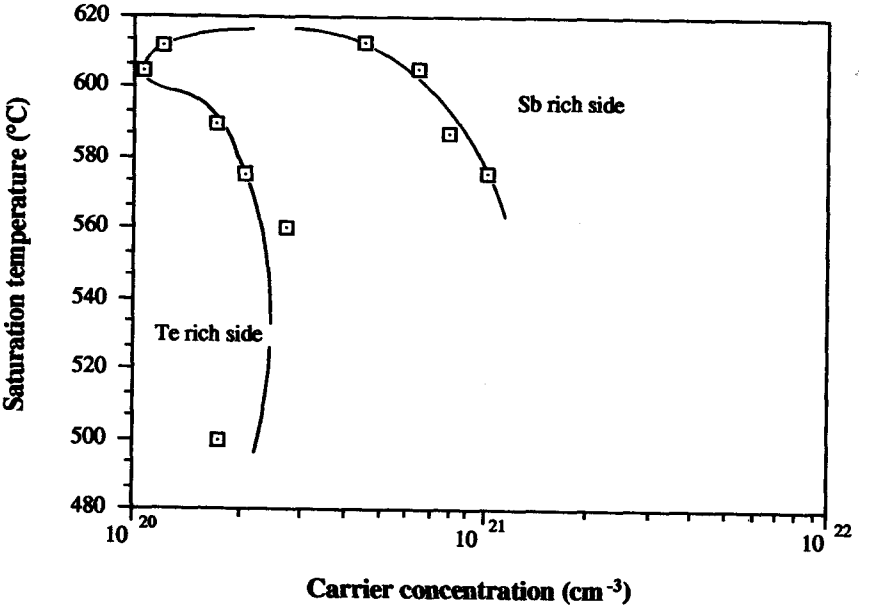

FIGURE 9 Solidus of Sb_2Te_3 for different saturation temperatures plotted as a function of carrier concentration.

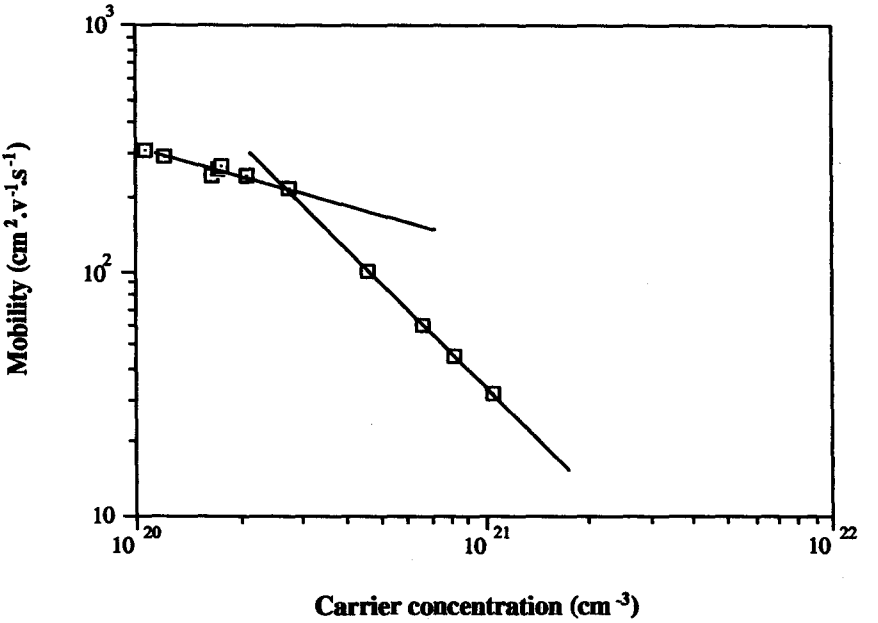

FIGURE 10 Hall mobility of Sb_2Te_3 at room temperature vs. carrier concentration.

The estimated figure-of-merit is higher along the c-axis (Z_{33}) than in the perpendicular direction (Z_{11}), as shown in Figure 14. The optimal values are $Z_{11} = 0.65 \times 10^{-3}\ K^{-1}$, $Z_{33} = 1.6 \times 10^{-3}\ K^{-1}$, corresponding to carrier concentrations of $1.1 \times 10^{20}\ cm^{-3}$ and $2.1 \times 10^{20}\ cm^{-3}$, respectively. These values are lower than the ones obtained for Bi_2Te_3. Consequently the compound Sb_2Te_3 is not of interest as a thermoelectric material.

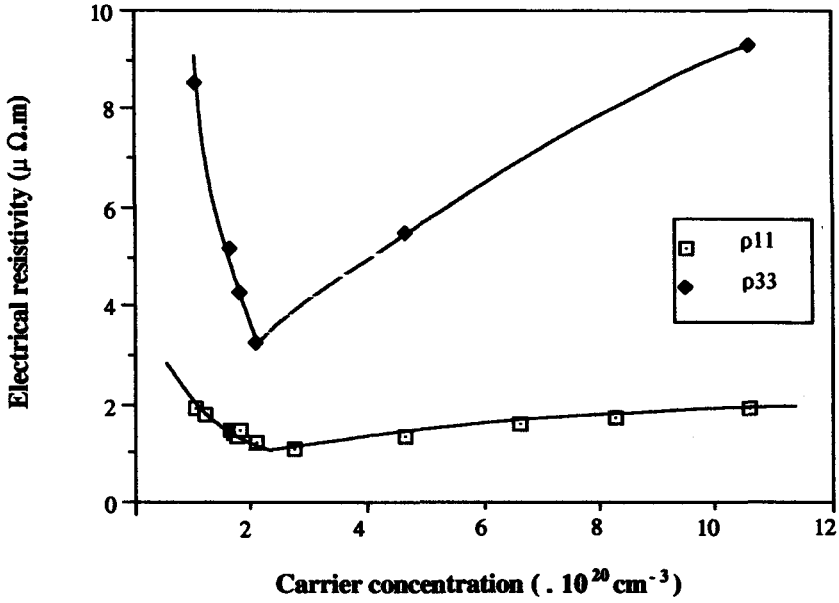

FIGURE 11 Electrical resistivity as a function of carrier concentration for Sb_2Te_3.

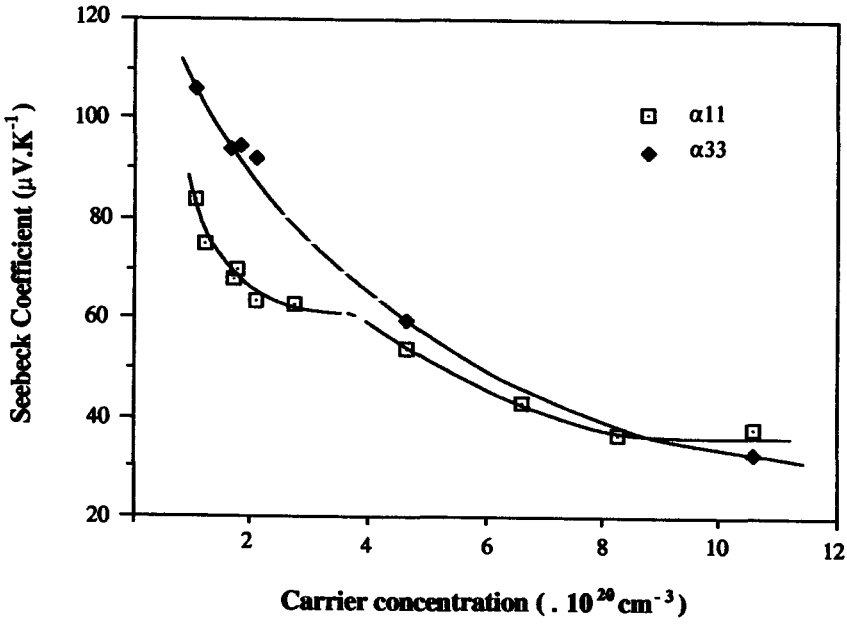

FIGURE 12 Seebeck coefficient as a function of carrier concentration for Sb_2Te_3.

The model[42] enables the lattice thermal conductivity to be estimated at room temperature $\lambda_{11L} = 2.2\ W\ m^{-1}\ K^{-1}$ and $\lambda_{33L} = 0.34\ W\ m^{-1}\ K^{-1}$. The extrapolation of the thermal conductivity from the experimental law $\lambda(\sigma)$ is not valid because the Lorentz coefficient is not a constant. The lattice component λ_{11L} appears to be a high value, but it decreases with alloying as is normal for the Bi_2Te_3-Sb_2Te_3 alloy system.

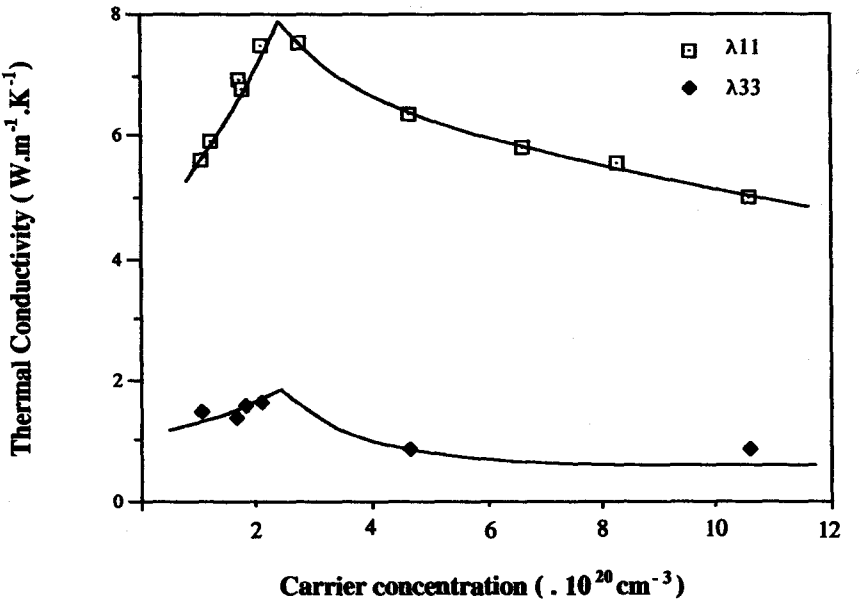

FIGURE 13 Thermal conductivity as a function of carrier concentration for Sb_2Te_3.

Table 4. Experimental Results for Sb_2Te_3 on the Sb-Rich Side

Saturation temperature °C	575	587	605	613
At.% Te	44.2	47.5	52.0	56.3
ρ_{11} μΩ.m	1.90	1.69	1.57	1.36
ρ_{33} μΩ.m	9.29	—	—	5.50
α_{11} μV K^{-1}	38.0	36.6	43.0	53.9
α_{33} μV K^{-1}	32.6	—	—	59.2
λ_{11} W m^{-1} K^{-1}	5.01	5.56	5.83	6.35
λ_{33} W m^{-1} K^{-1}	0.85	—	—	0.89
μ_H 300 K cm^2 V^{-1} s^{-1}	31	45	60	99
p.10^{20} cm^{-3}	10.6	8.26	6.63	4.66
$Z_{11}.10^{-4}$ K^{-1}	1.52	1.43	2.02	3.37
$Z_{33}.10^{-4}$ K^{-1}	1.36	—	—	7.16

Table 5. Experimental Results for Sb_2Te_3 on the Te-Rich Side

Saturation temperature °C	615	612	605	590	575	560	500
At.% Te	62.5	63.5	67.0	70.5	72.5	74	82
ρ_{11} μΩ.m	1.44	1.79	1.89	1.40	1.22	1.07	1.34
ρ_{33} μΩ.m	5.18	—	8.55	—	3.23	—	—
α_{11} μV K^{-1}	—	74.8	83.4	67.5	63.1	62.5	69.8
α_{33} μV K^{-1}	94	—	110	—	92	—	—
λ_{11} W m^{-1} K^{-1}	—	5.92	5.62	6.92	7.47	7.52	6.77
λ_{33} W m^{-1} K^{-1}	1.38	—	1.46	—	1.63	—	—
μ_H 300 K cm^2 V^{-1} s^{-1}	262	288	313	260	244	215	266
p.10^{20} cm^{-3}	1.65	1.21	1.06	1.71	2.10	2.72	1.75
$Z_{11}.10^{-4}$ K^{-1}	—	5.28	6.54	4.7	4.37	4.86	5.37
$Z_{33}.10^{-4}$ K^{-1}	12.3	—	9.0	—	16.1	—	—

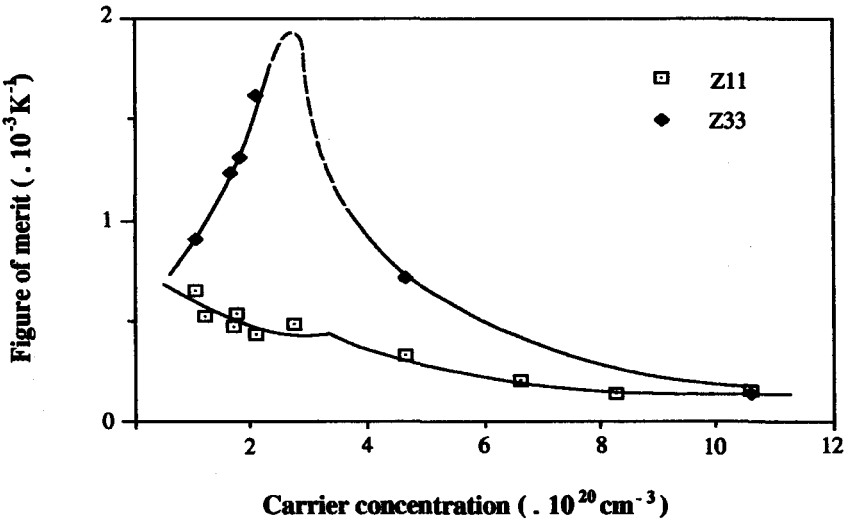

FIGURE 14 Figure-of-merit as a function of carrier concentration for Sb_2Te_3.

19.4 Bi_2Te_3-Sb_2Te_3 Solid Solutions

Phase Diagram

Ternary compounds must be prepared for use as a reference material and in commercial applications. The preparation of this material by THM requires knowledge of the Bi-Sb-Te phase diagram.

Smith and coworkers[60] determined the Bi_2Te_3-Sb_2Te_3 pseudobinary section of the phase diagram, where the distribution coefficient was equal to unity at compositions 33.3 and 66.7 mol% of Bi_2Te_3. Abrikosov and Poretskaya[61] carried out a determination of this pseudobinary region where the solidus and liquidus lines are situated close to one another. They also studied the liquidus surface of the Bi_2Te_3-Sb_2Te_3-Te region of the ternary system. Furthermore, two theoretical models[62,63] were developed to determine the Bi-Sb-Te ternary phase diagram, but the results were not in good agreement with previous experimental data. Steininger[64] shows how the determination of the liquidus and solidus temperatures by thermal analysis in many solid solution phase diagrams is often subject to error because of supercooling. The pseudobinary phase diagram[65] obtained from investigations where the sample compositions are kept constant, avoiding supercooling effects and phenomena connected with inefficacious quenching, is shown in Figure 15. This figure displays the boundaries of the liquid-solid phase in the pseudobinary region of Bi_2Te_3-Sb_2Te_3 as a function of the Bi_2Te_3 mole content. The melting point of bismuth telluride is 585°C and that of antimony telluride is 617°C. The maximum gap between the solidus and liquidus line is 7°C. In this case, the segregation coefficient is always larger than unity.

The ternary phase diagram (Bi,Sb,Te) is represented on the Te-rich side of the pseudobinary cross section in Figure 16. The liquidus temperatures of the Bi_2Te_3-Sb_2Te_3-Te region were obtained by DSC measurements. The liquidus surface bounded by the eutectic line E_1-E_2 and the Bi_2Te_3-Sb_2Te_3 pseudobinary region is represented by isothermal curves for temperatures ranging from 510 to 602°C. These curves allow insight to be obtained on the shape of the liquidus surface in the tellurium region. The information given by the ternary phase diagram will be complete if all the compositions of the liquidus in equilibrium at all temperatures with the solid $(Sb_{1-x}Bi_x)_2Te_3$ can be determined, x being fixed (isoconcentration lines). In the case of the figure, S_1 and S_2 correspond to $Bi_8Sb_{32}Te_{60}$ and $Bi_{10}Sb_{30}Te_{60}$ solid solutions, respectively. Tie-lines for each solid solution have been experimentally determined for temperatures ranging between 510°C and the melting point of each: 609°C for S_1 and 607°C for S_2. The isoconcentration lines are L_1 for S_1 and L_2 for S_2. The intersection of the isothermal line at 550°C and the isoconcentration line L_1 (point A) gives the liquidus composition in equilibrium with the solid solution S_1 at 550°C; then

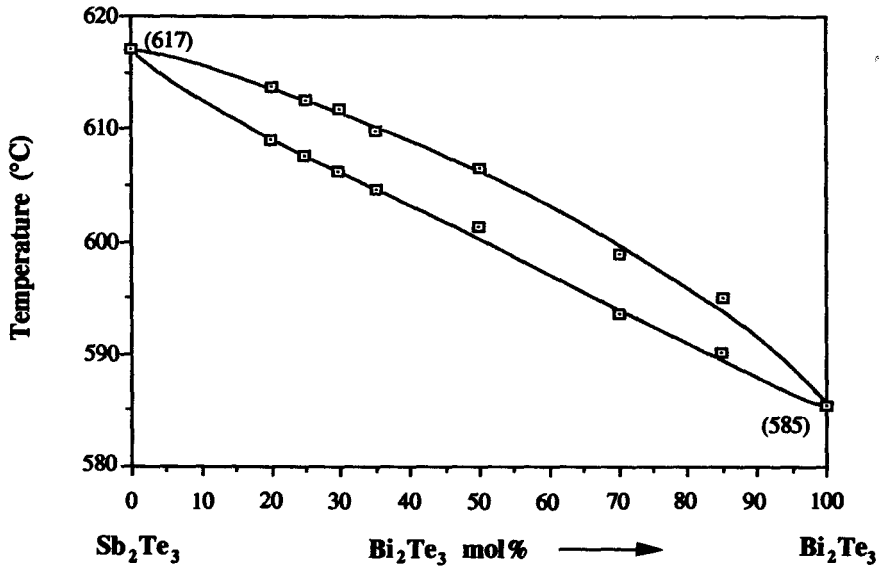

FIGURE 15 Liquidus and solidus temperatures for the Bi_2Te_3-Sb_2Te_3 pseudobinary section. (From Reference 65 with permission.)

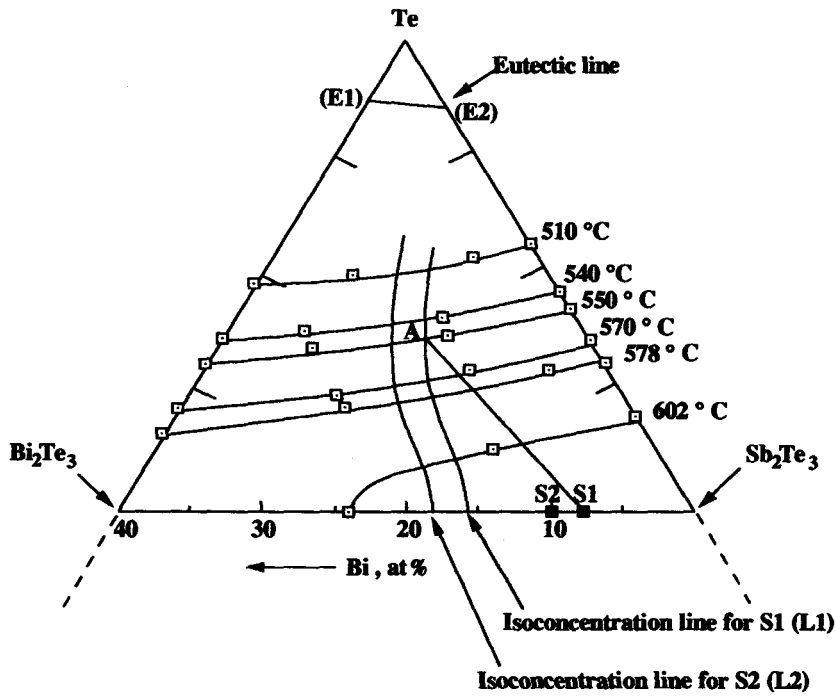

FIGURE 16 Liquidus temperatures and isoconcentration lines for $Bi_8Sb_{32}Te_{60}$ and $Bi_{10}Sb_{30}Te_{60}$ solid solutions for the Te-rich field. (From Reference 65 with permission.)

the line connecting A to S_1 represents the tie-line. The deviations from stoichiometry are not taken into account on the diagram.

The experimental data were used to construct a spatial illustration of the Bi-Sb-Te ternary diagram shown in Figure 17. This illustration is limited to the tellurium-rich region and to temperatures above 400°C. This diagram has been drawn with respect to temperatures but the true atomic scale was not conserved in order to include the boundaries of the solid solutions formed

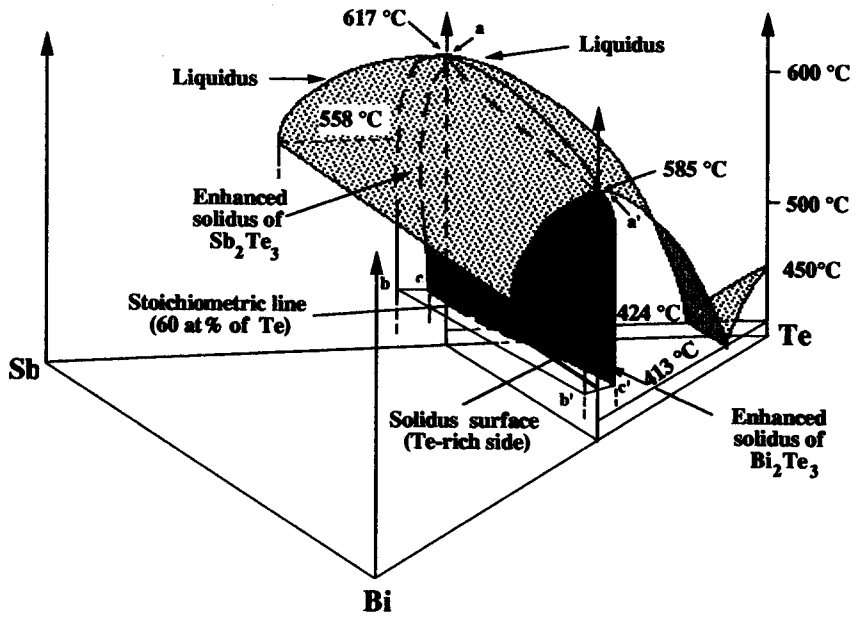

FIGURE 17 Schematic illustration of Bi-Sb-Te ternary phase diagram. (From Reference 65 with permission.)

by Bi_2Te_3 and Sb_2Te_3 compounds. It is well known that the compound Sb_2Te_3 always has p-type conductivity[42] and that the domain of existence (surface [a, b, c]) is outside of the stoichiometric composition and on the antimony-rich side.[66] This could be explained by the fact that the dominant defects are Sb_{Te} anti-site defects.[67] For Bi_2Te_3, both n- and p-type samples have been obtained and the domain of existence which contains the stoichiometric composition (surface [a', b', c']) expands when the temperature decreases.[45] In this compound, both Bi_{Te} and Te_{Bi} anti-site defects were identified and, thus, the dominant defects in solid solutions formed by Bi_2Te_3 and Sb_2Te_3 compounds would probably be Sb_{Te} and Bi_{Te} anti-site defects.[68] This could explain why $(Bi_xSb_{1-x})_2Te_3$ solid solutions are nonstoichiometric and deviate from stoichiometry toward bismuth and antimony.[69] In Figure 17, the volume (a, b, c, a', b', c') represents the boundaries of the whole solid solutions formed by bismuth telluride and antimony telluride. The boundary of tellurium-rich solidus corresponds to the shaded region. As the bismuth telluride content increases in the solid solutions, the strong deviation from stoichiometry observed for the Sb_2Te_3 compound decreases. Previous studies on p-type thermoelectric materials based on $(Bi_xSb_{1-x})_2Te_3$ solid solutions show that the solid solution with $x = 0.25$ has the higher efficiency. Most of the samples were grown from the melt by the Czochralski method, Bridgman method, or zone melting using initial melts with stoichiometric composition. It is clear that these methods would not allow the growth of samples with a controlled composition. Indeed, the isoconcentration line for the solid solution with $x = 0.25$ in Figure 16 shows how the direction of the tie-lines changes as the temperature decreases. Thus, crystals grown from the melt cannot have the same composition along the ingot because of the change in the initial melt composition. Knowledge of isoconcentration lines for $Bi_8Sb_{32}Te_{60}$ and $Bi_{10}Sb_{30}Te_{60}$ solid solutions will be very helpful to achieve growth of thermodynamically well-defined ternary crystals.

Preparation by THM

In this case, the growth process of the single crystal is achieved when the liquid ternary solvent zone is in thermodynamical equilibrium with the ternary source ingot and the single crystal at each interface. For example, suppose the compound $Bi_8Sb_{32}Te_{60}$ (S1) on Figure 16 is to be prepared. If a crystallization temperature of the compound at 550°C is chosen, the intersection labeled A between the isothermal liquidus curve at 550°C and the isoconcentration line (L_1) represents the composition of the solvent zone. In this example, the solvent zone is rich in tellurium. Single

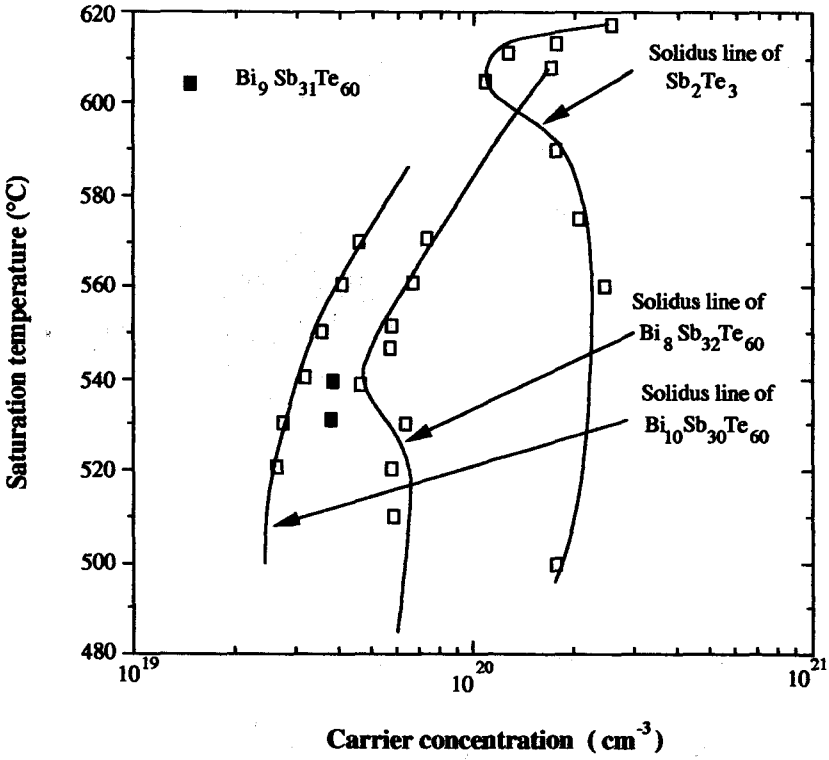

FIGURE 18 Hall carrier concentration as a function of saturation temperature for (S_1), (S_2) solid solutions and Sb_2Te_3 on the Te-rich side. (From Reference 70 with permission.)

crystals of $Bi_8Sb_{32}Te_{60}$ (S_1) and $Bi_{10}Sb_{30}Te_{60}$ (S_2) with cleavage planes parallel to the growth axis were obtained.[70]

Experimental Results

A ternary phase diagram is very useful when using the annealing saturation technique to prepare samples with compositions along the solidus line at different temperatures. In Figure 18 the number of excess carriers is displayed as a function of annealing temperature on the Te-rich side, for (S_1), (S_2) solid solutions and Sb_2Te_3 compound.[71] The carrier concentration is related to the concentration of intrinsic antistructure defects (Sb_{Te}) and (Bi_{Te}), and thus to stoichiometric deviations.[67] The strong decrease of the Hall carrier concentration with the increased mole contents of Bi_2Te_3 is related to the decrease of the (Sb_{Te}) antistructure defects. These results are in agreement with those of Abrikosov and Poretskaya.[61] Hall carrier concentrations range from 4.8 to 7.5 × 10^{19} cm^{-3} for (S_1) and from 2.8 to 5.0 × 10^{19} cm^{-3} for (S_2).

The saturated samples are characterized at 300 K by measuring the Seebeck coefficient and the thermal and electrical conductivities. Measurements were made in directions parallel (11) and perpendicular (33) to the cleavage planes. The different data are compiled in Tables 6 and 7 for (S_1) and (S_2) solid solutions, respectively.

The Seebeck coefficients show that the samples are always of p-type. The carrier mobilities are quite acceptable at about 150 and 180·cm^2 V^{-1} S^{-1}, respectively, for (S_1) and (S_2) solid solutions.

In Figures 19 and 20 Seebeck coefficient values are reported as a function of carrier concentration. A classical behavior was obtained for Seebeck coefficient α_{11} and α_{33}; as the carrier concentration of the samples increased, the Seebeck coefficient decreased. For (S_1) solid solution, Seebeck coefficient values ranged from 172 to 194 μV K^{-1} for α_{11} and from 180 up to 215 μV K^{-1} for α_{33}. A similar magnitude for the anisotropy of the Seebeck coefficient had already been observed for

Table 6. Experimental Results at 300 K for (S_1) Solid Solution

Saturation temperature °C	570	560	550	546	540	530	520	510
ρ_{11} μΩ.m	5.83	7.04	8.8	9.2	9.95	8.0	9.0	8.5
ρ_{33} μΩ.m	17.22	18.1	24.3	—	25.9	21.1	24.0	—
α_{11} μV K^{-1}	172	178	187	194	194	183	189	185
α_{33} μV K^{-1}	180	188	207	—	—	203	214	—
λ_{11} W m^{-1} K^{-1}	2.15	1.8	1.48	1.43	1.26	1.8	1.5	1.6
λ_{33} W m^{-1} K^{-1}	0.88	0.78	0.68	—	—	0.79	0.71	—
μ_H 300 K cm^2 V^{-1} s^{-1}	151	151	146	152	176	157	146	—
$p.10^{19}$ cm^{-3}	7.5	6.9	5.8	5.7	4.8	6.5	5.9	6.0
$Z_{11}.10^{-3}$ K^{-1}	2.3	2.4	2.7	2.84	2.95	2.34	2.6	2.6
$Z_{33}.10^{-3}$ K^{-1}	2.14	2.5	2.6	—	—	2.5	2.7	—

Table 7. Experimental Results at 300 K for (S_2) Solid Solution

Saturation temperature °C	570	560	550	540	530	520
ρ_{11} μΩ.m	8.9	11.0	12.3	12.8	14.2	15.9
ρ_{33} μΩ.m	29.1	—	38.7	40.4	45.65	—
α_{11} μV K^{-1}	205	218	225	225	227	232
α_{33} μV K^{-1}	200	—	—	225	226	—
λ_{11} W m^{-1} K^{-1}	1.75	1.57	1.45	1.37	1.36	1.37
λ_{33} W m^{-1} K^{-1}	0.75	—	—	0.75	0.7	—
μ_H 300 K cm^2 V^{-1} s^{-1}	170	177	179	177	182	178
$p.10^{19}$ cm^{-3}	4.9	4.2	3.7	3.34	2.9	2.85
$Z_{11}.10^{-3}$ K^{-1}	2.7	2.7	2.75	2.9	2.7	2.5
$Z_{33}.10^{-3}$ K^{-1}	1.84	—	—	1.7	1.65	—

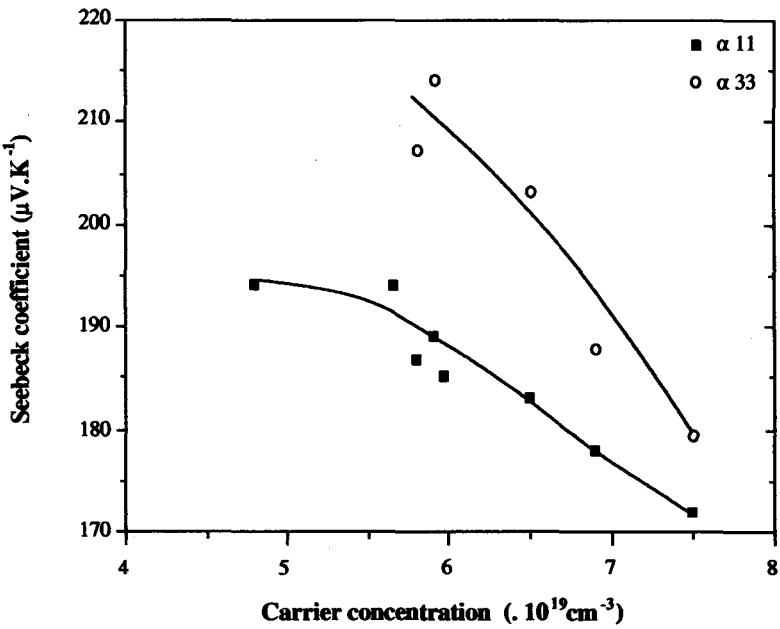

FIGURE 19 Seebeck coefficient as a function of carrier concentration for (S_1) solid solution. (From Reference 70 with permission.)

the Sb_2Te_3 compound. The Seebeck coefficient was relatively isotropic for (S_2) solid solution with samples exhibiting values between 200 and 230 μV K^{-1}.

Plots of the electrical resistivities ρ_{11} and ρ_{33} vs. carrier concentration are shown on Figures 21 and 22. For both solid solutions the values ρ_{11} and ρ_{33} decreased as the carrier concentration increased. The strong anisotropy between the electrical resistivities ρ_{11} and ρ_{33} could be explained by the anisotropy of the effective mass and the relaxation time.[72]

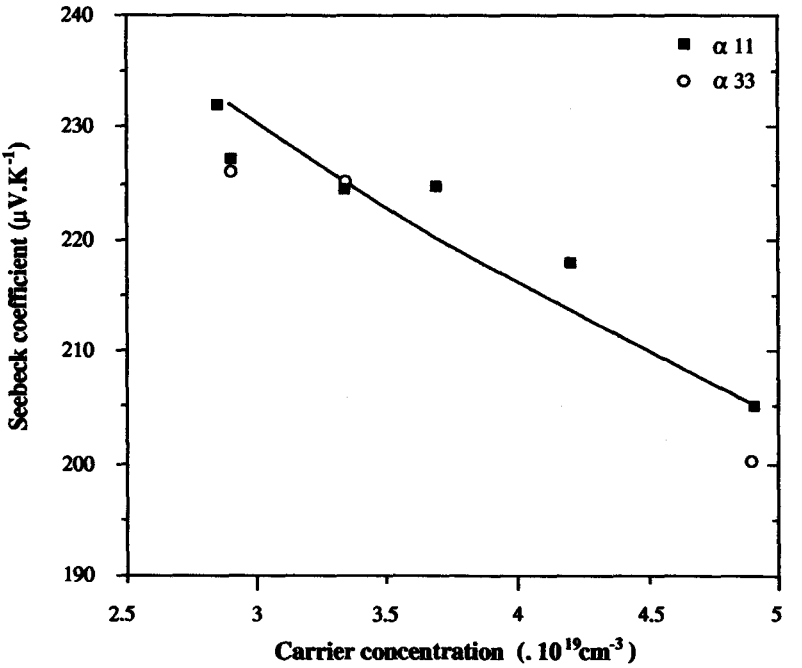

FIGURE 20 Seebeck coefficient as a function of carrier concentration for (S_2) solid solution. (From Reference 70 with permission.)

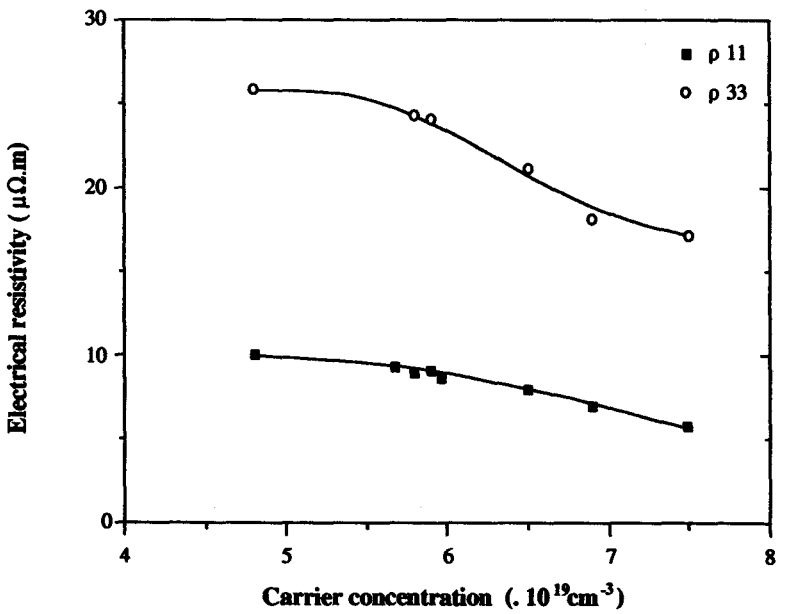

FIGURE 21 Electrical resistivity as a function of carrier concentration for (S_1) solid solution. (From Reference 70 with permission.)

The behaviors of the thermal conductivities λ_{11} and λ_{33} as a function of carrier concentration are displayed in Figures 23 and 24 for (S_1) and (S_2) solid solutions, respectively. All the values of λ_{11} are lower than those obtained for Bi_2Te_3 and Sb_2Te_3 compounds. The values of λ_{33} are nearly constant as a function of carrier concentration and lower than those of λ_{11}, showing strong anisotropic behavior for the (S_1) and (S_2) solid solutions. It is interesting to note that for the same carrier concentration, thermal conductivities measured on samples of (S_2) solid solution are higher

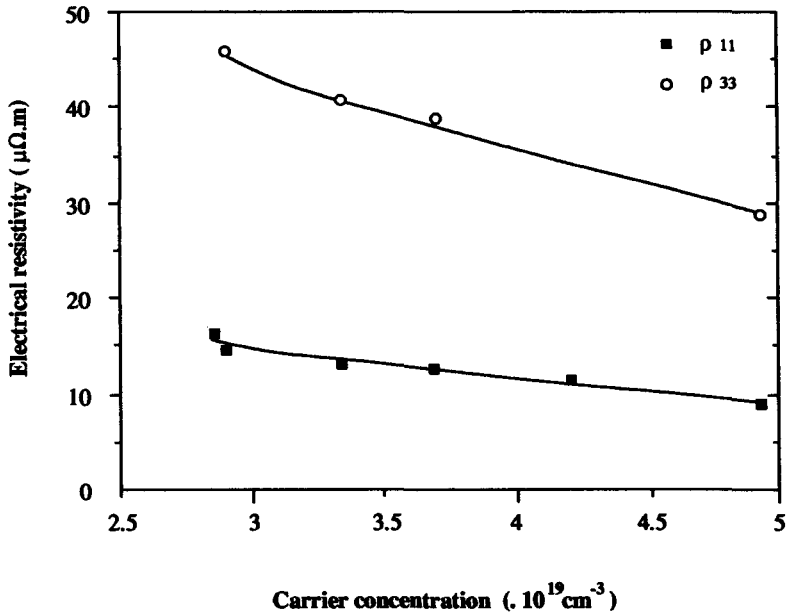

FIGURE 22 Electrical resistivity as a function of carrier concentration for (S_2) solid solution. (From Reference 70 with permission.)

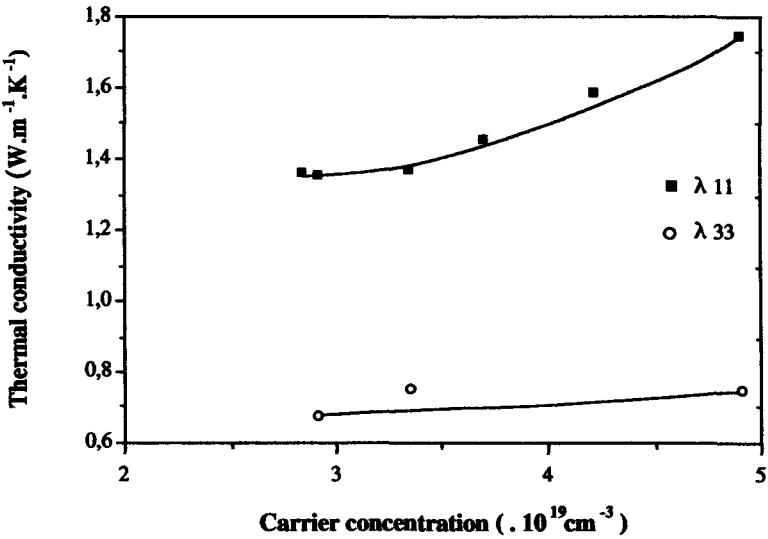

FIGURE 23 Thermal conductivity as a function of carrier concentration for (S_1) solid solution. (From Reference 70 with permission.)

than those obtained for (S_1) solid solution. It could be related to an increase of the lattice thermal conductivity for (S_2) solid solution.

Figures-of-merit ($Z = \alpha^2/\rho\lambda$) are plotted against carrier concentration for (S_1) and (S_2) solid solutions in Figures 25 and 26. The maximum Z_{11} value obtained for (S_1) solid solution was 2.95×10^{-3} K^{-1} with a carrier concentration of 4.8×10^{19} cm^{-3}. It should be noticed that the figure-of-merit was nearly isotropic for this solid solution ($Z_{11} \approx Z_{33}$) and similar results were previously obtained.[73]

A different behavior of the figure-of-merit was observed for (S_2) solid solution and the anisotropic figure-of-merit was maximum in a direction parallel to the cleavage planes (Z_{11}). A maximum value of 2.9×10^{-3} K^{-1} is obtained for $p = 3.4 \times 10^{19}$ cm^{-3}.

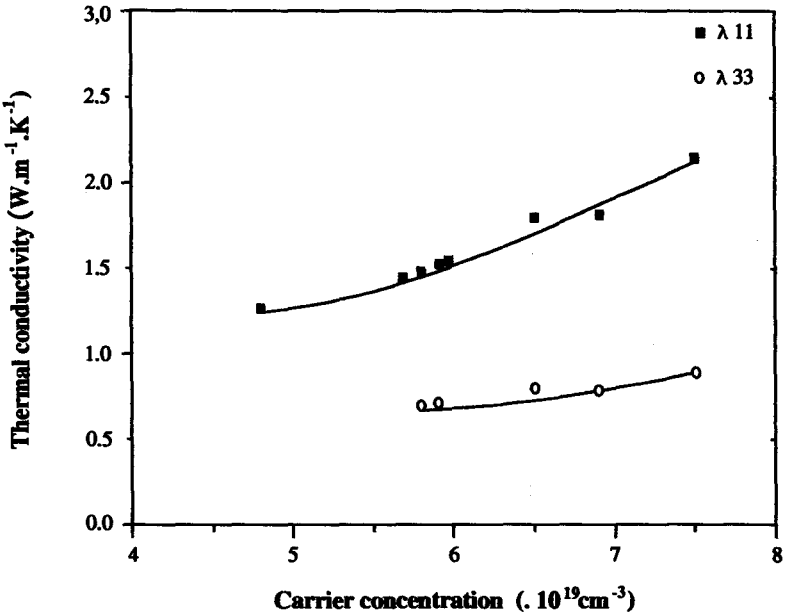

FIGURE 24 Thermal conductivity as a function of carrier concentration for (S_2) solid solution. (From Reference 70 with permission.)

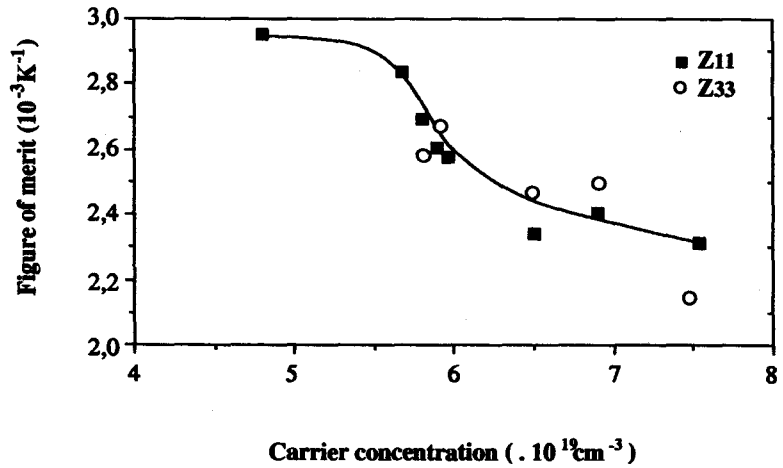

FIGURE 25 Figure-of-merit as a function of carrier concentration for (S_1) solid solution. (From Reference 70 with permission.)

It is of interest to study the thermoelectric properties of the solid solution (S_3) with a composition between (S_1) and (S_2). Indeed, the compensation between the thermoelectric properties of (S_1) and (S_2) could lead to a higher figure-of-merit. The results of measurements made on samples of $Bi_9Sb_{31}Te_{60}$ (S_3) solid solution saturated at 530 and 540°C are reported in Table 8. Values of the figure-of-merit were higher than those obtained for both (S_1) and (S_2) solid solutions. The maximum value was 3.2×10^{-3} K^{-1} for the sample saturated at 530°C with $p = 3.9 \times 10^{19}$ cm^{-3}.

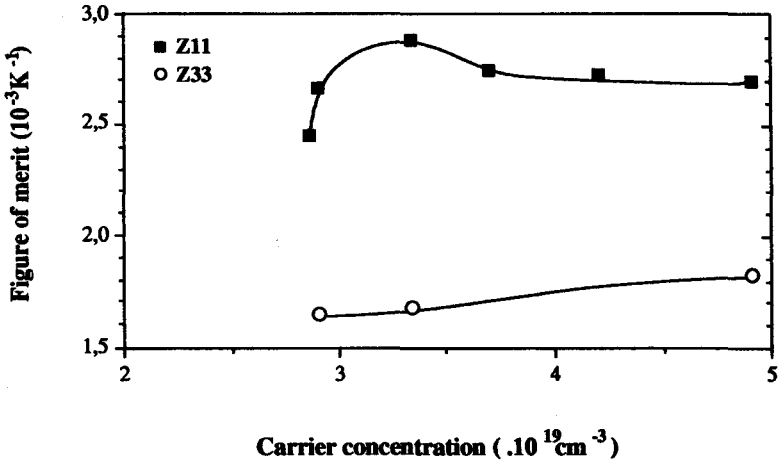

FIGURE 26 Figure-of-merit as a function of carrier concentration for (S_2) solid solution. (From Reference 70 with permission.)

Table 8. Thermoelectric Parameters for $Bi_9Sb_{31}Te_{60}$ Solid Solution

Saturation temperature °C	ρ_{11} μΩ.m	α_{11} μV K^{-1}	λ_{11} W m^{-1} K^{-1}	Z_{11} 10^{-3} K^{-1}	μ_H 300 K cm^2 V^{-1} s^{-1}	p.10^{19} cm^{-3}
540	8.87	205	1.51	3.13	186	4.1
530	8.89	206	1.49	3.2	190	3.9

19.5 Bi_2Te_3-Bi_2Se_3 Solid Solutions

Phase Diagram and Preparation by THM

As in the case of ternary phase diagram (Bi,Sb,Te), the pseudobinary section phase diagram Bi_2Te_3-Bi_2Se_3 on the Bi_2Te_3-rich side and the Bi_2Te_3-Bi_2Se_3-Te liquidus temperature field were determined by DSC measurements.[74] In Figure 27 the boundaries of the liquid-solid phase in the pseudobinary region Bi_2Te_3-Bi_2Se_3 as a function of the Bi_2Te_3-Bi_2Se_3 mole content (up to 30%) are displayed. Up to 12 mol% of Bi_2Te_3-Bi_2Se_3 in Bi_2Te_3-Bi_2Se_3 the results are the same as reported in the literature.[40–75] Over this composition, a second phase seems to appear and the liquidus temperature is constant.

The isothermal regions of the Bi_2Te_3-Bi_2Se_3-Te liquidus temperature field are displayed in Figure 28 for temperatures ranging from 560 to 592°C. $L_{2.5}$ and L_5 are the isoconcentration lines corresponding to Bi_2Te_3-Bi_2Se_3 solid solutions with x = 0.025 ($S_{2.5}$) and x = 0.05 (S_5).

The behavior of an isoconcentration curve and the interesting part of the ternary phase diagram are illustrated by the schematic Figure 29. The point L represents the composition of the solvent zone in equilibrium with the solid solution S at the interface of crystallization during the growth process by THM.

Experimental Results

Measurements were made on single crystals of Bi_2Te_3-Bi_2Se_3 ($S_{2.5}$) and Bi_2Te_3-Bi_2Se_3 (S_5) solid solutions with cleavage planes parallel to the growth axis. The samples are saturated to obtain the solidus composition on the Te-rich side between 540°C and the melting point. Then they are

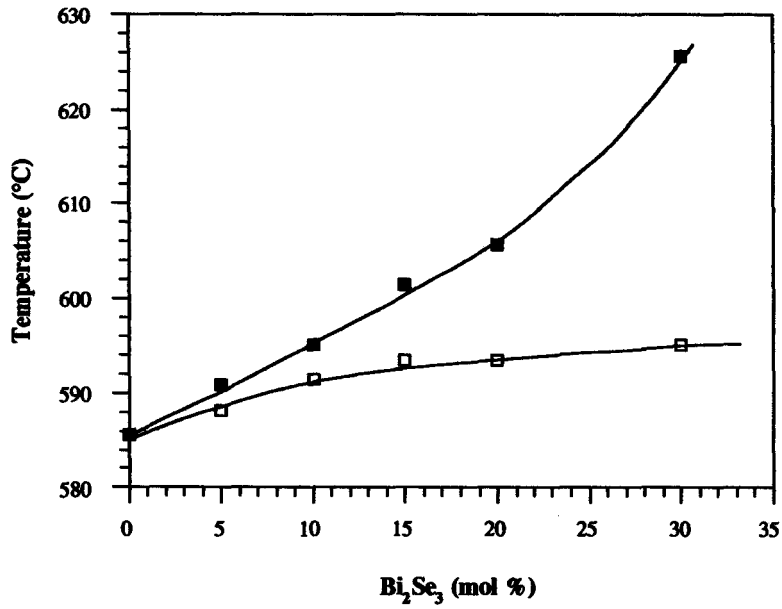

FIGURE 27 Liquidus and solidus temperatures for the Bi_2Te_3-Bi_2Se_3 pseudobinary section on the Bi_2Te_3-rich side.

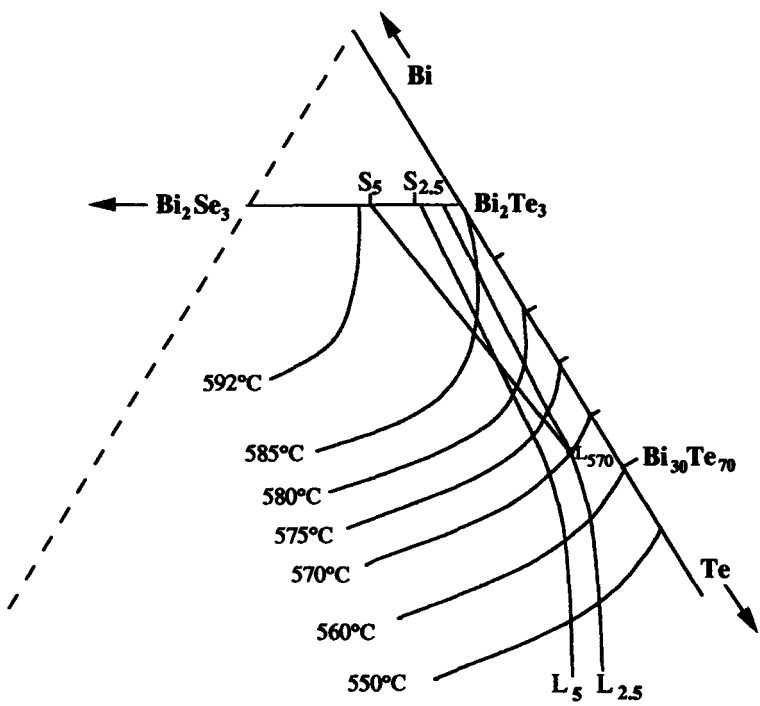

FIGURE 28 Liquidus and isoconcentration lines for $Bi_2(Te_{1-x}Se_x)_3$ solid solutions with x = 0.025 and x = 0.05.

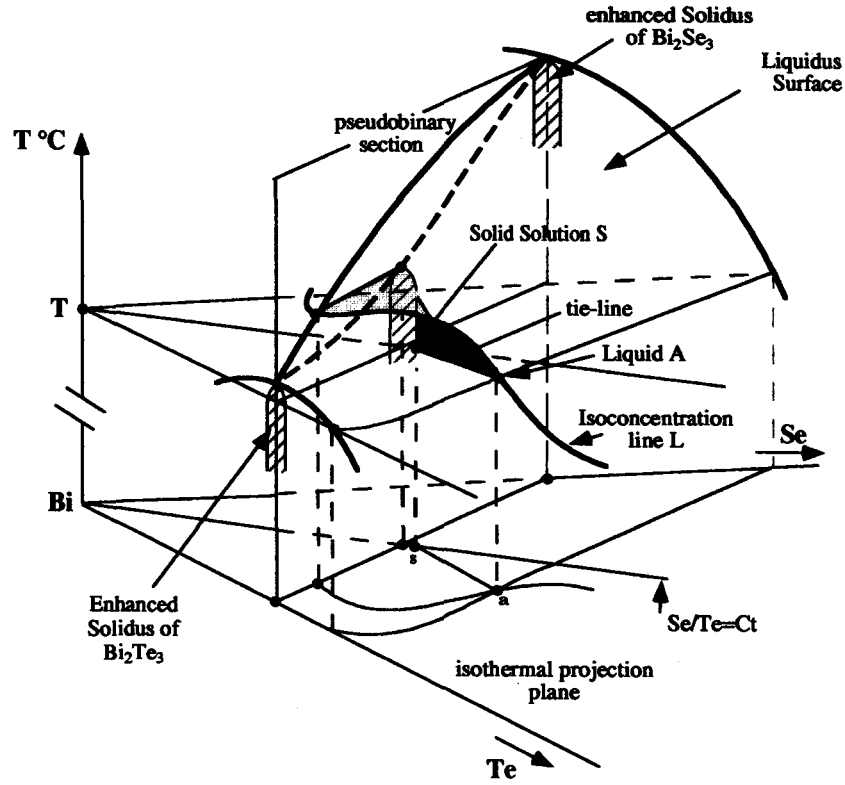

FIGURE 29 Schematic illustration of Bi-Te-Se ternary phase diagram.

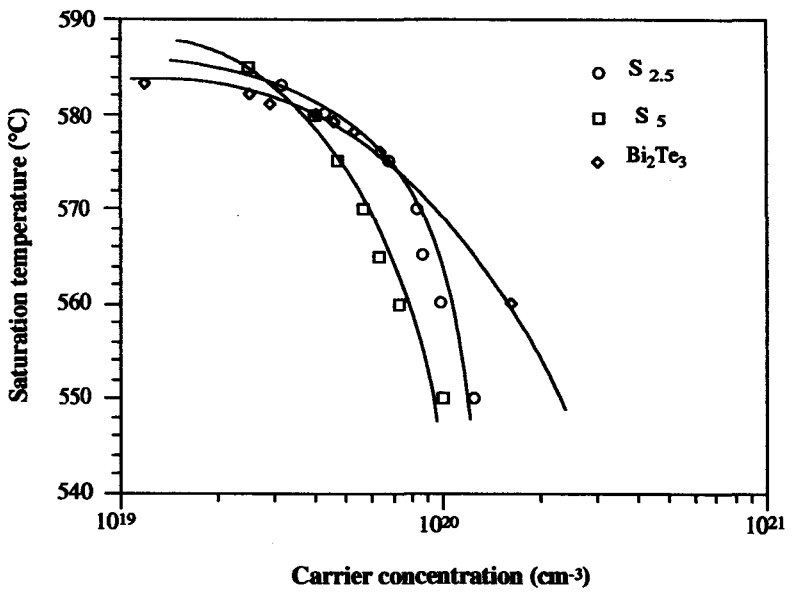

FIGURE 30 Hall carrier concentration as a function of saturation temperature for ($S_{2.5}$), (S_5) solid solutions and Bi_2Te_3 on the Te-rich side.

Table 9. Experimental Results at 300 K for ($S_{2.5}$) Solid Solution

Saturation temperature °C	583	580	575	570	565	560	550
ρ_{11} μΩ.m	14.8	11.05	8.25	7.1	7.0	6.9	5.4
α_{11} μV K^{-1}	246	230	201	189	186	187	160
λ_{11} W m^{-1} K^{-1}	1.62	1.66	1.80	1.95	1.97	2.05	2.15
n.10^{19} cm^{-3}	3.2	4.3	6.8	8.4	8.7	9.9	12.5
Z_{11}.10^{-3} K^{-1}	2.52	2.89	2.72	2.58	2.51	2.47	2.20

Table 10. Experimental Results at 300 K for (S_5) Solid Solution

Saturation temperature °C	585	580	575	570	565	560	550
ρ_{11} μΩ.m	16.3	11.1	10.5	9.8	9.2	8.3	6.7
α_{11} μV K^{-1}	243	223	215	207	203	197	175
λ_{11} W m^{-1} K^{-1}	1.47	1.59	1.65	1.70	1.75	1.83	1.95
n.10^{19} cm^{-3}	2.5	4	4.7	5.7	6.3	7.3	10
Z_{11} 10^{-3} K^{-1}	2.46	2.82	2.66	2.57	2.56	2.55	2.34

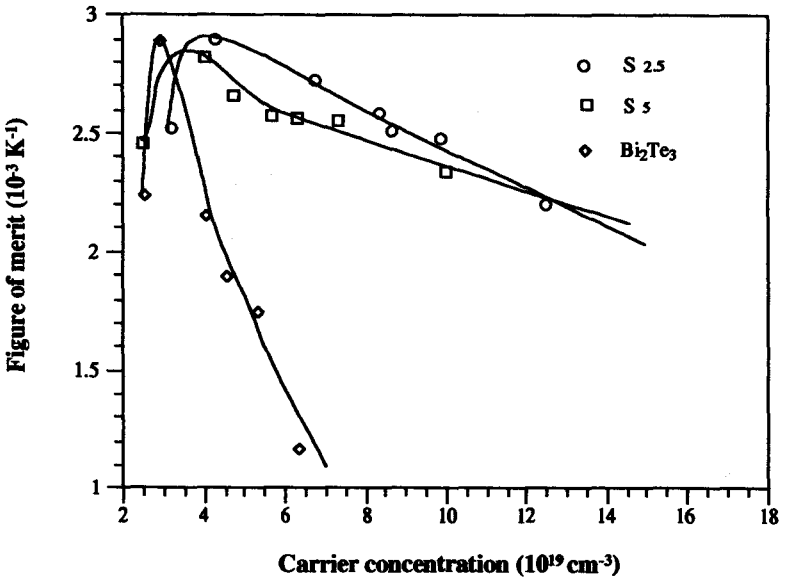

FIGURE 31 Figure-of-merit as a function of carrier concentration for ($S_{2.5}$), (S_5) solid solutions and Bi_2Te_3 on the Te-rich side.

characterized at 300 K by Hall effect measurements. Figure 30 displays the number of excess carriers as a function of annealing temperatures of the Te-rich side for ($S_{2.5}$), (S_5), and Bi_2Te_3 compound.

Assuming that the native major defects responsible for stoichiometric deviations are antistructure defects, as in Bi_2Te_3 compound,[76] the total number of defects (Te_{Bi} + Se_{Bi}) decreases as the content of selenium increases, and is probably connected with the formation energy of the Se_{Bi} defect being larger than that of Te_{Bi}. It should be noted that the temperature of the change in conductivity type increases with the content of selenium. All the measured samples on Figure 30 present n-type conductivity.

The results of Seebeck coefficient, thermal and electrical conductivities measured in a direction parallel to the cleavage planes (11) are collected in Tables 9 and 10 for ($S_{2.5}$) and (S_5) solid solutions, respectively. The Seebeck coefficient α_{11} and the electrical resistivity ρ_{11} for ($S_{2.5}$) (S_5) solid solutions decrease when the carrier concentration increases as in Bi_2Te_3. Nevertheless, for the same carrier concentration, the electrical resistivity λ_{11} of Bi_2Te_3 is lower than that of solid solutions.

Table 11. Anisotropy Measurements for ($S_{2.5}$) Solid Solution

Saturation temperature °C	583	575	565	560	550
$n.10^{19}$ cm^{-3}	3.2	6.8	8.7	9.9	12.5
α_{11}/α_{33}	1.03	1.05	1.05	1.06	1.07
ρ_{33}/ρ_{11}	4.38	5.47	6.08	6.16	6.71
$\lambda_{11}/\lambda_{33}$	2.15	2.28	2.32	2.35	2.41

Table 12. Anisotropy Measurements for (S_5) Solid Solution

Saturation temperature °C	585	580	570	560	550
$n.10^{19}$ cm^{-3}	2.5	4	5.7	7.3	10
α_{11}/α_{33}	1.02	1.04	1.06	1.05	1.06
ρ_{33}/ρ_{11}	4.29	5.03	5.51	6.26	6.56
$\lambda_{11}/\lambda_{33}$	2.10	2.21	2.27	2.34	2.40

This is consistent with the Hall mobility, about 150 $cm^2\ V^{-1}\ S^{-1}$ at 300 K, measured in ($S_{2.5}$) and (S_5) solutions and about 250 $cm^2\ V^{-1}\ S^{-1}$ in Bi_2Te_3 compound for a carrier concentration $n \approx 4 \times 10^{19}\ cm^{-3}$.

The thermal conductivity λ_{11} increases with the carrier concentration of the solid solutions. For the same carrier concentration the thermal conductivity for (S_5) is less than the thermal conductivity for ($S_{2.5}$) due to the decrease of the lattice thermal conductivity λ_L as expected.[77] The estimate of $\lambda_L = 1.27\ W\ m^{-1}\ K^{-1}$ for ($S_{2.5}$) solid solution, and $\lambda_L = 1.15\ W\ m^{-1}\ K^{-1}$ for (S_5) can be compared to $\lambda_L = 1.7\ W\ m^{-1}\ K^{-1}$ for Bi_2Te_3.

The best Z_{11} values of the figure-of-merit for the ($S_{2.5}$), (S_5) solid solutions are about $2.9 \times 10^{-3}\ K^{-1}$ with $n \approx 4 \times 10^{19}\ cm^{-3}$. Other Z_{11} values are higher than $2.5 \times 10^{-3}\ K^{-1}$ over a large carrier concentrations interval (2.0 to $9 \times 10^{19}\ cm^{-3}$), as shown in Figure 31. It should be noted that for Bi_2Te_3, the interesting Z_{11} values exist in a more limited carrier concentration domain.

The anisotropy of the thermoelectric properties of ($S_{2.5}$) and (S_5) is characterized by the results presented in Tables 11 and 12. The Seebeck coefficient is nearly isotropic ($\alpha_{11} \approx \alpha_{33}$) and similar results were previously reported.[36–78] The strong anisotropy of the electrical resistivity (ρ_{33}/ρ_{11}) increases with carrier concentrations. However, the anisotropy of the thermal conductivity ($\lambda_{11}/\lambda_{33}$) is nearly independent of the content of selenium and increases weakly with the carrier concentrations. The results of the anisotropy for ($S_{2.5}$) and (S_5) differ little from that of Bi_2Te_3[51–79] ($Z_{11} \approx 2Z_{33}$ for the lower carrier concentrations).

19.6 Conclusion

The authors have described a method to prepare single crystals of high quality, under well-defined thermodynamic conditions. Employing saturation techniques the domain of existence of the Bi_2Te_3 and Sb_2Te_3 compounds and their solid solutions has been explored, together with the behavior of their thermoelectric parameters as a function of the stoichiometric deviation along the solidus line. The solid solution ternary phase diagrams in the region of interest for thermoelectric applications were determined. The establishment of the tie-lines has facilitated the use of saturation techniques to study the dependence of the thermoelectric properties on stoichiometric deviation. The properties reported represent the fundamental behavior of the bulk material. Theoretical modeling[53,72–80] has been undertaken, based on a complex band structure and using mixed acoustic phonon and ionized impurity carrier scattering. The optimal figure-of-merit corresponds to a carrier concentration about $2.10^{19} cm^{-3}$ for the n-type solid solutions and about $4.10^{19} cm^{-3}$ for the p-type solid solutions. Very little change in the maximum values of the thermoelectric properties is found upon alloying. Increasing the energy gap reduces the influence of the minority carriers and results in acceptable figures-of-merit over a larger range around the optimal carrier concentration.

Some practical improvement in the figure-of-merit of these thermoelectric materials may be possible by suitable doping. Progress could also be made in investigating the effect of new scattering

mechanisms (e.g., resonance charge carrier scattering).[81] It may also be possible to increase the figure-of-merit by preparing the materials with special structures (e.g., two dimensions).[82]

References

1. Ainsworth, R. S. and Scanlon, W. W., *Phys. Rev.*, 111, 1029, 1958.
2. Birkholz, U. and Haacke, G., *Z. Naturforsch.*, 17a, 161, 5, 1962.
3. Goldsmid, H. J., *Thermoelectric Refrigeration*, Pion Ltd., London, 1986.
4. Yim, W. and Rosi, F. D., *Solid State Electron.*, 15, 1121, 1972.
5. Rosi, F. D., Abeles, B., and Jensen, R. V., *J. Phys. Chem. Solids*, 10, 191, 1959.
6. Rosi, F. D. and Ramberg, F. G., *Thermoelectricity*, Egli, P.M., Ed., John Wiley & Sons, New York, 1960.
7. Satterthwaite, C. D. and Ure, R. W., *Phys. Rev.*, 108, 1164, 1957.
8. Brebrick, R. F., *J. Phys. Chem. Solids*, 30, 719, 1969.
9. Lange, P. W., *Naturwissenschaften*, 27, 133, 1939.
10. Francombe, M. H., *Br. J. Appl.* 9, 415, 1958.
11. Brebrick, R. F., *J. Appl. Crystallogr.*, 1, 241, 1968.
12. Drabble, J. R. and Goodman, C. H. L., *J. Phys. Chem. Solids*, 5, 142, 1958.
13. Jenkins, J. O., Rayne, J. A., and Ure, R. W., *Phys. Rev. B*, 5, 3171, 1972.
14. Wagner, V., Dolling, G., Powell, B. M., and Landwehr, G., *Phys. Status Solidi (b)*, 85, 311, 1978.
15. Thuler, M. R., Benbow, R. L., and Hurych, Z., *Chem. Phys.*, 71, 265, 1982.
16. Kullmann, W., Geurts, J., Richter, W. et al., *Phys. Status Solidi (b)*, 125, 131, 1984.
17. Drabble, J. R. and Wolfe, R., *Proc. Phys. Soc.*, 69, 113, 1957.
18. Black, J., Conwell, E. M., Seigle, L., and Spencer, C. W., *J. Phys. Chem. Solids*, 2, 240, 1957.
19. Austin, I. G., *Proc. Phys. Rev.*, 72, 545, 1958.
20. Austin, I. G. and Sheard, A., *J. Electron. Contrib.*, 3, 236, 1957.
21. Köhler, H., *Phys. Status Solidi (b)*, 73, 95, 1976.
22. Köhler, H., *Phys. Status Solidi (b)*, 74, 591, 1976.
23. Semiletov, S. A., *Kristallografiya*, 1, 403, 1956.
24. Shunk, F. A., *Constitution of Binary Alloys, second supplement*, McGraw-Hill, New York, 1969.
25. Langhammer, H. T., Stordeur, M., Sobotta, H., and Riede, V., *Phys. Status Solidi (b)*, 123, K47, 1984.
26. Sehr, R. and Testardi, I. R., *J. Phys. Chem. Solids*, 23, 1219, 1962.
27. Von Middendorf, A., Dietrich, K., and Landwehr, G., *Solid State Commun.*, 13, 443, 1973.
28. Smith, M. S., Knight, R. S., and Spencer, C. W., *J. Appl. Phys.*, 33, 7, 1962.
29. Testardi, L. R. and Wiese, J. R., *Trans. Met. Soc. AIME*, 221, 1961.
30. Volotskii, M. P., Gudkin, T. S., Dashevskii, Z. M., Kaidanov, V. I., and Syibnev, I. V., *Sov. Phys. Semicond.*, 8, 682–683, 1974.
31. Stölzer, M., Stordeur, M., Sobotta, H., and Riede, V., *Phys. Status Solidi (b)*, 138, 259, 1986.
32. Süssmann, H. and Heiliger, W., *Phys. Status Solidi (a)*, 80, 535, 1989.
33. Stordeur, M. and Sobotta, H., *Proc. 1st European Conference on Thermoelectrics*, Rowe, D. W., Ed., Cardiff, 1987.
34. Köhler, H. and Freudenberger, A., *Phys. Status Solidi (b)*, 84, 195, 1977.
35. Lidorenko, N. S., Galev, V. N., Dashevskü, Z. N., and Kolomets, N. V., *Sov. Phys. Dokl.*, 20, 10, 1976.
36. Kutasov, V. A., Svechnikova, T. E., and Chizhevskaya, S. N., *Sov. Phys. Solid State*, 10, 1724, 1987.
37. Greenaway, D. L. and Harbeke, G., *J. Phys. Chem. Solids*, 26, 1585, 1965.
38. Muragi, B. D. and Zope, J. K., *J. Mater. Sci. Lett.*, 3, 663, 1984.
39. Miller, G. R., Li, C. Y., and Spencer, C. N., *J. Appl. Phys.*, 34, 1398, 1963.
40. Bankina, V. F. and Abrikosov, N. Kh., *Russ. J. Inorg. Compounds*, 9 (4), 502, 1964.
41. Wiese, J. R. and Muldawer, L., *J. Phys. Chem. Solids*, 15, 13, 1960.
42. Gaillard, L., doctoral thesis, Nancy, 1989.
43. Scherrer, H., Weber, S., and Scherrer, S., *Phys. Lett. A*, 77, 189, 1980.
44. Hansen, M., *Constitution of Binary Alloys*, McGraw-Hill, New York, 1958.
45. Fleurial, J. P., Gailliard, L., Triboulet, R., Scherrer, H., and Scherrer, S., *J. Phys. Chem. Solids*, 49, 1237, 1988.

46. Zhukov, A. A., Frolov, V. V., Davysov, S. V., Roshchina, V. R., and Kuleshova, N. N., *Izv. Akad. Nauk SSSR*, Metaly I, 183, 1983.
47. Miller, G. R. and Li, C. Y., *J. Phys. Chem. Solids*, 26, 173, 1965.
48. Pecheur, P. and Toussaint, G., *Proc. 1st European Conference on Thermoelectrics*, Rowe, D. M., Ed., Cardiff, 1987, 394.
49. Scherrer, S., Scherrer, H., Chitroub, M., and Fleurial, J. P., *Proc. 6th Int. Conf. on Thermoelectric Energy Conversion*, 3, Arlington, 1986.
50. Scherrer, S., Scherrer, H., Chitroub, M., and Samuel, A., *Proc. 20th Intersociety Energy Conversion Engineering Conf.*, Miami Beach, 1985.
51. Drabble, J. R., Groves, R. D., and Wolfe, R., *Proc. Phys. Soc.*, 71, 430, 1957.
52. Goldsmid, H. J., *Proc. Phys. Soc.*, 71, 633, 1958.
53. Fleurial, J. P., Gailliard, L., Triboulet, R., Scherrer, H., and Scherrer, S., *J. Phys. Chem. Solids*, 49, 1249, 1988.
54. Eichler, W. and Kurg, T., *Phys. Status Solidi (b)*, 101, K1, 1980.
55. Gaidukova, V. S., Dudkin, L. D., and Sokolov, O. B., *Izv. Akad. Nauk SSSR Neorg. Mater.*, 14, 437, 1978.
56. Langhammer, H. T., Stordeur, M., Sobotta, H., and Riede, V., *Phys. Status Solidi (b)*, 123, K47, 1984.
57. Simon, G. and Eichler, W., *Phys. Status Solidi (b)*, 103, 289, 1981.
58. Stordeur, M. and Simon, G., *Phys. Status Solidi (b)*, 124, 799, 1984.
59. Rowe, D. M. and Bhandari, C. M., *Modern Thermoelectrics*, Holt, Reinhardt, and Winston, Eds., London, 1983.
60. Smith, M. J., Knight, R. J., and Spencer, C. W., *J. Appl. Phys.*, 33, 7, 1962.
61. Abrikosov, N. Kh. and Poretskaya, L. V., *Izv. Akad. Nauk SSSR Neorg. Mater.*, 1, 503, 1965.
62. Basr, R., *CALPHAD*, 2, 113, 1978.
63. Cholinski, J., Lasocka, M., and Matyja, H., *Rev. Phys. Appl.*, 12, 1, 1977.
64. Steininger, J., *J. Appl. Phys.*, 41, 6, 1970.
65. Caillat, T., Carlé, M., Perrin, D., Scherrer, H., and Scherrer, S., *J. Phys. Chem. Solids*, 53, 227, 1992.
66. Castanet, R., Bergman, C., and Mathieu, J. C., *CALPHAD*, 3, 205, 1979.
67. Stary, Z., Horak, J., Stordeur, M., and Stolzer, M., *J. Phys. Chem. Solids*, 49, 29, 1988.
68. Caillat, T., doctoral thesis, Nancy, 1991.
69. Abrikosov, N. Kh., Bankina, V. F., Kolomoets, L. A., and Dzhliashvili, N. V., *Izv. Akad. Nauk SSSR, Neorg. Mater.*, 13, 827, 1975.
70. Caillat, T., Carle, M., Pierrat, P., Scherrer, H., and Scherrer, S., *J. Phys. Chem. Solids*, 53, 1121, 1992.
71. Gaillard, L., Caillat, T., Scherrer, H., and Scherrer, S., *Proc. 8th Int. Conf. on Thermoelectric Energy Conversion*, Scherrer, H. and Scherrer, S., Eds., Nancy, 1989.
72. Caillat, T., Gailliard, L., Scherrer, H., and Scherrer, S., *J. Phys. Chem. Solids*, 54, 525–581, 1993.
73. Süssmann, H. and Heiliger, W., *Phys. Status Solidi (a)*, 51, K20, 1979.
74. Carle, M., doctoral thesis, Nancy, 1992.
75. McHugh, J. P. and Tiller, W. A., *Trans. Met. Soc. AIME*, 215, 651, 1959.
76. Scherrer, H., Hammow, B., Fleurial, J. P., and Scherrer, S., *Phys. Lett. A*, 130, 161, 1988.
77. Golts'man, B. M., Ikonnikova, G. N., Kutasov, V. A., and Shapiro, E. Kh., *Sov. Phys. Solid State*, 12, 1103, 1970.
78. Kaibe, H., Tanaka, Y., Sakata, M., and Nishida, I., *J. Phys. Chem. Solids*, 50, 945, 1989.
79. Fleurial, J. P., doctoral thesis, Nancy, 1988.
80. Fleurial, J. P., *Proc. 11th Int. Conf. on Thermoelectrics*, Rao, K. R., Ed., Arlington, 1992.
81. Ravich, Y. I. and Vedernikov, M. V., *Proc. of the 9th Int. Conf. on Thermoelectrics*, Vining, C. B., Ed., Pasadena, 1990.
82. Hicks, L. D. and Dresselhaus, M. S., *Proc. of the 1st Natl. Thermogenic Cooler Conf.*, Fort Belvoir, 1992.

20

Valence Band Structure and the Thermoelectric Figure-of-Merit of $(Bi_{1-x}Sb_x)_2Te_3$ Crystals

M. Stordeur
Martin Luther University, Halle-Wittenberg, Germany

20.1 Introduction

The thermoelectric figure-of-merit Z is the "hardware" of a thermoelectric material and is a measure of its performance in thermoelectric devices as solid state coolers (Peltier effect) or generators (Seebeck effect). Z is defined by

$$Z = \frac{\alpha^2\sigma}{\lambda} \tag{1}$$

where α is the Seebeck coefficient and σ and λ are the electrical conductivity and the thermal conductivity, respectively.

From a solid-state physics point of view the thermoelectric figure-of-merit is a complex quantity which includes both the charge and heat transport properties of the crystal. So Z is influenced by the system of free charge carriers (in general, electrons and holes), by the phonon system, and by the interaction between both systems. Consequently, the thermoelectric figure-of-merit can be described in terms of the electronic band structure, the lattice dynamical properties, and the charge carrier scattering mechanisms such as phonons and crystal impurities. Finally, all these properties are determined by the chemical bonding in the solid state.

During the last decade there has been a worldwide search for new materials with higher thermoelectric figures-of-merit and attempts to improve the thermoelectric properties of the known compounds.[1] It is anticipated that the successful development of such materials will lead to new fields of application for thermoelectric devices and related technologies based on bulk crystals and

0-8493-0146-7/95/$0.00+$.50

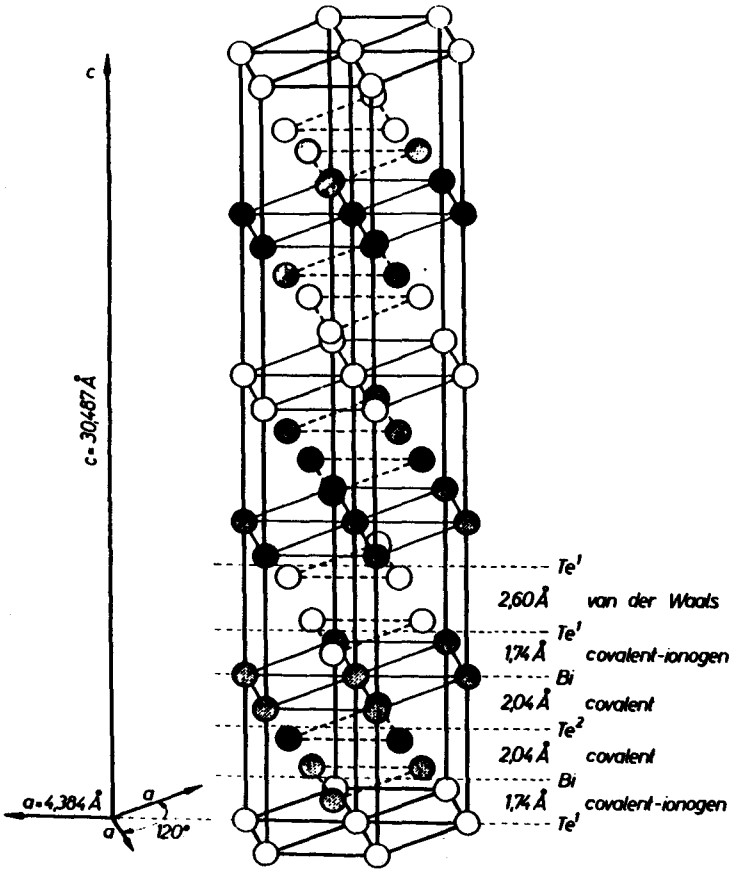

FIGURE 1 Layer structure of a Bi_2Te_3 crystal in the hexagonal system with data on atomic distances and predominant binding forces (after Reference 5).

on films. However, the improvement of thermoelectric materials requires a detailed knowledge of all the factors which determine their properties.

At present solid solutions of the compounds bismuth telluride (Bi_2Te_3), antimony telluride (Sb_2Te_3), and bismuth selerride (Bi_2Se_3) have the highest thermoelectric figures-of-merit in the temperature range around room temperature.[2] The most suitable materials for the n-leg and the p-leg of thermocouples are the suitably doped mixed crystals n-$Bi_2(Te_{1-y}Se_y)_3$ ($y = 0.1$) and p-$(Bi_{1-x}Sb_x)_2Te_3$ ($x = 0.75$) and in the following sections the connection between the valence band structure and the thermoelectric figure-of-merit of $(Bi_{1-x}Sb_x)_2Te_3$ will be considered in detail.

20.2 Fundamental Properties of $(Bi_{1-x}Sb_x)_2Te_3$ Mixed Crystals

A review of the physical properties of $(Bi_{1-x}Sb_x)_2Te_3$ is given in References 3 and 4. The lattices of the isomorphous semiconductors Sb_2Te_3, Bi_2Te_3, and Bi_2Se_3 (tetradymite Bi_2Te_2S structure) which crystallize in the trigonal system, have a rhombohedral unit cell which is based on five atoms per molecule. In order to demonstrate more clearly the layered structure which is typical of these crystals a transformation into the hexagonal system is frequently carried out, as exemplified by the Bi_2Te_3 crystal in Figure 1.

The lattice consists of a sequence of atomic layers:

$$\ldots VI^1 - V - VI^2 - V - VI^1 \ldots$$

arranged in such a way that after each five layers the stacking sequence is repeated and can be considered as a sandwich, with three stacks forming the hexagonal unit cell.

The crystals have three energetically different lattice sites:

1. VI^2-sites: the Te^2, Se^2 atoms are covalently bound to the surrounding six Bi, Sb atoms by sp^3d^2 hybrids.
2. V-sites: the metal atoms Bi, Sb have six Te, Se atoms as neighbors where one *p*-electron of the Te^1, Se^1 atoms transfers to the metal atom in order to fill the sp^3d^2 hybrid. The mixed covalent bond to the Te^1, Se^1 atoms has a shorter bond length and is stronger than that to the Te^2, Se^2 atoms.[3]
3. VI^1-sites: the Te^1, Se^1 atoms have a covalent-ionogen bond on one side with the three Bi, Sb atoms via the four *p*-electrons of Te, Se, while on the other side they are only weakly bound to the atoms of the next Te^1, Se^1 layer.

Originally there was a consensus (see Reference 5) that the bonding between the VI^1-VI^1 layers is exclusively of the van der Waals type, but now there is evidence that results from investigations on the thermoelastic properties[6] and from the study of the pressure dependence of the Raman active lattice vibrations[7] which indicates that the Te^1-Te^1 bond between the layers is weak. There is also a significant proportion of covalent bonds.

It can be seen from the crystal structure (Figure 1), whose symmetry elements are described by the point group D_{3d}, that all mechanical, transport, and optical crystal properties exhibit a marked anisotropy. For example, single crystals of the $(Bi_{1-x}Sb_x)_2Te_3$ system possess an easy cleavage with mirror-like planes perpendicular to the trigonal c-axis (optical axis).

In spite of crystallographic similarities the real crystals also reveal marked differences. Point defects, which result from deviations from stoichiometry (metal components Sb and Bi, respectively, are preferentially built-in), induce Bi_2Te_3 and Sb_2Te_3 always to crystallize as p-type semiconductors from stoichiometric melts, whereas Bi_2Se_3 is n-type. In Sb_2Te_3 this disorder is so strong that no inversion to the n-type is possible.[8,9]

In order to change the transport properties of crystals intentionally, the behavior of impurity dopants (Mn, Mg, Ge acceptors; I, Tl doners; and Cu in Sb_2Te_3 amphoteric) was extensively studied.[10–15] The effect of Pb and Ge acceptors is discussed in Reference 16.

It is also remarkable that the electronic transport properties of components at the edge of the system $(Bi_{1-x}Sb_x)_2Te_3$, Bi_2Te_3 (x = 0), and Sb_2Te_3 (x = 1) show a qualitatively different anisotropy behavior.[3,17–21]

20.3 Thermoelectric Figure-of-Merit of p-$(Bi_{1-x}Sb_x)_2Te_3$ Crystals—Experimental Results

From Equation 1 it can be seen that Z becomes larger when the Seebeck coefficient and electrical conductivity increase and the thermal conductivity decreases. It is usual to vary α and σ by changing the hole concentration, e.g., by ensuring that there is a tellurium excess in the melt from which the crystals are grown. But a decrease in the free carrier concentration results in an increase in the Seebeck coefficient and a decrease in electrical conductivity so the carrier density has to be optimized to attain a high product $\alpha^2\sigma$.[22] Another way of increasing the thermoelectric figure-of-merit is to minimize the thermal conductivity λ. Here it must be taken into consideration that λ is composed of an electronic part λ_e and a lattice component λ_L:

$$\lambda = \lambda_e + \lambda_L \tag{2}$$

and for λ_e the Wiedemann-Franz law is valid:

$$\lambda_e = L\sigma T \tag{3}$$

Here L is the Lorentz number and T the absolute temperature. Whereas λ_e depends on the carrier concentration via the reduced Fermi level η, λ_L is only influenced by the lattice properties.

According to Ioffe[23] the lattice thermal conductivity can be minimized by forming mixed crystals. In the mixed crystal system $(Bi_{1-x}Sb_x)_2Te_3$, the minimum of λ_L is expected to correspond with the point of maximum disorder of both compounds Bi_2Te_3 and Sb_2Te_3 (x = 0.5). This presumption is confirmed by the following lattice thermal conductivity data (in $Wm^{-1}\,K^{-1}$): $\lambda_L(x = 0.5) = 0.60$, $\lambda_L(x = 0.75) = 0.67$,[24] $\lambda_L(x = 0.5) = 0.70$, $\lambda_L(x = 0.75) = 0.90$.[25]

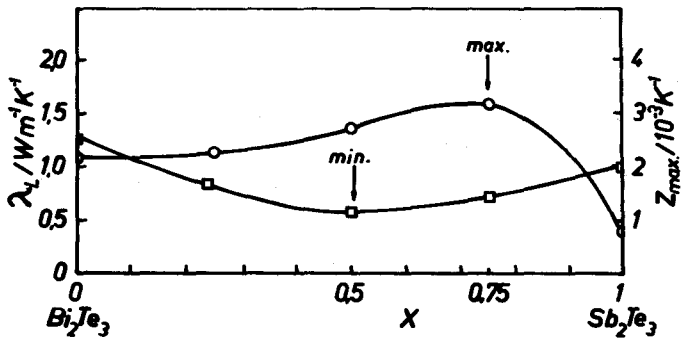

FIGURE 2 Maximum thermoelectric figure-of-merit Z_{max} (optimum doped crystals) and lattice thermal conductivity λ_L for $(Bi_{1-x}Sb_x)_2Te_3$ single crystals as a function of composition x ○, Z_{max}; □, λ_L (after Reference 26).

It could be expected that the maximum thermoelectric figure-of-merit in the $(Bi_{1-x}Sb_x)_2Te_3$ system also corresponds to the composition x = 0.5, but this is not the case. Extensive and careful experimental investigations led to the conclusion[4,24] that the maximum thermoelectric figure-of-merit in the mixed crystal series $(Bi_{1-x}Sb_x)_2Te_3$ is obtained at the composition x = 0.75 and that the optimum carrier concentration reaches a value $Z = 3.3 \cdot 10^{-3}\,K^{-1}$ at room temperature. Consequently, it is necessary to obtain a deeper understanding of the solid-state properties that limit Z and to provide a quantitative explanation of the common p-Bi_2Te_3-type materials.

The maximum thermoelectric figure-of-merit of an optimally doped $(Bi_{1-x}Sb_x)_2Te_3$ single crystal is displayed in Figure 2 as a function of composition.[26]

20.4 Influence of the Valence Band Structure on the Thermoelectric Figure-of-Merit of $(Bi_{1-X}Sb_X)_2Te_3$

Band structure calculations are unavailable for the mixed crystal series $(Bi_{1-x}Sb_x)_2Te_3$. Theoretical results are given only for the compound Bi_2Te_3.[27–29] We cannot use these results directly for the calculation of the thermoelectric figure-of-merit and consequently the parameters of the band structure model (e.g., effective masses, mobilities, relaxation time constants) and models for the scattering mechanisms are used. Thus, in the following section the relationship between the band structure parameters and the thermoelectric figure-of-merit is considered in a phenomenological manner.

Phenomenological Considerations

If it is assumed that only holes that obey a parabolic energy dispersion relationship contribute to the electronic transport (single band conduction) and the charge carriers are only scattered by the acoustic phonons during their drift through the crystal, then a valid expression for the thermoelectric figure-of-merit is[26,30]

$$Z = \frac{\dfrac{\mu_{cl}\left(\dfrac{m_d}{m_0}\right)^{3/2}}{\lambda_L} g_1(\eta)}{1 + \dfrac{\mu_{cl}\left(\dfrac{m_d}{m_0}\right)^{3/2}}{\lambda_L} g_2(\eta)} \tag{4}$$

where μ_{cl}, the classical hole mobility, is given by

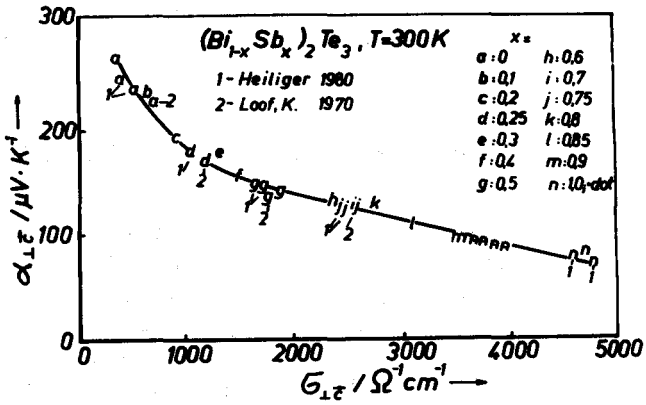

FIGURE 3 Seebeck coefficient $\alpha_{\perp c}$ and electrical conductivity $\sigma_{\perp c}$ for doped and undoped crystals of the system $(Bi_{1-x}Sb_x)_2Te_3$ (after Reference 31).

$$\mu_{cl} = \frac{4}{3\sqrt{\pi}} \frac{q\tau_o^{ac}}{m_{\perp c}} (k_0 T)^{-1/2} \tag{5}$$

where $m_{\perp c}$ is the effective mass perpendicular to the trigonal c-axis (only this direction is considered here and is a reasonable simplification in the case of these materials), m_d is the total density-of-states effective mass, τ_o^{ac} the energy-independent factor in the relaxation time, and q, k_0, m_0 are the elementary charge, Boltzmann constant, and free electron mass, respectively. At constant temperature $g_l(\eta)$ and $g_2(\eta)$ are functions of the reduced Fermi level η only and can be represented by the usual Fermi-Dirac integrals $F_\nu(\eta)$:

$$g_1(\eta) = \frac{k_0^2 m_0^{3/2}}{q\hbar^3\sqrt{2}\pi^{3/2}} (k_0 T)^{3/2} F_0(\eta) \left\{ 2\frac{F_1(\eta)}{F_0(\eta)} - \eta \right\}^2 \tag{6}$$

$$g_2(\eta) = \frac{k_0^2 m_0^{3/2}}{q\hbar^3\sqrt{2}\pi^{3/2}} (k_0 T)^{3/2} F_0(\eta)\, T \left\{ 3\frac{F_2(\eta)}{F_0(\eta)} - 4\frac{F_1^2(\eta)}{F_0^2(\eta)} \right\} \tag{7}$$

Similarly it follows that the Seebeck coefficient α is given by

$$\alpha = \frac{k_0}{q} \left\{ 2\frac{F_1(\eta)}{F_o(\eta)} - \eta \right\} \tag{8}$$

and the electrical conductivity σ as

$$\sigma = \frac{q m_0^{3/2}}{\hbar^3\sqrt{2}\pi^{3/2}} (k_0 T)^{3/2} m \mu_{cl} \left(\frac{m_d}{m_0} \right)^{3/2} F_0(\eta) \tag{9}$$

where $\hbar$ is Planck's constant divided by 2π.

It can be seen from Equations 4 and 5 that Z is strongly influenced by the solid-state parameters and can be expressed in the form:

$$Z_{appr.} \propto \tau_0^{ac} m_{\perp c}^{-1} \left(\frac{m_d}{m_0} \right)^{3/2} \lambda_L^{-1} \tag{10}$$

where $m_{\perp c}^{-1}(m_d/m_0)^{3/2}$ represents the contribution of the electronic band structure to the thermoelectric figure-of-merit. A review of the experimental results for the Seebeck coefficient $\alpha_{\perp c}$ and the electrical conductivity $\sigma_{\perp c}$ is presented in Figure 3.

In order to study the quantitative influence of the valence band parameter $m_{\perp c}^{-1}(m_d/m_0)^{3/2}$ on the thermoelectric figure-of-merit (Equation 4), it is necessary to determine the dependence of this parameter on the composition x of the mixed crystal series $(Bi_{1-x}Sb_x)_2Te_3$. This can be achieved

by using a combination of optic-spectroscopic and transport investigations and by interpreting the data in terms of the electronic band structure and the scattering mechanisms. This is done in the following sections.

Band Structure and Charge Carriers Scattering Model for $(Bi_{1-x}Sb_x)_2Te_3$ Crystals

The valence band structure model developed by Drabble and Wolfe (DW model)[33,34] for Bi_2Te_3 crystals has proved to be fundamental for the interpretation of the electronic transport properties in this anisotropic crystal. In spite of all the changes and modifications that have taken place it still serves as the standard model, especially for the description of anisotropic transport and optical free carrier phenomena in Bi_2Te_3 and in the $(Bi_{1-x}Sb_x)_2Te_3$ system. In the case of Bi_2Te_3 this model had been previously verified by the successful explanation of galvanomagnetic measurements.[35,36]

In accordance with the DW model the following assumptions are made: the top of the highest valence band is sixfold degenerate, the valleys have elliptical isoenergetic surfaces, and the following dispersion law operates.

$$\gamma(E) = \frac{\hbar^2}{2m_0}(a_{11}^H k_1^{H^2} + a_{22}^H k_2^{H^2} + a_{33}^H k_3^{H^2}) \tag{11}$$

where k_i^H are the components of the holes' wave number vector in the ellipsoid main axis system and E is the carrier energy. In k-space (for the Brillouin zone of the crystals see, for example, Reference 37) k_1^H is parallel to the twofold axes, k_2^H and k_3^H include the tilt angle ϑ with the bisectric and trigonal axes of the crystal coordinate system, respectively, and a_{ii}^H is connected with the momentum effective masses m_{ii}^H by the relationship

$$m_{ii}^{H-1} = m_0^{-1} a_{ii}^H \left(\frac{d\gamma}{dE}\right)^{-1} \tag{12}$$

For nonparabolicity, which is included in the relationships, the first-order approximation $\gamma(E) = E + \gamma_1 E^2$ holds where γ_1 is a constant.

Carrier scattering is by acoustic phonons and is assumed to be isotropic, frequency independent, and can be described by the relaxation time

$$\tau(E) = \tau_0^{ac} \gamma^{-1/2}(E) \left(\frac{d\gamma}{dE}\right)^{-1} \tag{13}$$

The complicated anisotropic mixed scattering mechanism due to acoustic phonons and ionized impurities used in the interpretation of the anisotropic behavior of the transport properties of single crystals Sb_2Te_3 ($x = 1$)[19,20] is not given further consideration.

Based on this model the carrier density is given by[38]

$$p = \frac{2\sqrt{2}}{3\pi^2\hbar^3} m_d^{3/2} \langle 1 \rangle \tag{14}$$

The symbol $\langle A(E) \rangle$ represents the usual integration of the function A(E) over energy,[39] m_d^v is the density-of-states mass in a single valley,

$$m_d = 6^{2/3} m_d^v, \; m_d^v = m_0 (a_{11}^H a_{22}^H a_{33}^H)^{-1/3} \tag{15}$$

The effective susceptibility masses used to describe the free carrier optical effects are given by

$$m_{\perp,\|_c}^{(\chi)-1} = m_{\perp,\|_c}^{-1} \frac{{}_0^{3/2}L_{-1}}{{}_0^{3/2}L_0} \tag{16}$$

and in the parabolic case they are identical with the conductivity masses $m_{\perp c}$ and $m_{\|_c}$ at the band edges with

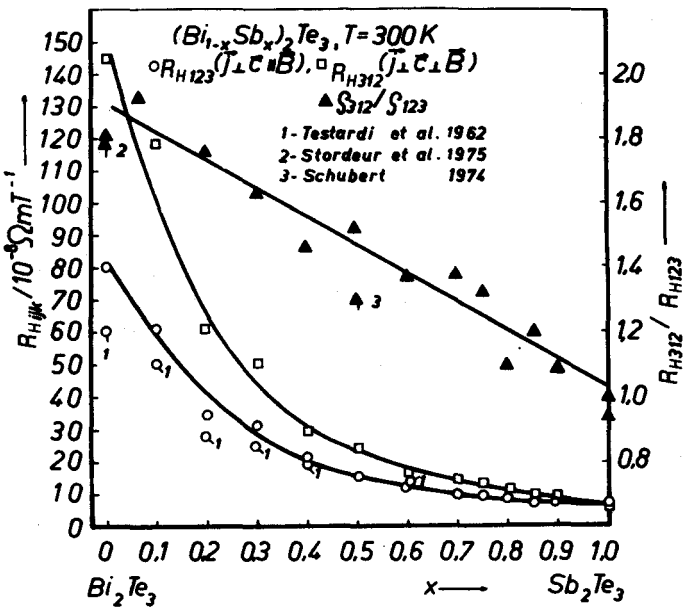

FIGURE 4 Dependence of both Hall coefficients R_{H123} and R_{H312} and their anisotropy ratio R_{H312}/R_{H123} on the mixed crystal composition x (after References 31 and 38).

$$m_{\perp c}^{-1} = (2m_0)^{-1}\,(a_{11}^H + c^2a_{22}^H + s^2a_{33}^H),\; m_{\parallel c}^{-1} = m_0^{-1}\,(s^2a_{22}^H + c^2a_{33}^H) \qquad (17)$$

${}^nL_k^m(\eta, \beta)$ stands for the generalized Fermi-Dirac integrals.[39] The reduced Fermi level is given by $\eta = E_F/(k_0T)$, $\beta = \gamma_1 k_0 T$ represents the nonparabolicity parameter, and c and s mean $\cos\vartheta$ and $\sin\vartheta$, respectively.

All parameters required for the quantitative determination of relevant band structure data from the following transport and optical measurements results have been defined in Equations 11 to 17.

Investigations of the Electrical Transport and Optical Properties of $(Bi_{1-x}Sb_x)_2Te_3$ Single Crystals

In addition to the electrical conductivity $\sigma_{\perp c}$ and the Seebeck coefficient $\alpha_{\perp c}$ (Figure 3), the behavior of both the weak field Hall coefficient $R_{H123}(j \perp c \parallel B)$ and $R_{H312}(j \perp c \perp B)$ dependences on the mixed crystal composition x is displayed in Figure 4. j and B are the electrical current density and magnetic induction, respectively.

Both the coefficients R_{H123} and R_{H312} decrease with increasing x from Bi_2Te_3 to Sb_2Te_3. This is due to the rising carrier density which accompanies an increase in the Sb_2Te_3 component in the $(Bi_{1-x}Sb_x)_2Te_3$ solid solution. However, the Hall anisotropy R_{H312}/R_{H123} shows a monotonic decrease with increasing x. This experimental result can only be interpreted by a change of the Hall structure factors (Equations 25 and 26). This means that, at least quantitatively, the valence band structure dependence on x also changes along the mixed crystal series. This trend and its effect on the thermoelectric figure-of-merit will be studied.

The response of the free carrier gas to an external perturbation in the form of an electromagnetic light wave has been used to measure the plasma reflection spectra of p-$(Bi_{1-x}Sb_x)_2Te_3$ single crystals over a wave number range from about 300 to 4000 cm^{-1}. All measurements were carried out on polished surfaces at room temperature with polarized infrared light incident at an angle of 20°. The reflectivity results for the polarization E ⊥ c and E ∥ c (E radiation electrical field strength) in the free carrier plasma resonance range are shown in Figures 5 and 6, respectively.

Interband excitations in the spectra were also observed for higher wave numbers $\bar{\upsilon}$ (2000 $cm^{-1} \le \bar{\upsilon} \le$ 4000 cm^{-1}) essentially in the Bi_2Te_3-rich part of the mixed crystals ($x \le 0.8$).[42] All details

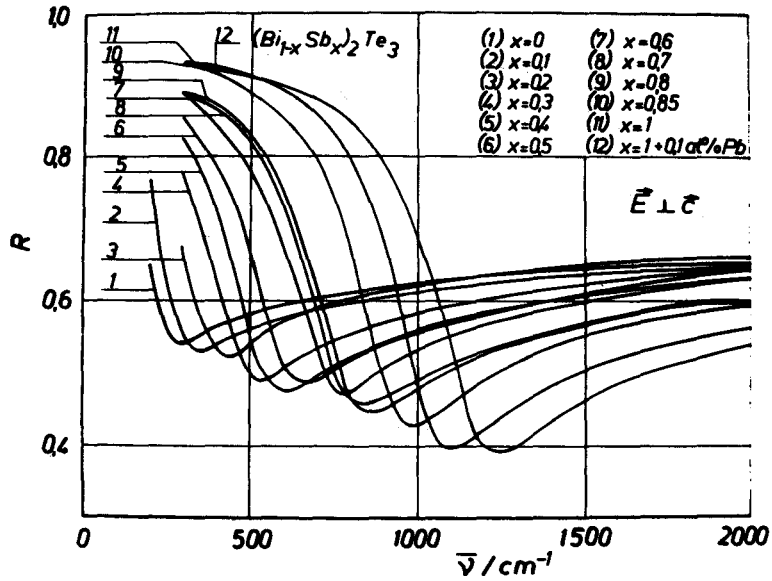

FIGURE 5 Plasma reflectivity R dependence on wave number $\bar{\nu}$ for the polarization E ⊥ c of p-$(Bi_{1-x}Sb_x)_2Te_3$ single crystals (after References 31 and 38).

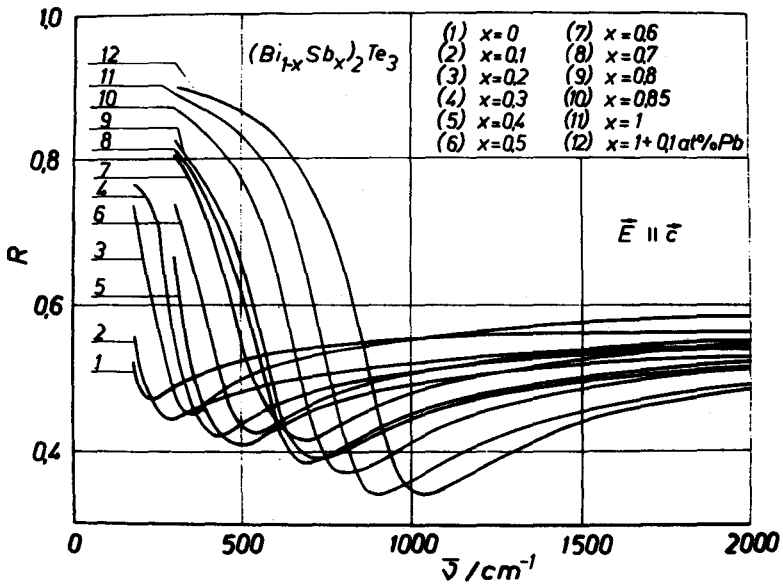

FIGURE 6 Plasma reflectivity R dependence on wave number $\bar{\nu}$ for the polarization E‖c of p-$(Bi_{1-x}Sb_x)_2Te_3$ single crystals (after References 26, 31, and 38).

relating to the preparation of samples and their measurement are described in Reference 42. Here only the free carrier excitations are of interest. In order to demonstrate the distinct optical anisotropy of all reflectivity spectra, the spectra for the crystals x = 0.75 and 0.9 are presented separately in Figure 7.

The plasma edges of all spectra in Figures 5, 6, and 7 show a clear shift towards higher frequencies as the carrier density increases with the increasing Sb_2Te_3 contribution. This is in agreement with the change in the transport coefficients along the mixed crystal series. With increasing x the electrical conductivity $\sigma_{\perp c}$ is also increased, whereas the Hall coefficients ρ_{123}, ρ_{312} and the thermoelectric power $\alpha_{\perp c}$ are lowered (see Figures 3 and 4).

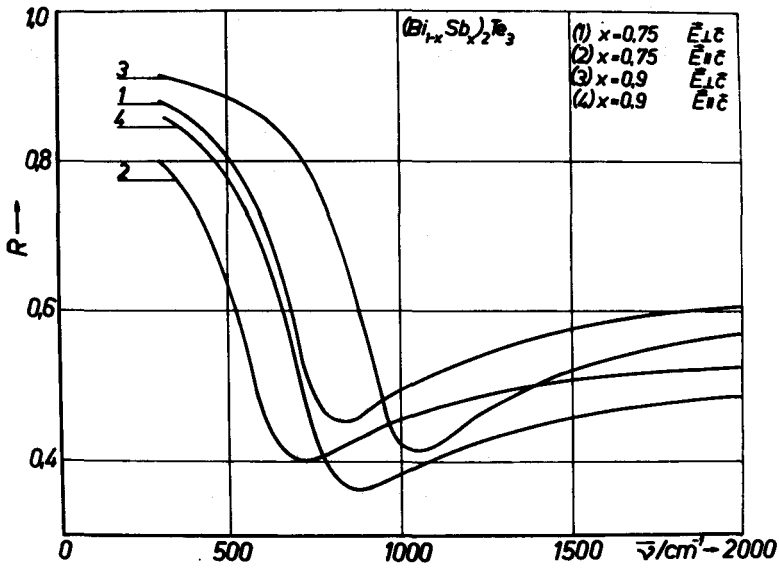

FIGURE 7 Example of the reflection spectra (polarization E ⊥ c and E ∥ c) anisotropy of the mixed crystals $(Bi_{1-x}Sb_x)_2Te_3$ with the compositions x = 0.75 and x = 0.9 (after References 26, 31, and 38).

Determination of the Band Structure Data of $(Bi_{1-x}Sb_x)_2Te_3$ Single Crystals

The basis for the calculation of the band structure data by using experimental results was defined earlier in Section 20.4. Commence with the numerical interpretation of the plasma reflectivity. For small angles of incidence α the reflectivity R is given by Reference 43.

$$R = \frac{(n-1)^2 + k^2}{(n+1)^2 + k^2}\left(1 + \frac{2n}{n^2 + k^2}\alpha^2\right) \tag{18}$$

where the refractive index n and the index of absorption k can be represented by the dielectric function $\varepsilon_{\perp,\,\|}{}^*{}_c(\omega)$, and ω is the angular frequency of the radiation

$$\varepsilon^*_{\perp,\,\|}(\omega) = \varepsilon_{\infty\perp,\|} + \frac{q^2}{\varepsilon_0}\frac{p}{m^{(x)}_{\perp,\|c}}\frac{\tau_{opt\perp,\|}}{1 + \omega^2\tau^2_{opt\perp,\|}}\left(-\tau_{opt\perp,\|} + \frac{i}{\omega}\right) \tag{19}$$

with

$$\varepsilon^{(1)} = n^2 - k^2,\ \varepsilon^{(2)} = 2nk \tag{20}$$

In Equation 19 the interband contribution to the dielectric function $\varepsilon^*(\omega)$ is taken into account only by the high-frequency dielectric constant term ε_∞. ε_0 is the dielectric constant of space. The damping of the plasma excitation is described by an averaged frequency-independent optical relaxation time τ_{opt}. It is seen that $\varepsilon^*(\omega)$ is connected with the valence band structure via the magnitudes $m^{(x)}_{\perp,\,\|c}$ (Equation 16).

The expression for the electrical conductivity $\sigma_{\|c}$ (Equation 9) can also be described in the modified manner

$$\sigma_{\perp,\|c} = qp\mu_{\perp,\|c'} \tag{21}$$

where $\mu_{\perp,\|c}$ are the phenomenological drift mobilities.

$$\mu_{\perp,\|c} = \frac{q}{m_{\perp,\|c}}\frac{\left(\left(\frac{d\gamma}{dE}\right)^{-1}\tau(E)\right)}{(1)}. \tag{22}$$

In the model used here (see previous page) the following relationships are valid for the Hall coefficients and thermoporer $\alpha_{\perp c}$, which enable possible nonparabolicity of the valence band structure to be taken into consideration.

$$\rho_{123} = \frac{R_H}{pq} B_{123}, \quad \rho_{312} = \frac{R_H}{pq} B_{312}, \tag{23}$$

$$\gamma_{\perp c} = \frac{k_0}{q} \left(\frac{{}^1L^1_{-2}}{{}^0L^1_{-2}} - \eta \right). \tag{24}$$

B_{ijk} are the structure factors and γ_H is the scattering factor in the Hall coefficients.

$$B_{123} = \frac{4a^H_{11}(c^2a^H_{22} + s^2a^H_{33})}{(a^H_{11} + c^2a^H_{22} + s^2a^H_{33})^2}, \tag{25}$$

$$B_{312} = \frac{a^H_{11}(s^2a^H_{22} + c^2a^H_{33}) + a^H_{22}a^H_{33}}{(s^2a^H_{22} + c^2a^H_{33})\,(a^H_{11} + c^2a^H_{22} + s^2a^H_{33})} \tag{26}$$

$$\gamma_H = \frac{{}^0L^{1/2}_{-4}\,{}^0L^{3/2}_{0}}{({}^0L^1_{-2})^2}. \tag{27}$$

These equations are all that are required to obtain information about the microscopic parameters of p-$(Bi_{1-x}Sb_x)_2Te_3$ single crystals from the experimental data.

As a first step all spectra (see Figures 5 to 7) were fitted to Equations 18 to 20. This process enabled the numerical data to be calculated for $\varepsilon_{\infty\perp,\|c}$, $\tau_{opt\perp,\|c}$ and the important ratios $p/m^{(x)}_{\perp,\|c}$. If, as a next step, the $p/m^{(x)}_{\perp,\|c}$ data are combined with the results of the transport measurements (see Figures 3 and 4), it can be seen from Equations 11 to 17 and 23 to 27 that for a known nonparabolicity parameter β the magnitudes $p/m^{(x)}_{\perp c}$, $p/m^{(x)}_{\|c}$, ρ_{123}, ρ_{312} and $\alpha_{\perp c}$ form a system of equations that enables relevant band structure data in the model employed such as a^H_{11}, a^H_{22}, a^H_{33}, ϑ, and η to be calculated.

Band Structure Data of p-$(Bi_{1-x}Sb_x)_2Te_3$ Single Crystals

The fitted values $p/m^{(x)}_{\perp,\|c}$, the mass anisotropy ratio $m^{(x)}_{\|c}/m^{(x)}_{\perp c}$, and the conductivity ratio $\sigma_{\perp c}/\sigma_{\|c}$ are presented in Figure 8 as a function of x. It is apparent that the mass anisotropy $m^{(x)}_{\|c}/m^{(x)}_{\perp c}$ calculated from the optical spectra is in full agreement with the DC conductivity anisotropy $\sigma_{\perp c}/\sigma_{\|c}$ obtained from transport measurements.[24]

Examination of Equations 21 and 22 indicates that the assumption of an isotropic relaxation time (Equation 13) is correct. This is confirmed by a comparison of the fitted optical relaxation times $\tau_{opt\perp c}$ and $\tau_{opt\|c}$ which have a difference of about 5%. The quantitative values were determined as $3.6 \cdot 10^{-14}$ s for Bi_2Te_3 and $2.1 \cdot 10^{-14}$ s for Sb_2Te_3 decreasing from x = 0 to x = 1.[31] For the third fitted parameter $\varepsilon_{\infty\perp,\|c}$ the following two examples are given: for x = 0, $\varepsilon_{\infty\perp c} = 63.2$, $\varepsilon_{\infty\|c} = 39.8$, and for x = 1, $\varepsilon_{\infty\perp c} = 56.1$, $\varepsilon_{\infty\|c} = 34.4$.[31]

The numerical results for the effective masses at the valence band edge m^H_{ii}, the related masses $m_{\perp c}$, $m_{\|c}$, m_d, and the ellipsoid tilt angle θ calculated with the method described in the previous section are presented in Figure 9. For mixed crystals with the composition $0 \le x \le 0.85$ a parabolic band was assumed ($\beta = 0$) and for crystals with x = 0.9, 1.0 a weak nonparabolic band with $\beta = 0.01$ was more suitable to describe the physical properties being investigated.

In Figure 9 the clear anisotropy of the elliptical Fermi surface represented by the masses m^H_{ii} is shown. Over the whole system the relation $m^H_{22} \gg m^H_{33} > m^H_{11}$ was found to be valid. The increase of m^H_{22} in the range $0.5 \le x \le 0.85$ causes the formation of a distinct maximum in the total density-of-states effective mass m_d near x = 0.8. Consideration of the change of the chemical bonds in the series $(Bi_{1-x}Sb_x)_2Te_3$ over the range $0.5 \le x \le 1.0$ also predicts the maximum of the density-of-state mass at $x \approx 0.8$.[47] This is in agreement with the author's conclusion. The tilt angle ϑ slowly increases from x = 0 to 1.

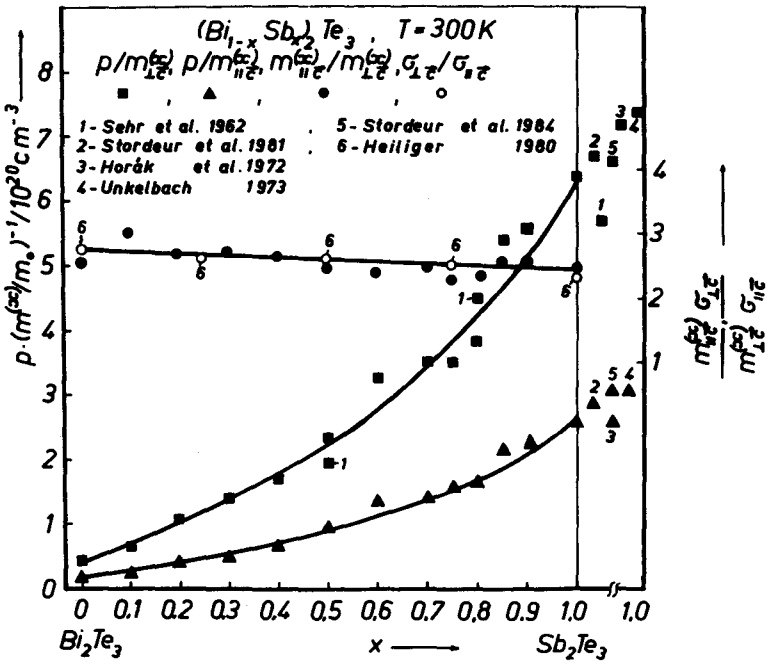

FIGURE 8 The fitted parameter $p/m^{(x)}{}_{\perp}{}_{\|c}$, their anisotropy $m^{(x)}{}_{\|}{}_{c}/m^{(x)}_{\perp c}$, and the comparison with the conductivity anisotropy $\sigma_{\perp c}/\sigma_{\|}c$ (after References 26 and 38).

The alloying of Sb_2Te_3 and Bi_2Te_3 is also accompanied by an increase of the tilt angle[48] based on measurements at low temperatures (4 K) and in high magnetic fields.

The masses $m_{\perp c}$ and $m_{\|c}$ determine the electrical conductivity anisotropy (see Equations 21 and 22) and show a slow increase with rising x. Further discussion of the valence band data given here together with the references leads to the conclusion that the value for m_d ($x = 0.75$) is practically the same as previously reported.[49] This excellent agreement indicates that the valence band parameters are typical for this specific composition. If the band parameter for Sb_2Te_3 which was derived from transport data is compared with the reflectivity spectra[20] which were calculated using a more complicated model by numerical analysis of the temperature dependence of transport coefficients, then there is a maximum difference of 18%. Considering that the use of totally different interpretation methods leads to similar results, the masses can be considered as typical for this semiconducting compound ($x = 1$). This can also be demonstrated by a comparison of the data for $m_{\perp c}$ and $m_{\|c}$ with the values published in Reference 50, which reveal that the maximum difference is 16%. This is remarkable because these values[50] were calculated based on the observation of coupled plasmom-LO-phonon modes by IR-reflectivity and Raman scattering experiments without making any assumption about the band structure and carrier scattering.

Values for the carrier density p, the mobility $\mu_{\perp c}$, and the Fermi energy E_F which correspond to the effective masses are given in Figure 10. The representation of the dependence of E_F on the mixed crystal composition leads to an averaged curve with only a small amount of scatter which increases with increasing x. Whereas between $x = 0.7$ and 0.85 the Fermi energy only increases slightly, the carrier density increases continuously due to the increase of the density-of-states effective mass in the same range (see Reference 14 and Figure 9).

The mobility $\mu_{\perp c}$ is calculated using the experimental values of the electrical conductivity $\sigma_{\perp c}$ (see Figure 3). $\mu_{\perp c}$ decreases as the fraction of Sb_2Te_3 in the crystals increases, although there is a 30% scatter around the curve in Figure 10.

The energy-independent term of the relaxation time τ_0^{ac} (see Equation 13) does not change along the mixed crystal series and shows the same order of scattering about the mean mobility value of $0.28 \cdot 10^{-23}\ W^{-1/2}\ s^{3/2}$.[31]

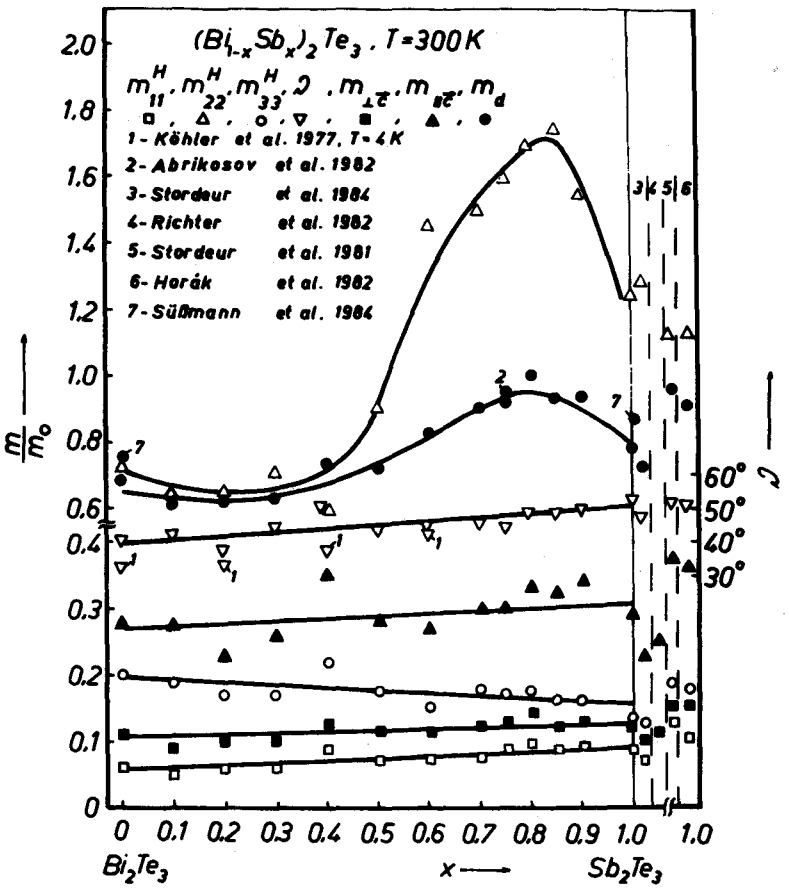

FIGURE 9 The dependence on composition x of the effective main axis masses m_{ii}^H (E = 0), the ellipsoid tilt angle ϑ, the band edge masses $m_{\perp c}$, $m_{\parallel c}$, and the total density-of-states mass m_d (E = 0) for single crystal $(Bi_{1-x}Sb_x)_2Te_3$. (Numerical values based on Figure 9 are published in Reference 38.)

Returning once more to the question of the high anisotropy of the effective main-axis masses m_{ii}^H (see Figure 9), it is not possible to support the values of the effective masses by further theoretical calculations based on the band structure framework developed earlier in this chapter. However, a qualitative analysis of the chemical bonds and geometrical arrangements of the lattice sites leads to the following picture: two nonequivalent Te sites exist in the layered-structure lattices of V_2VI_3 semiconducting compounds.[3] The Te^1 atoms have covalent-ionogen bonds on one side with three metal atoms (Bi, Sb), and on the other side there is only a weak bond to the next layer of Te^1 atoms (see Figure 1 and Section 20.2.). The Te^2 atoms, however, are surrounded by six metal atoms in an octahedral configuration. A schematic comparison of corresponding directions of the direct and the reciprocal lattice for Sb_2Te_3 is drawn in Figure 11.

In the crystal coordinate system the z, k_3-axis represents the trigonal optical axis, whereas x, k_1 and y, k_2 stand for the binary and the bisectric axes, respectively. In k-space one of the iso-energy ellipsoids is centered on the (k_2, k_3) mirror plane with the tilt angle ϑ between the k_2, k_2^H directions. In the direct lattice on this mirror plane Te^2 atoms (center of inversion) and Sb atoms are localized as nearest neighbors. The chemical bond between these atoms is realized by sp^3d^2 hybrids[3] and forms a bond angle of 38° for Sb_2Te_3 and 39° for Bi_2Te_3. This chemical bond probably leads to the ellipsoid tilt angle ϑ of a similar magnitude in the k-space (40° for Bi_2Te_3 and 52° for Sb_2Te_3). The high effective mass in the k_2 direction, m_{22}^H, supports the proposition of a weak overlap of the corresponding wave functions in this direction.[52]

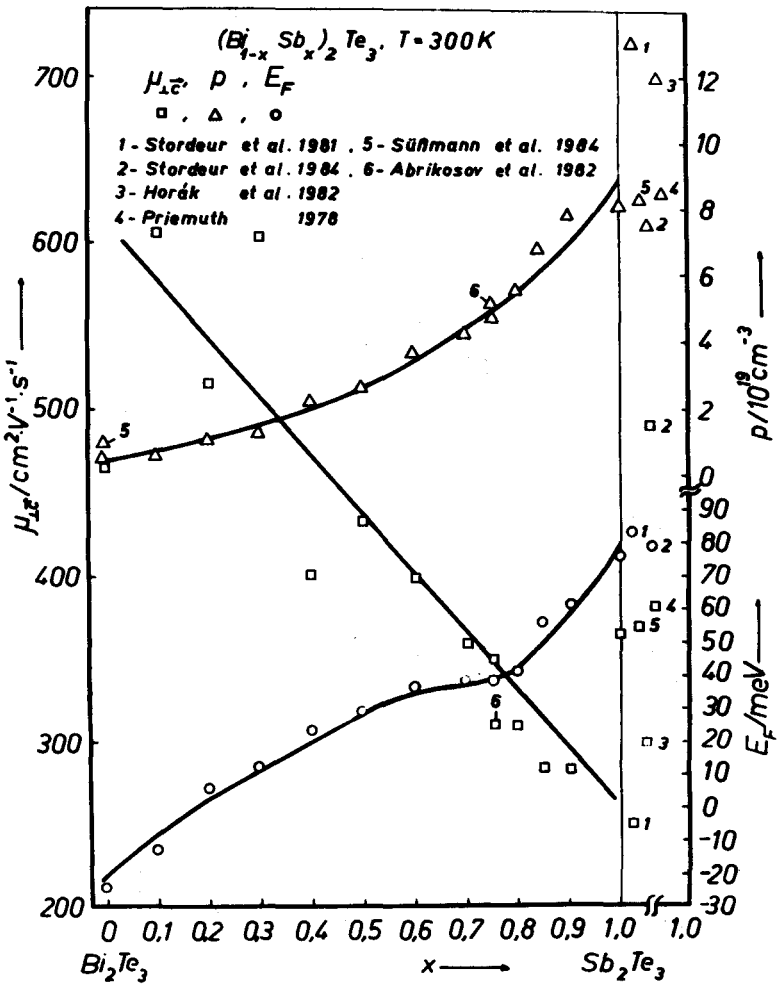

FIGURE 10 Dependence on composition x of the carrier density p, mobility $\mu_{\perp c}$, and the Fermi energy E_F of single crystal $(Bi_{1-x}Sb_x)_2Te_3$ (after References 26 and 38).

Relating to Figure 11 a further aspect is given. In the Sb_2Te_3 lattice the Te^2-Sb separation amounts to 3.17 Å, whereas in Bi_2Te_3 the corresponding distance is 3.24 Å. If Bi_2Te_3 is alloyed to Sb_2Te_3 the Bi atoms are predominately built-in on metal sites. This means that the available Te^2-Sb distance in a Sb_2Te_3 host lattice is too small for a Bi atom on a Sb site. Consequently the chemical bond in the Te^2-(Bi, Sb) direction is mainly influenced by the alloying and we can also expect a quasi-direction-dependent effect, i.e., the effective mass m_{22}^H is most strongly influenced by alloying, whereas m_{11}^H and m_{33}^H hardly depend on the composition x.

20.5 Interpretation of the Thermoelectric Figure-of-Merit in the p-$(Bi_{1-x}Sb_x)_2Te_3$ System

In Section 20.4 the influence of the valence band structure to the thermoelectric figure-of-merit Z via the parameter $m_{\perp c}^{-1}(m_d/m_0)^{3/2}$ was discussed. Employing a consistent interpretation of the combined optic-spectroscopic and transport investigations (see earlier sections) all relevant valence band mass data were determined and it was found that τ_0^{ac} is nearly independent of x. On this basis the electronic parameter $m_{\perp c}^{-1}(m_d/m_0)^{3/2}$ was calculated and is displayed in Figure 12 together with

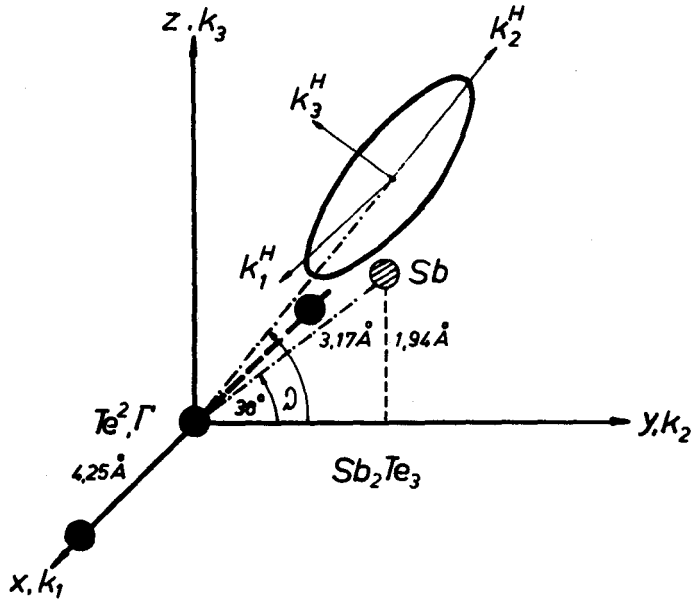

FIGURE 11 Schematic comparison between the location of one of the six iso-energy ellipsoids in k-space and the atomic sites and bond angles in the direct lattice of a Sb_2Te_3 crystal. Lattice constants and bond angles from Reference 3.

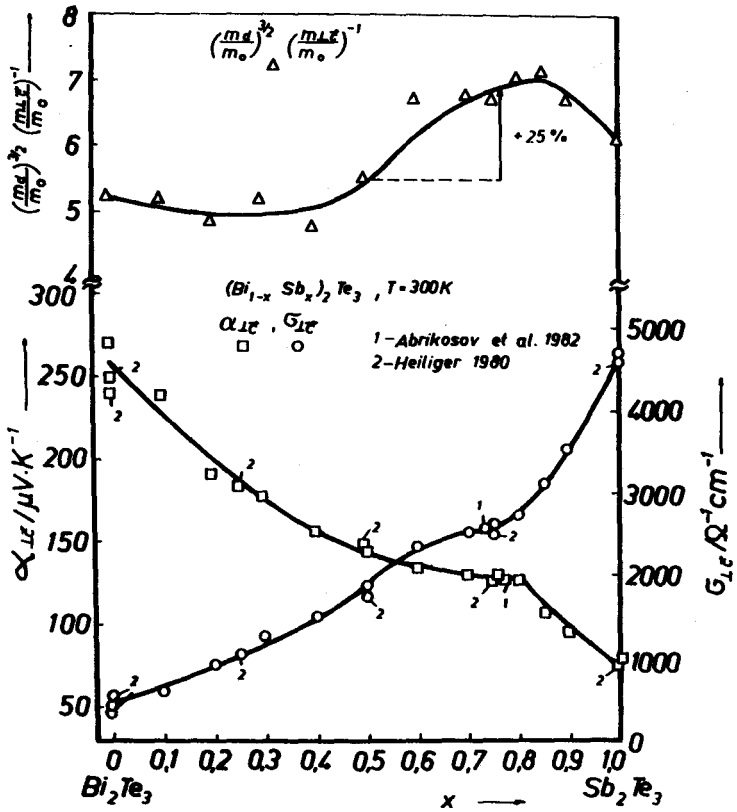

FIGURE 12 Dependence on composition x of the calculated band parameter $m_{\perp c}^{-1}$ $(m_d/m_0)^{3/2}$, electrical conductivity $\sigma_{\perp c}$, and Seebeck coefficient $\alpha_{\perp c}$ for undoped p-$(Bi_{1-x}Sb_x)_2Te_3$ single crystals (after Reference 30).

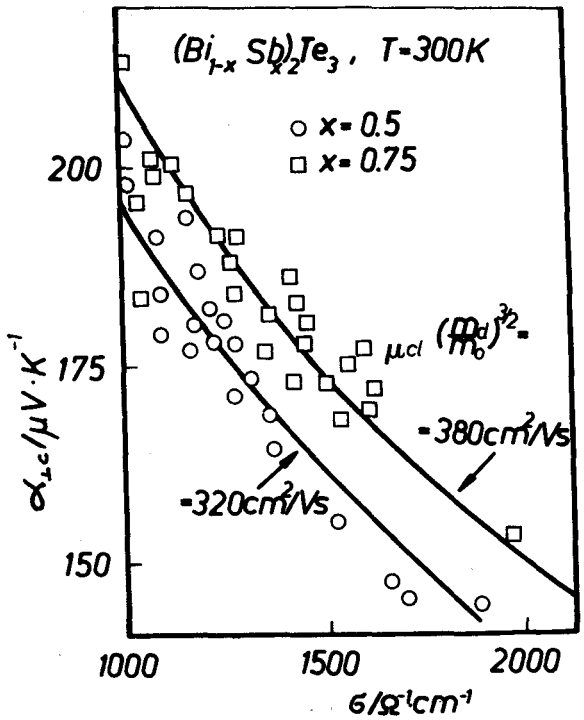

FIGURE 13 Thermoelectric power $S_{\perp c}$ dependence on electrical conductivity $\sigma_{\perp c}$ for $(Bi_{1-x}Sb_x)_2Te_3$ crystals with x = 0.5 and x = 0.75 with different doping levels (after References 26 and 30). The curves were calculated using Equations 5, 8, and 9; the experimental data are from Reference 53.

the experimental values for $\alpha_{\perp c}$ and $\sigma_{\perp c}$ (see also Figure 3). It is seen that crystals with $x \approx 0.8$ have a band parameter which is about 25% higher than crystals with x = 0.5. Therefore crystals with x = 0.5 possess the most favorable band structure for obtaining the highest thermoelectric figure-of-merit in the mixed crystal system $(Bi_{1-x}Sb_x)_2Te_3$. The competitive aspects of the influences of band structure and lattice thermal conductivity (see Equation 10) on the thermoelectric figure-of-merit are discussed in the following section.

According to the results presented in Figure 12 it is expected that differently doped crystals with x = 0.75 will have a greater value of $\mu_{cl}(m_d/m_0)^{3/2}$ than crystals with x = 0.5. This is confirmed in Figure 13. The $\alpha_{\perp c}(\sigma_{\perp c})$ plots for differently doped crystals with x = 0.5 and 0.75 show that the electric parameter $\mu_{cl}(m_d/m_0)^{3/2}$ is only dependent on the Bi-Sb ratio and the theoretical curves are calculated using the parameters 380 cm^2/Vs (x = 0.75) and 320 cm^2/Vs (x = 0.5).

With the use of Equations 4, 6, and 7 it is possible to calculate the dependence of the thermoelectric figure-of-merit on the Seebeck coefficient (Equation 8) via the reduced Fermi level η. This has been done for $(Bi_{0.25}Sb_{0.75})_2Te_3$ crystals with an electronic parameter of 380 cm^2/Vs and a lattice thermal conductivity $\lambda_L = 0.85\ W\ m^{-1}\ K^{-1}$. The result is presented in Figure 14.

The good agreement between the theoretical values and the experimental figure-of-merit data confirms the validity of the model employed and the value of λ_L obtained lies between the data reported in References 24 and 25 (see Section 20.3).

The results displayed in Figures 13 and 14 also enable the influence of lattice thermal conductivity and valence band structure on the maximum of the thermoelectric figure-of-merit for crystals with the composition x = 0.75 in the series $p\text{-}(Bi_{1-x}Sb_x)_2Te_3$ at room temperature to be understood.

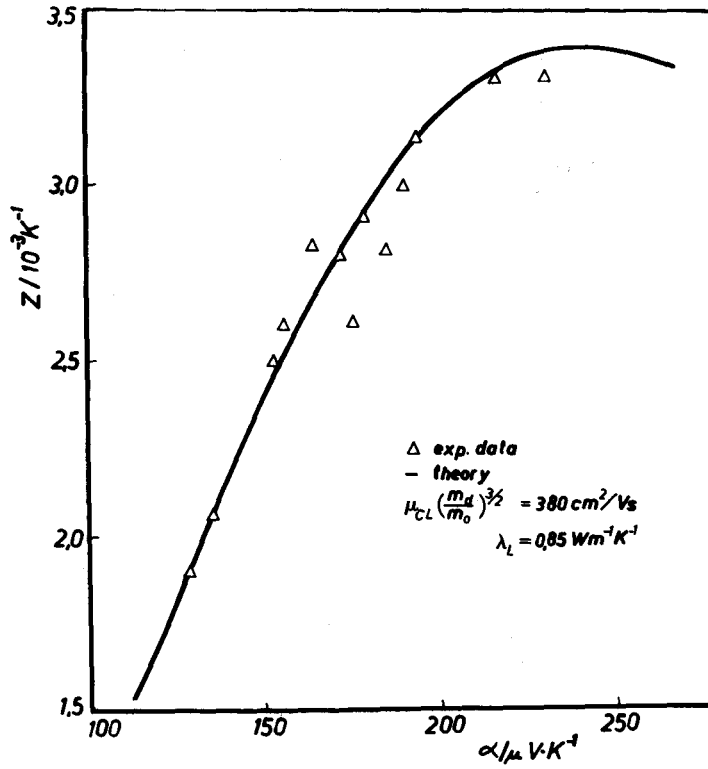

FIGURE 14 The dependence of the thermoelectric figure-of-merit Z on the Seebeck coefficient $\alpha_{\perp c}$ for differently doped $(Bi_{0.25}Sb_{0.75})_2Te_3$ crystals (T = 300 K). (After Reference 53.) Experimental data (symbols) after References 53 and 54, full line calculated with the parameters $\mu_{cl}(m_d/m_0)^{3/2}$ = 380 cm²/Vs and λ_L = 0.85 W m^{-1} K^{-1}.

References

1. Goodman, C. H. L., *Mater. Res. Bull.*, 20, 231 (1985).
2. Sher, A., Shiloh, M., Ilzycer, D., and Eger, D., *J. Electron. Mater.*, 12, 247 (1983).
3. Krost, A., Landolt-Börnstein New Series Group III, Vol. 17, Subvol. f, Springer-Verlag, Berlin, 1983, 234.
4. Stecker, K., Stordeur, M., and Langhammer, H. T., *Verbindungshalbleiter*, Unger, K. and Schneider, H. G., Eds., Akademische Verlagsgesellschaft Geest & Portig, Leipzig, 1986, 304.
5. Wiese, J. R. and Muldawer, L., *J. Phys. Chem. Solids*, 15, 13 (1960).
6. Dato, P. and Köhler, H., *J. Phys. C Solid State Phys.*, 17, 3711 (1984).
7. Kullmann, W., Geurts, J., Richter, W., Lehner, N., Rauh, H., Steigenberger, U., Eichhorn, G., and Geick, R., *Phys. Status Solidi (b)*, 125, 131 (1984).
8. Süβmann, H. and Loof, K., *Phys. Status Solidi (a)*, 37, 467 (1976).
9. Priemuth, A., *Phys. Status Solidi (a)*, 67, 505 (1981).
10. Tichý, L., Horák, J., Vaško, A., and Frumar, M., *Phys. Status Solidi (a)*, 20, 717 (1973).
11. Horák, J., Matyaš, M., and Tichý, L., *Phys. Status Solidi (a)*, 27, 621 (1975).
12. Horák, J., Lošták, P., Šiška, L., and Stordeur, M., *Phys. Status Solidi (b)*, 114, 39 (1982).
13. Lošták, P., Horák, J., and Koudelka, L., *Phys. Status Solidi (a)*, 84, K143 (1984).
14. Horák, J., Lošták, P., and Beneš, L., *Philos. Mag. B*, 50, 665 (1984).
15. Starý, Z., Horák, J., Stordeur, M., and Stölzer, M., *J. Phys. Chem. Solids*, 49, 29 (1988).
16. Süβmann, H., Priemuth, A., and Pröhl, U., *Phys. Status Solidi (a)*, 82, 561 (1984).
17. Stordeur, M. and Kühnberger, W., *Phys. Status Solidi (b)*, 69, 377 (1975).
18. Stordeur, M. and Heiliger, W., *Phys. Status Solidi (b)*, 78, K103 (1976).
19. Stordeur, M., *Phys. Status Solidi (b)*, 124, 439 (1984).

20. Stordeur, M. and Simon, G., *Phys. Status Solidi (b)*, 124, 799 (1984).
21. Eichler, W. and Simon, G., *Phys. Status Solidi (b)*, 86, K85 (1978).
22. Stecker, K., Süβmann, H., Eichler, W., Heiliger, W., and Stordeur, M., *Wiss. Z. Univ. Halle (Germany)*, 27, 5 (1978).
23. Ioffe, A. F., *Physik der Halbleiter*, Akademie-Verlag, Berlin, 1960, 272.
24. Heiliger, W., Thesis MLU, Halle (Germany), 1980.
25. Küchler, M., Thesis MLU, Halle (Germany), 1984.
26. Stordeur, M. and Sobotta, H., in *Proc. First European Conf. on Thermoelectrics*, Rowe, D. M., Ed., IEE Materials & Devices Ser. 7, P. Peregrinus Ltd., London, 1988, 209.
27. Lee, P. and Pincherle, L., *Proc. Phys. Soc.*, 81, 461 (1963).
28. Borghese, F. and Donato, E., *Nuovo Cimento*, 53, 283 (1968).
29. Katsuki, S. I., *J. Phys. Soc. Jpn.*, 26, 58 (1969).
30. Stordeur, M., *Phys. Status Solidi*, 161, 831 (1990).
31. Stordeur, M., Thesis B, MLU, Halle (Germany), 1985.
32. Loof, K., Diploma work, MLU, Halle (Germany), 1970.
33. Drabble, J. R. and Wolfe, R., *Proc. Phys. Soc. B*, 69, 1101 (1956).
34. Drabble, J. R., *Proc. Phys. Soc.*, 72, 380 (1958).
35. Efimova, B. A., Korenblit, I. J., Novikov, W. I., and Ostroumov, A. G., *Fiz. Tverd. Tela*, 3, 2746 (1961).
36. Caywood, L. P. and Miller, G. R., *Phys. Rev. B*, 2, 3209 (1970).
37. Greenaway, D. L. and Harbeke, G., *J. Phys. Chem. Solids*, 26, 1585 (1965).
38. Stordeur, M., Stölzer, M., Sobotta, H., and Riede, V., *Phys. Status Solidi (b)*, 150, (1988).
39. Zawadzki, W., *Adv. Phys.*, 23, 435 (1974).
40. Testardi, L. R., Bierly, J. N., and Donahoe, F. J., *J. Phys. Chem. Solids*, 23, 1209 (1962).
41. Schubert, H., Diploma work, MLU, Halle (Germany), 1974.
42. Stordeur, M., Langhammer, H. T., Sobotta, H., and Riede, V., *Phys. Status Solidi (b)*, 109, 673 (1981).
43. Langhammer, H. T., Thesis, MLU, Halle (Germany), 1980.
44. Sehr, R. and Testardi, L. R., *J. Phys. Chem. Solids*, 23, 1219 (1962).
45. Horák, J., Tichý, L., Vaško, A., and Frumar, M., *Phys. Status Solidi (a)*, 14, 289 (1972).
46. Unkelbach, K. H., Thesis, RWTH, Aachen (Germany), 1973.
47. Gaidukova, V. S., Erofeev, R. S., and Oveshkina, N. V., *Izv. Akad. Nauk SSSR Ser. Neorg. Mater.*, 17, 244 (1981).
48. Köhler, H. and Freudenberger, A., *Phys. Status Solidi (b)*, 84, 195 (1977).
49. Abrikosov, N. Ch. and Ivanova, L., *Izv. Akad. Nauk SSSR Ser. Neorg. Mater.*, 18, 560 (1982).
50. Richter, W., Krost, A., Nowak, M., and Anastassakis, E., *Z. Phys. B*, 49, 191 (1982).
51. Priemuth, A., Thesis, MLU, Halle (Germany), 1978.
52. Kirejew, P. S., *Physik der Halbleiter*, Akademie-Verlag, Berlin, 1974.
53. Süβmann, H., Stecker, K., Eichler, W., Langhammer, S., Yuen, N. H., Sung, N. W., Voung, N. W., Hoau, S. S., Trishenikov, V. M., and Sherbina-Samoilova, M. B., *Salut-6-Sojus*, Izd. Nauka, Moscow, 1985, 37.
54. Süβmann, H. and Heiliger, W., in *Proc. Conf. Transport in Compound Semiconductors*, MLU, Halle (Germany), KTB Series 1982, 100.

21

Lead Telluride and Its Alloys

V. Fano
University of Parma
Parma, Italy

21.1 Introduction

Lead telluride and lead telluride-based thermoelectric materials, $Pb_{1-x}Sn_xTe$ "lead-tin-telluride", belong to a class of semiconductors represented by the general formula $A^{IV}B^{VI}$. Their physicochemical properties have much in common: they have the same type of chemical bond (ionic-covalent) and they are isomorphous (cubic sodium chloride-type lattice).

Their thermoelectric properties, such as the type of carrier, concentration, mobility, Seebeck coefficient, and electrical and thermal conductivities are determined by the deviation from stoichiometry, doping element concentration and defect, i.e., by the synthesis conditions. A prerequisite for the synthesis of materials, irrespective of their crystalline habitus (single crystals, polycrystals, sintered materials, or epitaxial layers), is knowledge of the phase diagrams. These provide information about the solid phases grown from the melt, the stoichiometry for the formation of a compound or solid solution, and the solubility of cationic or anionic excess in the solid phase. A large amount of information has been reported on all the above-mentioned topics in the literature. During the past decade interest in lead telluride-based materials has focused mainly on obtaining reliable data pertinent to the material technology and the role of defects. Lead telluride-based materials have been used for a range of purposes in the hot-junction temperature range 600 to 900 K.[1] Comprehensive reviews of these materials have been given in the literature.[1–5]

21.2 Phase Diagrams

Lead Telluride

Lead telluride has a congruent melting point in the lead telluride-rich zone of the phase diagram (923 or 924°C). The composition at this point is 50.012 at.% tellurium. Below the melting point lead telluride exhibits a homogeneous range of composition extending from the tellurium-rich to the lead-rich region and having its maximum width around 780°C (from 50.012 at.% tellurium to 49.994 at.% tellurium[6,7]). The T-x (temperature-composition) phase diagrams have been reported.[8–10] Thus, lead telluride exhibits p-type and n-type electrical conductivity and carrier concentration, which can vary in the range from 10^{15} to 10^{21} cm^{-3}. Material solidified from a stoichiometric melt exhibits a carrier concentration which randomly ranges from $\approx 2 \times 10^{18}$ to

0-8493-0146-7/95/$0.00+$.50

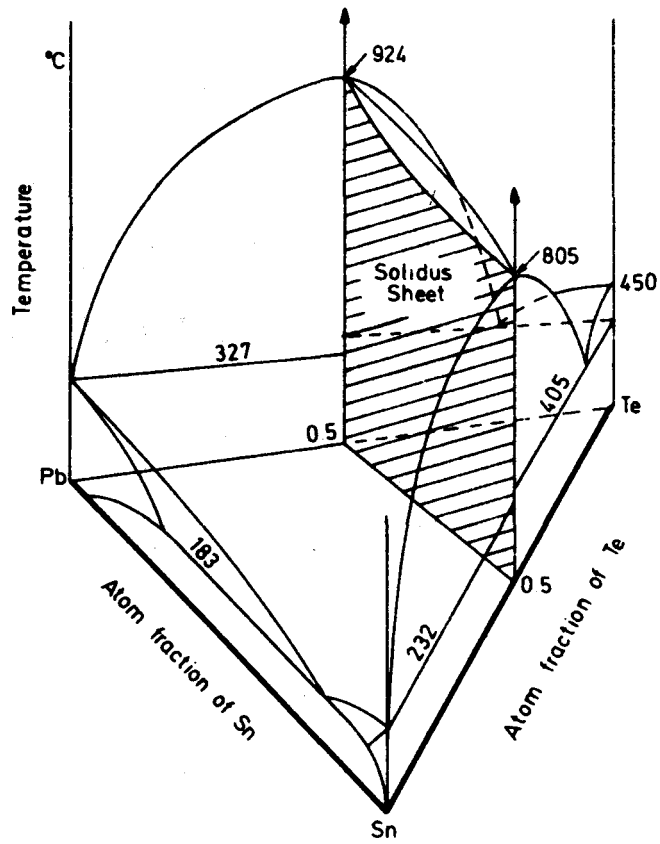

FIGURE 1 Temperature-composition phase diagram for the ternary $(Pb_{1-x}Sn_x)_{1-y}Te_y$. (After Maier and Hesse, Reference 20.)

$\approx 17 \times 10^{18} cm^{-3}$ at room temperature. The change in carrier concentration and carrier type of the undoped lead telluride is obtained by thermal annealing in a lead-rich (for n-type conductivity) or tellurium-rich (for p-type conductivity) atmosphere.[11,12] This method enables the stoichiometry to be changed.

The lead-tellurium system forms a eutectic at 85.5 at.% tellurium and a melting point of 405°C.

Lead Tin Telluride

This system forms a continuous series of solid solutions which obey Vegard's law. Information on the pseudobinary phase diagram is reported in References 13 to 16.

The more general ternary systems, $(Pb_{1-x}Sn_x)_{1-y}Te_y$, where $0 \leq x \leq 1$ and $0 \leq y \leq 1$ have been studied[17–21] and are presented in Figure 1. Typical properties are collected in Table 1. The maximum melting point of the alloys occurs at nonstoichiometric compositions. In Figure 2 the phase diagrams around the stoichiometric composition of some $Pb_{1-x}Sn_xTe$ alloys are reported in terms of the equivalent carrier concentrations. In all these alloys the congruent melting point is in the tellurium-rich zone. The curves represent the metal-saturated and tellurium-saturated solidus lines for different compositions x; the tin and lead ions are randomly distributed on the sublattice occupied by the electropositive ions. The other sublattice is occupied by the electronegative tellurium ions.[22] To date the influence of doping elements on the phase diagrams has not been described in detail.

Table 1. Physical Properties of $Pb_{1-x}Sn_xTe$ (x = 0, 0.2, 0.25, 1)

	PbTe	$Pb_{0.8}Sn_{0.2}Te$ (A) $Pb_{0.75}Sn_{0.75}Te$ (B)	SnTe
Lattice constant (a, 300 K) (Å)	6.460	6.4321 (A)	6.302 (Te salt) 6.327 (Sn salt)
Density (ρ, 300 K) (g cm^3)	8.242	7.91 (A)	6.445
Vol. compressibility (cm^2dyn) × 10^{-12}	2.43	2.76 (B)	2.64
Heat cap. (Cp,300 K) (cal $mol^{-1}K^{-1}$)	12.1 (210 < T < 260)		12 (300 K)
Band gap, E_g (E_g, 300 K) (eV)	0.32	0.20 (A)	0.18
dE_g/dT (300 K) (10^{-4} eV K^{-1})	4.85	4.85 (B)	
Effective masses (4 K)			
m_c^*/m_o	0.034		
m_v^*/m_o	0.032		
Therm. exp. coeff. (α, 300 K) (10^{-6} K^{-1})	19.8	20 (A)	
Melting point (K)	1197	1178 (A) 1174 (B)	1078

Sources: References 2, 3, 5, and 20.

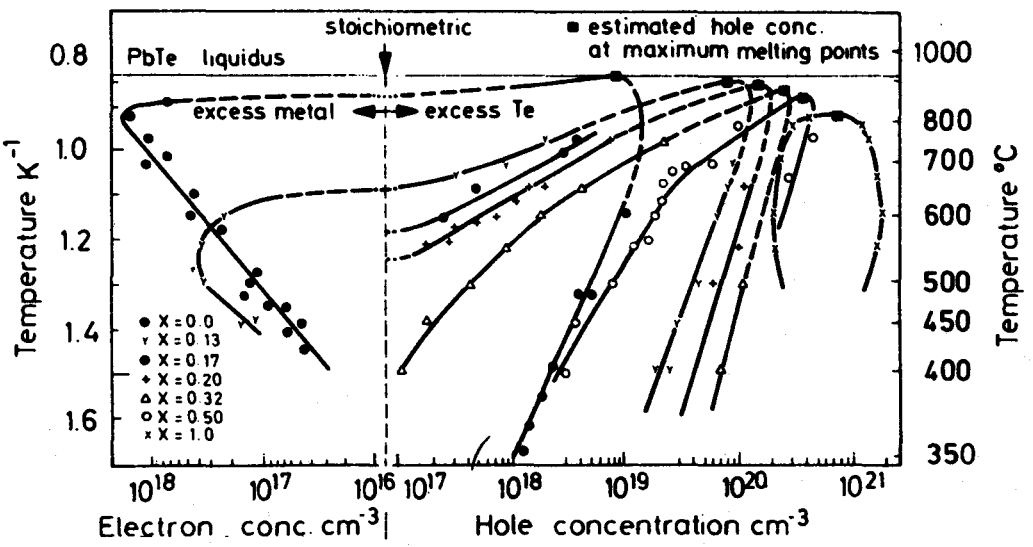

FIGURE 2 Temperature-composition phase diagram around the stoichiometric composition of $Pb_{1-x}Sn_xTe$ in terms of the equivalent carrier concentration. The curves represent the metal-saturated and tellurium-saturated solidus lines for different compositions x. (After Maier and Hesse, Reference 20.)

21.3 Properties

Lead Telluride

The electrical and thermoelectric properties are dependent on the carrier concentration and temperature. When materials with carrier concentration higher than 10^{18} cm^{-3} are required, doping elements are added to the lead telluride melt. Electrical and thermoelectric properties of materials solidified from the melt or from the vapor phase have been investigated intensively and reported in several works.[1,23–34] It was observed that the Hall coefficient ratio $R_{H295°}/R_{H77°C}$ increases from about 1:1 to 2:5 as the nominal p-type carrier concentration ($1/R_He$) increases from 3.5 × 10^{17} to 1.5 × 10^{20} cm^{-3}. This behavior is attributed to the presence of a second valance band, separated

from the first by about 0.1 e V. An analysis of the experimental temperature dependence of the Hall coefficient gives the following value for the energy gap between the valence bands:

$$E = 0.17 - 4x10^{-4}T\ eV \quad (1)$$

Consequently, the edges of the two valence bands are at approximately the same level at 400 K. At temperatures higher than 400 K the main contribution to the transport properties is the heavy hole band[3,35] and the energy gap between the edges of the conduction and heavy hole bands remains constant. The Hall coefficient of n-type lead telluride as a function of temperature is constant (≈ -0.1 cm^3/K). Between 4.2 and 150 K the Hall coefficient of p-type samples has constant values; it then increases and reaches a maximum at about 430 K. The carrier concentration does not affect this maximum, but does influence its value. The Hall mobility varies with temperature; at T >20 to 50 K, it approximately follows the law $\mu \approx T^{-5/2}$ for "as grown" crystals from stoichiometric melt. For doped crystals the power exponent decreases when the carrier concentration increases.

The thermoelectric properties of n- and p-type materials with different dopants have been reported.[1,3,36,37] The maximum figure-of-merit (Z_{max}) value of n-type lead telluride was reached at T ≈150°C and n ≈5 × 10^{18} cm^{-3}. When the carrier concentration is higher, the Z_{max} is lower and shifts towards higher temperatures. The Z_{max} of p-type lead telluride is reached at ≈400°C (Z_{max} ≈1.6 × 10^{-3} K^{-1}) and remains practically fixed at this temperature for a wide range of carrier concentrations higher than 6 × 10^{19} cm^{-3} due to the influence of the second valence band. This heavy-hole valence band in doped p-type lead telluride affects the carrier concentration and the thermoelectric power, when the temperature is varied.[28]

In Figures 3a and 3b the figures-of-merit of some n- and p-type samples are presented. The curves 4 and 5 of Figure 3a and curves 1 and 5 of Figure 3b are from Reference 3; there is some uncertainty in the curves because of the different behavior of the electrical and thermoelectrical properties vs. the temperature of "real" samples (particularly p-samples) which have nominally the same carrier concentration.

Lead Tin Telluride

The energy gap of $Pb_{1-x}Sn_xTe$ is a function of composition[38] and temperature and is given by the relationship

$$E(eV) = 0.180 - 0.48\,x + 4x10^{-3}T(K) \quad (2)$$

It has been shown that the energy gap of $Pb_{1-x}Sn_xTe$ close to 0 K is zero at x ≈ 0.35 and increases on both sides of this composition and changes sign; it is negative on the lead-rich side and positive on the tin-rich side. Schematic representation of the valence and conduction band for PbTe, $Pb_{0.65}Sn_{0.35}Te$, and SnTe at 12 K is shown in Figure 4. Various other band structures have been suggested to explain the electrical, optical, and thermal properties. However, these models do not explain all the experimental data.[39] The p-type carrier concentration in these alloys increases from about 1–7 × 10^{18} cm^{-3} for lead telluride to ≈ 10^{21} cm^{-3} for tin telluride. The mobility decreases as one moves away from lead telluride[40] and reaches the minimum at x ≈ 0.8 at 77 K. In general, the mobility is inversely proportional to the carrier concentration.[41] The Hall mobility in both n- and p-type $Pb_{0.8}Sn_{0.2}Te$ has been measured as a function of carrier concentration. For both n- and p-type materials at 77 K the Hall mobility varies monotonically with carrier concentration over a wide range. At 300 K the Hall mobility in both n- and p-type materials is independent of carrier concentration up to about 10^{19} cm^{-3}, while above this value, the mobility decreases with an increase in carrier concentration. To eliminate spurious effects (Righi-Leduc, Nernst-Ettingshausen), a Hall effect method employing alternating magnetic and electric fields has been reported;[43] other Hall effect apparatus are reported in Reference 1. The Seebeck coefficient reaches the maximum value[44] ($\alpha \approx 220$ μV/K) for x = 0.15 at 300 K. For lead-rich samples, when x increases the maximum shifts towards higher temperatures: for x = 0.2, $\alpha \approx 200$ μV/K at T = 360 K; for x = 0.3, $\alpha \approx 195$ μV/K at T = 420 K; for x = 0.4, $\alpha \approx 150$ μV/K at T = 520 K. Some samples show a transition from p-type conduction at low temperature to n-type conduction at high temperature.

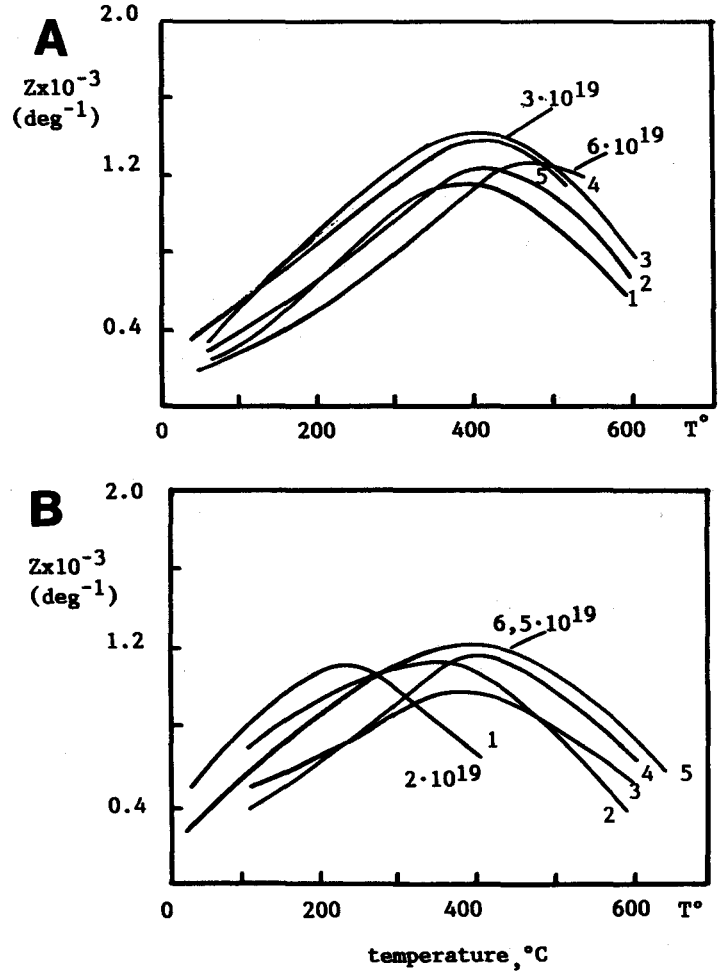

FIGURE 3 (A) The figure-of-merit of n-type PbTe samples; curves 3 and 4 are from Reference 3, the other curves correspond to n = 3 × 10^{19} cm^{-3}. (B) The figure-of-merit of p-type PbTe samples; curves 1 and 5 are from Reference 3, the other curves correspond to p = 3 × 10^{19} cm^3.

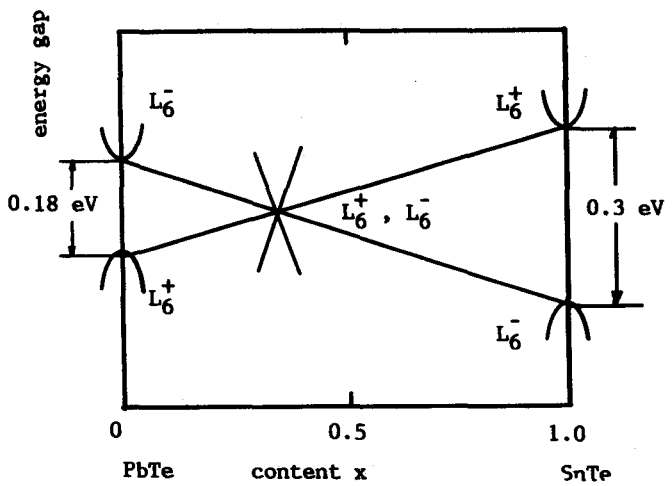

FIGURE 4 Schematic representation of the valence and the conduction band for PbTe, $Pb_{0.65}Sn_{0.35}Te$, and SnTe at 12 K.

The tin-rich samples show a similar behavior. For x = 0.4 the Seebeck coefficient shows a peak, $\alpha \approx 150$ μV/K, at 500 K. As the amount of tin increases the peak value drops and shifts to higher temperatures.

21.4 Preparation

PbTe and $Pb_{1-x}Sn_xTe$ have been obtained as fine-grained polycrystalline, as well as single, crystals. Polycrystalline materials are obtained by direct synthesis from oxygen-free elements whose purity is 99.90% or more. The synthesis is carried out in a well-cleaned and out-gassed quartz tube (1 to 1.5 mm wall thickness is sufficient to avoid breaking the ampoule when the temperature decreases after the melting). Sometimes, although the doping action of oxygen (p-type) is not eliminated, pyrolitic graphite-coated quartz ampoules are used so that the quartz tube does not break during cooling. The melting is carried out in an inert (He,N) or hydrogen atmosphere or under vacuum (10^{-5} to 10^{-6} mmHg) in a sealed ampoule.

Several elements with different doping characteristics have been employed: Na, Au, Tl, O behave as acceptors; Zn, Cd, In, Bi, Cl, Bi are considered donors; whereas Cu, Ag, As, Sb are amphoteric.[45–48] The data, which refer to PbTe, may be applied in a qualitative way to many $Pb_{1-x}Sn_xTe$ compositions. However, the different stabilized forms of doping element in the crystalline matrix (substitutional or interstitial on the metal or tellurium sites) complicate the behavior. Generally, the following rules are valid: elements of group Ia and b are acceptors in the metallic sites and donors in interstitial sites; the elements of group III are donors, excluding Tl; the elements of group V are acceptors if they substitute the metallic ions and donors if they substitute the tellurium. The elements of group VII are donors.

The electrical and thermoelectric properties are affected significantly by the fabrication method. In fact any synthesis method induces specific defects, some of which are electrically active. Materials obtained by the two main fabrication methods, the sintering process and single crystal growth, are now discussed briefly.

Sintered Materials

Although most data refer to experiments with lead telluride, the results may be generalized to include $Pb_{1-x}Sn_xTe$. The as-pressed p-type lead telluride obtained by powdering polycrystals or single crystals possess a very low Hall mobility;[49,50] the powdering operation appears to introduce donor levels, which can cause a cross-over in carrier sign. Annealing in an inert or hydrogen atmosphere tends to eliminate the donor levels. In n-type lead bromide doped lead telluride annealing increases the electron concentration. In all materials, which have low conductivity when powdered and pressed, the electrical conductivity increases after annealing.

The best temperature range for sintering appears to be $650°C < T° < 750°C$. In this temperature range the evaporation of constituents during the sintering period (10 to 20 h) does not significantly change the stoichiometry: at 700°C the saturation vapor pressure of lead telluride is 6.5×10^{-2} mmHg; the molecules of the vapor are partially dissociated (the dissociation energy of vapor molecules is 2.2 eV). A higher sintering temperature results in significant constituent evaporation, but does not eliminate completely the defects introduced by the powdering operation. Figure 5 shows the structure of a PbTe sample prepared by sintering.

Single Crystals

Single crystals of lead telluride can be prepared by almost any of the standard methods, but large single crystals with a high degree of perfection and a homogeneous distribution of the components are difficult to prepare. The solid materials do not undergo any phase transformation between room temperature and melting temperature. However, the specificity of the phase diagrams and the growth conditions cause defects in the crystal such as precipitates, inclusions, and grain growth. Generally, the vapor growth techniques produce small crystals, thus growths from the melt

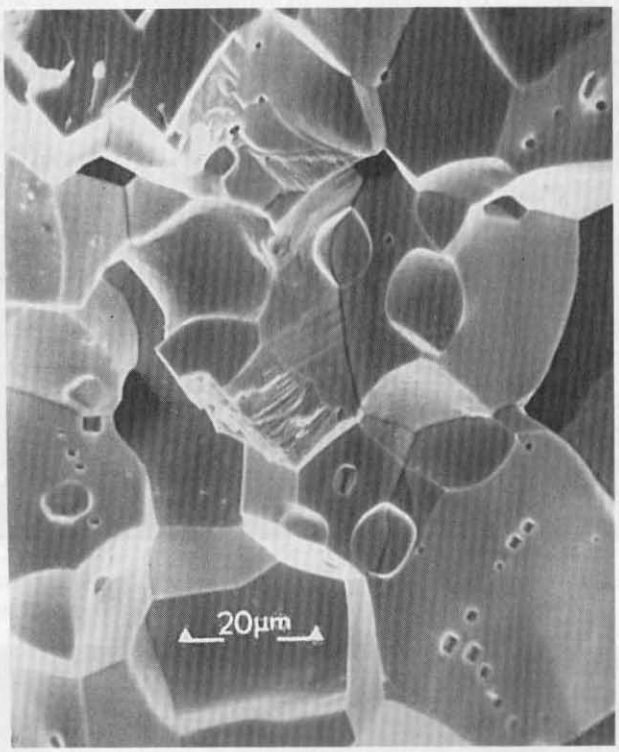

FIGURE 5 The structure of sintered PbTe.

methods are more suitable for manufacturing device thermoelements because large standard size single crystals can be obtained. Recently[51,52] the growth of PbTe and $Pb_{1-x}Sn_xTe$ a few centimeters from the vapor phase on oriented barium fluoride sticks, $Pb_{1-x}Sn_xTe$ substrates, or on red quartz has been reported. Bridgman and Czochralski techniques are used to grow crystals from the melt.

Single crystals grown by the Bridgman technique, or modifications of it, are reported in References 15, 53, and 54. Usually single crystals of 60 to 100 g are obtained. In Reference 57 thermoelectric power measurements were used to monitor the precipitation process in p-type PbTe. In References 58 to 61 micro-size defects in PbTe single crystals grown by the vertical Bridgman technique have been seen in samples selected from different regions of ingots. The influence of both the Pb:Te ratio in the melt and the different growth conditions on the Te-rich or Pb-rich microphase formation has also been tested.[58] Inclusions, microprecipitates, dislocations, and grains can be seen easily by optical microscopy, scanning electron microscopy, or transmission electron microscopy on polished and chemically or electrochemically etched surfaces. Figure 6 shows the typical etch pits on the (100) planes. The average concentration of dislocation is 10^5 to 10^6 cm^{-2}. A Te-rich precipitate in undoped PbTe is shown in Figure 7. Their density is about 10^{-3} to 10^{-4} cm^{-2} in PbTe[58] and is much lower in $Pb_{1-x}Sn_xTe$. Metallic inclusions and cellular substructures in $Pb_{1-x}Sn_xTe$ are reported in Reference 62. A modified Bridgman technique has been described in Reference 54. The isothermal annealing technique has been used to obtain various carrier concentrations.

The normal Czochralski technique for pulling single crystals is useful for materials of relatively low vapor pressure. In the case of volatile materials precautions are taken to ensure that the exposed surface of the melt and the pulled crystals are encapsulated with a nonvolatile liquid (molten boric oxide, B_2O_3). PbTe and $Pb_{1-x}Sn_xTe$ have been grown in this way.[63,64] The growth of $Pb_{1-x}Sn_xTe$ single crystals from near-stoichiometric melts and from melts with slight deviation from stoichiometry has been reported.[65] Pull rates of 1 to 3 mm h^{-1} were used; crystals were 0.5 to 1 cm diameter and weighed 10 to 20 g.

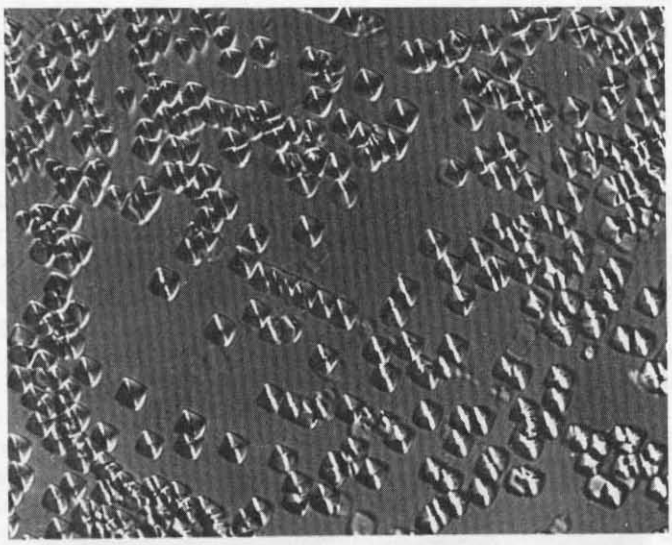

FIGURE 6 Etch pits on the (100) plane of PbTe.

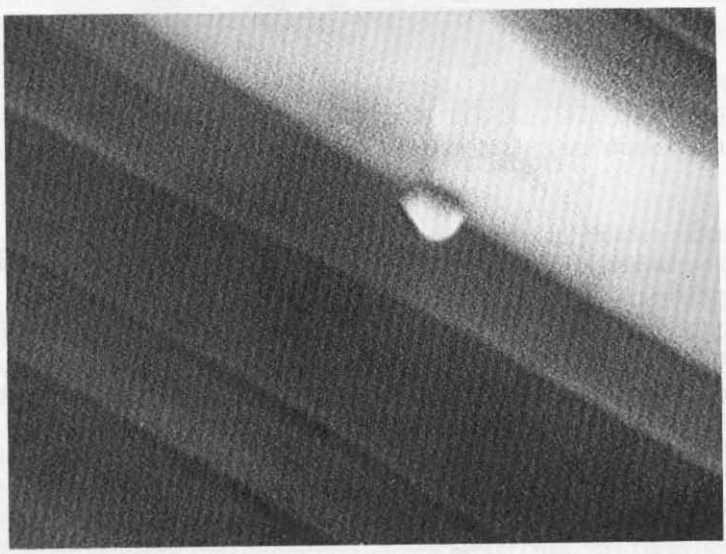

FIGURE 7 Te-rich precipitate in PbTe matrix. (× 30)

References

1. Rowe, D. M. and Bhandari, C. M., *Modern Thermoelectrics,* Holt, Rinehart, and Winston, London, 1983.
2. Parker, S. G. and Johnson, R. E., Preparation and properties of (Pb,Sn)Te, in *Preparation and Properties of Solid State Materials,* Vol. 6, Wilcok, W. R., Ed., Dekker, New York, 1981.
3. Ravich, Y. I., Efimova, B. A., and Smirnov, I. A., *Semiconducting Lead Chalcogenides,* Stilbans, L. S., Ed., Plenum Press, New York, 1970.
4. Iordanishvili, E. K., *Thermoelectriceskie Istochniki Pitania,* Sovietskoe Radio, Moscow, 1968.
5. Abrikosov, N. Kh., Bankina, V. F., Poriezkaia, L. V., Scudnova, E. V., and Scelimova, L. E., *Poluprovodnicovie Soedinenia, ich Poluchenia i Svoistva,* Nauka, Moscow, 1968.
6. Brebrik, R. F. and Allgaier, R. S., Composition limits of stability of PbTe, *J. Chem. Phys.,* 32, 1826, 1960.

7. Brebrick, R. F. and Gubner, E., Composition stability limits of PbTe, *J. Chem. Phys.*, 36, 1283, 1962.
8. Brebrick, R. F., Non-stoichiometry in binary semiconductor compounds, in *Progress in Solid State Chemistry*, Vol. 3, Reiss, H., Ed., Pergamon Press, New York, 1966.
9. Gomez, M. P., Stevenson, D. A., and Huggins, R. A., Self-diffusion of Pb and Te in lead telluride, *J. Phys. Chem.*, 32, 335, 1971.
10. Brebrick, R. F., Analysis of the solidus lines for PbTe and SnTe, *J. Electron. Mater.*, 6, 659, 1977.
11. Sato, Y., Fujimoto, M., Kobayashi, A., Effects of heat treatment on lead telluride under tellurium pressure, *Jpn. J. Appl. Phys.*, 2, 688, 1963.
12. Fujimoto, M. and Sato, Y., P-T-x phase diagram of lead telluride, *Jpn. J. Appl. Phys.*, 5, 128, 1966.
13. Melngailis, I. and Harman, T. C., Single-crystal lead-tin chalcogenides, in *Semiconductors and Semimetals*, Vol. 5, Beer, A. C. and Willardson, R. K., Eds., Academic Press, New York, 1970.
14. Wagner, J. M. and Willardson, R. K., Growth and characterization of single crystals of PbTe-SnTe, *Trans. Metall. Soc. AIME*, 242, 366, 1968.
15. Calawa, A. R., Harman, T. C., Finn, M., and Youtz, P., Crystal growth, annealing and diffusion of lead-tin chalcogenides, *Trans. Metall. Soc. AIME*, 242, 374, 1968.
16. Harris, J. S., Longo, J.T., Gertner, E. R., and Clarke, J. E., The Pb-Sn-Te phase diagram and its application to the liquid phase epitaxial growth of $Pb_{1-x}Sn_xTe$, *J. Crystal Growth*, 28, 334, 1975.
17. Linden, K. J. and Kennedy, C. A., Phase diagram of the ternary system Pb-Sn-Te, *J. Appl. Phys.*, 40, 2595, 1969.
18. Hatto, P. and Crocker, A. J., Solidus of the Pb-Sn-Te alloy system, *J. Crystal Growth*, 57, 507, 1982.
19. Laugier, A., Cardoz, J., Faure, M., and Moulin, M., Ternary phase diagram and liquid phase epitaxy of Pb-Sn-Se and Pb-Sn-Te, *J. Crystal Growth*, 21, 235, 1974.
20. Maier, H. and Hasse, J., Growth, properties and applications of narrow-gap semiconductors, in *Crystal Growth, Properties, and Applications*, Vol. 4, Freyhardt, H. C., Ed., Springer-Verlag, Berlin, 1980.
21. Brebrik, R. F., Composition stability limits for the rocksalt-structure phase $(Pb_{1-y}Sn_y)_{1-x}Te_x$ from lattice parameter measurements, *J. Phys. Chem. Solids*, 32, 551, 1971.
22. Reti, A. M., Jena, A. K., and Bever, M. B., The solid solution of tin telluride and lead telluride, *Trans. Metall. Soc. AIME*, 242, 371, 1968.
23. Miller, E., Komarek, K., and Cadoff, I., Interrelation of electronic properties and defect equilibria in PbTe, *J. Appl. Phys.*, 32, 2457, 1961.
24. Shogenij, K. and Uchiyama, S., On electrical resistivity and Hall coefficient of PbTe crystals, *J. Appl. Soc. Jpn.*, 12, 252, 1957.
25. Fedorov, V. I. and Machnev, V. I., The thermal conductivity of PbTe, SnTe, and GaTe in the solid and liquid phases, *Sov. Phys. Solid State*, 11, 1116, 1969.
26. Greig, D., Thermoelectricity and thermal conductivity in the lead sulfide group of semiconductors, *Phys. Rev.*, 120, 358, 1960.
27. Allgaier, R. S. and Houston, B. B., Mobility studies in semiconductors with very high carrier densities, in *Proc. Int. Conf. on the Physics of Semiconductors*, Exeter, Inst. Phys. and Phys. Soc., London, 1962, 172.
28. Allgaier, R. S., Valence bands in lead telluride, *J. Appl. Phys.*, 32, 2185, 1961.
29. Stavizkaia, T. S., Long, V. A., and Efimova, B. A., Termoelectriceskie sboistva n-PbTe pri vissokikh temperaturakh, *Izv. Akad. Nauk SSSR Neorg. Mater.*, 2, 2096, 1966.
30. Smirnov, I. A., Vinogradova, M. N., Kolomoez, N. V., and Sisoeva, L. M., Teploprovodnost silno leghirovannovo p-PbTe, *Fiz. Tverd. Tela*, 9, 2638, 1967.
31. Allgaier, R. S., Comment on the interpretation of transport measurements in PbTe, *Int. J. Electron.*, 18, 397, 1965.
32. Crocker, A. J. and Rogers, L. M., Interpretation of the Hall coefficient, electrical resistivity and Seebeck coefficient of p-type lead telluride, *Br. J. Appl. Phys.*, 18, 563, 1967.
33. Johnson, G. W., The Seebeck coefficient and electrical resistivity of n-type PbTe between 20°C and 500°C, *J. Electron. Control*, 16, 497, 1964.
34. Andreev, A. A., Temperaturnaia savissimost coeffizenta Kholla PbTe, *Fiz. Tverd. Tela*, 8, 2818, 1966.
35. Andreev, A. A. and Radionov, V. N., O zonnoi structure telluride svinza iz ismereni effecta Kholla pri vissokikh temperaturakh, *Fiz. Tekh. Poluprovodn.* 1, 183, 1967.
36. Koval'chik, T. L. and Maslakovets, P. I., Vlianie primesei na electriceskie svoistva telluride svinza, *Zh. Tekh. Fiz.*, 26, 2417, 1956.

37. Bass, J. C. and Elsner, N. B., Segmented selenide thermoelectric generator, in *Proc. 3rd Int. Conf. Thermoelectric Energy Conversion*, Rao, K. R., Ed., University of Texas at Arlington, 1980, 8.
38. Melngailis, I. and Harman, T. C., Single crystal lead-tin chalcogenides, in *Semiconductors and Semimetals*, Vol. 5, Willardson, R. K. and Beer, A. C., Eds., Academic Press, New York, 1970.
39. Dixon, J. R. and Bis, R. F., Band inversion and electrical properties of $Pb_{1-x}Sn_xTe$, *Phys. Rev.*, 176, 942, 1968.
40. Wagner, J. W., Thompson, A. G., and Willardson, R. K., Carrier mobilities in $Pb_{1-x}Sn_xTe$, *J. Appl. Phys.*, 42, 2515, 1971.
41. Ocio, M., Hall coefficient and mobility in $Pb_{1-x}Sn_xTe$ with high carrier density, *Phys. Rev. B*, 10, 4274, 1974.
42. Zoutendyk, P. J. A., Carrier concentration and Hall mobility in as grown bismuth-doped $Pb_{0.8}Sn_{0.2}Te$ crystals, in *Proc. Int. Conf. Physical Semi-Metallic and Narrow Gap Semi-Conductors*, Bate, R. T. and Carter, D. L., Eds., Pergamon Press, New York, 1971, 424.
43. Fano, V., Growth and characterization of $A^{IV}B^{VI}$ single crystals for IR technology and thermoelectric energy conversion, *Prog. Crystal Growth Charact.*, 3, 287, 1981.
44. Machonis, A. A. and Cadoff, I. B., Investigation of alloys of the system PbTe-SnTe, *Trans. Metall. Soc. AIME*, 230, 333, 1964.
45. Strauss, A. J., Effect of Pb- and Te-saturation on carrier concentrations in impurity-doped PbTe, *J. Electron. Mater.*, 2, 553, 1973.
46. Antcliffe, G. A. and Wrobel, J. S., Spontaneous and laser emission from $Pb_{1-x}Sn_xTe$ diodes prepared by Sb diffusion, *Appl. Phys. Lett.*, 17, 290, 1970.
47. Silberg, E. and Zemel, A., Cadmium diffusion studies of PbTe and $Pb_{1-x}Sn_xTe$, *J. Electrochem. Mater.*, 8, 99, 1979.
48. Crocker, A. J., The role of sodium in lead telluride, *J. Phys. Chem. Solids*, 28, 1903, 1967.
49. Breschi, R., Olivi, A., Camanzi, A., and Fano, V., Induced defects in sintered lead telluride, *J. Mater. Sci.*, 15, 918, 1980.
50. Breschi, R. and Fano, V., The sintering of lead telluride, *J. Mater. Sci.*, 20, 2990, 1985.
51. Golacki, Z., Furmanik, Z., Gorska, M., Szczerbakow, A., and Zahorowski, W., Vapour phase growth of large crystals of PbTe and $Pb_{1-x}Sn_xTe$, *J. Crystal Growth*, 60, 150, 1982.
52. Saunina, T. V., Chesnokova, D. B., and Jaskov, D. A., Thermodynamic analysis of the conditions of growth of $Pb_{1-x}Sn_xTe$ from the gas phase, *J. Crystal Growth*, 71, 75, 1985.
53. Miller, J. F., Moody, J. W., and Himer, R. C., The preparation of PbTe crystals, *Trans. Metall. Soc. AIME*, 239, 342, 1967.
54. Dionne, G. and Woolley, J. C., Crystal growth and isothermal annealing of $Pb_{1-x}Sn_xTe$ alloys, *J. Electrochem. Soc.*, 119, 784, 1972.
55. Lawson, W. D., Preparation of oxygen-free single crystals of lead telluride, selenide, sulfide, *J. Appl. Phys.*, 23, 435, 1952.
56. Akchurin, R. Kh., Vigdorovich, V. N., Lobanov, A. A., Marychev, V. V., and Ufimtsev, V. B., Preparation and physicochemical characteristics of crystals of the solid solutions PbTe-SnTe grown by directed crystallization, *Inorg. Mater.*, translated from *Izv. Akad. Nauk SSSR, Neorg. Mater.*, 12 (15), 838, 1976.
57. Scanlon, W. N., Precipitation of Te and Pb in PbTe crystals, *Phys. Rev.*, 15, 509, 1962.
58. Breschi, R., Camanzi, A., and Fano, V., Defects in PbTe single crystals, *J. Crystal Growth*, 58, 399, 1982.
59. Mühlberg, M. and Hesse, D., TEM precipitation studies in Te-rich as grown PbTe single crystals, *Phys. Status Solidi (a)*, 76, 513, 1983.
60. Watanabe, T. and Kinoshita, K., Study of precipitation in Bridgman-grown $Pb_{1-x}Sn_xTe$ single crystals by TEM, *J. Crystal Growth*, 80, 393, 1987.
61. Fano, V., Precipitation in chalcogenides of groups II and IV, *J. Crystal Growth*, 106, 510, 1990.
62. Butler, J. F. and Harman, T. C., Metallic inclusions and cellular substructure in $Pb_{1-x}Sn_xTe$ single crystals, *J. Electrochem. Soc.*, 116, 260, 1969.
63. Metz, E. P. A., Miller, R. C., and Mazelski, R., A technique for pulling single crystals of volatile materials, *J. Appl. Phys.*, 33, 2016, 1962.
64. Laugier, A., Cadoz, J., Faure, M., and Moulin, M., Ternary phase diagram and liquid phase epitaxy of Pb-Sn-Se and Pb-Sn-Te, *J. Crystal Growth*, 21, 235, 1974.
65. Wagner, J. W. and Willardson, R. K., Growth and characterization of single crystals of PbTe-SnTe, *Trans. Metall. Soc. AIME*, 242, 366, 1968.

22

Properties of the General TAGS System

E. A. Skrabek
Orbital Sciences Corporation
Germantown, Maryland, U.S.A.

D. S. Trimmer
Teledyne Brown Engineering
Huntville, Maryland, U.S.A.

22.1 Background

In the early 1960s great emphasis was placed on developing high-efficiency thermoelectric materials for use with radioisotope heat sources for space power supplies. At that time lead telluride, PbTe, was the standard material for this temperature regime. While the n-type PbTe exhibits good stability, reasonably good mechanical properties, and can be joined to metallic shoes with stable bonds, the p-type PbTe formulations have a number of weaknesses. The alkali-doped (2P) material becomes unstable at high temperatures, is very susceptible to poisoning during processing and operation, has poorer mechanical properties, and is difficult to bond. The manganese-doped material (3P) overcomes some of these drawbacks but has a much lower energy conversion efficiency.

Therefore, a replacement for the p-type PbTe was sought. The fundamental approach was to look for a highly degenerate semiconductor material with minimal thermal conductivity in the 300 to 900 K temperature range. The Ag-Sb-Te system fit these criteria fairly well and has been studied extensively.[1–4] However, it was not capable of high-temperature operation, and it was plagued with stability problems.

Several alloys capable of good power generation over a reasonable temperature range were formed by alloying silver antimony telluride, $AgSbTe_2$, with germanium telluride, GeTe.[5] There appeared to be a monotonic increase of the Seebeck coefficient, electrical resistivity, and thermal conductivity with increasing GeTe content, and an apparent maximum in performance at 90% GeTe. Because the existence of a room temperature transformation from a rhombohedral (89.2°) to cubic sodium chloride (NaCl) structure somewhere between the 75% and 90% GeTe compositions was considered to be a stability problem, this range was not studied.[5]

22.2 Uniqueness of TAGS-80 and TAGS-85

The present authors were of the opinion that permanent lattice strains in these compositions might lead to reduced thermal conductivity and enhanced thermoelectric performance. A number of compositions of the basic TAGS-type materials $(AgSbTe_2)_{1-x}(GeTe)_x$, including those reported on

0-8493-0146-7/95/$0.00+$.50

Table 1. TAGS Compositions Studied

Values of x in $(AgSbTe_2)_{1-x}(GeTe)_x$			
90	85 5/7	83.7	78
87 1/2	85.1	83 1/3	75
87	85	83	50
86	84	80	20

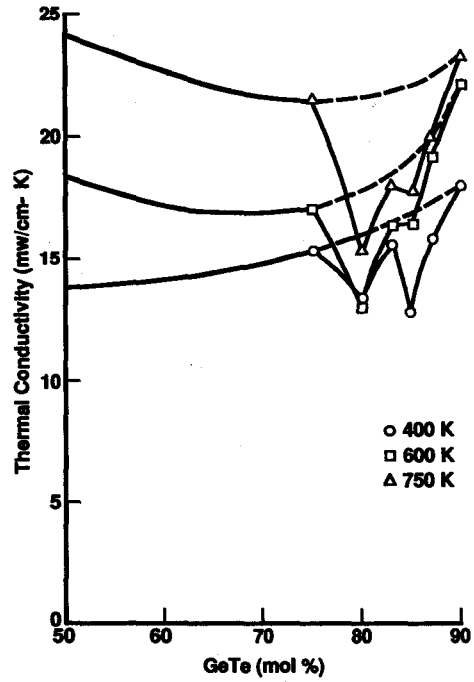

FIGURE 1 Thermal conductivity of various TAGS compositions at selected temperatures.

earlier,[5] were examined (see Table 1). Many of the properties of these alloys were found to vary smoothly with compositions up to 75% GeTe (and indeed, if the points between 75 and 90% GeTe were ignored, the variations would be smooth over the entire range, right to pure GeTe.) However, definite departures from these trends were observed in the 75 to 90% GeTe range.[6–9] Higher than expected values were found for the Seebeck coefficient and the electrical conductivity. A more dramatic effect was the double minima in thermal conductivity observed at 80 and 85% GeTe (Figure 1). These all combined to give a sharp double peak of the dimensionless figure-of-merit (ZT) at these two compositions (Figure 2). The TAGS-80 composition actually exhibits better initial thermoelectric properties than TAGS-85. However, mechanical strength and stability problems with this composition lead to the choice of TAGS-85 as the preferred material for use in generators. Other physical properties of the system confirm the unique character of the TAGS-85 formulation. Both the crystal lattice spacing and the thermal coefficient of expansion (Figure 3) have definite minima at this composition.[6]

Preliminary differential thermal analysis data also point up the uniqueness of this composition range. An attempt was made to analyze this system by means of a pseudobinary phase diagram constructed on the assumption that $AgSbTe_2$ and GeTe behave as single entities in this alloy system.[9] Although this system is too complex for this approach to work, it did indicate possible peritectic compound formation at both the TAGS-80 and TAGS-85 compositions. Further it shows another phase shift at 516°C over the entire 80 to 90% range.

Minor phases consisting primarily of Ag/Te, Sb/Te, Sb, and Ge have been identified in varying amounts in these materials.[10,11] Some of these reduce in size on annealing, supporting the idea of

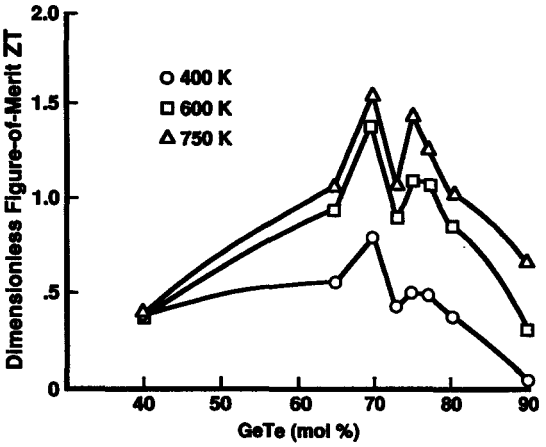

FIGURE 2 Dimensionless figure-of-merit (ZT) of various TAGS compositions at selected temperatures.

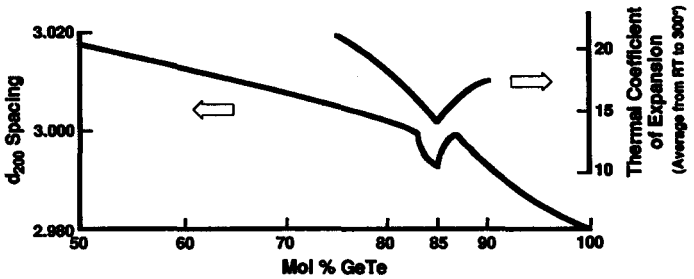

FIGURE 3 Variation of lattice parameter and coefficient of thermal expansion with GeTe content in TAGS alloys.

incomplete peritectic compound formation. Visual examination of several samples during a controlled heat-up cycle revealed thermal etching just above the 516°C phase transition temperature.[12] Sublimation becomes so rapid as to be visibly noticeable above 550°C. Even at lower temperatures it is significant in a vacuum environment.[13] Because of all of these effects the recommended upper limit on the operating temperature is 510°C.

There was originally some concern that the phase transitions and the accompanying change in thermal expansion would cause problems, but multiple thermal cycles of complete couples containing TAGS-85 showed no adverse effects either immediately or in long-term operation.

22.3 High-Performance Materials

The most important feature contributing to the exceptionally high performance of TAGS-80 and TAGS-85 is their very low lattice conductivity. The thermal conductivity (λ) of all of the compositions in this study were measured over the temperature range 25 to 500°C using an absolute method,[14] and the data for TAGS-85 was corroborated by an outside laboratory using a thermal diffusivity technique.[15] The lattice component of thermal conductivity (λ_L) was calculated from experimental data at each temperature and was found to yield a very good 1/T relationship[7] with a lower limit near 0.003 W cm^{-1} K^{-1}. A comparison of manganese-doped PbTe with TAGS-85 is given in Figure 4.

These low values of λ_L are important in that they indicate that the electronic component of the thermal conductivity is approximately 80% of the total (as compared to 50% for PbTe). Thus, when during long-term operation, the Seebeck coefficient (α) and the electrical resistivity (ρ) both

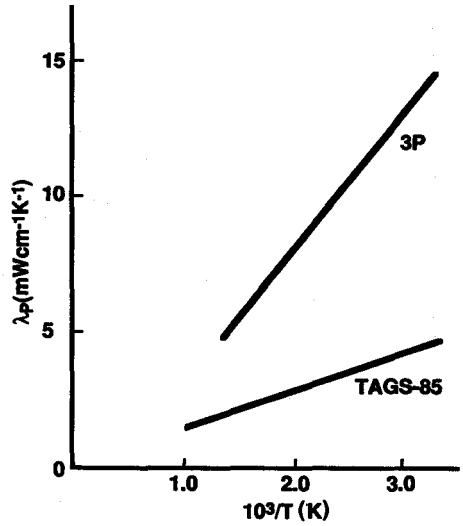

FIGURE 4 Dependence of lattice thermal conductivity on temperature for TAGS-85 and Mn-doped PbTe.

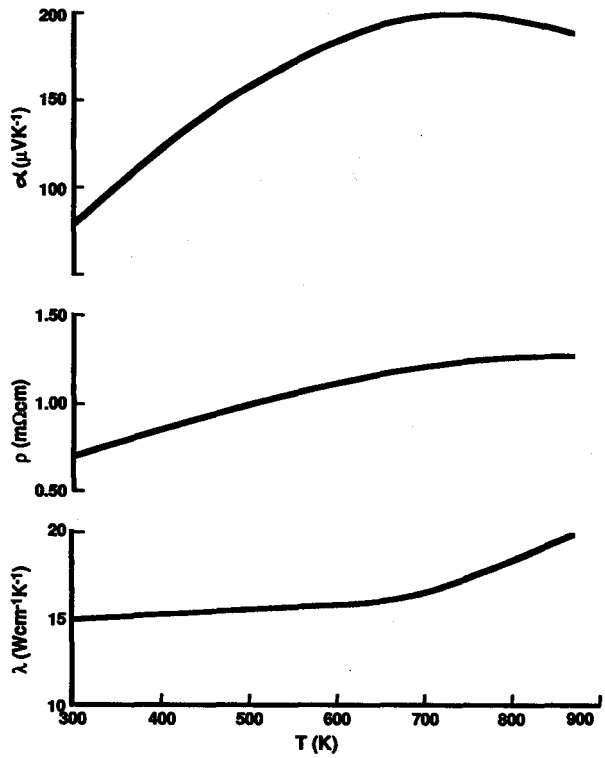

FIGURE 5 Temperature dependence of thermoelectric properties of TAGS-85.

increase to some extent, the figure-of-merit remains relatively unchanged. This follows since about 80% of its change in the $\rho\lambda$ product due to the increase in ρ is compensated for by a decrease in λ and the corresponding increase in Seebeck coefficient essentially compensates for the rest of the change. This effect has been demonstrated experimentally by the authors[8] when precautions were taken to eliminate sublimation effects.

The basic thermoelectric properties of the standard TAGS-85 composition are given in Figure 5.

Table 2. TAGS-Type Compositions Studied $[(Ag_2Te)_x(Sb_2Te_3)_y]_{1-n}$

Sb/Ag Ratio	x	y	n	Ref.
1.078	0.477	0.514	0.843	9, 16
1.084	0.475	0.515	0.856	9, 16
1.10	0.471	0.518	0.913	9, 16
1.10	0.471	0.518	0.856	9, 16
1.10	0.471	0.518	0.851	9, 16
1.128	0.47	0.53	0.85	11
1.154	0.456	0.526	0.834	9, 16
1.166	0.453	0.528	0.848	9, 16
1.203	0.444	0.534	0.853	9, 16
1.25	0.432	0.540	0.84	9, 16
1.274	0.427	0.544	0.853	9, 16
1.30	0.50	0.65	0.90	9, 16
1.30	0.50	0.65	0.85	9, 16
1.30	0.50	0.65	0.75	9, 16
1.30	0.50	0.65	0.50	9, 16
1.333	0.414	0.552	0.832	9, 16
1.363	0.408	0.556	0.846	9, 16
1.439	0.41	0.59	0.87	11
1.439	0.41	0.59	0.85	11
1.439	0.41	0.59	0.84	11
1.439	0.41	0.59	0.83	11
1.439	0.41	0.59	0.81	11
1.45	0.390	0.566	0.838	9, 16
1.50	0.4	0.6	0.80	23
1.50	0.4	0.6	0.60	23
1.506	0.381	0.574	0.851	9, 16
1.524	0.41	0.625	0.87	11
1.524	0.41	0.625	0.86	11
1.524	0.41	0.625	0.85	11
1.524	0.41	0.625	0.84	11
1.524	0.41	0.625	0.83	11
1.524	0.41	0.625	0.81	11
1.545	0.373	0.576	0.83	9, 16
1.60	0.364	0.582	0.843	9, 16
3.0	0.25	0.75	0.80	23
3.0	0.25	0.75	0.60	23

22.4 "Nonstoichiometric" Compositions

Since work on the Ag-Sb-Te system[1–4] indicated that the best thermoelectric material was not $AgSbTe_2$, but rather a material with an Sb/Ag ratio of about 1.5:1, the authors investigated a large range of such "nonstoichiometric" silver antimony tellurides in GeTe. Many of those studied are listed in Table 2. The power factor (α^2/ρ) of these materials at 600 K (about midrange) is compared to that of some "stoichiometric" TAGS compositions in Figure 6. From this data it would appear that several of these nonstoichiometric materials would be better for thermoelectric power generation than even TAGS-85. However, when thermal conductivity is taken into account all of these materials fall below TAGS-80 and TAGS-85 in efficiency.[16]

Nevertheless, it should be noted that very few of the alloys in Table 2 were at the exact 0.80 or 0.85 GeTe compositions. More recently, a study of 80% GeTe alloys with high ratios of Sb to Ag has reported an alloy with an appreciably higher ZT than standard TAGS-85 over the entire operating range.[23] The long-term stability and mechanical properties of this material have yet to be determined, but it looks very promising. This material is compared with TAGS-85 and several other commonly used p-type materials in Figure 7.

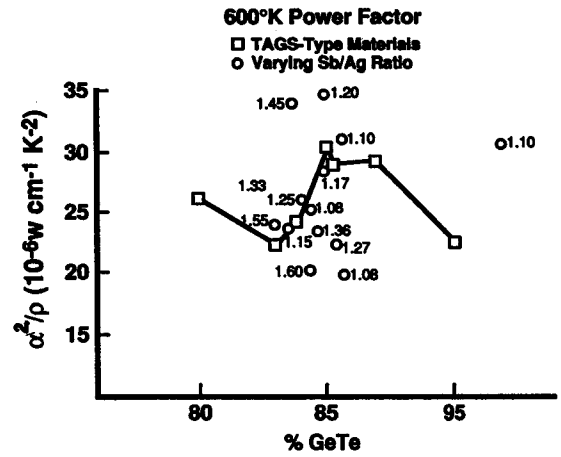

FIGURE 6 Power factor (α^2/ρ) vs. composition for TAGS-type materials with varying Ag/Sb ratios.

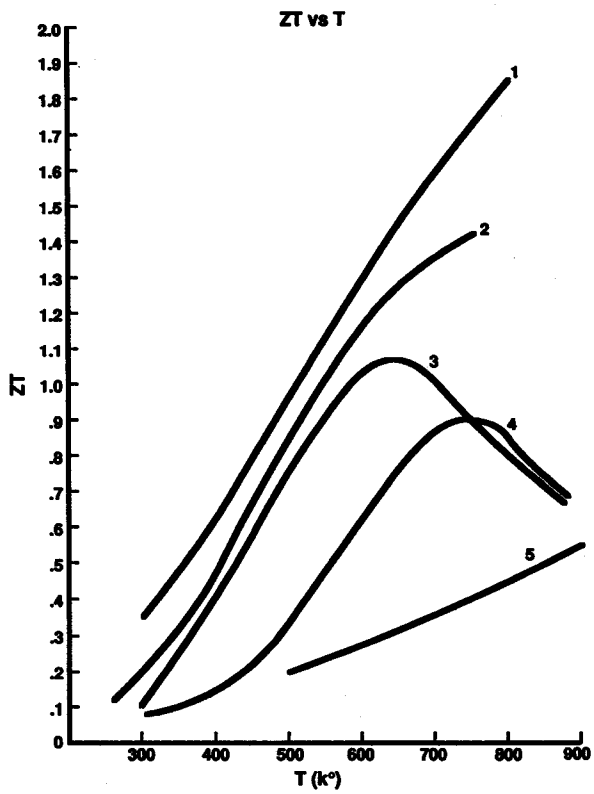

FIGURE 7 Dimensionless figure-of-merit (ZT) vs. temperature for several p-type thermoelectric materials. 1, (1.5:1) TAGS-80; 2, TAGS-85; 3, 2P-PbTe (alkali doped); 4, 3P-PbTe (Mn doped); 5, SiGe.

22.5 Doping

There has been some disagreement as to the optimum formulation and stability of the Ag-Sb-Te system. But it appears that it owes its low thermal conductivity and strong p-type thermoelectric character to a defect structure.[1–4] Similarly, germanium telluride exists as a tellurium-rich compound,[17] and gains its p-type characteristics from this defect structure.[18] The characteristics of the

TAGS-type materials (all p-type with very low lattice conductivities) would definitely seem to arise in the same way.

The thermoelectric properties of these materials have not been found amenable to fine adjustment through ordinary doping techniques. Among the doping agents investigated with very negligible (or actually deleterious) effects were Cu, Sn, In, Ga, Mn, Pb, Se, I, Si, Cd, Fe, Cr, Ni, Ca, Mg, Bi, Li, and excess or deficient Te.[19]

This is not all bad, since it means that TAGS materials are also not easily susceptible to poisoning or oxidation effects.

22.6 Mechanical Properties

At this point, the work was concentrated on the exceptionally efficient TAGS-80 and -85 compositions in order to get them in working devices. The TAGS-80 gave higher efficiency indications than the TAGS-85 material and was initially considered to be the prime composition. However, in the course of early couple development work, TAGS-85 was found to be significantly stronger and less prone to cracking.[7]

Compression tests comparing TAGS-85, TAGS-80, and 2P-PbTe shifted preference to TAGS-85. It failed in compression at an average 21.4 ksi for cast samples and 26.9 ksi for hot-pressed samples (3/8 in. diameter × 1/2 in. long cylinders). 2P-PbTe failed at 13.2 ksi, and 3P-PbTe at 10.9 ksi. TAGS-80 behaved more like PbTe. The tensile strength determined for p-legs bonded to hot and cold shoes was ~890 psi for TAGS-85 and only 122 psi for 3P-PbTe. 2N-PbTe was >340 psi.

In another simple test used to evaluate handling and shock responses, p-legs were dropped 12 in. onto a steel ball. Four TAGS-85 hot-pressed samples survived five drops with no damage. Two of the four TAGS-85 cast samples did so also. The other two cracked on the fifth drop. All four 2P-PbTe pressed and sintered samples failed, three on the first drop and one on the fifth drop.

Then a 25-g steel ball was dropped onto the samples from a height of 4.5 in. The same TAGS-85 samples were used for this test, but four new PbTe samples had to be used since all of the original ones had been broken. All of the TAGS-85 hot-pressed samples survived five drops, while the remaining TAGS-85 cast samples and all of the new PbTe samples either cracked or split apart the first time the ball was dropped on them.

These superior mechanical properties of TAGS-85 have allowed it to be used in rather severe conditions where high dynamic loads are encountered, such as spacecraft launch and landing, and in remote terrestrial locations where sophisticated gear is unavailable for transport and installation.

22.7 Long-Term Performance

As mentioned above, TAGS is essentially self-adjusting to small changes in its thermoelectric properties due to phase shifts from annealing and/or in-gradient operation. However, rather noticeable degradation in output has been observed in low-pressure environment operation of couples in the laboratory and on several space probes. Much of this is attributable to the reduction in hot end area of the element due to vaporization losses, and a corresponding increase in resistance. Directly associated with this is a compositional variation in this area due to a concurrent diffusion of excess Ag_2Te toward the cold end.[19]

Using a 3.5 by 0.5 in. diameter TAGS-85 sample instrumented with 14 thermocouple/voltage probes and operated for a year at 500/25°C, the authors found that the Seebeck coefficient and the electrical resistivity varied much more with time at the cold end than at the hot end of the thermoelement.[8] Other studies with elements containing Mo diffusion barriers one third of the way from the hot end showed that most of these changes were due to the diffusion of Ag_2Te to the cold end. When the diffusion barrier prevented the migration of Ag_2Te, sublimation of GeTe from the hot end was significantly reduced.[19]

The vapor pressure of TAGS-85 at 500°C is over an order of magnitude higher than for PbTe, with GeTe being the predominant vapor species.[13] Therefore, these materials cannot be operated in vacuum. Both baffling with fibrous insulation and ceramic coating of the hot ends of the elements have been used to substantially reduce the power degradation rates for long periods of

time.[20,21] These can reduce the power degradation rates as much as an order of magnitude if properly applied. Generally, a cover gas has also been used in actual devices.[20,22]

22.8 Production of TAGS-85 and Fabrication of Couples

TAGS material is normally produced by casting in an evacuated Vycor tube in a rocking furnace for 1 h at 800°C. It is then cooled slowly in the furnace to 525°C and annealed for 16 h, after this it is cooled to room temperature. If the casting is of the correct diameter, the ingot can be sliced to size and used for couple fabrication with no further treatment.

However, if large batches are cast in large-diameter tubes, they can be remelted under inert atmosphere and cast in graphite molds. The annealing time then required is only about an hour.

Hot-pressed legs have the same thermoelectric properties as the cast ones, but have somewhat better mechanical properties. The process uses −35 mesh material compacted at 20,000 psi at room temperature, and then hot-pressed at 5,000 psi at 525°C for half an hour.

Cold pressing and sintering, which is used extensively with other materials such as PbTe, has been found to be very unsatisfactory for producing TAGS legs.[6]

Common contacting materials such as copper, iron, and nickel react with TAGS at temperatures below 500°C. Therefore, it is necessary to insert a layer of semiconductor between the TAGS leg and the metallic strap. Tin telluride has been shown to provide low bond resistance and good aging characteristics in this application.

Couples have been fabricated with a wide number of n-leg materials. The most commonly used is lead iodide doped PbTe. In order to fully utilize the temperature capability of the PbTe legs, a thin segment of SnTe is used to maintain the hot-side temperature of the TAGS below 525°C while allowing the PbTe to operate nearer 600°C. This causes a slight degradation in p-leg performance but an overall increase in couple output.

22.9 Applications

TAGS-85 has been used successfully in numerous space and terrestrial applications. The Pioneer 10 and Pioneer 11 spacecraft were the first to traverse the asteroid belt and visit the giant gas planets Jupiter and Saturn, and were also the first man-made objects to leave the solar system. After more than 20 years, these TAGS radioisotope thermoelectric generators (RTG) are still delivering enough power to run the 11 onboard experiments and power the radio which is returning useful data from more than 10 billion km away from earth. Data from these spacecraft are still being received approximately biweekly, and being reduced at Fairchild to monitor the continuing performance of the RTGs. The current overall power degradation rate, including fuel decay, helium buildup, and all other effects is approximately 0.00007 W/h per generator. As far as is known, these are the longest lived autonomous electrical power sources ever produced.

The Viking Landers 1 and 2, which conducted man's first searches for life on the surface of Mars, were also powered by TAGS RTGs. These were still producing power above the design level when other problems caused a loss of communication with each of the landers.

SENTINEL generators using TAGS-85 have been used for numerous terrestrial applications ranging from deserts to arctic environments. One SENTINEL RTG has been continuously supplying power to a meteorological data collection and transmission system off the coast of California since 1970. Another ten TAGS-85 RTGs deployed at five sites are currently supplying the power for a series of seismic detectors in Alaska.

References

1. Stegher, A., Wald, F., and Eckerlin, P., Über eine ternäre Phase im System Ag-Sb-Te, *Z. Naturforsch.*, 16a, 130, 1961.
2. Stegherr, A., U.S. Patent 3,249,469.

3. Burmeister, R. A. and Stevenson, D. A., Preparation and electrical properties of silver antimony telluride, *Trans. Metall. Soc. AIME*, 230, 329, 1964.
4. Johnson, R. G. R. and Brown, J. T., Preparation and properties of silver-antimony-tellurium alloys for thermoelectric power generation, in *Metallurgical Soc. Conferences*, Vol. 15, 285, Interscience Publishers, New York, 1962.
5. Rosi, F. D., Dismukes, J. P., and Hockings, E. F., Semiconductor materials for thermoelectric power generation up to 700°C, *Electron. Eng.*, 79, 450, 1960.
6. Skrabek, E. A. and Trimmer, D. S., U.S. Patents 3,695,867, 3,762,960, 3,945,855.
7. Skrabek, E. A., Advanced Technology Symposium, Martin-Marietta Corp., Baltimore, MD, MND-3314, August, 1967.
8. McGrew, J. W., A report on the properties and performance of TAGS, in *Proceedings of the 5th Intersociety Energy Conversion Engineering Conference*, Las Vegas, NE, September 21–25, 1970, 15–31.
9. Skrabek, E. A., A discussion of the properties of the general TAGS system, presented at the 8th Intersociety Energy Conversion Engineering Conference, Philadelphia, PA, August 13–18, 1973.
10. ———, Electron Beam Microanalysis of Microconstituent Phases in Te-Ge-Sb-Ag Alloys, Report AMR-2024, Advanced Metals Research Corp., July 1965.
11. Elsner, N. B., personal communication, 1972.
12. Evans, D. B., personal communication, 1968.
13. Elsner, N. B., Selleck, E. G., and Staley, H., Vaporization characteristics of (GeTe) · 85(AgSbTe2) · 15 (TAGS) alloys, in *Proceedings of the 5th Intersociety Energy Conversion Engineering Conference*, Las Vegas, NE, September 21–25, 1970, 15–34.
14. Bienert, W. B., Trimmer, D. S., and Skrabek, E. A., Technique for measuring thermal conductivity of T/E materials, in *Proceedings of the IEEE/AIAA Thermoelectric Specialist Conference*, Washington, D.C., May, 1966.
15. Mueller, J. J. and Lagedrost, J. P., Final Report on Electrical and Thermal Properties of TAGS-85 Thermoelectric P-Type Alloy, Battelle Memorial Institute, Columbus Laboratories, April 18, 1969.
16. Skrabek, E. A., Compositional variations of TAGS-type materials, presented at Fourth RTG Working Group Meeting, Daytona Beach, FL, March, 1973.
17. McHugh, J. P. and Tiller, W. A., *Trans. Metall. Soc. AIME*, 218, 187, 1960.
18. Kolomoets, N. V., Lev, E. Ya., and Sysoeva, L. M., Nature of charge carriers in GeTe, *Soviet Phys. Solid State*, 5, 2101, 1964.
19. Skrabek, E. A., Improved long term performance of TAGS thermoelements, in *Proceedings of the 9th Intersociety Energy Conversion Engineering Conference*, San Francisco, CA, August, 1974, 160.
20. Goebel, C. J., Snap 19 Pioneer 10 and 11 RTG deep space performance, in *Proceedings of the 10th Intersociety Energy Conversion Engineering Conference*, Newark, DE, August 18–22, 1975, 868.
21. Skrabek, E. A., Effects of coatings and temperature on long term performance of TAGS thermoelements, in *Proceedings of the 11th Intersociety Energy Conversion Engineering Conference*, Lake Tahoe, NV, September, 1976, 1567.
22. Brittain, W. M. and Skrabek, E. A., SNAP 19 RTG performance update for the Pioneer and Viking missions, in *Proceedings of the 18th Intersociety Energy Conversion Engineering Conference*, Orlanda, FL, August, 1983, 1056.
23. Christakudis, G. Ch., Plachkova, S. K., Shelimova, L. E., and Avilov, E. S., Thermoelectric figure of merit of some compositions in the system $(GeTe)_{1-x}[(Ag_2Te)_{1-y}(Sb_2Te_3)_y]_x$, in *Proceedings of the 8th International Conference on Thermoelectric Energy Conversion*, Nancy, France, July 10–13, 1989, 125.

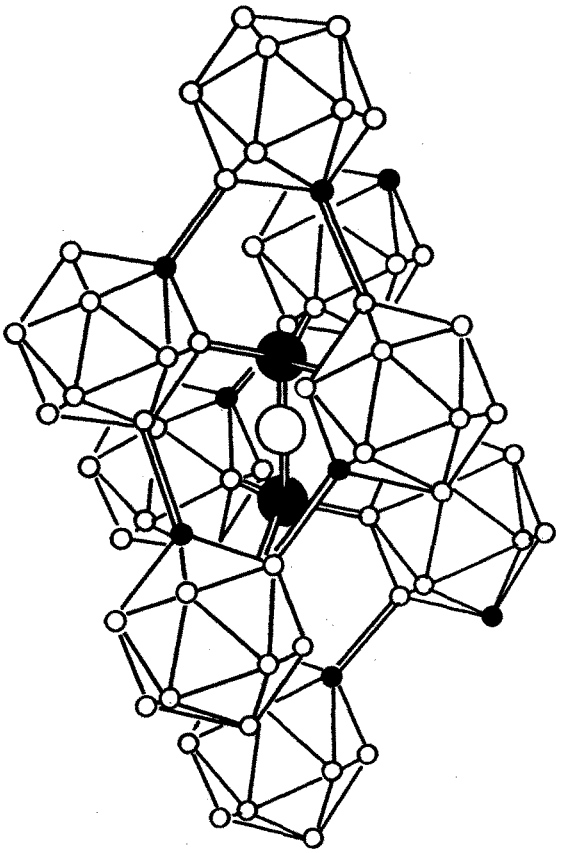

FIGURE 2 Crystal structure of boron carbide. Open circles represent boron atoms, filled circles represent carbon atoms in the ideal B_4C structure.

has long been a matter of controversy. A detailed discussion of the various proposals is beyond the scope of this chapter. As shown in a recent review article,[29] the composition dependences of a wide variety of physical properties of boron carbide may be understood within a simple structural model of the boron carbide solid solution. This model, which was originally proposed[30] to explain the electrical transport properties of boron carbides, will be adopted in this article. Details of the various models are provided in References 1, 16, 29, 31, and 32.

The prominent feature of our structural model is the presence of carbon atoms within many of boron carbide's icosahedra at all compositions. As the carbon concentration is reduced from the ideal B_4C composition, CBC chains are first replaced by CBB chains, $(B_{11}C)[CBC \rightarrow CBB]$. The replacement proceeds until the supply of CBC chains is nearly exhausted, at a composition of 13.3 at.% carbon. Further reductions in carbon concentration are achieved by replacing some of the icosahedral carbon atoms with boron atoms, $(B_{11}C \rightarrow B_{12})[CBB]$. Even at the lowest carbon concentration of about 9 at.%, carbon is located within some 35% of the icosahedra. Disorder, arising from the distribution of carbon atoms among different icosahedral sites, from the mixing of different types of icosahedra and chains, and from the two possible orientations of CBB chains, is present at all boron carbide compositions. The relationship between these structural effects and the electrical and thermal transport properties of boron carbides will be explored in the following sections.

31.5 Electrical Transport Properties

The electrical transport properties of boron carbides have been measured over wide ranges of temperatures by a number of authors.[12–14,23,26,33–38] The essential features are reproduced in most of

23

Thermoelectric Properties of Silicides

Cronin B. Vining
Consultant
Webster Groves, Missouri, U.S.A.

23.1 Abstract

For the most commonly used thermoelectric materials (Bi_2Te_3, PbTe, SiGe), the conduction and valence bands are derived from *s*- and *p*-orbitals. But most thermocouple wire materials (chromel, alumel, WRe, PtRh) consist of alloys with partially filled *d*-bands, because Seebeck values are much larger for *d*-band alloys than for metals with filled or empty *d*-bands (such as Cu or Na, respectively). Certain silicide semiconductors that exhibit *d*-band character in the valence and/or conduction band may be able to combine the Seebeck enhancement effect characteristic of transition metal alloys, with the ability to achieve optimum doping levels typical of conventional thermoelectric materials. In this chapter, the thermoelectric properties of compounds of silicon combined with elements from groups 1 through 8, including the *d*-band elements, are reviewed. A number of materials are identified which appear to have the potential for ZT values much greater than ZT ~1 typical of current state-of-the-art materials.

23.2 Introduction

Even after more than 30 years of experience with thermoelectric technology, efficiencies remain relatively low, seldom exceeding 1/8 of the limiting Carnot efficiency. The difficulty is that available materials have limited performance, as characterized by the usual dimensionless figure-of-merit

$$ZT = \frac{\sigma\alpha^2 T}{\lambda}$$

where σ is the electrical conductivity, α is the Seebeck coefficient, and λ is the thermal conductivity. Each of the most commonly used thermoelectric materials, such as Bi_2Te_3, PbTe, and SiGe, have a maximum ZT ~1. Since there is no fundamental upper limit on ZT the room for growth must nevertheless be considered quite large, amounting to almost an order of magnitude in efficiency.

0-8493-0146-7/95/$0.00+$.50

In order to achieve significantly higher efficiencies, new materials are needed. Probably these new materials will differ from the conventional thermoelectric materials in some fundamental way. Fortunately, candidate materials are not difficult to identify, because in some ways the most commonly used thermoelectric materials represent an extremely narrow class of materials: all are composed exclusively of elements from the right-hand portion of the periodic table and all are dominated by *s*- and *p*-bonding. One promising class of materials is the transition metal silicides, where the *d*-electrons qualitatively alter the bonding and transport properties compared to simple *s*-, *p*-bonded materials. A few silicides, such as $FeSi_2$ and the higher manganese silicides ($MnSi_{-1.75}$), are discussed in more detail in chapters elsewhere in this handbook. But for many promising materials, insufficient data are available to reliably estimate thermoelectric performance.

This chapter examines the occurrence and properties of silicide semiconductors with an emphasis on the possibility of attaining high thermoelectric conversion efficiencies. Section 23.3 discusses the general criteria used to evaluate the available literature on a candidate thermoelectric material. Section 23.4 reviews the properties of silicides as they pertain to thermoelectric applications and Section 23.5 summarizes the results of this survey.

23.3 Evaluation Criteria

Before considering specific materials, this section provides a brief summary of the characteristics which suggest potential for a high figure-of-merit material. Characteristics to be considered include those needed: (1) to achieve a high figure-of-merit and (2) to use in applications. When establishing such search criteria, care must be taken to avoid excluding promising materials due to excessively narrow selection criteria. At the same time the criteria must be sufficiently definite to limit the search to a tractable number of candidate materials.

The principles for achieving a high figure-of-merit have been discussed by Ioffe[1] for a standard band-type semiconductor:

1. High value of $A' = (T/300)\,(m^*/m_e)^{3/2}\,\mu/\lambda_{ph}$ where m^* is the carrier effective mass, μ is the mobility in $cm^2/V\text{-}s$, and λ_{ph} is the lattice thermal conductivity in mW/cm-K (for simplicity, the units for A′ will be omitted throughout this chapter)
2. Band gap, E_g, greater than about 4 k_BT
3. Dopable to the extrinsic regime

The trade off in properties represented by the factor A′ comes from a simple, single band model for semiconductors. ZT actually depends on a large number of additional factors, but A′ captures the essential features. Moreover, the parameters entering A′ may be estimated with a minimum of experimental information and can therefore be useful as a screening tool, at least for conventional band-type semiconductors.

So, ZT may be improved by increasing the effective mass, increasing the mobility, and/or reducing the lattice thermal conductivity. The large energy gap requirement stems from the need to suppress the thermal excitation of minority carriers, which quenches the Seebeck coefficient and increases the thermal conductivity. The doping requirement stems from the need to achieve the optimum doping level: overdoping results in a small Seebeck coefficient, while underdoping results in excessively large resistivity values.

The considerations for practical utilization of a material can depend strongly on the anticipated application. However, some general criteria include:

1. Chemical, structural, and thermal stability
2. Ability to form sound electrical and thermal connections
3. Manufacturable in suitable quality and quantity

There is often some trade off between these two types of requirements. If ZT is high enough, even very substantial applications difficulties may be overcome with heroic device development efforts. On the other hand, even a relatively low ZT may be useful if the material is sufficiently inexpensive and easy to use.

Table 1. Representative Thermoelectric Parameters at 300 K and Maximum ZT for Selected Materials

Material Name	Melting Point, K	Type	m^*/m_e	μ cm²/V-s	λ_{ph}mW/cm-K	A′	ZT_{max}	E_geV	Ref.
(Si,Ge)	1550	n	1.4	68	44	2.6	1.0	0.7	2, 3
(Si,Ge)	1550	p	1.2	40	44	1.2	0.7	0.7	2, 4
$Mg_2(Si,Sn)$	1300	n	(1)			14	0.8	0.7	12, 13
$Mg_2(Si,Ge)$	1360	n	1.2	108	21	6.8	1.07	0.74	14, 15
$Mg_2(Si,Ge)$	1360	p	2.3	22	21	3.7	1.68	0.74	14, 15
$CrSi_2$	1763	p	5	15	68	2.5		0.35	23–26
$CrSi_2$	1763	n	20.2	0.15	68	0.2		0.35	22–23
$MnSi_{\sim 1.75}$	1550	p	(1)	40	29	1.4	0.7	0.67	32,33,36,37
$ReSi_2$	2250	p	(1)	105	55	1.9		0.12	24, 27
$FeSi_2$	1255	p	4	4	40	0.8	0.2	0.9	43
$FeSi_2$	1255	n	(1)	2	40	0.05	0.4	0.9	44
Ru_2Si_3	1970	n	2.9	10	40	1.2		1.08	49, 52
Ru_2Si_3	1970	p	2.9	29	40	3.6		1.08	49, 52

For space power applications, state-of-the-art SiGe alloys have ZT values among the best known[2] and are excellently suited for high-temperature applications. Since transition metals are relatively refractory materials, SiGe alloys are a reasonable baseline for comparison purposes. For SiGe, using parameters taken from recent theoretical models (see Table 1), we find $A' = 2.6$ and $ZT_{max} = 1$ for n-type SiGe[3] and $A' = 1.2$ and $ZT_{max} = 0.7$ for p-type SiGe.[4]

This example serves to highlight the fact that the relationship between A′ and ZT_{max} is only qualitative, even for an extensively studied material such as SiGe. There is considerable error for most of the entries in Table 1 and because they were extracted from a wide variety of sources, considerable caution must be exercised in any comparisons. Still, large values of A′ do generally correlate with high ZT values, so these values can be of some use as a qualitative guide.

23.4 Properties of Metal Silicides

In this section each of the metal-silicon systems from the first ten groups of the periodic table will be reviewed. Useful reviews are available on the preparation,[5,6] thermodynamics,[7] electrical properties,[8] and thermoelectric properties[9] of transition metal silicides. In many cases sufficient transport data are available to estimate A′ for the silicides and these data are summarized in Table 1. The number of possible doping and alloying combinations, however, is very large. This, combined with the technical difficulties of preparing and characterizing high-quality samples of refractory materials, has meant that little or no data are available for a great many very promising materials.

With the exception of the alkali and alkaline earth silicides, semiconducting behavior is observed in only the more silicon-rich silicides. This is a straightforward result of the usual requirement that all bands must be either completely filled or completely empty for a material to exhibit semiconducting behavior. The alkali and alkaline earth elements have only one or two valence electrons and it is relatively easy to use all of the valence electrons in bonds, regardless of the proportion of metal to silicon atoms. Transition metals have many more valence electrons and if the silicon content is too low, there will almost certainly be metal-metal bonds, resulting in metallic conduction behavior. All known metal-rich transition metal silicides are metallic. Many of the more silicon-rich compounds, however, do exhibit semiconducting behavior and each of the metal silicides from groups 1 through 8 will be examined in the following sections.

Alkali and Alkaline Earth Silicides

Many of the alkali and alkaline earth silicides and germanides are known to be semiconductors. Several of the alkali monosilicides and monogermanides (NaSi, NaGe, KGe), are semiconductors with band gaps near 0.5 to 1 eV,[10] but little else is known about them. Notable are Mg_2Si, Ca_2Si,

Sr_2Si, and their germanide and even stannide analogs. Based on the known semiconducting properties of these materials,[11] Nicolaou has predicted ZT = 3 and larger for certain solid solutions.[12] Recently, ZT = 0.8 has been reported for $Mg_2(Si,Sn)$ solid solutions.[13] Marchuk et al.[13] report μ/λ_{ph} values for $Mg_2(Si,Sn)$ which, using $m^*/m_e = 1$, yields the extraordinary value of A′ = 14. Results of Noda et al.[14,15] also indicate large values for A′ and ZT as large as 1.68 for $Mg_2Si_{0.6}Ge_{0.4}$. The large values of A′ and the band gap (0.7 eV), combined with the ability to alloy these materials, are all excellent indications that even higher ZT values will be achieved with further development.

$BaSi_2$, with $E_g \cong 0.48$ eV, has been reported to have $\alpha^2\sigma = 1.0$ $\mu W/K^2$-cm for a sample with $\alpha = +600$ $\mu V/K$.[11] Assuming acoustic phonon scattering and a constant mobility, an optimum power factor of $\alpha^2\sigma \cong 11$ $\mu W/K^2$-cm is estimated. Combined with $\lambda_{ph} = 16$ mW/cm-K[16] yields ZT = 0.2 at 300 K. With optimized doping and alloying, this material may also be of interest. For all the alkali and alkaline earth compounds, however, considerable handling difficulties can be anticipated due to chemical reactivity. Also, many systems exhibit low melting point eutectic compositions.

Rare Earth Silicides

All of the rare earth elements (Sc, Y, La-Lu) form metallic silicides, with the possible exception of α-$LaSi_2$ which may be described as a small band gap (0.19 eV)[11] n-type semiconductor. The binary rare earth-silicon compounds, therefore, appear to be of little interest for thermoelectric applications.

Groups IVB and VB Silicides

The group IVB (Ti, Zr, and Hf) and group VB (V, Nb, and Ta) elements all form metallic disilicides. Nevertheless, $Nb_xTa_{1-x}Si_yGe_{2-y}$ alloys have been investigated and a sample of NbSiGe was reported to have ZT = 0.5[17] or ZT = 1.5[18] at 1300 K. The ZT = 1.5 value is particularly suspicious, however, since the quoted electrical resistivity and thermal conductivity values violate the Wiedemann-Franz law. It is worth pointing out here that the crystal structure of $TiSi_2$[19] is the prototype for a large family of materials[20] known as Nowotny chimney-ladder compounds. The unit cell in this family can be very large, consisting of a chimney-ladder of subcells, each of which is similar to the $TiSi_2$ unit cell. The metal atoms occupy nearly regular sites, similar to the β-Sn structure type, while the silicon (or other group IV) atoms occupy sites that vary slightly from subcell to subcell.

An interesting characteristic of the Nowotny chimney-ladder compounds is the "magic" number of 14 valence electrons per metal atom (VEC = 14), a remarkable predictive rule for the occurrence of a band gap in these materials.[20] The rule was thought to originate from the observation that 14 valence electrons are enough to fill the 4 *s*-*p*-type bonding states of the β-Sn structure type, plus 10 more to fill all of the *d* states for each metal. Recent calculations, however, suggest that the gap is found within the *d* states, contrary to the filled *d*-band interpretation.[21] The rule itself remains useful, even if the causal relationship is unclear, because chimney-ladder compounds with VEC = 14 are typically semiconductors while others, such as $TiSi_2$ with only VEC = 12, are found to be good conductors.

Cr, Mo, and W Silicides

Although not a member of the Nowotny chimney-ladder structure type, $CrSi_2$ is a large effective mass[22] semiconductor, consistent with the "magic" number of VEC = 14, and has a reasonably large A′ value of 2.5 for p-type material, which compares well to the value for SiGe (see Table 1). While the value of A′ can be further increased by lowering λ through alloying,[23,24] $CrSi_2$ is intrinsic at high temperatures due to the small band gap (0.35 eV)[25,26] and therefore of little interest for high-temperature thermoelectric applications.

α-$MoSi_2$ and WSi_2 are p-type semimetals with relatively low carrier concentrations (4.0 and 7.5×10^{21} cm^{-3}, respectively) and high mobilities (59 and 67 cm^2/V-s, respectively).[27] In this case

it seems the "magic" number of VEC = 14 was not sufficient to actually create a band gap, but instead resulted in a reduced density of states at the Fermi level and a small number of carriers. All three of the compounds $CrSi_2$, $MoSi_2$, and WSi_2 might be made into useful thermoelectrics, if only they exhibited a larger band gap.

Mn and Re Silicides

MnSi[11,16,28,30] and the higher manganese silicides[11,27,29,31,37] are of some interest as thermoelectrics. While the monosilicide probably has too small a band gap to be useful at high temperatures, the higher silicides have ZT values up to 0.8–0.9 (32, 36, 37). Using $m^*/m_e = 1$ for holes, we estimate $A' = 1.4$, which again compares well to SiGe.

Early work was uncertain as to the precise composition of the material. It is now known that the higher manganese silicides actually form with a variety of compositions such as $Mn_{11}Si_{19}$, $Mn_{15}Si_{26}$, $Mn_{27}Si_{47}$ (38) and probably others, each of which is a Nowotny chimney-ladder compound with VEC near 14. Al substitutions result in the ternary compound $MnAl_{0.75}Si_{1.25}$ which exhibits opposite signs for the Hall and Seebeck coefficients, explained by an unusual band structure.[39] Clearly, much remains to be done in this system and even higher ZT values can be expected with proper development.

$ReSi_2$, like $CrSi_2$, has a favorable $A' = 1.9$ (again assuming $m^*/m_e = 1$), but has a small band gap (0.12 eV), and therefore cannot be expected to have a large ZT (see Table 1). Still, the number of alloying possibilities, such as $Re_{1-x}Mo_xSi_2$ or the closely related $Cr_{1-x}V_xSi_2$ (40) is rather large and some of these materials may be sufficiently inexpensive to be of some interest.

Fe, Ru, and Os Silicides

β-$FeSi_2$ is a useful, inexpensive thermoelectric material, currently under development for use in automobiles[41] and as a source of small amounts of emergency power.[42] Birkholz has reviewed the properties of β-$FeSi_2$,[43] which are summarized in Table 1. The relative ease of preparation and low cost compensate in some applications for the relatively low ZT values. The very low value of $A' = 0.05$ for n-type β-$FeSi_2$ is reconciled with the fairly substantial ZT = 0.4 by analysis of both transport[44] and optical properties[45] which indicate the conduction mechanism is by small polaron hopping. In this case, the parameter A′ may still be of some use, but cannot be readily compared to A′ values for more conventional materials with band-type conduction. There has also been some interest, mostly in Japan, in β-$FeSi_2$ prepared by a novel RF-plasma technique.[46]

The compounds Ru_2Si_3, Os_2Si_3, and Os_2Ge_3 are isostructural, VEC = 14, Nowotny chimney-ladder compounds,[47] with structures similar to Ru_2Ge_3 and Ru_2Sn_3.[48] Ru_2Si_3, Ru_2Ge_3, and Os_2Si_3 are semiconductors, as expected, with reported band gaps of 1.08 eV,[49] 0.34 eV,[50] and 2.3 eV,[51] respectively, although electronic structure calculations for Ru_2Si_3 suggest the band gap is within the *d*-states, rather than above,[21] as discussed above.

A model for the thermoelectric properties of doped Ru_2Si_3 has been developed based on high-temperature measurements of electrical resistivity, Hall effect, Seebeck coefficient, and thermal conductivity in the intrinsic region.[52] Based on this model, ZT_{max} for p-type Ru_2Si_3 has been predicted to be up to three times larger than p-type SiGe and n-type Ru_2Si_3 is predicted to be 50% better than n-type SiGe. To date, large ZT values have not yet been realized for Ru_2Si_3 due to doping difficulties, in spite of efforts to identify suitable dopants.[53,54]

Finally, in the Os-Si system, one more semiconductor has been reported: $OsSi_2$, isostructural with β-$FeSi_2$ and has been reported to have a band gap of 1.8[55] or 2.3 eV.[51] The much greater mass of Os compared to Fe suggests $OsSi_2$ will have a much lower thermal conductivity than $FeSi_2$. Measurements on high-quality samples of $OsSi_2$ to estimate the effective mass, mobility, and thermal conductivity values would be very interesting.

Co, Rh, and Ir Silicides

The cobalt silicides, CoSi and $CoSi_2$, are inexpensive but have too large a carrier concentration[27] to be particularly useful as thermoelectrics. Two compounds of possible interest (Rh_3Si_4, Rh_4Si_5)

have been reported in the Rh-Si system.[56] Although transport properties have not been reported for either rhodium compound, their Ir analogs (Ir_3Si_4 and Ir_4Si_5) have recently been found to be metallic.[57] Two further compounds in the Ir-Si system, Ir_3Si_5 and $IrSi_3$, appear to have no other isostructural compounds, but exhibit some semiconducting behavior and may be of some interest for thermoelectric applications.

Ni, Pd, and Pt Silicides

All of the Ni group silicides are metallic and of little use as thermoelectrics. It is worth noting, however, that alloys based on Ni and Pt are important thermocouple materials due to their relatively large Seebeck coefficient values, a result of the *d*-band character of the electronic structure of these metals.

23.5 Summary

Many silicide semiconductors have been identified and most of these are of at least some interest as thermoelectric materials. ZT values nearly as large as achieved in SiGe have already been achieved for $Mg_2(Si,Sn)$ alloys and $MnSi_{\sim 1.75}$, and probably higher ZT values can be achieved with optimum alloying and doping in oriented single crystals. $CrSi_2$ and $ReSi_2$ probably could be turned into useful thermoelectric materials, except for their low band gap values.

Several Ru, Os, and Ir silicides are semiconductors, but much too little is known about them to satisfactorily estimate their figure-of-merit values. Among the more interesting compounds in this group are the Nowotny chimney-ladder compounds Ru_2Si_3 and Os_2Si_3, which have the "magic" number of 14 valence electrons per transition metal element. These compounds are essentially isostructural with $MnSi_{\sim 1.75}$, which is known to have reasonable ZT values, but are more refractory and, because of the heavier elements involved, expected to have lower thermal conductivity values.

The trends observed among the silicides may generally be expected to be followed by the analogous germanides. Germanides will tend to have lower melting points and smaller band gap values, both of which restrict their use to temperatures somewhat less than the silicides. But, they may also have both lower thermal conductivity values and larger mobility values, which could prove useful. Even less is known about the germanides than is known about the silicides, however, and considerable exploratory work will be required.

As this survey shows, many silicides with the potential for large ZT values have hardly been examined. The development of detailed theoretical models for this kind of *d*-band semiconductor, combined with experimental results on high-quality samples of a few representative systems, such as Ru_2Si_3, are needed to evaluate the potential of this class of materials to exhibit high ZT values.

References

1. Ioffe, A. F., *Semiconductor Thermoelements and Thermoelectric Cooling*, Infosearch Limited, London, 1957.
2. Dismukes, J. P., Ekstrom, L., Steigmeier, E. F., Kudman, I., and Beers, D. S., Thermal and electrical properties of heavily doped Ge-Si alloys up to 1300 °K, *J. Appl. Phys.*, 35, 2899, 1964.
3. Vining, C. B., A model for the high-temperature transport properties of heavily doped n-type silicon-germanium alloys, *J. Appl. Phys.*, 69, 331, 1991.
4. Vining, C. B., A model for the high-temperature transport properties of heavily doped p-type silicon-germanium alloys, in *Modern Perspectives on Thermoelectrics and Related Materials, Materials Research Society Symposium Proceedings*, Vol. 234, Allred, D. D., Vining, C. B., and Slack, G. A, Eds., Materials Research Society, Pittsburgh, Pennsylvania, 1991, 95.
5. Mason, K. N., Growth and characterization of transition metal silicides, *Prog. Crystal Growth Charact.*, 2, 269, 1979.
6. Nicolet, Marc-A., and Lau, S. S., Formation and characterization of transition-metal silicides, in *VLSI Electronics: Microstructure Science*, Vol. 6, 1983, chap. 6.

7. Schlesinger, M. E., Thermodynamics of solid transition-metal silicides, *Chem. Rev.*, 90, 607, 1990.
8. Murarka, S. P., Transition metal silicides, *Annu. Rev. Mater, Sci.*, 12, 117, 1983.
9. Sakata, T. and Nishida, I., Thermoelectric properties of semiconducting 3 d-transition metal disilicides (in Japanese), *Nippon Kinsoku Gakkaishi*, 15, 11, 1976.
10. Tegze, M. and Hafner, J., Electronic structure of semiconducting alkali-metal silicides and germanides, *Phys. Rev. B*, 40(14), 9841, 1989.
11. Samsonov, G. V. and Vinitskii, I. M., *Handbook of Refractory Compounds*, Plenum Press, New York, 1980.
12. Nicolaou, M. C., Material for direct thermoelectric energy conversion with a high figure of merit, in *Proc. 1st Int. Cong. on Thermoelectric Energy Conversion*, Rao, K., Ed., University of Texas at Arlington, Arlington, Texas, 1976, 59.
13. Marchuck, N. D., Zaitsev, V. K., Fedorov, M. I., and Kaliazin, A. E., Thermoelectric properties of some cheap n-type materials, *Proc. 8th Int. Conf. of Thermoelectric Energy Conversion*, Scherrer, H. and Scherrer, S., Eds., Institute National Polytechnique de Lorraine, Nancy, France, 1989, 210.
14. Noda, Y., Kon, H., Furukawa, Y., Otsuka, N., Nishida, I. A., and Masumoto, K., Preparation and thermoelectric properties of $Mg_2Si_{1-x}Ge_x$ ($x = 0.0 \sim 0.4$) solid solution semiconductors, *Mater. Trans. JIM*, 33(9), 845, 1992.
15. Noda, Y., Kon, H., Furukawa, Y., Otsuka, N., Nishida, I. A., and Masumoto, K., Temperature dependence of thermoelectric properties of $Mg_2Si_{0.6}Ge_{0.4}$, *Mater. Trans. JIM*, 33(9), 851, 1992.
16. Spitzer, D. P., Lattice thermal conductivity of semiconductors: a chemical bond approach, *J. Phys. Chem. Solids*, 31, 19, 1970.
17. Brixner, L. H., X-ray study and thermoelectric properties of the $NbSi_xGe_{2-x}$ and $TaSi_xGe_{2-x}$ systems, *J. Inorg. Nucl. Chem.*, 25, 257, 1963.
18. Brixner, L. H., Thermoelectric compositions of $Nb_xTa_{1-x}Si_yGe_{2-y}$, U.S. Patent No. 3298777, du Pont de Nemours and Company, 1967.
19. Jeitschko, W. and Parthé, E., The crystal structure of $Rh_{17}Ge_{22}$, an example of a new kind of electron compound, *Acta Crystallogr.*, 22, 417, 1967.
20. Nowotny, H., Crystal chemistry of transition element defect silicides and related compounds, in *The Chemistry of Extended Defects in Non-Metallic Solids*, Eyring, L. R. and O'Keefe, M., Eds., North-Holland, Amsterdam, 1970, 223.
21. Pécheur, P. and Toussaint, G., Electronic structure and bonding of the Nowotny chimney-ladder compound Ru_2Si_3, *Phys. Lett. A*, 160, 193, 1991.
22. Oshugi, I. J., Kojima, T., and Nishida, I. A., Temperature dependence of the magnetic susceptibility of a $CrSi_2$ single crystal, *Phys. Rev. B*, 42(16), part B, 10761, 1990.
23. Nikitin, E. N., Thermoelectric properties of the silicon-chromium system, *Sov. Phys. Solid State*, 2(11), 2389, 1961.
24. Neshpor, V. S. and Samsonov, G. V., Electron structure, chemical bonding and physical properties of rhenium disilicide and some of its alloys, *Izv. Akad. Nauk SSSR, Neorg. Mater.*, 1(5), 655, 1965.
25. Shinoda, D., Asanabe, S., and Sasaki, Y., Semiconducting properties of chromium disilicide, *J. Phys. Soc. Jpn.*, 19, 269, 1964.
26. Nishida, I., The crystal growth and thermoelectric properties of chromium disilicide, *J. Mater. Sci.*, 7, 1119, 1972.
27. Neshpor, V. S. and Samsonov, G. V., Hall effect studies on transition metal silicides (in Russian), *Dokl. Akad. Nauk SSSR*, 134(6), 1337, 1960.
28. Mayer, S. E. and Mlavsky, A. I., Thermal and electrical properties of some silicides, in *Properties of Elemental and Compound Semiconductors*, Gatos, H. C., Ed., Interscience Publishers, New York, 1960, 261.
29. Nikitin, E. N., Study of temperature dependence of electrical conductivity and thermal EMF of silicides, *Sov. Phys. Tech. Phys.*, 3, 20, 1958.
30. Nikitin, E. N., Electrical conductivity and thermal EMF of silicides of transition metals, *Sov. Phys. Tech. Phys.*, 3, 23, 1958.
31. Neshpor, V. S. and Samsonov, G. V., Study of the electrical conductivity of silicides of the transition metals, *Sov. Phys. Solid State*, 2, 1966, 1960.
32. Bienert, W. B. and Skrabek, E. A., A new manganese-silicon p-type thermoelectric material, *Proc. IEEE/AIAA Thermoelectrics Specialists Conf.*, 1966, 10-1.

33. Bienert, W. B. and Gillen, F. M., Process of making Mn_4Si_7 thermoelectric element and product of said process, U.S. Patent No. 3407037, Martin Marietta Co., 1968.
34. Ivanova, L. D., Abrikosov, N. Kh., Elagina, É. I., and Khvostikova, V. D., Production and investigation of the properties of single crystals of the higher manganese silicide, *Inorg. Mater.*, 5(11), 1645, 1969.
35. Levinson, L. M., Investigation of the defect manganese silicide Mn_nSi_{2n-m}, *J. Solid State Chem.*, 6, 126, 1973.
36. Korshunov, V. A. and Gel'd, P. V., Thermoelectric properties of the higher manganese silicide, in *Thermoelectric Properties of Semiconductors*, Kutasov, V. A., Ed., Consultants Bureau, New York, 1964, 54.
37. Vedernikov, M. V., Engalychev, A. E., Zaitsev, V. K., Ordin, S. V., and Fedorov, M. I., Thermoelectric properties of materials based on the higher manganese silicide and cobalt monosilicide, in *Proc. 7th Int. Conf. on Thermoelectric Energy Conversion*, Rao, K. R., Ed., University of Texas at Arlington, Arlington, Texas, 1988, 151.
38. Zwilling, G. and Nowotny H., The anisotropy of the electrical conductivity in the manganese defect silicide $Mn_{27}Si_{47}$ (in German), *Monatsh. Chem.*, 105, 666, 1974.
39. Fedorov, M. I., Kalyazin, A. E., Zaitsev, V. K., and Engalychev, A. R., Transport phenomena in $MnAl_{0.75}Si_{1.25}$, *Sov. Phys. Solid State*, 31(6), 1079, 1989.
40. Long, R. G. and Mahan, J. E., Two pseudobinary semiconducting silicides: $Re_{1-x}Mo_xSi_2$ and $Cr_{1-x}V_xSi_2$, *Appl. Phys. Lett.*, 56, 1655, 1990.
41. Birkholz, U., Groβ, E., Stöhrer, U., Voss, K., Gruden, D. O., and Wurster, W., Conversion of waste exhaust heat in automobiles using $FeSi_2$-thermoelements, *Proc. 7th Int. Conf. on Thermoelectric Energy Conversion*, Rao, K. R., Ed., University of Texas at Arlington, Arlington, Texas, 1988, 124.
42. Uemura, K., Mori, Y., Imai, T., Nishida, I., Horie, S., and Kawaguchi, M., Candle-type portable power source employing iron disilicide thermoelements, *Proc. 8th Int. Conf. on Thermoelectric Energy Conversion*, Scherrer, H. and Scherrer, S., Eds., Institute National Polytechnique de Lorraine, Nancy, France, 1989, 151.
43. Birkholz, U., Irondisilicide as thermoelectric generator material, *Proc. 8th Int. Conf. on Thermoelectric Energy Conversion*, Scherrer, H. and Scherrer, S., Eds., Institute National Polytechnique de Lorraine, Nancy, France, 1989, 98.
44. Hesse, J., The influence of density on the thermoelectric properties of sintered β-$FeSi_2$ (in German), *Z. Metallkde.*, 60, 652, 1969.
45. Birkholz, U. and Naegele, J., Optical investigation of the small polaron in β-$FeSi_2$, *Phys. Status Solidi*, 89, 197, 1970.
46. Matsubara, K., Miki, T, Nagao, K., Kishimoto, K., Nakanshi, O., Ueeda, O., and Fujii, K., Characterization and thermoelectric properties of new β-$FeSi_2$ ceramics developed by an RF-plasma processing in O_2 and SiH_4 gases, *Proc. 11th Int. Conf. on Thermoelectric Energy Conversion*, Rao, K. R., Ed., University of Texas at Arlington, Arlington, Texas, 1992, 24.
47. Poutcharovsky, D. J. and Parthé, E., The orthorhombic crystal structure of Ru_2Si_3, Ru_2Ge_3, Os_2Si_3, and Os_2Ge_3, *Acta Crystallogr. B*, 30, 2692, 1974.
48. Poutcharovsky, D. J., Yvon, K., and Parthé, E., Diffusionless phase transformations of Ru_2Si_3, Ru_2Ge_3, and Ru_2Sn_3. I. Crystal structure investigations, *J. Less-Common Metals*, 40, 139, 1975.
49. Vining, C. B. and Allevato, C. E., Intrinsic thermoelectric properties of single crystal Ru_2Si_3, *Proc. 10th Int. Conf. on Thermoelectrics*, Rowe, D. M., Ed., Babrow Press, 1991, 167.
50. Susz, C. P., Muller, J., Yvon, K., and Parthé, E., Diffusionless phase transformations of Ru_2Si_3, Ru_2Ge_3, and Ru_2Sn_3. II. Electrical and magnetic properties, *J. Less-Common Metals*, 71, P1, 1980.
51. Schellenberg, L., Braun, H. F., and Muller, J. The osmium-silicon phase diagram. *J. Less-Common Metals*, 144, 341, 1988.
52. Vining, C. B., Extrapolated thermoelectric figure-of-merit of ruthenium silicide, in *Ninth Symposium on Space Nuclear Power Systems, AIP Conf. Proc. 246*, El-Genk, M. S. and Hoover, M. D., Eds., American Institute of Physics, New York, 1992, 338.
53. Vining, C. B. and Allevato, C. E., Progress in doping of ruthenium silicide (Ru_2Si_3), in *27th Intersociety Energy Conversion Engineering Conference Proceedings*, Vol. 3, Society of Automotive Engineers, Warrendale, Pennsylvania, 1992, 3.489.

54. Ohta, T., P-type thermoelectric characteristics of polycrystal ruthenium sesquisilicide, *Proc. 11th Int. Conf. on Thermoelectric Energy Conversion*, Rao, K. R., Ed., University of Texas at Arlington, Arlington, Texas, 1992, 74.
55. Mason, K. and Müller-Vogt, G., Osmium disilicide: preparation, crystal growth, and physical properties of a new semiconducting compound, *J. Crystal Growth*, 63, 34, 1983.
56. Schellenberg, L., Jorda, J. L., and Muller, J., The rhodium-silicon phase diagram, *J. Less-Common Metals*, 109, 261, 1985.
57. Allevato, C. E. and Vining, C. B., Phase diagram and electrical behavior of silicon-rich iridium silicide compounds, *J. Alloys Compounds*, 200, 99, 1993.

24

Polycrystalline Iron Disilicide as a Thermoelectric Generator Material

Ulrich Birkholz, Erwin Groβ, and Ulrich Stöhrer
Institut für angewandte Physik, Universität Karlsruhe, Germany

24.1 Introduction

The compound iron disilicide ($FeSi_2$) exists in a metallic high-temperature phase (α-$FeSi_2$) and a semiconducting low-temperature phase (β-$FeSi_2$). According to the phase diagram established by Piton and Fay,[1] the transition temperature is 955°C (Figure 1) and β-$FeSi_2$ is a peritectic phase. Consequently, the semiconducting phase cannot be grown from the melt. So far three types of β-$FeSi_2$ samples have been prepared:

- Tiny single crystals by growth from the vapor phase for X-ray investigations[2]
- Thin polycrystalline layers by electron beam evaporation[3] or plasma ion processing[4]
- Polycrystalline bulk material by powder metallurgical methods[5–8]

In this chapter only the properties of polycrystalline bulk material will be discussed. This material was first proposed by Ware and McNeill[9] for thermoelectric generation. Since the publication of their paper in 1964 the metallurgical and thermoelectric properties have been studied in detail. Methods of making contacts to the hot and cold junctions of a $FeSi_2$ thermocouple were also described.

The following properties characterize β-$FeSi_2$ as a good thermoelectric generator material for terrestrial applications:

- Sufficiently high figure-of-merit
- Stability with respect to oxidation, sublimation, evaporation, and diffusion
- Nontoxic components
- Low price components
- Simple technology

0-8493-0146-7/95/$0.00+$.50

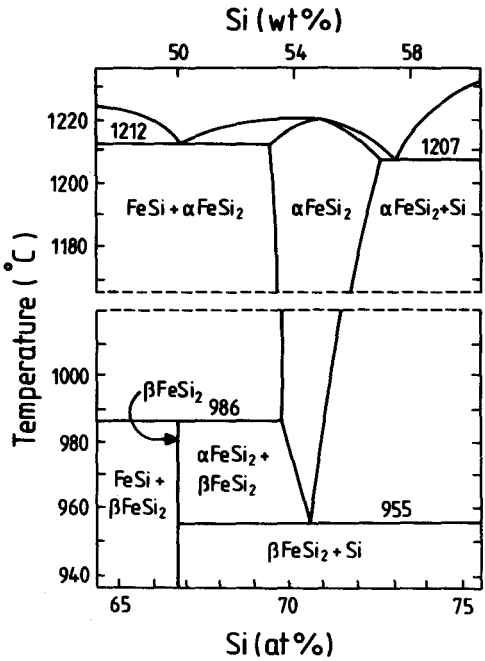

FIGURE 1 Phase diagram for the system Fe-Si. (From Piton, J. P. and Fay, M. F., *C.R. Acad. Sci. (Paris)*, 266, 514, 1968. With permission.)

As a result it may be stated that β-$FeSi_2$ is a good candidate for many civil applications, e.g., electrical power supply of heating systems, hot air fans, and use of waste heat in automobiles. In the last section of this chapter it will be shown that β-$FeSi_2$ can be combined with other silicides in order to improve the efficiency of the thermocouple.

24.2 Powder Metallurgical Preparation of Iron Disilicide

The best way to prepare bulk samples of β-$FeSi_2$ is the powder metallurgical method. For this process the following steps are necessary:

- Smelting of the ingot
- Powder preparation
- Densification by cold pressing with subsequent sintering or hot pressing
- Annealing

These preparation techniques are described in detail in several papers.[10–12]

Smelting of the Ingot

The compounds are usually of high purity, e.g., Fe 99.99% and Si 99.999%. But, due to the high doping level employed lower grade starting material will also give good results. The elements Co, Al, and Mn act as dopants. In order to improve the thermal shock stability a small amount of boron (0.01 at.%) may also be added. The dopants substitute the components in the following way: $Fe_{1-x}Co_xSi_2$ for n-type and $Fe_{1-x}Mn_xSi_2$ or $FeSi_{2-x}Al_x$ for p-type. In the case of Al-doping a certain loss of Al during the preparation process has to be taken into account. The raw materials are smelted under argon or Ar/H_2 atmosphere in a quartz crucible using resistance or induction heating.

Powder Preparation

There are two ways to obtain a powder from the ingot:

- The liquid material can be sprayed into a protective atmosphere
- The ingot can be crushed and the lumps ground in a ball mill.

Powder production by spraying — The cheapest method suitable for industrial application is to spray the liquid material through a valve into an inert or a reducing atmosphere. The powder then consists of frozen drops and the grains are spherical. A typical sieved fraction of $FeSi_2$ powder (<53 μm) has a mean grain diameter of about 16 μm.[13] The spherical shape permits only point contacts between the grains, and stable greens cannot be obtained without the use of a binder and lubricant.

Powder production by grinding — The powder can also be produced by crushing and grinding the ingot. Milling in a planetary steel ball after 4 h results in powder with a mean grain size of 4 μm. The milling process consists of crushing, but also of agglomeration of the powder particles. The equilibrium grain size depends strongly on the temperature. To obtain small grain sizes it is useful to employ a periodic process: 15 min. milling, 30 min. cooling, and so on. To facilitate heat transport and to reduce agglomeration, a milling fluid, e.g., *n*-hexane, should be used. For industrial application, where easy handling of the powder is necessary, binder and lubricant have to be used also in the case of ground powder. Polyvinyl alcohol and colloidal paraffine (1 wt%) allow the powder to be granulated and filled into dies automatically.

Densification of the Powder

The densification of $FeSi_2$ powder can be performed either by cold pressing with subsequent sintering treatment or by hot pressing.

Cold pressing and sintering — The greens can be obtained by uniaxial pressing in a hardened steel die or by hydrostatic pressing, e.g., in a silicon rubber box. A pressure of 400 MPa is applied, and the resulting density of the greens is ≥3 g/cm³. For the subsequent sintering process the sintering theories established or reviewed by Coble,[14] Shaw,[15] and Exner[16] have to be considered. Densification and grain growth during the sintering process can be understood from a thermodynamic viewpoint. The free enthalpy of the sample is lowered by the diffusion of the vacancies to the boundaries. The gas/solid interface is substituted by a solid/solid interface, which results in densification. Grain growth occurs when the isolated or connected grains grow together in order to lower the surface energy. If grain growth is not observed, the densification may be described by Coble's shrinking law for isothermal sintering:

$$P(t) = P_0 - C\,ln(t/t_o) \tag{1}$$

P(t) is the porosity at time, t, P_0 the porosity at the starting time t_0.

Experimental procedure — Binder and lubricant are removed by annealing in air from 300 to 700 K at a heating rate of 80 K/h.[11] The greens are sintered at 1175°C for 6 to 8 h in a stream of Ar/H_2 or in high vacuum. When these parameters are employed, the sintering temperature is close to the melting point of 1212°C and a density of 95% can be obtained. The density vs. sintering time follows Coble's law.[12]

Hot pressing — Hot pressing, i.e., simultaneous application of heat and pressure, also leads to densification. In the beginning of the process there are only small contact areas between the particles, resulting in localized pressure peaks. Material is transported away from the high-pressure zones by plastic flow. According to Thümmler and Thomma[17] this plastic deformation predominates the densification over wide ranges. Murray et al.[18] described this fast process by the formula:

$$dP(t)/dt = -3/4\ \sigma/\eta \cdot P(t) \tag{2}$$

with P the porosity, σ the applied pressure, and η the viscosity at the hot pressing temperature. When the contact areas have grown, the critical stress cannot be reached; further densification only takes place by diffusion, which is a slow process compared to plastic flow.

Experimental procedure — $FeSi_2$ can be uniaxially hot pressed in a graphite die at a maximum pressure of 50 MPa. The hot pressing temperature is in the range between 800 and 1200°C. Figure 2 shows the densification of sprayed powder during hot pressing at 880°C. In the semilogarithmic presentation two straight lines are observed corresponding to a fast densification process (plastic flow) and a nearly constant density after some minutes, when only diffusion takes place. At 37.5 MPa a density of 95% and at 50 MPa a density of 97% can be obtained.

Annealing

To obtain β-$FeSi_2$ a phase transition has to be induced after sintering by annealing.[19,20] The optimum annealing temperature is about 800°C. At lower temperatures, the diffusion rate decreases rapidly; for higher temperatures the chemical potential difference between α- and β-phase is low. For cobalt-doped specimens an annealing time of 20 h is sufficient. For aluminum-doped samples at least 100 h are needed, because aluminum precipitations contained in the α-phase have to be dissolved during the annealing process.[12] The phase transition can be observed by *in situ* measurements of the electrical resistivity (Figure 3).

24.3 Thermoelectric Properties of β-$FeSi_2$

The high-temperature α-phase of $FeSi_2$ is metallic. The low-temperature β-phase, however, is a semiconductor with a band gap $E_g = 0.9$ eV at 0 K.[6,7,21,22] The transport properties are related to the narrow *3d*-bands. For p-type $FeSi_2$ the thermoelectric power, electrical conductivity, Hall mobility, and near infrared absorption can be explained in terms of an energy band model, the hole mobility decreasing with increasing temperature. In the case of n-$FeSi_2$, however, the results of Hall and optical measurements do not fit the band model. Here, the electronic properties may be ascribed to small polaron conduction.[5,21]

The carrier density can be controlled by cobalt doping (n-type) or aluminum doping (p-type) over a wide range. The dopants substitute the components according to the formulas $Fe_{1-x}Co_xSi_2$ or $FeSi_{2-x}Al_x$. As a result of the mass difference the thermal conductivities are reduced by doping. Manganese doping also produces p-type material according to $Fe_{1-x}Mn_xSi_2$. The activation energy of the manganese acceptor, however, is high and the carrier density in the temperature range of interest is low.

The different conduction mechanism for p-type and n-type material can be identified clearly in Figures 4 and 5. For p-type material the reflectivity can be explained by Drude's formula; in the case of n-type material small polaron resonance is observed.

Typical temperature dependences of the thermoelectric power for p-type and n-type $FeSi_2$ is shown in Figure 6. In both cases four ranges can be distinguished:

- Range of impurity band conduction
- Range of carrier activation (extrinsic)
- Range of constant carrier density (extrinsic)
- Range of intrinsic conduction

It should be emphasized that there is no need to introduce optical phonon drag in order to explain the peak of the thermoelectric power. At all doping levels the curves can be fitted by assuming a

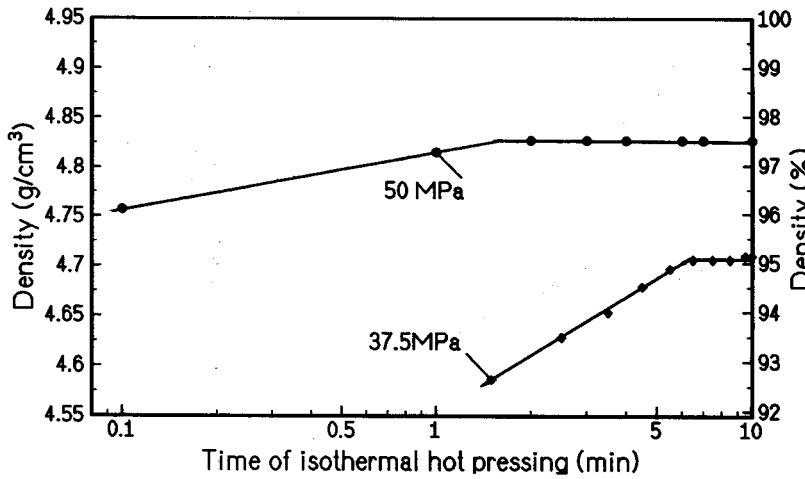

FIGURE 2 Densification of sprayed powder by hot pressing for 37.5 MPa and 50 MPa at 880°C.

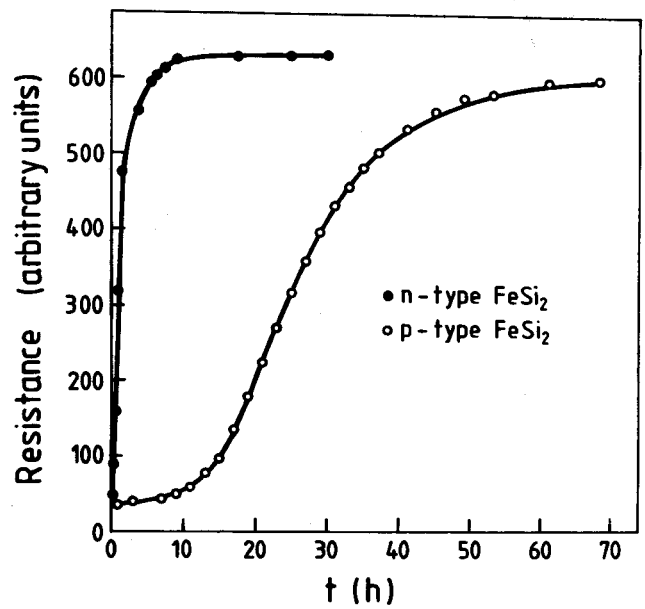

FIGURE 3 Observation of the phase transition α-$FeSi_2$ → β-$FeSi_2$ during annealing by resistance measurement (annealing temperature 800°C). (From Birkholz, U., in *Proc. 8th Int. Conf. on Thermoelectric Energy Conversion*, Scherrer, H. and Scherrer, S., Eds., Institute National Polytechnique de Lorraine, Nancy, France, 1989, 151. With permission.)

combination of impurity-band conduction and extrinsic conduction. The extension of the different ranges can be controlled by doping. For thermoelectric application the range of constant thermoelectric power should be extended as far as possible. The optimum doping level is rather high (about 10^{20} cm^{-3}) as a result of high density-of-states (about 10^{22} cm^{-3}). In spite of the high carrier density the electrical conductivity is rather low (about 10^2 Ω^{-1} cm^{-1}) because of a low mobility (about 10 cm^2/Vs). The precise value for the carrier mobility depends on the density of the samples prepared by powder metallurgy. Therefore, it is sometimes difficult to compare

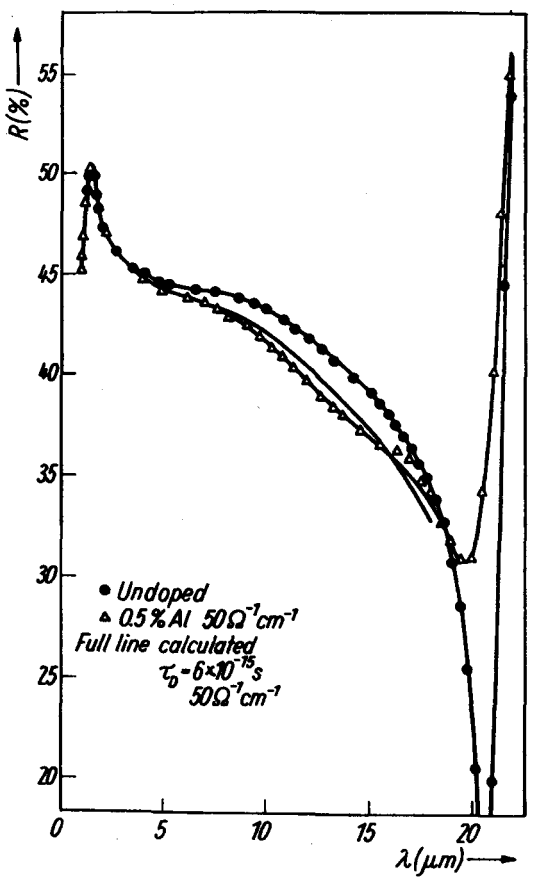

FIGURE 4 Reflectivity of p-type β-$FeSi_2$. (From Birkholz, U. and Naegele, J., *Phys. Status Solidi*, 39, 197, 1970. With permission.)

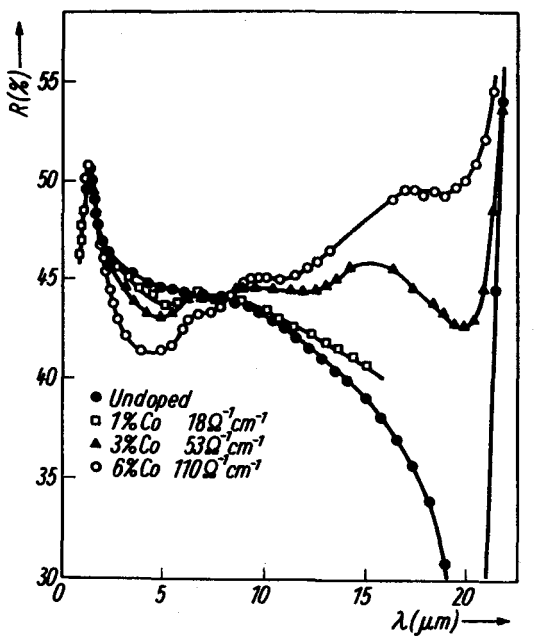

FIGURE 5 Reflectivity of n-type β-$FeSi_2$. (From Birkholz, U. and Naegele, J., *Phys. Status Solidi*, 39, 197, 1970. With permission.)

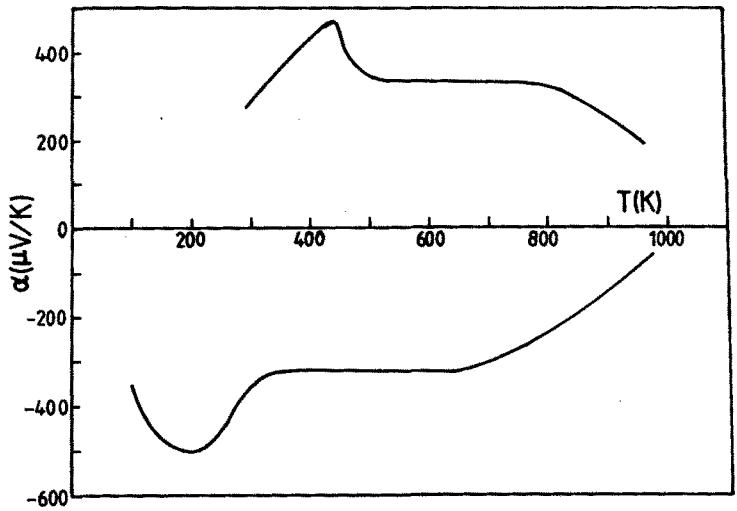

FIGURE 6 Thermoelectric power of $FeSi_2$: p-type, Al-doped, $N_a = 0.8 \cdot 10^{20}$ cm^{-3} and n-type, Co-doped, $N_d = 2.6 \cdot 10^{20}$ cm^{-3}. (From Birkholz, U., in *Proc. 8th Int. Conf. Thermoelectric Energy Conversion*, Scherrer, H. and Scherrer, S., Eds., Institute National Polytechnique de Lorraine, Nancy, France, 1989, 151. With permission.)

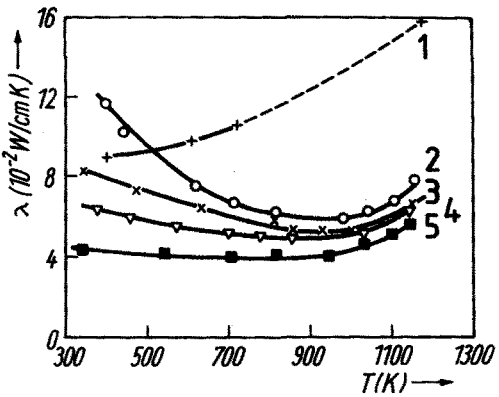

FIGURE 7 Thermal conductivity of α- and β-$FeSi_2$. (1) α-$FeSi_2$; (2) β-$FeSi_2$; (3) $FeSi_{1.96}Al_{0.04}$; (4) $Fe_{0.97}Co_{0.03}Si_2$; (5) $Fe_{0.94}Co_{0.06}Si_2$. (From Waldecker, G., Meinhold, H., and Birkholz, U., *Phys. Status Solidi (a)*, 15, 143, 1973. With permission.)

published data. This is also true for the thermal conductivity. Results obtained by Waldecker et al.[23] using Angström's method for undoped, p-type and n-type β-$FeSi_2$ and also for metastable α-$FeSi_2$ are shown in Figure 7. The thermal conductivity is strongly reduced by doping; cobalt is more effective than aluminum. The figure-of-merit $z = \alpha^2\sigma/\lambda$ can be measured directly by Harman's method. Results obtained by Stöhrer[24] are presented in Figure 8. With these data a generator efficiency of approximately 3% is predicted at $\Delta T = 600$ K.

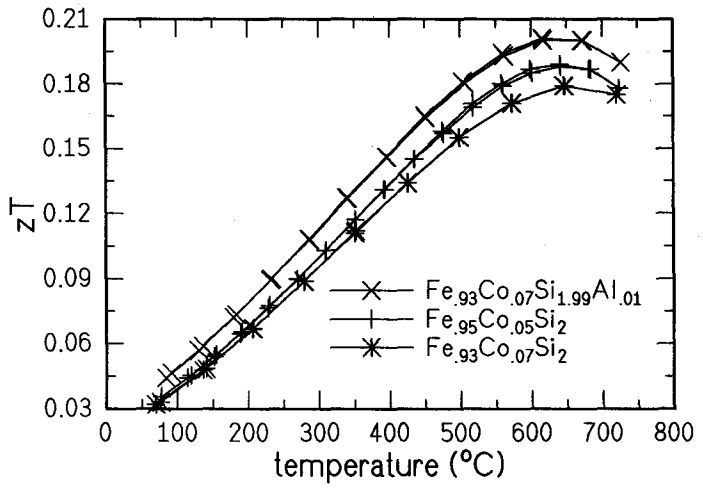

FIGURE 8 Dimensionless thermoelectric figure-of-merit ZT for $FeSi_2$. (From Stöhrer, U., in *Proc. 11th Int. Conf. on Thermoelectrics*, Rao, K.R., Ed., University of Texas, Arlington, 1992. With permission.)

24.4 $FeSi_2$ Thermogenerators

The design of a thermoelectric generator requires good electrical and thermal contacts for the hot and cold junctions. The calculation of cross section and length has not only to take into account the thermoelectric properties, but also the electrical and thermal contact resistivity and finally the heat resistance between the thermogenerator and the heat reservoirs.

Electrical Contacts at the Cold Junction

Assuming that a good electrical contact also implies a good thermal contact, only the preparation of contacts with low contact electrical resistivity has to be discussed. For the cold side of the couple, solders are of interest whose melting points lie between 200 and 400°C and several lead- and zinc-based solders have been used.[25–30] To prepare contacts using $PbAg_3$ solder,[26–30] the surface was polished and a silver foil 0.1 mm thick used as an electrode. It was necessary to apply a flux and solder above the eutectic temperature of 303°C. The solder was sufficiently ductile to eliminate problems related to different coefficients of expansion. The contact resistivity was $r_c = 1.3 * 10^{-4}$ Ωcm^2, thus, the condition $r_c/\rho\ell \ll 1$ was met (ρ resistivity of the leg, ℓ length of the leg). These contacts were stable up to 250°C.

Nakajima et al.[27] have developed a doubledecker structural contact electrode. This means ultrasonic soldering using a zinc-based solder with multi-components. The advantage of this solder is the high melting point (653 K). Copper leads wires or sheets were welded onto this solder. Groβ et al.[28,29] established a cold junction contact suitable for $FeSi_2$ and higher manganese silicide (HMS) by ultrasonic soldering[31] using a zinc-based solder ($Zn_{90}Al_5Cu_5$) and a nickel-plated iron sheet as an electrode. The electrical contact resistivity was $r_c = 8 * 10^{-5}$ Ωcm^2, thus considerably lower than in the case of the $PbAg_3$ solder described above.

Electrical Contacts at the Hot Junction

There are two types of hot junction contacts: soldered contacts and direct sintered contacts (Figure 9).

Soldered hot junction contacts — The soldered contacts were prepared using a solder and a conducting bridge, which connects the p- and the n-leg of the generator. The bridge consisted of

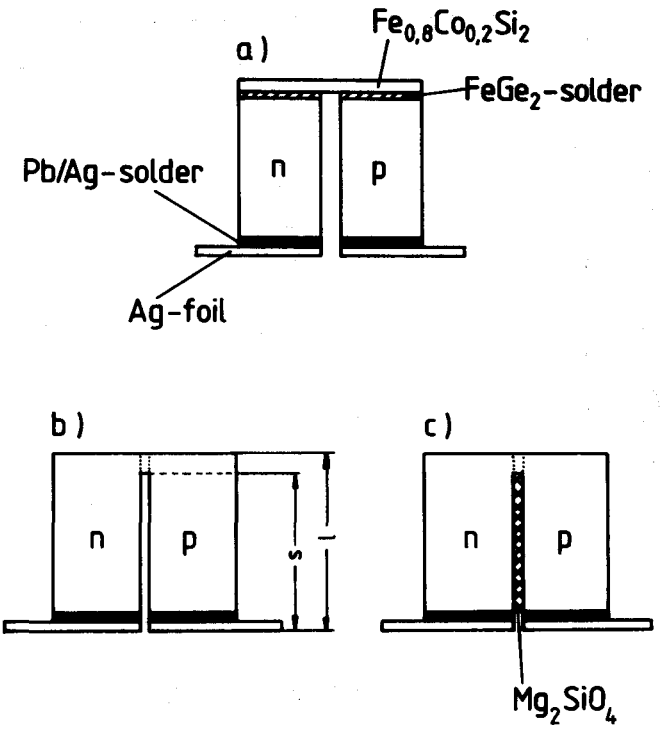

FIGURE 9 $FeSi_2$ thermoelements for power generation: (a) with soldered hot junction; (b) with sintered hot junction; (c) with sintered hot junction and electrically insulating separation layer. (From Birkholz, U., in *Proc. 8th Int. Conf. on Thermoelectric Energy Conversion,* Scherrer, H. and Scherrer, S., Eds., Institute National Polytechnique de Lorraine, Nancy, France, 1989, 151. With permission.)

Table 1. Solders for $Fe_{0.8}Co_{0.2}Si_2$

Solder Composition	Melting Temperature (°C)
AgCu 27 In 13 (60 wt% Ag, 27 wt% Cu, 13 wt% In)	720
MnGe 40.6 (59.4 wt% Mn, 40.6 wt% ge)	700
MgGe 17.7 (82.3 wt% Mg, 17.7 wt% ge)	680

heavily doped $FeSi_2$ (for example $Fe_{0.8}Co_{0.2}Si_2$,[6] $TiSi_2$,[29] or iron).[26] The bridge must exhibit a matching coefficient of expansion and possess high electrical and thermal conductivities. Solders applied to $Fe_{0.8}Co_{0.2}Si_2$ have been tested by Hesse[6] and compiled in Table 1.

A hot junction made with AgCu 27 In 13 was tested for 2000 h at a hot junction temperature of 650°C. The diffusion depth of the solder components was between 50 and 100 μm. Therefore, a degradation of electrical and mechanical properties of the contact is not to be expected.

Using $FeGe_2$ (melting point 850°C) contacts with low contact resistivity can be prepared. Unfortunately, however, operation at 800°C causes severe aging by oxidation after a few days. Recently a promising hot junction contact was reported consisting of a titanium disilicide ($TiSi_2$) bridge and titanium-activated silver solder.[29] The contact resistance with a $FeSi_2$ leg was $r_c = 6 \cdot 10^{-4}$ Ωcm^2. The $TiSi_2$ bridge and titanium-activated solder are also useful for HMS contacts. It should be mentioned that $AgSi_3$ was reported as a good solder for use in high-temperature Harman measurements.[24]

Direct sintered hot junction contacts — Direct sintered contacts are prepared by pressing p-type and n-type material in the same die and avoiding mixing of the powders. After burning the binder and lubricant the sample is sintered and annealed. Separation between the p- and n-leg can

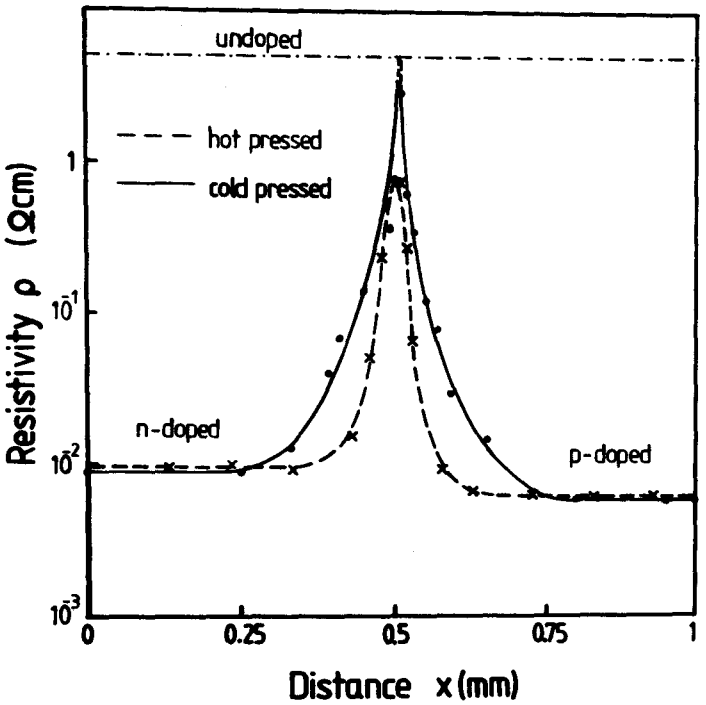

FIGURE 10 Resistivity profiles across cold and hot pressed contacts. (From Groβ, E. and Stöhrer, U., in *Proc. 2nd Eur. Conf. on Thermoelectrics*, Scherrer, H. and Scherrer, S., Eds., Institute National Polytechnique de Lorraine, Nancy, France, 1989, 151. With permission.)

be achieved in three different ways: one method is the use of a U-shaped die;[10,11,27] another is to separate the legs by an appropriate incision;[8,12,26,30] the third is to insert an insulating powder between the n- and p-material before sintering and annealing.[32] Kojima,[10] Nakajima et al.,[27] and Uemura et al.[11] described direct sintered contacts for cobalt- and manganese-doped material. Uemura exposed the hot junction to a propane gas flame and tested the thermocouple with temperature cycles.

Several authors[8,12,26,30,32] have investigated direct sintered contacts for Co- and Al-doped material. Groβ and Stöhrer[8] compared direct sintered thermocouples prepared by cold and hot pressing. They observed a diffusion layer in the contact zone due to the diffusion of aluminum from the p-leg into the Co-doped n-leg. The corresponding resistivity profiles in the contact zone are presented in Figure 10. The thermocouples with cold-pressed junctions were tested for 2 months in air at 800°C. Several cycles between 100 and 800°C were performed. No significant change was observed after this treatment.

Properties of the Generators

The efficiency of $FeSi_2$ thermoelectric generators according to published data[6,12,28,30] does not exceed 3% at a temperature difference of 600°C irrespective of the method of fabrication. The experimental data show that the internal resistance of direct sintered couples decreases strongly with increasing temperature difference, whereas in the case of soldered couples the internal resistance is nearly constant. Open circuit voltage, internal resistance, and power output for a $FeSi_2$ couple are shown in Figure 11.

Preliminary results show that an efficiency above 3.5% may be obtained using a thermocouple with a n-$FeSi_2$[24] leg and p-HMS[33] leg.

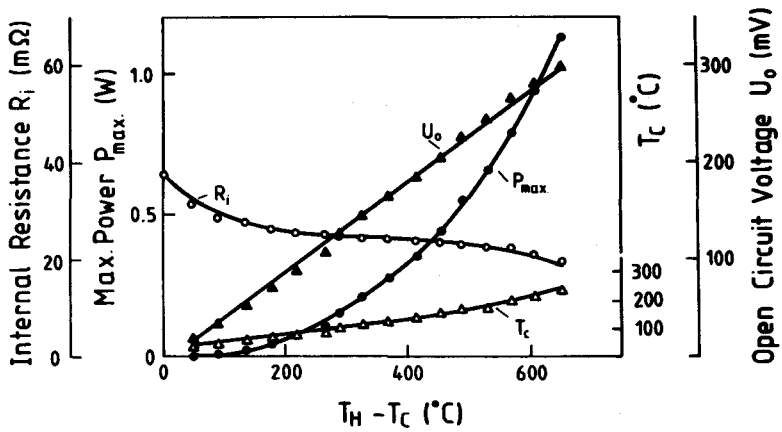

FIGURE 11 Open circuit voltage, internal resistance, and power output of a $FeSi_2$ thermocouple. (From Stöhrer, U., Voggesberger, R., Wagner, G., and Birkholz, U., *Energy Convers. Manage.*, 30 (2), 143, 1990. With permission.)

References

1. Piton, J. P. and Fay, M. F., Sur les changements de phases des alliages de compositions voisines de $FeSi_2$, *C.R. Acad. Sci. (Paris)*, 266, 515, 1968.
2. Wandji, R., Dusansoy, J., and Roques, B., Preparation et étude du silicure $FeSi_2\beta$ à l'état monocristallin, *C.R. Acad. Sci. (Paris)*, 267, 1587, 1968.
3. Geserich, H. P., Sharma, S. K., and Theiner, W. A., *Philos. Mag.*, 27, 1001, 1973.
4. Matsubara, K., Minemura, N., Miyata, J., Kishimoto, K., Kawamura, K., Koyanagi, T., and Miki, T., Thermoelectric properties of $FeSi_2$ ceramics developed by plasma ion processing, in *Proc. 10th Int. Conf. on Thermoelectrics*, Rowe, D.M., Ed., Babrow Press, Cardiff, 1991, 40.
5. Birkholz, U. and Schelm, J., Mechanism of electrical conduction in β-$FeSi_2$, *Phys. Status Solidi*, 27, 413, 1968.
6. Hesse, J., Leistungsthermoelemente aus Esiendisilizid für die Stromerzeugung, *Z. Angew. Phys.*, 28, 133, 1969.
7. Nishida, I., Study of semiconductor-to-metal transition in Mn-doped $FeSi_2$, *Phys. Rev. B*, 7, 2710, 1972.
8. Groβ, E. and Stöhrer, U., Comparison of cold and hot pressed $FeSi_2$ thermoelements, *Proc. 2nd Eur. Conf. on Thermoelectrics*, Scherrer, H. and Scherrer, S., Eds., Institute National Polytechnique de Lorraine, Nancy, France, 1989, 151.
9. Ware, R. M. and McNeill, D. J., Iron disilicide as a thermoelectric generator material, *Proc. IEE*, 111, 178, 1964.
10. Kojima, T., Semiconducting and thermoelectric properties of sintered irondisilicide, *Phys. Status Solidi (a)*, 111, 233, 1989.
11. Uemura, K., Mori, Y., Imai, T., Nishida, I., Horie, S., and Kawaguchi, M., Candle type portable power source employing iron disilicide thermoelements, *Proc. 8th Int. Conf. on Thermoelectric Energy Conversion*, Scherrer, H. and Scherrer, S., Eds., Institute National Polytechnique de Lorraine, Nancy, France, 1989, 151.
12. Stöhrer, U., Voggesberger, R., Wagner, G., and Birkholz, U., Sintered $FeSi_2$ for thermoelectric power generation, *Energy Convers. Manage.*, 30 (2), 143, 1990.
13. Stöhrer, U., Taibon, U., Groβ, E., and Birkholz, U., Figure-of-merit of cold and hot pressed $FeSi_2$ measured with the Kohlrausch method, *Proc. 9th ICT*, Vining, C.B., Ed., Jet Propulsion Laboratory, Pasadena, 1990, 242.
14. Coble, R. L., Sintering crystalline solids, *J. Appl. Phys.*, 32, 787, 1961.
15. Shaw, N. J., Densification and coanstuing during solid state sintering of ceramics, a review of the models, *Powder Metall. Int.*, 21, 3, 1989.
16. Exner, H. E., *Grundlagen von Sintervorgängen*, Petzow, G., Ed., Gebrüder Bomträger, Berlin, 1978.
17. Thümmler, F. and Thomma, W., private communication.

18. Murray, P., Rodgers, E. P., and Williams, E., Practical and theoretical aspects of the hot pressing of refractory oxides, *Trans. Br. Ceram. Soc.*, 53, 474, 1954.
19. Kojima, T., Masumoto, K., Okamoto, M. A., and Nishida, I., Formation of β-$FeSi_2$ from the sintered eutetic alloy FeSi-Fe_2Si_5 doped with cobalt, *J. Less-Common Metals*, 159, 299, 1990.
20. Sakata, T., Sakai, Y., Yoshino, H., Fujii, H., and Nishida, I., Studies on the formation of $FeSi_2$ from the FeSi-Fe_2Si_5 eutectic, *J. Less-Common Metals*, 61, 301, 1978.
21. Birkholz, U. and Naegele, J., Optical investigation of the small polaron in β-$FeSi_2$, *Phys. Status Solidi*, 39, 197, 1970.
22. Dubovtsev, I. A. and Sidorenko, F. A., Observation of small polarons in β-$FeSi_2$ with the aid of the Mössbauer effect, *Zh Eksp. Teor. Fiz. Pis'ma Red.*, 14, 205, 1971.
23. Waldecker, G., Meinhold, H., and Birkholz, U., Thermal conductivity of semiconducting and metallic $FeSi_2$, *Phys. Status Solidi (a)*, 15, 143, 1973.
24. Stöhrer, U., High temperature measurements on thermoelectric materials, in *Proc. 11th Int. Conf. on Thermoelectrics*, Rao, K.R., Ed., University of Texas, Arlington, 1992, 191.
25. Wagner, Th., *Diplomarbeit*, Universität Karlsruhe, 1989.
26. Birkholz, U., Stöhrer, U., and Wagner, Th., Electrical contacts for $FeSi_2$-thermocouples, in *Proc. 7th Int. Conf. on Thermoelectric Energy Conversion*, Rao, K.R., Ed., University of Texas, Arlington, 1988.
27. Nakajima, T., Suzuki, M., and Ohta, J., Iron disilicide thermoelectric generator for home appliance use, in *Proc. Intersociety Energy Conversion Engineering Conf.*, American Society of Mechanical Engineers, 1981, 2013.
28. Groβ, E., Stöhrer, U., Neu, V., and Birkholz, U. Powdermetallurgic preparation of HMS, in *Proc. 10th Int. Conf. on Thermoelectrics*, Rowe, D.M., Ed., Babrow Press, Cardiff, 1991, 178.
29. Birkholz, U., Groβ, E., Riffel, M., Roth, H., Stöhrer, U., and Wittmer, W., Measurements of the efficiency of a HMS-$FeSi_2$ thermoelectric generator, in *Proc. 11th Int. Conf. on Thermoelectric Energy Conversion*, Rao, K.R., Ed., University of Texas, Arlington, 1992, 51.
30. Stöhrer, U., Voggesberger, R., Wagner, G., and Birkholz, U., Semiconducting $FeSi_2$-thermocouples for power generation, in *Proc. 8th Int. Conf. on Thermoelectric Energy Conversion*, Scherrer, H. and Scherrer, S., Eds., Institute National Polytechnique de Lorraine, Nancy, France, 1989, 104.
31. Rudolf, R., Groβ, E., Stöhrer, U., and Birkholz, U., Thermoelectric generators on the basis of bismuth-telluride, in *Proc. 10th Int. Conf. on Thermoelectrics*, Rowe, D.M., Ed., Babrow Press, Cardiff 1991, 102.
32. Groβ, E., Powalla, M., Stöhrer, U., and Birkholz, U., Thermocouples with insulating layers, in *Proc. 9th Int. Conf. on Thermoelectrics*, Vining, C.B., Ed., Jet Propulsion Laboratory, Pasadena, 1990, 336.
33. Groβ, E., Neu, V., and Stöhrer, U., Harman and Hall measurements on higher manganese silicide, in *Proc. 11th Int. Conf. on Thermoelectrics*, Rao, K.R., Ed., University of Texas, Arlington, 1992, 107.

25

Thermoelectric Properties of Anisotropic $MnSi_{1.75}$

V. K. Zaitsev
A. F. Ioffe Physical Technical Institute
St. Petersburg, Russia

25.1 Crystal Structure Properties of the Higher Manganese Silicides

The crystal structure of the higher manganese silicides (HMS) has been determined by Novotny.[1] The range of composition of the HMS synthesized from the liquid phase lies between $MnSi_{1.71}$ and $Mn_{1.75}$[2] and possibly extends to the composition $MnSi_{1.77}$[3] at temperatures below the peritectic line. Atomic positions were measured for the four phases: $Mn_{11}Si_{19}$,[4] $Mn_{15}Si_{26}$,[5] $Mn_{27}Si_{47}$,[6] and Mn_4Si_7,[7] which have similar tetragonal cells (space group D_{2d} directed along the tetragonal axis C (Figure 1). It was shown[8] that the various commensurate crystal structures in the HMS can be described on the basis of a manganese sublattice with a tetragonal cell and a rather labile silicon sublattice forming a helix winding along the C-axis.

The silicon sublattice spacing C_{si} is a function of composition. Generally the sublattice spacings C_{Si} and C_{Mn} are incommensurate. Incommensurate structures in a number of HMS compositions were studied in detail by means of electron diffraction and high-resolution electron microscopy.[9] Most of the HMS crystal is of almost homogeneous composition with one of the commensurate structures, separated by narrow regions where the composition changes abruptly. The silicon sublattice in these regions is larger and the manganese concentration increased. It can be shown that the existence of such a quasi-periodic structure with an increased manganese concentration can stimulate the separation of the monosilicide phase. Such regions are arranged across the C-axis and manifest themselves as a striped microstructure of HMS monocrystals.

25.2 Structural Ordering in the Higher Manganese Silicide

An inherent feature of HMS monocrystals, prepared by different methods and in different laboratories, is the presence of well-developed cleavage planes and an ordered system of striped precipitates of second-phase manganese monosilicide (Figure 2) without the sample becoming non-monocrystal.[10] The planes of formation of $MnSi_{1.75}$ are in all cases arranged perpendicular to the C-axis, and their orientation does not depend on the growth direction. Consequently it is

0-8493-0146-7/95/$0.00+$.50

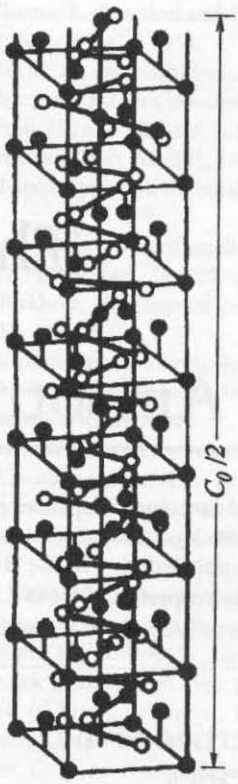

FIGURE 1 Structure of $Mn_{15}Si_{26}$.[2]

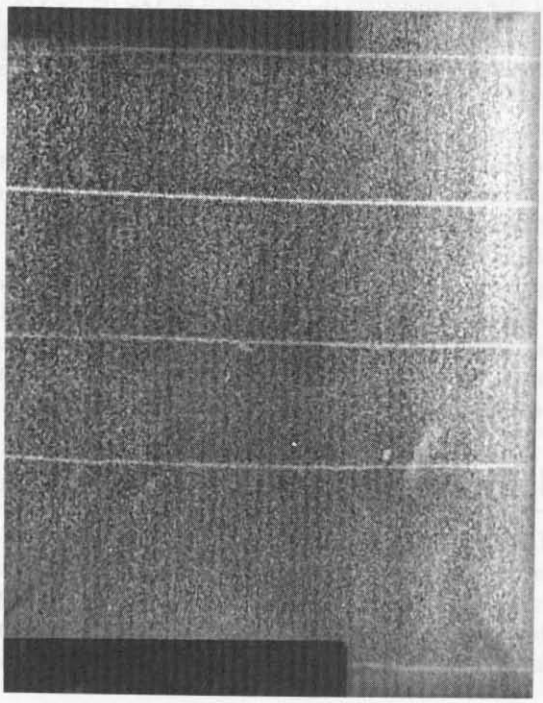

FIGURE 2 Striped microstructure of the HMS: plane parallel to C-axis.

evident that the forming microstructure does not depend on the preparation technique or on specific crystallization features of the HMS, but is a result of solid-state transformations. It is evident from the theory of incommensurate structures[11] that in relatively weakly interacting systems with incommensurate spacings the creation of a soliton structure is possible. This is characterized by broad regions of a commensurate phase separated by soliton walls, their composition being occasionally different from the average. When T = 0 (e.g., without taking into account thermal fluctuations) the presence of two sublattices with different spacings leads to a structure which is determined by the competition between the deformation energy of the "soft" sublattice and the energy of their interaction. Obviously, a weak interaction results in incommensurate structure with a short period which is characteristic of the majority of crystals. In an intermediate case, starting from some value of the interaction energy, transition to an inhomogeneously deformed state favors a "soft" sublattice and leads to the creation of a soliton lattice. Since in the HMS the one-dimensional superlattice is formed along the tetragonal axis, this incommensurate structure can be represented by a reciprocal lattice vector G^i directed along the C-axis. The free energy function can be written as

$$F(\Phi) = \int d^3r \Big\{ q\,(d_x\,\Phi - h)^2 + \nu\,(d_y\,\Phi + d_z\,\Phi)^2 + \Sigma_{G_x^i} V_{G^i} \exp \Big| iG_x^i x + iG_x^i\,\Phi\,(x) \Big| + \frac{1}{2} B_{ijlm}\,u_{ij}u_{lm} + \Gamma_{ij_k}\,u_{ij} \cdot \frac{d\Phi}{dx_k} \Big\}. \tag{1}$$

Here $\Phi(x)$ is a displacement of the soft sublattice atoms (Si sublattice) from the equilibrium position they occupy if the interaction with the rigid sublattice (Mn) is removed; u_i and u_{ij} are the displacement vector and deformation tensor, respectively, which describe the deformation of the hard sublattice; q and ν are elastic constants for the soft sublattice; B is an elastic constant for a hard sublattice; V_{Gi} are the space harmonics of the hard sublattice potential and Γ_{ijk} are intersublattice interaction constants. The parameter h is a measure of the incommensurability of sublattices and is given by

$$h \approx \frac{Na - Mb}{Nb} \tag{2}$$

where a/b = M/N + δ and a and b are sublattices spacings; M and N are whole numbers. If only one potential harmonic is taken into account the well-known sine-Gordon model is obtained:

$$\frac{d^2\Phi}{dx^2} + V \cdot \sin(\Phi) = 0 \tag{3}$$

Here the first term is due to the elasticity of the "soft" sublattice and the second is due to the influence of the "hard" sublattice on the "soft" one. When h is more than some value h_c a phase transition into the incommensurate state with a soliton lattice takes place (see Figure 3). The regions of constant phase in Figure 3 correspond to a stretched Si sublattice which, as the author's estimates show, can stimulate nucleation of the monosilicide phase. Regions of this kind are arranged across the C-axis and are revealed macroscopically as a striped structure in the HMS (Figure 2).

Superstructures $Mn_{11}Si_{19}$, $Mn_{15}Si_{26}$, and Mn_4Si_7 having the longer C-axis dimensions of 48.136, 65.311, and 17.463 Å, respectively, can be fitted using the approximation a/b = 1/2 + h; this means a low order of commensurate phase (1:2). Assuming a typical value of the constant which links the stress tensor and phase change to be $\nu = 10^4$ dyn · cm, the critical potential V_a^c can be evaluated which corresponds to the appearance of the soliton solution in this model: $V_a^c \cong 4.6 \cdot 10^{-2}$, $4.3 \cdot 10^{-2}$, and $3.75 \cdot 10^{-2}$ eV, respectively, for the indicated compositions. For all monocrystals discussed the value of δ is approximately equal to 0.07 and is determined by the parameter:

$$h = (\nu l^2 \delta^2 / V_a)^{\frac{1}{2}} \tag{4}$$

where l is the width of the soliton wall. When h takes values around $h_c = 4/\pi$ and provided $V_a \to V_a^c$, the scale of the soliton structure increases further and can be observed with a scanning electron microscope (SEM).

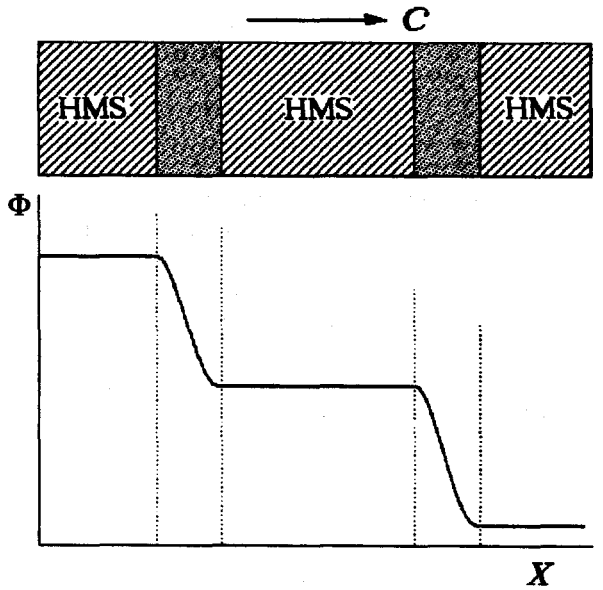

FIGURE 3 Solition microstructure formation mechanism in the HMS.

An SEM microstructure study of HMS samples revealed the strong influence of dopant composition and thermal treatment on the heterogenization of available crystals.[12] In all cases the structural transformations are accompanied by distinctive changes in the striped monosilicide precipitates. Moreover, the total combination of structural and microscopic transformations may be described as a single phase transition during which a crystal structure passes incommensurate states along a "devil's staircase" of superstructures, and a lattice of soliton concentrations arises. The equilibrium period of this lattice approaches infinity when the temperature approaches that of the transformation into the commensurate state. As the number of particles remains constant this increase in soliton concentration leads to their local condensation—sticking together. The resulting local increase in manganese concentration promotes the creation of the monosilicide phase.

The results of the SEM study of the microstructure of HMS monocrystals (subjected to different thermal processing) agree qualitatively with the model of soliton ordering of the compound crystal lattice discussed above. It applies to both precipitates and the temperature dependence of the period of the soliton concentration observed on the "hardened" and thermally processed samples. The mean size of manganese monosilicide precipitates in the undoped HMS monocrystals ranges from 10 to 150 μm, with their dispersion and positions of center of gravity depending on composition and thermal processing.

The SEM study of doped HMS monocrystals revealed a profound change in the scale of microprecipitation, which indicated the strong influence of doping on the HNS crystal lattice formation. Thus, the introduction of Fe and Re atoms decreases the regular precipitate size to approximately several microns while the introduction of germanium has a stronger influence with a 0.5 at.% concentration of this element reducing the precipitates to approximately 1 μm.

The dependence of structure order in HMS on composition and temperature manifests itself most effectively in the thermal expansion. In Figures 4 and 5 the results of relative lengthening (RL) and linear expansion coefficient (LEC) study on the HMS in the incommensurate state region are presented. The measurements were made in the C-axis direction. The sharp dependence of the state of the system on the heating regime is apparent. The following aspects of LEC and RL behavior on temperature changes can be derived from an analysis of the data:

1. In all the temperature range covered, a non-monotonic change of RL and LEC is observed indicating a set of phase transitions.

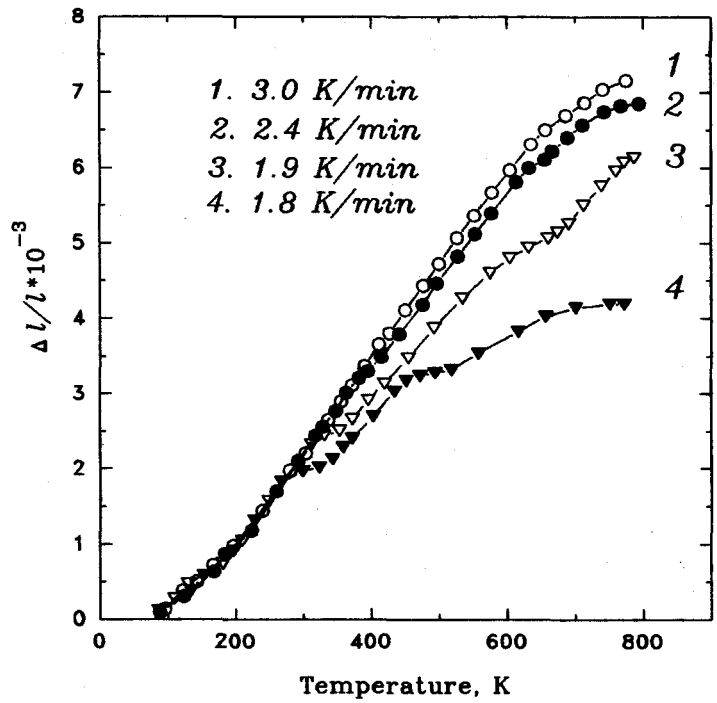

FIGURE 4 Temperature dependence of relative lengthening for the HMS monocrystals in directions along the C-axis at different heating rates.

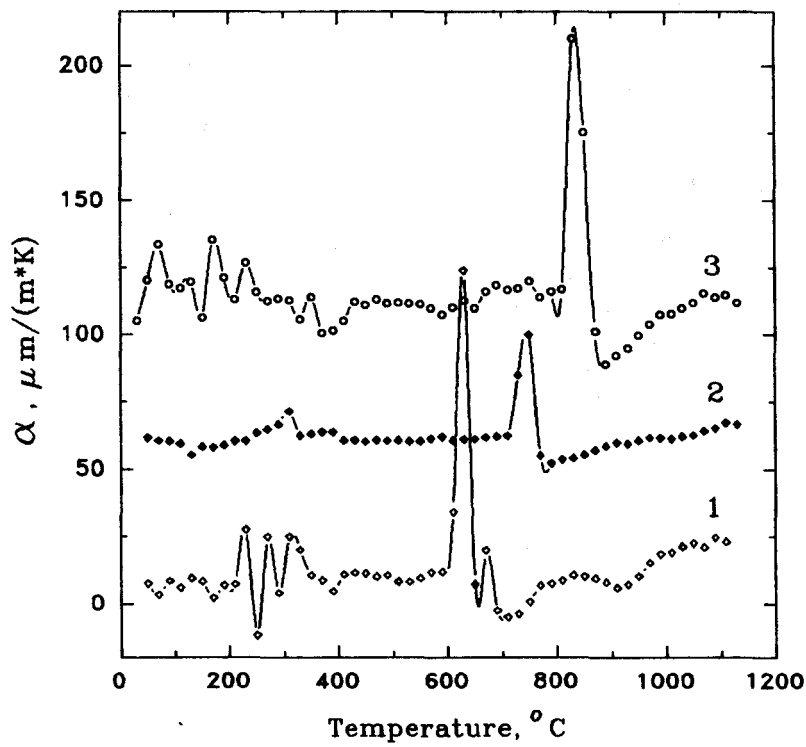

FIGURE 5 Thermal expansion coefficient (α) for HMS monocrystals of different compositions: (1) $MnSi_{1.77}$; (2) $MsSi_{1.75}$; (3) $MnSi_{1.73}$.

2. Figure 5 reveals the strong influence of stoichiometry on the phase diagram of the incommensurate state. An increase of silicon concentration in HMS reduces the temperature of the high-temperature transition.

The observed phase transformations are linked to transitions between different commensurate and incommensurate states. The most intensive high-temperature peak in the linear expansion coefficient correlates with the transition of an incommensurate (soliton) state into a disordered one. The results obtained confirm the existence of incommensurate structures of HMS; a satisfactory description has been given in Reference 13. The observed behavior can be traced back to a difference in the sublattices' partial linear expansion coefficients.

25.3 Kinetic Properties of HMS

Based on its electrical properties, HMS can be regarded as a self-doped, p-type semiconductor with a high carrier concentration ($p \sim 10^{21}$ cm^{-3}) over the temperature range studied and a relatively low carrier mobility ($\mu_p \sim 10$ cm^2/V · s at T = 300 K).

Very little data have been reported hitherto regarding the energy spectrum and carrier scattering mechanism in HMS. However, based on the electrical conductivity and Hall coefficient data, in the intrinsic region the thermal width of the energy gap is 0.6 to 0.8 eV.[14] This value is close to the direct transition energy derived from the light absorption coefficient at room temperature (0.67 ± 0.01 eV).[15] The hole effective mass has been determined from the thermoelectric power and Hall coefficient in the extrinsic region and from an analysis of reflection data on germanium- and chromium-doped HMS samples.[16] In spite of the low accuracy of effective mass determination in these experiments, the close values of the effective mass obtained from the density-of-states and optical conductivity indicate that the valence band extremum lies in the center of the Brillouin zone, although the high effective mass values ($\sim 10 m_o$, m_o—free electron mass) apparently indicate a narrow valence band.

It is well known that HMS monocrystal samples exhibit a strong anisotropy in their kinetic properties over a wide temperature range.[17,18] In addition, it has been established that the anisotropy of the thermoelectric power is of the order of $\alpha_\perp/\alpha_\parallel \cong 1.7$ where $\alpha_\perp, \alpha_\parallel$ are the thermoelectric power across and along the C-axis, respectively, and depend weakly on the composition. It appears that the electrical conductivity σ in the perpendicular direction also depends weakly on the composition, although a highly non-monotonic dependence was observed in conductivity measurements along the C-axis. The conductivity anisotropy $\sigma_\perp/\sigma_\parallel$ at 300°C reaches 5 to 10 while the thermal conductivity anisotropy $\lambda_\perp/\lambda_\parallel$ is 2. The anisotrophic transport properties, typical for HMS single crystals, measured in the temperature range 4.2 to 1000 K, are shown in Figure 6. A prominent feature is the marked anisotropic behavior of the thermoelectric power over a wide temperature range and a wide plateau in the thermal conductivity vs. temperature plot. As described above, the characteristic peculiarity of the HMS microstructure is a precipitate of a high-conducting second phase in planes perpendicular to the C-axis.

In the general case the oriented arrangement of this phase with conductivity much exceeding that of the matrix can initiate an anisotropy in the thermoelectric power and electrical conductivity. However, it can be estimated in this case that anisotropy originating in manganese monosilicide precipitation cannot exceed 15 to 20% of the thermopower and electric conductivity. Therefore, the most probable origin of strong anisotropy in the thermoelectric power and the electrical conductivity is the incommensurate structure of the HMS.

Consider an inhomogeneous deformed state formed by an array of equidistant or randomly arranged solitons. The large regions of commensurate state, which occupy the greater part of volume, will be separated by thin, shallow (almost two-dimensional) layers, formed by the soliton walls (kinks). If an inhomogeneous modulation occurs which consists of a regular or random array of kinks then a commensurate state exists in the bulk except in the vicinities of the two-dimensional layers. In this case transport processes can be studied by considering these kinks as perturbations of the initial homogeneous state.

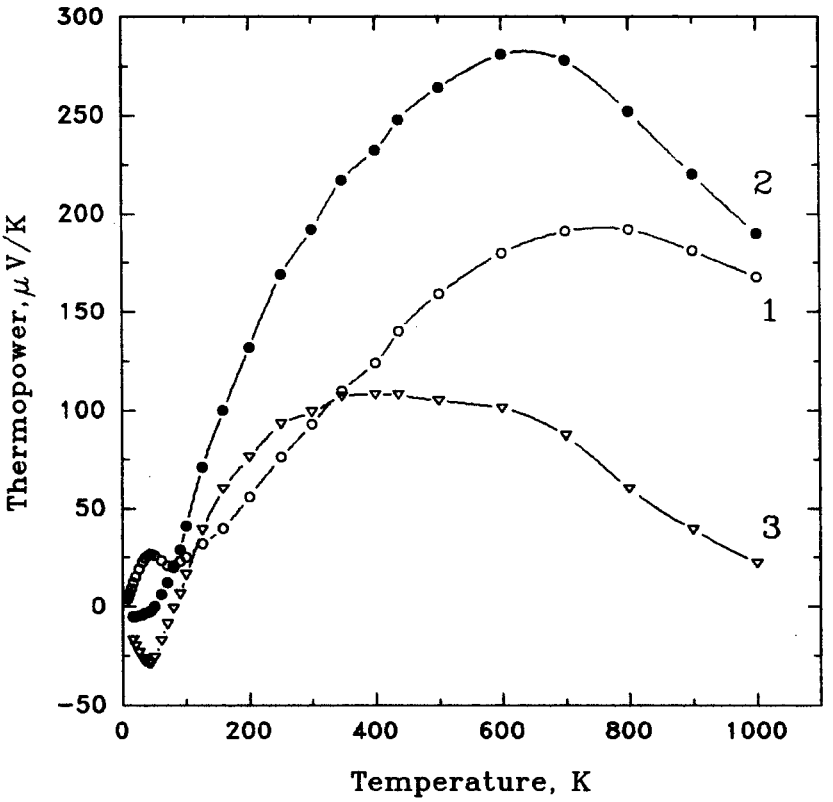

FIGURE 6 Temperature dependence of the thermoelectric power (1,2) and its anisotropy ($S_{\parallel}$-$S_{\perp}$-3) for HMS monocrystals with the composition $MnSi_{1.75}$; 1 parallel and 2 perpendicular to the C-axis direction.

If the electron mean free path $l \gg$ L, where L is the mean distance between kinks, the well-known problem of the finite band potential is obtained (there are only a few gaps in the spectrum). In the case $l \ll$ L the electrical conductivity can be calculated using the Landauer formula. Electron scattering on the kinks results in the conductivity and thermopower anisotropy. The additional resistance in the C-axis direction due to scattering on the soliton wall is given by

$$\delta R_{\parallel} = \frac{(2\pi)^2 h^3}{2e^2 mS \int_o^{\infty} dE \cdot f(E) \cdot D(E)} \tag{6}$$

where S is the cross section area, m is the electron effective mass, f(E) is a distribution function, and D(E) is the transparency coefficient for the barrier. The thermoelectric power can be calculated in a similar manner.

$$\delta\alpha_{\parallel} = \frac{1}{eT} \cdot \frac{\int_o^{\infty} (e-\mu)\frac{df}{d\mu} \cdot \int_0^{E} D(E-E_{\perp})dE_{\perp}}{\int_o^{\infty} dE \frac{df}{d\mu} \cdot \int_o^{E} D(E-E_{\perp})dE_{\perp}} \tag{7}$$

Here μ is a chemical potential and $E_{\perp}$ is the kinetic energy for a transversal movement. For a single soliton the effective potential takes the Peschle-Teller form:

$$U = \frac{U_0}{ch^2 \frac{X - X_0}{l_s}} \tag{8}$$

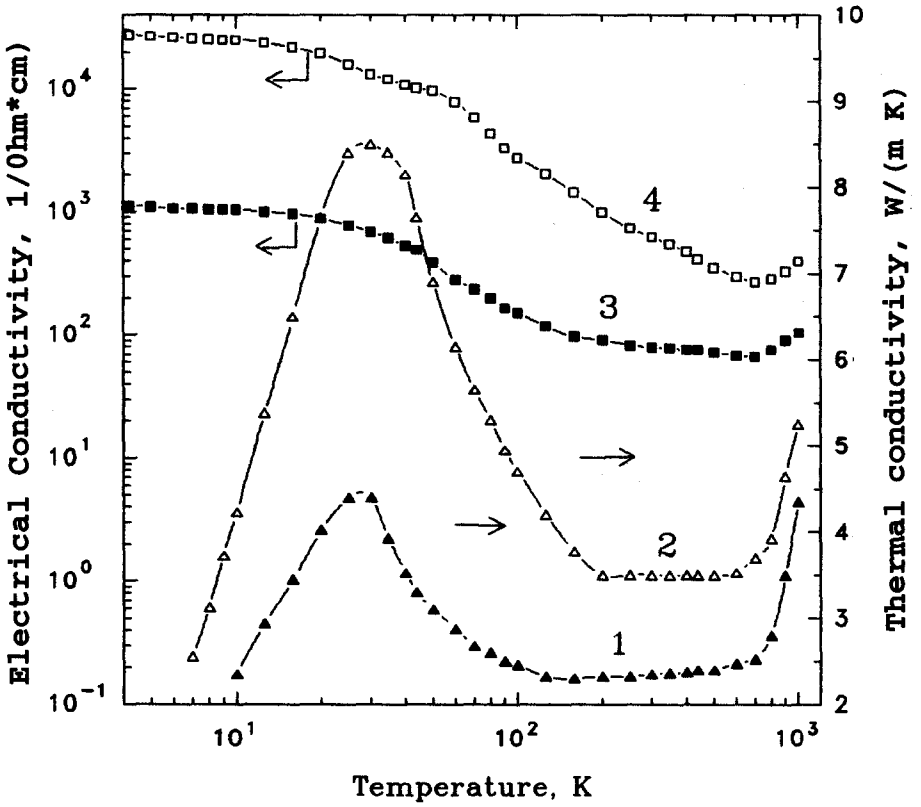

FIGURE 7 Temperature dependence of the thermal (1,2) and electrical conductivity (3,4) for HMS monocrystals with the composition $MnSi_{1.75}$; (1,3) parallel and (2,4) perpendicular to the C-axis direction.

where U_0 and l_s are the barrier (well) amplitude and width. In the case of a well ($U < 0$):

$$D(k) = \frac{sh^2 nkl_s}{sh^2 nkl_s + ch^2\left(\frac{\pi}{2}(1 - \frac{8m}{h^2} U_0 l_s^2)^{\frac{1}{2}}\right)} \tag{9}$$

and in the case of a barrier ($U_0 > 0$):

$$D(k) = \frac{sh^2 nkl_s}{sh^2 nkl_s + ch^2\left(\frac{\pi}{2}(\frac{8m}{2} U_0 l_s^2 - 1)^{\frac{1}{2}}\right)} \tag{10}$$

where $\hbar^2 k^2/2m = E$; k is the $\vec{k}$ vector component in the C direction.

The experimental data available give evidence of the very strong influence of kinks and stripes which appear due to incommensurability, upon the kinetic properties and, in particular, upon their anisotropy. In fact reducing the soliton structure by doping or thermal treatment leads to a significant decrease in the anisotropy of the kinetic coefficients. Unfortunately, the model of thinly dispersed soliton walls provides a qualitative, but not a quantitative, fit to the experimental anisotropy data. For a quantitative fit it is necessary to develop a theory for the case of a dense soliton array which takes into account the multiple scattering effects.

The wide plateau region on the thermal conductivity vs. temperature curve (Figure 7) indicates the presence of an additional heat transfer mechanism in the temperature range 200 to 700 K compared with the low-temperature region where a classical maximum is usually observed in pure, well-ordered crystals. On the basis of a comparison between the optical phonon decrement and

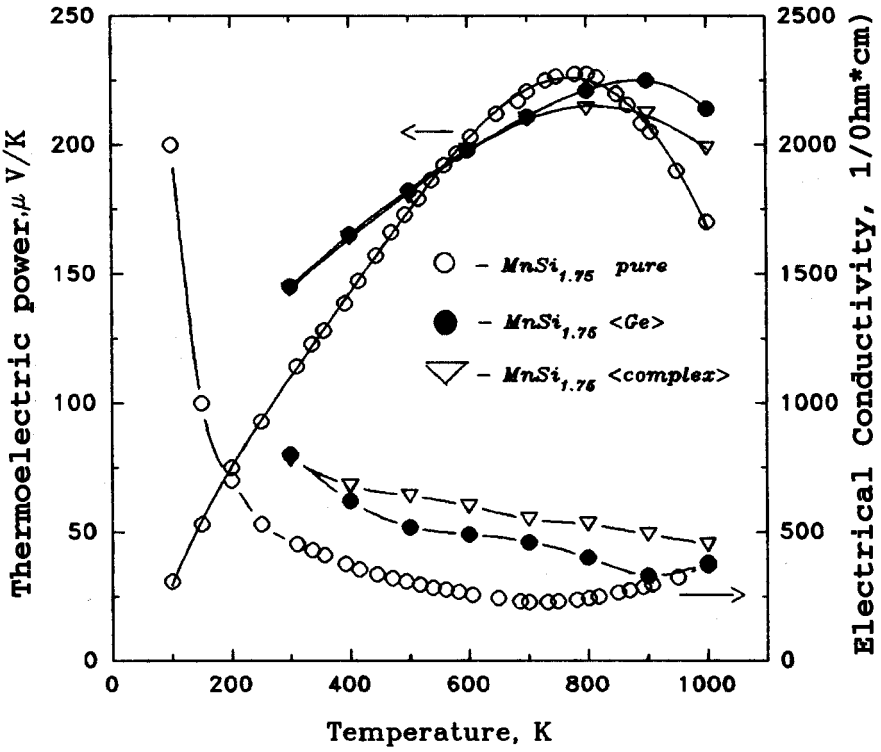

FIGURE 8 Temperature dependence of thermoelectric power and electrical conductivity for pure and doped $MnSi_{1.75}$.

the thermal conductivity of solid solitons of the HMS with iron disilicide it was shown[16] that optical phonons may make a substantial contribution to the phonon scattering as well as to heat transport. This process results in a weaker temperature dependence of the thermal conductivity and the appearance of a plateau.

High values of thermoelectric power anisotropy over an extremely wide temperature range support the prospect of using the HMS as a base for the development of anisotropic thermal to electrical energy converters which may offer substantial advantages compared with traditional thermoelements.

25.4 Figure-of-Merit of Material Based on the HMS

The complex crystal structure, strong anisotropy of the charge and heat transport properties, and shortcoming of existing theories make any estimates of the thermoelectric figure-of-merit of material based on the HMS extremely difficult.

Undoped samples of HMS, prepared using a hot-pressing technique, have low values of Z. The introduction of impurities into the HMS samples results in apparently unpredictable complex changes of the structure, carrier concentration, and phonon spectrum. For instance, a small concentration of a neutral impurity such as Ge very effectively and unusually produces changes in the thermoelectric parameters.[19] The primarily current carrier concentration increases up to $9 \cdot 10^{21}$ cm^{-3}, the electrical conductivity also increases, and the maximum of the thermoelectric power shifts to a higher temperature (Figure 8). In addition, the thermal conductivity increases continuously with the increase in temperature while in undoped HMS it does not depend on temperature over a wide temperature range. It can be seen from the temperature dependence of the thermoelectric figure-of-merit that it is much higher in doped samples and slightly depends on temperature within a wide temperature range. Figure 9 shows that the figure-of-merit of materials based

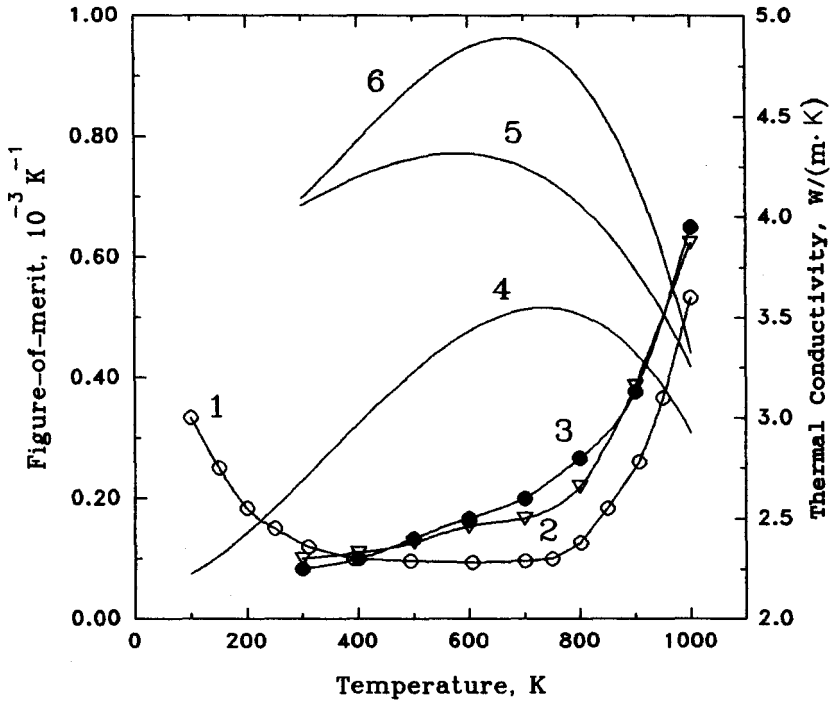

FIGURE 9 Temperature dependence of thermal conductivity (1–3) and figure-of-merit (4–6) for pure (1,4), complex doped (2,6), and Ge-doped (3,5) $MnSi_{1.75}$.

on the HMS increases to $10^{-3}K^{-1}$ due to doping, which induces complicated changes in the phonon spectrum and crystal structure. These materials possess low vapor pressure, good stability at high temperature, are rather cheap, are comprised of nontoxic main components, and are mechanically strong. All these features make these materials good prospects for use in thermoelectric generators.

References

1. Novotny, H., *The Chemistry of Extended Defects in Non-Metallic., Sol*l (ed), Eyring, L. and O'Keefe, M., Eds., North-Holland, Amsterdam, 1970, 223.
2. Geld, P. V. and Sidorenko, F. A., Silicides of transition metals of fourth period, *Metalluriga,* Moscow, 1971, chap. 2.
3. Nikitin, E. M. and Zaitsev, V. K., Production of higher manganese silicide by reaction of gas transport, *Izv. Akad. Nauk SSR Neorg. Mater.*, 1, 1526, 1965.
4. Schwomma, O., Presinger A., Nowotny, H., and Wittman, A., Kristall Structure von $Mn_{11}Si_{19}$ und deren Zusammenhang mit Disilicid Typen, *Monatsh. Chem.*, 95, 1527, 1964.
5. Knott, H. W., Mueller, M. H., and Heaton, L., The crystal structure of $Mn_{15}Si_{26}$, *Acta Crystallogr.*, 23, 549, 1967.
6. Flicher, G. H., Völlenkle, H., and Nowotny, H., Die Kristallstructur von $Mn_{27}Si_{47}$, *Monatsh. Chem.*, 98, 2173, 1967.
7. Karpinski, O. G. and Evseev, B. A., Crystal structure of Mn_4Si_7, *Izv. Akad. Nauk SSSR Neorg. Mater.*, 5, 525, 1969.
8. Zaitsev, V. K., Ordin, S. V., Rahimov, K. A., and Engalychev, A. E., The crystal structure peculiarities and thermopower of higher manganese silicide, *Fiz. Tverd. Tela,* 23, 621, 1981.
9. Ye, H. Q. and Amelinckx, S., High-resolution electron microscopic study of manganese silicides $MnSi_{2-x}$, *J. Solid State Chem.*, 61, 8, 1986.
10. Levinson, L. M., Investigation of the defect manganese silicide Mn_nSi_{2n-m}, *J. Solid State Chem.*, 6, 126, 1973.

11. Currat, R. and Janssen, T., Excitation in incommensurate crystal phases, *Solid State Phys.*, 41, 202, 1988.
12. Ordin, S. V., Zaitsev, V. K., Engalychev, A. E., and Soloviev, V. A., Electron microscopic study of materials based on higher manganese silicide, in *Materials for Thermoelectric Converters*, Leningrad, 1987, 99.
13. Zaitsev, V. K., Ktitorov, S. A., Kalyazin, A. E., Marchuk, N. D., and Ordin, S. V., Thermal expansion in higher manganese silicide, *Fiz. Tverd. Tela*, 34, 2589, 1992; Zhdanova, V. V., Zaitsev, V. K., Ktitorov, S. A., and Engalychev, A. F., Thermal expansion in higher manganese silicide, in *Semiconductor Materials for Thermoelectric Converters*, Leningrad, 1985, 80.
14. Nikitin, E. N., Tarasov, V. I., Andreev, A. A., and Shumilova, L. N., Electrical properties of higher manganese silicide, *Fiz. Tverd. Tela*, 11, 3389, 1969.
15. Zaitsev, V. K., Ordin, S. V., Tarasov, V. I., and Fedorov, M. I., Optical properties of higher manganese silicide, *Fiz. Tverd. Tela*, 21, 2517, 1979.
16. Zaitsev, V. K., Fedorov, M. I., Rahimov, K. A., Engalychev, A. E., and Popov, V. V., Lattice thermoconductivity and reflection spectra of higher manganese silicide and some solid solitons on its base, *Fiz. Tverd. Tela*, 126, 819, 1984.
17. Voronov, B. K., Dudkin, L. D., and Trusova, N. N., Anisotrophy of thermoelectric properties in chromium disilicide and higher manganese silicide single crystals, *Kristallografia*, 12, 519, 1967.
18. Ivanova, L. D., Abrikosov, N. Kh., Elagina, E. I., and Khvostikova, V. D., Preparation and study of properties of higher manganese silicide single crystals, *Izv. Akad. Nauk SSSR Neorg. Mater.*, 5, 1933, 1969.
19. Abrikosov, N. Kh., Ivanova, L. D., and Murav'ev, V. G., Preparation and study of single crystals solid solutions of higher manganese silicide with GE and $CrSi_2$, *Izv. Akad. Nauk SSSR Neorg. Mater.*, 8, 1194, 1972.

26

Low Carrier Mobility Materials for Thermoelectric Applications

V. K. Zaitsev, S. A. Ktitorov, and M. I. Fedorov
A. F. Ioffe Physical Technical Institute
St. Petersburg, Russia

26.1 Introduction

Materials that exhibit hopping conductivity and low mobility have not been considered to be prospective candidates for use in thermoelectric power converters because, in accordance with the criterion $Z \sim \mu/\lambda_L$ (μ is the mobility and λ_L is the lattice thermal conductivity), their efficiency is smaller than that of band-conducting materials. Recently it has been discovered that some materials with hopping conductivity (the higher borides and iron disilicide, for example) possess a high efficiency compared with that of band-conducting semiconductors. Material based on α-AlB_{12} holds the record efficiency value at high temperatures.[1]

In this chapter some of the peculiarities of the transport properties of low mobility materials are discussed in connection with the possibility of obtaining higher thermoelectric efficiencies.

The problem of nonstandard (i.e., non-Boltzmann) transport in semiconductors and metals is one of the intriguing problems of modern physics. The calculation of the conductivity of disordered and polaron semiconductors is a difficult enough problem, but the difficulties are connected mainly with solving mathematical physics problems, whereas the formulation of the problem is quite obvious. At the same time, the formulation of the problem of the thermoelectric power calculation encounters serious difficulties. The Kubo formulas give general expressions for the transport coefficients but the problem is that the heat flux operator cannot be uniquely defined in the presence of the electron-phonon interaction. One of the difficulties is that it is impossible to take the thermal perturbation into account within the Hamiltonian formalism in the nonrelativistic theory.

0-8493-0146-7/95/$0.00+$.50

26.2 Inequilibrium Thermodynamics Relations and the Kubo Formulas

In-equilibrium thermodynamics give the following relations between the external forces and the correspondent currents:[2]

$$j = L_{11}(E + -\nabla(\mu/T)) + L_{12} \cdot \frac{1}{T} \cdot \nabla T \tag{1}$$

$$q = -L_{21}(E + -\nabla(\mu/T)) - L_{22} \cdot \frac{1}{T} \cdot \nabla T \tag{2}$$

where E is the electric field, μ is the chemical potential of electrons, and j and q are the electric current and the thermal flux, respectively. The kinetic coefficients L_{ik} obey the Onsager symmetry relations

$$L_{ik} = L_{ki} \tag{3}$$

The electrical conductivity σ, the thermal conductivity λ, and the thermopower (Seebeck) coefficient α can be expressed in terms of the coefficients L_{ik}:

$$\begin{aligned} \sigma &= L_{11} \\ \lambda &= [L_{22} - L_{21}L_{12}/L_{11}]/T \\ \alpha &= [L_{12}/L_{11} - \mu/e]T \end{aligned} \tag{4}$$

These relations are valid for any statistically homogeneous system with an arbitrary disorder. The Kubo formulas

$$L_{11} = \sigma = \lim_{s\to 0} \int_0^\infty dt e^{-st} \int_0^\beta <\hat{j}(0)\hat{j}(t + i\hbar\lambda)>d\lambda \tag{5a}$$

$$L_{12} = L_{21} = \lim_{s\to 0} \int_0^\infty dt e^{-st} \int_0^\beta <\hat{j}^H(0)\hat{j}(t + i\hbar\lambda)>d\lambda \tag{5b}$$

$$L_{22} = \chi = \lim_{s\to 0} \int_0^\infty dt e^{-st} \int_0^\beta <\hat{j}^H(0)\hat{j}^H(t + i\hbar\lambda)>d\lambda \tag{5c}$$

give general expressions for the kinetic coefficients. In these formulas $\hat{j}^H(t)$ is the energy flux operator and $\hat{j}(t)$ is the Heisenberg current operator, which satisfies the continuity equation:

$$div\,\hat{j} + \partial\rho/\partial t = 0 \tag{6}$$

where $\rho = e\,\psi^+(x)\psi(x)$ is the charge density operator; and $\psi(x)$ and $\psi^+(x)$ are the annihilation and creation field operators, respectively.

Notwithstanding the simple form of the Kubo formulas, calculations using them are not simple, because the direct application of perturbation theory to them leads to divergencies. Summing up the leading terms leads to the kinetic equation.

26.3 Thermoelectric Power Without an Electron-Electron Interaction in Disordered Systems

Luttinger[3] has given a recipe for taking thermal perturbation into account using the fact that the condition of the thermodynamic equilibrium for a system interacting with a gravitation field is

$$Tg_{00}^{1/2} = const.,$$

with g_{00} the time component of the metric tensor. In the limit of the weak Newtonian field Ψ:

$$g_{00} = 1 + 2\Psi/c^2 \tag{7}$$

For the case of the homogeneous gravitational field

$$\Psi = \nabla\Psi \cdot r \text{ with } \nabla\Psi = const.$$

Since the energy density h(r) behaves as a mass density $h(r)/c^2$, we have an interaction term of the form:

$$F = \int \rho(r)\phi(r)d^dr + \int h(r)\Psi(r)d^dr \tag{8}$$

leading to Equation 5b, with the energy flux $\hat{j}^H$ satisfying the continuity equation:

$$div\,\hat{j}^H + \partial h/\partial t = 0 \tag{9}$$

The study of the thermoelectric effects in a disordered system was stimulated by Mott's work (see, for instance, Reference 4). The following formula for the Seebeck coefficient was suggested:

$$\alpha = -\frac{k}{e}\int dE\,\frac{E - E_F}{kT}\,\sigma(E)/\sigma \tag{10}$$

where $\sigma = \int \sigma(E)dE$, E_F is the Fermi energy. Neglecting the electron correlations effects one can write:

$$\sigma(E) = e \cdot g(E) \cdot u(E) \cdot f(E) \cdot (1 - f(E)) \tag{11}$$

with g(E) being the electron density-of-states, u(E) the mobility, and f(E) the distribution function. The Equation (10) is valid only in the absence of inelastic collisions.

In the high temperature limit $kT \gg < E >$, i.e., when kT exceeds the width of the band,

$$\alpha \approx \frac{1}{e}\cdot\frac{E_F}{T} = \frac{k}{e}\cdot \ln\frac{n}{N-n} \tag{12}$$

where n is the charge carrier concentration and N is the concentration of sites. Note that Equation 12 is valid for any system with negligible transport of the kinetic energy. The main consequences of Equations 7 and 8 are as follows:

1. The sign of the thermoelectric power is determined by the type of conduction. For $n < N/2$ $\alpha < 0$ transport is by electrons and for $n > N/2$ $\alpha > 0$ it is hole-type.
2. The Seebeck coefficient is isotropic in the hopping regime.

At low temperatures the Mott formula derived for metals is valid for systems with hopping transport:

$$\alpha = \frac{\pi^2}{3}\cdot\frac{k^2T}{e}\cdot\frac{dln\sigma(E)}{dE}\Big|_{E=E_F} \tag{13}$$

For low-temperature transport with hops in the vicinity of the Fermi level the $T^{-1/2}$ law holds. Then

$$\alpha = \frac{\pi^2}{3}\cdot\frac{k^2T}{e}\cdot\frac{dlnN(E_F)}{dE_F}\cdot\left(1 + \frac{1}{4}\left(\frac{T_0}{T}\right)^{1/4}\right) \tag{14}$$

Another expression for the thermopower was obtained in Reference 5.

$$\alpha \approx -\frac{1}{e}\cdot\frac{(\Delta E)^2}{T}\cdot\frac{dlnN(E_F)}{dE_F} \tag{15}$$

where $\Delta E \approx kT_0(T/T_0)^{3/4}$ is an energy range near the Fermi level within which hops take place, giving rise to the $T^{-1/4}$ law. Thus, we have

$$\alpha \propto T^{1/2}$$

Qualitatively different results for the thermopower in the hopping regime follow from the above-mentioned difficulty in determining the energy flux operator in the systems under consideration.

The effect of inequilibrium phonons on the thermoelectric power is discussed in the next section.

26.4 The Influence of Inequilibrium Phonons on the Thermoelectric Power

The possible effect of an inequilibrium state of the phonon subsystem was discussed by Fritzche.[6] Inelastic processes and inequilibrium phonons were shown to change Equation 10 into the following:

$$\alpha = -\frac{k}{e} \cdot \int dE \frac{E - E_F + D(E,T)}{kT} \cdot \frac{\sigma(E)}{\sigma} \tag{16}$$

where the D term takes into account the heat transport by phonons. In Reference 7 the term D(E,T) was calculated using the two-site model. The thermoelectric power between two sites is given by

$$\alpha = -\frac{1}{e}\left[\frac{E_i + E_j}{2} + E_T^{ij} - E_F\right]/T \tag{17}$$

$$E_T^{ij} = kT^2\left[\frac{\partial \ln(R_{ij}/R_{ji})}{\partial T_i} + \frac{\partial \ln(R_{ji}/R_{ij})}{\partial T_j}\right]_T$$

Here E_i is the equilibrium energy of the system when the electron occupies site i and R_{ij} is the rate characterizing a phonon-assisted hop $i \rightarrow j$.

These formulas predict nonvanishing thermoelectric power even in the case of the symmetric hopping of electrons about the Fermi level: $(E_i + E_j - 2\zeta) = 0$:

$$\alpha = -\frac{<E_T^{ij}>}{eT} \tag{18}$$

In this case the thermoelectric power is a measure of the mean square disorder energy characteristic of the dominant conducting paths. In Mott's variable-ranging hopping regime[4] the thermoelectric power acquires the following temperature dependence, $\alpha \propto T^{1/2}$. Thus, a non-zero thermoelectric power can be observed even in the case of the symmetric distribution of hopping states.

The most interesting variant can arise in the case of strong electron-phonon interaction (for example, polaron type). A polaron state results from the strong interaction of a carrier with the polar phonon and leads to a lowering of energy. In the theory of small polarons the propagation of such a "dressed" electron has been considered in detail.[8]

Until now, the case has not been studied where the phonon system is in an inequilibrium state with a directed flow of optical phonons due to a temperature gradient. It is natural to suppose that, if the electron-phonon interaction is strong enough, a phonon drift can induce asymmetry in polaron hops and, as a result, an electron drift appears too, i.e., an effect which is analogous to the well-known acoustic phonon drag effect. A possible value of the effect can be estimated.

Near the Debye temperature acoustic as well as optical branches contribute to the heat flux so it is necessary to take account of the corresponding inequilibrium contribution. The polaron-forming phonon branch is also in an inequilibrium state. It is apparent that the phonon "wind" can induce an additional asymmetry of back and forward hops and therefore an additional contribution to the thermoelectric power.

The thermoelectric power can be calculated using Equations 4, 5a, 5b, and 5c. If the electron contribution to the energy flow only is taken into account we get the Morin formula (Equation 12). The phonon contribution to the energy flux gives the required effect; the correlator L_{12} does not vanish only for the phonon mode which strongly interacts with the electron forming the

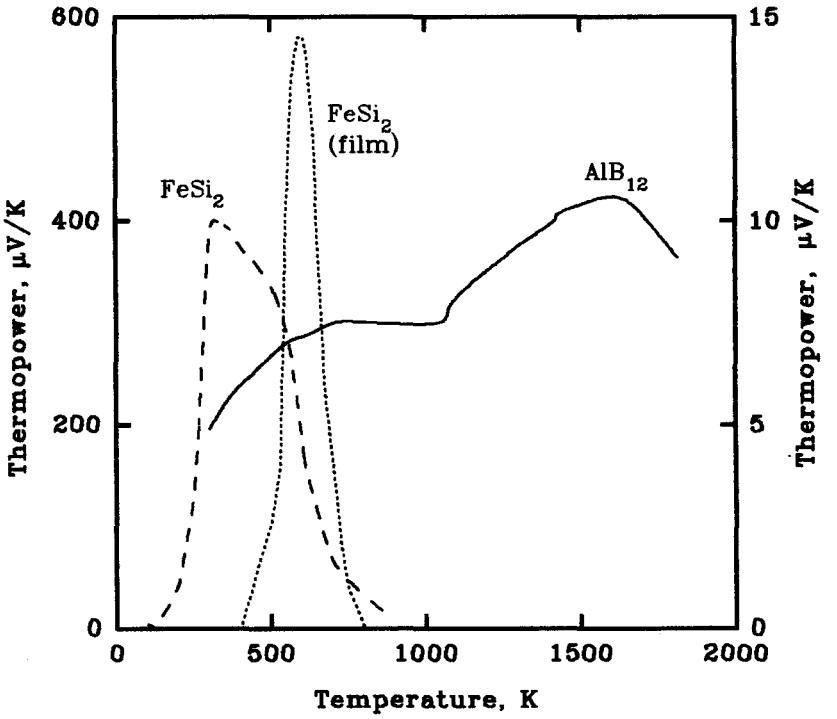

FIGURE 1 Temperature dependencies of thermopower in AlB_{12} (solid),[1] bulk β-$FeSi_2$ (dashed) and $FeSi_2$ amorphous film (dotted).[9] The right scale corresponds to $FeSi_2$ amorphous film and the left one to other materials.

polaron state. Difficulties in attempts to estimate the effect arise from the lack of data relating to the electron-phonon interaction constants and phonon scattering rates. Note that the effect of interest is given by the off-diagonal (in the secondary quantization representation) flux operator matrix elements. Actually in the hopping regime at $T > T_D$ (T_D is the Debye temperature) the polaron band is very narrow ($J \ll kT$) and the main contribution is given by the off-diagonal elements. As such elements are absent in the equilibrium density matrix, the off-diagonal elements of the energy flux operator have to be taken into account.

The simplest estimate for the optical phonon drag effect can be done by omitting details of the electron-phonon interaction in analogy with the acoustic phonon drag effect:

$$S_{ph} = \frac{1}{3} \frac{v_{ph} \cdot l_{ph}}{T \cdot u_e} \tag{19}$$

where v_{ph}, l_{ph} are a dispersion parameter (with the dimension of velocity) and the free path of optical phonons, respectively, and u_e is a drift mobility of electrons. For $v_{ph} \approx 10^5$ cm/s, $l_{ph} \approx 10^{-7}$ cm, and $u_e \approx 10^{-2} \div 10^{-7}$ cm^2/(V · s), S_{ph} can reach a value of the order of 10 mV/K. Extremely high values of thermoelectric power (~10 mV/K) were observed in amorphous films of $FeSi_2$,[9] prepared using the ionized cluster beams method. The temperature dependence of the thermoelectric power shows an anomalous maximum (Figure 1). It should be noted that to obtain a thermoelectric power of 10 to 12 mV/K it is necessary for an electron to acquire an energy of about 6 to 12 eV, that is, more than the work function in solids. Evidently such a value of thermoelectric power can exist only as a result of some collective effect when electrons obtain their energy by small quanta.

The observed shape of the thermoelectric power-temperature dependence can be explained qualitatively as follows. The sharp increase of the thermoelectric power can be traced back to the

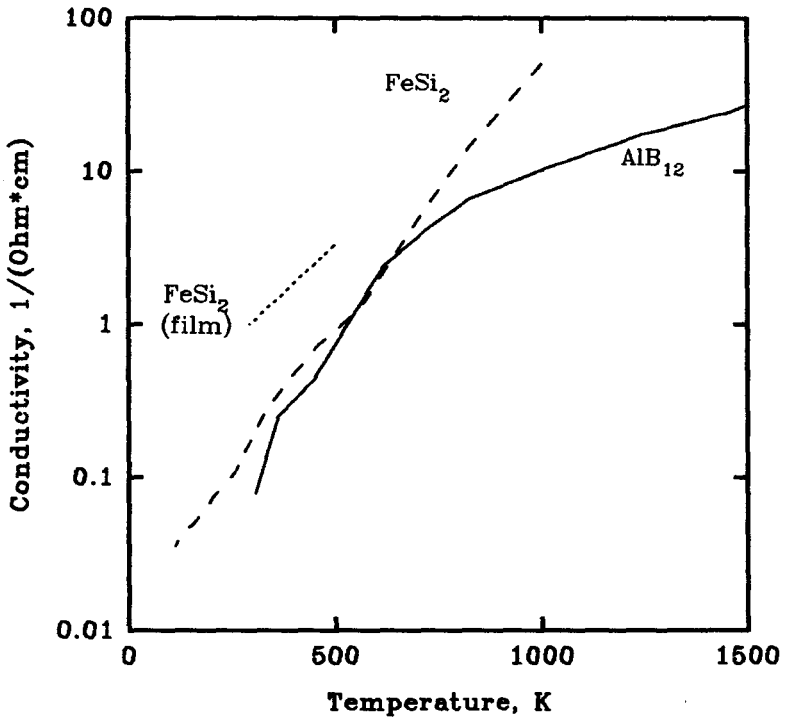

FIGURE 2 Temperature dependencies of conductivity in AlB_{12} (solid),[1] bulk β-$FeSi_2$ (dashed), and $FeSi_2$ amorphous film (dotted).[9]

excitation of optical phonons with characteristic frequencies for $FeSi_2$ in the range of 250 to 700 K as revealed by spectra.[10] The sharp decrease can be explained by the exponential increase of carrier mobility and decrease of the phonon free path with an increase in temperature. Figures 1 and 2 show the temperature dependencies of the thermoelectric power and electric conductivity for a few materials with a polaron-type hopping conductivity mechanism. It is apparent that the temperature dependencies of the thermoelectric power, analogous to that of amorphous $FeSi_2$ films, can be observed in bulk samples of β-$FeSi_2$ and of AlB_{12} in the higher temperature region. However, the maximum values of the thermoelectric power are lower in these materials. A sharp increase in thermoelectric power (in this case) begins at temperatures corresponding to the energy of optical phonons. Thus, in order for the optical phonon drag effect to be effective, optical branches with rather strong dispersion (high group velocity) have to be present. A sufficiently strong electron-phonon interaction is necessary and the phonon-phonon scattering has to be rather weak.

All the considerations discussed above allow the search for prospective thermoelectric materials to be widened substantially to include the vast class of materials with low mobility.

26.5 Thermoelectric Properties Near the Mobility Edge

This section discusses the phenomena that take place when the Fermi level is situated on the border between band and localized states. In some important thermoelectric compounds a transition from band to hopping conductivity takes place at some position of the Fermi level (E_c). This means the existence of a mobility edge and the carrier localization at energies lower than E_c. Such a transition has been discovered in the solid solutions $MnSi_{1.7}$-$FeSi_2$[11] and in some other materials.[4] In such a system when the Fermi level is near or above E_c the transport is carried out mainly by delocalized carriers with $E > E_c$. Opposite to barrier structures[12] such a system is macroscopically homogeneous and the kinetics are more or less standard. The mobility edge appears at energies for which

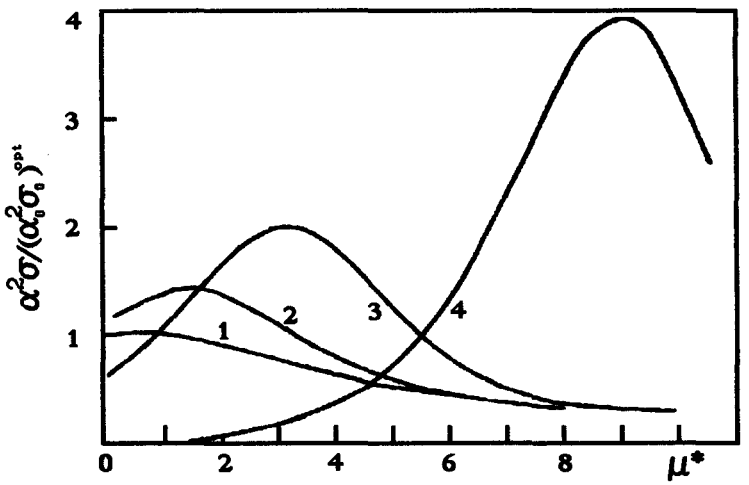

FIGURE 3 The dependencies of the ratio of $\alpha^2\sigma$ for a system with mobility edge to the optimal value of $\alpha_0^2\sigma_0$ for a standard parabolic band on the Fermi level at various x_c. x_c: 1–0, 2–2, 3–4, 4–10.

the Landau-Peierls parameter (kinetic equation parameter) $\hbar/\tau E_c \approx l/\lambda$ becomes smaller than unity, where τ is the carriers' relaxation time, l is their mean free path, and λ is their wavelength.

It is interesting to discuss qualitatively the possible thermoelectric advantages of such systems. The thermoelectric power value is generally determined by a difference of "hot" ($E > E_F$) and "cool" ($E < E_F$) carriers. In a standard one-band semiconductor at $E_F \approx kT$ the thermoelectric power is rather high ($\alpha \sim k/e$), but the electrical conductivity ($\sigma \propto p_F^2 l$) is small because of the small Fermi momentum (p_F). On the other hand, at higher E_F, σ is large, but α is small due to the compensation of the "hot" and "cool" carrier contributions. In both cases $\alpha^2\sigma$ is rather low. In systems with a mobility edge ($E_c > 0$), it is possible to establish the state when $E_F \approx E_c$ and E_c is high. Then σ is large, but cool carriers ($E < E_c$) have a low mobility and, therefore, $\alpha \sim k/e$.

Consider a kinetic model with vanishing diffusion near the mobility edge, so that at $E > E_c$, the standard band transport with $l > \lambda$ takes place and at $E < E_c$ the mobility is extremely low due to localization. Since carriers with $E > E_c$ give the main contribution to the electrical conductivity the following expression can be written:[13]

$$\frac{\sigma}{\sigma_0} = \frac{F_1(\mu^* - x_c) + x_c F_0(\mu^* - x_c)}{F_1(\mu^*)} \tag{20}$$

$$\frac{\alpha}{\alpha_0} = \frac{-(\mu^* - x_c) + \dfrac{F_2(\mu^* - x_c) + x_c F_1(\mu^* - x_c)}{F_1(\mu^* - x_c) + x_c F_0(\mu^* - x_c)}}{-\mu^* + \dfrac{F_2(\mu^*)}{F_1(\mu^*)}} \tag{21}$$

Here σ_0 and α_0 are the thermoelectric power and electrical conductivity of the standard band, $\mu^* = E_F/kT$, $x_c = E_c/kT$.

In Figure 3 the product $\alpha^2\sigma$ is shown as a function of μ^* for different x_c. It determines the transformed power of the material relative to the optimum value $\alpha_0^2\sigma_0$ for the standard band. This figure shows that the maximum $\alpha^2\sigma$ increases with x_c as does the Fermi momentum p_F and, therefore, the conductivity increases too. Notwithstanding the fact that thermoelectric power slightly decreases, the product $\alpha^2\sigma$ is high.

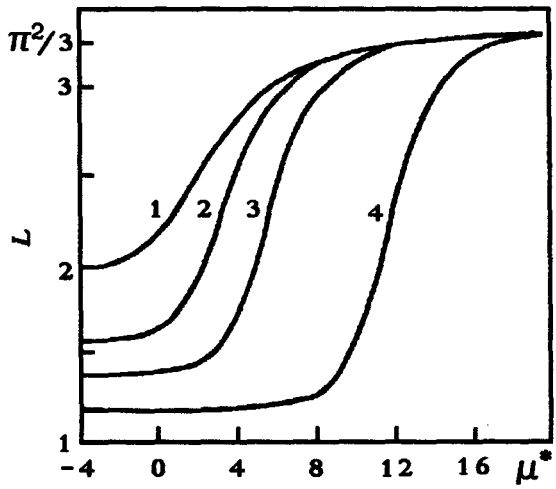

FIGURE 4 The dependencies of the Lorenz number L for a system with mobility edge on the Fermi level at various x_c. The designations are the same as on the Figure 3.

Consider the influence of the mobility edge on the electron component of the thermal conductivity. The ratio of the electron component of the thermal conductivity (λ_e) for a system with a mobility edge to that for standard band (λ_{e0}) can be represented as follows:[14]

$$\frac{\lambda_e}{\lambda_{e0}} = \frac{F_3(\mu_1^*) + (x_c - 2\mu_1^*)F_2(\mu_1^*) - (2x_c - \mu_1^*)\mu_1^* F_1(\mu_1^*) + x_c\mu_1^{*2}F_0(\mu_1^*)}{F_3(\mu_1^*) - \frac{F_2^2(\mu_1^*)}{F_1(\mu_1^*)}} - \frac{[F_2(\mu_1^*) + (x_c - \mu_1^*)F_1(\mu_1^*) - x_c\mu_1^* F_0(\mu_1^*)]^2}{[F_1(\mu_1^*) - x_c F_0(\mu_1^*)] \cdot \left[F_3(\mu_1^*) - \frac{F_2^2(\mu_1^*)}{F_1(\mu_1^*)}\right]} \quad (22)$$

where $\mu_1^* = \mu^* - x_c$. In this case the Lorentz number L [$L = (e/k)^2\chi_e/(\sigma T)$] for the system with a mobility edge is given by

$$L = \frac{\chi_e}{\chi_{e0}} \cdot \frac{F_1(\mu^*)}{F_1(\mu_1^*) + x_c F_0(\mu_1^*)} \cdot \left[\frac{F_3(\mu^*)}{F_1(\mu^*)} - \left(\frac{F_3(\mu^*)}{F_1(\mu^*)}\right)^2\right] \quad (23)$$

The dependence of the Lorentz number L on μ^* at various x_c, which was calculated using Equation 23, is displayed in Figure 4.

The figure shows that at $\mu^* > x_c$, L, as should be expected, aspires to $\pi^2/3$. The L (μ^*) dependence at $\mu^* \leq x_c$ is of practical interest. In this case $L < 2$, i.e., L is less than the minimum value in the case of a simple parabolic band. The result can be explained qualitatively because the mean energy of carriers decreases in transporting a unit charge. In this case the Lorentz number L decreases. Figure 4 shows that the practical realization of a system with a mobility edge can result in the essential decrease of the electron component of the thermal conductivity (λ_e) at the optimal position of the Fermi level. This decrease in λ_e and growth of the $\alpha^2\sigma$ parameter allows the thermoelectric efficiency of such systems to increase.

References

1. Berezin, A. A., Golikova, O. A., Zaitsev, V. K., Kazanin, M. M., Orlov, V. M., Stilbans, L. S., and Tkalenko, E. N., The electrical properties, reflection spectrum and conductivity mechanism of aluminium dodecaboride (α-AlB_{12}), *Fiz. Tverd. Tela*, 15, 952, 1973.
2. Zyrianov, P. S. and Klinger, M. I., *Quantum Theory of the Electronic Transport in Semiconductors*, Nauka, Moscow, 1976.

3. Luttinger, J. M., Theory of thermal transport coefficients, *Phys. Rev. A*, 135, 1505, 1964.
4. Mott, N. F. and Davis, E. A., *Electronic Processes in Noncrystalline Materials*, Clarendon Press, Oxford, U.K., 1971.
5. Čapek, V., Theory of the hopping thermoelectric effects in amorphous semiconductors and glasses, *Phys. Status Solidi (b)*, 57, 733, 1973.
6. Fritzche, H., A general expression for the thermoelectric power, *Solid State Commun.*, 9, 1813, 1971.
7. Emin, D., Thermoelectric power due to electronic hopping motion, *Phys. Rev. Lett.*, 35 (N13), 882, 1975.
8. Firsov, Yu. A., Ed., *Polarons*, Nauka, Moscow, 1975.
9. Matsubara, K., Koyanagi, T., and Takagi T., Amorphous $FeSi_2$ films as a new thermoelectric material prepared by ionized-cluster beam (ICB) technique, in *Proc. VIth Int. Conf. on Thermoelectric Energy Conversion*, Rao, K. R., Ed., University of Texas, Arlington, 1986, 1.

9a. Morimoto, K. and Takagi, T., U.S. Patent 4500742, 1984.

10. Birkholz, U. and Naegele, J., Optical investigations of the small polaron in β-$FeSi_2$, *Phys. Status Solidi*, 39, 197, 1970.
11. Zaitsev, V. K., Tarasov, V. K., and Adilbekov, A., The metal-nonmetal transition in compensated higher manganese silicide, *Fiz. Tverd. Tela*, 17, 581, 1975.
12. Bytensky, L. I., Gudkin, T. S., Iordanishwili, E. K., Kazmin, S. A., Kaidanov, V. I., Nemov, S. A., and Ravich, Yu. I., Potential barriers influence on thermoelectric properties of lead halcogenides, *Fiz. Tekh. Polyprovodn.*, 11, 1522, 1977.

12a. Moizhes, B. Ya. and Nemchinsky, V., Nontraditional methods of improvement of the thermoelectric figure-of-merit based on size effects, in *Proc. of the XIth Int. Conf. on Thermoelectrics*, Rao, K. R., Ed., University of Texas, Arlington, 1992, 232.

13. Zaitsev, V.K., Petrov, Yu. V., and Fedorov, M. I., The kinetic properties and thermoelectric parameters of partially disordered systems with mobilty edge, *Fiz. Tekh. Poluprovodn.* 13, 1359, 1979.
14. Zaitsev, V. K., Petrov, Yu. V., and Fedorov, M. I., Electron thermal conductivity in the systems with mobility edge, *Fiz. Tekh. Poluprovodn.*, 13, 205, 1979.

27

Semimetals as Materials for Thermoelectric Generators

M. I. Fedorov and
V. K. Zaitsev
A. F. Ioffe Physical Technical Institute
St. Petersburg, Russia

27.1 Introduction

The possibility of using semimetals as thermoelectric materials is considered in this chapter. Prospective methods of increasing the thermoelectric efficiency of semimetals based on a study of their kinetic and optical properties are discussed and cobalt monosilicide and the compound $Mn_4Al_3Si_5$ presented as examples.

It is generally thought that semimetals have no prospects as thermoelectric materials. Nevertheless, there are a few thermoelectric generator designs whose n-legs are made of a typical semimetal, cobalt monosilicide (CoSi),[1,2] for example, the "SNAP-11" generator.[2]

27.2 The Properties of CoSi

Physical-Chemical Properties

The thermoelectric properties of cobalt monosilicide have been studied by a number of workers.[3–6] Cobalt monosilicide has a cubic crystal structure (B20-type). Its space group[7] is $P2_13$-T^4, with a lattice spacing[8] of 4.445[8] and a density[9] of 6.58 g/cm^3. CoSi has an expansion coefficient Å of $(11.1 \pm 1.0) \cdot 10^{-6}$ K^{-1} and melts[10] at 1730 K. Monocrystals of cobalt monosilicide can easily be obtained by the Bridgman method.[6] This compound is mechanically and chemically strong and can be used in aggressive environments without any protection.

Cobalt monosilicide has a wide region of homogeneity (about 2 at.%). As shown in Reference 8 the thermoelectric power depends very strongly on composition. In this region stoichiometric CoSi exhibits a maximum absolute thermoelectric power of 83 μV/K at room temperature. It has been shown that stoichiometric CoSi also has a maximum value of electrical conductivity.[11] The low values of thermoelectric power indicate that most of the investigations of the kinetic properties of CoSi were carried out on nonstoichiometric CoSi. Even stoichiometric CoSi possesses some extra electrons with a carrier concentration about 10^{20} cm^{-3}.

The electron concentration can be changed by preparing solid solutions of CoSi with NiSi or FeSi.[5] FeSi and CoSi form a continuous series of solid solutions and up to 10 mol% of NiSi can

0-8493-0146-7/95/$0.00+$.50

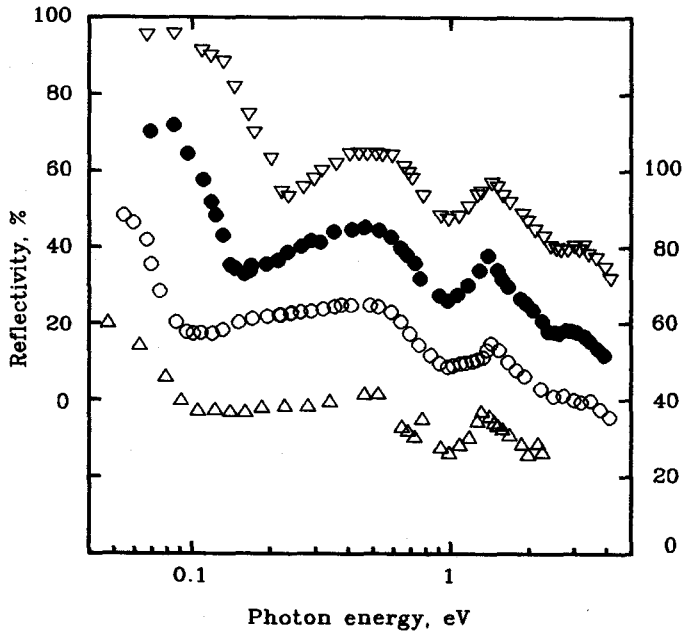

FIGURE 1 The reflectance spectra of CoSi (○), $Co_{0.93}Ni_{0.07}Si$ (▽), $Co_{0.95}Ni_{0.05}Si$ (●), and $Co_{0.99}Fe_{0.01}Si$ (△). The left scale corresponds to $Co_{0.93}Ni_{0.07}Si$ and the right one corresponds to CoSi. The $Co_{0.95}Ni_{0.05}Si$ spectrum is shifted down 20% relative to the left scale. The $Co_{0.99}Fe_{0.01}Si$ spectrum is shifted down 20% relative to the right scale.

be dissolved in CoSi. The electron concentration increases when cobalt atoms are replaced by nickel ones and decreases when cobalt atoms are replaced by iron. The properties of CoSi can be discussed in terms of the "rigid band" model. According to this model the solid solutions $Co_{1-x}Ni_xSi$ and $Co_{1-y}Fe_ySi$ have the same band structure. Only the Fermi level changes with a change in composition.

Optical Properties

Optical methods are widely used to study band structure. They enable the band structure parameters to be determined directly and in detail. Figure 1 shows the reflectance spectra of CoSi and its solid solutions with FeSi and NiSi. There are two main features on all these spectra: the plasma minimum and a peak at ≈1.5 eV. The plasma minimum is situated in the infrared wavelength region and is caused by reflection from free carriers. Free carrier gas parameters can be obtained from a mathematical analysis of this part of the spectra. The spectra were analyzed using the methods described in Reference 12. The conductivity effective mass and the relaxation times of electrons and holes were obtained by analyzing the plasma reflection. The CoSi density-of-state masses for the valence and conduction bands are $m_{dv} = 6m_e$ and $m_{dc} = 2m_e$, respectively. These were obtained from the dependences of the thermoelectric power on carrier concentration for solid solutions of $Co_{1-x}Fe_xSi$ and $Co_{1-y}Ni_ySi$. The positions of the valence and conduction bands extrema were determined by comparing the conductivity effective masses with those of the density-of-states. The modified Kramers-Kronig method[13] was used to analyze the high-frequency part of the spectra.

The Band Structure of CoSi

In Figure 2 a schematic of the band structure of CoSi that is based on the experimental study of its optical and kinetic properties is shown.[14,15] This schematic and the rigid band model are in good agreement with later calculations of the density-of-states of CoSi, FeSi, and NiSi.[16] Because

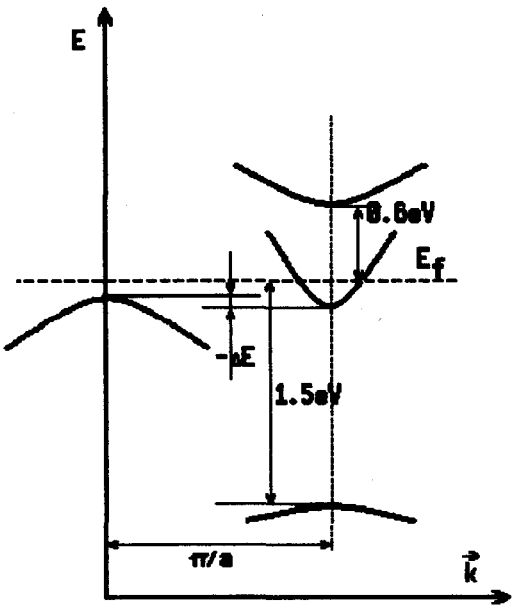

FIGURE 2 The band structure of CoSi.

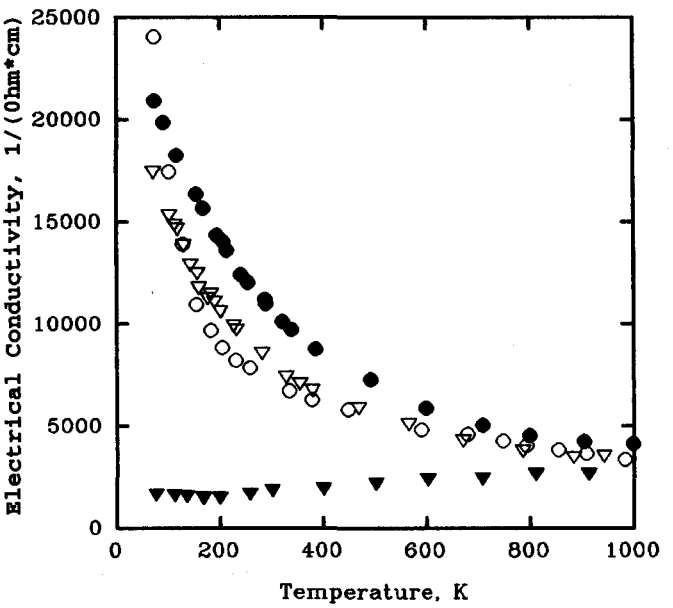

FIGURE 3 The conductivity of CoSi and its solid solutions with NiSi and FeSi. CoSi, ○; $Co_{0.96}Ni_{0.04}Si$, ●; $Co_{0.99}Ni_{0.01}Si$, ∇; and $Co_{0.95}Fe_{0.05}Si$, ▼.

the electron effective mass is much less than that of holes, the hole mobility is much less than that of electrons. As was mentioned above, in all samples of CoSi there are some extra electrons. In this case all the kinetic properties at low temperatures depend only on the concentration and mobility of electrons. At higher temperature when the concentration of holes becomes approximately equal to that of electrons both type of carriers are involved in kinetic processes. All the features described above are well illustrated by the plots presented in Figures 3 to 5. The temperature dependences of the figures-of-merit of CoSi and $Co_{0.96}Ni_{0.04}Si$ are also shown in Figure 5.

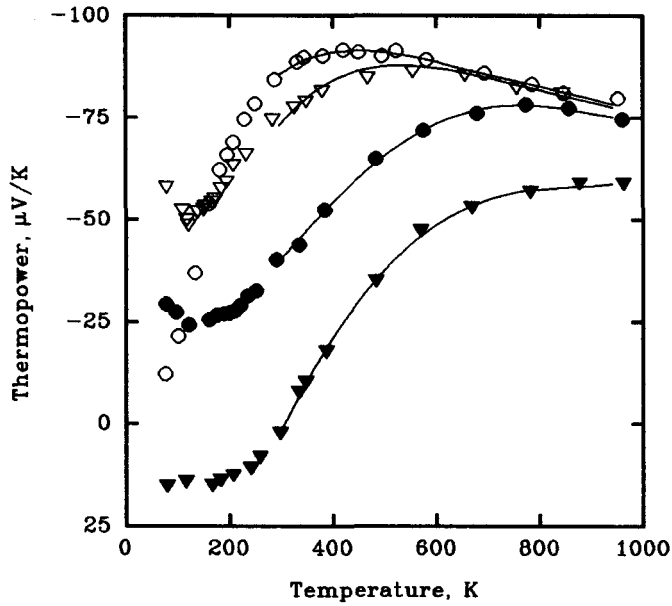

FIGURE 4 The thermopower of CoSi and its solid solutions with NiSi and FeSi. The designations are the same as in Figure 3.

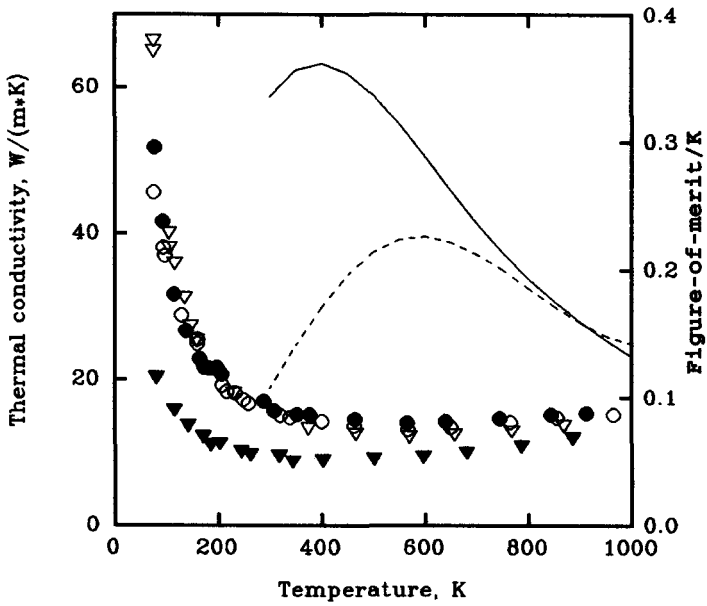

FIGURE 5 The figure-of-merit of CoSi (solid) and $Co_{0.96}Ni_{0.04}Si$ (dashed) and the thermal conductivity of CoSi and its solid solutions with NiSi and FeSi. The designations are the same as in Figure 3.

Suggesting the validity of the "rigid band" model for CoSi and its solid solutions with FeSi and NiSi, some band structure parameters were calculated.[15] These were the overlapping energy value at 0 K (ΔE), the overlapping temperature coefficient (β), the concentration of extra electrons (n_0), and the mobility ratio (b). It was assumed that all bands are parabolic, that acoustic phonon scattering is the principal scattering mechanism, and that all the parameters are independent of

Table 1. CoSi Energy Band Parameters

Composition	ΔE, meV	β, meV/K	$n_0 10^{27}$, m^{-3}	$b = u_p/u_n$
$Co_{0.95}Fe_{0.05}Si$	0	0.148	−0.94	0.119
CoSi	−41	0.085	0.31	0.156
$Co_{0.99}Ni_{0.01}Si$	−32	0.048	0.43	0.196
$Co_{0.96}Ni_{0.04}Si$	−30	0.026	1.02	0.286

Table 2. CoSi Heat Conduction Mechanisms

	Thermal Conductivity at 1000 K, W/(m · K)			
Composition	Total	Electronic	Bipolar Diffusion	Lattice
$Co_{0.95}Fe_{0.05}Si$	12.4	4.6	4.6	3.2
CoSi	14.6	6.0	5.7	2.9
$Co_{0.99}Ni_{0.01}Si$	14.9	6.5	6.9	1.5
$Co_{0.96}Ni_{0.04}Si$	15.0	7.8	6.1	1.1

temperature. The calculated temperature dependences of the thermoelectric power are shown in Figure 4 as solid lines. The calculated parameter values are collected in Table 1.

Heat Transport in CoSi

Based on the calculated parameters, the contributions of the various heat conduction mechanisms were evaluated[15] and are presented in Table 2.

27.3 The Possibilities of Increasing the Thermoelectric Efficiency

According to Table 2 the crystal lattice thermal conductivity at high temperature is about 20% of the total thermal conductivity. This means that a significant increase in thermoelectric efficiency cannot be achieved by decreasing the lattice thermal conductivity.

There are two ways to increase the thermoelectric efficiency of a semimetal. The first is to decrease the valence and conduction band overlapping. This can be achieved by deforming the crystal lattice. In Figure 6 the dependences of the thermoelectric power and electrical conductivity of the solid solution $Co_{0.95}Fe_{0.05}Si$ on the applied hydrostatic pressure are shown. This plot indicates that a real possibility exists of increasing the thermoelectric efficiency of semimetals.[17] In practice such deformation can be obtained by producing doped material with an impurity the atomic size of which differs considerably from that of the host atoms.

Another way is to design a structure that will strongly scatter one type of carrier. It can be a barrier structure[18] or a compound in which carriers of one sign are strongly scattered. Such a situation is probably realized in the compound $Mn_4Al_3Si_5$.[19] This compound is not an optimized thermoelectric material but it may exhibit strong interband scattering.

27.4 The Properties of $Mn_4Al_3Si_5$

In Figures 7 and 8 the thermoelectric parameters and Hall coefficient measured on polycrystalline samples of $Mn_4Al_3Si_5$ are displayed. The temperature dependences of the electrical conductivity, thermoelectric power, and thermal conductivity are similar to those of CoSi. However, the sign of the Hall coefficient is opposite to that of the thermoelectric power. As the material is weakly paramagnetic there are two main possible explanations.

The first supposes that there are both electrons and holes involved in kinetic processes. In this case a combination of their concentrations and mobilities can cause the different signs of the thermoelectric power and Hall coefficient. However, the temperature range of the existence of different signs cannot be as wide as shown in Figure 8.

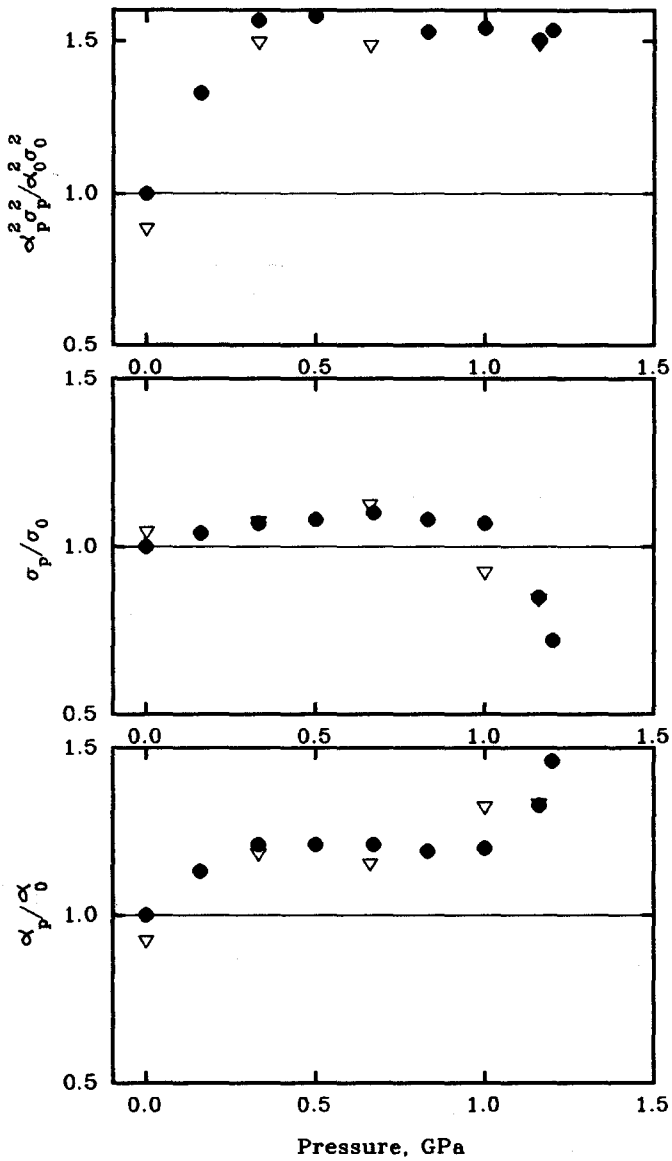

FIGURE 6 Dependences of $Co_{0.95}Fe_{0.05}Si$ thermopower (α), conductivity (σ), and power parameter ($\alpha^2\sigma$) on hydrostatic pressure. ●, increase of pressure; ▽, decrease of pressure.

The second explanation is that there are two types of holes and strong interband scattering. This possibility has been discussed in detail in Reference 19. The temperature dependences of the thermoelectric power, Hall coefficient, and electrical conductivity were calculated as well as the partial thermal conductivities. The two heat transport mechanisms—free carrier and bipolar diffusion—were taken into account.

The calculated temperature dependence of the Hall coefficient and thermoelectric power have opposite signs over a very wide temperature range, as shown in Figure 8. However, the calculated values of the Hall coefficient are a hundred times larger than the experimental ones. This discrepancy cannot be caused by a simple mechanism. One of the reasons may be possible anisotropy of the material as analogous materials (higher manganese silicide [HMS] and chromium disilicide) have very anisotropic kinetic properties.[20]

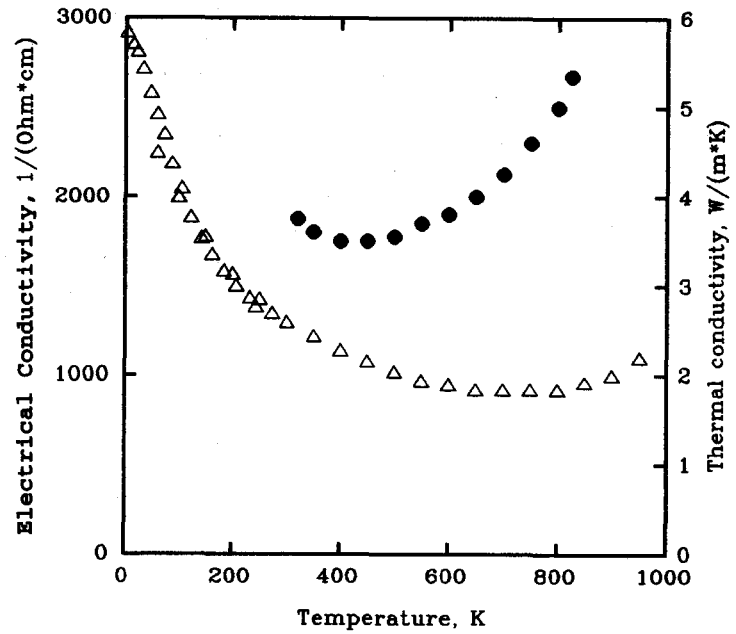

FIGURE 7 The conductivity (△) and thermal conductivity (●) of $Mn_4Al_3Si_5$.

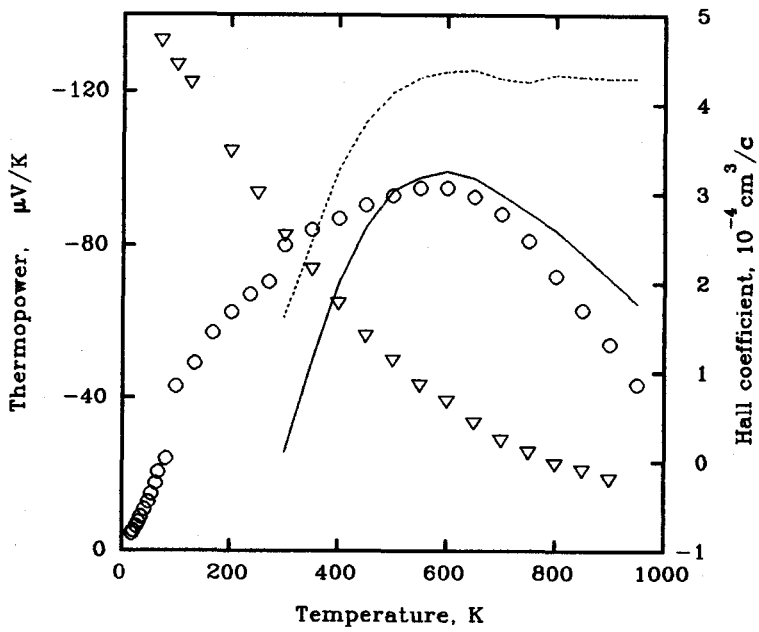

FIGURE 8 The thermopower (▽) and Hall coefficient (○) of $Mn_4Al_3Si_5$. The curves are calculated values of thermopower (solid) and Hall coefficient multiplied by 100 (dashed).

27.5 Semimetals as the Materials for Passive Legs

There is another possible use of semimetals in thermoelectric devices without increasing their efficiency. If two materials with different efficiencies are made into a thermocouple the less efficient leg is referred to as passive. Semimetals are very good materials for use as passive legs of thermoelements.

Consider two materials having equal thermoelectric efficiencies—a semiconductor and a semimetal. In this case the carrier concentration of the semimetal will be higher than that of the semiconductor and therefore the semimetal has the larger ratio of electrical to thermal conductivity. The amount of waste heat passing through the passive leg due to lattice thermal conductivity will be less in the semimetal than in the semiconductor. Consequently the couple with a semimetallic passive leg will be more effective than that with a semiconductor one. Moreover, as semimetals have very high electrical and thermal conductivities, the cross section of the semimetallic leg is much less than that of the semiconductor leg. Consequently the total thermoelement mass will be much less than that with two semiconductor legs. These advantages, together with the possibility of improving their thermoelectric parameters, make semimetals prospective thermoelectric materials.

References

1. Tokushima, T., Nishida, I., Sakata, K., and Sakata, T., The $CrSi_2$-CoSi thermomodule and its applications, *J. Mater. Sci.*, 4, 978, 1969.
2. Corliss, W. R. and Harvey, D. G., *Radioisotopic Power Generation*, New York, 1964.
3. Asanabe, S., Shinoda, D., and Sasaki, Y., Semi-metallic properties of $Co_{1-x}Fe_xSi$ solid solution, *Phys. Rev.*, 134, 774, 1964.
4. Mayer, S. E. and Mlavsky, A. L., Thermal and electrical properties of some silicides, in *Properties of Elemental and Compound Semiconductors*, 1960, 261.
5. McNeil, D. J. and Ware, R. M., Thermoelectric power and resistivity of some transition metal monosilicides, *Br. J. Appl. Phys.*, 15, 1517, 1964.
6. Nikitin, E. N., Tamarin, P. V., and Tarasov, V. I., Thermal and electrical properties of cobalt monosilicide between 4.2 and 1600K, *Sov. Phys. Solid State*, 11, 2002, 1970.
7. Boren, B., *Arkiv for kemi, Mineralogi och Geologi*, 11A, 2, 1933.
8. Zelenin, L. P., Sidorenko, F. A., and Gel'd, P. V., Structural peculiarities of ε-phase in CoSi system, *Izv. Vyssh. Uchebn. Zaved. Tsvetn. Metall.*, 7, 146, 1964.
9. Zhuravlev, N. N. and Stepanova, A. A., X-ray diffraction studies of thermal expansion coefficients of manganese and cobalt monosilicides, *At. Energ.*, 13, 183, 1962.
10. Hashimoto, U., *Nippon Kinzoku Gakkai-Shi*, 1, 135, 1937.
11. Vedernikov, M. V., Engalychev, A. E., Zaitsev, V. K., Ordin, S. V., and Fedorov, M. I., Thermoelectric properties of material based on higher silicide of manganese and cobalt monosilicide, in *Proc. of the VIIth International Conference on Thermoelectric Energy Conversion*, Rao, K. R., Ed., University of Texas, Arlington, 1988, 150.
12. Zaitsev, V. K., Fedorov, M. I., Tarasov, V. I., and Adilbekov, A., Plasma reflection from CoSi and $Co_{1-x}Ni_xSi$ solid solutions, *Sov. Phys. Solid State*, 19, 996, 1977.
13. Zaitsev, V. K. and Fedorov, M. I., On the phase correction in the Kramers-Kronig Analysis, *Opt. Spectrosc.*, 44, 1186, 1978.
14. Zaitsev, V. K., Fedorov, M. I., Ordin, S. V., and Tarasov, V. I., Plasma reflection from CoSi in the temperature range 80–300K, *Sov. Phys. Solid State*, 20, 890, 1978.
15. Alekseeva, G. T., Zaitsev, V. K., Petrov, A. V., Tarasov, V. I., and Fedorov, M. I., Electrical properties and thermal conductivity of cobalt monosilicide and the solid solutions $Co_{1-x}Fe_xSi$ and $Co_{1-x}Ni_xSi$, *Sov. Phys. Solid State*, 23, 1685, 1981.
16. Vinokurova, L. I., Vlasov, A. V., and Kulatov, E. T., Electronic band structure of the transition metal silicides, in *Silicides* (Proc. IOFAN, v.32) Nauka, Moscow, 1991, 26.
17. Zaitsev, V. K., Fedorov, M. I., and Zyuzin, A. Yu., About thermoelectric efficiency of the materials based on cobalt monosilicide, *Geliotekhnika*, N4, 18, 1981.
18. Bytensky, L. I., Gudkin, T. S., Iordanishwili, E. K., Kazmin, S. A., Kaidanov, V. I., Nemov, S. A., and Ravich, Yu. I., Potential barriers influence on thermoelectric properties of lead halcogenides, *Fiz. Tekh. Polyprovodn.*, 11, 1522, 1977.
19. Fedorov, M. I., Kalyazin, A. E., Zaitsev, V. K., and Engalychev, A. E., Transport phenomena in $MnAl_{0.75}Si_{1.25}$, *Sov. Phys. Solid State*, 31, 1079, 1989.
20. Anatychuk, L. I., *Thermoelements and Thermoelectric Devices*, Naukova dumka, Kiev, 1979, 278.

28

Silicon Germanium

Cronin B. Vining
Consultant
Webster Groves, Missouri, U.S.A.

28.1 Abstract

This chapter summarizes the preparation techniques and material properties required for practical applications of silicon germanium alloys. The relationship between the phase diagram and choice of preparation technique is discussed and two proven methods, zone leveling and hot pressing, are described. Key physical properties such as thermal expansion and mechanical strength are summarized and trends in thermoelectric properties as functions of composition, doping level, and temperature are illustrated. Representative thermoelectric property data are presented in tabular form and the critical degradation mechanisms of sublimation and dopant precipitation are discussed. Finally, the agreement between modern theory and proven experimental results is presented.

28.2 Introduction

Silicon germanium alloys (SiGe) were first used in space in the SNAP-10A nuclear reactor and have been the exclusive choice for radioisotope thermoelectric generators (RTGs) launched by the U.S. since 1976.[1] Primary considerations for space power applications are reliability and high operating temperatures to take advantage of the T^4 dependence of radiator heat rejection rates. In addition to having attractive thermoelectric and physical properties, SiGe devices can operate at temperatures up to about 1300 K without significant degradation. A number of reviews of the properties of SiGe alloys are available[2–6] and the principles of generator design and fabrication are discussed elsewhere in this handbook. This chapter will therefore emphasize aspects of SiGe required for practical applications.

28.3 Preparation

Although silicon and germanium are completely miscible in both the liquid and solid states, a large separation exists between the liquidus and the solidus, which complicates the preparation of homogeneous solids. Figure 1 illustrates solidification of $Si_{0.8}Ge_{0.2}$ (C_S) from a liquid with composition $Si_{0.545}Ge_{0.455}$(C_L). Upon cooling, the first solid deposited is enriched in Si, compared to the melt, and as a result cast ingots typically exhibit severe alloy segregation. Preparation of homogeneous solids requires either a method to maintain the composition of the melt during

0-8493-0146-7/95/$0.00+$.50

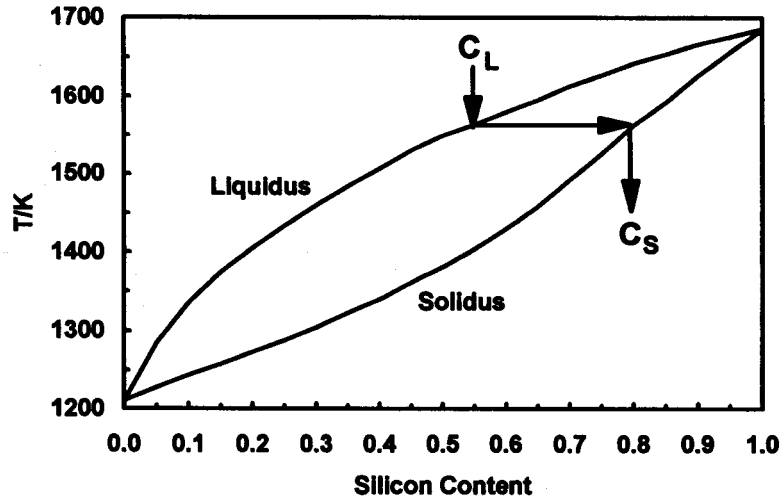

FIGURE 1 Si-Ge phase diagram indicating solidification of $Si_{0.8}Ge_{0.2}$. (Data from Reference 7.)

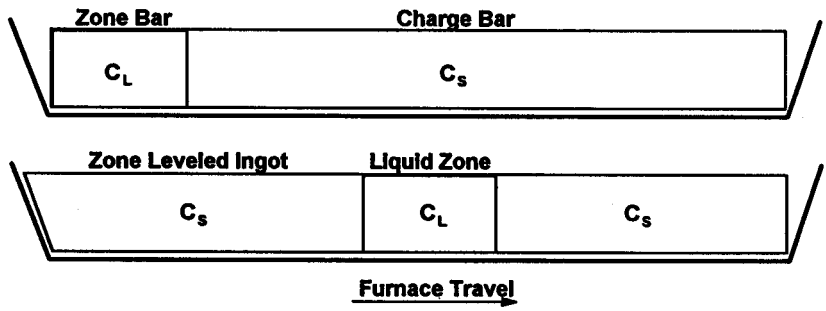

FIGURE 2 Schematic of the zone leveling procedure showing the initial arrangement of the materials (above) and the situation during zoning (below).[2]

solidification or some process to homogenize the solid phase. A variety of methods employing either strategy are available and two successful variants are described in the following sections.

While the effect of each parameter will not be discussed in detail here, it should be emphasized that variations in many process parameters will significantly affect the properties of the resulting material. Accurate process control is therefore critical to preparing a reproducible product. Porosity, density, thermoelectric power, and electrical resistivity measurements are relatively simple to perform and provide a great deal of quality control information. Porosity provides a sensitive measure of densification and density is a reliable indicator of composition. Doping level may be monitored by measuring the thermoelectric power at room temperature and electrical resistivity provides a sensitive measure of overall sample quality.

Zone Leveling

The zone leveling method was used for the first space application of SiGe thermoelements in the SNAP-10A nuclear reactor.[1] The procedure is illustrated schematically in Figure 2. A charge bar is prepared by any convenient method (e.g., casting, powder metallurgy) with the desired final composition (C_S). A zone bar is similarly prepared with a composition (C_L) chosen to have a freezing point at the same temperature as the melting point of the charge bar, as indicated in Figure 1. The zone bar is then heated to the melting point of the charge bar and the resulting liquid zone caused to traverse the length of the charge bar. As the liquid zone moves to the right, the charge bar is consumed at the leading edge of the liquid zone and a homogeneous ingot of SiGe

freezes out of the trailing edge. To prevent consitutional supercooling, growth rates typically cannot exceed about 0.5 to 1 mm/h.

Phosphorus is the preferred dopant for n-type materials and boron is the only p-type dopant sufficiently soluble for thermoelectric applications. Either of these dopants may be added to the charge and zone bars. When preparing n-type materials it is desirable to control the vapor pressure of phosphorus over the liquid zone to achieve the high doping levels required for optimum figure-of-merit (Z). With proper choice of conditions zone leveling can provide high-quality polycrystalline materials with transport properties indistinguishable from single crystals. The primary disadvantage of this technique is the long time required to prepare samples.

Hot-Pressing

Today, powder metallurgical methods are generally preferred for production of significant quantities of SiGe, primarily because large, good-quality samples can be prepared from powders in a single day. Also, relatively large variations of preparation conditions can be tolerated while still producing satisfactory thermoelectric properties.[8] Hot-pressed SiGe has been used in RTGs aboard the LES 8, LES 9, Voyager I, Voyager II, Galileo, and Ulysses spacecrafts. The following preparation procedure is representative of, although not identical to, the procedure used to prepare SiGe for RTGs.

Typically, a 4-to-1 atomic ratio of silicon and germanium is induction melted in fused silica crucibles under vacuum. For p-type materials 0.08 wt% boron is placed in the crucible before heating and for n-type materials 0.55 wt% phosphorus is added directly to the melt to minimize losses due to vaporization. The melt is cast into a water-cooled copper mold and mechanically pulverized to −80 mesh powder. A planetary ball mill may be used to further reduce the median particle diameter to 2–10 μm, which improves both the homogeneity and strength of the final compact. The powders are placed in dies and molds made of an alloy of titanium, zirconium, and molybdenum (TZM), lightly coated with graphite to reduce friction during compact ejection. Pressure sintering is performed under 180 MPa of pressure, applied after reaching 1513 K. Pressure is released after 30 min when the compact is ejected from the die and allowed to cool. SiGe compacts 5.08 cm in diameter and 2.54 cm thick have been routinely prepared in this manner and larger sizes have occasionally been produced.

28.4 Properties

A wide variety of physical, thermal, and thermoelectric properties are required for the design of reliable thermoelectric devices. The most essential properties are summarized in the following sections.

Physical

Thermal expansion and mechanical strength considerations are critical to the design of thermoelectric devices and some of the more important properties for SiGe are summarized in Table 1. The greatest stresses often arise when the device cools following the final high-temperature fabrication processes. Differential thermal expansion at the joints between dissimilar materials results in stresses that can easily exceed the maximum stress of the thermoelectric material. As is typical of ceramic materials, SiGe is three to four times stronger in compression than in tension. It is therefore preferred that the materials in contact with SiGe have a somewhat larger thermal expansion, so that they contract more than SiGe on cooling and keep the SiGe in compression rather than under tension. It is interesting to note that p-type SiGe can typically withstand greater stress than n-type SiGe.

Thermoelectric

This section provides an overview of some of the more important effects of composition, temperature, doping level, and dopant type on the thermoelectric properties of SiGe. Figure 3 illustrates the composition dependence of the dimensionless figure-of-merit ZT for silicon-rich alloys.

Table 1. Typical Physical Properties of Hot-Pressed Silicon Germanium

	T (K)	Units	p-Type $Si_{0.8}Ge_{0.2}$	n-Type $Si_{0.8}Ge_{0.2}$
Density	300	g/cm^3	2.99	2.99
Thermal expansion	300	10^{-6}/K	3.98	4.20
	600	10^{-6}/K	4.26	4.43
	900	10^{-6}/K	4.55	4.66
	1200	10^{-6}/K	4.84	4.89
	1400	10^{-6}/K	5.03	5.05
Porosity			1%	1%
Dopant			Boron	Phosphorus
Nominal composition		at.%	0.23	0.59
Compressive strength[a]				
Maximum stress	300	MPa (±20%)	653	473
Maximum strain	300	% (±25%)	0.42	0.37
Modulus	300	GPa (±7%)	154	129
Tensile strength[b]				
Maximum stress	300	MPa (±20%)	201	129
	875	MPa (±20%)	292	143
	1375	MPa (±20%)	310	182[c]
Maximum strain	300	% (±25%)	0.15	0.11
	875	% (±25%)	0.20	0.10
	1375	% (±25%)	0.49	>0.69[c]
Modulus	300	GPa (±7%)	137	145
	875	GPa (±7%)	151	165
	1375	GPa (±7%)	103	114[c]

Test methods: [a]Cylinders; [b]4-point flexure; [c]Two of three samples tested did not fail due to high ductility at 1375 K.

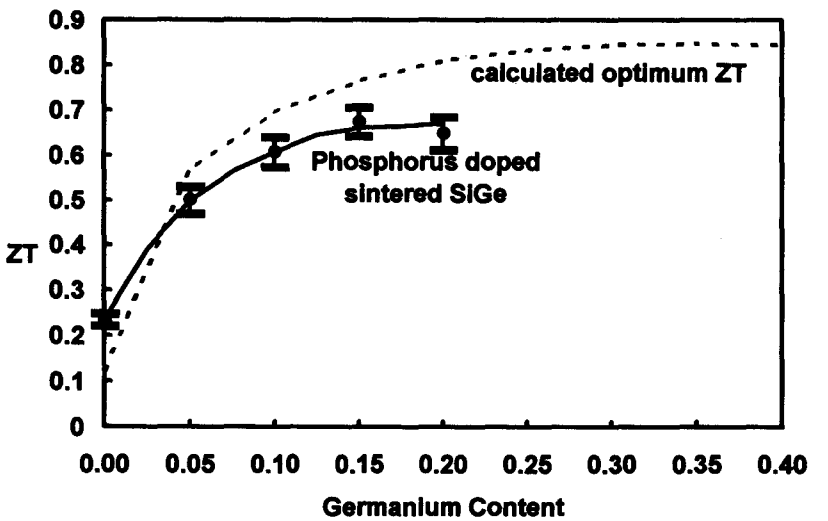

FIGURE 3 Dimensionless figure-of-merit averaged from 575 to 1275 K. The points are experimental results on sintered n-type Si-Ge with 2 at.% phosphorus[9] and the dashed line is the theoretical maximum ZT calculated using the model described in Reference 10.

The addition of germanium to silicon increases ZT to technically useful values, primarily due to increased scattering of phonons associated with the random distribution of Si and Ge atoms in the alloy. Except with very near pure silicon, ZT is seen to be relatively insensitive to composition, and for this reason sintered materials can yield good performance even when homogenization is incomplete.

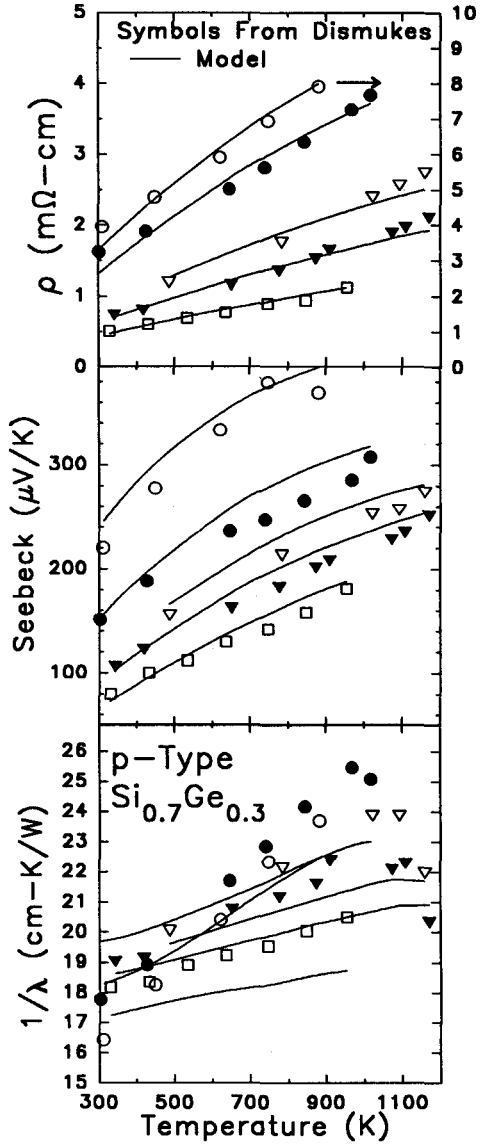

FIGURE 4 Resistivity, Seebeck coefficient, and thermal conductivity for p-type $Si_{0.7}Ge_{0.3}$. The points are experimental results[11] and the lines are calculated.[10]

Figure 4 illustrates the temperature dependence of the thermoelectric properties for boron-doped, zone leveled $Si_{0.7}Ge_{0.3}$ with several different doping levels. At these doping levels, the electrical resistivity and Seebeck coefficient generally increase with increasing temperature, which is more characteristic of metals than semiconductors. Up to about 1000 K, the thermal resistivity also increases with temperature, a behavior typical of electrical insulators. As temperatures are further increased, the Seebeck coefficient, electrical resistivity, and thermal resistivity will all decrease with increasing temperature due to the thermal excitation of charge carriers. Another effect, associated with the solubility and diffusion characteristics of the dopants, will be discussed below.

Note that while the individual properties vary strongly with doping level, as illustrated in Figure 4, the figure-of-merit is relatively insensitive to doping level in the vicinity of the optimum doping level, as illustrated in Figure 5 for zone leveled n-type $Si_{0.7}Ge_{0.3}$. The precise value of the optimum doping level varies somewhat with composition and temperature, but is usually in the range of $1–3 \times 10^{20}$ cm^{-3} for n-type SiGe and $2–4 \times 10^{20}$ cm^{-3} for p-type SiGe (not shown).

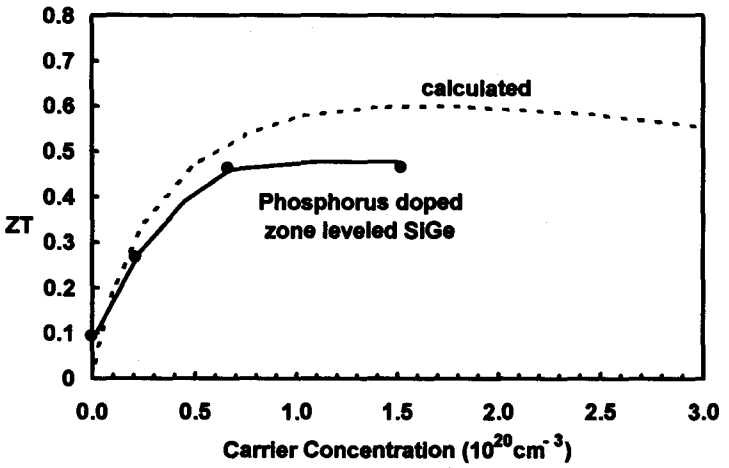

FIGURE 5 Dimensionless figure-of-merit (averaged from 300 to 1000 K) for zone leveled n-type $Si_{0.7}Ge_{0.3}$[11] and the dashed line is calculated using the model described in Reference 10.

Table 2. Typical Thermoelectric Properties for p-Type Silicon Germanium

T (K)	Electrical Resistivity (10^{-5} Ω-m)	Seebeck Coefficient (μV/K)	Thermal Conductivity (W/m-K)	Heat Capacity (J/g-K)	ZT unitless
300	1.14	121			
400	1.32	144	4.80	0.647	0.131
500	1.51	161	4.70	0.649	0.184
600	1.71	176	4.57	0.658	0.237
700	1.93	189	4.41	0.672	0.295
800	2.16	203	4.25	0.687	0.359
900	2.41	216	4.12	0.703	0.423
1000	2.68	228	4.07	0.719	0.478
1100	2.96	237	4.14	0.736	0.505
1200	3.19	240	4.38	0.754	0.501
1300	3.26	233	4.84	0.772	0.446

Achieving precisely optimum ZT values can be rather difficult and it should be emphasized that almost any variation in processing will affect the individual thermoelectric properties. But often reproducibility is more important than the absolute maximum ZT and satisfactory results can generally be achieved using preparation and process monitoring methods such as outlined above. Tables 2 and 3 summarize typical thermoelectric properties for p-type and n-type sintered SiGe.

Degradation Modes

SiGe thermocouples have accumulated over 250 million device hours in space applications without a single known thermoelectric failure. This remarkable success has been achieved by following conservative design principles and paying close attention to the possible failure mechanisms and degradation modes. This section describes some of the more important lifetime-limiting degradation modes for SiGe alloys.

Sublimation—Sublimation is one of the primary degradation mechanisms for a high-temperature SiGe thermoelectric device. SiGe sublimation degrades performance in at least two ways. First, SiGe deposits on the surroundings can result in either thermal or electrical shorts around the thermoelectric device. Second, continued sublimation can eventually erode the thermoelectric device to the point of electrical open circuit and/or mechanical failure. Figure 6 illustrates steady-state loss rates for uncoated SiGe and for SiGe coated with Si_3N_4 which, combined with a knowledge of the exposed surface area and temperature profile of the device, allows estimates of erosion

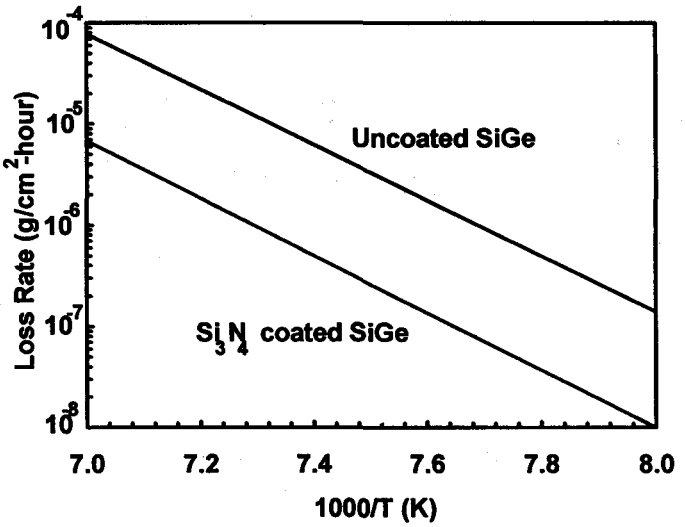

FIGURE 6 Material loss rates for $Si_{0.78}Ge_{0.22}$ with and without a 1200-nm coating of Si_3N_4. (Data from Reference 13.)

Table 3. Typical Thermoelectric Properties for n-Type Silicon Germanium

T (K)	Electrical Resistivity (10^{-5} Ω-m)	Seebeck Coefficient (μV/K)	Thermal Conductivity (W/m-K)	Heat Capacity (J/g-K)	ZT unitless
300	0.85	−108			
400	1.01	−136	4.45	0.647	0.165
500	1.17	−165	4.31	0.649	0.269
600	1.36	−190	4.19	0.658	0.380
700	1.61	−213	4.08	0.672	0.486
800	1.86	−233	3.99	0.687	0.583
900	2.06	−247	3.93	0.703	0.679
1000	2.11	−253	3.93	0.719	0.775
1100	1.97	−250	4.01	0.736	0.870
1200	1.78	−242	4.20	0.754	0.938
1300	1.91	−243	4.53	0.772	0.890

rates. SiGe devices for space applications have typically been coated with Si_3N_4 and wrapped with a quartz yarn.

Dopant precipitation—SiGe thermoelectric materials are intentionally supersaturated with dopants in order to achieve the highest possible figure-of-merit. Therefore, under most operating conditions (below about 1400 K), dopants will tend to precipitate from solid solution forming localized precipitates and decreasing the carrier concentration within the thermoelectric material. For practical purposes this effect is well described by the conventional Lifshitz-Slyozov model. Particles smaller than a critical radius (the size of which depends on temperature) tend to dissolve, which can actually result in a temporary increase in the carrier concentration with time until the smallest particles are consumed. Larger precipitates tend to grow in size, at a rate which is determined by the diffusion constant of the dopant. For phosphorus-doped SiGe, precipitation rates are most pronounced between about 600 and 900 K, as illustrated by the changes in the electrical resistivity shown in Figure 7. It should be emphasized that Figure 7 illustrates the time dependence of material held at a fixed temperature. Measurements performed as a function of temperature on any particular sample would appear very different. At lower temperatures the degree of supersaturation may be very large, but because diffusion is so slow that precipitation occurs at a negligible rate and the resistivity increases only slowly with time. At higher temperatures diffusion is very

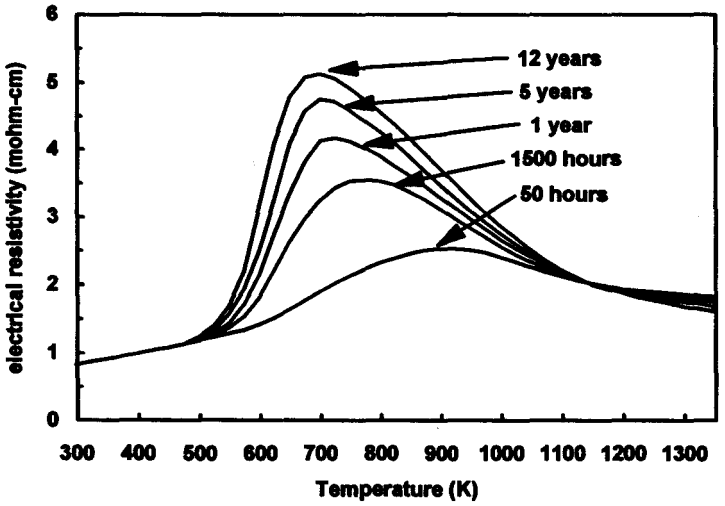

FIGURE 7 Estimated time dependence of the electrical resistivity of n-type $Si_{0.8}Ge_{0.2}$ for samples held isothermally at the indicated temperatures.[14]

fast, but dopants are more soluble and again precipitation is relatively slow. Indeed, phosphorus diffusion is so fast at high temperatures that the peak typically observed in the resistivity of n-type SiGe at about 1000 K (see the 50-h curve in Figure 7) is due to precipitated phosphorus dissolving into the SiGe matrix and increasing the carrier concentration during the measurement. This effect is sometimes misinterpreted as the onset of excitation of minority carriers, which is a physically very distinct effect.

Fortunately for practical applications, the effect of dopant precipitation on the Seebeck coefficient and thermal conductivity is smaller than the effect on the electrical resistivity, and the overall effect on ZT is smaller still due to compensatory changes in the individual properties. Also, the effects are less pronounced in boron-doped materials because boron is both more soluble and has a lower diffusion rate compared to phosphorus.

28.5 Theory

The theory of the thermoelectric properties of SiGe alloys is beyond the scope of this chapter, but may be described as a specialization of the general theory of semiconductors. Basically, the electrical and thermal properties of SiGe are considered to arise from electrons, holes, and phonons simultaneously contained within the solid. Heat and electrical currents are attributed to the motion of these particles in response to applied forces, in the form of thermal or electrical gradients. Electrons and holes transport both electrical charge and heat through the solid, while phonons (which are nothing more than wave-like oscillations of the atoms about their equilibrium positions) transport only heat. Figure 4 shows an example of the excellent agreement that has been achieved between this type of microscopic theory and experimental results.

28.6 Summary

Key aspects of SiGe preparation have been presented and typical material properties critical to the design of practical thermoelectric devices have been summarized. While to date SiGe has been used almost exclusively for space applications, the mature basis of the technology and attractive physical and chemical properties summarized here make this material a viable alternative for any application where reliable, long-term performance in a demanding high-temperature environment is required.

References

1. Wood, C., Materials for thermoelectric energy conversion, *Rep. Prog. Phys.*, 51, 459, 1988.
2. Rosi, F. D., Thermoelectricity and thermoelectric power generation, *Solid-State Electron.*, 11, 833, 1968.
3. Bhandari, C. M. and Rowe, D. M., Silicon-germanium alloys as high-temperature thermoelectric materials, 21, 219, 1980.
4. Rowe, D. M., Recent advances in silicon-germanium alloy technology and an assessment of the problems of building the modules for a radioisotope thermoelectric generator, *J. Power Sources*, 19, 247, 1987.
5. Vining, C. and Fleurial, J. F., Silicon germanium—an overview of recent developments, in *Proc. of the Tenth Int. Conf. on Thermoelectrics*, Rowe, D. M., Ed., Babrow Press, Cardiff, 1991, 1.
6. Slack, G. A. and Hussain, M. A., The maximum possible conversion efficiency of silicon-germanium thermoelectric generators, *J. Appl. Phys.*, 70, 2694, 1991.
7. Bergman, C., Chastel, R., and Castanet, R., Thermodynamic investigation on the Si-Ge binary system by calorimetry and Knudsen cell mass spectroscopy, *J. Phase Equilibria*, 13, 113, 1992.
8. Vining, C. B., Laskow, W., Hanson, J. O., Van der Beck, R. R., and Gorsuch, P. D., Thermoelectric properties of pressure-sintered $Si_{0.8}Ge_{0.2}$ thermoelectric alloys, *J. Appl. Phys.*, 69, 4333, 1991.
9. Gorsuch, P. D., Nakahara, J., Slack, G. A., Feingold, E., and Vining, C. B., Development of Improved Thermoelectric Materials for Space Nuclear Power Systems, Final report for contract no. DE-AC01-84NE-32123, U.S. Department of Energy, Washington, D.C., 1989.
10. Vining, C. B., A model for the high-temperature transport properties of heavily doped n-type silicon-germanium alloys, *J. Appl. Phys.*, 69, 331, 1991.
11. Dismukes, J. P., Ekstrom, L., Steigmeier, E. F., Kudman, I., and Beers, D. S., Thermal and electrical properties of heavily doped Ge-Si alloys up to 1300 K, *J. Appl. Phys.*, 35, 2899, 1964.
12. Vining, C. B., A model for the high-temperature transport properties of heavily doped p-type silicon-germanium alloys, *Modern Perspectives on Thermoelectrics and Related Materials*, Materials Research Society Symp. Proc. Vol. 234, Allred, D. D., Vining, C. B., and Slack, G. A., Eds., Materials Research Society, Pittsburgh, Pennsylvania, 1991, 95.
13. Shields, V. and Noon, L., Sublimation measurements and analysis of high temperature thermoelectric materials and devices, in *Proc. of the 18th Intersociety Energy Conversion Engineering Conference*, Vol. 1, American Institute of Chemical Engineers, New York, 1983, 235.
14. Raag, V., The time and temperature dependence of the thermoelectric properties of silicon germanium alloys, in *Proc. of the 10th Intersociety Energy Conversion Engineering Conference*, Institute of Electrical and Electronics Engineers, New York, 1975, 156.

29

Rare Earth Compounds

B. J. Beaudry and
K. A. Gschneidner, Jr.
Ames Laboratory,
Iowa State University
Ames, Iowa, U.S.A.

29.1 Introduction

With the development of the ion exchange technique for the separation and purification of the rare earth elements during World War II, fairly pure rare earths became readily available by the mid-1950s. Because of this availability, a number of groups of scientists made survey studies of the electrical, magnetic, optical, thermal, and mechanical properties of many rare earth materials. One group in particular from Battelle Memorial Institute concentrated on the electrical behavior of semiconducting rare earth materials,[1,2] while most of the other pioneering groups concentrated on either the magnetic or the optical behaviors of rare earth materials. As a result of the Battelle studies, it became clear that some of the rare earth selenides and tellurides had interesting thermoelectric properties; however, it took about another 20 years before much effort was focused on these semiconducting materials. A few other rare earth compounds formed with the nonmetallic elements have also been examined for their semiconducting behavior, but not nearly as much effort has been devoted to these materials as has been placed on the chalcogenide compounds. For this reason, the chalcogenides will be discussed first, followed by the pnictides, oxides, and silicides.

29.2 Chalcogenides

Binary Systems

After their initial study of the electrical properties of rare earth compounds,[1] the Battelle group made a more complete study, including thermoelectric properties of the rare earth selenides and tellurides.[2] These studies also included the rare earth compounds of arsenic and antimony, which will be discussed below in the pnictide section. By this time, the use of thermoelectric generators for space applications was established, and the possibility of developing new and better thermoelectric materials was a goal of many researchers. Thus, Seebeck coefficient and resistivity were measured and reported for a number of compounds. These studies indicated that the rare earth selenide and telluride R_3X_4 to R_2X_3 solid solution region "showed distinct promise as thermoelectric materials for power generation". The results of studies on binary rare earth chalcogenides were summarized in reviews by Gschneidner et al.[3] and Wood.[4]

Rare earth-chalcogen binary systems generally contain the compounds RX, R_3X_4, R_2X_3, and RX_2, where R represents a rare-earth metal and X represents S, Se, or Te. A typical phase diagram

0-8493-0146-7/95/$0.00+$.50

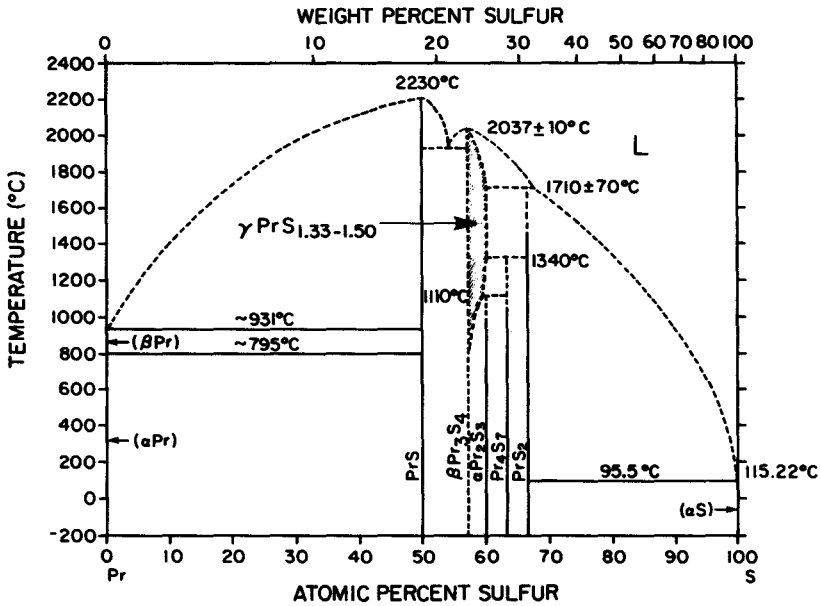

FIGURE 1 The praseodymium-sulfur phase diagram.[5] The shaded region at high temperatures is known as the γ-phase region.

(Pr-S[5]) is shown in Figure 1, where it is seen that at high temperatures a solid solution extends from Pr_3S_4 to Pr_2S_3, which is readily retained as a metastable solid solution at room temperature for many of the R_3S_4-R_2S_3 systems. The lanthanide-selenium systems, where R = La, Ce, Pr, and Nd are notable exceptions, i.e., they are monomorphic and thus stable at room temperature. From a thermoelectric material standpoint, both the RX and RX_2 compounds are of little interest because they are metallic conductors, and the RX_2 compounds have an additional problem in that they readily dissociate by evolution of the chalcogen at a temperature well below their melting points. Those rare earth-chalcogenide systems that contain the R_3X_4-R_2X_3 solid solution based on the Th_3P_4 structure offer the most promise for thermoelectric materials.[2] In this solid solution region the composition varies from $RX_{1.333}$ to $RX_{1.500}$ by the random removal of metal atoms from the X anion network while maintaining the Th_3P_4 structure, and has the general formula $R_{3-y}\upsilon_yX_4$, where υ is the cation vacancy. More commonly, however, the equivalent formula, RX_x, is used to describe the solid solution region, which is known as the γ-phase. The vacancy concentration in atomic percent, N_υ, is given by

$$N_\upsilon = (3x-4)/7x \tag{1}$$

and varies from 0 at x = 1.333 to 4.76 at.% at x = 1.500. Because of the rigid anion network the lattice parameter hardly changes from x = 1.333 to x = 1.500 (e.g., 8.728 to 8.723 Å for La_3S_4 to La_2S_3, respectively). The crystallographic details of the Th_3P_4-type structure have been given by Gschneidner et al.[3] When the electrically neutral R_2X_3 composition is reached, a vacancy structure exists which has the properties of a narrow gap semiconductor. By addition of metal atoms to the vacancy sites, self-doping takes place and valence electrons are added with each metal atom. As the metal to chalcogen ratio increases, the conducting properties of the compound change from semiconducting to semimetallic to metallic. It is this self-doping property that makes the rare earth chalcogenides based on the Th_3P_4 structure interesting as thermoelectric materials. The concentration of conduction electrons per atom, N_e, is given by the expression

$$N_e = (3-2x)/(1 + x), \tag{2}$$

and varies from 0 at x = 1.500 to 0.143 at x = 1.333. This variation of the electron concentration with changing composition, while maintaining a constant volume, makes these materials attractive

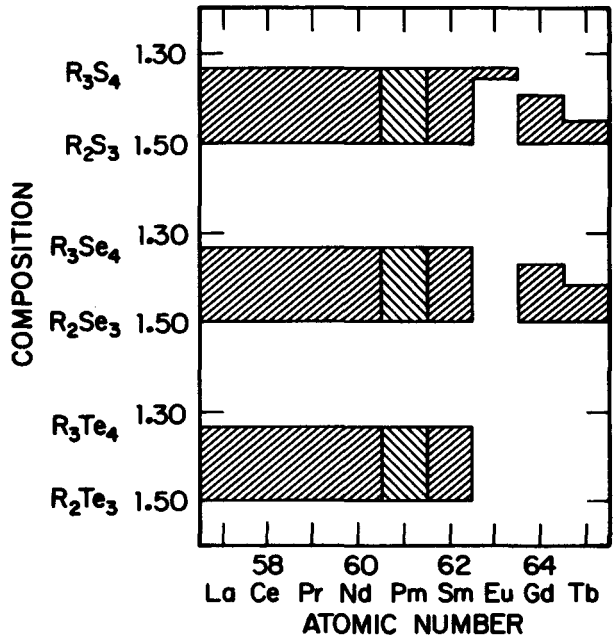

FIGURE 2 The extent of the R_3X_4-R_2X_3 solid solution region in the light to middle lanthanide systems. Promethium compounds have not been studied, but systematics would indicate the behavior shown.

for basic scientific studies as well as potential refractory semiconductors because of their high melting points, >1500°C (Figure 1).

Not all of the binary rare earth-chalcogenide systems form the Th_3P_4-type phases. In general, La through Sm form this type with S, Se, and Te (excluding radioactive Pm, for which no information is available), while Gd, Tb, and Dy form a limited composition range with S and Se and do not form the Th_3P_4-type structure with Te (see Figure 2). A more complete discussion of the existence of this type of compound was given previously.[3] Recent studies have shown that the γ-phase at the R_2S_3 composition can be prepared in a metastable state at room temperature by mechanical milling for the rare earths Y, Dy, Er, Tm, Yb, and Lu.[6,7] However, for the Tm_2S_3 and Lu_2S_3 compositions, the metastable γ-phase coexists with the respective room temperature equilibrium phase δ-Tm_2S_3 and ε-Lu_2S_3.[7]

The fundamental property measurements of resistivity, ρ, Seebeck coefficient, α, and thermal conductivity, λ, which are required to determine the figure-of-merit, Z, have been carried out on several of the lanthanide sulfides, selenides, and tellurides that have the Th_3P_4 structure. Plots of room temperature resistivities, Seebeck coefficients, and thermal conductivity vs. composition for some R_3X_4-R_2X_3 alloys presented in Figures 3, 4, and 5 show the great similarity between these properties of the sulfides and selenides of the various light lanthanides. The data shown in Figures 3, 4, and 5 are representative values for all of the known results and show that the resistivity, thermoelectric power, and thermal conductivity vs. x for the R_3S_4-R_2X_3 alloys fall on a universal curve regardless of the lanthanide or chalcogenide element in the alloy. That is, the resistivity, thermoelectric power, and thermal conductivity depend only upon the electron concentration of the sample, which is expected from the relationship between N_e and x (see Equation 2).

These properties have also been measured at high temperatures (up to 1000°C).[3,4,8] Calculations of the figure-of-merit, where

$$Z = \alpha^2/\rho\lambda, \tag{3}$$

show that these lanthanide chalcogenide phases are potentially useful high-temperature n-type thermoelectric materials, and have values comparable to the state-of-the-art n-type $Si_{80}Ge_{20}$ alloys, (see Table 1).

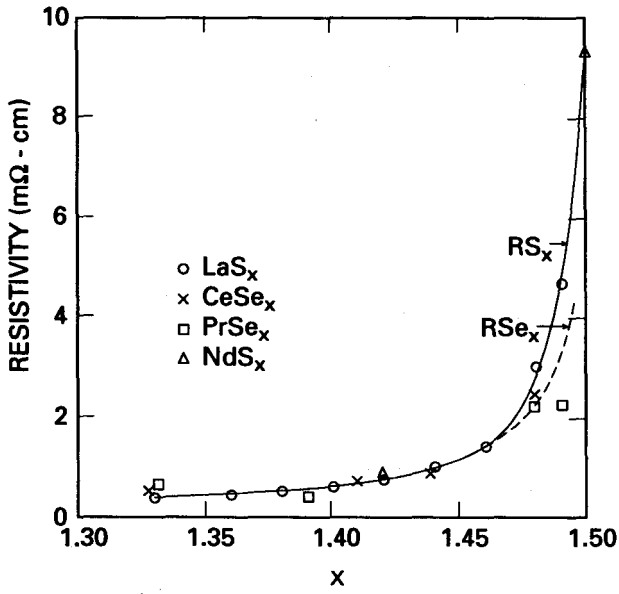

FIGURE 3 Resistivity vs. x at room temperature for several lanthanide sulfides (RS_x) and selenides (RSe_x).

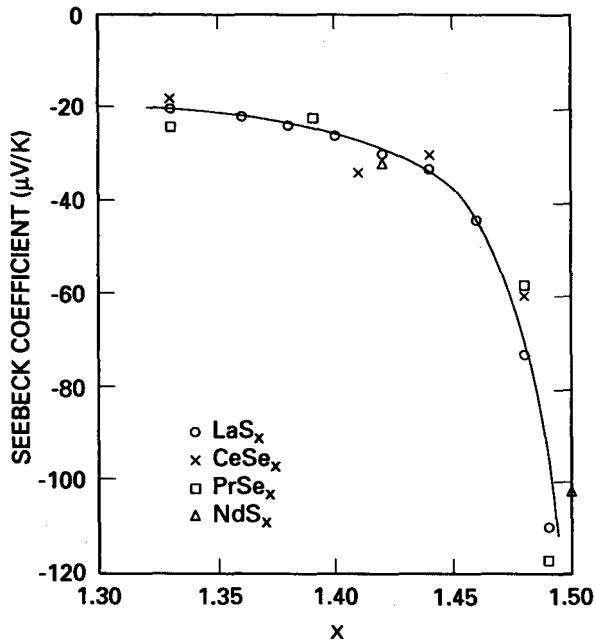

FIGURE 4 Seebeck coefficient vs. x at room temperature for several lanthanide sulfides (RS_x) and selenides (RSe_x).

Early studies by Cutler et al.[9] and Ryan et al.[10] on the thermoelectric properties of the binary $Ce_{3-x}S_4$ system had indicated a potential for extending the useful temperature to a higher temperature range. However, $Ce_{3-x}S_4$ exists in two or three forms depending upon the temperature and/or the purity of the sample. The high-temperature γ-phase, which is metastable below 900°C, deteriorates slowly below this temperature, forming either the α-Ce_2S_3 form (in the absence of oxygen) or the "β-Ce_2S_3" form (which is actually $Ce_{10}S_{15-x}O_x$, where $x \simeq 1$),[11] and the good thermoelectric properties are lost. The same is true for $La_{3-x}S_4$, $Nd_{3-x}S_4$, and $Pr_{3-x}S_4$. Fitzpatrick

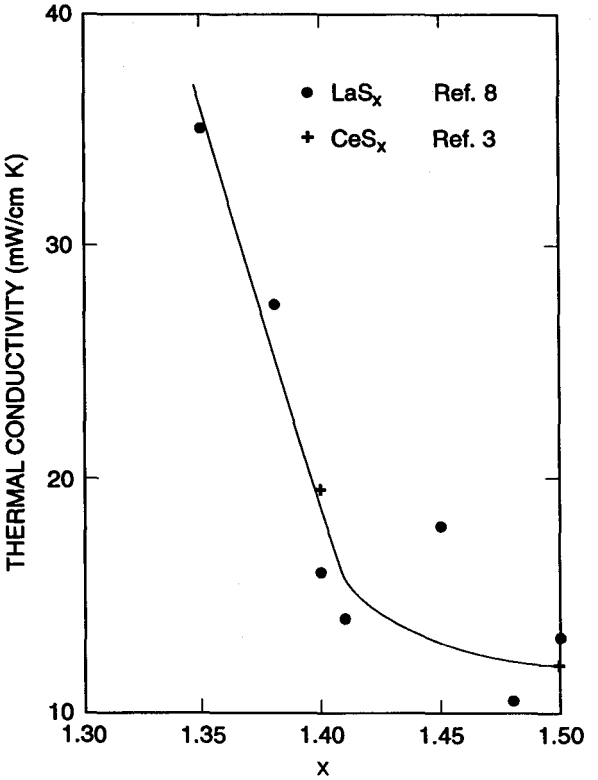

FIGURE 5 The thermal conductivity vs. x at room temperature for several lanthanide sulfides (RS_x).

Table 1. Figure-of-Merit for Some RX_x Alloys

Composition	Temperature (°C)	Figure-of-Merit $Z \times 10^3$ (K^{-1})	Ref.
$LaS_{1.42}$	1000	0.75	8
$LaS_{1.48}$	1000	0.5	8
$NdS_{1.49}$	500	0.53	3
$NdS_{1.50}$	800	0.93	3
$GdSe_{1.49}$	900	1.17[a]	13
$LaTe_{1.46}$	925	0.96	16
$La_{2.2}Eu_{0.8}S_4$	1000	0.52	19
$Si_{80}Ge_{20}$ (n-type)	800	0.8	[b]

[a]See text.
[b]State-of-the-art.

and Munir[12] reported that the γ-form was stabilized by the addition of BaS. However, their stability tests were not carried out for a sufficiently long period of time to be conclusive. For long-term applications, the sulfides are not sufficiently stable even with BaS or other alkaline earth additives.

In the 1970s an extensive effort was made to use $GdSe_x$ (with x = 1.490 to 1.495) as the n-leg of a thermoelectric energy conversion device for space applications.[13] Thermal conductivity measurements reported by Hampl et al.[13] for $GdSe_{1.495}$ were a factor of two or three lower than those measured on LaS_x[8], and the resulting figures-of-merit greater than one were reported (see Table 1), indicating $GdSe_{1.495}$ was an excellent thermoelectric material. Rowe[14] summarized the work of Hampl and indicated "serious difficulties were encountered". Hampl et al.[13] intended to use copper-silver selenide ($Cu_{1.97}Ag_{0.03}Se_{1.008}$) as the p-leg. But, unfortunately, this material has a high

Table 2. Room Temperature Resistivity and Seebeck Coefficient of Rare Earth Nitrides

	Resistivity (m Ω cm)		Seebeck Coefficient (μV/K)	
Nitride	Ref. 21	Ref. 22	Ref. 21	Ref. 22
ScN	0.13		−39	
YN	0.093		−37	
LaN	0.10	0.17	−35	
CeN		0.03		+20
PrN	0.11	0.1	−34	
NdN	0.075	0.074	−36	
SmN		0.15		−65
EuN		1.0		−15
GdN		0.2		
TbN		0.2		
DyN	0.10	0.15	−36	
HoN	0.11	0.09	−37	
ErN	0.079	0.13	−36	
TmN		0.2		
YbN		9		−10
LuN		0.4		

partial pressure of selenium at elevated temperatures. When tested as a couple, the selenium vapor from the copper-silver selenide caused the composition of the $GdSe_{1.49}$ leg to change to $GdSe_{1.50}$. At this composition the transition from the γ-form to the α-form is rapid, and the clear ruby red α-form appears quickly and destroys the thermoelectric properties of the $GdSe_{1.49}$. Wei[15] reported that even the $GdSe_{1.49}$ composition transformed to the low-temperature form in 300 h at 1000°C. The transformation problem can be alleviated by replacing Gd with La, Ce, Pr, or Nd. These light rare earth selenides exist only in the γ-form and therefore do not transform. Thermoelectric properties of $NdSe_x$ and other light rare earth selenides have been summarized by Gschneidner et al.[3]

A comprehensive study of the $LaTe_x$ compound with $1.33 \leq x \leq 1.48$ by Danielson et al.,[16] which was in agreement with previous studies,[3] showed the highest figure-of-merit for any of the binary rare earth-chalcogen systems. A representative value is given in Table 1. But since then no additional results have been reported on the high-temperature behavior of these telluride thermoelectric materials.

Ternary Systems

In an effort to improve thermoelectric properties by lowering thermal conductivity, ternary sulfide systems of La with Sm, Eu, and Yb[17] and La with Ca, Sr, and Hg[18] were studied. Results of resistivity and Seebeck coefficient measurements,[17] when coupled with thermal conductivity measurements[19] for lanthanum sulfides with Sm, Eu, or Yb additives, did not show an improvement in the figure-of-merit.[19] The highest Z in the ternary system was found for the ternary La-Eu-S system.[19] However, the maximum Z reported did not exceed that of the binary $LaS_{1.42}$ composition (see Table 1).

29.3 Pnictides

The rare earth pnictides, which have the NaCl-type structure and have the 1:1 composition, have been studied extensively, and in an early review Wachter[20] concluded that the rare earth nitrides had the largest band gap of the pnictides and even they were semimetallic. Difficulties were experienced by many experimenters in obtaining stoichiometric nitrides. Sclar[21] prepared many of the rare earth nitrides with about 90% of the theoretical nitrogen content. Measurements of resistivity and thermoelectric power at room temperature were made and are given in Table 2. Didchenko and Gortsema[22] had prepared all of the lanthanide nitrides and their results are also

Table 3. Resistivity and Seebeck Coefficient for Several Rare Earth Oxides at 650°C

Oxide	Resistivity (m Ω cm)	Seebeck Coefficient (μ V/K)
La_2O_3	0.6	
Pr_2O_3[a]	0.4	10
Nd_2O_3	0.7	
Sm_2O_3	1.1	70[b]
Eu_2O_3	6.7	2000
Gd_2O_3	7.7	500[b]
Tb_2O_3	5	1
Ho_2O_3	6.2	800
Yb_2O_3	20	
Y_2O_3	18	2500
$PrO_{1.833}$[a]	1.2×10^{-5}	−50
$TbO_{1.81}$[c]	0.16	−92
$TbO_{1.81}$[d]	0.006	−102
$TbO_{1.81}$[a]	0.0006	−78

[a]600°C.
[b]Data from Reference 27.
[c]200°C.
[d]400°C.
Data from Reference 26.

given in Table 2. The similarity in the common results of References 21 and 22 indicates approximately the same purity was achieved in both studies. Both of these early studies concluded the nitrides were semimetallic. The question whether their semimetallic behavior was intrinsic or due to impurities was discussed by Wachter.[20] More recently, high-purity GdN[23] and ScN[24] have been prepared as nearly stoichiometric single crystals and both were shown to be semimetallic. Additions of oxygen to GdN[23] increased the carrier concentration, making them more metallic. Thus, the rare earth monopnictides show little promise as high-temperature thermoelectric materials.

An extensive discussion is presented by Hulliger[25] on pnictides of compositions other than a 1:1 ratio. The most interesting one from a thermoelectric material standpoint is Yb_5Sb_3, which has a Seebeck coefficient of +323 μV/K at room temperature. However, the resistivity has a negative temperature coefficient and presumably the Seebeck drops rapidly with increased temperature.

29.4 Oxides

Electrical transport properties of some of the rare earth sesquioxides determined by Subba Rao et al.[26] and Verma et al.[27] are given in Table 3. As will be noted, the Seebeck coefficients are positive for all of the sesquioxides while the oxygen-rich (multivalent) oxides are n-type. Resistivities are sufficiently low and Seebeck coefficients are high enough at 200°C to make $TbO_{1.81}$ of interest as a thermoelectric n-type material. However, the Seebeck coefficient falls rapidly with increasing temperature.[26] The high resistances of the rare earth sesquioxides coupled with their low Seebeck coefficients make their potential as practical thermoelectric materials extremely limited.

Oxygen-containing compounds such as chromites ($YCrO_3$ and $LaCrO_3$) have been studied and various dopants have been added to achieve n- or p-type behavior.[28–30] Resistivities in all cases were high and the Seebeck coefficients were nearly independent of temperature. Thus, the ternaries studied to date have the same limitation as the binary systems with respect to their potential as thermoelectric materials.

29.5 Silicides

Studies of the thermoelectric properties of $CeSi_x$ compounds where $x < 2$ were made primarily to confirm the existence of a transition from the paramagnetic to the ferromagnetic state in $CeSi_x$[31]

or some other low-temperature anomalies.[32] Resistivity and Seebeck coefficient measurements made below 300 K indicated metallic conductivity with low Seebeck coefficients. It was also noted[32] that large anisotropic expansions caused cracking to occur and resulted in extremely large resistivities for compositions near x = 1.85. Neither results suggest any potential for these compounds as useful thermoelectric materials, at least near the $CeSi_{1.75}$ to $CeSi_{1.95}$ compositions.

29.6 Concluding Remarks

Of the compounds formed between the rare earth metals and the nonmetallic elements, only some silicide, pnictide, oxide, and chalcogenide compositions offer the potential of being semiconductors, i.e., RN, R_2O_3, R_2S_3, etc. Examination of these possible systems by scientists over the past 40 years has shown that to date only the compositions near the R_2S_3 stoichiometry show any exceptional promise as thermoelectric materials with reasonably large figures-of-merit (slightly less than $1 \times 10^{-3} \cdot K^{-1}$). Attempts to utilize these R_2S_3 materials as high-temperature thermoelectric materials have been disappointing because of the lack of phase stability of the compositions studied to date and the availability of a compatible p-type material. The R_2Se_3 and R_2Te_3 compounds also seem to exhibit similar problems as the R_2S_3 phases, but not nearly as much effort has been devoted to these materials, and so the prospects of useful thermoelectric materials among the selenides and tellurides is better than for the sulfides.

The RN phases, which might be expected to be interesting semiconductors, exhibit too low resistivities and Seebeck coefficients to be interesting thermoelectric materials. But one of the main problems has been the preparation of truly stoichiometric RN, and so one cannot rule out these compounds. Another problem is the reported reactivity of the RN phase with H_2O, but some evidence indicates that if one has stoichiometric RN, it is quite stable in ambient atmospheric conditions.

The R_2O_3 phases and several of the ternary oxides that have been studied indicate that these materials are insulators with large band gaps and though they may have large Seebeck coefficients, their resistivities are much too large for practical thermoelectric materials at any reasonable temperature.

The silicides also are not of much interest because they are metallic conductors with low Seebeck coefficients.

Ternary rare earth semiconductors and the potentially interesting thermoelectric materials based on them remain a wide-open field of research. Little or no effort is being made in this field at the present time. Although many ternary compounds have been identified as to composition and structure, there is a tremendous lack of physical property data on such phases, especially their electrical and thermoelectric behaviors. This is the area where the next big advance in thermoelectric materials is most likely to occur.

Acknowledgment

Ames Laboratory is operated for the U.S. Department of Energy by Iowa State University under contract No. W-7405-Eng-82. This work was supported by the Office of Special Applications, U.S. Department of Energy.

References

1. Miller, J. F., Reid, F. J., and Himes, R. C., Rare earth compound semiconductors, *J. Electrochem. Soc.*, 106, 1043, 1959.
2. Reid, F. J., Matson, L. K., Miller, J. F., and Himes, R. C., Electrical properties of selected rare earth compounds and alloys, *J. Electrochem. Soc.*, 111, 943, 1964.
3. Gschneidner, K. A., Jr., Nakahara, J. F., Beaudry, B. J., and Takeshita, T., Lanthanide refractory semiconductors based on the Th_3P_4 structure, *Mater. Res. Soc. Symp. Proc.*, 97, 359, 1987.

4. Wood, C., Materials for thermoelectric energy conversion, *Rep. Prog. Phys.*, 459, 1988.
5. Gschneidner, K. A., Jr., Comment. The paper, Pr-S [praseodymium-sulfur], *J. Phase Equil.*, 13, 586, 1992.
6. Han, S. H., Gschneidner, K. A., Jr., and Beaudry, B. J., Preparation of a metastable high temperature phase (γ-Dy_2S_3) and a metastable high pressure phase (γ-Y_2S_3) by mechanical alloying and mechanical milling, *Scr. Metall. Mater.*, 25, 295, 1991.
7. Han, S. H., Gschneidner, K. A., Jr., and Beaudry, B. J., Preparation of the metastable high pressure γ-R_2S_3 phase (R = Er, Tm, Yb, and Lu) by mechanical milling, *J. Alloys Compds.*, 181, 463, 1992.
8. Wood, C., Lockwood, A., Parker, J., Zoltan, A., and Zoltan, D., Thermoelectric properties of lanthanum sulfide, *J. Appl. Phys.*, 58, 1542, 1985.
9. Cutter, M., Leavy, J. F., and Fitzpatrick, R. L., Electronic transport in semimetallic cerium sulfide, *Phys. Rev.*, 133, A1143, 1964.
10. Ryan, F. M., Greenberg, I. N., Carter, F. L., and Miller, R. C., Thermoelectric properties of some cerium sulfide semiconductors from 4° to 1300°K, *J. Appl. Phys.*, 33, 864, 1962.
11. Flahaut, J., Sulfides, selenides and tellurides, in *Handbook on the Physics and Chemistry of Rare Earths*, Vol. 4, Gschneidner, K. A., Jr. and Eyring, L., Eds., North Holland, Elsevier, Amsterdam, 1979, 1.
12. Fitzpatrick, R. L. and Munir, Z. A., Studies on the stabilization of gamma phase cerium sulfide, *Mater. Res. Bull.*, 2, 939, 1967.
13. Hampl, E. F., Hinderman, J. D., Mitchell, W. C., Reylek, R. S., and Wald, D. A., Design of a thermoelectric converter using 3M high performance thermoelectric material, *Proc. 10th Intersoc. Energy Convers. Eng. Conf.*, 2, 714, 1975.
14. Rowe, D. M., Recent developments in thermoelectric materials, *Appl. Energy*, 24, 139 1986.
15. Wei, G. C., Phase transformation and processing of polycrystalline gadolinium selenide, $GdSe_{1.49}$, *J. Am. Ceram. Soc.*, 67, 664, 1984.
16. Danielson, L. R., Alexander, M. N., Vining, C., Lockwood, R. A., and Wood, C., Thermoelectric properties of $LaTe_y$, *Proc. of the Seventh International Conference on Thermoelectric Energy Conversion*, Rao, K. R., Ed., The University of Texas at Arlington, TX, 1988, 71.
17. Nakahara, J. F., Takeshita, T., Tschetter, M. J., Beaudry, B. J., and Gschneidner, K. A., Jr., Thermoelectric properties of lanthanum sulfide with Sm, Eu and Yb additives, *J. Appl Phys.*, 63, 2331, 1988.
18. Nakahara, J. F., Takeshita, T., Tschetter, M. J., Beaudry, B. J., and Gschneidner, K. A., Jr., A study of the thermoelectric properties of Ca, Sr and Hg substituted lanthanum sulfides, *The First European Conference on Thermoelectrics*, Rowe, D. M., Ed., Peter Peregrinus Ltd., 1988, 161.
19. Kokos, G. B., Gschneidner, K. A., Jr., Cook, B. A., and Beaudry, B. J., Thermal conductivity of $La_{3-x}R_xS_4$ where R = Sm, Eu, and Yb, *J. Appl. Phys.*, 66, 2356, 1989.
20. Wachter, P., The optical electrical and magnetic properties of the europium chalcogenides and the rare earth pnictides, *Crit. Rev. Solid State Sci.*, 3, 189, 1972.
21. Sclar, N., Properties of rare-earth nitrides, *J. Appl. Phys.*, 35, 1534, 1964.
22. Didchenko, R. and Gortsema, F. P., Some electric and magnetic properties of rare earth monosulfides and nitrides, *J. Phys. Chem. Solids*, 24, 863, 1963.
23. Wachter, P. and Kaldis, E., Magnetic interaction and carrier concentration in GdN and $GdN_{1-x}O_x$, *Solid State Commun.*, 34, 241, 1980.
24. Travaglini, G., Marabelli, F., Monnier, R., Kaldis, E., and Wachter, P., Electronic structure of ScN, *Phys. Rev. B*, 34, 3876, 1986.
25. Hulliger, F., Rare earth pnictides, in *Handbook on the Physics and Chemistry of Rare Earths*, Vol. 4, Gschneidner, K. A., Jr. and Eyring, L., Eds., North-Holland, Elsevier, Amsterdam, 1979, 153.
26. Subba Rao, G. V., Ramdas, S., Mehratra, P. N., and Rao, C. N. R., Electrical transport of rare-earth oxides, *J. Solid State Chem.*, 2, 377, 1970.
27. Verma, B. K., Pratap, V., and Lal, H. B., Transport properties of monoclinic rare-earth sesquioxides, *Indian J. Pure Appl. Phys.*, 18, 150, 1980.
28. Weber, W. J., Bates, J. L., Griffin, C. W., and Olsen, L. C., Electrical conductivity and Seebeck coefficient of divalent-metal-doped $YCrO_3$, *Mater. Res. Soc. Symp. Proc.*, Vol. 60, Chen, Y., Kingery, W. D., and Stokes, R. J., Eds., Mat. Res. Soc., Pittsburgh, PA, 1986, 235.
29. Karim, D. P. and Aldred, A. T., Localized level hopping transport in $La(Sr)CrO_3$, *Phys. Rev. B*, 20, 2255, 1979.

30. Minaev, I. M., Teterin, G. A., Zinchenko, V. F., and Kozlov, V. D., Electrophysical and thermoelectric characteristics of lanthanide chromites in the high-temperature region, *Inorg. Mater.*, 27, 1083, 1991.
31. Aliev, F. G., Moohchalkov, V. V., Petrenko, O. V., and Balich, O. I., Galvanomagnetic and thermoelectric properties of $CeSi_x$ compounds, *Soviet Solid State Phys.*, 28, 637, 1986.
32. Gschneidner, K. A., Jr., Lee, W. H., Damento, M. A., Tang, J., Cook, B. A., Shinar, J., Dehner, B., and Shelton, R. N., Resistance anomaly near the localized-delocalized crossover point in the $CeSi_x$ system, *Phys. Rev. B*, 39, 2099, 1989.

30

Thermoelectric Properties of High-Temperature Superconductors

M. Cassart and J.-P. Issi
Université Catholique de Louvain
Louvain-la-Neuve, Belgium

30.1 Abstract

A few selected examples among the large variety of results are chosen to discuss the thermoelectric properties of high-T_c superconductors. The main high-T_c families are first briefly introduced. Then, the electrical resistivity, thermoelectric power, and thermal conductivity are successively discussed and the possible use of high-T_c ceramics in thermoelectric coolers is contemplated. Attention is focused on the $La_{2-x}(Sr,Ba)_xCuO_4$ compounds, and their properties are compared to those of some of the other high-T_c superconductors.

30.2 Introduction

Six years after the discovery of high-temperature superconductivity in the cuprates by Bednorz and Müller (1986),[1] and despite a large variety of proposed theoretical models, the exact mechanism for high-T_c superconductivity is still a matter of conjecture.[2–4] One reason for this is that even the normal-state properties of these systems are not well understood, even though an enormous amount of experimental and theoretical effort has been dedicated to their investigation.

Nowadays, there are two main problems in discussing the transport properties of high-T_c superconductors. The first is that, in order to analyze electronic transport, a reliable model for the

0-8493-0146-7/95/$0.00+$.50

electronic structure is a prerequisite. Unfortunately, there is not an appropriate model that describes the strongly correlated electron systems in the high-T_c materials. The other problem is the quality of the samples investigated, even when they are single crystals, in regard to control of stoichiometry, doping, crystal perfection . . . This makes it difficult to compare data from various sources.

The thermoelectric properties are no exception and the abundant literature on the subject, where reported results are often contradictory, does not facilitate the job of the reviewer. Consequently, in this chapter a few illustrative experimental facts are selected which are fairly representative of the field. The description is phenomenological rather than explanatory, with correlations being established between the results when applicable. The abundant literature, including appropriate review papers, is referred to wherever appropriate.

After briefly introducing the main high-T_c families (Section 30.3), the salient results pertaining to the thermoelectric properties: electrical resistivity (Section 30.4), thermoelectric power (Section 30.5), and thermal conductivity (Section 30.6) are discussed. Before concluding, the possible use of high-T_c ceramics in thermoelectric coolers (Sections 30.7 and 30.8) is contemplated.

Because there exists such a large variety of compounds that display different properties, attention is focused on the first-discovered family of high-T_c ceramics, the $La_{2-x}(Sr,Ba)_xCuO_4$ compounds. Finally their properties are compared to those of the other high-T_c superconductors.

30.3 The High-T_c Ceramic Families

Sample Preparation[5,6]

The most common way of preparing oxides containing several cations consists first in thoroughly mixing different oxides (e.g., La_2O_3, CuO, Bi_2O_3, BaO, Tl_2O_3, . . .), carbonates (Ba_2CO_3, $SrCO_3$, $CaCO_3$, . . .), and/or nitrates [$Sr(NO_3)_2$, $Ba(NO_3)_2$, . . .] to provide the necessary spatial uniformity. The mixing is most frequently achieved by grinding the powders in an agate mortar for an extended time. Alternative techniques include the coprecipitation of the powders and the sol-gel process, both designed to produce a more intimate mixture of the constituents. The mixing process is normally carried out in air under ambient conditions.

The prepared powders are then subjected to a series of heat treatments in order to achieve the solid-state reaction at a temperature where solid-state diffusion becomes fast enough and where the desired structures are stable. A prefiring at a lower temperature to eliminate the moisture accumulated during the grinding process is often performed. Sometimes, in order to decompose some reactants like carbonates or nitrates into the corresponding oxides, intermediate grindings are needed. While a variety of crucible materials have been successfully used, the most commonly used are platinum and alumina. The details of the initial heat treatment vary from case to case. For the $La_{2-x}(Sr,Ba)_xCuO_4$ compounds, consistent results are obtained by reacting the powders in air at 1100 to 1140°C for 24 to 48 h. This reaction step is usually repeated after regrinding the material.

The powders obtained are pressed into pellets and sintered, experiencing a heat treatment similar to that used for the preparation of the powder. After this stage, the correct phase is usually obtained, but the oxygen content may be nonstoichiometric. Thus, an oxygen recovery state at temperatures below the initial reaction temperature is usually required. Some compounds like $Nd_{2-x}Ce_xCuO_4$ require heat treatment in a reducing atmosphere.

The major part of the data reported in the literature relates to sintered materials, although some good thin films and single crystals have now been successfully prepared for some families of high-T_c compounds.[7,8] The most important problem with the use of sintered materials, in addition to the loss of information on anisotropy, is the masking of some intrinsic properties by grain boundary effects. Nevertheless, polycrystalline samples present some advantages: material composition can be controlled rather precisely and fairly easily, large-size samples can be prepared, and equilibrium in oxygen stoichiometry or treatments like fluorination (see below) is easier to achieve.

Table 1 High-T_c Families

Superconductor Family		T_c max
$MBa_2Cu_{3+x}O_{6+\delta}$	M = Y or rare earth	92 K
$La_{2-x}M_xCuO_4$	M = Ca, Sr, Ba, . . .	40 K
$Bi_2(Ca,Sr)_{n+1}Cu_nO_{2n+4}$		115 K
$M_y N_{n+1} Cu_n O_{2n+2+y}$	M = TL, Pb, Cu, Hg; N = Ca, Ba, Sr (Hg compounds under pressure)	- - -> 155 K
$Ln_{2-x}M_xCuO_{4-y}F_y$	Ln = Pr, Nd, Sm, Eu; M = Ce, Th	38 K
$Sr_{1-y}M_xC_nO_{2+y}$	"infinite layer"	40 K
	(1) M = Nd	110 K
	(2) M = Ba	
$Ba_{1-x}K_xPb_{1-y}Bi_y$		30 K

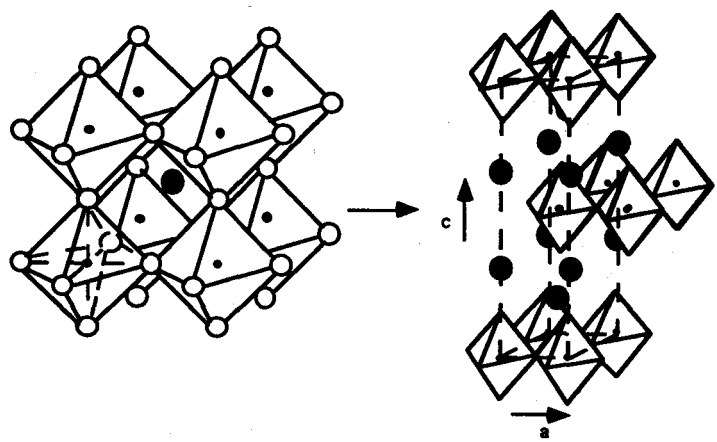

FIGURE 1 Structure of the $La_{2-x}(Ba,Sr)_xCuO_4$ (right) 18 compared with that of the typical perovskite cage (left). The large black circles represent the La, Ba, or Sr atoms while the small black circles represent the Cu atoms. The oxygen atoms are located at the vertices of the polyhedra.

Structure

The high-temperature superconductors discovered so far belong to seven chemical families (see Table 1). The superconducting cuprates (the first six families) have layered structures, with closely spaced electronically active CuO_2 planes separated by "charge reservoir" layers.[9,10] The $La_{2-x}Ba_xCuO_4$ compounds can be taken as an example. The parent compound La_2CuO_4, which crystallizes in the orthorhombic-distorted K_2NiF_4-type structure, has a single CuO_2 plane separated by La-oxygen planes and, as with all the other high-T_c families, its structure is closely related to that of perovskite (see Figure 1).[11,12] In addition to the first six families of high-T_c superconductors, there is the cubic perovskite $Ba_{1-x}K_xBiO_{3-y}$ where the CuO_2 layers are missing, with an onset transition temperature of 30 K.

Prior to the discovery of high-temperature superconductivity in the copper oxide materials, the perovskite systems were already well known to exhibit drastic changes in their electronic and magnetic properties as a result of small chemical substitutions. Substitutions or insertions of atoms could distort the cubic perovskite structure and lead to the occurrence of tetragonal, rhombohedral, or orthorhombic symmetry. It is these small structural transformations which introduce important changes in the magnetic and electric properties.

Phase Diagram

The parent compounds of the high-T_c copper oxides, such as La_2CuO_4, $YBa_2Cu_3O_6$, and Nd_2CuO_4, are characterized by strong antiferromagnetic exchange interactions in the Cu^{2+} lattice. These are

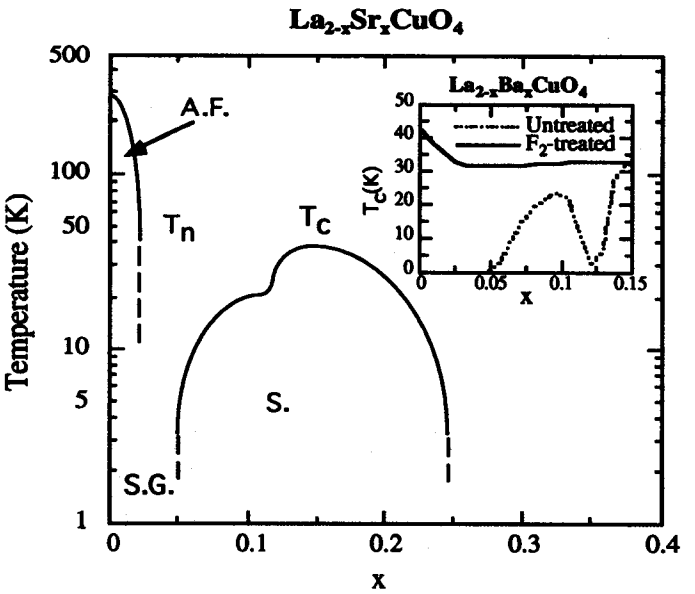

FIGURE 2 Phase diagrams: variation of T_c and T_n as a function of Sr concentration (x) for the $La_{2-x}Sr_xCuO_4$ compound. The regions where the samples are superconducting and antiferromagnetic are clearly shown. The inset shows schematically the peculiar concentration dependence of T_c of the $La_{2-x}Ba_xCuO_4$ compounds around x = 0.125, for untreated or F_2-treated samples.[22]

reduced by the addition of holes or electrons, and disappear with the emergence of the superconducting properties. This may be seen in the phase diagram of the $La_{2-x}(BaSr)_xCuO_4$ compound that could exemplify, with minor differences, nearly all high-T_c copper oxides families (see Figure 2).[13] A more complete phase diagram which also represents compounds other than $La_{2-x}(Ba,Sr)_xCuO_4$ vs. the charge carrier per copper atom in the CuO_2 plane is given by Torrence.[20]

The La_2CuO_4 compound is an antiferromagnetic insulator with copper in the $3d^9$ state, and a band gap of about 2 eV. On adding substitutional Sr, for example, the Neel temperature drops to zero. Then a spin glass region follows and with further increase in Sr substitution an insulator-metal transition occurs accompanied by superconducting properties. At large Sr concentrations, a region is reached where the superconducting properties disappear. This region is commonly and erroneously called the "overdoping region" in the literature. As for other classes of materials, e.g., conducting polymers, the word "doping" is commonly incorrectly used in the high-T_c literature. It is often used instead of inserting or substituting.

In the $La_{2-x}(Ba,Sr)_xCuO_4$ system, the three phases, i.e., the insulating, superconducting, and the region of high concentration of added atoms, can easily be covered. This is one of the reasons that led the authors to focus in this chapter on the $La_{2-x}(Sr,Ba)_xCuO_4$ system. However, it is obvious now that the phase diagram of $La_{2-x}(Ba,Sr)_xCuO_4$ has a singularity at x = 0.125 (see inset to Figure 2), that shows up in the most pronounced way in the barium-substituted sample. Indeed, for the $La_{1.875}Ba_{0.125}CuO_4$ sample, the superconductivity disappears, magnetic order is restored, and an energy gap appears to open for the charge excitations below 60 K. This temperature coincides with a structural transition from the orthorhombic structure to a low-temperature tetragonal phase (LTT). The transport properties that are discussed here are also all drastically affected at this temperature. However, all these anomalies may be suppressed by means of a fluorination treatment,[15] which probably stabilizes the lattice and the electronic system. Indeed, up to now, it is not clear whether the anomaly in the phase diagram is driven by some electronic instability inherent to the hole density for x = ⅛ or whether it is related to lattice instabilities. Also, it is not known whether the phenomenon is specific to the $La_{2-x}(Ba,Sr)_xCuO_4$ system. A recent work has

shown that the occurrence of a structural phase transition near x = 0.2 is related to the disappearance of superconductivity in $La_{2-x}Sr_xCuO_4$.[16] At the same time, the results obtained confine the bulk superconducting phase in a much narrower composition range than that presented in Figure 2. These results indicate a close relationship between superconductivity and minor structural changes.

Most of the high-T_c superconductors are highly inhomogeneous in composition, on a scale that is likely to influence both normal state and superconducting properties. Although some authors have considered these inhomogeneities as evidence for phase separation, the authors believe that most of these electronically inhomogeneous materials are single phase according to our usual thermodynamic and structural definitions.[5,6,17]

The $La_{2-x}Ba_xCuO_4$ system can be taken as an example for the discussion of the relationship between point defects and carrier concentration. Point defects resulting from the substitution of Ba for La are considered and other defects, such as oxygen interstitials and vacancies or other impurities, are ignored. The substitution tends to create regions where electrons are delocalized in the insulating La_2CuO_4 matrix. For low Ba concentrations, the electronic properties of these single-phase materials are only modified in the vicinity of the substitutional atom. With an increase in Ba concentration, the regions that are strongly influenced by the added atoms could connect and then appear homogeneous to most probes, while only the La_2CuO_4 sample is really homogeneous. As a consequence of this inhomogeneity, some probes may be more sensitive to Ba-rich regions and others may be more sensitive to the Ba-deficient regions. That is why reconciling the results of two different studies may prove sometimes rather difficult. The situation becomes even more complex when the oxygen stoichiometry and the presence of extended defects is considered. An example of this problem is discussed in the recent paper of Takagi et al.,[23] who show that for samples of the $La_{2-x}Sr_xCuO_4$ family, heat treated for 1 month, the range for bulk superconductivity is narrower than was previously known.

The lack of homogeneity pervades most of the systems where high-T_c superconductivity has been observed. Another particular example could be found in the n-type copper oxides (i.e., $Nd_{2-x}Ce_xCuO_4$ and $Nd_2CuO_{4-x}F_x$), where superconductivity is only observed for a very small range of x. A variation of x at a microscopic level will inevitably lead to materials that are not electronically homogeneous.

30.4 Electrical Resistivity[18]

The existence of "charge reservoir" layers seems to play a crucial role in all high-T_c compounds. From these layers, holes are injected into the copper oxide planes through a charge transfer mechanism. In La_2CuO_4, the presence of Ba or of interstitial oxygen defects in the La_2O_2 layers converts the latter into charge reservoir layers which are responsible for the presence of charge carriers in the CuO_2 planes. The Cu-O chains in $YBa_2Cu_3O_7$, the Bi-O layers in the bismuth compounds, and the Tl-O layers in the thallates may also act as charge reservoirs when they contain the appropriate defects.

The composition and temperature dependence of the electrical resistivity presented in Figure 3 clearly illustrate the drastic changes introduced by substitution of atoms in the La_2CuO_4 compound. This stoichiometric compound is known to possess a resistivity which is typical of a charge-transfer insulator, in which the copper moments undergo a three-dimensional antiferromagnetic ordering near room temperature. Following either a small increase in oxygen excess or the substitution of Ba, Sr, or Ca . . . for La, the La_2CuO_4 compound undergoes an insulator to "metallic" transition, a typical example of a Mott-Anderson transition.

For low concentrations of added atoms, i.e., for small x, most of the $La_{2-x}Ba_xCuO_{4+\delta}$ compounds are usually reported to exhibit a variable range hopping behavior but with different coefficients, α, for the temperature dependence. In that case, the electrical resistivity could be expressed by the following relation:[19]

$$\rho \approx \rho_0 \exp\left(\frac{T_0}{T}\right)^{\alpha} \tag{1}$$

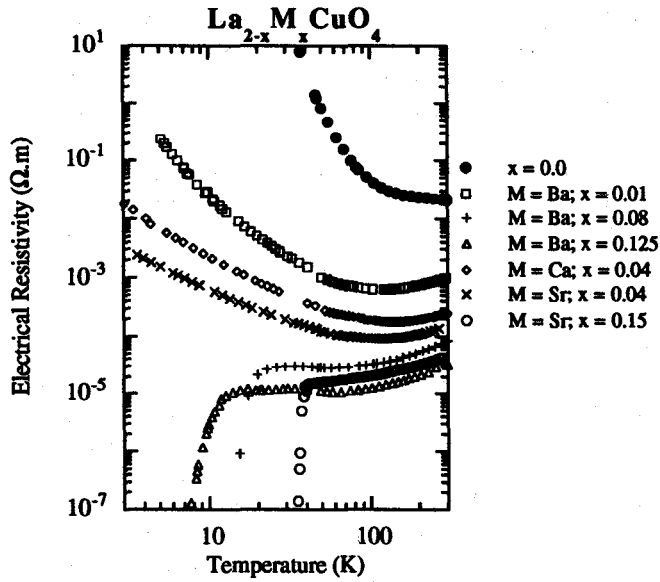

FIGURE 3 Temperature dependence of the electrical resistivity of sintered $La_{2-x}M_xCuO_4$ samples showing the drastic effect of substituting various atomic species for La.

where α is a function of the dimensionality of the hopping process and of the energy dependence of the density of states in the vicinity of the Fermi energy.

In the case of an energy-independent density of states, we are in the Mott's variable range hopping regime, with $\alpha = \frac{1}{3}$ for two dimensions and $\alpha = \frac{1}{4}$ for three dimensions. Shklovskii and Efros[20] have analyzed the case of low carrier concentrations, where electrons interact via the unscreened Coulomb potential, and they obtained $\alpha = \frac{1}{2}$ for any dimensionality.

Though most of the data in the literature are analyzed using only one of the above-mentioned values for α, all the electrical resistivity data of high-T_c superconductors cannot be described by means of a simple Mott or Shklovskii-Efros mechanism alone. A more generalized approach is needed where, for example, one should allow α to vary with the carrier concentration.[21] It is also possible to describe the temperature dependence of the low-temperature electrical resistivity of the $La_{2-x}Ba_xCuO_4$ system by means of a T^{-n} relation, with n decreasing with increasing barium substitution.

For higher substitutional atom concentrations, localization effects are reduced and the electrical resistivity starts to exhibit a linear temperature dependence and superconductivity may occur. Since the electrical resistivity of metals should vary linearly with temperature around and above the Debye temperature, most authors erroneously consider this linear dependence as a characteristic metallic behavior. In traditional metals the linear temperature dependence of the electrical resistivity originates from large-angle scattering of electrons by Debye phonons. The linear temperature dependence of the resistivity of the high-T_c compounds, which sometimes extends over a surprisingly wide temperature range, does not seem to be due to the interactions between electrons and phonons. Indeed, the $Bi_{2.1}Sr_{1.9}CuO_{6+\delta}$ compound displays a linear behavior down to 9 K, the superconducting transition temperature, and at this temperature, large-angle electron-phonon scattering is not likely to occur.[22] Also, at high temperature, where one expects a resistivity saturation, which is expected to occur in metals when the mean free path begins to be comparable to the interatomic distances,[23] the temperature dependence of the resistivity still remains linear in high-T_c compounds. In addition, the magnitude of the resistivity is usually high compared to that of typical metals.

The unusually high values of the electrical resistivity of high-T_c compounds have led some authors to invoke a novel mechanism for the inelastic scattering of charge carriers.[18] Lee and Read have considered a carrier-carrier interaction modified by an effect of two-dimensional van Hove

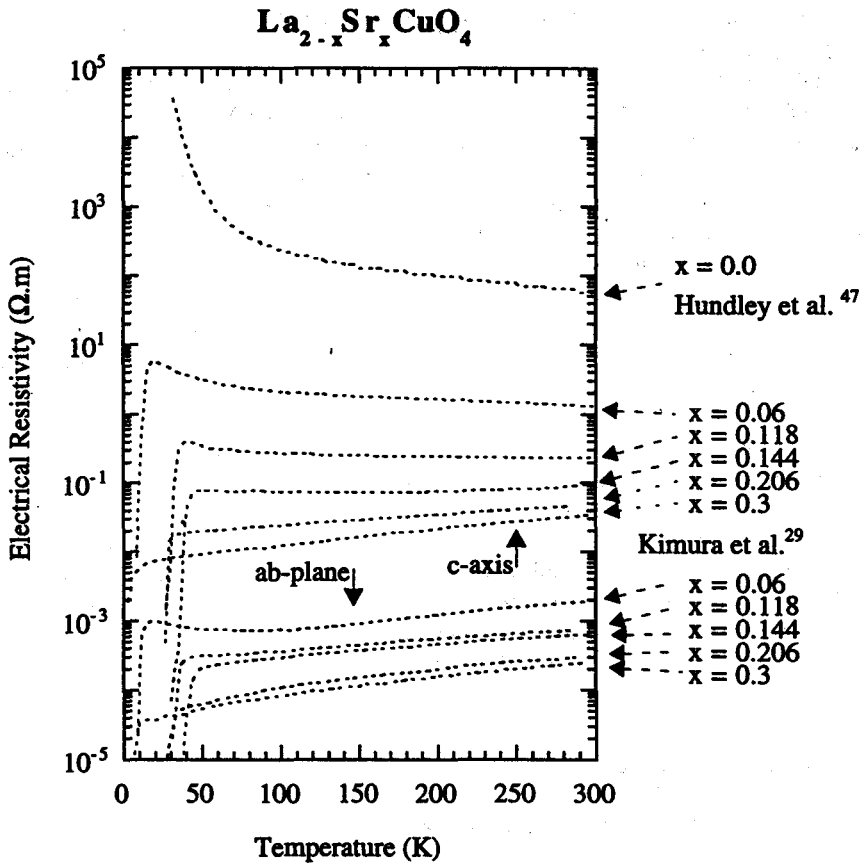

FIGURE 4 Temperature dependence of the resistivity along the ab-plane (five bottom curves) and along the c-axis (top curves) of $(La_{1-x}Sr_x)_2CuO_4$ single crystals.

singularities as a mechanism for the inelastic scattering.[24,25] Anderson and Zou have proposed, on the basis of their resonating valence bond (RVB) theory, a holon-spinon scattering model.[26] Phillips relates the particular electronic properties to the presence of extensive inhomogeneous micromorphologies.[17]

Substitution of different elements for Cu could also lead to metal-insulator transition owing to the superposition of two factors, namely the change in charge carrier concentration and the impurity-induced disorder. For some impurity species, superconductivity disappears for concentrations smaller than that of the metal-insulator transition, leaving a range of concentrations where the specimens have a linear resistivity but are not superconductors.[27,28]

As one might expect from the crystal structure, the electrical properties of the layered cuprates are highly anisotropic. The room-temperature electrical resistivity of $Bi_2Sr_2CaCu_2O_8$, for example, can be up to 10^5 times larger in the c-direction than it is in the a- or b-directions, while in $La_{2-x}Sr_xCuO_4$, the anisotropy ratio is usually found to be between 10^3 and 10^4 according to the importance of the Sr substitution (see Figure 4). The anisotropy ratio is specific to the family of compounds. The mechanisms responsible for the resistivities, parallel and perpendicular to the planes, are also different in character. The in-plane resistivity behaves like that of a metal for "good" superconducting samples, while the out-of-plane in most cases decreases upon heating with a value several orders of magnitude greater than the maximum metallic value. A possible exception is found for the $YBa_2Cu_3O_{7-\delta}$ system, which is the material with the lowest anisotropy ratio. Some good crystals of this compound exhibit a linear behavior of the out-of-plane resistivity, although its absolute value is more than ten times larger than in the ab-plane.[18,30,31] More recently,

the c-axis electrical resistivity of $Tl_2Ba_2CuO_{6+\delta}$ single crystals was also found to show a linear temperature dependence.[18]

The metal-insulator transition could be found in all high-T_c superconducting families. In the case of the $YBa_2Cu_3O_{7-\delta}$ compounds, it is possible to change the linear behavior of the resistivity into that typical of localized charge carriers by changing each element of the compound separately. This may be performed either by decreasing the oxygen concentration, or by substituting different elements for copper, or by substituting La for Ba, or Pr for Y by irradiation. As a result of these modifications, the electrical resistivity follows the behavior characteristic of a hopping process.

The substitution of Pr for Y is particularly interesting, since in addition to providing some elements for our understanding of the superconducting mechanisms, this unique system could be used to develop thin film junctions: superconductor-normal conductor-superconductor and superconductor-insulator-superconductor. The electrical resistivity of the $YBa_2Cu_3O_{7-\delta}$ compounds, where Pr is totally substituted for Y is more than four orders of magnitude greater than that of the nonsubstituted sample.[32]

Electrical transport in the $Ba_{1-x}K_xBiO_3$ system is also found to follow a variable range hopping law in the range between the high-temperature superconductor behavior that appears for $x \geq 0.4$ and the charge density wave behavior for $x = 0$.[33]

The cross-over between localized states to linear temperature dependence appears to be the universal behavior for the electrical resistivity of high-T_c materials. It is possible to cross more than seven orders of magnitude in the electrical resistivity near room temperature and to shift from an insulator to a perfect electrical conductor by only small substitutions or intercalation effects. However, none of the different states in which these compounds could exist are correctly understood or, at least, simply explained.

30.5 Thermoelectric Power[34]

Thermoelectric Power and Superconducting Transition

Thermoelectric phenomena in traditional superconductors have been studied for more than 60 years. It was established that thermoelectric effects are negligibly small in the superconducting state. Therefore, thermoelectric effects have naturally been almost exclusively studied in the normal state, i.e., above the critical temperature T_c. Meanwhile, it was soon noted that in the superconducting state the thermoelectric effects should not formally vanish, though it is generally not possible to observe them experimentally. Since they cannot exchange energy with the lattice, the Cooper pairs do not contribute to the thermoelectric effects. However, below T_c, the diffusion of unpaired electrons down the temperature gradient is balanced by an opposing supercurrent that flows without the need for a thermoelectric voltage. Thus, a circulating current pattern is set up in the isolated superconductor, the normal current being transformed into a supercurrent. In high-T_c superconductors, pronounced Seebeck effects have been reported which have been related to the resistivity caused by flux motion.[35]

Just above T_c, superconducting fluctuations are expected to produce a precursory reduction in thermopower magnitude, since supercurrents tend to short out the thermoelectric voltage. The superconducting fluctuations, which are reflected in the temperature variation of the electrical resistivity above T_c, are more pronounced in high-T_c oxides because of their relatively low normal-state conductivity and the low values of the coherence lengths.[36] However, some authors find a sharp peak just above T_c. Kaiser and Uher suggested that this peak could be attributed to an increase of the phonon drag.[37] On the other hand, Howson et al.[38] suggested that the peaks could be a fluctuation effect due to a flow of holes against the temperature gradient, driven by the density gradient of the fluctuations. In untwinned crystals this sharp peak was only found to be important in the a-direction.[39] It is important to note, however, that such a peak is not always observed.

$La_{2-x}(Ba,Sr)_xCuO_4$ Compounds

The thermoelectric power for disordered conductors, where electrical conduction is governed by variable range hopping between localized states in the gap, is complicated to analyze. In that case,

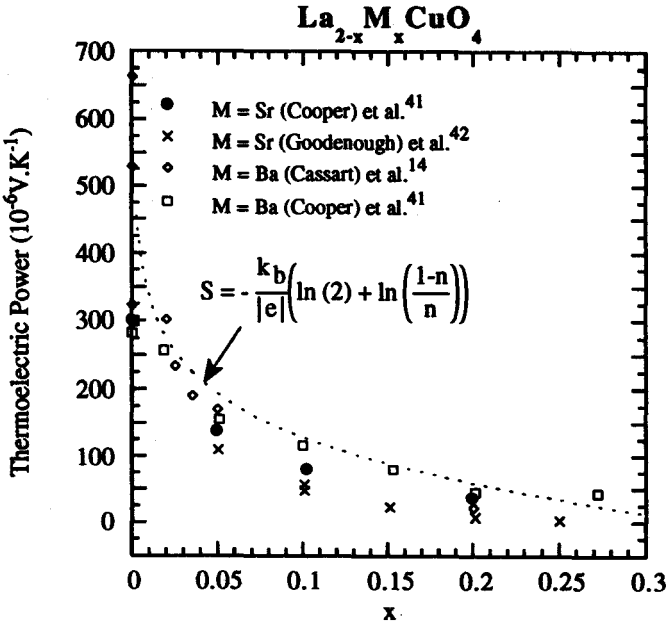

FIGURE 5 Room-temperature thermoelectric power vs. concentration in substitutional atoms for various $La_{2-x}M_xCuO_4$ compounds. The dashed line shows the concentration dependence computed from the modified Heikes formula (1).

the thermoelectric power is generally expected to exhibit an intermediate behavior between that of metals and semiconductors and should vary as $T^{1/2}$ in the case of a 3-D variable range hopping and as $T^{1/3}$ for 2-D.[40]

From the Hubbard model, where correlated hopping is concerned, the thermoelectric power is expected to be large and independent of temperature at high temperature. Then, to explain the constant thermoelectric power sometimes observed at high temperature for $La_2CuO_{4+\delta}$ and for samples with small amounts of Sr or Ba, Cooper et al.[41] suggested that the expression derived from the configurational entropy for correlated hopping of electrons in the Hubbard model was applicable. They proposed to use the following adapted Heikes formula:

$$S = -\frac{k_b}{|e|}\left(1n(2) + 1n\left(\frac{1-n}{n}\right)\right) \tag{2}$$

where n is the number of carriers per Cu^{2+} site. This expression also accounts for the strong decrease in magnitude of the thermoelectric power as the concentration of added elements is increased (see Figure 5). In that case, the thermoelectric power has a contribution from spin entropy which should be quenched by a large magnetic field. Since a field-independent thermoelectric up to 30 T was measured in a $La_{1.85}Sr_{0.15}CuO_{4-\delta}$ sample,[43] and though Allen et al.[44] suggested that a field of 30 T might still not be sufficient, the applicability of the correlated model for samples displaying linear "metallic" resistivity remains an open question.

There are discrepancies concerning the results obtained for La_2CuO_4 samples. As is the case for polycrystalline samples, some results obtained on single crystals indicate a temperature dependence of the ab-plane thermoelectric power consistent with the variable range hopping prediction ($T^{1/2}$),[45] while it is sometimes found to increase with decreasing temperature. In addition to these different temperature dependencies, the thermoelectric power in the c-axis direction is found to be surprisingly smaller than in the ab-plane and increases almost linearly with temperature.[46,47] Temperature dependencies of thermoelectric power measurements of various $La_2CuO_{4+\delta}$ samples are presented in Figure 6. It may be noted that around room temperature the thermoelectric power of these compounds varies from 700 to 10 $\mu V\ K^{-1}$.

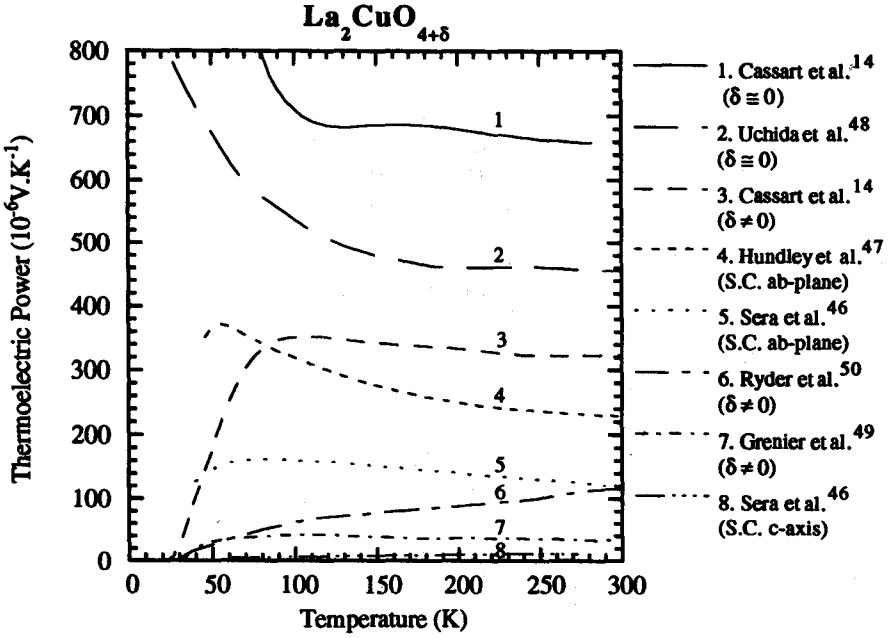

FIGURE 6 Temperature dependence of the thermoelectric power for various $La_2CuO_{4+\delta}$ single crystals and sintered samples. This figure shows the scatter in the data available from the literature.

The important differences observed in the results presented in Figure 6 could be explained by invoking the existence of a superconducting phase for the $La_2CuO_{4+\delta}$ with an excess in oxygen.[51] The presence of excess oxygen in the case of the $La_2CuO_{4+\delta}$ leads to an important decrease of the electrical resistivity, the thermoelectric power, and the Neel temperature.[14,51] Neutron-diffraction investigations as a function of temperature indicate that for such samples with excess oxygen, a reversible phase separation into two closely related structures occurs below room temperature.[52] Below the phase separation temperature, the material consists of a nonsuperconducting stoichiometric phase and a superconducting oxygen-rich phase. The important modification in the thermoelectric power observed for only small excesses in oxygen could then be explained by invoking electrical circuits where the antiferromagnetic and superconducting phases are in parallel with some resistances in series.[14]

The most commonly used way to decrease the thermoelectric power of the stoichiometric compounds consists in substituting Ba or Sr for La (see Figure 5). For low concentrations of substitutional atoms, the in-plane thermoelectric power is usually found to follow that measured on polycrystalline materials. This is not very surprising since the thermoelectric power is generally dominated by that of the most conducting component. However, for the low Sr concentrations, the thermoelectric power is found to be smaller in the c-axis direction than in the ab-direction and increases with increasing temperature as in the nonsubstituted La_2CuO_4.[46] So the thermoelectric power is higher in the direction where the electrical resistivity is the lowest.

The presence of fluorine in the ceramics of the $La_{2-x}Ba_xCuO_{4+\delta}$ family has a strong influence on the transport properties (see Figure 7).[14] It either leads to a superconducting behavior for samples that are not initially superconductors or increases the temperature of the superconducting transition. Above T_c, the fluorine treatment causes a decrease in the magnitude of the electrical resistivity and thermoelectric power that was attributed to an increase of the charge carrier density introduced by the fluorination treatment. The effect of fluorine treatment was found to be qualitatively the same as that of an increase in barium concentration.

At high concentration of added atoms, thermoelectric measurements performed on ceramic samples revealed a change of sign at high temperatures.[53,54] This result has been invoked to postulate the existence of a two-carrier model with opposite charges. Moreover, one possible explanation of the temperature dependence and of the substitution dependence of the Hall coefficient

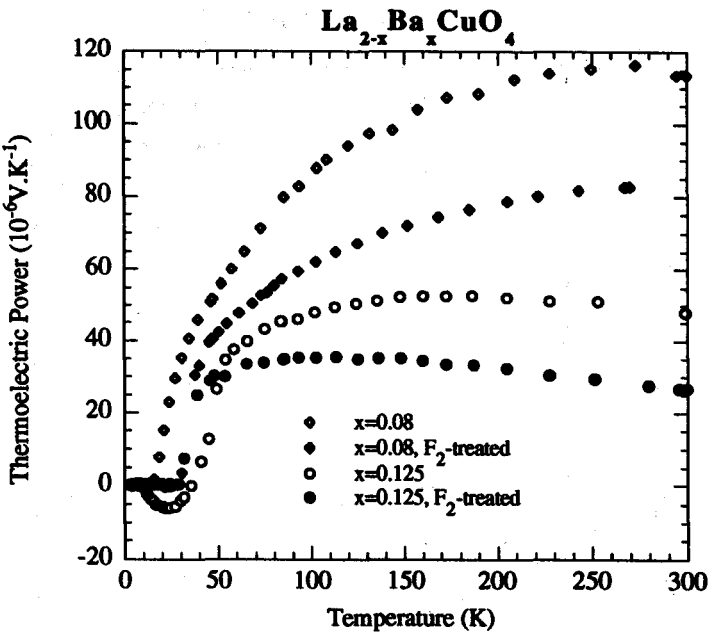

FIGURE 7 Temperature dependence of the thermoelectric power of $La_{2-x}Ba_xCuO_4$, for x = 0.08 and x = 0.125, either untreated (open symbol) or treated (filled symbols) with fluorine gas. The Seebeck coefficient of the untreated x = 0.125 sample exhibits a sharp drop below 60 K (the temperature of the low-temperature structural transition), and even becomes negative.

observed in the $La_{2-x}Sr_xCuO_4$ compounds could be partially found in the existence of two energy bands with different mobilities.[55] By contrast, there also exist good arguments against ascribing the anomalous temperature dependence of the Hall effect to a multiband model.[18,56]

The authors believe that the anomalies observed at the low-temperature structural transition in the particular composition x = 0.125 could hardly be explained in the frame of a single carrier model.[14] Indeed, near the occurrence of the low-temperature tetragonal phase, the thermoelectric power decreases drastically and changes sign, while the Hall coefficient presents a sharp decrease and the electrical resistivity increases.[57,58]

Different works have shown similar results for the $La_{2-x-y}Sr_xM_yCuO_4$ system with M = Nd, Eu, Gd, Dy, Tb.[59,60] For example, the $La_{1.85-y}Sr_{0.15}Nd_yCuO_4$ compounds with $0 \leq y \leq 1.0$ exhibit bulk superconducting behavior only for $y \leq 0.4$.[36,37] For $y \geq 0.18$, a low-temperature structural transition occurs which could be associated with the decrease or the disappearance of the superconducting properties. In this system, a decrease in the thermoelectric power and in the Hall coefficient, and a change of sign of the thermoelectric power, were also found.[59,61] These observations were also related to the existence of two types of carriers.[62]

For $La_{1.875}$ $Ba_{0.125}$ CuO_4 which corresponds to the formation of the (LTT) phase, the F_2-treatment leads to the appearance of bulk superconductivity at 32 K, and suppresses all the anomalies usually reported for the transport properties.[15] These results enable one to suppose that fluorination suppresses the low-temperature structural transition, as in the case of the $La_{1.85-x}Nd_x$ $Sr_{0.15}CuO_4$ system.[62]

Other Compounds

For the $YBa_2Cu_3O_{7-\delta}$ family, one of the clear trends is that the thermoelectric power increases as the oxygen deficiency increases (see Figure 8).[63,66] When $\delta \cong 0$, the thermoelectric power is found to be small and for very small oxygen deficiencies, negative values of α are observed. This behavior is also sometimes attributed to the existence of two-band conduction with carriers of opposite signs. Substitution, intercalation, neutron irradiation, or other treatments that decrease or suppress

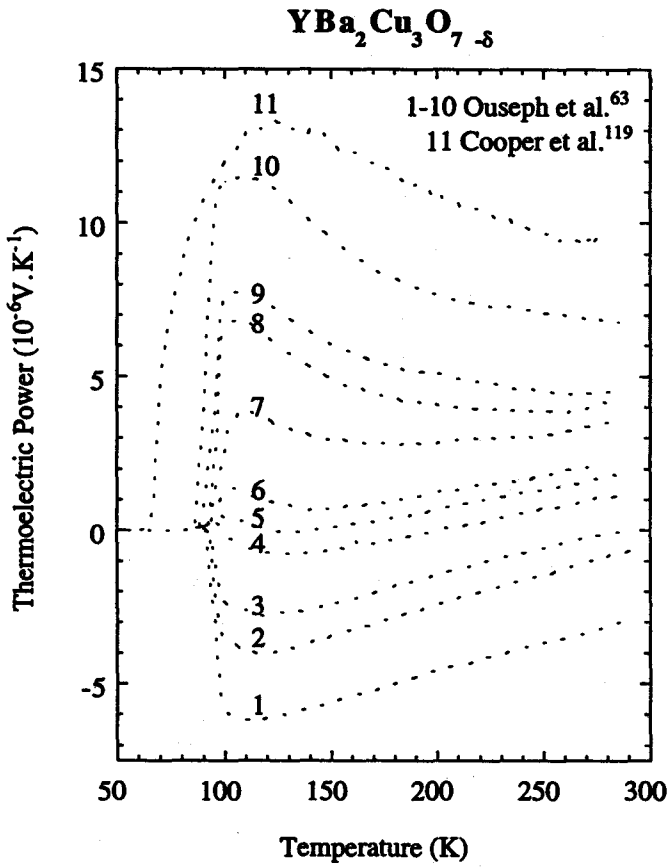

FIGURE 8 Variation of thermoelectric power for $YBa_2Cu_3O_{7-\delta}$ as a function of temperature with different oxygen content. $\delta = 0$ for curve 1; 0.02 for curve 2; 0.06 for curve 3; 0.07 for curve 4; 0.09 for curve 5; 0.10 for curve 6; 0.14 for curve 7; 0.16 for curve 8; 0.17 for curve 9; 0.19 for curve 10; and 0.3 for curve 11.

superconducting properties are usually found to have consequences on the thermoelectric power similar to a reduction in oxygen content.

The thermoelectric power of the Bi or Tl compounds is usually found to follow a similar behavior to that of the $YBa_2Cu_3O_{7-\delta}$ compounds.[67,68] It is, for example, drastically dependent on substitution and on oxygen concentration.[69] While the insulator compounds have very large thermoelectric powers with a temperature dependence characteristic of a variable range hopping behavior, the superconducting samples have thermoelectric powers similar to those of the other high-T_c materials. A change of sign with temperature or with composition is also frequently observed, and is sometimes related to the existence of two groups of carriers with opposite charges.[70–74]

While the in-plane thermoelectric power results for twinned $YBa_2Cu_3O_{7-\delta}$ single crystals are very different from one author to another, the out-of-plane thermoelectric power data are more consistent. All results show a positive thermoelectric power that increases approximately linearly with temperature (Figure 9).[70,75–77] The thermoelectric power in the a-direction of $YBa_2Cu_3O_{7-\delta}$ untwinned single crystals is found to be positive near T_c, becomes negative with increasing temperature, and then varies almost linearly with temperature (Figure 9).[39,78] This behavior is quite similar to the in-plane thermoelectric power of the Bi and the Tl materials (Figure 9), while the same features have been observed for the $Nd_{2-x}Ce_xCuO_4$ crystals.

A controversial problem has been the nature of the charge carriers in the $Nd_{2-x}Ce_xCuO_4$ compounds. Initial observations of negative thermoelectric power and Hall coefficient appeared to

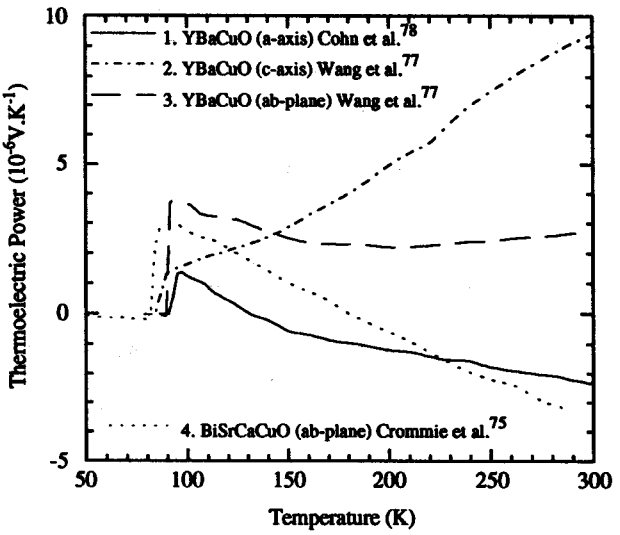

FIGURE 9 Temperature dependence of the thermoelectric power of various single crystals. The negative slope seems to be a "universal" behavior for the CuO_2 planes.

confirm that Ce contributes electron-like carriers to the CuO_2 planes.[79] On the other hand, other reports of positive Hall effect and thermoelectric power have suggested that holes may be the dominant carriers as in other cuprates.[80–82] In a more recent paper, it was speculated that the thermoelectric power of the $Nd_{2-x}Sr_xCuO_4$ compound contains a contribution from both a highly correlated system in the CuO_2 planes and from electron-like carriers possibly residing in the Nd_2O_2 layers.[83] At low substitutional atoms concentration the CuO_2 planes generate a large and negative thermoelectric power.[84] With increasing Ce contents, the correlation contribution is decreased to a small value, while the diffusion thermoelectric power of the electron band contributes a negative slope to the thermoelectric power. Also, in order to explain the temperature dependence of the thermoelectric power of $Nd_2CuO_{4-x}F_x$ samples, the effect of a magnon drag contribution was considered.[85]

The first measurements on $Ba_{1-x}K_xBiO_3$ have suggested that their thermoelectric power follows the traditional behavior of a diffusion metallic type thermoelectric power rather than a pattern similar to that of the Cu-O plane superconductors.[86] However, the data of Uher et al. show some similar trends for the thermoelectric powers of the Bi-O and the Cu-O planes superconductors.[87]

Model for the CuO_2 Thermoelectric Power

The increase with decreasing temperature and the shift from negative to positive values, which seem to be intrinsic to the CuO_2 planes, have been interpreted as indicating a negative diffusion thermoelectric power for the CuO_2 plane. In 1988 the calculation made by Allen et al. predicted the sign of thermoelectric power of good superconducting samples to be negative in the ab-plane and positive along the c-axis.[88] Opposite signs for the Hall coefficient and thermoelectric power may be due, for example, to the presence of many groups of carriers, with complicated Fermi surfaces. The weighting factors for combining thermoelectric power and Hall coefficient contributions may then be different.

The temperature dependence of the thermoelectric power is usually found to result from the competition between a T-dependent diffusion part and an important phonon drag contribution. In order to fit their results, Cohn et al. have suggested the addition of a freeze-out of electron-phonon umklapp scattering involving holes in the CuO_2 planes and optical-mode phonons.[66,78] However, instead of phonon drag, a T^{-1} additional contribution is sometimes attributed to electron-electron interactions.[89,90]

Mawdsley et al. have proposed a strong electron-phonon enhancement of the diffusion thermoelectric power.[91] Then they propose to use the following expression to explain the temperature dependence of the thermoelectric power:

$$S = X_b T + A\lambda_s(T)T \tag{3}$$

where λ_s is the temperature-dependent enhancement of thermoelectric power, X_b is the bare unenhanced thermoelectric parameter, usually taken as a constant, and A is a constant depending on the mass enhancement and on the materials. Using this expression they found that the thermoelectric power of single crystals from different families of high-T_c superconductors is consistent with strong large electron-phonon interactions in the plane, while the out-of-plane electron-phonon coupling is smaller.

In all these discussions, one should bear in mind that the thermoelectric power is the transport property that is the most sensitive to the details of the band structure. Since it depends on a balance resulting from the energy dependencies of the density of states and relaxation time, the sign of the diffusion thermoelectric power might be different from that of the charge carriers, even for the case of a single Fermi surface.

The explanation of the thermoelectric power behavior in high-temperature superconductors is controversial and presents a major challenge to the various models proposed for the superconducting mechanism. Unfortunately, few predictions for the thermoelectric behavior have been made. In all these compounds the thermoelectric power appears to be very sensitive to the chemical composition which drastically affects the density and sign of the charge carriers. Such sensitivity of the thermoelectric power is well illustrated by the drop of more than three orders of magnitude when x is varied from 0 to 0.2 in the $La_{2-x}Sr_xCuO_4$ compounds.

High-T_c superconductors have extended the temperature range in which thermoelectric powers could be determined with good precision. Indeed, an ideal reference material to determine the absolute Seebeck coefficient of solids should have zero thermoelectric power and be insensitive to external magnetic fields. It is interesting to note that with the discovery of high-T_c an ideal reference material becomes available to calibrate and determine the absolute thermoelectric power of a solid in a thermoelectric circuit. Furthermore, in a wide range of temperatures, magnetic fields have no effect.[92]

30.6 Thermal Conductivity[93–95]

Thermal Conductivity and Superconducting Transition

Generally speaking, the low-temperature thermal conductivity is mainly the sum of two contributions the electronic, λ_e, and the lattice, λ_L, thermal conductivities:

$$\lambda = \lambda_e + \lambda_L \tag{4}$$

where λ is the total measured thermal conductivity. For most of the compounds of the high-T_c families, simultaneous electrical and thermal conductivity measurements have indicated that λ_e is small with respect to λ_L. Indeed, using the Wiedemann-Franz relation:

$$\lambda_e = L_o T \rho^{-1} \tag{5}$$

the higher limits for the relative contribution of the electronic thermal conductivity in the normal state may be estimated from the temperature variation of the electrical resistivity. L_o is the free electron Lorenz number ($L_o = 2.44\ 10^{-8}\ V^2\ K^{-2}$). The fact that electron-phonon scattering is most probably inelastic above 100 K should lead to a decrease of the Lorenz ratio $(\lambda_e \cdot \rho)/T$ with respect to L_o.

In its simplest form, the lattice or phonon thermal conductivity may be expressed in the frame of the Debye model as[96]

$$\lambda_L = \frac{1}{3} C_v V l \tag{6}$$

where C_v is the lattice specific heat at constant volume, V is the velocity of sound, and l is the phonon mean free path. At low temperature the specific heat is found to vary as T^3 with, in some cases, the presence of an additional linear term which seems to be of extrinsic origin, i.e., related to impurities. For a polycrystalline electrical insulator, where the phonon mean free path is constant when it is limited by grain boundary scattering, the thermal conductivity is thus expected to vary as T^3 when the specific heat varies as T^3. As will be seen later, such a simple observation is not always made for compounds of the high-T_c superconductor families.

For traditional superconducting metallic alloys, when the lattice thermal conductivity is dominant, it is primarily limited by phonon-electron scattering.[97] Defect scattering may also play an important role.[98] Thus, one observes an increase in λ_L below T_c, since the phonons are not scattered by the fraction of the electrons which form Cooper pairs. On the other hand, λ_e decreases with decreasing temperature because the density of Cooper pairs, which do not carry heat, increases with decreasing temperature. Since in high-T_c compounds the phonons seem to provide the largest fraction of the total normal-state thermal conductivity, an increase of the total thermal conductivity with decreasing temperature below T_c should be expected. This is exactly what was observed by most investigators.[93–95] A first discussion of this result on the $YBa_2Cu_3O_{7-\delta}$ compounds was done assuming that the charge carriers experience band conduction in the Boltzmann approximation and that the heat carriers are those usually responsible for the low-temperature thermal conductivity of solids, as described above, i.e., the phonons and the charge carriers.[99] The results, which were thus qualitatively interpreted in terms of the ordinary electronic and phonon transport theory applied to superconducting metallic alloys, were found to be self-consistent. It was suggested that a strong electron-phonon coupling should be considered, at least partly, in the interpretation of superconductivity in these materials.[99] There now exist theoretical models adapted from the Bardeen, Rickayzen, and Tewordt theory, which have been used to fit satisfactorily the thermal conductivity of different high-T_c compounds.[100–102]

La_{2-x} (Ba,Sr) × CuO_4 Compounds

The first report on the thermal conductivity of La_2CuO_4 single crystals revealed a peculiar temperature dependence (see Figure 10).[103] In contrast, a subsequent measurement performed on another single crystal failed to observe the out-of-plane minimum.[104] The presence of such a minimum has been attributed by Morelli et al. to a reduction of the phonon-disordered spin interactions below the temperature of magnetic ordering.[103] The position of this minimum should therefore be related directly to the Neel temperature. As already stated, the Neel temperature of La_2CuO_4 decreases from 320 to 230 K when the excess of oxygen increases. Subsequent measurements made on two sintered samples with different Neel temperatures (300 and 235 K) have not shown any modification of the temperature at which the minimum thermal conductivity occurs.[14,15] However, it has been observed in those two sintered samples that in the temperature range where the thermal conductivity increases, the electrical resistivity increases drastically. Furthermore, the sample with an excess oxygen also presents a maximum in the thermal conductivity around 210 K where a maximum in the electrical resistivity is observed.[14,15] Since there is an obvious correlation between the electrical resistivity and the thermal conductivity, it was then proposed that the measured minimum in the thermal conductivity has to be related to electron-phonon interactions.[14,15]

The partial substitution of Sr or Ba for La leads to a decrease of the thermal conductivity which could be attributed to increased scattering by the lattice defects introduced by the substituting atoms, which is not overweighted by the effect of an increased carrier density at low concentration of substitutional atoms (see Figure 11).[105,106] This decrease in the thermal conductivity with increasing added atoms concentration is more important for the case of Ba than for the case of Sr. This should be attributed to the larger difference between the atomic radii of Ba^{2+} and La^{3+}. Since no important increase in thermal conductivity has been observed below the superconducting transition for good superconducting samples, it could be concluded that for $x \leq 0.2$ the lattice thermal conductivity, which is dominant in this family of samples, is essentially limited by phonon-defects interactions.

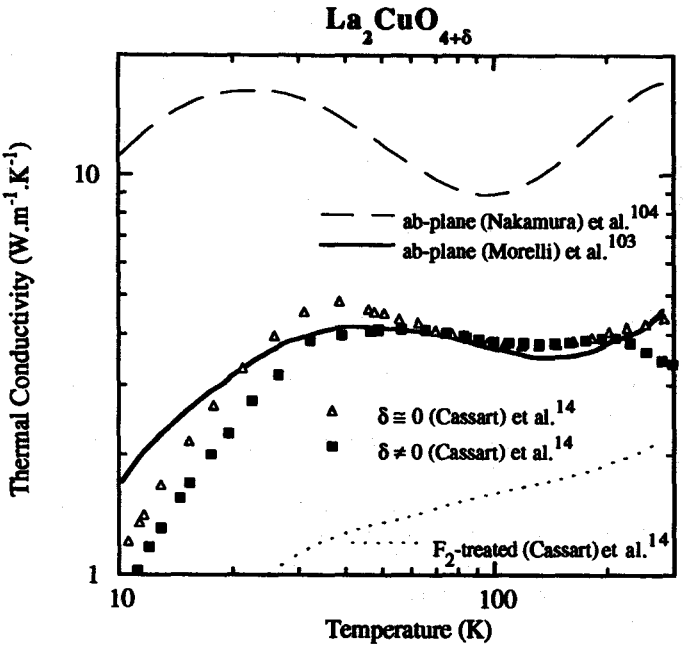

FIGURE 10 Comparison of the temperature dependence of the thermal conductivity for $La_2CuO_{4+\delta}$ single crystal and for sintered samples treated either at 450°C in O_2, or at 600°C in Ar, or at 200°C in F_2 atmosphere.

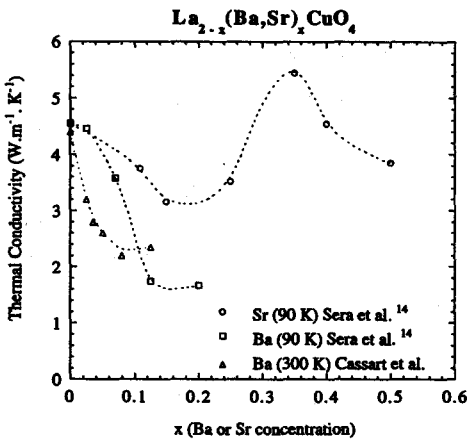

FIGURE 11 Concentration dependence of the thermal conductivity of sintered samples of $La_{2-x}(Sr/Ba)_xCuO_4$.

The thermal conductivity for the x = 0.125 (Ba) sample has been found to be partially at variance with this behavior and was found to present an anomaly at a temperature that corresponds to the low-temperature structural transition (Figure 12).[14–57] While the thermal conductivity was found to first decrease with decreasing temperature, a drastic increase was observed below the temperature at which the LTT phase appears, i.e., around 60 K. Below 10 K, the thermal conductivity reaches similar values to that of the La_2CuO_4 sample. The observed temperature of the minimum thermal conductivity corresponds reasonably well to the temperature of the upturn observed in the electrical resistivity, showing that in this particular sample the electron-phonon interactions are one of the most important scattering events for phonons. When Nd is substituted for La in

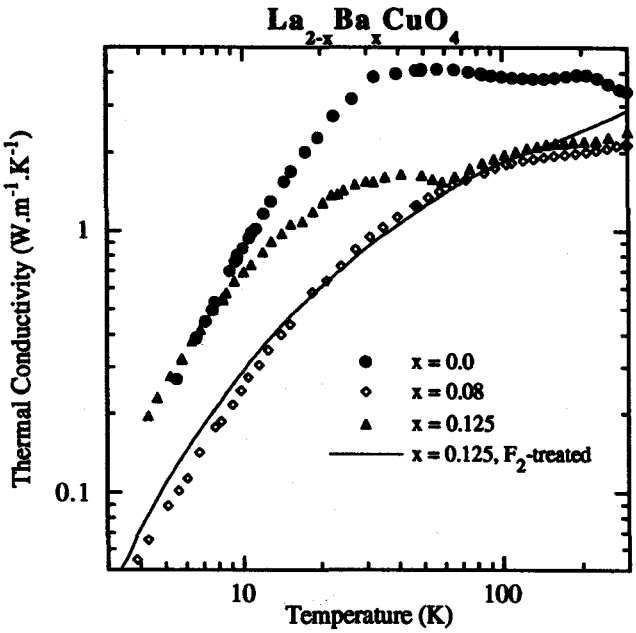

FIGURE 12 Temperature dependence of the thermal conductivity for various samples of the $La_{2-x}Ba_xCuO_4$ family. The plain curve shows the temperature dependence of the F_2-treated (x = 0.125) sample.

$La_{1.85}Sr_{0.15}CuO_4$, the thermal conductivity also exhibits a minimum at a temperature that corresponds to the low-temperature structural transition.[62]

In summary, in the $La_{2-x}(BaSr)_xCuO_4$ compounds, for $x \leq 0.2$ the two most important scatterers for phonons are the electrons and the imperfections introduced by substitution. For good samples, according to the doping concentration, either the phonon-electron or the phonon-defect interaction explains the temperature dependence of the thermal conductivity above 4 K. In the $x \gg 0.2$ range, the electronic thermal conductivity becomes comparable to the phonon contribution and its presence leads to an increase in the total thermal conductivity (see Figure 11).

At low temperature, while the temperature dependence of the thermal conductivity of sintered samples of these compounds generally follows a T^2 law, single crystals data usually show a temperature dependence in the ab-plane closer to a T^3 law, sometimes with the presence of an additional linear term.[93,95] In the out-of-plane direction, a T^2 law is observed.[95]

The thermal conductivity of La_2CuO_4 is reduced after fluorination whatever the starting material. For superconducting alloys where the lattice thermal conductivity is dominant and primarily limited by phonon-electron scattering, an increase in the thermal conductivity below T_c is observed, since the phonons are not scattered by the fraction of electrons which are in the superconducting state. In contrast, in the fluorinated samples, only a very small increase is observed. This may imply that the drastic decrease of the thermal conductivity due to the fluorine treatment cannot be attributed only to the increase of the interactions between phonons and charge carriers. It suggests that a fraction of the decrease in thermal conductivity can be attributed, as in the case of the barium-doped La_2CuO_4, to lattice disorder introduced by the fluorination process (see Figure 10).[14] It can be observed in Figure 12 that, after fluorination, the peculiar increase measured below 60 K in the thermal conductivity of the untreated $La_{1.85}Ba_{0.125}CuO_4$ sample is suppressed.

Other Compounds

It is worth adding that the in-plane thermal conductivity enhancement in the superconducting state is nearly a general property of high-T_c superconductors (see Figure 13). The two exceptions

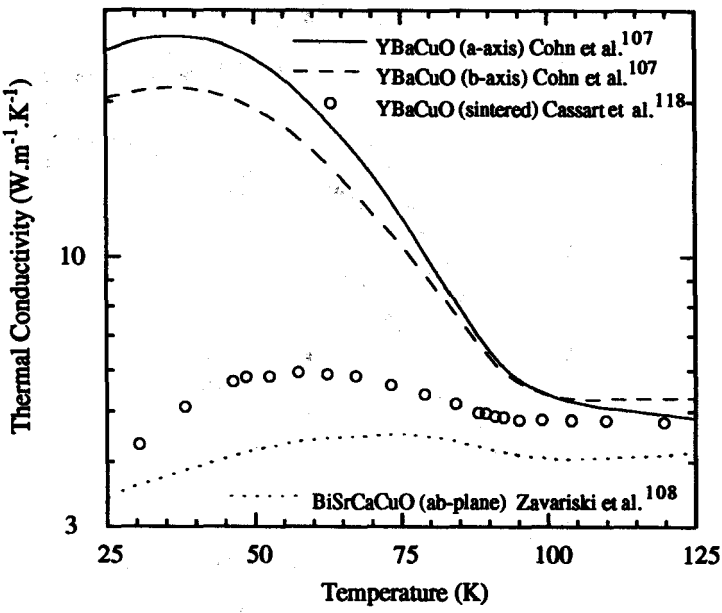

FIGURE 13 Temperature dependence of the thermal conductivity of various superconductor samples near the superconducting transition. The two upper curves (plain and dashed) and the lower curve (points) are relative to single crystals, while the intermediate curve (open circles) is relative to a sintered sample.

are the copperless family, i.e., $Ba_{1-x}K_xBiO_3$, and the $Nd_{2-x}Ce_xCuO_4$ family. However, in the c-direction, such an enhancement of the thermal conductivity is not always observed.[95]

In summary, the most common explanation for the temperature dependence of the thermal conductivity is the following: in the normal state the thermal conductivity is assumed to be dominated by the lattice thermal conductivity, which is significantly limited by phonon-electron scattering, but also by phonon-defect scattering and phonon-phonon scattering.[93–95] Below T_c, the number of electrons available to scatter phonons drops progressively due to the superconducting condensation.

By contrast, Yu et al.[109] have recently proposed that the strong suppression of the quasi-particle scattering rate observed below the superconducting transition is responsible for the enhancement of the superconducting state temperature. They assume that the electron-phonon scattering may not be significant in comparison with phonon-phonon or phonon-defect scattering.

A large number of in-plane low-temperature thermal conductivity results obtained on superconducting samples could be fitted by expressing the thermal conductivity as the sum of a linear and a cubic term. The cubic contribution reflects the boundary scattering of phonons, as expected.[93,95] Other results showing a T^2 dependence for the low-temperature data are related to resonant phonon scattering with low-energy excitations, i.e., tunnelling systems similar to those found in disordered materials.[94] However, the T^2 dependence seems to be a general feature of the Bi-Sr-Ca-Cu-O compounds where it could be related to the more important anistropy ratio of this material, i.e., to a classical 2-D behavior.

The thermal conductivity is a unique tool to provide information about both the normal and superconducting states. An analysis of the results could be used, for example, to obtain information on the superconducting energy gap, the strength of the electron-phonon coupling, fluctuation effects, etc.[102,110] It could also be used, as proposed by Richardson et al., as a probe of the vortex state.[111,112]

30.7 Passive Elements in Thermoelectric Coolers

Copinathan et al.[113] have proposed the use of high-T_c superconductors as passive thermoelements. Indeed, in the liquid nitrogen temperature range, the best materials for thermoelectric refrigeration

are the n-type bismuth-antimony alloys. High figures-of-merit are obtained when the electric current is directed along the trigonal axis. A significant drawback which hampers the practical use of thermoelectric couples based on these alloys is the fact that the n-type branch has thermoelectric parameters far superior to those of any material which might be used as the p-type branch. Then, rather than decreasing the figure-of-merit of the couple by using a p-type material with inferior thermoelectric properties, it is advantageous to substitute a high-T_c superconductor for the p-type branch for operating at the liquid nitrogen temperature range.

An important consideration in any practical use of this concept is the current density needed to maximize the thermoelectric cooling. Copinathan et al.[113] estimate that for a convenient length of 10 mm and the typical transport parameters of Bi-Sb, a critical current density of the order of 120 A cm^{-2} is needed to achieve maximum cooling effect. This is now possible to realize with oriented grains ceramics. Different workers have investigated this particular use of high-T_c compounds.[114–116] It has been shown that a thermocouple of an n-type $Bi_{1-x}Sb_x$ and a high-T_c ceramic has a higher figure-of-merit than that of a thermocouple with the same negative branch and with samples with a lower figure-of-merit like $Bi_{2-x}Sb_xTe_{3-y}Se_y$ for the positive branch. It has been shown that the use of high-T_c compounds is also efficient when the passive element is not fully in the superconducting state. Indeed, if the current through these superconductors is above the critical level, its resistivity increases, but very slowly. Then, within a limited region above the theoretical critical current density, the cooling efficiency continues to grow with increasing electrical current. This implies that the requirements on the critical current are less stringent than those first estimated by Copinathan.

30.8 Figure-of-Merit

Among the new materials developed during the last decade, the oxide compounds of the $La_{2-x}M_xCuO_4$ family are, up to now, the most promising potential candidates for thermoelectric conversion. In sintered samples, figures-of-merit greater than 10^{-4} K^{-1} have been obtained.[117] There are no other families of materials, except traditional thermoelectric materials, which present figures-of-merit comparable to this value. This is still a very low value, but this result could most probably be improved by using single crystals. Indeed, the thermoelectric power in the ab-plane is found to be higher than in the c-direction while the electrical resistivity is more than two orders of magnitude higher in the c-direction. Unfortunately, the thermal conductivity of single crystals is greater than that of sintered materials. The most promising compounds for thermoelectric cooling are those that have not yet been intensively studied since they do not present superconducting properties.

From the results available in the literature it is possible to estimate α^2/ρ higher than 3.10^{-4} W $m^{-1}K^{-2}$ for sintered samples of the $YBa_2Cu_3O_{7-\delta}$ family, with δ in the range 0.65 to 0.75, while the thermal conductivity lies between 2 and 6 W m^{-1} K^{-1} for ceramic samples with lower oxygen depletion and decreases with decreasing oxygen concentration. Once again, the use of single crystals would certainly increase the figure-of-merit. Unfortunately, it is very difficult to obtain large crystals with homogeneous spatial distribution of oxygen.

A few compounds for which it is possible to modify drastically the thermoelectric power by modifying the stoichiometry could be envisaged as candidates for thermoelectric conversion. It would certainly be interesting to investigate the copper oxide materials in which superconducting properties were not found.

30.9 Concluding Remarks

By means of a few examples, the authors have discussed the thermoelectric properties—electrical resistivity, thermoelectric power, and thermal conductivity—of the main high-T_c superconductor families.

Though the absence of reliable models for the electronic structure and the low quality of most of the samples usually investigated render a rigorous discussion of the transport effects difficult, at least some general trends are followed by most of the high-T_c families.

The electrical resistivity and thermoelectric power are very sensitive to the concentration of substituted atoms and to other lattice defects. Many conductivity regimes are proposed for the normal state, but none of them is yet fully understood.

The intrinsic lattice thermal conductivity seems to be limited by a strong electron-phonon interaction. This observation, which had already been made from earlier results pertaining to the behavior around the transition temperature, is confirmed for higher temperatures.

Though the thermoelectric figures-of-merit of high T_c are still too low compared to those of traditional thermoelements, further investigations on the non-superconducting compounds might reveal promising candidates for Peltier cooling.

Acknowledgements

This work was carried out under the financial support of the program "Action de Recherche Concertée." sponsored by "D.G.E.S.R. de la communauté Francaise de Belgique." The authors thank Professors J. P. Michenaud, B. Chevalier, and A. Tressaud, and doctors V. Bayout, L. Piraux, and E. Grivei for critical reading of the manuscript and fruitful discussions. The authors acknowledge also support for the work by the U.S. Navy under contract n°N00167–92–K0052.

References

1. Bednorz, J. G. and Müller, K. A., *Z. Phys. B*, 64, 189, 1986.
2. Allen, P. B., in *High Temperature Superconductivity*, Lynn, J. W., Ed., Springer-Verlag, Berlin, 1990, 303.
3. Schrieffer, J. R., *Phys. Scr.*, T42, 5, 1992.
4. Anderson, P. W. and Schrieffer, R., *Phys. Today*, 44, 55, 1991.
5. Sleight, A. W., in *High Temperature Superconductivity*, Tunstall, D. P. and Barford, W., Eds, Co-published by S.U.S.S.P. Publications and I.O.P. Publishing Ltd., Bristol, 1991, 97.
6. Sleight, A. W., *Phys. Today*, 44, 24, 1991.
7. Stupp, S. E. and Ginsberg, D. M., in *Physical Properties of High Temperature Superconductors III*, Ginsberg, D. M., Ed., World Scientific, Singapore, 1992, 1.
8. Lemberger, T. R., in *Physical Properties of High Temperature Superconductors III*, Ginsberg, D. M., Ed., World Scientific, Singapore, 1992, 471.
9. Tokura, Y., *Physica C*, 185–189, 174, 1991.
10. Batlogg, B., *Phys. Today*, 44, 44, 1991.
11. Santoro, A., in *High Temperature Superconductivity*, Lynn, J. W., Ed., Springer-Verlag, Berlin, 1990, 84.
12. Raveau, B., Michel, C., Hervieu, M., and Groult, D., in *Crystal Chemistry of High-T_c Superconducting Copper Oxides*, Springer Series in Materials Science, 15, Springer-Verlag, Berlin, 1991.
13. Torrance, J. B., Bezinge, A., Nazzal, A. I., and Parkin, S. S. P., *Physica C*, 162–164, 291, 1989.
14. Cassart, M., Grivei, E., Issi, J.-P., Ben Salem, E., Chevalier, B., Brisson, C., and Tressaud A., *Physica C*, 213, 327, 1993.
15. Cassart, M., Grivei, E., Issi, J.-P., Robin-Brisson, C., Ben Salem, E., Chevalier, B., Tressaud, A., and Etourneau, J., in *Icmas 92-Superconductivity*, Chu, C. W. and Fink, J., Eds, I.I.T.T. International, Paris, 1992, 185.
16. Takagi, H., Cava, R. J., Marezio, M., Batlogg, B., Krajewski, J. J., Peck, W. F., Bordet, P., and Cox, D. E., *Phys. Rev. Lett.*, 68, 3777, 1992.
17. Phillips, J. C., *Phys. Rev. B*, 46, 8542, 1992.
18. Iye, Y., in *Physical Properties of High Temperature Superconductors III*, Ginsberg, D. M., Ed., World Scientific, Singapore, 1992, 287.
19. Mott, N. F. and Davis E. A., in *Electronic Processes in Non-Crystalline Materials*, 2nd ed., Clarendon Press, Oxford, 1979.
20. Shklovskii, B. I. and Efros, A. L., in *Electronic Properties of Doped Semiconductors*, Springer Series in Solid-State Sciences, Cardon, M., Ed., Springer-Verlag, Berlin, 1984.
21. Quitmann, C., Andrich, D., Jarchow, C., Fleuster, M., Beschoten, B., Güntherodt, G., Moshchalkov, V. V., Mante, G., and Manske, R., *Phys. Rev. B*, 46, 11813, 1992.

22. Fiory A. T., Martin, S., Fleming, R. M., Scheenmeyer, L. F., Waszcak, J. V., Hebard, A. F., and Sunshine, S. A., *Physica C*, 162–164, 1145, 1989.
23. Grimvall, G., in *The Electron-Phonon Interaction in Metals*, Wohlfarth, E. P., Ed., Selected Topics in Solid State Physics 16, North-Holland, Amsterdam, 1981, 232.
24. Lee, P. A. and Read, N., *Phys. Rev. Lett.*, 58, 2691, 1987.
25. Newns, D. M., Tsuei, C. C., Pattnaik, P. C., and Kane, C. L., *Comments Condensed Matter Phys.*, 15, 273, 1992.
26. Anderson, P. W. and Zou, Z., *Phys. Rev. Lett.*, 60, 132, 1988.
27. Cieplak, M. Z., Guha, S., Kojima, H., Indenfeld, P. L., Xiao, G., Xiao, J. Q., and Chien, C. L., *Phys. Rev. B.*, 46, 5536, 1992.
28. Awana, V. P. S., Agarwal, S. K., Das, M. P., and Narlikar, A. V., *J. Phys.*, 4, 4971, 1992.
29. Kimura, T., Kishio, K., Kobayashi, T., Nakayama, Y., Motohira, N., Kitazawa, K., and Yamafuji, K., *Physica C*, 192, 247, 1992.
30. Iye, Y., *Int. J. Mod. Phys. B*, 3, 367, 1989.
31. Ito, T., Takagi, H., Shibashi, S., Ido, T., and Uchida, S., *Nature*, 350, 596, 1991.
32. Radousky, H. B., *J. Mater. Res.*, 7, 1917, 1992.
33. Hellman, E. S., Miller, B., Rosamilia, J. M., Hartford, E. H., and Baldwin, K. W., *Phys. Rev. B*, 44, 9719, 1991.
34. Kaiser, A. B. and Uher, C., in *Studies of High Temperature Superconductors*, Vol. 7, Narlikar, A. V., Ed., Plenum Press, New York, 1990, 353.
35. Ginzburg, V. L., *Superconductor Sci. Technol., 4, S1, 1991.*
36. Akinaga, M., in *Studies of High Temperature Superconductors*, Vol. 8, Narlikar, A. V., Ed., Plenum Press, New York, 1990, 297.
37. Kaiser, A. B. and Uher, C., *Aust. J. Phys.*, 41, 597, 1988.
38. Howson, M. A., Salamon, M. B., Freidmann, T. A., Rice, J. P., and Ginsberg, D. M., *Phys. Rev. B*, 41, 300, 1990.
39. Lowe, A. J., Regan, S. E., and Howson, M. A., *J. Phys. Condensed Matter*, 4, 8843, 1992.
40. Chaikin, P. M., in *Organic Superconductivity*, Kresin, V. Z. and Little, W. A., Eds., Plenum Press, New York, 1990.
41. Cooper, J. R., Alavi, B., Zhou, L.-W., Beyermann, W. P., and Grüner, G., *Phys. Rev. B*, 35, 8794, 1987.
42. Goodenough, J. B. and Manthiram, A., in *Studies of High Temperature Superconductors*, Vol. 5, Narlikar, A. V., Ed., Plenum Press, New York, 1990.
43. Yu, R. C., Naughton, M. J., Yan, X., Chaikin, P. M., Holtzberg, F., Greene, R. L., Stuart, J., and Davies, P., *Phys. Rev. B*, 37, 7963, 1988.
44. Allen, P. B., Fisk, Z., and Migliori, A., in *Physical Properties of High T_c Superconductors*, Ginsberg, D. M., Ed., World Scientific, Singapore, 1989, 217.
45. Cheong, S.-W., Fisk, Z., Kwok, R. S., Remeika, J. P., Thompson, J. D., and Gruner, G., *Phys. Rev. B*, 37, 5916, 1988.
46. Sera, M., Shamota, S., and Sato, M., *Solid State Commun.*, 68, 649, 1988.
47. Hundley M. F., Kwok, R. S., Cheong, S. W., Thompson, J. D., and Fisk, Z., *Physica C*, 172, 455, 1991.
48. Uchida, S.-I., Takagi, H., Ishii, H., Eisaki, H., Yabe, T., Tajima, S., and Tanaka, S., *Jpn. J. Appl. Phys.*, 26, L440, 1987.
49. Grenier, J. C., Wattiaux, A., Lagueyte, N., Park, J. C., Marquestaut, E., Etourneau, J., and Pouchard, M., *Physica C*, 173, 139, 1991.
50. Ryder J., Midgley, P. A., Exley, R., Beynon, R. J., Yates, D. L., Afalfiz, L., and Wilson, J. A., *Physica C*, 173, 9, 1991.
51. Demazeau, G., Tresse, F., Plante, Th., Chevalier, B., Etourneau, J., Michel, C., Hervieu, M., Raveau, B., Lejay, P., Sulpice, A., and Tournier, R., *Physica C*, 153–155, 824, 1988.
52. Jorgensen, J. D., Dabrowski, B., Shiyou Pei, Hinks, D. G., Soderholm, L., Morosin, B., Schirber, J. E., Venturini, E. L., and Ginley, S. G., *Phys. Rev. B*, 38, 11337, 1988.
53. Uher, C., Kaiser, A. B., Gmelin, E., and Walz, L., *Phys. Rev. B*, 36, 5676, 1987.
54. Ohtani T., Kobatake, K., and Takehara, T., *Physica C*, 179, 376, 1991.
55. Ruvalds, J. and Virosztek, A., *Phys. Rev. B*, 42, 399, 1990.

56. Ong, N. P., in *Physical Properties of High Temperature Superconductors II*, Ginsberg, D. M., Ed., World Scientific, Singapore, 1990, 459.
57. Sera, M., Ando, Y., Kondoh, S., Fukuda, K., Sato, M., Watanabe, I., Nakashima, S., and Kymagai, K., *Solid State Commun.*, 69, 851, 1989.
58. Suzuki, T., Tagawa, M., and Fujita, T., *Physica C*, 162–164, 983, 1989.
59. Büchner, B., Cramm, M., Braden, M., Braunisch, W., Hoffels, O., Schnelle, W., Harnischmacher, J., Borowski, R., Gruetz, A., Heymer, B., Hohn, C., Müller, R., Maldonado, O., Freimuth, A., Schlabitz, W., Heger, G., Khomskii, D. I., and Wohlleben, D., in *Physics and Materials Science of High Temperature Superconductors, II*, Kossowsky, R., Raveau, B., Wohlleben, D., and Patapis, S. K., Eds., NATO Asi Series, Kluwer Academic Publishers, Dordrecht, 1992, 349.
60. Crawford, M. K., Harlow, R. L., Mccarron, E. M., Farneth, W. E., Axe, J. D., Chou, H., and Huang, Q., *Phys. Rev. B*, 44, 7449, 1991.
61. Nakamura, Y. and Uchida, S., *Phys. Rev. B*, 46, 5841, 1992.
62. Cassart, M., Grivei, E., Issi, J.-P., Hetjmanek, J., Robin-Brisson, C., Ben Salem, E., Chevalier, B., Tressaud, A., and Etourneau, J., *J. Alloys Compounds*, 195, 335, 1993.
63. Ouseph, P. J. and O'Bryan, M. R., *Phys. Rev. B*, 41, 4123, 1990.
64. Cooper, J. R., Obertelli, S. D., Carrington, A., and Loram, J. W., *Phys. Rev. B*, 44, 12086, 1991.
65. Borchi, E., Degennaro, S., and Simoncini, M., *Phys. Lett. A*, 170, 102, 1992.
66. Cohn, J. L., Wolf, S. A., Selvamanickam, V., and Salama, K., *Phys. Rev. Lett.*, 66, 1098, 1991.
67. Munakata, F., Matsuura, K., Kubo, K., Kawano, T., and Yamauchi, H., *Phys. Rev. B*, 45, 10604, 1992.
68. Kosuge, M., Maeda, T., Sakuyama, K., Yamauchi, H., Koshizuka, N., and Tanaka, S., *Physica C*, 182, 157, 1991.
69. Forro, L., Lutatela, J., and Keszei, B., *Solid State Commun.*, 73, 501, 1990.
70. Kaiser, A. B. and Mountjoy, G., *Phys. Rev. B*, 43, 6266, 1991.
71. Smits, A. J., Elion, W. J., van Ruitenbeek, J. M., de Jongh, L. J., and Groen, W. A., *Physica C*, 199, 276, 1992.
72. Jha, S. R., Rajput, R., Kumar, D., Reddy, Y. S., and Sharma, R. G., *Solid State Commun.*, 81, 603, 1992.
73. Rao, C. N. R., Ramakrishnan, T. V., and Kumar, N., *Physica C*, 165, 183, 1990.
74. Song, Y. S., Choi, Y. S., Park, Y. W., Jang, M. S., and Han, S. K., *J. Moscow Phys. Soc.*, 1, 3, 1992.
75. Crommie, M. F., Zettl, A., Barbee, T. W., III, and Cohen, M. L., *Phys. Rev. B*, 37, 9734, 1988.
76. Li, L., Bei-hai, M., Shu-Yuan, L., Hong-Min, D., and Dian-Lin, Z., *Europhys. Lett.*, 7, 555, 1988.
77. Wang, Z. Z. and Ong, N. P., *Phys. Rev. B*, 38, 7160, 1988.
78. Cohn, J. L., Skelton, E. F., Wolf, S. A., and Liu, J. Z., *Phys. Rev. B*, 45, 13140, 1992.
79. Tokura, Y., Takagi, H., and Uchida, S., *Nature*, 337, 345, 1989.
80. Fortune, N. A., Murata, K., Yokoyama, Y., Ishibashi, M., and Nishihara, Y., *Physica C*, 178, 437, 1991.
81. Mazov, L. S., *Phys. Lett. A*, 148, 115, 1990.
82. Wang, Z. Z., Chien, T. R., Ong, N. P., Tarascon, J. M., and Wang, E., *Phys. Rev. B*, 43, 3020, 1991.
83. Xu, X. Q., Hagen, S. J., Jiang, W., Peng, J. L., Li, Z. Y., and Greene, R. L., *Phys. Rev. B*, 45, 7356, 1992.
84. Hagen, S. J., Xu, X. Q., Jiang, W., Peng, J. L., Li, Z. Y., and Greene, R. L., *Phys. Rev. B*, 45, 515, 1992.
85. Sugiyama J., Matsuura, K., Kosuge, M., Yamauchi, H., and Tanaka, S., *Phys. Rev. B*, 45, 17, 9951, 1992.
86. Sera, M., Kondoh, S., and Sato, M., *Solid State Commun.*, 68, 647, 1988.
87. Uher, C., Peacor, S. D., and Kaiser, A. B., *Phys. Rev. B*, 43, 7955. 1991.
88. Allen, P. B., Pickett, W. E., and Krakauer, H., *Phys. Rev. B*, 37, 7482, 1988.
89. Marino, A. and Rodriguez, J. E., *Solid State Commun.*, 82, 775, 1992.
90. Dey, T. K., Ghatak, S. K., Srinivasan, S., Bhattacharya, D., and Chopra, K. L., *Solid State Commun.*, 72, 525, 1989.
91. Mawdsley, A., Trodahl, H. J., Tallon, J., Sarfati, J., and Kaiser, A. B., *Nature*, 328, 233, 1987.
92. Uher, C., *J. Appl. Phys.*, 62, 4636, 1987.
93. Uher, C., *J. Superconductivity*, 3, 337, 1990.
94. Nunez Regueiro, M. D. and Castello, D., *Int. J. Mod. Phys. B*, 5, 2003, 1991.

95. Uher, C., in *Physical Properties of High Temperature Supercondutors III*, Ginsberg, D. M., Ed., World Scientific, Singapore, 1992, 159.
96. Berman, R., in *Thermal Conduction in Solids*, Clarendon Press, Oxford, 1976.
97. Olsen, J. L., *Proc. Phys. Soc. A*, 65, 518, 1952.
98. Klemens, P. G. and Tewordt, L., *Rev. Mod. Phys.*, 36, 118, 1964.
99. Bayot, V., Delannay, F., Dewitte, C., Erauw, J.-P., Gonze, X., Issi, J.-P., Jonas, A., Kinany-Aloui, M., Lambricht, M., Michenaud, J.-P., Minet, J.-P., and Piraux, L., *Solid State Commun.*, 63, 983, 1987.
100. Bardeen, J., Rickayzen, G., and Tewordt, L., *Phys. Rev.*, 113, 982, 1959.
101. Tewordt, L. and Wölkhausen, Th., *Solid State Commun.*, 70, 839, 1989.
102. Peacor, S. D., Richardson, R. A., Nori, F., and Uher, C., *Phys. Rev. B*, 44, 9508, 1991.
103. Morelli, D. T., Heremans, J., Doll, G., Picone, P. J., Jenssen, H. P., and Dresselhaus, M. S., *Phys. Rev. B*, 39, 1989.
104. Nakumara, Y., Uchida, S., Kimura, T., Motohira, N., Kishio, K., Kitazawa, K., Arima, T., and Tokura, Y., *Physica C*, 185–189, 1409, 1991.
105. Sera, M., Shamota, S., and Sato, M., *Physica C*, 185–189, 1335, 1991.
106. Sera, M., Shamota, S., and Sato, M., *Solid State Commun.*, 68, 649, 1988.
107. Cohn, J. L., Skelton, E. F., Wolf, S. A., Liu, J. Z., and Shelton, R. N., *Phys. Rev. B*, 45, 13144, 1992.
108. Zavaritsky, N. V., Samoilov, A. V., and Yurgens, A. A., *Physica C*, 169, 174, 1990.
109. Yu, R. C., Salamon, M. B., Lu, J. P., and Lee, W. C., *Phys. Rev. Lett.*, 69, 1431, 1992.
110. Cohn, J. L., Wolf, S. A., Vanderah, T. A., Selvamanickam, V., and Salama, K., *Physica C*, 192, 435, 1992.
111. Richardson, R. A., Peacor, S. D., Nori, F., and Uher, C., *Phys. Rev. Lett.*, 67, 3856, 1991.
112. Peacor, S. D., Cohn, J. L., and Uher, C., *Phys. Rev. B*, 43, 8721, 1991.
113. Copinathan, K. K., Goldsmid, H. J., Matthews, D. N., and Taylor, K. N. R., in *Proc. 7th International Conference on Thermoelectric Energy Conversion*, Rao, K. R., Ed., University of Texas, Arlington, 1988, 58.
114. Sidorenko, N. A. and Mosolov, A. B., in *Proc. 10th International Conference on Thermoelectric Energy Conversion*, Rowe, D. M., Ed., University of Wales, Cardiff, 1991, 80.
115. Dashevskii, Z. M., Sidorenko, N. A., Skipidarov, S. Y., Tsvetkova, N. A., and Mocolov, A. B., in *Proc. 10th International Conference on Thermoelectric Energy Conversion*, Rowe, D. M., Ed., University of Wales, Cardiff, 1991, 142.
116. Vedernikov, M. V., Kuznetsov, V. L., Ditman, A. V., Melekh, B. T., and Burkov, A. T., in *Proc. 10th International Conference on Thermoelectric Energy Conversion*, Rowe, D. M., Ed., University of Wales, Cardiff, 1991, 96.
117. Cassart, M. and Issi, J.-P., in *Proc. 8th International Conference on Thermoelectric Energy Conversion*, Institute National Polytechnique de Lorraine, Nancy, 1989, 121.
118. Cassart, M., Issi, J.-P., Chevalier, B., Tressaud, A., and Etourneau J., *Physica C*, 201, 305, 1992.
119. Hundley, M. F., Kwok, R. S., Cheong, S. W., Thomson, J. D., and Fisk, Z., *Physica C*, 172, 455, 1991.

31

Boron Carbides

Terrence L. Aselage
and David Emin
Sandia National Laboratories
Albuquerque, New Mexico, U.S.A.

31.1 Introduction

Boron carbides may be produced as ceramics by the reaction of boron and carbon at high temperatures. The exceptional properties of these refractory materials are utilized in several important industrial applications. Boron carbide is among the hardest materials known to man;[1-3] only cubic boron nitride and diamond are harder. Thus, boron carbides are employed in abrasive, grinding, and wear-resistant applications.[1-3] Applications as lightweight ceramic armor[4] are based on this hardness together with boron carbide's low density. A lack of oxidation resistance[1] limits high-temperature structural applications of boron carbide, even though it exhibits little decrease in strength with increasing temperature in inert atmospheres.[3]

Another major industrial use of boron carbide is in the nuclear industry. The ^{10}B isotope (naturally 20% abundant) has a large capture cross section for thermal neutrons. Therefore, boron carbides are utilized as neutron moderators in reactors.[5] In this application, boron carbides must sustain large amounts of radiation damage. This radiation tolerance will be discussed in greater detail in a following section. Films containing boron and carbon are also under investigation as first wall materials in Tokamaks.[6]

The potential for utilizing boron carbide and other boron-rich compounds in high-temperature electronics has long been recognized.[7-9] This interest led to a continuing series of international conferences focused primarily on boron and boron-rich solids.[10,11] In particular, boron carbides have potential application in very-high-temperature thermoelectric power conversion.[12-14] Here, a moderately large, thermally activated electrical conductivity, "anomalously" large Seebeck coefficient, and surprisingly low, glasslike thermal conductivity combine to yield a thermoelectric figure-of-merit that is orders of magnitude larger than expected. The relatively recent introduction[15] of a commercial boron carbide/graphite thermocouple with operating temperatures as high as 2200°C and output voltages of up to 500 mV illustrates the realizability of this potential for very-high-temperature applications of boron carbide.

In this chapter, the phase diagram, preparation, and structure of boron carbides will be reviewed. Then, the electrical and thermal transport properties of boron carbides will be described, and application to thermoelectrics will be discussed. Finally, unresolved questions that require additional research will be mentioned.

0-8493-0146-7/95/$0.00+$.50

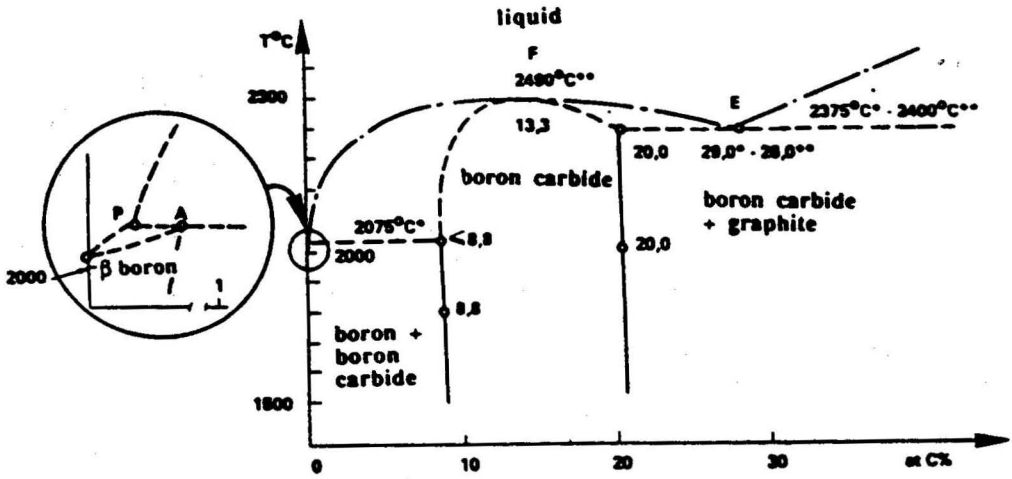

FIGURE 1 Boron-carbon phase diagram. (From Thevenot, F., *J. Eur. Ceram. Soc.*, 6, 205, 1990. With permission.)

31.2 Phase Diagram

Binary compounds of boron and carbon have been produced with a range of stoichiometries. The large number of phase diagrams reported for the boron-carbon system has been described in previous review articles.[2,3] Early phase diagrams showed boron carbides with different stoichiometries as distinct phases. These phases ranged in carbon content from greater than 30 at.% ($B_{12}C_5$) to less than 8 at.% ($B_{12}C$). Later work considered the range of stoichiometries to arise from solid solution within a single phase. The boron-rich boundary of the solid solution is generally placed at about 9 at.% carbon.[16–18] The carbon-saturated boundary has usually[1,3,17,18] been located at the customary B_4C composition, with 20 at.% carbon. However, a recent study[19] of this phase boundary by electron microprobe techniques shows that carbon saturation occurs at a boron carbide composition of about 19 at.% carbon. This upper boundary is consistent with earlier suggestions, based on entropic arguments[20] and electrical conductivity,[14,20] that the carbon concentration achieved in single-phase boron carbide samples is always somewhat less than the 20 at.% of the ideal B_4C limit.

The idea that boron carbides constitute a continuous solid solution between about 9 and 19 at.% carbon is generally accepted. Nonetheless, the nomenclature of boron carbide samples in the literature often has unfortunately followed from the designation of distinct phases. Thus, a sample with 13.3 at.% carbon will frequently be called $B_{13}C_2$, and a sample with 10 at.% carbon B_9C. "B_4C" is used to designate the carbon-saturated composition of about 19 at.% carbon. Although this convention is anachronistic, it is widespread. In this article, the composition of boron carbide is specified by its carbon concentration in atomic percent.

The high-temperature phase diagram of boron carbide is shown in Figure 1. Carbon-saturated boron carbide and graphite mixtures melt eutectically at 2375 to 2400°C, whereas boron-saturated boron carbide and β-rhombohedral boron melt peritectically at 2075°C. Between these two limits, the maximum melting temperature of the solid solution, about 2490°C, is reached. Although this maximum melting point is shown at a composition of 13.3 at.% carbon in Figure 1, the actual composition of this point is not well known. Similar phase diagrams place the maximum melting composition as high as 18.5 at.% carbon.[21]

Although no other binary compounds of boron and carbon have been produced by high-temperature synthesis, boron-rich tetragonal and orthorhombic modifications have been prepared by chemical vapor deposition at low temperatures.[22] Furthermore, amorphous films containing boron and carbon (and hydrogen) are frequently referred to as "boron carbides". The properties of these films are quite different from the crystalline material that is the subject of this chapter.

31.3 Preparation

Nearly all boron carbide for industrial use is prepared by the reduction of boron oxide by carbon through Equation 1:[1-3]

$$2B_2O_3 + 7C = B_4C + 6CO. \quad (1)$$

This reaction is carried out at temperatures of 2200 to 2500°C in electric arc furnaces.[3] The product is crushed and milled to an appropriate grain size for final application, and leached in acid to remove metallic impurities introduced in the milling. Compositional control is difficult in this approach, and a small amount of free carbon is frequently present in the material.

Boron carbide may also be produced by reducing B_2O_3 with magnesium in the presence of carbon:[1,2]

$$2B_2O_3 + 6Mg + C = B_4C + 6\,MgO. \quad (2)$$

Reaction (2) is thermodynamically favorable at lower temperatures than (1), so furnace temperatures of 1000 to 1200°C may be used. Stoichiometry control is again difficult, and the product may be contaminated with magnesia, magnesium borides (e.g., MgB_2), and, potentially, free carbon. Acid washing is successful in reducing the amount of some of these impurities.

Boron carbide powder is very difficult to sinter into a dense ceramic. Pressureless sintering of pure boron carbide is only possible at temperatures near the melting point.[1] Sintering is promoted at lower temperatures by the introduction of free carbon or other impurities.[1] Most boron carbide ceramic parts are prepared by hot pressing the powder in graphite dies.[23,24] Temperatures of 2100°C or greater and pressures of 5500 psi or greater are required to prepare samples of near-theoretical density.

Stoichiometric control of boron carbides over the entire single-phase region can be achieved by direct synthesis from the elements at high temperatures.[16,17] Mixtures of boron and carbon powders may be hot pressed under the same conditions as boron carbide powders to yield a ceramic with the desired composition. The carbon content of these ceramics may be semiquantitatively confirmed by lattice constant determination[16] and by Raman spectroscopy.[23] Raman spectroscopy sensitively detects the presence of free (amorphous or graphitic) carbon in boron carbide samples.[25] Carbon concentration gradients arising from contact with graphite dies are present in hot-pressed samples with low carbon concentrations.[23,24] These gradients may be prevented by using high-purity boron nitride die liners, or may be removed by mechanical grinding. Nearly all of the samples that have been used to study the thermoelectric properties of boron carbides have been prepared by such reactive hot pressing.[26]

A number of other procedures are available for preparing boron carbide crystals, powders, and films. These procedures are described with many references in existing review articles.[1,2]

31.4 Structure

The atomic positions within the crystal structure of boron carbide were determined independently by Zhdanov and Sevastyanov[27] and by Clark and Hoard[28] in the 1940s. Boron carbide's rhombohedral unit cell, space group $R\bar{3}m$, is depicted in Figure 2. This 15-atom unit cell may be represented as being composed of two distinct units. Slightly distorted, 12-atom boron-rich icosahedra are located at the vertices of the rhombohedron, and a linear 3-atom chain lies along the threefold axis. The initial studies[27,28] proposed all-boron, B_{12}, icosahedra, and all-carbon, CCC, chains for the ideal $B_{12}C_3$, or B_4C, composition. It is now generally accepted,[29] however, that this composition corresponds to a carbon atom residing within each icosahedron, $B_{11}C$, with the central atom of the chain being a boron, CBC, as depicted in Figure 2. Because carbon atoms reside in inequivalent sites in adjacent icosahedra (as illustrated in Figure 2), this ideal B_4C structure is disordered.

As discussed above, the ideal B_4C composition is never reached in real boron carbide samples. Rather, boron carbides always have compositions between about 19 and 9 at.% carbon. The location of carbon atoms within the boron carbide structure as a function of carbon concentration

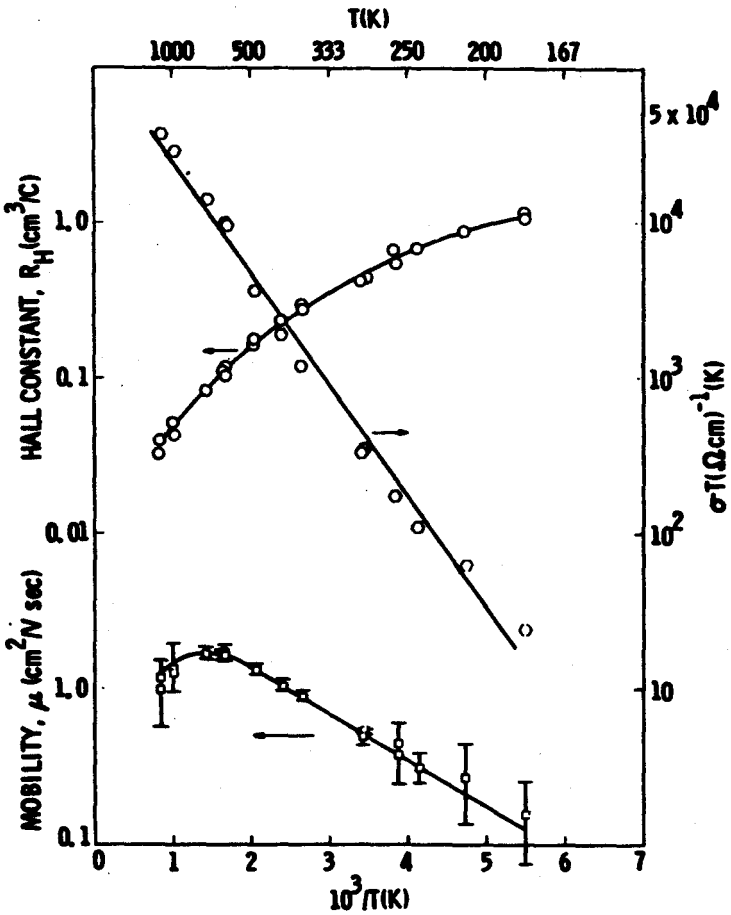

FIGURE 3 Temperature dependence of the electrical conductivity, Hall mobility, and Hall constant of a representative 19 at.% boron carbide sample. (From Wood, C. and Emin, D., *Phys. Rev. B*, 29, 4582, 1984. With permission.)

these studies. Impurities, such as free carbon,[35] and inhomogeneities are believed to dominate the samples that are inconsistent with the majority. The experimental electrical conductivity, Hall mobility, and Seebeck coefficient will be described in the following paragraphs. This section then concludes with a brief description of the theory that relates these transport properties to the structural model discussed above.

The electrical conductivity, Hall mobility, and Hall constant of a representative boron carbide with composition near 19 at.% carbon is shown in Figure 3. The electrical conductivities of boron carbides are thermally activated at high temperatures, with activation energies that are relatively small (0.15 to 0.18 eV). The preexponential factor of the conductivity is found to vary inversely with temperature, so that plots of the logarithm of (σT) vs. 1/T are linear at high temperature, as in Figure 3. Although the activation energy is found to be nearly independent of carbon concentration,[13,14,34,37] the magnitude of the conductivity at a given temperature varies non-monotonically with carbon concentration. As carbon content is reduced from 19 at.%, the electrical conductivity increases to a maximum at about 13.3 at.% carbon. The DC conductivity then falls once again as carbon concentration is reduced toward the low-carbon phase boundary.[13,14,26] At room temperature, the conductivity varies from a low of 3 (Ω-cm)$^{-1}$ for samples near 19 at.% carbon to a peak of about 23 (Ω-cm)$^{-1}$ at 13.3 at.% carbon.[23] Below room temperature, the conductivity of boron carbides continues to decrease with temperature with a progressively decreasing activation energy . At temperatures below 50 K, the resistivities of boron carbides are greater than 10^5 Ω-cm.[14,38]

As illustrated in Figure 3, the Hall mobilities of boron carbides are low (≤ 1 cm^2/V-s) and also thermally activated, with activation energies of about 0.05 eV.[34,37] Although the Hall mobility is low for boron carbides with several different compositions,[37] its dependence on carbon concentration has not been accurately determined. The sign of the Hall constant of boron carbides is positive for nearly all samples. Negative Hall constants have been reported for multiphase samples with very low carbon concentrations.[34,39]

Positive Seebeck coefficients for boron carbides of all compositions show that the conduction is intrinsically p-type. The magnitude of the Seebeck coefficient of boron carbides of all compositions is large (>100 μV/K at room temperature).[13,14,26,34,37,38] Additionally, the Seebeck coefficient is generally found to increase with temperature, reaching values greater than 200 μV/K at 1000 K.[13,26,34,37] Despite sharing these qualitative features, the experimental data for a given carbon composition and temperature show wide variations.[14] This variability is most pronounced near the carbon-rich end of the phase diagram,[14,33] where inclusions of free carbon may have the largest influence. Experimental values of the Seebeck coefficient are, on average, lowest for carbon-rich samples and increase with decreasing carbon content.

The electronic transport properties of boron carbides are understood within a theory developed by Emin.[30,34,40] In this view, the charge carriers in boron carbides are self-trapped, small bipolaronic holes that hop adiabatically between carbon-containing icosahedra. In the following paragraphs, the essential features of this theory are described.

A small polaron forms when charge carriers interact with the lattice sufficiently to stabilize displacements of the nearby atoms.[41] This local distortion produces a potential well which serves to bind the carrier at that site. Because the well is stabilized by its occupation by the carrier itself, the carrier is said to be "self-trapped". A small polaron consists of a self-trapped charge carrier and the associated atomic distortions. If the increase in the depth of the potential well caused by the localization of an additional charge carrier is greater than the Coulomb repulsion between carriers of like sign, two carriers may be bound in the same potential well. These localized pairs are called small bipolarons.[41] Because the motion of small (bi)polarons requires the motion of the atomic displacements, low mobilities are characteristic of small (bi)polarons. Increasing temperature results in increasing thermal motion of the atoms about their equilibrium positions, increasing the likelihood of atomic displacements on sites neighboring the polaron. Since such displacements aid the motion of the charge carrier, the hopping motion of small (bi)polarons is thermally assisted. At low temperatures, the mobility follows a non-Arrhenius temperature dependence.[41] At sufficiently high temperature, the mobility is expressed as follows:[30]

$$\mu = (qa^2\nu/k_BT)\exp(-E_A/k_BT), \tag{3}$$

where q is the carrier's charge, a is the mean distance a carrier hops, ν is a characteristic vibrational frequency, k_B is the Boltzmann constant, and E_A is the activation energy to produce an atomic distortion at a neighboring site that is equivalent to that associated with the polaron. This expression assumes that the carrier will follow the motion of the atoms (adiabatic approximation) and hop as soon as such an equivalence is achieved.

The thermally activated mobilities observed in boron carbides are the signature of small polaron hopping. Furthermore, the high-temperature conductivity characteristic of the hopping of a temperature-independent density of small (bi)polarons is thermally activated with a preexponential factor that is proportional to the inverse temperature. As shown in Figure 3 (and for many other boron carbide samples), the high-temperature conductivity of boron carbides exhibits just this temperature dependence. From this result, one deduces that the density of small (bi)polarons in boron carbides is independent of temperature. We shall show below that this density is of the order of 10^{21}/cm^3. Unlike conductors with nearly free carriers, the Hall mobilities, obtained as the conductivity times the Hall constant, and drift mobilities of small polaronic conductors do not manifest the same thermal activation energy.[40,41] The Hall constants measured in boron carbides and other small polaronic conductors are then not simply related to the carrier densities.

Small polarons and bipolarons give rise to similar electrical transport properties. As the hopping motion is slowed by cooling to very low temperatures, the localized spins associated with small polarons will contribute to the overall paramagnetism of the material; but small bipolarons in a

singlet state will not. Thus, a comparison of the carrier density with the low-temperature spin density observed by magnetic susceptibility or electron spin resonance provides a means of distinguishing small polarons from small bipolarons. The spin density observed[42–44] in boron carbides is of the order of $10^{19}/cm^3$, or two orders of magnitude lower than the carrier density. Therefore, the carriers in boron carbides are spinless, singlet bipolarons.[30]

The insensitivity of the activation energy to carbon concentration in boron carbides suggests that the hopping sites are similar throughout the single-phase region. This insensitivity also suggests that the non-monotonic carbon concentration dependence of the conductivity comes from the conductivity prefactor. Since a and ν in Equation 3 are not expected to vary significantly with carbon concentration, the carbon concentration dependence of the conductivity primarily reflects changes in the carrier density. This non-monotonic dependence shows that carbon is not acting as a simple dopant.

Having described the evidence that bipolarons form in boron carbides, we now address the question of their location and dependence on carbon concentration. We begin by considering the bonding of "ideal" B_4C, $(B_{11}C)[CBC]$. A neutral $B_{11}C$ icosahedron has a total of 37 valence electrons. Of these, 12 are required for bonding to the neighboring icosahedra and chains, leaving 25 for intra-icosahedral bonding. Filling the internal bonding orbitals of boron-rich icosahedra requires 26 electrons.[45] Thus, the stable state of the $B_{11}C$ icosahedra is negatively charged, $(B_{11}C)^-$. The twofold coordinated central boron atom in the CBC chain readily ionizes, CB^+C, and donates its extra valence electron to the icosahedra. This ionization is reflected in the vibrational frequencies, interatomic separations, and X-ray "thermal" factors of the chain.[29] With all of the bonding requirements of both icosahedra and chains fulfilled, this simple picture predicts an electrical insulator at B_4C. Insulating behavior is also predicted for B_4C by band structure calculations.[46] At lower carbon concentrations, band structure calculations predict metallic behavior resulting from an unfilled valence band.[46] The electrical transport properties of boron carbides are, however, distinctly nonmetallic.

CBB chains, which are isoelectronic with CB^+C chains, are not capable of electron donation to icosahedra. Because some CBB chains are present at all realizable boron carbide compositions, some of the $B_{11}C$ icosahedra should be neutral rather than negatively charged. A neutral icosahedron, with 25 electrons, would give rise to paramagnetic spins at low temperature. Because these spins are unobserved, it is presumed[30] that a strong driving force for pairing leads to the following disproportionation:

$$2(B_{11}C)^0 \rightarrow (B_{11}C)^+ + (B_{11}C)^-. \quad (4)$$

The bipolaronic holes in boron carbide are thus associated with positively charged, carbon-containing icosahedra. The hopping motion of these carriers involves the exchange of charge between positively and negatively charged icosahedra:

$$(B_{11}C)^+ + (B_{11}C)^- \rightarrow (B_{11}C)^- + (B_{11}C)^+. \quad (5)$$

The disproportionation proposed in Equation 4 readily explains the p-type conduction observed for all boron carbide compositions. The disproportionation alone leads to half of the $B_{11}C$ icosahedra being negatively charged, that is the $B_{11}C$ band is half full. With some charge donation from CB^+C chains, more of the icosahedra are $(B_{11}C)^-$ rather than $(B_{11}C)^+$, the $B_{11}C$ band is more than half full, and p-type conduction results.

The carrier density in boron carbides is equal to the density of $(B_{11}C)^+$ icosahedra. This density is just the product of the concentration of $B_{11}C$ icosahedra and the fraction that are positively charged. From the structural model presented above, the concentration of $B_{11}C$ icosahedra is constant at one per unit cell as the carbon content is reduced from 19 to 13.3 at.%. As the concentration is further reduced from 13.3 at.% carbon to the low-carbon phase boundary, the $(B_{11}C)$ concentration falls from one per unit cell to roughly one per three unit cells. At the ideal B_4C composition, the fraction of the $B_{11}C$ icosahedra that are positively charged is zero. Decreasing the carbon content increases the fraction of $B_{11}C$ icosahedra that are positively charged until, at about 13.3 at.% carbon, nearly 50% are $(B_{11}C)^+$. Because of the predominance of CBB chains at this and lower carbon concentrations, this fraction remains constant between 13.3 at.% carbon

and the low-carbon phase boundary. Thus, the product of the $B_{11}C$ concentration and the fraction that are positively charged is low at either phase boundary and peaks at about 13.3 at.% carbon, in qualitative agreement with the observed conductivity.

At 13.3 at.% carbon, the density of $B_{11}C$ icosahedra at one per unit cell is about $3 \times 10^{21}/cm^3$ from measurements of boron carbide's lattice constants.[16] With nearly half of these positively charged, the density of bipolaronic holes is $1.5 \times 10^{21}/cm^3$. With this carrier density, the experimental activation energy, and a charge per carrier of 2e, the observed high-temperature conductivity of samples with 13.3 at.% carbon yields physically reasonable values of a ($\approx$8Å) and ν ($\approx$1000 cm^{-1}).[14] Moreover, attributing the difference in conductivity between 13.3 at.% carbon and carbon-saturated samples solely to reduced carrier concentration, a carrier concentration of about $2.3 \times 10^{20}/cm^3$ is suggested for the carbon-saturated composition.[14] This carrier density corresponds to 7.5% of the $B_{11}C$ icosahedra being positively charged. Since two CBB chains produce one bipolaron, 15% of the chains at the carbon-saturated boundary must be CBB. This formula unit, $(B_{11}C)[CBC_{0.85}B_{0.15}]$ corresponds to a carbon-saturated concentration of 19 at.%, in excellent agreement with the microprobe results of Schwetz and Karduck.[19] Thus, the theory provides physically meaningful agreement with the observed electrical conductivities as a function of carbon concentration.

With a carrier density as high as $10^{21}/cm^3$, the value of the Seebeck coefficient would be small if boron carbides had conventional transport. One would also expect carbon-saturated samples, with the smallest carrier density, to have the largest value of the Seebeck coefficient. Both of these expectations are contradicted in boron carbides. Additionally, the Seebeck coefficient of boron carbides increases with increasing temperature, contrary to expectations of a conventional semiconductor. The anomalously large value of the Seebeck coefficient and the increase with temperature were predicted by Emin[30,40,47] for polaronic systems in which disorder leads to differences among site energies and electron-lattice interactions. As noted previously, boron carbides are intrinsically disordered materials at all carbon concentrations. Each of the various sources of disorder in boron carbides could affect the icosahedral hopping sites. Because of the possibility of controlling the nature of the disorder in boron carbides as a function of the carbon concentration, the interplay between disorder and the magnitude of the Seebeck coefficient in boron carbides remains an area of research interest.

31.6 Thermal Transport Properties

Boron carbides are extremely hard, stiff materials with correspondingly large sound velocities. Between 13.3 and 19 at.% carbon, the sound velocity is nearly independent of carbon concentration, with a magnitude of about 1.4×10^6 cm/s.[48] By comparison, the sound velocity in diamond is 1.8×10^6 cm/s; for most solids it is near 5×10^5 cm/s. For carbon concentrations below 13.3 at.%, the sound velocity of boron carbide falls with carbon content, to a (still large) value of 1.2×10^6 cm/s at 10 at.% carbon.[48] Accordingly, one might expect boron carbides to be extremely good thermal conductors. However, the thermal diffusivities λ' of boron carbides,[40,49] shown in Figure 4, are relatively low. For example, the largest room temperature thermal diffusivity (at 19 at.% carbon) is about 0.2 W/cm-K, two orders of magnitude smaller than diamond. The thermal diffusivities of boron carbides with lower carbon concentrations are even smaller.

The striking carbon concentration dependence of the thermal diffusivity illustrated in Figure 4 has been observed, if less clearly, in previous studies.[13,50] The thermal diffusivity of a boron carbide with 19 at.% carbon is 400% larger at 600 K than that of a sample with 10 at.% carbon. Moreover, the temperature dependence changes from that typical of crystalline solids (falling with increasing temperature) at high carbon concentrations to one characteristic of glass (nearly independent of temperature) at low carbon concentrations. This transition at about 17 at.% carbon occurs within a range of compositions where the sound velocity is nearly constant. Phonon mean free paths as short as several Angstroms calculated from the experimental thermal diffusivities and sound velocities are unphysically small. These results suggest the inadequacy of treatment of the thermal transport in boron carbides by acoustic phonon scattering.

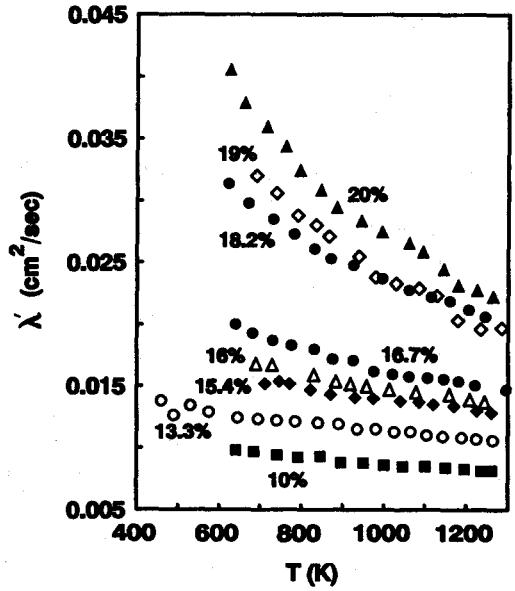

FIGURE 4 Temperature and composition dependences of the thermal diffusivities of boron carbides. (From Emin, D., in *Boron-Rich Solids*, Emin, D. et al., Eds., American Institute of Physics, New York, 1991, 65. With permission.)

Emin[40] has proposed the idea of vibrational localization to qualitatively understand the thermal transport in boron carbides. Localization of vibrational energy occurs when differences in the local vibrational frequencies exceed the frequency of the coupling between locations (the beat frequency). Disorder clearly fosters such differences. When localization occurs, vibrational energy may be transferred from site to site only when anharmonicities in the vibrations provide an occasional coincidence of frequencies. This is the vibrational analogue of polaron hopping.

Because the icosahedra in boron carbides are soft[48] and inherently disordered, it is presumed[40] that most of the heat is conducted through the intericosahedral chains. At high carbon concentrations in boron carbide, these chains are predominantly CBC. At either end of these CBC chains, carbon is stiffly bonded to the boron atoms of three adjacent icosahedra.[51] As the carbon content is reduced, increasing numbers of CBB chains replace CBC chains. The bonding between the chain-end boron and its surrounding icosahedral boron neighbors is believed to be much softer, with lower vibrational frequencies, than the carbon-boron bonds at the other end of the chain.[51] The two ends of the chain are only weakly coupled through the ionized boron atom at the central position. Therefore, the chains qualitatively fit the requirements of the vibrational localization picture. The crystal-like to glass-like transition in thermal diffusivity in boron carbides is believed to be related to this replacement of CBC chains by CBB chains. The experimentally observed crossover at 17 at.% carbon corresponds roughly to a 50/50 mix of CBC and CBB chains.

An alternate idea, originally proposed by Einstein, has been adopted[52] to describe the thermal diffusivity of disordered solids. Here, one supposes an array of independently vibrating harmonic oscillators with random phases. The time constant for the diffusion of elastic energy between such oscillators is assumed to be approximately half a vibrational period. With this jump period, the interatomic spacing, and the specific heat of the oscillator, the thermal diffusivity may be calculated. The resulting thermal diffusivity, termed Λ_{min}, is similar at high temperatures to the observed diffusivity of a number of amorphous and disordered crystalline solids.[52]

The quantitative description of the thermal diffusivity of boron carbides remains a theoretical challenge. More generally, boron carbides provide an interesting case study of thermal diffusion in disordered materials because of the ability to control and understand the nature of the disorder through changes in carbon concentration.

31.7 Thermoelectric Figure-of-Merit

A solid with a carrier density of $10^{21}/cm^3$ and a hardness and sound velocity approaching those of diamond would hardly be a candidate for a high-temperature thermoelectric based on standard formulas. Nevertheless, the "anomalously" large Seebeck coefficient, the unexpectedly low, glass-like thermal conductivity, and the thermally activated electrical conductivity combine to make boron carbide an attractive p-type material for very-high-temperature application.[12] The intrinsic thermoelectric figure-of-merit Z ($= \alpha^2\sigma/\lambda$) of boron carbides is highest for samples with 13.3 at.% carbon or less.[12,14,26] Z for samples in this composition range reaches as high as 0.25×10^{-3} K^{-1} at 1000°C.[14,26] In this low-carbon region, decreasing electrical conductivity with decreasing carbon concentration is balanced by a decrease in the thermal conductivity, making Z relatively insensitive to carbon content. Samples with higher carbon concentrations than 13.3 at.% exhibit lower values of Z due to higher thermal conductivity and lower electrical conductivity.

The large Z reported in Reference 13 (0.85×10^{-3} K^{-1} at 977°C) for a sample with 13.3 at.% carbon is based on linear extrapolations of carbon concentration dependences rather than experimental data. A value of Z near 0.5×10^{-3} K^{-1} at 1000°C has also been reported[12] for a boron carbide with 10 at.% carbon and 0.5 at.% Mg addition. The raw data from which this value is obtained have not been published.

The thermoelectric figure-of-merit of boron carbide is smaller at 1000°C than that for p-type Si/Ge alloys. Unlike Si/Ge and other high-temperature thermoelectric materials, however, the figure-of-merit of boron carbide is still increasing at 1000°C. Combined with the high melting temperatures of boron carbides, this raises the possibility of high-efficiency thermoelectric power generation using boron carbides at temperatures up to and above 2000°C. The potential for such high-temperature operation is illustrated by the B_4C/C thermocouple mentioned in the introduction to this chapter. Thermoelectric converter designs which couple boron carbide with a refractory, high-efficiency n-type material such as lanthanum sulfide have been proposed.[26] The possibility of producing an n-type, boron carbide-based material is a subject of ongoing investigation, as discussed below.

31.8 Considerations for Future Work

In this concluding section, several of the unresolved questions concerning the transport properties of boron carbides and their potential for thermoelectric application at high temperatures are briefly discussed. Specifically, the measurement of the transport properties above 1000°C, the possibility of producing an n-type boron carbide-based material, and the application of boron carbides in high radiation environments will be considered.

A fundamental difficulty in making transport measurements on boron carbide above 1000°C is the formation of electrical contacts. Refractory metals generally react with boron carbide to form stable metal borides and free carbon in this temperature range. Noble metals such as Pt and Pd form low-melting eutectics with boron, and have even been used as liquid solvents for the growth of boron carbide crystals.[53] Graphite may be used in contact with carbon-saturated materials, but carbon diffusion into samples with lower carbon contents precludes its use at high temperatures. A potential solution to these difficulties lies in the use of transition metal diborides as high-conductivity electrodes. TiB_2 and ZrB_2 have been shown[14] to be nonreactive toward boron carbides at temperatures above 2000°C. Both materials have very high electrical conductivities. Thin film electrodes of these materials will now be used for high-temperature measurements.

Interest in the electrical transport properties above 1000°C stems from measurements of the conductivity of a few boron carbide samples by Wood.[37] Rather than a simple extension of the lower-temperature results, a dramatic increase in conductivity was observed at and above about 1000°C. The origin of such an increase is not currently understood, nor has the Seebeck coefficient been measured in this high-temperature range. Confirmation of this experimental result would present an interesting problem for theoretical understanding. Additionally, a much higher electrical

conductivity coupled with a still larger Seebeck coefficient would produce dramatic enhancement of the thermoelectric figure-of-merit at very high temperature.

Attempts to prepare n-type boron carbides have not as yet been successful. These attempts have primarily involved the addition of metallic impurities to boron carbide.[27] Although two-phase, CVD-produced samples produced a negative Hall constant at very low carbon concentrations,[39] these materials are thermally unstable. An alternate approach to preparing n-type materials is to introduce an electron donor such as phosphorus into carbon-saturated material. A boron-rich phosphide, $B_{12}P_2$, is structurally similar to boron carbide with B_{12} icosahedra and P-P chains. Phosphorus, because of its size, is also expected to occupy a chain site in boron carbide. Initial attempts to prepare P-doped boron carbides have incorporated up to 0.67 at.% phosphorus. This level corresponds to one phosphorus every ten unit cells. The phosphorus was found to be present homogeneously and quantitatively at this doping level.[14] Although the Seebeck coefficient was still positive, the electrical conductivity was lower than undoped boron carbide with 19 at.% carbon by about a factor of 50. Measurement of the temperature dependence of the conductivity showed that this reduction arose from a combination of lower carrier density and lower mobility due to higher activation energy.[54] Further efforts to increase the concentration of phosphorus dopant have not been successful.[54]

Boron carbides, as noted in the introduction, are used as neutron moderators in reactors. As such, radiation damage in boron carbides has been extensively studied. The absorption of a neutron by the ^{10}B isotope produces energetic α particles and Li atoms. Each neutron absorption results in the creation of about 3000 vacancy-interstitial pairs.[55] Studies of neutron-irradiated single crystals[56] suggest that the central atom of the boron carbide chain is particularly susceptible to vacancy formation. Annealing these irradiated single crystals at 700 to 900°C resulted in substantial recombination of these vacancy-interstitial pairs. The predominant secondary defect observed in irradiated boron carbides is the presence of He bubbles caused by the coalescence of the α particles.[55] The internal stresses generated by these bubbles can cause extensive swelling and microcracking.[55]

Neutron irradiation of boron carbides with natural abundance or enrichment of ^{10}B is known to cause large reductions in both thermal[57,58] and electrical[58] conductivity. Whether these reductions are due primarily to point defect generation or to cracking is not certain. Both the thermal and electrical conductivity show some recovery with annealing.[58] The swelling, microcracking, and α particle-generated point defects may be nearly eliminated by utilizing highly ^{11}B-enriched boron carbides. Although such studies have not yet been performed, Stoto and coworkers[59] have performed effective simulations by studying the radiation damage induced by high-energy (1 MeV) electrons. The formation and stability of point defects were confirmed by observing swelling proportional to the radiation dose. No clustering of these point defects was observed at damage levels of up to 3 d.p.a. even when the irradiation was carried out at 12 K. At this low temperature, recombination and/or migration to the surface are slow processes. This result suggests that boron carbide is able to accommodate point defects at high concentration.

The robust nature of the structure of boron carbides suggests the possibility of their utilization in a neutron radiation environment. The effect of stable point defect populations on the thermoelectric properties of boron carbide are unknown. The electrons involved in intraicosahedral bonding are delocalized over the surface of the icosahedra, with peak densities at the centers of the triangular faces.[60] The electronic levels associated with this "metallic-like" bonding within the icosahedra[61] may not be greatly perturbed by removing an atom from the icosahedron. This might explain the relative stability of such structures to radiation damage.[59] Unlike conventional semiconductors with high mobilities and relatively low carrier densities, the low-mobility carriers in boron carbides are present in concentrations that are greater than or comparable to defect densities. The structural insensitivity to radiation damage and presence of a high density of low-mobility carriers suggest that the electrical properties of ^{11}B-enriched boron carbides might be relatively insensitive to neutron irradiation. Indeed, the Seebeck coefficient, already enlarged by the presence of disorder in the icosahedra, might be further enhanced by radiation-induced disorder. The thermal conductivity will, at worst, remain low and glass-like. Thus, the properties of ^{11}B-enriched boron carbides under neutron irradiation is an interesting experimental question that may lead to efficient thermoelectric applications of boron carbides in harsh environments.

Acknowledgments

This work was supported by the Division of Materials Sciences, Office of Basic Energy Sciences of the U.S. Department of Energy under contract #DE-AC04-76DP00789.

References

1. Thevenot, F., Boron carbide—a comprehensive review, *J. Eur. Ceram. Soc.*, 6, 205, 1990.
2. Makarenko, G. N., Borides of the IVb group, in *Boron and Refractory Borides*, Matkovich, V. I., Ed., Springer-Verlag, New York, 1977, 310.
3. Lipp, A., Boron carbide—production, properties, application, *Tech. Rundsch.*, 14,28,33 (1965) and 7 (1966).
4. Wilkins, M. L., Use of boron compounds in lightweight armor, in *Boron and Refractory Borides*, Matkovich, V. I., Ed., Springer-Verlag, New York, 1977, 633.
5. Mahagin, D. E. and Dahl, R. E., Nuclear applications of boron and the borides, in *Boron and Refractory Borides*, Matkovich, V. I., Ed., Springer-Verlag, New York, 1977, 613.
6. Veprek, S., Boron carbide large area in-situ coatings for controlled nuclear fusion research, in *Boron-Rich Solids*, AIP Conf. Proc. Vol. 231, Emin, D., Aselage, T. L., Switendick, A. C., Morosin, B., and Beckel, C. L., Eds., American Institute of Physics, New York, 1991, 617.
7. Samsonov, G. V., in *Boron, its Compounds and Alloys*, Academy of Sciences of the Ukrainian SSR, Kiev, 1960, chap. 6.
8. Searcy, A. W. and Meschi, D. J., Chemical considerations in high temperature thermoelectric power development, in *Thermoelectricity*, Egli, P. H., Ed., John Wiley & Sons, New York, 1960, 165.
9. A number of patents were issued in the 1960s in the name of C. M. Henderson and coworkers related to thermoelectric devices based on boron-rich materials. The primary emphasis of these patents was on the improvement in Z by dispersing second-phase materials within the matrix. See, for example, U.S. Patent 3,343,373, Two-phase thermoelectric body comprising a boron-carbon matrix, Sept. 26, 1967.
10. Starks, R. J., Buford, J. T., and Grayson, P. E., Boron since Asbury Park: the first International Boron Conference, September 18–19, 1959, in *Boron-Rich Solids*, AIP Conf. Proc. Vol. 140, Emin, D., Aselage, T. L., Beckel, C. L., Howard, I. A., and Wood, C., Eds., American Institute of Physics, New York, 1986, 373.
11. The most recent of these conferences was held in Tsukuba, Japan in August of 1993, the prior conference was held in Albuquerque, NM in 1990. The proceedings from the 1990 conference are cited in Reference 6; the 1993 proceedings are found in Jap. J. Appl. Phys., Series 10, Uno, R. and Higashi, I., Eds.
12. Wood, C., Boron carbides as high temperature thermoelectric materials, in *Boron-Rich Solids*, AIP Conf. Proc. Vol. 140, Emin, D., Aselage, T. L., Beckel, C. L, Howard, I. A., and Wood, C., Eds., American Institute of Physics, New York, 1986, 362.
13. Bouchacourt, M. and Thevenot, F., The correlation between the thermoelectric properties and stoichiometry in the boron carbide phase B_4C-$B_{10.5}C$, *J. Mater. Sci.*, 20, 1237, 1985.
14. Aselage, T. L., High-temperature thermoelectric properties of boron carbide, in *Modern Perspectives on Thermoelectrics and Related Materials*, MRS Symp. Proc. 234, Allred, D., Vining, C., and Slack, G., Eds., Materials Research Society, Pittsburgh, 1991, 145.
15. Hunold, K., B_4C/C thermoelement fur hohe temperaturen, *Chemie-Technik*, 14, 82, 1985.
16. Aselage, T. L. and Tissot, R. G., Lattice constants of boron carbides, *J. Am.. Ceram. Soc.*, 75, 2207, 1992.
17. Bouchacourt, M. and Thevenot, F., The properties and structure of the boron carbide phase, *J. Less-Common Met.*, 82, 227, 1981.
18. Matkovich, V. I., Extension of the boron-carbon homogeneity range, *J. Less-Common Met.*, 47, 39 1976.
19. Schwetz, K. A. and Karduck, P., Investigations in the boron-carbon system with the aid of electron probe microanalysis, in *Boron-Rich Solids*, AIP Conf. Proc. Vol. 231, Emin, D., Aselage, T. L., Switendick, A. C., Morosin, B., and Beckel, C. L., Eds., American Institute of Physics, New York, 1991, 405.

20. Emin, D., Structure and single phase regime of boron carbides, *Phys. Rev. B*, 38, 6041, 1988.
21. Elliot, R. P., in *Constitution of Binary Alloys*, 1st suppl., McGraw-Hill, New York, 1965, 110.
22. Ploog, K., Gasphasenabscheidung von binaren bor-kohlenstoff-phasen bei substrattemperaturen von 900 bis 1800°C, *J. Less-Common Met.*, 25, 115, 1974.
23. Aselage, T. L., Tallant, D. R., Gieske, J. H., Van Deusen, S. B., and Tissot, R. G., Preparation and properties of icosahedral borides, in *The Physics and Chemistry of Carbides, Nitrides and Borides*, Freer, R., Ed., Kluwer, Dordrecht, 1990, 97.
24. Shelnutt, J. A., Morosin, B., Emin, D., Mullendore, A., Slack, G. A., and Wood, C., Raman spectroscopy of boron carbides and related boron-containing materials, in *Boron-Rich Solids*, AIP Conf. Proc. Vol. 140, Emin, D., Aselage, T. L., Beckel, C. L, Howard, I. A., and Wood, C., Eds., American Institute of Physics, New York, 1986, 312.
25. Bouchacourt, M., Brodhag, C., and Thevenot, F., The hot pressing of boron and boron rich compounds: B_6O, $B_{10.5}C$-B_4C, *Sci. Ceram.*, 11, 231, 1982.
26. Elsner, N. B., Reynolds, G. H., Norman, J. H., and Shearer, C. H., Preparation and verification of boron carbide based thermoelectric alloys, in *Boron-Rich Solids*, AIP Conf. Proc. Vol. 140, Emin, D., Aselage, T. L., Beckel, C. L, Howard, I. A., and Wood, C., Eds., American Institute of Physics, New York, 1986, 59.
27. Zhdanov, G. S. and Sevastyanov, N. G., Crystal structure of boron carbide (B_4C), *Dokl. Akad. Nauk SSSR*, 32, 832, 1941.
28. Clark, H. K. and Hoard, J. L., The crystal structure of boron carbide, *J. Am. Chem. Soc.*, 65, 2115, 1943.
29. Aselage, T. L. and Emin, D., Structural model of the boron carbide solid solution, in *Boron-Rich Solids*, AIP Conf. Proc. Vol. 231, Emin, D., Aselage, T. L., Switendick, A. C., Morosin, B., and Beckel, C. L., Eds., American Institute of Physics, New York, 1991, 177.
30. Emin, D., Electronic transport in boron carbides, in *Boron-Rich Solids*, AIP Conf. Proc. Vol. 140, Emin, D., Aselage, T. L., Beckel, C. L, Howard, I. A., and Wood, C., Eds., American Institute of Physics, New York, 1986, 189.
31. Yakel, H. L., Recent developments in the structural crystallography of boron and the higher borides, in *Boron-Rich Solids*, AIP Conf. Proc. Vol. 140, Emin, D., Aselage, T. L., Beckel, C. L, Howard, I. A., and Wood, C., Eds., American Institute of Physics, New York, 1986, 97.
32. Kirfel, A., Gupta, A., and Will, G., The nature of the chemical bonding in boron carbide $B_{13}C_2$. I. Structure refinement, *Acta Crystallogr., B*, 35, 1052, 1979.
33. Werheit, H. and De Groot, K., Metal-insulator transition in boron carbide, *Phys. Status Solidi (b)*, 97, 229, 1980.
34. Wood, C. and Emin, D., Conduction mechanism in boron carbide, *Phys. Rev. B*, 29, 4582, 1984.
35. Bandyopadhyay, A. K., Beuneu, F., Zuppiroli, L., and Beauvy, M., The role of free carbon in the transport and magnetic properties of boron carbide, *J. Phys. Chem. Solids*, 45, 207, 1984.
36. Samara, G. A., Emin, D., and Wood, C., Pressure and temperature dependences of the electronic conductivity of boron carbides, *Phys. Rev. B*, 32, 2315, 1985.
37. Wood, C., Transport properties of boron carbide, in *Boron-Rich Solids*, AIP Conf. Proc. Vol. 140, Emin, D., Aselage, T. L., Beckel, C. L, Howard, I. A., and Wood, C., Eds., American Institute of Physics, New York, 1986, 206.
38. Kormann, R. and Zuppiroli, L., Low temperature electronic transport properties of boron carbide, in *Boron-Rich Solids*, AIP Conf. Proc. Vol. 140, Emin, D., Aselage, T. L., Beckel, C. L., Howard, I. A., and Wood, C., Eds., American Institute of Physics, New York, 1986, 216.
39. Campbell, A. N., Mullendore, A. W., Tallant, D. R., and Wood, C., Low-carbon boron carbides produced by CVD, in *Novel Refractory Semiconductors*, MRS Conf. Proc. Vol. 97, Emin, D., Aselage, T. L., and Wood, C., Eds., Materials Research Society, Pittsburgh, 1987, 113.
40. Emin, D., Electronic and vibrational hopping transport in boron carbides, in *Boron-Rich Solids*, AIP Conf. Proc. Vol. 231, Emin, D., Aselage, T. L., Switendick, A. C., Morosin, B., and Beckel, C. L., Eds., American Institute of Physics, New York, 1991, 65.
41. Emin, D., Small polarons, *Physics Today*, June 1982, p. 2.
42. Azevedo, L. J., Venturini, E. L., Emin, D., and Wood, C., Magnetic susceptibility of boron carbides, in *Boron-Rich Solids*, AIP Conf. Proc. Vol. 140, Emin, D., Aselage, T. L., Beckel, C. L., Howard, I. A., and Wood, C., Eds., American Institute of Physics, New York, 1986, 288.

43. Venturini, E. L., Azevedo, L. J., Emin, D., and Wood, C., Electron spin resonance study of hot-pressed boron carbide, in *Boron-Rich Solids,* AIP Conf. Proc. Vol. 140, Emin, D., Aselage, T. L., Beckel, C. L., Howard, I. A., and Wood, C., Eds., American Institute of Physics, New York, 1986, 292.
44. Venturini, E. L., Emin, D., and Aselage, T. L., Origin of paramagnetic defect in single crystal and ceramic B_4C, in *Novel Refractory Semiconductors,* MRS Conf. Proc. Vol. 97, Emin, D., Aselage, T. L., and Wood, C., Eds., Materials Research Society, Pittsburgh, 1987, 57.
45. Longuet-Higgins, H. C. and Roberts, M. de V., The electronic structure of an icosahedron of boron atoms, *Proc. R. Soc. London, Ser. A,* 230, 110, 1955.
46. Bylander, D. M., Kleinman, L., and Lee, S., Self-consistent calculations of the energy bands and bonding properties of $B_{12}C_3$, *Phys. Rev. B,* 42, 1394, 1990; Bylander, D. M. and Kleinman, L., Structure of $B_{13}C_2$, *Phys. Rev. B,* 43, 1487, 1991.
47. Emin, D., Thermoelectric power due to electronic hopping motion, *Phys. Rev. Lett.,* 35, 882, 1975.
48. Gieske, J. H., Aselage, T. L., and Emin, D., Elastic properties of boron carbide, in *Boron-Rich Solids,* AIP Conf. Proc. Vol. 231, Emin, D., Aselage, T. L., Switendick, A. C., Morosin, B., and Beckel, C. L., Eds., American Institute of Physics, New York, 1991, 376.
49. Wood, C., Aselage, T. L., and Emin, D., unpublished data.
50. Wood, C., Emin, D., and Gray, P. E., Thermal conductivity of boron carbides, *Phys. Rev. B,* 31, 6811, 1985.
51. Tallant, D. R., Aselage, T. L., and Emin, D., Structure of icosahedral borides by Raman spectroscopy, in *Boron-Rich Solids,* AIP Conf. Proc. Vol. 231, Emin, D., Aselage, T. L., Switendick, A. C., Morosin, B., and Beckel, C. L., Eds., American Institute of Physics, New York, 1991, 301.
52. Cahill, D. G. and Pohl, R. O., Is there a lower limit to the thermal conductivity of solids?, in *Modern Perspectives on Thermoelectrics and Related Materials,* MRS Symp. Proc. 234, Allred, D., Vining, C., and Slack, G., Eds., Materials Research Society, Pittsburgh, 1991, 27.
53. Aselage, T. L., Van Deusen, S. B., and Morosin, B., Solution growth, structure, and composition of boron carbide crystals, *J. Less-Common Met.,* 166, 29, 1990.
54. Aselage, T. L., Samara, G. A., Tallant, D. R., Van Deusen, S. B., Eatough, M. O., Emin, D., and Johnson, S., Phosphorus doping of boron carbides, *Phys. Rev. B,* 48, 11759, 1993.
55. Zuppiroli, L. and Lesueur, D., Modelling the swelling and microcracking of boron carbide under neutron irradiation, *Philos. Mag. A,* 60, 539, 1989.
56. Tucker, C. and Senio, P., X-ray scattering by neutron-irradiated single crystals of boron carbide, *Acta Crystallogr.,* 8, 371, 1955.
57. Froment, K., Gosset, D., Guery, M., Kryger, B., and Verdeau, C., Neutron irradiation effects in boron carbides: evolution of microstructure and thermal properties, *J. Nucl. Mater.,* 188, 185, 1992.
58. Iseki, T., Ito, M., Suzuki, H., and Honda, T., Effect of neutron-irradiation on thermal conductivity, electric resistivity, and thermal expansion of boron carbide, *J. Nucl. Sci. Technol.,* 10, 632, 1973.
59. Stoto, T., Zuppiroli, L., and Pelissier, J., Absence of defect clusters in electron irradiated boron carbide, *Radiat. Effects,* 90, 161, 1985.
60. Morosin, B., Mullendore, A. W., Emin, D., and Slack, G. A., Rhombohedral crystal structure of compounds containing boron-rich icosahedra, in *Boron-Rich Solids,* AIP Conf. Proc. Vol. 140, Emin, D., Aselage, T. L., Beckel, C. L., Howard, I. A., and Wood, C., Eds., American Institute of Physics, New York, 1986, 70.
61. Emin, D., Theory of electronic and thermal transport in boron carbides, in *The Physics and Chemistry of Carbides, Nitrides and Borides,* Freer, R., Ed., Kluwer, Dordrecht, 1990, 691.

32

Thermoelectric Properties of Metallic Materials

A.T. Burkov and
M.V. Vedernikov
A.F. Ioffe Physico-Technical Institute
Russian Academy of Sciences
St. Petersburg, Russia

32.1 Introduction

Thermoelectric properties play an important role in a wide variety of practical applications of metals. Metallic materials can be used in thermoelectric generators and in cooling devices in a combination with semiconducting materials as an arm of a thermoelement, as well as bonding materials used to connect the two semiconductor arms of a thermoelement. Thermoelectric applications require the material to have large thermoelectric parameters. On the other hand, in low-voltage electronic circuits, such as DC micro- and nanovoltmeters, scanners, and electrical sensors, a low thermoelectric power relative to copper is required.

In this chapter a survey of the thermoelectric properties of metallic materials such as pure metals, metallic alloys, and intermetallic compounds will be given. Basic theoretical concepts are outlined and main experimental results are discussed. For additional information readers are referred to the books and review articles listed at the end of the chapter.

32.2 Formal Theory of Transport Properties of Metals

Based on the linearized Boltzmann transport equation the following expressions can be derived for the electrical conductivity (σ), thermoelectric power (α), and thermal conductivity (λ):[1-3]

$$\sigma = e^2 \cdot K_0 \tag{1}$$

$$\alpha = \frac{1}{e \cdot T} \cdot K_1 \cdot K_0^{-1} \tag{2}$$

$$\lambda = \frac{1}{T} \cdot K_2 \tag{3}$$

where the kinetic coefficients K are defined as

$$K_n = \int_0^\infty \omega(\varepsilon,T) \cdot (\varepsilon - \mu)^n \cdot \left(-\frac{\partial f^0}{\partial \varepsilon}\right) \cdot d\varepsilon \tag{4}$$

0-8493-0146-7/95/$0.00+$.50

with

$$\omega(\varepsilon,T) = \frac{1}{12 \cdot \pi^3 \cdot \hbar} \cdot \oint \tau \cdot V \cdot V \cdot \frac{dS}{|V|} \tag{5}$$

τ, v, μ, ε are relaxation time, velocity, electrochemical potential, and energy of electrons, respectively; f^0 is the Fermi-Dirac distribution function. The integral in Equation 5 is taken over a surface of constant energy in the electron momentum space. Equations 2 to 5 are of a general nature and can be applied to describe transport properties of semiconductors and of metals. The area of their validity is limited by the boundaries of applicability of the linearized Boltzmann transport equation, which for metals may be considered as fully substantiated. For metals a further approximation is employed, which is associated with the fact that the electron gas in metals is strongly degenerated. This means that the function $-\partial f^0/\partial\varepsilon$ has a sharp peak at $\varepsilon = \mu$.

In this case, the integrand in Equation 4 is exponentially small at all energies except a narrow (compared with the Fermi energy) region near the Fermi energy. Expanding the function $\omega(\varepsilon,T)$ in a Taylor series in the vicinity of $\varepsilon = \mu$ and considering only the first nonvanishing terms, the following expressions can readily be obtained for the electrical conductivity, thermoelectric power, and thermal conductivity:

$$\sigma(T) = e^2 \cdot \omega(\mu,T) \tag{6}$$

$$\alpha(T) = -\frac{\pi^2 k_B^2}{3|e|} \cdot T \cdot \left[\frac{1}{\omega} \cdot \frac{\partial\omega}{\partial\varepsilon}\right]_{\varepsilon=\mu} \tag{7}$$

$$\lambda(T) = \frac{\pi^2 k_B^2}{3} \cdot T \cdot \omega(\mu,T) \tag{8}$$

It follows from Equations 6 and 8 that:

$$\lambda(T) = \frac{\pi^2 k_B^2}{3e^2} \cdot T \cdot \sigma(T) = L_0 \cdot T \cdot \sigma(T) \tag{9}$$

Equation 9 is known as the Wiedemann-Franz law with L_0 the Sommerfeld value of the Lorentz number ($L_0 = 2.45 \cdot 10^{-8} V^2 K^{-2}$). It should be emphasized here that λ is the electronic component (λ_e) of the total thermal conductivity which includes a lattice contribution (λ_L). For metals, the electronic part of the thermal conductivity is usually much larger than the lattice contribution. Consequently the lattice thermal conductivity can be neglected in estimations of the thermoelectric figure-of-merit Z:

$$Z = \frac{\alpha^2 \cdot \sigma}{\lambda} = \frac{\alpha^2}{L_0 \cdot T} \tag{10}$$

Thus, to a first approximation, the thermoelectric efficiency of metallic materials is determined only by the thermoelectric power. The so-called Bloch-Grüneisen law for the temperature dependence of the electrical conductivity follows from Equation 6. This law predicts the linear temperature dependence of the electrical resistivity in the high-temperature region (usually at temperatures above approximate room temperature). As a consequence of the Wiedemann-Franz law the thermal conductivity should be temperature independent in the high-temperature domain. The Mott formula for the thermoelectric power (Equation 7), also predicts a linear variation of the thermoelectric power with the temperature in the high-temperature region and absolute values of about 1 μ V/K. From Equations 7 and 9 it is concluded that the figure-of-merit Z increases linearly with the temperature.

These are the results based on the standard transport theory for an idealized metal. However, the real situation is much more complicated. Experimental data on the temperature-dependent thermoelectric power of metals, some alloys, and intermetallic compounds are presented in the following sections.

Several specific low-temperature phenomena have not been considered. For example, in pure metals at temperatures of about $\theta_D/6$ a phonon drag peak is observed. The magnitude of this peak in most cases does not exceed 1 to 2 μ *V/K*. This has been interpreted to mean that at low temperatures, momentum and energy from the nonequilibrium phonon system can be imparted to the conduction electron system producing an additional charge flow.[8]

At very low temperatures impurity scattering dominates all other scattering processes. One of the most interesting effects of the electron-impurity interaction is the Kondo effect. This will be briefly discussed in the last section of the chapter. In general, at the lowest temperatures the thermoelectric power tends to zero with decreasing temperature.

32.3 Experimental Data on Thermoelectric Power of Metallic Materials

Pure Metals

A number of books and review articles have been devoted to the thermoelectric properties of metals.[4–11] It has been shown that at high temperatures the thermoelectric power and the electrical resistivity of many metals follow more complex laws, rather than simply varying with temperature according to the Mott formula and Bloch-Grüneisen law. Although the electrical resistivity of a number of metals at high temperatures increases with temperature at a rate which is slower than a linear law and may trend to saturation, there are metals whose resistivity increases with temperature faster than a linear rate. The high-temperature thermoelectric power exhibits a diverse behavior which cannot be described by a linear dependence based on Mott's expression even to a first approximation. A significant observation has been made on pure metals: all metals belonging to the same group of the periodic table can, to a first approximation, be characterized by a common dependence of the thermoelectric power on temperature but the temperature dependences for metals from different groups are qualitatively different.[5] The complicated behavior of thermoelectric power has not, in general, been theoretically explained, but it is believed that the temperature dependences of both the thermoelectric power and electrical resistivity are intimately related to the structure of the electronic spectrum near the Fermi level. In Table 1 the available experimental thermoelectric power data are collected. Most of the data are for polycrystalline samples; although in some cases data were obtained using single crystals. For those metals the reported $\alpha(T)$ values are averaged over the crystallographic directions. For more information the reader is referred to the review article of Foiles.[10]

The temperature dependence of the thermoelectric power for a number of metals is collected in Figure 1. The temperature variation of the thermoelectric power of copper is to a first approximation in agreement with the standard transport theory with respect both to its absolute value and the temperature dependence. The strong influence of magnetic ordering on the thermoelectric power is clearly evident for Cr, Ni, and Co. Its pronounced nonlinearity and large absolute value in the case of W, Mo, and Pd demonstrate the deviations from the predictions of the standard transport theory.

Many metals crystallize with anisotropic lattices and consequently the respective thermoelectric power also exhibits rather large anisotropies. These metals can be used in anisotropic thermoelectric converters, for example, in thermoelectric detectors of radiation. Figure 2 shows the temperature-dependent thermoelectric power for Re and Be measured along the principal crystallographic axis.

Pure copper, platinum, and gold are widely used in thermocouples and in thermoelectric power measurements as reference electrodes. The measured voltage (ΔV) in thermoelectric power determinations is proportional to the difference of the thermoelectric power of the sample under investigation (α_s) and the thermoelectric power (α_r) of the electrode used to measure the voltage along the sample:

$$\Delta V = (\alpha_s - \alpha_r) \cdot \Delta T \tag{11}$$

Table 1

	Thermoelectric Power $\alpha(T)$, μV/K					
Metal	100 K	300 K	500 K	1000 K	1500 K	Ref.
Ag	0.73	1.51	2.82	7.95		11
Al	−2.2	−1.66	1.96			10
Au	0.82	1.94	2.86	3.85		11
Ba	−4	12.1	28.5			10
Be	−2.5	1.7	2.7	7.9		10
Ca	1.05	10.3	17.1			10
Cd	−0.05	2.55				10
Ce	13.6	6.2	5.2	−4.8		10
Co	−8.43	−30.8	−44.8	−35.9	−7.8	5
Cr	5	21.8	16.6	17.9	5.7	10
Cs		−0.9				10
Cu	1.19	1.83	2.83	5.36		11
Dy	−4.1	−1.8	0.9	2.3		9
Er	−3.8	−0.1	1.9	4.2		9
Eu	5.3	24.5	46			10
Fe	11.6	15	3	0.4		10
Ga	0.5					10
Gd	−4.6	−1.6	−0.5	−0.8		9
Hf	0	5.5	5.7	−0.5		15
Ho	−6.7	−1.6	1.4	2.8		9
In	0.56	1.68				10
Ir	1.42	0.86	−0.1	−2.7	−5.7	10
K	−5.2	−13.7				10
La	0.1	1.7	2	−1.7		9
Li	4.3					10
Lu	−6.9	−4.3	−2.6	0		9
Mg	−2.1	−1.46				10
Mn	−2.5	−9.8	−8.4	−1.5		10
Mo	0.1	5.6	11.4	17.4	13.7	12
Na	−2.6	−6.3				10
Nb	1.05	−0.44	−1.1	0.45	3.2	15
Nd	−4	−2.3	0	−1.2		9
Ni	−8.5	−19.5	−25.8	−29.9		10
Np	8.9	−3.1				10
Os	−3.2	−4.4	−4.7	−6.3	−8.5	10
Pb	−0.58	−1.05	−1.5			14
Pd	1.1	−10.7	−16.3	−32.3	−46.4	10
Pu	12					10
Rb	−3.6	−10				10
Re	−1.4	−5.9	−5.9	−1.9	1.8	10
Rh	0.8	0.6	0.5	−1.5		10
Ru	0.3	−1.4	−1.8	−4.2	−7.5	10
Sc	−14.3	−19	−17.5	−5.4	10.2	15
Sm	0.7	1.2	0.6	−3		9
Sn	−0.04	−1				10
Sr	−3	1.1	4.2			10
Ta	0.7	−1.9	−2.3	1.6	7.2	15
Tb	−1.6	−1	0.3	0.6		9
Th	0.6	−3.2	−9.2	−14.3	−10.3	10
Ti	−2	9.1	5.3	−3.1	−0.5	15
Tl	0.6	0.3	−1.5			10
Tm	−1.3	1.9	2.7	2.2		9
U	3	7.1	11	16.7		10
V	2.9	0.23	1.1	4.6		10
W	−4.4	0.9	9	19.8	21.3	12
Y	−5.1	−0.7	0.3	2.9	6.6	10
Yb	5.1	30	20.3	12.3		10
Zn	0.7	2.4				10
Zr	4.4	8.9	4.6	−3	1.1	15

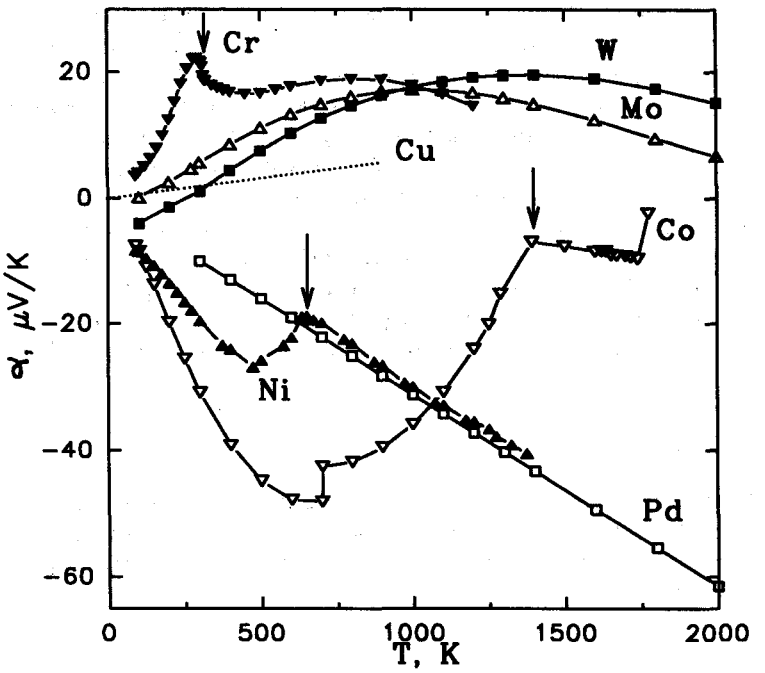

FIGURE 1 Temperature-dependent thermoelectric power of Co, Cr, Cu, Pd, Mo, Ni, and W. For references see Table 1. The arrows show the temperatures of the magnetic transitions for Cr, Ni, and Co.

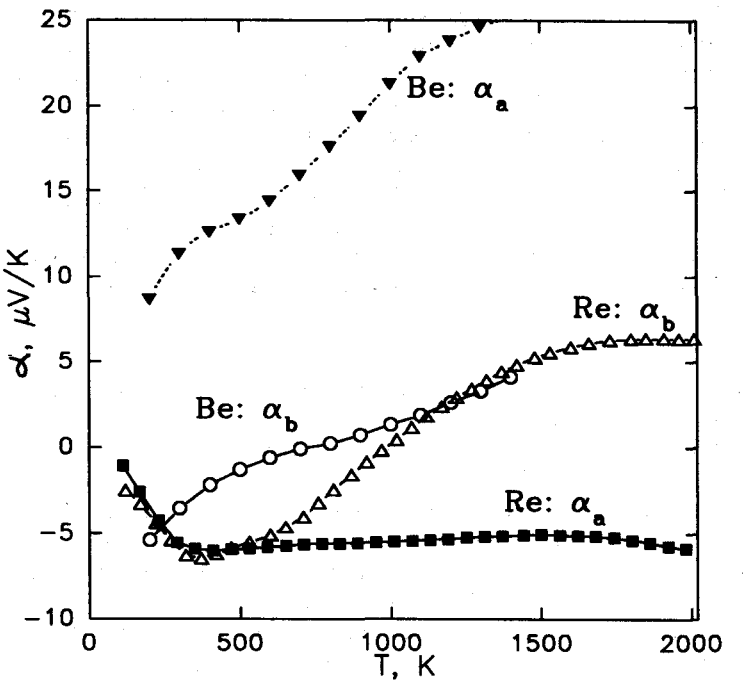

FIGURE 2 Temperature-dependent thermoelectric power of Be and Re single crystals measured when a heat flow passes along (a_a) or perpendicular to (a_b) the hexagonal axis of the crystals.

Therefore, it is necessary to know the thermoelectric power of the electrode in order to calculate the absolute thermoelectric power (α_s) of the sample. The most reliable and precise data on absolute thermoelectric power have been obtained for lead by Roberts[14] from Thomson heat measurements using the Onsager relation for thermoelectric coefficients.[8] Consequently Pb is used as a primary reference electrode in the temperature range 0 to 350 K. At higher temperatures Cu, Pt, Mo, or W can be used as reference electrodes. The absolute thermoelectric power of these metals has been calculated by Cusack and Kendall[12] using the Thomson heat measurements of Lander.[13]

Within the group of pure metals, Eu has the largest positive thermoelectric power but because of its extremely high chemical activity this metal cannot be used in any thermoelectric device. Other metals like Cr, Mo, and W possess positive thermoelectric power of up to 20 μ V/K at high temperatures and can be used up to 2000 K. "Magnetic" metals like Ni or Co and "nearly magnetic" metals such as Pd or Pt have negative thermoelectric power of up to -60 μ V/K at 2000 K.

Metallic Alloys

Because of the practically unlimited variety of metallic alloys more or less general relations have only been established for the simplest alloys—binary alloys. The Matthiessen rule can be applied for the electrical resistivity of dilute binary alloys. The total electrical resistivity ρ of a dilute alloy can be expressed as:[1]

$$\rho(T) = \rho_i(c) + \rho_{ph}(T) \tag{12}$$

where c is the impurity concentration. This expression shows that the total resistivity of an alloy consists of two independent parts: the temperature-dependent phonon contribution $\rho_{ph}(T)$ and the concentration-dependent (but temperature-independent) impurity resistivity ρ_i. In analyzing the thermoelectric power of dilute alloys the Nordheim-Gorter expression is sometimes used:[8]

$$\alpha = (\alpha_{ph} - \alpha_i) \cdot \rho_{ph}/(\rho_{ph} + \rho_i) + \alpha_i \tag{13}$$

The thermoelectric power α_{ph} and α_i are considered as the characteristic thermoelectric power of the solvent and solute, respectively. This expression is based in the first instance on the assumption that scattering processes involving conduction electrons on phonons and on impurities are independent and, secondly, on the validity of the Wiedemann-Franz law. It follows from Equation 13 that at any given temperature the measured thermoelectric power α is a linear function of the reciprocal total resistivity $\rho = (\rho_{ph} + \rho_i)$. Another important observation has been made for the binary continuous solid solutions of metals:[15] it has been established that all alloys of this class can be divided into two types according to the dependence of their electrical resistivity and thermoelectric power on the alloy composition. In the alloys of the first type the impurity resistivity depends on composition and follows the well-known Kurnakov-Nordheim rule:[1]

$$\rho_i = A \cdot c \cdot (1 - c) \tag{14}$$

where c is the atomic concentration of one of the alloy components. Figure 3a demonstrates this type of behavior for Nb-Ta alloys.

In alloys of the second type the electrical resistivity does not obey this rule, the dependence of the impurity resistivity on an alloy composition being depicted by a curve which is asymmetric relative to the equi-atomic composition (see Figure 4a for Pd-Ag alloys). The alloys of the first type can be formed only of isoelectronic metals (i.e., belonging to the same group of the periodic table), whereas those of the second type are made primarily of nonisoelectronic metals. This classification is also confirmed by an analysis of the thermoelectric power.[15] In alloys of the first type the thermoelectric power varies smoothly with the alloy composition. Usually a relatively strong composition dependence is observed for the dilute alloys, whereas a comparatively weak variation is observed for the concentrated alloys. Figure 3b presents the composition dependence of the thermoelectric power for Nb-Ta alloys and shows it to be nearly composition independent. As

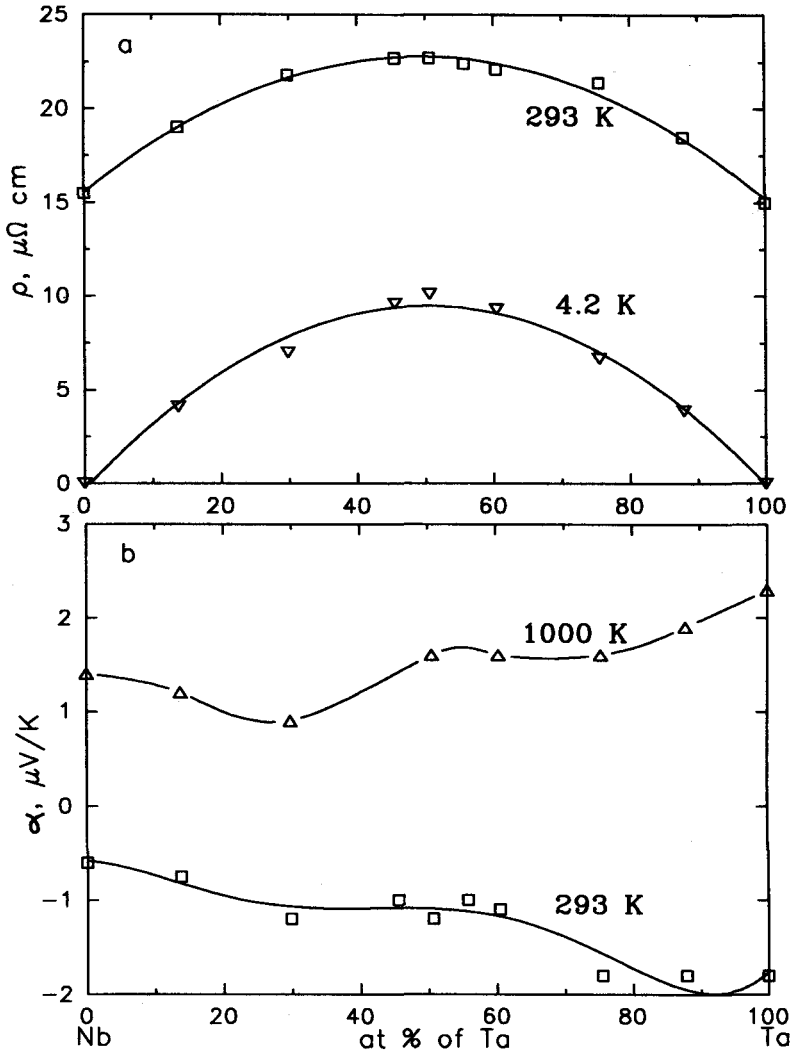

FIGURE 3 Electrical resistivity (a) and thermoelectric power (b) of Nb-Ta alloys vs. composition.[15]

already mentioned, metals belonging to the same group of the periodic table exhibit similar temperature dependences of the thermoelectric power, whereas nonisoelectronic metals possess qualitatively different temperature dependencies. In alloys of isoelectronic metals the variations of the temperature dependences of thermoelectric power and resistivity with the alloy composition are purely quantitative. This is demonstrated for the Ta-Nb alloys in Figure 5b. The temperature-dependent thermoelectric power of the alloys have the same typical features as those of pure Ta and Nb: a minimum around 500 K, change of sign near 800 K, and a maximum at about 1800 K. The resistivity temperature dependences of pure Ta, Nb, and of their alloys have similar negative curvatures, as can be seen in Figure 5a. So far the only, but quite interesting, exception to this rule is the Ag-Au alloys whose temperature dependences of thermoelectric power differ markedly from those of the pure metals.

A substantially different situation is observed in the case of nonisoelectronic metal alloys where the thermoelectric power depends strongly on the composition for any component ratio, with a clearly pronounced extremum being usually observed in the middle of the thermoelectric power-composition diagram. As an example, the thermoelectric power of Pd-Ag alloys is presented in

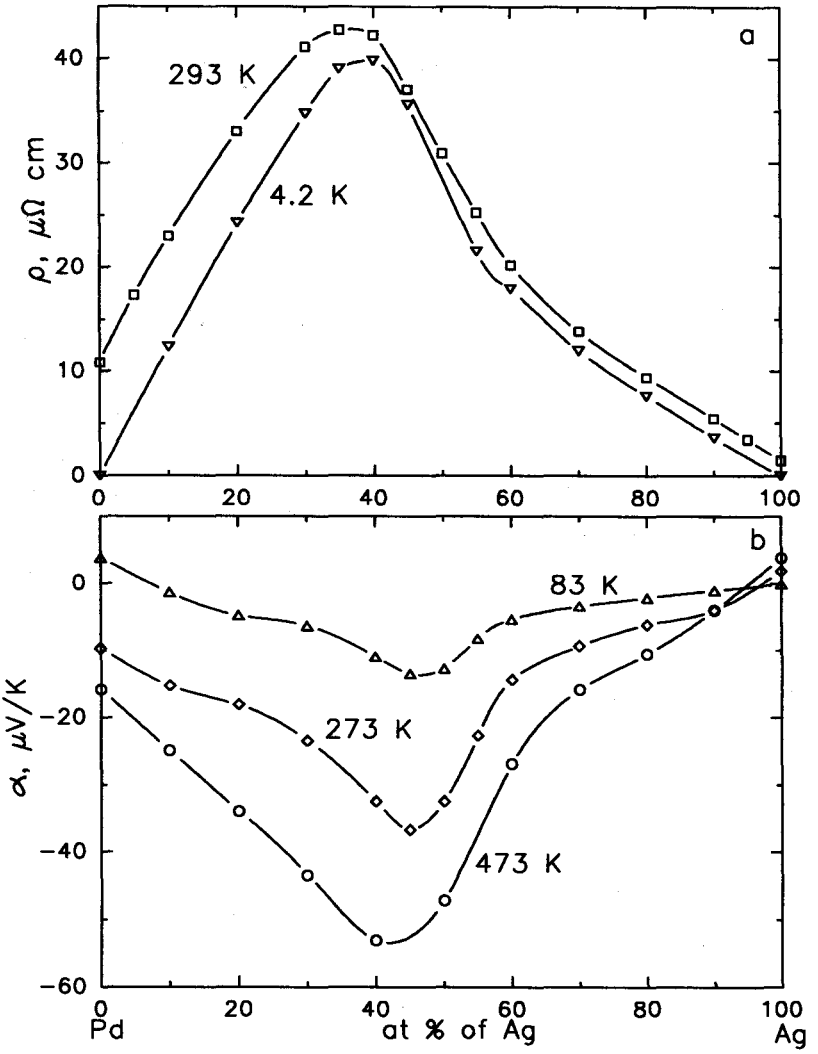

FIGURE 4 Electrical resistivity (a) and thermoelectric power (b) of Pd-Ag alloys vs. composition.[11]

Figure 4b. The thermoelectric power, and to some extent, the resistivity temperature dependences of these alloys undergo qualitative transformations as the alloy composition is varied. This is demonstrated in Figure 6.

Metallic alloys are the principal materials for thermocouples. Mostly, Cu-, Ni-, Pt-, and W-based alloys are used in this application. The data for the widely used Ni-Cr alloys with positive thermoelectric power are presented in Figure 7, and for some Cu-Ni alloys with negative values in Figure 8. Some of these alloys have also been used in thermoelectric generators and radiation detectors. More efficient metallic alloys exist, such as Pd + 11% at. U[20] and Cr + 10% Mn[10] which have large positive thermoelectric power values at high temperatures (up to 40 μ V/K above room temperature), whereas alloy Pd + 40% Ag exhibits values of about −75 μ V/K at 1000 K.[11] However, the high price of the materials precludes their wide-scale application.

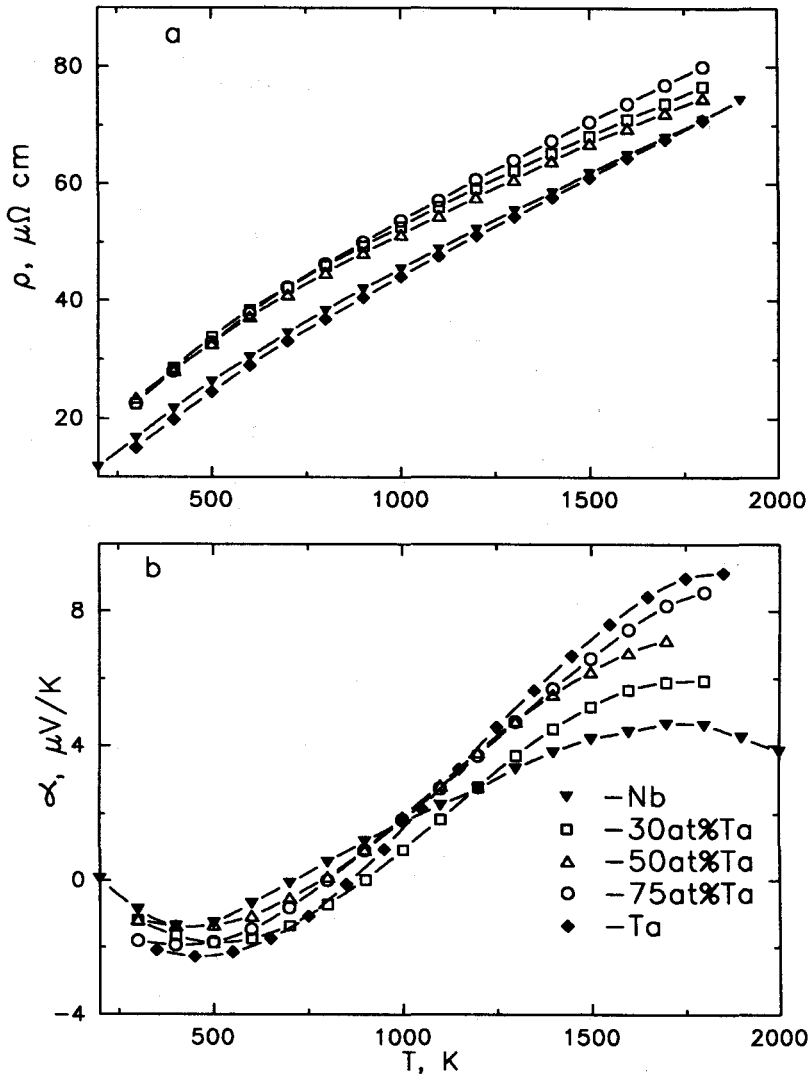

FIGURE 5 Temperature-dependent electrical resistivity (a) and thermoelectric power (b) of pure Ta, Nb, and Ta-Nb alloys.[11]

Intermetallic Compounds

The intermetallic compounds of diluted Kondo alloys and heavy-fermion compounds are briefly discussed. Kondo alloys, which have found a practical application in low-temperature thermometry, are the dilute alloys of magnetic transition metals in the noble metals. The characteristic feature of these alloys is the large thermoelectric power at very low temperatures—about 10 μ V/K at 10 K. This large value, as well as the resistivity minima in the same temperature range, is the result of conduction electron spin-flip scattering by the localized magnetic moments of *3d* or *4d* impurities.[8] Very dilute alloys of iron in gold (about 0.01 at.%), usually in a combination with the 90% Ni + 10% Cr alloy (Chromel), are commonly used as low-temperature thermocouples. These thermocouples show reasonable sensitivity from about 5 K up to room temperature.

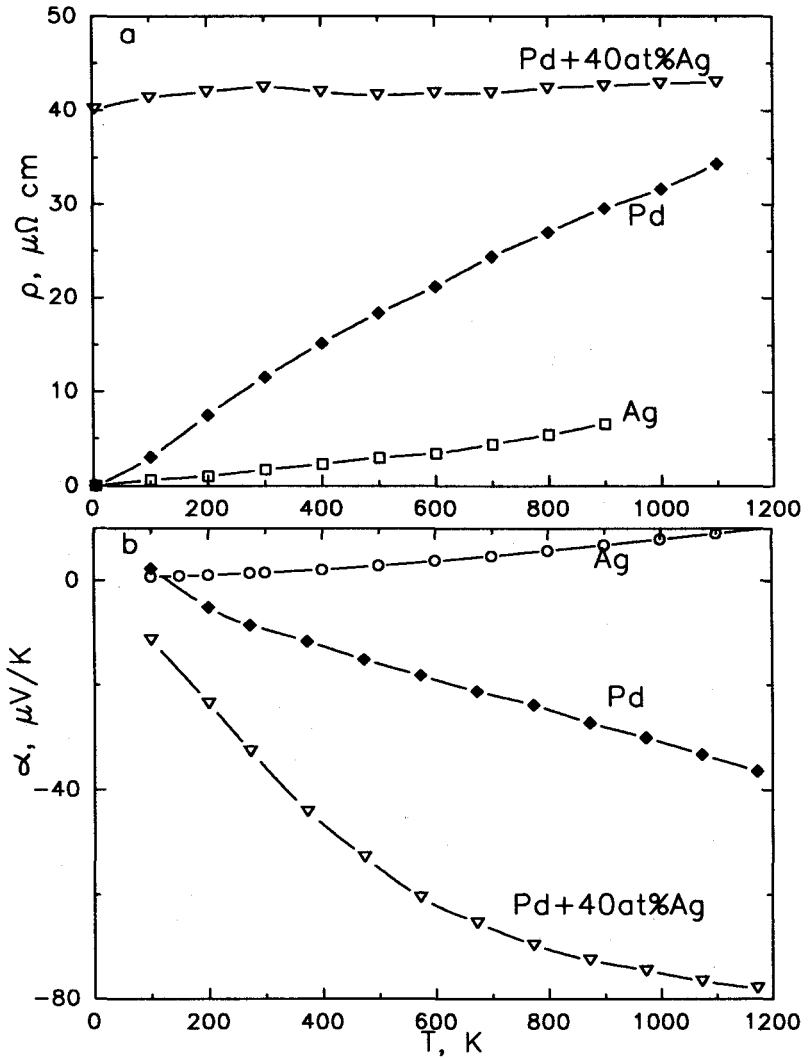

FIGURE 6 Temperature-dependent electrical resistivity (a) and thermoelectric power (b) of pure Ag, Pd, and of Pd + 40 at.% Ag alloy.[15]

Heavy-fermion compounds behave in many respects like concentrated Kondo systems. The spin-flip scattering resulting in a large thermoelectric power and resistivity minima is attributed to the well-localized magnetic moments of rare earth elements like cerium and ytterbium.[16,17] Heavy-fermion compounds have not found practical thermoelectric application but, because of the comparatively large thermoelectric power which they exhibit at very low temperatures, this class of materials can probably find a use in low-temperature thermoelectric devices. A few examples of the temperature-dependent thermoelectric power of heavy-fermion compounds are shown in Figure 9. Low-temperature applications have become especially important since the discovery of new high-temperature superconducting materials. The temperature of the superconducting transition for these materials is within a temperature range from 80 to 135 K. On the one hand such temperatures can probably be achieved by using thermoelectric cooling devices and on the other hand, thermoelements can be used for a precise regulation of the temperature in the vicinity of the superconducting transition.

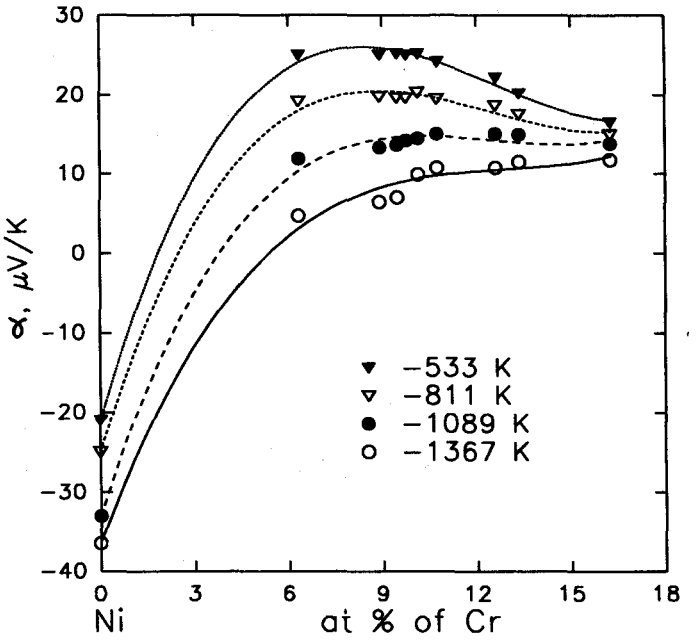

FIGURE 7 Composition-dependent thermoelectric power of Ni-Cr alloys at different temperatures.[18]

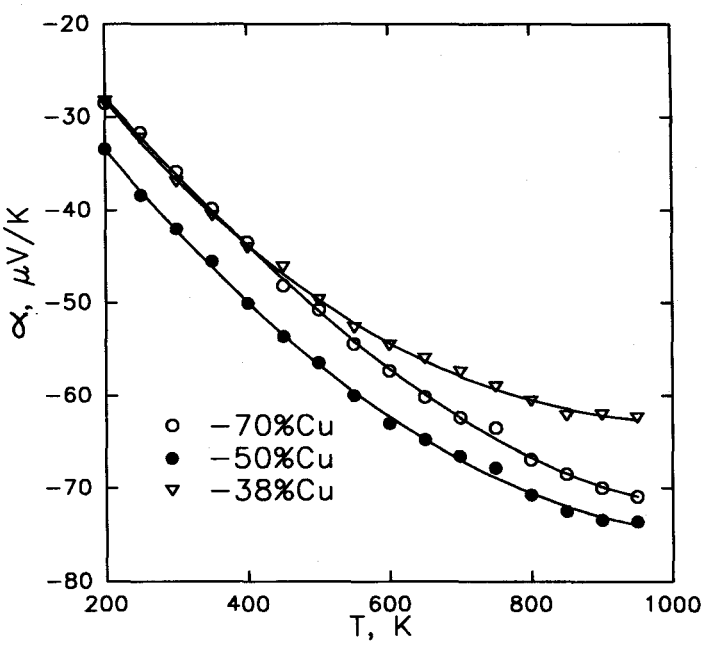

FIGURE 8 Temperature-dependent thermoelectric power of Cu-Ni alloys.[19]

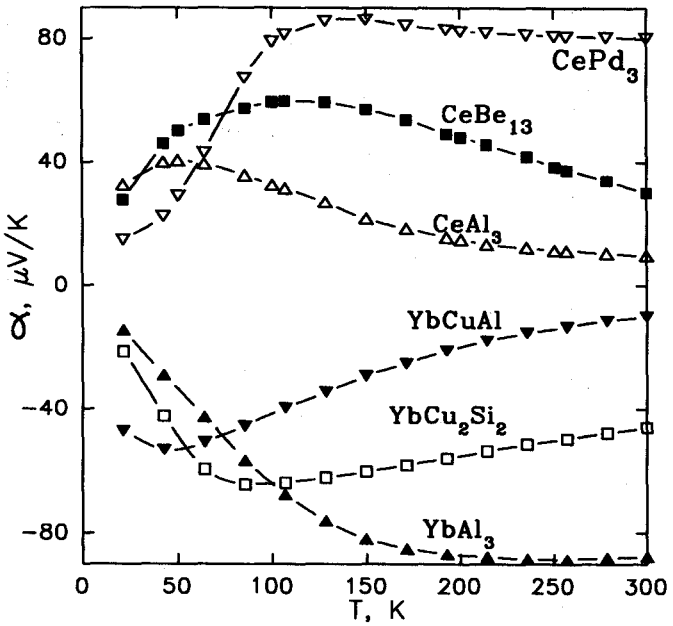

FIGURE 9 Temperature-dependent thermoelectric power for various heavy-fermion compounds.[16,17]

Defining Terms

c—Atomic concentration of an alloy component
e—Electron charge
L_0—Sommerfeld value of the Lorentz number
$\boldsymbol{k}$—Conduction electron wave vector
k_B—Boltzmann constant
K_n—Kinetic coefficients
f^0—Fermi-Dirac distribution function
T—Absolute temperature
$\boldsymbol{v}$—Conduction electron velocity
Z—Thermoelectric figure-of-merit
$d\boldsymbol{S}$—Area element of a constant energy surface in the wave vector space
α—Thermoelectric power
α_s—Thermoelectric power of the sample under investigation
α_r—Thermoelectric power of a reference electrode
α_i—Impurity thermoelectric power
α_{ph}—Phonon thermoelectric power
ε—Energy of an electron
λ—Thermal conductivity
λ_e—Electronic thermal conductivity
λ_L—Lattice thermal conductivity
Θ_D—Debye temperature
μ—Chemical potential
ρ—Electrical resistivity
ρ_i—Impurity contribution to the resistivity
ρ_{ph}—Phonon contribution to the resistivity
σ—Electrical conductivity

τ—Conduction electron relaxation time
$\omega(\varepsilon,T)$—Conductivity of electrons on a constant energy surface $e(\boldsymbol{k})$ = const
ΔT—Temperature difference
ΔV—Potential difference along a sample

Acknowledgments

One of the authors (A.B.) would like to express his gratitude to the Institute of Experimental Physics of Vienna Technical University for facilitating a two-month stay during which a substantial part of this work was completed. In particular he would like to thank Professor E. Gratz, Dr. E. Bauer, and Mr. R. Resel.

References

1. Mott, N. F. and Jones, H., *The Theory of the Properties of Metals and Alloys*, Oxford University Press (Clarendon), London, 1936.
2. Ziman, J. M., *Electrons and Phonons*, Oxford University Press (Clarendon), London, 1960.
3. Blatt, F. J., *Physics of Electronic Conduction of Solids*, McGraw-Hill, New York, 1968.
4. Nystrom, J., *Thermospannungen*, in Landolt-Bornstein. Zahlenwerte und Funktionen, Bd.2, teil 6, Springer, Berlin, 1959.
5. Vedernikov, M. V., Thermopowers of transition metals at high temperatures, *Adv. Phys.*, 18, 337, 1969.
6. Blatt, F. J., Shroeder, P. A., Foiles, C. L., and Greig, D., *Thermoelectric Power of Metals*, Plenum Press, New York, 1976.
7. Hubener, R. P., *Thermoelectricity in Metals and Alloys, Solid State Physics*, Vol. 27, Academic Press, New York, 1972.
8. Barnard, R. D., *Thermoelectricity in Metals and Alloys*, Taylor & Frances, London, 1972.
9. Vedernikov, M. V., Burkov, A. T., Dvunitkin, V. G., and Moreva, N. I., The thermoelectric power, electrical resistivity and Hall constant of rare earth metals in the temperature range 80–1000 K, *J. Less-Common Met.*, 52, 221, 1977.
10. Foiles, C. L., *Thermopower of pure metals and dilute alloys*, in Landolt-Bornstein. Numerical Data and Functional Relationships in Science and Technology. New Series. Group III, v.15, Metals, Springer-Verlag, New York, 1985.
11. Rudnitskii, A. A., *Thermoelektricheskie Svoistva Blagorodnykh Metallov i ikh Splavov* (Thermoelectric Properties of Noble Metals and their Alloys), Izdatelstvo Akademii Nauk SSSR, Moscow, 1956 (in Russian).
12. Cusack, N. and Kendall, P., The absolute scale of thermoelectric power at high temperature, *Proc. Phys. Soc.*, 72, 898, 1958.
13. Lander, J. J., Measurements of Thomson coefficients for metals at high temperatures and of Peltier coefficients for solid-liquid interfaces of metals, *Phys. Rev.*, 74, 479, 1948.
14. Roberts, R. B., The absolute scale of thermoelectricity, *Philos. Mag.*, 36, 91, 1977.
15. Vedernikov, M. V., Dvunitkin, V. G., Zhumagulov, A., Regularities in electrical resistivity and thermopower of metallic binary continuous solid solutions, *Fiz. Tverd. Tela*, 20, 3302, 1978 (in Russian).
16. Brandt, N. B. and Moshchalkov, V. V., Concentrated Kondo systems, *Adv. Phys.*, 33, 373, 1984.
17. Bauer, E., Anomalous properties of Ce-Cu- and Yb-Cu-based compounds, *Adv. Phys.*, 40, 417, 1991.
18. Wang, T. P., Starr, C. D., and Brown, N., Thermoelectric characteristics of binary alloys of nickel, *Acta Metall.*, 14, 649, 1966.
19. Ahmad, H. M. and Greig, D. J., The electrical resistivity and thermopower of nickel-copper alloys, *J. Phys. (Paris)*, 15, C4-223, 1974.
20. Vedernikov, M. V., Terekhov, G. I., Sinyakova, S. I., and Ivanov, O. S., Thermoelectric properties of alloys of palladium with uranium, Communications of Academy Sc. USSR-Metals, N4, 191, 1969 (in Russian).

33

Neutron Irradiation Damage in SiGe Alloys

Jan W. Vandersande
Jet Propulsion Laboratory
California Institute of Technology
Pasadena, California, U.S.A.

33.1 Introduction and Background

Silicon-germanium (SiGe) thermoelectric alloys have been used very successfully in space power sources in several space missions during the past two decades. In these power sources (called radioisotope thermoelectric generators—RTGs) the heat is produced by the decay of ^{238}Pu and converted to electricity by the SiGe material. The thermoelectric alloy in these RTGs experiences a very low neutron flux and fluence (on the order of 10^{11} n/cm^2), which appears to have no adverse effect on the thermoelectric properties. In some future space missions nuclear reactors will very likely be used to supply the heat needed for the conversion into electrical power, and thermoelectric energy conversion is one of the main conversion options. The SiGe material will in that case experience a larger neutron fluence (from on the order of 10^{15} n/cm^2 behind a shield to on the order of 10^{21} n/cm^2 next to the reactor, over a 7-year period). The effect of this fluence neutron irradiation on the thermoelectric properties definitely needs to be studied. The irradiation damage could either result in no change in properties due to the annealing out at the temperatures of operation (typically 600 to 1000°C), or change the properties, either deteriorate or improve them. The net change in performance of the material will depend on how the figure-of-merit, Z (a measure of how good a thermoelectric material it is), changes. It is given by:

$$Z = \frac{\alpha^2}{\rho\lambda} \tag{1}$$

where α is the Seebeck coefficient, λ is the thermal conductivity, and ρ the resistivity, which is given by

$$\rho = \frac{1}{ne\mu} \tag{2}$$

where n is the carrier concentration, e the charge, and μ the mobility. All these parameters can change as a result of the neutron irradiation so the net change in Z will depend on the magnitude of the changes in α, ρ, and λ.

Very little work has been done on the effect of neutron irradiation on SiGe thermoelectric material until very recently. One study was very inconclusive[1] while an RCA study[2] was very detailed but was limited to neutron fluences on the order of 1 to 4 × 10^{18} n/cm^2 with irradiation at 100 and 400°C and with subsequent anneals up to 500°C. It was found that fast and thermal neutrons

0-8493-0146-7/95/$0.00+$.50

resulted in an increase in resistivity (both a decrease in mobility and carrier concentration) which only partially (in some cases up to about 90%) annealed out after a heat treatment at 500°C for 2 to 4 h. Very little work was done on studying the effect on the thermal conductivity. The few measurements indicated a reduction of up to around 10%. In silicon irradiated to a fluence of 10^{18} n/cm^2 it was found that all the damage annealed out after a heat treatment at 800°C.[3] The most detailed study of irradiation damage on a thermoelectric material (SiGe) is by Vandersande and Farmer.[4] Their results will be presented in detail in this chapter.

In $Si_{80}Ge_{20}$ alloys, most of the heat is carried by intermediate-frequency phonons, since the high-frequency (short wavelength) phonons are scattered by the Si-Ge mass difference and other point defects and the low-frequency (long wavelength) phonons by electrons and grain boundaries. The intermediate-frequency phonons will be scattered by defects that are 40 to 100 Å in size.[5] Irradiation-produced Frenkel pairs will thus not scatter these phonons. Only larger stable defects, such as vacancy chains or clusters, will do that. There is evidence for these types and sizes of irradiation-produced defects in KCL[6] and diamond.[7] It is believed that the size and required concentration of these extended defects that will be needed to scatter the intermediate-frequency phonons, will not scatter the electrons to the same degree.[4] The reduction in thermal conductivity is thus expected to be greater than the increase in resistivity, resulting in a net increase in Z.

The above-mentioned previous work gives no clear indication as to what to expect for the neutron irradiation effect on SiGe alloys. However, it does suggest that a heat treatment at the highest temperature of future operation (1000°C) is needed to determine if the damage anneals out or not. A detailed discussion of the Vandersande and Farmer[4] results now follows.

33.2 Experimental

Four different types of $Si_{80}Ge_{20}$ alloys were studied: zone-leveled (ZL) and hot-pressed (HP) n- and p-type. The ZL samples were fabricated by RCA in the early 1960s and the HP samples by GE. The samples were 12.6 mm in diameter by 1 mm thick. The HP samples have grain sizes from 1 to 10 μm compared to at least several millimeters for the ZL samples. Also, the HP samples have about 2 a/o oxygen present compared to very little in the ZL samples. The effect, if any, of grain boundaries and oxygen on the irradiation-produced defects can thus be determined.

The samples were irradiated at the University of Missouri Research Reactor. Two sets of samples were irradiated, one set in the first row of the reflector and the second in the flux trap. The neutron spectra are similar for the two positions; however, the dose rate is approximately ten times higher in the flux trap. The reflector position has a thermal flux of 8.0×10^{13} n/cm^2-s and a fast flux of neutrons (with energy greater than 10 KeV) of 2.1×10^{13} n/cm^2-s. For the samples that were irradiated in the reflector the total thermal fluence was 1.5×10^{19} n/cm^2 and the fast fluence was 4.0×10^{18} n/cm^2. The dose for the first set of samples corresponds to displacement of 1.5×10^{20} atoms/cm^3. In the flux trap the thermal neutron flux is 3×10^{14} n/cm^2-s and the fast flux of neutrons (with energies greater than 10 keV) is 9×10^{13} n/cm^2-s. The samples irradiated in the flux trap were irradiated to a total thermal fluence of 1.8×10^{20} n/cm^2 and a total fast fluence of 5.4×10^{19} n/cm^2. This dose corresponds to displacement of approximately 2×10^{21} atoms/cm^3. The irradiation position also has a relatively high gamma field. The combination of the neutron and gamma fields results in an ambient temperature during the irradiation of 200 to 300°C.

The electrical resistivity, carrier concentration, and mobility were measured at room temperature in a Hall effect apparatus. The thermal diffusivity, which is directly proportional to the thermal conductivity, was measured at 177 to 192°C in a flash diffusivity apparatus. The samples were measured before and after irradiation and after each anneal at 350, 600, and 1000°C. The anneals were for 2 h each in air. Initially (pre-irradiation), the samples were heated at 1050°C for 1/2 h and measured. This "resetting" of the samples puts the dopant (phosphorus for n-type and boron for the p-type) in solution. That ensures that meaningful comparisons with the post anneal measurements are possible. It was decided to anneal at three different temperatures so that the effect of each on the irradiation damage could be observed.

Table 1 Characterization of Neutron-Irradiated SiGe Samples to a Fluence of 4×10^{18} n/cm^2

Sample	Treatment	Resistivity (mΩ-cm)	Hall Mobility (cm^2/V-s)	Carrier Concentration (cm^{-3})	Diffusivity at 450–465 K (cm^2/s)
Zone-Leveled	Pre-irradiation	0.786	59.8	$1.33 \cdot 10^{20}$	0.0239
(RCA)	1050°C "reset"	0.630	52.4	$1.89 \cdot 10^{20}$	
n-type	Post-LF irradiation	4.11	29.4	$5.16 \cdot 10^{19}$	0.0207
	350°C anneal	1.65	57.0	$6.63 \cdot 10^{19}$	0.0260
	600°C anneal	0.835	61.6	$1.21 \cdot 10^{20}$	0.0256
	1000°C anneal	0.630	53.7	$1.79 \cdot 10^{20}$	0.0252
Hot-Pressed	Pre-irradiation	1.70	26.6	$1.38 \cdot 10^{20}$	0.0179
(GE)	1050°C "reset"	1.43	26.0	$1.69 \cdot 10^{20}$	
n-type	Post-LF irradiation	10.10	11.5	$5.36 \cdot 10^{19}$	0.0166
	350°C anneal	2.62	24.7	$9.62 \cdot 10^{19}$	0.0186
	600°C anneal	1.81	32.1	$1.07 \cdot 10^{20}$	0.0182
	1000°C anneal	1.41	25.1	$1.71 \cdot 10^{20}$	0.0182
Zone-Leveled	Pre-irradiation	1.04	38.6	$1.56 \cdot 10^{20}$	0.0359
(RCA)	1050°C "reset"	1.02	38.8	$1.57 \cdot 10^{20}$	
p-type	Post-LF irradiation	8.38	19.5	$3.82 \cdot 10^{19}$	0.0249
	350°C anneal	3.13	24.2	$8.26 \cdot 10^{19}$	0.0362
	600°C anneal	1.48	31.1	$1.35 \cdot 10^{20}$	0.0348
	1000°C anneal	1.03	39.1	$1.55 \cdot 10^{20}$	0.0343
Hot-Pressed	Pre-irradiation	1.01	36.4	$1.70 \cdot 10^{20}$	0.0257
(GE)	1050°C "reset"	1.00	36.1	$1.74 \cdot 10^{20}$	
p-type	Post-LF irradiation	4.17	22.4	$6.69 \cdot 10^{19}$	0.0218
	350°C anneal	2.26	24.9	$1.11 \cdot 10^{19}$	0.0286
	600°C anneal	1.32	31.1	$1.52 \cdot 10^{20}$	0.0259
	1000°C anneal	1.00	36.1	$1.73 \cdot 10^{20}$	0.0266

33.3 Results and Discussion

The results of the two different fluence neutron irradiations are summarized in Tables 1 and 2. The dramatic effect of the irradiation on the resistivity can be seen clearly in both cases: increases from a factor of 4 to 8 for the lower fluence, to 50–3 $\times$ 10^4 for the higher fluence. This increase is due to both a large drop in mobility in most cases and in carrier concentration in all cases. The HP n-type sample, which had the smallest grain size (1 to 2 μm), showed by far the largest drop in mobility, from 26.0 to 0.469 cm^2/V-s compared to 10–50% drops for the other samples. This suggests that the small grain size does have a dramatic effect, probably by trapping vacancies and/or interstitials. The 10-μm grain size for the p-type HP high fluence sample does not appear to have had any effect. The thermal diffusivity decreased only up to 10–15% in both cases. This indicates that only small defects were produced by the neutron irradiation and that this additional point defect scattering by vacancies and interstitials, besides the Si-Ge mass difference, reduced the thermal conductivity only slightly. The presence of these small defects is confirmed by the observed reduction in mobility, which would be expected to be decreased more by these defects than extended defects.

For moderate levels of irradiation, both the displacement damage and the free carrier removal rate are linear with fluence. Thus, the free carrier removal rate is a good indicator of the number of defects introduced by irradiation. The dose for the irradiation performed in the reflector position ("low fluence") is already at the upper limit of the expected linear regime. The free carrier removal rate measured for n-type material is approximately 32 cm^{-1} and for p-type it is 28 cm^{-1}. Both numbers are consistent with earlier work at lower fluences; however, the p-type removal rate in the present study is somewhat lower than that reported earlier.[2] The difference for p-type material is probably because, even at the low fluence dose, the damage has exceeded the linear regime. These free carrier removal rates are quite high. Calculations of the number of atomic displacements produced by the neutron irradiation yield similar introduction rates for atomic displacements. This

Table 2 Characterization of Neutron-Irradiated SiGe Samples to a Fluence of 5.4×10^{19} n/cm^2

Sample	Treatment	Resistivity (mΩ-cm)	Hall Mobility (cm^2/V-s)	Carrier Concentration (cm^{-3})	Diffusivity at 450–465 K (cm^2/s)
Zone-Leveled	As received	0.795	60.1	$1.31 \cdot 10^{20}$	0.0236
(RCA)	1050°C "reset"	0.630	52.4	$1.89 \cdot 10^{20}$	
n-type	Post-HF irradiation	69.8	22.3	$4.02 \cdot 10^{18}$	0.0216
	350°C anneal	18.9	35.5	$9.32 \cdot 10^{18}$	0.0258
	600°C anneal	0.837	60.7	$1.23 \cdot 10^{20}$	0.0253
	1000°C anneal	0.627	52.9	$1.88 \cdot 10^{20}$	0.0246
Hot-Pressed	As received	1.66	26.8	$1.41 \cdot 10^{20}$	0.0179
(GE)	1050°C "reset"	1.43	26.0	$1.69 \cdot 10^{20}$	
n-type	Post-HF irradiation	41960	0.469	$3.17 \cdot 10^{17}$	0.0147
	350°C anneal	2992	0.321	$6.49 \cdot 10^{18}$	0.0151
	600°C anneal	2.01	25.4	$1.22 \cdot 10^{20}$	0.0183
	1000°C anneal	1.41	25.4	$1.75 \cdot 10^{20}$	0.0190
Zone-Leveled	As received	1.03	39.1	$1.55 \cdot 10^{20}$	0.0328
(RCA)	1050°C "reset"	1.02	38.8	$1.58 \cdot 10^{20}$	
p-type	Post-HF irradiation	109	71.6	$7.98 \cdot 10^{17}$	0.0309
	350°C anneal	37.5	38.0	$4.39 \cdot 10^{18}$	0.0345
	600°C anneal	8.48	25.9	$2.84 \cdot 10^{19}$	0.0328
	1000°C anneal	1.03	39.1	$1.56 \cdot 10^{20}$	0.0323
Hot-Pressed	As received	1.01	36.3	$1.71 \cdot 10^{20}$	0.0266
(GE)	1050°C "reset"	0.96	36.1	$1.74 \cdot 10^{20}$	
p-type	Post-HF irradiation	45.2	31.0	$4.46 \cdot 10^{18}$	0.0235
	350°C anneal	26.8	34.3	$6.80 \cdot 10^{18}$	0.0257
	600°C anneal	8.73	25.0	$2.86 \cdot 10^{19}$	0.0240
	1000°C anneal	1.00	35.7	$1.74 \cdot 10^{20}$	0.0262

similarity is unexpected, since at the temperature of irradiation, more than 90% of the displaced atoms should spontaneously anneal. Either the alloy structure is somehow stabilizing the point defects, or the neutron irradiation is producing defects which can remove several carriers. The latter is more likely the case since even the simple vacancy defect can remove up to four carriers. Even so, the free carrier removal rate is surprisingly high.

The carrier removal rates for the high fluence irradiations are much lower (3.3 and 3.0 cm^{-1} for n- and p-type, respectively). These rates are consistent with the fact that the irradiation damage is well into the saturation regime. (Once most of the free carriers have been removed, further irradiation will continue to produce atomic displacement damage, but the defects will not be as effective in removing the free carriers.)

The 350 and 600°C heat treatments each restored the properties only partially, confirming the RCA[2] results. The 1000°C heat treatment restored all the properties to almost exactly their original "reset values." Thus, there appears to be no evidence for permanent extended defects. The presence of grain boundaries and oxygen does not appear to have acted as traps or nucleation sites for permanent extended defects, even the HP high fluence n-type sample came back to its "reset" values.

As mentioned above, the irradiation-induced drop in carrier concentration is very probably due to irradiation-produced defects acting as traps for the carriers. The slight decrease and even the increase in mobility for both the p-type higher fluence samples is due to the decrease in carrier concentration being roughly equivalent to or less than the increase in irradiation-induced scattering centers. The decrease in the carrier concentration of the higher fluence ZL n-type sample was not as large (about a factor of 10 less) with the expected result that the mobility decreased (mobility μ is proportional to $n^{-3/2}$).

Any transmutation of the dopants P and B is expected to have a negligible effect on the carrier concentration because of the very high doping levels ($\sim 1 \times 10^{20}$ cm^{-3}) compared to the low concentration of transmuted P and B ($\sim 1 \times 10^{16}$ cm^{-3}). Likewise, the transmutation of the dopants themselves is expected to be negligible. It was not attempted to heat treat longer at 600°C to

determine if the original properties could be restored at this temperature, due to the limited number of samples available.

The very large doses of neutron irradiations were used in an attempt to form large, stable defect clusters. These clusters could have a larger effect on phonon scattering than on the electrical resistivity of the material. Under such conditions, an increase in the figure-of-merit would be observed. However, it was found that even at these very high levels of irradiation, based on thermoelectric measurements, no large clusters were formed. In addition, the annealing results demonstrated complete recovery of all the electrical properties. The complete recovery is surprising and further indicates that large, stable defect clusters were not formed during the irradiation or during the subsequent anneals.

33.4 Conclusion

The main conclusion of their work is that fast neutron irradiation, up to a fluence of 5.4×10^{19} n/cm, does not have any effect on the thermoelectric properties of SiGe alloys and does not produce any permanent defects after heat treatment at 1000°C.

References

1. J. W. Winslow, Radiation Effects in Thermoelectrics, Report USNRDL-TR-67-83, 1967.
2. RCA, private company report, 1962.
3. G. Pompe, N. abd el Rehim, and M. Mertig, *J. Low Temp. Phys.*, 74, 475, 1989.
4. J. W. Vandersande and J. Farmer, *Radiation Effects and Defects in Solids*, 118, 125–130, 1991.
5. P. Klemens, private communication.
6. R. A. Guenther and H. Weinstock, *J. Appl. Phys.*, 42, 3790, 1971.
7. J. W. Vandersande, Thermal Conductivity Reduction in Electron Irradiated Type IIa Diamonds at Low Temperatures, *Phys. Rev. B*, 15, 2355, 1977.

34

New Materials and Performance Limits for Thermoelectric Cooling

Glen A. Slack
Rensselaer Polytechnic Institute
Troy, New York, U.S.A.

34.1 Introduction

There has long been an interest in the question of the ultimate performance limits for thermoelectric materials, both for generators and for coolers. Since the figure-of-merit, Z, depends inversely on the thermal conductivity of the material from which the device is made, it is clear that low thermal conductivity values are desirable. The highest Z values are likely to be found in materials with very low thermal conductivities. The total thermal conductivity, λ_{total}, is a sum of the lattice thermal conductivity, λ_L, and the electronic thermal conductivity, λ_e. Thus:

$$\lambda_{total} = \lambda_L + \lambda_e \tag{1}$$

It has been pointed out[1] that for each material there is a well-defined value for its minimum lattice thermal conductivity, λ_{min}. This value is reached when all phonons have a mean free path equal to their wavelength. An alternative model[2] sets this minimum at the point where the limit is one-half wavelength. These minimum values differ exactly by a factor of two if acoustic phonons carry the heat.

The effect of such a λ_{min} concept on predicting the ultimate performance limit of silicon-germanium thermoelectric generators has been demonstrated by Slack and Hussain.[3] The highest possible values of the dimensionless figure-of-merit, ZT, in this system are for n-type material with ZT = 1.75 at 1050 K. The highest values achieved to date are ZT ≅ 1.0 at 1050 K.

For thermoelectric cooling materials the analysis must be broader than it was for Si-Ge because we need to consider not only the lower limits on the thermal conductivity but also the upper limits

0-8493-0146-7/95/$0.00+$.50

on the power factor, $P = \alpha^2\sigma$. Therefore, an exploration has been made of a large number of known elemental and binary compound semiconductors in order to fix reasonable limits on both P_{max} and λ_{min}. The conclusion is that in the temperature range between 77 and 300 K one might obtain ZT values as high as 4, but that substantially larger values are highly unlikely.

34.2 Systematic Search

For this review of the possibilities a systematic search of the elements in the periodic table has been undertaken. This search has been divided into four steps, which are as follows.

The first step is a review of the currently available cooling materials, such as Bi_2Te_3, Bi-Sb, and PbTe. The second step is a model calculation of possible ZT values employing a few not unreasonable physical parameters, such as thermal conductivity, λ; carrier mobility, μ; and effective mass values, m^*. This calculation shows that ZT values as large as 4 in the 77 to 300 K temperature range might be found in materials somewhat better than those presently employed. The third step is a study of the weighted mobility, $\mu(m^*/m_o)^{3/2}$, as a function of the average electronegativity difference, $\overline{\Delta X}$, of a large number of known semiconductors. This study suggests a limited number of possible transition metal antimonides or tellurides as possible high-performance candidates. The fourth step shows that these candidates will have high ZT values only if their lattice thermal conductivity can be reduced to values very close to their minimum thermal conductivity without affecting the charge carrier mobility. The more promising materials are listed, and those deemed most fruitful are suggested as being worthy of future research effort.

34.3 Historical Review

The best cooling materials found to date are Bi-Sb mixed crystals and modifications of Bi_2Te_3. The material presently employed for thermoelectric coolers is based on Bi_2Te_3.[4–6] The n-type leg is usually made of Bi_2Te_3 with 10 mol% Bi_2Se_3 doped to have a carrier concentration of 1 to 3 × $10^{19}/cm^3$ while the p-type leg is usually made of Bi_2Te_3 with 75 mol% Sb_2Te_3 doped to have a similar carrier concentration. The mixed crystals of $(Bi\text{-}Sb)_2Te_3$ and $Bi_2(Se\text{-}Te)_3$ are used so that the random variation of the atomic masses on the cation or anion site will produce some phonon scattering and thus reduce the lattice component of the thermal conductivity. These mixed crystals also have somewhat different conduction- and valence-band properties than pure Bi_2Te_3.

The performance of these materials can be described by the ZT product. A plot of ZT vs. T is shown for such Bi_2Te_3-based mixed crystals in Figure 1. The data for Figure 1 have been assembled from the literature.[7–10] Aivazov et al.[10] were particularly interested in samples like P2 in Figure 1 for low-temperature use.

Clearly Bi_2Te_3 fails to meet the modest goal of $ZT \geq 1$ over the 77 to 300 K temperature range, but does exceed $ZT = 1$ for a small temperature range above 300 K. Somewhat better low-temperature performance has been obtained in Bi-Sb mixed crystals, as shown in Figure 2. The literature data[11–13] show $ZT \geq 0.5$ in zero magnetic field for these samples where the temperature gradient is along the trigonal axis. The ZT can be raised[12] by operating in a DC magnetic field, but such devices are unwieldy and are not considered further in the present discussion.

The first thermoelectric measurements on SnTe, Bi_2Te_3, and Sb_2Te_3 were made in 1910 by Haken.[14] He discovered that Seebeck coefficients, α, as high as 690 μV/K could be found in compound semiconductors. High Seebeck coefficients in the elemental semiconductors B, Si, and Ge were discovered by Uno, Wick, and Bidwell.[15] The first thermoelectric measurements on compound semiconductors such as PbS and ZnSb were made by Seebeck[16] in 1822.

These discoveries paved the way for the modern thermoelectric generators and coolers made by Ioffe[17] in the late 1940s. Very little improvement in performance of these materials has been made since Ioffe's time. The big advance that Ioffe made over the work of Haken is that he employed the mass fluctuation scattering of phonons discovered in 1928 by Eucken and Kuhn[18] in the development of thermoelectric materials. Ioffe discovered that in certain selected mixed crystals the

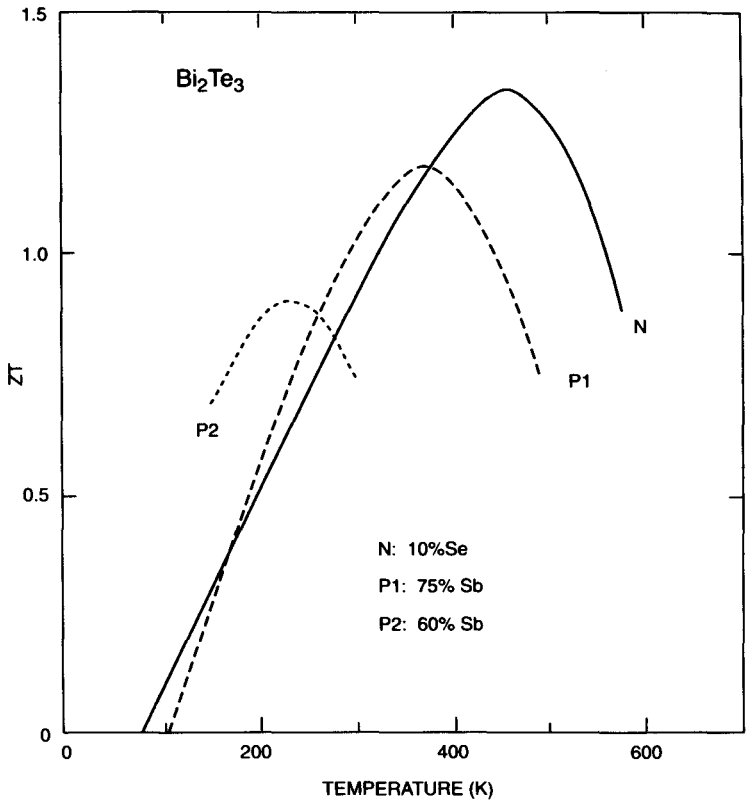

FIGURE 1 The dimensionless figure-of-merit, ZT, of Bi_2Te_3 mixed single crystals as a function of temperature. The curves are labeled with the composition. The n-type crystal has 10 atom% of the Te replaced by Se. For p-type samples some Bi is replaced by Sb. The heat flow is perpendicular to the rhombohedral axis.

lattice thermal conductivity, λ_L, is reduced more rapidly than the electrical conductivity, σ, by the incorporation of a third element into crystals of Bi_2Te_3, PbTe, or Ge. Thus, Z is given by:

$$Z = \frac{\alpha^2\sigma}{\lambda_{TOT}}, \quad \lambda_{TOT} = \lambda_e + \lambda_L \tag{2}$$

The value of Z increases with increasing alloy content. This increase often ceases after 20 or 30 mol% of the third element is added. For example, in the binary silicon-germanium thermoelectric generator materials the optimum concentration is 20 to 30 mol% of germanium in the silicon.

Since Ioffe's work there have probably been studies on at least 100 or more different mixed-crystal semiconductors. None of these have been found to have higher ZT values than Bi_2Te_3 in the temperature range of interest. Thus, the important questions are, first, where to look for materials that are better than Bi_2Te_3, and, second, why should they be better?

34.4 New Materials

Calculations in the Appendix are based on a model material, and show that ZT = 4 can, in principle, be reached for temperatures in the 77 to 300 K range. The search for real materials that approach this model is based on the electronegativity scale of the elements. The concept of a minimum thermal conductivity is important in this search.

A hypothetical thermoelectric material that resembles PbTe has been postulated in the Appendix. There we have used a high-temperature ($T \geq 300$ K) limiting value of $\lambda_{min} = 2.6 \times 10^{-3}$ W/cmK and have estimated the ZT vs. carrier concentration curves at several temperatures.

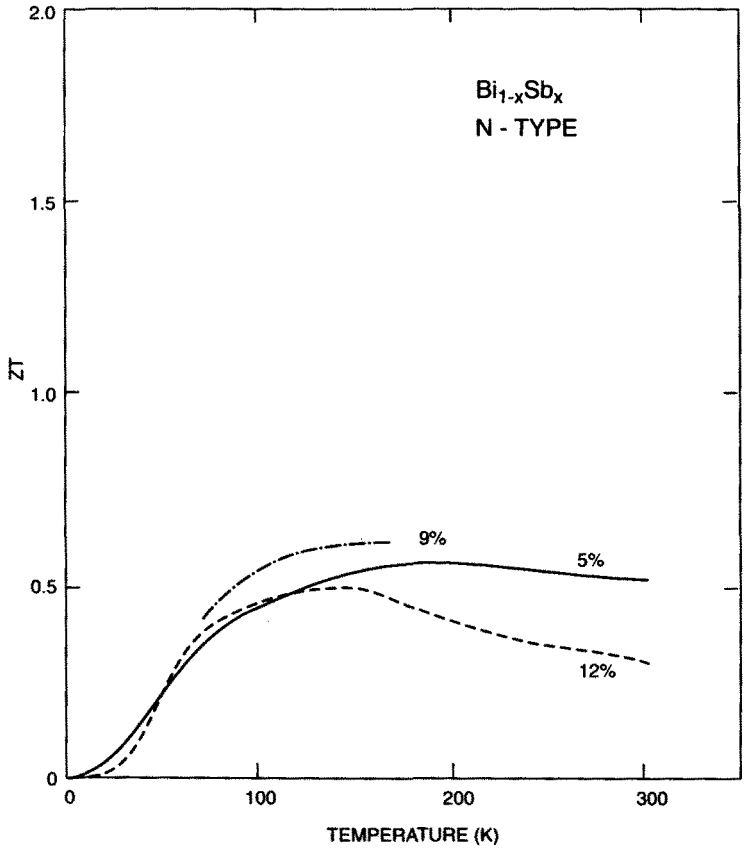

FIGURE 2 The dimensionless figure-of-merit, ZT, of Bi-Sb mixed single crystals as a function of temperature. The curves are labeled with the atom% of Sb in the crystals. They are undoped. The heat flow is along the rhombohedral axis. All samples are n-type.

One sees that, at least for this hypothetical material doped at a level of 10^{17} to $10^{18}/cm^3$, one can obtain ZT $\geq$4 from 78 to 300 K. This hypothetical material is termed "PGEC", which means "a phonon glass and an electron single crystal". Thus, in the search for new materials we possess a hypothetical material whose properties are not unreasonable and which yields high ZT values. We note that if $\lambda \cong 12\ \lambda_{min}$ for our hypothetical material, then ZT $\cong$ 1. So we have to be within a factor of 10 of λ_{min} in order to find materials that will meet the present goal of ZT $\geq$1 between 77 and 300 K.

Phonon "Glasses"

Ever since the analysis by Kittel,[19] it has been known that glasses possess phonon mean free paths of atomic dimensions. The relationship of glass-like thermal conductivities to the minimum thermal conductivity was pointed out by Slack[1] in 1979. Some special large single crystals have been discovered that also possess thermal conductivity values very close to or equal to λ_{min}. The first of those found[20] was YB_{68} in 1971. The important result is that good crystals with long-range atomic order as well as glasses with no long-range order can both have very short phonon mean free paths.

Desired Performance

The goal of the present study is to select or discover materials that possess ZT values greater than 1 over the temperature range from 77 to 300 K. Based upon the same arguments used by Ioffe[1]

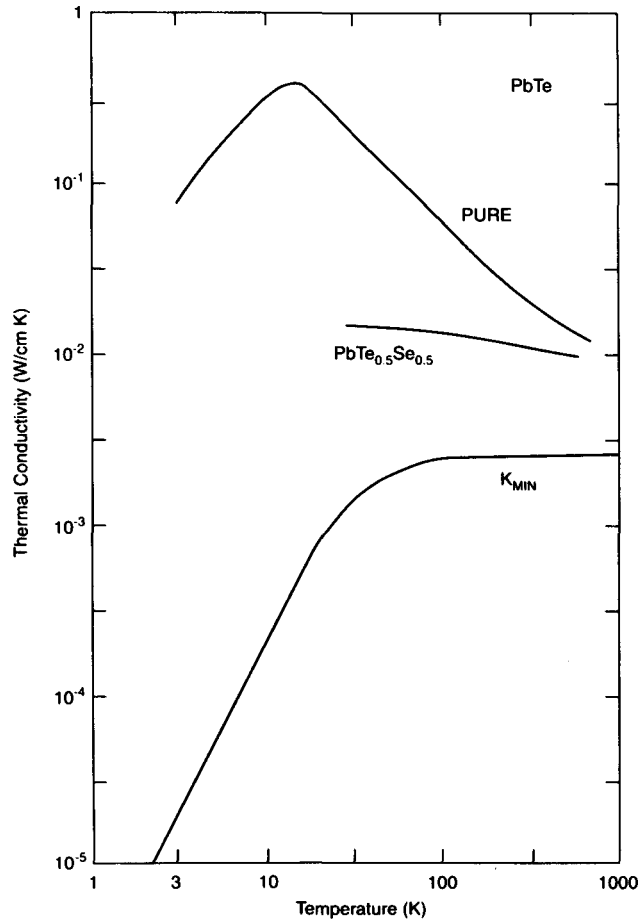

FIGURE 3 The lattice thermal conductivity of PbTe and a mixed crystal of $PbTe_{0.5}Se_{0.5}$ as a function of temperature. The curve labeled λ_{min} has been calculated for PbTe if all phonons have a mean free path equal to one wavelength.

such materials are expected to be elements or binary or ternary compounds formed from the heavy elements near the bottom of the periodic table. One example is elemental bismuth and bismuth-antimony mixed crystals, whose use in thermoelectric coolers has been reviewed by Yim and Amith.[12] As can be seen in Figure 2, these are not adequate to meet the required ZT goal. Elemental Te, even though it is a semiconductor, is not adequate. Its mobility is too low and its thermal conductivity is too high. Furthermore, it has a chain-like structure and only conducts electricity well along the z-axis. Thus, compounds should be used instead of elemental semiconductors as candidate materials. This means that primarily compounds of Sn, Sb, Bi, or Te with various heavy metals are of interest.

PGEC

In surveying various known candidates for desirable properties a material is required that resembles a phonon glass and an electron single crystal or "PGEC". This means a material in which the phonon mean free paths are as short as possible and in which the electron mean free paths are as long as possible. Consider PbTe as a starting point. The thermal conductivity, λ, of pure PbTe vs. temperature is shown in Figure 3, and is based on data from the literature.[21–24] λ vs. T for a mixed crystal of 50 mol% PbTe plus 50 mol% PbSe given in Figure 3 is based on other measurements.[25–29] The data from 28 to 90 K is from Soltys.[26] There is another data point for $Pb_{0.5}Ag_{0.25}Sb_{0.25}Te$ from Rosi et al.,[30] who found a thermal conductivity at room temperature of

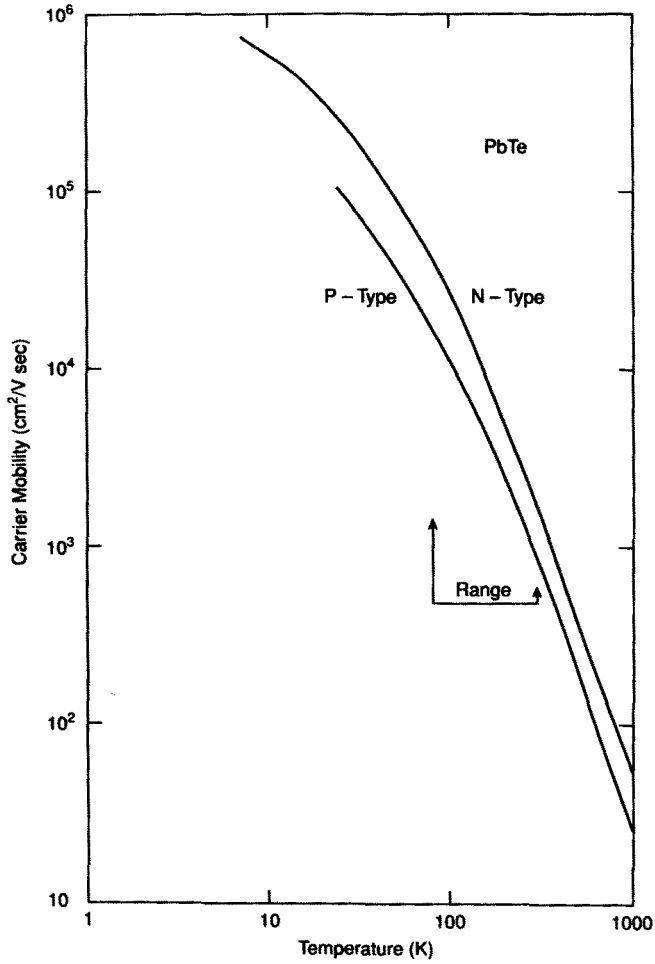

FIGURE 4 The charge carrier mobility in very lightly doped ($\leq 10^{18}/cm^3$) PbTe single crystals as a function of temperature. The present range of interest is 77 to 300 K.

4.5 mW/cmK. The minimum thermal conductivity of PbTe, as defined by Slack,[1] is about 2.50 mW/cmK at room temperature. The minimum thermal conductivity of most other heavy element semiconductors will be similar in magnitude, i.e., 1 to 5 mW/cmK. The temperature dependence of λ_{min} of PbTe is shown in Figure 3 as a function of temperature, as calculated from Equation (20.5) of Slack[1] using a Debye temperature of $\theta_o = 160$ K. Note that λ_{min} only starts to decrease rapidly at a temperature below $\theta_o/4$. Thus, λ_{min} will be nearly independent of temperature in the temperature range of 77 to 300 K for the materials that we shall be considering. This nearly constant value simplifies the calculations considerably.

Next, the assumption is made that in the model material, PGEC, the carrier mobility will be twice that of p-type PbTe, and vary in a similar manner with temperature. The experimental values for intrinsic p-type PbTe have been collected from the literature,[31–33] and are shown in Figure 4 vs. temperature. The n-type PbTe has a slightly higher mobility[31,34,35] than the p-type. Note that it is assumed that: $\mu(300\ K) = 1800\ cm^2/V\ s$ and the temperature dependence between 77 and 300 K is given by $\mu = AT^{-b}$ where A is some constant and $b = 2.30$. Furthermore, assume, for the time being, that this mobility is independent of carrier concentration. This assumption will be returned to later. It is, in general, not true but turns out to be approximately true for many heavy-element semiconductors up to carrier concentrations of $10^{19}/cm^3$.

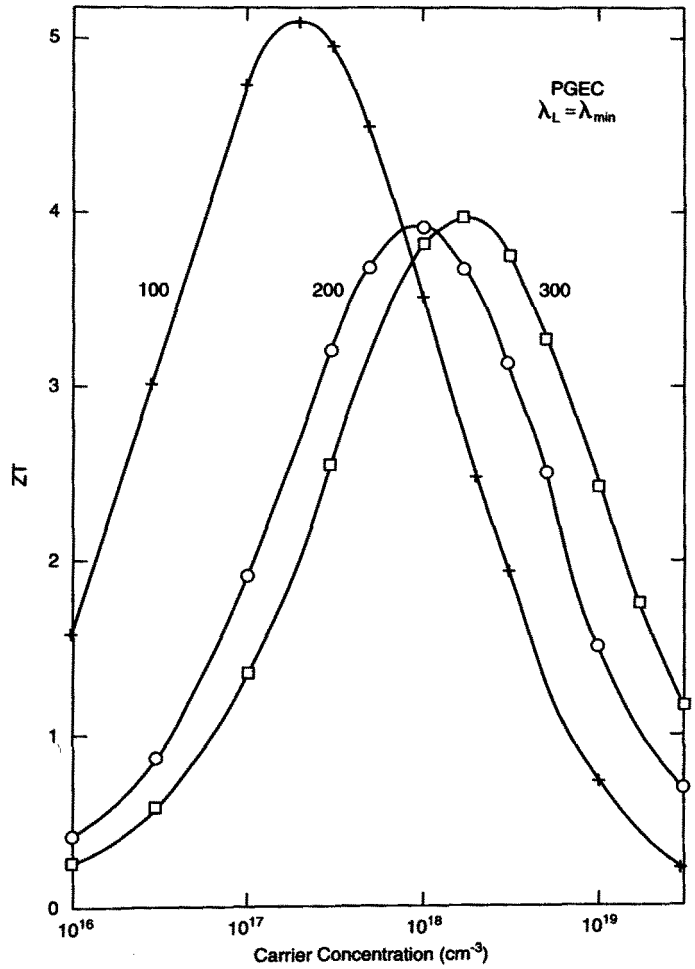

FIGURE 5 The calculated dimensionless figure-of-merit, ZT, vs. carrier concentration for the model material PGEC where $\lambda_L = \lambda_{min}$. Curves are shown for three separate temperatures.

The fourth assumption for "PGEC" is that the density of states effective mass, m^*, of the charge carriers is equal to the free electron mass, m_o. Further, the assumption is made that there is a single valence band and a single conduction band, both with $m^* = 1\ m_o$. The m^* values for PbTe are actually smaller than this, but relatively large m^* values are required in order to obtain high ZT values.

Following the arguments of Mahan[37] for useful thermoelectric materials, it is assumed that the band gap is ≥ 10 kT, where T is the hot junction temperature. The five assumptions are

1. $\lambda_L = \lambda_{min} = 2.5 \times 10^{-3}$ W/cmK
2. $\mu_N = \mu_P = 1800\ (300/T)^{+2.30}\ cm^2/V \cdot s$
3. $m^* = 1\ m_o$
4. $E_g \geq 0.25$ eV
5. μ, λ_L, and m^* are independent of the carrier concentration, and λ_L and m^* are independent of temperature as well.

With these assumptions the ZT vs. carrier concentration curves have been calculated at three temperatures: 100, 200, and 300 K, as shown in Figures 5 to 8. The calculations are described in the

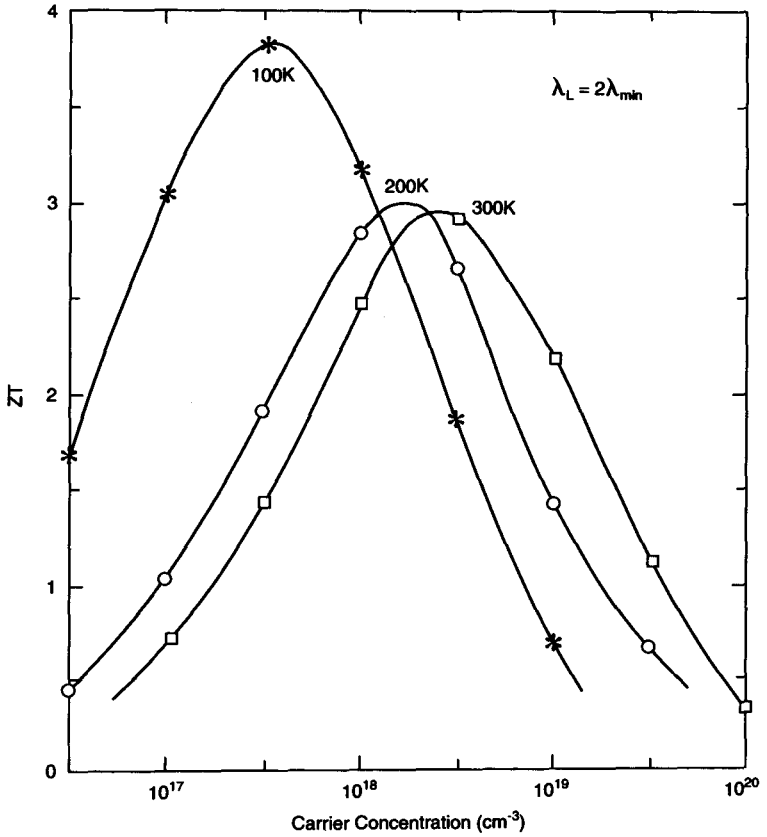

FIGURE 6 The calculated dimensionless figure-of-merit, ZT, vs. carrier concentration for $\lambda_L = 2\ \lambda_{min}$ at three temperatures.

Appendix. Figure 5 shows that ZT $\geq$4 can be achieved at all temperatures with a doping level of 10^{17} to $10^{18}/cm^3$. The optimum doping level does change somewhat with temperature.

Relaxation of λ_{MIN} Assumption

If reducing λ_L to λ_{min} for a real material is unsuccessful, what are the consequences? The next step is to assume λ_L = 2, 6, or 12 λ_{min} and recalculate ZT, as shown in Figures 6, 7, and 8. Note that at $\lambda_L = 6\ \lambda_{min}$, ZT = 3 can no longer be obtained at any carrier concentration, but that ZT = 1.5 is possible. At $\lambda_L = 12\ \lambda_{min}$, as in Figure 8, ZT = 1 can just be reached over the whole temperature range.

Instead of raising λ_L to reduce the maximum ZT, μ can be reduced. Since the quantity μ/λ_L appears in the expression in the Appendix for ZT, it is apparent that reducing μ or increasing λ_L has similar effects. However, the "window" of acceptable parameters needed for ZT $\geq$1 is fairly narrow. Only minor variations from the assumptions used for "PGEC" can be tolerated if high ZT values are the goal, particularly to reach ZT = 4. A similar calculation was done by Goldsmid[36] who also obtained ZT = 4 as a reasonable upper limit for thermoelectric coolers.

Band Gaps of Semiconductors

The necessity of having a Seebeck coefficient larger than 100 μV/K for a thermoelectric cooler means that semiconductors rather than metals are the required materials. Mahan[37] has shown that the optimum band gap of such semiconductors should be about 10 kT. For T = 300 K this means

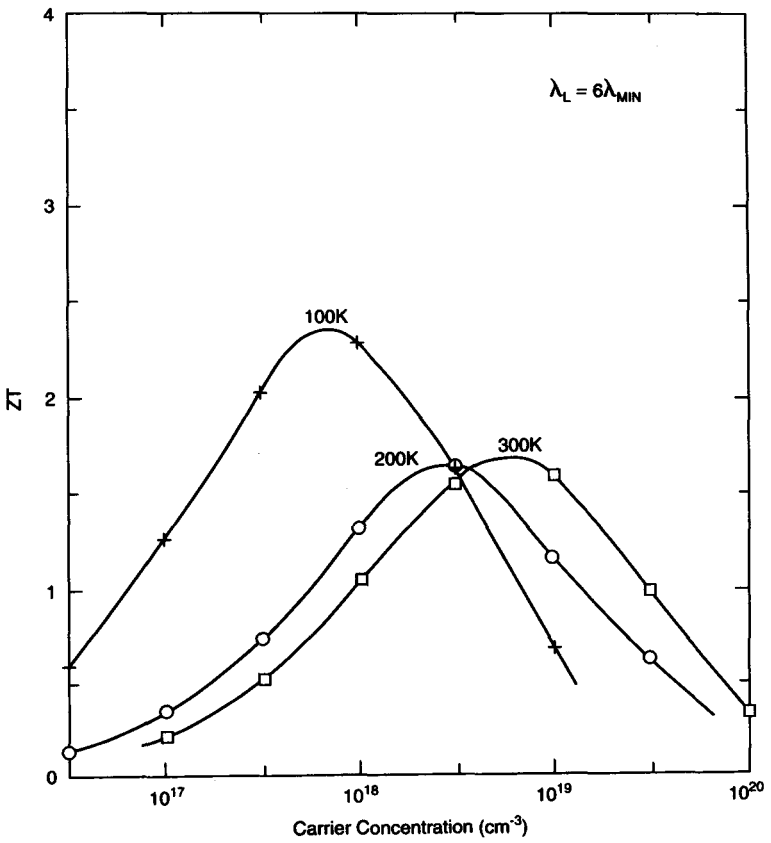

FIGURE 7 The calculated dimensionless figure-of-merit, ZT, vs. carrier concentration for $\lambda_L = 6\ \lambda_{min}$ at three temperatures.

$E_g = 0.25$ eV, whereas for 77 K it is 0.064 eV. If one uses materials with larger band gaps the mobilities tend to be lower or the thermal conductivities larger, or both. If one uses materials with smaller band gaps, then the Seebeck coefficients tend to decrease and the bipolar thermal conductivity rises. The question now is where to look in the periodic table for compound semiconductors with the required band gap.

Data have been considered for the room temperature values of the thermal band gap of a number of semiconductors in Figure 9. Here are plotted E_g values of elements and compounds across several rows of the periodic table, such as the series diamond, BN, BeO, and LiF vs. the electronegativity difference between the elements in the compounds. The electronegativity scale used is that of Pauling,[38] as modified by Allred.[39] Some of the values in this scale for selected elements are given in Table 1. In some cases the charge state of the ion was not specified,[38,39] and an assumed charge state is given with a question mark. From Figure 9 it is clear that in order to obtain $E_g \cong 0.25$ eV it is necessary to use the heavier elements in the periodic table and to find average $|\overline{\Delta X}|$ values of less than 1. An expanded version of Figure 9 is shown in Figure 10 for these low E_g compounds. One should notice that the standard thermoelectric compounds PbTe and Bi_2Te_3 appear in Figure 10 in the lower left-hand corner at low E_g and low $|\overline{\Delta X}|$ values.

For compounds such as Bi_2Te_3 where Te-Te bonds as well as Bi-Te bonds occur the average $|\overline{\Delta X}|$ for the compound can be defined as an average over the ΔX values of the several different kinds of bonds in the structure. Thus:

$$\overline{\Delta X} = \frac{4}{5}[X(\text{Bi}) - X(\text{Te})] + \frac{1}{5}[X(\text{Te}) - X(\text{Te})] \tag{3}$$

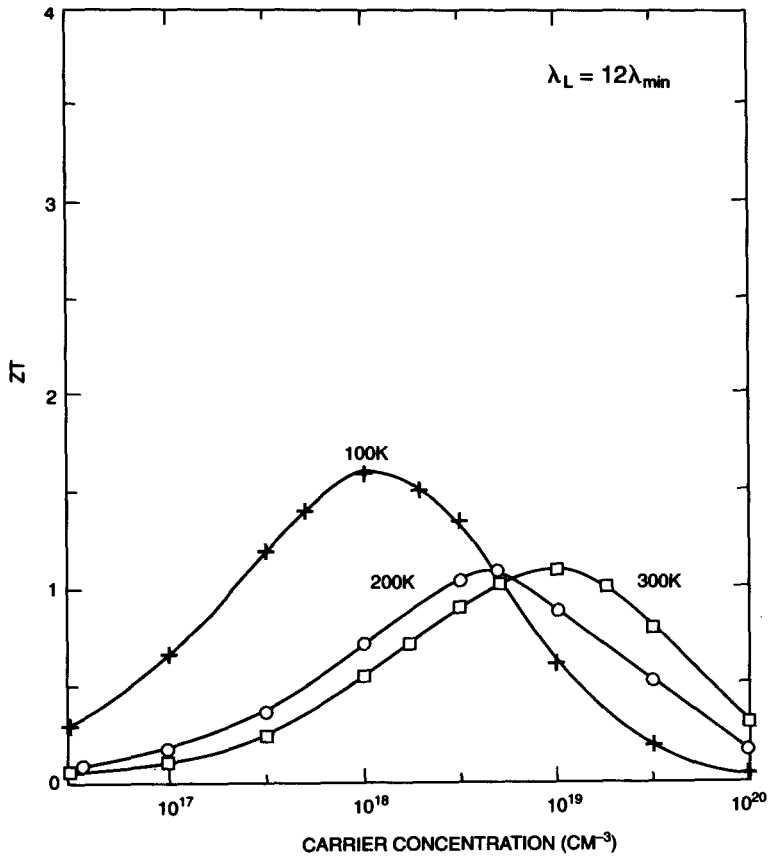

FIGURE 8 The calculated dimensionless figure-of-merit, ZT, vs. carrier concentration for $\lambda_L = 12\ \lambda_{min}$ at three temperatures.

because 80% of the bonds are Bi-Te bonds while 20% are Te-Te bonds. Of course, X(Te) − X(Te) = 0. Thus $|\overline{\Delta X}| = 0.30$ for Bi_2Te_3. The same type of calculation is used for ternary compounds where two or three different kinds of bonds may occur.

Carrier Mobilities

The electrical conductivity, σ, depends on the carrier mobility, μ, for n-type samples, according to:

$$\sigma_N = n\, e\, \mu_N \tag{4}$$

where n = electron concentration, and e = electron charge. A similar expression holds for p-type samples. According to Ioffe,[17] Goldsmid,[6] and Mahan,[37] the important parameter for thermoelectric materials is $\mu(m^*/m_o)^{3/2}$, where m^* is the density of states effective mass for the conduction (or valence) band and m_o is the free electron mass. A large value of $\mu(m^*/m_o)^{3/2}$ means, possibly, a good thermoelectric material; a small value definitely means a poor one. Define a weighted mobility, U, as:

$$U = \mu[m^*/m_o]^{3/2} \tag{5}$$

Data have been collected on μ and (m^*/m_o) for a large number of semiconductors at room temperature from the Landolt-Bornstein[40] tables, and U_N and U_P calculated. These values are meant to be those at very low doping levels such as 10^{14} to 10^{17} cm^{-3} and are considered "intrinsic".

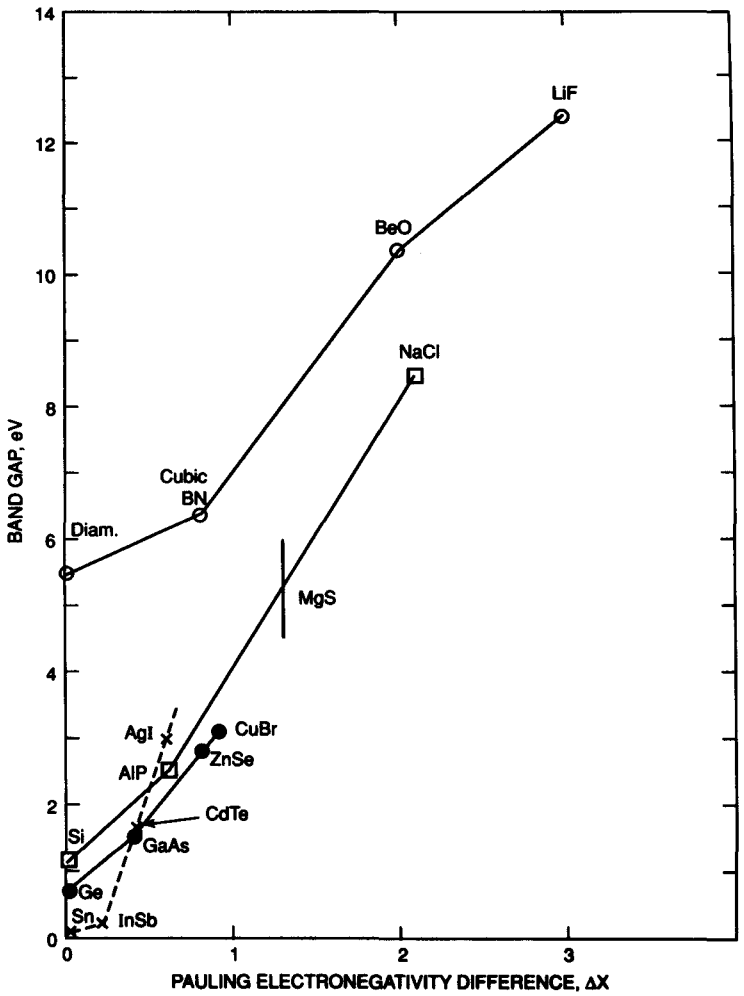

FIGURE 9 The band gap in electron volts of elements and compounds from four horizontal rows across the periodic table as a function of the electronegativity difference, $|\Delta X|$, between the two elements.

Values for the energy gap E_g at room temperature and for the Debye temperature at absolute zero, θ_o, are tabulated in Table 2. For some of the compounds other data sources were employed. For example, for PbSe and PbTe the m* values are from Dalven.[41] The intrinsic mobilities are from Allgaier and Scanlon[31] and others,[32–35] see Figure 4. For Bi_2Te_3 the values are for conduction perpendicular to the rhombohedral axis. The literature values for the effective masses are for low doping levels[42] where only the light mass valence and conduction bands are populated. The measured Hall mobility values in Bi_2Te_3 are complicated by the anisotropy corrections, B, as explained by Drabble.[43] The μ values in Table 2 for Bi_2Te_3 are the experimentally measured Hall mobilities, μ, divided by B, i.e., μ/B, in the limit of low carrier concentration. Similar comments hold for Bi_2Se_3. The values for $PtSb_2$ have been taken from Abdullaev et al.,[44] while its θ_o has been calculated from the elastic constants of Damon et al.[45] The data for $IrSb_3$ are from Slack and Tsoukala.[46]

Figure 11 shows the trend of U as a function of $|\overline{\Delta X}|$, the average electronegativity value. In Figure 11 is plotted, for each compound, the larger of the two values, U_N or U_P. The solid line in Figure 11 is only intended to indicate the general trend; it has no theoretical significance. However, it is clear from Figure 11 that compounds with low $|\overline{\Delta X}|$ are required if we wish to come close to the U values for PGEC, which has

$$U_N = U_P = 1800 \text{ cm}^2/V \cdot \text{sec.} \tag{6}$$

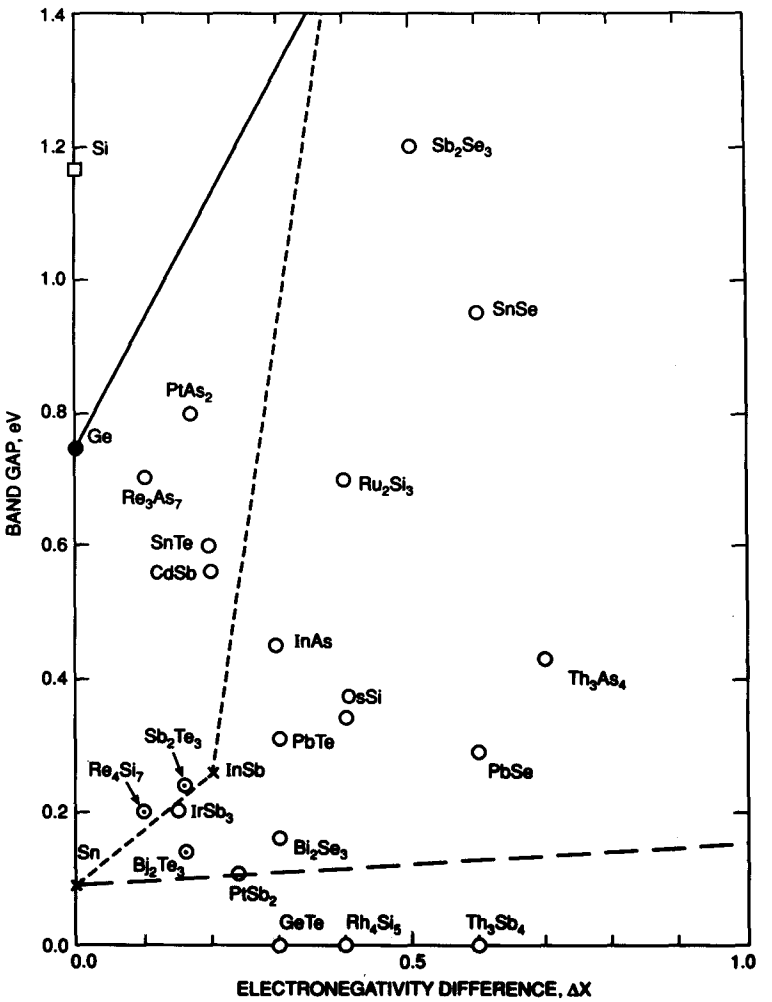

FIGURE 10 The band gap in electron volts of three elements and many compounds as a function of the average electronegativity difference, $|\Delta X|$, across the bonds in the compounds.

The second important observation is that, of all the presently known semiconductors, very few qualify. Clearly Si and Ge do, and they are already employed in high-temperature thermoelectric generators.[3] A reasonable upper limit can be set of $|\overline{\Delta X}| \leq 0.5$ for compounds that will ever have ZT = 4 at room temperature. For a ZT = 1, U $\geq$150 cm^2/V · s and $|\overline{\Delta X}| \leq 1$, while for ZT = 2, U $\geq$300 cm^2/V · s and $|\overline{\Delta X}| \leq 0.8$. These values are shown in Table 3 and were obtained by drawing an imaginary line in Figure 11 through the points for diamond and Th_3A_4. The $|\overline{\Delta X}|$ values listed under the main sequence in Table 3 are the values for the solid black line in Figure 11.

From Table 3 and Figure 11 it can be seen that $Bi_{0.85}Sb_{0.15}$ with $|\overline{\Delta X}| = 0.020$ clearly qualifies as a possible candidate for ZT = 4. The compound Bi_2Te_3 with $|\overline{\Delta X}| = 0.30$ also qualifies. Their main problem is that their λ_L values are too high, and their ZT values are presently limited by this factor, as shown in Figures 1 and 2.

Background Explanation

The reason for the systematic variation of the carrier mobility with $|\overline{\Delta X}|$ needs some explanation. First, in completely covalent semiconductors such as Si and Ge, the carriers are scattered by interaction with the acoustic phonons. The mobility is high since there is no charge motion associated with phonons in a purely covalent lattice. In the compound semiconductors made of two

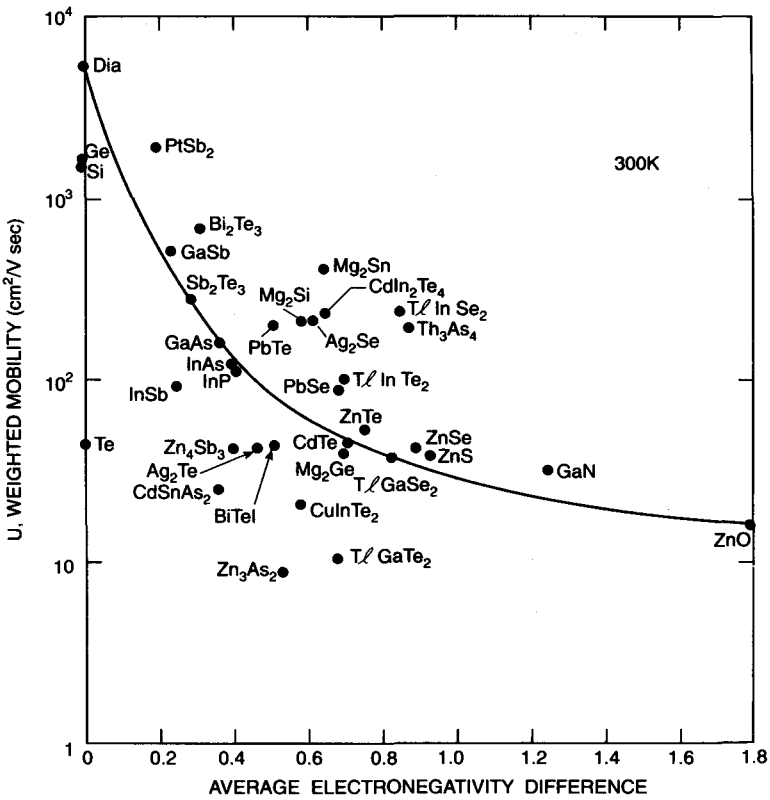

FIGURE 11 The weighted mobility, U, at room temperature for lightly doped or intrinsic samples as a function of the average electronegativity difference, $|\overline{\Delta X}|$.

Table 1 Pauling and Allred Electronegatives of Some Selected Elements

Element	Charge State	X	Element	Charge State	X
La	+3	1.10	(Ge)	(+4)	(2.01)
Ce	+3	1.12	Bi	+3	2.02
Lu	+3	1.27	B	+3	2.04
Th	+4	~1.3	(Tl)	(+3)	(2.04)
Mg	+2	1.31	Sb	+3	2.05
Sc	+3	1.36	Mo	+2	2.16
U	+6	1.38	As	+3	2.18
Ta	+5	~1.5	P	−3	2.19
Be	+2	1.57	Os	+2?	~2.20
Nb	+5	1.6	Pd	+2	2.20
Tl	+1	1.62	Ir	+3	2.20
Zn	+2	1.65	Ru	+2?	~2.25
Cd	+2	1.69	Rh	+3	2.28
In	+3	1.78	Pt	+2	2.28
Sn	+2	1.80	Re	+7?	~2.30
Ga	+3	1.81	(Pb)	(+4)	(2.33)
Ge	+2	~1.85	(Mo)	(+6)	(2.35)
Pb	+2	1.87	W	+6	2.36
Co	+2	1.88	Te	−2	~2.40
Si	+4	1.90	Au	+1	2.54
Cu	+1	1.90	Se	−2	2.55
Ni	+2	1.91	S	−2	2.58
Ag	+1	1.93	I	−1	2.66
(Sn)	(+4)	(1.96)	O	−2	3.44
Hg	+2	2.00	F	−1	3.98

Note: ( ) indicates a second, higher valence state.

Table 2 Properties Affecting the Carrier Mobilities at 300 K for a Collection of Semiconductors

Crystal	E_g eV	θ_o K	$\overline{\lvert\Delta X\rvert}$	m_N^*/m_o	m_P^*/m_o	μ_N	μ_P	U_N	U_P
						$cm^2/V \cdot s$			
Diamond	5.50	2240	0.0	1.87	1.21	2500	2100	5370	2810
Si	1.12	645	0.0	1.06	0.69	1550	500	1692	287
Ge	0.66	374	0.0	0.553	0.357	4600	2100	1892	448
AlAs	2.16	416	0.57		0.804		~200		~154
AlSb	1.61	290	0.44		0.976	200	450		434
GaN	3.4		1.23	0.218		300	—	31	—
GaP	2.27	444	0.38	0.365	0.83	200	150	44	113
GaAs	1.42	345	0.37	0.067	0.53	9200	400	160	154
GaSb	0.75	269	0.24	0.0412	0.64	6000	1000	50	512
InP	1.34	302	0.41	0.0765	0.58	5370	150	114	66
InAs	0.35	251	0.40	0.0239	0.39	33000	450	122	110
InSb	0.17	207	0.27	0.0136	0.2	60000	850	95	76
ZnO	3.35	416	1.79	0.275	—	110	—	16	—
ZnS	3.68	339	0.93	0.34	1.82	200		39	
ZnSe	2.70	271	0.90	0.142	0.97	600	45	32	43
ZnTe	2.28	226	0.75	0.122	0.6	800	115	34	53
CdTe	1.49	161	0.71	0.094	0.82	1110	60	32	45
HgSe	0.0		0.55	0.0265		15000		65	
PbS	0.41	220	0.72						
PbSe	0.28	156	0.68	0.21	0.18	1000	860	94	67
PbTe	0.31	160	0.53	0.24	0.215	1750	790	200	79
$Bi_{0.85}Sb_{0.15}$[a]	0.020	124	0.009				—		—
Te[a]	0.33	145	0.0		0.109	—	1260	—	45
Mg_2Si	0.60	578	0.59	0.53	2.2	550	60	212	196
Mg_2Ge	0.55	492	0.70	0.18	0.31	530	110	40	19
Mg_2Sn	0.23	340	0.65	1.17	1.28	320	260	405	377
In_2Te_3	1.03		0.62	0.70	1.23				
Sb_2Se_3	1.11	240	0.40			15	42		
Sb_2Te_3	0.22	160	0.28	—	0.97	—	270	—	258
Bi_2Se_3 ($\perp$C)	0.12	182	0.42	0.155		780	42	48	
Bi_2Te_3 ($\perp$C)	0.13	165	0.30	0.43	0.68	1440	1085	406	608
Ag_2Se	0.15		0.62	0.20	0.54	2000	550	179	218
Ag_2Te	0.67		0.47	0.077	1.5	2000	20	43	37
$IrSb_3$		310[b]	0.10		0.167		≥1320		≥90
$PtSb_2$	0.11	215[b]	0.20	3.34	2.55	245	485	2320	4072
Th_3As_4	0.43		0.88	0.55		470		192	
Zn_3As_2	0.98		0.53		0.65		17		8.9
β-Zn_4Sb_3	1.0		0.40		0.12		998		42
$CuInTe_2$	1.06		0.58		0.75	150	35		23
$CdSnAs_2$	0.26		0.36	0.014	0.13	15000	43	25	2.0
$CdIn_2Te_4$	1.15		0.65	0.15		4000		232	
$TlGaSe_2$	2.03		0.83	0.37	0.68	26	65	5.9	37
$TlGaTe_2$	1.2		0.68	0.12	0.23	66	96	2.7	11
$TlInSe_2$	1.14		0.85	0.31	0.65	225	450	39	236
$TlInTe_2$	0.68		0.70	0.08	0.31	420	600	9.5	104
BiTeI	0.45		0.51	0.22		445		46	

[a]Along the c-axis.
[b]Calculated from sound velocities.

Table 3 Weighted Mobility and Limits for Obtaining ZT Goals at Room Temperature

ZT	U $cm^2/V \cdot s$	$\overline{\lvert\Delta X\rvert}$ Upper Limit	$\overline{\lvert\Delta X\rvert}$ Main Sequence
1	≥150	≤1.0	0.38
2	≥300	≤0.8	0.29
3	≥900	≤0.5	0.13

Note: Assumed λ_L = 2.5 mW/cm K.

Table 4 Binary Semiconducting Tin Compounds

Elements A,B	$X_A - X_B$	Compounds	$\overline{\lvert\Delta X\rvert}$	f[a]	Structure
Sn-Te	−0.60	SnTe	0.60	1	Rock salt
Mg-Sn	−0.65	Mg_2Sn	0.65	1	Calcium fluoride

[a] f = fraction of the bonds that possesses an electronegativity difference equal to $X_A - X_B$.

or more elements with differing electronegativity values there is an electron charge transfer between the ions. The amount of charge transfer increases with the electronegativity difference, $\overline{|\Delta X|}$. At a finite temperature the phonons in such a lattice produce modulations in the local electrostatic field and thus an increase in the charge carrier scattering. This gives rise to a mobility decrease as $\overline{|\Delta X|}$ increases.

34.5 Electronegativities and Good Thermoelectric Semiconductors

A number of compound semiconductors can be selected based on the electronegativities of the bonds between the atoms. Since there are many known semiconducting compounds whose mobilities and effective masses have never been measured we need a method of selecting promising candidates solely from $\overline{\Delta X}$ values, i.e., from their chemical compositions, their crystal structures, and Table 1. The electronegativity scale in Table 1 allows the selection of binary pairs and ternary triplets that might make useful thermoelectric cooling materials. The requirement $\overline{|\Delta X|} \leq 0.50$ is a first-cut screening based on Table 3. This condition suggests those pairs listed in Tables 4 through 6. In these tables all compounds containing the monovalent ions Cu, Ag, Au, and Tl have been excluded. These ions tend to diffuse rapidly and drift under a direct current applied voltage. As impurities, they are known to seriously degrade the performance of Bi_2Te_3 thermoelements. Also excluded are compounds of the first transition metal series Fe, Co, Ni, because these compounds generally have "high-spin" *d*-shell configurations, and the resultant magnetic scattering of the conduction electrons is apt to seriously lower the carrier mobility. However, $CoSb_3$ is known to be zero spin, and so is included. The compounds of the second and third transition metal series generally tend to have "zero-spin" *d*-shells and so are reasonable prospects.

The $\overline{|\Delta X|}$ values given in Tables 4 through 6 are based on bond counting. Thus, one must know the structures of the compounds in order to calculate $\overline{|\Delta X|}$. In some complex cases the structures are not known. Therefore, literature references[47–49] have been given. However, the atomic structure of $GeTe_4$ is unknown,[50] but it is cubic, it has a low packing density, and may have $GeTe_4$ tetrahedra in the structure.

The compounds in Tables 4 through 6 show some interesting trends. In Table 4 it is seen that $\overline{|\Delta X|}$ values of the semiconducting Sn compounds are rather large. Compounds of Sn with smaller $\overline{|\Delta X|}$ tend to be metallic. The compound Mg_2Sn has a rather high U value in Figure 11, which makes it interesting. The compound SnTe is often used in mixed crystals with PbTe to make thermoelectric generator materials.

Table 5 shows the Bi-Sb mixed crystals whose ZT properties appear in Figure 2, as well as Sb_2Te_3, which is the major constituent of the Pl material in Figure 1. However, note that the $\overline{|\Delta X|}$ value of Sb_2Te_3 is rather large, and there are many other unexplored candidates with lower $\overline{|\Delta X|}$ values. The prime candidate is $IrSb_3$ with $\overline{|\Delta X|} = 0.10$. The much-studied 3-5 compounds, GaSb and InSb, have larger $\overline{|\Delta X|}$ values which limit U. The mixed crystal (In-Ga)Sb has been studied extensively as a thermoelectric generator material.[51]

Table 6 shows the much-studied semiconductors Bi_2Te_3, PbTe, In_2Te_3, and CdTe. Again, note that these are at the high end of the $\overline{|\Delta X|}$ scale, and that there are a number of candidates with lower $\overline{|\Delta X|}$ that have been studied very little. Particularly interesting are the cluster compounds Re_6Te_{15} and Mo_6Te_8, which contain Me_6Te_8 clusters, where Me = metal. The formation of these clusters attests to the predominantly covalent nature of the metal-tellurium bonds. At present there is no knowledge of their carrier mobilities, thermal conductivity values, effective masses, etc. At least one of these may have very good thermoelectric properties. An attempt has been made in Tables 4 through 6 to list *all* of the known binary semiconductors with small band gaps and small $\overline{|\Delta X|}$ values. All of the currently used low-temperature thermoelectric materials appear in these

Table 5 Binary Semiconducting Antimony Compounds

Elements	$X_A - X_B$	Compounds	$\overline{\lvert\Delta X\rvert}$	f[a]	Structure
Bi-Sb	−0.03	$Bi_{1-x}Sb_x$ (M.C.)[b]	≤0.03	?	Bismuth
Ir-Sb	+0.15	$IrSb_2$	0.13	6/7	Arsenopyrite
	+0.15	$IrSb_3$	0.10	2/3	Skutterudite
Os-Sb	+0.15	$OsSb_2$	0.13	6/7	Marcasite
Co-Sb	−0.17	$CoSb_2$	0.15	6/7	Arsenopyrite
		$CoSb_3$	0.11	2/3	Skutterudite
Ru-Sb	+0.20	$RuSb_2$	0.17	6/7	Marcasite
Rh-Sb	+0.23	$RhSb_2$	0.20	6/7	Arsenopyrite
	+0.23	$RhSb_3$	0.15	2/3	Skutterudite
Pt-Sb	+0.23	$PtSb_2$	0.20	6/7	Pyrite
Ga-Sb	−0.24	GaSb	0.24	1	Zincblende
In-Sb	−0.27	InSb	0.27	1	Zincblende
Sb-Te	−0.35	Sb_2Te_3	0.28	4/5	Tetradymite
Sb-Se	−0.50	Sb_2Se_3	0.40	4/5	Tetradymite

[a] f = fraction of the bonds that possesses an electronegativity difference equal to $X_A - X_B$.
[b] M.C. = mixed crystals.

Table 6 Possible Binary Tellurium Compounds

Elements A, B	$X_A - X_B$	Compounds	$\overline{\lvert\Delta X\rvert}$	f[a]	Structure
Mo-Te	−0.05	Mo_6Te_8[b]	0.04	5/7	Ref. 45, 46
Re-Te	−0.10	Re_6Te_{15}	0.06	3/5	Ref. 47
Rh-Te	−0.12	Rh_3Te_8	0.10	6/7	Defect pyrite
Ru-Te	−0.15	$RuTe_2$	0.13	6/7	Pyrite
Os-Te	−0.20	$OsTe_2$	0.17	6/7	Pyrite
Ir-Te	−0.20	Ir_3Te_8	0.17	6/7	Defect pyrite
As-Te	−0.22	As_2Te_3	0.18	4/5	Tetradymite
Bi-Te	−0.38	Bi_2Te_3	0.30	4/5	Tetradymite
Ge-Te	−0.39	$GeTe_4$	≤0.39	?	Cubic, Ref. 48
Pb-Te	−0.53	PbTe	0.53	1	Rock salt
In-Te	−0.62	In_2Te_3	0.62	1	Defect zincblende
Cd-Te	−0.71	CdTe	0.71	1	Zincblende

[a] f = fraction of the bonds that possesses an electronegativity difference equal to $X_A - X_B$.
[b] Mo_6Te_8 is metallic, but when modified by replacing some of the Mo by Re or Ru it may become semiconducting. Some Te replacement by Se may also be needed.

tables, plus some new ones. Hence, there *may be no other candidates,* or very few others, for binary compounds with values of $ZT \geq 1$. There are, of course, many more ternary compounds, too many to list here. However, low $\overline{\lvert\Delta X\rvert}$ values, heavy mass atoms, and small band gaps will still be required in such ternaries.

34.6 Dopant and Mixed-Crystal Effects on Mobilities

In this section, it is demonstrated that the carrier mobilities in the useful compound semiconductors are not degraded by ionized impurity scattering but are degraded by mixed-crystal formation. The carrier concentration in a semiconductor is generally controlled by the substitution of a p-type or n-type impurity into the structure. Such impurity centers, when ionized, end up having a net positive or negative charge. As such, they scatter the mobile charge carriers (electrons or holes) by the long-range coulomb interaction. This is clearly the case[3] in Si and Ge thermoelectric generator materials, and this impurity scattering seriously degrades their performance at high doping levels. The effective masses in Si and Ge are almost unaffected by the impurity doping level, but the carrier mobilities decrease rapidly[3] with increasing impurity content. Thus, the weighted mobility, U, at room temperature drops rapidly with increasing impurity content above about $10^{16}/cm^3$ donors or acceptors.

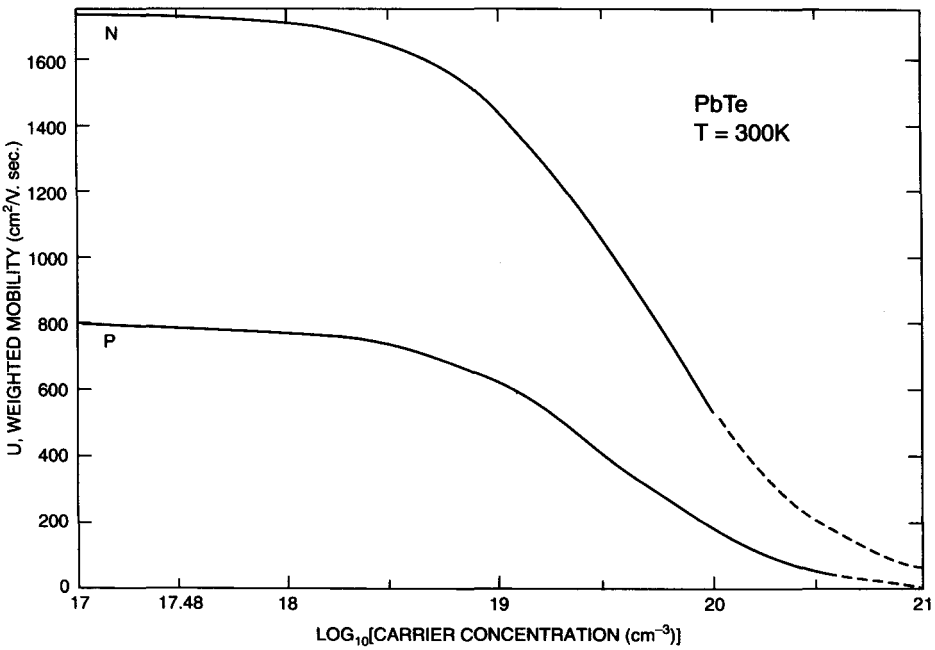

FIGURE 12 The carrier mobility at room temperature in n-type and p-type single-crystal PbTe as a function of the carrier concentration. The dashed lines are extrapolations of the existing data toward higher carrier concentrations.

This effect of the carrier concentration on the carrier mobility has also been studied in some of the heavy element semiconductors. Figures 12 and 13 show this effect in PbTe and Bi_2Te_3 single crystals at room temperature. The mobility decrease starts at a carrier concentration of about $10^{18}/cm^3$ and is substantial by the time it reaches $10^{20}/cm^3$. Figures 12 and 13 are based on collected data from the literature for PbTe[31–35] and Bi_2Te_3.[6,42,43,52–56] The Hall mobility data for PbTe are straightforward. The curve in Figure 13 for Bi_2Te_3 is actually the mobility product, μB, where μ is the true mobility and B is the anisotropy factor, see Drabble.[43] At low (10^{17} to $10^{18}/cm^3$) carrier concentrations[6,43] $B = 0.33$ for n-type and $B \cong 0.48$ for p-type Bi_2Te_3. However, at high carrier concentrations near $10^{20}/cm^3$ the value of B is unknown, but may approach $B = 3$. The carrier concentration dependence of B has never been studied. The simple interpretation of the Hall-effect data always yields μB. Likewise, the carrier concentration given in Figure 13 is really n/B or p/B. This means that the true values of n and p are unknown except at low carrier concentrations. The vertical arrow in Figure 13 is the approximate carrier concentration above which both the heavy mass conduction-band and heavy mass valence-band[42] start becoming populated.

A very similar decrease in room temperature mobility with increasing carrier concentration has been found[57] in InSb crystals.

Dopant Effects on the Weighted Mobility

The important parameter that affects the thermoelectric properties is the weighted mobility, U. The critical question is the effect of the carrier concentration on U, not its effect on μ. U has been calculated for PbTe and InSb from the measured mobility values, μ, and measurements of the effective mass, m^*, as a function of the carrier concentration. For n-type InSb the m^* values were taken from Zawadski;[57] the results are shown in Figure 14. Note that U_N actually *increases* with increasing carrier concentration from a value of 95 $cm^2/V \cdot s$ at low carrier concentration (see Table 2 also). It peaks at a value of 125 $cm^2/V \cdot s$ at about $8 \times 10^{17}/cm^3$ and only drops below 95 $cm^2/V \cdot s$ for $n > 1.2 \times 10^{19}/cm^3$. This increase in U with increasing carrier concentration is

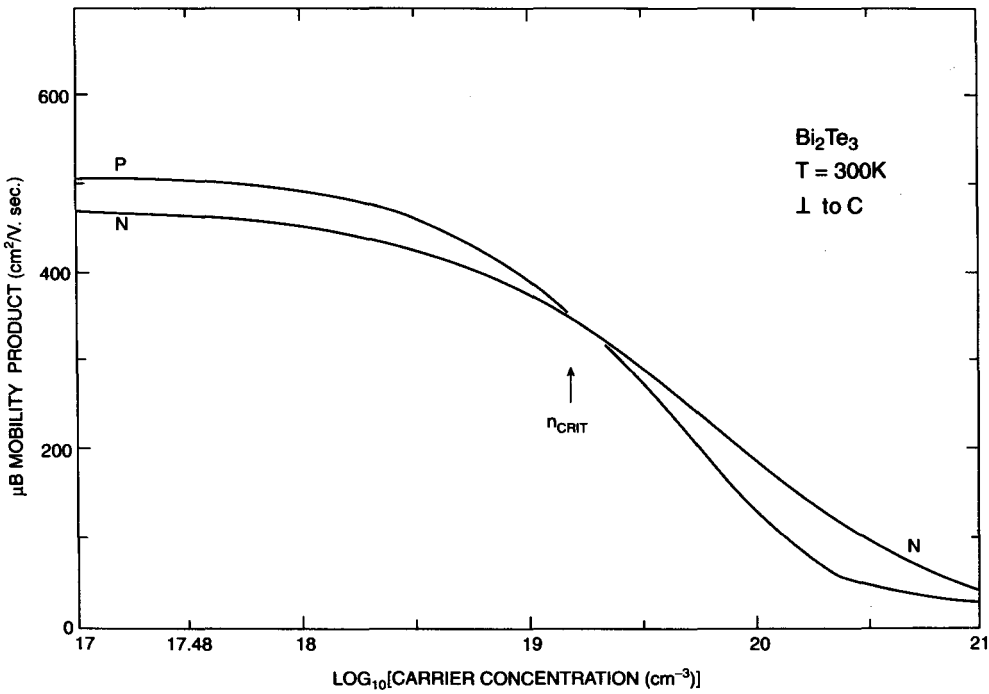

FIGURE 13 The carrier mobility at room temperature in n-type and p-type single-crystal Bi_2Te_3 as a function of the carrier concentration. The values of mobility are for current flow perpendicular to the rhombohedral or hexagonal c-axis. See text for a discussion of the anisotropy parameter B and n_{CRIT}.

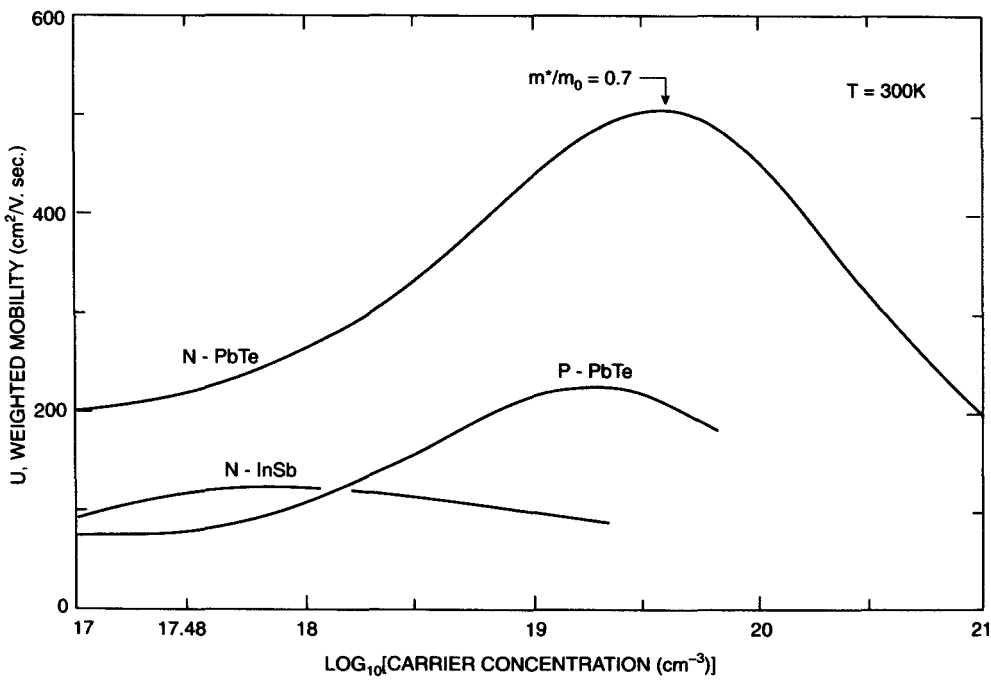

FIGURE 14 The weighted mobility of InSb and PbTe as a function of the carrier concentration at room temperature.

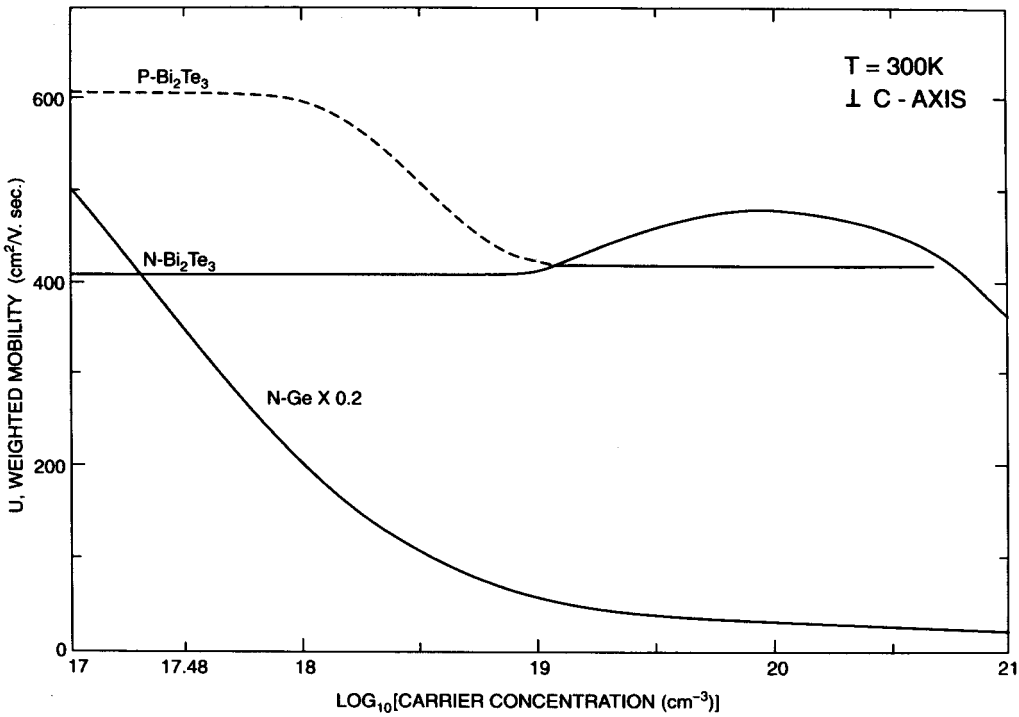

FIGURE 15 The weighted mobility at room temperature in Bi_2Te_3 and Ge as a function of the real (unweighted) carrier concentration. For Bi_2Te_3 the current flow is perpendicular to the rhombohedral axis. The U values for Ge from Slack and Hussain[18] have been multiplied by 0.2 in order to fit the scale employed.

even more dramatic for PbTe, as shown in Figure 14. The m* values for n-type PbTe are from Zawadski,[57] Das and Nag,[58] and Zhitinskaya et al.[59] Those for p-type are from Jensen et al.[60] The m* values used in the present calculations are those appropriate to room temperature. The m* values vary linearly with the band gap, and the band gap is temperature dependent.[35]

From Figure 14 it can be seen that the U values in both n-type and p-type PbTe increase considerably from those given in Table 2 for carrier concentrations $\leq 10^{17}/cm^3$. The increase is a factor of more than 2.5 times. The reason for the increase is that the valence- and conduction-band m* values increase as the Fermi level rises. The $(m_N^*/m_o) = 0.24$ for PbTe at low doping level, but increases to 0.66 at $4 \times 10^{19}/cm^3$, the peak of the curve in Figure 14. This feature explains why PbTe is useful in thermoelectric generators at high temperatures where the doping level is 10^{19} to $10^{20}/cm^3$. From Figures 5, 6, 7, and 8 it is seen that doping levels of 10^{18} to $10^{19}/cm^3$ are desirable for refrigeration purposes. Thus, PbTe is not as useful in this application.

The U values for Bi_2Te_3 shown in Figure 15 have been calculated separately from μ and (m^*/m_o) values only at $10^{17}/cm^3$. The $(m_N^*/m_o) = 0.43$ is from Kutasov and Lukyanova,[61] see also Mallison et al.[62] The value of $(m_P^*/m_o) = 0.68$ at room temperature is based on the 4.2 K value[63,64] of 0.525 corrected for the temperature change. These effective masses combined with the corrected mobilities of $\mu_N = 1440\ cm^2/V \cdot s$ and $\mu_P = 1085\ cm^2/V \cdot s$ yield the U_N and U_P values in Table 2. These appear in Figure 15 at a carrier concentration of 10^{17} to $10^{18}/cm^3$. Just how U_P varies with carrier concentration from 10^{17} to $10^{19}/cm^3$ is uncertain, and is shown as a dashed line in Figure 15.

The U values in Figure 15 above $10^{19}/cm^3$ have been derived from measurements of σ and α. Literature data have been taken from Goldsmid,[65] Goltsman et al.,[54] Süssmann and Heiliger,[66] and Testardi et al.[67] A comparison of Figure 15 with Figure 13 suggests strongly that the effective mass of Bi_2Te_3 increases strongly with increasing carrier concentration. Evidence[42] points to heavy mass conduction and valence bands slightly separated in energy from the main bands. The effective

masses of these bands have been measured[62,64] for n-type as $(m_N^*/m_o) = 1.5$ and for p-type as $(m_P^*/m_o) = 1.25$ by von Middendorf and Landwehr,[68] or 2.5 by Sologub et al.[64]

An attempt was made to use the data from Figures 13 and 15 and to adjust the assumed values of both m* and B as a function of the carrier concentration in order to find out how m* and B vary. For n-type Bi_2Te_3 at $1 \times 10^{21}/cm^3$ at room temperature it appears that $B \simeq 3$ and $(m_N^*/m_o) \simeq 3$. Using this approach B has been calculated as a function of carrier concentration for n-type Bi_2Te_3. Thus, the carrier concentration given in Figure 15 is (approximately) the true carrier concentration, not n/B as in Figure 13.

The conclusion to be drawn from Figures 14 and 15 is that the weighted mobility U values for intrinsic, undoped crystals of InSb, PbTe, and Bi_2Te_3 do not decrease with increasing carrier concentration from the effects of ionized impurity scattering. However, U does decrease for just this reason in Ge and in Si. The difference, as pointed out by Zawadski,[57] is that these heavy mass, low-band-gap materials are very polarizable and have high dielectric constants. Thus, the impurity core charge is effectively screened in its effects on the mobile charge carriers for impurity concentrations up to about $10^{20}/cm^3$. Furthermore, Zawadski[57] points out that in these small-band-gap materials the bands are, in general, nonparabolic. The effective mass always increases with increasing doping level. In Bi_2Te_3 this effect is enhanced by two low-lying heavy mass bands (one valence, one conduction). It appears that m* in the single bands in Bi_2Te_3 also increases with increasing carrier concentration. The result is that the intrinsic U values in Table 2 may well be approximately correct for small-band-gap semiconductors at doping levels from $10^{17}/cm^3$ up to $10^{19}/cm^3$. The assumption made earlier for PGEC that μ and m* should not change with carrier concentration can now be recast as U should not decrease with carrier concentration. This is reasonably well obeyed. This means that Figure 11 is useful over the range of carrier concentrations up to $10^{19}/cm^3$ for low-band-gap, heavy element crystals.

A second result of this charge screening is that it is not necessary to make multilayer thermoelectric cooling elements by MBE or CVD where the conducting layers and the charge donor (or acceptor) layers are interleaved. There is nothing to be gained in thermoelectric cooling performance from such structures.

Mixed-Crystal Effects on Mobility

The useful method of reducing the lattice thermal conductivity of thermoelectric materials is to make mixed-crystal samples. For example, in Ge-Si thermoelectric materials[3] the thermal conductivity has been reduced by the mass fluctuation scattering of the phonons. The Ge or Si atoms randomly occupy the lattice sites in the structure, and this random variation in the mass on the lattice sites scatters the otherwise coherent sound wave vibrations (phonons). This alloy scattering technique is employed in all of the currently used thermoelectrics, such as Bi-Sb, $Bi_2(Se\text{-}Te)_3$, $(Bi\text{-}Sb)_2Te_3$, Pb(Te-Se), (Pb-Sn)Te, and Ge-Si. This randomness in the structure can also reduce the carrier mobilities to unacceptably low levels. The purpose of the present discussion is to point out just how the carrier mobilities are affected.

Consider Si-Ge mixed crystals. It can be seen from Table 1 that the electronegativities of Si and Ge are close but not equal. Thus, X(Ge) − X(Si) = 0.11. This difference means that in a mixed crystal the electrons or holes will experience a fluctuating potential on the atomic cores. The alloy scattering mobility[3] is given by:

$$\mu_{alloy} = \frac{\mu_a}{4\,x\,(1-x)} \left(\frac{300}{T}\right)^{0.5} \text{cm}^2/V \cdot \text{sec.} \tag{7}$$

with $\mu_a = 160\ \text{cm}^2/V \cdot \text{s}$.

It can be seen from Equation 7 that for a 50 mol% Ge-50 mol% Si mixed crystal at room temperature:

$$\mu_{alloy} = \mu_a = 160\ \text{cm}^2/V \cdot \text{sec.}$$

In $In(P_{1-x}As_x)$ mixed crystals Ehrenreich[69] found

$$\mu_a \cong 30{,}000 \text{ cm}^2/V \cdot \text{sec.} \tag{8}$$

From Table 1, X(P) − X(As) = 0.01.

From Wiley,[70] the mobility determined by polar optical phonon scattering of the charge carriers varies as:

$$\mu \sim \frac{1}{(e^*)^2} \tag{9}$$

where e* is the effective charge on the ions in the compound semiconductor. If it is assumed that e* is proportional to ΔX, then, very approximately:

$$\mu_a = \frac{C}{(\Delta X)^2} \tag{10}$$

For both Si-Ge and In(P-As) an approximate value for C (at room temperature) is

$$C = 2.0 \text{ cm}^2/V \cdot \text{sec.} \tag{11}$$

Consider the mobility data for mixed crystals of PbTe-PbSe in Figure 16. The data in Figure 16 are from Hohnke and Hurley[71] for doping levels $\leq 5 \times 10^{17}/\text{cm}^3$. The curves for n-type and p-type samples are almost identical. At T = 300 K the value derived from Figure 16 is

$$\mu_a = 330 \text{ cm}^2/V \cdot \text{sec.}$$

From Table 1 X(Se) − X(Te) = 0.15. Thus, at room temperature:

$$\mu_a \cong \frac{7.5}{(\Delta X)^2} \text{cm}^2/V \cdot \text{sec.} \tag{12}$$

The constant C is now somewhat larger than in Si-Ge or In(P-As) because of the higher dielectric screening in the lead salts. Assume C = 7.5 $\text{cm}^2/\text{V} \cdot \text{s}$ for most or all of the heavy element semiconductors that are of interest. If the carrier mobilities in the mixed crystals are to be like those in PGEC, the alloy scattering should be small compared to 1800 $\text{cm}^2/\text{V} \cdot \text{s}$ at room temperature. Thus, setting the desired value of:

$$\mu_a \geq 3000 \text{ cm}^2/V \cdot \text{sec.}$$

the measured total mobility will be given by:

$$\mu_{tot}^{-1} = \mu_{normal}^{-1} + \mu_a^{-1} \tag{13}$$

The effect of μ_a on PGEC will be to give a value of

$$\mu_{TOT} \geq 1125 \text{ cm}^2/V \cdot \text{sec.} \tag{14}$$

Even this much reduction in μ_{TOT} from 1800 $\text{cm}^2/\text{V} \cdot \text{s}$ is not good; it drops the maximum ZT ≃ 3, but it sets a limit on $|\overline{\Delta X}|$ of:

$$|\overline{\Delta X}| \leq 0.05 \tag{15}$$

Thus, any mixed crystals that are formed in order to reduce the lattice thermal conductivity will have to be selected from two elements that are intended to occupy the same type of lattice site which differ in X by less than 0.05. Some of the possible pairs of elements that might substitute for one another in mixed crystals that satisfy this requirement are given in Table 7. The Sb-Bi pair in Table 7 is almost the only useful one among the constituents of heavy element semiconductors. The small value of X(Sb) − X(Bi) is one of the reasons that Bi-Sb mixed crystals work well for thermoelectric cooling, see Figure 1. This small ΔX difference is also the reason for the success of $(\text{Bi-Sb})_2\text{Te}_3$ mixed crystals in Figure 2. The limited use of only 10% Se in $\text{Bi}_2(\text{Se-Te})_3$ mixed crystals

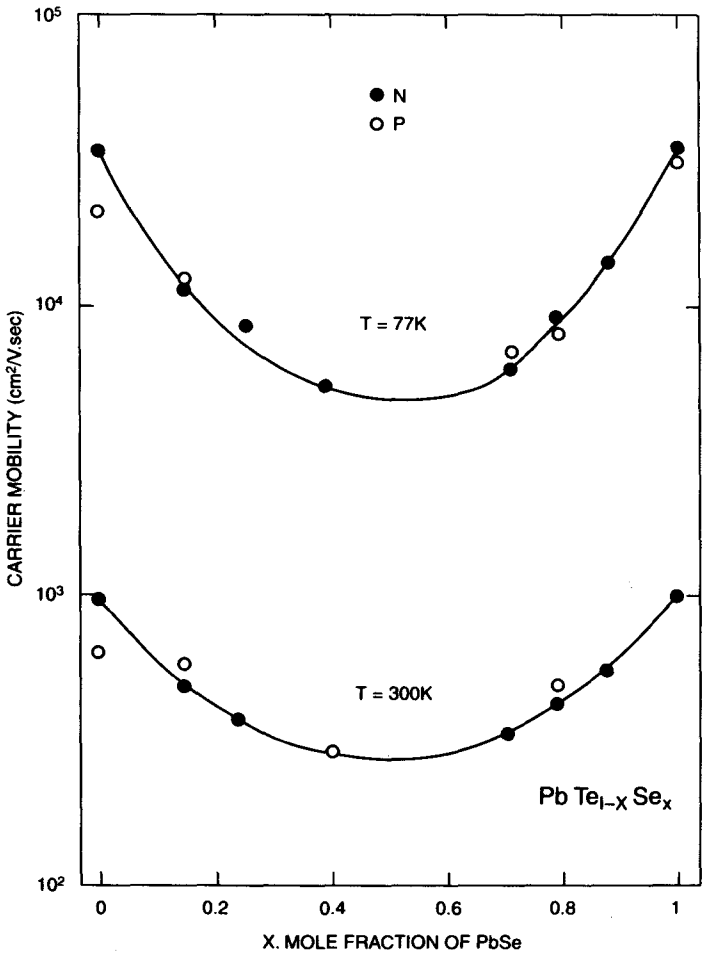

FIGURE 16 The carrier mobility in mixed crystals of PbTe-PbSe as a function of composition for two different temperatures. Both n-type and p-type samples have been measured.

Table 7 Matched Pairs of Elements for Mixed Crystals that Possess Low $|\Delta X|$

Pair	$X_A - X_B$	Pair	$X_A - X_B$
P^{3-}-As^{3-}	0.01	Pb^{2+}-Sn^{2+}	0.07
W^{6+}-Mo^{6+}	0.01	Rh^{3+}-Ir^{3+}	0.08
Ce^{3+}-La^{3+}	0.02	Ge^{4+}-Si^{4+}	0.11
Ga^{3+}-In^{3+}	0.03	As^{3-}-Sb^{3-}	0.13
Sb^{3+}-Bi^{3+}	0.03	Se^{2-}-Te^{2-}	0.15
Cd^{2+}-Zn^{2+}	0.04	Tl^{3+}-In^{3+}	0.26
		Pb^{2+}-Ge^{2+}	0.32

for n-type elements in Figure 1 is caused by the relatively large value of X(Se) − X(Te) = 0.15, see Table 7.

It must also be realized from Figure 16 that the relative importance of alloy scattering on the mobility increases with decreasing temperature. The curve for 77 K in Figure 16 exhibits a much more pronounced dip at the x = 0.5 composition than does the one at 300 K. The result is that good thermoelectric cooling materials are more sensitive to alloy scattering than are thermoelectric generator materials.

Clearly there is a dilemma here. High mobility is needed for good thermoelectric cooling materials. The standard method used for controlling their thermal conductivity has reduced the mobility below acceptable limits. One method for overcoming this problem was suggested by Ioffe.[72] This is the idea that in mixed-crystals cation substitutions scatter electrons while anion substitutions scatter holes. The data of Efimova et al.[72] have been analyzed, and can be recast to give $\mu_a = 450$ cm^2/V · s for holes and 1800 cm^2/V · s for electrons in $PbTe_{0.5}Se_{0.5}$ at room temperature. The more recent data on Pb(Te-Se) shown in Figure 16 indicate that the electron scattering is about the same as the hole scattering and $\mu_a = 330$ cm^2/V · s for both. Thus, the carrier scattering in mixed crystals *cannot* be avoided by substituting anion randomness for cation randomness or vice versa. Ioffe's concept[72] that these substitutions will always act as neutral impurities was wrong. He did *not* consider the ΔX difference between the substituting pairs.

Weighted Mobility

Consider the weighted mobility, U, in PbTe-PbSe mixed crystals. The effective mass of n-type mixed crystals as a function of composition, x, has been measured by Faradzhev et al.[73] These m^* values have been adjusted to those appropriate at room temperature and U_N vs. x has been calculated for $PbTe_{1-x}Se_x$. The results are shown in Figure 17. It is clear that the weighted mobility also shows a minimum at $x = 0.5$. Thus, the carrier scattering effect by the coulomb potential fluctuations is *real*, and is not just a manifestation of changes in the band structure and in m^* as a result of the mixed-crystal formation. As a consequence, the best Pb(Te-Se) thermoelectric materials only contain about 10 mol% PbSe, as shown by Kudman.[74] Larger amounts of Se clearly degrade U, as shown in Figure 17. This is the same story as in $Bi_2(Te\text{-}Se)_3$.

Table 7 lists the pairs with small X differences. Consider the In-Ga pair in the form of (In-Ga)Sb mixed crystals. U vs. x has been calculated at room temperature for these samples based on the mobility[75] and effective mass[76] data in the literature. The result is the curve shown in Figure 17 for n-type $In_{1-x}Ga_xSb$. Clearly there is little or no alloy scattering in this system, and U has a maximum near 67 mol% GaSb. Thermoelectric measurements on this system by Kudman et al.[51] show that the highest Z values are for mixed crystals containing about 45 mol% GaSb. This result agrees with Figure 17. The value of $|\Delta X| = 0.03$ for the In-Ga pair is acceptable, the $|\Delta X| = 0.15$ for the Te-Se pair is not. From Equation 10, it is seen μ_a^{-1} varies as $|\Delta X|^2$. Thus, these pairs, In-Ga and Se-Te, differ by a factor of 25 in their effect on the mobility.

It is clear from Figure 17 that the alloy scattering effects on U can be substantial, and that low $|\Delta X|$ pairs should always be selected whenever possible in order to obtain high Z values. Figure 17 also demonstrates that the cation substitution in (In-Ga)Sb does not scatter the electrons while the anion substitution in Pb(Te-Se) does. This is just opposite of Ioffe's model. The real difference is $|\Delta X|$, not whether one has cation or anion substitution.

34.7 Lattice Thermal Conductivity

The lattice thermal conductivity should approach the minimum possible value in good single-crystal thermoelectric materials. Some methods of achieving this are explained in this section.

The thermal conductivity value that enters into the expression for ZT contains[3] the sum of the lattice thermal conductivity, λ_L, the polar electronic thermal conductivity, $\lambda_p = L_o \sigma T$, and the bipolar thermal conductivity, λ_b. As long as the band gap, E_G, is ≥ 10 kT we can neglect λ_b. Thus:

$$\lambda_{TOTAL} = \lambda_L + L_o \sigma T. \tag{16}$$

Here L_o is the Lorentz number and is almost always close to its classical value[3] of $L_o = 2.443 \times 10^{-8}$ V^2/K^2. The critical quantity that influences ZT is λ_L. In order to have a chance of coming close to the desired ZT values from 77 to 300 K, the λ_L values must be close to λ_{min}. This means values close to 2.5×10^{-3} W/cmK. This limit has been discussed earlier.

The method used by Ioffe[17] for reducing λ_L in PbTe and Bi_2Te_3 was mass fluctuation scattering produced by using mixed crystals, such as Ge-Si or (Pb-Sn)Te, etc. It has two distinct limitations.

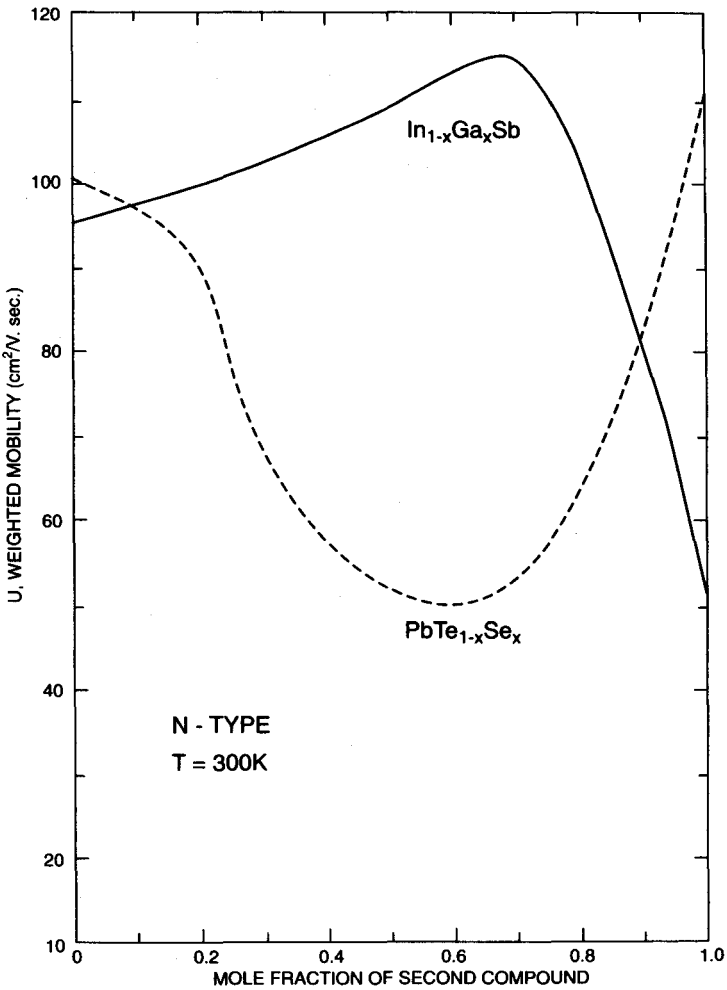

FIGURE 17 The weighted mobility vs. mixed-crystal composition for single crystals of n-type (In-Ga)Sb and Pb(Te-Se) at room temperature.

First it does not reduce λ_L to values anywhere near λ_{min}. Second, it often lowers the carrier mobility unless the $|\Delta X|$ difference for the mixed pair is close to zero, see Table 7. Clearly, a method of reducing λ_L is needed that is both more effective in reducing the mean free path of phonons and which also has a smaller effect on the charge carriers.

Consider first the increased phonon scattering. Note that the mass fluctuation scattering has a scattering strength that varies as ν^4, where ν is the phonon frequency. The short-wavelength phonons are strongly affected by this scattering, but the intermediate- and long-wavelength phonons are not much affected by this scattering mechanism. The λ_L of a crystal is made up of almost equally weighted contributions from all wavelengths of the phonon spectrum. This means one would like a phonon scattering mechanism that is uniform over the whole spectrum. There are a few crystals that are known to have λ_L values close to or equal to λ_{min}, and thus they tend to approach this desired behavior. It is known[77,78] that amorphous semiconductors such as Si, Ge, or $CdGeAs_2$ have minimum thermal conductivity values. Since the electrical conductivities of these amorphous solids are very low, they are not of interest for thermoelectric cooling. The next class consists of those compounds in which one of the kinds of ions is disordered but the others are all ordered. Some examples are YB_{68}, Tl_3AsSe_3, NH_4Cl, AgI, and ice clathrates.

In YB_{68} the boron atoms form a well-ordered structure but the Y ions occupy a dumbbell-shaped cavity in which each Y ion can move easily between the two equivalent ends of the cavity. Its

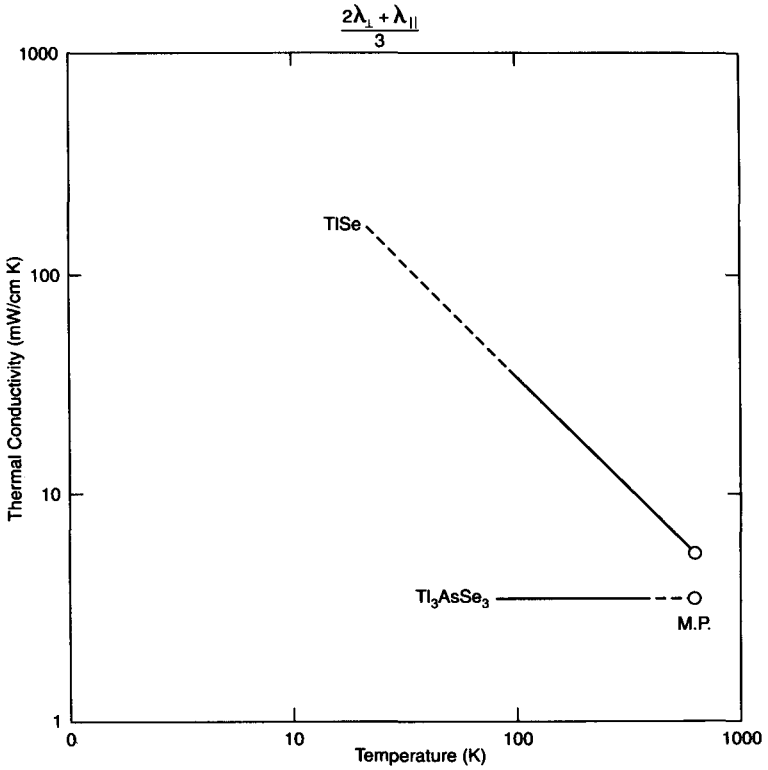

FIGURE 18 The average thermal conductivity of TlSe and Tl_3AsSe_3 as a function of temperature. The average values for TlSe have been computed from $\lambda_\perp$ and $\lambda_\parallel$ for this anisotropic crystal. The melting points are denoted by M.P.

thermal conductivity has been shown[79] to be equal to λ_{min} from 1 to 300 K. This low thermal conductivity is believed to be caused by the "rattling" motion of the Y ions.

In Tl_3AsSe_3 the As atom position appears to be unstable.[80] The thermal conductivity of large single crystals have been measured[81] from 77 to 300 K. The results are shown in Figure 18, where the data for Tl_3AsSe_3 are compared to those[82] for TlSe, which has no As. The thermal conductivities of these compounds are fundamentally anisotropic, so in TlSe we have used the average thermal conductivity $(2\lambda_\perp + \lambda_\parallel)/3$. In Tl_3AsSe_3 the thermal conductivity appears[81] to be isotropic although the crystal structure is rhombohedral. Note the substantial difference between Tl_3AsSe_3 and TlSe in Figure 18, both in magnitude and temperature dependence. TlSe behaves like a normal crystal, Tl_3AsSe_3 does not; its thermal conductivity is just that of λ_{min}.

In NH_4Cl there is a sharp drop in the thermal conductivity[83] at 250 K. Above this temperature the NH_4 ions are rotating freely in the crystal and continue to do so up to the melting point at about 800 K. Below 250 K they are locked into the structure, and in this temperature region the thermal conductivity behaves normally. Above 250 K the thermal conductivity is low, almost independent of temperature, and very close to λ_{min}. The low thermal conductivity is caused by the interaction of the rotating NH_4 ions with the propagating phonons.

The results for AgI from Goetz and Cowan[84] are shown in Figure 19. Note that the thermal conductivity of AgI behaves normally below 420 K. At 420 K there is a sharp drop in the curve. Above 420 K the silver ions are very mobile. The material is now a superionic conductor, and the mobile silver ions strongly scatter the phonons, yielding λ_{min} values of ~2 mW/cm K up to the melting point. Such mobile silver ions are probably responsible for the low thermal conductivity of $Ag_{0.25}Pb_{0.5}Sb_{0.25}Te$ as well, see Figure 3.

The thermal conductivity of single-crystal ice (the normal 1h phase) is shown[85] in Figure 20. The results show normal $K \sim T^{-1}$ behavior. Ice can also be crystallized with various molecules

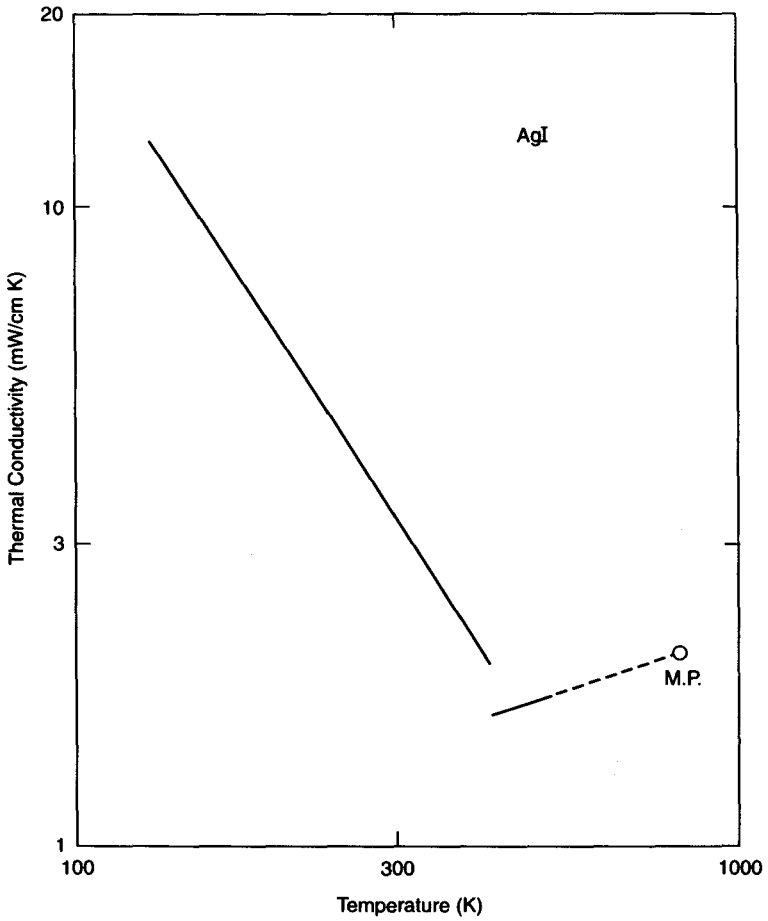

FIGURE 19 The thermal conductivity of AgI as a function of temperature. The melting point is M.P.

trapped within the structure. These crystals are called ice clathrates, and exhibit the thermal conductivity properties also shown in Figure 20. For example, trapped tetrahydrofuran (THF) molecules have been studied by Ross and Andersson[86] and Ashworth et al.[87] from 40 to 270 K. The results in Figure 20 indicate a nearly temperature-independent thermal conductivity even less than that of water, the "amorphous" phase of ice. This is clearly λ_{min} behavior. The THF curve from 2 to 40 K has been estimated by comparison with the results[88] on dioxolane clathrates. Ice clathrates can also be made[88,90] with methane (CH_4) or xenon (Xe) inclusions. Their thermal conductivities are also shown in Figure 20, and have values at or close to λ_{min}, and clearly less than that of amorphous ice (i.e., water). The results for xenon are especially interesting because they show that a spherical molecule without any "arms or legs" on it has a sufficiently strong interaction with the host, i.e., ice, to produce λ_{min} behavior.

A comparison of Figures 18, 19, and 20 with Figure 3 shows that the thermal conductivity of $PbTe_{0.5}Se_{0.5}$ does not behave like λ_{min} vs. temperature. Thermal conductivity results have also been collected for bismuth[91,92] and bismuth-antimony[12,93] mixed crystals, as shown in Figure 21. The data are for heat flow parallel to the rhombohedral axis ($K_{33}=\lambda_{33}$). For $Bi_{0.85}Sb_{0.15}$ the thermal conductivity is not at all close to λ_{min}. Thus, the ZT performance shown in Figure 2 could be greatly improved if values of K approaching λ_{min} could be realized. The same type of comment applies to the ZT curves in Figure 1 for Bi_2Te_3-type compounds.

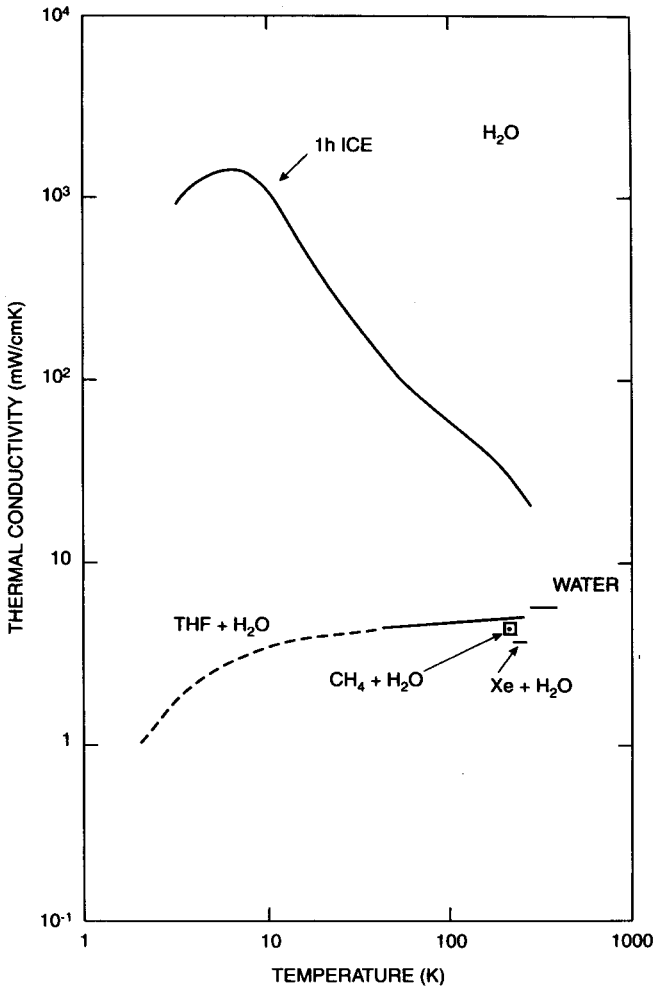

FIGURE 20 The thermal conductivity of water, single crystal ice, and several polycrystalline ice clathrates as a function of temperature.

Phonon Scattering Mechanisms

It has been shown that minimum thermal conductivity values do occur in crystalline solids for materials such as YB_{68}, Tl_3AsSe_3, NH_4Cl, AgI, and H_2O. Cahill et al.[2] have enumerated a number of mixed-crystal systems that possess minimum thermal conductivities. The common features of all of these materials are

1. They possess atoms or molecular groups whose translational positions or angular orientations are not exactly defined. There may be two or more possible semistable positions.
2. There is no long-range correlation between the positions or orientations of these loose or "rattling" atoms or molecules. One needs to be above the "freeze-out" temperature below which they do order.
3. The mass of such "rattling" atoms or molecules should be at least 3% of the total mass of the crystal.

Furthermore, they[2] concluded that simple mass substitution, as in K(Cl-Br) or other mixed crystals, *never* leads to λ_{min} behavior.

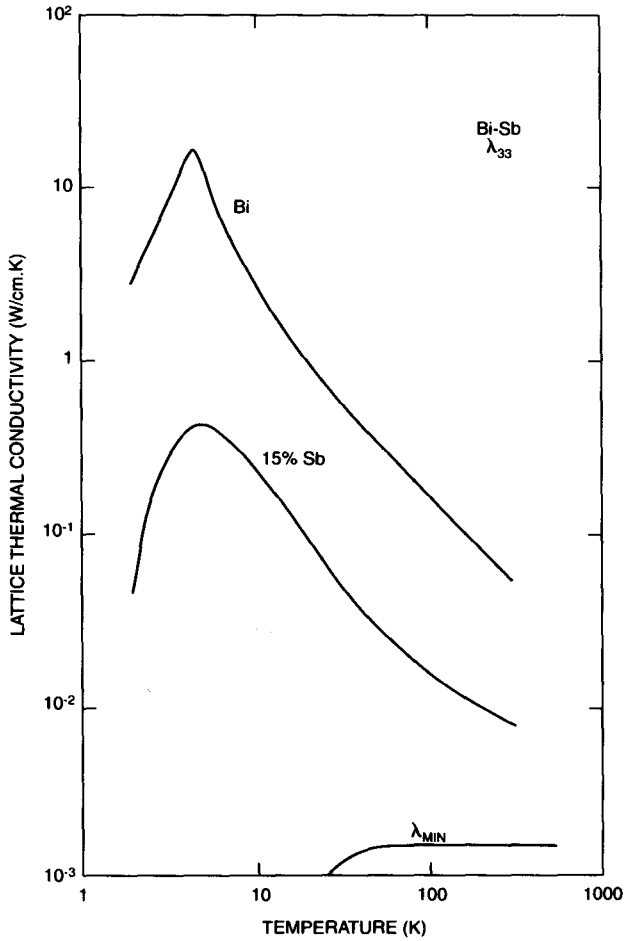

FIGURE 21 The lattice thermal conductivity of Bi and $Bi_{0.85}Sb_{0.15}$ single crystals vs. temperature for heat flow along the rhombohedral axis. The calculated λ_{min} is also given.

34.8 New λ_{min} Crystals and New Thermoelectrics

Using the guidelines above, what crystals or kinds of crystals might be found with λ_{min} behavior that are also semiconductors? The compound Tl_3AsSe_3 is not a useful thermoelectric semiconductor. However, it suggests that one should look for ternary semiconducting compounds A_xBC_y where the conducting framework is $A_x + C_y$ and the B atoms are used to scatter the phonons. Possible types of candidates are K_3SbTe_3[94] or Cs_2GaSb_2.[95] One of the long-term thermoelectric projects should be to synthesize and study a large range of heavy element ternary compounds with this in mind. Then one might find thermoelectric cooling materials that approach the limiting values of $ZT \simeq 4$ at and below room temperature. Careful attention will have to be paid to the average electronegativity differences between the elements in these compounds in order to obtain high carrier mobilities.

34.9 Conclusions From the Analysis

Nine conclusions are given based on the preceding analysis.

1. There are no currently known materials that have R values, where $R = U/\lambda_L$, sufficiently high to produce $ZT = 1$ over the temperature range from 77 to 300 K.

2. The model for PGEC indicates that a ZT = 4 is possible from 77 to 300 K if a material with U = 1800 $cm^2/V \cdot s$ and λ_L = 2.5 mW/cm · K can be found. The decisive ratio is R = U/λ_L = 7.20 $cm^2\ s^2$ K/g V.
3. It seems unlikely that cooling materials with ZT >4 will ever be found.
4. The goal of ZT = 1 can be obtained with R = 0.60 $cm^2\ s^2$ K/g V.
5. The place to look for such materials is in small-band-gap, heavy element compound semiconductors with electronegativity differences of $|\overline{\Delta X}| \leq 0.5$.
6. For doping levels less than $10^{19}/cm^3$ charged impurity scattering that might lower the mobility will be screened out by the high dielectric constants.
7. For ZT = 4 materials the traditional use of mixed crystal formation to enhance the ZT values will fail because alloy scattering of the charge carriers increases as $[\Delta X]^2$. There are very few pairs of elements with small $|\Delta X|$ values available.
8. For ZT = 1 materials mixed crystals might help in a few special cases.
9. Minimum thermal conductivity values can sometimes be found in crystals that contain "rattling" atoms or molecular groups.

Appendix: Calculation of ZT for PGEC

A model thermoelectric material is "a phonon glass and an electron crystal". Its ZT values are calculated as a function of carrier concentration and temperature.

The figure-of-merit, Z, for a thermoelectric material is given[5,6] by:

$$Z = \frac{\alpha^2 \sigma}{\lambda_{TOT}} \tag{A1}$$

$$\lambda_{total} = \lambda_L + L_o \sigma T \tag{A2}$$

where α = Seebeck coefficient, σ = electrical conductivity, λ_L = lattice thermal conductivity, L_o = Lorentz number, and T = absolute temperature. This can be rewritten as:

$$ZT = \frac{(\alpha/\sqrt{L_o})^2}{1 + \left[\frac{\lambda_L}{L_o \sigma T}\right]} \tag{A3}$$

The Seebeck coefficient for degenerate statistics and hence no carrier freeze-out at low temperatures is given by:

$$\alpha = \pm \frac{k}{e}\left[\frac{2 F_1(\eta)}{F_o(\eta)} - \eta\right], \eta = \frac{\zeta}{kT} \tag{A4}$$

Here k = Boltzmann's constant, e = electron charge, $F_i(\eta)$ = the *ith* Fermi integral, η = reduced Fermi energy, and ζ = Fermi energy. We have assumed pure lattice phonon scattering of the charge carriers. The value of η for a p-type sample is given by:

$$F_{1/2}(\eta) = \frac{p}{[m^*/m_o]^{1.5}} \cdot \frac{6\pi^2 \hbar^3}{[2 m_o k T]^{1.5}} \tag{A5}$$

where p = the hole concentration, m^* = effective mass of the valence band, m_o = the free electron mass, and $\hbar$ = Planck's constant divided by 2π. The resultant α vs. carrier concentration curves are given in Figure 22.

The electrical conductivity for p-type material is given by:

$$\sigma_p = p\, e\, \mu_p \tag{A6}$$

where μ = the carrier mobility. Define the weighted mobility, U_p, by:

$$U_p = \mu_p [m^*_p/m_o]^{1.5} \tag{A7}$$

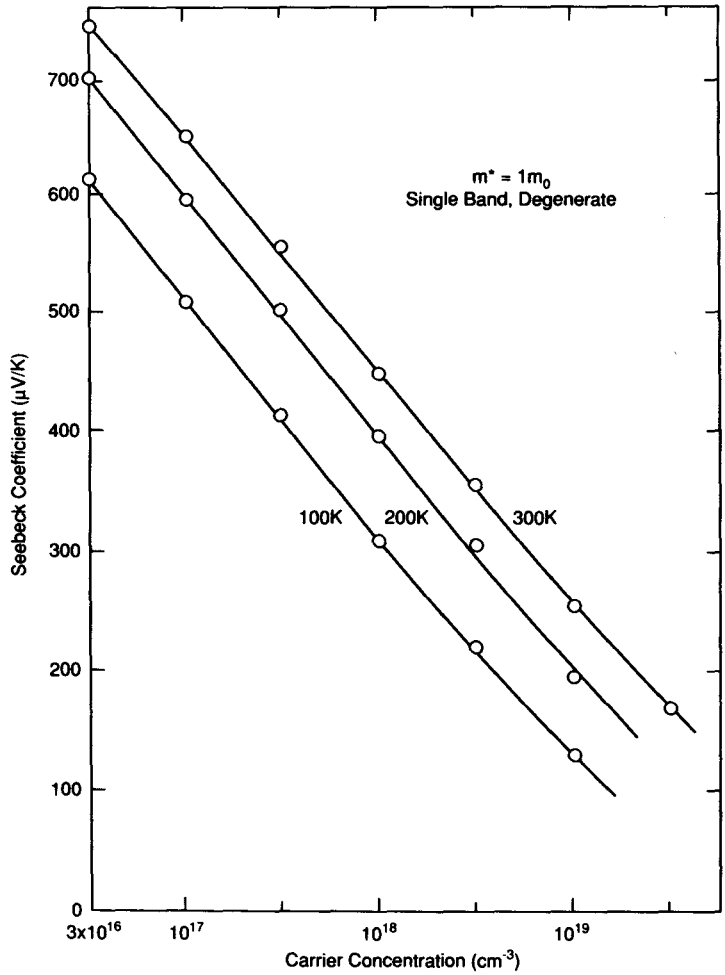

FIGURE 22 The calculated Seebeck coefficient as a function of carrier concentration for three different temperatures from Equation A4. The effective mass is assumed to be the free electron mass.

Then Equation A3 can be rewritten as:

$$Z_pT = \frac{(\alpha/\sqrt{L_o})^2}{1 + \frac{1}{L_o\, e\, T}\left[\frac{\lambda_L}{U_p}\right]\left[\frac{[m^*_p/m_o]^{1.5}}{p}\right]} \tag{A8}$$

From Equations A5 and A8 it can be seen that ZT depends on the material parameters:

$$R_p = \frac{U_p}{\lambda_L} \text{ and } \frac{[m^*_p/m_o]^{1.5}}{p} \tag{A9}$$

The first of these, R_p, is governed by the choice of the material. The second parameter in Equation A9 can be adjusted by controlling the doping level.

The value of ZT for the model material PGEC was calculated using:

$$U_p = U_N = 1800\left[\frac{300K}{T}\right]^{2.30} \text{ cm}^2/V \cdot \text{sec.} \tag{A10}$$

For λ_L, the λ_{min} vs. T curve from Figure 3 or various multiples of it were used (2 λ_L, 6 λ_L, and 12 λ_L). The α vs. carrier concentration curves are given in Figure 22. The ZT vs. carrier concentration curves are given in Figures 5, 6, 7, and 8.

References

1. G.A. Slack, "The thermal conductivity of nonmetallic crystals", in *Solid State Physics*, Vol. 34, p. 1 (1979), ed. by H. Ehrenreich, F. Seitz, and D. Turnbull, Academic Press, New York.
2. D.G. Cahill, S.K. Watson, and R.O. Pohl, "Lower limit to the thermal conductivity of disordered crystals", *Phys. Rev. B*, 46, 6131 (1992).
3. G.A. Slack and M.A. Hussain, "The maximum possible conversion efficiency of silicon-germanium thermoelectric generators", *J. Appl. Phys.*, 70, 2694 (1991).
4. W.M. Yim and F.D. Rosi, "Compound tellurides and their alloys for Peltier cooling—a review", *Solid-State Electron.*, 15, 1121 (1972).
5. D.M. Rowe and C.M. Bhandari, *Modern Thermoelectrics*, Holt, Rinehart, and Winston, London, 1983.
6. H.J. Goldsmid, *Electronic Refrigeration*, Pion Ltd., London, 1986.
7. J. Rupprecht, "Thermoelectric properties of one p-type and one n-type bismuth telluride alloy in the temperature range 100 to 300°K", *Z. Angew. Phys.*, 16, 304 (1964).
8. W.M. Yim, E.V. Fitzke, and F.D. Rosi, "Thermoelectric properties of bismuth telluride-antimony telluride-antimony selenide pseudo-ternary alloys in the temperature range 77 to 300°K", *J. Mater. Sci.*, 1, 52 (1966).
9. D.A. Wright, "Materials for direct-conversion thermoelectric generators", *Metall. Rev.*, 15, 147 (1970) [see Metals and Materials, Vol. 4, 1970, Review #148].
10. A.A. Aivazov, A.I. Anukhin, A.I. Mazina, and N.A. Boboshko, "Thermoelectric properties of the solid solutions bismuth-antimony telluride in the temperature range 150–350°K", *Neorg. Mater.*, 27, 2072 (1991) [*Inorg. Mater.*, 27, 1761 (1991)].
11. G.E. Smith and R. Wolfe, "Thermoelectric properties of bismuth-antimony alloys", *J. Appl. Phys.*, 33, 841 (1962).
12. W.M. Yim and A. Amith, "Bismuth-antimony alloys for magneto-thermoelectric and thermomagnetic cooling", *Solid-State Electron.*, 15, 1141 (1972).
13. Z.M. Dashevskii, N.A. Sidorenko, N.A. Tsvetkova, C.Ya. Skipidarov, and A.B. Mosolov, "Cryogenic thermoelectric coolers with passive high-T_c superconductor branches", *Supercond. Sci. Technol.*, 5, 690 (1992).
14. W. Haken, "Contribution to the knowledge of the thermoelectric properties of metallic alloys", *Ann. Phys.*, 32, 291 (1910).
15. R. Uno, "On the electrical properties of polycrystalline boron", *J. Phys. Soc. Jpn.*, 13, 667 (1958); F.G. Wick, "Some electrical properties of silicon. I. Thermoelectric behavior of metallic silicon", *Phys. Rev.*, 25, 382 (1907); C.C. Bidwell, "Resistance and thermoelectric power of metallic germanium", *Phys. Rev.*, 19, 447 (1922).
16. T.J. Seebeck, "Magnetic polarization of metals and minerals by temperature differences", *Abh. Preuss. Akad. Wiss.*, p. 265 (1822–1823).
17. A.F. Ioffe, *Semiconductor Thermoelements and Thermoelectric Cooling*, Infosearch Ltd., London, 1957.
18. A. Eucken and G. Kuhn, "Results of new measurements of the thermal conductivity of crystalline solids at 0°C and −190°C", *Z. Phys. Chem.*, 134, 193 (1928).
19. C. Kittel, "Interpretation of the thermal conductivity of glasses", *Phys. Rev.*, 75, 972 (1949).
20. G.A. Slack, D.W. Oliver, and F.H. Horn, "Thermal conductivity of boron and some boron compounds", *Phys. Rev., B*, 4, 1714 (1971).
21. D. Greig, "Thermoelectricity and thermal conductivity in the lead sulfide group of semiconductors", *Phys. Rev.*, 120, 358 (1960).
22. A.D. Stuckes, "Measurement of thermal conductivity of semiconductors at high temperatures", *Br. J. Appl. Phys.*, 12, 675 (1961).

23. E.D. Devyatkova, A.V. Petrov, and I.A. Smirnov, "Heat transfer during bipolar diffusion of current carriers in lead telluride and lead selenide", *Fiz. Tverd. Tela,* 3, 1338 (1961) [*Sov. Phys.-Solid State,* 3, 970 (1961)].
24. S.S. Shalyt, V.M. Muzhdaba, and A.D. Galetskaya, "Lattice and electronic thermal conductivity of lead telluride, lead selenide, and lead sulfide", *Fiz. Tverd. Tela,* 10, 1277 (1968) [*Sov. Phys.-Solid State,* 10, 1018 (1968)].
25. A.V. Ioffe and A.F. Ioffe, "Thermal conductivity of semiconductors", *Izv. Akad. Nauk S.S.S.R., Ser. Fiz.,* 20, 65 (1956).
26. T.J. Soltys, General Electric R and D Center (1957), private communication.
27. A.V. Ioffe and A.F. Ioffe, "Thermal conductivity of semiconductor solid solutions", *Fiz. Tverd. Tela,* 2, 781 (1960) [*Sov. Phys.-Solid State,* 2, 719 (1960)].
28. A.F. Ioffe, "Heat transfer in semiconductors", *Can. J. Phys.,* 34, 1342 (1956).
29. E.D. Devyatkova and V.V. Tikhonov, "Scattering of phonons and electrons in solid solutions", *Fiz. Tverd. Tela,* 7, 1770 (1965) [*Sov. Phys.-Solid State,* 7, 1427 (1965)].
30. F.D. Rosi, E.F. Hockings, and N.E. Lindenblad, "Semiconducting materials for thermoelectric power generation", *RCA Rev.,* 22, 82 (1961) [see page 108]; T. Irie, "Lattice thermal conductivity of disordered alloys of ternary compound semiconductors", *Jpn. J. Appl. Phys.,* 5, 854 (1966).
31. R.S. Allgaier and W.W. Scanlon, "Mobility of electrons and holes in PbS, PbSe, and PbTe between room temperature and 4.2°K", *Phys. Rev.,* 111, 1029 (1958).
32. I.A. Chernick, V.I. Kaidanov, M.I. Vinogradova, and N.V. Kolomoets, "Investigation of the valence band of lead telluride using transport phenomena", *Fiz Tekh. Poluprovodn.,* 2, 773 (1968) [*Sov. Phys.-Semic.,* 2, 645 (1968)].
33. N.V. Kolomoets, T.S. Stavitskaia, and L.S. Stilbans, "An investigation of the thermoelectric properties of lead selenide and lead telluride", *Zh. Tekh. Fiz.,* 27, 73 (1957) [*Sov. Phys.-Tech. Phys.,* 2, 59 (1957)].
34. T.S. Stavitskaya, L.V. Prokofeva, Yu. I. Ravich, and B.A. Efimova, "Influence of conduction-band nonparabolicity on the transport coefficients of lead telluride in the temperature range 100–1000°K", *Fiz. Tekh. Poluprovodn.,* 1, 1138 (1967) [*Sov. Phys.-Semic.,* 1, 952 (1968)].
35. Yu. I. Ravich, B.A. Efimova, and V.I. Tamarchenko, "Scattering of current carriers and transport phenomena in lead chalcogenides. II. Experiment", *Phys. Status Solidi B,* 43, 453 (1971).
36. H.J. Goldsmid, *Electronic Refrigeration,* Pion Ltd., London, 1986, p. 89.
37. G. Mahan, "Figure of merit for thermoelectrics", *J. Appl. Phys.,* 65, 1578 (1989).
38. L. Pauling, *The Nature of the Chemical Bond,* Cornell University Press, Ithaca, New York, 1960, third edition, p. 93.
39. A.L. Allred, "Electronegativity values from thermochemical data", *J. Inorg. Nucl. Chem.,* 17, 215 (1961).
40. Landolt-Bornstein, Neue Serie, Gruppe III, Band 17, ed. by O. Madelung, M. Schulz, and H. Weiss, Springer-Verlag, Berlin, 1985.
41. R. Dalven, "Electronic structure of PbS, PbSe, and PbTe", in *Solid State Physics,* Vol. 28, p. 179 (1973), ed. by H. Ehrenreich, F. Seitz, and D. Turnbull, Academic Press, New York.
42. I.A. Smirnov, E.V. Shadrichev, and V.A. Kutasov, "Heat conductivity of stoichiometric and heavily-doped bismuth telluride crystals", *Fiz. Tverd. Tela,* 11, 3311 (1969) [*Sov. Phys.-Solid State,* 11, 2681 (1970)].
43. J.R. Drabble, "The physical properties of single crystal bismuth telluride", in *Progress in Semiconductors,* Vol. 7, p. 47 (1963), ed. by A.F. Gibson and R.E. Burgess, John Wiley & Sons, New York.
44. A.A. Abdullaev, L.A. Angelova, V.K. Kuznetsov, A.B. Ormont, and Yu. I. Pashintsev, "Galvano- and thermomagnetic properties of platinum antimonide", *Phys. Status Solidi A,* 18, 459 (1973).
45. D.H. Damon, R.C. Miller, and A. Sagar, "Semiconducting properties of platinum antimonide", *Phys. Rev. A,* 138, 636 (1965).
46. G.A. Slack and V.G. Tsoukala, "Some properties of semiconducting $IrSb_3$", *J. Appl. Phys.,* 76, 1665 (1994).
47. F.J. Berry, C.D. Gibbs, and C. Greaves, "Structural properties of the molybdenum-ruthenium telluride of composition $Mo_9Ru_3Te_{16}$", *J. Solid State Chem.,* 92, 148 (1991).
48. W. Hönle, H.D. Flack, and K. Yvon, " "Single crystal X-ray study of Mo_6Se_8-type selenides containing partially substituted clusters", *J. Solid State Chem.,* 49, 157 (1983).

49. F. Klaiber, W. Petter, and F. Hulliger, "The structure type of Re_2Te_5, a new $[M_6X_{15}]$ cluster compound", *J. Solid State Chem.*, 46, 112 (1983).
50. A.G. Moore, C. Maghrabi, and J.M. Parker, "A new compound in the germanium-tellurium system", *J. Mater. Sci.*, 13, 1127 (1978).
51. I. Kudman, L. Ekstrom, and T. Seidel, "High-temperature thermal and electrical properties of gallium antimonide-indium antimonide alloys", *J. Appl. Phys.*, 38, 4641 (1967).
52. J.R. Drabble, R.D. Groves, and R. Wolfe, "Galvanomagnetic effects in n-type bismuth telluride", *Proc. Phys. Soc. London*, 71, 430 (1958).
53. R.W. Ure, Jr., "High mobility n-type Bi_2Te_3", *Proc. Fifth Int. Conf. Phys. Semic.*, Exeter, 1962, p. 659, Inst. Phys. & Phys. Soc., London.
54. B.M. Goltsman, B.M. Kudinov, and I.A. Smirnov, *Thermoelectric Semiconductor Materials Based on Bismuth Telluride*, Nauka, Moscow, 1972. [Translation available NTIS, U.S. Dept. of Commerce, as AD783734 (1973)].
55. J.P. Fleurial, L. Gaillard, R. Triboulet, H. Scherrer, and S. Scherrer, "Thermal properties of high quality single crystals of bismuth telluride, II", *J. Phys. Chem. Solids*, 49, 1249 (1988).
56. Yu. A. Boikov, O.S. Gribanov, V.A. Danilov, and V.A. Kutasov, "Electrophysical parameters of epitaxial n-type bismuth telluride films", *Fiz. Tverd. Tela*, 33, 3414 (1991) [*Sov. Phys.-Solid State*, 33, 1926 (1991)].
57. W. Zawadski, "Electron transport phenomena in small-gap semiconductors", *Adv. Phys.*, 23, 435 (1974).
58. A.K. Das and B.R. Nag, "Free-carrier absorption and electron mobility in n-type lead telluride", *J. Phys. Chem. Solids*, 39, 259 (1978).
59. M.K. Zhitinskaya, V.I. Kaidanov, and I.A. Chernik, "Nonparabolicity of the conduction band of lead telluride", *Fiz. Tverd. Tela*, 8, 295 (1966) [*Sov. Phys.-Solid State*, 8, 246 (1966)].
60. J.D. Jensen, B. Houston, and J.R. Burke, "Fermi-surface parameters of p-type lead telluride as a function of carrier density", *Phys. Rev. B*, 18, 5567 (1978).
61. V.A. Kutasov and L.N. Lukyanova, "The conduction band parameters and scattering mechanisms in solid solutions based on bismuth telluride", *Phys. Status Solidi B*, 154, 669 (1989).
62. R.B. Mallison, J.A. Rayne, and R.W. Ure, Jr., "DeHaas-VanAlphen effect in n-type bismuth telluride", *Phys. Rev.*, 175, 1049 (1968).
63. L.R. Testardi, P.J. Stiles, and E. Burstein, "DeHaas-VanAlphen and high field galvanomagnetic studies of the bismuth telluride valence band structure", *Solid State Commun.*, 1, 28 (1963).
64. V.V. Sologub, A.D. Goletskaya, and R.V. Parfenev, "Some features of the valence band of bismuth telluride", *Fiz. Tverd. Tela*, 14, 915 (1972) [*Sov. Phys.-Solid State*, 14, 783 (1972)].
65. H.J. Goldsmid, "The electrical conductivity and thermoelectric power of bismuth telluride", *Proc. Phys. Soc. Lond.*, 71, 633 (1958).
66. H. Süssmann and W. Heiliger, "Seebeck coefficient and electrical conductivity in p-bismuth-antimony telluride at room temperature", *Phys. Status Solidi A*, 80, 535 (1983).
67. L.R. Testardi, J.N. Bierly, Jr., and F.H. Donahoe, "Transport properties of p-type bismuth telluride-antimony telluride alloys in the temperature range 80 to 370°K", *J. Phys. Chem. Solids*, 23, 1209 (1962).
68. A. von Middendorf and G. Landwehr, "Evidence for a second valence band in p-type bismuth telluride from magneto-Seebeck and Shubnikov-DeHaas data", *Solid State Commun.*, 11, 203 (1972).
69. H. Ehrenreich, "Electron mobility of indium arsenide-phosphide", *J. Phys. Chem. Solids*, 12, 97 (1959).
70. J.D. Wiley, "Mobility of holes in III-V compounds", in *Semiconductors and Semimetals*, Vol. 10, Chap. 2 (1975), ed. by R.K. Willardson and A.C. Beer, Academic Press, New York.
71. D.H. Hohnke and M.D. Hurley, "Growth and electrical properties of epitaxial lead selenide-telluride layers", *J. Appl. Phys.*, 47, 4975 (1976).
72. B.A. Efimova, T.S. Stavitskaya, L.S. Stilbans, and L.M. Sysoeva, "Carrier scattering mechanisms in some solid solutions based on lead and bismuth tellurides", *Fiz. Tverd. Tela*, 1, 1325 (1959) [*Sov. Phys.-Solid State*, 1, 1217 (1960)].

73. F.E. Faradzhev, V.I. Tagirov, A. Sh. Mektiev, E.A. Akopyan, and G.A. Galandarov, "Effective mass of electrons in lead selenide-telluride", *Fiz. Tekh. Poluprovodn.*, 16, 908 (1982) [*Sov. Phys.-Semic.*, 16, 583 (1982)].
74. I. Kudman, "Thermoelectric properties of p-type lead telluride-lead selenide alloys", *J. Mater. Sci.*, 7, 1027 (1972).
75. W.M. Coderre and J.C. Woolley, "Conduction bands in gallium-indium antimonide alloys", *Can. J. Phys.*, 47, 2553 (1969).
76. M.J. Aubin, M.B. Thomas, E.H. vanTongerloo, and J.C. Woolley, "Electron effective-mass values in gallium-indium antimonide alloys", *Can. J. Phys.*, 47, 631 (1969).
77. D.G. Cahill and R.O. Pohl, "Thermal properties of a tetrahedrally bonded amorphous solid: $CdGeAs_2$", *Phys. Rev. B*, 37, 8773 (1988).
78. D.G. Cahill, H.E. Fischer, T. Klistner, E.T. Swartz, and R.O. Pohl, "Thermal conductivity of thin films: measurements and understanding", *J. Vac. Sci. Technol.*, A7, 1259 (1989).
79. D.G. Cahill, H.E. Fischer, S.K. Watson, R.O. Pohl, and G.A. Slack, "Thermal properties of boron and borides", *Phys. Rev. B*, 40, 3254 (1989).
80. H.Y.P. Hong, J.C. Mikkelsen, Jr., and G.W. Roland, "Crystal structure of Tl_3AsSe_3", *Mater. Res. Bull.*, 9, 365 (1974).
81. M.D. Ewbank, P.R. Newman, and H. Kuwamoto, "Thermal conductivity and specific heat of the chalcogenide salt Tl_3AsSe_3", *J. Appl. Phys.*, 53, 6450 (1982).
82. J.K. Viscakas, J.J. Vaitkus, G.D. Guseinov, S.G. Abdullayeva, F.M. Seidov, M.Z. Ismailov, and Kh. J. Khalilov, "Heat conductivity of $Tl_xGa_{1-x}Se$ monocrystals", *Mater. Res. Bull.*, 11, 377 (1976).
83. R.G. Ross and O. Sandberg, "Thermal conductivity and heat capacity of solid phases of NH_4Cl under pressure", *J. Phys. C*, 12, 3649 (1979).
84. M.C. Goetz and J.A. Cowen, "The thermal conductivity of silver iodide", *Solid State Commun.*, 41, 293 (1982).
85. G.A. Slack, "Thermal conductivity of ice", *Phys. Rev. B*, 22, 3065 (1980).
86. R.G. Ross and P. Andersson, "Clathrate and other solid phases in the tetrahydrofuran-water system: thermal conductivity and heat capacity under pressure", *Can. J. Chem.*, 60, 881 (1982).
87. T. Ashworth, L.R. Johnson, and L.P. Lai, "Thermal conductivity of pure ice and tetrahydrofuran clathrate hydrates", *High Temp. High Press.*, 17, 413 (1985).
88. N. Ahmand and W.A. Phillips, "Thermal conductivity of ice and ice clathrate", *Solid State Commun.*, 63, 167 (1987).
89. J.G. Cook and D.G. Leaist, "An exploratory study of the thermal conductivity of methane hydrate", *Geophys. Res. Lett.*, 10, 397 (1983).
90. Y.P. Handa and J.G. Cook, "Thermal conductivity of xenon hydrate", *J. Phys. Chem.*, 91, 6327 (1987).
91. G. White and S.B. Woods, "The thermal and electrical resistivity of bismuth and antimony at low temperatures", *Philos. Mag.*, 3, 342 (1958).
92. C.F. Gallo, B.S. Chandrasekhar, and P.H. Sutter, "Transport properties of bismuth single crystals", *J. Appl. Phys.*, 34, 144 (1963).
93. T.K. Dey and K.D. Chaudhuri, "Lattice thermal conductivity of bismuth-antimony alloy single crystals at low temperatures", *J. Low Temp. Phys.*, 23, 419 (1976).
94. J.S. Jung, B. Wu, E.D. Stevens, and C.J. O'Connor, "Synthesis and crystal structure of a novel Zintl phase: K_3SbTe_3", *J. Solid State Chem.*, 94, 362 (1991).
95. G. Cordier and H. Ochmann, "Crystal structure of Cs_2GaSb_2", *Z. Kristallogr.*, 195, 310 (1991).

Section E
Thermoelectric Generation

35
Miniature Semiconductor Thermoelectric Devices

David M. Rowe
University of Wales
Cardiff, U.K.

35.1 Introduction

The range of output power provided by thermoelectric generators is remarkable (Figure 1). It extends over 15 orders of magnitude, from milli-microwatts generated in miniature thermocouple arrays integrated into a semiconductor microelectronic chip[1] to the multikilowatt nuclear reactor-powered generators being built for the SP-100 project.[2] Miniature thermoelectric semiconductor devices (those with an output power of milliwatts or less) are extensively employed as sources of electrical power and as sensors. As detectors and sensors miniature thermocouple arrays (thermopiles) have found wide application as pyrometers and as sensor elements used in the measurement of magnetic, radiation, chemical, and mechanical signals.[3]

In this chapter a brief introduction to thermoelectric materials and the basic components of a thermoelectric generator is followed by a comparison of the "performance" of conventional metal-metal alloy thermoelectric materials with modern semiconductors. The changes in module fabrication technologies, which have resulted in a progressive reduction in device dimensions, are

0-8493-0146-7/95/$0.00+$.50

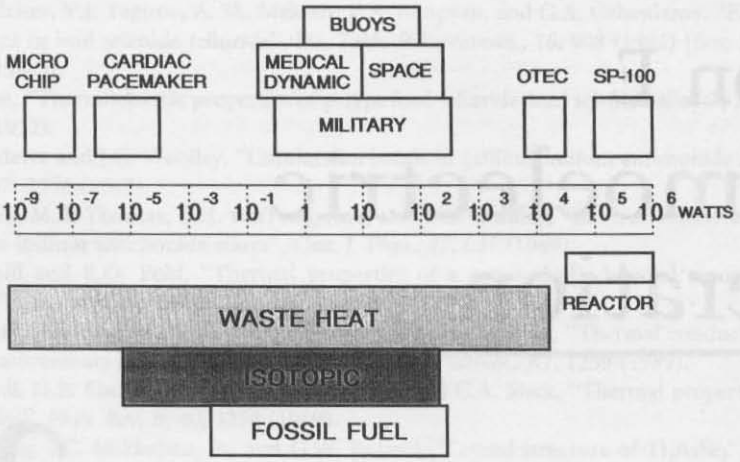

FIGURE 1 Power range and fuel sources of thermoelectric generators.

discussed. This is followed by a comprehensive review of miniature thermoelectric generating devices and sensors. Finally, conclusions are drawn regarding future developments in this area of thermoelectric applications.

35.2 Thermoelectric Materials

The "worth" of a semiconductor in a thermoelectric application is expressed by its figure-of-merit Z, which itself depends upon the electrical and thermal properties of the material, expressed as $\alpha^2\sigma$ where α is the Seebeck coefficient, σ the electrical conductivity, and λ is the thermal conductivity. A good thermoelectric material must have a large Seebeck coefficient to produce the required voltage, high electrical conductivity to minimize the thermal noise, and a low thermal conductivity to decrease thermal losses from the thermocouple junctions.

Established thermoelectric semiconductors can be conveniently grouped into three technologies depending on their temperature range of operation, as shown schematically in Figure 2, i.e., those based on bismuth telluride-type materials, lead telluride, and silicon germanium alloys. Materials based on bismuth telluride have the highest figure-of-merit but are restricted in operation to below about 250°C. Lead telluride has the next highest average figure-of-merit over an operating temperature range of up to around 500°C. Finally, silicon germanium has the lowest figure-of-merit but is able to operate for long periods of time at temperatures around 1000°C. The conversion efficiency is given approximately as ZT/4 where T is the temperature difference between the hot and cold junctions of the thermocouple. So, although the figures-of-merit of the three materials differ substantially, their performance is comparable when each is being used over the extreme of its operating temperature range. Material "performance" is often conveniently expressed in terms of a dimensionless figure-of-merit ZT. However, the conversion efficiency is not the only consideration, and when a material is selected for a specific application other factors such as the direct output voltage, thermal losses, and reliability must be taken into account. In addition, when fabricating miniature sensors the availability of appropriate fabrication technology must be assessed.

A comprehensive coverage of thermoelectric transport phenomena and material properties is given in Chapter 4.

35.3 Miniature Power Generators

General Considerations

A schematic thermoelectric generator is shown in Figure 3. In essence, it consists of a large number of thermocouples connected electrically in series to form a module. (The module is the basic

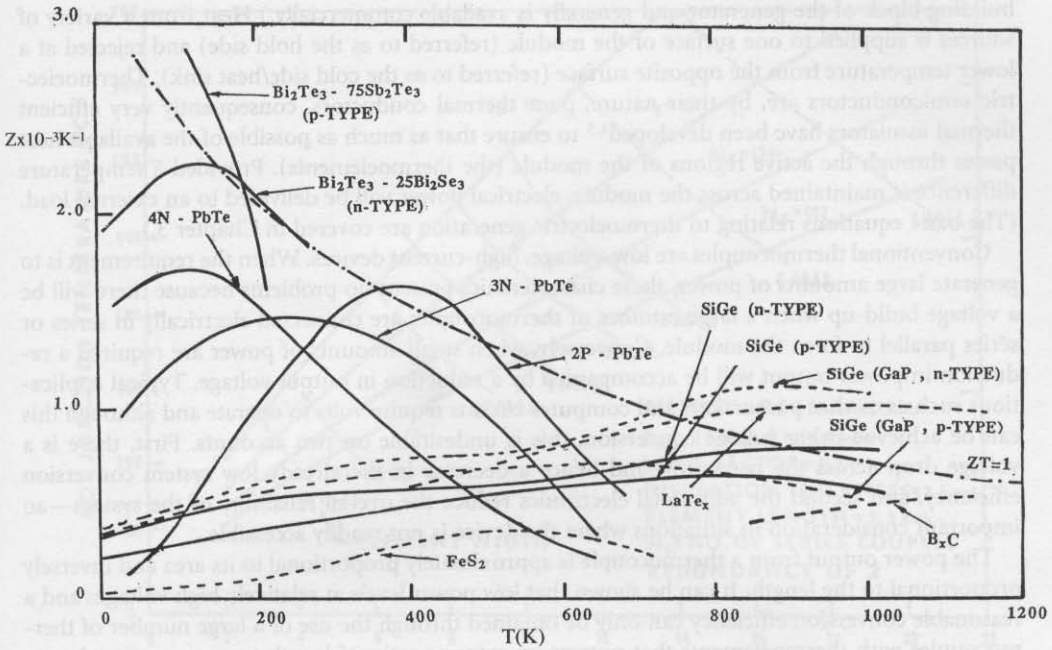

FIGURE 2 Figure-of-merit as a function of temperature.

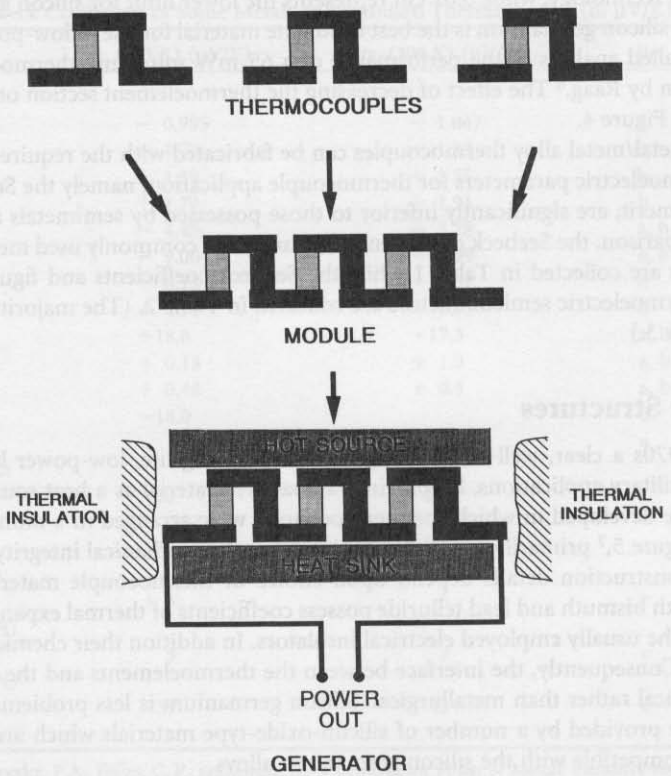

FIGURE 3 Schematic thermoelectric generator.

building block of the generator and generally is available commercially.) Heat from a variety of sources is supplied to one surface of the module (referred to as the hold side) and rejected at a lower temperature from the opposite surface (referred to as the cold side/heat sink). Thermoelectric semiconductors are, by their nature, poor thermal conductors, consequently very efficient thermal insulators have been developed[4,5] to ensure that as much as possible of the available heat passes through the active regions of the module (the thermoelements). Provided a temperature difference is maintained across the module, electrical power will be delivered to an external load. (The basic equations relating to thermoelectric generation are covered in Chapter 3.)

Conventional thermocouples are low-voltage, high-current devices. When the requirement is to generate large amounts of power, these characteristics present no problems because there will be a voltage build-up when a large number of thermocouples are connected electrically in series or series parallel to form the module. Conversely, when small amounts of power are required a reduction in power output will be accompanied by a reduction in output voltage. Typical applications such as cardiac pacemakers and computer circuits require volts to operate and although this can be achieved using voltage conversion, this is undesirable on two accounts. First, there is a voltage drop across the convertor, and hence a decrease in the already low system conversion efficiency, and second the additional electronics reduce the overall reliability of the system—an important consideration in situations where the device is not readily accessible.

The power output from a thermocouple is approximately proportional to its area and inversely proportional to the length. It can be shown that low power levels at relatively high voltages and a reasonable conversion efficiency can only be obtained through the use of a large number of thermocouples with thermoelements that possess an extreme ratio of length to cross-sectional area, i.e., wire-like.

Unfortunately the fragile nature of these established thermoelectric semiconductor materials sets a limitation to the manufacture of thermoelements that have small cross sections. For example, bismuth telluride and lead telluride element widths of 0.06 cm are just at the limit of present manufacturing technology, while 0.01 cm represents the lower limit for silicon germanium alloys. Consequently, silicon germanium is the best candidate material for use in low-power, high-voltage devices. A detailed analysis of the performance of a 65-mW miniature thermoelectric generator was undertaken by Raag.[6] The effect of decreasing the thermoelement section on the load voltage is displayed in Figure 4.

Although metal/metal alloy thermocouples can be fabricated with the required geometry, their principle thermoelectric parameters for thermocouple application, namely the Seebeck coefficient and figure-of-merit, are significantly inferior to those possessed by semimetals and semiconductors. As a comparison, the Seebeck coefficient of a number of commonly used metals and standard thermocouples are collected in Table 1 while the Seebeck coefficients and figures-of-merit of a number of thermoelectric semiconductors are collected in Table 2. (The majority of data is taken from Reference 3.)

Monolithic Structures

In the early 1970s a clear, well-defined requirement for long-life, low-power batteries arose in medical and military applications. Employing radioactive material as a heat source, a number of generators were developed in which the thermocouples were arranged in a monolithic structure, as shown in Figure 5,[7] primarily to assist in maintaining the mechanical integrity of the modules.

Monolith construction details depend upon choice of thermocouple material and, as Raag points out,[6] both bismuth and lead telluride possess coefficients of thermal expansion which differ from those of the usually employed electrical insulators. In addition their chemical properties are incompatible. Consequently, the interface between the thermoelements and the electrical insulation is mechanical rather than metallurgical. Silicon germanium is less problematic; effective insulation can be provided by a number of silicon-oxide-type materials which are chemically and mechanically compatible with the silicon germanium alloys.

The method of making the electrical connection between the thermoelements will depend upon the thermocouple material and upon the intended temperature of operation. A variety of methods

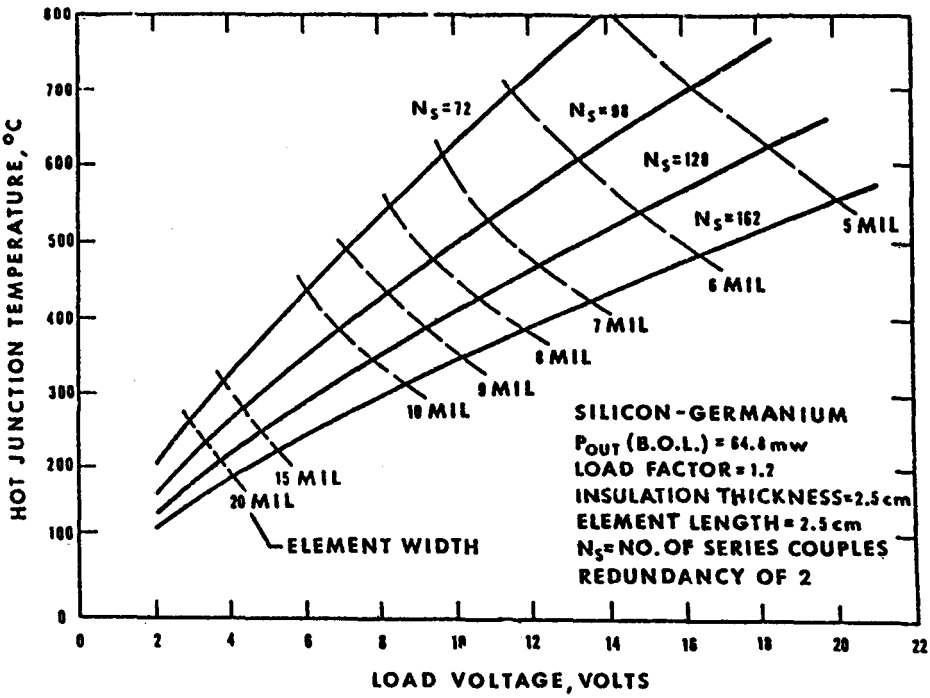

FIGURE 4 65-mW silicon-germanium RTG; effect of decreasing thermoelement section on load voltage (after Raag, Reference 6).

Table 1 The Seebeck Coefficient of Some Metals and Standard Thermocouples (in μV/K)

	α_s (273 K) (μV/K)	α_s (300 K) (μV/K)	Ref.
Metals			
Pb	− 0.995	− 1.047	c
Cu	+ 1.70	+ 1.83	b
Ag	+ 1.38	+ 1.51	b
Au	+ 1.79	+ 1.94	b
Pt	− 4.45	− 5.28	a, b
Pd	− 9.00	− 9.99	a, b
W	+ 0.13	+ 1.07	b
Mo	+ 4.71	+ 5.57	b
Cr	+18.8	+17.3	a, b
V	+ 0.13	+ 1.0	a, b
Rh	+ 0.48	+ 0.4	a, b
Ni	−18.0		a
Al		− 1.7	a
Thermocouple			
Type J (Fe/Cu-Ni)	50	51	c
Type K (Ni-Cr/Ni-Al)	39	41	c
Type R (Pt-13% Rh/Pt)	5	6	c
Type S (Pt-10% Rh/Pt)	5	7	c
Type T (Cu/Cu-Ni)	39	41	c

[a] Blatt, F. J., Schroeder, P.A., Foiles, C. F., and Greig, D., *Thermoelectric Power of Metals*, Plenum Press, New York, 1976.
[b] Barnard, R.D., *Thermoelectricity in Metals and Alloys*, Taylor and Francis, London, 1972.
[c] Quinn, T. J., *Temperature*, Academic Press, London, 1983.

Table 2 The Figure-of-Merit of Some Thermoelectric Materials

Material	ρ (Ω m)	α_s (μV/K)	Z (K^{-1})	Ref.
Si	3.5×10^{-5}	450	4.0×10^{-5}	a
Positive thermoelements				
ZnSb			1.0×10^{-3}	b
PbTe			$<1.2 \times 10^{-3}$	b
PbSe			$<1.2 \times 10^{-3}$	b
Sb_2Te_3	5.0×10^{-6}	+130	1.2×10^{-3}	b
Bi_2Te_3		+190	1.8×10^{-3}	b
Ge (thin film)	8.3×10^{-4}	+420	3.3×10^{-6}	c
InAs	2.0×10^{-5}	+200	8.0×10^{-5}	d, e
Bi_2Te_3	1.2×10^{-5}		2.2×10^{-3}	f
$Bi_2Te_3-25\%Bi_2Se_3$			2.7×10^{-3}	f
$Bi_2Te_3-10\%Bi_2Se_3$			2.8×10^{-3}	f
Negative thermoelements				
PbTe	7.7×10^{-6}		1.5×10^{-3}	b
Bi_2Te_3		−210	2.3×10^{-3}	b
Ge (thin film)	6.9×10^{-3}	−548	6.8×10^{-7}	c
InAs	2.0×10^{-5}	−180	2.7×10^{-5}	d, e
$InP_{0.1}As_{0.9}$			6.0×10^{-4}	d
Bi_2Te_3	8.2×10^{-6}		2.6×10^{-3}	f
$Bi_2Te_3-25\%Sb_2Te_3$			2.2×10^{-3}	f
$Bi_2Te_3-50\%Sb_2Te_3$			2.8×10^{-3}	f
$Bi_2Te_3-74\%Sb_2Te_3$			3.0×10^{-3}	f

[a] Van Herwaarden, A. W., The Seebeck effect in silicon IC's, *Sensors Actuators*, 6, 245, 1984.

[b] Goldsmid, H. J., *Applications of Thermoelectricity*, Butler and Tanner, London, 1960.

[c] Onuma, Y., Thermoelectric power of a vacuum deposited germanium thin film, *Electr. Eng. in Jpn.*, 89, 72, 1969.

[d] Kekelidge, N.P., Kuindadze, Z. N., Davitaya, Z. F., Eritayan, G. N., Saakyan, V. A., and Karapetya, E. K., Studies of thermoelectric characteristics of InP_xAs_{1-x} alloys, *Phys. Status Solidi A*, 38, K49, 1976.

[e] Hocking, E. F. et al., Thermal and electrical transport in InAs-GaAs alloys, *J. Appl. Phys.*, 37, 2879, 1966.

[f] Heikes, R. R. and Ure, R. W., *Thermoelectricity, Science and Engineering*, Interscience Publishers, New York, 1961.

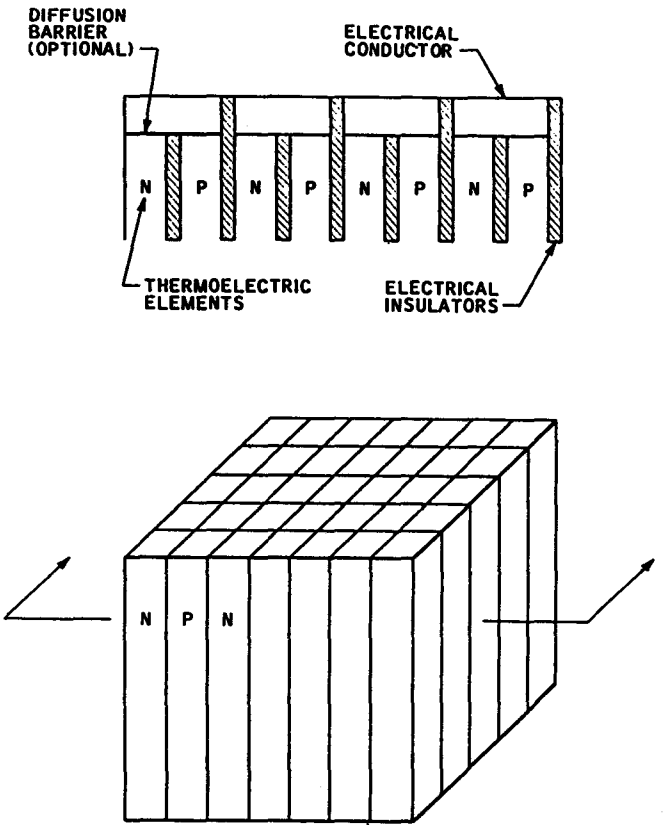

FIGURE 5 Typical monolithic module construction.

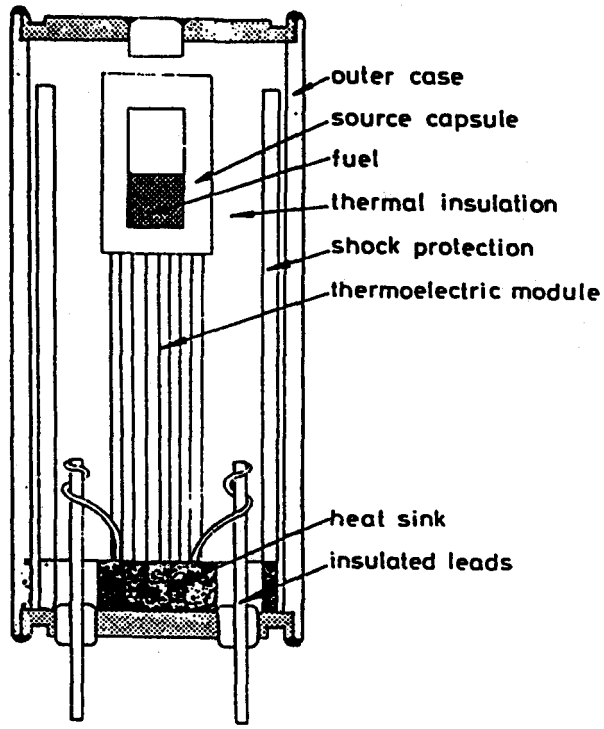

FIGURE 6 General layout of miniature nuclear battery (after Reference 8).

have been employed and include the use of metallic pastes, solders, vaporization, and pressure bonding.

The geometric arrangement of the modules around the heat source also requires careful consideration. An optimum configuration would appear to be washer-shaped modules located around the periphery of a cylindrical fuel capsule. Although such an arrangement possesses good mechanical strength, the required output power and voltage can only be achieved if the thermoelements are extremely thin, less than 0.001 in.[6] The configuration that has been almost universally adopted is a parallelepiped monolithic structure located at one or both ends of a cylindrical fuel capsule. A typical general layout is shown in Figure 6.

Applications

Although considerable effort was made in the development of monolithic thermoelectric generators for military and naval applications their power output is of the order of a watt and they do not fall into the miniature category. However, monolithic devices have found widespread medical applications in cybernetic devices where the power requirement is less than a milliwatt and they are essentially stimulators. The best-known medical application of miniature thermoelectric batteries is in the cardiac pacemaker. Pacemakers control heart rhythms by delivering electrical pulses to the muscle. A device manufactured by General Atomic (under license from Harwell UK) is shown in Figure 7.

Information relating to nuclear-powered thermoelectric batteries is collected in Table 3. Output power ranges from the 33 μW of the Coratomic battery to the 600 μW of the Atomcell™ battery. Of the seven batteries listed, four use bismuth telluride thermocouples, one uses silicon germanium thermocouples, one uses silicon p-n junctions, and one couplon-tophel wire tapes. The radioactive heat source (usually plutonium-238) is extremely poisonous and the amount used must be kept to a minimum. The battery manufactured by the Nuclear Battery Corporation uses evacuated multifoil insulation in an attempt to obtain the required output power[10] which is achieved with a

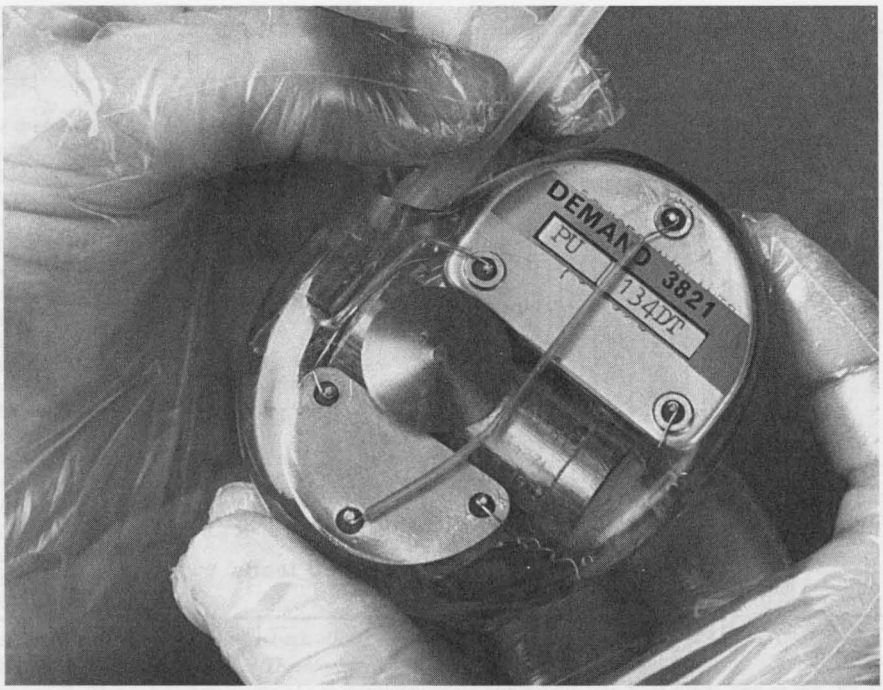

FIGURE 7 Pacemaker device (courtesy UKAEA).

Table 3 Nuclear Batteries for Cardiac Pacemakers

Manufacturer	Size cm	Weight grams	Output Power microwatts	Input Power watts	Conversion Elements	Thermal Insulation
1. Nuclear Battery Corp. Atomcell™	4.6 × 1.7D	28	600 @ .3 V	.080 (as PuO_2)	Bismuth telluride thermopile	Evacuated multifoil
2. General Atomic[1]	3.8 × 1.6D	26	400 @ .4 V	.100 (as PuO_2)	Bismuth telluride thermopile	1 atm inert gas
3. ARCO Nu-5[2]	6.5 × 3.2	120	200 @ end of 11 years	.226 (as PuO_2)	Cupron-Tophel wire tapes	Evacuated multifoil
4. McDonnell Douglas Betacel™	2.4 × 2.3D	98	370 @ 3.6 V BOL 70 μW @ 2.9 V after 5 years	.036 (as Pm_2O_3) (.009 after 5 years)	Silicon pn junctions	Not applicable
5. Syncal	3.8 × 1.3D	28	300 @ 5.0 V	.075 (as PuO_2)	Silicon germanium thermopile	Evacuated multifoil
6. CIT-Alcatel[3]	4.7 × 2.3D	30	250 @ .55 V	.096 (as PuO_2)	Bismuth telluride thermopile	Fibrous insulation
7. Coratomic[4]	6 × 4.70 × 1.92	61	33 @ 4.05 V	.142 (as PuO_2)	Bismuth telluride thermopile	Evacuated multifoil

[1] General Atomic possesses the license to manufacture the Harwell battery in the U.S. This battery was initially developed by the British Atomic Energy Research Establishment at Harwell, England.

[2] This pacemaker was developed under sponsorship of the U.S. Atomic Energy Commission. Size and weight numbers refer to the total pulse generator. Four of six redundant tapes can fail and unit will still operate.

[3] Fuel capsule for Alcatel battery was developed by the French Atomic Energy Commission (CEA).

[4] Size, weight, and output refer to total pulse generator.

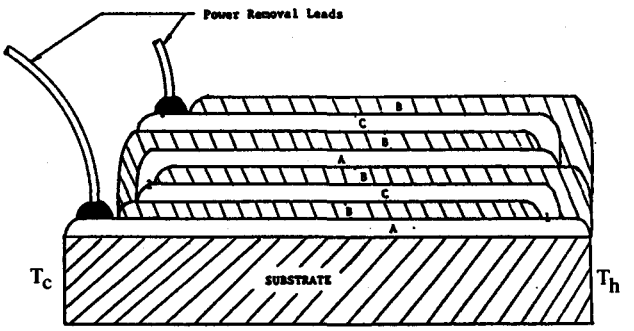

FIGURE 8 Vacuum-deposited thin films (after Reference 15).

minimum of nuclear fuel loading by using evacuated multifoil insulation. Maintaining battery integrity under extreme conditions is also critically important in clinical applications and the batteries are subjected to exhaustive safety tests.

Usually the required voltage is achieved using a DC-to-DC converter but the Syncal battery, using silicon germanium thermoelements, does not require a separate convertor.[11] The performances of the CIT-Alcatel and Medronoc Laurene-Alacatel Model 9000 have been described in a number of publications (see Reference 9). This battery was used in the first implant, which took place at Hospital Broussais, Paris, in April 1970.

Films and Tapes

The machining limitations imposed by the semiconductor material properties resulted in the development of films or tapes as alternative methods of fabricating thermocouples with extreme geometry. Early attempts at fabricating thin-film semiconductor thermocouples involved the deposition of bismuth and antimony, bismuth and tellurium, and n- and p-type lead telluride.[12] However, serious problems were encountered associated with the thermoelectric properties changing with time.

An early investigation into the use of thin films for power generation was undertaken by Abowitz et al.[13] with thin-film thermoelements being deposited onto glass slides in single layers with the number of elements being limited by the size of the substrates. The n-leg was fabricated from Bi_2Te_3 (75 w/o) + Bi_2Se_3 (25 w/o) plus halogen compound, and the p-leg from Bi_2Te_3 (25w/o) + Sb_2Te_3 (75 w/o) plus excess Te. Annealing the films at 350°C after deposition resulted in Seebeck coefficients in good agreement with bulk material. Fractionation of the films was also minimized by heating the source extremely rapidly.

A method for making thermoelectric generators using a chemical vapor deposition technique was patented by Thorp.[14] Unlike Abowitz's configuration the thermoelements are stacked one on top of another, being electrically insulated by layers of SiO_2. A suggested material for the thermoelements was n- and p-type silicon germanium alloy.

Attempts to fabricate very small DC power supplies capable of large voltage outputs were made as early as 1972,[15] as shown schematically in Figure 8. The proposal was to vacuum-deposit thin films to make thousands of thermoelectric couples in a small volume. Thermoelectric material and insulators would be deposited onto a thin substrate to create a multistage thermoelectric generator in which the legs were deposited on top of one another. Elemental bismuth and antimony were chosen to test the feasibility of the concept. The electrical properties of the deposited films were shown to agree to within about 10% of that of bulk material. However, the proposal met with limited success, as only a single couple was fabricated due to pin-holing of the insulation between the thermoelements.

Siemens of Germany[16] developed a conversion system intended as a cardiac pacemaker battery consisting of thin-film thermocouples deposited by a flash evaporation technique onto a type of polyamide as a substrate. The device is shown in section in Figure 9. ZnSb was the p-type material

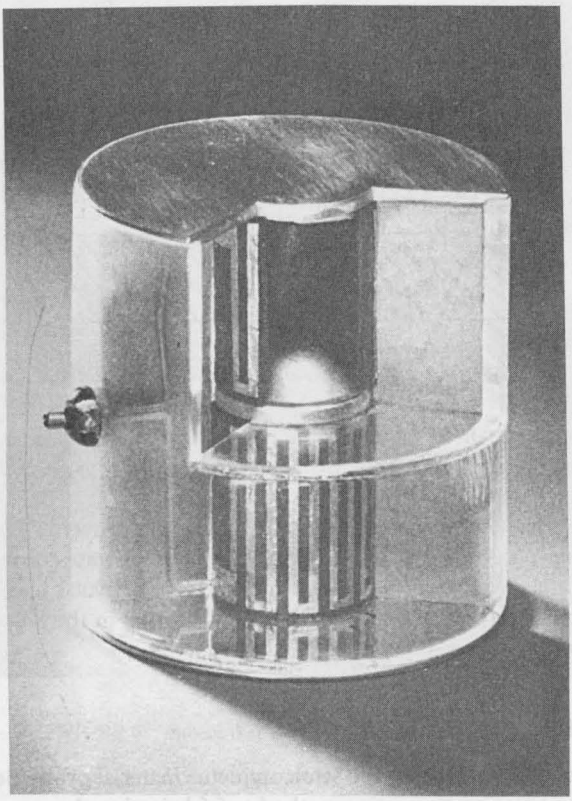

FIGURE 9 Isotopic battery, showing fuel capsule and tape generator (after Reference 16).

and bismuth the n-type, the latter being later replaced with Bi_2Te_3. Two tapes are connected in parallel to ensure reliability and upwards of 700 thermocouples of Bi_2Te_3/ZnSb give 3 to 6 V under load. The authors presented expressions which expressed the pertinent operating data such as output voltage, power, and conversion efficiency as a function of tape length (i.e., the number of thermocouples) and layer thickness. The results of these calculations corresponding to a thermal input power of 100 mW are displayed in Figure 10.

The possibility of powering a watch using the heat from the human body resulted in the conceptual generator shown in Figure 11.[17] The thermocouples are prepared by depositing germanium and indium antimonide on the two sides of an insulator about 1 mm thick (simulating a watch strap), connections between the thermoelements being made with metallic strips. It was estimated that 2875 elements, connected in series, would be required to obtain the required 2 V at 1 W.

Although ultimately intended as a low-cost, mass-produced, thermoelectric material for large-scale thermoelectric energy conversion,[18,19] thin films based on the bismuth telluride system have also been deposited by vacuum deposition onto a 25 μm thick milar substrate. Film thickness was usually of the order of 1 μm. The preparation of films of thermoelectric material using a screen printing and sintering process has also been reported.[20] Also intended for use in large-scale power conversion, thick-film thermoelements of about 0.3 mm thick have been manufactured using this technique.[21] The composition of the p-type and n-type starting material was (Sb_2Te_3) 72 at.%, (Bi_2Te_3) 25 at.%, (Sb_2Se_3) 3 at.% plus dopant, and (Bi_2Te_3) 95 at.%, (Sb_2Se_3) 5 at.% plus dopant, respectively. The typical element size was 4 mm × 5 mm × 0.3 mm. Although the Seebeck coefficient of the film material compared favorably with that of the bulk material the figures-of-merit of both n- and p-type thick-film elements were shown to be only about one half to one third of that of the bulk element, which was principally due to an increased electrical resistivity.

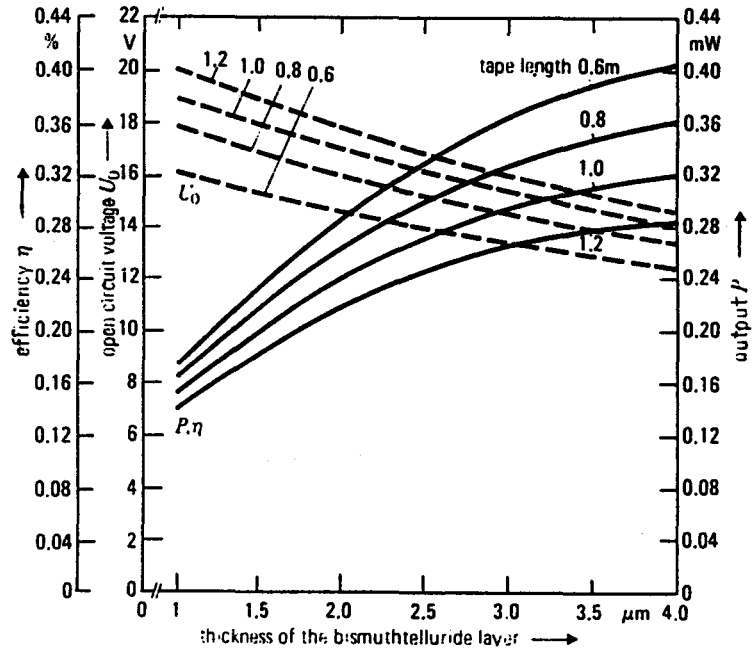

FIGURE 10 Output efficiency and open current voltage as a function of the thickness of the deposited layers and of the tape length of a Bi_2Te_3/ZnSb thermocouple. α = 360 μV/K thermal power of the heat source as 100 mW (after Reference 16).

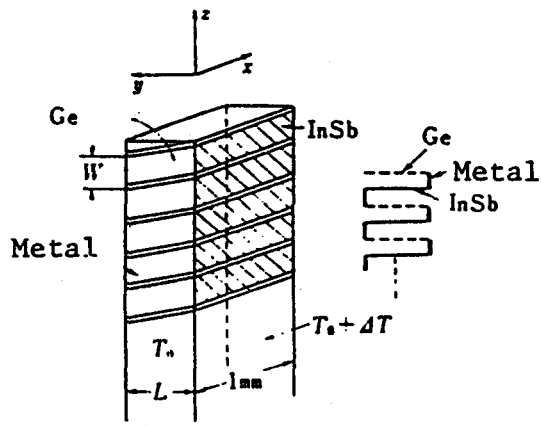

FIGURE 11 Conceptual watch-strap generator (after Reference 17).

Integrated Circuit Technology

Integrated circuit technology readily lends itself to the fabrication of miniature low-power, high-voltage sources and to detectors/sensors, the latter being covered in Section 35.4.

An industrial requirement for a long-life voltage source which was independent of the electric utilities resulted in the development of a thermoelectric convertor which generates 1.5 V when a temperature difference of a few degrees is established across its thermoelements.[22] SOS (silicon on sapphire) technology, which was readily available, was used to demonstrate the feasibility of the fabrication method. Wafers of near-intrinsic silicon (>100 Ω cm) which had been epitaxially

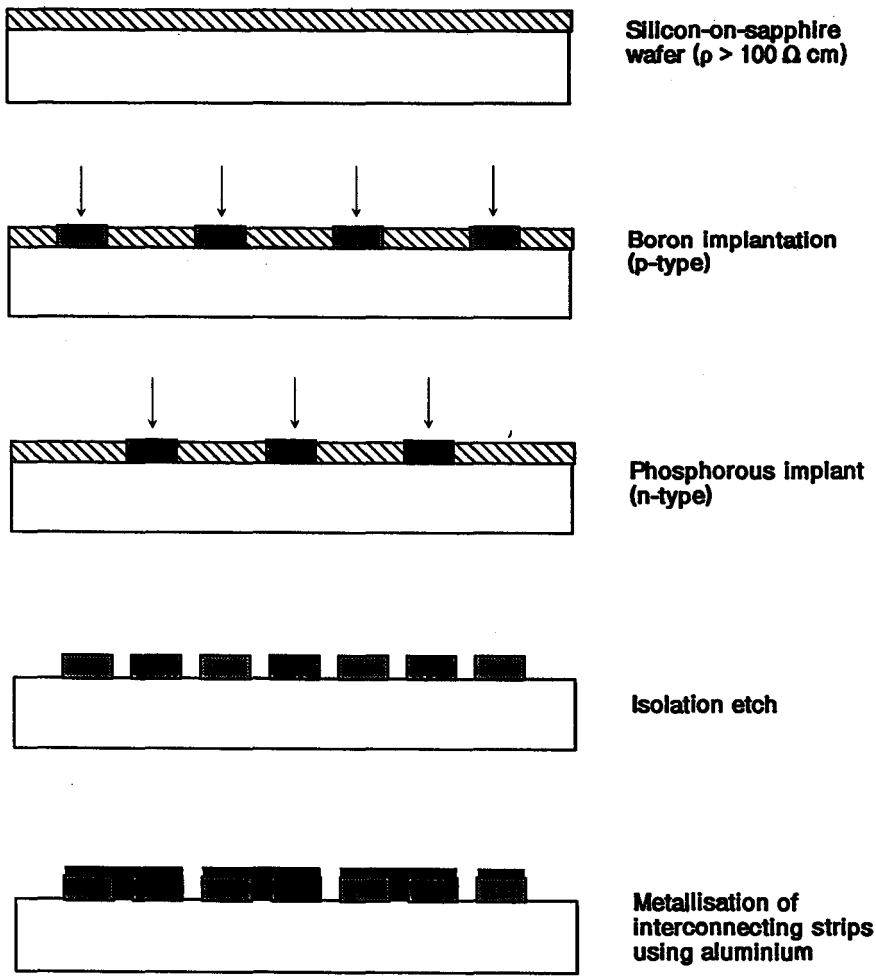

FIGURE 12 SOS fabrication sequence (after Reference 24).

grown on sapphire were used as the substrate.[23] The second phase of the work involved the deposition of polycrystalline silicon on a quartz substrate.[24]

A typical fabrication sequence for both silicon on sapphire and polycrystalline silicon on quartz is shown in Figure 12. The p- and n-type strips were produced by ion implantation. This technique enables precise control to be maintained over the depth of the implanted ions and their number and, consequently, the geometry and transport properties of the thermoelements. Phosphorus and boron are widely employed in implantation and relevant implantation data were available.[25] An optical microphotograph of the generator chip is shown in Figure 13.

35.4 Detectors/Sensors

General Considerations

Descriptions of the general construction, mode of operation, and parameters that govern the performance of infrared detectors and thermal sensors are dealt with in Chapter 55. Only a brief coverage will be given here. The principal parameters that are used to evaluate the performance of an infrared detector are responsivity, spectral response, time constant, and detectivity.

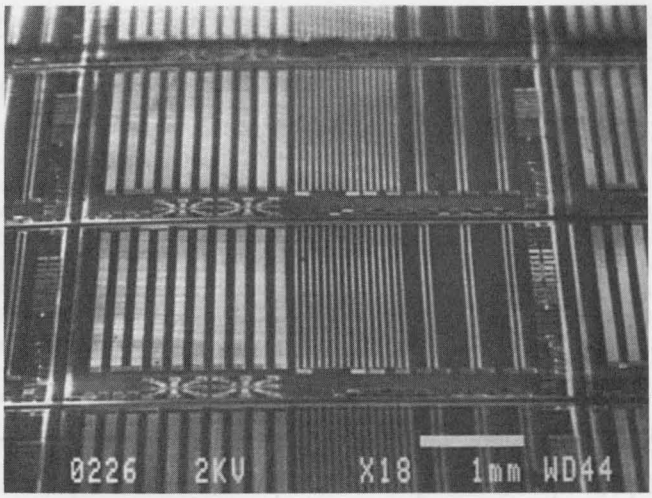

FIGURE 13 Scanning electron micrograph of a typical chip on a wafer.

The responsivity, RV(volts/watt), is given by the ratio of the open circuit voltage to the power incident on the detector. Spectral response—in theory, within the infrared region of the spectrum—thermal detectors should be independent of the wavelength of the incident radiation; however, in practice, different materials used in the detector have different absorption coefficients. The response speed of the detector is determined by its time constant. Typical values are 10 to 100 msec. Finally, detectivity is the reciprocal of the minimum detectable power and is defined as the minimum incident radiation which produces a signal-to-noise ratio of unity.

Infrared Detectors/Thermopiles

Infrared detectors can be classified into thermal detectors and photon detectors.[26] Photon detectors do not depend upon thermoelectric phenomena for their operation and will not be discussed further. In infrared thermal detectors, radiation is absorbed at the sensitive region of the detector, which heats up. A temperature difference is established across the thermocouples and an electrical signal generated by the Seebeck effect.

Although germanium films suitable for detector application have been deposited on very small flexible organic substrates using replica techniques,[27] conventional thermopiles are fabricated by evaporating a thin film of thermoelectric material through a shadow mask onto a thin plastic or alumina substrate.[28,29] Sputtering procedures have also been employed.[30] However, this fabrication technology does not lend itself to batch fabrication production methods. Silicon technology has been applied to the fabrication of a basic silicon thermopile infrared detector structure.[31] A monolithic silicon thermopile detector fabricated using integrated circuit technology is shown in Figure 14. Typical performance characteristics of some thin-film thermopiles are summarized in Table 4.

Anatychuk et al.[32] have described the fabrication of a thin-film thermoelectric battery based on silicon for pyrometer application. The p-type material based on bismuth telluride is deposited onto the oxide layer by magnetron sputtering. The stages in fabricating the device and a general view of the receiver are given in Figures 15 and 16.

Thermal Sensors

Thermal sensors are similar to infrared detectors, inasmuch as they operate by establishing a temperature gradient across a thermopile, but in these devices the heat detected is transferred by conduction and convection rather than radiation. The production of thermal sensors by evaporating

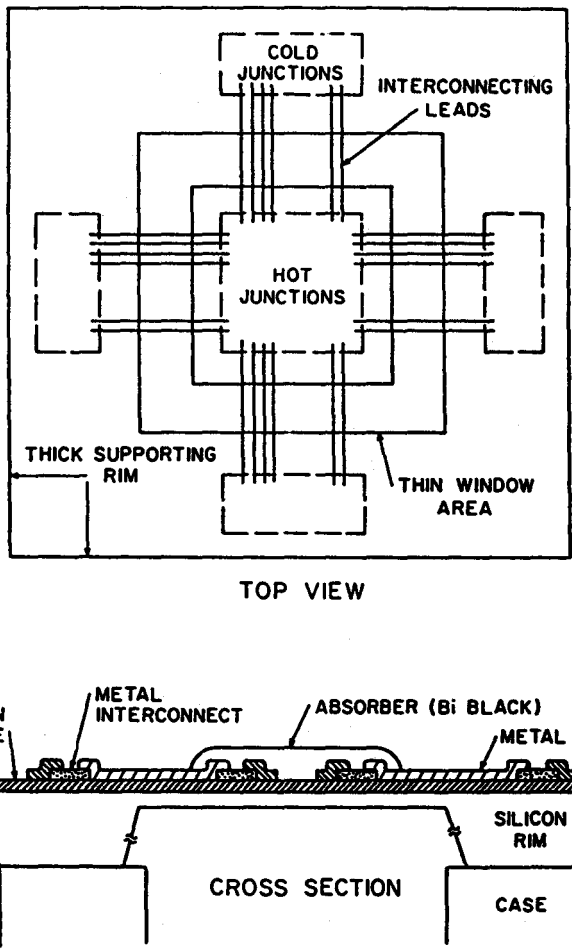

FIGURE 14 Monolithic silicon thermopile detector fabricated using integrated circuit technology (after Reference 31).

semiconductor thermoelements onto electrically insulating substrates has resulted in a substantial increase in sensitivity compared to traditional metal wire thermocouples formed from NiCr-NiAl. BiTeSb and PbTe have also been deposited with Seebeck coefficients of 160 μ V K^{-1} and 500 μ V K^{-1}, respectively.[33] A comprehensive review of the construction and application of thermal sensors has been given by Van Herwaarden and Sarro.[3] A variety of silicon integrated thermal sensors has also been fabricated.[34] An integrated thermopile can be used in one of two ways. It can be integrated into the silicon chip which is mounted on its substrate and used to detect temperature differences. In this case the silicon substrate, which is considerably thicker than the thermopile structure, acts as an effective thermal shunt and reduces the device's sensitivity. An alternative method, which results in significantly increased sensitivity, is to remove the silicon by means of micromachining, resulting in a membrane or cantilever beam structure supporting the thermopile. Various other structures, such as the floating membrane, are also employed, as shown in Figure 17. Integrated thermopiles have been used to measure the amplitude of AC signals,[35] as a true rms converter,[36] a vacuum sensor,[37–40] and as a flow sensor.[41,42]

Table 4 Typical Performance Characteristics of Some Thermopile Infrared Detectors (after Reference 3)

Number of Couples	Materials	Active Area (mm^2)	Sens. (V/W)	Time Constant (msec)	R_{tp} (kΩ)	D^* 10^8 cm $Hz^{1/2}/W$	Ref.
6		1	15	80	8	1.3	a
15		0.78	23.5	32	3	3.0	a
12		0.78	9.5	40	3.25	1.1	a
60	Bi-Sb	0.36	6	15	36	0.6	b
60	p-polySi Au	0.36	7	15		0.35	b
60	n-polySi Au	0.36	9.6	15		0.48	b
32	n-polySi Au		20–25	25	73–82	0.5–0.6	c
32	p-polySi Au		52–56	25	220–280	0.68–0.73	c
54	Te-InSb	1	95	30	500	1.1	d
11	Te-Ag		1.1	300	70		e
50	Bi-Sb	1	30–50	15–30	20	3	f
44	(p)Si-Al	7.3	10.6	128	50	1.05	g

[a] Wollman, L. R., The thermopile: the commercial infrared detector, *Electro-Opt. Syst. Des.*, 37, 1979.

[b] Lahiji, G. R. and Wise, K. D., A batch-fabricated silicon thermopile infrared detector, *IEEE Trans. Electron Devices*, ED-29, 14, 1982.

[c] Choi, I. L. and Wise, K. D., A silicon-thermopile-based infrared sensing array for use in automated manufacturing, *IEEE Trans. Electron Devices*, ED-33, 72, 1986.

[d] Shibata, C., Kimura, C., and Mikami, K., Far infrared sensor with thermopile structure, *Proc. 1st Sensor Symp. Japan*, 1981, p. 221.

[e] Kimura, M., Microbridge infrared detector, *Proc. 1st Sensor Symp. Japan*, 1981, 227.

[f] Elbel, Th., Muller, J. E., and Volklein, F., Miniaturisierte thermische Strahlungssensoren: Die neue Thermosaule TS-50.1, *Feingeratetechnik (Berlin)*, 34, 113, 1985.

[g] Sarro, P. M. and van Herwaarden, A. W., An integrated silicon thermopile infrared detector, accepted for presentation at ESSDERC '86, Cambridge, U.K., Sept. 1986.

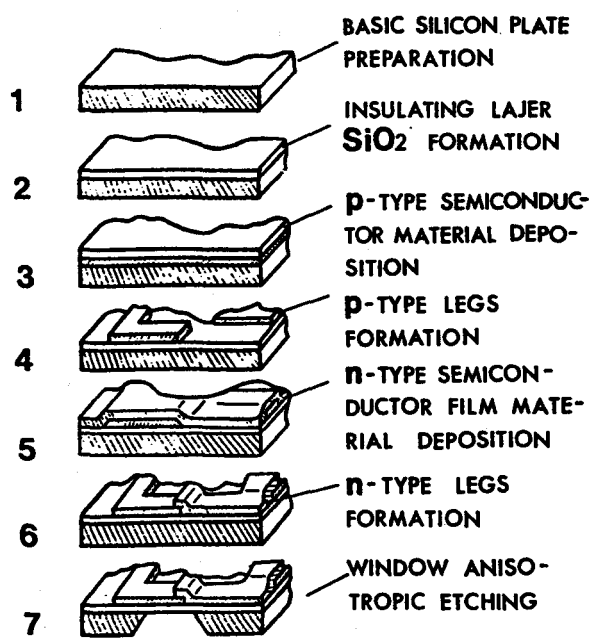

FIGURE 15 Fabrication steps of film thermoelectric "receiver" (after Reference 32).

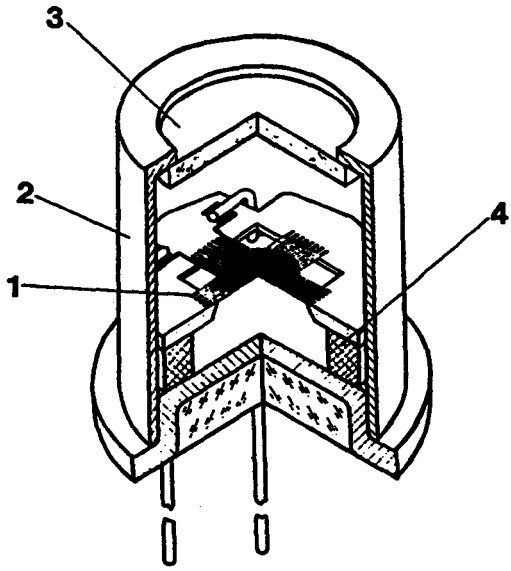

FIGURE 16 General view of receiver (after Reference 32).

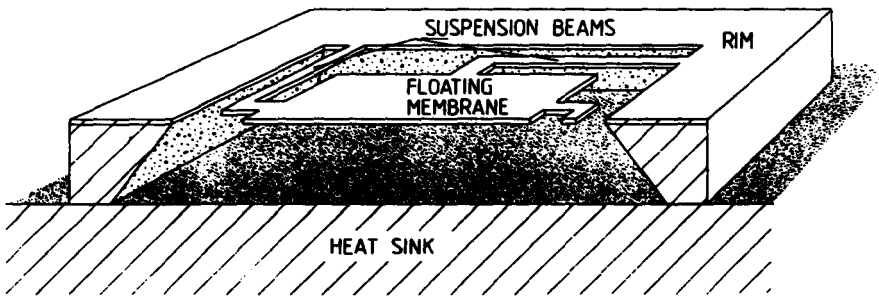

FIGURE 17 Floating membrane structure (after Reference 34).

35.5 Discussion and Conclusion

The technology for fabricating thermoelectric devices which generate milliwatts of electrical power at relatively high voltages using monolithic "bundles" of thermocouples is well established. However, as the devices are generally fueled by a radioactive source, their application has been restricted to situations where their proven reliability outweighs their relatively low efficiency and high cost. In recent years the development of integrated circuit technology for the microelectronics industry has provided an ideal pick-a-back for the miniaturization of generators and sensors. Both devices can be mass-produced with reproducible performance. Future developments in thermoelectric sensor technology are assured with the commercial market expanding rapidly on a broad front. Although integrated circuit technology enables miniature low-power, high-voltage devices to be incorporated in a semiconductor chip, to date this device has not been commercially exploited. However, future developments in microelectronics, with a relentless drive towards smaller and smaller circuits, are likely to be accompanied by a requirement for localized integrated power and voltage sources.

References

1. Rowe, D. M., Morgan, D. V., and Keily, J., Fabrication of a miniature thermoelectric generator, *Proc. 8th International Conference on Thermoelectric Energy Conversion,* (Eds) Scherrer, H. and Scherrer, S., Nancy, France, July 10–13, 1989, 133.
2. Stapfer, G. and Carroll, W., Thermoelectric Power Conversion for SP-100, *Proc. 8th International Conference on Thermoelectric Energy Conversion,* (Eds) Scherrer, H. and Scherrer, S., Nancy, France, July 10–13, 1989, 143.
3. Van Herwaarden, A. W. and Sarro, P. M., Thermal sensors based on the Seebeck effect, *Sensors Actuators,* 10, 1986, 321.
4. Notaro, F., Nies, C. E., and Hedel, R., Multi-layer vacuum insulation and its application to a silicon germanium converter, *Proc. IVth IECEC,* Washington, D.C., September 22–26, 1969, 400.
5. Paquin, M. L., The multi-foil thermal insulation development programme, *Proc. IVth IECEC,* Washington, D.C., September 22–26 , 1969, 408.
6. Raag, V., Review of thermoelectric conversion in micro/milliwatt power range for bio-medical applications, *Proc VIth IECEC,* Boston, MA, August 3–5, 1971, 245.
7. Caputo, R. S. and Truscello, V. C., Two-watt radioisotope power generator for underwater applications, *Proc. IXth IECEC,* San Francisco, CA, August 26–30, 1974, 637.
8. Penn, A., Small electrical power sources, *Phys. Technol.,* 5, 114, 1974.
9. Gasper, A. and Fester, K. E., Cardiac pacemaker power source, *Proc. Xth IECEC,* University of Delaware, Newark, NJ, August 18–22, 1975, 1205.
10. Greathatch, W. and Bustard, T. S., A Pu238O2 nuclear power source for implantable cardiac pacemaker, *IEEE Trans. Biomed. Eng.,* BME-20, (No. 5), September 1973.
11. Raag, V., The use of silicon germanium alloys in radioisotope thermoelectric generators, *Proc. XIth IECEC,* State Line, Nevada, September, 1976, 1586.
12. Vacuum deposited thermocouple development, Denver Research Institute Armed Services Technical Information Agency, AS278384, 1962.
13. Abowitz, G., Klints, V., Levy, M., Lancaster, D., and Mountvala, A., Thin film thermoelectrics, *SCP Solid State Technol.,* February 1965, 18.
14. Thorp, W., Manufacture of thermoelectric generators, U.S. Patent 3434203, 1969.
15. Collier, R. K. and Backus, C.E., Thin film thermoelectric generators, *Proc. VIIth IECEC,* San Diego, CA, September 25–29, 1972, 216.
16. Renner, T., Rittmayer, G., Falkenberg, D., and Grubmiller, An isotopic thermoelectric battery for cardiac pacemakers, *Proc. IInd International Symposium on Power from Radioisotopes,* Madrid, 1972, 207.
17. Sakai, S., Takeda, S. I., Onuma, Y., and Kobayashi, M., Thermoelectric properties of deposited semiconductor films and their application, *Electrical Engineering in Japan,* Vol. 105, 2, 1985, 387.
18. Trefny, J. U. and Jayadev, T. S., Thermoelectric properties of bismuth-antimony thin films, *Proc. XVth IECEC,* Seattle, WA, August 18, 1980.
19. Trefney, J. U., Bi-Sb thin films for thermoelectric energy conversion, *Proc. XVIth IECEC,* Atlanta, GA, 1981, 2019.
20. Ohta, T. and Kajikawa, T., Thermoelectric properties of chalcogenides based on thick film elements for low temperature operation, *Proc. VIth International Conference on Thermoelectric Energy Conversion,* University of Texas at Arlington, 1986, 55.
21. Kajikawa, T. and Ohta, T., Chalcogenides based thick film thermoelectric elements for power generation module, *Proc. Ist European Conference on Thermoelectrics,* University of Wales, Cardiff, (Ed) Rowe, D. M., 1987, 330.
22. Rowe, D. M., Miniature Thermoelectric Convertors, U.S. Patent No. 14698, 1988.
23. Rowe, D. M., Morgan, D. V., and Keily, J., Miniature low-power/high voltage thermoelectric generators, *Electron. Lett.,* 25 (No. 2), 166, 1989.
24. Keily, J., Morgan, D. V., Rowe, D. M., and Humphreys, J., Low cost miniature thermoelectric convertor, *Electron. Lett.,* 27 (No. 25), 2332, 1991.
25. Carter, G. and Grant, W. A., *Ion Implantation of Semiconductors,* Edward Arnold, London, 1976.
26. Smith, R. A., Jones, F. E., and Chasmer, R. P., *The Detection and Measurement of Infra-Red Radiation,* Clarendon Press, Oxford, England, 1968.

27. Onuma, Y. and Sakai, Y., Preparation of replicated germanium films and their application to sensors, *J. Appl. Phys.*, 44 (No. 7), 3046, 1973.
28. Smith, R. A., Jones, F. E., and Chasmar, R. P., *The Detection and Measurement of Infra-Red Radiations,* Oxford University Press, New York, 1957.
29. Wolfe, W. L. and Zissis, G. H., *The Infra-Red Handbook,* The Infra-Red Information and Analysis (IRIA) Centre, Environmental Research Institute of Michigan, 1978.
30. Wollman, L. R., The thermopile: the commercial O + IR detector, *Electro-Opt. Syst. Des.*, 37, 1979.
31. Lahiji, G. R. and Wise, K. D., A batch fabricated silicon thermopile infra-red detector, *IEEE Trans. Electron Devices,* ED 29 (No. 1), 14, 1982.
32. Anataychuk, L., Thermoelectric batteries for pyrometers, *Xth International Conference on Thermoelectrics,* University of Wales, Cardiff, September 10–12, 1991, (Ed) Rowe, D. M., 108.
33. Chudnovskii, A. F. and Shinderov, B. L., Semiconductor thermoelectric elements as radiation temperature sensors, *Inzh. Fiz. Zh.*, 20 (No. 4), 633, 1971.
34. Van Herwaarden, A. W., Van Duyn, D. C., Van Oudheusden, B. W., and Sarro, P. M., Integrated thermopile sensors, *Sensors Actuators,* A21-A23, 621, 1989.
35. Kerkoff, H. Q. and Meijer, G. C. M., An integrated electrothermal amplitude detector using the Seebeck effect, *Proc. ESSCIRC,* Southhampton, UK, 1979, 31.
36. Van Herwaarden, A. W., Hockstenback, H. P., and Hermans, C. J. P. M., Integrated true RMS converter, *IEEE Trans. Instrum. Meet.*, IM-35, 1986, 224.
37. Van Herwaarden, A. W. and Sarro, P. M., Double beam integrated thermal vacuum sensors, *J. Vac. Sci. Technol.*, A5 (4), 2454, 1987.
38. Van Herwaarden, A. W. and Sarro, P. M., Integrated vacuum sensor with extended range, *Vacuum,* 38, 449, 1988.
39. Van Herwaarden, A. W. and Sarro, P. M., Floating membrane thermal vacuum sensors, *Sensors Actuators,* 14, 259, 1988.
40. Van Herwaarden, A. W. and Sarro, P. M., Performance of integrated thermopile vacuum sensors, *J. Phys. E.*, 21, 1162, 1988.
41. Van Oudheusden, B. W. and Huijsing, J. H., An electronic wind metre based on a silicon flow sensors, *Sensors Actuators,* A21-A23, 420, 1990.
42. Van Oudheusden, B. W. and Van Herwaarden, A. W., High sensitivity 2-D flow sensor with an etched thermal isolation structure, *Sensors Actuators,* A21-A23, 425, 1990.

36

Commercially Available Generators

Alan G. McNaughton
Global Thermoelectric Inc.
Calgary, Canada

36.1 Introduction

Thermoelectric generators (TEGs) have been available commercially since the early 1960s. They have been used since that time in industrial applications all over the world. Over 20 different models of thermoelectric generators are currently available with power outputs ranging from 10 to 550 W.

The four primary characteristics of TEGs that make them desirable and economic to use are high reliability, a long interval between service, low maintenance, and a long life. Most TEGs are relied on to operate continuously for over 8000 h, then be serviced for a few hours with minimal part replacement, and then be put back into operation for another year. TEGs that have been in service since the early 1960s have come back in the 1990s for overhaul and update of their fuel system and electronics because the thermoelectrics are still sound after 30 years of operation.

36.2 Available Generators

There are currently two companies that regularly manufacture commercial thermoelectric generators: Teledyne Energy Systems in the U.S. and Global Thermoelectric Inc. in Canada. Both companies offer a range of generators and market them worldwide. Most of the generators that are sold operate on gaseous fuels such as propane (C_3H_8) or natural gas (CH_4). A few generators operate on liquid fuels, primarily diesel.

Gas-Fueled Generators

All of the currently available generators that operate on gaseous hydrocarbon fuel are intended for stationary outdoor applications. The vast majority of the generators are used in applications where they operate 24 hours per day, 365 days of the year. The generators have been designed so that they need maintenance only once per year when used continuously. Figure 1 shows a pole-mounted 220-W generator located in a forest in western Canada.

The output of these generators is fixed. The generators produce a constant amount of power regardless of the power draw of the equipment being powered.

Table 1 lists the gas-fueled generators currently offered, excluding hazardous area generators.

0-8493-0146-7/95/$0.00+$.50

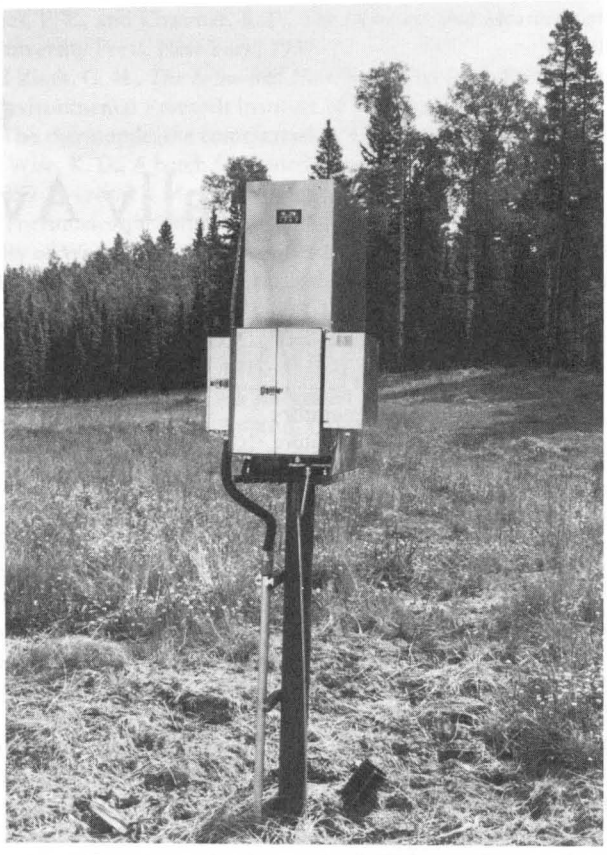

FIGURE 1 A 220-W TEG mounted on a pole.

Table 1 Gas-Fueled TEGs

Manufacturer	Basic Model	Nominal Wattage	Natural Voltage	Watts at 12 V DC	Watts at 24 V DC	Fuel (LPG) kg/d	Price[a] USD
Teledyne	2T1	10	4.8	8	8	0.73	2295
Teledyne	2T2	20	9.6	17	17	1.46	2995
Global	5030	30	2.5	24	24	1.50	2715[b]
Teledyne	2T3	30	14.4	30	25	2.19	3420
Teledyne	2T4	40	19.2	36	36	2.91	4295
Global	TCELL50	50	3.5	40	40	2.90	2284
Teledyne	2T5	50	24	50	50	3.63	5075
Global	5060	60	6.7	54	54	2.90	5220
Teledyne	2T6	60	28.8	60	60	4.36	5975
Teledyne	2T7	70	33.6	68	68	5.09	6895
Teledyne	2T8	80	38.4	79	74	5.81	7800
Teledyne	2T9	90	43.2	90	89	6.54	8500
Global	5120	120	6.7	108	108	5.8	5481
Global	5220	220	15	220	176	14.2	8039
Global	8550	550	27	480	550	38.0	16443

[a] Prices are based upon manufacturers' published list prices. Prices are in U.S. dollars.
[b] Price includes a DC-DC convertor.

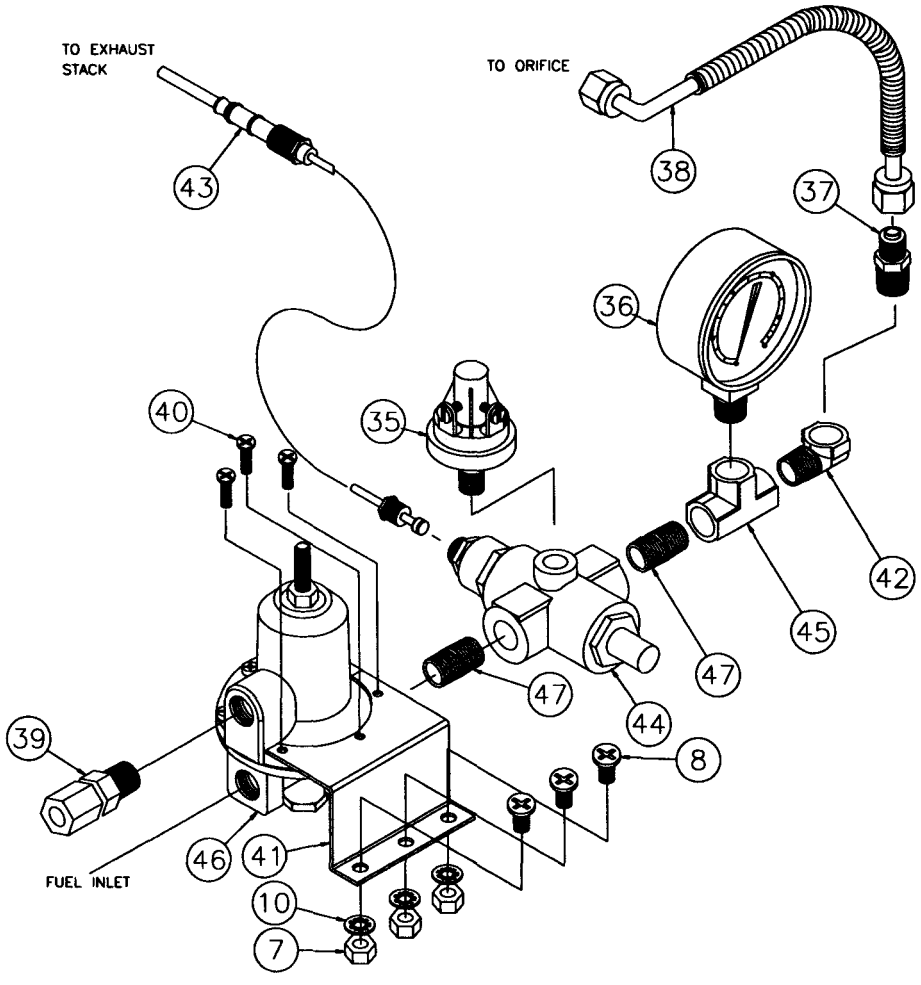

FIGURE 2 Typical fuel delivery system complete with automatic gas shut off. (See Legend to Figures located at the end of the chapter.) (From Global Thermoelectric, Inc., Calgary, Canada. With permission.)

Generator Construction

A complete thermoelectric generator system consists of much more than the thermoelectrics. A useful generator must also have a fuel system, a burner, a heat sink, cabinet or housing, and electronics. These other systems make up a considerable portion of the cost and complexity of a complete generator. They also must be designed with care or they detract from the inherent advantages of thermoelectrics: reliability and low maintenance.

Fuel System

The primary function of the fuel system in a typical TEG is to regulate the gas pressure of the supplied fuel to an appropriate and constant pressure. All of the gas-fueled generators offered by Global and Teledyne use fixed-opening orifices and regulated gas pressure to control the amount of fuel delivered to the burner. The only adjustment on these generators to compensate for the varying energy content of various gas sources is the fuel pressure. In most applications the outlet fuel pressure is only adjusted once per year.

In most generators the only difference between the models that operate on propane (also known as liquified petroleum gas or LPG) and those that operate on natural gas is the size of the fuel orifice. This makes it a simple process to change from one type of fuel to another. An exploded view of a typical fuel system is shown in Figure 2.

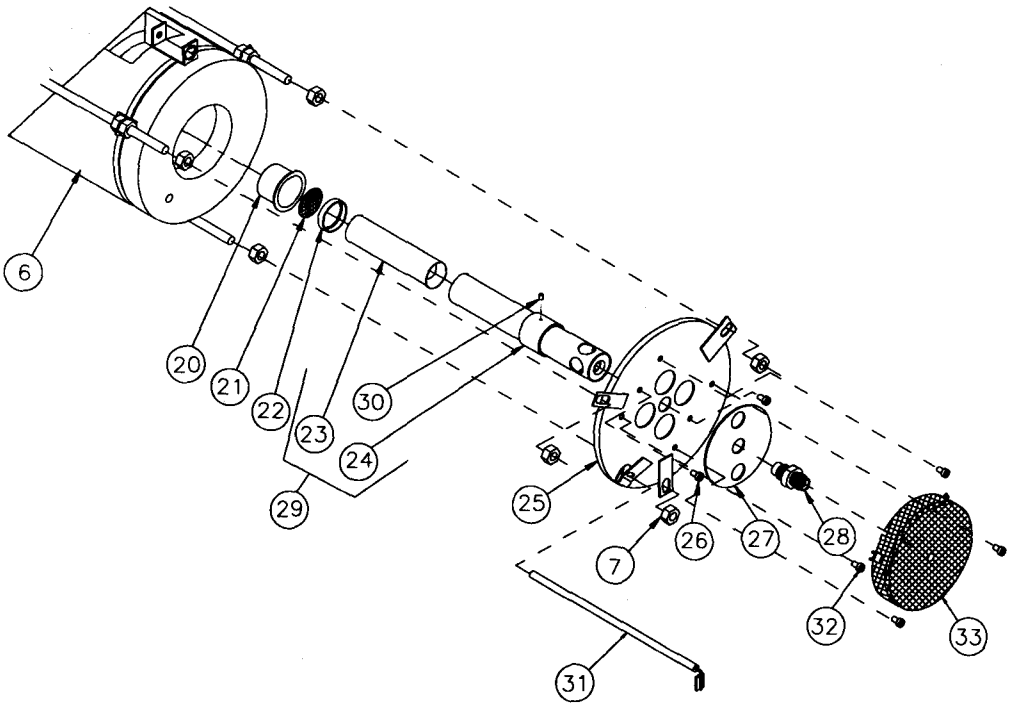

FIGURE 3 Exploded view of a typical TEG burner. (See Legend to Figures located at the end of the chapter.) (From Global Thermoelectric, Inc., Calgary, Canada, *User's Manual.* With permission.)

The fuel systems in some generators include a small filter. Any major particulate filtration or other gas cleanup, such as sulfur or water removal, is not part of the standard generators. These fuel cleanup systems, when needed, are added upstream of the generator. They are usually not needed when commercial propane or natural gas is used. They are occasionally required when natural gas is used directly from a gas well.

The fuel systems use the pressure of the gaseous fuel to deliver the fuel and combustion air to the burner. The fuel system and burner can then be designed with no moving parts.

Burner

The burner of a TEG must combust the fuel to create heat in sufficient quantity, at appropriate temperatures, and with even heat distribution. All of the currently available generators are intended for outdoor use in many climactic extremes. The burners must, therefore, continue to operate in high winds, at extreme ambient temperatures and humidities, and in heavy snow and rain.

Two types of burners are used, open-flame burners, known as "meeker" burners, and catalytic burners. The catalytic burners have a lower temperature than meeker burners and are used with bismuth telluride thermoelectrics. Meeker-type burners are used with all of the lead telluride TEGs. An exploded view of a meeker-type burner is shown in Figure 3 and a cut-away view is shown in Figure 4.

The burners can be started with a match or, as is more commonly done, with a high-energy spark. Some burners are designed to restart automatically if the burner goes out or if the fuel supply has been interrupted and has been restored.

Thermoelectric Convertor

The thermoelectric convertor of a TEG is located between the burner and the heat sink, as shown in Figure 5. It converts a small portion of the heat passing through it into electricity. Typically between 4 and 9% of the heat that enters the thermoelectric convertor is turned into electricity. The efficiency is dependent upon the generator model and construction, the type of thermoelectric

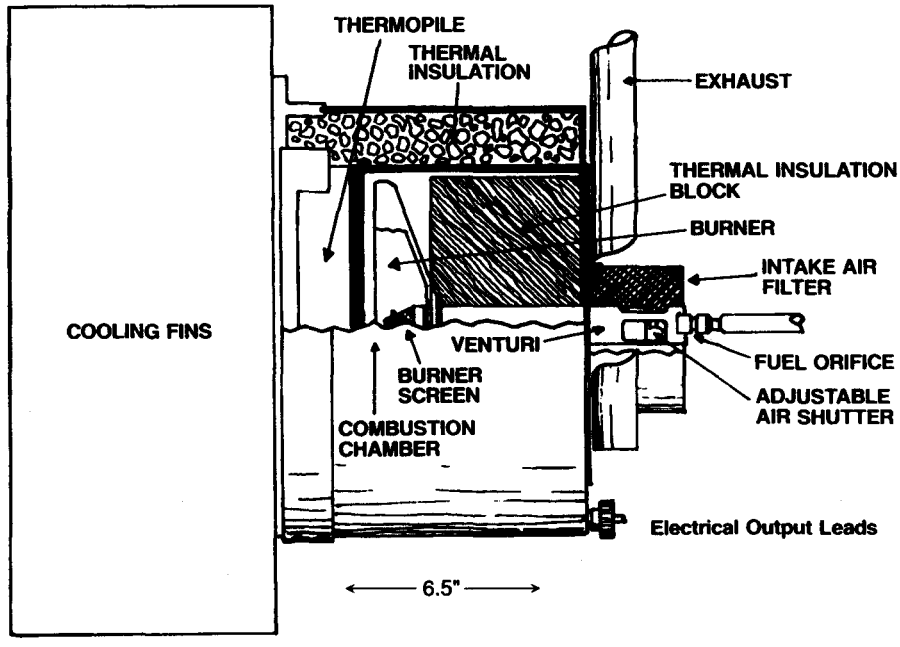

FIGURE 4 Cut-away view of a burner for a gas-fueled TEG. (From Global Thermoelectric, Inc., Calgary, Canada, *User's Manual.* With permission.)

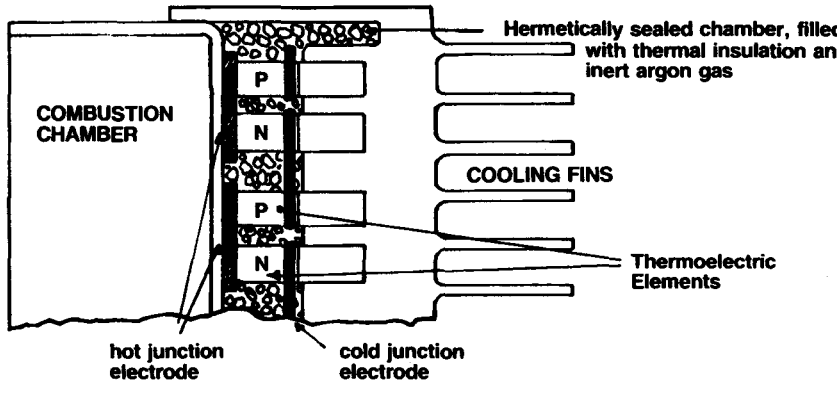

FIGURE 5 Thermoelectric convertor, cut-away view (not to scale). (From Global Thermoelectric, Inc., Calgary, Canada, *User's Manual.* With permission.)

material used, and the ambient temperature. In a typical TEG, over half of the heat produced does not even pass through the thermoelectric convertor; it is lost through the walls of the burner and thermoelectric convertor, and out the exhaust.

The thermoelectric convertors used in commercial TEGs use either lead telluride or bismuth telluride. All of the TEGs offered by Global use lead telluride, while most of the TEGs offered by Teledyne use bismuth telluride.

When lead telluride is used it is hermetically sealed in an inert atmosphere to prevent the lead telluride from oxidizing. These sealed thermoelectric convertors have less than 0.2% degradation in power output per year of operation.

Heat Sink

The heat sink of a TEG rejects the heat that has passed through the thermoelectric convertor. The heat sinks are usually a series of aluminum fins. Natural convection is used to move sufficient air

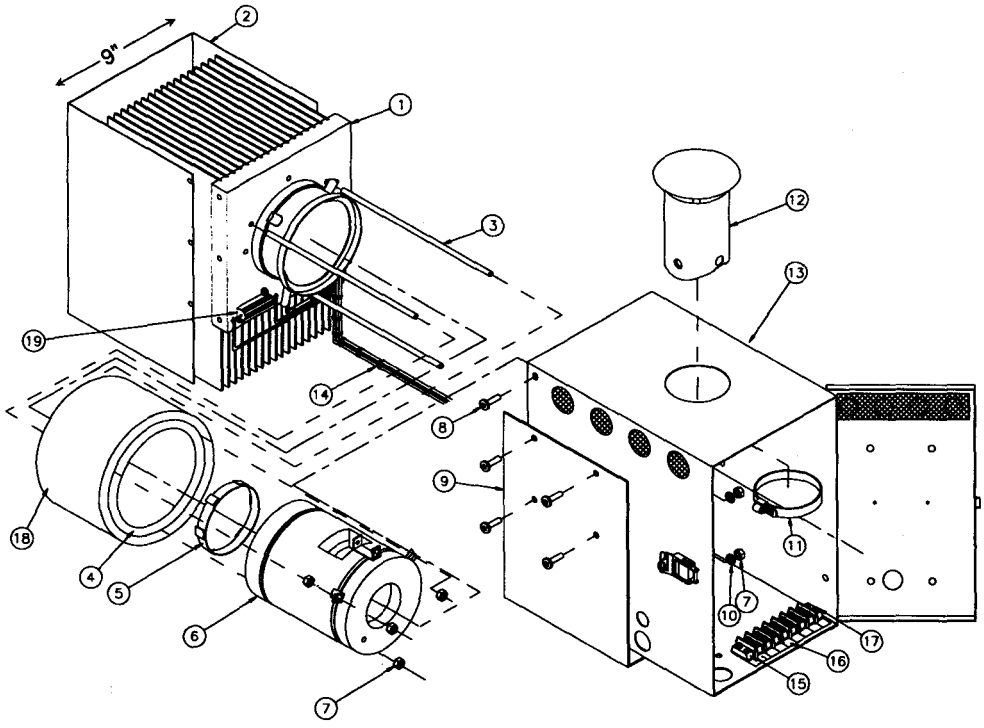

FIGURE 6 Components of a 50-W TEG, fuel system and electronics not shown. (See Legend to Figures located at the end of the chapter.) (From Global Thermoelectric, Inc., Calgary, Canada, *User's Manual.* With permission.)

to provide the cooling. The use of natural convection results in relatively large heat sink assemblies. The heat sink comprises between half and two thirds of the volume of a TEG. Smaller heat sinks could be achieved with forced air, but the fan would impact reliability and be a parasitic power draw. Figure 6 shows the aluminum fins that form the heat sink on a 50-W generator.

Housing

The housing or case of a TEG is designed to protect the fuel system, electronics, burner, and thermoelectrics from the weather. It also provides physical security to prevent unauthorized adjustments to the fuel or electrical settings. On the majority of generators currently sold, the housings are made from stainless steel. Figure 7 shows a typical housing.

Electronics

An important part of a TEG is its electronics which provide an ignition system, DC-DC voltage conversion, output power conditioning, and safety shut down. The ignition system is usually a high-voltage spark. It is turned on when there is gas pressure present. A small battery provides the power for the igniter. This battery is recharged by the TEG when it is operating.

In applications that require a precise voltage, DC-DC convertors are used to provide a regulated voltage. Normally the DC-DC convertors are stepping up a low voltage to a higher voltage. The majority of the data gathering and telecommunication equipment powered by TEGs operate at either a nominal 12 or 24 V DC. A typical application that uses a battery will actually require a higher voltage to charge the battery. For example, a "12-V" system with a battery may require 13.8 or 14.2 V to charge the battery. The DC-DC convertors provide an adjustment that allows the voltage to be set at any voltage over a range. Typical ranges are 12 to 16 V for a 12-V system and 24 to 31 V for a 24-V system.

In applications that do not require a DC-DC convertor, power conditioning is provided by a voltage limiter. The voltage limiter prevents the voltage from rising to the point that it could

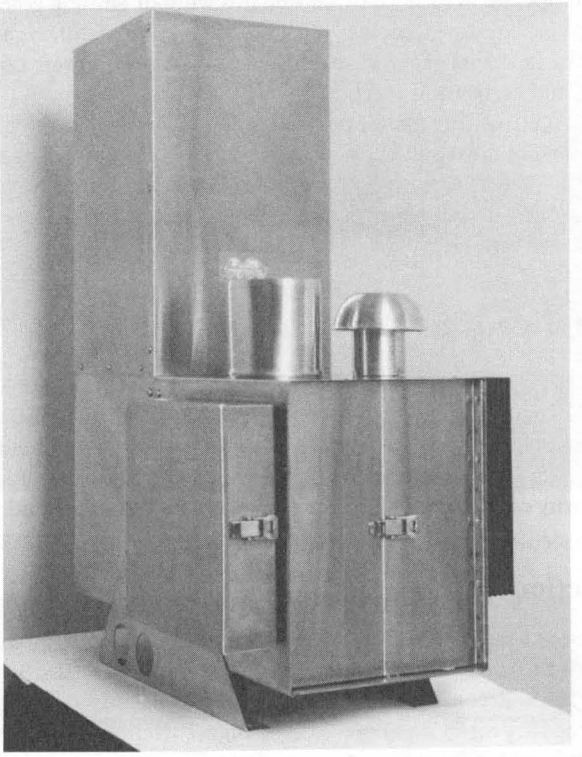

FIGURE 7 Global model 5120 TEG.

damage the TEG. As the electrical load on the TEG diminishes, the voltage of the TEG rises. When the voltage rises to a certain preset point, the voltage limiter presents an artificial resistive load to the TEG, thereby limiting the voltage.

The reason that a voltage limiter is required is that the thermoelectrics move more heat from the hot side to the cold side when there is a load on the TEG. In an open-circuit condition (no electrical load) the temperature of the hot side of the thermoelectrics will rise because less heat is passing through the thermoelectrics. The voltage limiter keeps the hot side of the thermoelectrics at a temperature that results in a long thermoelectric life.

Most TEGs have a safety shutdown that turns off the fuel if the burner goes out. This is accomplished with a solenoid valve held open by a thermocouple located in the exhaust of the burner.

Liquid-Fueled Generators

Thermoelectric generators that use liquid fuels such as kerosene and diesel have been designed. Only a few models in the 100-W range are currently offered for sale and all of these have moving parts. These generators are distinguished from gas-fueled TEGs in that they have moving parts and a much shorter interval between scheduled maintenance. While it may be theoretically possible to design a liquid-fueled TEG with no moving parts, most practical implementations will have some moving parts. Typically a fuel pump, a combustion air blower, and a fuel atomizing system all use devices that must be maintained or replaced periodically.

The interest in liquid-fueled TEGs was originally dominated by military applications. Some commercial applications are now emerging.

Hazardous-Area Generators

A small number of models of TEGs have been designed and certified for use in hazardous areas. These generators can operate in explosive atmospheres without igniting gases external to the generators. Many oil and gas locations, such as offshore production platforms and metering stations, either have or have the potential of having explosive gases. Any equipment operating within these areas must be tested and certified as meeting certain standards.

In order to make a TEG qualify for use in these areas, major changes to the basic generator are required. The exhaust gases must pass through a heat exchanger to cool the gases sufficiently before they exit the generator. The TEG must be constructed so that no external surface is hotter than a certain temperature which is well below ignition temperatures. Both the air intake and exhaust must pass through flame arresters.

36.3 Common Applications

It is useful to review the major applications of TEGs to better understand the type of product they are. The uses of TEGs are extremely broad and include applications as varied as powering ventilation fans in outhouses in national parks; powering navigational equipment used in precise surveys; and powering landing lights at airports. However, the three most common applications that account for the majority of sales are cathodic protection, data gathering, and telecommunications.

Cathodic Protection

One of the original uses of commercial TEGs was to provide power for cathodic protection systems. Cathodic protection is the use of an electrical current to prevent a metal structure from corroding. Cathodic protection is still a major use of TEGs. Typically TEGs are used to protect gas well casings and pipelines. In cathodic protection a low-voltage, high-current power source is usually needed. This matches very well with thermoelectrics, which are naturally low-voltage and high-current. Many TEGs can be used for cathodic protection without a DC-DC convertor.

The generators usually used for cathodic protection have outputs of 60 W or higher. Often when the TEG is used to protect a gas well casing, natural gas from the well is used to fuel the generator. The same is true when TEGs are used to cathodically protect gas pipelines. A pressure reduction system is usually required when gas is taken from a gas transmission line. When TEGs are used to protect oil pipelines or other structures, containerized propane is used as the fuel source. Figure 8 shows a TEG being used for cathodic protection in New Mexico.

The combined efficiency of the combustion system and the thermoelectrics translates into a fuel consumption rate. The fuel consumption in cathodic protection applications is usually not a primary concern because most sites are readily accessible by road for propane delivery, or they use natural gas directly from the well or pipeline that they are protecting.

Data Gathering

A very common and growing use of TEGs is to power a variety of data gathering equipment. In many applications the data are either continuously or intermittently transmitted by radio to a central site. In some applications instructions are transmitted by radio to the system powered by the TEG. These systems are sometimes referred to as SCADA systems (Supervisory Control and Data Acquisition). Figure 9 shows a 50-W TEG mounted on the side of a pipeline metering station. The gas for the TEG comes from the pipeline, and the TEG powers flow measuring devices and a flow computer.

The type of data gathered by equipment powered by TEGs includes weather, seismic, pipeline flows and pressures, water levels, and gas well monitoring. The power requirement in these applications is usually under 100 W, with most systems requiring less than 50 W. The peak power

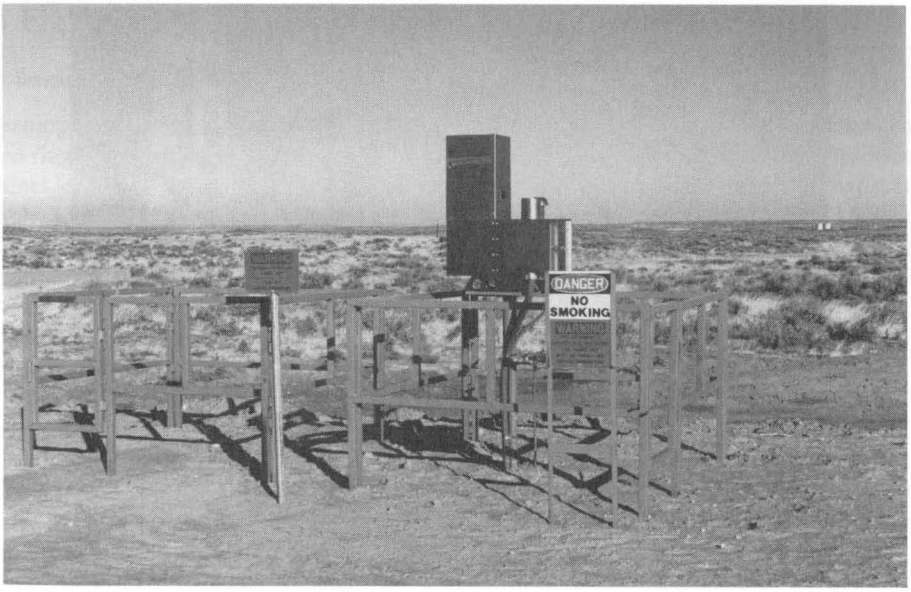

FIGURE 8 120-W TEG used in cathodic protection in New Mexico.

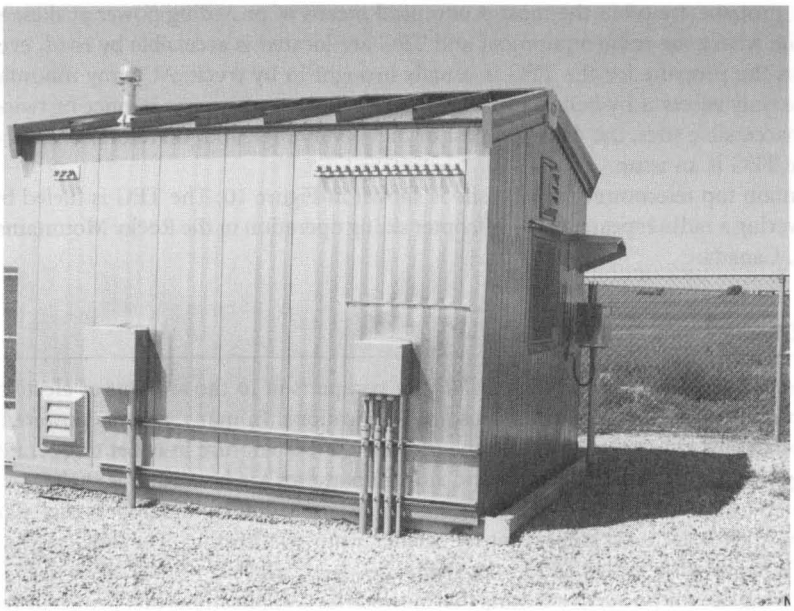

FIGURE 9 50-W TEG used in a data gathering application on a gas pipeline.

requirements are much higher but are very brief, occurring only when the system's radio is transmitting. These surge power requirements are met by a storage battery that is charged by the TEG.

Telecommunications

TEGs have been used successfully to power microwave, VHF, cellular, television, commercial radio, and two-way radio repeaters. In these applications it is highly desirable to locate the repeater or

FIGURE 10 Mountain top telecommunications site powered and heated by a TEG.

rebroadcast site in a high location such as a mountain top or hill top. Typically commercial grid power is not available at these sites and would be very expensive to extend to the site. TEGs fueled by bottled propane are often the most economical means of providing power at these sites.

If the site where the radio equipment and TEG are located is accessible by road, even for part of the year, the propane for the TEG is usually brought in by truck. At many mountain top locations the only access is by helicopter, and propane tanks are brought in once or twice per year. In these inaccessible sites, the delivered cost of fuel is very high and, therefore, the fuel consumption of the TEG is an issue.

A mountain top telecommunication site is shown in Figure 10. The TEG is fueled by propane and is powering a radio repeater for a helicopter skiing operation in the Rocky Mountains of British Columbia, Canada.

36.4 Heaters and Generators

A TEG produces a significant amount of heat in comparison to the amount of electricity it produces. Some of this heat is put to use in some applications. In many systems powered by TEGs, the electronics and radios must be kept above a certain temperature in order to operate properly. In cold regions the electronics, radios, and storage batteries are housed in a shelter or enclosure that is heated by the waste heat from the TEG. Expansion bellows and dampers that allow outside air into the shelter are used to prevent the shelter from overheating. The TEG in the shelter in Figure 10 is heating the radios within the shelter.

An emerging use for power-generating thermoelectrics is applications that primarily require heat but also need some electricity. These devices have been dubbed "self-powered heaters". Typically the electricity is needed to power components necessary to produce the heat and to distribute the heat. To produce the heat, electrical power may be needed for a control and safety system, a combustion air blower, fuel pump, and fuel atomization system. Distribution of the heat may be by fans or water circulating pumps or a combination of these. Some excess electricity is often desirable to power some other minor equipment, such as a radio or security system.

36.5 Future Generators

The future of commercial thermoelectric generators will probably include more models of TEGs with power outputs under 20 W, increased availability of liquid-fueled TEGs, and new generators aimed more at the consumer market than the industrial market.

Legend to Figures

The following items are referenced in Figures 2, 3, and 6.

1, Thermopile assembly; **2,** fin wrapper; **3,** burner mounting rod; **4,** burner insulation kit; **5,** combustion ring; **6,** burner asembly; **7,** hex nut, ¼–20, stainless steel; **8,** screw, ¼–20, ⅝″ stainless steel; **9,** cabinet leg; **10,** lock washer, ¼″ stainless steel; **11,** clamp, 3″, stainless steel; **12,** exhaust stack assembly; **13,** cabinet assembly; **14,** wiring assembly; **15,** terminal block, seven position; **16,** marker strip, 7 terminal; **17,** screw, 10–32, ¾″ stainless steel; **18,** burner insulation wrapper; **19,** resistor assembly; **20,** screen holder; **21,** burner screen, natural gas, burner screen, propane; **22,** insert ring; **23,** Venturi, natural gas, Venturi, propane; **24,** Venturi weldment; **25,** top plate assembly; **26,** screw, truss head 8–32, ⅜″; **27,** air shutter; **28,** orifice, P6, natural gas, orifice, P4, propane; **29,** Venturi assembly, natural gas, Venturi assembly, propane; **30,** screw, socket head 6–32, 0.128″; **31,** ignitor rod; **32,** screw, truss head 8–32, ¼″; **33,** air screen; **34,** manifold block; **35,** pressure switch; **36,** gauge, 0–15 psi; **37,** connector, male ¼″ NPT × ¼″ tube; **38,** fuel line kit; **39,** connector, ¼″ tube × ¼″ NPT, nylon; **40,** screw, 8–32 × ¾″ stainless steel; **41,** fuel system mounting bracket; **42,** elbow, street ¼″ NPT; **43,** thermocouple; **44,** shut-off valve; **45,** tee ¼″ NPT; **46,** regulator, 0–35 psi; **47,** nipple, close ¼″ NPT 304 SS; not shown: fuel filter; limiter convertor; cathodic protection box; battery, spark ignitor.

37 Modular RTG Technology

Robert F. Hartman
Martin Marietta Corp.
Valley Forge, Pennsylvania, U.S.A.

37.1 Modular RTG Technology

The Modular RTG design concept was initiated at Fairchild Industries[1] and developed by the General Electric Astro Space Division for the U.S. Department of Energy, Office of Special Applications. The Modular RTG (MOD-RTG) design incorporates the next generation of radioisotope thermoelectric generator (RTG) technology. The distinguishing features of its design are its modularity, its high specific power compared to predecessor RTGs, and its ability to provide spacecraft voltage (28 to 30 V DC) over a wide range of power levels.

The MOD-RTG design utilizes the modular General Purpose Heat Source (GPHS) and a multicouple thermoelectric device to provide a totally modular thermoelectric converter. The reference design is shown in Figure 1. The reference design contains eighteen GPHS modules and produces 340 W (e) of electrical power. The design, however, is modular and can be scaled down to provide decreased power. Eight multicouples, connected in series, surround each GPHS module, forming a modularized power segment which provides ~19 W (e) at 30.8 V DC. The number of GPHS modules utilized is dependent upon the user's power requirements. The RTG is capable of accommodating up to 18 GPHS modules within the converter. The range of power output can be varied (in 19-W increments) from 19 W (e) for a converter with a single GPHS module, to 340 W (e) for a converter with 18 GPHS modules.

The multicouples penetrate a multifoil insulation system which is used to insulate the isotope heat source. The heat source is mounted in the converter with a support system which utilizes titanium spring washers to maintain the required axial preload. An aluminum outer shell, with heat rejection fins, provides containment for the converter components.

The design and performance attributes for the reference design containing 18 GPHS modules are shown in Table 1. The design provides a significant improvement in specific power compared to predecessor RTGs, due to the use of lighter-weight converter components and the improved efficiency of the thermoelectric multicouple device. Specific power vs. power output for the modular RTG is shown in Figure 2. The specific power of the predecessor GPHS-RTG design is shown, for reference.

0-8493-0146-7/95/$0.00+$.50

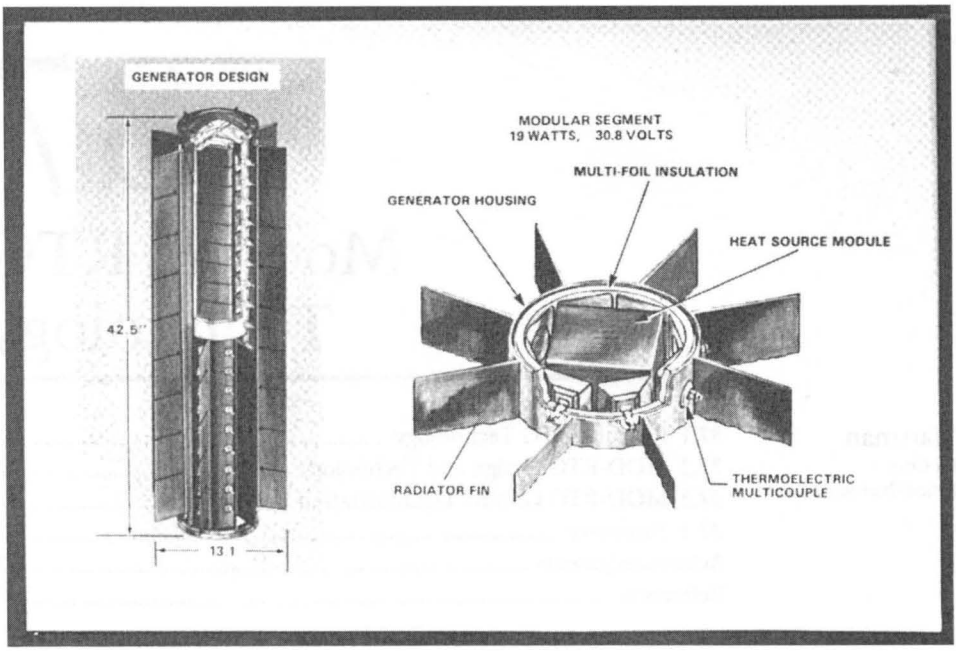

FIGURE 1 Modular RTG design. (Courtesy of Martin Marietta Corporation, Bethesda, Maryland.)

Table 1 MOD-RTG Reference Design and Performance Attributes

Design Attribute	Design/Performance Parameter
Load voltage, volts	30.8
Power output, watts	340
Specific power, W/kg	7.9
Cold/hot junction temperature, K	573/1273
Converter efficiency, %	7.5
Number of GPHS modules (250 W (t) per module)	18
Number of multicouples	144
Length, M	1.08
Overall diameter, M	0.33
Weight, kg	42.2

37.2 MOD-RTG Design and Technology

The MOD-RTG design combines proven RTG technology with new technologies developed specifically to enhance its performance. The design utilizes the flight qualified and proven GPHS to provide the required thermal energy and a 2219 aluminum converter housing/radiator to dissipate the waste heat. New technologies were developed to enhance thermoelectric material efficiency and device performance. These technologies are incorporated into a new thermoelectric multicouple device. The multifoil insulation system selected for the design also incorporates new technologies designed to reduce its overall weight. The paragraphs below describe the major MOD-RTG components and the new technologies developed to enhance their performance.

The General Purpose Heat Source (GPHS) is a modular design concept (Figure 3). Each GPHS module is designed to provide 250 W of thermal energy at Beginning of Life (BOL). The modules are designed to be stacked vertically to provide the thermal inventory required by the radioisotope thermoelectric generator.

Each module contains four pressed and sintered ^{238}Pu oxide fuel pellets, each pellet having a thermal inventory of 62.5 W (t). Each fuel pellet is individually encapsulated in a vented, iridium

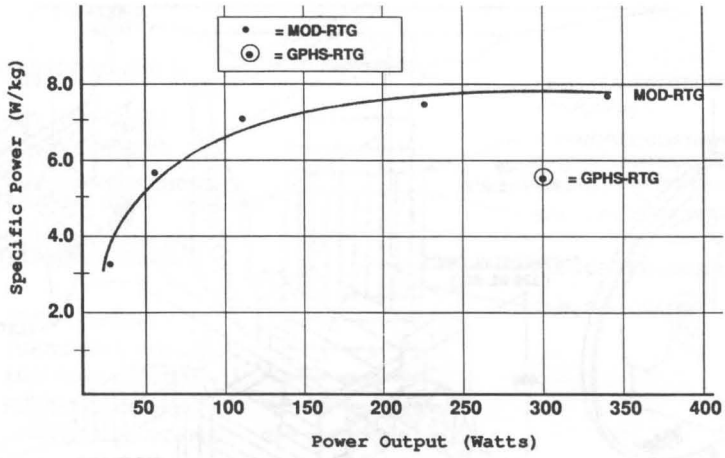

FIGURE 2 MOD-RTG enhanced specific power. (Courtesy of Martin Marietta Corporation, Bethesda, Maryland.)

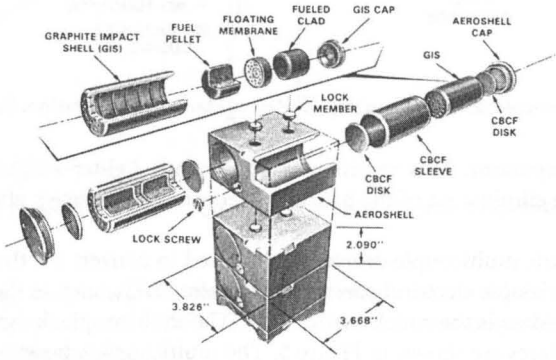

FIGURE 3 General-purpose heat source. (Courtesy of Martin Marietta Corporation, Bethesda, Maryland.)

cladding. The cladding provides primary containment of the fuel pellet in the event of re-entry impact or launch abort/accident environments. The fueled clads are enclosed within a Graphite Impact Shell (GIS) to provide additional impact protection. The Graphite Impact Shells are fabricated from a Fine Weave Pierced Fabric (FWPF), carbon carbon composite material. Thermal insulation sleeves of Carbon Bonded Carbon Fiber (CBCF) graphite are used to ensure that safe iridium temperature limits are achieved during re-entry heating and adequate iridium ductility is maintained during subsequent impact. These components are contained within a FWPF aeroshell which provides structural integrity within the generator and aerodynamic heating protection in the event of re-entry.

The GPHS has been qualified for RTG space flight after extensive safety analysis and testing. It is currently operating in the GPHS-RTGs which are providing electrical power to the Galileo and Ulysses Spacecrafts. Its modular design is well suited for the Modular RTG application and it represents proven flight qualified technology.

A new lightweight multifoil insulation system has been developed for the MOD-RTG design. Predecessor RTGs utilized a multifoil insulation system consisting of 60 layers of 7.6×10^{-5} m thick molybdenum, with each layer separated by Astro quartz spacers. The new insulation system, which was initially developed by ThermoElectron Corporation, eliminates the quartz spacers between foils and replaces them with zirconia powder, which is electrostatically sprayed onto each

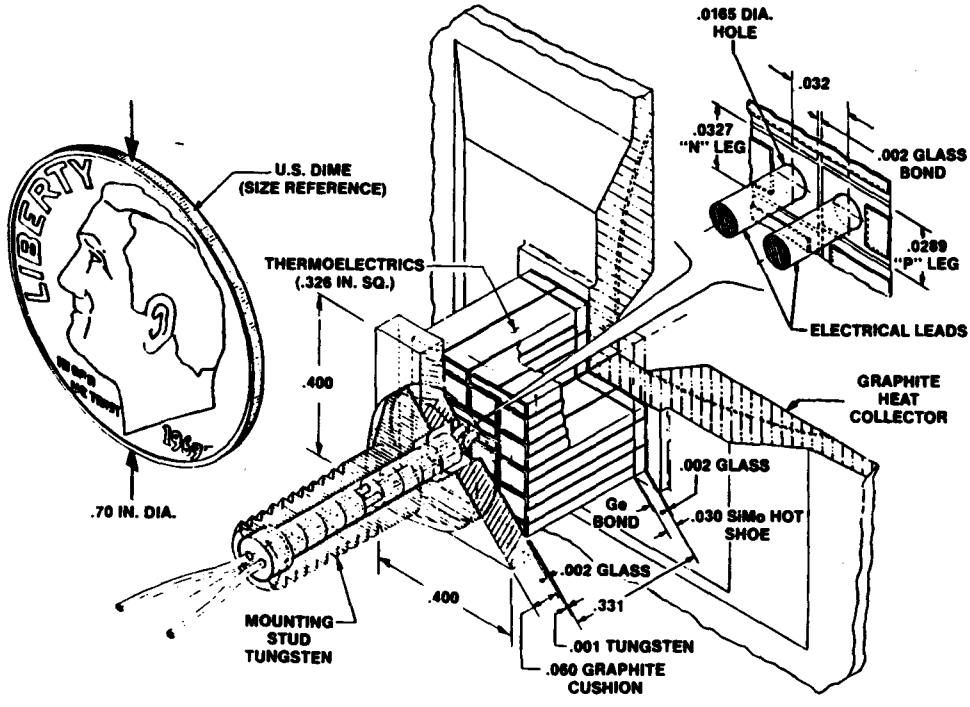

FIGURE 4 Multicouple design. (Courtesy of Martin Marietta Corporation, Bethesda, Maryland.)

foil to serve as the separator. This results in a significantly lighter-weight system (65% weight reduction) due to the elimination of the quartz spacers and the reduced, effective thickness of the insulation system.

A new thermoelectric multicouple device is being used to convert the thermal energy from the isotope heat source to usable electrical energy. Predecessor RTGs, such as the GPHS-RTG, MHW-RTG, etc., utilized unicouple thermoelectric devices. The multicouple design is shown in Figure 4 and its material interfaces are shown in Figure 5. The multicouple consists of a graphite heat collector, thermoelectric couples connected electrically in series, a graphite cold cushion, and a tungsten mounting stud for attachment to the outer shell. The heat collector, slotted for stress relief, tapered and centrally dished to minimize weight, maintains the heat source at 1373 K and the thermoelectric hot junction at 1273 K. The heat collector is bonded to the thermoelements with a high-temperature alumino-silicate glass to provide electrical isolation. SiGe p-type and SiGe/GaP n-type thermoelements are used in the multicouple design.

The 40 individual thermoelectric elements, arranged in a four-by-ten array, are coated with Si_3N_4/SiO_2 and bonded with a high-temperature alumino-silicate glass (nominal composition: 62 SiO_2:24 Al_2O_3:6 MgO:8 CaO). N-doped silicon molybdenum hot shoes and silver-plated tungsten cold contacts are bonded to the thermoelements to provide the electrical series circuit.

Nickel-plated molybdenum wire is brazed to the centrally located thermoelements to provide the power output leads. The outer surfaces of the thermopile are coated with Si_3N_4/SiO_2 and glass to provide sublimation suppression. The graphite cold cushion is bonded to the thermoelements using CV-635 solder glass to maintain electrical isolation and is brazed to the tungsten mounting stud using an aluminum silicon braze alloy (88 Al:12 Si). The power leads exit through the tungsten mounting stud and glass headers isolate the leads from the mounting stud and provide a hermetic seal.

The multicouple is designed to operate at a 1273 K hot junction temperature and a 573 K cold junction temperature. It currently produces approximately 2.1 W (e) at BOL and produces 3.5 V; however, advances in thermoelectric material efficiencies are expected to increase the power output

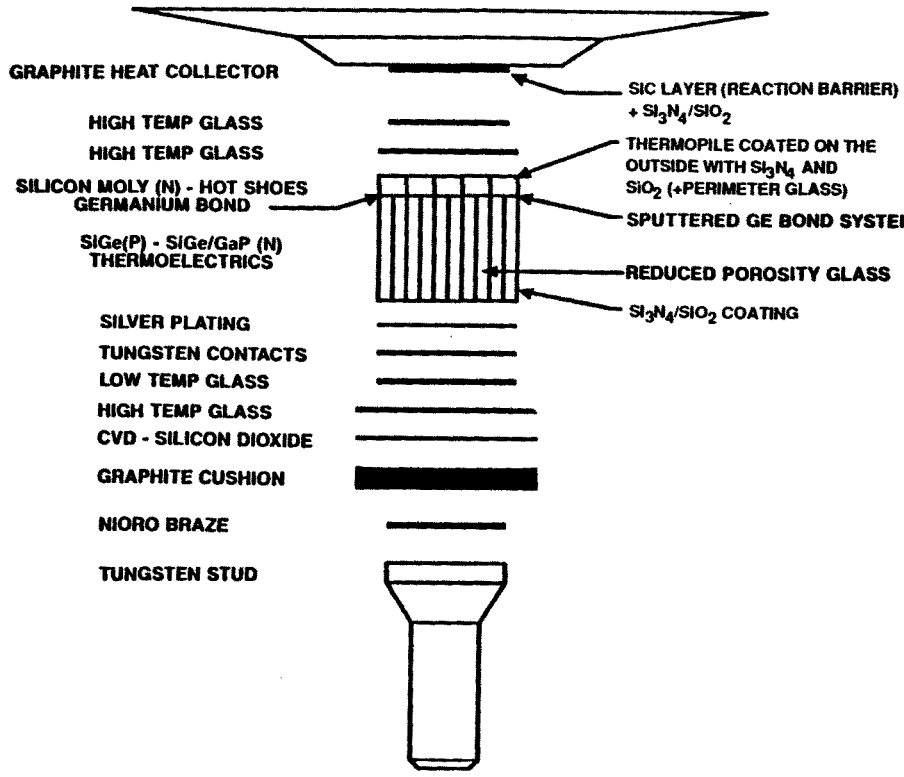

FIGURE 5 Multicouple material interfaces. (Courtesy of Martin Marietta Corporation, Bethesda, Maryland.)

by 15%. Its high-voltage output is particularly attractive for missions requiring low power at spacecraft voltage, which is typically 28 to 30 V. This requires eight multicouples connected in a series string to achieve the desired voltage.

The selection of SiGe alloys for use in the multicouple is based on extensive experience with a variety of thermoelectric materials. A thermoelectric energy conversion device is essentially a heat engine in which the majority charge carriers (electrons or holes) comprise the working fluid. Like any other heat engine, this system has a maximum conversion efficiency given by $\eta_C = (T_{hot} - T_{cold})/T_{hot}$. The extent to which the thermoelectric materials fall short of the Carnot ideal is expressed by a factor multiplying the Carnot efficiency. To maximize the Carnot term, the MOD-RTG multicouple has been designed to operate between $T_{cold} = 573$ K and $T_{hot} = 1273$ K. While this increases the efficiency, it limits the choice of materials to refractory semiconductors which must be mechanically and chemically compatible with the refractory metals and insulators used to construct the remainder of the device.

The multicouple thermoelectric materials consist of a silicon germanium alloy in which 80% of the atoms are Si and 20% are Ge. This basic alloy is doped either with boron, in the case of the p-type material or a combination of Ga and P in the case of the n-type material. The addition of the dopants modifies the percentage of Si and Ge slightly. The nominal compositions given here are based on the amount of each material placed in the initial melt. A small amount of material is lost in the subsequent processing and the nominal composition is not adjusted to account for this. A p-type compact is prepared from a nominal composition, $Si_{0.798}Ge_{0.199}B_{0.0025}$, by vacuum-casting from a melt and hot pressing. An n-type compact is prepared from a nominal composition, $Si_{0.796}Ge_{0.198}Ga_{0.019}P_{0.025}$, by vacuum-casting from a melt of Si, Ge, and P, hot pressing, recrushing the compact, adding GaP, powder blending, and repressing.

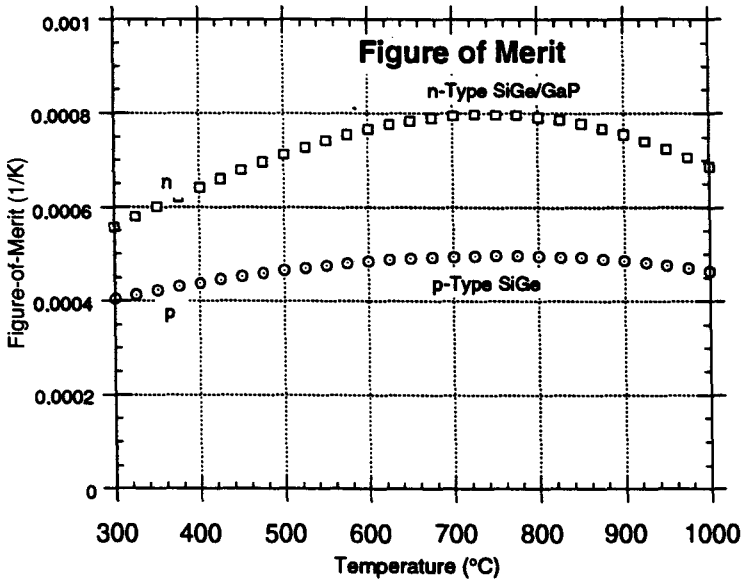

FIGURE 6 The figures-of-merit of the n- and p-type baseline MOD-RTG alloys are shown here. The integrated averages over the 300 to 1000°C range are 0.72×10^{-3} (K^{-1}) and 0.47×10^{-3} (K^{-1}) for n and p, respectively. (Courtesy of Martin Marietta Corporation, Bethesda, Maryland.)

The conversion efficiency of thermoelectric materials is characterized by figure-of-merit, Z, defined as the square of the Seebeck coefficient α, multiplied by the electrical conductivity σ, divided by the thermal conductivity, λ, or $Z = \alpha^2\sigma/\lambda$. The figures-of-merit for the SiGe/GaP n-type and SiGe p-type material are shown in Figure 6. Efforts are in progress to further improve the efficiency of these materials by modification of the dopant concentrations as well as the introduction of nanophase materials to increase the scattering of phonons.

Reliable, long-term performance of the multicouple thermoelectric device is required to meet the power requirements for 8- to 12-year deep space missions. Multicouple analyses and tests have been conducted to identify life-limiting degradation mechanisms and degradation models are being established to predict long-term performance. The principal life-limiting degradation mechanism has been shown to be degradation of the high-temperature insulating glass between thermoelements or between heat collector and thermopile. Testing has shown that alkali contaminants can severely degrade the electrical and mechanical properties of the insulating glass at operating conditions, thereby enabling electrolysis and dielectric breakdown to occur. This mechanism was shown to be operative even when alkali contaminants were present in materials located external to the multicouple. In this case alkali ions were transported into the multicouple insulating glass by electrochemical migration. Extreme care is taken to minimize the alkali concentration in all multicouple materials and all materials adjacent to the multicouple in the converter.

Testing at the GE Corporate Research and Development Center has also shown that gallium and gallium phosphide can migrate from the n-leg into the insulating glass and produce internal shorts after long periods of time. This mechanism was shown to be voltage driven and only operative when the anode contained gallium phosphide. Diffusion barrier coatings of Si_3N_4 were shown to be effective in suppressing this migration, except where flaws (microcracks) were present. Alternative coatings, such as AlN, are also being evaluated for this application. This mechanism is also controlled by limiting the voltage between thermoelements and/or the concentration of GaP in the n-leg.

The long-term performance characteristics of the multicouple have been determined. Figure 7 shows the performance trends for two multicouple configurations, defined as Build #3 and Build #4, when operating at normal RTG operating conditions. Testing reached 14,000 h in February,

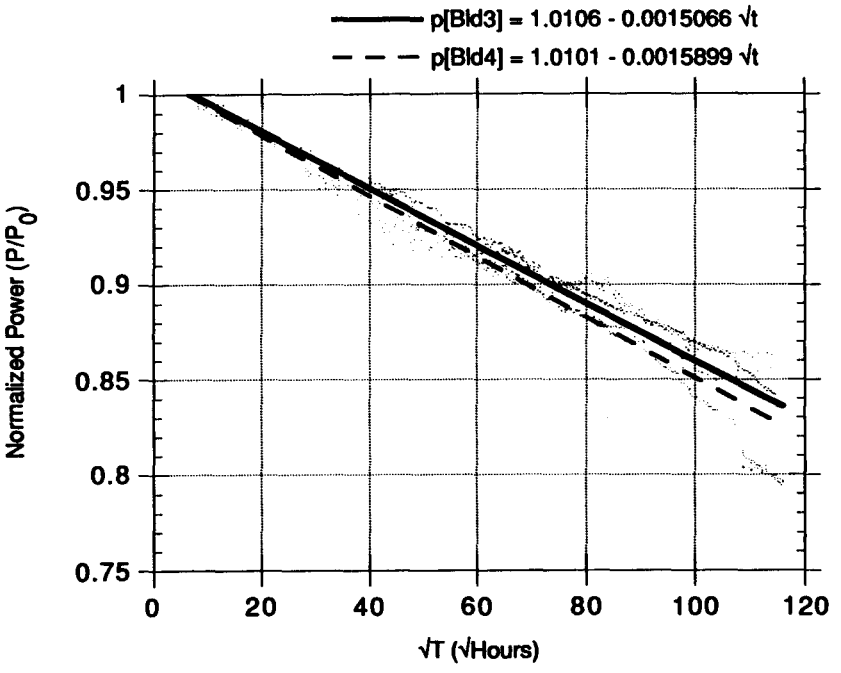

FIGURE 7 Multicouple power trend. (Courtesy of Martin Marietta Corporation, Bethesda, Maryland.)

Table 2 GDS Design Attributes and Predicted Performance

Design Attribute	Design/Performance Parameter
Number of equivalent GPHS modules	6
Number of multicouples	48
Length, M	0.44
Overall diameter, M	0.33
Operating life, Years	8 to 12
Load voltage, voltage	30.8
Power output, watts	100
Cold/hot junction temperatures, K	573/1273

1993 and is continuing. Design modifications have been identified that will further enhance the long-term performance of the multicouple. These include further optimization of dopants in the silicon molybdenum hot shoes and possibly further refinements to the thermoelectric material grain size and/or leg geometry to minimize dopant loss. These improvements are necessary to achieve the 8- to 12-year operating life requirements for deep-space missions.

37.3 MOD-RTG Ground Demonstration System

An electrically operated Ground Demonstration System (GDS) has been designed to demonstrate the modularity and long-life performance of the MOD-RTG design. Its design is shown in Figure 8 and its operating characteristics summarized in Table 2. The GDS converter is designed to accept an electric heat source whose geometry, mass, and power level simulate the equivalent of six GPHS modules. The size of the GDS was selected on the basis of demonstrating modularity or scalability of power level while minimizing size to reduce cost. The GDS design incorporates all of the key features of the conceptual flight design.

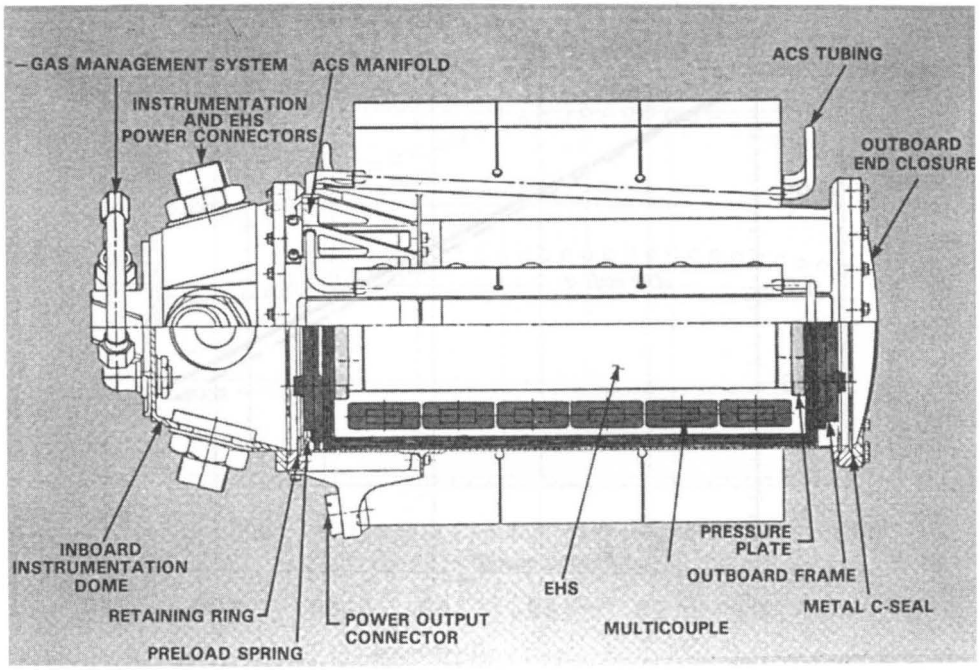

FIGURE 8 Design features of the MOD-RTG GDS. (Courtesy of Martin Marietta Corporation, Bethesda, Maryland.)

37.4 Summary

The MOD-RTG design combines proven and new technologies to provide enhanced performance. Its unique modular design adapts to a wide range of power levels. The development of new, lightweight component designs, improved thermoelectric material efficiencies, and a new multicouple thermoelectric device has resulted in significant improvement in RTG specific power. Achieving reliable, long-life performance of the multicouple is the key technology issue. Analyses and tests have defined the life-limiting degradation mechanisms and the appropriate measures have been identified to achieve the required performance.

Acknowledgments

MOD-RTG technology development was performed by the General Electric Company for the U.S. Department of Energy's Office of Special Applications under Contract DE-AC01-83NE32112. The author gratefully acknowledges the innovative work and dedicated support of the GE MOD-RTG team members and the numerous organizations (industry, government and national laboratories) who have assisted in the development of the MOD-RTG technology.

Reference

1. Shock, A., Modular Isotopic Thermoelectric Generator, Proceedings of the 1981 IECEC, Volume I, p. 327.

38

Peltier Devices as Generators

Gao Min
Kunming Institute of Physics
Kunming, China

David M. Rowe
University of Wales
Cardiff, U.K.

38.1 Introduction

Thermoelectric devices can be used either in the Peltier mode for refrigeration or in the Seebeck mode for electrical power generation. The basic requirements to achieve a significant thermoelectric performance are the same for both generators and coolers.[1,2] However, in practice both types of devices are usually very different from each other in design and construction, due to the difference in the temperature range of operation and the intended application.[3–5] Thermoelectric coolers usually utilize Bi_2Te_3 materials and are employed in applications below room temperature, whereas generators are fabricated from high-temperature materials such as PbTe or SiGe alloys and are used in the temperature region 400 to 1200 K. Generally it is inefficient for a generator to be used as a cooler and vice versa.

However, an increasing interest in low-temperature "waste heat" energy conversion employing thermoelectric devices[6,7] has encouraged investigations into the use of conventional Peltier devices as generators.[8,9] Figure 1 shows the power outputs of conventional Peltier devices as a function of temperature differences.[10] In order to obtain the maximum power output, it is necessary to reoptimize the geometry of the Peltier device thermoelements, which have already been optimized for obtaining the maximum coefficient of performance.

In this chapter, a theoretical model is presented which provides guidelines in selecting or modifying the geometry of thermoelements to achieve maximum power output. A method for optimizing the "generating system" when using hot water as a heat source is also presented. Finally the economic prospects of this application of thermoelectrics are discussed.

38.2 Models for Power Output Calculation

"Ideal" Model

A simplified model of a Peltier device is shown in Figure 2a. It consists of an n-type and p-type semiconductor thermoelement connected in series by highly conducting copper strips. If the

0-8493-0146-7/95/$0.00+$.50

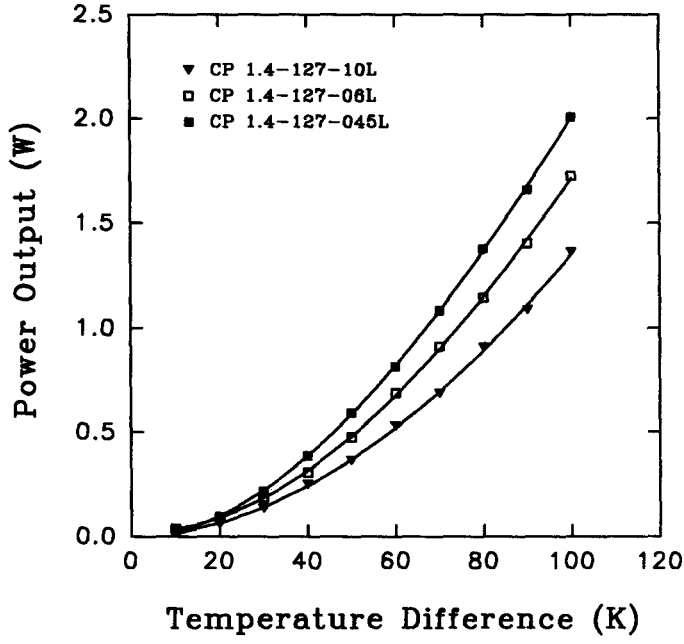

FIGURE 1 Power output of conventional Peltier devices as a function of temperature differences.

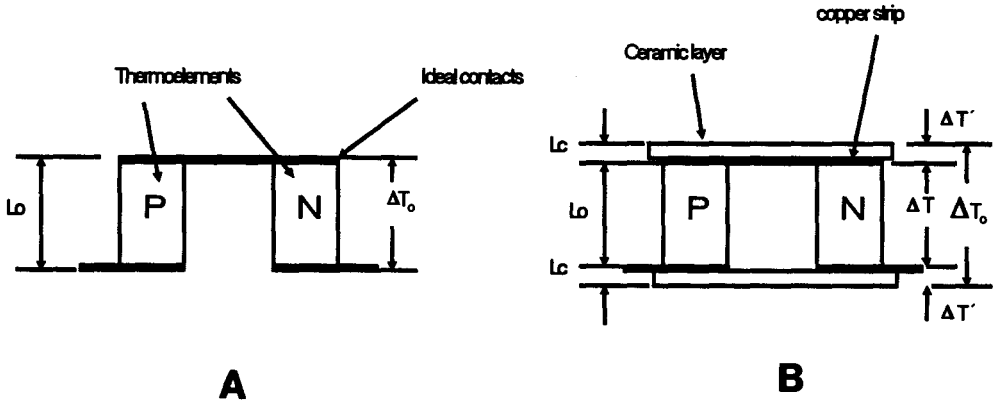

FIGURE 2 Schematic diagram of Peltier devices: (a) "ideal" device; (b) realistic device.

contact resistances (thermal and electrical) between the thermoelements and copper strips are neglected, the calculated power output P_i based on this "ideal" model is given by:[11]

$$P_i = \frac{(2\alpha\Delta T_o)^2}{4R_o} \tag{1}$$

where α is the Seebeck coefficient, ΔT_o is the temperature difference across the thermoelements, and R_o the total series electrical resistance of the two thermoelements.

$$R_o = 2\rho\left(\frac{L_o}{A_o}\right) \tag{2}$$

where ρ is the electrical resistivity, and L_o/A_o the ratio of the thermoelement length to cross-sectional area. Equation 1 can then be expressed as:

$$P_i = \left(\frac{\alpha^2}{\rho}\right)\left(\frac{\Delta T_o^2}{2}\right)\left(\frac{A_o}{L_o}\right) \tag{3}$$

In formulating the above three equations it is assumed that the two thermoelements have the same dimensions and very similar thermoelectric properties.

A prerequisite for the use of Equation 1 or 3 is that the Peltier device should possess relatively long thermoelements so that the contact effects can be neglected. This model is usually adequate when estimating the output power of a device with relatively long thermoelements that has been optimized to achieve the maximum coefficient of performance or maximum temperature difference for cooling.

Realistic Model

For low-temperature waste "heat to electrical power" conversion using the Peltier device as a generator, the thermoelement length should be optimized for maximum power output. Usually the required length is relatively shorter in power generation than in the case of refrigeration where coefficient of performance or temperature difference is an over-riding requirement. However, Equation 3, which was derived from the "ideal" model, indicates that the power output approaches infinity as the length of the thermoelements goes to zero. This is obviously unrealistic for an actual device. In practice, as the ratio of length to cross-sectional area of the thermoelements is decreased, the contact effects become significantly more important and can no longer be neglected.

A more realistic model of a Peltier device is shown in Figure 2b. It comprises the simple structure of an "ideal" model sandwiched by two plates of high thermally conducting but electrically insulating ceramics. When the effects associated with the ceramic layers are taken into account, the actual temperature difference across the thermoelements of the device, ΔT, is related to the applied temperature difference across the two ends of the device, ΔT_o, by:

$$\Delta T = \frac{\Delta T_o}{1 + 2(\lambda/\lambda_c)(L_c/L_o)} \tag{4}$$

or

$$\Delta T = \frac{\Delta T_o}{1 + 2rw} \tag{5}$$

where λ and λ_c are thermal conductivity of the thermoelements and the contacting layers, respectively. L_c is the thickness of the ceramic layers, $r = \lambda/\lambda_c$, and $w = L_c/L_o$.

Similarly, when the contact's contribution is taken into account the total electrical resistance of the device can be expressed as $R = R_o + R_c$, or

$$R = 2\rho\left(\frac{L_o}{A_o}\right)\left(1 + \frac{n}{L_o}\right) \tag{6}$$

where $R_c = 4\rho_c/A_o$ and $n = 2\rho_c/\rho$. R_c and ρ_c are electrical contacting resistance and resistivity, respectively.

Substituting for ΔT_o and R_o in Equation 1 with Equations 5 and 6, the power output P_{co} is then given by:

$$P_{co} = \frac{P_i}{(1 + n/L_o)(1 + 2rw)^2} \tag{7}$$

Furthermore, if a realistic device with thermoelements having a ratio of cross-sectional area to length A/L is compared with the "ideal" device which possesses a ratio of A_o/L_o, the relative change of the power output D(x) can be obtained from

$$D(x) = P_c/P_i = \frac{ax^2}{(x + n/L_o)(x + 2rw)^2} \tag{8}$$

where $a = A/A_o$, $x = L/L_o$, and

$$P_c = \frac{(A/A_o)P_i}{(L/L_o + n/L_o)[1 + 2(\lambda/\lambda_c)(L_c/L)]^2} \tag{9}$$

P_c is the power output of a realistic device with reference to an "ideal" device.

38.3 Optimization of Peltier Device for Thermoelectric Generation

An experimental investigation using the more realistic model has shown[10] that it can provide a more accurate estimation of power output for commercially available Peltier devices, especially when the length of the thermoelements decreases. Furthermore, as shown in Figures 3a to 3d, the model indicates that the power output increases with decreasing thermoelement length until it reaches a maximum and then decreases with a further reduction in the length of the thermoelements. This provides a theoretical guideline for optimizing the device geometry to obtain the maximum power output. It is especially useful in the application of low-temperature waste heat electrical power conversion, where maximum power output is required. However, most commercially available Peltier devices have been optimized to attain the largest temperature difference or coefficient of performance. The length of thermoelements that have been optimized in terms of the largest temperature difference or maximum coefficient of performance is usually much more than is required for use in low-temperature power generation. Consequently, the length of the thermoelements has to be modified to its optimum value for maximum power output.

It can also be seen that the power output of the device is significantly affected by the contact properties, such as the thermal and electrical contacting resistances, the thermal conductivity, and the thickness of the ceramic layer. The effects of these contact properties on the power output of the device are also illustrated in Figures 3a to 3d. In practice a more substantial increase in power output can be achieved by improving the thermal contacts rather than the electrical contacts. A more substantial increase in power output can also be achieved by reducing the thickness of the insulating ceramic plates rather than by reducing their thermal conductivity.

Once the properties of the thermal and electrical contacts are determined, the optimum length of the thermoelements can be obtained from the graphs displayed in Figures 3a and b. In the case of a commercially available Peltier device fabricated using state-of-the-art technology, values of 0.20 and 0.10 mm have been obtained for the parameters r and n, respectively.[12]

38.4 Efficiency of Optimized Devices

For the "ideal" device with a matched load, the conversion efficiency is given by:[13]

$$\phi = \left(\frac{T_h - T_c}{T_h}\right)\left[2 - \frac{1}{2}\left(\frac{T_h - T_c}{T_h}\right) + \frac{4}{ZT_h}\right]^{-1} \tag{10}$$

where T_h and T_c are the temperatures at the hot and cold sides of the device, and z is the thermoelectric figure-of-merit. Equation 10 is only a function of temperature and the figure-of-merit. This indicates that the conversion efficiency of the "ideal" device is independent of the length of the thermoelements. Equation 10 can only be used to calculate the conversion efficiency of devices with relatively long thermoelements.

When a Peltier device is used as a generator for "low-temperature" electrical power conversion, the contact effects cannot be neglected because of the relatively short length of the thermoelements. Using a similar calculation to that for the power output based on the realistic model, the conversion efficiency of a Peltier device can readily be derived and is given by:

$$\phi = \left(\frac{T_h - T_c}{T_h}\right)\left\{(1 + 2rw)^2\left[2 - \frac{1}{2}\left(\frac{T_h - T_c}{T_h}\right) + \left(\frac{4}{ZT_h}\right)\left(\frac{1 + n/L_o}{1 + 2rw}\right)\right]\right\}^{-1} \tag{11}$$

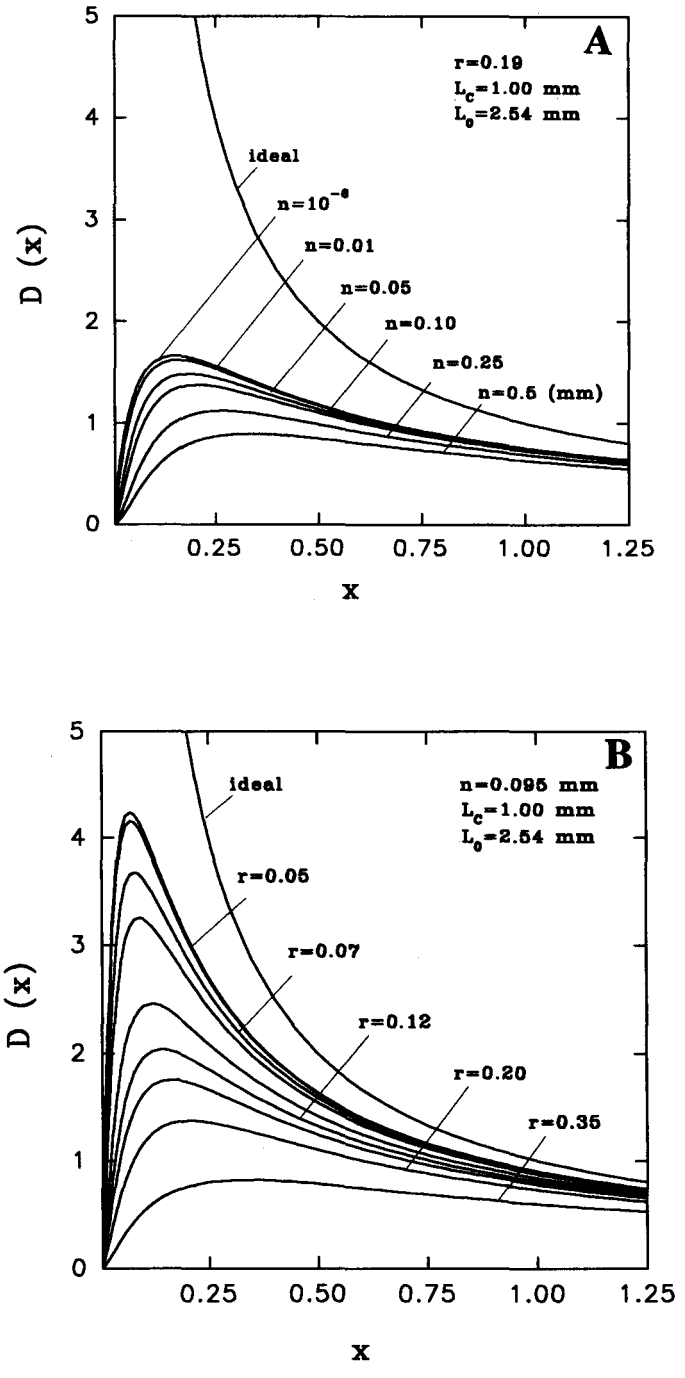

FIGURE 3 Power output of thermoelectric modules as a function of length of thermoelements. (a) Effect of electrical contacting resistance; (b) effect of thermal contacting resistance; (c) effect of thermal resistivity of ceramic layer; (d) effect of thickness of ceramic layer.

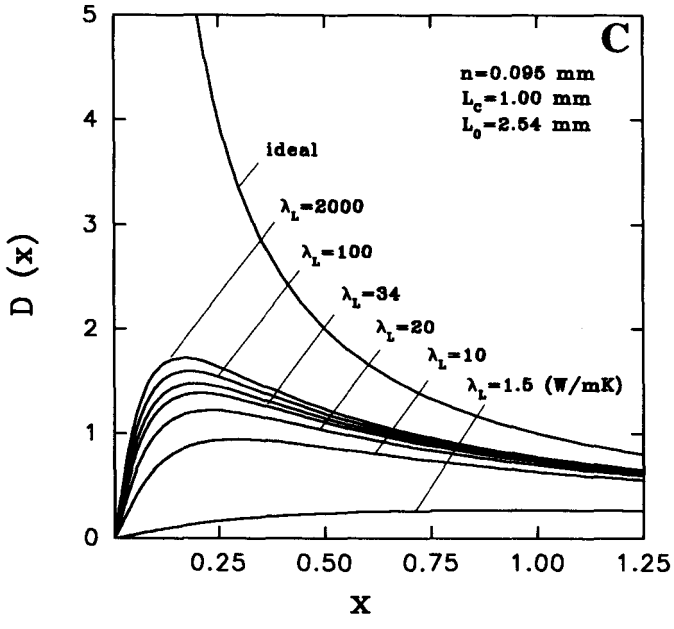

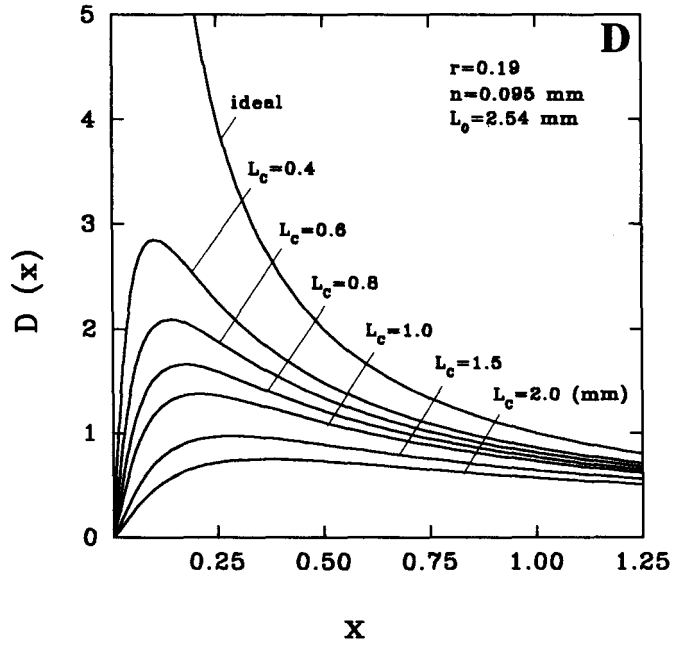

FIGURE 3 Continued.

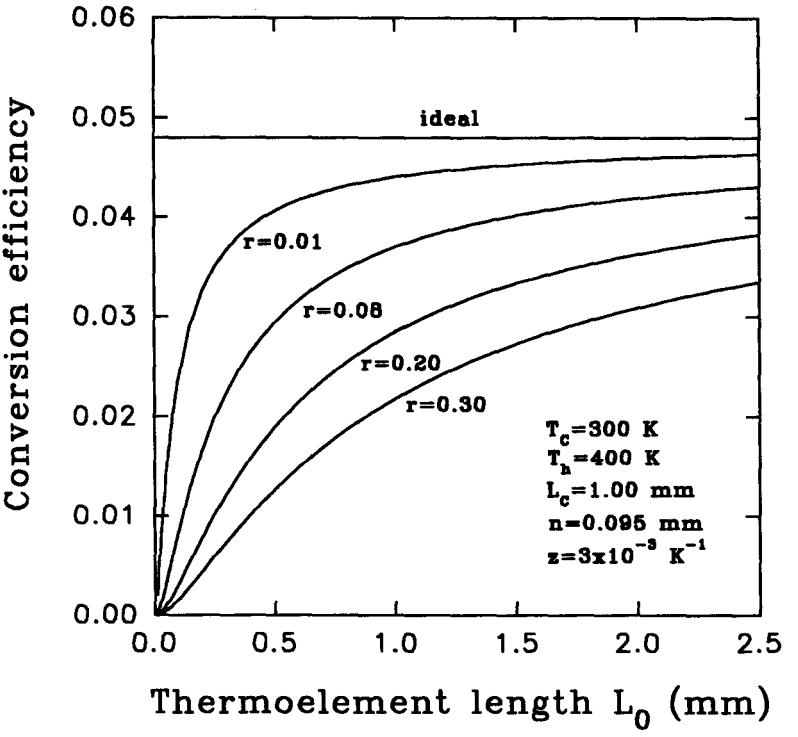

FIGURE 4 Conversion efficiency vs. length of thermoelements of the modules.

Obviously, the conversion efficiency is also affected by the length of the thermoelements, which reflects the dependence of the conversion efficiency of the device on the properties of the thermal and electrical contacts. Figure 4 illustrates the change of conversion efficiency with thermoelement length and contact properties. The conversion efficiency of the actual device will decrease with a reduction in the length of the thermoelements and this decrease will become more significant when the length of the thermoelements is very short. Therefore, optimization of the length should be a trade-off between the maximum power output and the conversion efficiency. Fortunately, in applications such as electrical power generation employing low-temperature waste heat, the conversion efficiency is not an overriding requirement. Moreover, the decrease in conversion efficiency is not very significant at the thermoelement length that corresponds to maximum power output.

38.5 Optimization of the System

Convenient low-temperature waste heat sources are usually in the form of warm water (see Chapter 44). Utilizing this type of heat source to drive a thermoelectric generator involves heat transfer from the liquid (water) to solid (device). A temperature difference will exist across the interface between the liquid and the solid. A conceptual electrical power generating system that uses Peltier devices as generators and "waste" hot water as a heat source is shown in Figure 5. Due to the extra thermal resistance that exists between the liquid and the solid interface, the thermoelement length has to be reoptimized to take into account the temperature drops at the solid-liquid interface.

If the heat transfer coefficient of the water to the ceramics of the device is h, the power output of this system will be further decreased, giving:

$$S(x) = \left[\frac{x + 2rw}{x + 2rw + 2\lambda/hL_o}\right]\left[\frac{ax^2}{(x + n/L_o)(x + 2rw)^2}\right] \tag{12}$$

where S(x) is the relative change in power output of the system as a function of the relative change in thermoelement length. The effect of the heat transfer coefficient on the power output of the

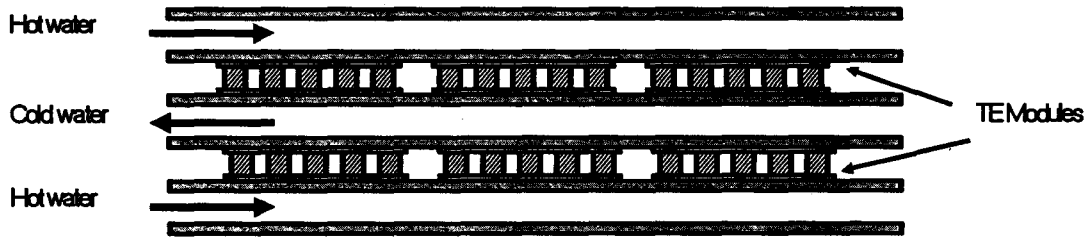

FIGURE 5 Schematic diagram of thermoelectric conversion system using flow of hot water as heat source.

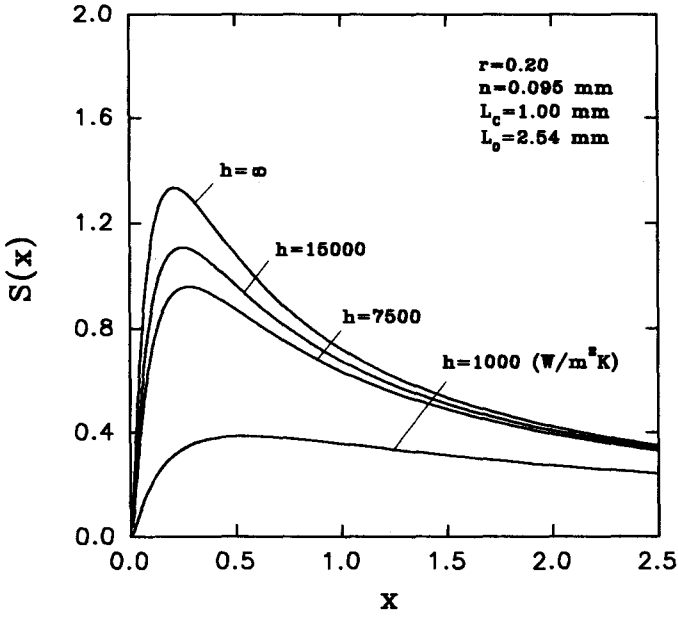

FIGURE 6 Effect of heat transfer coefficient on power output of system.

system is shown in Figure 6. An investigation of a prototype conversion system has shown that the maximization of the heat transfer from the water to the device is also vitally important.[8]

38.6 Economic Prospects

The increase in output power per unit area has significant economic benefits. Table 1 lists the increases in the power outputs that accompany a reduction in the thermoelement length (three Peltier devices investigated were obtained from MELCOR, U.S. and were identical apart from having thermoelements that differed in length). A decrease in thermoelement length results in not only an increase in power output but also a reduction in volume and amount of material. Currently available Peltier devices of the type investigated generate about 1 W (CP 1.4–127–10L) when operating at a temperature difference of around 80 K and cost about $20 a unit. The cost is likely to reduce to around $10 a unit for orders of several thousand. The calculated cost of generating electrical power using thermoelectrics is presented in Figure 7. It is evident that electricity can be

Table 1 Length Dependence of Power Output of Commercially Available Peltier Modules

Modules	L (mm)	L/L_o	Pc (W)	F_e (%)	F_i (%)	F_r (%)
CP 1.4–127–10L	2.54	1.00	1.36	0	0	0
CP 1.4–127–06L	1.52	0.60	1.72	26	68	30
CP 1.4–127–045L	1.14	0.45	2.01	48	120	50

L_o = 2.54 mm; Pc was measured at a temperature difference of 80 K; F is the fractional increase in power output; subscripts e, i, and r indicate that the values were obtained from experiment, "ideal" model, and realistic model, respectively.

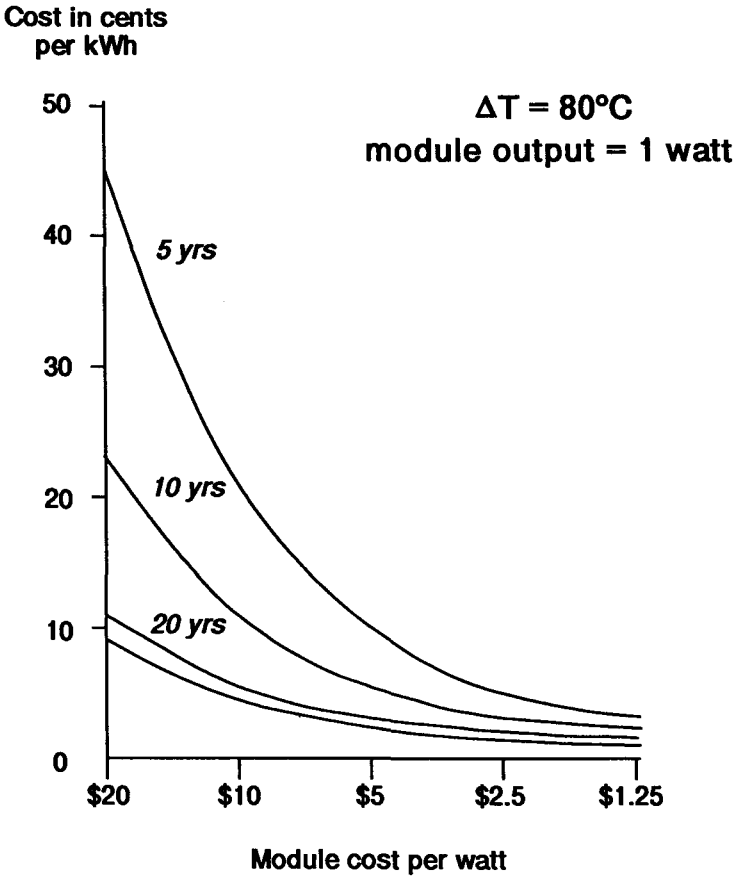

FIGURE 7 Cost of electricity as a function of module cost and power output per module.

generated on-site over 20 years at a cost of around 6 cents per kilowatt hour. Employing a module with shorter thermoelements (producing 1.75 W) reduces the cost to about 3.5 cents per kilowatt hour.

The modules will be the most costly items in any large-scale thermoelectric generating system. If the system construction costs are assumed to be of similar order to the cost of the modules, the system's generation cost will double. Nevertheless, the total on-site generating cost of around 7 cents per kilowatt hour would compare very favorably with the price of between 5 and 7 cents paid for electricity generated by conventional methods.[14]

In an actual conversion system, the heat input is provided by a flow of water and the optimization of thermoelements is different. Nevertheless, the results shown in Figure 6 indicate that for heat transfer coefficient of 7550 W m^{-2} K^{-1} the relative increase in output power per module would achieve a maximum at 0.9. This corresponds to an actual power output of about 1.4 W (e) when the temperature difference is 80 K. As is evident from Figure 7 any increase in the cost per kilowatt hour will be marginal.

References

1. Thomson, W., On a mechanical theory of thermoelectric currents, *Proc. R. Soc. Edinburgh*, 91–98, 1851.
2. See, for example, S. R. de Groot, *Thermodynamics of Irreversible Processes*, North Holland Publishing, Amsterdam, 1952.
3. Cadoff, I. B. and Miller, E., *Thermoelectric Materials and Devices*, Reinhold, New York, 1959.
4. Rowe, D. M. and Bhandari, C. M., *Modern Thermoelectrics*, Holt, Rinehart and Winston, 1983.
5. Goldsmid, H. J., *Electronic Refrigeration*, Pion Limited, London, 1986.
6. Benson, D. K. and Jaydev, T.S., *Proc. Third Int. Conf. Thermoelectric Energy Conversion*, Arlington, Texas, March 12–14, 1980.
7. Watt Committee Report, Profiting from Low Grade Heat, presented at the Institute of Mechanical Engineers, Feb. 26, 1991.
8. Burke, E. J. and Burist, R. J., *Proc. Fifth Int. Conf. Thermoelectric Energy*, Arlington, Texas, March 14–16, 1984, p. 91.
9. Matsuura, K. T., IEE Japan, 107-B (6), 307, 1987.
10. Min, G. and Rowe, D. M., Optimisation of thermoelectric module geometry for "waste" heat electrical generation, *J. Power Sources*, 38, 253, 1992.
11. Ioffe, A. F., *Semiconductor Thermoelements and Thermoelectric Cooling*, Infosearch Ltd., London, 1957.
12. Min, G., Rowe, D. M., Assis, O., and Williams, S.G.K., Determining the electrical and thermal contact resistance of a thermoelectric module, *Proc. 11th Int. Conf. Thermoelectrics*, Arlington, Texas, 1992.
13. Heikes, R. R. and Ure, R. W., *Thermoelectricity Science and Engineering*, Interscience Publishers, New York, 1961.
14. Crook, J., Some uses of low grade heat, in *Power Generation Technology*, Sterlin Publications International, London, in press, 1992.

39

Calculations of Generator Performance

Milan H. Cobble
New Mexico State University
Las Cruces, New Mexico, U.S.A.

39.1 Introduction

An analysis of a thermoelectric generator is presented and expressions derived for the thermoelectric efficiency, optimum efficiency, maximum power output, and maximum power output per unit area. Important parameters are computed for both a single-couple thermoelectric generator (TEG) and a multicouple device (MTEG). The effect of thermoelement contact resistance is discussed. A list of the terms used in this chapter can be found at the end of the chapter.

39.2 Thermodynamic (Thermoelectric) Efficiency

The thermodynamic efficiency of a single-couple thermoelectric generator (Figure 1) without contact resistance is given by

$$\eta_t = P_o/Q_h \tag{1}$$

where

$$P_o = I^2R_o \text{ electrical power output} \tag{2}$$

and

$$Q_h = K\Delta T + \alpha T_h I - \frac{1}{2}I^2R, \text{ heat input} \tag{3}$$

0-8493-0146-7/95/$0.00+$.50

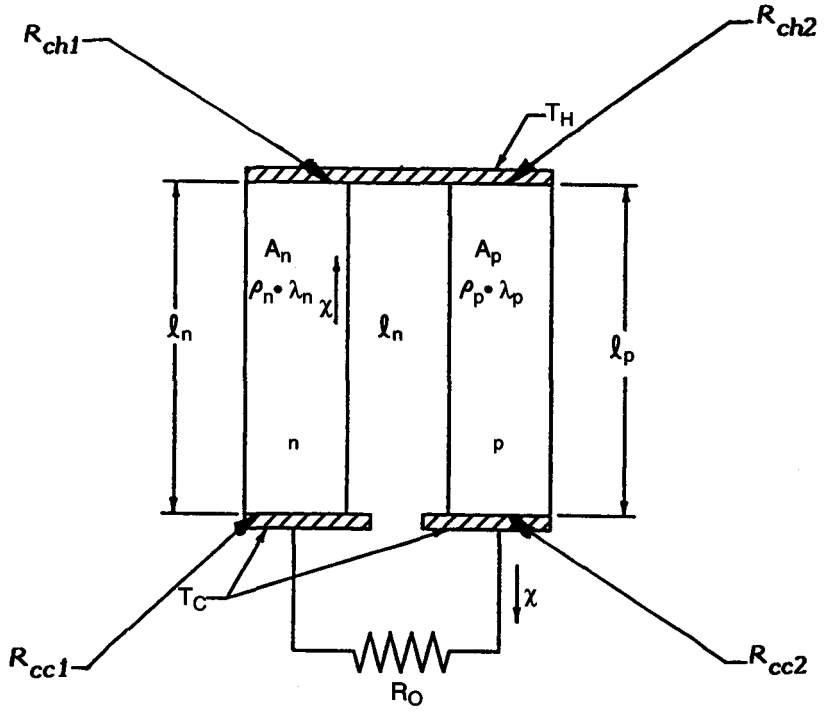

FIGURE 1 A thermoelectric generator.

In the above equations, the following relationships apply:

$$I = V_{oc}/R_t = V_{oc}/(R + R_o) \tag{4}$$

$$K = \lambda_n\gamma_n + \lambda_p\gamma_p \tag{5}$$

$$\gamma_i = A_i/l_i,\ i = n,p \tag{6}$$

$$\Delta T = T_h - T_c \tag{7}$$

$$\alpha = |\alpha_n| + |\alpha_p| \tag{8}$$

$$R = \rho_n/\gamma_n + \rho_p/\gamma_p \tag{9}$$

$$V_{oc} = \alpha\Delta T \tag{10}$$

If we now define

$$\mu = R_o/R \tag{11}$$

and

$$\eta_c = \Delta T/T_h, \text{ (the Carnot efficiency)} \tag{12}$$

then the above expressions in Equation 1 gives

$$\eta_t = \frac{\mu\eta_c}{[KR(\mu + 1)^2/\alpha^2 T_h + (\mu + 1) - \eta_c/2]} \tag{13}$$

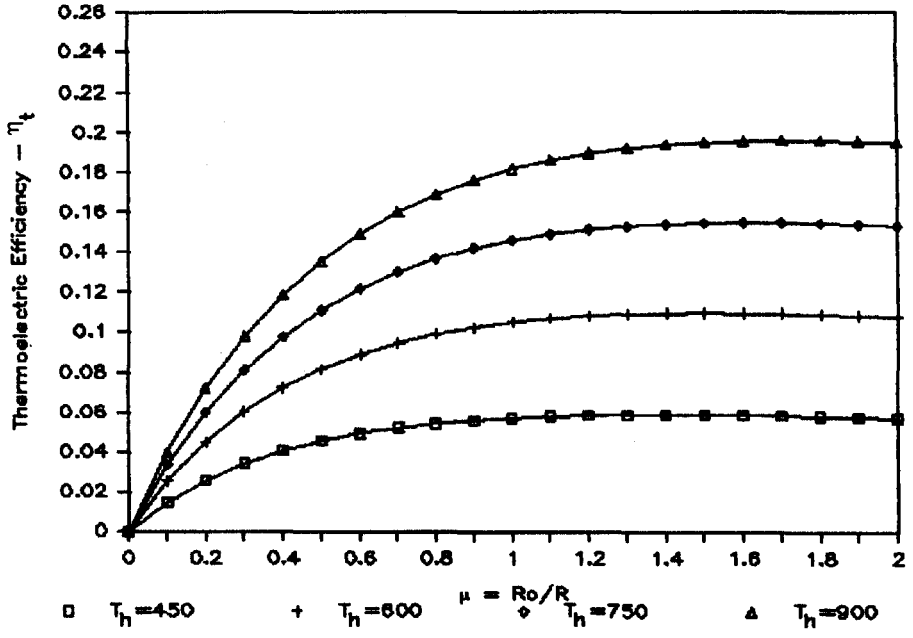

FIGURE 2 Thermoelectric efficiency as a function of μ and T.

and in Equation 13

$$KR = \lambda_n\rho_n + \lambda_n\rho_p\Psi + \lambda_p\rho_n/\Psi + \lambda_p\rho_p = KR(\Psi) \tag{14}$$

where

$$\Psi = \gamma_n/\gamma_p \tag{15}$$

Consequently,

$$\eta_t = \eta_t(\mu,\Psi) \tag{16}$$

By definition

$$Z = \alpha^2/KR = Z(\Psi), \text{ (Ioffe figure-of-merit)} \tag{17}$$

So we may write

$$\eta_t = \frac{\mu\eta_c}{[(\mu + 1)^2/ZT_h + (\mu + 1) - \eta_c/2]} \tag{18}$$

This is the well-known expression for the thermodynamic (thermoelectric) efficiency of a thermoelectric generator (single couple).[1] Using Equation 18 and assuming $Z = 2.22 \times 10^{-3}\ K^{-1}$, a graph of the thermoelectric efficiency of a generator is shown in Figure 2 as a function of μ and T_h; the cold junction is at 300 K.

39.3 Optimizing the Efficiency

To optimize η_t the following conditions are applied:

$$\frac{\partial}{\partial\Psi}(\eta_t)_\mu = 0 \tag{19}$$

$$\frac{\partial}{\partial\mu}(\eta_t)_\Psi = 0 \tag{20}$$

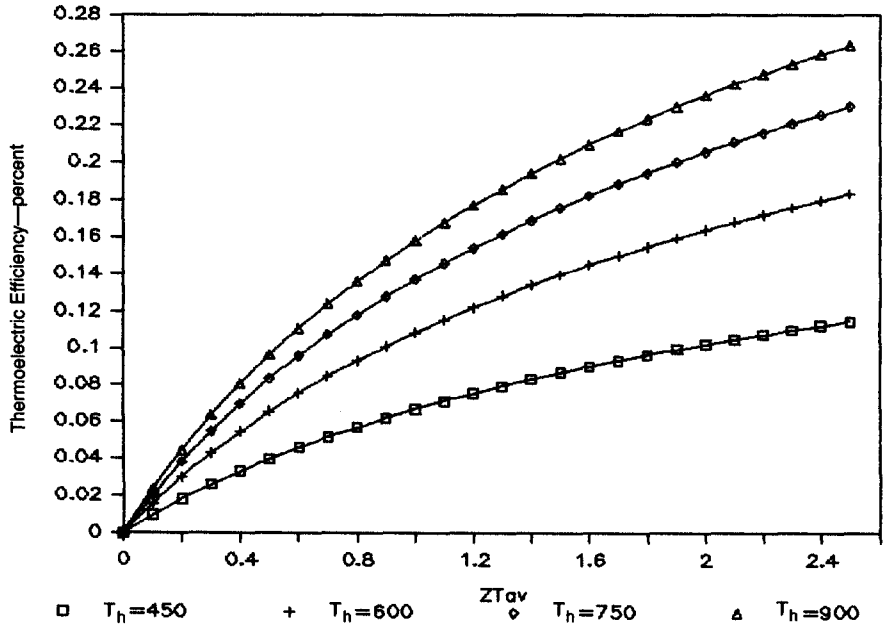

FIGURE 3 Optimum thermoelectric efficiency as a function of ZT_{av}.

Using the operator of Equation 19 on Equation 18 gives

$$KR'(\Psi) = 0 = \lambda_n\rho_p - \lambda_p\rho_n/\Psi^2 \tag{21}$$

Consequently,

$$\Psi(optimum) = \Psi_{o\eta} = [\lambda_p\rho_n/\lambda_n\rho_p]^{1/2} \tag{22}$$

and

$$KR(optimum) = KR_{o\eta} = KR(\Psi_{o\eta}) = [(\lambda_n\rho_n)^{1/2} + (\lambda_p\rho_p)^{1/2}]^2 \tag{23}$$

Also, from Equation 21:

$$Z(optimum) = Z^* = \alpha^2/KR_{o\eta} = \frac{\alpha^2}{[(\lambda_n\rho_n)^{1/2} + (\lambda_p\rho_p)^{1/2}]^2} \tag{24}$$

Using the operator of Equation 20 on Equation 18 gives relationships[3,4]

$$\mu_{o\eta} = [1 + ZT_{av}]^{1/2} \tag{25}$$

where

$$T_{av} = (T_h + T_c)/2 \tag{26}$$

$$\eta_{to} = (\mu_{o\eta} - 1)\eta_c/(\mu_{o\eta} + T_c/T_h) \tag{27}$$

Figure 3 shows a plot of the optimum thermoelectric efficiency as a function of ZT_{av}, obtained using Equations 25 and 27 for a range of hot junction temperatures; the cold junction at 300 K.

39.4 Maximum Power

The expression for power is

$$P_o = I^2R_o = V_{oc}^2\mu/R(\mu + 1)^2 = P(\mu,R) \tag{28}$$

For optimum power at a fixed R, the following condition is applied:

$$\frac{\partial}{\partial\mu}(P_o)_R = 0 \tag{29}$$

Using the operator of Equation 29 on Equation 28 gives

$$\mu(optimum\ power) = \mu_{op} = 1 \tag{30}$$

The optimum power is[5]

$$P_o(\mu_{op},R) = V_{oc}^2/4R = P_o(ideal\ maximum) = P_{omi} \tag{31}$$

39.5 Maximum Power per Unit Area

If we now define

$$\Phi = P_o/A_t = \frac{v_{oc}{}^2\mu}{RA_t(\mu + 1)^2} \tag{32}$$

where

$$RA_t = (A_n + A_p)[\rho_n/\gamma_n + \rho_p/\gamma_p] = l[\rho_n(1 + 1/\Psi) + \rho_p(1 + \Psi)] = RA_t(\Psi) \tag{33}$$

In the above it is assumed that

$$l = l_n = l_p \tag{34}$$

So

$$\Phi = \Phi(\mu,\Psi) \tag{35}$$

To optimize Φ

$$\frac{\partial}{\partial\mu}(\Phi)_\Psi = 0 \tag{36}$$

$$\frac{\partial}{\partial\Psi}(\Phi)_\mu = 0 \tag{37}$$

Using the operator of Equation 36 on Equation 32 gives

$$\mu(optimum\ power) = \mu_{o\Phi} = 1 = \mu_{op} \tag{38}$$

Using the operator of Equation 37 on Equation 32 gives

$$\Psi(optimum\ power) = \Psi_{o\Phi} = [\rho_n/\rho_p]^{1/2} \tag{39}$$

Then,

$$RA_t(optimum\ \Phi) = RA_t(\Psi_{o\Phi}) = l[(\rho_n)^{1/2} + (\rho_p)^{1/2}]^2 \tag{40}$$

Thus,

$$\Phi(maximum) = \Phi(\mu_{o\Phi},\Psi_{o\Phi}) = \frac{V_{oc}{}^2}{4l[(\rho_n)^{1/2} + (\rho_p)^{1/2}]^2} \tag{41}$$

39.6 Multicouple Generators

The efficiency of a multicouple generator (voltage in series) is given by

$$\hat{\eta}_t = \hat{P}_o/\hat{Q}_h \tag{42}$$

If it is assumed that:

$$\begin{aligned} \hat{P}_o &= nP_o & \hat{I} &= I \\ \hat{Q}_h &= nQ_h & \hat{n} &= \hat{V}_{oc}/V_{oc} \\ \hat{R} &= nR & \hat{R}_o &= nR_o \end{aligned} \tag{43}$$

and

$$\hat{V} = \hat{I}\hat{R}_o = I\hat{R}_o = nV$$

Then

$$\hat{\eta}_t = \frac{I^2R_o}{[K\Delta T + \alpha T_h I - \tfrac{1}{2}I^2R]} = \eta_t \tag{44}$$

Thus,

$$\hat{\eta}_t = \frac{\mu\eta_c}{\{(\mu + 1)^2/ZT_h + (\mu + 1) -)\eta_c/2\}} = \eta_t \tag{45}$$

A plot of Equation 45 for a single or multicouple generator is shown in Figure 2.

In addition, the following ratios of parameters are describable for both single and multicouple generators:

1. Power

$$P_r = \hat{P}_o/\hat{P}_{omi} = P_o/P_{omi} = \frac{4\mu}{(\mu + 1)^2} \tag{46}$$

2. Current

$$I_r = \hat{I}/\hat{I}_{ssi} = I/I_{ssi} = \frac{1}{(\mu + 1)} \tag{47}$$

where

$$\hat{I}_{ssi} = I_{ssi} = \hat{V}_{oc}/\hat{R} = V_{oc}/R \tag{48}$$

3. Voltage

$$V_r = \frac{\hat{V}}{\hat{V}_{oc}} = \frac{V}{V_{oc}} = \frac{\mu}{(\mu + 1)} \tag{49}$$

Figure 4 shows a plot of P_r, I_r, and V_r vs μ for a single or multicouple generator. Equivalent graphs are shown in References 6 and 7.

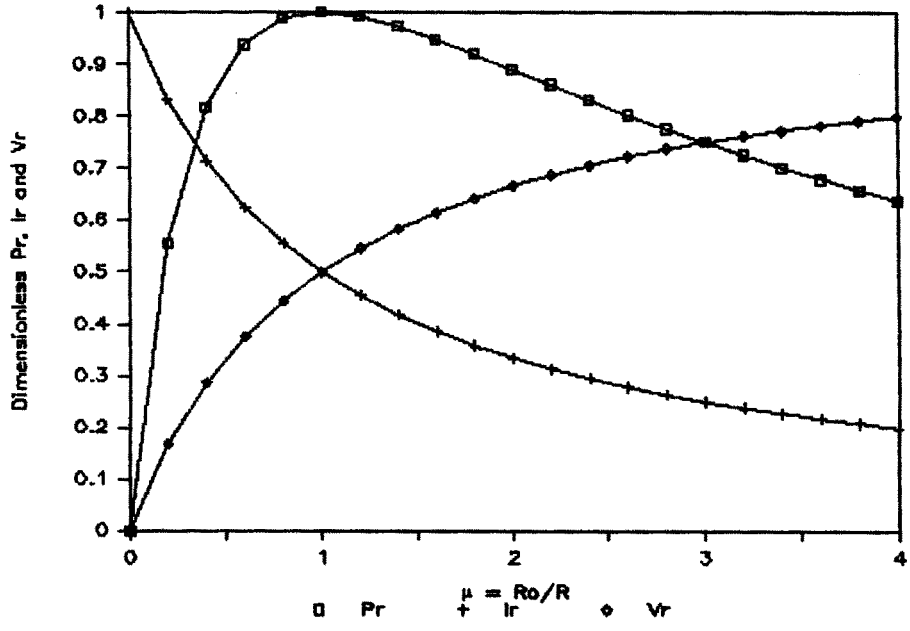

FIGURE 4 Plot of P_r, I_r, and V_r as a function of μ for a single or multicouple.

39.7 Computations

Using the equations developed above and some typical assumed values for the thermoelectric parameters for a bismuth telluride-type device,[8] a range of values is computed for three types of devices, single couples as well as multicouples. The maximum efficiency and maximum power per unit area is computed as well as the power for a device with identical n-leg and p-leg cross-sectional areas.

Assumed Data

T_c = 300 K, T_h = 600 K, η_c = 0.5, T_{av} = 450 K, ΔT = 300 K.

n-leg
α_n = −190E-6 V/K
ρ_n = 1.35E-3 ohm cm
λ_n = 1.40 E-3 W/cm K
l_n = 1 cm, A_n = 1 cm^2
γ_n = 1 cm, $\hat{V}_{oc}$ = 12 V

p-leg
α_p = 230E-6 V/K
ρ_p = 1.75E-3 ohm cm
λ_p = 1.20E-3 W/cm K
l_p = 1 cm

Results

1. (Maximum efficiency, $\Psi = (\rho_n\lambda_p/\rho_p\lambda_n)^{1/2}$ = 0.813)

K = 28.757E-3 W/K
Z = Z* = 2.265E-3/K
μ_{on} = 1.421
I_{ssi} = 45.979 A
$P_{o\eta}$ = 1.42125 W
A_t = 2.2297 cm^2
Q_h = 12.964 W

R = 2.773E-3 ohm
γ_p = 1.22974 ohm cm
$R_{o\eta}$ = 3.94E-3 ohm
$I_{o\eta}$ = 18.99 A
A_p = 1.2297 cm^2
$\Phi_{o\eta}$ = 0.6374 W/cm^2
η_{to} = 0.10958

I_{mp} = 22.989 A
Φ_{omp} = 0.6572 W/cm^2
$\hat{R}$ = 0.26099 ohms
P_{omp} = 1.4655 W
n = 94.117 Tegs
$\hat{P}_{omp}$ = 137.93 W

2. (Maximum $\Phi_o = P_t/A_{o\phi}$, $\psi = (\rho_n/\rho_p)^{1/2} = 0.878$)

K = 28.87E-3 W/K
Z = 2.262E-3/K
$\mu_{o\Phi}$ = 1.430477
I_{ssi} = 44.1628 A
$P_{o\Phi}$ = 1.3652 W
A_t = 2.13855 cm^2
Q_h = 12.47083 W
I_{mp} = 22.081 A
Φ_{omp} = 0.658245 W/cm^2
$\hat{R}$ = 0.271 ohms
R = 2.887E-3 ohms
γ_p = 1.13855 cm
R_o = 4.1E-3 ohms
$I_{o\Phi}$ = 18.24 A
A_p = 1.13855 cm^2
$\phi_{o\Phi}$ = 0.63838 A/cm^2
η_{to} = 0.109472
P_{omp} = 1.40769 W
n = 94.117 Tegs
$\hat{P}_{omp}$ = 132.488 W

3. (Equal areas, $\Psi = \gamma_n/\gamma_p = 1$)

K = 26.0E-3 W/cm K
Z = 2.241E-3/K
μ_{oea} = 1.4171
I_{ssi} = 41.129 A
P_{oea} = 1.2719 W
A_t = 2 cm^2
Q_h = 11.6901 W
I_{mp} = 20.5645 A
Φ_{omp} = 0.65549 W/cm^2
$\hat{R}$ = 0.2917 ohms
R = 3.1E-3 ohms
γ_p = 1 cm
R_{oea} = 4.393E-3 ohms
I_{oea} = 17.0151 A
A_p = 1 cm^2
Φ_{oea} = 0.63597 W/cm^2
η_{to} = 0.108804
P_{omp} = 1.31099 W
n = 94.711 Tegs
$\hat{P}_{omp}$ = 123.38 W

39.8 Thermoelectric Efficiency (Contact Resistance Included)

Referring to Figure 1, the effect of contact resistance (CR) can be determined.[9] The thermoelectric efficiency is given by

$$\eta_t = P_o/Q_h \tag{1}$$

where

$$P_o = I^2R_o, \text{ electrical output} \tag{2}$$

and

$$Q_h = K\Delta T + \alpha T_h I - \frac{1}{2}I^2R - I^2R_{ch}, \text{ heat input} \tag{50}$$

where, in addition to the terms defined on page 1, the following hold:

$$R_t = R + R_o + R_c \tag{51}$$

$$R_c = R_{ch} + R_{cc} = R_{ch1} + R_{ch2} + R_{cc1} + R_{cc2} \tag{52}$$

If we now define

$$\delta = \delta_c = R_c/R \tag{53}$$

$$\delta_{ch} = R_{ch}/R \tag{54}$$

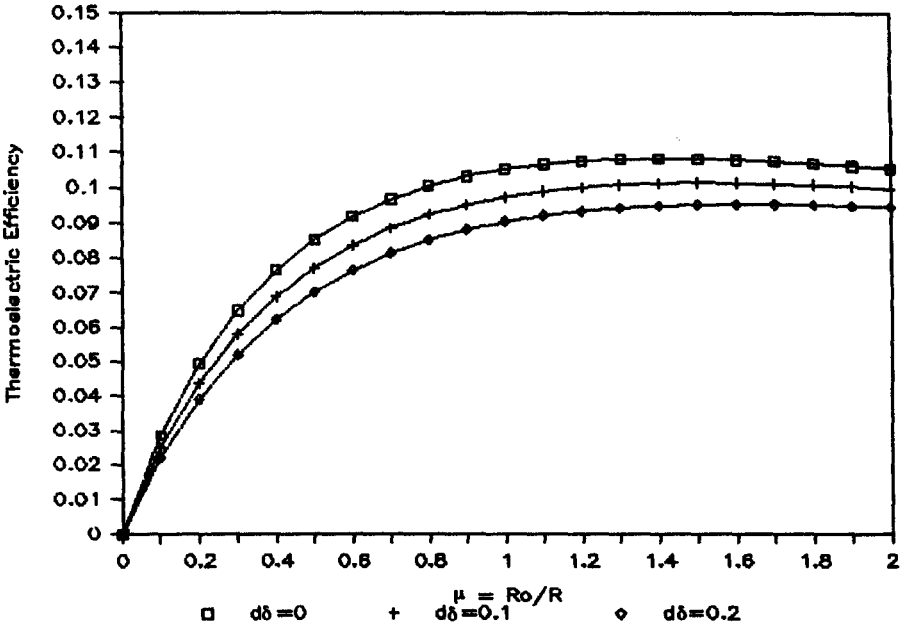

FIGURE 5 Thermoelectric efficiency as a function of μ and δ.

$$\phi_c = 1 + 2\delta_{ch} \tag{55}$$

using the above, and previously defined terms in Equation 1, gives

$$\eta_t = \frac{\mu\eta_c}{[KR(\mu + 1 + \delta)^2/\alpha^2 T_h + (\mu + 1 + \delta) - \phi_c\eta_c/2]} \tag{56}$$

As noted before

$$\eta_t = \eta_t(\mu,\psi) \tag{57}$$

Now, by definition

$$Z = \alpha^2/KR = Z(\psi), \text{ Ioffe figure-of-merit} \tag{58}$$

So,

$$\eta_t = \frac{\mu\eta_c}{[(\mu + 1 + \delta)^2/ZT_h + (\mu + 1 + \delta) - \phi_c\eta_c/2]} \tag{59}$$

Using Equation 59 a graph of the thermoelectric efficiency of a thermoelectric generator is shown as a function of μ and δ in Figure 5; T_h = 600 K, T_c = 300 K, and Z = 2.22 × 10^{-3} K^{-1}. When $\delta_{ch} \to 0$ and $\delta \to 0$ we have the limiting case, namely Equation 18.

39.9 Optimizing η_t with Contact Resistance

To optimize η_t, Equations 19 and 20 must be satisfied. Applying them to Equation 61, when $\delta = 2\,\delta_{ch}$, gives

$$\mu(optimum) = \mu_{o\eta} = [(1 + \delta)^2 + (1 + \delta)ZT_{av}]^{1/2} = \mu_{o\eta}(\delta,Z) \tag{60}$$

Using Equation 60 in Equation 59 gives

$$\eta_t(\mu_{o\eta},Z) = [\mu_{o\eta} - (1 + \delta)]\eta_c/[\mu_{o\eta} + (1 + \delta)T_c/T_h] = \eta_t(optimum) = \eta_{to} \tag{61}$$

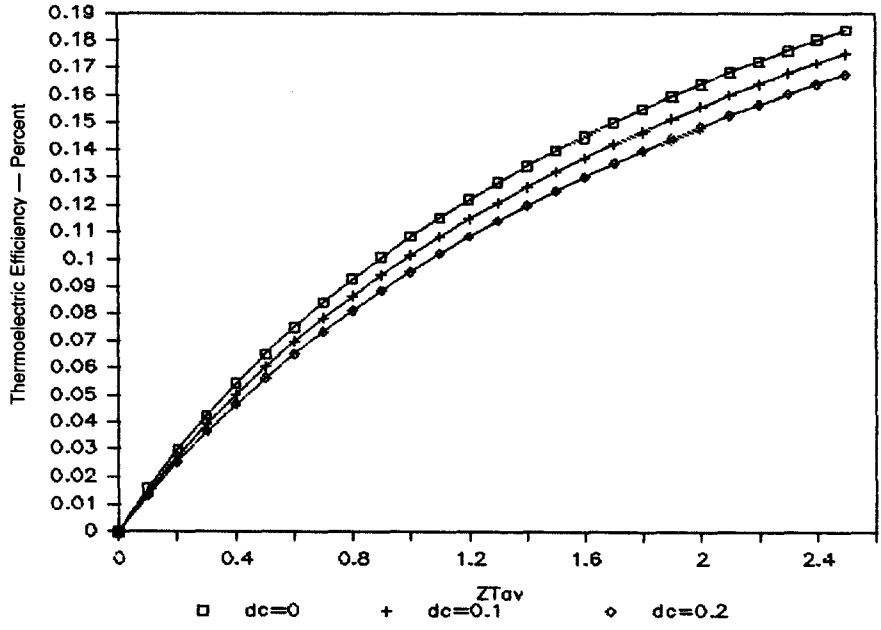

FIGURE 6 Optimum thermoelectric efficiency as a function of ZT_{av} and δ for a single or multicouple generator.

Now if

$$\delta_{ch} \rightarrow 0 \tag{62a}$$

$$\delta \rightarrow 0 \tag{62b}$$

then Equation 60 reduces to Equation 25 and Equation 61 reduces to Equation 27. Additionally, as with no contact resistance

$$\psi(optimal) = \psi_{o\eta} = (\lambda_p \rho_n / \lambda_n \rho_p)^{1/2} \tag{22}$$

Figure 6 shows a plot of the optimum thermoelectric efficiency as a function of ZT_{av} and δ, using Equations 62 and 63. $T_c = 300$ K, $T_h = 600$ K.

39.10 Maximum Power with Contact Resistance

The expression for power is

$$P_o = I^2 R_o = V_{oc}^2 \mu / R[\mu + (1 + \delta)]^2 = P_o(\mu, R) \tag{63}$$

For optimum power at a fixed R, satisfying Equation 29 and using Equation 63 gives

$$\mu(optimum\ power) = \mu_{op} = 1 + \delta \tag{64}$$

The optimum power is

$$P_o(\mu_{op} R) = V_{oc}^2 / 4R(1 + \delta) \tag{65}$$

When $\delta \rightarrow 0$, then we obtain Equation 31.

39.11 Maximum Power per Unit Area with Contact Resistance

From the definition of ϕ, Equation 32,

$$\Phi = P_o / A_t = \frac{V_{oc}^2 \mu}{R A_t [\mu + (1 + \delta)]^2} \tag{66}$$

where RA_t is defined in Equations 33 and 34 and so, as before,

$$\Phi = \Phi(\mu,\psi) \tag{67}$$

To optimize Φ, apply the conditions of Equations 36 and 37 to Equation 66 and obtain

$$\mu(optimum\ power) = \mu_{o\Phi} = 1 + \delta = \mu_{op} \tag{68}$$

and, as before,

$$\psi(optimum\ power) = \psi_{o\Phi} = [\rho_n/\rho_p]^{1/2} \tag{69}$$

Then

$$RA_t(optimum\ power\ \phi) = RA_t(\psi_{o\Phi}) = l[(\rho_n)^{1/2} + (\rho_p)^{1/2}]^2 \tag{70}$$

Thus,

$$\Phi(maximum) = \Phi(\mu_{o\Phi}, \psi_{o\Phi}) = \frac{V_{oc}^2}{4l[(\rho_n)^{1/2} + (\rho_p)^{1/2}]^2(1 + \delta)} \tag{71}$$

39.12 Multicouple Generators with Contact Resistance

The efficiency of a multistage generator (voltage in series) is given by

$$\hat{\eta}_t = \hat{P}_o/\hat{Q}_h \tag{42}$$

If, in addition to the previous assumptions (Equation 43), we assume:

$$\begin{aligned} \hat{R}_c &= nR_c \qquad \hat{R}_o = nR_o \\ R_{ch} &= R_{cc} \qquad \hat{R}_{ch} = nR_{ch} \end{aligned} \tag{72}$$

then

$$\hat{\eta}_t = \frac{I^2R_o}{[K\Delta T + \alpha T_h I - \tfrac{1}{2}I^2R(1 + 2\delta_{ch})]} = \eta_t \tag{73}$$

So

$$\hat{\eta}_t = \frac{\mu\eta_c}{\{[\mu + (1 + \delta)]^2/ZT_h + [\mu + (1 + \delta)] - (1 + \delta)\eta_c/2\}} = \eta_t \tag{74}$$

A plot of this, for a single and multicouple generator, is shown in Figure 5.

Additionally, the following ratios are desirable for multicouple generators having contact resistance, as well as single-couple TEGS.

1. Power

$$P_r = \hat{P}_o/\hat{P}_{omi} = P_o/P_{omi} = \frac{4\mu}{[\mu + (1 + \delta)]^2} \tag{75}$$

2. Current

$$I_r = \hat{I}/\hat{I}_{ssi} = I/I_{ssi} = \frac{1}{[\mu + (1 + \delta)]} \tag{76}$$

I_{ssi} is given in Equation 48.

3. Voltage

$$V_r = \frac{\hat{V}}{\hat{V}_{oc}} = \frac{V}{V_{oc}} = \frac{\mu}{[\mu + (1 + \delta)]} \tag{77}$$

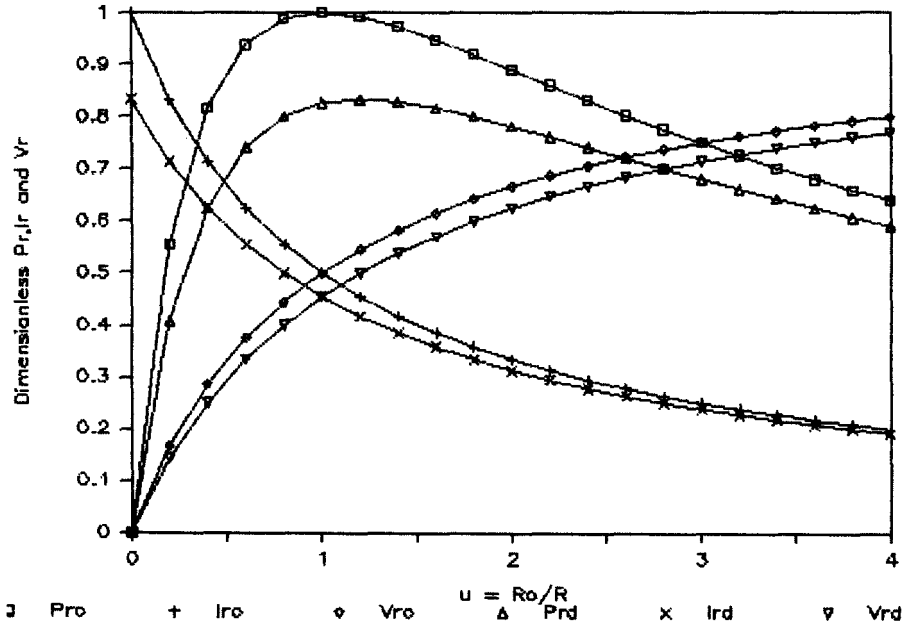

FIGURE 7 Plots of power, current, and voltage ratios as a function of μ for $\delta = 0$ and 0.2.

Figure 7 shows a plot of P_r, I_r, and V_r vs. μ for a single or multicouple generator; $\delta = 0$, 0.2. Equivalent graphs are published in References 6 and 7.

39.13 Conclusion

Expressions for the thermoelectric efficiency η_t, power P_o, power per unit area Φ, relative power ratio P_r, relative current ratio I_r, and the relative voltage ratio V_r have been derived. The thermoelectric efficiency, power, and power per unit area have been optimized, and the resulting equations reported. The results, shown graphically, are for a single-couple generator (TEG) and a multistage generator (MTEG) having contact resistance. Additionally, the results of computations for a typical bismuth telluride type of device are shown for three types of TEGS and MTEGS. The effect of contact resistance on thermal efficiency, power, power per unit area, the relative power ratio, the relative current ratio, and the relative voltage ratio is given in equations and also presented graphically.

39.14 Nomenclature

A_t	Total area, cm^2
A_n, A_p	Cross-sectional area of the n and p legs, cm^2
I	Current, A
$\hat{I}$	Current in multistage generator, A
I_r	Current ratio, dimensionless
K	Thermal conductance, W/K
λ_n, λ_p	Thermal conductivity of the n and p legs, W/cm K
l	Leg element length, cm
l_n, l_p	Length of n and p elements, cm
n	Number of single stages in multistage generator, dim.
P_o	Electric power output, W
$\hat{P}_o$	Electrical power output of MTEG, W

P_r	Power ratio, dimensionless
Q_h	Thermal input, W
$\hat{Q}_h$	Thermal input to MTEG, W
R	Device resistance, ohms
$\hat{R}$	MTEG resistance, ohms
R_c	Contact resistance, ohms
$\hat{R}_c$	MTEG contact resistance, ohms
R_{cc}	Contact resistance at cold temperature, ohms
$\hat{R}_{cc}$	MTEG contact resistance at cold temperature, ohms
R_{ch}	Contact resistance at hot temperature, ohms
$\hat{R}_{ch}$	MTEG contact resistance at hot temperature, ohms
R_t	Total resistance, ohms
$\hat{R}_t$	MTEG total resistance, ohms
T_{av}	Average temperature, K
T_c	Cold junction temperature, K
T_h	Hot junction temperature, K
V	Load voltage, V
$\hat{V}$	MTEG load voltage, V
V_r	Voltage ratio, dimensionless
V_{oc}	Open circuit voltage, V
$\hat{V}_{oc}$	MTEG open circuit voltage, V
Z	Ioffe figure-of-merit, 1/K
Z^*	Optimal Ioffe figure-of-merit, 1/K
α	Seebeck coefficient, V/K
α_n, α_p	Seebeck coefficients of n and p legs, V/K
γ_i	A_i/l_i, i = n, p, cm
δ	$\delta_c = R_c/R$, dimensionless
δ_{ch}	R_{ch}/R, dimensionless
μ	R_o/R, dimensionless
η_c	Carnot efficiency, dimensionless
η_t	Thermodynamic (thermoelectric) efficiency, dimensionless
$\hat{\eta}_t$	MTEG thermodynamic efficiency, dimensionless
ρ_n, ρ_p	Electrical resistivity of n and p legs, ohm cm
Φ	P_o/A_t, W/cm^2
ϕ_c	$1 + 2\delta_{ch}$, dimensionless
Ψ	γ_n/γ_p, dimensionless

References

1. Angrist, S. W., *Direct Energy Conversion,* Third Edition, 1976, Allyn and Bacon, Boston, p. 138.
2. Angrist, S. W., *Direct Energy Conversion,* Third Edition, 1976, Allyn and Bacon, Boston, p. 138.
3. Angrist, S. W., *Direct Energy Conversion,* Third Edition, 1976, Allyn and Bacon, Boston, pp. 138–9.
4. Ioffe, A. F., *Semiconductor Thermoelements and Thermoelectric Cooling,* Infosearch Limited, London, 1957, p. 40.
5. Angrist, S. W., Direct Energy Conversion, Third Edition, 1976, Allyn and Bacon, Boston, p. 140.
6. *Global Thermoelectric Instruction Manual,* A 1829–2000–82110, Global Thermoelectric Power Systems Ltd., Bassano, Alberta, Canada, p. 1–5.
7. *3M Brand Thermoelectric Generators—Installation Manual,* 3M Minnesota Mining and Manufacturing Co., St Paul, Minnesota, Section VIII.
8. Angrist, S. W., Direct Energy Conversion, Third Edition, 1976, Allyn and Bacon, Boston, p. 150.
9. Cobble, M. H., Analysis of a Thermoelectric Device Having Contact Resistance, *Proceedings of the XIth International Conference on Thermoelectrics,* University of Texas, Arlington, October 7–9, 1992.

Section F
Generator Applications

40
Terrestrial Applications of Thermoelectric Generators

William C. Hall
Teledyne Brown Engineering
Hunt Valley, Maryland, U.S.A.

40.1 Introduction

The thermoelectric principle was discovered in the first quarter of the 19th century, but only in the past 30 years has there been sustained production of thermoelectric power-generating devices. There were a few early attempts at a practical design—there is a record of a German firm offering such a device in 1899, but it wasn't until the post-World War II period that a technological breakthrough in the development of semiconductor materials made a reasonably efficient generator possible.

Also, it wasn't until the development of modern communications and data acquisition equipment that a need arose which matched the attributes of a thermoelectric generator. Such equipment has evolved over the years to have characteristically low power requirements, high reliability, and is designed for operation at remote sites. Without the thermoelectric generator, power supply options under these conditions were limited to batteries, primitive solar cells, engine-driven generators, or extended land lines. Each of these has its disadvantages which may encourage the use of an alternate independent power source, the thermoelectric generator.

Although the subject of this chapter is Terrestrial Applications, we must make at least a nodding reference to the space power requirements which prompted the milestone production of the SNAP-3 (Systems for Nuclear Auxiliary Power). In January 1959 this grapefruit-sized generator, fueled with polonium-210 as a heat source, was demonstrated to President Eisenhower. Although there had been a few primitive configurations earlier, the SNAP-3 is recognized as the first really

0-8493-0146-7/95/$0.00+$.50

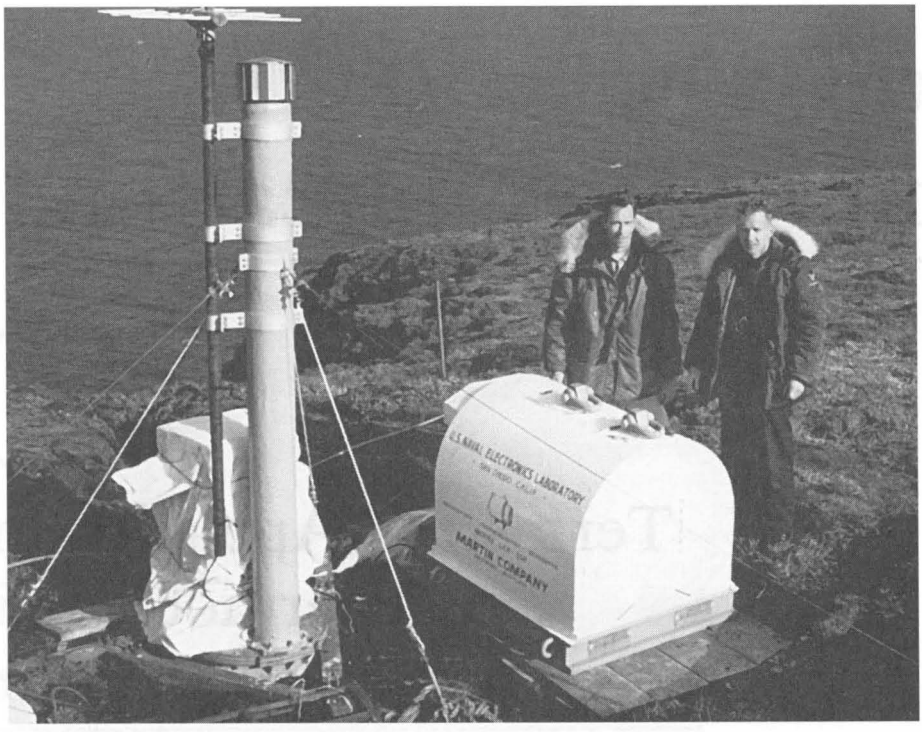

FIGURE 1 Installation of SENTINEL 25A, Fairway Rock, Alaska, 1966. (Courtesy of Teledyne Brown Engineering.)

practical thermoelectric power conversion device and formed the basis for a thermoelectric generator industry.

40.2 Radioisotope Thermoelectric Generators (RTG)

Weather Stations

Two years following the SNAP-3's debut the first atomic-powered weather station was established on Axel Heiberg Island, which is part of the Canadian Northwest Territories and is located on the 80th parallel of north latitude. This application set the tone for many of the first isotopic-powered thermoelectric generator installations. Here was a remote, mostly inaccessible, hostile environment which had heretofore created a significant gap in the regional weather network. The strontium-90 source, using a lead-telluride converter, provided a constant 5 W of power, enabling the collection and transmission of wind, temperature, and barometric pressure data. Shortly after this, during the Austral summer of 1962, a similar installation was established at Minna Bluff in the Antarctic, using the SNAP-7C. This station operated for 7 years before being supplanted by a new configuration in 1968 which used a SENTINEL 25C. In 1966 a SENTINEL 25A with appropriate data collection and transmission equipment was implanted on Fairway Rock, a speck of land in the Bering Strait (Figure 1). It provided uninterrupted power until 1981 when that generator was replaced by a newer model.

Other Antarctic weather installations were established and used throughout the 1960s and 1970s. A SNAP-21 was used on the Ross Ice Shelf, and an URIPS-8 was installed at Marble Point. This latter automatic weather station was temporarily relocated to the South Pole, and operated during the year 1975, after which it was returned to Marble Point.

This technology was not confined to the Arctic and Antarctic. In vivid environmental contrast, in 1976 three meteorological data collection stations were installed in a desert kingdom of the Middle East, each powered by a SENTINEL 25F. Plessey Radar Ltd. designed and constructed the

stations, which employed an EDASS data collection system and Racal's PICCOLO communication system. The data were transmitted to a central station and from there were made available to the World Meteorological Organization's World Weather Watch System. Since the installations' area is a breeding ground for significant weather patterns, this project provided a valuable addition to the meteorological data base.

A SENTINEL-8 RTG was deployed in 1970 to San Miguel Island off the coast of California. It continues to charge a 15-V nickel-cadmium battery, furnishing power to a meteorological data collection system; the data are transmitted to the Naval Air Station at Point Mugu for use in Pacific operations. This is probably the oldest continuously operating terrestrial RTG; earlier models have either been relocated for other uses, placed in storage, or decommissioned.

Radioisotopic thermoelectric generator weather stations were not exclusively land-based. In several cases, buoy-mounted weather stations were powered by radioisotope thermoelectric generators. Most notable were a SNAP-7D, which spent 7 years in the Gulf of Mexico, and a NOMAD buoy with three SENTINEL-25Ds, which was deployed in 1969.

Navigational Aids

A logical extension from weather station applications was to the field of navigational aids. In 1965 the British Atomic Energy Research Establishment (AERE) at Harwell designed and built several RIPPLE (RadioIsotope Powered Pulsed Light Equipment) generators, which, using strontium-90 as fuel, were used to power navigational aids, frequently xenon flash tubes, in the U.K. and Scandinavia. At or about the same time, the French Hispano-Suiza Division of SNECMA developed the MARGUERITE, and over the years the Soviet Union deployed a number of strontium-fueled ANGARA generators powering navigational aids along the Arctic coast of that country.

In North America in 1972, the Atomic Energy of Canada Limited (AECL) installed several navigational aids along the St. Lawrence Seaway, using the cobalt-60-fueled MAPLE (Minor Atomic Powered Life Equipment). The U.S. Coast Guard also installed a SNAP-7A-powered light buoy in Curtis Bay, Maryland in 1961, where it operated for 6 years and in 1964 a SNAP-7B was installed on Baltimore Light at that city's channel entrance into the Chesapeake Bay.

Subsea Operations

In 1968 an attempt was made to utilize an RTG in a purely industrial installation. The design mounted two 3-W RTGs on a subsea petroleum wellhead, where they charged batteries. The batteries provided electrical power to close and open four wellhead valves and also, upon command, report wellhead conditions. Communications with the surface platform, 5000 feet away, used acoustic signals generated at the surface triggering a response by the subsea control system. The system was installed in 90 feet of water in the Gulf of Mexico on a platform owned by Sinclair Oil and Gas Company. The operation was successful, but the assembly was retrieved after a few years, not because the RTGs were deficient, but because the system used motor-operators on the valves and might fail "as-is". This was not acceptable from a safety standpoint, since "fail-safe" would require failure to the "closed" position. However, this design also represented an early use of coded acoustic communication, which was to be used later on other offshore applications.

Other Terrestrial Applications

Often the RTG found employment in military or governmental applications. The United States' Antarctic installations came under the purview of the U.S. Navy, which provided logistical support to "Operation Deepfreeze", a multiyear effort involving the U.S. scientific community, including the National Science Foundation. Other applications have been in the area of supplying power to military communications or detection systems in environmentally hostile environments, sometimes submerged or buried.

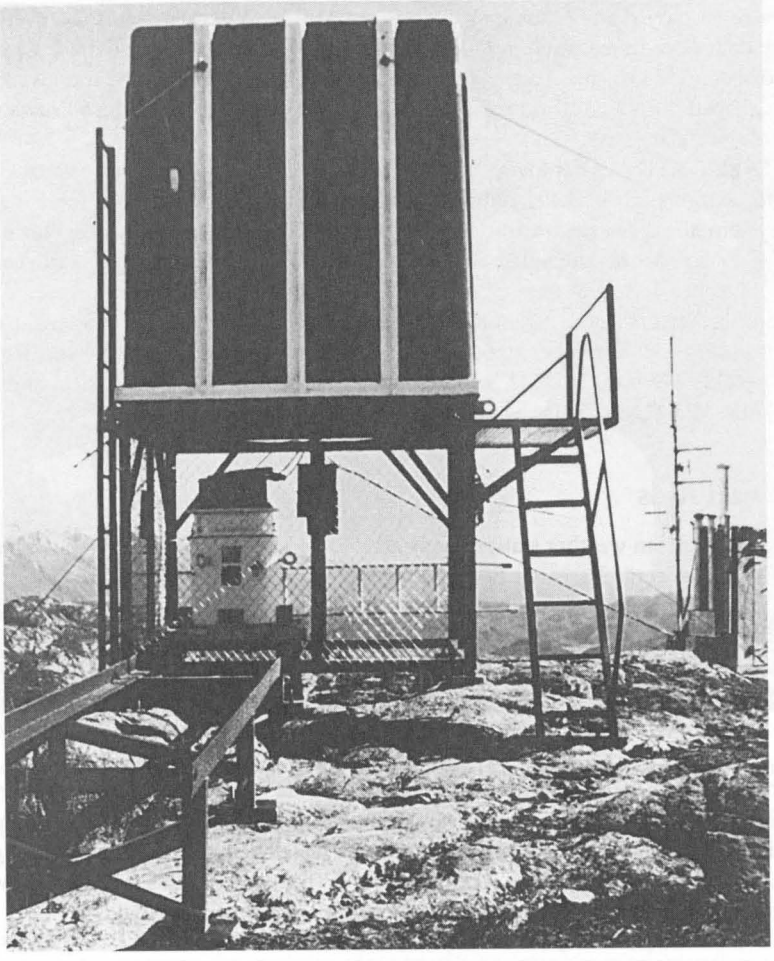

FIGURE 2 RTG-powered FAA installation, Lake Clark Pass, Alaska.

In other remote areas, such as Alaska, the Federal Aviation Agency (FAA) for years had a number of RTGs operating communications relay stations, most notably in Lake Clark Pass on the west side of Cook Inlet (Figure 2). During underground nuclear tests conducted by the Atomic Energy Commission in 1968 in the Aleutians, several RTGs were deployed to furnish power to the test monitoring instruments. At the time of writing, ten RTGs are deployed at five U.S. Air Force sites on Burnt Mountain in northern Alaska. They furnish power to sensitive seismic detector stations associated with the monitoring of the provisions of the nuclear test-ban treaties.

The Outlook for Terrestrial RTGs

Most, if not all, of these terrestrial RTGs use a form of strontium-90, in either the titanate or fluoride form, as a heat source. The strontium was initially available as a waste by-product of the nuclear weapons industries established after World War II. In 1974, the U.S. ceased separating the strontium from the waste streams at the production plants. Since that time, the specific activity of the available strontium has been decaying at its half-life of 28.6 years. Concurrently, the cost of encapsulation and licensing has increased. A mounting increase in the public's antinuclear sentiment, coupled with technological advances and the increased availability of competing power sources (batteries and photovoltaics), has resulted in a lessened demand for RTGs. Another factor, namely that the life of the RTG frequently outlasts the mission, has resulted in double or even

triple missions for a single unit. One might say that they have proven too reliable for their continued success.

40.3 Fossil-Fueled Thermoelectric Generators

Background

Shortly after the RTG research and development projects started, a parallel effort commenced to find useful commercial designs for thermoelectric generators; it was obvious that the market for RTGs was limited both by the nature of the radioactive fuel itself, and by the cost of the device. One of the pioneers in the production of useful commercial TEG technology was Minnesota Mining & Manufacturing Company (later 3M), which has been a consistently innovative organization. The first TEGs were produced in the early 1960s, and in 1966 General Instrument Corporation began marketing its own version. TEGs from both these companies used propane, butane, or natural gas as a fuel, and that has been the general pattern ever since.

These two firms and their successor companies have been the leading producers of fossil-fueled thermoelectric generators. In 1970, General Instrument sold its product line to Teledyne, and in 1975 the 3M technology was acquired by a group of 3M employees who relocated to Alberta, Canada, and organized under the name of Global Thermoelectric Inc. There has been some activity on the part of others to enter the market, but these have been, in general, short-lived.

Terrestrial applications have naturally been limited by the need for combustion air and by the necessity of providing an adequate supply of fuel. Even so, during the past 20 years or more, thermoelectric generators have found their way to all the seas and continents. At the time of writing, probably something in excess of 12,000 fossil-fueled thermoelectric generators have been placed into operation.

Many of the attractive characteristics of the RTGs are also attributable to the fossil-fueled thermoelectric generator (TEG), viz.:

Continuous and predictable power output
Highly reliable output in useful power ranges
Long service life
Independence from external power sources
Adaptability to hostile environments
Low maintenance requirements

To be sure, there are alternative methods of providing power under similar circumstances. Batteries come to mind, as do photovoltaics. Both have advantages and both have disadvantages *vis-à-vis* the TEG, and the design engineer should take all aspects into consideration. Sometimes the battery wins, sometimes the solar cell, and sometimes the TEG. Usually the selected method is paired with one or more of the others. Naturally the solar panel needs batteries for night-time support, and frequently a variable load requires that the TEG be paired with a battery. One must consider the annual insolation when the photovoltaic technology is considered; the fuel supply problem in the case of the TEG (unless near a gas pipeline or well), and the need for access for recharging when the battery is installed.

Communications

The most obvious user of this level of power production is the communications industry: radio, television, microwave, and telephone. In the mountains of the U.S. and Canada there are a number of television relay stations, using the power of a TEG to operate translators, which bring television signals to areas that are otherwise in topographical shadows. Microwave stations throughout the world enable telephone communications to span the deserts and prairies. Without the modularity and independence of the thermoelectric generator it would be necessary to run expensive land-line extensions, to install engine-driven generators, or to consider the photovoltaic option.

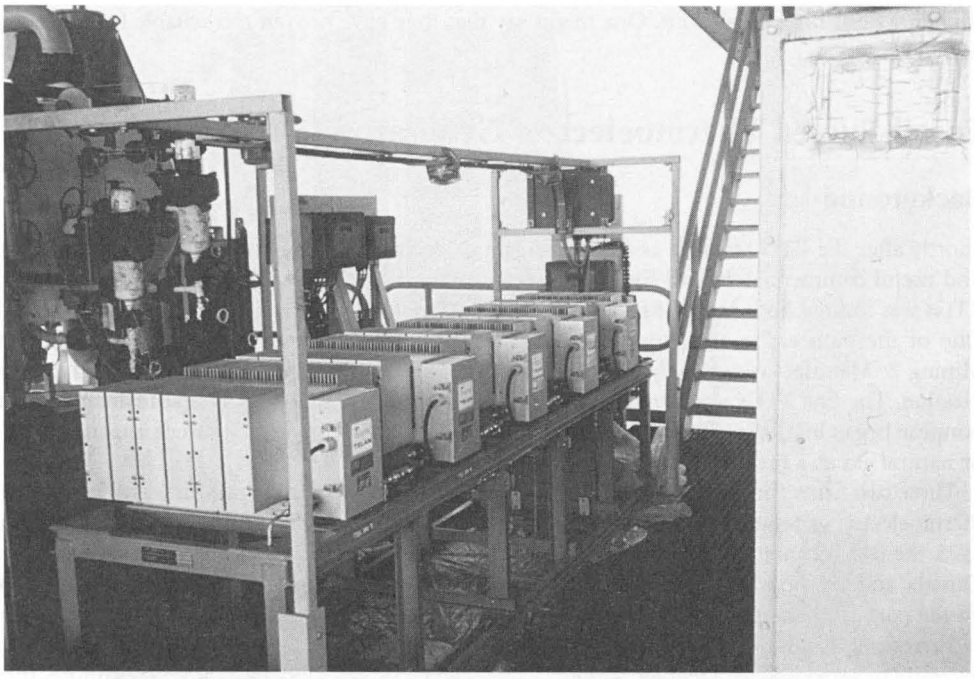

FIGURE 3 300-W TEG installation, offshore gas platform, Middle East. (Courtesy of Teledyne Brown Engineering.)

Along many of the world's petroleum product transport lines the transported gas fuels thermoelectric generators, which in turn provide power to SCADA systems with sensors and transmitters to advise the central stations of the product status. This same application is also a feature of many of the industry's offshore petroleum-gathering platforms where, in addition to the data collection and transmission activities, the generator also frequently provides an independent emergency power supply to energize an unattended platform shutdown in the event of fire, leaks, or adverse weather conditions. By tapping into the gas source, the thermoelectric generator has fuel available in quantities that would be a serious logistics problem for bottled gas (Figure 3). In these cases the major constraint becomes the capital cost of the generator itself. So where such fuel supplies are available, one sees TEG installations of several hundred watts, even into the kilowatt range.

Still on the subject of communications, the increased accessibility of remote areas to the general public has required the establishment of emergency communications systems, for disasters such as fire, floods, accidents, or sudden illness. These isolated installations require small amounts of dependable power at reasonable capital and operating costs and this is where the thermoelectric generator fits.

Speaking of disasters, active or potential, seismic stations around the tectonic plate boundaries or in volcanic areas are frequently powered by thermoelectric generators. TEG-powered creep monitors keep an eye on the various earthquake faults and, although they might not provide immediate warning signals, the long-term data collected are invaluable information to the geological community. Currently several TEGs support the U.S. Geological Survey's monitoring of Mount St. Helens, both through cameras and seismometers. Snow-depth measuring devices need power to measure the potential spring flow from the mountain ranges. Water management benefits both by these installations and also by water-level monitors on the remote reservoirs (Figure 4).

In the area of the display of visual information, TEGs have long been used in railway signaling stations where land-line power was unavailable. Recently we have seen the installation of electric signs warning of adverse weather or poor road conditions where such signs use the power of TEGs. This is especially applicable to snowy or rainy climates where photovoltaics cannot depend upon the availability of sunlight.

FIGURE 4 Installation of TEG-powered self-contained rainfall data logging and broadcasting system, New Zealand. (Published in the Levin (NZ) Chronicle, 1991.)

During the 1980s, with the advent of satellite communication technology, geophysical scientists specializing in Antarctic operations became excited by the possibility of unmanned stations capable of operating for extended periods in remote locations, where they would collect significant geophysical data and transmit it to geosynchronous satellites. Such stations not only required electric power but also heat to provide an acceptable environment for the data collection and ancillary equipment. After an exhaustive comparison of the alternatives (thermoelectric generators [radioisotope and fossil-fueled], closed-cycle turbine-generators, windmills, gasoline engine generators, and diesel engine generators), the fossil-fueled TEG was selected. Although the RTG had been a stellar performer in earlier trials its cost was a prime factor. Solar panels and windmills do not produce heat as a by-product, and the maintenance requirements for the rotating machinery were not attractive.

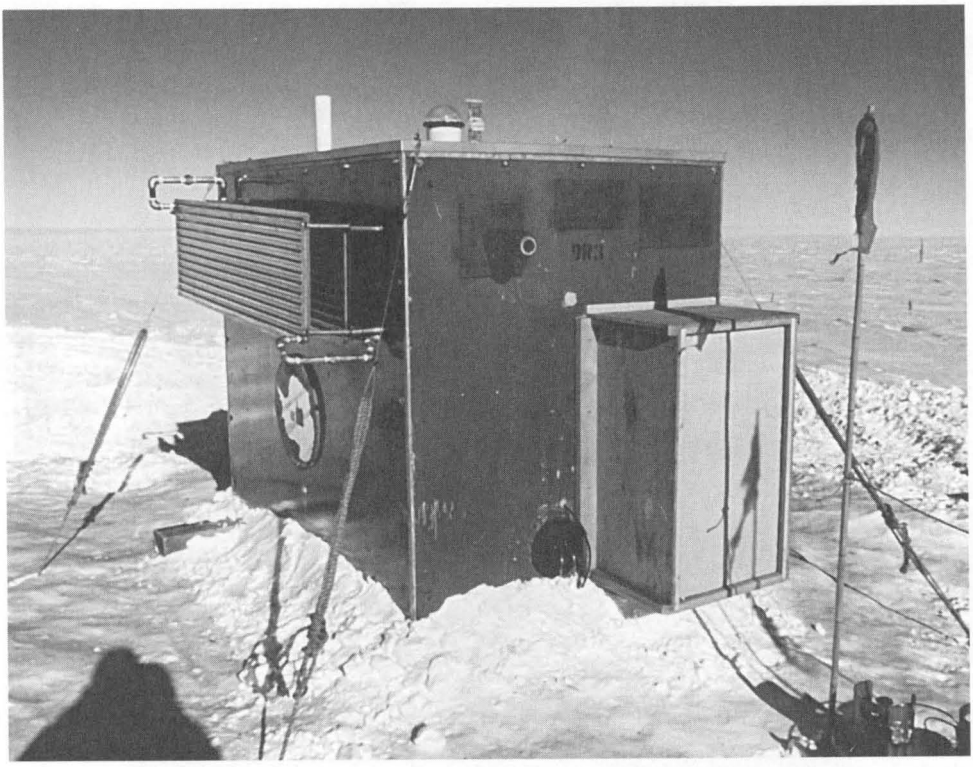

FIGURE 5 Automatic geophysical laboratory, Antarctica. (From Lockheed Missiles and Space Co., Report LMSC-F171145, 1986. With permission.)

Lockheed Missiles and Space Company's Research and Development Division at Palo Alto designed an ingenious system which captures the TEG's waste heat after power conversion and releases it through thermostatic controls either to the interior of the shelter or to the environment. Enough liquified petroleum gas (LPG) for the mission is palletized and transported to the site, and a nitrogen pressurization system ensures that the fuel will be delivered to the heated shelter during extremely cold conditions when the propane remains liquid. Several of these stations are deployed and are currently operational (Figure 5).

Navigation Aids

Navigation aids, either visual or electronic, are another application for TEGs. The most immediate and obvious use is for lights. During the late 1960s and early 1970s rugged shorelines like the west coast of South America were dotted with lights using thermoelectric generators. Of course, these lights required only small amounts of power, so as battery technology improved and the photovoltaics emerged, the TEG market here decreased.

However, radionavigation aids are another story. The 1970s and early 1980s brought extensive petroleum exploration, both offshore and onshore. Not only that, but military operations such as clearing the Suez Canal and Haiphong Harbour of mines as well as routine channel dredging, demanded precise navigational techniques. Since satellite navigation was still in its infancy equipment bearing the names of Argo, Raydist, Cubic, Omega, Racal, Motorola, and the like demanded power in higher levels, beyond the capability of the batteries and solar cells. Each system used one transmitter and one or more transponders. The portability and capacity of the TEG made it a very attractive power supply (Figure 6).

FIGURE 6 TEG-powered radionavigation transponder, Canada.

Other Terrestrial Applications

Corrosion has long been a problem affecting the petroleum production and gas transport industries. A subterranean pipeline is subject to a constant migration of naturally occurring electrically charged ions to and from its surface, resulting in induced corrosion. Several methods of counteracting this effect are in use. Some are passive, such as improved coatings or materials, but the active use of electrical current is one of the most effective methods in the cathodic protection of wells and pipelines. An electrical current is generated in a direction opposite to the natural one, effectively neutralizing its effect.

Thermoelectric generator cathodic protection installations at power levels of several hundred watts are not uncommon, especially if the material being transported is natural gas or LPG. In these cases the fuel is essentially free, and the thermoelectric generator can and does compete effectively with photovoltaics and other methods of power production (Figure 7).

A recent development in the utilization of thermoelectric generation principles has been the self-powered heater. Although it would appear that a conventional free-standing space heater, fueled by gas or liquid fuel, fills most requirements, users of such devices have observed that the heat, being radiant in most cases, is selective in its benefits. The part of the body facing the heat source gets too warm, while the other side cools off. Additionally, the lack of circulation means that the floor of the space stays cold while the uppermost reaches are stiflingly hot. There is also a possible problem with exhaust fumes being vented into the space.

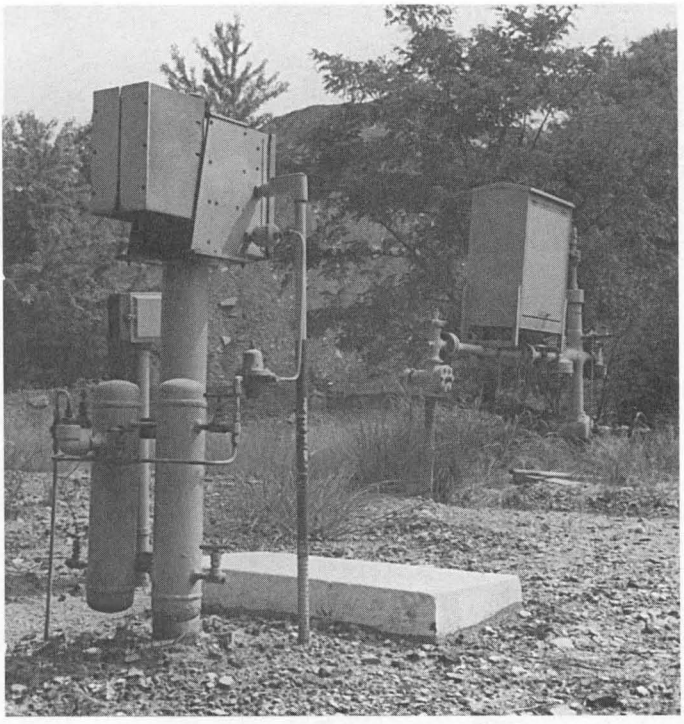

FIGURE 7 Cathodic protection, natural gas pipeline, New Mexico.

By incorporating a number of thermoelectric elements in the heat flow path configuration one can convert some of the heat flux to electricity before it arrives in the air heating stream. The electricity, in turn, can drive any number of moving components: circulating and exhaust fans, pumps, and so forth. It can even be used to charge an auxiliary battery for supplying a limited amount of power for lights or a radio.

This type of application is of interest not only to the consumer market but also to the military. Consider a detachment bivouacked in adverse weather conditions. Conventional heaters do not keep the tents uniformly warm and therefore do not keep the troops warm enough. In order to provide the heat circulation equivalent to that which the self-powered heater could furnish, an external source of electrical power is required, which dictates either a battery bank or a dynamic-cycle generator. The first will run down rapidly; the second is noisy and prone to failure. The thermoelectric conversion unit is silent and will furnish power for air circulation so long as the heater is running.

An adaptation of this usage of available heat for electrical power production is in the military field kitchen. The conventional field kitchen uses a gasoline or alcohol burner. These fuels are volatile and have no other use in the field. If one could use safer diesel fuel, which is supplied for vehicle use anyway, these two objections would be overcome. However, diesel fuel, by virtue of its stability, does not vaporize easily for use in a passive combustion system. The incorporation of thermoelectric power allows the introduction of a pump, which in turn permits mechanical fuel vaporization.

These applications are still in the stage of being developed to an economical design. As in most areas of product development the expansion of a market depends upon an attractive product price, which in turn depends upon a demand for high production. High production rates require capital investment and an occasional "leap of faith". Sometimes the user is willing to make the up-front investment, especially in matters of safety and security; sometimes the manufacturer must invest his own funds based upon his own good judgement, ingenuity, and design capability. Over the

years we have seen applications for thermoelectric generators peak, fade, and peak again as a function of the economy and the relative availability and viability of competitive technologies. Most likely this cycle will continue.

Bibliography

1. Power from Radioisotopes, in *Understanding the Atom* series, U.S. Atomic Energy Commission, Washington, D.C., 1964.
2. *RTG Facts and Applications,* Martin Marietta Nuclear Division, Baltimore, 1967.
3. *Radioisotope Thermoelectric Generators of the U.S. Navy,* 10, 1978–785–930/1221 9–1, U.S. Government Printing Office, Washington, D.C.
4. *Communications,* December 1974.
5. *Interim report on the first British radioisotope isotope powered thermoelectric generators, RIPPLE I and II,* AERE- M 1594, Atomic Energy Research Establishment, Harwell, U.K., 1965.
6. *Radioisotope Power,* Ind-55, Atomic Energy of Canada.
7. *Development of an Automatic Geophysical Observatory for use in Antarctica,* LSMC-F171145, Lockheed Missiles and Space Company, Palo Alto, 1986.
8. *Modern Thermoelectrics,* Rowe, D. M. and Bhandari, C. M., Holt, Reinhart and Winston, 1983.

41

Space Applications

Gary L. Bennett
NASA Headquarters (retired)
c/o Boise, Idaho

41.1 Introduction

All of the nuclear power sources (NPS) flown by the U.S. to date (1993) and reportedly all but two of the NPS flown by the former Soviet Union have achieved their power conversion through the use of thermoelectric generators. In the case of the U.S. these NPS have greatly enhanced or enabled a number of challenging space missions, including the first flights to the outer planets.[1-5]

The U.S. began studying the use of NPS in the late 1940s and early 1950s. By the mid- to late 1950s the U.S. had active programs to develop both space radioisotope and space reactor power sources. The first known actual use of a NPS on a spacecraft came in 1961 with the launch of the small SNAP-3B radioisotope thermoelectric generator (RTG) by the U.S. (SNAP is an acronym for Systems for Nuclear Auxiliary Power. All odd-numbered SNAP power sources used radioisotope fuel and all even-numbered SNAP power sources used nuclear fission reactors.) In total, as shown in Table 1, the U.S. has launched 41 RTGs and one reactor to provide power for 25 space systems. (Thirty-eight of these NPS on 22 space systems are still in space or on other planetary bodies. Four U.S. RTGs have returned to Earth in one form or another because of spacecraft or launch vehicle malfunctions.) The U.S. has also used small radioisotope heater units (RHUs) on some of its RTG-powered science missions and on the Apollo 11 science package. All of the U.S. RTGs have used ^{238}Pu as the source of heat because of its long half-life (87.8 years) and its comparatively low level of radiation emission. The only U.S. space reactor flown used ^{235}U as the fuel.[1] The former Soviet Union has reportedly placed at least 35 reactor-powered and two RTG-powered satellites in orbit and placed at least two RHU-heated rovers on the Moon. In addition the former Soviet Union has reportedly had at least six re-entries of NPS (two of radioisotope units and four of reactors).[4]

Initially the U.S. NPS were used to supplement solar power sources but gradually with the improvement of NPS technology and with the ever-increasing requirements of spacecraft power (particularly for outer planet missions) NPS became the sole source of power. NPS have a number of important attributes, including compact size, self-sufficiency, reliability, survivability, long lifetimes, and operational flexibility. Figure 1 shows qualitatively the regimes of possible space power applicability.

Figure 2, which is a schematic of a SNAP-3B RTG, illustrates the basic features of an NPS: a heat source (either a naturally decaying radioisotope or a nuclear reactor) and a converter (which

Table 1 Summary of Space Nuclear Power Systems Successfully Launched by the U.S.

Power Source[a]	No. of NPS	Initial Avg Power/NPS (W)	Spacecraft (Mission Type)	Launch Date[b] (Launch Site)	Initial Orbit	Status
SNAP-3B7	1	2.7	Transit 4A (Navigational)	29 Jun 1961 (ETR)	~890 × 1000 km 67.5°, 104 min	RTG operated for ~15 years. Satellite now shutdown but operational.
SNAP-3B8	1	2.7	Transit 4B (Navigational)	15 Nov 1961 (ETR)	~960 × 1130 km 32.4°, 106 min	RTG operated for 9 years. Satellite operation was intermittent after 1962 high-altitude nuclear test. Last reported signal in 1971.
SNAP-9A	1	>25.2	Transit 5BN-1 (Navigational)	28 Sep 1963 (WTR)	~1090 × 1150 km 89.9°, 107 min	RTG operated as planned. Non-RTG electrical problems on satellite caused satellite to fail after 9 months.
SNAP-9A	1	26.8	Transit 5BN-2 (Navigational)	5 Dec 1963 (WTR)	~1080 × 1110 km 90.0°, 107 min	RTG operated for >6 years. Satellite lost navigational capability after 1.5 years.
SNAP-10A	1	>500	SNAPSHOT (Experimental)	3 Apr 1965 (WTR)	1296 × 1329 km 90.2°, 111.5 min	Reactor successfully operated for 43 d until shutdown by electrical component failure on spacecraft.
SNAP-19B3	2	28.2	Nimbus III (Meteorological)	14 Apr 1969 (WTR)	1070 × 1131 km 99.9°, 107 min	RTGs operated for >2.5 years (no data taken after that).
SNAP-27	1	73.6	Apollo 12 (Lunar)	14 Nov 1969 (KSC)	Lunar trajectory	RTG operated for ~8 years (until station was shut down).
SNAP-27	1	72.5	Apollo 14 (Lunar)	31 Jan 1971 (KSC)	Lunar trajectory	RTG operated for ~6.5 years (until station was shut down).
SNAP-27	1	74.7	Apollo 15 (Lunar)	26 Jul 1971 (KSC)	Lunar trajectory	RTG operated for > 6 years (until station was shut down).
SNAP-19	4	40.7	Pioneer 10 (Planetary)	2 Mar 1972 (ETR)	Solar system escape trajectory	RTGs still operating. Spacecraft successfully operated to Jupiter and is now beyond orbit of Pluto.
SNAP-27	1	70.9	Apollo 16 (Lunar)	16 Apr 1972 (KSC)	Lunar trajectory	RTG operated for ~5.5 years (until station was shut down).
Transit-RTG	1	35.6	"Transit" (TRIAD-01-1X)	2 Sep 1972 (WTR)	716 × 863 km 90.1°, 101 min	RTG still operating.

Table 1 *Continued*

Power Source[a]	No. of NPS	Initial Avg Power/NPS (W)	Spacecraft (Mission Type)	Launch Date[b] (Launch Site)	Initial Orbit	Status
SNAP-27	1	75.4	Apollo 17 (Lunar)	7 Dec 1972 (KSC)	Lunar trajectory	RTG operated for ~5 years (until station was shut down).
SNAP-19	4	39.9	Pioneer 11 (Planetary)	5 Apr 1973 (ETR)	Solar system escape trajectory	RTGs still operating. Spacecraft successfully operated to Jupiter and Saturn and is now beyond orbit of Pluto.
SNAP-19	2	42.3	Viking 1 (Mars lander)	20 Aug 1975 (ETR)	Trans-Mars trajectory	RTGs operated for > 6 years (until lander was shut down).
SNAP-19	2	43.1	Viking 2 (Mars lander)	9 Sep 1975 (ETR)	Trans-Mars trajectory	RTGs operated for >4 years until relay link was lost.
MHW-RTG	2	153.7	LES-8 (Communications)	14 Mar 1976 (ETR)	35,787 km 25.0°, 1436 min	RTGs still operating.
MHW-RTG	2	154.2	LES-9 (Communications)	14 Mar 1976 (ETR)	35,787 km 25.0°, 1436 min	RTGs still operating.
MHW-RTG	3	159.2	Voyager 2 (Planetary)	20 Aug 1977 (ETR)	Solar system escape trajectory	RTGs still operating. Spacecraft successfully operated to Jupiter, Saturn, Uranus, Neptune, and beyond.
MHW-RTG	3	156.7	Voyager 1 (Planetary)	5 Sep 1977 (ETR)	Solar system escape trajectory	RTGs still operating. Spacecraft successfully operated to Jupiter, Saturn, and beyond.
GPHS-RTG	2	287.1	Galileo (Jupiter orbiter)	18 Oct 1989 (KSC)	Trans-Jupiter trajectory	RTGs still operating.
GPHS-RTG	1	~282 (power inferred)	Ulysses (Solar orbiter)	6 Oct 1990 (KSC)	Solar polar orbit	RTG still operating.

[a]SNAP stands for Systems for Nuclear Auxiliary Power. All odd-numbered SNAP power plants use radioisotope fuel. Even-numbered SNAP power plants have nuclear fission reactors as a source of heat. MHW-RTG stands for the Multi-hundred Watt Radioisotope Thermoelectric Generator. GPHS-RTG stands for the General-Purpose Heat Source Radioisotope Thermoelectric Generator.

[b]Key to launching stations: ETR, Eastern Test Range; WTR, Western Test Range; KSC, Kennedy Space Center.

could utilize any number of conversion systems, such as thermoelectric, thermionic, Brayton, Rankine, Stirling, magnetohydrodynamic, etc.) to change the thermal power into electrical power. As noted earlier the U.S. has only used thermoelectric converters because of their proven reliability and longevity and the lack of a requirement to provide powers high enough to warrant the use of more efficient conversion systems such as turbine/alternators.[3] The former Soviet Union launched two thermionic reactors, which had limited lifetimes because of the limited supply of cesium (among other problems).[4]

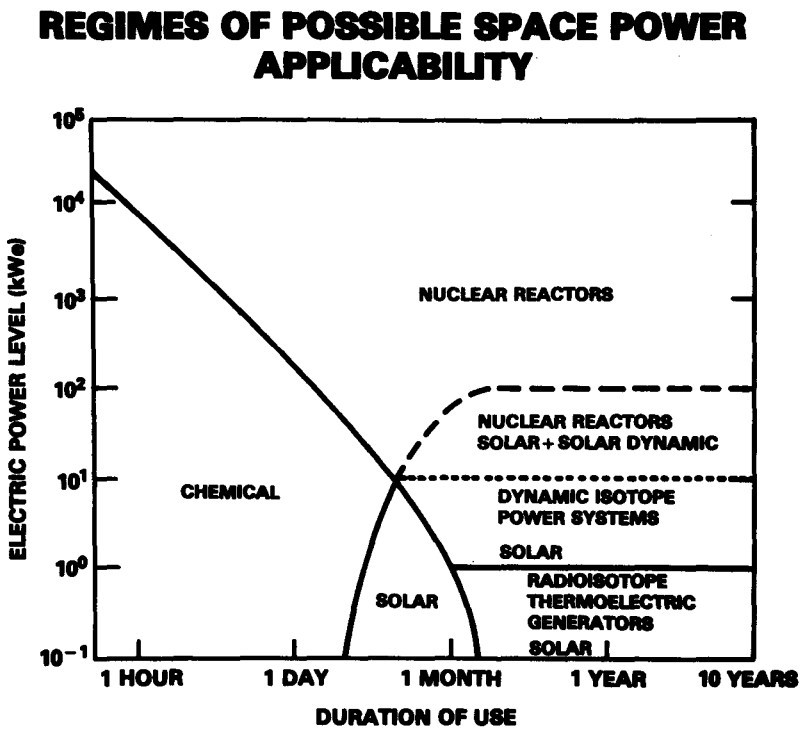

FIGURE 1 Regimes of possible space power applicability.

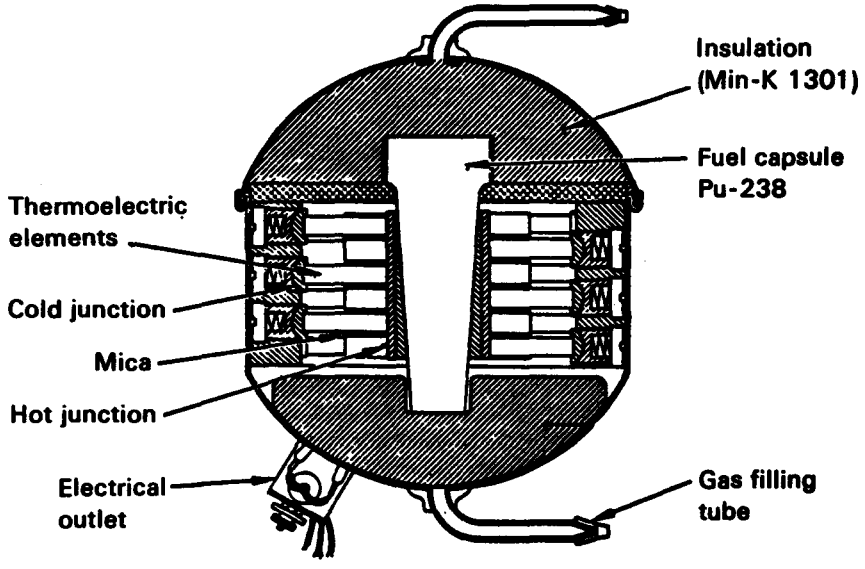

FIGURE 2 Schematic of the SNAP-3B RTG. The overall dimensions were 12.1 cm in diameter by 14 cm high.

The following sections provide an overview of the NPS flown by the U.S. and the former Soviet Union. In the case of the U.S. program this overview is broadly grouped into four general classifications covering nine converter designs, as listed in Table 2. As can be seen from Table 2 the general technology trend for each of the RTG design concepts has been to improve generator performance, efficiency, and specific power. This has led to improvements in the technology of

Table 2 General Characteristics of U.S. Nuclear Power Sources in Space

Spacecraft	Power Source	T/E Materials	NPS Intern. Environ.	Thermal Coupling	T/E Mounting	T_h/T_c (K)[a]	Nominal Efficiency[a]	Specific Power (W [e]/kg)[a]
Transit 4A	SNAP-3B7	PbTe 2n/2p	Soft vacuum	Conduction	Spring + piston	783/366	.051	1.3
Transit 4B	SNAP-3B8	PbTe 2n/2p	Kr + H_2	Conduction	Spring + piston	783/366	.051	1.3
Transit 5BN-1	SNAP-9A	PbTe 2n/2p	Ar + He	Conduction	Spring + piston	790/431	.051	2.2
Transit 5BN-2	SNAP-9A	PbTe 2n/2p	Ar + He	Conduction	Spring + piston	790/431	.051	2.2
SNAPSHOT	SNAP-10A	SiGe	Vacuum	Conduction	Bonded	777/611	.013	1.2
Apollo 12	SNAP-27	PbTe 3n/3p	Argon	Conduction	Spring + piston	866/547[b]	.05	2.3[c]
Apollo 14	SNAP-27	PbTe 3n/3p	Argon	Conduction	Spring + piston	866/547[b]	.05	2.3[c]
Apollo 15	SNAP-27	PbTe 3n/3p	Argon	Conduction	Spring + piston	866/547[b]	.05	2.3[c]
Apollo 16	SNAP-27	PbTe 3n/3p	Argon	Conduction	Spring + piston	866/547[b]	.05	2.3[c]
Apollo 17	SNAP-27	PbTe 3n/3p	Argon	Conduction	Spring + piston	866/547[b]	.05	2.3[c]
TRIAD	Transit-RTG	PbTe 2n/3p	Vacuum	Radiation	Panel	674/410	.042	2.6
Nimbus III	SNAP-19B	PbTe 2n/3p	Ar + He	Conduction	Spring + piston	800/452	.045	2.1
Pioneer 10	SNAP-19	PbTe 2n/TAGS-85	Ar + He	Conduction	Spring + piston	785/430	.062	3.0
Pioneer 11	SNAP-19	PbTe 2n/TAGS-85	Ar + He	Conduction	Spring + piston	785/430	.062	3.0
Viking Lander 1	SNAP-19[d]	PbTe 2n/TAGS-85	Ar + He	Conduction	Spring + piston	819/450	.062	2.8
Viking Lander 2	SNAP-19[d]	PbTe 2n/TAGS-85	Ar + He	Conduction	Spring + piston	819/450	.062	2.8
LES-8	MHW-RTG[e]	SiGe	Vacuum	Radiation	Cantilever	1273/570	.066	4.2
LES-9	MHW-RTG[e]	SiGe	Vacuum	Radiation	Cantilever	1273/570	.066	4.2
Voyager 1	MHW-RTG[e]	SiGe	Vacuum	Radiation	Cantilever	1273/570	.066	4.2
Voyager 2	MHW-RTG[e]	SiGe	Vacuum	Radiation	Cantilever	1273/570	.066	4.2
Galileo	GPHS-RTG[f]	SiGe	Vacuum	Radiation	Cantilever	1273/570	.066	5.1[g]
Ulysses	GPHS-RTG[f]	SiGe	Vacuum	Radiation	Cantilever	1273/570	.066	5.0[g,h]

[a]These values have been averaged over the different RTGs for the beginning-of-mission (where data were available) and do not represent individual RTG performance.

[b]These values are based on design analysis and ground tests. The Apollo 12/SNAP-27 initial data indicated a lunar night-day variation of about 855 to 890 K at the hot junction and about 470 to 520 K at the cold junction.

[c]The SNAP-27 specific power is calculated including the fuel-cask mass.

[d]The SNAP-19s used on the Viking Landers were modified for use on the surface of Mars. The modifications included the addition of a dome gas reservoir.

[e]MHW-RTG is an acronym for Multi-Hundred Watt Radioisotope Thermoelectric Generator.

[f]GPHS-RTG is an acronym for General-Purpose Heat Source Radioisotope Thermoelectric Generator.

[g]The specific powers for Galileo and Ulysses are shown for the actual launch dates (1989 and 1990, respectively). Had the launches gone as planned in 1986 the specific powers would have been at least 5.3 W (e)/kg.

[h]The Ulysses power is not measured directly by the spacecraft; rather, it is determined from other measurements.

thermoelectric materials, from the lead telluride (PbTe) used in the first RTG concepts to the silicon germanium (SiGe) used in the multi-hundred watt (MHW) RTGs and the general-purpose heat source (GPHS) RTGs. As will be seen their performance has demonstrated that thermoelectric NPS generators can be engineered safely and reliably to meet a variety of space-mission requirements.[2,3]

41.2 Lead Telluride Generators

Except for the SNAP-10A reactor, all of the U.S. NPS flown in the 1960s and the early 1970s used telluride (usually lead telluride, PbTe) thermoelectric materials to make up the elements of the converter. With the exception of the Transit RTG all of these telluride-based RTGs operated by means of a conductive coupling between the plutonium heat source and the thermoelectric elements. Bulk insulation was used to minimize heat losses and a cover gas was used to retard sublimation of the thermoelectric material at the hot end of the couples. The Transit RTG operated in a vacuum using a radiant heat transfer coupling between thermoelectric elements and the heat source. To control sublimation the Transit RTG operated at a lower hot junction temperature than did the other telluride generators. The SNAP-3B7 RTG on the Transit 4A satellite also operated under vacuum conditions to minimize conduction losses through the insulation.[2,5]

SNAP-3B

The SNAP-3B RTGs, which were developed out of an earlier SNAP-3 program, were used to provide 2.7 W (e) of power to radio transmitters and other electronic equipment aboard the U.S. Navy's Transit 4A and Transit 4B navigation satellites. The SNAP-3B RTGs were also flown to prove the practicality of radioisotope power sources in space.[2,6]

Prior to the use of NPS, continuous electrical power had been obtained by solar arrays and nickel-cadmium (NiCd) batteries. Concern over possible degradation of solar cells in the inner Van Allen belt and battery breakdown from repeated charge-discharge cycles had led the Navy to fly RTGs.[3]

Each 2.1-kg SNAP-3B RTG contained 27 spring-loaded, series-connected pairs of PbTe thermoelectric elements operating at a hot junction temperature of about 783 K and a cold junction temperature of about 366 K. The n elements were doped with lead iodide and the p elements were doped with sodium. Each radioisotope heat source provided about 52.5 W (t). The design life was 5 years. Figure 3 shows the first mounting of an NPS to a spacecraft in 1961. At the time Transit 4A, which is shown in Figure 4, had the longest operating life of any satellite launched by the U.S.—over 15 years. The RTG on Transit 4B was still operating 10 years after launch when the last signals were received.[2,6–8]

From the test experience with the SNAP-3B RTGs and later PbTe RTGs, two general modes for the degradation of generator power output were identified:

1. Outgassing of the thermal insulation (water from the Min-K bulk insulation), which can lead to oxygen attack on PbTe elements and bonds. (The Min-K insulation can also experience structural instability caused by the loss of impurities during high-temperature service.)
2. Increases in generator internal resistance, which occur when the sublimation or loss of thermoelectric material at the hot junction leads to a reduced leg cross section and hence a higher contact resistance.

The second mode was judged to be the more probable, especially in the Transit 4A generator, which had essentially no inert fill gas to retard sublimation.[9]

SNAP-9A

The SNAP-9A RTGs, which became the foundation for the follow-on, highly successful SNAP-19 RTGs, were built to provide all of the electrical power for the Navy Transit 5BN navigation

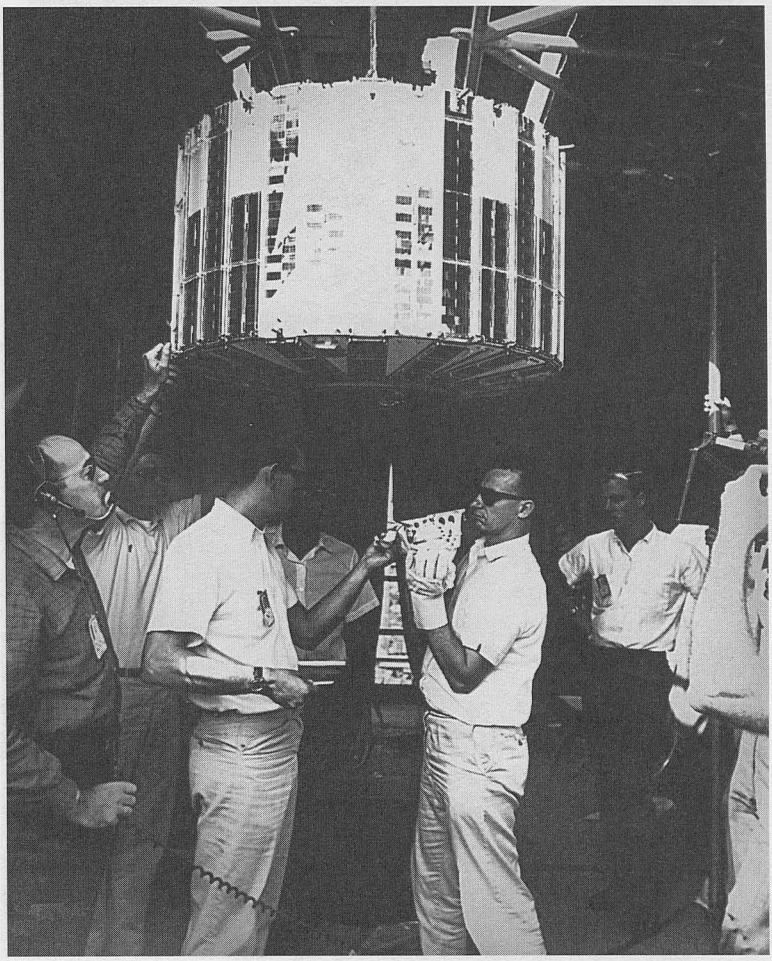

FIGURE 3 Paul J. Dick of Teledyne Energy Systems is shown installing the SNAP-3B7 RTG on the Transit 4A satellite in June 1961. This was the first flight of an NPS.

satellites. Of special significance is that Transit 5BN-1, which was launched in 1963, was the first satellite to obtain all of its power from an RTG. Transit 5BN-2, which was also launched in 1963, was the first operational navigational satellite. The RTG approach was selected because RTGs are inherently radiation resistant, whereas the solar-cell primary power system of Transit 4B had been adversely affected by a 1962 high-altitude nuclear explosion.[9] Each 12.3-kg SNAP-9A was designed to provide 25 W (e) at a nominal 6 V for 5 years in space after 1 year of storage on Earth.[10] Spacecraft problems prevented obtaining data from Transit 5BN-1 after June 1, 1964; however, Transit 5BN-2 telemetry showed the SNAP-9A RTG still functioning in June 1970.[7]

One of the objectives of the Transit 5BN program was to demonstrate the satisfactory operation and long-life potential of the SNAP-9A power supply. The Johns Hopkins University Applied Physics Laboratory, which built the satellites, reported that the objective was fully satisfied. In fact Transit "5BN-1 demonstrated the extreme simplicity with which thermoelectric generators may be integrated into the design, not only to provide the electrical power but also to aid in thermal control".[7] Some waste heat from the RTG was used to maintain electronic instruments within the satellite at a temperature near 293 K.

SNAP-19

The SNAP-19 technology-improvement program built on the SNAP-9A development program, with the SNAP-19B power source specifically designed for use on NASA's Nimbus meteorology

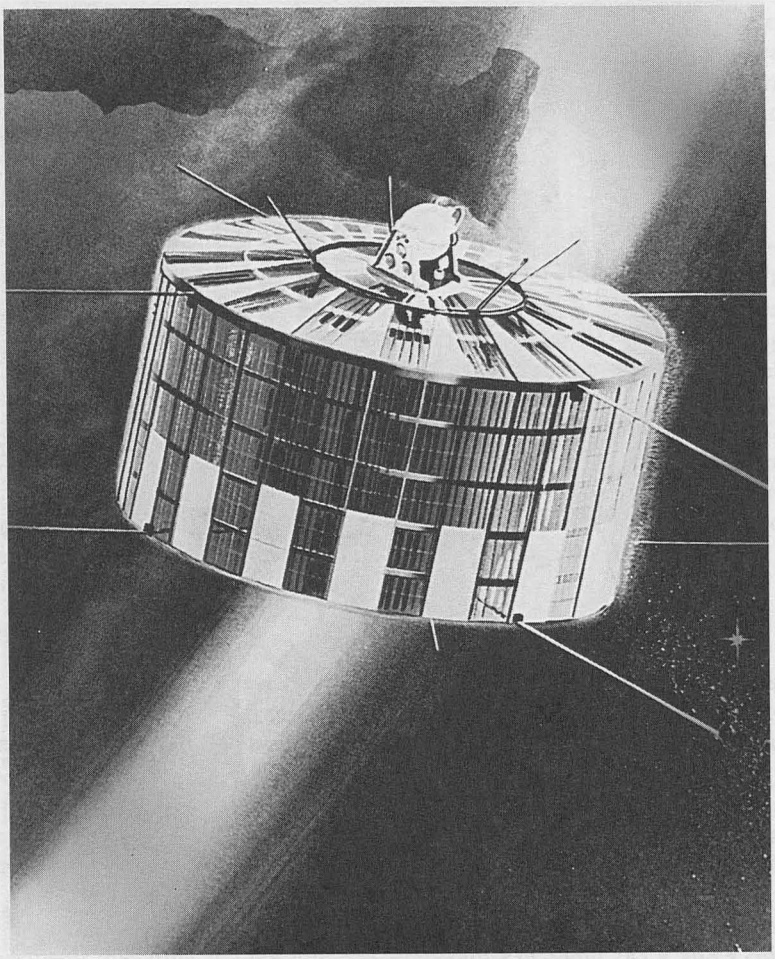

FIGURE 4 Artist's concept of the Transit 4A satellite in orbit showing the SNAP-3B7 RTG mounted on one end.

satellites. The Nimbus SNAP-19 program was the first demonstration of RTG technology aboard a NASA spacecraft, and, as such, it developed the data and experience to support interplanetary missions using RTGs. Subsequent modifications were made in the SNAP-19 design to power NASA's Pioneer and Viking missions. The Viking SNAP-19, which represents the culmination of the SNAP-19 program, is shown schematically in Figure 5. Figure 6 illustrates the configuration of a SNAP-19 thermoelectric couple assembly.

Each Viking SNAP-19 thermoelectric converter, like those on Nimbus III and Pioneers 10 and 11, had six thermoelectric modules, each consisting of 15 thermoelectric couples (for a total of 90 couples per generator), Johns-Manville Type 1301 Min-K thermal insulation, interconnecting electrical straps, and associated cold-end hardware. The cold-end hardware, which consisted of springs, pistons, alignment buttons, and heat sink bar, was located between the modules and the cylindrical generator housing where it could provide a compressive load on each thermoelectric element to maintain adequate electrical and thermal paths in the converter. The thermoelectric couples were fabricated from Teledyne Energy Systems TAGS-85 material (with a thin SnTe segment at the hot side) for the p-leg and from 3M Company 3M-TEGS 2N(M) material for the n-leg. (The acronym TAGS is derived from the names of its major constituents: tellurium, antimony, germanium, and silver. TAGS is a solid solution of silver antimony telluride in germanium telluride. TAGS is an undoped inherent "p" material. TAGS thermoelectric elements were designed to provide higher

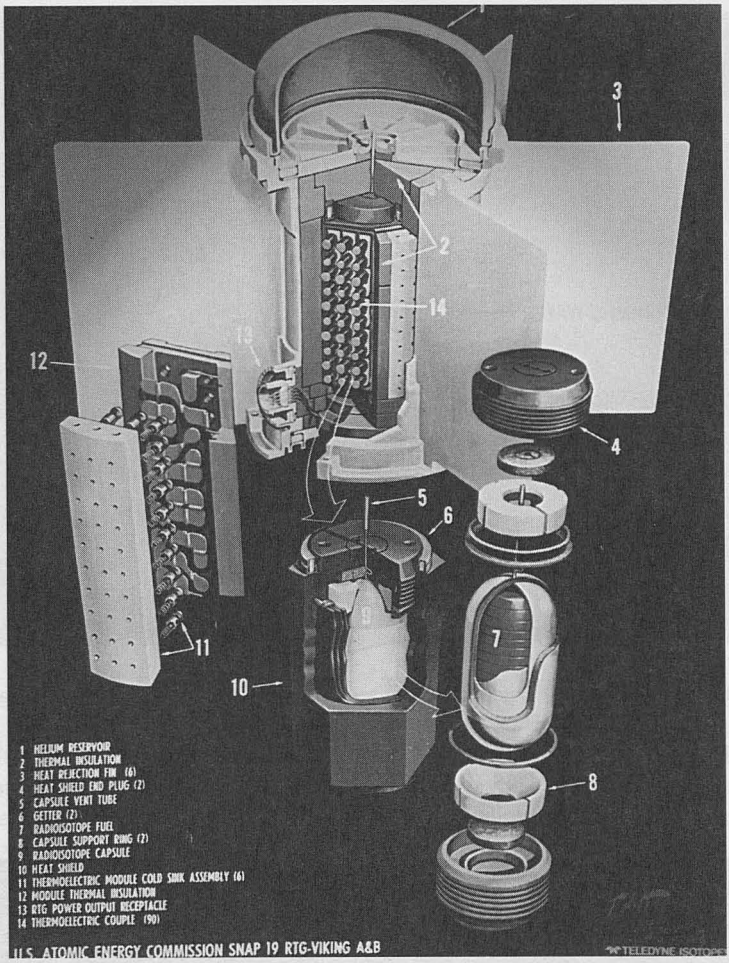

FIGURE 5 Schematic of the Viking/SNAP-19 RTG. The height is 40.4 cm and the fin span is 58.7 cm. The three SNAP-19 RTG concepts shared a common technology heritage which can be traced back to the SNAP-9A program.

efficiency and improved, longer-term power performance over the PbTe 2n/2p on the SNAP-3Bs and PbTe 2n/3p on the Nimbus SNAP-19B.)[11]

For Nimbus III, two 13.4-kg SNAP-19B RTGs were mounted on the spacecraft to provide a total of 56.4 W (e) at beginning of mission (BOM) to augment the solar power source. During the design lifetime of 1 year, nuclear power comprised about 20% of the total power delivered to the regulated power bus, allowing a number of extremely important atmospheric-sounder experiments to operate in a full-time duty cycle. Without the RTGs the total delivered power would have fallen below the load line about 2 weeks into the mission.[12,13]

Four SNAP-19 RTGs were carried on both the Pioneer 10 and 11 spacecrafts, as shown in Figure 7. Pioneer 10 was the first spacecraft to flyby Jupiter and the first to leave the Solar System. The Pioneer RTGs performed so well that Pioneer 11 was retargeted for the first flyby of Saturn.[14] Both spacecraft are still operating over 20 years after their launches, well beyond their 3-year design life requirement, and they are providing valuable information about the heliosphere. The RTGs continue to provide reliable power.[2,5,15,16]

The SNAP-19 design was further modified for the Viking Mars Landers to accommodate high-temperature (400 K) sterilization, storage during the spacecraft's cruise to Mars, and, on the surface of Mars, the thermal cycling caused by the rapid and extreme temperature changes of the Martian

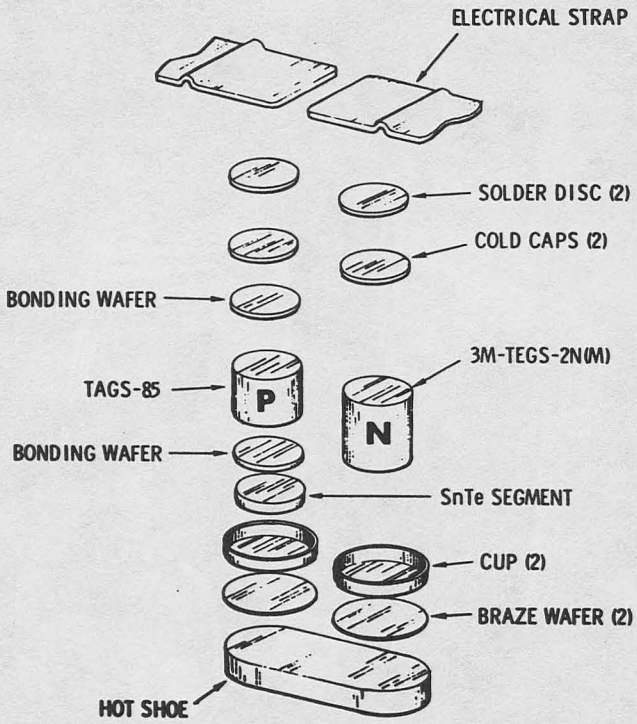

FIGURE 6 SNAP-19 TAGS-85/2n thermoelectric couple configuration.

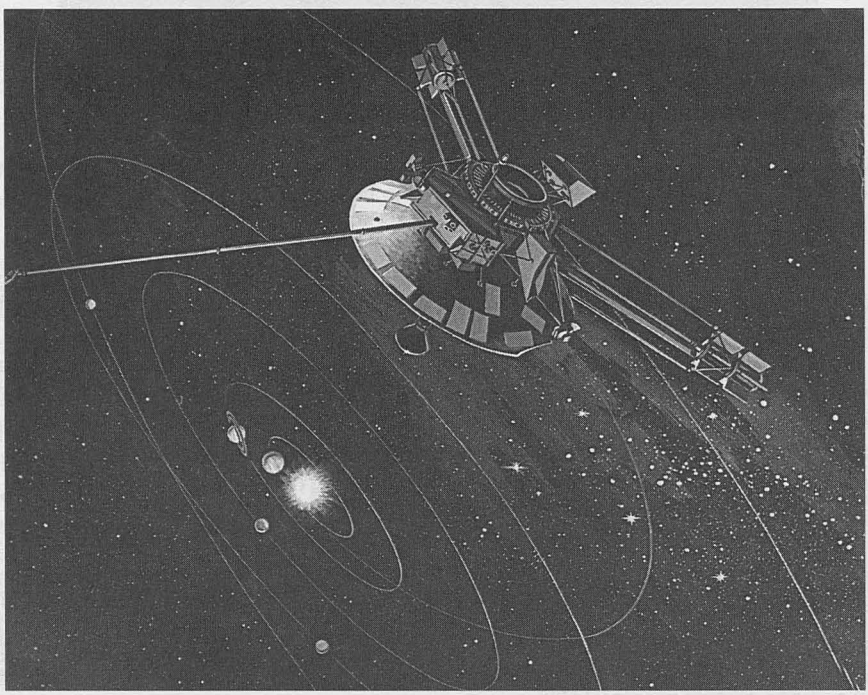

FIGURE 7 Pioneer 10 shown in an artist's concept on June 13, 1983 crossing the orbit of Neptune, making the spacecraft the first flight beyond the Solar System. The four SNAP-19 RTGs are shown mounted in pairs on the two booms.

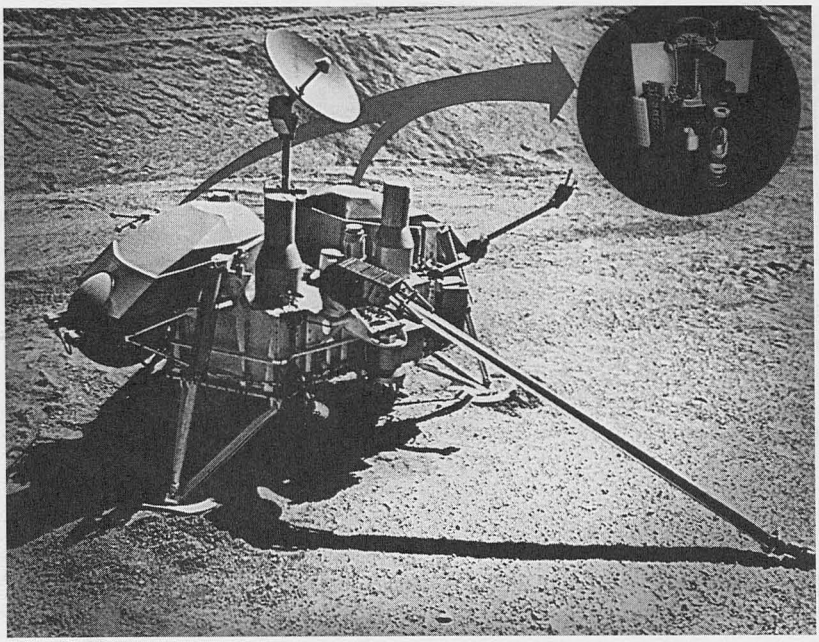

FIGURE 8 Engineering mockup of the Viking Lander with the location of the two SNAP-19 RTGs indicated.

day-night cycle. One modification from the Pioneer/SNAP-19 RTG and shown in Figure 5 was the addition of a dome reservoir. The initial fill gas for the converter was a 90:10 helium-argon mixture, while the reservoir was filled with a 95:5 argon-helium mixture. The purpose of this configuration was to permit a controlled interchange of gases in these two volumes to minimize heat-source operating temperatures up to launch while maximizing electrical output at the end of the mission.[17] As shown in Figure 8 each Viking Lander carried two of the 15.2-kg RTGs which produced a total power of over 85 W (e) at BOM. The RTGs were to produce a total of 70 W (e) for the primary mission of 90 d on the surface of Mars. All four RTGs met the 90-d requirement and they were still operating 4 (Viking Lander 2) to 6 years (Viking Lander 1) later when the Landers were separately and inadvertently shut down on commands from Earth.[5,15,17] Based on their power performance, it had been estimated that the RTGs on Viking Lander 1 were capable of providing sufficient power for operation until 1994—*18 years beyond the mission requirement.*[18]

Both the Pioneer and Viking RTGs demonstrated the operability and usefulness of RTGs in interplanetary spacecraft. All of these RTGs performed beyond their mission requirements.

SNAP-27

The SNAP-27 RTGs (see schematic in Figure 9) were developed to power the experiments of NASA's Apollo Lunar Surface Experiments Package (ALSEP). The RTG design requirement was to provide at least 63.5 W (e) at 16 V DC 1 year after lunar emplacement. (In the case of Apollo 17, the requirement was 69 W (e) 2 years after emplacement.) The use of RTGs to power the ALSEPs was a natural choice because of their low mass, reliability, and ability to produce full electrical power during the long lunar night-day cycle. Since the ALSEPs were to be manually positioned by the astronauts, the RTG designers took advantage of this assembly capability. The converter and the sealed-fuel-capsule assembly were kept separately in the Lunar Module and integrated on the Moon as shown in Figure 10. This approach allowed optimization of the electrical, mechanical, and thermal interfaces of the two major hardware subsystems of the RTG.[19]

A total of five RTG-powered ALSEPs were placed on the Moon. In each case the RTGs exceeded their mission requirements in both power and lifetime (all were still operating when the ALSEPs were shut down on September 30, 1977 for budgetary reasons). Through this performance beyond

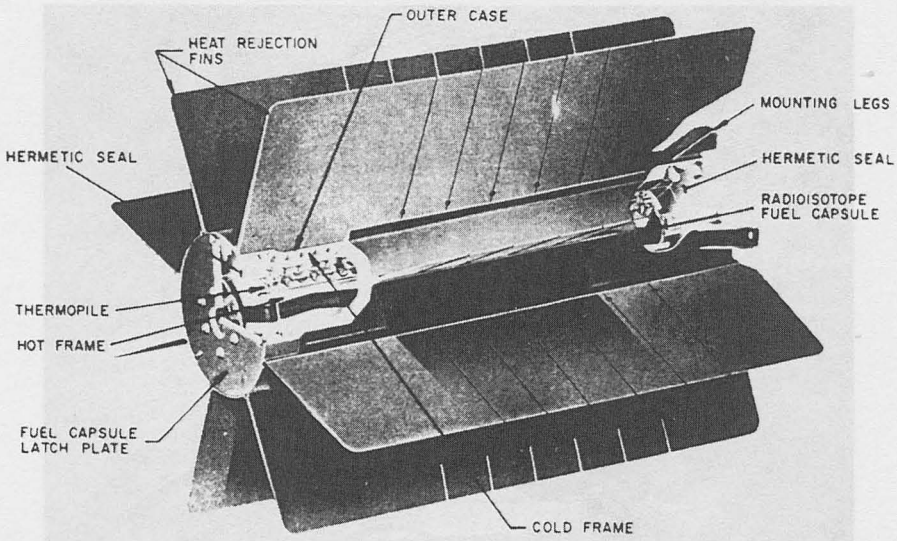

FIGURE 9 Schematic of the SNAP-27 RTG. The overall dimensions were 46 cm long and 40.0 cm in diameter (including the fins).

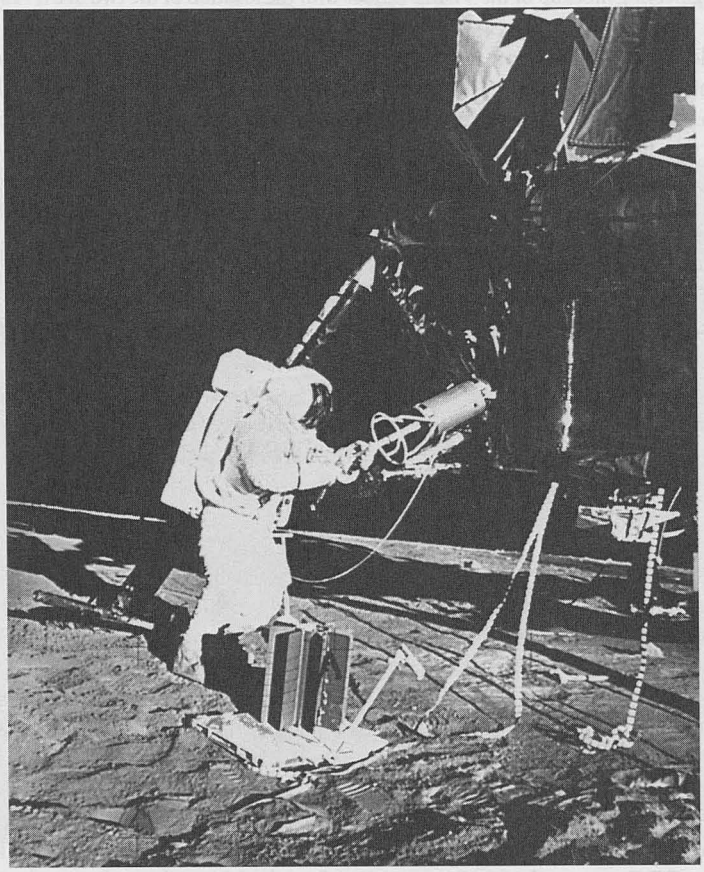

FIGURE 10 Astronaut Alan L. Bean is shown removing the SNAP-27 heat source in preparation for insertion into the converter shown in the foreground during the Apollo 12 mission in November 1969.

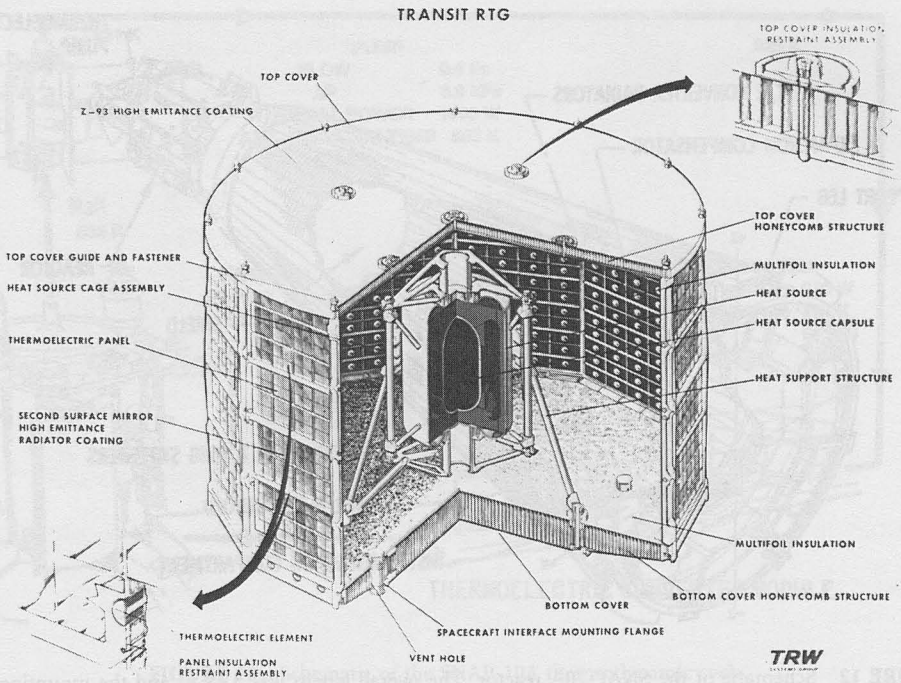

FIGURE 11 Schematic of the Transit RTG. The distance across flats is 61 cm and the panel height is 36.3 cm.

mission requirements, the SNAP-27 RTGs enabled the ALSEP stations to gather long-term scientific data on the internal structure and composition of the Moon, the composition of the lunar atmosphere, the state of the lunar interior, and the genesis of lunar features.[20]

Transit RTG

The Transit RTG was developed specifically as the primary power for the TRIAD navigational satellite, with auxiliary power to be provided by four solar-cell panels and one 6-Ah NiCd battery. The 13.6-kg Transit RTG, shown in Figure 11, was a modular RTG with a 12-sided converter surrounding the radioisotope heat source. The low hot-side temperature (673 K) allowed operation of the PbTe thermoelectric elements in a vacuum.[21] Transit TRIAD operated for over 13 years—well beyond the design requirement of 5 years.

41.3 Silicon Germanium Generators

The use of high-temperature SiGe alloys as thermoelectric power-conversion materials was a direct outgrowth of spacecraft requirements for higher NPS power levels and lower NPS masses (i.e., improved efficiencies). In general, a higher hot-side operating temperature means a higher efficiency, although the optimum temperature is dictated by the mission life (i.e., minimizing sublimation). The cold-side temperature is optimized to obtain the desired power-to-mass ratio (specific power). To a first approximation, PbTe can be used from room temperature to about 900 K before material properties and the figure-of-merit become concerns. The SiGe alloy can be used from room temperature to about 1300 K and offers the potential of higher power with an improved efficiency. Furthermore, SiGe NPS generally do not require an inert atmosphere for space operation because the temperatures (1300 K or less) are normally below those at which sublimation presents a problem. (The use of multifoil insulation, such as molybdenum, does necessitate sealing an RTG NPS under an inert atmosphere on Earth to protect the molybdenum foil against oxidation.)[2]

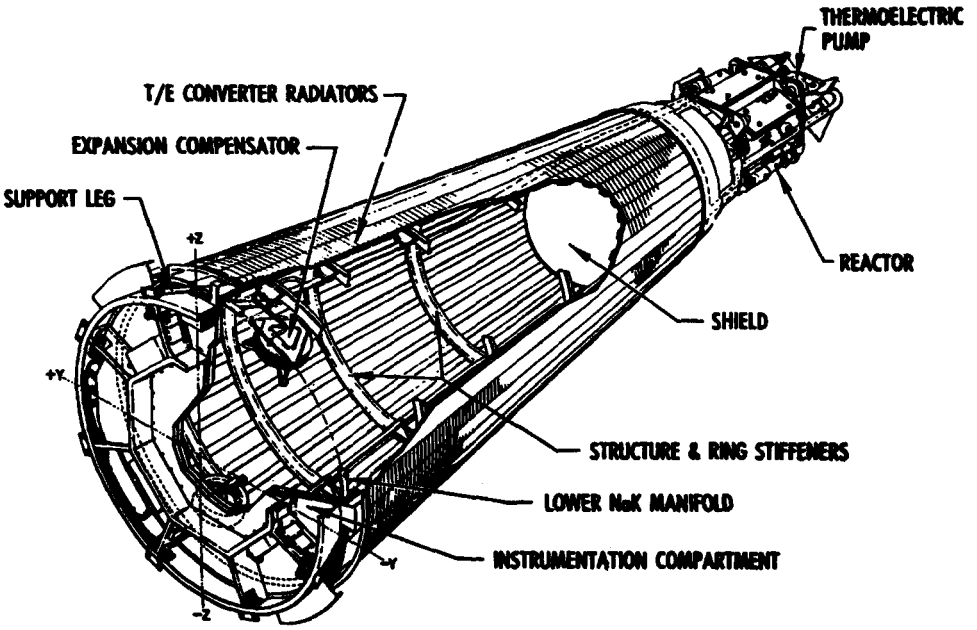

FIGURE 12 Schematic of the SNAP-10A reactor. The overall length was 3.48 m and the mounting base diameter was 1.27 m.

SNAP-10A

SNAP-10A, which is shown schematically in Figure 12, was the first, and so far the only, U.S.-built space reactor flown by the U.S. and it was also the first silicon germanium (SiGe) generator flown by the U.S. SNAP-10A evolved out of earlier U.S. reactor concepts and was launched in 1965 as part of a joint U.S. Air Force (USAF)-U.S. Atomic Energy Commission (USAEC) experiment known as SNAPSHOT. The requirement of the reactor was to provide not less than 500 W (e) with a 1-year operating lifetime.[22,23] The truncated cone shape of SNAP-10A was dictated by minimum mass shield requirements, especially the requirement to eliminate neutron scattering around the steel-reinforced lithium hydride shadow shield. The base diameter was established by the Agena vehicle payload and the upper diameter was determined by the effective area of the reactor. The length was determined by the total radiator area requirement for the 43-kW (t) reactor. The total system mass of the final flight unit was 435 kg including the shield.[22]

The power conversion system basically consisted of 2880 SiGe thermoelectric elements mounted in groups of 72 along 40 stainless steel tubes through which the sodium-potassium (NaK) alloy coolant flowed. Figure 13 shows the overall thermodynamic cycle, including a thermoelectric module. Despite its lower figure-of-merit at the SNAP-10A operating temperatures SiGe was chosen over PbTe because of (1) its stability to higher temperatures; (2) its potential for future performance growth; (3) its ease of manufacture; and (4) its mechanical properties.[22]

Once safely in its final orbit the command was sent for the automatic startup of SNAP-10A. Net power output ranged from a transient high of 650 W (e) in the early part of the mission to a low of 527 W (e) in the Sun after 43 d. The system operated exactly as intended. On May 16, 1965, after 43 d of successful operation, the reactor was shut down by a spurious command caused by a failure of a voltage regulator on the Agena unregulated bus. There was no evidence of any malfunction in the SNAP-10A system. The ground test twin to the flight unit successfully operated at full power for 10,000 h, thereby demonstrating the capability of SNAP-10A to operate unattended for a year.[22]

The SNAP-10A reactor successfully completed most of its objectives, including the following significant achievements:[22]

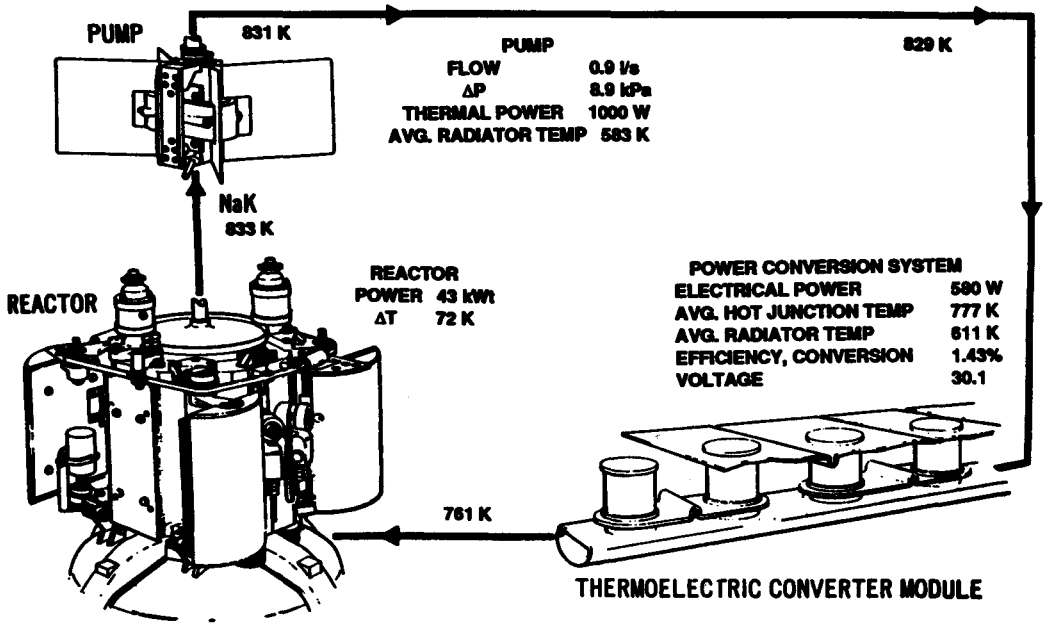

FIGURE 13 Schematic of the SNAP-10A thermodynamic cycle.

- First application of a nuclear reactor in space
- First development of a reactor thermoelectric power system and the first use of such a system in space
- First remote automatic startup of a nuclear reactor in space
- First application of a high-temperature (810 K) liquid metal transfer system in space and the first application of a high-temperature spacecraft in space
- First use of a nuclear shadow shield in space
- Development and application of the highest powered thermoelectric power system to that time (and to date still the highest power single thermoelectric NPS flown by the U.S.) and the first use of a thermoelectric power system of that size in space.
- First thermoelectric-powered liquid metal pump and the first use of such a pump in space

Multi-Hundred Watt (MHW) RTG

The designs of the USAF Lincoln Experimental Satellites 8 and 9 (LES 8/9) and NASA's Voyager 1 and 2 spacecrafts led to a doubling of the power requirement compared to the SNAP-27 RTGs. The MHW-RTG, which is shown in Figure 14, was designed to produce over 150 W (e) at BOM. Two MHW-RTGs were flown on each LES and, as shown in Figure 15, three MHW-RTGs were flown on each Voyager spacecraft. The maximum prelaunch lifetime requirement was 5 years.

The MHW-RTG thermoelectric element (called a "unicouple") is illustrated in Figure 16 and the manufacturing flow is illustrated in Figure 17. Each MHW-RTG contained 312 unicouples with a multifoil (layers of molybdenum and Astroquartz) insulation packet. The n-type material was doped with phosphorus and the p-type with boron. The MHW-RTGs were the first U.S. space RTGs to use SiGe as the thermoelectric material. The use of SiGe permitted higher operating temperatures and higher specific powers all within a space vacuum operating environment.

During and after the MHW-RTG development program, a number of analytical and experimental studies were undertaken to determine the long-term performance of the MHW-RTGs. Four principal degradation modes were identified: (1) dopant-precipitation effects; (2) increases in the conductance of the thermal insulation; (3) degradation of the electrical insulation; and (4) carbon

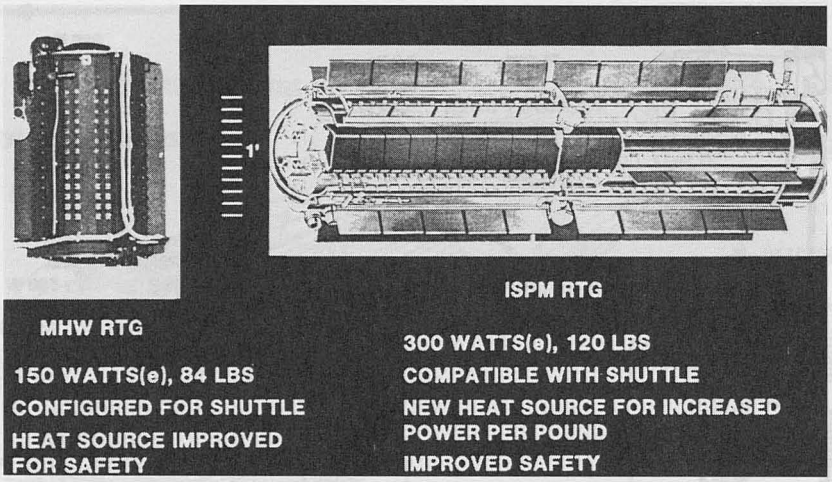

FIGURE 14 Comparison of the MHW-RTG (as modified for Space Shuttle use) and the GPHS-RTG.

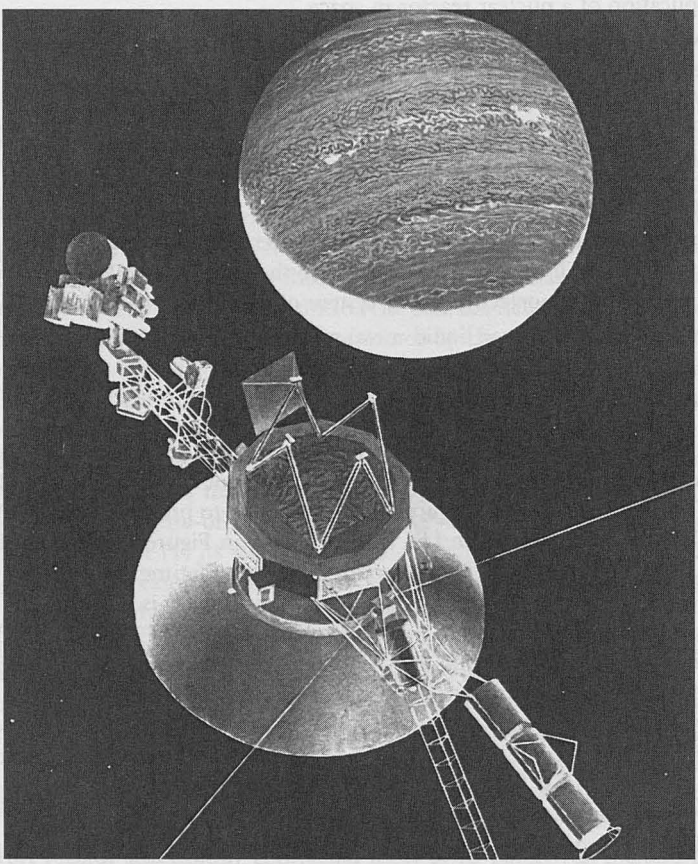

FIGURE 15 Artist's conception of the Voyager 2 spacecraft passing Neptune in August 1989. The three MHW-RTGs are mounted on a boom attached to the lower right of the spacecraft.

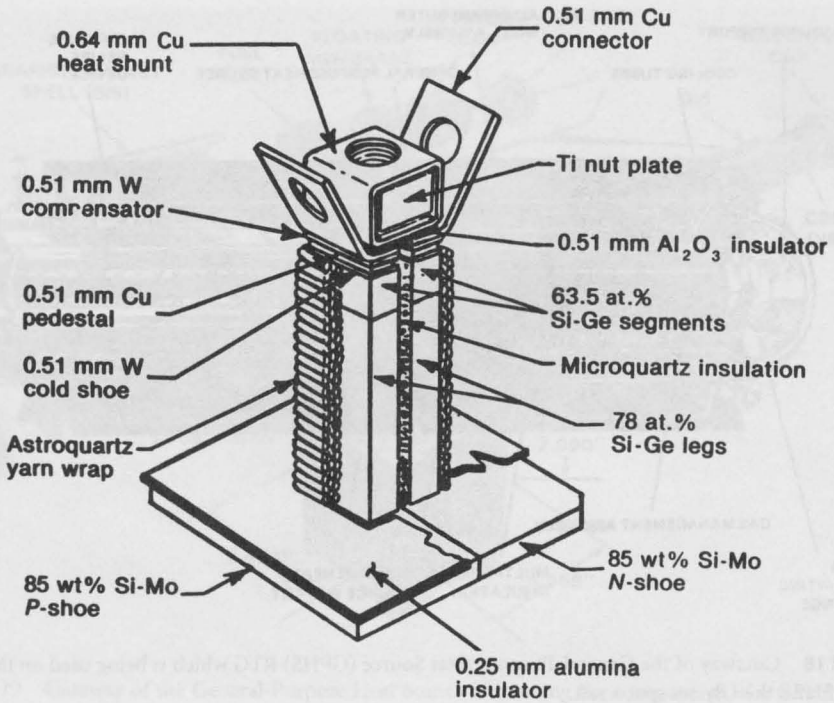

FIGURE 16 Cutaway of the silicon germanium thermoelectric element ("unicouple") used in the MHW-RTGs and GPHS-RTGs. The unicouple length is 3.11 cm and the hot shoe measures 2.29 × 2.29 × 0.19 cm thick.

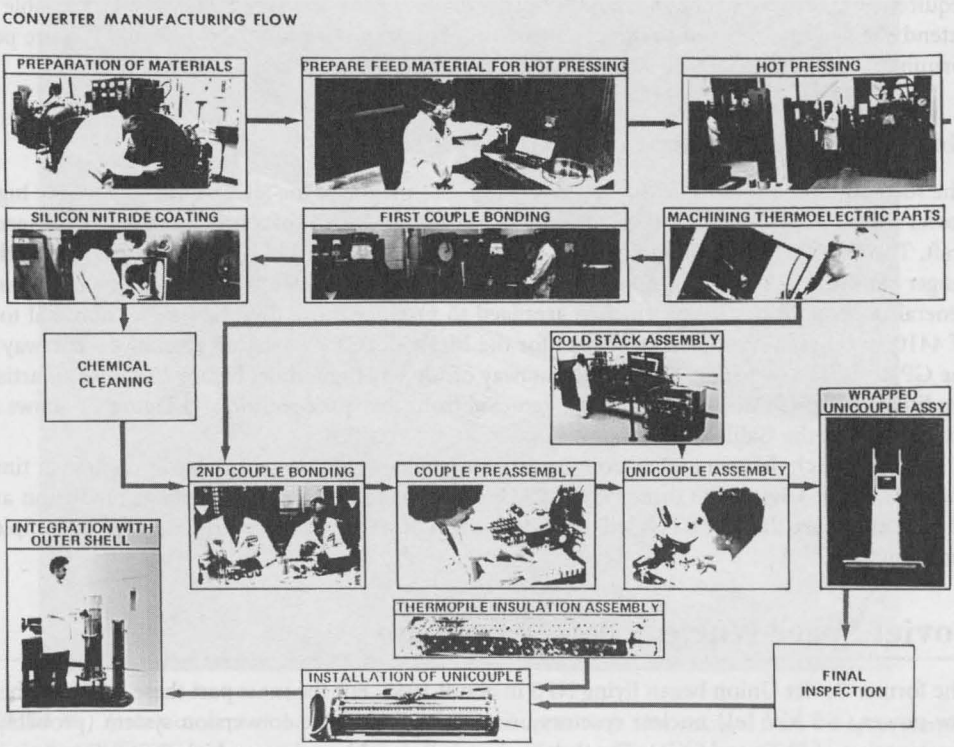

FIGURE 17 Manufacturing flow for silicon germanium converter (GPHS-RTG example).

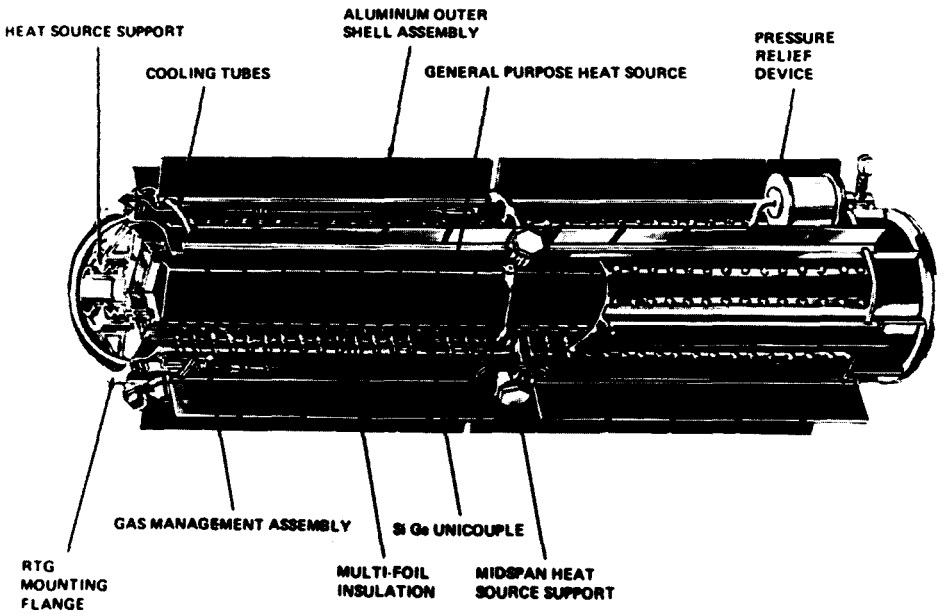

FIGURE 18 Cutaway of the General-Purpose Heat Source (GPHS) RTG which is being used on the Galileo spacecraft and the Ulysses spacecraft.

monoxide (CO) effects.[24] The flight data have shown a steady decrease in overall degradation as the effect of dopant precipitation has diminished. No evidence of appreciable contributions from the other degradation modes has been found in the flight data.

The MHW-RTGs on LES 8/9 and Voyagers 1/2 continue to operate well beyond their mission requirement. Because of the outstanding performance of the Voyager RTGs, NASA was able to extend the Voyager mission to include flybys of Uranus and Neptune.[2,5,25,26] The RTGs are performing so well that scientific data will be received into the early 21st century.[27]

General-Purpose Heat Source (GPHS) RTG

The successful performance of the MHW-RTGs led to the use of the SiGe technology for the high-power (≥285 W [e]) GPHS-RTGs currently in use on the Galileo spacecraft and the Ulysses spacecraft. The GPHS-RTG employs the same unicouple design as used in the MHW-RTGs but with a longer converter (114 vs. 58 cm for the MHW-RTG) and a modular heat source (hence the name general-purpose heat source) which is arranged to produce more thermal power (nominal total of 4410 W (t) vs. a nominal 2400 W (t) for the MHW-RTG).[28–36] Figure 18 shows a cutaway of the GPHS-RTG and Figure 19 shows a cutaway of the GPHS module. Figure 20 shows an artist's rendition of the Ulysses spacecraft after removal from the space shuttle and Figure 21 shows an artist's view of the Galileo spacecraft at Jupiter.

Despite launch delays ranging from 3 years for Galileo (plus a 4-year delay in the transit time) and 4 years for Ulysses the three GPHS-RTGs continue to perform according to prediction and all indications are that the RTGs will provide enough power to enable both spacecraft to complete their missions.[37,38]

41.4 Soviet Space Nuclear Power Program

The former Soviet Union began flying NPS in about 1965. For the most part these NPS have been low-power (≤5 kW [e]) nuclear reactors using a thermoelectric conversion system (probably a combination of PbTe and SiGe). The thermoelectric Romashka reactor, which the Soviets unveiled

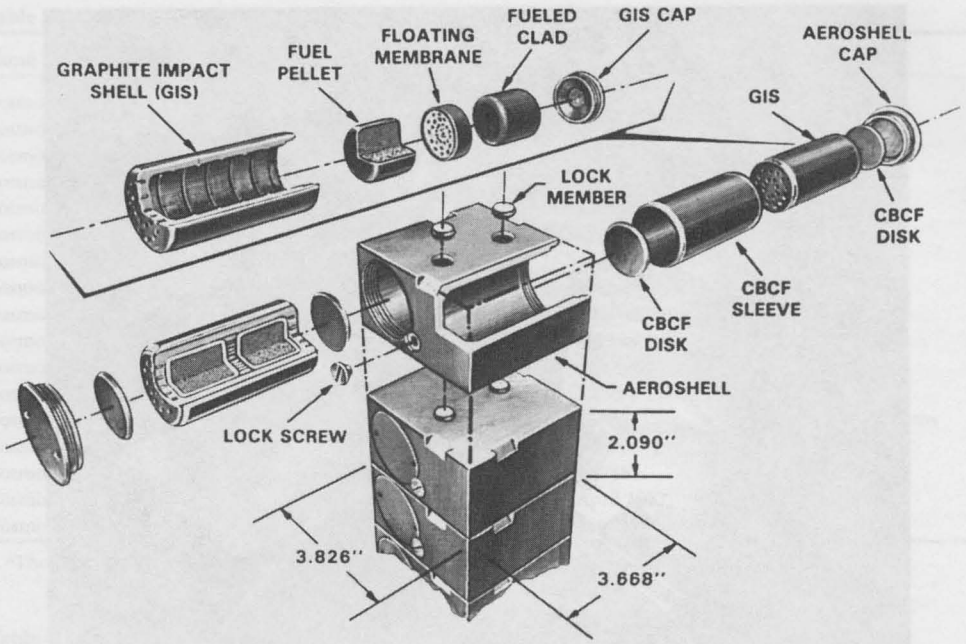

FIGURE 19 Cutaway of the General-Purpose Heat Source illustrating the components of a GPHS module which produces a total of almost 250 W (t) from four plutonia pellets. Eighteen modules are used in each GPHS-RTG.

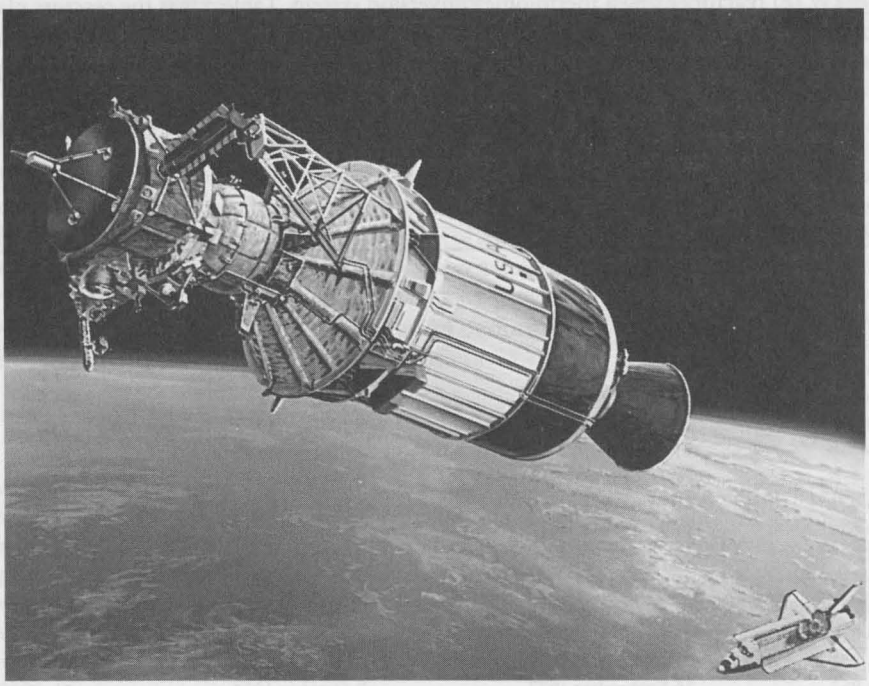

FIGURE 20 Artist's concept of the Ulysses spacecraft and upper stage after removal from the space shuttle. The single GPHS-RTG is the cylinder mounted on the side of the spacecraft.

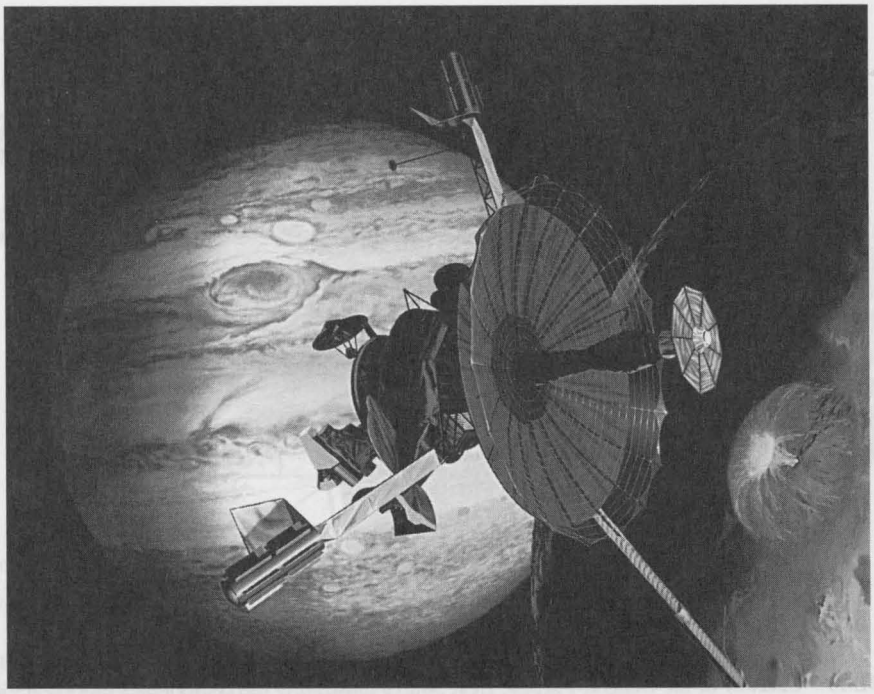

FIGURE 21 Artist's concept of the Galileo spacecraft at Jupiter showing the two GPHS-RTGs mounted one per boom. (At the time of publication the antenna had not been unfurled.)

in 1964, was ground tested using SiGe thermoelectric elements. The former Soviet Union also flew two ~6-kW (e) reactors using a thermionic conversion system. Table 3 lists the reactors placed in orbit by the former Soviet Union. All but the satellites designated as Cosmos 1818 and Cosmos 1867 used thermoelectric conversion. Table 4 summarizes the radioisotope power sources reported to have been launched by the former Soviet Union. Unfortunately, the types of missions flown and the anecdotal character of much of the information does not permit a good extrapolation of what the ultimate lifetimes could be.[4]

Table 3 Soviet Orbital Reactor Program History

Name	Launch Date	Termination Date	Lifetime
Cosmos 198	27 December 1967	28 December 1967	1 d
Cosmos 209	22 March 1968	23 March 1968	1 d
Cosmos 367	3 October 1970	3 October 1970	<3 h
Cosmos 402	1 April 1971	1 April 1971	<3 h
Cosmos 469	25 December 1971	3 January 1972	9 d
Cosmos 516	21 August 1972	22 September 1972	32 d
Cosmos 626	27 December 1973	9 February 1974	45 d
Cosmos 651	15 May 1974	25 July 1974	71 d
Cosmos 654	17 May 1974	30 July 1974	74 d
Cosmos 723	2 April 1975	15 May 1975	43 d
Cosmos 724	7 April 1975	11 June 1975	65 d
Cosmos 785	12 December 1975	12 December 1975	<3 h
Cosmos 860	17 October 1976	10 November 1976	24 d
Cosmos 861	21 October 1976	20 December 1976	60 d
Cosmos 952	16 September 1977	7 October 1977	21 d
Cosmos 954	18 September 1977	~31 October 1977	~43 d
Cosmos 1176	29 April 1980	10 September 1980	134 d
Cosmos 1249	5 March 1981	18 June 1981	105 d

Table 3 Continued

Name	Launch Date	Termination Date	Lifetime
Cosmos 1266	21 April 1981	28 April 1981	8 d
Cosmos 1299	24 August 1981	5 September 1981	12 d
Cosmos 1365	14 May 1982	26 September 1982	135 d
Cosmos 1372	1 June 1982	10 August 1982	70 d
Cosmos 1402	30 August 1982	28 December 1982	120 d
Cosmos 1412	2 October 1982	10 November 1982	39 d
Cosmos 1579	29 June 1984	26 September 1984	90 d
Cosmos 1607	31 October 1984	1 February 1985	93 d
Cosmos 1670	1 August 1985	22 October 1985	83 d
Cosmos 1677	23 August 1985	23 October 1985	60 d
Cosmos 1736	21 March 1986	21 June 1986	92 d
Cosmos 1771	20 August 1986	15 October 1986	56 d
Cosmos 1818	1 February 1987	~July 1987	~6 months
Cosmos 1860	18 June 1987	28 July 1987	40 d
Cosmos 1867	10 July 1987	~July 1988	~1 year
Cosmos 1900	12 December 1987	~14 April 1987	~124d[a]
Cosmos 1932	14 March 1988	19 May 1988	66 d

[a]The Cosmos 1900 reactor continued to operate past the 124-d mission lifetime.

Table 4 Summary of Radioisotope Power Sources Reported to Have Been Launched by the Former Soviet Union

Power Source	Spacecraft	Mission Type	Launch Date	Status
RTG (?)	Cosmos 84	Navigation (?)	3 Sept 1965	In orbit
RTG (?)	Cosmos 90	Navigation (?)	18 Sept 1965	In orbit
RHU	Luna 17 (Lunokhod-1)	Lunar rover	10 Nov 1970	Shutdown
RHU	Luna 21 (Lunokhod-II)	Lunar rover	8 Jan 1973	Shutdown

41.5 Conclusions

The U.S. thermoelectric space nuclear power sources have proved to be reliable, long-lived sources of electrical power that have enabled the conduct of a number of important U.S. space missions, including the first long-term study of the surfaces of the Moon and Mars and the first exploratory visits to Jupiter, Saturn, Uranus, and Neptune. In general, the NPS, from SNAP-3B to the GPHS-RTG, met or exceeded their design requirements by providing power at or above that required and beyond the planned lifetime. This successful performance has laid a secure foundation for future U.S. missions that will use nuclear power.

References

1. Bennett, G. L., Lombardo, J. J., and Rock, B. J., Development and use of nuclear power sources for space applications, *J. Astronaut. Sci.*, 29, 321, 1981.
2. Bennett, G. L., Lombardo, J. J., and Rock, B. J., U.S. radioisotope thermoelectric generator space operating experience (June 1961–December 1982), paper 839171, *Proceedings of the 18th Intersociety Energy Conversion Engineering Conference*, Orlando, Florida, August 21–26, 1983 [Reprinted as U.S. radioisotope thermoelectric generators in space, *Nucl. Eng.*, 25, 49, 1984].
3. Bennett, G. L., Historical overview of the U.S. use of space nuclear power, *Space Power*, 8, 259, 1989.
4. Bennett, G. L., A look at the Soviet space nuclear power program, *Proceedings of the 24th Intersociety Energy Conversion Engineering Conference*, Crystal City, Virginia, August 6–11, 1989, pp. 1187–1194.

5. Skrabek, E. A., Performance of radioisotope thermoelectric generators in space, *Proceedings of the Seventh Symposium on Space Nuclear Power Systems*, Part Two, El-Genk, M. S. and Hoover, M. D., Eds., 1990, 819.
6. Dick, P. J. and Davis, R. E., Radioisotope power system operation in the Transit satellite, presentation at the *American Institute of Electrical Engineers Summer General Meeting*, Paper no. CP 62–1173, Denver, Colorado, June 17–22, 1962.
7. Johns Hopkins University Applied Physics Laboratory, *Artificial Earth Satellites Designed and Fabricated by the Johns Hopkins University Applied Physics Laboratory*, JHU/APL report SDO-1600 (revised), August 1980.
8. Harvey, D. G., Dick, P. J., and Fink, C. R., Isotope-generator reliability and safety, *Nucleonics*, 21, 56, 1963.
9. Hittman Associates, Inc., Radioisotope powered space systems, *U.S. Atomic Energy Commission report NYO–3165–11*, August 23, 1963. [Additional discussion of survivability issues may be found in Bennett, G. L., Survivability considerations in the design of space power systems, *Proceedings of the 23rd Intersociety Energy Conversion Engineering Conference*, Paper 889159, Denver, Colorado, July 31–August 5, 1988.]
10. Martin Marietta Corporation, *SNAP-9A Pu-238 Fueled Thermoelectric Power Supply for Auxiliary Space Power, Final Report*, Volume 1, Martin Nuclear Division report MND–P–3098–1, October 1964.
11. Teledyne Energy Systems, *SNAP 19 Viking Lander System Program Final Report*, July 1, 1970–June 30, 1976, report TES–3069–54, June 1976.
12. Fihelly, A. W. and Baxter, C. F., Orbital performance of the SNAP-19 radioisotopic thermoelectric generator experiment, paper 719152, *Proceedings of the 6th Intersociety Energy Conversion Engineering Conference*, Boston, Massachusetts, August 3–5, 1971.
13. Jaffe, H. and O'Riordan, P., Isotope power systems for unmanned spacecraft applications, paper 729088, *Proceedings of the 7th Intersociety Energy Conversion Engineering Conference*, San Diego, California, September 25–29, 1972.
14. Goebel, C. J., SNAP-19 Pioneer 10 and 11 RTG deep space performance, *Record of the 10th Intersociety Energy Conversion Engineering Conference*, paper 759130, Newark, Delaware, August 18–22, 1975.
15. Brittain, W. M. and Skrabeck, E. A., SNAP-19 RTG performance update for the Pioneer and Viking missions, paper 839172, *Proceedings of the 18th Intersociety Energy Conversion Engineering Conference*, Orlando, Florida, August 21–26, 1983.
16. Skrabek, E. A. and McGrew, J. W., Pioneer 10 and 11 RTG performance update, in *Space Nuclear Power Systems 1987*, Vol. 7, Orbit Book Co., Malabar, Florida, 1988, 587.
17. Brittain, W. M., SNAP-19 Viking RTG mission performance, paper 769255, *Proceedings of the 11th Intersociety Energy Conversion Engineering Conference*, State Line, Nevada, September 12–17, 1976.
18. Britting, A. O., Jr., Viking lander battery performance, degradation, and reconditioning, paper 819110, *Proceedings of the 16th Intersociety Energy Conversion Engineering Conference*, Atlanta, Georgia, August 9–14, 1981.
19. Pitrolo, A. A., Rock, B. J., Remini, W. C., and Leonard, J. A., SNAP-27 program review, paper 699023, *Proceedings of the 4th Intersociety Energy Conversion Engineering Conference*, Washington, D.C., September 22–26, 1969.
20. Bates, J. R., Lauderdale, W. W., and Kernaghan, H., ALSEP termination report, *NASA Reference Publication 1036*, April 1979.
21. Bradshaw, G. B. and Postula, F. D., Beginning of mission flight data on the TRANSIT RTG, paper 739091, *Proceedings of the 8th Intersociety Energy Conversion Engineering Conference*, Philadelphia, Pennsylvania, August 13–16, 1973.
22. Staub, D. W., SNAP 10A summary report, *Atomics International Report NAA–SR–12073*, March 25, 1967.
23. Bennett, G. L., On the application of nuclear fission to space power, in *50 Years with Nuclear Fission*, American Nuclear Society, La Grange Park, Illinois, 1989, 916.
24. Kelly, C. E., The MHW converter (RTG), paper 759132, *Record of the 10th Intersociety Energy Conversion Engineering Conference*, Newark, Delaware, August 18–22, 1975. [An excellent summary of the MHW-RTG program may be found in the Addendum to the *8th Intersociety Energy Conversion Engineering Conference Proceedings*, August 13–16, 1973, Philadelphia, Pennsylvania.]

25. Kelly, C. E., MHW RTG performance during LES 8/9 and Voyager missions, *Transactions of 4th Symposium on Space Nuclear Power Systems,* 1987, 197.
26. Packard, L. A., Flight performance of the Voyager electrical power system, *Proceedings of the 16th Intersociety Energy Conversion Engineering Conference,* Vol. 1, 1981, 446.
27. Cesarone, R. J., Sergeyevsky, A. B., and Kerridge, S. J., Prospects for the Voyager extra-planetary and interstellar mission, *J. Br. Interplanetary Soc.,* 37, 99, 1984.
28. Schock, A., Shostak, A., and Sookiazian, H., Design, analysis, and optimization of RTG for solar polar mission, *Proceedings of the 14th Intersociety Energy Conversion Engineering Conference,* Boston, Massachusetts, 1979, 1444.
29. Schock, A., Design evolution and verification of the "general-purpose heat source", *Proceedings of the 15th Intersociety Energy Conversion Engineering Conference,* Seattle, Washington, 1980, 1032.
30. Cockfield, R. D., Hartman, R. F., and Kelly, C. E., RTG power sources for the International Solar Polar Mission, *Proceedings of the 15th Intersociety Energy Conversion Engineering Conference,* Seattle, Washington, 1980, 1043.
31. Cockfield, R. D., Engineering development testing of the GPHS-RTG converter, *Proceedings of the 16th Intersociety Energy Conversion Engineering Conference,* Atlanta, Georgia, 1981, 321.
32. Kelly, C. E. and Ambrose, G. R., Testing of the GPHS electrically heated thermoelectric converter, *Proceedings of the 17th Intersociety Energy Conversion Engineering Conference,* Los Angeles, 1982, 1382.
33. Bennett, G. L., Lombardo, J. J., and Rock, B. J., Power performance of the General-Purpose Heat Source Radioisotope Thermoelectric Generator, in *Space Nuclear Power Systems 1986,* Orbit Book Company, Malabar, Florida, 1987, 437.
34. Bennett, G. L., Lombardo, J. J., Hemler, R. J., and Peterson, J. R., The General-Purpose Heat Source Radioisotope Thermoelectric Generator: power for the Galileo and Ulysses missions, *Proceedings of the 21st Intersociety Energy Conversion Engineering Conference,* San Diego, California, 1986, p. 1999.
35. Cockfield, R. D., Qualification of GPHS-RTG for the Galileo and Ulysses missions, *Proceedings of the 21st Intersociety Energy Conversion Engineering Conference,* San Diego, California, 1986, 2012.
36. Bennett, G. L., Whitmore, C. W., and Amos, W. R., On the development of the power sources for the Ulysses and Galileo missions, *Proceedings of the European Space Power Conference,* European Space Agency publication ESA SP-294, 1989, 117.
37. Hemler, R. J. and Cockfield, R. D., GPHS-RTG performance on the Galileo mission, *Proceedings of the Eighth Symposium on Space Nuclear Power Systems,* Part Two, American Institute of Physics, New York, CONF-910116, 1991, 910.
38. Hemler, R. J. and Kelly, C. E., Flight performance of Galileo and Ulysses RTGs, *Proceedings of the 10th Symposium on Space Nuclear Power and Propulsion,* American Institute of Physics, January 10–14, 1993, Albuquerque, New Mexico.

42

SP-100 Space Subsystems

Jack F. Mondt
Jet Propulsion Laboratory
California Institute of Technology
Pasadena, California, U.S.A.

42.1 Introduction

The space subsystems for SP-100 are the Heat Transport, Converter, and Heat Rejection Subsystems, as shown in Figure 1. The most critical technology required to make the SP-100 Program a reality is the conversion of heat from the reactor to electricity for operating a spacecraft and/or electric thrusters. The heat-to-electric Converter Subsystem must be high-temperature, low-mass, highly reliable, and have a very long life. The SP-100 Project is developing a Converter Subsystem made up of many conductively coupled thermoelectric (TE) multicouple cells to convert the reactor thermal power to electricity. The TE cell uses the basic silicon germanium material which has operated for more than 12 years in space on the JPL Voyager spacecraft with a radioisotope heat source. The main differences between the SP-100 TE cell and the Voyager TE couple are shown below.

SP-100	Voyager
Conductively coupled	Radiation coupled
± 100 V DC	30 V DC
Improved SiGe material	SiGe material
T_h = 1273 K	T_h = 1273 K
T_c = 833 K	T_c = 573 K
P_o = 12.5 W @ 1.2 V	P_o = 0.5 W @ 0.2 V
Size = 1.04″ × 1.04″ × 0.51″	Size = 0.9″ × 0.9″ × .81″
Eight (8) couples	One (1) couple

The converter technical development challenges were the hot-side, high-voltage electrical insulator, the hot and cold compliant pads, and the hot and cold electrodes. These were all new developments that were needed for the SP-100 conductively coupled TE cells. The high-voltage electrical insulator and the compliant pads were not needed nor used on the Voyager radiation-coupled TE cells.

The next most critical space technology required for the SP-100 system was in the Heat Transport Subsystem. This subsystem must remove the heat from the surface of the reactor fuel pins and transport that heat at an end-of-life temperature of 1375 K to the hot side of the TE cell. The Heat Transport Subsystem must have low heat loss, low mass, be highly reliable, and have a 10-year

0-8493-0146-7/95/$0.00+$.50

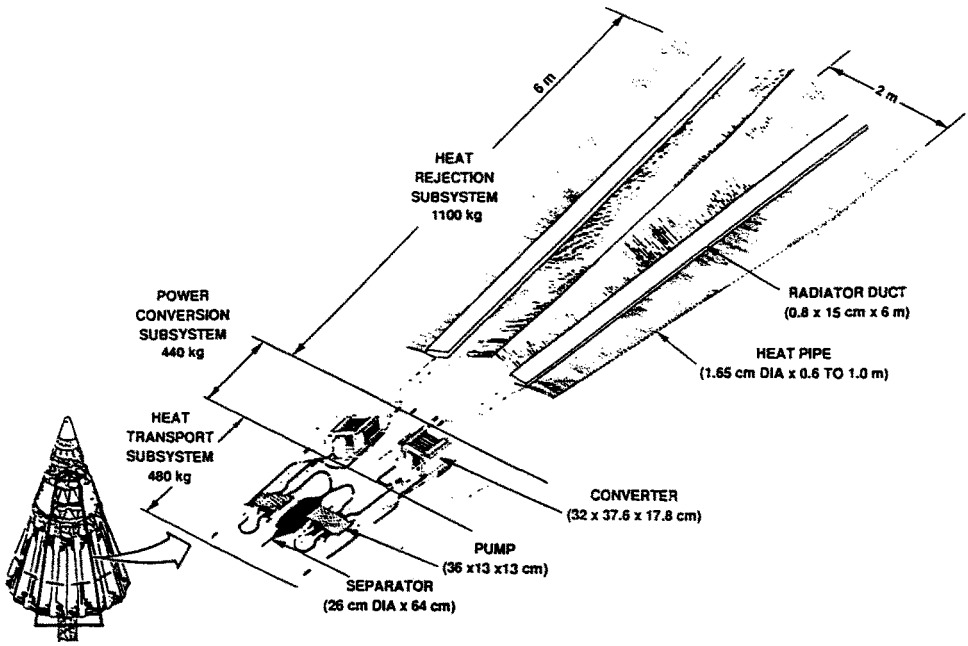

FIGURE 1 Space subsystems.

life. The subsystem being developed consists of liquid lithium circulating in niobium 1% zirconium piping, thermoelectric electromagnetic pumps, and helium/lithium gas separators.

The other critical space technology required for the SP-100 system is in the Heat Rejection Subsystem. This subsystem must remove the waste heat from the cold side of the TE cell at an end-of-life temperature of 880 K and radiate this heat to space. The waste heat radiator must have low temperature gradients, low mass, be highly reliable in a meteoroid environment, and have a 10-year life. The SP-100 Program is developing a Heat Rejection Subsystem consisting of liquid lithium circulating in titanium ducts and many potassium heat pipes with carbon-carbon armor material thermally bonded to the ducts and heat pipes for meteoroid protection.

42.2 Converter Subsystem Progress

The Converter Subsystem design for a 100-k W (e) space reactor power system was completed in May 1988 and consists of 12 identical power conversion assemblies (PCA), one of which is shown in Figure 2. The PCA is made of six identical thermoelectric converter assemblies (TCA), each with one set of hot-side headers and manifolds, and two sets of cold-side headers and manifolds, as shown in Figure 3. The headers and manifolds get the heat to the hot side of the TE cells and away from the cold side of the TE cells. One TCA consists of 120 TE cells, one of which is shown in Figure 4. The TE cell consists of three major components which are (1) the TE module shown in Figure 5, (2) the compliant pads shown in Figure 6, and (3) the high-voltage insulator shown in Figure 7.

High-Voltage Insulator

The SP-100 Project developed a single-crystal sapphire ($S_xAL_2O_3$) insulator, 0.127 mm thick, metallurgically bonded to thin niobium sheets on both sides, which allow bonding to a niobium 1% zirconium (Nb1Zr) heat exchanger on one side and a niobium compliant pad on the other side. For the SP-100 application, which uses lithium as the heat exchanger fluid from the reactor heat source, the $S_xAl_2O_3$ insulator must be protected from the lithium by a non-oxygen-permeable

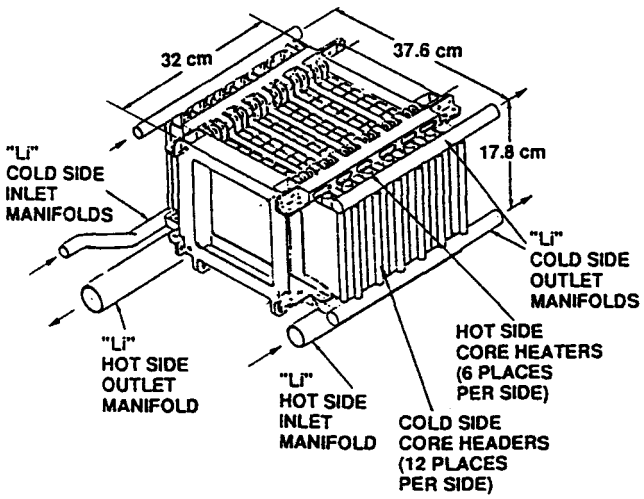

FIGURE 2 Power conversion subsystem.

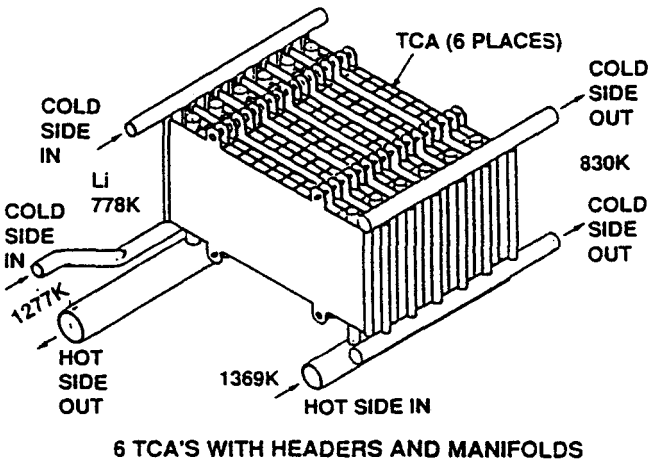

FIGURE 3 Power converter assembly.

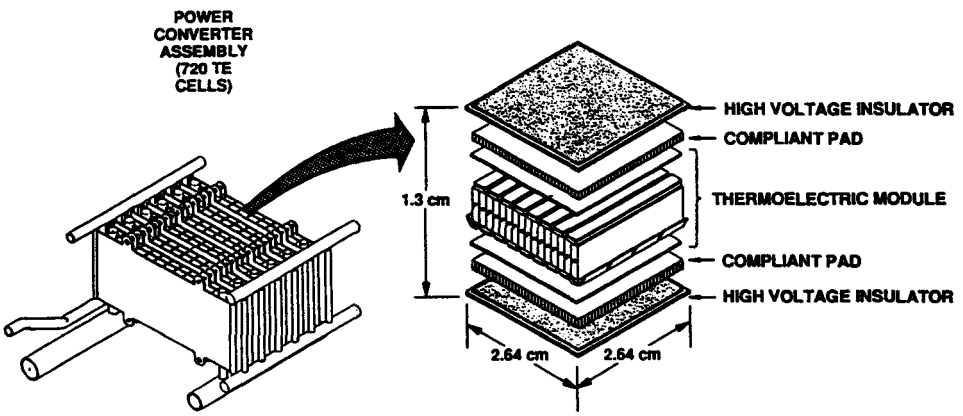

FIGURE 4 SP-100 thermoelectric cell.

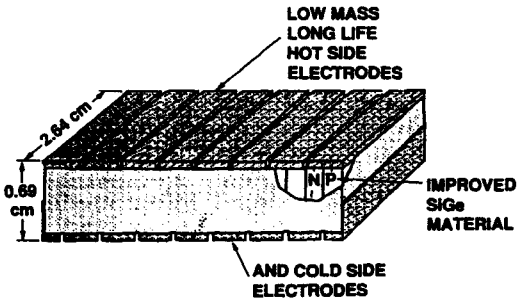

FIGURE 5 Thermoelectric module.

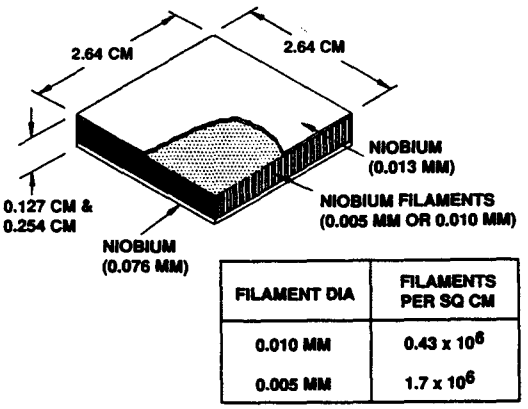

FILAMENT DIA	FILAMENTS PER SQ CM
0.010 MM	0.43×10^6
0.005 MM	1.7×10^6

FIGURE 6 Compliant pad.

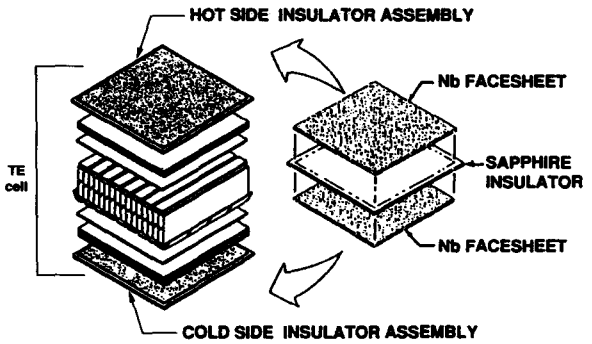

FIGURE 7 High-voltage insulator.

material to prevent rapid loss of oxygen from the insulator. The prevention of oxygen loss from the insulator was confirmed by accelerated tests using a molybdenum barrier, bonded between the lithium heat exchanger and the niobium face sheets on the sapphire insulator. The effectiveness of the molybdenum barrier has been proven by tests up to 1875 K, which verified the calculations that predict greater than 10 years life at 1375 K. Therefore, the insulator technology for SP-100 has been validated and is ready for use in flight space reactor power systems.

Compliant Pad

The SP-100 Program developed a compliant pad with a 0.075 mm thick niobium face sheet on the insulator side and a 0.013 mm thick niobium face sheet on the TE module side with 0.635 mm long by 0.010 mm diameter niobium filaments in between. A sketch of this compliant

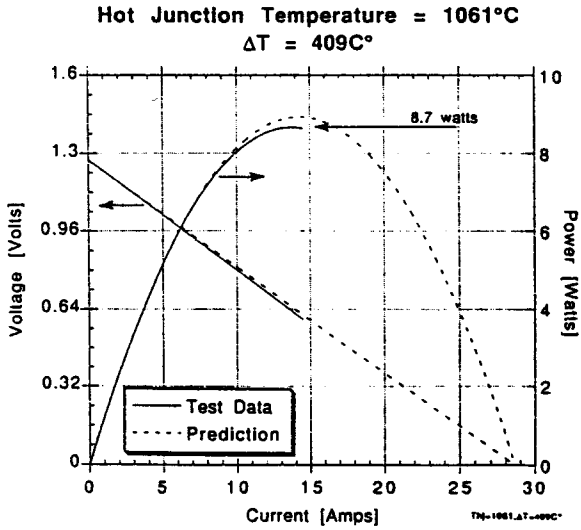

FIGURE 8 PD2A thermoelectric cell test data.

pad is shown in Figure 6. During the assembly development of the second series of predevelopment cells (PD2), it was discovered that during the 1200°C bonding step, to bond the insulator to the compliant pad, the niobium filaments were also partially bonding together. This increased the stiffness of the compliant pad beyond the allowable load. So now yttrium oxide Y_2O_3 is injected into the filament matrix of the compliant pad as a colloidal suspension of Y_2O_3 in water. The water is subsequently vaporized, leaving Y_2O_3 particles on the surfaces of the filaments. The effectiveness of this approach has been demonstrated by analyses and tests. A full-size Y_2O_3-coated pad was examined and tested to demonstrate that the coating method prevents niobium filament bonding. The tensile cycle test of the full size compliant pad produced a stiffness which meets the designed allowable load.

The compliant pad developed in SP-100 has been integrated into two TE cells. One TE cell (PD2) failed by cracking of the SiGe material after cool down from the final brazing step. It is predicted, by stress analyses and strength tests, that the SiGe failure in PD2 was caused by weak tungsten and a stiff compliant pad, which developed because of the cell fabrication process. This process has been corrected. The second-series predevelopment cell fabricated according to the corrected process (PD2A) was put on test, operated for more than 600 h with a temperature gradient of 330°C and a power level of 6 W. The TE cell was operated for a short time at a maximum temperature gradient of approximately 400°C and a maximum output power of 8.7 W. Figure 8 shows the predicted and experimental current/voltage curve and the power/current curve. The design temperature gradient of about 440°C could not be reached because of lower thermal conductivities in the components and bonds on the hot and cold sides of the TE module. This was the first successful test of a conductively coupled TE cell with the niobium compliant pads. Therefore, this test verifies the calculations that the compliant pad allows the SiGe module to bow with a 400°C thermal gradient without fracturing. Additional development for the compliant pad was completed. Reproducible pads with low stiffness for use in TE cells with thermal gradients of about 440°C, were manufactured and successfully tested.

Thermoelectric Module

The TE module developed by SP-100 for a 100-kW (e) system is shown in Figure 5. The TE module consists of eight improved SiGe thermoelectric n and p couples, with tungsten graphite bilayer hot- and cold-side electrodes.

Improving the SiGe thermoelectric alloy material for SP-100 results in a 20% mass savings for thermoelectric space reactor power systems. Several improved (20 to 30%) n-type SiGe/GaP

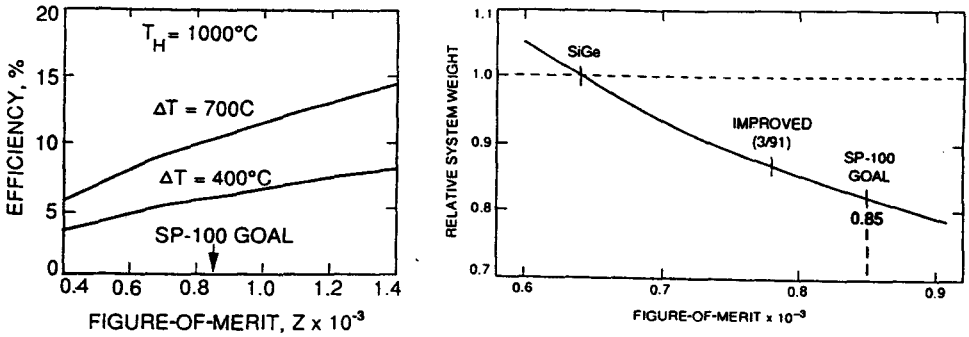

FIGURE 9 Improved SiGe material.

samples have been obtained by heat treating the material at very high temperatures. More recently, two theoretical models (a thermodynamic model and an electrical and thermal transport model) have been developed which explain the cause of the improvement. The cause of the improvement is the gallium-phosphorous (Ga-P) interaction (ion-pairing), which results in the solubility of phosphorus increasing beyond normal levels. As a result of this understanding, several improved thermoelectric material samples have been produced at JPL and at Thermotrex Corporation. Routine fabrication of the improved n-type material has been achieved.

Work on the improvement of p-type SiGe started in 1990. The improvement approach being taken is to reduce the thermal conductivity. It is planned to add very fine scattering centers to the alloy in order to scatter the intermediate-frequency phonons, which carry most of the heat. The work is taking place at the Thermotrex Corporation, which has developed a special spark erosion apparatus that can produce the very fine particulates needed.

The improved efficiency and the relative system mass as a function of the TE figure-of-merit are shown in Figure 9. The SiGe material presently used on outer-planet spacecraft has a figure-of-merit of 0.65×10^{-3} K^{-1}. The SP-100 system is based on an improved SiGe material with a 0.85×10^{-3} K^{-1} figure-of-merit. The SP-100 development to date has achieved a figure-of-merit of 0.78×10^{-3} K^{-1} with the SP-100 design value of 0.85×10^{-3} K^{-1} in sight. With predicted improvements, both analytically and experimentally, in both the electrical and thermal properties, a design value of 1.0×10^{-3} K^{-1} is thought possible with this improved SiGe material.

The electrode development has concentrated on developing a tungsten-graphite electrode because the graphite makes a good bond to the SiGe and the tungsten thermal coefficient of expansion is close to matching SiGe. The tungsten will also be used as an intercell electrical lead that can be welded. The most critical requirement is to maintain the electrical contact resistance for all material interfaces within the TE cell to less than 100 micro-ohms-cm^2. The tungsten-to-graphite contact resistivity easily meets the requirement while the graphite-to-SiGe bond can be made with an initial contact resistivity of less than the requirement. However, the contact resistivity increases very rapidly with time at temperature. By sealing the graphite material with pyrolytic graphite prior to bonding to SiGe, the low contact resistance has been maintained for up to 1000 h at 1000°C, as shown in Figure 10.

The original flight design consists of tungsten foil brazed to graphite sheet. These brazes formed brittle carbides with large expansion coefficients and the design was changed to use the chemical vapor deposition (CVD) process to bond tungsten to graphite. The CVD process provides a strong bond, but does not provide a very good method for interconnection of cells. Interconnection of cells is proposed by applying CVD tungsten continuously over the graphite and over the glassed edges of the TE module. Interconnecting tungsten tabs would then be attached to the CVD tungsten along the sides of the module. In this configuration, the tungsten would be continuous and approximately the same thickness across the graphite and up the sides of the TE module.

The TE cell electrode design and interconnections remain as a key technical challenge for SP-100 and is planned to be completed for the prototype development cell, called (TA) for type approval. The interconnect design is to be demonstrated with a 2 × 2 TE cell array test.

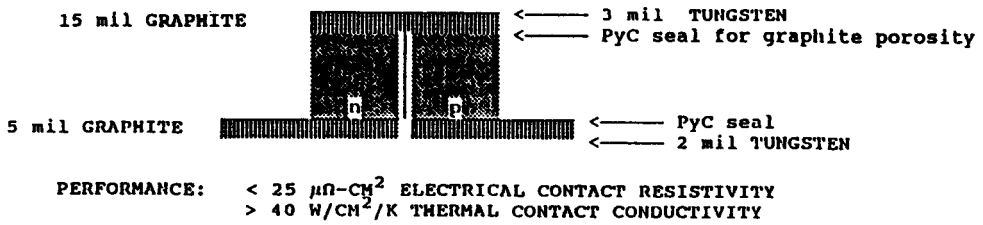

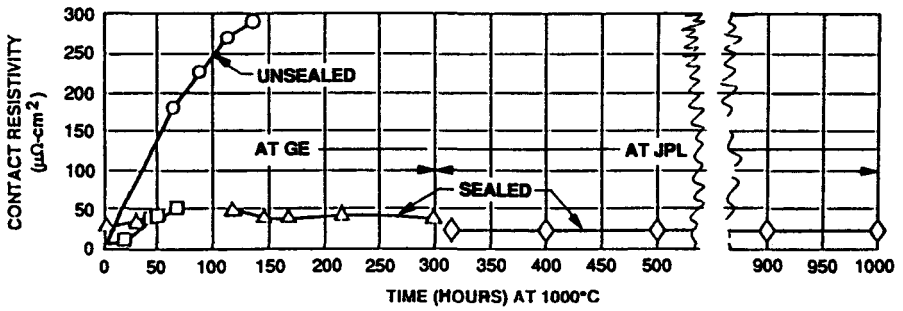

FIGURE 10 Contact resistivity for unsealed and sealed bilayer electrode.

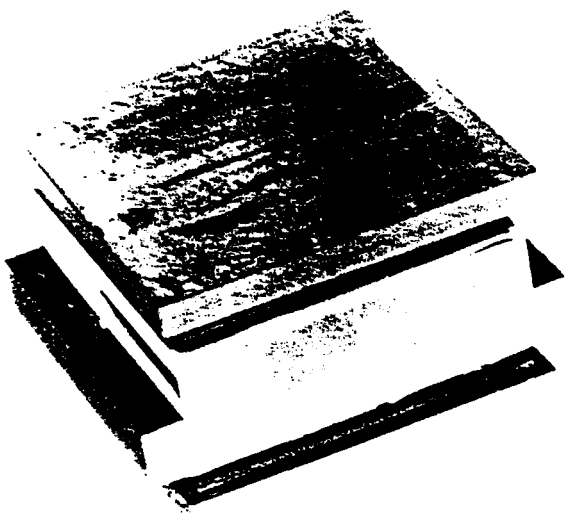

FIGURE 11 Second-series predevelopment cell (PD2A).

TE Cell Assembly and Test

The insulator, compliant pad, and TE module with silicon molybdenum electrodes (Voyager RTG electrodes) were assembled and put on test at the end of June 1991 and operated for more than 600 h. This second-series predevelopment cell (PD2A) has demonstrated that the basic three subassemblies can be bonded and will produce power as predicted. A photograph of PD2A after final brazing and before instrumenting is shown in Figure 11. The next step incorporated the flight system electrodes and tested eight prototypic TE cell assemblies which included all the technologies developed specifically for the SP-100 reactor space power system. This type approval (TA) cell concluded a major development step toward a successful space reactor power system.

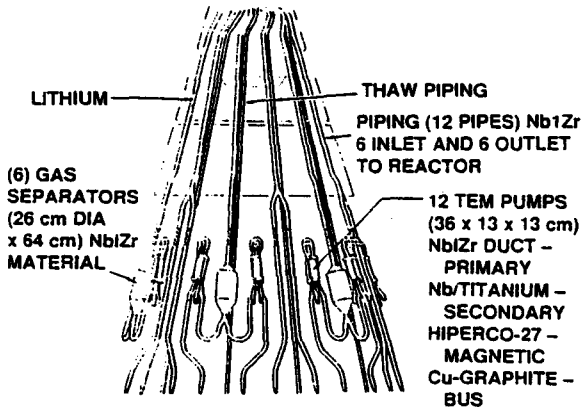

FIGURE 12 Heat transport subsystem.

42.3 Heat Transport System Progress

The Heat Transport (HT) Subsystem includes the TEM pump, the gas separator, and the lithium containment piping, which must remain leak tight for the 10-year life of the system. The HT subsystem is shown in Figure 12.

A Nb1Zr materials convection test loop was assembled and operated up to 1460 K to demonstrate that the cleaning, welding, and heat treatment processes for Nb1Zr have been reestablished. A schematic of the materials test loop is shown in Figure 13. The first loop was assembled, filled, and operated to reestablish and complete the process specifications and procedures to be used for complex weld geometries and assemblies. The second materials loop was built in strict adherence to the process specifications and procedures presently documented for complex weld geometries and assemblies of Nb1Zr material and was filled with lithium. The second loop operated up to 1500 K and validated the cleaning, pickling, welding, and post-weld treatment specification and procedures. This loop also successfully tested Nb1Zr post-weld heat treatment welded coupons and niobium 1% zirconium 0.1% carbon (Nb1Zr0.1C) welded coupons.

TEM Pump

The pump design has been completed and magnetic tests were successfully conducted which verified the analytical, magnetic codes. The pump design, dimensions, and materials are shown in Figure 14. An electromagnetic integration test (EMIT) was completed and verified the integrated electric and magnetic design codes followed by design fabrication and test of the flight design pump. A TEM pump was fabricated using prototypic materials and TE cells to demonstrate a viable fabrication process.

Gas Separator

A gas separator concept to remove helium from lithium in zero gravity has been well defined. Using the helium-lithium analytical codes, but substituting the properties of air for helium and water for lithium, a room-temperature gas separator was designed, fabricated, and tested both horizontally and vertically against gravity. The device separated air from water even against one g as predicted by the analyses. A design and test with helium and lithium verified the analytical design codes for this component. The gas separator design is shown in Figure 15.

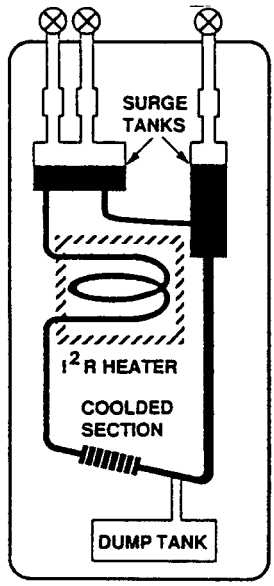

FIGURE 13 Materials test loop schematic.

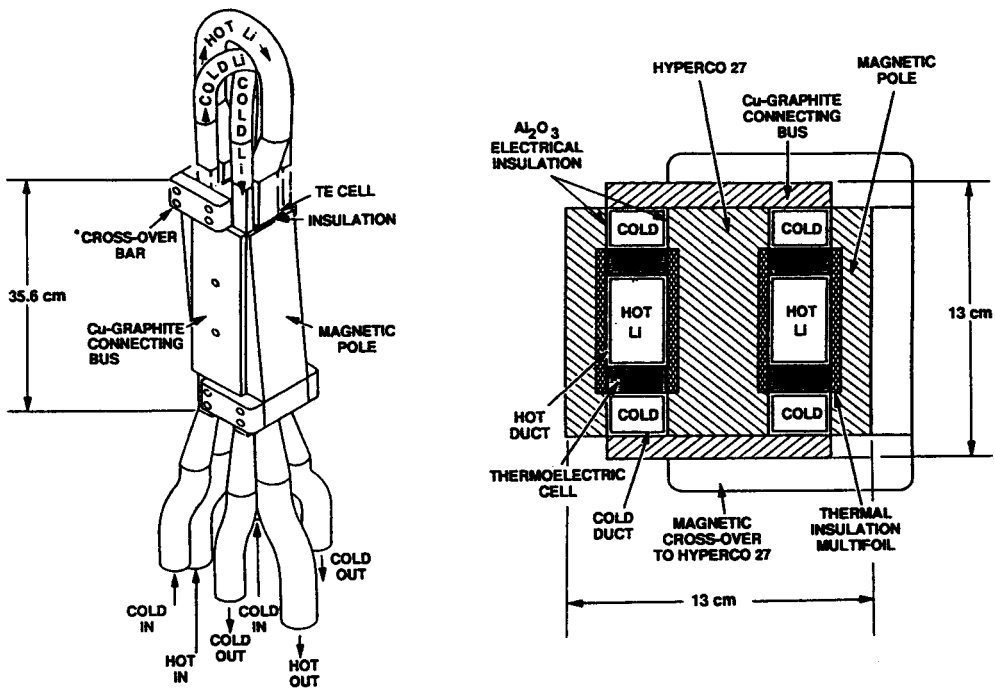

FIGURE 14 Thermoelectric electromagnetic pump.

42.4 Heat Rejection Subsystem

The Heat Rejection Subsystem consists of lithium circulating in titanium ducts protected from meteoroids by bumpers and potassium-titanium heat pipes with carbon-carbon meteoroid protection over the exposed radiating sections of the heat pipes. The radiator panel design is shown

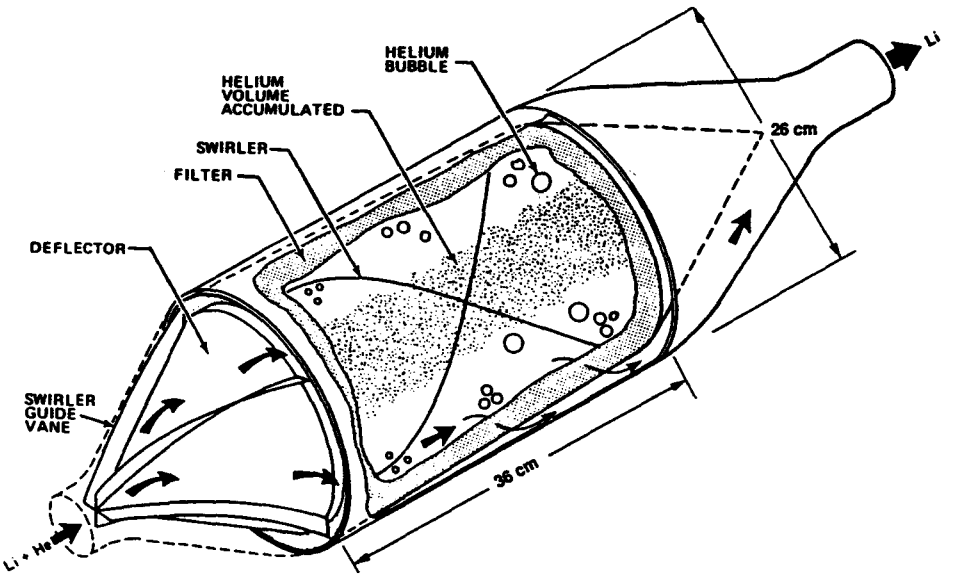

FIGURE 15 Gas separator/accumulator.

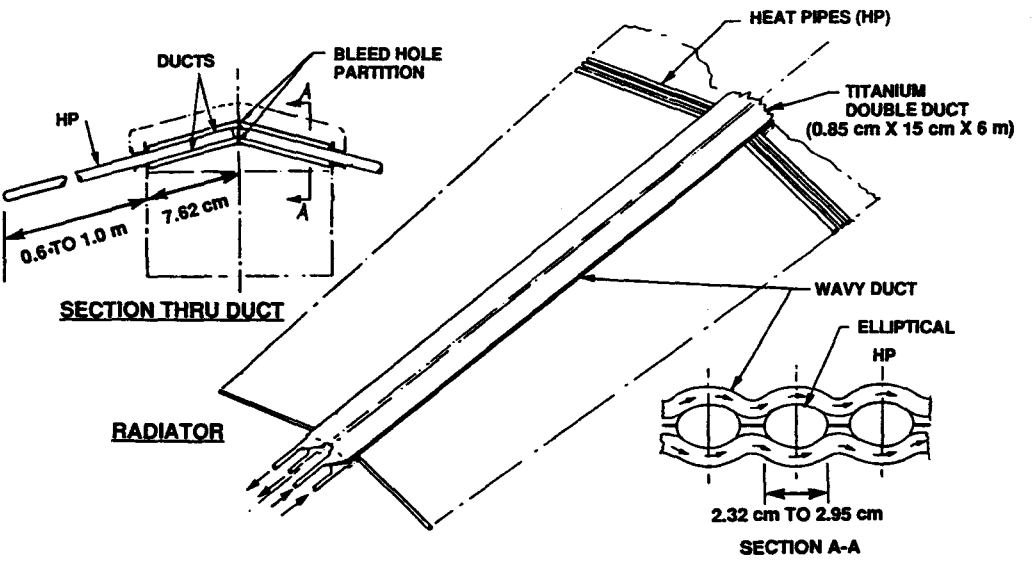

FIGURE 16 Heat rejection radiator panel.

in Figure 16. The titanium heat pipes have been fabricated and tested and have verified the heat pipe analytical codes. The SP-100 program has not had sufficient funding to pursue this subsystem development. The critical key technology is bonding titanium to carbon-carbon and creating a 10-year life, high-thermal-conductivity joint at 750 to 850 K temperature. NASA LeRC developed the nobium to carbon-carbon bond at a very low funding level as part of the advanced, which could be used for SP-100 technology.

42.5 Conclusion

The space technology effort has been primarily concentrated over the last 2 years on the Converter Subsystem. Excellent progress has been made on some very difficult challenges. The high-temperature, high-voltage insulator in the presence of lithium is technology-ready. The compliant

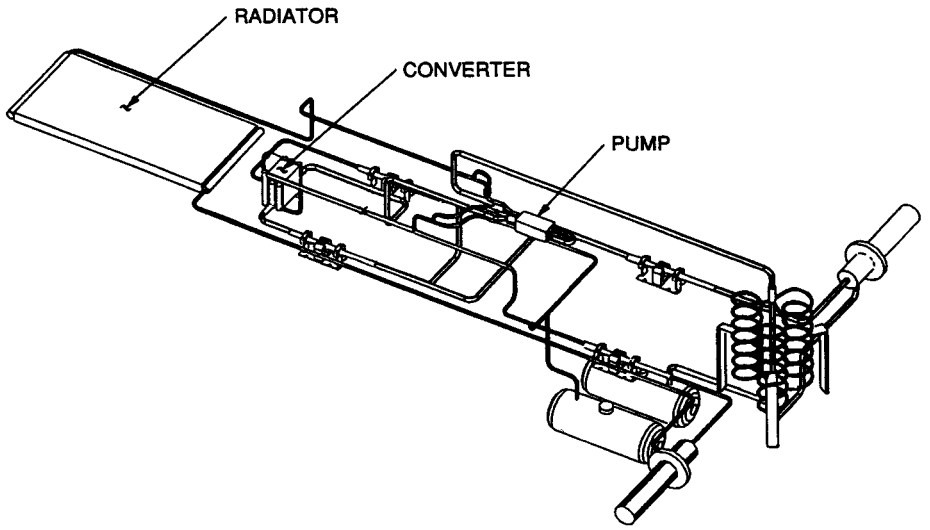

FIGURE 17 Converter, pump, radiator test.

pad, essential to conductively coupled thermoelectric converters, is technology-ready. A compliant pad has been operated successfully in a TE cell at the design temperature gradient across the SiGe material. The bilayer electrode contact resistance has shown encouraging lifetime results. The TE module, compliant pad, and insulator assembly development has resulted in ten operating TE multicells, with eight of the ten successfully operated at higher than design end-of-life hot-side temperatures.

The Heat Transport Subsystem progress on Nb1Zr fabrication, cleaning, and welding necessary to contain lithium at 1375 K, has been excellent and is technology-ready. The thermoelectric, electromagnetic pump magnetics operated as designed and a new gas separator concept operated as predicted with air and water.

The Heat Rejection Subsystem progress has shown that a low-cost, manufacturable heat pipe can be designed and will operate as designed at the required performance values for SP-100. The radiator thaw bleed-hole design has also been shown to behave as predicted and meet SP-100 requirements.

There is still development needed in the space subsystems. However, the most critical technical challenges have been resolved and the remaining ones are well defined. The three major components (converter, pump, and radiator) of the space subsystems need to be built and tested in a liquid metal lithium double loop facility. An isometric of this double loop facility is shown in Figure 17 with the SP-100 converter, pump, and radiator in place.

Acknowledgment

Prepared by the Jet Propulsion Laboratory, California Institute of Technology, for the U.S. Department of Energy through an agreement with the National Aeronautics and Space Administration (NASA).

43

Safety Aspects of Thermoelectrics in Space

Gary L. Bennett
NASA Headquarters (retired)
c/o Boise, Idaho

43.1 Introduction

The purpose of this chapter is to describe the safety review and approval process used in the U.S. for the launch of any nuclear-powered spacecraft. This process can be traced back to 1961 with the first launch of a nuclear power source (NPS) by the U.S. From the beginning there has been an emphasis on the safe use of NPS, including a requirement to obtain launch approval from the Office of the President because of the international policy implications of such launches.[1–5] The latest codification of the launch approval process is Presidential Directive NSC/25, dated December 14, 1977, which covers any federal undertaking (non-nuclear as well as nuclear) that may have "major and protracted effects on the physical or biological environment". With regard to space nuclear systems, the Presidential Directive states:[6]

> A separate procedure will be followed for launching space nuclear systems. An environmental impact statement or a nuclear safety evaluation report, as appropriate, will be prepared. In addition, the President's approval is required for launches of spacecraft utilizing radioactive sources containing more than 20 curies of material in Radiotoxicity Groups I and II and for more than 200 curies of material in Radiotoxicity Groups III and IV (as given in Table I of the NASC report of June 16, 1970 on "Nuclear Safety Review and Approval Procedures"). An ad hoc Interagency Nuclear Safety Review Panel consisting of members from the Department of Defense, Department of Energy, and National Aeronautics and Space Administration will evaluate the risks associated with the mission and prepare a Nuclear Safety Evaluation Report. The Nuclear Regulatory Commission should be requested to participate as an observer when appropriate. The head of the sponsoring agency will request the President's approval for the flight through the Office of Science and Technology Policy. The Director is authorized to render approval for such launchings, unless he considers it advisable to forward the matter to the President for decision.

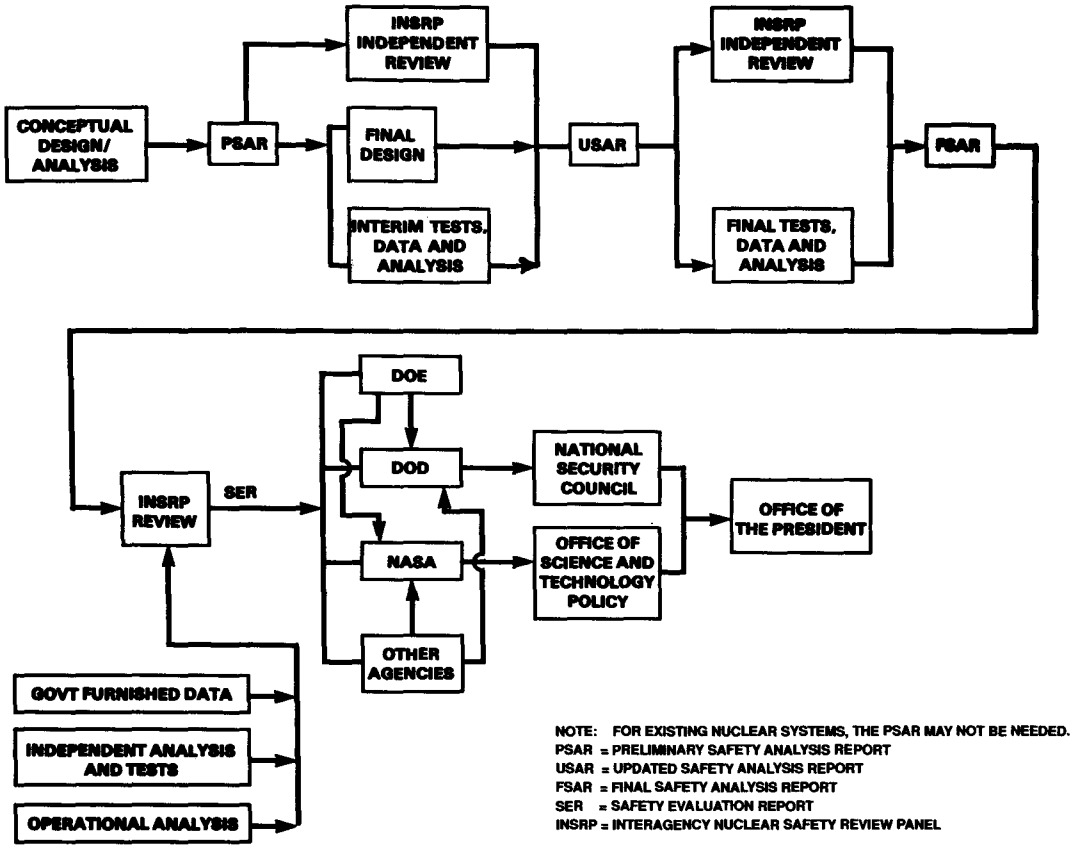

FIGURE 1 Review process for the safety of space nuclear power systems.

Figure 1 illustrates the review process for the safety of space nuclear systems.

43.2 Safety Review Process

As shown in Figure 2 for the general-purpose heat source radioisotope thermoelectric generator (GPHS-RTG), safety is one of the two principal design requirements on an NPS (the other being performance). The primary safety objective is to minimize the potential interaction of the radioactive materials with earth's population and environment.[1] A formal review process has been established for the assessment of the safety of an NPS, as shown diagrammatically in Figure 1.

The safety review process consists of three sequential and required documents:

1. An Environmental Impact Statement (EIS) prepared very early in the project at the time of the initial decision to undertake the mission. Figure 3 illustrates the U.S. federal EIS process.
2. A Safety Analysis Report (SAR) prepared during the development of the NPS program.
3. A Safety Evaluation Report (SER) prepared by an independent interagency panel known as the Interagency Nuclear Safety Review Panel (INSRP) during the late stages of the program as independent input into the governmental decisions to launch the NPS.

Figure 4 shows the overall NPS program logic, illustrating how the safety, design, fabrication, and testing processes are interrelated. Table 1 lists the generic types of safety-related documents required for launch and space use of an NPS. The SAR, which is the major compilation of safety information and analyses by the U.S. Department of Energy (DOE) program office, and the SER, which provides an independent review of the SAR and is considered in the launch approval process, are the primary focus of this chapter. Although the focus is on the flight-related SARs and SER,

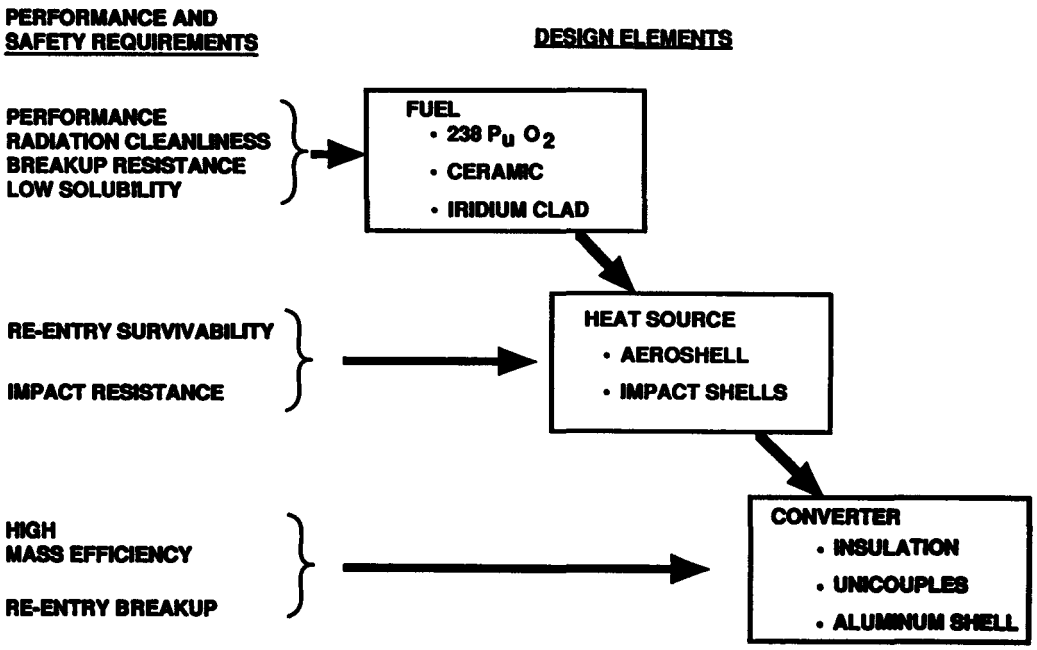

FIGURE 2 Diagram relating the performance and safety requirements to the design elements.

it is important to note that there are DOE (and other agency) orders governing safety, security, and safeguards in the fabrication, assembly, testing, handling, and transportation of NPS prior to launch. Another requirement is set forth in the Federal Radiological Emergency Response Plan and further codified in the various agency orders and plans for contingency planning in preparation for the launch of an NPS.[7]

43.3 Interagency Nuclear Safety Review Panel

As discussed in Section 43.1 the Interagency Nuclear Safety Review Panel (INSRP) is chartered to conduct an independent safety review (including technical risk assessment) of each proposed U.S. nuclear-powered space mission prior to launch. INSRP does not make a recommendation of launch approval or disapproval; rather, it provides the necessary independent risk evaluation that will be used in risk management by decision makers who must weigh the benefits of the mission against the potential risks.

The general process of forming an INSRP begins with a request to DOE and either NASA or the Department of Defense (DoD) from a user agency (NASA or DoD) when the user agency has an approved mission. An INSRP is chaired by three coordinators appointed by the Secretary of Defense, the Administrator of NASA, and the Secretary of Energy. DOE is involved because it provides the NPS and has statutory responsibility for the nuclear safety of its NPS. DoD and NASA are involved because of their launch vehicle safety expertise. The coordinators come from independent safety offices within the three agencies. The general INSRP operating plans, including organizational structure (subpanels) and support requirements, are established by the three coordinators. Under the Presidential Directive, the U.S. Nuclear Regulatory Commission (NRC) is invited to send representatives to INSRP meetings, although NRC is not part of the official review and approval process.[1-5] Historically, the U.S. Environmental Protection Agency (EPA) and the U.S. National Oceanic and Atmospheric Administration (NOAA) have participated as observers in these reviews. (EPA has a key role in emergency planning and NOAA has provided valuable input to meterological analyses.) At the time of Publication the Office of Science and Technology Policy has made NRC and EPA full-fledged members of INSRP for the planned Cassini mission to Saturn. Figure 5 shows the structure of INSRP as it was established for the Galileo mission and

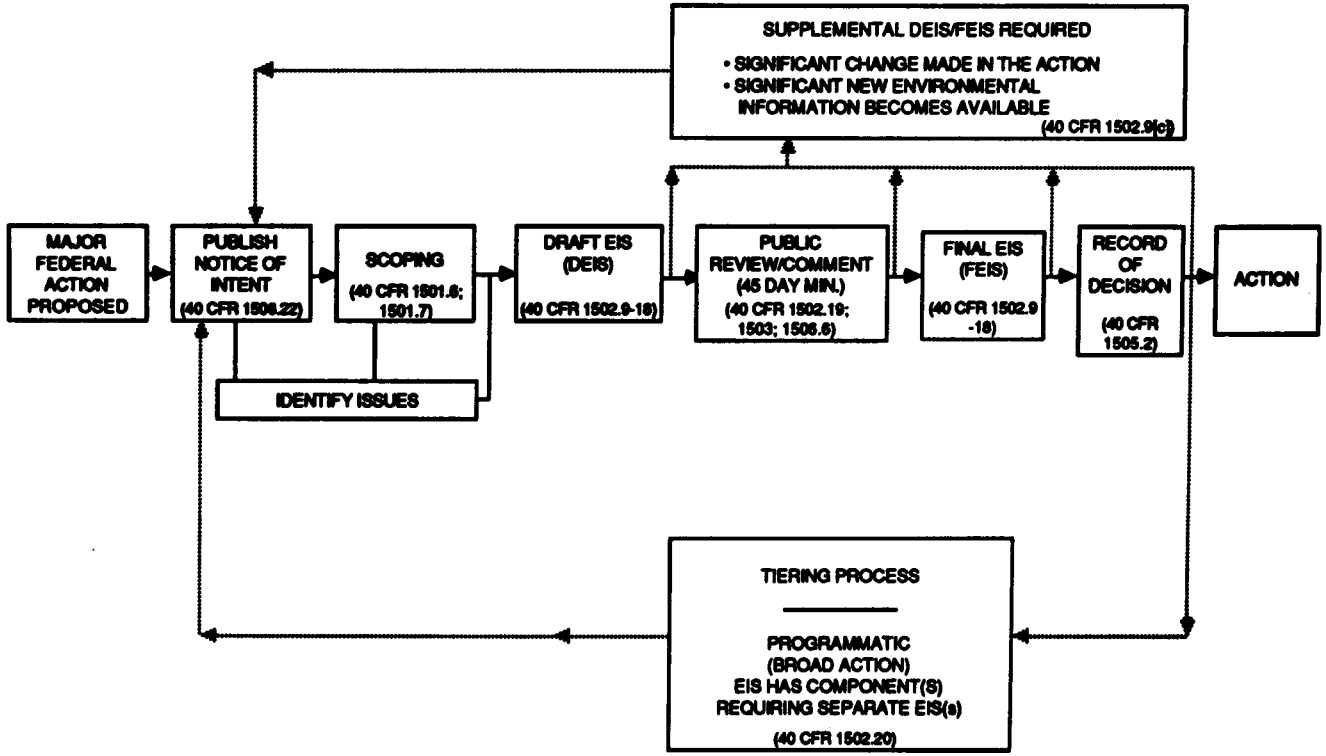

FIGURE 3 Federal EIS process.

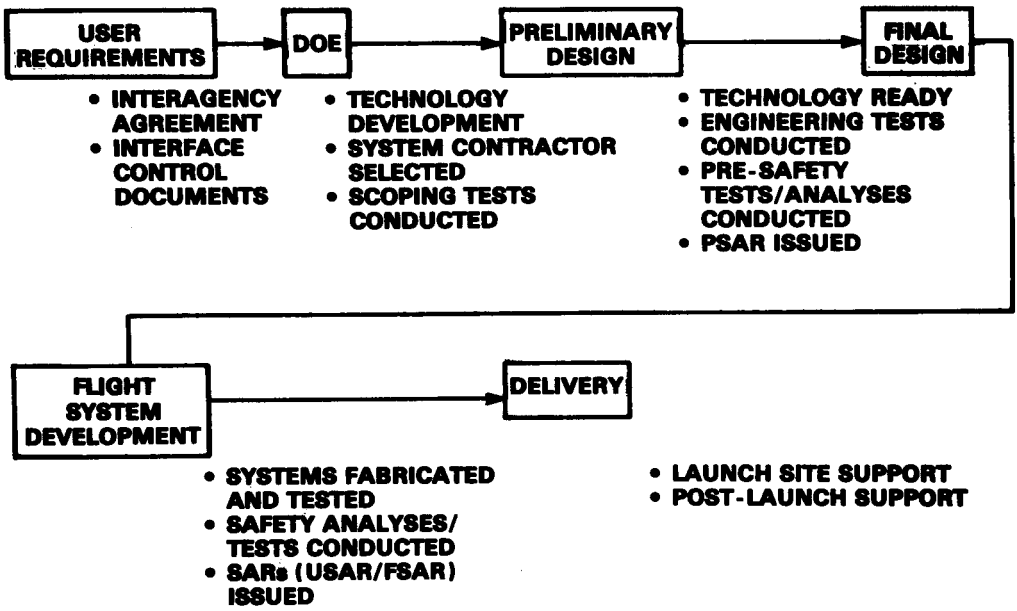

FIGURE 4 Overall program logic.

Table 1 Minimum Safety Documentation Requirements

Safety Assessment Report—Defines safety aspects of design and mission
Safety Program Plan—Outlines total safety program to achieve safety objectives
Radiological Protection Plan—Presents radiological protection and health physics program to protect people
Ground Safety Analysis Report (GSAR)—Assesses safety of site-specific operations, facilities, personnel, training, and equipment
Criticality Assessment Report—Assesses critically aspects of reactor or RTG/heat source, multiple storage/ transportation configurations
Safety Analysis Reports (Flight)—Provides overall nuclear risk analysis of the mission
Safety Analysis Report for Packaging (SARP)—Qualifies the shipping container for issuance of "certificate of compliance" for transportation
Emergency Preparedness and Responses Plan—Provides interagency plan to protect people and the environment in accident situations
Safety Evaluation Report (Flight)—Provides independent nuclear risk analysis of the mission

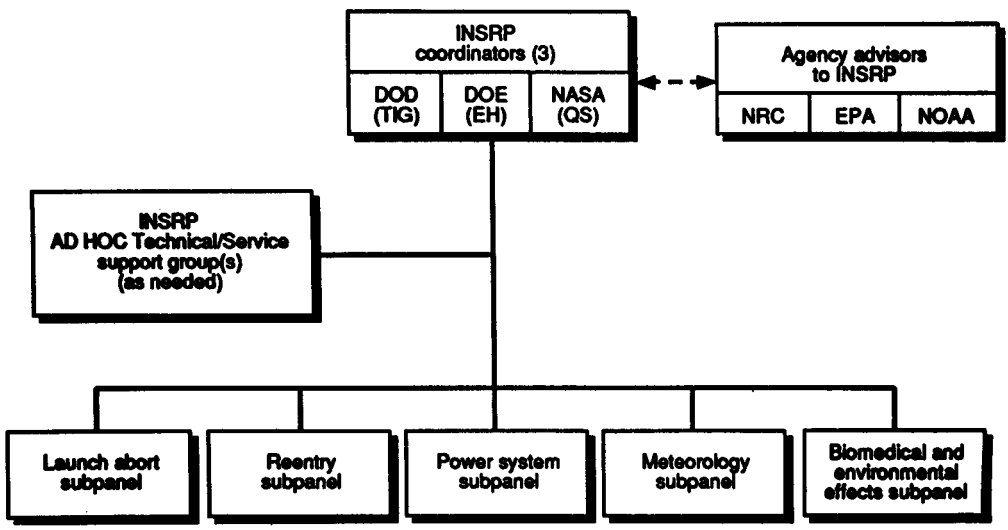

FIGURE 5 Organization of the Interagency Nuclear Safety Review Panel (INSRP).

the Ulysses mission, the two most recent U.S. space nuclear-powered missions. For the Galileo and Ulysses missions, the five subpanels were composed of approximately 50 scientists and engineers from a number of government agencies, national laboratories, industry, and universities, covering such specialties as missile flight analysis, chemical engineering, nuclear engineering and safety, thermal protection, and inhalation toxicology. The subpanels for Galileo and Ulysses were as follows:[4]

- *Launch Abort Subpanel:* Identifies and characterizes prelaunch, launch, and ascent accidents and their probabilities.
- *Reentry Subpanel:* Identifies and characterizes reentry accidents, their probabilities, and their effects on the nuclear system.
- *Power System Subpanel:* Characterizes the nuclear system response to prelaunch, launch, ascent, and post-re-entry Earth impact accidents, including any fuel releases postulated.
- *Meteorology Subpanel:* Characterizes the transport of postulated fuel releases within the atmosphere.
- *Biomedical and Environmental Effects Subpanel:* Characterizes the environmental and health effects of postulated fuel releases, including overall risks.

The INSRP approach has the following advantages:

1. A unified nuclear risk assessment is prepared and provided for the launch approval process of the three agencies and higher approval authorities. In the early missions, it was possible for each agency to conduct its own review, with the potential for three uncoordinated SERs. INSRP provides a mechanism to coordinate the independent reviews that the agencies are required to undertake.
2. Expertise common to a specific participating agency can be made available to the other agencies, which will eliminate possible duplication of effort.
3. At least one coordinator will not be involved in agency sponsorship of the mission nor will the representatives from NRC, EPA, and NOAA; therefore, their participation ensures an objective view and enhances the independence of the review.
4. The INSRP approach produces an environment conducive to free, open, and timely flow of information.

43.4 Safety Analysis Reports

The safety analysis report (SAR), which is generally prepared for the DOE program office, is the first step in the safety review process. As noted Figure 1, the INSRP review is a three-stage process with, in most instances, at least three formal INSRP reviews: one for the Preliminary Safety Analysis Report (PSAR), one for the Updated Safety Analysis Report (USAR), and one for the Final Safety Analysis Report (FSAR). Having three separate and sequential SARs allows INSRP to become familiar with the NPS and its proposed use and to provide input on the kinds of information they would like to see in the next SAR.

The PSAR is issued soon after a design concept is selected for a given mission. The PSAR includes a description of the NPS and the mission, as well as probabilistic radiological risk assessments as supported by the available conceptual design data base. The USAR is issued as soon as practical after the NPS design freeze. The USAR includes updated information on the mission, the failure modes analysis, and the radiological risk assessment, plus any safety tests and data required. The FSAR is normally issued about 1 year before the scheduled launch. The FSAR provides a description of the final design of the system, the mission, and radiological safety assessment data, including the results of the safety tests.[1–5]

The PSAR usually consists of two volumes: a Reference Design Document (RDD) and an Accident Model Document (AMD). The USAR (if sufficient information is available) and the FSAR include these two plus a third volume called the Nuclear Risk Analysis Document (NRAD). Table 2 shows an outline of the contents of the three volumes of the Ulysses FSAR.[8]

Table 2 Outline of the Ulysses Final Safety Analysis Report

Executive Summary
Volume 1—Reference Design Document
- Nuclear power system
- Spacecraft description
- Launch vehicle
- Inertial upper stage description
- Trajectory and flight characteristics
- Flight contingency modes
- Launch site
- References
- Appendix A—Plutonium fuel properties/characteristics
- Appendix B—Properties of heat source and converter materials

Volume II (Book 1)—Accident Model Document
- Introduction
- Summary of accident evaluation
- Accident evaluation and failure mode analysis

Volume II (Book 2)—Accident Model Document—Appendices
- A—Accident definition and probabilities
- B—Accident environments
- C—Hydrocode analysis of RTG response to accident environments
- D—Launch accident scenario evaluation program (LASEP)
- E—JPL re-entry breakup analysis
- F—Deleted (not applicable to Ulysses—for Galileo this was the appendix on the GPHS re-entry response for Venus-Earth-Earth-Gravity Assist (VEEGA) conditions)
- G—Safety test program summary and results
- H—Vaporization of PuO_2 in a space shuttle fireball
- I—RTG/GPHS re-entry response

Volume III (Book 1)—Nuclear Risk Analysis Document
- Introduction
- Methodology
- Major accident scenarios and consequences
- Integrated mission risk analysis
- References

Volume III (Book 2)—Nuclear Risk Analysis Document—Appendices
- A—Risk assessment methodology
- B—Biomedical aspects of plutonium-238 dioxide
- C—Kennedy Space Center (KSC) meteorology
- D—Particle size considerations
- E—KSC vicinity demography and land use
- F—KSC vicinity oceanographic, ground, and surface water studies
- G—Worldwide demographic, land use, and oceanographic data

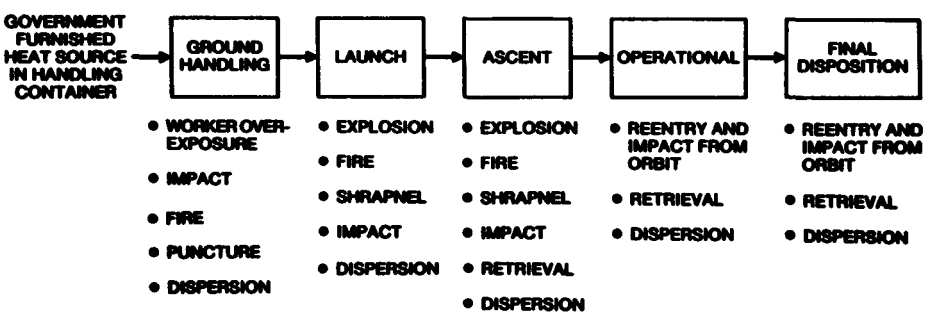

FIGURE 6 Safety encompasses evaluation of all mission phases.

In general, the SARs consider the following types of accident environments (categorized by mission phase; see also Figure 6):

1. Prelaunch, launch, and ascent phases:
   - Explosion overpressure
   - Projectile impact
   - Land or water impact
   - Liquid propellant fire
   - Solid propellant fire
   - Sequential combinations of the above
2. Orbit and/or flight trajectory phases:
   - Re-entry (which could follow an upper-stage explosion)
   - Land or water impact
   - Post-impact environment (land or water)

On-orbit contingency options (including using the spacecraft's propulsion system to boost a stranded spacecraft into a longer-lived orbit or retrieval) are considered as appropriate. Figure 7 shows the kinds of accidents considered for the Galileo mission.[9-11]

The safety analysis is conducted by evaluating each phase of the mission separately, as shown in Figure 8 for the Galileo mission. Each phase represents a change in configuration, location, and activity that can potentially affect the NPS in the event of a postulated accident. Since the mid-1960s, the U.S. has performed its safety analyses using probabilistic risk analysis (PRA) techniques. For Galileo and Ulysses the risk analysis begins with the construction of failure/abort sequence trees (FASTs) of the sort shown diagrammatically in Figure 9. Risk analysis, as used in this context, refers to a quantitative assessment of the potential for human exposure to radiation resulting from the use of an NPS in a space application. The concept of risk is more quantitatively defined in Figures 10 and 11.

The conduct of a risk analysis for a space mission using nuclear power requires (see Figure 12):[12]

- Definition of potential mission accidents and probabilities
- Determination of the types and severity of the resulting accident environments or stresses on the nuclear system
- Testing and/or analyzing the nuclear system to determine responses to the various accident environments
- Organization of the information on accidents, probabilities, and system responses into event trees (e.g., FASTs) for each mission phase (phases oriented to the potential for human risk)
- Analysis of radiological risk using radionuclide environmental pathway and dose models and worldwide data bases
- Appropriate contingency planning, launch safety preparations, and real-time accident analysis and recovery capability

References 9 to 11 describe in more detail the development and implementation of a space nuclear safety program that follows this logic. Figure 13 summarizes this process for the Galileo mission.

43.5 Safety Evaluation Report

The SER is prepared by INSRP to document its independent risk assessment. Table 3 is an outline of the SER prepared for the Ulysses mission. For the Ulysses mission the INSRP concluded that "Compared with the nominal 20-percent lifetime cancer fatality risk that everyone faces, the highest calculated added individual risk associated with the Ulysses mission increased lifetime cancer risk to no more than 20.00015 percent. If one considers that the likelihood of an accidental release that results in fatal cancer was less than 1 in 100,000, the actual added risk of fatal cancer associated with the Ulysses mission was much smaller than 0.00015%.

"Thus, the INSRP analysis suggested that the radiological risks associated with the Ulysses mission were relatively small".[13]

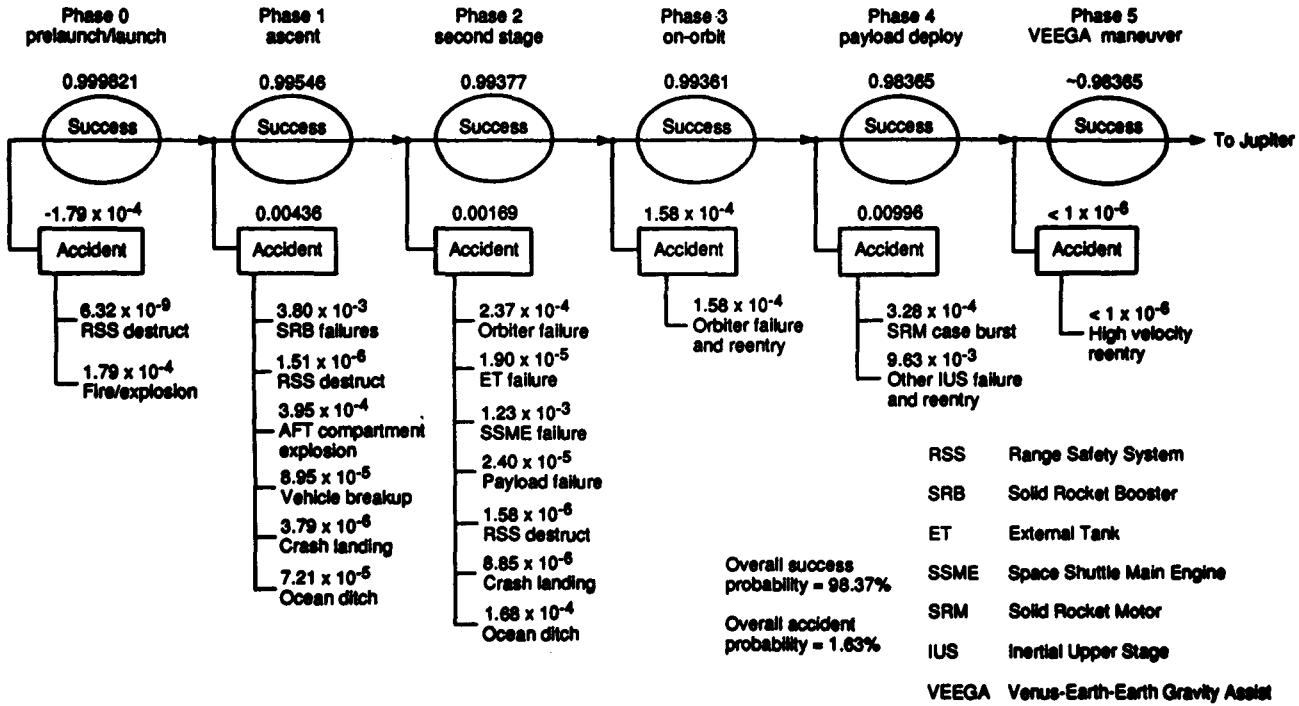

FIGURE 7 Mission success and accident probabilities for the Galileo mission.

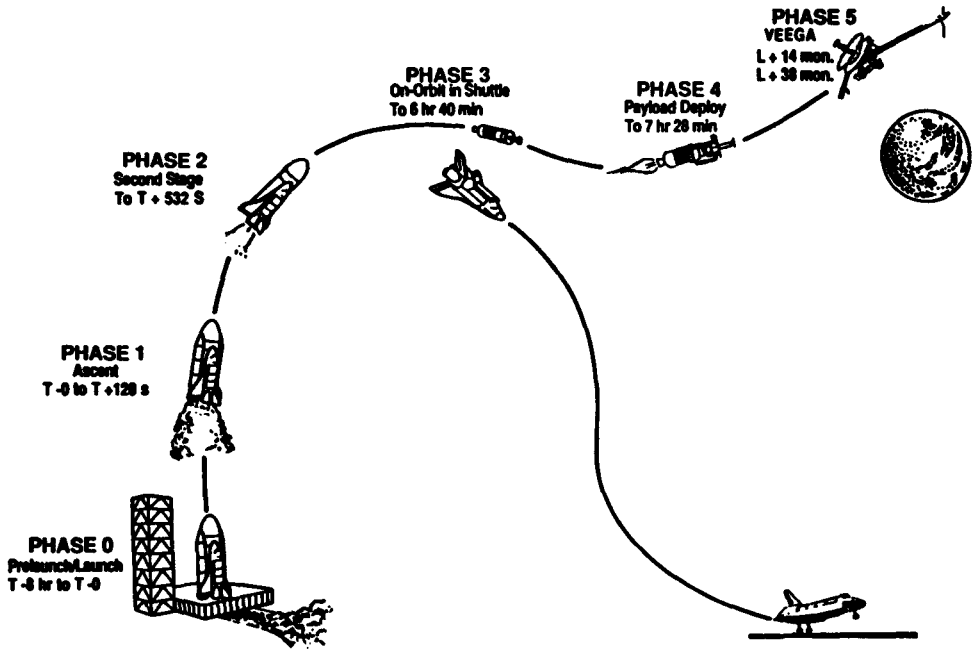

FIGURE 8 Mission phases for the Galileo mission.

43.6 Launch Approval

The completed SER is provided to DOE, NASA, and DoD for their review and concurrence. Upon receipt of letters of concurrence from the other two coordinating agencies on the INSRP signifying that their needs have been met, the launching agency submits a request for launch approval, along with the SER and other documentation if needed, to the Office of the President. Under Presidential Directive NSC/25, the Director of the Office of Science and Technology Policy (OSTP) is empowered to approve the launch. Military missions are also reviewed by the National Security Council (NSC). Consultation with and deferral to the President for launch approval may take place as circumstances warrant.

Flight approval constitutes an affirmative judgment by the U.S. Government, based on an overall risk-benefit evaluation, that the risks associated with the use of an NPS are warranted by the benefits to be derived from its use.

43.7 Historical Experience

The safety analysis and review process have a very practical aspect in that they provide information that can be used by contingency planners in responding to accidents that could occur. The U.S. has had three accidents involving NPS:[1,3,5]

- Failure of the Transit 5BN-3 navigational satellite with a SNAP-9A RTG to achieve orbit (April 21, 1964). The SNAP-9A burned up and dispersed as designed. (SNAP is an acronym for Systems for Nuclear Auxiliary Power.)
- Abort of the launch of the Nimbus-B 1 meteorological satellite with two SNAP-19B RTGs (May 18, 1968). The RTG heat sources were recovered intact, as designed.
- Damage to the Apollo 13 spacecraft after a successful launch on April 11, 1970, which led to the intact re-entry (as designed) of the SNAP-27 RTG fuel cask over the South Pacific Ocean on April 17, 1970.

A fourth incident affected the SNAP-10A reactor, which was successfully launched on April 3, 1965. Following approved guidelines, the spacecraft was placed in a high-altitude orbit, and the

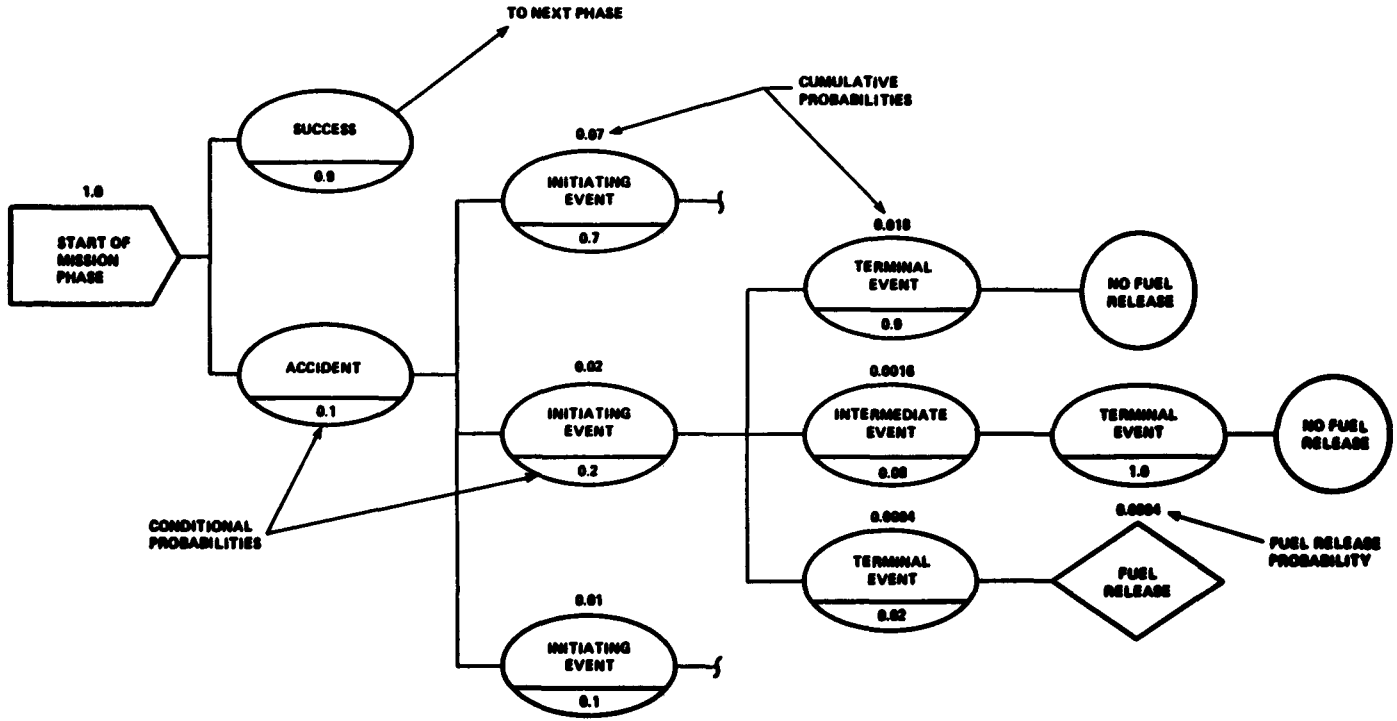

FIGURE 9 Simplified failure/abort sequence tree (FAST) displaying one of its sub-branches.

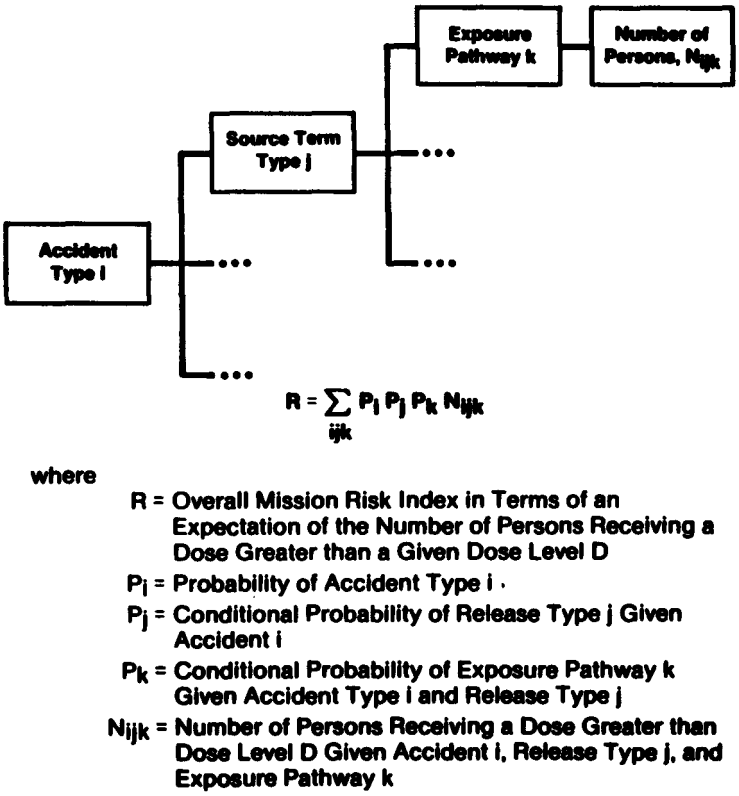

FIGURE 10 Process for evaluating overall mission risk.

reactor was not started until this altitude was confirmed. The reactor operated for 43 d when a shutdown was safely and automatically effected following a malfunction of a voltage regulator on the spacecraft payload (not on the reactor).[14]

In each case cited, the NPS performed as they were designed to do and there were no measurable health effects. The existence of SARs coupled with teams of safety experts has provided decision makers with the necessary information to select the appropriate responses. The SARs also served to guide designers in improving the safety margins of succeeding NPS.

The former Soviet Union has had at least six re-entries of NPS as listed in Table 4.[15] In addition there was a close call with the reactor-powered Cosmos 1900 in 1988. All of the Soviet reactor incidents involved thermoelectric reactors (although the reactors apparently had nothing to do with the causes of the incidents).

43.8 Safety Criteria

This section discusses the general safety criteria applied to U.S. NPS, specifically, the GPHS-RTG, now in use on Galileo and Ulysses, and the SP-100 space nuclear reactor power system. Safety criteria have also been the subject of discussions in several organs of the United Nations following the re-entry of the reactor-powered satellite Cosmos 954 over Canada in 1978.[16] U.S. safety criteria are consistent with the original 1981 criteria developed by a U.N. working group.[16,17] More recent recommendatory but legally nonbinding criteria are being modified to improve their ". . . technical credibility and consistency with proven U.S. methods".[18]

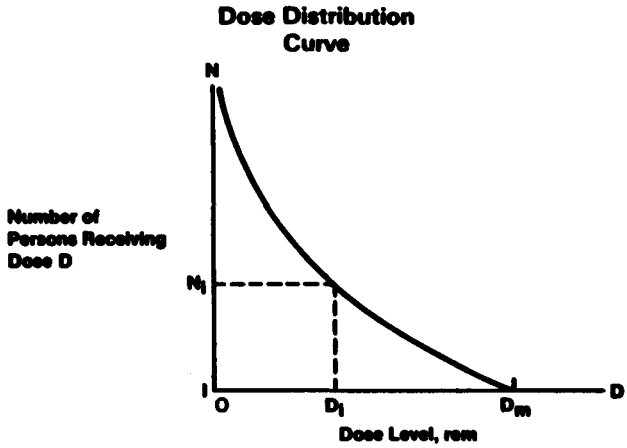

- Maximum Individual Dose, D_m
- Number of Persons, N_i, Receiving Dose $\geq D_i$
- Total Population Dose in Person-rem

$$PD = \int_0^{D_m} N \, dD$$

- Potential Health Effects

$$H = k \times PD$$

FIGURE 11 Measures of radiological consequences.

Radioisotope Thermoelectric Generators

All of the RTGs flown by the U.S. have used ^{238}Pu as the radioisotope to provide the thermal power in the heat source. Plutonium-238 has been chosen to fuel the heat sources because this radioisotope satisfies the various safety and operational criteria. Plutonium-238 decays primarily by emitting alpha particles, which are completely absorbed in the heat source to produce the heat; hence, no special radiation shielding for these alpha particles is required. This radioisotope has an appropriately long half-life (about 87.8 years) and a power density that reduces the number of curies per gram while still permitting reasonable sizes for the heat source and long operational lifetimes. The principal safety objective associated with the use of ^{238}Pu is to keep it contained or immobilized to prevent inhalation or ingestion by humans and consequent exposure of the internal organs and bones to radiation.[1,3,5] How this is accomplished with the GPHS-RTGs in use on Galileo and Ulysses can be seen by referring first to Figure 14, which shows diagrammatically the layout of a GPHS-RTG. The basic components of the GPHS-RTG are the converter and the heat source. The RTG external envelope is based on a cylindrical geometry with an overall diameter of 0.42 m across the fins and a length of 1.14 m. The average mass of a flight RTG is about 56 kg.

The GPHS, shown in Figure 15, supplies the thermal energy to the thermoelectric converter. The GPHS is comprised of rectangular parallelepiped modules, each having dimensions of 93 × 97 × 53 mm, a mass of about 1.43 kg, and a thermal output of at least 245 W (t). Each GPHS-RTG contains 18 independent GPHS modules stacked into a single column. The GPHS was designed and tested for improved safety and power performance, and it represents a major step forward in RTG technology.[9,10]

Each GPHS module contains four plutonia fuel pellets of nominal thermal inventory of 62.5 W (t) (equivalent to about 1875 Ci of ^{238}Pu). The plutonium is enriched to about

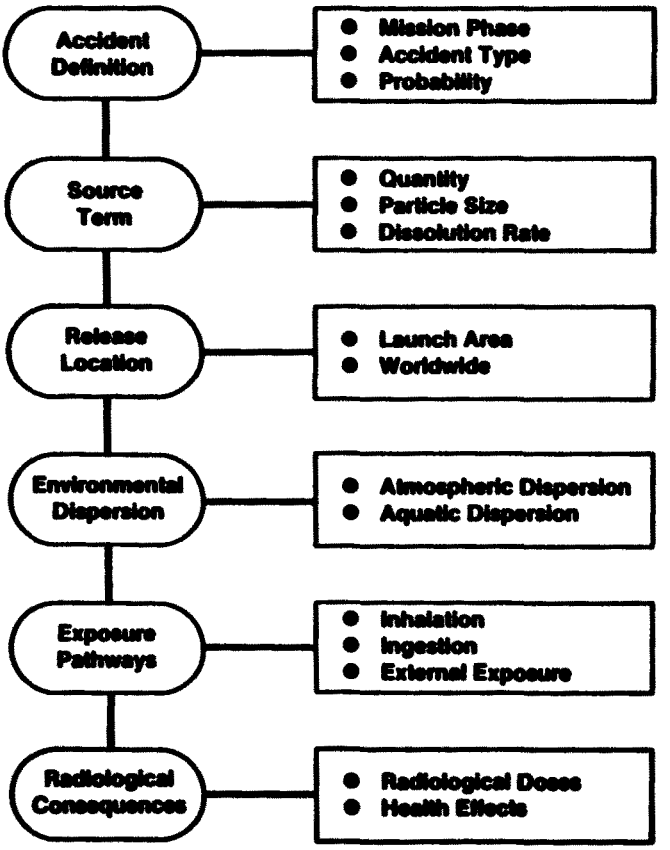

FIGURE 12 Logic diagram for analyzing radiological consequences.

83.5% ^{238}Pu. The GPHS thermal power requirement of 4.4 kW (t) translates into about 8.1 kg of ^{238}Pu per generator. Safety considerations were key factors in the design of the GPHS. The physical form of the fuel is a cylindrically shaped, ceramic pellet having an average diameter of 27.5 mm and an average length of 27.6 mm. The fuel is high fired to more than 1700 K and so is expected to remain chemically stable if released into the environment. Each pellet is individually contained in a post-impact containment shell or cladding made from an alloy of iridium. This alloy is capable of resisting oxidation in the post-impact environment while providing chemical and metallurgical compatibility with the fuel and graphitic components during high-temperature operation and postulated accidents. The iridium cladding has a frit vent that allows release of the helium produced by the alpha decay of the ^{238}Pu without releasing plutonium particles. The combination of fuel pellet and cladding is referred to as a fueled clad.[9,10]

Two of these fueled clads are encased in a graphic impact shell (GIS) machined from Fine Weave Pierced Fabric (FWPF)™, a three-dimensional carbon-carbon composite material produced by AVCO Corporation. Two of these graphite impact shell assemblies are inserted into an aeroshell, also machined from FWPF. A thermally insulating graphite sleeve made of carbon-bonded carbon fiber (CBCF) fits between each GIS assembly and the aeroshell and serves to control the temperature of the iridium during a postulated re-entry accident.[9,10]

The aeroshell, which is also made from FWPF, a material originally developed for re-entry vehicle nose cones, is designed to protect the two GIS assemblies from the severe aerothermodynamic

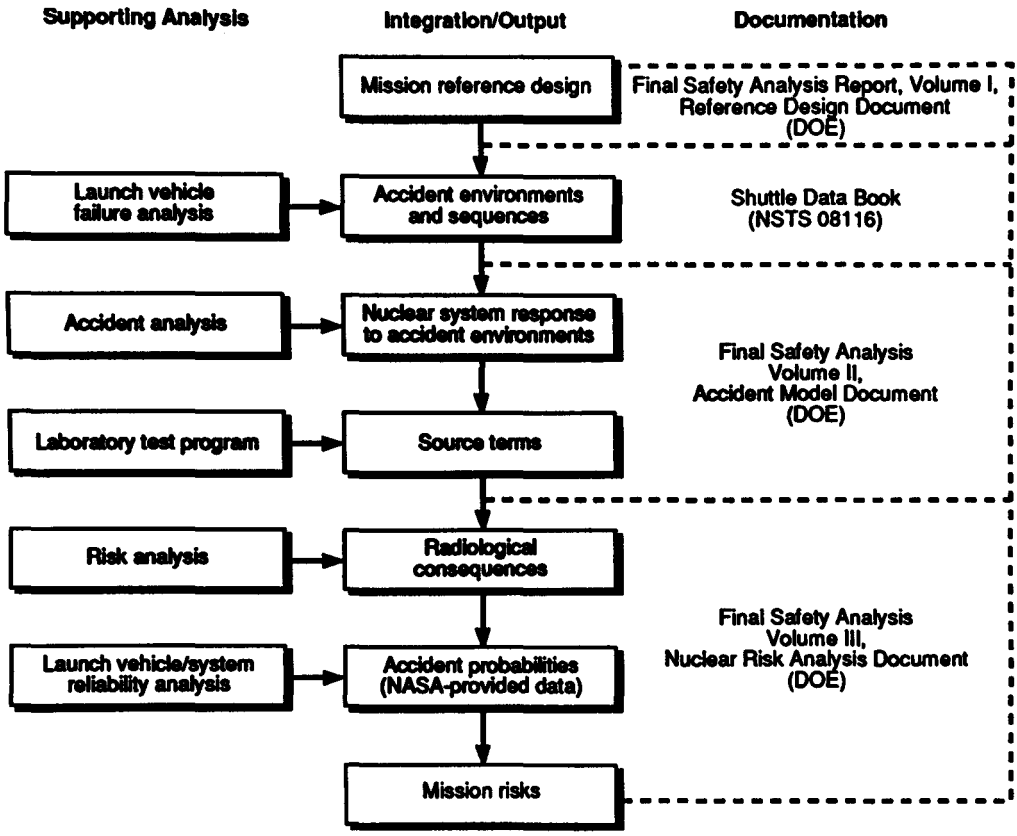

FIGURE 13 The safety analysis report process.

environment that may be encountered during a postulated re-entry. The GIS is designed to provide impact protection for the fueled clads under impact conditions associated with GPHS module terminal velocity. The cladding is intended to provide post-impact containment of the fuel.[9,10] Figure 16 shows the actual GPHS hardware. Figures 17 to 19 illustrate various tests that have been performed on GPHS hardware.

Reactors

As noted earlier, the U.S. has launched only one reactor, SNAP-10A, which coincidentally used thermoelectric conversion. Until 1993, the principal ongoing U.S. thermoelectric reactor technology program was the SP-100, which was jointly supported by NASA and DOE. The safety philosophy governing the SNAP-10A program and the SP-100 program is to keep the reactor subcritical in accident situations. In the case of SNAP-10A, the 44-kW (t) reactor was not operated at power before launch or until the final orbit was achieved. The final orbit (1288 × 1307 km) was chosen to be one with an orbital lifetime of more than 3000 years, well beyond the time (about 300 years) required for the decay of the majority of the fission products. At the time of the SNAP-10A launch, the U.S. safety philosophy on accidental re-entries was to disperse the reactor into small, nonrespirable-sized particles so that no significant doses occurred and no recriticality or safeguards issues would occur. Because of uncertainties over the ability to actually achieve such dispersion, the SP-100 reactor re-entry philosophy was to design for intact re-entry and burial.[19–21]

Table 3 Outline of the Ulysses Safety Evaluation Report

INSRP 90–01: Volume I—Executive Summary
- Introduction
- Mission and system description
- Launch site and environs
- Safety procedures and equipment
- Accidents considered and their probabilities
- Analysis and conclusions
- Appendix A—References
- Appendix B—Ulysses INSRP participants
- Appendix C—Acronyms and abbreviations

INSRP 90–01: Volume II—Overview of INSRP SER for Ulysses
- Purpose
- SER methodology and approach
- Reference documents
- Appendix A—Tables used to determine source terms
- Appendix B—Analysis of uncertainties inherent in the INSRP assessment of Ulysses mission risks
- Appendix C—Acronyms and abbreviations

INSRP 90–01:Volume III—Compendium of Biographical Sketches of the INSRP Members

INSRP 90–02—Launch Abort Subpanel Report
- Introduction
- Approach
- Activity summary
- Launch abort subpanel conclusions
- Appendix 1—Selected detail scenarios
- Appendix 2—Supporting analysis summary for analytical studies and reviews
- Appendix 3—Technical comments on the FSAR
- Appendix 4—Resumes

INSRP 90–03—Re-Entry Subpanel Report
- Subpanel responsibility and membership
- Background
- Failure modes
- Re-entry scenarios
- Ulysses spacecraft breakup during re-entry
- Re-entry modeling and experimental verification
- Response to re-entry environments
- Velocity at impact
- Attitude at impact
- Re-entry footprint
- Surface at impact
- Summary and conclusions
- Recommendations
- List of references

INSRP 90–04—Power System Subpanel Report
- Executive summary
- Introduction
- Mission and system description
- Launch site and environs
- Range safety procedures and equipment
- Accidents considered and their probabilities
- Power system subpanel review and evaluation
- Results and conclusions
- Appendix A—References
- Appendix B—ORIGEN code calculations for Ulysses

Table 3 Outline of the Ulysses Safety Evaluation Report *Continued*

INSRP 90–05—Meteorology Subpanel Report
- Executive summary
- Summary of recommendations of the meteorology subpanel
- Introduction and background
- Exceptions taken with the dispersion and deposition FSAR procedures
- KSC climatology
- Dispersion methodology of the FSAR
- Deposition methodology of the FSAR
- Other key (and potentially problematic) assumptions
- Tests with a different dispersion methodology
- Estimates of uncertainties
- Conclusions
- References
- Appendix 1—The use of atmospheric transport and dispersion models in risk assessment
- Appendix 2—Deposition to the surface
- Appendix 3—Recommendations
- Appendix 4—Hourly wind roses for the period of the Ulysses launch: Kennedy Space Center and Orlando

INSRP 90–06—Biomedical and Environmental Effects Subpanel Report
- Executive summary
- Preface
- Introduction
- Radiological source terms
- Environmental transport and fate
- Land contamination and mitigation
- Radiation dose assessment
- Radiological consequences
- Summary
- References
- Biographies of the biomedical and environmental effects subpanel

INSRP 90–07—Uncertainty Analysis Report (Volume I)
- Introduction and summary
- Review of FSAR risk analysis methodology

INSRP 90–07—Uncertainty Analysis Report (Volume II)
- Introduction
- Objectives of the Ulysses risk analysis
- Technical approach
- Assessment of the significant factors
- Presentation of results
- Appendix A—Procedure of the Ulysses risk analysis

Table 4 Re-Entries of Soviet Space Nuclear Power Sources

Name	Launch Date	Re-Entry Date	Type of Power Source	Comments
—	Jan 25, 1969	Jan 25, 1969	Reactor	Possible launch failure of a RORSAT (Radar Ocean Reconnaissance Satellite)
Cosmos 300	Sept 23, 1969	Sept 27, 1969	Radioisotope	One or both of these payloads may have been a Lunokhod and carrying a ^{210}Po heat source.
Cosmos 305	Oct 22, 1969	Oct 24, 1969	Radioisotope	Upper stage malfunction prevented payloads from leaving Earth orbit.
—	Apr 25, 1973	Apr 25, 1973	Reactor	Probable launch failure of RORSAT
Cosmos 954	Sept 18, 1977	Jan 24, 1978	Reactor	Payload malfunction caused re-entry near Great Slave Lake in Canada.
Cosmos 1402	Aug 30, 1982	Jan 23, 1983 (spacecraft) Feb 7, 1983 (reactor core)	Reactor	Payload failed to boost to storage orbit on Dec 28, 1982. Spacecraft structure re-entered at 25°S, 84°E. Fuel core re-entered at 19°S, 22°W.

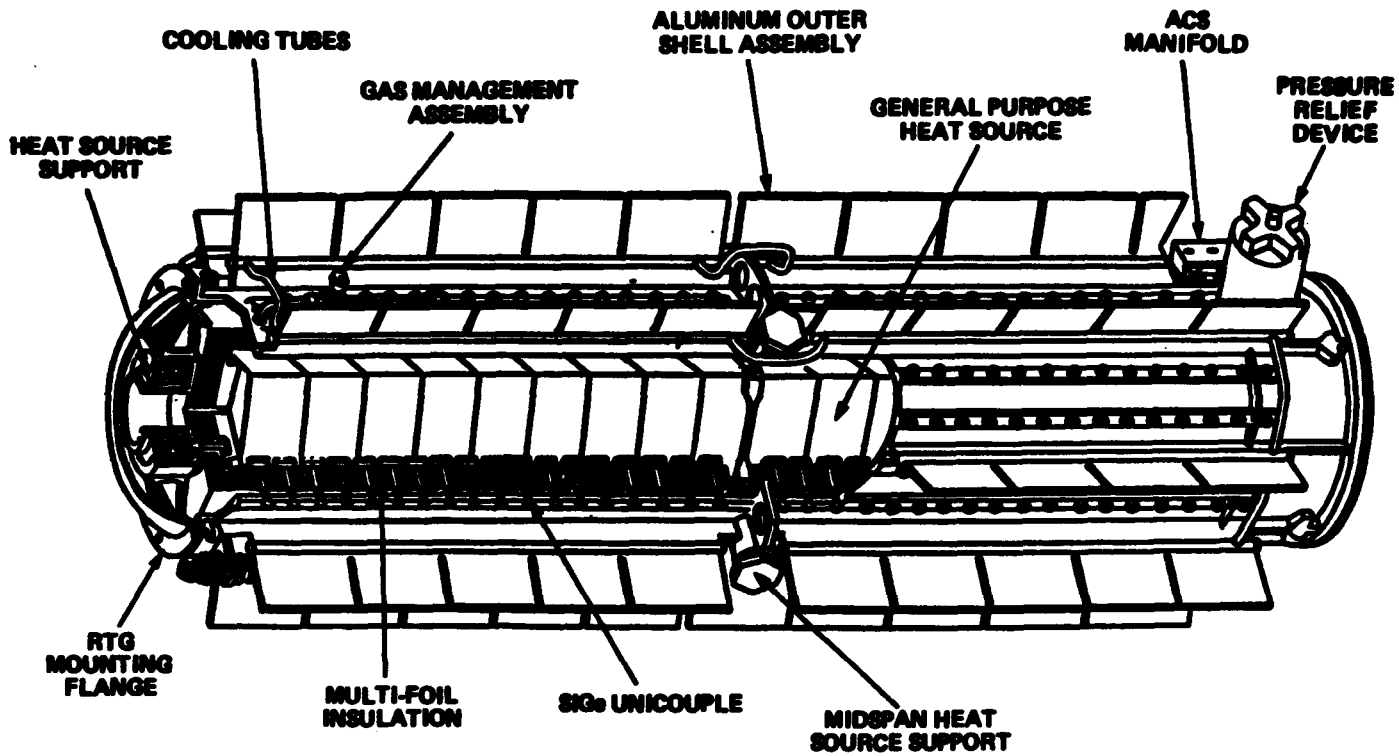

FIGURE 14 The general-purpose heat source radioisotope thermoelectric generator (GPHS-RTG).

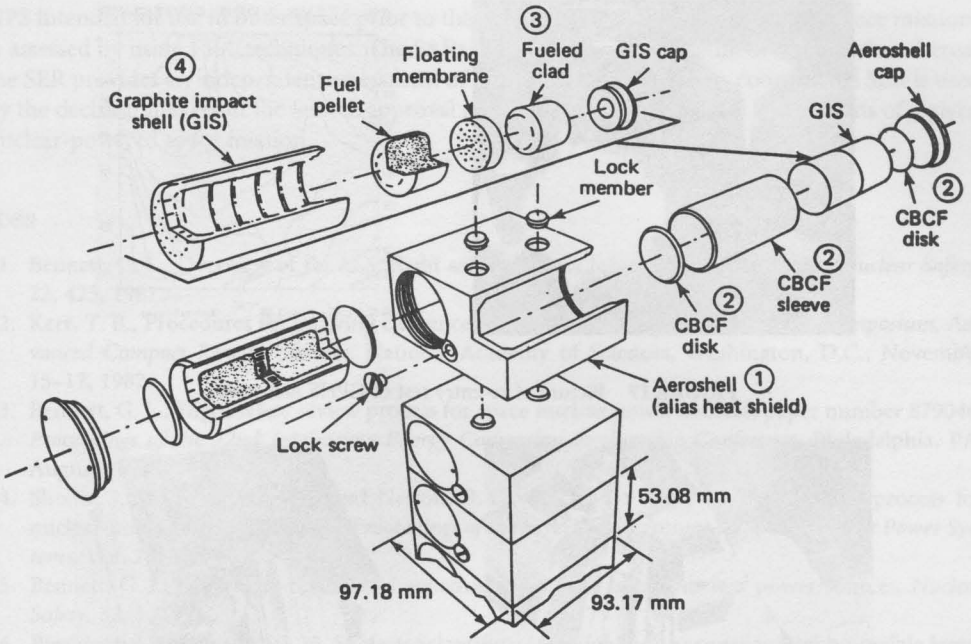

FIGURE 15 General-purpose heat source (GPHS) module component and assemblies.

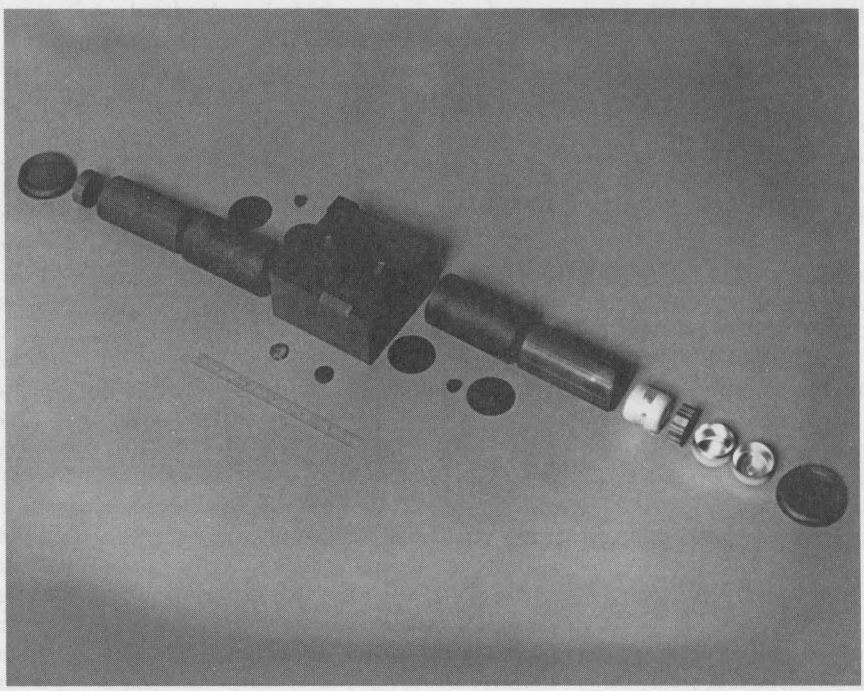

FIGURE 16 Picture of GPHS hardware.

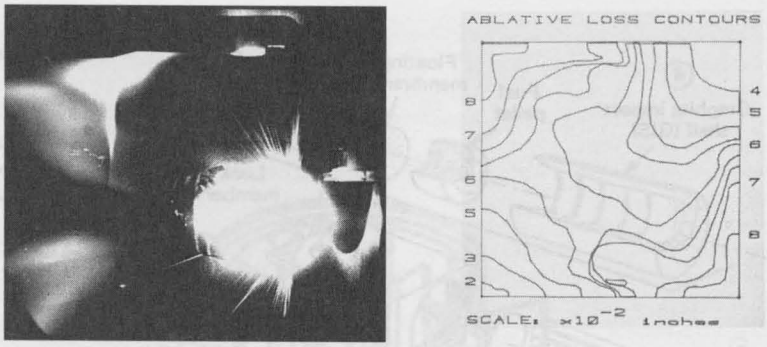

FIGURE 17 Picture of re-entry test of GPHS materials.

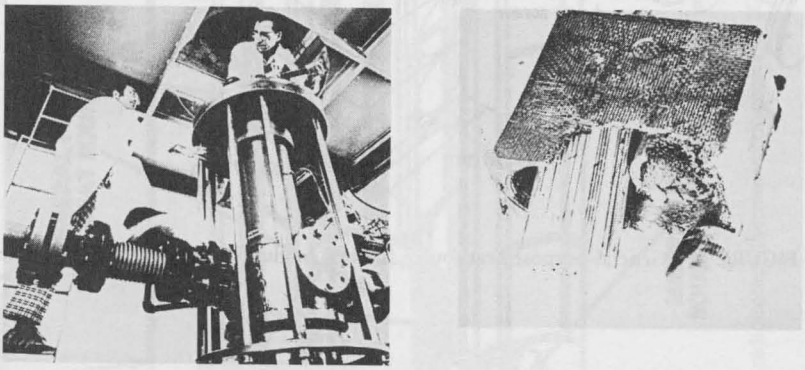

FIGURE 18 Picture of impact test of GPHS module.

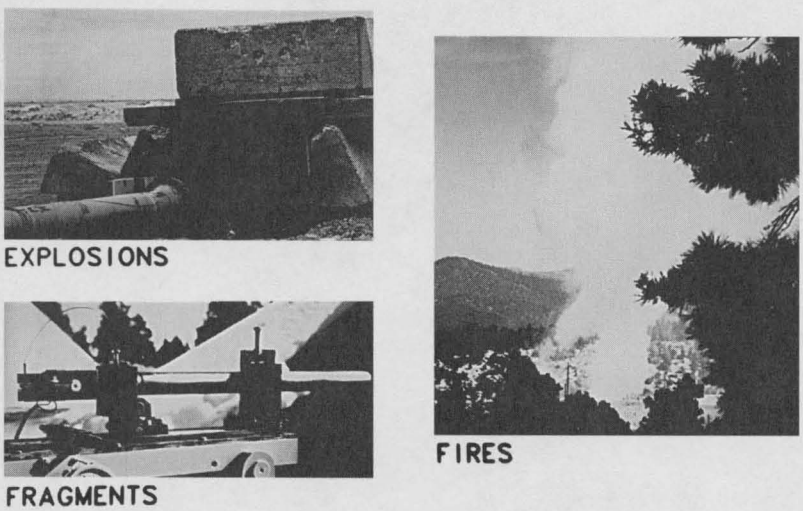

FIGURE 19 Picture of launch accident tests of GPHS hardware.

43.9 Conclusions

Overall, the flight safety review and approval process as developed and implemented in the U.S. has been successful and accepted at the various involved levels of government. These procedures have led to a rigorous space nuclear safety program that provides for the testing and analysis of

NPS intended for use in outer space prior to their actual use. The safety of the NPS space missions is assessed by using PRA techniques. The SARs provide a project assessment of the risks, whereas the SER provides an independent assessment of the risks by the INSRP. A coordinated SER is used by the decision makers in the launch approval process to evaluate the risks and benefits of a given nuclear-powered space mission.

References

1. Bennett, G. L., Overview of the U.S. flight safety process for space nuclear power, *Nuclear Safety*, 22, 423, 1981.
2. Kerr, T. B., Procedures for securing clearance to launch reactors, *Proceedings of a Symposium, Advanced Compact Reactor Systems*, National Academy of Sciences, Washington, D.C., November 15–17, 1982.
3. Bennett, G. L., Flight safety review process for space nuclear power sources, paper number 879046, *Proceedings of the 22nd Intersociety Energy Conversion Engineering Conference*, Philadelphia, PA, August 10–14, 1987.
4. Sholtis, J. A., Jr., Joyce, J. P., and Nelson, R. C., U.S. flight safety review/approval process for nuclear-powered space missions, *Proceedings of the Seventh Symposium on Space Nuclear Power Systems*, Vol. 2, 1990, 569.
5. Bennett, G. L., The safety review and approval process for space nuclear power sources, *Nuclear Safety*, 32, 1, 1991.
6. Presidential Directive/NSC-25, Subject: Scientific or technological experiments with possible large-scale adverse environmental effects and launch of nuclear systems into space, The White House, December 14, 1977.
7. Federal Emergency Management Agency, Federal radiological emergency response plan (FRERP), Concurrence by all twelve federal agencies and publication as an operational plan, *Federal Register*, 50, 46542, 1985.
8. General Electric Company and NUS Corporation, Final safety analysis report for the Ulysses mission, report numbers ULS-FSAR-001 to ULS-FSAR-006, 1990.
9. Bennett, G. L., Lombardo, J. J., Mowery, A. L., Jr., Bartram, B. W., Englehart, R. W., Bradshaw, C. T., Conn, D. W., Hagan, J. C., Schock, A., Skrabek, E. A., and Zocher, R. W., Development and implementation of a space nuclear safety program, in *Space Nuclear Power Systems 1987*, Orbit Book Company, Malabar, Florida, 1988.
10. Bennett, G. L., Bradshaw, C. T., Bartram, B. W., Englehart, R. W., Cull, T. A., Zocher, R. W., Eck, M. B., Mukunda, M., Brenza, P. T., Chan, C. C., Conn, D. W., Hagan, J. C., Lucero, E. F., and Lutz, S. A., Update to the safety program for the general-purpose heat source radioisotope thermoelectric generator for the Galileo and Ulysses missions, in *Space Nuclear Power Systems 1988*, Orbit Book Company, Malabar, Florida, 1992.
11. General Electric Company and NUS Corporation, Final safety analysis report for the Galileo mission, GE Document No. 87SDS4213 (and supplementary document number 89SDS4221) and NUS-5126, 1988 and 1989, Report DOE/NE/32134–T.1–V.3–BK.1 and 2 (NUS-5126-Rev. 1–Vol. 3–BK. 1 and 2), 1989.
12. Englehart, R. W., Mechanics of space nuclear safety, in *Space Nuclear Power Systems 1984*, Orbit Book Company, Malabar, Florida, 1985.
13. Sholtis, J. A., Jr., Huff, D. A., Gray, L. B., Klug, N. P., and Winchester, R. O., Conduct and results of the Interagency Nuclear Safety Review Panel's evaluation of the Ulysses space mission, *Proceedings of the Eighth Symposium on Space Nuclear Power Systems*, CONF-910116, 1991, 132.
14. Bennett, G. L., On the application of nuclear fission to space power, in *50 Years with Nuclear Fission*, American Nuclear Society, La Grange Park, Illinois, 1989.
15. Bennett, G. L., Soviet space nuclear reactor incidents: perception versus reality, *Space Nuclear Power Systems 1989*, Orbit Book Companion, Malabar, Florida, 1992.
16. Bennett, G. L., Sholtis, J. A., Jr., and Rashkow, B. C., United Nations deliberations on the use of nuclear power sources in space: 1978–1987, in *Space Nuclear Power Systems 1988*, Orbit Book Company, Malabar, Florida, 1989.
17. Bennett, G. L., Proposed principles on the use of nuclear power sources in space, paper number 889027, in *Proceedings of the 23rd Intersociety Energy Conversion Engineering Conference*, Denver, Colorado, July 31–August 5, 1988.

18. Brown, C. E. and Lange, R. G., International activities concerning the use of special nuclear materials in space, *Proceedings of the 27th Intersociety Energy Conversion Engineering Conference*, 1, 1.7, 1992.
19. Bennett, G. L. and Buden, D., Use of nuclear reactors in space, *Nucl. Eng.*, 24, 108, 1983.
20. Josloff, A. J., Matteo, D. N., and Bailey, H. S., SP-100 generic flight system design and development progress, in *Proceedings of the 25th Intersociety Energy Conversion Engineering Conference*, Vol. 1, 1990, 173.
21. Bennett, G. L., Safety status of space radioisotope and reactor power sources, in *Proceedings of the 25th Intersociety Energy Conversion Engineering Conference*, Vol. 1, 1990, 162.

44

Low-Temperature Heat Conversion

Kenji Matsuura
Osaka University
Osaka, Japan

David M. Rowe
University of Wales
Cardiff, U.K.

44.1 Introduction

Most present-day commercial thermoelectric generators operate at a hot-side temperature of several hundred degrees centigrade and use isotopic or fossil fuel heat sources to generate levels of electrical power in the milli-microwatt to hundred-watt range. The generators are employed in a number of specialized medical, civil and military terrestrial/marine applications, and in space.[1] In a number of terrestrial applications combinations of the desirable properties of thermoelectric generators, viz., reliability, absence of moving parts, and ruggedness, outweigh their low thermal to electric conversion efficiency. However, in space applications system weight and fuel cost/availability are important considerations and parameters such as power-to-weight ratio and conversion efficiency become as important as reliability. In recent years space has become a dominant application area and the major research effort has concentrated on improving the overall performance of the thermoelectric conversion system. This has been achieved by marginally increasing the figure-of-merit of the thermocouple materials, significantly reducing parasitic losses through the development of better thermal insulation, and by operating the device at increasingly higher temperatures.

Little attention has been paid to thermoelectric generation at low temperatures. A combination of a relatively low material thermoelectric figure-of-merit and a low Carnot efficiency would appear to make this method of power generation an unattractive commercial proposition. However, when the heat source is free, as in the case of waste heat, conversion efficiency is not a main consideration.

0-8493-0146-7/95/$0.00+$.50

In addition thermoelectric generators are environmentally friendly. They differ from other methods of generating electricity in that they are silent, do not require a working fluid, and consequently do not exhaust pollutants—an important consideration.

In this chapter the possibility of converting low-temperature (waste) heat into electrical power is addressed. The major sources of low-grade heat are reviewed, the basic concepts of thermoelectric energy conversion outlined, and the thermocouple materials best suited for operating at relatively low temperatures identified. A fundamental analysis of the thermoelectric conversion of low-temperature heat is followed by a description of a generating system. Finally, two case studies are presented as examples of potential applications.

44.2 Sources of Low-Temperature Heat

Geothermal

Geothermal energy is the earth's natural heat which is derived mainly from the radioactive decay of long-lived isotopes of uranium, thorium, and potassium. Geothermal heat sources vary considerably in quality and accessibility and are generally classified into those with temperatures ranging from 150 to 200°C (high enthalpy) and those sources at a temperature of less than 150°C (low enthalpy). High-enthalpy geothermal energy sources in which naturally occurring steam or hot water is available have been used directly with conventional steam turbines since the turn of the century. Steam turbines typically operate at an inlet temperature of about 180°C and an outlet temperature of around 50°C; usually associated with active tectonic and volcanic regions, some 3200 MW of electrical power was generated by this method in 1983.[2] Techniques have also been developed to extract heat from hot dry rocks (HDR system) where there is insufficient natural fluid available to transfer the heat to the surface. This concept has been put into practice, notably by the Los Alamos National Laboratory in the U.S. and the Camborne School of Mines, Cornwall (Rosemanowes Project).[3] In the U.K. a study has also been undertaken to assess marine-based geothermal operations and in particular to convert redundant oil platforms to geothermal power stations.[4] The majority of reservoirs are at about 100°C which is too low a temperature at which to use conventional steam turbines. As alternative generating methods the organic Rankine cycle or thermoelectrics were proposed (see Section 44.8).

Ocean Thermal Energy

There are several areas of the oceans, particularly those in the tropics, where the temperature of the surface water may be 20 to 25°C higher than that of water at a depth of 500 m or so and in some regions, for example the Red Sea, similar temperature changes occur over considerably shorter distances.[5]

During the early 1970s and 1980s a considerable research effort was made, particularly in Japan and the U.S., to develop OTEC (Ocean Thermal Energy Conversion).[6,7] This system in its present form is based on a Rankine cycle heat engine using low-boiling-point organic liquids as the working fluid with the hot surface water used to boil the working fluid and the cold sea water pumped from depth used to condense it after it has driven a turbine generator.

Peat Deposits

Peat deposits extend over hundreds of square kilometers of Ireland and over considerably greater areas of Russia and often reach depths of hundreds of meters. The petrifaction process during the formation of the peat is accompanied by the release of heat, which in some cases is at sufficiently high temperatures to result in spontaneous combustion. Some studies have been undertaken to apply geothermal-type techniques to extracting the heat.

Solar Ponds

Solar ponds have been employed in many parts of the world as an energy storage device and as a means of distilling saline water.[8] A modification of the solar pond is the so-called salt gradient

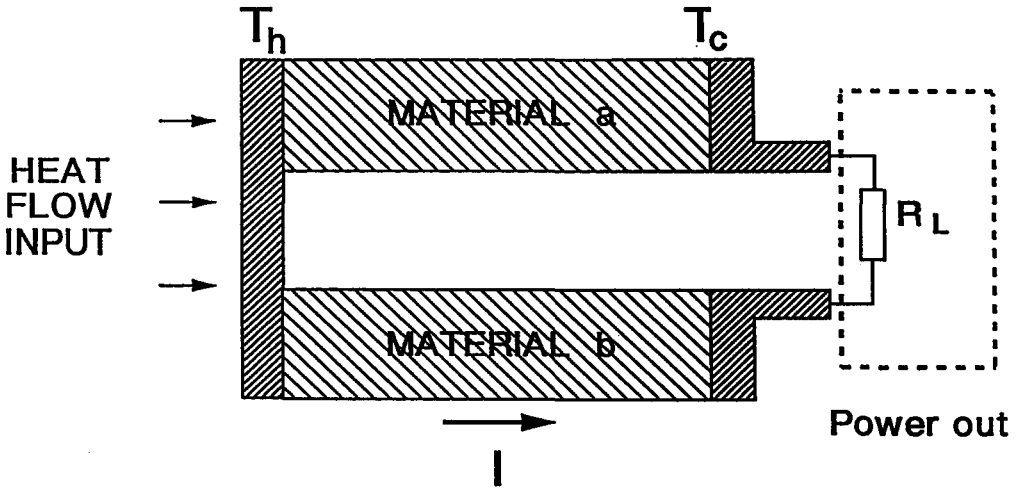

FIGURE 1 A thermocouple as a power generator.

stabilized solar pond (SGSSP).[9] In this system solar energy heats up the pond to temperatures as high as 90°C. Locally available salts are used to establish a stabilized density gradient between the top and bottom of the pond which substantially reduces convection heat losses from the surface. Radiative heat loss from the pond is also reduced by the strong absorption of long wavelengths by the water.

Waste Heat

Large quantities of heat are contained in waste cooling water associated with power stations and other large utilities. Modern electricity generating installations operate at best with an efficiency of around 40%. A considerable proportion of the waste energy is used in heating the cooling water, in some installations to in excess of 40°C. Similar sources of low-grade heat are associated with other industrial operations such as paper production and steel making (see Section 44.8).

44.3 Basic Thermoelectric Concepts

Whenever heat flows along a solid, the charge carriers in the material are also swept along and a potential difference is established between the hot and cold ends. Based on this phenomenon, a simple thermoelectric generating device can be formed by connecting the hot ends of two dissimilar conductors at a junction and closing the cold ends with a load to complete an electric circuit (Figure 1). Heat supplied to the hot junction causes an electric current to flow in the circuit and electric power is delivered to the load. The thermoelectric conversion efficiency is given by the ratio of the electric energy supplied to the load to the heat energy absorbed at the hot junction. It can be shown that the maximum conversion efficiency can be expressed:[10]

$$\phi_{max} = \gamma\eta \text{ where } \gamma = \frac{T_{hot} - T_{cold}}{T_{hot}} \tag{1}$$

$$\eta = \frac{(1 + Z_c T)^{1/2} - 1}{(1 + Z_c T)^{1/2} + T_{hot}/T_{cold}} \text{ with } T = \frac{T_{hot} - T_{cold}}{2} \tag{2}$$

and temperatures are in degrees Kelvin.

The efficiency is thus the product of the Carnot limiting efficiency γ, which is clearly less than unity, and η, which embodies the parameters of the thermocouple material. The conversion efficiency depends upon the temperature difference over which the device is operated, its average

temperature of operation, and the "goodness factor" or so called figure-of-merit Z_c of the thermocouple:

$$Z_c = \alpha_c^2 / R\lambda' \tag{3}$$

where α_c is the Seebeck coefficient of the couple, λ' is the thermal conductance of a and b in parallel, and R is the sum of the branch resistances. If the geometries of a and b are matched to nominal heat absorption then:

$$Z_c = \frac{(\alpha_a - \alpha_b)^2}{[(\lambda_a/\sigma_a)^{1/2} + (\lambda_b/\sigma_b)^{1/2}]} \tag{4}$$

where λ_a, λ_b, and σ_a, σ_b are the thermal conductivities and electrical conductivities, respectively, of the two branches.

In practice the two branches of the junction have similar material constants, in which case the concept of a figure-of-merit for an individual material is employed and given by:

$$Z = \frac{\alpha^2 \sigma}{\lambda} \tag{5}$$

the thermal conductivity λ is essentially the sum of a contribution λ_L arising from the lattice wave and λ_e, a contribution from the charge carriers. All three parameters occurring in the expression for the figure-of-merit depend upon the carrier concentration and the expected dependencies of α, σ, and λ are shown in Figure 2. Metals have high electrical conductivity but the Seebeck coefficient is too low. Insulators have high Seebeck coefficients but are electrically resistive. A good compromise is reached in heavily doped semiconductors (carrier concentrations of 10^{19} to 10^{20} cm^{-3}) with α and σ values intermediate between the properties of insulators and metals. Figure 3 illustrates the dependence of the conversion efficiency upon the temperature difference of operation and the thermocouple's material figure-of-merit. (Cold junction maintained at 300 K [27°C].) A thermocouple fabricated from a material with a Z value of 3×10^{-3} K^{-1} when operating over a temperature difference of 100°C would convert heat into electrical energy with an efficiency of around 5.5%. In a practical thermoelectric generator system heat losses would reduce the efficiency by about 50%, resulting in an overall system efficiency of around 3%.

44.4 Low-Temperature Thermoelectric Material

In Figure 4 the figure-of-merit of a number of established thermoelectric semiconductors identified as suitable for use over the temperature range from room temperature to about 150°C is displayed. Alloys/compounds based on the bismuth chalcogenides exhibit high figures-of-merit with Bi_2Te_3-$75Sb_2Te_3$, the best p-type material, and Bi_2Te_3-$25Bi_2Se_3$, the best n-type, exhibiting an average figure-of-merit in excess of 2.5×10^{-3} K^{-1}.[11] Alloys/compounds based on lead telluride possess figures-of-merit of around 1.5×10^{-3} K^{-1}.[12] These are identified by designation such as TEGS-2N: this is n-type and indicates a specific semiconductor composed essentially of a compound of lead and tellurium with small additions of electrically active PbI_2. On the other hand, 2P signifies that the lead telluride is doped p-type with Na. More complicated materials, such as TAGS (tellurium-antimony-germanium-silver), have also been developed.[13]

Materials based upon the intermetallic compounds of germanium and silicon with the general formula $Mn_2Si_xGe_ySn_{1-x-y}$ are predicted to possess figures-of-merit as large as 10^{-2}.[14] The preparation of semiconductors with significantly higher figures-of-merit than those of materials based on the bismuth or lead chalcogenides has been reported in the literature and Z values as high as 5.7×10^{-3} are claimed for AgTlTe and its related compounds.[15] However, the best thermoelectric materials for use in "low-temperature" applications, and which have a proven track record in device applications, are those used in thermoelectric coolers and are based on bismuth telluride. These materials are capable of converting at maximum about 20% of the available heat energy (Carnot fraction) into electrical energy and when operating at hot and cold junction temperatures of 100°C and ambient, respectively, the thermoelectric conversion efficiency is around 5%.

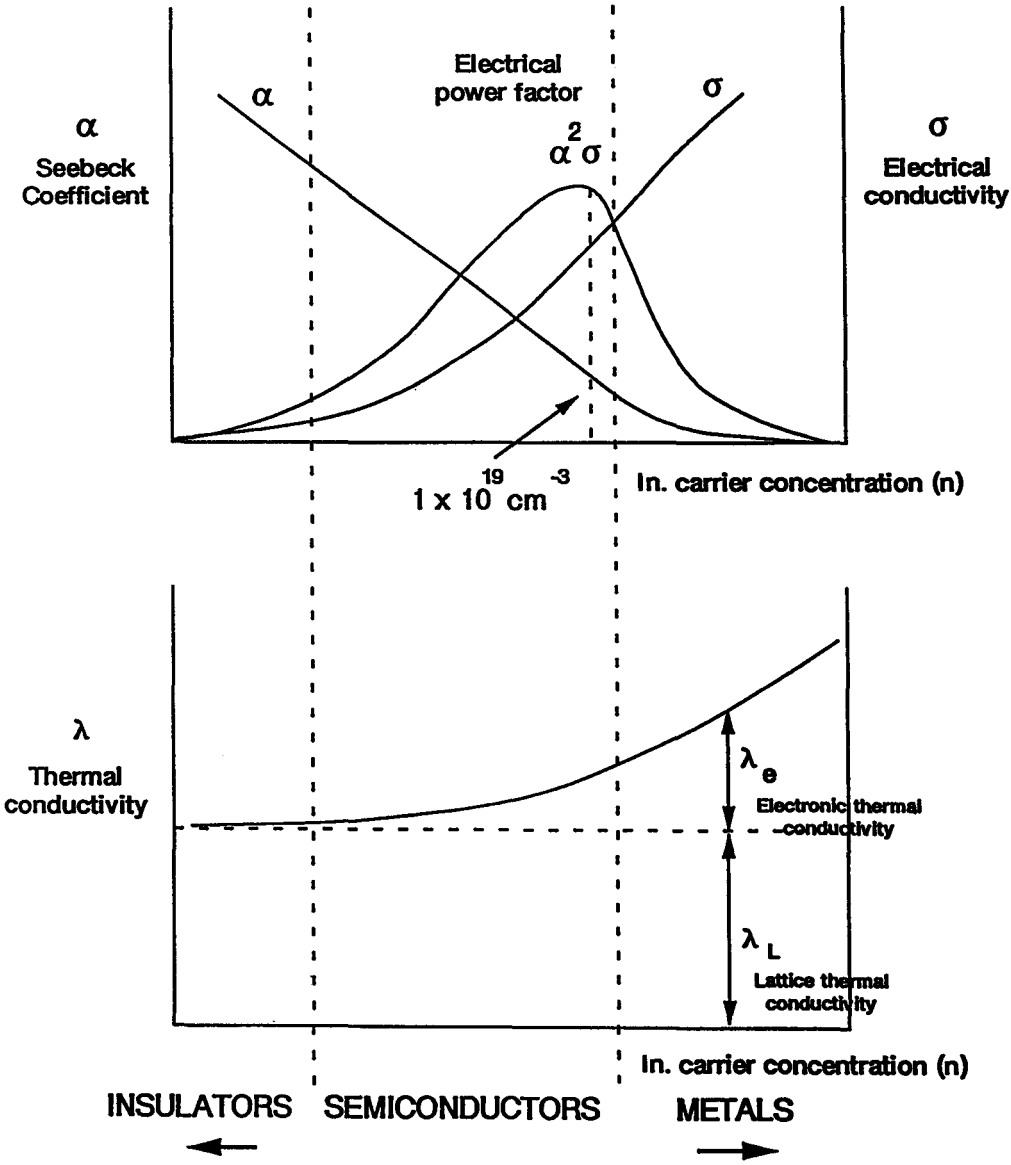

FIGURE 2 Thermoelectric properties of metals, semiconductors, and insulators.

44.5 A Fundamental Analysis of the Thermoelectric Conversion of Low-Temperature Heat

Introduction

An essential feature of the thermoelectric conversion of low-temperature heat is the utilization of heat which is at too low a temperature to drive a turbogenerator. A significant reduction in performance results from parasitic losses in the temperature difference between the module and heat exchanger. The effect of these losses on the power output conversion efficiency requires careful consideration when calculating the system's performance.

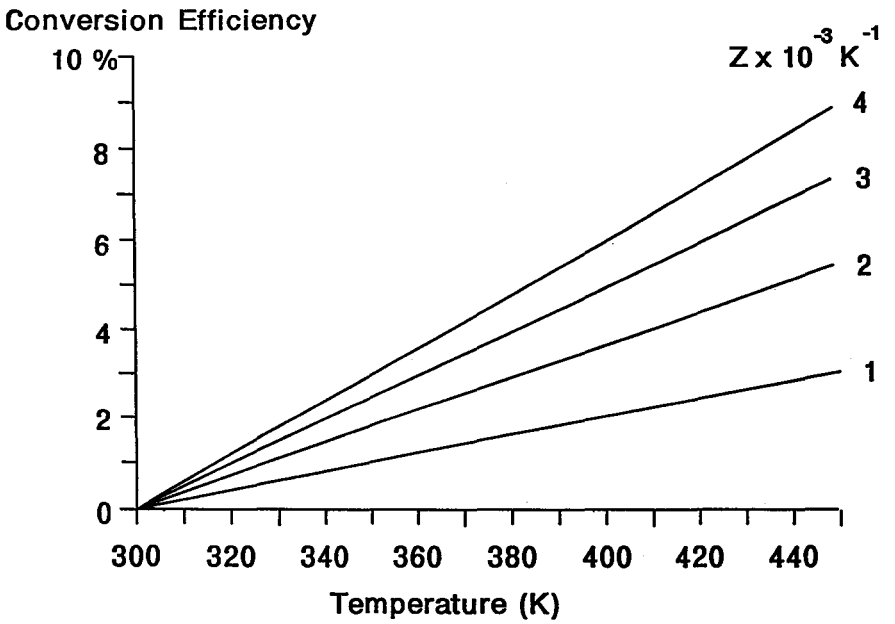

FIGURE 3 Maximum conversion efficiency as a function of hot junction temperature and Z value. (T_{cold} = 300 K)

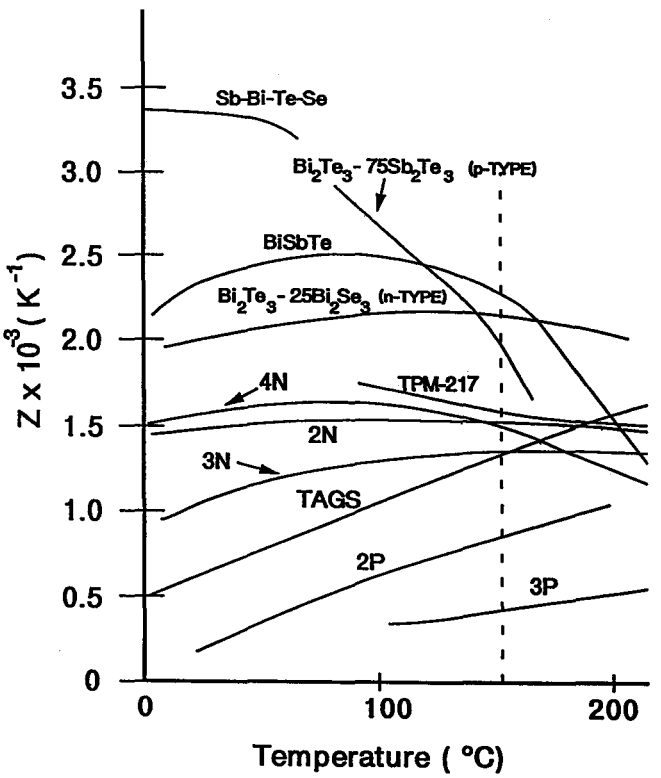

FIGURE 4 Figure-of-merit as a function of temperature.

List of Symbols

h_{ec}	Heat transfer conductance between the cold flow and the cold electrode per unit area
h_{ew}	Heat transfer conductance between the warm flow and the warm electrode per unit area
h_{1ec}	Heat transfer coefficient between the cold flow and the inner surface of the heat transfer tube
h_{1ew}	Heat transfer coefficient between the warm flow and the inner surface of the heat transfer tube
h_{2ec}	Heat transfer conductance through the insulator and the heat transfer tube faced to the cold flow per unit area
h_{2ew}	Heat transfer conductance through the insulator and the heat transfer tube faced to the warm flow per unit area
I	Current
K	Heat transfer conductance through a thermoelectric element composed of a couple of p-type and n-type semiconductors in the module
N	Number of thermoelectric elements in the module
P	Power output
P_{max}	Maximum power output
q_c	Heat flux at the cold junction
q_w	Heat flux at the warm junction
R	Electrical resistance of a single thermocouple
R^*	Effective internal resistance for a single thermocouple
R_l	External load resistance
S	$S = S_c = S_w$ (this stands for a special module design)
S_c	Heat exchanging surface area corresponding to a single thermocouple (cold flow side)
S_w	Heat exchanging surface area corresponding to a single thermocouple (warm flow side)
T_c	Cold fluid temperature
T_{cj}	Cold junction temperature
T_w	Warm fluid temperature
T_{wj}	Warm junction temperature
ΔT_c	Temperature difference between the electrode at cold junction and the cold flow
ΔT_{teg}	Temperature difference across a block of thermoelectric semiconductor
ΔT_w	Temperature difference between the electrode at the warm junction and the warm flow
V	Terminal voltage
V_{open}	Open terminal voltage
α	Seebeck coefficient of a single thermocouple

Analytical Model and Power Equation

A schematic of the heat exchanger-thermocouples model employed in the basic analysis is displayed in Figure 5. In converting the low-temperature heat into electricity the steady-state voltage V, current I, and power output P are expressed as a function of load resistant R_l in equations 6, 7, and 8.[16]

$$V = \frac{N(1 - AI)}{B} \tag{6}$$

$$I = \frac{1}{\mathrm{A} + \dfrac{R_l}{N} B} \tag{7}$$

$$P = VI = \frac{R_l}{(\mathrm{A} + \dfrac{R_l}{N} B)^2} \tag{8}$$

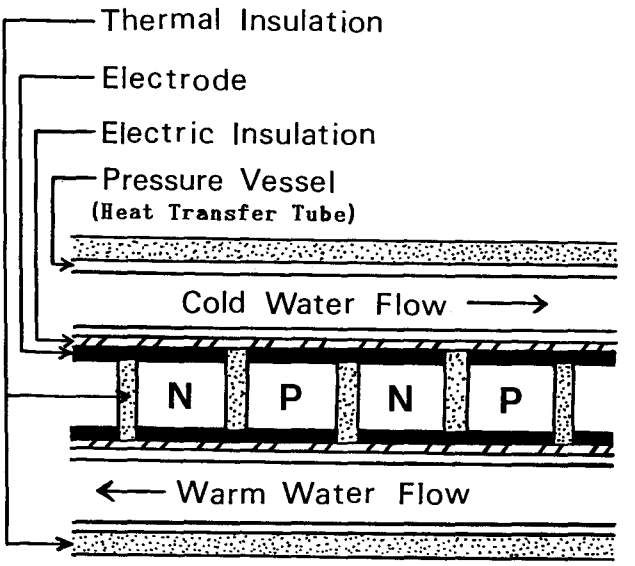

FIGURE 5 A typical construction of a thermoelectric converter.

where

$$A = \frac{R + \dfrac{KR(h_{ew} + h_{ec})}{Sh_{ew}h_{ec}} + \dfrac{\alpha^2(T_w h_{ew} + T_c h_{ec})}{Sh_{ew}h_{ec}}}{\alpha(T_w - T_c)} \tag{9}$$

$$B = \frac{1 + \dfrac{K(h_{ew} + h_{ec})}{Sh_{ew}h_{ec}}}{\alpha(T_w - T_c)} \tag{10}$$

Derivation of Power Output Formula

Assume that the Thomson effect is negligibly small and the thermoelectric material properties remain constant over the small operating temperature difference of the thermoelectric converter. Then the heat flux equations are as follows:

$$q_w = S_w h_{ew} \Delta T_w = K\Delta T_{teg} + \alpha I T_{wj} - \frac{1}{2} I^2 R \tag{11}$$

$$q_c = S_c h_{ec} \Delta T_c = K\Delta T_{teg} + \alpha I T_{cj} + \frac{1}{2} I^2 R \tag{12}$$

The first term on the right side of Equation 11 is the conduction heat flux from the hot to cold junction and the second term the Peltier cooling heat at the hot junction. The third term represents a net Joule heat transfer to the hot junction. The three terms on the right side of Equation 12 represent the heat fluxes due to the same physical phenomena at the cold junction.

The temperature relationships are:

$$T_{wj} = T_w - \Delta T_w \tag{13}$$

$$T_{cj} = T_w - \Delta T_w - \Delta T_{teg} \tag{14}$$

$$\Delta T_c = T_w - \Delta T_w - \Delta T_{teg} - T_c \tag{15}$$

Relationships between the electrical parameters are given by:

$$I = \frac{N\alpha\Delta T_{teg}}{NR + R_l} \tag{16}$$

$$V = IR_l \tag{17}$$

$$P = I^2R_l \tag{18}$$

Equations 11 to 18 are the basic equations for the thermoelectric converter. Algebraic manipulation of these equations gives a third-order polynomical in ΔT_{teg}:

$$a\Delta T_{teg}^3 + b\Delta T_{teg}^2 + c\Delta T_{teg} + d = 0 \tag{19}$$

with

$$\begin{aligned} a &= \frac{2N^2\alpha^4R_l}{NR + R_l} \\ b &= N\alpha^2(NR + 2R_l)(S_wh_{ew} - S_ch_{ec}) \\ c &= -2N(NR + R_l)(S_wh_{ew}T_w + S_ch_{ec}T_c)\alpha^2 \\ &\quad -(NR + R_l)^2\{S_wh_{ew}S_ch_{ec} - K(S_wh_{ew} + S_ch_{ec})\} \\ d &= 2(NR + R_l)^2S_wh_{ew}S_ch_{ec}(T_w - T_c) \end{aligned}$$

In a low-temperature heat conversion application, the numerical values of the parameters may be of the following orders: $\alpha \simeq 10^{-3.5}$ V K^{-1}, $R + R_l/N \simeq 10^{-2}$ to 10^{-3} Ω, $K \simeq 10^{-0.5}$ to 10^{-1} W K^{-1}, $S_w \simeq S_c \simeq 10^{-4}$ m^2, $h_{ew} \simeq h_{ec} \simeq 10^2$ to 10^4 W K^{-1} m^{-2}, $T_c \simeq T_w \simeq 300$ K and $T_w - T_c \simeq$ 10 to 20 K. Then the first term on the left side of Equation 19 is negligibly small compared with the second, third, or fourth term. With this approximation Equation 19 can be simplified to:

$$b\Delta T_{teg}^2 + c\Delta T_{teg} + d = 0 \tag{20}$$

Taking into consideration the conditions $c^2 \gg 4bd$, $c < 0$ and $S_w = S_c = S$ for the standard module design, this gives a solution for ΔT_{teg} in the following simple form:

$$\begin{aligned} \Delta T_{teg} &= \frac{-c - \sqrt{c^2 - 4bd}}{2b} \simeq -\frac{d}{c} \\ &= \frac{T_w - T_c}{\dfrac{N(h_{ew}T_w + h_{ec}T_c)\alpha^2}{(NR + R_l)Sh_{ew}h_{ec}} + \left\{1 + \dfrac{K(h_{ew} + h_{ec})}{Sh_{ew}h_{ec}}\right\}} \end{aligned} \tag{21}$$

Henderson[17] used the method of Lagrange multipliers to solve numerically the thermoelectric converter model based on a polynomical equation similar to Equation 19. This technique would result in a more precise solution but is rather tedious. Equation 21 is an approximate solution but it is simple and useful over the range of practical applications.[16]

Eliminating ΔT_{teg} from Equations 16 and 21, Equation 7 is obtained as:

$$I = \frac{1}{\mathrm{A} + \dfrac{R_lB}{N}}$$

where A and B are defined by Equations 9 and 10, respectively.

Eliminating R_l from Equations 7 and 17, Equation 6 is obtained as:

$$V = \frac{N(1 - AI)}{B}$$

Since $P = I^2R_l$, substitution for I from Equation 7 yields Equation 8 as:

$$P = \frac{R_l}{\left(A + \frac{R_l B}{N}\right)^2}$$

Differentiating Equation 6 with respect to I gives:

$$-\frac{\partial V}{\partial I} = \frac{NA}{B} = NR^* \tag{22}$$

where

$$R^* = R + \frac{\alpha^2(T_w h_{ew} + T_c h_{ec})}{Sh_{ew}h_{ec} + K(h_{ew} + h_{ec})} \tag{23}$$

R^* in Equations 22 and 23 is defined as an effective internal resistance for a single thermocouple composed of a p-type and n-type semiconductor block. It is noticeable that R^* is larger than R, the purely electrical resistance of the single thermoelectric element, and is affected by fluid conditions.

Under steady-state conditions A and B are kept constant. For maximum power $\partial P/\partial R_l = 0$. This maximum power condition gives the following relationship when applied to Equation 8:

$$P_{\max} = \frac{V_{open}^2}{4NR^*} \tag{24}$$

in which case

$$\frac{R_l}{N} = \frac{A}{B} = R^* \tag{25}$$

and

$$V_{open} = \frac{N}{B} \tag{26}$$

where V_{open} is the open terminal voltage and is obtained by putting $I = 0$ in Equation 6.

Conversion Efficiency

The conversion efficiency η of heat into electricity is defined by:

$$\eta = \frac{P}{q_w} \tag{27}$$

From the heat flux equation 11 and the temperature relation equation 13, q_w is expressed as:

$$q_w = \frac{K\Delta T_{teg} + \alpha I T_{wj} - \frac{1}{2}I^2R}{1 + \frac{\alpha I}{Sh_{ew}}} \tag{28}$$

Substitution for q_w from Equation 28 yields:

$$\eta = \frac{P\left(1 + \frac{\alpha I}{Sh_{ew}}\right)}{K\Delta T_{teg} + \alpha I T_{wj} - \frac{1}{2}I^2R} \tag{29}$$

η should be estimated as a function of load resistance R_l by using the relations for P from Equation 8, I from Equation 7, and ΔT_{teg} from Equation 21.

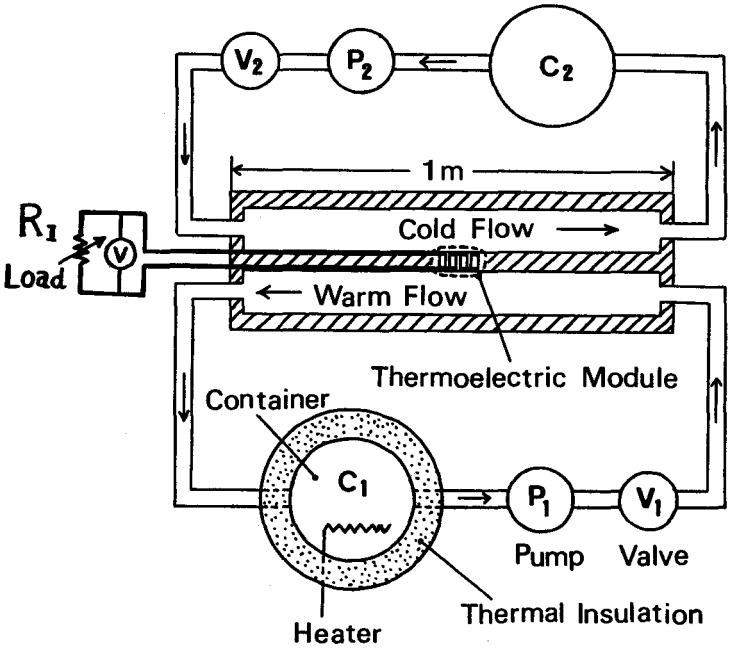

FIGURE 6 Schematic arrangement of an experimental thermoelectric converter for low-temperature heat.

Table 1 Properties of a single thermoelectric element in the module

	Characteristic value	Remark
Seebeck Coefficient, α	3.14×10^{-4} VK^{-1}	$\alpha = \lvert\alpha_n\rvert + \lvert\alpha_p\rvert$
Mean Resistivity, ρ	9.85×10^{-6} Ωm	$\rho = (\rho_n + \rho_p)/2$
Mean Thermal Conductivity, λ	1.15 WK^{-1} m^{-1}	$\lambda = (\lambda_n + \lambda_p)/2$
Electrical Resistance, R	7.34×10^{-3} Ω	$R = R_n + R_p$
Thermal Conductance, K	6.17×10^{-3} WK^{-1}	$K = K_n + K_p$

Subscripts n and p denote the n-type and the p-type semiconductors respectively.

Table 2 Properties of Flowing Fluids Subjected to the Experiments

Physical Characteristics	A Fluorocarbon Liquid
Specific heat (JK^{-1}m^{-3})	963
Density (k_gm^{-3})	$\sqrt{4530000-7491T}+316$
Heat transfer coefficient	0.0769
(WK^{-1}m^{-1})	-5.53×10^{-5}T
Viscosity	2.232 x exp (−0.0244T)
(Pas)	$+3.49 \times 10^{-4}$

T is temperature of fluid in Kelvin.

44.6 Experimental Verification

In order to verify the basic performance characteristics of the low-temperature heat thermoelectric converter embodied in Equations 6 to 8 and 23 to 26 an experiment was carried out at Osaka University using the test thermoelectric converter shown in Figure 6.[16] The system consists essentially of a thermoelectric module with 32 pairs of bismuth telluride-based p-type and n-type elements connected electrically in series and thermally in parallel, each p-type or n-type block being 1.1×10^{-5} m^2 in the cross-sectional area and 4.1×10^{-3} m in length. The thermoelectric properties of a single couple are summarized in Table 1. The surfaces of the module are directly interfaced to an insulating fluorocarbon liquid. The physical properties of the liquid are given in Table 2.

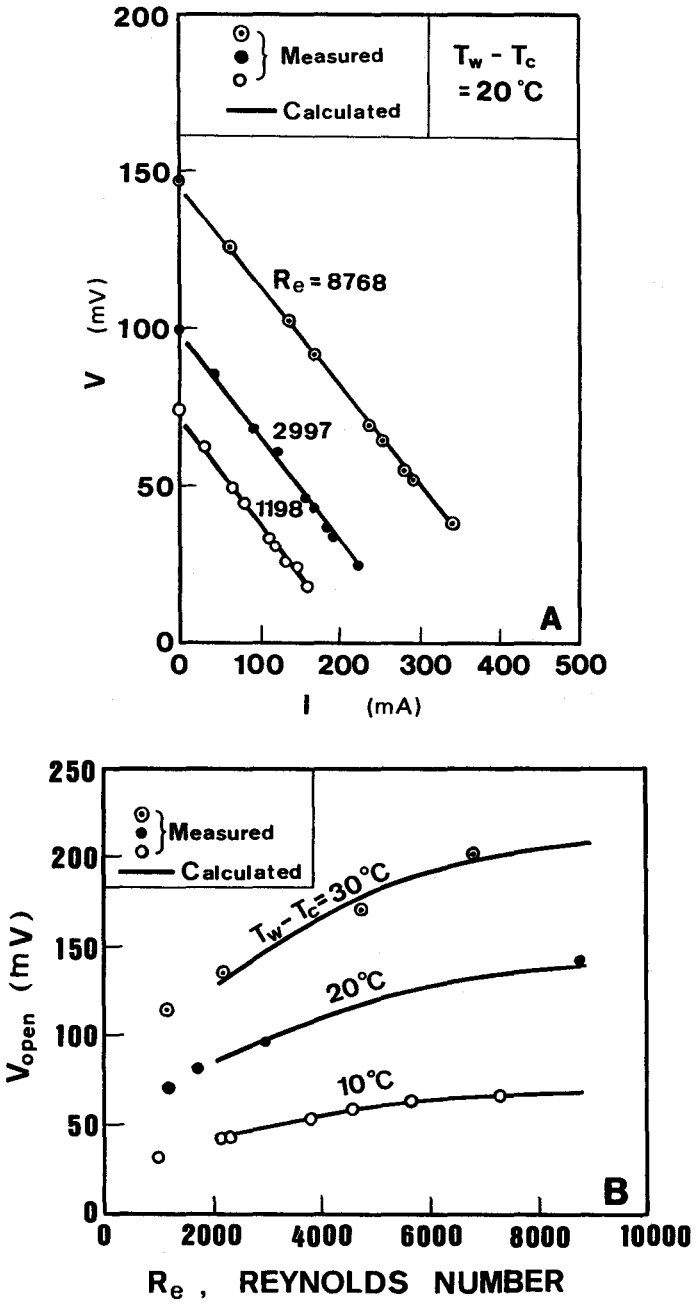

FIGURE 7 Experimental verification of fundamental equations for estimating performance characteristics of low-temperature thermoelectric converter. (a) Output voltage vs. current; (b) open terminal voltage vs. Reynolds number; (c) effective inner resistance vs. Reynolds number; (d) maximum power output vs. Reynolds number; (e) power output vs. current.

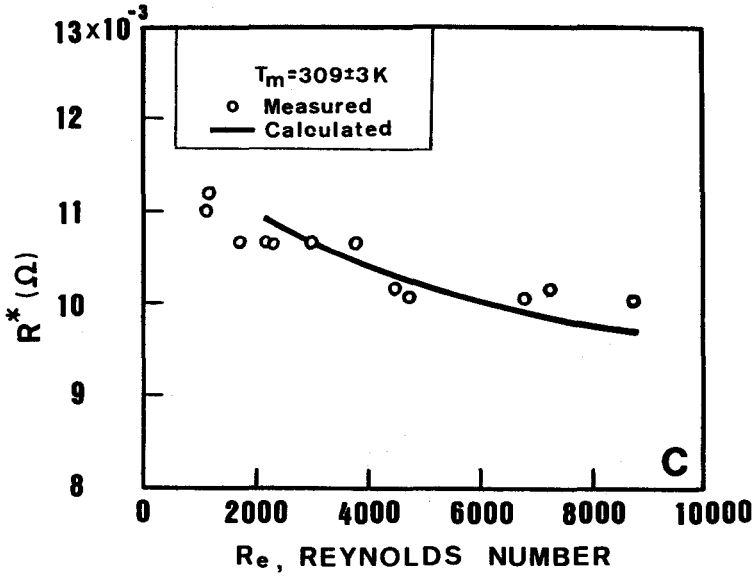

FIGURE 7 continued.

Pumps P_1 and P_2 produce a warm and cold flow in the respective ducts, which are 1.5×10^{-2} m wide and 5.3×10^{-2} m in height. The warm and cold flow rates were controlled by adjusting the valves V_1 and V_2, respectively. A thermally insulated fluid container (0.05 m^3) having an electric heater enables the warm flow to be heated to a desired temperature and keeps the temperature constant during an experimental run. The electric power generated by the thermoelectric converter was fed to a pure resistance load R_l. Load characteristics of the converter were obtained by measuring the terminal voltage and current simultaneously with varying R_l.

A special condition $h_{ew} = h_{ec} = h_e$ was employed in all experimental runs in order to simplify the analysis of V_{open}, R^*, and P_{max}. It was assumed that h_e was related to the Reynolds number R_e by the Sieder Tate equation in the turbulent flow range.

In Figure 7a the load characteristic at $T_w - T_c = 20$ K for various fluid flow conditions in the converter is shown. It is noticeable that a straight line relationship is obtained in each load characteristic, circumstantial evidence that the total effective internal resistance NR^* is constant under flow conditions. The open terminal voltage V_{open} and the effective internal resistance R^* are plotted as functions of R_e in Figures 7b and c, respectively. On the other hand, the relationships between V_{open} and R_e, and R^* and R_e were calculated for the thermoelectric converter using Equations 26 and 23, respectively, where h_e was related to R_e by the Sieder Tate equation. The results are shown by solid lines in Figure 7b for V_{open} and Figure 7c for R^*. The following constants were used for the numerical calculations: $N = 32$, $S = 4.5 \times 10^{-5}$ m^2, $\alpha = 3.14 \times 10^{-4}$ V K^{-1}, $K = 6.17 \times 10^{-3}$ W K^{-1}, $R = 7.34 \times 10^{-4}$ Ω, $T_m = (T_w + T_c)/2 = 309$ K. The calculated and measured V_{open} and R^* are dependent on R_e or h_e and this provides evidence of the appreciable temperature drops at the boundary layers in the working fluid facing the module electrodes. In particular the second term on the right side of Equation 23 shows that the temperature drops at the boundary layers due to the Peltier effect heat flux increase proportionally with increasing current. It is noticeable that in the turbulent flow range R^*/R is about 1.4 due to this effect. If pure water is used as the working fluid, the ratio R^*/R will reduce further and approach unity. The measured power outputs at $T_w - T_c = 20$ K are plotted as a function of current in Figure 7d for various values of the Reynolds number. Referring to the theoretical treatment, the maximum power output P_{max} was calculated using the relationship $P_{max} = V^2_{open}/(4NR^*)$. The calculated and measured maximum power outputs are plotted as a function of R_e in Figure 7e for various values of $T_w - T_c$. They exhibit good agreement through the range of R_e and it was proved that the maximum power output of the thermoelectric low-temperature heat converter can be reasonably calculated using Equation 24.

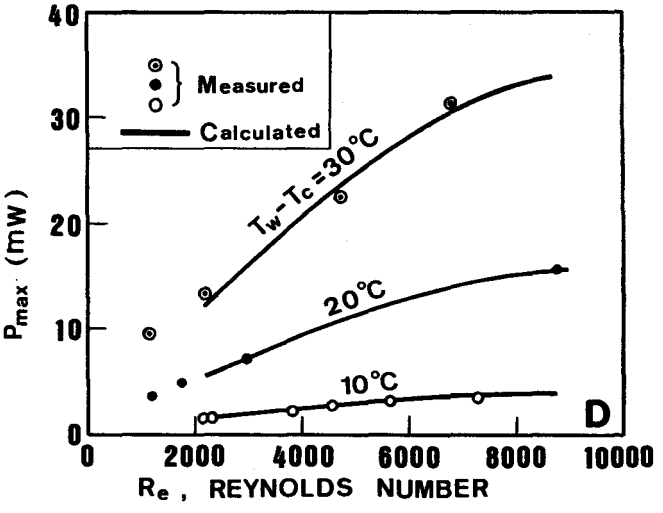

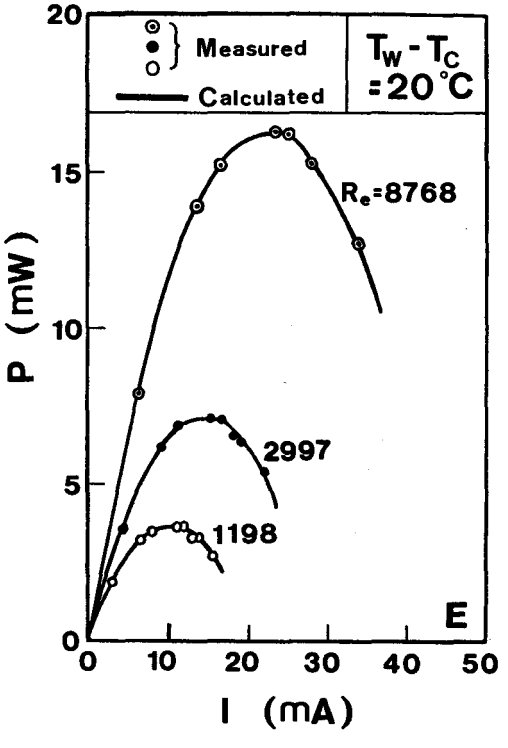

FIGURE 7 continued.

44.7 Thermoelectric Generator for Low-Temperature Heat Conversion

Generator System Studied

To investigate the performance of a thermoelectric generator using low-temperature heat (below 150°C [423 K]), a thermoelectric conversion system was assembled, as shown schematically in Figure 8.[18] An array of 20 modules, Figure 8b, is located between the hot and cold heat transfer tubes. Each heat transfer tube is 1.5 m long and of rectangular cross section, as indicated in Figure 8c. The specifications of the modules, which consisted of 31 couples of n- and p-type thermoelements, are given in Table 3. The modules, which are commercially available, are based

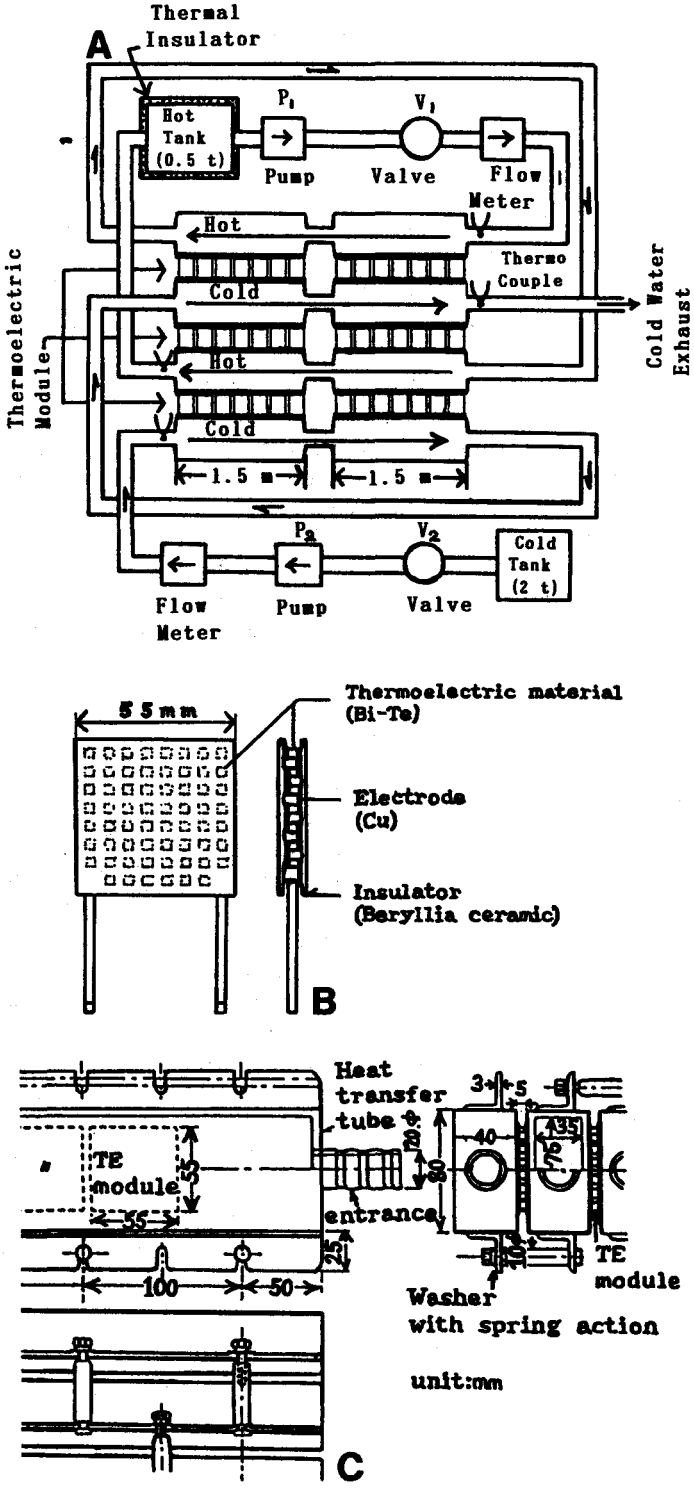

FIGURE 8 A laboratory-scale, low-temperature thermoelectric generator system and the components. (a) Schematic illustration of the system; (b) thermoelectric module; (c) heat transfer tube.

Table 3 Thermoelectric Module Specifications

		Insulator	Electrode	T.E. Element
Thickness	(mm)	0.7	0.7	2.4
Cross section	(mm^2)	49	23	19
Thermal conductivity	(w/cm·K)	2.30	4.03	0.0097
Specific heat	(J/g·K)	1.089	0.385	0.545
Density	(g/cm^3)	2.87	8.91	8.00
Electrical properties of thermoelectric element				
Seebeck coefficient		$(\lvert\alpha_p\rvert + \lvert\alpha_n\rvert)/2 = 1.70 \cdot 10^{-4}$		(V/K)
Resistivity		$(\rho_p + \rho_n)/2 = 1.33 \cdot 10^{-5}$		$(\Omega \cdot m)$

on bismuth telluride technology and are designed for cooling (Peltier applications). The generator consists of two units, with each unit having four aluminum heat transfer tubes and 60 modules in three arrays. The modules are connected electrically in series and thermally in parallel along the heat transfer tubes. The complete generator thus consists of 120 modules (3720 p-n thermoelements). In the construction of the generator the modules have been carefully integrated with the heat transfer tubes so that the thermal resistance between the two has a minimal effect on the performance of the generator. This was achieved by carefully polishing and greasing the facing surfaces. Pumps P_1 and P_2 produce the hot and cold water flows while valves V_1 and V_2 control the flow rate. The hot water is pumped from a large, thermally well-insulated tank, with a controllable electric heater.

Generator Performance

The performance of the laboratory-scale, low-temperature thermoelectric generator was monitored by measuring the steady-state output power as a function of inlet water temperature and flow rate. In Figure 9 the output electrical power is shown as a function of the current through the external load for different values of Reynolds number. In general there is good agreement between the experimental and theoretical data, which were obtained by the analysis developed by Mathiprakasam et al.[19] One of the theoretical curves in Figure 9a takes into account the temperature dependencies of the thermoelectric material parameters. These are displayed in Figure 10.[19] The temperature difference between the inlet hot water temperature T_h and the outlet cold water T_c was 60 K. When using larger temperature differences the temperature dependences of the thermoelectric material parameters must be included in the generator's design calculation. Evidently over the temperature range of interest both the electrical resistivity and the Seebeck coefficient increase with an increase in temperature. The absolute values of these parameters and their temperature dependences vary to some extent between samples. Figure 10 represents an average of measurements made on several samples.[18]

In Figure 9b the maximum power output (matched load) as a function of hot and cold water flow Reynolds numbers for various inlet water temperatures is displayed. An increase in flow rates results in an increase in the maximum power output of the generator. This is due to the fact that the heat transfer coefficient of water at the inner surface of the heat transfer tube increases with an increase in flow rate. However, an increase in flow rate increases the power requirement of the water pumps. Evidently the maximum net output is obtained at an optimum flow rate which is determined by the design of the heat transfer tube. Regarding this point Henderson gave an illustration in Figure 11, which shows a typical relationship between gross generator power and net system power for a range of Reynolds numbers. As is found from the graph, the net power generation of a thermoelectric generator system achieves a maximum at a specific Reynolds number.[17] This is because the heat transfer coefficient increases roughly linearly with the Reynolds number, while pumping losses are more closely related to the cube of the Reynolds number. More detailed analysis was performed by Matsuura and Kinoshita.[20] The results of the analysis revealed that the maximum net electric power output from a water flow-powered thermoelectric generator using commercially available BiSbTeSe alloy elements (figure-of-merit $\sim 2.2 \times 10^{-3}\ K^{-1}$) is 20 to

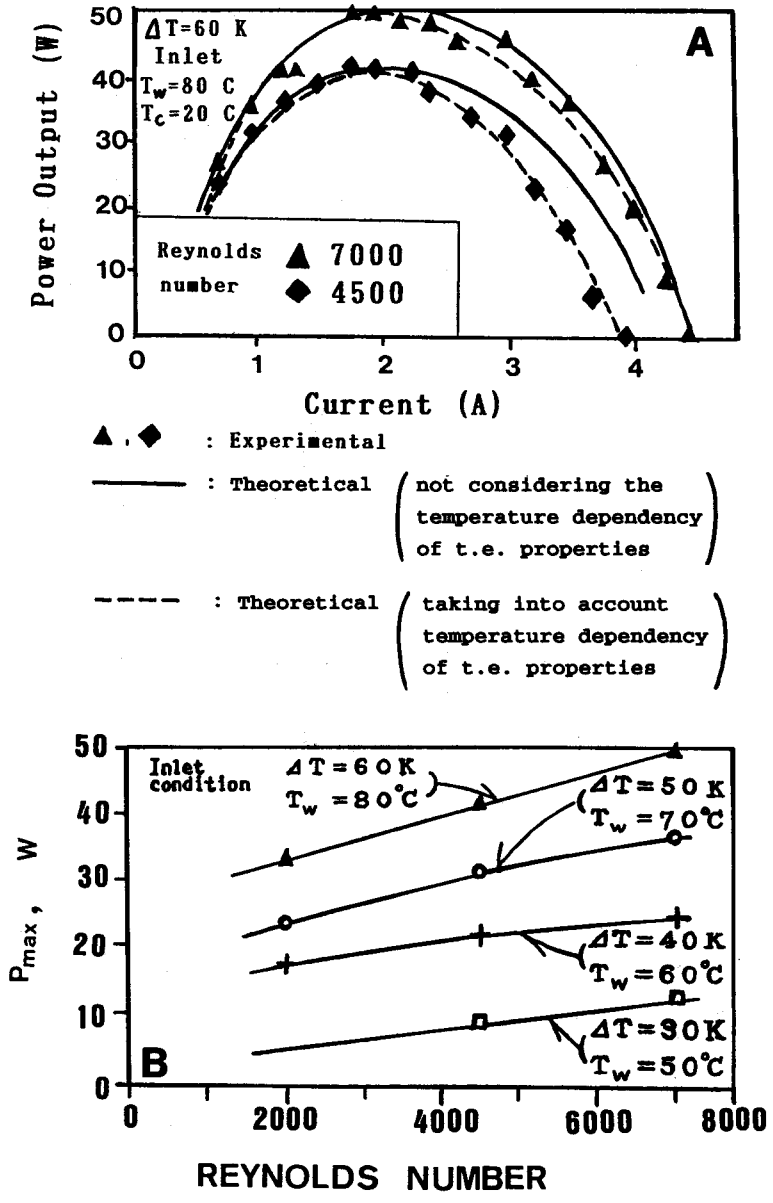

FIGURE 9 Performance characteristics of a laboratory-scale, low-temperature thermoelectric generator. (a) power output vs. current; (b) maximum power output vs. Reynolds number.

25 W/m^2 if the temperature difference between the thermoelectric module surface at the heat source temperature and the heat exchanger is 25 K and the mean Reynolds number is 4100.

The design optimization of a large-scale, low-temperature thermoelectric generator has been investigated,[21] in particular (1) optimizing the module geometry for maximum power output, (2) minimizing the generator volume, and (3) maximizing the conversion efficiency under operating conditions. The results indicate that a reduction in commercially available Bi_2Te_3 thermoelement length from 2.54 to 0.5 mm results in an increase in power output accompanied by an acceptable decrease in conversion efficiency of 8%. As for the heat transfer system, it is concluded that the optimum depth of the warm and cold water channels is around 20 mm and the performance of the system is relatively insensitive to channel width when a simply rectangular configuration is assumed for the water channel and the operation temperature is below 120°C.

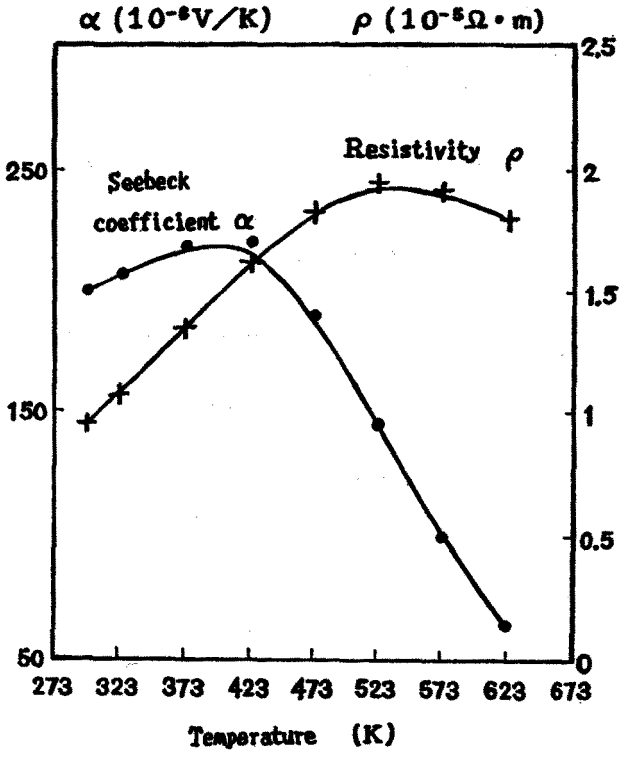

FIGURE 10 Temperature dependence of the properties of a Bi-Te-based thermoelectric material.

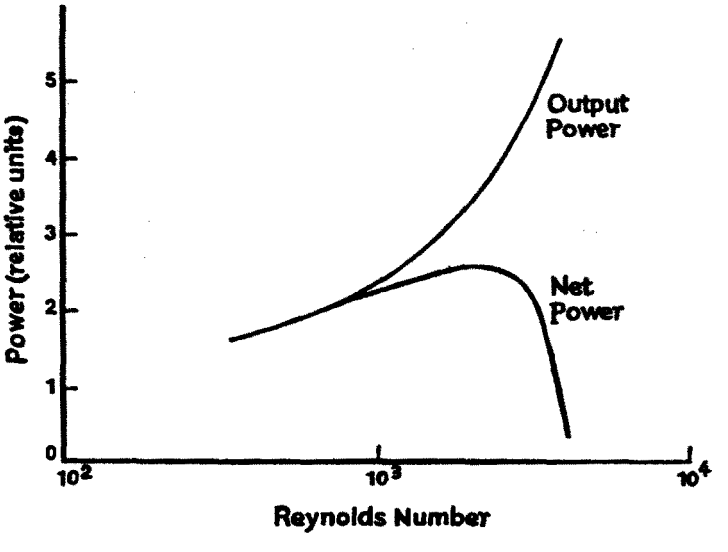

FIGURE 11 Thermoelectric generator power output and heat exchanger thermoelectric power output. (From Henderson, J., Proc. XIV Intersoc. Energy Conversion Eng. Conf., 1979, p. 1835. Copyright 1979 American Chemical Society.)

44.8 Low-Temperature Applications

The low-temperature thermoelectric conversion system described above can be employed to convert low-temperature "waste" heat to electrical power provided the heat is in a suitable form. The system can be used for gases or liquids, but clearly liquids with their much greater heat capacity

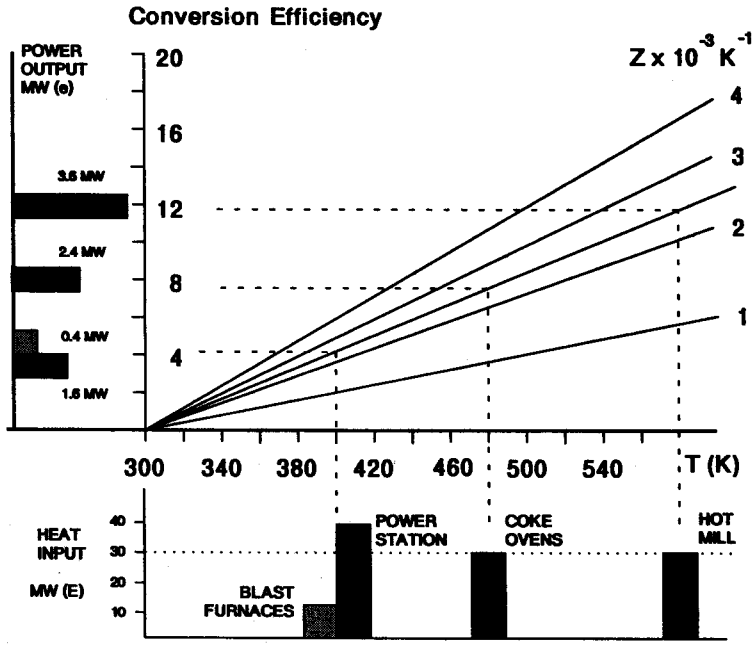

FIGURE 12 Thermoelectric recovery from a typical steel plant.

are preferred. As an example of the potential of this large-scale conversion concept two case studies of current interest to the authors are briefly discussed: cooling water associated with steel-making plants and geothermal heat from redundant oil wells.

Steel Plants

An inventory of the main sources of waste heat associated with a typical steel-making plant is presented in Figure 12. The figure displays the potential electrical power as a function of the figure-of-merit of the semiconductor material and the thermocouple conversion efficiency. The total waste heat amounts to about 115 MW, which could be recovered to produce about 8 MW of electrical power using available thermoelectric materials. The cooling water from the larger blast furnaces is rejected at a temperature of around 95°C. A waste water throughput of 50 to 60 m^3 per minute would provide around 10 MW of electrical power. The water pumps currently employed are rated at 350 KW. Thermoelectrically recovered waste heat would be sufficient to meet the on-site electrical requirements.

Redundant Oil Wells

In a recent Department of Energy publication[22] it was reported that the decommissioning of North Sea oil platforms would commence in 1992. (The authors note that at the time of going to press the decommissioning had not started.) The cost of complying with current government regulations regarding the decommissioning of all the platforms is estimated to be in excess of 5 billion pounds Sterling with the least expensive costing about 3 million pounds Sterling and with an average cost of decommissioning of about a million pounds Sterling. Understandably alternative uses for these installations have been proposed. One use which has received serious consideration is to convert the redundant platforms to geothermal power stations. In this concept the hot water pumped under pressure from oil-exhausted reservoirs converts to steam with reduction of pressure at the surface and drives turbine electric generators on the platform. The electricity generated is transmitted to the mainland grid system by submarine cable. Unfortunately the majority of the available hot water is under 140°C which makes this method of thermal to electric energy conversion unviable. However, this low-temperature heat can be converted into electricity using organic Rankine

cycle or thermoelectric generators. Although thermoelectric generators are less efficient than Rankine cycles they do offer a number of advantages, not the least of which is that they are environmentally friendly. Information relating to actual platform operations is commercial property but a realistic doublet flow rate based on general information on reservoirs and platforms is 5000 l/min.[22] Operating at an input temperature of 90°C and a sea temperature of 10°C gives a Carnot efficiency of 22%. Modern thermocouple materials are capable of operating at 20% efficiency which gives an upper operating system efficiency of 4.4%. Each extractor thus has a potential to produce at maximum around 1 MW (e) continuous. Assuming that 10 pairs of injector and extractor pipes can be accommodated on a single platform the total output is of the order of 10 MW per platform.

44.9 Conclusions

Waste cooling water associated with steel-making plants and redundant North Sea oil reservoirs provides a readily accessible source of geothermal heat; however, the temperature of the majority of the heat is too low for conversion into electricity using conventional electricity-generating technology. Thermoelectric conversion may be a viable alternative, although information on the performance of thermoelectric generators in converting low-grade heat into electricity is confined to a laboratory-scale generator producing around 150 W (e).

Volume production of thermoelectric modules is predicted to reduce their cost to around $2 per watt. If the thermoelectric component of the conversion system is the major cost factor, generating electricity by this method over 20 years would be competitive with existing utilities. However, in an actual generating system a number of factors must be taken into account, such as the cost of the generator's supporting structure and its maintenance. In addition thermoelectricity is generated as DC and conversion to AC and its subsequent transmission is expensive. The hot water supply of the two examples cited will also contain chemicals which corrode the inlet pipe and the thermoelectric generator while the cold water flow will also require preventative filtering.

Nevertheless this method of reclaiming waste heat is environmentally friendly and a detailed cost analysis should be undertaken to ascertain its economic viability.

References

1. Rowe, D. M. and Bhandari, C. M., *Modern Thermoelectrics*, Holt, Reinhart and Wilson, New York, 1983.
2. Di Pippo, R., *Worldwide Geothermal Power Development Bulletin*, Geothermal Research Council, 13, 4, 1984.
3. Downing, R. A. and Gray, D. A., *Geothermal Energy—the Potential in the United Kingdom*, British Geological Survey, 1986.
4. Rowe, D. M., Thermoelectric generation, in *Profiting from Low Grade Heat*, chapter 10, (ed.) Crook, A. W., published on behalf of the Watt Committee on Energy by IEEE, London, 1994.
5. Brandsetter, A., The hot deeps of the Red Sea as a potential heat source for thermoelectric power generation, *Proc. IXth Intersociety Energy Conversion Engineering Conference*, August 26–30, 1974, San Francisco, CA, 277.
6. Trimble, C. and Owens, W. L., *Proc. XVth Intersociety Energy Conversion Engineering Conference*, 1983, 1331.
7. *Renewable Energy Sources, Report No. 22* published on behalf of the Watt Committee on Energy by Elsevier Applied Sciences, 1990.
8. Garg, H. P., Solar ponds as an energy storage device, Paper H4, SMR/156–12 *Workshop on the Physics of Non-Conventional Energy Sources and Material Science for Energy*, Trieste, Italy, September 2–20, 1985.
9. Jayadev, T. S. and Edesess, M., Solar ponds and their applications, *Proc. VIIth Energy Technology Conference*, Washington, D.C., March 1980.
10. Rosi, F. D., Thermoelectricity and thermoelectric power generators, *Solid State Electron.*, 11, 833, 1968.

11. Writght, D. A., Materials for direct conversion thermoelectric generators, *Metall. Rev.*, 15, 147, 1970.
12. Fritts, R. W., Lead telluride alloys, in *Thermoelectric Materials and Devices*, (ed.) Cardoff, I. B. and Miller, G., Reinhold, New York, 1959.
13. McGrew, J. W., A report on the properties and performance of TAGS, *Proc. Vth Intersociety Energy Conversion Engineering Conference*, Las Vegas, Nevada, 1970, 1531.
14. Nicolau, M. C., The magnesium silicide germanide stannide alloy, *Proc. IVth International Conference on Thermoelectric Energy Conversion*, University of Texas at Arlington, March 10–12, (ed.) Rao, K. R., 1982, 83.
15. Ayral-Marin, R. M. et al., $Ag_{(1-x)}Cu_{(x)}TITe$ a new low temperature p-type thermoelectric material, *Proc. Ist European Conference on Thermoelectrics*, (ed.) Rowe, D. M., University of Wales, Cardiff, September 15–17, 1987, 24.
16. Matsuura, K., Honda, T., and Kinoshita, H., Thermoelectric generation by direct heat exchange in ocean thermal energy conversion, *Technology Report of the Osaka University*, Vol. 33, No. 1691, 1983, p. 59.
17. Henderson, J., Analysis of a heat exchanger-thermoelectric generator system, *Proc. XIVth Intersociety Energy Conversion Engineering Conference*, 1979, 1835.
18. Matsuura, K., Rowe, D. M., Tsuyoshi, A., and Min, G., The large scale thermoelectric conversion of low temperature heat, *Proc. Xth ITC*, 1991, 233.
19. Mathiprakasam, B., Sutikno, T., and Beeson, J., Analytical model for predicting the performance of thermoelectric generators, *Proc. IVth ITC*, 1982, 61.
20. Matsuura, K. and Kinoshita, H., An improved method in generating thermoelectric power from low-grade heat, *Proc. Vth ITC*, 1984, 10.
21. Matsuura, K., Rowe, D. M., Koumoto, K., Min, G., and Tsuyoshi, A., Design optimisation for a large scale, low temperature thermoelectric generator, *Proc. XIth ITC*, 1992, 10.
22. Preliminary Assessment of Offshore Platform Conversion to Geothermal Power Station, *Department of Energy Report* ETSUG 145, Washington, D.C., 1989.

Section G
Thermoelectric Refrigeration

45
Introduction

H. J. Goldsmid
University of New South Wales, Australia

The basic building block of a thermoelectric refrigerator is the thermocouple, which consists of a positive and negative branch. It is usually convenient for the two branches to be of rectangular cross section and of the same length. Strictly, when the lengths are equal, the cross-sectional areas A_p and A_n of the branches should satisfy the relationship:[1]

$$\frac{A_p}{A_n} = \left(\frac{\rho_p \lambda_n}{\rho_n \lambda_p}\right)^{1/2} \tag{1}$$

where ρ and λ represent electrical resistivity and thermal conductivity, respectively. However, at ordinary temperatures, ρ and λ are of comparable value for the positive and negative materials and, therefore, it is usual for A_p and A_n to be nominally equal.

The ratio A/L, where L is the length, for each thermoelement is determined by the electric current that is to be passed. In principle, any required cooling power can be reached using a single couple if its cross-sectional area is large enough but this might involve an impracticably large current. Thus, in practice, a number of thermocouples are linked together, thermally in parallel and electrically in series, so as to form what is known as a thermoelectric module. The links are formed by strips of metallic conductor which must be thick enough so as not to offer any significant electrical resistance. On one face of the module the metallic strips are in thermal contact with the heat source while at the other face they are in contact with the heat sink. It goes without saying that the strips must be electrically insulated from one another, other than through the thermoelements.

In theory the cooling power and current for each thermocouple in the module are determined solely by the thermoelectric properties and by the ratio A/L. Thus, economic use of material suggests that both A and L should be as small as possible provided that their required ratio is

0-8493-0146-7/95/$0.00+$.50

maintained. However, the adoption of very small lengths is undesirable since this magnifies the relative effect of any electrical resistance at the contacts and it also makes it more difficult to avoid heat transfer between the source and sink around the sides of the thermoelements. It will be appreciated that the overall cross section of a module cannot be made too small without there being substantial thermal barriers to the source and sink. In practice, it has been possible in commercial modules to reduce the length of the thermoelements to 1 or 2 mm.

The design of thermoelectric modules will be considered in subsequent chapters by other authors but the basic principles will be discussed briefly here. It will be supposed that the cooling power and the temperature difference between the source and sink are specified. It is then a simple matter to calculate the optimum coefficient of performance in terms of the figure-of-merit of the thermocouple materials. The electric current I that is require to yield this optimum coefficient of performance is given by:

$$I = \frac{(\alpha_p - \alpha_n)(T_2 - T_1)}{R[(1 + ZT_M)^{1/2} - 1]} \tag{2}$$

where $(\alpha_p - \alpha_n)$ is the differential Seebeck coefficient, T_1, T_2, and T_M are the source temperature, the sink temperature, and the mean temperature, respectively, and Z is the figure-of-merit. R is the electrical resistance of the two branches of the thermocouple in series. Clearly, then, the value of the resistance R for a given current can be calculated and this, in turn, determines the ratio A/L. The cooling power of each couple is given by:

$$q_c = (\alpha_p - \alpha_n)IT_1 - K(T_2 - T_1) - I^2R/2 \tag{3}$$

so it is possible to determine the number of couples that are needed in the module to give the required overall cooling power. It should be noted that the potential drop across each thermocouple is rather small. At the maximum coefficient of performance it is given by:

$$V = (\alpha_p - \alpha_n)(T_2 - T_1)\left[\frac{(1 + ZT_M)^{1/2}}{(1 + ZT_M)^{1/2} - 1}\right]. \tag{4}$$

Typically $(1 + ZT_M)^{1/2}/[(1 + ZT_M)^{1/2} - 1]$ is of the order of 4, $(\alpha_p - \alpha_n)$ is of the order of 4×10^{-4} volt and $(T_2 - T_1)$ is of the order of 20 K, so V is of the order of 3×10^{-2} volt. Direct current power sources cannot provide such a small voltage efficiently but it is rare for a thermoelectric cooling device to consist of a single couple. Typical commercial modules contain some tens of couples so that the potential drop across a module is of the order of one or more volts.

In actual fact, one does not usually design a thermoelectric module for a specific application. Rather, a range of standard modules having specified characteristics is available from each manufacturer, and one must select that which has enough cooling capacity for one's requirements and which, at the same time, operates within the appropriate current or voltage range.

Reference

1. Ioffe, A. F., *Semiconductor Thermoelements and Thermoelectric Cooling*, Infosearch, London, 1957.

46

Module Design and Fabrication

Raymond Marlow and
Edward Burke
Marlow Industries
Dallas, Texas U.S.A.

46.1 Introduction

Thermoelectric refrigeration is a versatile technology that can be customized to meet the needs of a wide range of customers. This flexibility comes from the options available in the design and also fabrication of the thermoelectric module. The following chapter reviews the details involved in the design and fabrication of thermoelectric refrigeration modules.

46.2 General Theory of Operation

Thermoelectric refrigeration is achieved when a direct current is passed through one or more pairs of n- and p-type semiconductor materials.[1] Figure 1 is a diagram of a single pair consisting of n- and p-type semiconductor materials. In the cooling mode, direct current passes from the n- to the p-type semiconductor material. The temperature T_c of the interconnecting conductor decreases and heat is absorbed from the environment. This heat absorption from the environment (cooling) occurs when electrons pass from a low energy level in the p-type material through the interconnecting conductor to a higher energy level in the n-type material. The absorbed heat is transferred through the semiconductor materials by electron transport to the other side of the junction T_H and liberated as the electrons return to a lower energy level in the p-type material. This phenomenon is called the Peltier effect.

A second phenomenon is also important in thermoelectric refrigeration. When a temperature differential is established between the hot and cold sides of the semiconductor material, a voltage is generated. This voltage is called the Seebeck voltage, and it is directly proportional to the temperature differential. The constant of proportionality is referred to as the Seebeck coefficient.

The Peltier effect is controlled by the Peltier coefficient, defined as the product of the Seebeck coefficient of the semiconductor material and the absolute temperature. The Peltier coefficient

0-8493-0146-7/95/$0.00+$.50

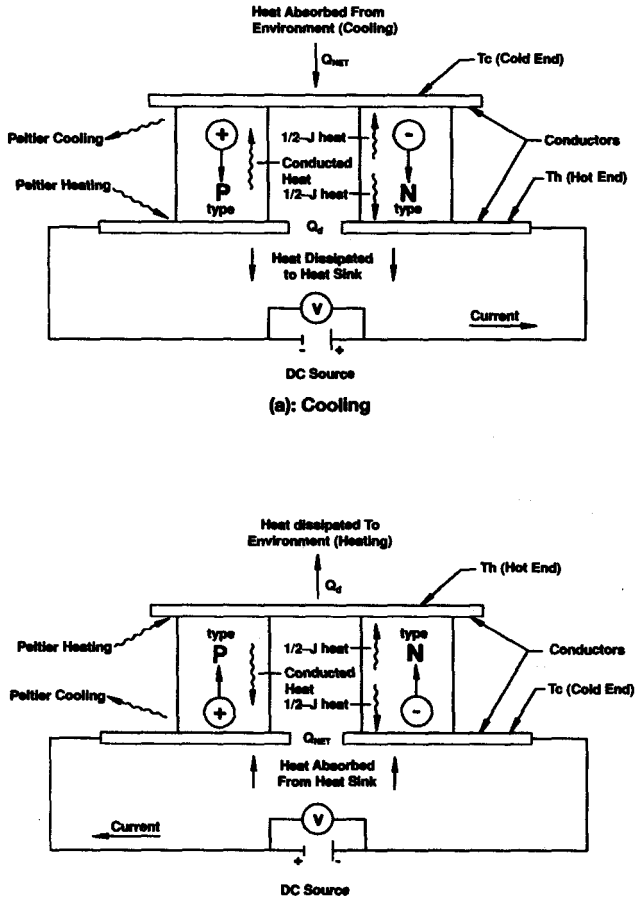

FIGURE 1 Thermocouple.

relates to a cooling effect as current passes from the n-type material to the p-type material, and a heating effect when current passes from the p-type material to an n-type material, as shown in Figure 1. Reversing the direction of the current reverses the temperature of the hot and cold sides.

$$Q_{net} = \alpha T_c I - \frac{1}{2}(I^2 R) - K\,\Delta T \tag{1}$$

where Q = rate of heat absorbed at cold junction, in watts; $\alpha = \alpha_{pn} = \alpha_p - \alpha_n$ = the difference between the absolute Seebeck coefficient of the p and n materials; $\Delta T = (T_h - T_c)$ operating temperature difference, degrees Celsius; T_h = hot junction temperatures, Kelvin; T_c = cold junction temperature, Kelvin; $R = R_n + R_p$ electrical resistances of the couple legs per degree Celsius and K the thermal conductance.

Ideally, the amount of heat absorbed at the cold side and the heat dissipated at the hot side are dependent on the product of the Peltier coefficient and the current flowing through the semiconductor material. Practically the net amount of heat absorbed at the cold side due to the Peltier effect is reduced by two sources, conducted heat and Joule heat. Due to the temperature differential between the cold and hot sides of the semiconductor material, heat will be conducted through the semiconductor material from the hot to the cold side. As the current is increased, the temperature differential, and thus the conducted heat, increases because the Peltier cooling effect increases. When a steady state is established at the cold junction, the Peltier cooling equals the heat conducted down the couple legs, plus heat absorbed (useful heat pumped).

As the current continues to increase and Joule heating becomes the dominating factor, a point is reached where additional current will result in less net cooling. The current at which no further

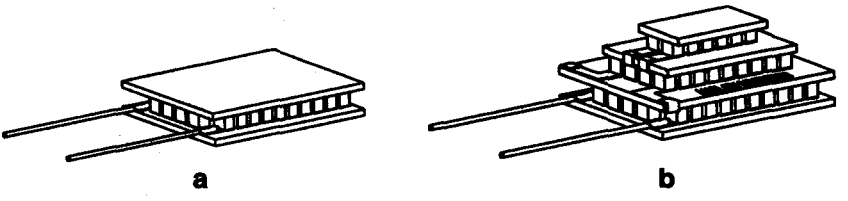

FIGURE 2 Typical thermoelectric module designs: (a) single-stage module, (b) multistage module.

cooling can be achieved is the maximum current (I_{max}). Maximum voltage (V_{max}) and maximum temperature differential ΔT_{max} will also occur for any given heat load at the maximum current.

The net heat dissipated at the hot side is the sum of the net heat absorbed at the cold side plus the applied electric power. The coefficient of performance (COP) used to define the cooling "efficiency" is defined as the net heat absorbed at the cold side divided by the applied electric power.

The properties of semiconductor materials—electrical resistivity, thermal conductivity, and Seebeck coefficient—that define their maximum cooling capabilities are temperature dependent. This is why simple formulas are not dependable for thermoelectric refrigeration design. For any one semiconductor material there is a temperature range over which that particular material has the best performance. The most widely used thermoelectric material for refrigeration in the temperature range of −184 to 446°F (−120 to 230°C) is a pseudo-binary alloy, $(Bi,Sb)_2(Te,Se)_3$, commonly referred to as bismuth telluride.

The refrigeration capability of a semiconductor material is dependent on a combined effect of the material's Seebeck voltage, electrical resistivity, and thermal conductivity over the operational temperature range between the cold and hot sides. The expression that contains these material parameters is referred to as the figure-of-merit, and is denoted by Z (in reciprocal Kelvin)

$$Z = \frac{\alpha^2}{\rho\lambda}$$

Each of the n- and p-type semiconductor material properties varies as a function of temperature, and therefore the figure-of-merit for each material is temperature dependent. It can be shown that the maximum temperature differential that can be achieved by a single pair of n- and p-type materials is directly proportional to the "temperature averaged" figure-of-merit of each semiconductor material. Therefore, maximizing the figure-of-merit is the major objective in the selection and optimization of thermoelectric materials. The figure-of-merit of the semiconductor material limits the temperature differential, whereas the length-to-area ratio of each n- and p-type semiconductor material defines the heat pumping capacity.

46.3 Description of a Thermoelectric Refrigeration Module

More than one pair of semiconductors are usually assembled together to form a thermoelectric module. Within the module each semiconductor is called an element, and a pair of elements is called a thermocouple. Thermoelectric modules, as shown in Figure 2, are typically classified as single-stage modules or multistage modules.

Single-Stage Module

A single-stage module as shown in Figure 2a consists of several thermocouples connected thermally in parallel and electrically in series to increase the operating voltage of the module. These thermocouples are interconnected with good electric conductors such as copper. The conductors must be electrically isolated from the device being cooled; otherwise the module will be electrically short-circuited to the surface being cooled. However, the electrical isolation material must also be thermally conductive material to minimize the temperature difference between the conductor and the device being cooled. The module shown in Figure 2a has a ceramic plate on the top and bottom surfaces of the module. Alumina ceramics typically provide the electrical isolation and thermal

conductance that satisfy this requirement. Beryllium oxide ceramics may also be used where maximum lateral heat transfer is desired such as in multistage coolers (Figure 2b).

Thermoelectric modules vary in size from a single pair of elements that may be as small as 0.06 in.^{2} (1.5 mm^2) up to groups of pairs that may be 2.0 in.^{2} (51 mm^2). The limit in making smaller modules is related to the assembly of smaller pellets and the mechanical integrity of the pellets.

A limiting factor in the use of single-stage modules is related to the figure-of-merit of the semiconductor material. Regardless of the amount of power applied to a single-stage module, the coldest temperature that can be reached with bismuth telluride with a hot-side temperature of 80°F (27°C) and no thermal load is approximately −29°F (−34°C) in still air and −53°F (−47°C) in a vacuum.

Multistage Module

When the desired temperature differential cannot be obtained with a single-stage module, a multistage module is required. A typical three-stage module is shown in Figure 2b. Multistage modules are essentially single-stage modules stacked in a vertical array. Typically a multistage module is pyramid shaped because the lower stage must pump the heat dissipated by the upper stages in addition to the active heat load on the top stage. Therefore, there are always more pellets in the lower stage than in the upper stages when all of the pellets are connected in series.

As additional stages are added to a module, colder temperatures can be achieved. A practical limit in the number of stages is presently between eight and ten stages. With an eight-stage module, a temperature of −218°F (−139°C) on the cold side has been achieved when the hot-side temperature was 127°F (53°C).[2]

46.4 Operational Characteristics

The basic operational characteristics of a thermoelectric module include the cold-side and hot-side temperatures, heat pumping capacity at the cold side, heat dissipated at the hot side, input current, and voltage. The acceptable range of each of these characteristics must be established by the design engineer in order to select a commercial thermoelectric module. Considerations in the final selection are typically performance, cost, and reliability.

Number of Stages

The first consideration in the selection of a module is to determine the number of stages required to obtain the desired temperature differential, which is defined by the desired cold- and hot-side temperatures. The temperature differential that is achievable for various modules depends on the atmosphere in which the module operates. A greater temperature differential can be reached when the module is operating in a vacuum compared with operation in dry air, nitrogen, or other gases because the passive heat load is less in a vacuum. Figure 3 shows the practical cold-side temperature range achievable with present thermoelectric materials for various numbers of stages in dry nitrogen and vacuum. Figure 3 also shows an overlap in the number of stages of a module relative to the desired temperature differential. This is an important design consideration since, in general, the cost of a module is influenced by the number of stages. As the number of stages increases, the cost of the module increases. For minimum cost, the modules with the fewest number of stages would normally be selected.

The design of multistage modules is complex. Typically multistage modules are custom designed for optimum performance in a specific application. Computer programs to assist in the design of complex multistage modules have been developed and applied by thermoelectric module manufacturers.

Temperature Differential and Heat Load

Manufacturers of thermoelectric modules provide tables that define the maximum performance capabilities of various modules. A typical format is shown in Table 1. The heat pumping capacities

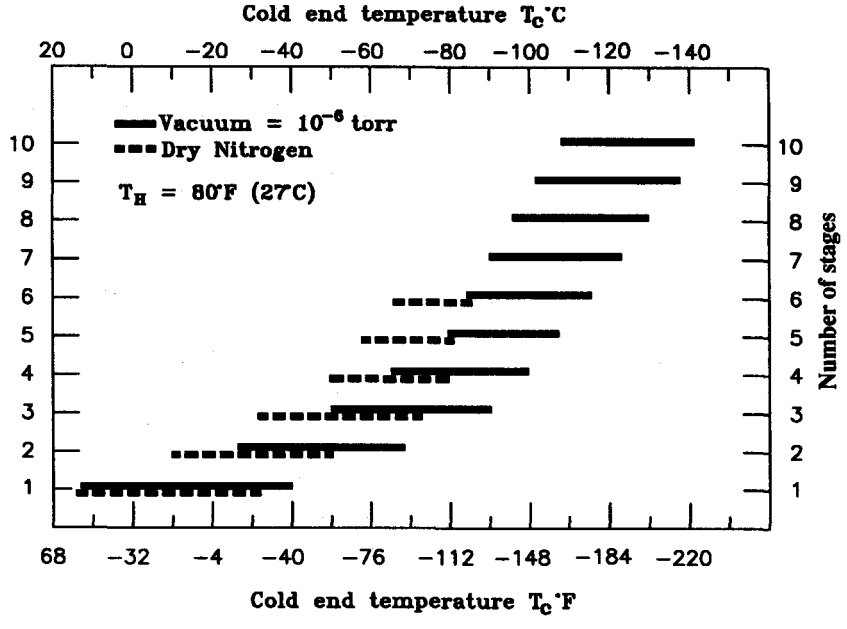

FIGURE 3 Typical performance range of thermoelectric modules.

Table 1 Summary Performance and Geometry of Typical Thermoelectric Cooling Modules

	ΔT_{max} when Q = 0 and T_H = 80.6°F (27°C)							Dimensions				
	Vacuum 10^{-6} torr		Dry N_2 760 mm Hg					Base Ceramic		Top Ceramic		
Module	°F	(°C)	°F	(°C)	Qmax W	Imax A	Vmax V	Width in(mm)	Length in(mm)	Width in(mm)	Length in(mm)	Height in(mm)
1	121	(67)	110	(61)	0.52	1.0	0.8	0.16 (3.96)	0.16 (3.96)	0.16 (3.96)	0.16 (3.96)	0.10 (2.41)
2	122	(68)	115	(64)	2.45	2.0	2.0	0.26 (6.60)	0.26 (6.60)	0.26 (6.60)	0.26 (6.60)	0.09 (2.20)
3	122	(68)	115	(64)	55.4	6.0	15.2	1.50 (38.1)	1.50 (38.1)	1.50 (38.1)	1.50 (38.1)	0.17 (4.40)
4	162	(90)	151	(84)	1.04	1.5	2.1	0.26 (6.60)	0.26 (6.60)	0.16 (3.96)	0.16 (3.96)	0.15 (3.80)
5	193	(107)	176	(98)	6.29	4.7	7.4	0.86 (21.72)	1.11 (28.27)	0.34 (8.61)	0.51 (12.98)	0.44 (11.10)
6	200	(111)	157	(87)	0.85	1.1	6.9	0.52 (13.26)	0.68 (17.22)	0.16 (4.06)	0.31 (7.98)	0.35 (8.80)
7	238	(132)	194	(83)	0.66	3.8	6.5	0.86 (21.72)	1.11 (28.27)	0.20 (5.08)	0.20 (5.08)	0.80 (21.10)

of various modules cover a wide range. The maximum heat pumping capacity is defined as the amount of heat required to suppress the temperature differential to zero. By dividing the maximum temperature differential that can be achieved with no heat load by the maximum heat pumping capacity with no temperature differential, the slope of the temperature differential vs. heat load line can be defined. The actual performance is such that the temperature differential suppression is linear with the heat load.

Performance Curves

After one or more candidate modules have been selected based on data similar to those in Table 1, more detailed performance characteristics need to be considered. Typical module performance

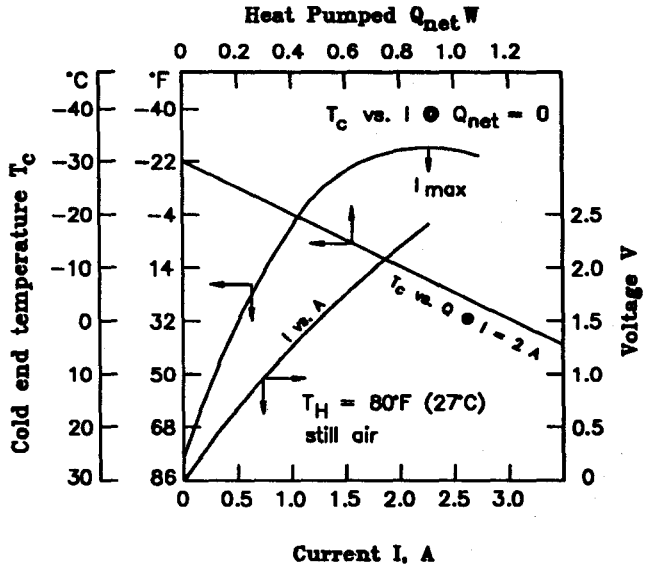

FIGURE 4 Thermal and electrical performance of typical thermoelectric modules.

curves are illustrated in Figure 4. One curve shows the effect of cold-side temperature T_c as a function of current I when the net heat load is zero ($Q_{net} = 0$). As discussed in the next paragraph, the condition of zero net heat load actually includes several parasitic heat loads that are present during the testing of a module. For single-stage modules the tests are normally conducted in room air conditions; for multistage modules they are typically conducted in a vacuum.

The relationship between the cold-side temperature and the net heat pumping capacity when operating at a maximum current is also given in Figure 4. As the heat load is increased, the temperature differential that can be achieved is decreased. The net heat pumped Q_{net}, defined in the performance curve, is the net heat load of the device being cooled. If the device being cooled is a small electrical component, the net heat load consists of the active Joule heating I^2R within the component and the heat conducted through the lead wires. The parasitic heat loads attributed to thermal radiation and convection on the lateral surfaces of the module are accounted for in the zero net heat load condition. Radiation and convection heat loads will need to be determined when the device being cooled has large surfaces.

The third curve in Figure 4 relates the input voltage to the input current. As the current increases, the voltage increases. The current is not linearly proportional to the voltage due to the temperature dependence of the material properties.

Design Options

There are three usual objectives in the design and application of thermoelectric modules: (1) maximum heat pumping, (2) maximum COP, and (3) maximum speed of response. Maximum heat pumping requires the module to operate at the current and voltage that pumps the maximum amount of heat over the specified temperature differential. The currents and voltages listed in Table 1 apply to operation at the current for maximum heat pumping.

The current for operation at the maximum COP is generally less than the current for maximum heat pumping. For example, when operating at the current for achieving maximum COP at a hot-side temperature of 80°F (27°C), the maximum COP is about 0.2 for a 104°F (40°C) temperature differential. When the temperature differential is 72°F (22°C), the maximum COP is about 1.0.

The design of a module for maximum speed of response is more complex. Consideration must not only be given to the thermal and electrical characteristics of the module, but also to the thermal mass of the module and the device being cooled. In addition, the characteristics of the heat sink

must be considered in the overall design. Temperature differentials of 144°F (80°C) from a hot-side temperature of 140°F (60°C) have been achieved in less than 2 s for properly designed modules with minimized heat loads. Typical single-stage or multistage modules will achieve the maximum cold-side temperature within 60 to 90 s after power is applied. This response time applies to the cold side of the module when there is no added mass on the cold side and the hot side is attached to a heat sink capable of absorbing the heat with a minimum rise in temperature.

Mechanical Dimensions

The dimensional characteristics of typical modules are shown in Table 1. Typically the top and bottom surface areas of a single-stage module have the same dimensions except for ledges for electrical connections on some modules. The cold-stage surface area of a multistage module is typically smaller than the hot-stage surface area.

The flatness of the cold and hot surfaces of a module, the parallelism between the cold and hot surfaces, and the tolerances on the height of the module are important mechanical characteristics of the modules. These tolerances become increasingly important to overall performance when groups of modules are sandwiched between two heat exchangers and these tolerances are typically ± 0.001 in. or less.

Electrical Characteristics and Control

Table 1 shows the maximum direct current together with the voltage that will achieve the maximum temperature differential in the cooling mode. For maximum performance the ripple component of the direct current should not exceed 10%.

Depending on the direction and the amount of current, thermoelectric modules have the ability to cool, heat, or stabilize temperatures regardless of whether or not the cold surface is above or below the ambient temperature. By applying the correct amount of current at the desired polarity, the temperature of a device can be stabilized as the ambient temperature oscillates. Temperature stability depends on the thermal mass and heat load capacity. Tolerances of ± 0.18 to ± 0.54°F (± 0.1 to ± 0.3°C) at a stabilized temperature are reasonable.

The module with the lowest current would normally be selected because it makes the power supply temperature controllers less expensive for a given output power. However, the total power to the module is the major factor. Low-current modules will, therefore, require higher voltages to maintain the same power input. High-voltage modules require a larger number of pellets, thereby increasing the cost of the module. Therefore, when selecting a module, a tradeoff is made between module cost and power supply or temperature controller cost, or both.

46.5 Practical Considerations

Thermal

The practical heat load (pumping) for thermoelectric modules ranges from a few milliwatts to tens of watts. This practical limitation is related to the competitiveness of other refrigeration methods in both cost and efficiency. Conventional mechanical refrigeration systems are normally not competitive with thermoelectric refrigeration when the heat loads are under 25 W. Thermoelectric refrigeration can be used to pump heat loads much greater than 25 W, but these are usually for very specialized applications.

The lowest practically achievable temperature is about −148°F (−100°C). Since the efficiency of a thermoelectric module (single-stage or multistage) decreases as the temperature decreases, the heat pumping capacity is typically limited to only a few milliwatts at those cold temperatures.

In heating applications, the practical limit is about 176°F (80°C). This temperature limit is imposed primarily by the manufacturing techniques used to assemble the thermoelectric modules. Although typical thermoelectric modules are assembled at soldering temperatures of 280°F

(138°C), they are not capable of operating at these higher temperatures for extended periods of time without degrading in performance. The gradual degradation in performance with time is due to contaminants diffusing into the thermoelectric material resulting in changing cooling properties. It should be noted that much less input power is required to heat than to cool.

Environmental

Because thermoelectric modules are solid-state and have no moving parts, high reliability is an inherent feature. However, the reliability may be affected by environmental extremes.

Moisture

With power applied to the module, excessive moisture within the module can cause galvanic corrosion at the thermoelements, solders, and conductors. The moisture can also provide an electric short-circuit within the module, which would reduce the module's performance. Generally, a moisture barrier, gasket, or dry atmosphere is required to maintain reliability.

High Temperature

Continual operation at high temperatures accelerates thermal diffusion of metal ions into the pellets, thus decreasing the performance of the module. In addition, high temperature can cause the solder to migrate into the pellets, which results in a damaged joint, thereby reducing performance. Typically, this is not a problem below 176°F (80°C). However, the temperature at which these factors begin to affect the performance of specific modules should be defined to the design engineer by the module manufacturer.

Thermal Cycling

Rapid temperature cycling from cool to hot can also affect the performance of the module over time. As temperatures change, the module will expand or contract. This action stresses the pellets in the module. Although one major feature of thermoelectric modules is the ability to heat and cool, consideration should be given to minimizing rapid power cycling.

Mechanical Stress

Mechanical stresses applied during shock or vibration are not a major failure mode if the modules are properly mounted. In general, the module is strongest in the compression mode. The most likely failure mode of the solder joints is in the shear direction, which is parallel to the top or bottom surfaces of the module. Most modules will withstand shock levels of 1000 *g* over a frequency range of 10 to 2000 Hz and random vibration of about 65 *g* rms from an acceleration power density of 0.01 to 5.0 g^2 Hz over a frequency range 50 to 20,000 Hz.

Vacuum

A vacuum is the most reliable environment in which to use a module. Thermoelectric modules are not susceptible to failure as the result of any level of vacuum. When in a vacuum, the effective heat pumping capacity of the module is increased, thereby providing colder operating temperatures as compared to operating in air for the same input power.

Radiation

No form of radiation has been noted in the literature that has induced failure of thermoelectric modules. Several tests have demonstrated that high neutron bombardment and gamma radiation do not affect performance.

Installation

Mounting

The module may be pretinned and soldered to a heat sink. Usually the hot side is soldered to the heat sink and the cold side is greased with a nonsetting thermal compound for good heat transfer.

Table 2 Applications of Thermoelectric Modules

Electronic Components	Small Refrigerators	Instruments	Special
Infrared detectors	Boats	Dew point sensor	Dehumidifiers
Laser diodes	Mobile homes	Cold bath	Water coolers
Charge-couple devices	Offices	0°C reference source	Air-conditioning
Blackbody reference source	Hotels	Microtome	Display cabinets
Voltage reference source	Portable picnic boxes	Blood coagulator	Cream coolers

Soldering the top or bottom to a heat sink can lead to mechanical breaking of the thermal expansion mismatch between the module and the attached heat sink is large. This is especially true if the hot and cold sides are both mechanically constrained between the heat sinks.

A good thermal epoxy is another way of bonding or attaching the module. The same failure modes as for soldering also apply to epoxy. Another way of mounting a module is between two clamped plates. Extreme caution should be used for small or multistage modules. Improperly applied compression loads can cause very large shear loads, which will fracture the pellets.

The reason individual modules are not larger than about 2.0 in.^{2} (51 mm^2) is due to mechanical considerations. The modules tend to bow much like a thermostatic bimetallic element. This bowing between the hot and cold sides of the module is due to the fact that one side is contracting and the other side is remaining constant or expanding. The stress induced by these expansion coefficients tends to strain the individual pellets on the outer edge of the module. When the distance across the module increases beyond about 2.0 in. (51 mm), the strain can be too great for the pellets and they crack or break. For this reason, groups of modules are assembled onto heat exchangers rather than mounting one large module to the heat exchangers.

Handling

The module is a rigid assembly sandwiched between ceramic plates. The lead wires are attached to stiff lead conductors. Excessive torque on the lead wires will result in pulling the wires loose or snapping the lead conductor loose from the circuit. The ceramic plates on the top and bottom of the module may be cracked or broken by mishandling, which increases the probability of electric short circuits.

Heat Sinking

Adequate heat sinking is required to dissipate the heat load and power of the module without an excessive hot-side temperature rise. Failures have occurred where the solder joints on the hot side of the pellets were melted because of inadequate heat transfer to the heat sinks.

46.6 Range of Applications

The application of thermoelectric modules ranges from the cooling of electronic components such as infrared detectors with heat loads in the milliwatts and temperatures of −171°F (−113°C) to special applications where 5 tons of air-conditioning is achieved in a railroad passenger car with a temperature difference of 11°F (6°C).[3] Table 2 shows a list of typical applications for thermoelectric refrigeration.

46.7 Thermoelectric Module Fabrication

Thermoelectric modules consist of pairs of p- and n-type semiconductor elements that are electrically connected in series. The electrical circuit is accomplished by soldering the elements to electrical conductors. There are several methods to fabricate the individual components and overall assembly of thermoelectric modules.

Thermoelectric Elements

Thermoelectric p- and n-type elements can be fabricated by a variety of methods. The most common methods utilized by the thermoelectric industry are zone refining, Bridgman method,

and press and sintering. Most thermoelectric cooler manufacturers utilize a barrier material such as nickel applied to the sides of the elements to allow protection from diffusion of copper and solder constituents into the element and also this barrier provides a surface that can easily accept solder to insure good reliable solder joints. The thermoelectric elements are produced by slicing wafers from the ingot and then subsequently dicing the wafers into the individual elements. Tight dimensional tolerances (± 0.0005 in.) must be held to allow reliable fabrication and also to maintain the design integrity.

Ceramics

Ceramics (alumina, beryllium oxide) are used in the construction of thermoelectric modules due to their good thermal conduction and electrical isolation properties. The copper conductors can be affixed to the ceramics by a variety of methods. The most common method is to print and fire a circuit pattern using molymanganese or copper. The copper conductors are then soldered to this circuit pattern. Ceramics are produced in a variety of shapes, sizes, and such specialty features as holes.

Assembly

The fabrication of the module begins by loading the individual p- and n-type elements into a holding fixture. Special care is required to insure that no elements are misloaded, since this will result in a heater being produced instead of a cooler. The elements are then soldered to the electrical conductors. The solders that are most commonly used are bismuth tin (58% Bi/42% Sn; MP = 138°C), and tin lead (63% Sn/37% Pb; MP = 183°C). Various methods for solder reflow are utilized and range from manual soldering to vapor-phase reflow. Multistage coolers are constructed by assembling each individual stage and then soldering each subsequent stage on top of the next. All modules are then thoroughly cleaned to insure removal of all flux residue.

Testing

A variety of tests can be performed to understand the performance of each module and to insure their high reliability. A typical test sequence is as follows:

- Resistance measurement (AC resistance)
- Vacuum bake (T = 100°C, 2 h)
- Thermal cycle (0 to 100°C; 20 cycles)
- Performance test ($I = I_{max}$; $T_H = 27°C$)
- Resistance measurement

The performance test consists of heat sinking the module to a temperature-controlled surface, then applying power to the module at the "maximum" current and then measuring the temperature of the cold-side ceramic. Testing is best performed in a nitrogen or vacuum environment to minimize the forming of frost/ice on the top of the module. Performance testing can also be performed using a "transient" method that measures the Seebeck voltage and calculates the individual module's performance. The "transient" method requires a high-speed computer and special data acquisition software.[4]

46.8 Summary

Thermoelectric refrigeration is a highly reliable and practical method of cooling electronic components and small-volume refrigerators from a cost and efficiency viewpoint. When heat loads are less than 25 W and temperature requirements are not below −148°F (−100°C) or above 176°F (80°C), thermoelectric refrigeration is practical for a wide variety of applications. There are many

important considerations that need to be considered when designing thermoelectric coolers, but when properly analyzed will yield a product that can be optimized for a very wide variety of specific applications. Thermoelectric module fabrication and installation require tight tolerances and knowledge of the important process parameters, but with these considered will produce a very reliable, uncomplicated system.

References

1. Goldsmid, H. J., *Electronic Refrigeration,* Pion, London, 1986.
2. Buist, R., Fenton, J., and Tuomi, D., *Low Temperature Thermoelectric Cooler for 145K Operation,* Night Vision Laboratory, VA, Sept. 1971.
3. Stockholm, J. G., Prototype Thermoelectric Air Conditioning of a Passenger Rail Coach, *IVth International Conf. on Thermoelectric Energy Conversion,* TX, Mar. 1982.
4. Buist, R., A new methodology for testing thermoelectric materials and devices, *XIth International Conf. on Thermoelectrics,* Oct. 1992.

47 Cooling Thermoelements with Superconducting Leg

M. V. Vedernikov and
V. L. Kuznetsov
A. F. Ioffe Physical-Technical Institute
St. Petersburg, Russia

47.1 Introduction

According to A. F. Ioffe,[1] the figure-of-merit of a thermoelement, Z_{np} with optimized leg dimensions can be written:

$$Z_{np} = \frac{(\alpha_p - \alpha_n)^2}{((\lambda_n\rho_n)^{1/2} + (\lambda_p\rho_p)^{1/2})^2} \quad (1)$$

where α, λ, and ρ are the thermopower, thermal conductivity, and electrical resistivity of the leg materials, the indices n and p referring to the negative and positive legs, respectively. As seen from this equation, the figure-of-merit Z_{np} of a thermoelement is actually the result of an averaging of the leg figures-of-merit, Z_p and Z_n. For each leg one uses the most efficient materials with similar figures-of-merit. In this case Z_{np} is approximately equal to Z_n and Z_p. If the difference between the leg figures-of-merit is large, efficient cooling, while operating the thermoelement in the Peltier mode, cannot be provided, despite the high efficiency of one of the leg materials. This is exactly the situation in the temperature domain below 150 K where the figure-of-merit of the widely used materials based on the solid solution bismuth-antimony-tellurium-selenium, $(Bi,Sb)_2(Te,Se)_3$, decreases dramatically with decreasing temperature. Only one material, the solid solution of n-type $Bi_{1-x}Sb_x$, is known to have a high efficiency in this temperature domain. At temperatures of 80 to 100 K, the figure-of-merit of the $Bi_{1-x}Sb_x$ n-leg and of the Bi_2Te_3-based p-leg differ by a factor of between five and eight. This difference in the leg material properties has for many years been an obstacle to the successful low-temperature applications of thermoelectric cooling.

As shown by a straightforward analysis in Equation 1, this problem could be solved if, in place of the less efficient leg, a leg was used with such a low value of $\lambda\rho$ that it could be neglected in the denominator of this equation. In this case the Z_{np} of a thermoelement would approach the figure-of-merit of the n-leg material. This is, however, impossible for any material with normal conductivity (degenerate semiconductors, semimetals, metals), since the product $\lambda\rho$ for these materials cannot be noticeably different from the constant determined by the Wiedemann-Frantz law. The only class of materials with such properties are superconductors for which $\rho = 0$. The Seebeck coefficient of a superconductor (in the superconducting state) is also always zero. Therefore, the superconducting leg will not contribute to thermoelectric conversion and will be thermoelectrically

0-8493-0146-7/95/$0.00+$.50

passive. The figure-of-merit of a thermoelement consisting of an active and a passive leg is equal to that of the active leg if the passive leg also has zero thermal conductivity. Actually, it will be somewhat less than that because the superconducting leg has a finite thermal conductivity and, hence, will thermally shunt the active leg.

Nobody had considered the possibility of using a passive leg before the discovery of the high-T_c (critical temperature) superconductivity, since in the range where the traditional superconductors are used (below 20 K) the application of thermoelectric cooling was thought unrealistic. However, the advent of high-T_c superconductors (HTCS) with critical temperatures $T_c > 77$ K makes it possible to employ a passive leg. In 1989, Goldsmid and co-workers analyzed the problem. However, an attempt at preparing a thermoelement with a superconducting leg failed because of too low a critical current density in the HTCS ceramic, yttrium-barium-copper-oxygen ($YBa_2Cu_3O_{7-x}$) used.[2] In 1991, the authors of the present chapter published a paper in which they reported the successful experimental fabrication of a cooling thermoelement with the passive leg made of a HTCS material.[3] The present chapter is based on Reference 3 and some later data of the authors.

47.2 Active Leg Materials

The materials primarily used in thermoelectric coolers in the temperature range 200 to 300 K are at present n-type Bi_2Te_3-Bi_2Se_3 and p-type Bi_2Te_3-Sb_2Te_3 solid solutions. Below 150 K, however, the figure-of-merit of these materials drops dramatically. At 80 K the figure-of-merit of the best materials for the positive leg does not exceed $1.4 \cdot 10^{-3}$ K^{-1}.[4] Reports have appeared recently of the possibility of preparing Bi_2Te_3-Sb_2Te_3 samples with $Z = 2.2 \cdot 10^{-3}$ K^{-1} using an extrusion technique at 80 K.[5]

The only efficient thermoelectric material for use below 150 K is the single-crystal n-type $Bi_{1-x}Sb_x$ solid solution. The figure-of-merit of undoped $Bi_{0.85}Sb_{0.15}$ samples along the trigonal axis is $6.5 \cdot 10^{-3}$ K^{-1} at 80 K.[6] If a magnetic field of 1.5 kÖe is applied along the bisector axis, the Seebeck coefficient and electrical resistivity increase simultaneously by 50 to 60% with a slight decrease of the thermal conductivity. As a result, the value of the figure-of-merit increases to $11 \cdot 10^{-3}$ K^{-1}.[6]

If a magnetic field is applied, the figure-of-merit of a thermoelement made of the best active n- and p-legs mentioned above would not exceed $4.9 \cdot 10^{-3}$ K^{-1}, which is less than the corresponding value for $Bi_{0.85}Sb_{0.15}$ by more than a factor of two. The maximum temperature drop across such an element at a hot junction temperature of 77 K, as calculated from the properties of these materials, is 10.7 K, whereas if an ideal passive leg were used in combination with $Bi_{0.85}Sb_{0.15}$, figure-of-merit of the thermoelement $Z = 11 \cdot 10^{-3}$ K^{-1}, the temperature drop could reach as much 18.7 K.

47.3 Passive Leg Materials

The HTCS material intended for use in the passive leg of a thermoelement should meet a number of requirements. It should have a low thermal conductivity, a high critical current density, also in an external magnetic field, and the electrical resistance of contacts to the HTCS leg should not exceed 10^{-5} ohm · cm^2 (per unit area).

Two classes of HTCS materials are presently available, namely, those based on yttrium ($YBa_2Cu_3O_{7-x}$) and on bismuth (the Bi-Sr-Ca-Cu-O system). Of these, the lowest thermal conductivity is found in the bismuth-containing superconductors: $\lambda_{77K} = 0.7$ to 2.0 W/m · K, compared with $\lambda_{77K} = 3.0$ to 6.0 W/m · K for the yttrium-based superconductors.[7,8] The low thermal conductivity of the bismuth-based superconductors (1.5 to 2 times smaller than that of $Bi_{1-x}Sb_x$) favors their use in passive legs.

The desire to reduce the heat losses associated with the finite thermal conductivity of the HTCS thermoelement materials forces one to reduce the cross-sectional area of the passive leg. However, this places ever more stringent constraints on the critical current density, (j_c), that the HTCS material is capable of sustaining. The optimum current density which provides the largest cooling effect with $Bi_{0.85}Sb_{0.15}$ is 55 to 60 A/cm^2. The current density in the passive leg will be greater by

S_n/S_p times, where S_i is the leg cross-sectional area. Apart from this, the active leg should be placed in a fairly strong magnetic field to reach the maximum figure-of-merit. Being of necessity in close vicinity to the active leg, the passive leg will be in the magnet's stray field, and it is known that in a magnet field, the critical current density of a superconductor decreases.

In the case of ceramic and polycrystalline HTCS samples the critical current density does not exceed $5 \cdot 10^2$ A/cm^2, while for high plasticity ribbons and wires of HTCS materials at 77 K and in magnetic fields of up to 1 T, j_c can reach 10^4 to 10^5 A/cm^2. In thin films the magnitude of j_c may be even higher.

Another essential condition for making a "good thermoelement" with an HTCS passive leg is a low contact resistance. An analysis of the dependence of a thermoelement's figure-of-merit on electric contact resistance (per unit area) to a HTCS leg shows that if the contact resistance exceeds $1 \cdot 10^{-5}$ ohm · cm^2, the Joulean heat dissipated in the contacts drastically degrades the thermoelement characteristics, the figure-of-merit reaching practically its maximum at a contact resistance of $1 \cdot 10^{-6}$ ohm · cm^2. The preparation of low-resistance contacts to HTCS materials is dealt with in a number of publications where a variety of methods are used to deposit silver or gold layers on the sample surface followed by annealing,[9] the resistance reached in this way being less than $1 \cdot 10^{-7}$ ohm · cm^2.

It is concluded that methods for preparing HTCS samples suitable for use as passive legs in a thermoelement are presently available.

47.4 Testing a Thermoelement with an HTCS Leg

The authors used as active leg material a single-crystal $Bi_{0.85}Sb_{0.15}$ sample grown by horizontal zone melting. The measured temperature dependencies of the thermoelectric properties of the crystal along the trigonal axis practically coincided with the data of Reference 6. The figure-of-merit measured at 80 K without a magnetic field is $6.7 \cdot 10^{-3}$ K^{-1} and it tends to increase with a further decrease of temperature.

Polycrystalline molten bismuth-strontium-calcium-copper-oxygen, $BiSrCaCu_2O_x$, samples with critical temperature of $T_c = 87$ K and critical current density at 77 K of $j_c = 120$ A/cm^2, were used as the passive leg. Low-resistance contacts were obtained by the electrolytic deposition of a silver layer with subsequent annealing; the contact resistance between the HTCS material and the silver layer at 77 K being less than $1 \cdot 10^{-6}$ ohm · cm^2.

The operating conditions of the passive leg can be improved by reducing the stray magnetic field in its vicinity through appropriate screening and removing it from the strong field area. Thermoelements with the traditional Π-shaped configuration (Figure 1a) and with aligned legs (Figure 1b) have been fabricated. In the absence of a magnetic field they exhibit practically the same results. When the active leg is placed in an external magnetic field, the thermoelement with a linear leg arrangement provides greater cooling. The cooling is improved further by screening the passive leg in the second case with superconducting plates (a superconductor is the best possible magnetic screen). The legs are 1 cm long, the $Bi_{0.85}Sb_{0.15}$ cross-sectional area is 0.11 cm^2, and the passive leg cross section is optimized in accordance with the well-known relations which take due account of the variation of the electrical resistivity along the $BiSrCaCu_2O_x$ leg in the presence of an inhomogeneous external magnetic field.

The parameters of the thermoelement are measured in a small evacuated cell fully immersed in liquid nitrogen. Liquid nitrogen temperature is appropriate for two reasons: the critical current density of a superconductor increases with decreasing temperature below T_c and, in addition, it provides a reliable reference measurement temperature. The hot and cold junction temperatures are measured with copper-constantan thermocouples, with the copper leg 0.02 mm, and constantan leg 0.1 mm in diameter; the junctions of the measuring thermocouples with copper wires are placed in liquid nitrogen and the temperature difference on the thermoelement determined to within 0.01 K. The thermoelement parameters in a magnetic field are measured using permanent ferrite magnets placed in the cell in the immediate vicinity of the active leg (Figure 1b) and in good thermal contact with the cell base. The optimum value of the magnetic field which provides the maximum thermoelement efficiency is 1.4 kÖe; this was determined experimentally by varying

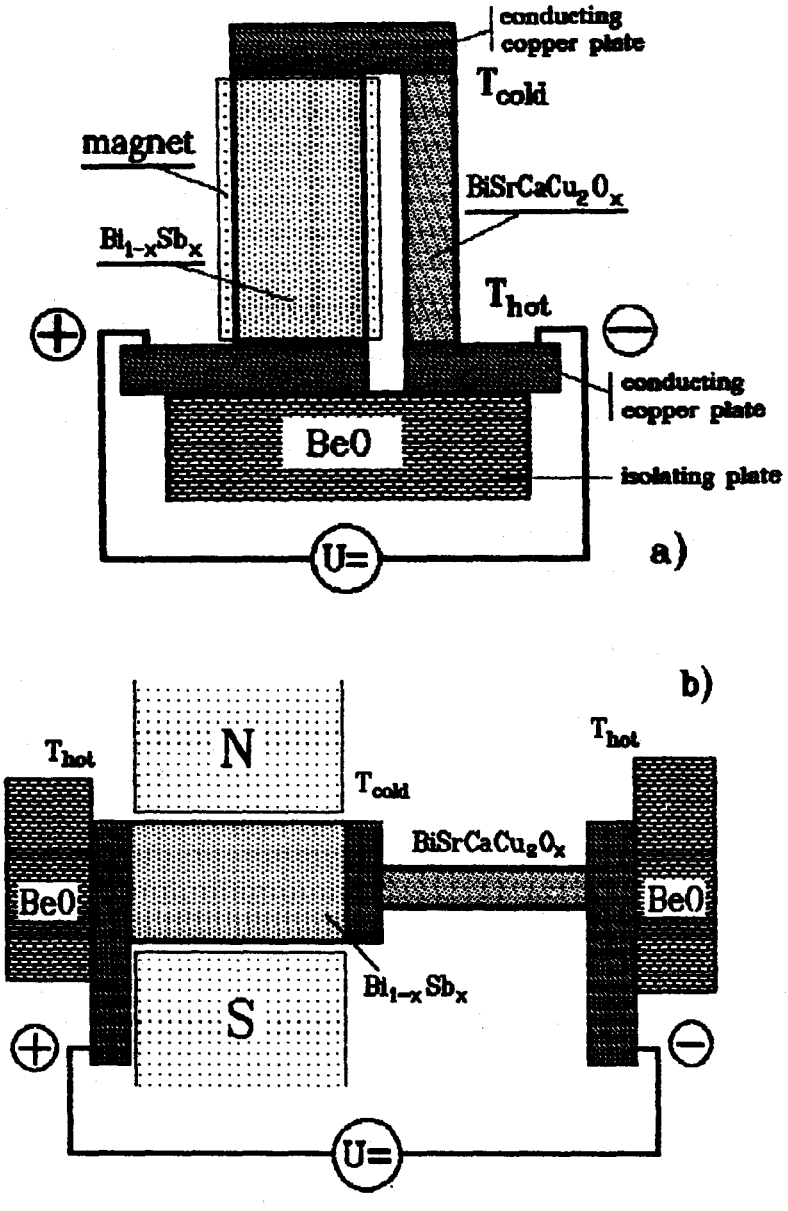

FIGURE 1 Thermoelement: (a) of traditional geometry, and (b) with linear leg configuration. $Bi_{1-x}Sb_x$ leg is placed between magnet poles.

the magnet pole gap. With a 1.4 kÖe magnetic field on the $Bi_{0.85}Sb_{0.15}$, the field strength on the $BiSrCaCu_2O_x$ varied from 0.2 kÖe at the end closest to the active leg to 0.03 kÖe at the farthest end.

The experimentally measured and calculated characteristics of the thermoelement with a linear leg arrangement are listed in Table 1 and displayed in Figure 2. The figure-of-merit of the thermoelement, Z_{exp}, is determined from the experimental values of ΔT_{max} using the relation $Z = (2 \cdot \Delta T_{max}) \cdot T_o^2$, where T_o is the cold junction temperature, and Z_{cal} is calculated from the leg material properties taking due account of the contact resistance, heat losses, and heat load introduced by the measuring thermocouple; ΔT_{max}^{cal} was calculated from Z_{cal}.

As seen from the table, with no magnetic field on the $Bi_{0.85}Sb_{0.15}$ leg the calculated and measured values are in good agreement. Taking into account unavoidable small losses, the figure-of-merit

Table 1 Experimentally Measured and Calculated Characteristics of Thermoelements

No.	T_{hot}, K	H, kÖe	ΔT_{max}^{exp}, K	ΔT_{max}^{cal}, K	Z_{exp}, K^{-1}	Z_{cal}, K^{-1}
1	78.5	0	13.4	13.6	$6.3 \cdot 10^{-3}$	$6.5 \cdot 10^{-3}$
2	78.3	1.4	16.4	—	$8.5 \cdot 10^{-3}$	—

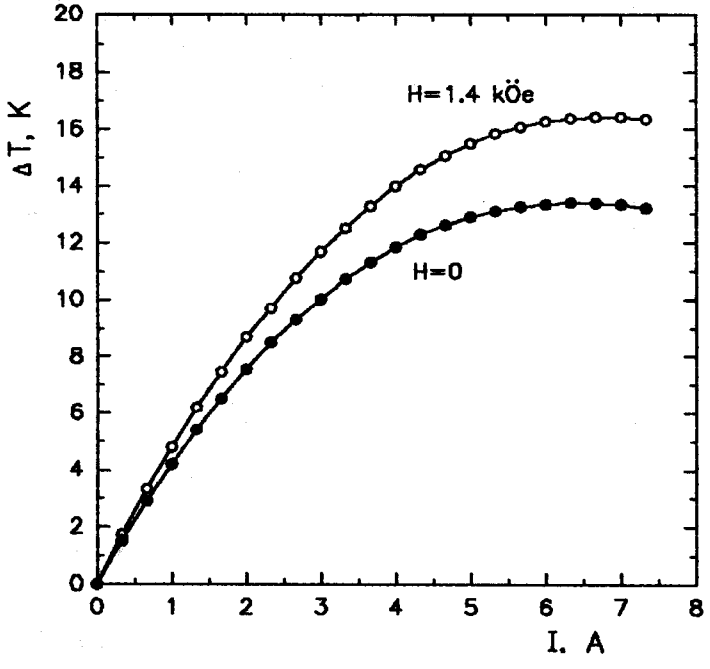

FIGURE 2 Temperature drop across thermoelement with passive leg vs. current through the thermoelement with and without magnetic field.

of the thermoelement is very close to that of the $Bi_{0.85}Sb_{0.15}$ active leg. The authors succeeded in fabricating a thermoelement with a practically ideal passive leg.

Since the characteristics of the $Bi_{0.85}Sb_{0.15}$ sample in the magnetic field were not measured, it was not possible in this case to calculate Z and ΔT_{max}. Recalling, however, the data cited above in Section 47.2, it is concluded that the experimentally measured figure-of-merit of the thermoelement in the magnetic field is considerably smaller than the limiting figure-of-merit value of the $Bi_{0.85}Sb_{0.15}$ leg. This may be due to an increase of the electrical resistivity of the passive leg in the external magnetic field. The fact is that the critical current density of the HTCS samples at the authors' disposal is not high enough. On increasing j_c the HTCS material can pass into a so-called "mixed state" of superconduction (for example, Reference 10). In connection with this phenomenon, the dependence of the resistivity of $BiSrCaCu_2O_x$ on magnetic field and current density has been studied at currents above the critical level, the measurements being performed at 77 K in magnetic fields that range from 0 to 1 kÖe, and at DC sample current densities from 10 to 350 A/cm^2 (Figure 3). As seen from the figure, when the current density in the sample exceeds the critical level, the resistivity of the HTCS material reaches a finite but very small value comparable with the resistivity of copper or silver at liquid nitrogen temperature. Note that while Joulean heat dissipation does occur, at certain current densities and magnetic fields it is not large. In addition it is smaller than the increment of the Peltier heat absorbed in the cold junction corresponding to the current increment. Thus, the limit to which the current through the passive leg can be increased is determined not by the critical current density of the HTCS material but rather by the permitted level of Joulean heat dissipation. The specific heats dissipated in $BiSrCaCu_2O_x$ are shown as dashed lines in Figure 3.

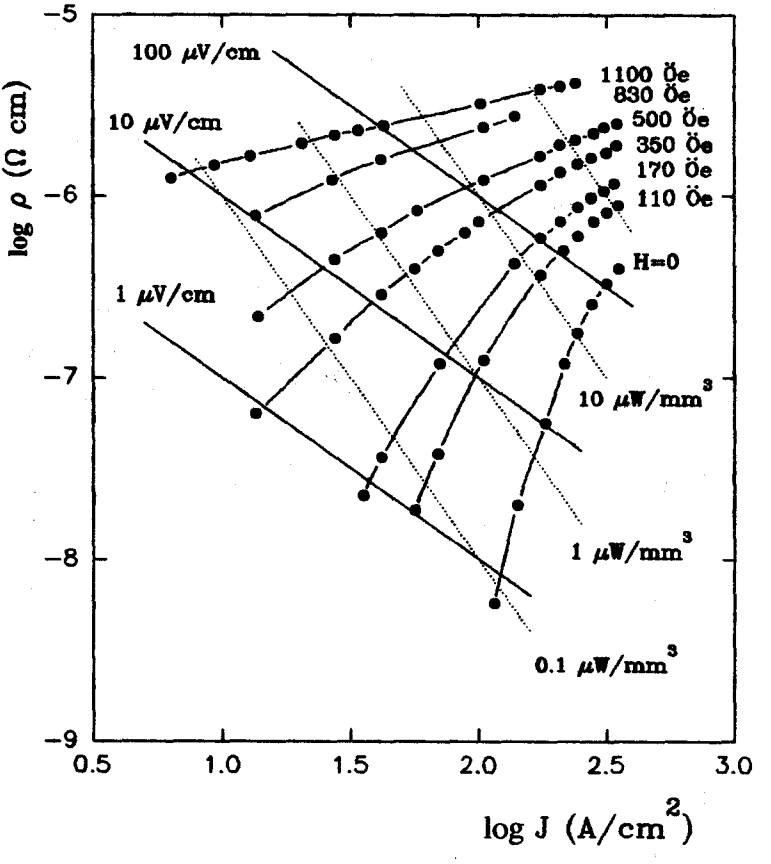

FIGURE 3 Resistivity of $BiSrCaCu_2O_x$ at 77 K vs. current density for different magnetic fields. Straight lines correspond to the same voltage drop per 1 cm of sample length, dashed lines connect points of equal heat generation in the sample.

The above experiments on the thermoelement at 77 K, and the natural interest in its behavior at other temperatures, prompted the authors to test the thermoelement with its linear leg maintained at various hot junction temperatures. The temperature could be lowered by pumping off the liquid nitrogen vapor and raised above 77 K by means of an electric heater located on the casing of the measuring cell. The results of the experiments are presented graphically in Figures 4 and 5. Figure 4 shows the maximum temperature drop across the thermoelement as a function of the hot junction temperature. Figure 5 also shows the dependence of the thermoelement figure-of-merit on the hot junction temperatures. The slight increase of the figure-of-merit observed to occur with decrease in temperatures (Figure 5) may be attributed to both a possible increase in the figure-of-merit of the $Bi_{0.85}Sb_{0.15}$ leg at $T < 80$ K, and an increase of critical current density in the passive leg as its temperature is decreased.

47.5 Conclusion

The fabrication of a thermoelement with a passive superconducting leg is the most recent development in thermoelectric energy conversion. Only one paper containing positive results has been published on this subject.[3] Consequently, further changes and improvements in thermoelement construction, together with optimization of material properties, are anticipated. The main result, however, has already been obtained: the fabrication of a new type of thermoelement with only one active leg. In addition, conversion characteristics are achieved that are equal to the calculated values. This means that the standard theory of thermoelectric conversion is totally applicable.

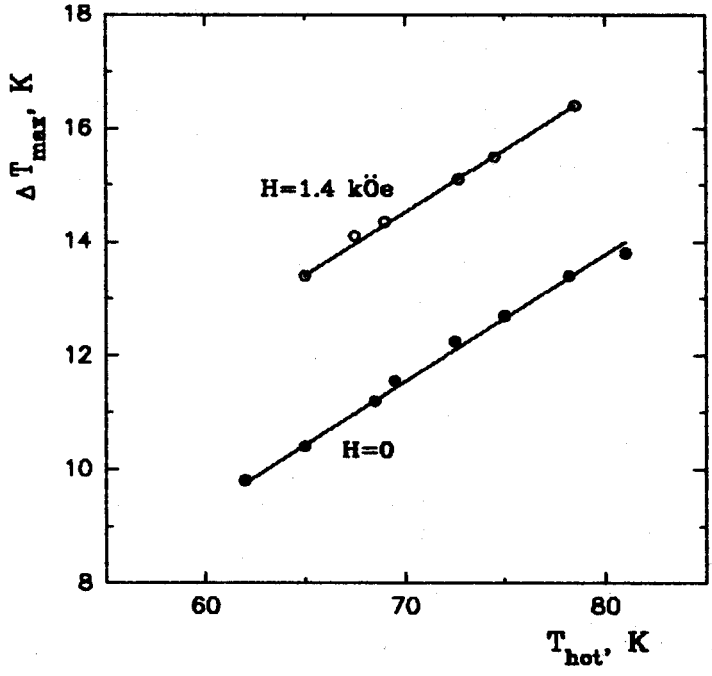

FIGURE 4 Maximum temperature drop across thermoelement with passive leg vs. hot junction temperature with and without magnetic field.

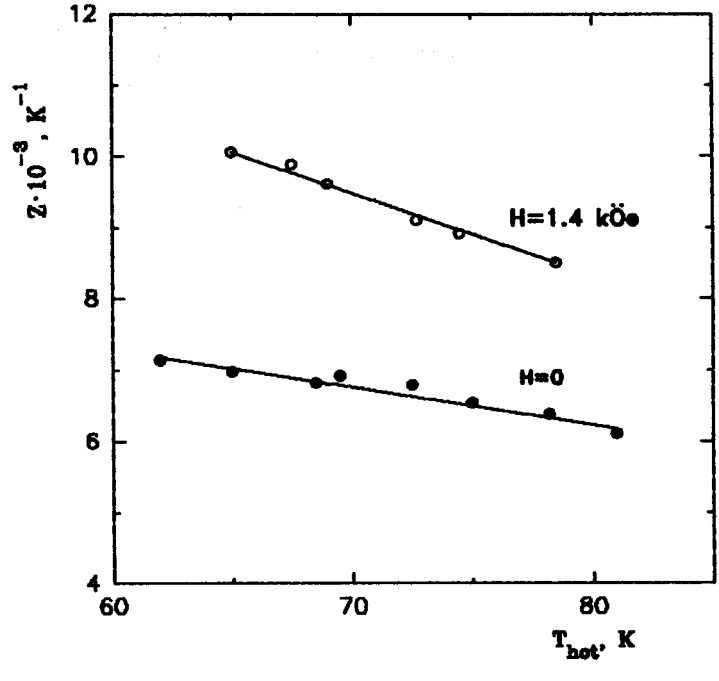

FIGURE 5 Figure-of-merit of thermoelement with passive leg vs. hot junction temperature with and without magnetic field.

Although at present there are no applications of this technology, it clearly would facilitate the operation of electronic sensors at liquid nitrogen temperatures with an accompanying reduction in noise level.

It is not easy to envisage the development of a thermoelectric material that operates more efficiently at this temperature than $Bi_{0.85}Sb_{0.15}$. However, it should be noted that undoped Bi-Sb solid solution was used in this investigation. A study of the effect of doping on the properties of this material at temperatures <77 K could provide useful information regarding possible improvements in the thermoelement.

The long-term reliability of the device and its response to cyclic operation should also be researched.

References

1. Ioffe, A. F., *Semiconductor Thermoelements and Thermoelectric Cooling,* Infosearch, London, 1957.
2. Goldsmid, H. J., Gopinathan, K. K., Matthews, D. N., Taylor, K. N. R., and Baird, C. A., High-T_c superconductors as passive thermoelements, *J. Phys. D,* 21, 344, 1988.
3. Kuznetsov, V. L., Vedernikov, M. V., Ditman, A. B., Melekh, B. T., and Burkov, A. T., The effective thermoelement with thermoelectrically passive leg from high-Tc superconductor, in *Superconductivity: Physics, Chemistry, Technology* (in Russian), 4, 616, 1991.
4. Yim, W. M. and Rosi, F. D., Compound tellurides and their alloys for Peltier cooling—a review, *Solid State Electron.,* 15, 1121, 1972.
5. Kolomoets, N. N., Skipidarov, S. Ya., Sidorenko, N. A., and Erofeev, R. S., Cryogenic temperature level thermoelectric coolers, in *Proceedings of the IXth International Conference on Thermoelectrics,* March 19–21, 1990, 128.
6. Yim, W. M. and Amith, A., Bi-Sb alloys for magneto-thermoelectric and thermomagnetic cooling, *Solid State Electron.,* 15, 1141, 1972.
7. Ctirad, U., Thermal conductivity of high-T_c superconductors, *J. Supercond.,* 3, 337, 1990.
8. Kirichenko, Yu. A., Rusanov, K. B., and Tyurina, E. G., Thermal conductivity of high-T_c superconductors. Survey of experimental data, *Superconductivity: Physics, Chemistry, Technology* (in Russian), 3, 1385, 1990.
9. Ekin, J. W., Larson, T. M., Bergren, N. F., Nelson, A. J., Swartzlander, A. B., Kazmerski, L. L., Panson, A. J., and Blankenship, B. A., High-T_c superconductor/noble-metal contacts with surface resistivities in the $10^{-10}\ \Omega \cdot cm^2$ range, *Appl. Phys. Lett.,* 52, 1819, 1988.
10. Rose-Innes, A. C. and Rhoderick, E. H., *Introduction to Superconductivity,* 2nd ed., Pergamon, New York, 1978.

Section H
Applications of Thermoelectric Cooling

48
Introduction

H. J. Goldsmid
University of New South Wales
Australia

When rapid improvements in the materials for Peltier cooling were made in the 1950s, notably by the introduction of semiconductor thermoelements,[1] there was some hope that this form of refrigeration would make all other techniques superfluous. Then, when further progress seemed slow, doubts began to be expressed as to the possibility of thermoelectric refrigeration having any real use whatever and, indeed, most of the world's leading electrical manufacturers withdrew from the field. Eventually it was realized that thermoelectric refrigerators possess unique advantages that make them the best solution to many problems, but they also have disadvantages that inhibit their use in many important areas.

Conventional refrigerators fall into two distinct classes. Most make use of mechanical pumps to actuate the compression and expansion of selected gases according to the principles of thermodynamics. There are also so-called absorption refrigerators that utilize some source of heat to drive, for example, ammonia out of solution and through a thermodynamic cycle. Before the advent of thermoelectric cooling, both types of refrigerator were to be found performing virtually all everyday tasks at ordinary temperatures.

Absorption refrigerators have the advantage of being noiseless and they can be operated from any heat source, e.g., oil or gas burners, so that they are useful in applications where main electricity is not available. One of their disadvantages is that they have a relatively low coefficient of performance. This is essentially because they combine a heat engine and a heat pump in one device. Thus, the overall coefficient of performance is the product of that of the heat pump and the efficiency of the heat engine (which must, of course, be less than unity). Another disadvantage is that they will not work properly if they are tilted and this makes them unsuitable for many marine applications.

Mechanical refrigerators can have remarkably high coefficients of performance, sometimes achieving a large fraction of the ideal thermodynamic value $T_1/(T_2 - T_1)$ where T_1 is the source temperature and T_2 is the sink temperature. They are also very reliable, in spite of their moving parts, operating for many years without any form of maintenance. However, they too have their

0-8493-0146-7/95/$0.00+$.50

disadvantages. They are never silent and can only achieve their potentially high coefficient of performance when the cooling power is large and the load is more or less constant. In order to adjust to some intermediate load, a mechanical refrigerator cannot be operated at reduced power but has to cycle between the "on" and "off" modes. This, for example, makes it particularly difficult to obtain a steady temperature in any enclosure that is cooled by a mechanical refrigerator. More recently, another disadvantage of mechanical refrigerators has become apparent. The special gases that are used as the working fluid often eventually find their way into the atmosphere, where they are known to have harmful environmental effects.

Thermoelectric refrigerators, it must be admitted, are generally much less efficient than mechanical refrigerators when the latter are operating under the conditions that suit them best. The maximum coefficient of performance ϕ_{max} of a Peltier cooler may be written as

$$\phi_{max} = \frac{T_1}{T_2 - T_1} \cdot \frac{[(1 + ZT_M)^{1/2} - T_2/T_1]}{[(1 + ZT_M)^{1/2} + 1]} \tag{1}$$

where Z is the figure-of-merit and T_M is the mean temperature. For the best materials that are available at present, $(1 + ZT_M)^{1/2}$ is equal to about 1.4. Since T_2/T_1 is close to unity for most refrigeration applications, the second fraction on the right-hand side of Equation 1 has a value close to 1/6, which means that the thermoelectric device has only about 17% of the ideal thermodynamic coefficient of performance. However, unlike mechanical refrigerators, they can maintain their efficiency down to very low cooling powers, of the order of milliwatts. The coefficient of performance, in fact, does not compare badly with that of an absorption refrigerator but it must, of course, be operated from an electrical source. The fact that a thermoelectric refrigerator is preferentially powered by a low-voltage direct current may or may not be a disadvantage, depending on the circumstances. It is no disadvantage, for example, if the refrigerator has to work directly from an automobile battery.

Thermoelectric refrigerators are silent and have neither moving parts to wear out nor gases to leak away. The fact that they are solid-state devices should give them an extremely long life, but this can only be achieved in practice if care is taken in the design and construction. For example, it is known that bismuth telluride thermoelements are sensitive to contamination by copper[2] and it is necessary to prevent diffusion of this element into the material both during manufacture of the modules and during their subsequent operation.

Perhaps one of the greatest advantages of thermoelectric refrigerators is their flexibility. Although they reach their maximum coefficient of performance (COP) only when operated with a specified load, the COP does not fall too disastrously if the conditions are varied. Suppose, for example, that a thermoelectric refrigerator is operated under the condition of maximum cooling power rather than maximum COP. The coefficient of performance then becomes

$$\phi_q = \frac{Z\,T_1^2/2 - (T_2 - T_1)}{Z\,T_1 T_2} \tag{2}$$

Consider a particular case with $Z = 3 \times 10^{-3}\ K^{-1}$, $T_1 = 250$ K, and $T_2 = 300$ K. We find that the maximum cooling power is about 1.7 times the cooling power for optimum COP. From Equations 1 and 2 we find that the coefficients of performance ϕ_{max} and ϕ_q are 0.32 and 0.19, respectively. In other words, the increased cooling power has been achieved at the cost of reducing the COP to some 60% of its maximum value.

The real benefit that stems from the flexibility of a thermoelectric refrigerator is its ability to operate in conjunction with a proportional control system rather than an on-off system. This means that thermoelectric coolers can be used to maintain enclosures at steady rather than fluctuating temperatures.

Perhaps the types of situation in which thermoelectric refrigerators are most suitable can best be appreciated by discussing some specific examples. Thus, portable boxes incorporating Peltier cooling have been available for many years,[3] being employed for carrying medical supplies and for the storage of perishable goods in automobiles. On the other hand, Peltier devices have so far found little use in larger domestic or industrial refrigerators. It is probably for this reason that one

often hears of an arbitrary upper limit of about 10 W of cooling power for practical thermoelectric devices. As shall be demonstrated, however, such a limit is quite artificial.

Perhaps the widest application of thermoelectric cooling has been in the control of temperature, particularly for scientific instruments and for electronic and optoelectronic systems. For example, as long ago as 1964, Wennerberg[4] was able to maintain an enclosure at 25°C to within 0.2°C with a load of 2.75 W and ambient temperatures ranging from −29°C to 85°C. Under more restricted conditions, much better control of temperature can be achieved. Thus, by utilizing the expansion of water on freezing to operate a switching system it has been possible to maintain the reference junctions of measurement thermocouples at within 10^{-2}°C of the ice point.[5] Another application that originates from the early days of semiconductor thermoelements is in dew-point hygrometry where the metallic link between the two branches of a refrigerating couple has formed the mirror on which condensation takes place.[3] Sometimes, accurate control of temperature is not needed but rather the reduction of temperature of some device so that its efficiency is improved or, perhaps, so that it can actually operate. Examples are to be found in the cooling of lasers[6] and infrared detectors.[7,8] In such cases it is the convenience of thermoelectric refrigeration for small-scale applications that is the key factor.

At the other extreme, we may discuss the use of the Peltier effect in air conditioning. Here the temperature differences are always well within the capacity of thermoelectric heat pumps, but one might expect the relatively poor coefficient of performance to be an insuperable disadvantage. However, the widely variable load causes some difficulty when the usual mechanical systems are employed and this allows the Peltier effect to become economically competitive. One of the most thorough assessments of thermoelectric air conditioning has been carried out by Stockholm et al.,[9] who installed such a system in a train carriage on the French railways. The consistent and reliable performance of the equipment was remarkable. Other successful large-scale applications, including a 27-kW industrial water cooler, have been described by Buffet and Stockholm.[10,11]

There is plenty of scope for thermoelectric refrigeration, even if new materials are not found, and if improved figures-of-merit can be obtained, the possibilities seem boundless.

References

1. Ioffe, A. F., *Semiconductor Thermoelements and Thermoelectric Cooling*, Infosearch, London, 1957.
2. Carlson, R. O., *J. Phys. Chem. Solids*, 13, 65, 1960.
3. Bean, J. E., *Ind. Electron.*, 1, 132, 1962.
4. Wennerberg, A. L., *Rev. Sci. Instrum.*, 35, 1191, 1964.
4. Goldsmid, H. J., *Thermoelectric Refrigeration*, Plenum, New York, 1964.
6. Matsumoto, K., Shirahata, H., and Fujioka, T., *Jpn. J. Appl. Phys.*, 19, 2187, 1980.
7. McMullan, D. and Oliver, M., *J. Phys. E.*, 1, 1255, 1968.
8. Marlow, R., Buist, R. J., and Nelson, J. L., *Proceedings, Fifth International Conference on Thermoelectric Energy Conversion*, Arlington, Texas, IEEE, New York, 1984, 125.
9. Stockholm, J. G., Pujol-Soulet, L., and Sternat, P., *Proceedings, Third International Conference on Thermoelectric Energy Conversion*, Arlington, Texas, IEEE, New York, 1982, 136.
10. Buffet, J. E. and Stockholm, J. G., *Proceedings, Eighteenth Intersociety Energy Conversion Engineering Conference*, Orlando, Florida, American Institute of Chemical Engineers, New York, 1983, 253.
11. Buffet, J. E. and Stockholm, J. G., *Proceedings, Fifth International Conference on Thermoelectric Energy Conversion*, Arlington, Texas, IEEE, New York, 1984, 95.

49

Commercial Peltier Modules

Kin-ichi Uemura
Institute for Thermoelectric Technologies
Yokohama, Japan

49.1 Introduction

A brief description of commercial modules is given. The modules can be characterized by four parameters: I_{max}, ΔT_{max}, Q_{c-max}, and V_{max}. Values of these parameters are given in graphs and in a table. The intermediate values of I, ΔT, Q_c, and V can be obtained from universal graphs. Numerical examples show how to use the graphs and choose a module that satisfies the given requirements.

49.2 Single-Stage Peltier Module

Construction

A Peltier module is composed of thermoelectric couples, connected electrically in series and thermally in parallel, and integrated between two ceramic plates. These plates form the cold and hot surfaces of the module and provide sound mechanical integrity and high electrical insulation from, as well as good thermal conduction to, the heat sink and body to be cooled. A single-stage Peltier module configuration is shown in Figure 1.

There are still modules without ceramic plates. On the one hand they have the advantage of eliminating the thermal resistance of the ceramic plates, on the other hand they also have the disadvantage of mechanical fragility and they require electrical insulation.

The thermoelectric couple consists of n- and p-type semiconductor material. For thermoelectric cooling a quaternary alloy of bismuth, tellurium, selenium, and antimony is used—heavily doped to create either an excess (n-type) or a deficiency (p-type) of electrons. The doping is required to produce extensive thermoelectric cooling, thus yielding higher performance.

0-8493-0146-7/95/$0.00+$.50

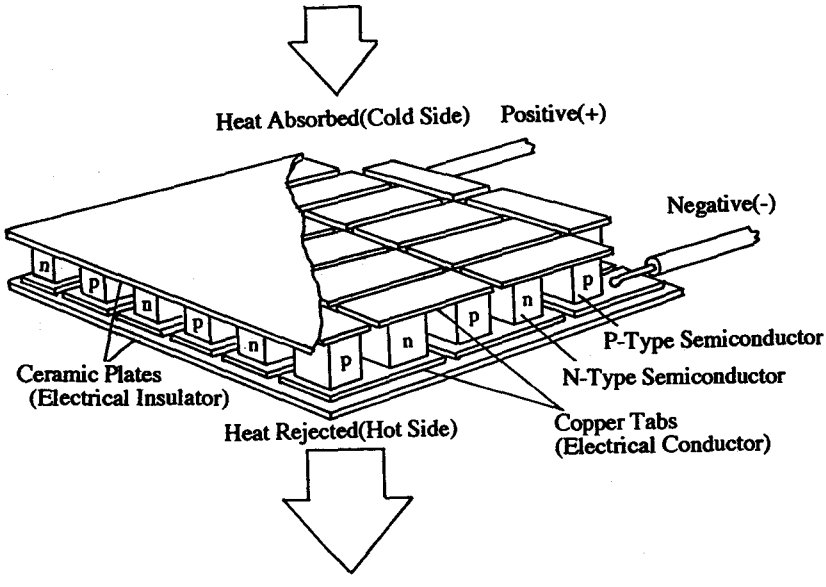

FIGURE 1 Single-stage Peltier module configuration.

Performance

Maximum Performance Parameters

Commercial Peltier modules are available in a great variety of sizes, shapes, operating currents, operating voltages, and ranges of cooling powers. The thermoelectric couple can be produced for an optimum operating current which defines the dimensions of the thermoelectric elements. We denote the geometric factor, G, of the element as the cross-sectional area A (m^2) divided by the length L (m): G = A/L (m). The cooling power of the module is proportional to the geometric factor G, and the number of the thermoelectric couples N.

Four maximum performance parameters with a hot junction temperature fixed at 298 K (25°C) or 300 K (27°C) are provided on the table and graphs for commercial single-stage Peltier modules:

- I_{max} (A): DC current that yields the maximum junction temperature difference ΔT_{max}; the cooling power is equal to zero, which means that there is no heat load on the cooled side. I_{max} is not a maximum value of I, but corresponds to the value of the current which gives ΔT_{max}.
- ΔT_{max} (K): the maximum junction temperature difference across the module at I_{max} with no heat load. The ΔT_{max} of commercial single-stage modules is about 67 to 70 K with the hot junction temperature at 300 K (27°C).
- Q_{c-max} (W): the cooling power that corresponds to a temperature difference across the module of $\Delta T = 0$ with current I_{max}.
- V_{max} (V): the terminal voltage for I_{max} with no heat load.

As all the physical properties of the thermoelectric material are dependent on temperature, the module's performance is temperature dependent and increases with increasing temperature over the operating hot junction temperature range, 123 K (−150°C) to 353 K (+80°C). The maximum parameters at an optimum hot junction temperature of T_h (K) can be estimated roughly for the commercial modules that are presented from Figure 2 or from the equations:

$$(\Delta T_{max})_{Th} = 67K + 0.4(T_h - 300) \quad (1)$$

$$(Q_{c-max})_{Th} = (Q_{c-max})_{300K} + 2.0(T_h - 300) \cdot G \cdot N \quad (2)$$

$$(V_{max})_{Th} = (V_{max})_{300K} + 0.0007(T_h - 300) \cdot N \quad (3)$$

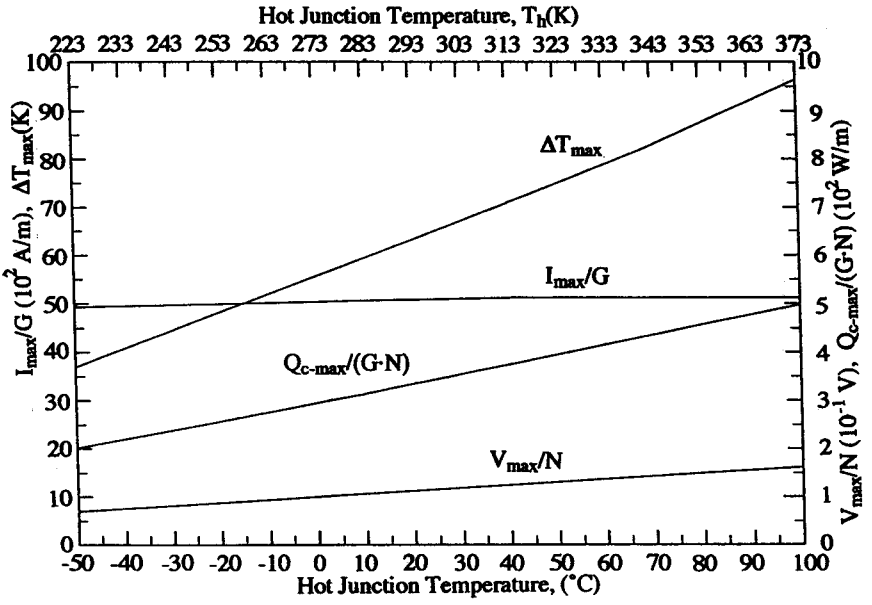

FIGURE 2 Maximum performance parameters of single-stage Peltier modules as a function of hot junction temperature, T_h.

I_{max} is virtually unaffected by the hot junction temperature T_h, and I_{max}/G is equal to about 5×10^3 A/m.

Commercial Single-Stage Peltier Modules

The commercial single-stage Peltier modules cover a wide range of ceramic face sizes from 1.8 × 3.4 mm^2 to 62 × 62 mm^2 and heights from 2.45 mm to 5.8 mm with Q_{c-max} from 0.2 to 125 W; I_{max} from 0.8 to 60 A; V_{max} from 0.4 to 15.4 V; and number of couples from 4 to 127. Figure 3 shows the maximum cooling powers Q_{c-max} of the leading commercial single-stage modules with hot junction temperature at 298 K (25°C) or 300 K (27°C) with their corresponding electrical input values, I_{max} and V_{max}.

Universal Characteristics

In practice, the modules are operated under conditions that satisfy the particular requirements of the application:

T_c (K): the temperature of the cold junctions
T_h (K): the temperature of the hot junctions
ΔT (K) = $T_h - T_c$: the junction temperature difference
Q_c (W): the cooling power, i.e., the amount of heat load to be absorbed by the cold junctions
Q_h (W): the amount of heat dissipated at the hot junctions
I (A): the applied current
V (V): the terminal voltage
P (W): the electrical input power, equal to I · V

The coefficient of performance, COP, is defined as the cooling power Q_c divided by the input electrical power P: Q_c/P. All these values have an interdependent relationship with each other which is specific to each module. These universal characteristics are a nondimensional presentation of the parameters $\Delta T/\Delta T_{max}$, I/I_{max}, Q_c/Q_{c-max}, V/V_{max} available for a wide range of hot junction temperatures.[1]

Figure 4 shows the universal relationship (chart I) between the operating current ratio I/I_{max}, the cooling power ratio Q_c/Q_{c-max}, and the coefficient of performance COP, as a function of the

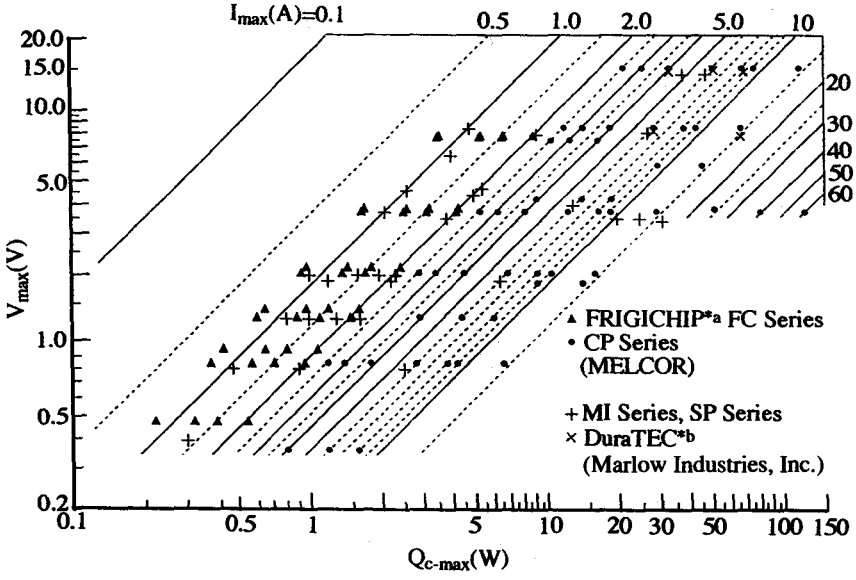

FIGURE 3 Maximum cooling powers Q_{c-max} of commercial single-stage Peltier modules, with hot junction temperature at 298 K (25°C) or 300 K (27°C), with their corresponding electrical input values I_{max} and V_{max}. *a, registered trademark of Materials Electronic Products Corporation, MELCOR, Trenton, NJ; *b, trademark of Marlow Industries Inc., Dallas, TX.

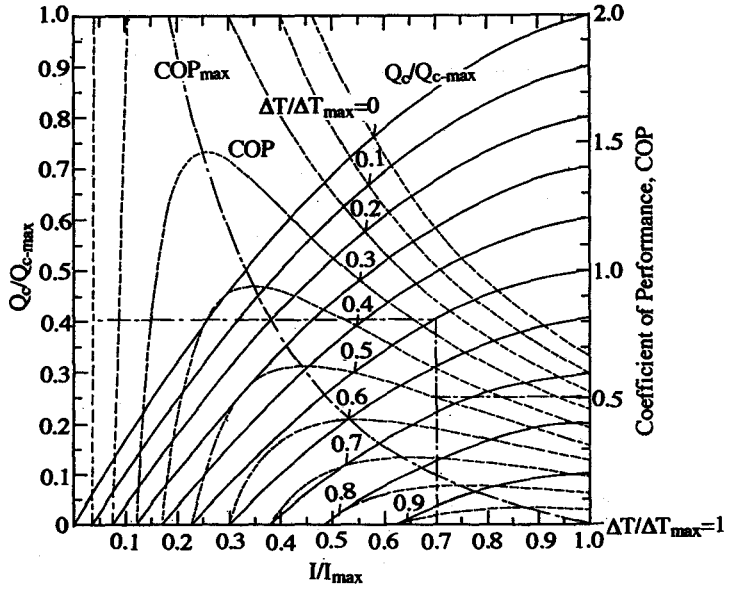

FIGURE 4 Universal chart I for commercial single-stage Peltier modules.

junction temperature difference ratio $\Delta T/\Delta T_{max}$. The higher the operating current ratio I/I_{max}, the greater the cooling power ratio Q_c/Q_{c-max}. As the current ratio I/I_{max} is decreased, the COP increases to the COP_{max} and then decreases. The higher the COP for a given cooling power the lower the ratio of electrical input power/cooling power and the heat generated at the hot junctions which must be dissipated by the heat dissipating exchanger. A suitable operating current is between the values corresponding to COP_{max} and I_{max}.

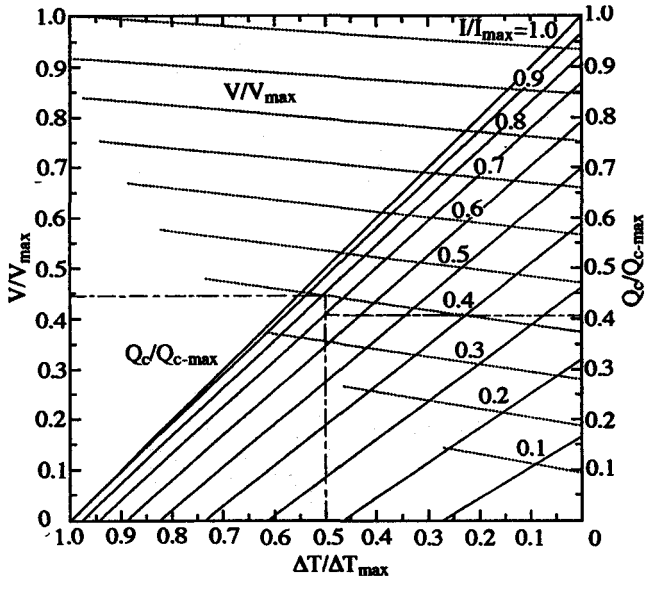

FIGURE 5 Universal chart II for commercial single-stage Peltier modules.

Figure 5 shows the universal relationship (chart II) between the three parameters operating junction temperature difference ratio $\Delta T/\Delta T_{max}$, the terminal voltage ratio V/V_{max}, and the cooling power ratio Q_c/Q_{c-max}, as a function of the operating current ratio I/I_{max}.

49.3 Multistage Peltier Module

Construction

The junction temperature difference ΔT of a single-stage Peltier module cannot exceed the maximum value ΔT_{max} given in Figure 2, and Figure 4 shows that when ΔT is equal to ΔT_{max} the cooling power Q_c and the COP are both zero for the single-stage Peltier modules. However, this limitation can be overcome by using several stages. A multistage Peltier module is essentially two or more single-stage Peltier modules stacked on top of each other. When the top stage is used for cooling then the lower stage requires greater cooling power to pump the heat dissipated by the upper stages. Therefore, when the module of each stage has the same thermoelectric elements with the same geometric factor G, all connected electrically in series, a lower stage requires more couples than an upper one. Figure 6a shows the configuration of a typical pyramid-shaped three-stage Peltier module. Figure 6b shows a configuration of a two-stage Peltier module in which the upper module consists of the same number of couples as the lower, but the geometric factor G is one half of the lower. The upper module is divided into halves which are connected in parallel.

Performance

Maximum Performance Parameters

The four maximum performance parameters I_{max}, ΔT_{max}, Q_{c-max}, and V_{max} with a hot junction temperature of the bottom module fixed at 300 K (27°C) are given for multistage commercial Peltier modules. Their definitions are the same as those for single-stage modules. However, the maximum temperature difference ΔT_{max} of a multistage is determined by the number of stages.

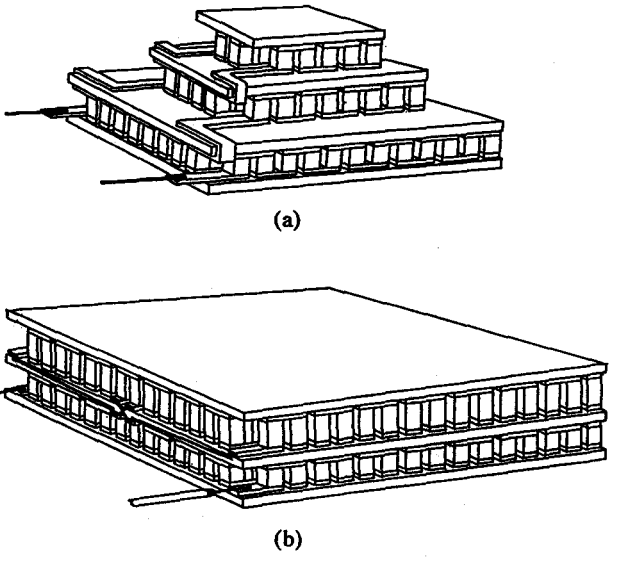

FIGURE 6 Multistage Peltier module configurations. (a) Three-stage Peltier module; (b) two-stage Peltier module.

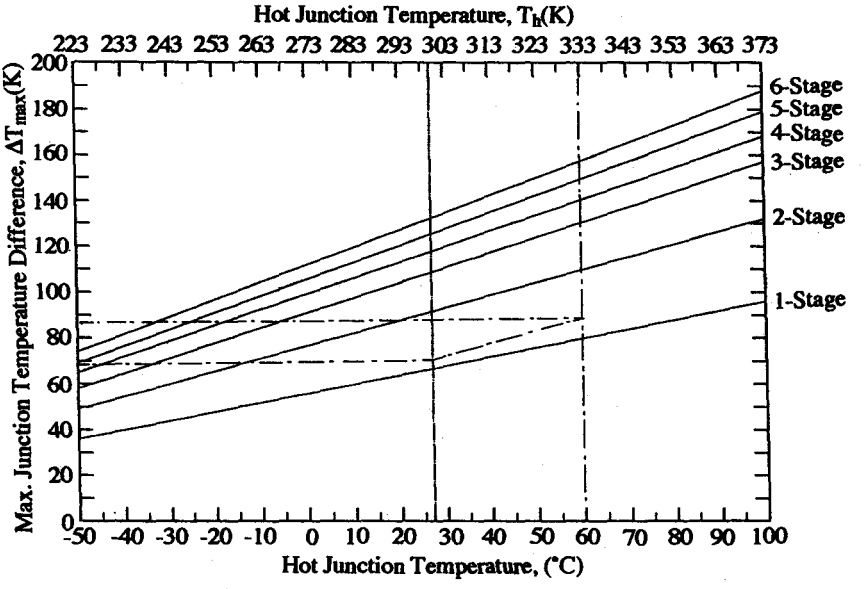

FIGURE 7 ΔT_{max} of multistage Peltier modules, as a function of bottom stage hot junction temperature T_h, for constant current = I_{max}.

Figure 7 shows the ΔT_{max} of multistage Peltier modules as a function of the bottom stage hot junction temperature T_h, for constant current I_{max}.

Commercial Multistage Peltier Modules

Commercial multistage Peltier modules cover a range of ceramic face sizes from 3.2 × 3.2 mm^2 to 62 × 62 mm^2 at the top (cooling side) and from 3.8 × 3.8 mm^2 to 62 × 62 mm^2 at the base (heated side), and heights from 3.8 to 21.4 mm with: I_{max} (A) from 0.7 to 9.5 A; Q_{c-max} (W) from 0.39 to 59 W; V_{max} (V) from 0.8 to 14 V; and number of stages from two to six. Table 1 shows

Table 1 Maximum Performance Parameters of Commercial Multi-Stage Peltier Modules, with Bottom Stage Hot Junction Temperature at 300 K (27°C)

Number of Stages (refers to graphs)	Model	ΔT_{max} (K)	Q_{c-max} (W)	I_{max} (A)	V_{max} (V)
2-Stage:					
(2- 1)	MI2022T	89	0.39	1.4	0.8
(2- 2)	2 CP 040 080–7-2	92	0.42	2.0	0.9
(2- 3)	MI2011T	90	0.47	0.7	1.9
(2- 4)	MI2021T	91	0.92	1.4	2.0
(2- 5)	MI2060	96	1.1	5.5	0.8
(2- 6)	SP1548	89	1.9	1.4	4.4
(2- 7)	2 CP 040 050–17–7	87	2.00	2.94	2.1
(2- 8)	MI2012T	86	2.4	1.2	5.4
(2- 9)	SP1412	84	3.1	1.9	3.9
(2–10)	2 CP 040 065–71–17	94	4.61	2.56	8.6
(2–11)	2 CP 040 065–127–31	94	8.40	2.57	15.5
(2–12)	MI2064	99	9.6	5.6	8.2
(2–13)	2 CP 085 100–71–17	94	13.67	7.7	8.6
(2–14)	MI2063	91	14.0	5.0	8.4
(2–15)	2 SC 040 050–127–63	84	16.2	2.8	15.6
(2–16)	2 CP 055 045–127–31	94	23.54	7.18	15.5
(2–17)	2 SC 055 045–127–63	84	34.83	5.96	15.6
(2–18)	2 SC 085 065–127–70	84	59.8	9.54	15.6
(2–19)	2 CP 085 065–127–71	82	60.09	9.49	15.7
3-Stage:					
(3- 1)	MI3021T	110	0.33	1.3	1.9
(3- 2)	3 CP 040 080–17–7-2	108	0.45	1.7	2.1
(3- 3)	MI3026T	109	0.62	1.3	3.4
(3- 4)	SP1056	105	5.6	4.5	7.3
(3- 5)	MI3040	109	5.6	4.5	7.3
(3- 6)	3 CP 085 065–71–17–7	109	8.7	10.1	7.9
(3- 7)	3 CP 085 065–127–71–31	98	30.27	8.3	15.5
4-Stage:					
(4- 1)	MI4010T	117	0.17	1.2	1.9
(4- 2)	MI4000T	110	0.43	0.6	7.0
(4- 3)	4 CP 040 080–71–17–7-2	124	0.52	1.67	7.6
(4- 4)	MI4012T	114	0.76	1.0	6.7
(4- 5)	MI4040	120	2.7	4.0	6.8
(4- 6)	4 CP 085 065–71–17–7-2	124	2.99	9.49	7.6
(4- 7)	4 CP 085 065–127–71–31–17	108	16.5	7.43	14.8
5-Stage:					
(5- 1)	5 CP 040 080–71–31–17–7-2	126	0.5	1.38	8.1
(5- 2)	5 CP 040 065–127–71–31–17–7	120	1.76	1.55	14.6
(5- 3)	5 CP 085 065–127–71–31–17–7	120	8.13	7.18	14.6
6-Stage:					
(6- 1)	MI6010T	122	0.31	0.7	5.8
(6- 2)	MI6020	122	0.28	1.8	6.4
(6- 3)	6 CP 040 080–127–71–31–17–7-2	132	0.52	1.25	14.6
(6- 4)	MI6030	133	0.58	3.6	6.3
(6- 5)	6 CP 055 065–127–71–31–17–7-2	132	1.24	2.99	14.6
(6- 6)	6 CP 085 085–127–71–31–17–7-2	132	2.95	7.15	14.6

Note: MI Series, SP series (Courtesy of Marlow Industries, Inc.)

SC Series, CP series Partial List of Cascades (Courtesy of Materials Electronic Products • MELCOR supplies custom designed multi-stage modules to meet customer's requirements).

the maximum performance parameters ΔT_{max}, Q_{c-max}, I_{max}, and V_{max} of the leading commercial multistage Peltier modules. The cooling power Q_c and the temperature difference ΔT can be calculated approximately from the equations:

$$Q_c = Q_{c-max} \cdot (1 - \Delta T/\Delta T_{max}) \tag{4}$$

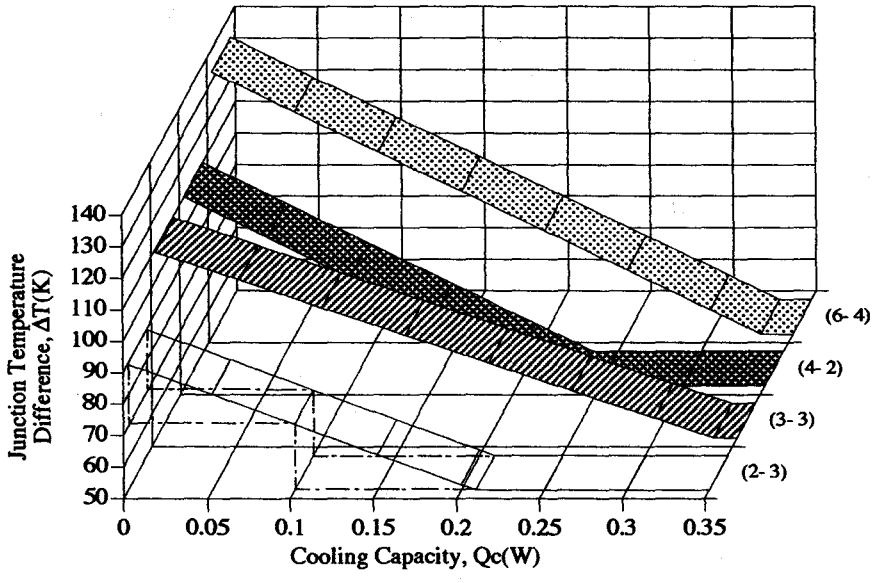

FIGURE 8 Cooling powers Q_c of commercial multistage Peltier modules for junction temperature difference ΔT, with bottom stage hot junction temperature at 300 K (27°C) – (I).

$$\Delta T = \Delta T_{max} \cdot (1 - Q_c/Q_{c-max}) \tag{5}$$

Figures 8 and 9 show the cooling powers Q_c of the several leading commercial standard multistage Peltier modules for the junction temperature difference ΔT above 50 K, with the bottom stage hot junction temperature at 300 K (27°C).

49.4 Selection of a Peltier Module

Thermal Resistances

Most of the performance curves described above are based on the cold and hot junction temperatures T_c, T_h of the thermoelectric couples in the Peltier modules. To select the Peltier module to satisfy the requirements, three specific module parameters must be determined:

T_c (K): the cold junction temperature
T_h (K): the hot junction temperature
Q_c (W): the cooling power, i.e., the amount of heat load to be removed by the cold side of the Peltier module

However, in an actual thermoelectric cooling system the interfacing layers, i.e., the electrical insulators, the thermal grease or adhesive, and the heat exchangers serve to inhibit the flow of heat through the system. We denote W_c (K/W) and W_h (K/W) as the cold- and hot-side thermal resistances of the system. So the cold junction temperature T_c is $\Delta T_c = Q_c W_c$, cooler than the ultimate desired temperature of the body T_{c-bod} by $\Delta T = Q_c W_c$, and the hot junction temperature T_h rises by $\Delta T_h = Q_h W_h$ above the ambient temperature T_{amb}. The effective temperature difference ΔT_{ef} for practical use is $\Delta T_{ef} = T_{amb} - T_{c-bod}$. If the body to be cooled is in direct contact with the cold ceramic plate of the Peltier module, the temperature of the cooled body can be considered to be the same as the temperature of the cold junctions of the Peltier module, $T_c = T_{c-bod}$ for the steady-state heat loads.

The thermal resistances W_h and W_c of the thermoelectric cooling units or systems are

1. From 2.0 to 0.5 K/W for natural convection
2. From 0.5 to 0.02 K/W for forced convection
3. From 0.02 to 0.005 K/W for liquid cooling

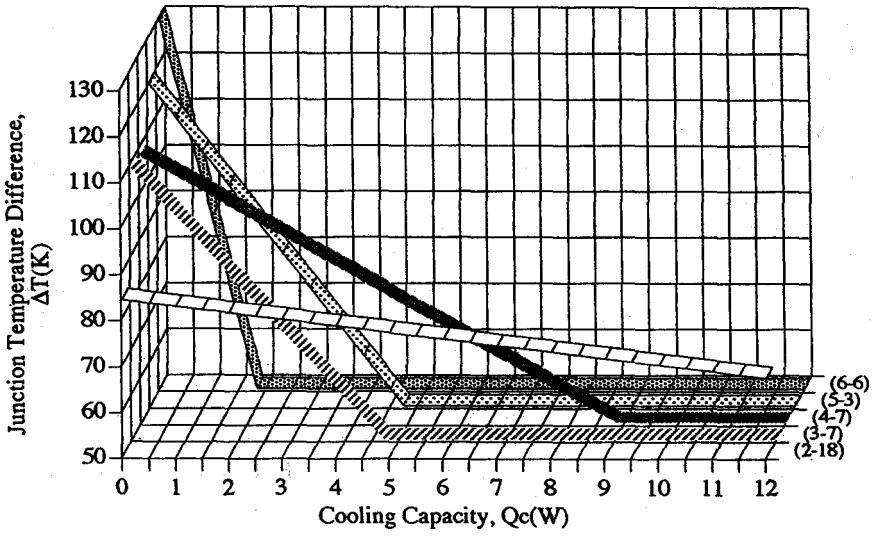

FIGURE 9 Cooling powers Q_c of commercial multistage Peltier modules for junction temperature difference ΔT, with bottom stage hot junction temperature at 300 K (27°C) – (II).

The Amount of Heat Load Q_c

Q_c (W) is comprised of active and passive heat loads. The active load Q_{act} (W) is the heat dissipated by the body to be cooled. When cooling an electronic device it corresponds to the electrical power input to the device. The passive load is comprised of radiation load Q_{rad}, convection load Q_{conv}, and conduction load Q_{cond}.

Finally, the total heat load O_c is equal to:

$$Q_c = Q_{act} + Q_{rad} + Q_{conv} + Q_{cond} \tag{6}$$

The principal heat load to be absorbed depends on the requirements for the application. In the case of air-conditioning the convective heat load Q_{conv} is predominant and the other heat loads are parasitic. But when cooling electronic devices such as infrared detectors, laser diodes, charge-coupled devices (CCDs), or ICs, the active heat loads Q_{act} are predominant. In cooling systems with small active loads and large temperature differences, the parasitic heat loads are dominant and must be minimized.

For the design of a heat exchanger and the heat load estimation refer to Chapter 14 by Richard J. Buist and to the literature.[2]

Examples

Single-Stage Peltier Module

A cold plate of the temperature T_{bod} = 277 K (4°C) requires a heat pumping power of Q_c = 48 W, with an ambient up to T_{amb} = 303 K (30°C). The junction temperatures are estimated: T_h = 308 K (35°C) and T_c = 273 K (0°C). The current should be about I = 10 A.

The required junction temperature difference is ΔT = 308 − 273 = 35 K. Figure 2 shows that the maximum junction temperature for T_h = 308 K (35°C) is ΔT_{max} = 70 K, and the temperature difference ratio is $\Delta T/\Delta T_{max}$ = 0.5. When choosing from Figures 4 and 5 an operating current ratio I/I_{max} of 0.7, the inputs are I/I_{max} = 0.7, $\Delta T/\Delta T_{max}$ = 0.5, the outputs are Q_c/Q_{c-max} = 0.4, COP = 0.5, and V/V_{max} = 0.45. Therefore, the required maximum performance parameters for the module are Q_{c-max} = 48/0.4 = 120 W for T_h = 308 K (35°C) and I_{max} = 10/0.7 = 14 A. From Figure 3 we see that the commercial Peltier module is one of the CP-Series. The cooling power Q_c = 120 W of the commercial CP-Series is based on a hot junction temperature of 298 K (25°C).

Using Figure 2 or Equation 2 we see that the cooling power of 120 W at a hot junction temperature of 298 K (25°C) corresponds to Q_c = 127 W at 308 K (35°C). To obtain the reference and details of the module the catalogues of Peltier module manufacturers must be consulted.

Multistage Peltier Module

To cool an electronic device the following conditions are required: T_{c-bod} = 246 K (−27°C) with a hot junction temperature T_h = 333 K (60°C) and the total heat load to be cooled Q_c = 0.1 W. The Peltier module will operate from a constant current power source.

From Figure 7, the point of intersection of T_h = 333 K (60°C) and ΔT = 87 K is above the one-stage but under the two-stage line, so a two-stage Peltier module should be selected. The cooling powers Q_c of commercial multistage Peltier modules for ΔT of Figures 8 and 9 are based on a bottom stage hot junction temperature of T_h = 300 K (27°C). Therefore, the junction temperature difference ΔT = 87 K must be converted to the equivalent ΔT for 300 K (27°C). In Figure 7 one must draw a line that goes through the point T_h = 333 K and ΔT = 87 K and is parallel to the two-stage line. On this line T_h = 300 K (27°C) and ΔT = 69 K. Figure 8 shows that module (2–2) can be used and Table 1 indicates that it is MI2011T which satisfies the requirements. See catalogues of Peltier module manufacturers for further information.

49.5 Reliability

Each couple has four solder joints. Leading manufacturers are producing Peltier modules on a production line under very severe quality control regulations. Click and Marlow reported that the average failure rate value for each solder joint was $\lambda_i = 3 \times 10^{-8}$ failures/h.[3] MELCOR assumes per module a conservative MTBF of 100,000 h/failure when operation and storage temperatures are limited to 353 K (80°C), based on overall field experience of their end users in systems. Stockholm reported that small systems with a few Peltier modules have a MTBF of the order of 120×10^6 module hours.[4] To maximize reliability, manufacturers' guidelines should be followed. They require the combination of (1) proper handling, (2) proper assembly techniques, and (3) maintaining the lowest possible hot-side temperatures.

49.6 Costs

It is difficult to detail prices of commercial Peltier modules since there are many types of modules manufactured by different companies. The leading manufacturing companies have continued to make a great effort to reduce the prices of Peltier modules over the last three decades. As a result current prices are as reasonable as they possibly can be. As the price of raw material, i.e., tellurium, is continuing to rise a dramatic cost reduction cannot be expected. When using a Peltier module a heat sink is necessary at the hot side of the module regardless of the cost. Low-cost Peltier modules which are smaller in size and thinner in thickness require a flatter smooth contact surface. They also require larger capacity heat sinks and thermal conductive blocks at the cold side of the module to maintain thick thermal insulation. In systems using one or two modules the module cost is only a small fraction, about 10%, of the total cooling system cost. These requirements may result in a rise in the cost of the cooling system in spite of the low-cost module. However, one should keep in mind that in systems requiring many modules the cost of the modules can represent 20% or more of the total system cost.

49.7 Manufacturers

Of the many Western companies which started up in the thermoelectric business in the 1960s and 1970s, only two survived into the early 1990s. These are MELCOR and Marlow Industries Inc. and between them these companies hold about 95% of the market in the western world. Even now, many companies start up but "go under" in the thermoelectric business, thus thermoelectric history repeats itself. At the present time new companies are being started in the CIS, China, and other countries. The following companies have agreed to be listed in this text.

1. Marlow Industries Inc., started 1973, 10451 Vista Park Road, Dallas, TX 75238–1645. Phone: (1) 214–340–4900, Fax: (1) 214–341–5212.
2. MELCOR (Materials Electronic Products Corporation), started 1959, 1040 Spruce Street, Trenton, NJ 08648. Phone: (1) 609–393–4178, Fax: (1) 609–393–9461.
3. Institute of Thermoelectricity, started 1980 (as Phonon Institute, renamed in 1990), General Post Office Box 86, Chernovtsy, 274000, Ukraine. Tel: (7) 03722–44422, Fax: (7) 03722–35118, Telex: 149113 WIWAT SU.
4. OSTERM, started 1958, 15, Grazhdanskaja St., St. Petersburg, 190031, Russia. Phone: (7) 812–312–57–32, Fax: (7) 812–315–17–01.
5. Nord/Telvis, started 1991, 3 Peschany Carier, Moscow 109383, Russia. Phone: (7) 095–356–61–86, Fax: (7) 095–348–07–00, Telex: 411965 ENEK SU.
6. Tecom, Berndt & Schöpke OHG, ThermoElectrische Componenten, started 1992, Schwoitscher Straβe 2, D-06184 Gröbers, Germany. Phone/Fax: (49) 34605–430.
7. Hainan Arctic Ocean Thermoelectric Cooling Co., started 1992, No.1 Xiuying Binya Road, Haikou, Hainan 570011, P. R. China. Phone: (86) 898664761, Fax: (86) 898–664761.
8. Qinhuangdao Fulianjing Electronics Co., Ltd., started 1993, Quinhuangdao Economic and Technical Development Zone, Quing Nian Street, Hebel Province of China, P. R. China. Phone: (86) 335–351208, Fax: (86) 335351159.
9. Komatsu Electronics Inc., started 1966, 2597 Shinomiya, Hiratsukashi, Kanagawa, 254 Japan. Phone: (81) 463–22–8722, Fax: (81) 463–23–3679.
10. Thermovonics & Co., Ltd., started 1983, 1–1-7, Shiohama, Kawasakiku, Kawasaki-shi, Kanagawa, 210 Japan. Phone: (81) 44–277–5155, Fax: (81) 44–277–5616.

References

1. Uemura, K. I., Universal characteristics of Bi-Te thermoelectrics with application to cooling equipments, in *Proc. Xth Int. Conf. Thermoelectrics*, Cardiff, U.K., 1991, p. 69.
2. Marlow, R. and Click, P. B., Jr., Estimating heat loads in multistage thermoelectric coolers, in *Proc. IInd Int. Conf. Thermoelectric Energy Conv.*, Arlington, TX, 1978, p. 72.
3. Click, P. B., Jr. and Marlow, R., Reliability and failure modes of thermoelectric heat pumps, in *Proc. IInd Int. Conf. Thermoelectric Energy Conv.*, Arlington, TX, 1978, p. 115.
4. Stockholm, J. G., Reliability of thermoelectric cooling systems, in *Proc. Xth Int. Conf. Thermoelectrics*, Cardiff, U.K., 1991, p. 228.

50

Thermoelectrically Cooled Radiation Detectors

L. I. Anatychuk
Institute of Thermoelectricity, Chernovtsky, Ukraine

50.1 Classification of Detectors

Photoelectric detectors occupy a particular place in the wide variety of optical and infrared detectors. Their principle of operation is based on the internal photoelectric effect. Photoelectric detectors can be classified depending upon the mechanism that converts the radiation into an electric signal (Figure 1).

Photoresistors

These are the simplest semiconductor photoelectric detectors. Following the absorption of incident radiation, additional electric charge carriers are generated in the semiconductor and result in an increase in electrical conductivity.

Photodiodes

These are semiconductors which contain two regions with different conducting types forming a p-n junction. A flux of incident photons results in a contact potential difference across the junction. The sensitivity of photodiodes increases when a reverse voltage is superimposed across the p-n junction.

Phototransistors

These are structures with two p-n junctions. Operation of a phototransistor is analogous to a typical transistor and virtually carries out the internal photocurrent application.

Multi-range Detectors

These contain structures in which photoelectric detectors having different spectral characteristics are arranged in series. In this case the short-wave receiver simultaneously serves as a filter for the long waves.

0-8493-0146-7/95/$0.00+$.50

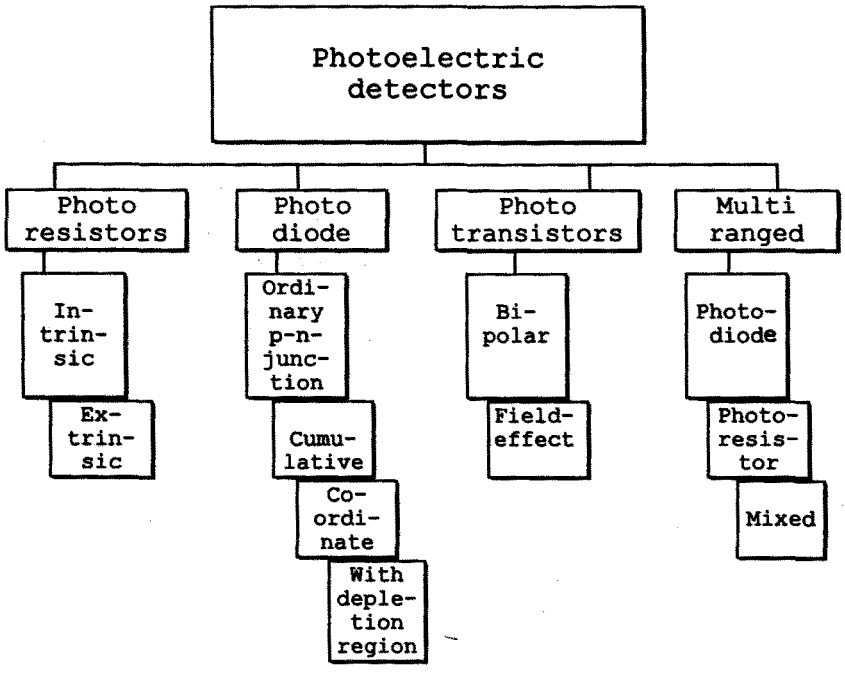

FIGURE 1 Classification diagram of photoelectric radiation detectors.

Photodetectors based on charge-coupled devices (CCD) are a radically new type of photoelectric detector. Their operation is based on the generation of current carriers (charges) and their accumulation in potential wells formed by MIS structures and the transfer of additional accumulated charge to the output of the device.

50.2 Parameters and Characteristics of Photoelectric Detectors

Photoelectric detectors are characterized by:

Threshold sensitivity or detectivity
Spectral sensitivity range
Operating temperature of photoelectric receiver

and other temperature-independent parameters, such as area of receiver, field of vision angle, and preamplifier "matching conditions."

All photoelectric detectors are by their nature selective. Consequently it is necessary to select optimum photoelectric material for each region of the spectrum. In excess of 25 semiconductors are used over the 0.4 to 20.0-mcm range covered by photoelectric detectors. Typical spectral characteristics of detectors made from different materials are displayed in Figure 2.

The temperature dependence of the maximum detectivity of the most popular photoelectric detectors are presented in Figure 3. The detectivity at liquid nitrogen temperatures of "long-wave" photoelectric electrons, based on HgCdTe, is two orders of magnitude higher than at intermediate temperatures (~200 K). Detectors based on InSb exhibit a slightly less marked dependence of detectivity on temperature while the detectivity of those based on PbSe is almost temperature independent over the range 77 to 200 K.

Thus, in general, the cooling of PbS and PbSe detectors to liquid nitrogen temperatures is unjustified. Photoelectric detectors based on InSb provide rather high sensitivity at intermediate temperatures. The use of HgCdTe detectors cooled to intermediate temperatures is justified only for use for middle-wavelength radiation.

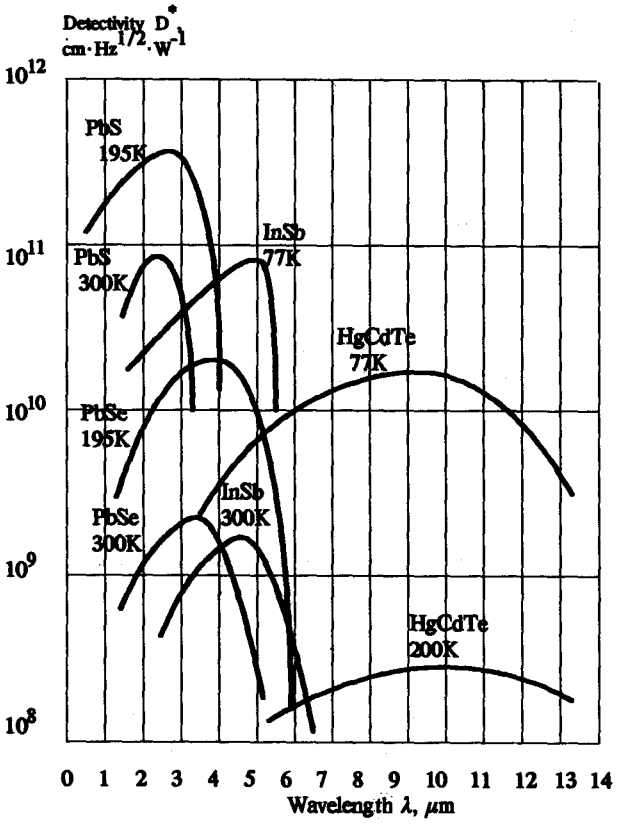

FIGURE 2 Spectral characteristics of photoelectric detectors made of different materials.

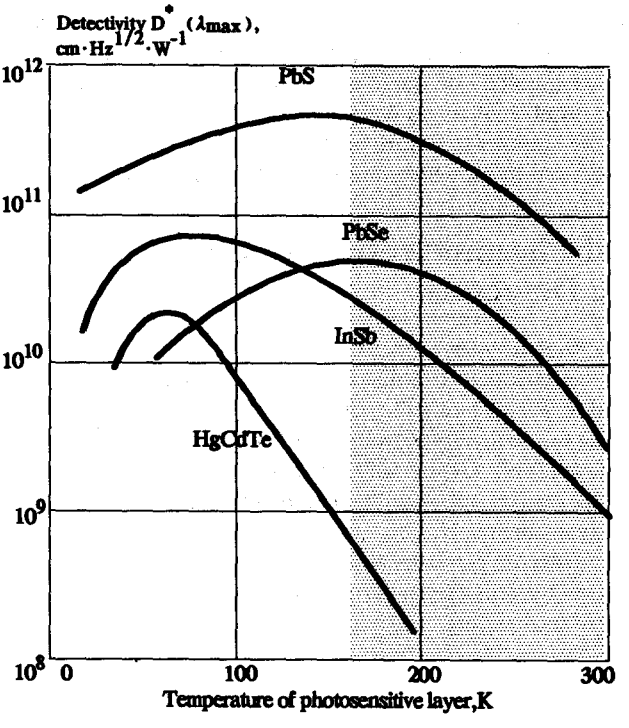

FIGURE 3 Temperature dependence of detectivity. Region of rational use of TE coolers is dashed.

50.3 Detector Cooling

There are four main methods for cooling photoelectric detectors.

Liquid gases
Utilizing the Joule-Thomson effect
Cryogenic apparatus
Peltier effect (thermoelectric cooling)

Liquid Gases

Different types of cryostats are used for this purpose. They are inconvenient to use because they are not self-contained. It is necessary to ensure that the cryostat is vertical when filling with the liquid gas.

Joule-Thomson Effect

The temperature is decreased by the Joule-Thomson effect when gas under a high pressure (20 to 40 MPa) expands. Liquid nitrogen temperature (77 K) is reached in minutes. The operation lifetime depends upon the volume of the compressed gas and results in mass-dimensional limitations.

Cryogenic Apparatus

Cooling is achieved using mechanical systems that operate on different thermodynamic cycles: Sterling, Jifford-McMagon, Willumier, and so on. This method of cooling is unacceptable for compact devices.

Thermoelectric Cooling

Thermoelectric cooling is an exceptionally convenient method for cooling photoelectric detectors. These coolers have a limitless lifetime, can operate at any orientation, and are mechanically robust. Coolers with different numbers of stages are employed depending upon the required level of cooling. Usually the number of stages does not exceed four to six, although coolers with more stages are available. An important feature of this method of cooling is that it can operate under closed and evacuated conditions, which results in a decrease in electric power consumption.

50.4 Parameters of Thermoelectrically Cooled Photoelectric Detectors

A great number of different types of thermoelectrically cooled detectors are currently available. Information on photoelectric detectors that are thermoelectrically cooled to similar operating temperatures is collected in Tables 1 to 5 for convenience.

The tables illustrate the versatility of thermoelectric coolers. In recent years new thermoelectric coolers have become available for use with infrared equipment: thermoelectric coolers are successfully used for CCD matrix cooling in the temperature range 200 to 220 K (Wight Instruments, U.K. and Princeton Instruments, U.S.).

The variety of photoelectric detectors available in company catalogues increases each year. The advantages of employing thermoelectric cooling for MCT and CCS will result in their increased application in infrared engineering.

Table 1 Parameters of Photodetectors Based on PbS

Producer Company, Country	Photodetector Model	No. of Cascade TE Coolers	Working Temperature K	Input Power TE Cooler W	Detectivity D^* (λ_{max}) cm · $Hz^{1/2}$ · W^{-1}	Spectral Range, μm	λ_{max}, μm	Package
IRA, U.S.	PS-1	1	253	—	$1.5 \cdot 10^{11}$	1–3	—	TO-37–1, TO-8–1
	PS-2	2	243	—	$2.5 \cdot 10^{11}$	1–3.2	—	TO-8–2, TO-37–2
	PS-3	3	203	—	$3 \cdot 10^{11}$	1–3.5	—	TO-3
Hamamatsu, Japan	P 2682	1	253	—	$4 \cdot 10^{11}$	—	2.5	TO-8
	K3413–01	1	263	—	$1 \cdot 10^{11}$	1.1–3	2.4	
Cal. Sensors, Inc. U.S.	AT 1	1	253	2.2	$1.5 \cdot 10^{11}$	—	2.5	TO-5 or
	AT 2	2	243	2.0	$2.5 \cdot 10^{11}$	—	2.6	TO-37
Infrared Industries Inc.,	2600	1	253	1.6	$1.5 \cdot 10^{11}$	—	—	TO-37
U.S.	2700	2	243	1.53	$2.5 \cdot 10^{11}$	—	—	TO-37
	2900	3	203	5.0	$3 \cdot 10^{11}$	—	—	TO-37
SBRS (Santa Barbara	PS-ITO	3	200	3.5–16	$2–6 \cdot 10^{11}$	—	2	54764–3
Research Center) U.S.		4	195	3–7		—	2.5	54764–4

Table 2 Parameters of Photodetectors Based on PbSe

Producer Company, Country	Photodetector Model	No. of Cascade TE Coolers	Working Temperature K	Input Power TE Cooler W	Detectivity D^* (λ_{max}) cm · $Hz^{1/2}$ · W^{-1}	Spectral Range μm	λ_{max}, μm	Package
IRA, U.S.	PE-1	1	253	—	$7.5 \cdot 10^9$	1–5.0	—	TO-37–1, TO-8–1
	PE-2	2	243	—	$1.8 \cdot 10^{10}$	1–5.2	—	TO-8–2, TO-37–2
	PE-3	3	203	—	$2 \cdot 10^{10}$	1–5.8	—	TO-3
Hamamatsu, Japan	P903 P2038–01 P2038–02	1	263	—	$3 \cdot 10^9$	—	4.1	TO-66 TO-8 TO-8
	P2680	2	253	—	$4 \cdot 10^9$	—	4.3	TO-8
	P4115	2	263	—	$3 \cdot 10^9$	—	4.1	TO-66
	K3413–02 (4 el. 2 colors)	1	263	—	$3 \cdot 10^9$	1.1–4.85	4.1	—
PO "Kvarts" Ukraine	FR-127	1	293	0.4	$1 \cdot 10^9$	2.6–4.8	3.6–3.8	—
Cal. Sensors, Inc. U.S.	BT-1	1	253	2.2	$7.5 \cdot 10^9$	—	4.3–4.5	TO-5
	BT-2	2	243	2.0	$1.3 \cdot 10^{10}$	—	4.4–4.6	TO-37
Optoelectronics Textron, U.S.	line	3	193	4.0	$6–7.3 \cdot 10^{10}$	3–5.0	—	—
PO "Orion" Russia	line 64 el.	4	196	6.3	$1.5 \cdot 10^{10}$	2–5.0	≥4.0	
Infrared Industries Inc.,	5600	1	253	1.6	$7.5 \cdot 10^9$	—	—	TO-37
U.S.	5700	2	243	1.53	$1.3 \cdot 10^{10}$	—	—	TO-37
	5900	3	203	5.0	$2.0 \cdot 10^{10}$	—	—	TO-3(5)
Barnes Engineering Co., U.S.	1003 1004	1	253	2.4	$1 \cdot 10^9–7.5 \cdot 10^9$	—	4.3–4.5	TO-37
SBRS (Santa Barbara	PE-ITO	3	200	3.5–16	$1.3 \cdot 10^{10}$	—	4.8	54764–3
Research Center) U.S.		4	195	3–7		—		54764–4

Table 3 Parameters of Photodetectors Based on HgCdTe

Producer Company, Country	Photodetector Model	No. of Cascade TE Coolers	Working Temperature K	Input Power TE Cooler W	Detectivity D^* (λ_{max}) cm · $Hz^{1/2}$ · W^{-1}	Spectral Range, μm	λ_{max}, μm	Package
IRA, U.S.	HCT-35-TE2-A	2	240	—	$1 \cdot 10^{10}$	3–5	—	TO-37
	HCT-35-TE3-A	3	220	—	$2 \cdot 10^{10}$	3–5	—	TO-3
	HCT-L-TE3	3	215	—	$2 \cdot 10^{8}$	—	10.6	TO-3
Hamamatsu, Japan	P3981	2	243	—	$5 \cdot 10^{10}$	—	3.6	TO-8, TO-66
	P3982	2	243	—	$1 \cdot 10^{11}$	—	2.9	TO-8, TO-66
	P2750	3	213		$2 \cdot 10^{10}$	—	4.8	TO-3
EG&G Judson, U.S.	J15-TE200	2	243	1.0	$3–5 \cdot 10^{9}$ (500 K)	—	4.5 ± 0.2	TE-200
	J15TE3:5	3	218	3.0	$4 \cdot 10^{10}$	2–5	—	TO-6, TO-3
	J15TE4:5	4	—	—	—	—	—	—
	J15-TE400–5	4	200	4.0	$5–7 \cdot 10^{10}$	—	5 ± 0.5	TE400
	J15-TE400–10	4	200	4.0	$2–8 \cdot 10^{8}$	—	10.6 ± 1.0	TE400
Vigo Ltd., Poland	PC-L-2TE	2	230	—	$\geq 1 \cdot 10^{8}$	—	—	TO-37, TO-8
	PC-L-2TE-3	2	230	—	$\geq 1 \cdot 10^{9}$	—	—	TO-37
Mullard, England	18RPW/G1810	3	203	3.0	$5.5 \cdot 10^{10}$	3.0–5.0	—	—
	18RPW/G1813 (8 el. SPRITE)	3	203	3.0	$2.2 \cdot 10^{11}$	—	5.2 ± 0.2	—
	18RPW/T1813	3	203	3.0	$1 \cdot 10^{9}$	—	10.6	—
SBRS (Santa Barbara Research Center), U.S.	H-PC-E	3	195	3.5–16	$2–5 \cdot 10^{10}$	—	4.5	54764–3
		4		3–7		—	5.5	54764–4

Table 4 Parameters of Photodetectors Based on Ge

Producer Company, Country	Photodetector Model	No. of Cascade TE Coolers	Working Temperature K	Input Power TE Cooler W	Detectivity D* (λ_{max}) cm · $Hz^{1/2}$ · W^{-1}	Spectral Range μm	λ_{max}, μm	Package
Polytec, Germany	GE-2	2	245	—	$4 \cdot 10^{11}$	0.6–1.9	1.5	TO-37–2, TO-8–2
	GE-3	3	—	—	—	0.6–1.9	1.5	TO-3
Hamamatsu, Japan	B2538	1	−10	—	$1–5 \cdot 10^{11}$	—	1.52	TO-8
	B2614	2	−30	—	$1 \cdot 10^{12}$	—	1.52	TO-8
EG&G Judson, U.S.	J16-TE200	2	243	1	$4 \cdot 10^{11}$	—	1.5	—
	J16-TE400	4	200	2–3	$>1 \cdot 10^{12}$	—	1.5	—
Germanium Power Devices Corp., U.S.	GM5TEC	1	258	—	—	0.8–1.8	—	TO-5
	GM8TEC	2	248	—	—	0.8–1.8	—	TO-8

Table 5 Parameters of Photodetectors Based on InAs

Producer Company, Country	Photodetector	No. of Cascade TE Coolers	Working Temperature K	Input Power TE Cooler W	Detectivity D* (λ_{max}), cm · $Hz^{1/2}$ · W^{-1}	Spectral Range μm	λ_{max}, μm	Package
Hamamatsu, Japan	P2837–01	2	243	—	$2 \cdot 10^{10}$	—	3.2	TO-8
EG&G Judson, U.S.	J12-TE200	2	250	1	$3 \cdot 10^{10}$	—	3.3	TE-200
	J12-TE3	3	218	2–3	$1 \cdot 10^{11}$	1–3.4		—
	J12-TE400	4	200	2–3	$8 \cdot 10^{10}$	—	3.2	TE400

51

Reliability of Peltier Coolers in Fiber-Optic Laser Packages

R.M. Redstall and
R. Studd
BT Laboratories, Ipswich, U.K.

51.1 Introduction

Laser modules of various types are used as the transmitters in fiber-optic telecommunications networks. Peltier coolers are employed in some of these laser modules to maintain the laser chip at a constant temperature, typically 25°C. The Peltier cooler removes both the heat generated by the laser chip itself (up to 200 mW), and that received from its surroundings. Many laser modules are intended for operation within telephone exchange buildings, where the maximum temperature is 45°C. In other locations, the temperature may be higher, for example 65 or 85°C.[1] The Peltier cooler is needed for two main purposes. The first is to ensure that the optical output power of the laser does not change if the outside temperature fluctuates—because its power output is temperature sensitive. Second, tight control of temperature is necessary for lasers where emission wavelength is critical.

A typical telecoms systems will be required to have an operating life of between 10 and 25 years. In order to perform adequately in such applications, therefore, the Peltier coolers are required to exhibit a high level of reliability. Hence, the telecom-grade coolers need to be designed for long-term reliability. Specifically, this means a very low rate of infant mortality, and very low wear-out and random failure rates over a period of years. Individual burn-in and screening may be necessary, and suggested methods have been described.[2] These may include thermal cycling.

Over several years BT Laboratories (BTL) has gained considerable experience of the reliability of laser modules, many of which include a Peltier cooler. BTL[3] and others[4] have found that Peltier coolers have shown reliability problems. Further, from test laser modules assembled at BTL which have contained Peltier coolers, it has been found that all the subsequent assembly methods are critical in determining cooler reliability. The bismuth telluride (BiTe) elements within the Peltier cooler are relatively fragile, and can be damaged when being assembled into the laser module package unless the process is carefully controlled.

In this chapter results are presented which are typical of this experience at BTL. Failure analysis is included, and areas for improvements are discussed.

0-8493-0146-7/95/$0.00+$.50

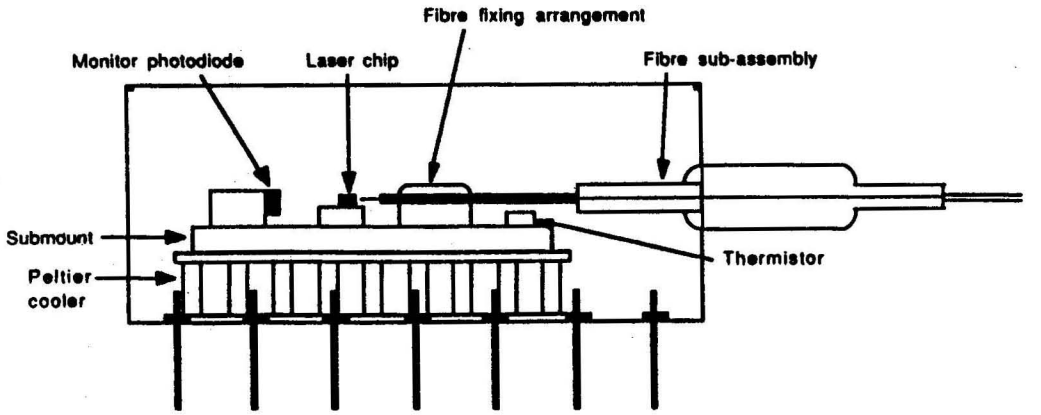

FIGURE 1 Sectional view through a typical rectangular-style laser module showing the key components.

51.2 Laser Module Package Design

One typical module design contains the laser and some other components mounted upon the Peltier cooler within a rectangular hermetic package. A schematic drawing of this arrangement is shown in Figure 1. The small laser chip is mounted precisely in line with the fiber pigtail, with a back-facet monitor photodiode behind. Also included is a thermistor for control of the laser temperature.

51.3 Life-testing

Life-tests have been carried out on Peltier-cooled laser modules at elevated temperatures. The lasers were operated under normal drive currents, and the Peltier coolers in the laser modules were powered in order to cool the laser chip to the predetermined temperature. The performance of the Peltier cooler and the laser chip was regularly monitored while the life-test progressed, by recording any changes in their drive currents. Two examples from such life-tests are detailed below.

The Peltier coolers in both cases were made of 36 elements of BiTe, with a specified maximum drive current of 1 A. Such coolers can generate a temperature difference (ΔT) between their cold side and their base of up to 65°C.

Life-testing with a Large Temperature Difference (ΔT)

In the first example, 20 laser modules containing Peltier coolers were subjected to an accelerated life-test with a relatively high temperature difference (ΔT) of 40°C, where the laser module was at a temperature of 85°C and the internal laser chip was cooled to 45°C. Throughout the life-test of 4000 h the laser was driven and provided a heat load of 20 mW. The ΔT used in this test is typical of that specified for this size of Peltier cooler.

The 20 laser modules were all nominally identical. The results are shown with the relative change in drive current plotted against life-test duration, in Figure 2.

Out of the 20 coolers tested there was one failure after 500 h. Such an early failure should have been screened out by an effective burn-in process. The other 19 coolers showed a wide distribution of behavior, with four degrading relatively rapidly—so that it is estimated that, had the test continued, these four would have failed in under 40,000 h. This wide distribution in itself indicates that these components might not be suitable for some telecoms applications.

At lower temperatures there would be an improvement in the life-times of these coolers. The effects of overstress in life-testing can be difficult to assess: it results in thermally accelerated degradation, for which there can be derived an acceleration factor. In this example an activation energy

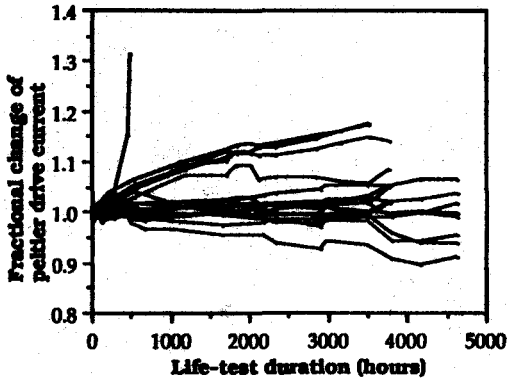

FIGURE 2 Peltier cooler life-test plot of the 20 Peltier coolers, showing the fractional change of drive current against life-test duration.

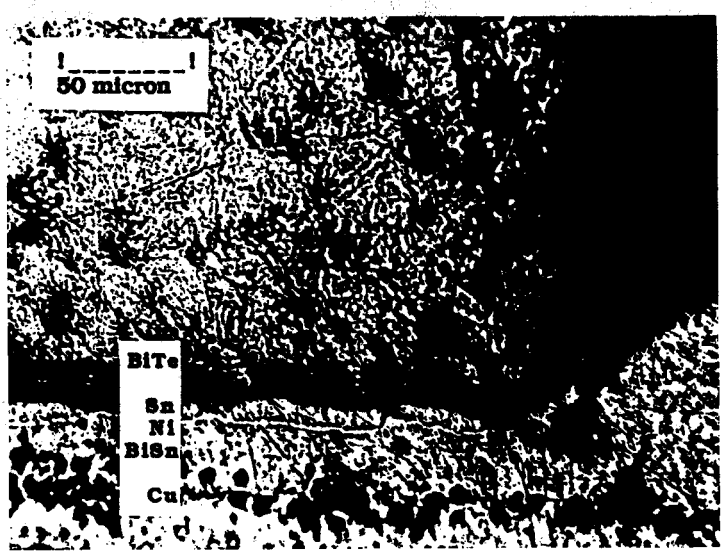

FIGURE 3 Optical micrograph of a section through a cooler element, showing a corner of the BiTe element, the Ni barrier, the BiSn solder, and the Cu track.

of 1.2 eV is used, from the experience of typical failure mechanisms involving the diffusion of metals, and a failure criterion of 1 A. At 65°C, as a typical example, this gives a ten times longer life. The early life-test failure would have occurred in 6 months. In addition, for a system containing several hundred coolers, and because of the wide distribution in behavior, an unacceptable number of wearout failures would be expected early in the system life.

Failure Analysis

Analysis was carried out on the failed cooler and two of those more rapidly degrading, by sectioning BiTe elements. Typical results are shown in two photographs, Figures 3 and 4.

The construction of the cooler was that the BiTe elements were attached with bismuth-tin (BiSn) solder to their copper interconnections on a ceramic plate. A nickel barrier metal was located on the end of the BiTe, to prevent diffusion of the solder material into the cooler elements. The nickel barrier can be seen as a bright wavy line about a half micron thick towards the bottom edge of Figure 3. Significantly, tin from the solder was found between the nickel and the BiTe element. The tin will have diffused through the nickel layer, indicating that the nickel was not an effective

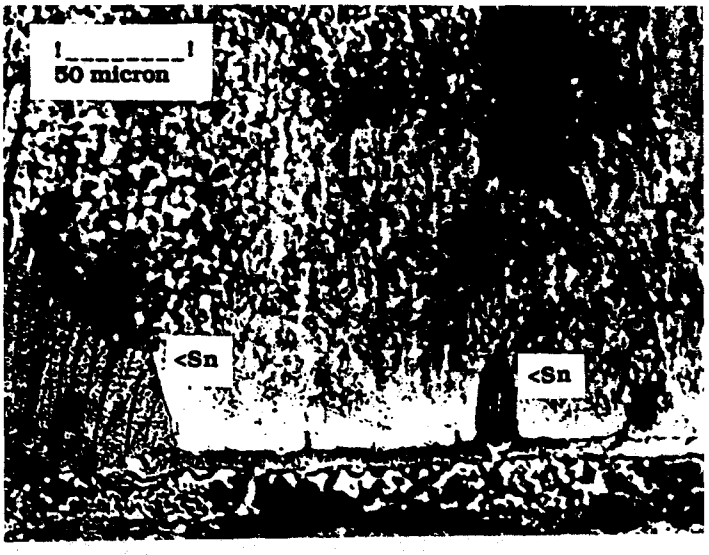

FIGURE 4 Optical micrograph of a section through a cooler element, showing two areas where the tin has migrated down cracks in the BiTe.

barrier to the diffusion of the components of the solder. In the second section of a cooler element, shown in Figure 4, areas can be seen in which a larger amount of tin has passed through the nickel barrier, and the tin has then followed the sites of a series of longitudinal cracks in the material, to the extent that the BiTe element has been swollen laterally.

Summary

In this example, the tin from the solder is clearly moving into the BiTe elements, showing that the nickel barrier is not performing its design function effectively. This represents a hazard which limits the cooler reliability. Further, the burn-in employed as a production screen was clearly not effective in removing early failures.

Life-testing with a Small Temperature Difference (ΔT)

In the second example three Peltier-cooled laser modules of a different design and from a different manufacturer to those in the first example were life-tested using a small ΔT of 5°C, where the module was at a temperature of 70°C, with the laser chip cooled to a slightly lower temperature of 65°C. During the lifetest of 5000 h small increases in drive current indicated that degradation was occurring, typical of wearout. However, for one of the coolers, at the end of the 5000-h test period, rapid degradation was observed during its remeasurement at a number of temperatures. Figure 5 shows how these characteristics changed even further during an additional short storage test of 170 h.

Failure analysis

When the failed cooler was disassembled the weakest point in its construction was found to be the junction of the element with its solder pads. Scanning electron microscope (SEM) micrographs of the interconnection pads indicated that there was poor adhesion between the p-type cooler elements and their pads. Energy dispersive X-ray analysis in the SEM confirmed that the elements had broken away relatively cleanly, leaving the nickel barrier metal on the pads.

It should be noted that there are several methods of depositing nickel barrier layers onto the BiTe cooler material, and not all of the methods will necessarily result in ideal adhesion properties.[5]

Summary

In this test, one out of three coolers failed prematurely. The failure is attributed to poor adhesion of the nickel barrier to the BiTe.

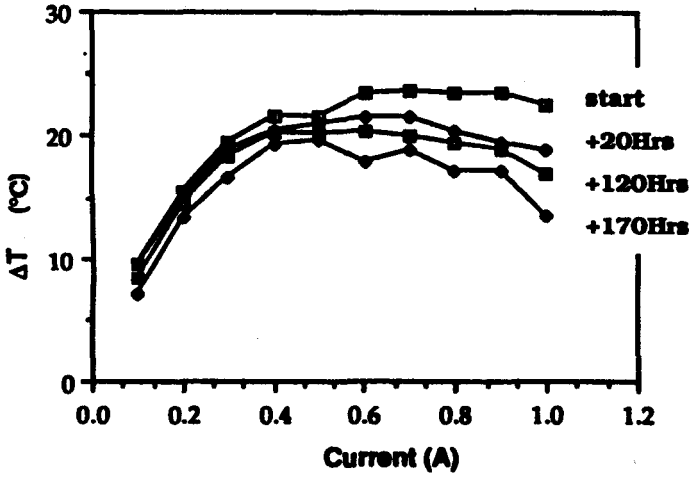

FIGURE 5 Successive characteristics of a failed Peltier cooler, after first life-testing at 70°C, and then baking at 60°C. The graph shows the cold-side temperature depression (ΔT) vs. drive current.

51.4 Conclusions

Peltier coolers represent a very significant reliability hazard when used in laser modules for typical telecoms fiber-optic applications.

To improve the situation:

1. Cooler manufacturers need to assess and revise their designs to take account of telecoms needs—paying particular attention to the thickness, composition, and adhesion of barrier layers and other metals.
2. Cooler manufacturers and laser module manufacturers both need to pay close attention to assembly methods and to the rigorous screening of their products to ensure that early failures are not experienced by the end users.

Acknowledgments

We gratefully acknowledge assistance from our colleagues, A. P. Skeats and C. J. Allen.

References

1. Bellcore. "Reliability Assurance Practices for Optoelectronic Devices in Loop Applications", *TA-TSY-000983, Issue 1,* January, 1990.
2. Spencer, J.L., "Assuring the reliability of lasers intended for the uncontrolled environment", *Bellcore Semiconductor Device Reliability,* Eds Christou, A., and Unger, B.A., 1989, p75–96.
3. Sim, S.P., Videlo, I.D.E., Redstall, R.M. and Nelson, D., 1991. "The reliability of laser transmitter modules for use in optical fibre transmission systems", *ESREF '91,* 1991.
4. Su, P., "Temperature stress testing of laser modules for the uncontrolled environment", *Fibre Optics Reliability: Benign and Adverse Environments IV, SPIE,* 1990 Vol. 1366.
5. Allred, D., et al., "Thermoelectric element thermoelectric device and methods of manufacturing the same", UK Patent GB2171254B, 1988.

52

Laboratory Equipment

Kin-ichi Uemura
Institute for Thermoelectric Technologies
Yokohama, Japan

52.1 Introduction

Since a fully comprehensive account of all available laboratory equipment using Peltier modules is beyond the scope of this text, the analysis is limited to the examples given below. The seven areas of practical usage that are listed below indicate the versatility and broad range of application of the Peltier module.

Typically, equipment consists of three components: (1) Peltier cooling unit, (2) DC power source/controller system, and (3) an accessory system which is highly specific to satisfy the desired purpose.

In this chapter equipment of relatively low cooling capacity, i.e., less than hundreds of watts are classified under the following categories:

1. Measurement
2. Biotechnology
3. Medical
4. Electronics
5. Industrial
6. General Purpose
7. Consumer

For large-scale systems of high cooling capacity, refer to Chapters 53 and 54 by John G. Stockholm; for equipment using thermoelectrically cooled detectors or electrical components, refer to Chapters 50 and 51.

52.2 Basic Construction of a Cooling Unit

The Peltier cooling unit in the equipment consists of three components: (1) the Peltier module, (2) the heat dissipator at the hot side of the module which is indispensable to the Peltier cooling unit, and (3) the cooling component at the cold side of the module.

The solid body to be cooled can be cooled in direct contact with the cold ceramic plate of the module, but in most cases the body is cooled through (1) a heat conducting plate, a block, and the bath; (2) the cooling heat exchanger, for example the forced air convection fin; or (3) the liquid jacket. Each type functions specifically. Figure 1 shows the typical configuration of the Peltier cooling system. These standardized systems are economical and suitable for general-purpose applications.

0-8493-0146-7/95/$0.00+$.50

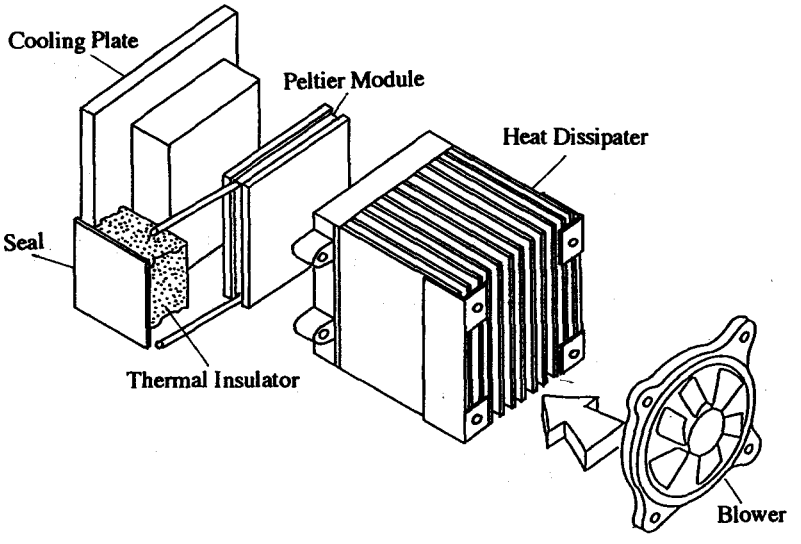

FIGURE 1 Configuration of a Peltier cooling unit.

The specifications of each Peltier cooling unit are indicated in Table 1:

1. The name of the equipment
2. The number of stages
3. Configuration of the cooling and heat dissipating system
4. Obtainable minimum temperature in the cooling mode, T_{min} (°C) of the cooled body
5. Maximum temperature in the heating mode, T_{max} (°C) of the heated body
6. Magnitude of the cooling power Q_c (W) at T_{min}
7. The Peltier cooling unit or the total system power consumption.

52.3 Laboratory Equipment Classified by Usage

Measurement

Micro photo calorie meter — The copper cavity is a Peltier-controlled black body (NiP-plating) that can be used to measure the power of light, its wavelength range; 0.4 to 1.8 μm, power range; 100 μW to 200 mW within ± 1% accuracy by isothermal control of a Peltier module.

Dew point sensor — The mirror is mounted from a single-stage to a five-stage Peltier module which can cool the mirror below the ambient temperature. An LED illuminates the mirror and a photodetector monitors light reflected from the mirror. Another LED/photodetector provides a reference measurement. When a sample gas is passed over the cooled mirror, dew begins to form and the dew droplets scatter the light. The detector on which the light is reflected from the mirror senses a drop in light intensity compared to the reference photodetector. The two photodetectors are arranged in an electrical bridge circuit. The mirror surface temperature is automatically and continuously controlled at the dew point temperature of the sample gas. Figure 2 shows the dew point temperature sensor using a two-stage Peltier module and Figure 3 shows the schematic configuration.

Freezing point apparatus[1] — This apparatus is used for detecting the freezing and melting points of hydrocarbon mixtures, such as aviation fuels. The test sample needs to be cooled to about −60°C to determine the freezing point and to be heated back to room temperature to determine the melting point. Cooling and heating are provided by two three-stage Peltier modules in the apparatus; the top stage has 71 couples (element length: 3 mm), the middle stage has 71 couples (element length: 6 mm), and the bottom stage has 127 couples (element length: 6 mm). To keep

Table 1 Laboratory Equipment

Name of Equipment	No. of Stages	Cold/Hot-Side Configuration	Cooling Mode Minimum Temp. T_{min} °C	Heating Mode Maximum Temp. T_{max} °C	Cooling Power Q_c at T_{min} W	Heat Dissipating Medium °C	TE Unit Power Consumption	Total System Power Consumption
1. Measurement								
Micro photo calorie meter	1	Cu-Cave (NiP-plating, L:5 mm)/NA	20		0.2	Air (20)		90 W
Dew point sensor 2-stage	2	Mirror/NA or LJ	−35	85	0.5	Air (25)		
Dew point sensor 5-stage	5	Mirror/LJ	−80	35	0.5	Water (15)		
Dew point sensor 1-stage	1	Mirror/NA or LJ	−15	80	1	Air (25)		
Dew point sensor 4-stage	4	Mirror/NA or LJ	−75	35	1	Water (15)		
Freezing point apparatus	3	Sample holder (28 × 28 × 4 mm)/ ice + water	−60	0	2	Water (20)	50 W	
Black body radiation standard	1	Black body plate (50 × 50 mm)/FA	0	70	3	Air (20)		250 W
Photomultiplier housing	1	Phototube block/FA or LJ	−20		5	Air (20)	100 W	
Gas sampling dehumidifier unit	1	GJ/FA	1	3	5	Air (40)		100 V × 1.4 A
Ice point reference chamber	1	Gas-tight casing (water)/FA	0		5	Air (35)	6 V × 4 A	50 W
Triple point of water	1	Gas-tight casing (water + air)/FA	0		10	Air (35)		144 W
Water bath for sampling SO_2 bubbler	1	WB (100 ml)/FA	7	17	10	Air (50)		
Oil clouding point	2	Test tube holder/FA	−25	25	15	Air (30)		
Refractometer	1	Liquid bath (1.8 l) LJ/FA	10	60	60	Air (30)		100 V × 7.5 A
2. Biotechnology								
Bioactivity monitor-calorie meter	1	Detector tube (I.D. 14 mm)/LB	20	80	0.0003	Water (20)		300 W
DNA sequence reactor	1	WJ/FA	37	37	1.5	Air (20)	3 V × 0.8 A	
Spectrophotometer cell thermoprogrammer	1	Cuvette (1 cm) × 4/FA	0	99.9	2	Air (25)	48 W	
Programmable thermal controller	1	Test tube (600.5 ml) × 60 holder/FA	0	100	10	Air (25)		
Minifridge for blood	1	Test tube block/FA	4		10	Air (25)		
Photosynthesis analyzer	1	Box (12 l) FA/LJ	5	45	15	Water (20)		100 V × 5 A
Osmometer	2	Bath (90% ethylene glycol 100 ml)/FA	−11		25	Air (35)		240 W
Chromatography column holders	1	Column holder Al-block/FA	30	70	30	Air (30)	3 V × 16 A	
Thermoprogrammer for bioactive analyzer	1	LJ/FA	−10	80	70	Air (25)		
Centrifuge	1	Case/FA	20		600	Air (25)		
3. Medical								
Hot/cold stimulator	1	Probe/NA	0	50	0.1	Air (25)		
Cryosurgical destroyer	2	Cryoprobe/LJ	−50		2	Water (20)	100 W	
Temperature sense organ tester	1	Probe/FA	10	40	0.3	Air (25)	0.5 W	
Hot/cold moxa	1	Probe/NA	15	57	2	Air (25)	8 W	
Microscope stage cooler	1	Stage (30 × 37 mm) with hole/LJ	−20	60	3	Water (20)		100 W
Microtome stage cooler	1	Stage/LJ	−35		4	Water (20)	3.7 V × 20 A	

Table 1 Laboratory Equipment *Continued*

Name of Equipment	No. of Stages	Cold/Hot-Side Configuration	Cooling Mode Minimum Temp. T_{min} °C	Heating Mode Maximum Temp. T_{max} °C	Cooling Power Q_c at T_{min} W	Heat Dissipating Medium °C	TE Unit Power Consumption	Total System Power Consumption
Portable mini(insulin) cool box	1	AB(30 ml)/FA	5	15	5	Air (45)	50 W	
Cold plate for dental cement	1	Al-Plate(90 × 160 mm)/FA	18	20	10	Air (25)		200 W
Cold/hot therapy blanket	1	LJ/LJ	4	40	30	Air (20)		120 V × 2 A
Mist tent	1	FA/FA	15	25	150	Air (20)	130 V × 1.5 A	345 W
4. Electronics								
Photodetector (InAs)	4	Detector (InAs)/NA	−73		0.05	Air (25)	5 V × 0.8 A	
CCD video camera heads	3	CCD (384 × 576 sci-grade)/FA	−45		0.05	Air (25)		
Photodetector (HgCdTe)	3	Detector (HgCdTe)/NA	−50		0.1	Air (25)	3 V × 1 A	
Photodetector (InAs, HgCdTe, Ge, PbS, PbSe)	2	Detector/NA	−30		0.2	Air (25)	0.4 V × 1 A	
X-Ray spectrometer	7	Detector (Si-Li)/FA	−100		0.164	Air (20)	12 V × 5 A	
Optical communication laser diode	1	LD/NA	25		0.5	Air (50)	1.4 V × 1 A	
Interferometer laser diode	1	LD/NA	25		0.5	Air (50)	1.5 V × 1 A	
Low-noise amplifier for satellite earth station	3	FET/FA	−45		1.5	Air (60)		600 W
Microprocessor-IC environmental controller	1	Al-plate (66 × 66 mm)/FA	0	4	8	Air (35)	12 V × 3.5 A	
5. Industrial								
Dopant cooler for semiconductor device production	1	WB/FA	0	40	5	Air (20)	200 W	
Si wafer cooler plate for semiconductor device production	1	Plate/LJ	20	25	200	Water (20)	310 W	
Chemical circulating system for semiconductor device production	1	WJ (contamination-free)/LJ	15	50	400	Water (20)		200 V × 5 A
6. General Purpose								
Vacuum pump baffle	1	Chevron fin/FA	−30		3	Air (20)		
Immersion cooler	1	Ni-plate case/LJ	−25	60	17	Water (20)	4.8 V × 4.8 A	
Cold plate	1	Plate/WJ or FA	0	70	70	Air (25)	240 W	
Liquid circulating apparatus	1	WJ/WJ or FA	−10	70	70	Air (25)		
Air conditioner	1	FA/FA	−5	70	50	Air (25)		115 V × 6.0 A
7. Consumer								
Portable cooler (picnic box)	1	AB (12 l)/FA	5		13	Air (35)	12 V × 4 A	
Helmet	1	Liquid-filled cushion/heat collector/FA	26		11	Air (38)	12 V × 2 A	
Cheese server	1	AB (20 l)/FA				Air (25)		60 W
Water cooler	1	WB (680 ml)/FA	10		100	Air (27)	115 V × 4 A	138 W
Wine cooler	1	AB (55 bottles)/FA						160 W

Legend: FA, forced air; NA, natural air; LB, liquid bath; AB, air box; LJ, liquid jacket; GJ, gas jacket.

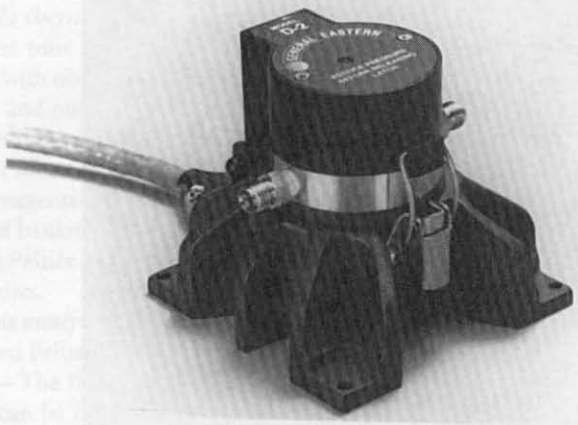

FIGURE 2 Dew point sensor with a two-stage Peltier module (courtesy General Eastern, U.S.).

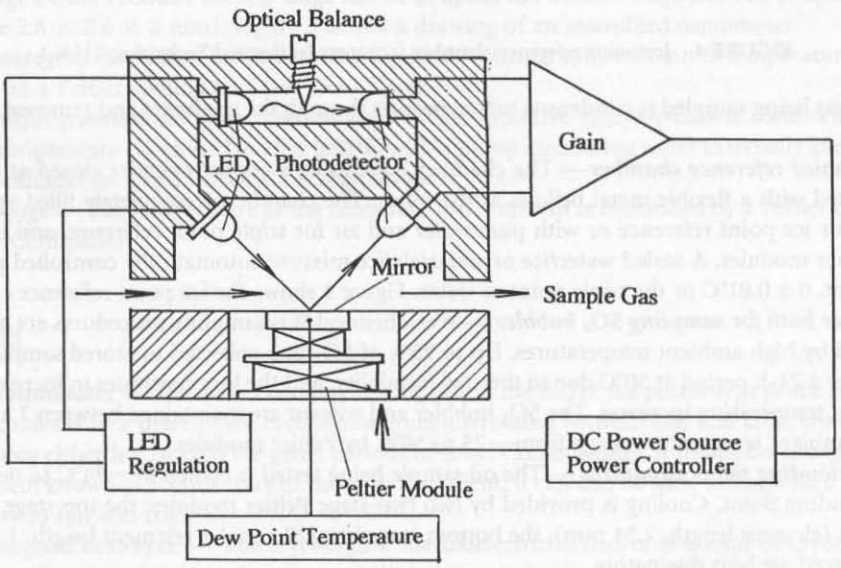

FIGURE 3 Principle of a Peltier-cooled dew point sensor.

the hot side of the Peltier modules below 20°C or so, a mixture of ice and water was chosen as a suitable medium.

Blackbody radiation standard — The blackbody plate, 50 × 50 mm, emissivity >0.98, is controlled at temperatures of −20 to 70°C, temperature uniformity ±0.1°C by the Peltier module. The plate provides the blackbody radiation standard at the desired temperature.

Photomultiplier housing — The Peltier-cooled housing for a photomultiplier provides low noise, low dark current operation, gain stability, and signal-to-noise ratio improvement for the photomultiplier measurement.

Gas sampling dehumidifier unit — Pollution gases, such as engine exhaust fumes, chimney smoke, etc. contain water vapor. When the gas is being sampled in an infrared analyzer, water vapor can give a false reading of the sample and/or the corrosive aqueous solution formed from the condensed water in the analyzer may damage the analyzer detector. The anticorrosive gas flow jacket is cooled by Peltier modules at a temperature of 1.5 to 3.0 ± 0.1°C. Water vapor contained

FIGURE 4 Ice point reference chamber (courtesy Isothermal Technology, U.K.).

in the gas being sampled is condensed before passing through the gas jacket and removed as drain water.

Ice point reference chamber — The chamber consists of a copper cylinder closed at one end and fitted with a flexible metal bellows at the other. The chamber is completely filled with pure water for ice point reference or with pure water and air for triple point reference, and is cooled by Peltier modules. A sealed water/ice or water/air/ice mixture automatically controlled gives the ice point, 0 ± 0.01°C or the triple point of water. Figure 4 shows the ice point reference chamber.

Water bath for sampling SO_2 bubbler — Wet-chemical SO_2 sampling procedures are adversely affected by high ambient temperatures. Up to 75% of SO_2 in a collected or stored sample can be lost over a 24-h period at 50°C due to thermal instability, and the loss continues to increase as the ambient temperature increases. The SO_2 bubbler and reagent are maintained between 7 and 17°C in an ambient temperature range from −25 to 50°C by Peltier modules.

Oil clouding point apparatus — The oil sample being tested is cooled to −34°C to determine the clouding point. Cooling is provided by two two-stage Peltier modules; the top stage has 127 couples (element length, 2.54 mm), the bottom stage has 127 couples (element length, 1.14 mm) with forced air heat dissipators.

Refractometer — A pump circulating water externally controls the environmental temperatures for refractometer using Peltier modules (see Liquid circulating apparatus).

Biotechnology

Bioactivity monitor-calorie meter — The direct and continuous monitoring of the very small heat effect associated with biological events in living organisms, up to 250 to 300 μW/ml, can be achieved by isothermal control of Peltier modules. The limit of detectability is 0.15 to 1.0 μW at 25 ± 0.01°C in a controlled environment with a pump circulating water externally and using Peltier modules (see Liquid circulating apparatus).

DNA sequence reactor — The DNA sequence reactor is maintained at the constant temperature of 37°C by a pump circulating water externally and using Peltier modules (see Liquid circulating apparatus).

Spectrophotometer cell thermoprogrammer — The temperature of the spectrophotometer cell holder is controlled with a Peltier cooling unit for DNA thermal denaturation-renaturation applications in nucleic acid and protein studies. It provides programmed heating and cooling of

samples in the spectrophotometer cell in the temperature range of 0 to 99.9 ± 0.1°C. Temperature agreement between cells is better than ±0.2°C at 40°C, better than ±0.5°C at 99°C, cooling rate 10°C per minute max.

Programmable thermal controller — The Peltier cooling unit provides rapid heat transfer to and from the test tube holder block with cooling rates up to 1°C per second from 0 to 100°C, accuracy ±0.5°C with no overshoot. It is a precise and convenient programmable thermal controller for DNA, RNA, and other samples. The accessory temperature control system has 2 kilobytes of nonvolatile memory available to store up to 100 user-defined programs.

Minifridge for blood — The bench-top Peltier cooler provides controlled pretest conditions for specimens and reagents, eliminating the need for containers of ice or repeated trips to the refrigerator. For blood banking, for coagulation heat-sensitive specimens and reagents should be stored at 4 to 8°C. The Peltier cooler is ideal for blood banking, radioimmunoassay (RIA), coagulation, and enzyme studies.

Photosynthesis analyzer — The photosynthesis analyzer environment is temperature controlled with a small-sized Peltier air conditioner (see Air conditioning).

Osmometer — The freezing point of a solution is determined precisely. The osmotic pressure of the solution can be indicated by mili-osmol with the freezing point method. A small amount of solution in the sample tube (0.3 to 2ml) is frozen by dipping it in a low-temperature 100-ml mixture of ethylene glycol 90% and water 10% in a bath cooled to the temperature of −11°C by a two-stage Peltier module; the top-stage has 32 couples; the bottom-stage has 128 couples (element size 2.8 × 2.8 × 2 mm). Figure 5 shows a drawing of an assembled osmometer.

Chromatography column holders — The liquid chromatography column is temperature controlled with a Peltier cooling unit (see Cold plate).

Thermoprogrammer for bioactive analyzer — The bioactive analyzer-calorie meter environment is temperature controlled at 25 ± 0.01°C with a pump circulating water externally and using Peltier modules (see Liquid circulating apparatus).

Centrifuge — The temperature of the centrifuge environment is controlled by a Peltier cooling unit (see Cold plate).

Medical

Hot/cold stimulator — The Peltier cooling/heating unit at the end of the pencil-type probe supplies heat or coldness in a determined cycle, sometimes alternating between hot and cold, sometimes maintaining either hot or cold for given periods of time. Consequently, it multiplies the function of treatment known as acupuncture or moxa in the Orient. It can also be used to diagnose a patient insensitive to hot and cold.

Cryosurgical destroyer[2] — The cryosurgical thermoelectric destroyer is a kind of cryotherapy based upon freezing of pathological tissue which is then rejected from an organism. The equipment consists of a control set-up and an operating cryoprobe. The temperature of the cryoprobe is −50 or −70°C using a two-stage Peltier module with water coolant for hot-side heat dissipation for the former temperature and with an autonomous cooling system for the latter temperature.

Microscope stage cooler — The Peltier-cooled microscope stage provides temperature control from −20 to 60 ± 0.1°C for specimens to be mounted on a microscope.

Microtome stage cooler — A sample tissue can easily be cut and sliced to a thin specimen for the microscope by freezing using a Peltier cooling stage. The stage is adaptable to any microtome. The temperature of the tissue is lowered or raised when desired by regulating the current flow to the Peltier module. A current-reversing switch is provided for rapid warming of the freezing plate, thus allowing the sample tissue to be removed quickly.

Portable mini (insulin) cool box — Insulin is maintained at the temperatures of 5 to 15°C by the portable Peltier cooling box at the ambient temperature of 45°C. The box has a self-contained power supply and an inner capacity of 30 cm^3.

Cold plate for dental cement — The temperature of dental cement is controlled on the Peltier-cooled plate. The plate delays the solidifying time for dental cement (see Cold plate).

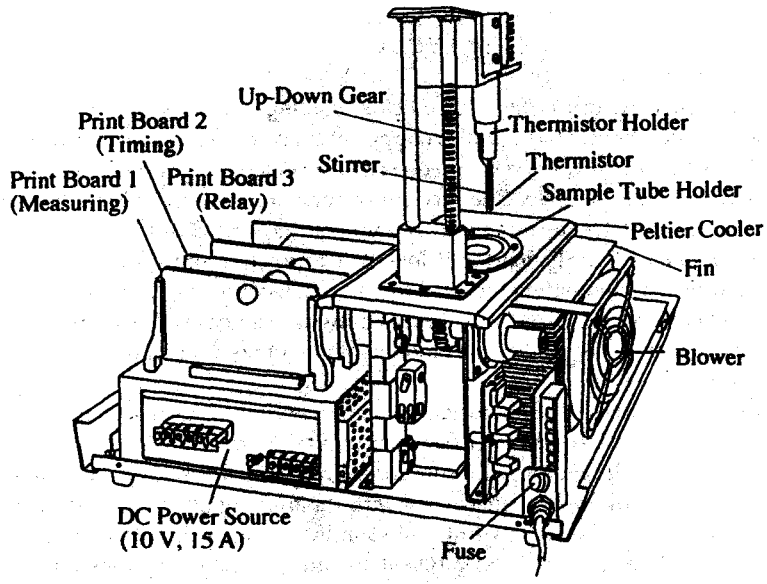

FIGURE 5 Osmometer with a two-stage Peltier module (courtesy Nikkiso Co., Japan).

Cold/hot therapy blanket — Water is pumped from the water jacket of the Peltier cooling unit and circulated through the blanket. The equipment is a closed loop blanket system for hot or cold therapy.

Mist tent — The environment in a tent is cooled by the Peltier air conditioner, providing an ideal environment for the use of inhalers (see Air conditioner).

Electronics

Refer to the Chapters 50 and 51.

Industrial

Dopant cooler for semiconductor device production — The Peltier cooling bath regulates the temperature of the chemical in the bubbler, which supplies chemical dopants to the semiconductor and fiber-optic industries within ±0.3°C of the selected temperature. Consequently, the thickness of the diffusion barrier of semiconductor devices or optical fibers is maintained, enabling precise quality control.

Silicon wafer cooling plate for semiconductor device production — A flat and contamination-free plate is cooled/controlled by the Peltier cooling unit for semiconductor wafers in the device production process. The wafer at the baking temperature of 150°C is cooled down to 20 ± 0.3°C in about 35 s. The photoresistant coating and developing process can be achieved under tightly controlled temperature conditions.

Chemical circulating system for semiconductor device production — The Peltier cooling system, comprising a circulator and filter, maintains the precise constant temperature required for the washing or etching process of the silicon wafers. It also facilitates the removal of small particles (larger than 0.1 μm) via filtering without the least contamination of the silicon wafers. The materials in contact with the chemical solution are carefully selected to match the working chemical solution, i.e., fluorine plastic tube, circulating pump, and silicone carbide (SiC) heat exchanger, etc.

General Purpose

Vacuum pump baffle — The Peltier-cooled baffle is incorporated for use on diffusion-pumped, high-vacuum systems and eliminates the need for compressors and cooling coils required by other baffle techniques. The temperature of chevron fins can be as low as −35°C.

Immersion cooler — The Peltier modules are enclosed in a heat exchanging metal case. With this type of immersion heat pump, the case facilitates the lowering of temperatures of small insulated laboratory baths.

Cold plate — The cold plates are the most basic type of Peltier cooling unit, as shown in Figure 1. Standardized Peltier cold plates for general purposes with an appropriate heat dissipator and waterproof sealing are available in a wide variety of sizes. The larger the size, the greater the cooling capacity and the higher the energy demand. They can be used in various types of liquid circulating apparatuses and air conditioning systems, custom built for a specific purpose.

Liquid circulating apparatus — The Peltier cooling system is easily operated for cooling/heating or automatically controlling the temperature of the circulating liquid. The liquid is pumped through the liquid jacket in contact with the Peltier module which has an appropriate heat dissipator. This is a universal liquid temperature-controlled system.

Air conditioner — The air convection heat exchanger fins are in contact with the Peltier module. The air passing between the fins is circulated by a blower. The heat can be rejected to air or to a liquid (e.g., water).

Consumer

Portable cooler (picnic box) — The portable Peltier cooling box is designed to work with a 12-V battery or a battery charger. It can be used on a boat, van, or camper by plugging it into a 12-V cigarette lighter socket or in fact anywhere by using a battery charger if AC power is available.

References

1. Mathiprakasam, B. and Fiscus, D., Development of Thermoelectric Freezing Point Apparatus, in *Proc. 6th Int. Conf. Thermoelectric Energy Conversion*, Arlington, Texas, 1986, 95.
2. Wartanowicz, T. and Czarnecki, A., Cryosurgical thermoelectric destroyer, in *Proc. 10th Int. Conf. Thermoelectrics*, Cardiff, 1991, 209.

53

Large-Scale Cooling: Integrated Thermoelectric Element Technology

John G. Stockholm
Marvel Thermoelectrics
Vernouillet, France

53.1 Introduction

Large-scale cooling is defined here as corresponding to cooling powers greater than several kilowatts. In this chapter integrated thermoelectric element technology is discussed because it is a logical design for large systems. The heat exchangers conduct electricity between consecutive n- and p-type pieces of thermoelectric material, referred to as elements. The size of the elements depends on the application.

In large systems, because of the cost of power, the electrical power consumption is important. The overall efficiency, which is characterized by the coefficient of performance (COP = cooling power/electrical power), becomes an important parameter when the cooling exceeds several kilowatts.

The thermal resistances characterize the thermal barriers that exist between the thermoelectric material and the fluid and correspond to temperature "drops" which decrease the performance. Evidently these temperature drops must be small when attempting to achieve high efficiencies.

Thermoelectric systems constitute an assembly of thermoelectric building blocks. A thermoelectric building block consists of thermoelectric material with a heat exchanger on the cooled side and on the heated side.

0-8493-0146-7/95/$0.00+$.50

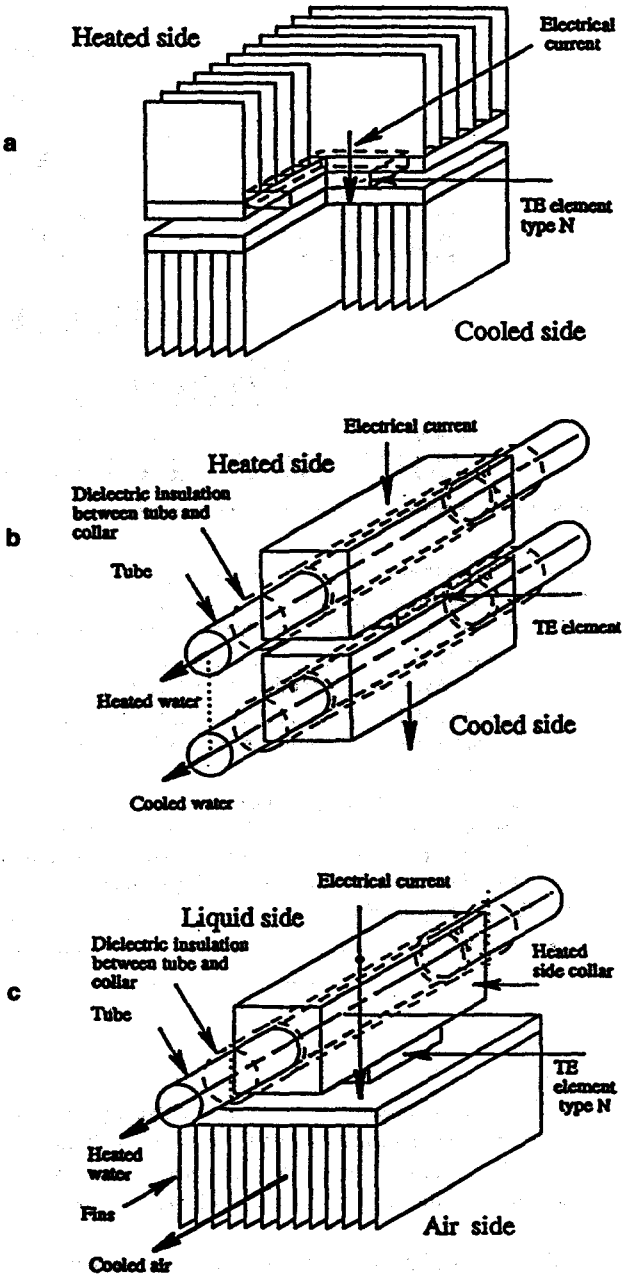

FIGURE 1 (a) Air-air thermoelectric building block; (b) water-air thermoelectric building block; (c) water-water thermoelectric building block. (With permission of the Institute of Electrical Engineers of Japan, Tokyo, Japan.)

53.2 Building Block Design

The design of the building block depends on the type of fluid employed, gas or liquid, and the three combinations, gas-gas, gas-liquid, and liquid-liquid, are considered. Generally the gas is air and the liquid is water. Typical building blocks for air-air, air-water, and water-water are shown in Figure 1.

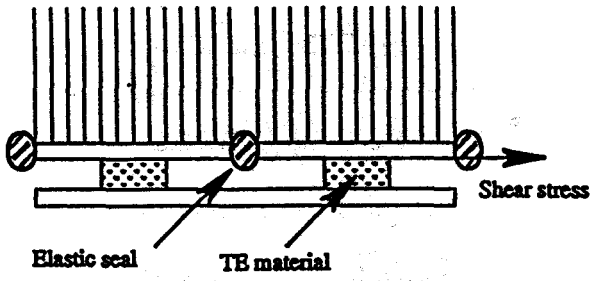

FIGURE 2 Air heat exchangers.

Constraints

There are a number of constraints when designing building blocks for large systems:

1. Electrical constraints—two aspects; the dielectric insulation where electrical codes specify tests between the electrical circuit and ground, which depend on the voltage of the system and the safety of people where electrical codes specify rules concerning the access to parts with an electrical potential, the codes depending on the maximum voltage on the system.
2. The continuity of the fluid circuit; this requires that the circuit be sealed and that adjacent heat exchangers along the fluid circuit are electrically insulated.
3. The mechanical means of absorbing shear stress, which is detrimental to thermoelectric material.

It is necessary to examine separately the constraints for gas and for liquid heat exchangers.

Air Heat Exchangers

All the air heat exchangers are in the electrical circuit which contains the thermoelectric material. Adjacent air heat exchangers along the air circuit are electrically connected through thermoelectric material and therefore they are at a different electrical potential; consequently there must not be a direct electrical connection which bypasses the thermoelectric material. This is relatively easy to achieve because, even with moist air, the metallic surfaces in contact with the air can be at an electrical potential without forming parasite electrical circuits through the air. The difficulty arises when there is a film of condensed water which joins adjacent heat exchangers.

So that condensation does not accumulate it must be eliminated, for example by gravity; one needs only to have sufficient space between adjacent heat exchangers. In practice several millimeters are sufficient because the voltage potential between the heat exchangers of adjacent building blocks is well below a volt.

In Figure 2 two adjacent air heat exchangers with a flexible elastic material between them which constitute a gas seal, an electrical insulator, and a means of absorbing the shear stress on the thermoelectric material are shown. The material can be silicone or rubber and can be applied with a gun or made in a mold.

Liquid-Heat Exchangers

For a non-electrically conducting fluid, such as an organic liquid, the liquid serves as its own electrical insulator. Nevertheless, the tube containing the liquid must be isolated electrically between adjacent pieces of thermoelectric material. In the case of an electrically conducting liquid such as water electrical insulation in theory is not necessary provided that the voltages are insufficient to create electrolysis. Nevertheless, a grounded water circuit constitutes safer and more reliable equipment.

At higher voltages a dielectric insulation is absolutely necessary to avoid electrolysis and the water circuit is consequently grounded. Figure 3 shows two methods of electrically separating

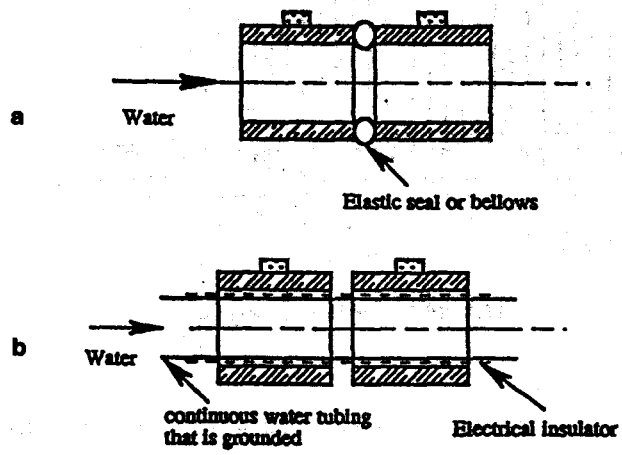

FIGURE 3 (a) Water heat exchanger, low-voltage operation; (b) high-voltage operation.

adjacent heat exchangers along the liquid flow which are not adjacent electrically. In Figure 3a two adjacent water heat exchangers with no dielectric insulation between the electrical circuit and the water are shown. The component between the heat exchangers can be a rubber-type seal, an "O ring", or bellows, etc. This technology is limited to an operating voltage of several volts. The component absorbs the shear stress and ensures that electrical insulation is maintained between two adjacent heat exchangers. A small electrical current will flow through the water from one heat exchanger to another, due to their small electric potential difference.

Figure 3b shows two adjacent heat exchangers with a tube which is grounded. There is a dielectric insulation between the tube and the electrically conducting collars. This technology satisfies the continuity and the dielectric aspect, but precautions must be taken relating to the transmission of shear stress to the thermoelectric material.

53.3 Assembly Structures

Types of Assemblies

Three types of structures will be defined which are characterized by the relative position of the pieces of thermoelectric material which are alternately of n-type and of p-type semiconductor. They are located with air heat exchangers on the cooled and on the heated sides.

1. Column structure (Figure 4a)—The heat exchangers have two bases which are perpendicular to the line formed by the electrical circuit.
2. Linear structure (Figure 4b)—The heat exchangers have only one base and are located on the side of the line formed by the electrical circuit
3. Planar structure (Figure 4c)—The thermoelectric material is situated in a plane and the electrical current passes alternatively up and down through the thermoelectric material.

Mechanical

The structure must be such that:

1. The thermoelectric material must always be under compression; this is achieved by using tie rods and bolts
2. The thermoelectric material should only be subjected to a small shear stress; this requires that the structure includes all necessary means for absorbing thermal expansion

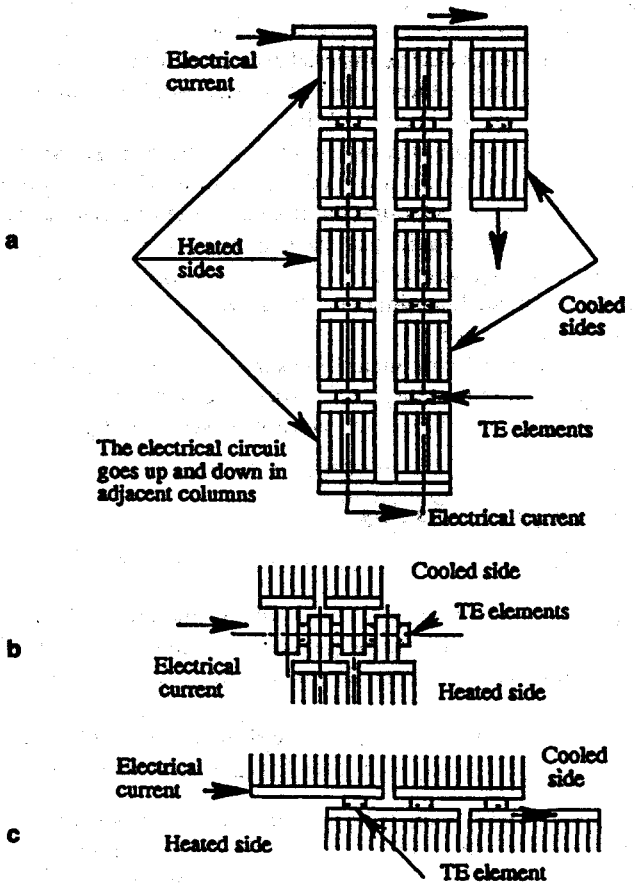

FIGURE 4 Types of assemblies; (a) column structure; (b) linear structure; (c) planar structure. (With permission of the Institute of Electrical Engineers of Japan, Tokyo, Japan.)

Air heat exchangers are shown because, should there be any shear stress due to the differential thermal expansion, it can be absorbed by an elastic seal which is located between the heat exchangers.

Liquid heat exchangers can be used instead of air gas heat exchangers in all three types of structure, provided that the shear stress is absorbed by the structure and not transmitted to the thermoelectric material.

Electrical

The electrical current must pass from one thermoelectric element to the next and there must be no short circuits between adjacent heat exchangers. This is achieved by having a gap between air heat exchangers and using an electrically insulating seal.

53.4 Fundamentals

The design of large systems requires the thorough study[1,2] of thermoelectric material interfacing and shear stress, sealing techniques, and fluid circuitry.

Thermal Aspects

This topic is covered in detail in books on thermoelectricity[3,4] and in heat transfer books.[5]

Structural Aspects

The mechanical properties of thermoelectric material require that the structure allows levels of compression in excess of 5 MPa on the thermoelectric material, while keeping the shear stress on the thermoelectric material to levels well below 5 MPa.

The shear stress essentially arises from the difference in the thermal expansion of the hot-side and the cold-side heat exchangers. For air heat exchangers an elastic seal is an efficient way of absorbing any thermal expansion parallel to the interface of the thermoelectric material.

Several techniques can be used for liquid heat exchangers: (1) compressible material, bellows, and "O" rings, which create segmentation on the liquid circuit and decrease the circuit's water tightness reliability, and (2) insulated continuous tubing, which requires capped thermoelectric material with a thermal grease interface.

The compression on the thermoelectric material ensures that the soldered interfaces between the thermoelectric material and intermediate parts (caps), or the interface with the heat exchangers, do not separate. Separation would result in high electrical resistance and possible arcing.

Thermoelectric Material Interfacing

There are several alternatives:

1. Direct soldering to the heat exchanger. This results in the lowest thermal and electrical interface resistances. However, it must be physically possible to solder the thermoelectric material to one or both heat exchangers *in situ* and the shear stress at the interface must be below 5 MPa.
2. Greased pressure contact at interface. Thermoelectric material is soldered to copper or aluminum caps with the outer surface of the caps flat (plane) or spherical.

The interface resistance varies considerably with pressure. When the pressure is below 0.5 MPa the resistance values can vary severalfold, so in practice it is necessary to have interface pressures in excess of 1 MPa. It is easy to maintain the quality control of thermoelectric elements with metallic caps.

53.5 Past Designs and Applications

Many companies were involved in thermoelectrics in the early 1960s and this period is covered in an excellent review by Lynch.[6] Although there were many designs, few large-scale applications were built. A convenient way to present the various designs is through the patents that were filed relating to large systems. Many of the designs did not mature into actual systems due to lack of development work, but nevertheless some of them are relevant and warrant attention.

Inventors

The most prolific of inventors in thermoelectric refrigeration was Elfving, who filed over 15 different patents. His most frequent air technology used tubes with fins but none of his ideas were ever used in large systems.

There are many people who have filed a few patents, some of which are of great importance because they influenced the trend of integrating the thermoelectric material to the heat exchangers. They are Lindenblad of RCA, A. B. Newton of Borg-Warner Corp., and C. J. Mole and H. D. Coe of Westinghouse Corp.

Patents were filed in 1964 on the column structure for air-air exchangers by C. J. Mole[7] of Westinghouse and by A. B. Newton[8] of the York Division of Borg-Warner. The Mole patent was published in 1965. However, the Newton patent was only published in 1970, which indicates that there was opposition to the publication of the patent, although the reasons are not publicly known.

A major concept, due to Coe[9] of Westinghouse, was a column assembly of alternating hot and cold heat exchangers which are compressed together by wires to form a cubic-type structure.

The patents of Newton, Mole, and Coe form the base of air-air subunits for large systems where elements of thermoelectric material are used and the electrical current goes through the air heat exchangers.

There were many patents in the 1960s on linear structures,[10–13] although none led to any known prototypes.

Mole[14] patented the concept of not electrically insulating the water heat exchangers in water-air units and having bellows between each heat exchanger in a planar structure. Benicourt et al.[15] and Buffet[16] patented a column structure for water-water systems with grounded tubing which uses capped thermoelectric material with a flat surface on one side and either a spherical or cylindrical surface on the other.

Borg-Warner

The York Division of Borg-Warner was only interested in air-air systems. The approach taken by Newton was to "solder" the entire "cubic" structure simultaneously in an oven. Borg-Warner had a policy of not publishing, so very little is known apart from the information in the patents. It appears that major difficulties were encountered when soldering all the junctions simultaneously.

Westinghouse

The same approach was employed for air-air[17] with the columns being tightened with a central tie rod. Small units were manufactured with cooling powers of several hundred watts for use in military prototypes, but none were commercialized.

In 1972 two highly documented papers[17,18] which covered the design of a water-water 7-kW unit, model 20GS, were published.

Westinghouse was very active in water-air systems for naval applications.[17–19] The design was based on the Mole patent.[14] The U.S. Navy had a thermoelectric unit made by Westinghouse for the air-conditioning on the USS Dolphin. It is a water-air unit with a planar structure and the water in direct contact with the electrical circuit. In order to avoid electro-corrosion the operating voltage is in the range of 5 V and the unit operated over a 10-year period.

ASEA

A prototype unit to air-condition and heat a passenger railway coach was built by ASEA for the Swedish railways. Two Swedish publications are available: one by Ridal[20] of the Swedish railways and one by Lundqvist[21] of ASEA. The design was based on two patents by Widakowich.[22,23] The first describes a planar structure that uses thermoelectric material, the second relates to capping the thermoelectric material with copper and using a pressure contact. The units operated for several years before being dismantled.

Air Industrie—Railway Application

Air Industrie was a manufacturer of compression cycle air-conditioning for passenger railway coaches. In 1973 J. P. Buffet initiated a development program for thermoelectric air-conditioning of passenger railway coaches for the French railways. The design was the column structure based on a patent by Gaudel.[24] This type of structure was retained after studying the planar and the linear structures and was considered to be the most sturdy of the three structures. Capped thermoelectric material was used because soldering a complete unit was found to be unreliable. The heat exchangers are based on patents by Buffet.[26] The program led to a coach being equipped in late 1977 with a 20-kW air-conditioning unit.[25] The coach was operated for over 10 years without a single thermoelectric failure.

Air Industrie—Naval Application

In 1980 the French Navy started a research and development program with Air Industrie to develop a water-water unit for producing cold water for air-conditioning. The column structure was chosen[15,16] with the water tubing electrically insulated from the heat exchangers which are in the electrical circuit.

The patent[15] describes capped thermoelectric material with, on one side a flat surface and on the other either a spherical or a cylindrical interface. During the tightening process this interface allows some movement of the cylinder or sphere to compensate for the nonparallelism of consecutive layers of water heat exchangers.

A patent[16] covers the mechanical linking of the hot and cold tubes so as to reduce the differential thermal expansion. Because of the differential thermal expansion of the hot and cold tubes capped thermoelectric material with one flat surface is used so as to absorb the mechanical shear stresses transmitted by the tubes.

The units have been described in the literature[27,28] and have undergone extensive endurance testing for more than 5 years.

Conclusions on Technologies for Large Systems

Interfaces

The soldering of thermoelectric material directly to both the heat exchangers presents the same difficulties as those in the manufacture of thermoelectric modules. The largest modules contain about 127 couples. Nobody has yet successfully soldered more than a few thermoelectric elements to heat exchangers in one operation. When thermoelectric elements are soldered on both sides to heat exchangers, and as most structures transmit shear stress to the thermoelectric element, that shear stress can be incompatible with the mechanical properties of the thermoelectric material.

If only one face is soldered and the other is a capped flat surface with a pressure contact, this surface can accommodate the shear stress.

A thermoelectric element when capped on both sides and with two pressure contacts facilitates the quality control of each piece. A safe and reliable design is a thermoelectric element with one flat cap and one spherical cap: the flat surface allows positioning and displacement without creating shear stress, while the spherical cap allows correct interfacing between nonparallel planes.

In large systems the area of the pieces of thermoelectric material is generally greater (0.5 to 3 cm^2) than in modules (0.2 cm^2).

Air-Air Systems

A column structure with a tightening mechanism per four columns is considered the most reliable of today's design. It is considered that direct soldering of the thermoelectric element to the heat exchangers can only be used for small individual columns. Capped thermoelectric material is more suitable for large subunits.

Water-Water Systems

There is published data on only two large water-water systems: a Westinghouse 7-kW model, 20GS, designed for low-voltage operation with the electrical circuit in contact with the water, and an Air Industrie 15-kW unit 10T925, designed for operating voltages in excess of 100 V with a grounded water circuit.

Water-Air Systems

In the case of water-air systems the only documented system built, and which has been in operation for a prolonged time, is from Westinghouse.[19] It was installed on the USS Dolphin for a period of 15 years. The design is a planar structure having a central tube with an air heat exchanger above

and below. The central tube consists of hollow blocks, as shown in Figure 3a, with bellows between each block. The thermoelectric elements (3 cm^2) are soldered to the hollow block and to the "double " air heat exchangers.

53.6 Future Applications

Currently a number of applications where large powers are involved are being examined, developed, and in some cases commercialized.

Parked aircraft — The air-conditioning of an aircraft parked at a terminal gate requires cooling powers of several tens of kilowatts. The systems that are being studied are air-air.[29]

Trains — The air-conditioning of passenger railway coaches[25] is on hold at the moment but applications to drivers' cabs are being studied. The cooling powers are of several kilowatts, but this application will no doubt come out sooner than the air-conditioning of a whole railway coach because the cooling powers are less and the electrical power consumption is less critical.

Automobiles — There is considerable interest in the thermoelectric cooling of automobiles, especially electric cars. At the present time people are more concerned with comfort cooling (blowing cool air onto the passengers) rather than reducing the overall temperature of the air in the car. Because of the large potential market some companies are examining the integrated technology.

Naval — Navies are pursuing the use of thermoelectrics for several reasons. In naval applications seawater is always available, where the heat can be rejected either directly or indirectly. Heat rejection to water leads to thermoelectric systems that are more efficient than those rejecting heat to air. When dealing with confined volumes (submarines) the elimination of a source of a CFC is always an asset. Large-scale water-water cooling is already a reality.[27] A water-water thermoelectric system has the advantage of replacing traditional compression systems, which produce chilled water. Another application is decentralized thermoelectric air-conditioning which produces directly cooled air. Another potential area for development is the cooling of naval containers. The commercialization of large two-stage modules has opened up areas where greater temperature differences are required, such as cold rooms and deep-freeze rooms.

Containers — There has been considerable interest in thermoelectric cooling by companies either manufacturing or using containers. The economics are such that a thermoelectric system is much more expensive than a compression cycle system, especially when one requires deep freeze temperatures. Specialized thermoelectrically cooled containers which are limited to maintaining +4°C may have a future.

53.7 Conclusions

Over the past 30 years the performance of thermoelectric material has increased by about 20% and the potential improvement of bismuth telluride is also about 20%. However, today we must work and design with existing materials.

The integrated thermoelectric technology which emerged in the 1960s is slowly progressing. This technology is necessary for large-scale cooling because it can be adapted to large electrical currents. It will really increase with mass production which will reduce costs considerably. Today there is no mass production; the only ongoing production using this technology is for naval systems, but the numbers are small so the costs are still high.

This technology can also be applied to medium powers using smaller thermoelectric elements but systems with thermoelectric modules are cheaper than systems with thermoelectric elements provided the production numbers are well below those of thermoelectric module production.

References

1. Stockholm, J. G., Modern Thermoelectric Cooling Technology, in *Proc. IXth Int. Conf. on Thermoelectrics*, Pasadena, California, March 1990.
2. Stockholm, J. G. and Schlicklin, P. M., Industrial thermoelectric air cooling in the kilowatt range with heat rejection to air, in *Proc. XXIst Intersociety Energy Conversion Engineering Conf.*, San Diego, CA, August 1986. (American Chemical Society, Washington, D.C.)
3. Heikes, R. H. and Ure, R. W., *Thermoelectricity: Science and Engineering*, Interscience Publishers, New York, 1961.
4. Goldsmid, H. J., *Electronic Refrigeration*, Pion Ltd., London, 1986.
5. McAdams, W. H., *Heat Transmission*, McGraw-Hill, New York, 1954.
6. Lynch, C. J., Thermoelectricity: The breakthrough that never came, *Uneven 7*, MIT Press, 1972, 47–57.
7. Mole, C. J., U.S. Patent 3,213,630, 1965.
8. Newton, A. B., U.S. Patent 3,527,621 (filed 1964), 1970.
9. Coe, H. D., U.S. Patent 3,626,704, 1971.
10. Minnesota Mining Company, U.S. Patent 2,944,404, 1960.
11. Whirlpool Corporation, U.S. Patent 2,949,014, 1960.
12. Alsing, C. F. (Westinghouse), U.S. Patent 3,004,393, 1961.
13. Siemens Corporation, U.S. Patent 3,071,495, 1963.
14. Mole, C. J., U.S. Patent 3,178,895, 1965.
15. Benicourt, M., Buffet, J. P., and Huard, J. F., U.S. Patent 4,499,329, 1985.
16. Buffet, J. P., G B Patent 2,027,534, 1983.
17. Mole, C. J. and Purcupile, J. C., Recent developments on direct transfer thermoelectric cooling for shipboard use, in *Proc. Annual ASHRAE Meeting*, Lake Placid, New York, June 1968, Paper No. 2078, II 3.1–II 3.12.
18. Mole, C. J., Foster, D. V., and Feranchak, R. A., Thermoelectric cooling technology, *IEEE Trans. Ind. Appl.*, 1A-8, No. 2, 108–125, March/April, 1972.
19. Blankenship, W. P., Rose, C. M., and Zemanick, P. P., Application of thermoelectric technology to naval submarine cooling, in *Proc XIIIth Int. Conf. on Thermoelectric Energy Conversion*, 224–231, July 1989, Eds. Scherrer, H. and Scherrer, S., Ecole des Mines, Nancy, France.
20. Ridal, J., Peltier-system för luftkonditionering i person vagnar Del II, *Järnvägs Teknik*, ref. DK 628.8:625.232, 40 No. 4, 74–82, 1972 (in Swedish).
21. Lundqvist, D., *Peltier Heat Pumps*, Translated by U.S. Department of Energy, 1975, ref. DOE-tr-5 (in Swedish, origin unknown).
22. Widakowich, Swedish Patent Appl. 16079/69, 1969.
23. Widakowich, Swedish Patent Appl. 14892/1967, 1967.
24. Gaudel, G., U.S. Patent 4,038,831, 1977.
25. Stockholm, J. G. and Pujol-Soulet, L., Prototype thermoelectric air-conditioning of a passenger railway coach, in *Proc. IVth Int. Conf. Thermoelectric Energy Conversion*, Arlington, Texas, 136–141, March 1982.
26. Buffet, J. P., U.S. Patent 4,420,940, 1983.
27. Buffet, J. P. and Stockholm, J. G., Industrial thermoelectric water cooling, in *Proc. XVIIIth Intersociety Energy Conversion Engineering Conf.*, Orlando, Florida, 253–258, August 1983 (American Institute of Chemical Engineers, New York).
28. Stockholm, J. G. and Schlicklin, P. M., Naval thermoelectrics, in *Proc. XIIIth International Conference on Thermoelectric Energy Conversion*, Nancy, France, 235–246, July 1989.
29. Gwilliam, S., Feasibility and prototype developments of a thermoelectric cooler for parked aircraft, in *Proc. Xth Int. Conf. on Thermoelectrics*, University of Wales, Cardiff, U.K., Sept. 1991, Barbow Press, Cardiff, U.K., 218–221, 1991.

54

Medium-Scale Cooling: Thermoelectric Module Technology

John G. Stockholm
Marvel Thermoelectrics
Vernouillet, France

54.1 Introduction

Medium-scale cooling is defined as the range in which thermoelectric modules are most suited for producing the cooling. This technology is used extensively for industrial equipment requiring small cooling powers, and where one or several modules are sufficient (see Chapter 52). This chapter will only address the technology that uses ten or more thermoelectric cooling modules.

The fundamental characteristic is that the modules are electrically insulated from the heat exchangers, so this technology is simpler than the technology in which thermoelectric elements are integrated to the heat exchangers (see Chapter 53).

54.2 Fundamentals

Types of Thermoelectric Modules

A thermoelectric module consists of a number of pieces of thermoelectric material referred to as thermoelectric elements. They are of n-type and of p-type semiconductor and are generally connected electrically in series inside a thermoelectric module (see Chapter 49).

There are two types of thermoelectric modules, as shown in Figure 1. Those with two ceramic plates, which support the thermoelectric elements, and those without ceramic plates, in which the thermoelectric elements are held together by a resin. Historically the first modules did not have ceramics, the electrical insulation between the copper connectors which link consecutive thermoelectric elements was achieved by placing a sheet of organic insulator such as Mylar (c)* between

*Registered trademark of E I Dupont de Nemours and Company, Inc., Wilmington, Delaware.

0-8493-0146-7/95/$0.00+$.50

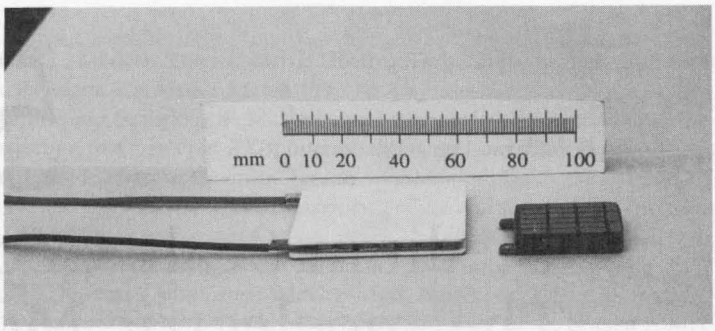

FIGURE 1 Photograph of a module without and with a ceramic insulating plate.

the thermoelectric module and the heat exchanger. Nowadays it is more economical to manufacture modules that use ceramic. The advantages are: (1) the ceramic is a good electrical insulator for low voltage operation, and (2) the ceramic, when used with a thermally conducting grease, provides a relatively low thermal resistance between the ceramic and the heat exchanger and allows easy assembly of the thermoelectric modules to the heat exchangers.

Thermal

The thermal requirements are not difficult to satisfy but the heat exchangers must be designed with a base plate to interface with the thermoelectric module. The thermal resistance of the base plate must be small compared to the overall thermal resistance. In addition the thermal resistance at the interfacing of the ceramic must be compatible with the rest of the thermal resistances. Heat losses between the two sides (cold and hot) must be minimized and the tightening screws must have thermally insulating washers.

Mechanical

The main problem with modules is that their structure, which today generally uses a ceramic on each side, cannot withstand any bending. Shear must be limited to the weakest shear component of the structure, which is the interface of the thermoelectric elements.

When several modules are assembled between two plates, the modules must all have the same thickness and the ceramics plates must be parallel to 0.02 mm. The heat exchanger plates must also be parallel, otherwise bending will occur and the thermoelectric modules damaged.

To decrease this problem, a large heat exchanger plate can be employed which holds n-modules on one side while on the other side there are several plates which are tightened separately. This reduces the number of modules that must have exactly the same thickness.

Electrical

The modules can be connected through their leads, either in series, in parallel, or any combination of both. The objective is to enable the total system to operate under a given voltage. The ceramic plates usually used are of alumina, although in very special circumstances beryllium oxide has been used because of its higher thermal conductivity. Aluminum nitride has also been used as it is a good thermal conductor and an excellent dielectric insulator; however, it is very expensive.

Alumina is excellent theoretically, but under severe operating conditions microcracks can develop over a long period and serve as the source of high-voltage breakdown. In the case of high-voltage operation requiring dielectric tests of several kilovolts, it is necessary to add to the alumina an organic insulator such as Mylar (c)™ or Kapton (c)*. In this case there is no advantage in using a ceramic unless the thermoelectric module is cheaper.

*Registered trademarks of E I Dupont de Nemours and Company, Inc., Wilmington, Delaware.

54.3 Heat Exchangers

There are two categories of heat exchangers, those using a gas such as air and those using a liquid such as water. Both will be examined briefly.

Air Heat Exchangers

Straight Fins

The cheapest fins are extruded fins (heat sinks), which are sold by many companies. The extrusion process does not produce thin, closely spaced fins. Consequently some companies manufacture heat exchangers by machining a flat plate with grooves into which the fins are stuck using epoxy resin. A higher fin surface is obtained but a drawback is the thermal resistance at the interface between the fins and the base (see Figure 2). Data on the performance of these fins are provided by some manufacturers.[1]

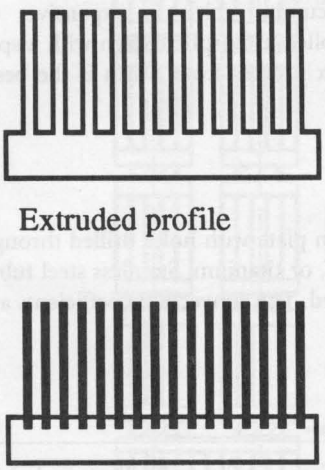

FIGURE 2 Detail of extruded fins and epoxied fins.

Straight fins can also be manufactured by a shaving process called "skyving." The initial patent belongs to Peerless of America, although several companies are licensees. Unfortunately, this process can only make straight fins.

Part of a skyved heat exchanger made by Showa of Japan is shown in Figure 3.

Other Types of Heat Transfer Surfaces

There are many heat transfer geometries for fins. The best reference is the book by Kays and London.[2] The surfaces can be flat, such as fins, or like pins. Efficient pins are difficult to manufacture and will not be discussed further.

Fins come in a great variety of shapes and sizes. There are two types, which both need to be attached to a base: (1) individually stamped fins, and (2) folded fins. The advantage of folded fins is that a group of fins are located together which simplifies the attaching process. The fins can be louvered, lanced, and perforated (see Figure 4).

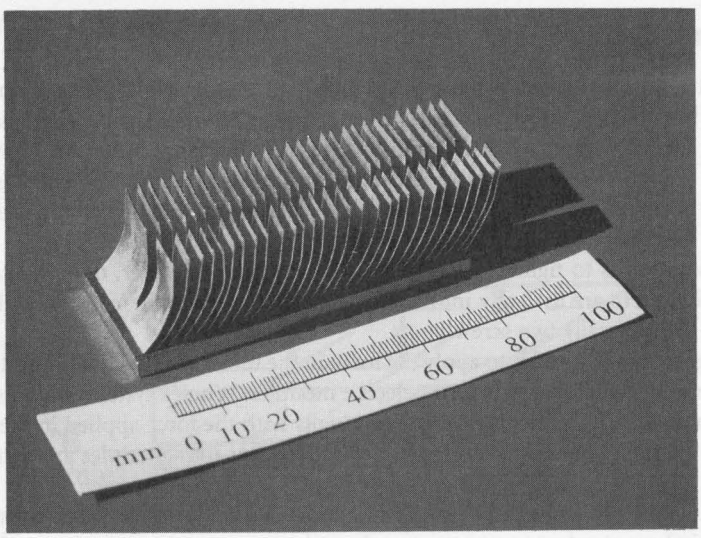

FIGURE 3 Photograph of a "skyved" heat exchanger.

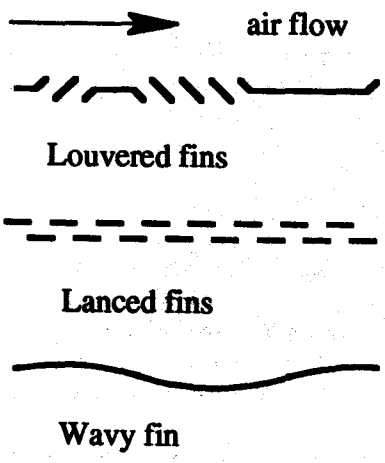

FIGURE 4 Schematic of fins: louvered, lanced, and wavy.

Fin-to-Base Attachment Processes

The process or material used to attach the fins to the base must have a low thermal resistance. The ideal solution is to have continuity of the material, but machining the fins out of a thick plate is very expensive. There is also the "skyving" process previously mentioned.

Fins are generally made of copper or aluminum. Aluminum is generally preferred because of the lower weight. Copper is easy to solder, whereas aluminum is more difficult. The techniques generally require that at least one of the parts be clad with an alloy of aluminum-silicium, which melts at a slightly lower temperature than pure aluminum. The parts can be bonded by: (1) dipping in a salt bath, which creates a pollution control problem; (2) brazing in a vacuum, which is expensive; or (3) brazing in a controlled-atmosphere oven with a special flux—the Nokolox process from Alcan is the best-known process.

Water Heat Exchangers

The water heat exchanger can consist of a copper or aluminum plate with holes drilled through it. Tubes can be used, manufactured out of copper, aluminum, or titanium. Stainless steel tubes constitute a thermal resistance that generally cannot be neglected. The convection coefficients are well known.[3]

54.4 Structures

There are three basic types of structures: planar, column, and linear (see Figure 5). Thermoelectric modules have two parallel surfaces traversed by thermal powers. These two surfaces have manufacturing tolerances on the thickness and the parallelism, these tolerances influence the choice of structure.

Planar Structure

The planar structure is the only one which employs a big plate on one side onto which many modules can be attached. A big heat exchanger is always cheaper than many small ones. This is probably the reason why all systems built to date use the planar structure. The most frequent method is to tighten two plates of the same size together (see Figure 6). There is a big plate on one side. The other plate serves to tighten several modules together, which reduces the number of modules that must have exactly the same thickness.

The ideal solution is to tighten the modules individually. However, the disadvantage of this is that on one side there are as many individual heat exchangers as there are modules and for each module there are generally two screws.

The best tightening method is to apply the force in the middle of the module and have individual heat exchangers on one side of the thermoelectric modules. When a system contains many modules there are several ways of tightening them individually with the force applied in the middle of each module. Two examples are given in Figure 7, where two or four modules are tightened with one central screw.

All tightening mechanisms must incorporate an elastic component such as a spring or a Belleville washer. This is because the structure expands and contracts when an electrical current passes through the modules.

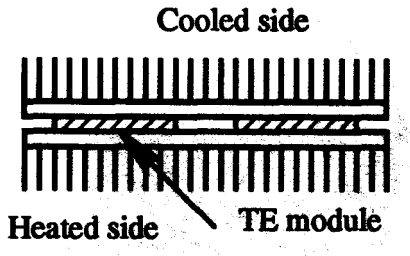

Figure 5a Planar structure.

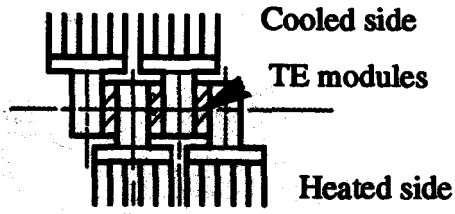

Figure 5c Linear structure.

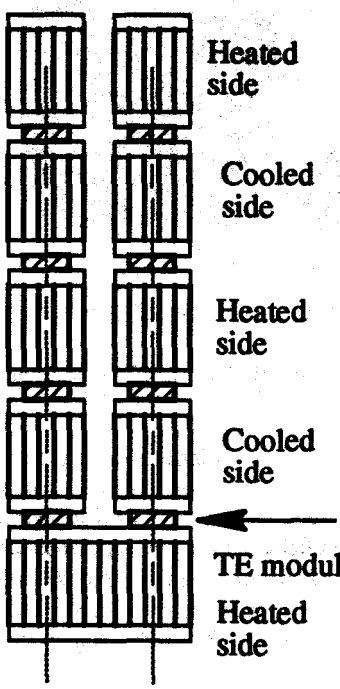

Figure 5b Column structure.

The wiring between modules is not shown.

FIGURE 5 Structures with thermoelectric modules.

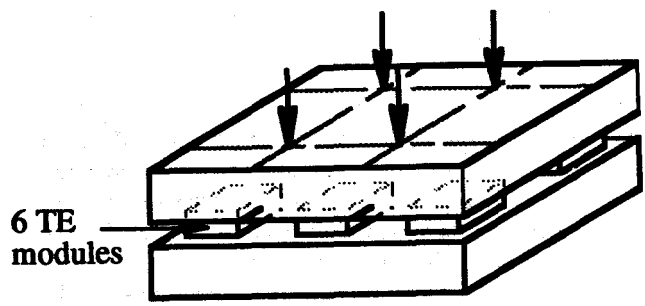

FIGURE 6 Traditional tightening mechanisms. (With permission of the Institute of Electrical Engineers of Japan, Tokyo, Japan.)

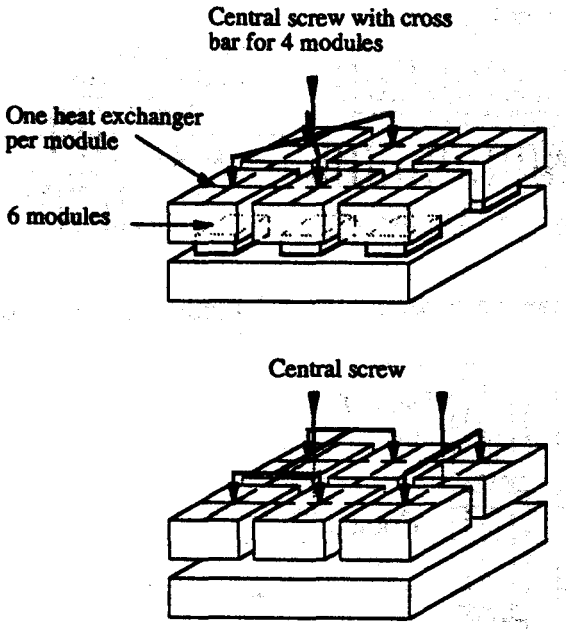

FIGURE 7 Central tightening mechanisms. (With permission of the Institute of Electrical Engineers of Japan, Tokyo, Japan.)

Linear and Column Structures

The difficulty with linear and column structures is the same as that of stacking a pile of bricks; if the top and bottom surfaces of the bricks are not parallel, then the pile is unstable and will topple over. It is similar when stacking TE modules. A disadvantage of this system is that each module requires an individual heat exchanger.

The tightening mechanisms are located alongside the lines or columns and it is practical to tighten four lines or four columns together.

54.5 Industrial Applications

Past Applications

Radio Corporation of America (RCA)

RCA was one of the first companies to invest heavily in thermoelectrics. They manufactured many small consumer-type products. In particular they made a 30-kW air-conditioning unit for the U.S. Navy[4] based on thermoelectric modules.

Carrier Corporation

This company worked on naval applications,[5,6] for example a 3.5-kW air-conditioning unit with heat rejection to water. The unit consists of six subunits, each one containing four thermoelectric modules. Each thermoelectric module is 13.7 × 17.8 cm and has 130 thermoelectric elements with an individual area of 1.13 cm^2 and a thermoelectric element height of 2.54 mm. This is much bigger than present-day commercial thermoelectric modules.

In the mid-1960s Carrier built a thermoelectric air-conditioning and heating system for the headquarters of S. C. Johnson in Racine, Wisconsin. Unfortunately nothing was ever published on the installation. The system consisted of about 30 decentralized air-conditioning units with heat rejection to a water circuit. In 1973 the system was operating and the only problem was the

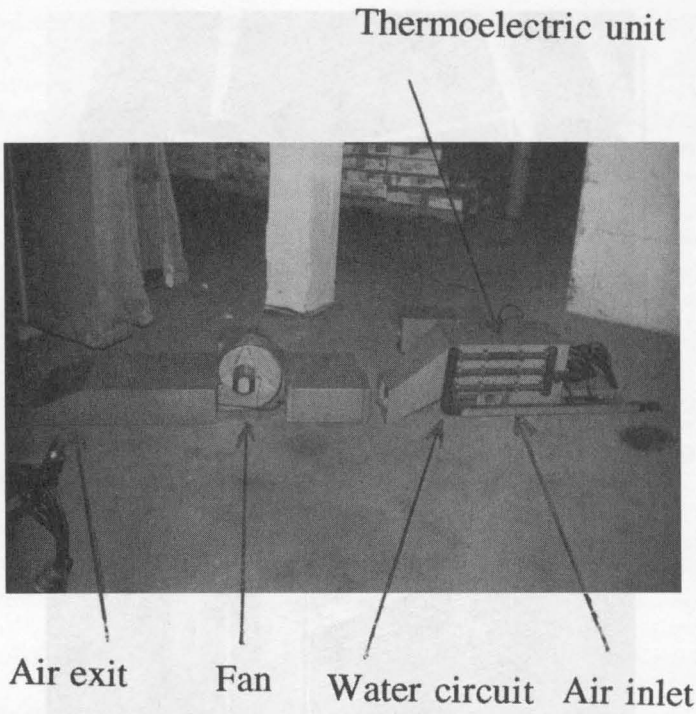

FIGURE 8 Photograph of Carrier Corp. unit at S. C. Johnson.

nonavailability of spares, especially concerning the power supplies and controls. A photograph of a unit when taken down for repair and laid out on the floor is shown in Figure 8. The cooling power of each unit is 1.5 kW and the heating power 1.8 kW.

The thermoelectric modules were made by Carrier. They are 12 × 12 cm, with 64 elements and a thickness of 2.5 mm. The exact thermoelectric element area is not known but is estimated to be around 60 mm^2. The maximum electrical current was 80 A in the cooling mode.

Carrier stopped all activity in thermoelectrics after completing this installation.

Borg-Warner Corporation

This company was very active but published practically nothing.[7] Their main activity was in small compact systems which used ceramic thermoelectric modules.

U.S. Navy

The U.S. Navy was a major driving force in developing thermoelectrics in the early 1960s. A very interesting paper describes a frozen and a chilled stores box.[8] The units produce cold air and reject the heat into a water circuit at 7°C. The cooling power is 0.7 kW for the chilled stores at −1°C and 2.5 kW for the frozen store at −18°C. The systems consist of subunits each containing 36 modules.

The thermoelectric modules are 8.4 × 8.4 cm and 15 mm high. Each module contains 48 thermoelectric elements of a diameter of 7.1 mm (area = 40 mm^2), with a height of 9.9 mm.

Present Applications

TECA

Today TECA of Chicago is the only company manufacturing multimodule cooling systems. A typical product is the C4000 air-conditioner. The heat is rejected to air and it has a cooling power of 400 W when the inlet temperatures on the cooled side and on the heated side are equal to 60°C.

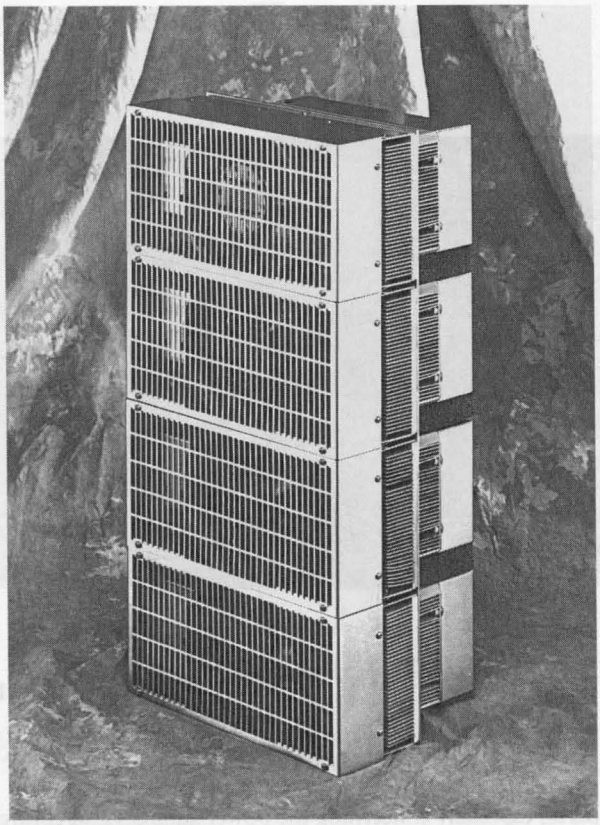

FIGURE 9 Photograph of a TECA Americool R4000 series unit.

It consists of four subunits joined together. All the air circuits are in parallel. A subunit is approximately 15 × 30 × 24 cm and cooling is obtained using commercially available thermoelectric modules. The number of modules and their characteristics is proprietary. A photograph of one unit is given in Figure 9 and the performances of a model Americool R4000 series are given in Figure 10.

Midwest Research Institute

Midwest Research Institute of Kansas City, Missouri, has developed a microclimate thermoelectric air-conditioning unit for the pilots of helicopters.[9] The unit has a cooling power of 1000 W. It contains 96 ceramic commercial modules, each one containing 254 thermoelectric elements. The size of the elements is proprietary. The thermoelectric modules are assembled six at a time between two continuous plates with folded lanced fins. They have developed a unit for ground vehicles[10], and also a liquid microclimate conditioner system.[11]

Future Applications

Equipment developed by the Midwest Research Institute will become commercial in the near future. Development work is ongoing on thermoelectric cooling systems with thermoelectric modules.

There are essentially two domains, space cooling for electronics and air-conditioning. The applications are numerous but are limited by the high cost. Prototypes have been built for air-conditioning telephone booths and feasibility studies have been undertaken for the air-conditioning of train driver's cabs and for cool rooms and deep freeze rooms for the navy.

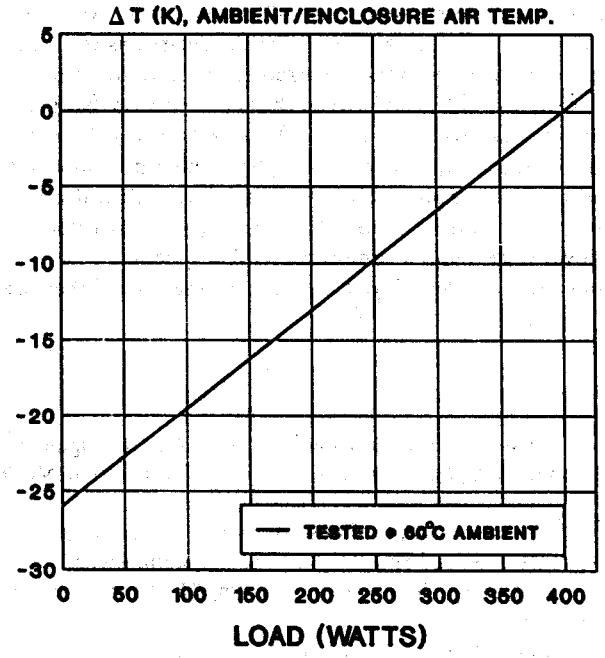

FIGURE 10 Performances of Americool R4000 series unit.

Although specifications change with time the basic difficulties remain the same. Fortunately, technology has progressed and today's systems can meet specifications that were unobtainable 30 years ago.

54.6 Advantages of the Thermoelectric Module Technology

Thermoelectric cooling systems today are essentially made with thermoelectric modules. The technology of integrating thermoelectric elements into the heat exchangers has only been used for very large systems (see Chapter 53).

Commercial thermoelectric modules have been available for over 30 years and their cost has decreased regularly. In cases where the number of systems is small, thermoelectric module technology is the most economic, for several reasons: (1) thermoelectric modules are standard off-the-shelf components; (2) the operating voltages are such that a system can contain series parallel electrical circuitry and commutation in the electrical circuits gives flexibility in the cooling power; (3) the parallel circuitry gives built-in redundancy; (4) they are relatively easy to install; and (5) the heat exchangers can be associated to several thermoelectric modules.

Integrated thermoelectric element technology is only appropriate for very large systems or when the equipment justifies mass production, which is not the case today.

54.7 Conclusions

Looking back 30 years history is seen to repeat itself. In the 1960s people expected to see material improvement, they wanted to have systems that would be as efficient power-wise as the compression cycle systems. When it was realized that this would not materialize all work on the thermoelectric cooling in the Western world stopped.

What has changed? The reasons are multiple: the compression cycle with its fluids is a source of problems with the CFCs likely to be banned. Thermoelectric systems are highly reliable and do not use any compression cycle fluid. Thermoelectric systems with their built-in redundancy do not require a back-up system, as is the case with compression cycles.

It is accepted that a thermoelectric system at full power cannot have an efficiency which approaches that of a compression cycle system but a thermoelectric system has a much more flexible cooling power than a compression cycle and a thermoelectric system can have an adjustable current (or voltage) DC power supply. The peculiarity of thermoelectrics is that the coefficient of performance (COP) increases very fast when the electrical current passing through the system is reduced which cannot be done with a compression cycle system where it is necessary to bypass some of the fluid flow around the compressor. This is far less efficient than decreasing the voltage of a thermoelectric system. It is interesting to note that at half power a thermoelectric system can often compete "electrical power wise" with a compression cycle system.

The applications of systems in the Kilowatt range that were studied then are now starting to be studied again.

References

1. High performance bonded heat sinks, Technical Brochure, AAVID Engineering Inc.
2. Kays, W. M. and London, A. L., *Compact Heat Exchangers*, Third Edition, McGraw-Hill, New York, 1984.
3. McAdams, W. H., *Heat Transmission*, McGraw-Hill, New York, 1954.
4. Crouthamel, M. S., Panas, J. F., and Shelpuk, B., Nine ton thermoelectric air-conditioning system, ASHRAE Semi-annual Meeting, New Orleans, LA, Jan. 27–29, 1964, paper N° 1872, *ASHRAE Trans.*, 70, 139–148, 1964.
5. Hudelson, G. D., Thermoelectric air-conditioning of totally enclosed environments, *Elect. Eng.*, 460–468, June, 1960.
6. Hudelson, G. D., Gable, G. K., and Beck, A. A., Development of a thermoelectric air-conditioner for submarine application, Proc. ASHRAE Semiannual Meeting, New Orleans, LA, January 27–29, 1964, paper N° 1874, *ASHRAE Trans.*, 70, 156–162, 1964.
7. Buist, R. J., Fenton J. W., and Lee J. S., A new concept for improving thermoelectric heat pump efficiency, in Proceedings Int. Conf. on Thermoeletric Energy Conversion, The University of Texas Arlington, Texas, Sept. 1–3, 1976, N° 76, *IEEE Cat.*, CH 1156–9 REG. 5, 80–83, 1976.
8. Neild, A. B., Scheider, W. E., and Henneke, E. G., Application study of submarine thermoelectric refrigeration systems, in *Proc. ASHRAE Semiannual Meeting*, Chicago, January 25–28, 1965, N° 1928, *ASHRAE Trans.*, 71, 183–191, 1965.
9. Jones, D., Mathiprakasam, B., Heenan, P., and Brantley, D., Development of a 1000 W thermoelectric air-conditioner, in *Proc. XIIIth Int. Conf. on Thermoelectric Energy Conversion*, Nancy, France, 232–234, July 1989.
10. Heenan, P. and Mathiprakasam, B., Development of two-man thermoelectric microclimate conditioner for use in army ground vehicles, in *Proc. XIth Int. Conf. on Thermoelectrics*, The University of Texas at Arlington, Department of Electrical Engineering, Oct. 7–9, 1992, 181–184, (Ed.) Rao, K. R.
11. Vincenc, T., Heenan, P., and Mathiprakasam, B., Development of a liquid thermoelectric microclimate conditioner system intended for use in Operation Desert Storm, in *Proc. Xth Int. Conf. on Thermoelectrics*, University of Wales, Cardiff, U.K., Sept. 1–12, 1991, 245–249, (Ed.) Rowe, D. M.

55

Modeling of Thermoelectric Cooling Systems

John G. Stockholm
Marvel Thermoelectrics
Vernouillet, France

55.1 Introduction

Thermoelectric cooling systems transfer thermal energy from a fluid at one temperature to thermal energy in a fluid at another temperature by using thermoelectric material and electrical power. A thermal thermoelectric model is presented of a system that consists of a number of cells referred to as thermoelectric building blocks. Each thermoelectric building block has three parts:

A quantity of thermoelectric material (thermoelectric component) through which an electrical current flows
A heat exchanger to cool a fluid (absorb heat from the fluid)
A heat exchanger to heat a fluid (exhaust heat)

55.2 Description of the Mathematical Thermal Thermoelectric Model

A system consists of:

A unit which is divided into a number of identical thermoelectric building blocks (Figure 1a)
Thermoelectric building blocks associated with a thermoelectric component and two heat exchangers (Figure 1b)

0-8493-0146-7/95/$0.00+$.50

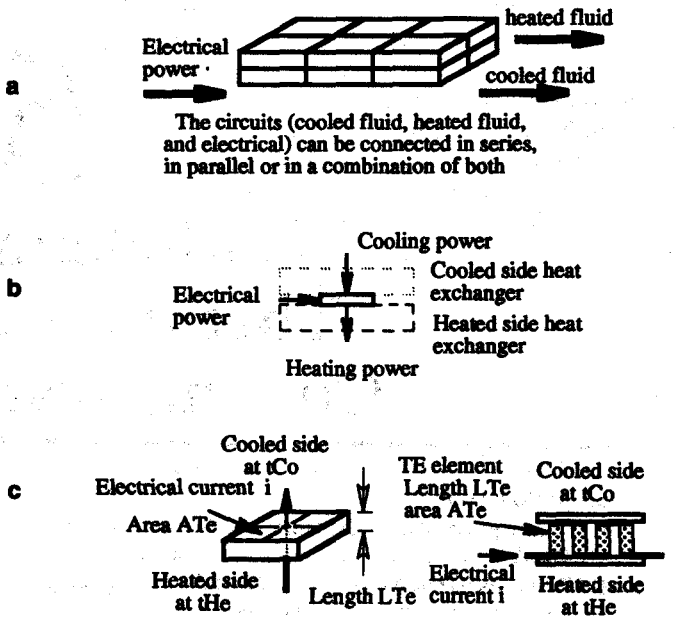

FIGURE 1 (a) Thermoelectric system with six building blocks; (b) building block power model; (c) one thermoelectric element: thermoelectric module two-dimensional representation with four thermoelectric elements.

Heat exchangers for gases, which can contain moisture, and for liquids

A thermoelectric component, which consists of one thermoelectric element or a thermoelectric module (Figure 1c)

Thermoelectric material characteristics

55.3 Thermoelectric Material and Modules

Thermoelectric Material

Bismuth telluride is the material used for cooling and is characterized by three parameters (expressed in SI units):

ρ_{Te} Electrical resistivity $\Omega \cdot m$
λ_{Te} Thermal conductivity $W/(m \cdot K)$
α_{Te} Seebeck coefficient V/K

These parameters vary with the average temperature, t_{av}, of the thermoelectric material; generally a polynomial correlation is used with second-order temperature terms. The thermoelectric material is of n- and p-type, generally the average values are used (value of n + value of p)/2.

The values depend on the manufacturer, and those used here are provided by Melcor Inc., the major world supplier of thermoelectric material and modules.

$$\rho_{Te}(t_{av}) = (10.8497 + 0.0535(t_{av} - 23) + 62.8 \cdot 10^{-6} \cdot (t_{av} - 23)\text{^}2\ )/10\text{^}6$$
$$\alpha_{Te}(t_{av}) = (210.9019 + 0.34426(t_{av} - 23) - 0.9904 \cdot 10^{-3} \cdot (t_{av} - 23)\text{^}2\ )/10\text{^}6$$
$$\lambda_{Te}(t_{av}) = 1.65901 - 3.32 \cdot 10^{-3}(t_{av} - 23) + 41.3 \cdot 10^{-6}(t_{av} - 23)\text{^}2$$

Thermoelectric Module

A thermoelectric module consists of a number of pieces of thermoelectric material, referred to as elements, which are alternately connected and form an electrical circuit of n-type and of p-type

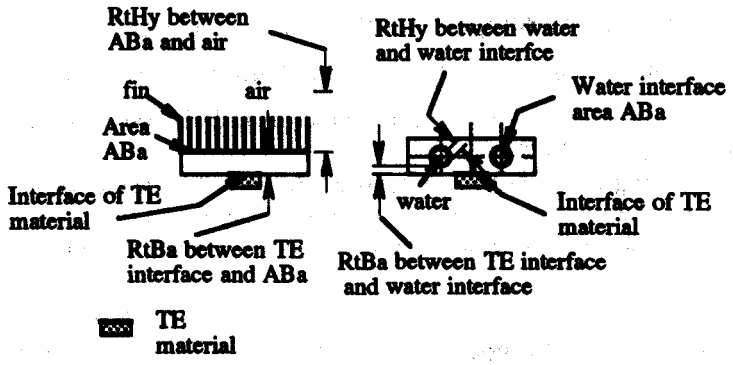

FIGURE 2 Schematic of an air heat exchanger and a water heat exchanger.

material. In addition to the material properties, the module is characterized by two other parameters: GF, the geometric factor of the thermoelectric element = A_{Te}/L_{Te} and Nb_{Te} = number of n-type elements + number of p-type elements in the module (sometimes the couple terminology is used: number of couples = $Nb_{Te}/2$).

A thermoelectric module and a single thermoelectric element can be characterized by:

$$Re_{Te} = Nb_{Te} \cdot \rho_{Te}/GF \quad = \text{total resistance } \Omega$$
$$S_{Te} = Nb_{Te} \cdot \alpha_{Te} \quad = \text{total Seebeck } V/K$$
$$C_{Te} = Nb_{Te} \cdot GF \cdot \lambda_{Te} = \text{thermal conductance } W/K$$

When dealing with one thermoelectric element $Nb_{Te} = 1$.

In this model the thermoelectric material characteristics are valid for a single thermoelectric element and for thermoelectric modules that contain a number of elements of n- and p-type material connected electrically in series. In the case of a thermoelectric module these characteristics include the thermal properties of the ceramic plates and of the electrical connectors, etc. This assumption is equivalent to saying that the temperature of the ceramic plate is the same as the temperature of the end of the element.

The following notations correspond either to a single thermoelectric element or to a thermoelectric module: α, the Seebeck coefficient, and C, the thermal conductance. A distinction is drawn between the electrical resistance of the cooled side and that of the heated side because when using a single thermoelectric element, the heat exchangers, which conduct the electricity between the pieces of thermoelectric material, have a non-negligible electrical resistance. This is defined as R_{Co} for the cooled side and R_{He} for the heated side.

The relevant equations are presented in Section 55.5. The terms representing Joule heating include for each side, half of the electrical resistance of the thermoelectric material plus the electrical resistance of the corresponding heat exchanger and are given by:

$$Re_{Co} = Re_{Te}/2 + R_{Co} \text{ and } Re_{He} = Re_{Te}/2 + R_{He}$$

In the case of modules, electricity is conducted from one module to the next by wires which are "dimensioned" so as to have a negligible electrical resistance, in which case $Re_{Co} = Re_{He} = Re_{Mod}/2$.

55.4 Heat Exchanger Characterization

An air heat exchanger and a water heat exchanger are shown schematically in Figure 2. When discussing the cooled side a subscript "Co" is added and when dealing with the heated side, a subscript "He." The model includes the thermal resistance of both heat exchangers and the thermal conductance (C_{xt}) of the seal and the air gap between the two heat exchangers. For practical reasons the thermal resistance is divided into two parts.

Thermal Resistance Through a Solid

The thermal resistance through the solid, RtBa (thermal base resistance, K/W):

- Water heat exchanger, it is between the interface of the thermoelectric material and the area ABa in contact with the water
- Air heat exchanger, it is the thermal resistance between the interface of the thermoelectric material and the area ABa at the base on which the fins are located; it is found more convenient to use this area rather than the area of the fins because it simplifies the calculation of RtBa

Contribution Due to Convection

The contribution due to convection RtHy (thermal hydraulic resistance, K/W) can be expressed as $RtHy = 1/(\text{hBa} \cdot \text{ABa})$ in K/W where ABa is the area of the base of the heat exchanger on the fluid side (m^2) and hBa is the convection coefficient as seen by the surface of the base $W/(m^2 \cdot K)$.

In the case of liquid heat exchangers the area of the liquid in contact with the base is ABa and the convection coefficient of the fluid at the interface between the fluid and the walls of the duct is hBa. An example with water is given in the Appendix.

In the case of air heat exchangers with fins RtHy is calculated in the following way: the base has an area of ABa, the fins on the base have an area of Afin, a fin efficiency of effFin and the convection coefficient of the fins is hFin. Consequently $hBa = \text{hFin} \cdot \text{Afin} \cdot \text{effFin/ABa}$ with $\text{effFin} = (t_{fin} - t_{air})/(t_{base} - t_{air})$. An example for air is also given in the Appendix.

Thermal Conductance of a Seal

The term C_{xt} represents the thermal conductance exterior (xt) to the thermoelectric material. It includes heat conduction through the air gap between the two heat exchangers, through the seal, and through the tightening mechanism. Experience has lead the author to express this heat loss between the temperature of the bases instead of between the interface temperatures of the thermoelectric material because the average temperature of the side of the base is much closer to the base temperature than to the temperature (tTE) at the ends of the thermoelectric material.

55.5 Equations for the Building Block

Equations

A set of equations for noncondensing air and for water, which correspond to the following parameters, can be written:[1]

Thermal power pumped out of cooled fluid

$$P_{Co} = -S_{te}{}^{*}i^{*}(tTe_{Co} + 273) + Re_{Co} \cdot \hat{i}^2 + C^{*}(tTe_{He} - tTe_{Co}) + C_{xt} \cdot (tBa_{He} - tBa_{Co}) \quad (1)$$

Thermal power exiting the module which is heating the fluid

$$P_{He} = S_{te}{}^{*}i^{*}(tTe_{He} + 273) + Re_{He} \cdot \hat{i}^2 - C^{*}(tTE_{He} - tTE_{Co}) + Cxt \cdot (tBa_{He} - tBa_{Co}) \quad (2)$$

Thermoelectric material temperature in contact with cooled base

$$tTE_{Co} = tFL_{Co} + P_{Co} \cdot (RtBa_{Co} + RtHy_{Co}) \quad (3)$$

Thermoelectric material temperature in contact with heated base

$$tTe_{He} = tFl_{He} + P_{He} \cdot (RtBa_{He} + RtHy_{He}) \quad (4)$$

Base temperature at interface with cooled fluid

$$tBa_{Co} = tFL_{Co} + P_{Co} \cdot RtHy_{Co} \tag{5}$$

Base temperature at interface with heated fluid

$$tBa_{He} = tFL_{He} + P_{He} \cdot RtHy_{He} \tag{6}$$

Solution

The six equations have six unknowns: tTe_{Co}, tTe_{He}, tBa_{Co},TBa_{He}, P_{Co}, and P_{He}. The inputs consist of the operating conditions: i, tFLCo, tFLHe; the characteristics of the thermoelectric material S_{te}, C_{te}, and Re_{Co}, Re_{He}, which include electrical resistances between the pieces of thermoelectric material and the characteristics of the heat exchangers, i.e., $RtBa_{Co}$, $RtBa_{He}$, $RtHy_{Co}$, $RtHy_{He}$, Cxt.

The equations are linear and the system is readily solved. The characteristics of the thermoelectric material are a function of their average temperature so an iteration method is necessary.

55.6 Inlet and Exit Equations

The above equations correspond to the thermoelectric building block, but as there are a succession of building blocks, the exit conditions from the inlet conditions[2] and the powers of each building block are calculated for each of the thermoelectric building blocks.

For noncondensing air and for a liquid such as water the following equations can be written: $tFL_{Co.ex} = tFL_{Co.in} + P_{Co}/Q_{Co} \cdot Cp_{Co}$ where Q_{Co} is the mass flow rate of the fluid (kg/s) and $Cp_{Co.in}$ is the specific heat of the fluid in J/(kg · K).

A model has been developed by Buffet and Stockholm[2,3] for condensing air.

55.7 Calculations of a Unit

Fluids and Temperature

The level of complexity of the calculation depends on whether a gas (air) or a liquid (water) is being considered. A thermoelectric building block varies in size and depends on the amount of thermoelectric material per building block, that is, the total area of thermoelectric material at the cold junction. The area of thermoelectric elements ranges from 15 mm^2 to more than 150 mm^2 while the module can exceed 500 mm^2. The cooling is generally between 2 and 10 W per cm^2. Assuming values of 150 mm^2 and 3 W/cm^2, with a coefficient of performance (COP) of 1, this corresponds to a cooling power of 4.5 W/cm^2 and a heating power per building block of 9 W/cm^2.

The mass flow rate of water through the base of a building block containing tubes is of the order of 0.15 kg/s while in the case of air the mass flow rate is of the order of 10 g/s. With a cooling power of 100 W the corresponding changes in temperature ΔT between inlet and outlet of a unit for air and water are as follows:

$$100\ W = (0.010\ kg/s) \cdot (1006\ J/(kg \cdot K) \cdot \Delta T \quad so\ \Delta T = 10K$$
$$100\ W = (0.15\ kg/s) \cdot (4{,}186\ J/kg \cdot K) \cdot \Delta T \quad so\ \Delta T = 0.16K$$

Water-Water

Therefore, with a water-water unit containing 500 building blocks in series on the cooled water circuit, with a cooling power of the order of 2.25 kW, the temperature of the water will decrease by 6.6°C. On the heated side if the flow rate is doubled and as the COP = 1, the increase in temperature of the heated water will also be 6.6°C. The flow configuration of the two circuits, the cooled and the heated ones (parallel, counter-flow, cross-flow, and combination of the above) is

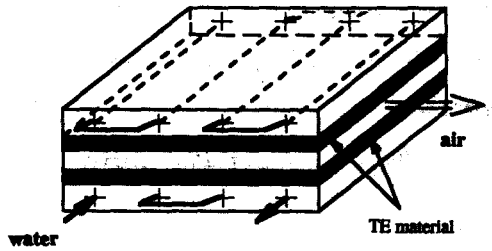

FIGURE 3 Water-air unit cross flow.

important. Buffet[6] has shown that the optimization is quite different to that of passive heat exchangers with two liquids.

When the temperature variations of the water are 10°C or less it is sufficient to calculate the performances of the average building block. This is the building block with fluid temperatures that correspond to the average fluid temperature of each circuit. This means that it is only necessary to calculate one building block, the total power being equal to the power of the building block multiplied by their number.

Water-Air

Consider the case of a water-air system containing, for example, 200 building blocks of which 50 are in parallel on the air and therefore 4 are in series. A schematic is shown in Figure 3; the individual building blocks are not shown. All the building blocks are in series in the water circuit, and as the water tube goes through the unit four times, there are four building blocks in series in the air circuit. The darkened areas correspond to the thermoelectric material.

The calculation is carried out for each row of building blocks in parallel in the air circuit. The building block is calculated with a water temperature equal to the average temperature of the water in each row of building blocks. So only the performances of four building blocks are required.

Air-Air

An air-air unit is shown schematically in three dimensions in Figure 4. For this cross flow it is necessary to calculate each building block shown in Figure 5. The calculation sequence can be ABCD then EFGH or AE then BF, CG and DH. It does not make any difference which sequence is chosen as in both cases all the building blocks are calculated. The total cooling power is obtained by adding the powers of each of the building blocks. The same is done for the heating and the electrical powers.

The average exit conditions are obtained by first obtaining a summation of the exit enthalpies of each of the building blocks, then calculating the exit temperatures and humidities.

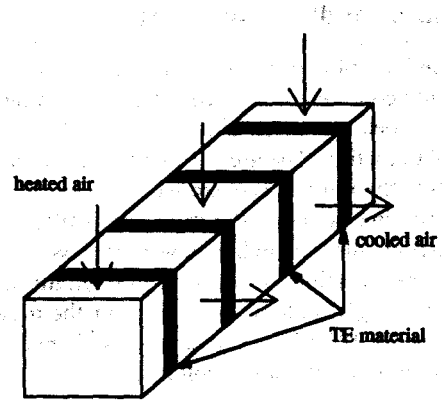

FIGURE 4 Air-air cross flow in three dimensions.

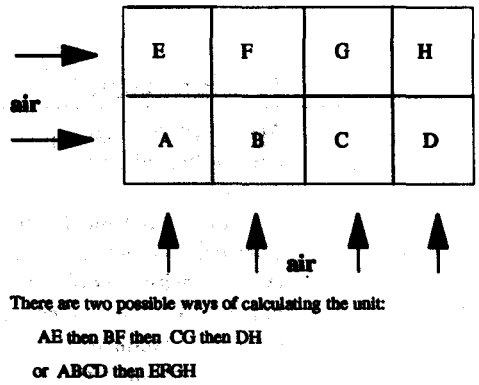

FIGURE 5 Air-air unit cross-flow calculation.

55.8 Conclusions

The modeling of thermoelectric systems based on the concept of building blocks has been presented. The parameters that are necessary to characterize a building block are given, together with the procedure to calculate a system. It has been shown that for water-water systems it is only necessary to calculate the thermoelectric building block that "sees" the average hot-side and the average cold-side fluid temperatures. For water-air units the average thermoelectric building block in each row along the air circuit has to be calculated. For air-to-air systems each thermoelectric building block which has different inlet conditions has to be calculated.

References

1. Stockholm, J. G. and Stockholm, D. W., Thermoelectric modeling of a cooling module with heat exchangers in *Proc. XIth Int. Conf. on Thermoelectrics*, Department of Electrical Engineering, University of Texas at Arlington, Arlington, Texas, Oct. 1992, 140–146.
2. Stockholm, J. G., Modélisation de systèmes thermoélectriques. Applications de la Thermoelectricité, *Demi-Journée Société Française des Thermiciens*, June 6, 1990, 1–15.
3. Buffet, J. P. and Stockholm, J. G., Thermoelectric air conditioning with water heat rejection, in *Proc. Vth Int. Conf. on Thermoelectric Energy Conversion*, University of Texas at Arlington, Arlington, Texas, March 1984, 95–101.
4. McAdams, W. H., *Heat Transmission*, Third edition, McGraw-Hill, New York, 1954.
5. Kays, W. M. and London, A. L., *Compact Heat Exchangers*, Third edition, McGraw-Hill, New York, 1984.
6. Buffet, J. P., A comparative study of flow optimization for thermoelectric units and surface heat exchangers, in *Proc. XIth Int. Conf. on Thermoelectrics*, Department of Electrical Engineering, University of Texas at Arlington, Arlington, Texas, Oct. 1992, 155–159.

Notations

Symbol	Units	Designation
ABa_{Co}	m^2	Area of cooled base
ABa_{He}	m^2	Area of heated base
$AFin$	m^2	Area of fin
A_{Te}		Area of one thermoelectric element
Cxt	W/K	Thermal conductance of seal
Cp_{Co}	J/(kg · K)	Heat capacity of cooled fluid
$effFin$	dimensionless	Fin efficiency = average t of fin/t at base of fin
GF	m	Geometric factor of thermoelectric element
$hFin$	W/(m^2 · K)	Convection coefficient of fin
i	A	Electrical current
L_{Te}	m	Length of thermoelectric element
Nb_{Te}	dimensionless	Number of thermoelectric elements in the module
P_{Co}	W	Cooling power
P_{He}	W	Heating power
Q_{Co}	kg/s	Mass flow rate of cooled fluid
R_{Co}	Ω	Electrical resistance of cold-side heat exchanger if in circuit
Re_{Co}	Ω	Electrical resistance $Re_{TE}/2 + R_{Co}$
Re_{He}	Ω	Electrical resistance $Re_{TE}/2 + R_{He}$
R_{He}	Ω	Electrical resistance of cold-side heat exchanger if in electrical circuit
$RtBa_{Co}$	K/W	Thermal resistance of cooled base
$RtBa_{He}$	K/W	Thermal resistance of heated base
$RtHy_{Co}$	K/W	Thermal hydraulic resistance of cooled base
$RtHy_{He}$	K/W	Thermal hydraulic resistance of heated base
t_{av}	°C	Average temperature of thermoelectric material
tFL_{Co}	°C	Temperature of cooled fluid
$tFL_{Co.ex}$	°C	Temperature of cooled fluid at exit of building block
$tFL_{Co.in}$	°C	Temperature of cooled fluid at inlet of building block
tFL_{He}	°C	Temperature of heated fluid
tTe_{Co}	°C	Temperature of thermoelectric material at the cooled end
tTe_{He}	°C	Temperature of thermoelectric material at the heated end
ρ_{Te}	Ω · m	Thermoelectric material electrical resistivity
λ_{Te}	W/(m · K)	Thermoelectric material thermal conductivity
α_{Te}	V/K	Thermoelectric material Seebeck coefficient
Ct_{Te}	W/K	Thermoelectric thermal conductance = $Nb_{Te} \cdot GF \cdot \lambda_{Te}$
Re_{Te}	Ω	Thermoelectric electrical resistance = $Nb_{Te} \cdot \rho_{Te}/GF$
S_{Te}	V/K	Thermoelectric Seebeck coefficient = $Nb_{Te} \cdot \alpha_{Te}$

Appendices

1. Convection coefficient of water in tubes

Generally considered, water flowing in circular ducts with a Reynolds number N_{Rey} in excess of 5000 with straight tubes having a length of less than 35 diameters. Experimentation has confirmed the formula given by MacAdams:

$$h = 1480 \cdot (1 + 0.015t)(V^{0.8})/D^{0.2} \text{ in SI units}$$

h = convection coefficient $W/(m^2 \cdot K)$
t = temperature of the water °C
V = velocity of the water, m/s
D = diameter of the tube, m

2. Convection coefficient of dry air

There exists many shapes of fins: flat fins, wavy fins, lanced fins, etc. Kays and London[5] give the convection coefficient in a nondimensional form.

When dealing with air the convection coefficient h $(W/(m^2 \cdot K)$ can be expressed as $h = a \cdot V^b$ where a and b are constants for a specific heat exchanger and for a defined range of velocities V in m/s.

A typical formula for wavy fins in air around the ambient temperature with velocities between 2 and 10 m/s in turbulent flow is $h = 21 \cdot V^{0.635}$.

0-8493-0146-7/95/$0.00+$.50

Index

A

B

C

D

E

F

G

H

I

J

K

L

M

N

O

P

Q

R

S

T

U

V

W

X

Y

Z

146
ISBN 0-8493-0146-7
90000
9 780849 301469

CRC PRESS
www.crcpress.com